AD-A052 845 ADVISORY GROUP FOR AEROSPACE RESEARCH AND DEVELOPMENT--ETC F/G 21/5
HIGH TEMPERATURE PROBLEMS IN GAS TURBINE ENGINES.(U)
FEB 78

UNCLASSIFIED AGARD-CP-229 NL

1 OF 7
AD A052845

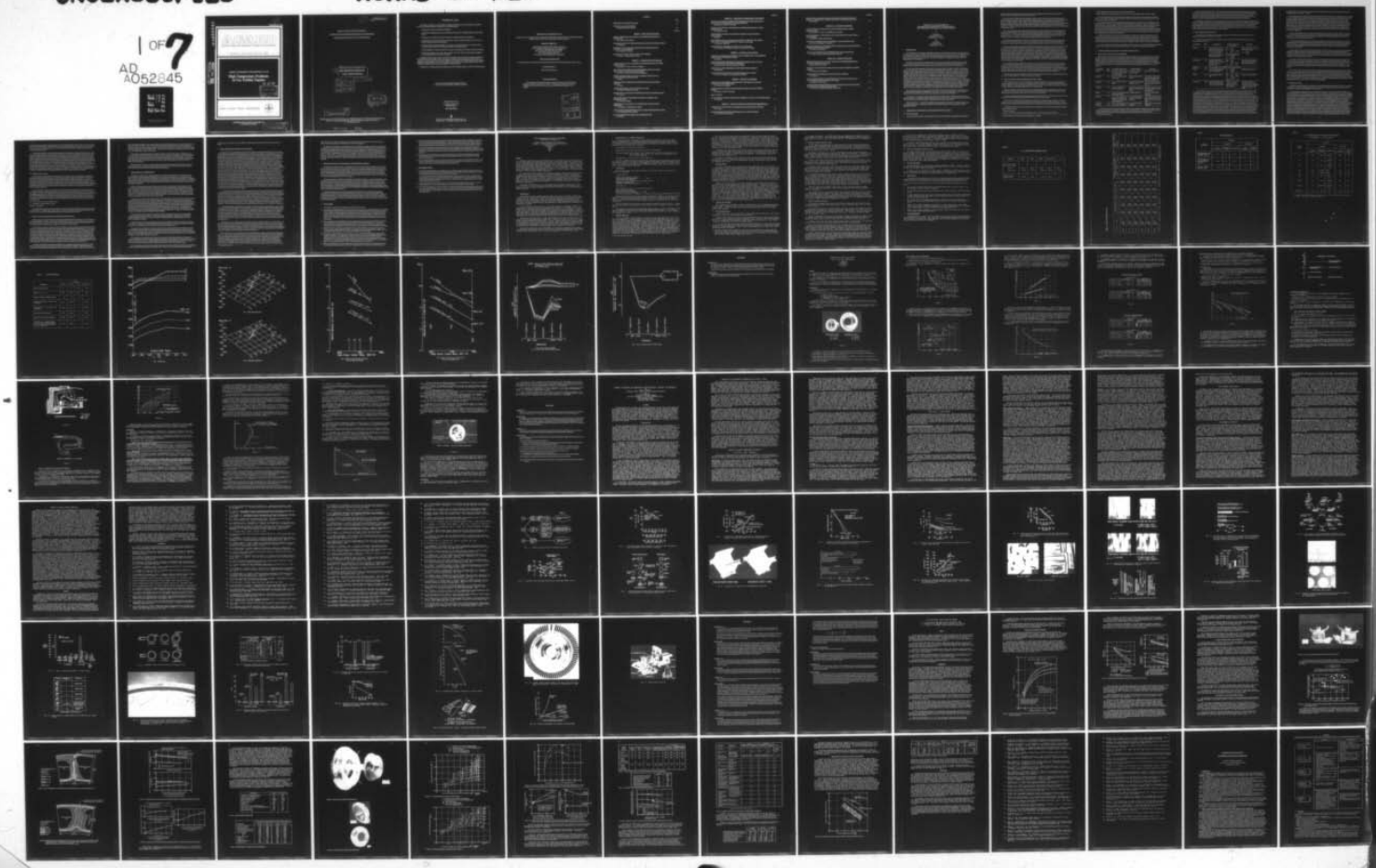

AGARD-CP-229

AGARD

ADVISORY GROUP FOR AEROSPACE RESEARCH & DEVELOPMENT

7 RUE ANCELLE 92200 NEUILLY SUR SEINE FRANCE

AGARD CONFERENCE PROCEEDINGS No. 229

High Temperature Problems in Gas Turbine Engines

NORTH ATLANTIC TREATY ORGANIZATION

(1) (14) AGARD-CP-229

NORTH ATLANTIC TREATY ORGANIZATION

ADVISORY GROUP FOR AEROSPACE RESEARCH AND DEVELOPMENT

(ORGANIZATION DU TRAITE DE L'ATLANTIQUE NORD)

AGARD Conference Proceedings No.229

(6) HIGH TEMPERATURE PROBLEMS IN GAS TURBINE ENGINES

(9) Conference proceedings,

(11) Feb 78

(12) 555 P.

Papers presented at the 50th Meeting of the AGARD Propulsion and Energetics Panel held at the Faculty of Engineering, Middle East Technical University, Ankara, Turkey from 19–23 September 1977

THE MISSION OF AGARD

The mission of AGARD is to bring together the leading personalities of the NATO nations in the fields of science and technology relating to aerospace for the following purposes:

- Exchanging of scientific and technical information;
- Continuously stimulating advances in the aerospace sciences relevant to strengthening the common defence posture;
- Improving the co-operation among member nations in aerospace research and development;
- Providing scientific and technical advice and assistance to the North Atlantic Military Committee in the field of aerospace research and development;
- Rendering scientific and technical assistance, as requested, to other NATO bodies and to member nations in connection with research and development problems in the aerospace field;
- Providing assistance to member nations for the purpose of increasing their scientific and technical potential;
- Recommending effective ways for the member nations to use their research and development capabilities for the common benefit of the NATO community.

The highest authority within AGARD is the National Delegates Board consisting of officially appointed senior representatives from each member nation. The mission of AGARD is carried out through the Panels which are composed of experts appointed by the National Delegates, the Consultant and Exchange Program and the Aerospace Applications Studies Program. The results of AGARD work are reported to the member nations and the NATO Authorities through the AGARD series of publications of which this is one.

Participation in AGARD activities is by invitation only and is normally limited to citizens of the NATO nations.

Published February 1978

ISBN 92-835-0209-4

Printed by Technical Editing and Reproduction Ltd
Harford House, 7–9 Charlotte St, London, W1P 1HD

PROPULSION AND ENERGETICS PANEL

Chairman: Dr Ing. G.Winterfeld, DFVLR, Institut für Antriebstechnik, Postfach 90 60 58, D-5000 Köln 90, Germany
Deputy Chairman: Dr J.Dunham, NGTE, Pyestock, Farnborough, UK

PROGRAM COMMITTEE

HOST NATION COORDINATOR

PANEL EXECUTIVE

ACKNOWLEDGEMENT

The Propulsion and Energetics Panel wishes to express its thanks to the Turkish National Delegate to AGARD for the invitation to hold its 50th Meeting at the Middle East Technical University in Ankara, Turkey and for the facilities and personnel made available for this meeting.

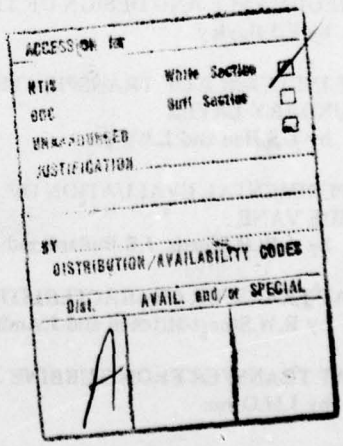

CONTENTS

TECHNICAL EVALUATION REPORT ON 50TH PROPULSION AND ENERGETICS PANEL MEETING ON HIGH TEMPERATURE PROBLEMS IN GAS TURBINE ENGINES

by

R.Eggebrecht
MTU München GmbH
8000 München 50, Germany

and

S.Lombardo
Curtiss-Wright Corp.
Wood-Ridge, N.J., USA

1. INTRODUCTION

The 50th Meeting of the Propulsion and Energetics Panel of the NATO Advisory Group for Aerospace Research and Development was held at the Middle East Technical University in Ankara, Turkey, from 19 to 23 September, 1977. The purpose of the meeting was to review the status of the technology associated with the design and operation of gas turbines at high turbine inlet temperatures. The conference program was arranged by a committee under the chairmanship of Dr. D.K.Hennecke.

The timing of the meeting was most appropriate, since the last meeting devoted to high temperature turbines was the 36th PEP Meeting in Florence, Italy, in 1970. Since that time, much progress has been made in the understanding and the application of increased entry temperatures to both military and civil aircraft gas turbines.

The maximum cycle temperature at which today's aircraft gas turbines are designed to operate is increasing as rapidly as the technology of high temperature materials and cooling methods will allow. Increases in cycle operating temperatures result in higher specific output and increased cycle efficiency. From an aircraft systems point of view, the higher specific output raises the thrust-to-weight ratio of the engine, with significant reduction in engine frontal area and nacelle drag. Thus, the benefits of operating an aircraft gas turbine at increased cycle temperatures can be translated into additional payload or range or a combination of both. All modern aircraft, as well as industrial gas turbines, operate at cycle temperatures which require turbine vane and blade cooling, as well as special cooling configurations for other hot section components such as combustors, shrouds, discs, afterburners, etc. In conjunction with cooling, special considerations in materials and coating selections are required to insure the integrity of the design and reliable operation of these advanced engines. In this meeting, major emphasis was placed on the state-of-the-art of high cycle temperature gas turbines, with regard to heat transfer, performance and materials technology and their interrelationships. In addition, the meeting covered new developments under investigation which offer significant improvements in the performance, cost, efficiency and reliability aspects of advanced gas turbine engines.

The conference consisted of 39 papers adequately balanced in subject matter and between representatives from industry and government-sponsored organizations. The number of countries providing papers was nine, though specialists from other NATO countries were present and took an active part in the discussions.

The conference was divided into eight sessions dealing with the general theme of high temperature problems in gas turbine engines. It is apparent from the attached listing of these session titles and reference papers that the meeting covered a broad scope of activities relating to the high temperature aspects of gas turbines.

The following review and evaluation uses slightly different headings for comments on the papers presented and for emphasis of some features which are thought to have an important impact on future developments of high temperature turbines.

2. PROGRESS OF NEW RESEARCH AND DEVELOPMENT TEST FACILITIES

2.1 Static Cascade Rigs

Many of the data presented at the meeting dealt with test results from different cascade rigs, and the progress

made to convert these data into a form which would be useful to designers for predicting the performance and durability aspects of high temperature hot section components.

The present status of highly developed cooling technologies was only reached with the help of sophisticated laboratory cascade testing which allows detailed analysis of basic phenomena for comparison with, and further development of, theoretical methods. However, there is still a fundamental need to increase cooling effectiveness with a minimum of engine performance losses, while the engine manufacturer is resorting to the use of improved manufacturing methods, materials and coatings, which will offer further temperature potential. One can easily foresee that future research work will be faced with new and sometimes more complex cooling configurations for all the hot-end components of advanced gas turbines.

The very encouraging progress is worth noting which has been achieved using the so-called short-duration test facilities at Oxford University, VKI and MIT reported during this meeting by D.L.Schultz (31)*, B.E.Richards (34) and J.F.Louis (28). The tests can be performed at actual engine Reynolds and Mach numbers and actual gas-to-wall temperature ratios. Heat transfer measurements are made by highly developed thin-film techniques, and fast data acquisition systems are available for recording and subsequent processing of transient data.

Interesting cascade testing with measurements of heat transfer along a PVD blade profile has been reported by B.W.Martin (32) from Wales University. These tests also employed a transient method by measuring temperature – time responses of blade surface thermocouples when the blade was suddenly introduced into a heated air stream.

One of the key problems in cascade testing, whether in the steady-state or transient mode, is the proper simulation of environmental conditions prevailing under actual engine conditions and influencing, for instance, the cooling performance of vanes, blades, shrouds and combustor liners. F.J.Bayley (37) stated the present position very clearly, when he pointed out that even the relevant characteristics of the engine flow are not yet definable, not to mention simulation under laboratory conditions. H.Köhler (6) in his paper compared surface temperature measurements and associated heat transfer coefficients from static cascade tests with results on a comparable rotor blade operated in an engine at similar Reynolds and Mach numbers and with the same gas-to-wall temperature ratio. The large discrepancies observed, mainly on the leading edge and pressure surface, highlight the possible effects of engine-related environmental conditions, such as main-stream turbulence originating from unsteady combustion, cooling air admixture and periodic velocity oscillations due to blade wakes.

For investigation of some separate effects of turbulence, F.J. Bayley (37) presented a new experimental set-up at Sussex University consisting of a static cascade with an upstream turbulence generator which was conceived as a rotating squirrel cage. This device allows the investigator to vary the turbulence intensity by using a range of bar diameters and to vary the frequency of velocity fluctuations through the rotational speed. The experiments he reported about were mainly done in the range of up to 6 kHz with measured velocity fluctuations in the range of 24% to 48% turbulence and showed some dramatic effect on local and mean blade profile heat transfer coefficients.

There was general agreement among the speakers that the data obtained from the above described laboratory tests are very useful and necessary for the design of hot-section components.

2.2 Turbine Aerodynamic Rigs and High Temperature Turbine Testing

For investigation of the effect of coolant injection on turbine aerodynamics, cold or warm air turbine rigs are commonly used, as referred to in papers by J.D.McDonel (29) and H.F.Due (4). As reported by A.W.H.Morris (12) at NGTE, a high-temperature single-stage research turbine has been used for recent testing of transpiration-cooled NGV's at design conditions of 1650 K gas temperature and 4.5 bar inlet pressure.

W.Kühl (7) described temperature measurements on rotating turbine blades in a single-stage test turbine at the Technische Hochschule, Aachen, which were aimed at analysing blade-profile heat transfer under moderate turbine inlet temperature and pressure conditions up to 1173 K and 1.5 bar respectively.

A major new test facility presented during this conference in the papers by J.Francois (5) and Y.Le Bot (33) is the so-called French MINOS (Montage inter ONERA-SNECMA) operated at CEPr, Saclay.

This test facility is basically a high-temperature test turbine with an upstream engine combustor, in which an attempt is made to simulate engine environmental conditions with respect to the combustor-turbine unit. The max. designed operating temperature is 1800 K and the max. entry pressure delivered from the plant feed system is 4.5 bar.

The authors (5) quote an impressive program of future investigations covering a broad range of high-temperature turbine problems including

- turbine aerodynamics
- various heat transfer and film cooling investigations on NGV's, rotor blades, casings and end walls

* Number in parentheses refers to the Paper in the main Conference Proceedings.

– thermal fatigue tests by means of cyclic variation of cooling air flows

– testing of abradable materials with respect to improvements in running clearances and reduced air leakages.

There is no doubt that each of these problem areas represents a major aspect in the development of advanced turbines. The ambitious targeting for this test facility essentially requires advanced measuring techniques, which are described in the paper by Y.Le Bot (33):

Total pressure and temperature probes designed for fast dynamic response and capable of operating under high temperatures have, for instance, been developed for measuring turbulence at turbine entry, and for analysing rotor downstream wakes. Laser anemometry is seen to be not yet ready for this application. Blade temperatures are being measured by embedded thermocouples and optical pyrometers. For heat transfer analysis on turbine blades, a transient technique involving sudden cooling air flow shut-off is being employed. Heat flux measurements on turbine casing liners can be performed with fluxmeters developed by SNIAS. For tracing cooling air flow paths and evaluating film cooling effectiveness, using the analogy between heat and mass transfer, the rig is designed to allow gas sampling with chromatographic analysis of gas concentrations.

It must be realized that the extent of the instrumentation used causes some changes in comparison with the actual engine situation such as, for instance, wider spacing between blade rows. Another limitation which must be recognized is the rather low operating pressure of the combustor, whose outlet conditions may alter in the actual core engine situation. This comment underlines the author's opinion that MINOS will at least help to bridge the gap between classical component rig testing and experimental investigations under real engine environmental conditions.

From the measurements already made and described in these two papers, it is evident that MINOS has the capability to make a major contribution to solving future high-temperature turbine research and development problems.

3. COOLING TECHNIQUES AND HEAT TRANSFER INVESTIGATIONS

3.1 Recent Work on Convection-Cooled Turbine Blades

Blade cooling is commonly used in present military and civil engines. However, surprisingly little information is available about the local gas-side and cooling-side heat transfer rate for different blade profiles and internal coolant passage configurations under actual engine operating conditions. In order to distinguish the physical phenomena occurring under these conditions, there is still a fundamental need for heat transfer investigations on cascades and research turbines, as reported on by several authors at this conference. The following table summarizes experimental and/or theoretical work devoted to external turbine blade heat transfer in the absence of boundary layer coolant injection.

Author/Ref.	Paper	Investigation Performed	Varied Parameters	Comments
J.F.Louis	(28)	profile heat transfer distribution (p.h.t.d.) for four transonic blade profiles	outlet Mach number; incidence angle	shock tunnel cascade rig
D.L.Schultz	(31)	p.h.t.d. for a high pressure turbine blade	outlet Reynolds number; Tu level	short-duration wind tunnel operating with single-stroke light piston compression
B.W.Martin	(32)	p.h.t.d. for PVD* turbine profile	outlet Mach and Reynolds numbers; Tu level	blades are shifted into hot gas duct and undergo transient heating
F.J.Bayley	(37)	p.h.t.d. for high pressure turbine rotor blade	outlet Mach and Reynolds numbers; Tu level and frequency	steady state cascade tests with upstream squirrel cage turbulence generator
W.Kühl	(7)	p.h.t.d. for turbine blade and cooling effectiveness	cooling air mass flow	test turbine with slip ring equipment
H.Köhler	(6)	p.h.t.d. and cooling effectiveness for four cooling configurations with unchanged outer blade profile	mainly outlet Reynolds number and cooling air mass flow	steady state cascade tests and engine measurements on rotor blades by means of thermal paints
J.Francois Y.Le Bot	(5) (33)	p.h.t.d. for internally cooled NGV behind combustor	no parameter variation reported	high temperature turbine rig "MINOS"

A review paper using these newly provided heat transfer data for comparison with previously published results by other authors appears to be very desirable. From the amount of available data one could expect that some fruitful incentives for improvements in heat transfer prediction by means of boundary layer theory may arise.

* Prescribed velocity distribution.

One paper, presented by W.D.Morris (38), dealt with heat transfer in rotating coolant channels as affected by Coriolis forces and rotational buoyancy. It turns out that the use of forced convection data obtained with stationary tubes for the prediction of heat transfer in rotating tubes can lead to significant errors of either over- or under-estimations. On the basis of the already available test results of this research work, which has just started, it seems advisable for blade cooling design engineers to closely watch the further outcome of these investigations.

Turbine blade cooling by means of a closed thermosyphon system would offer the advantage of high internal heat transfer coefficients. The paper by R.W.Stuart Mitchell (13) presented new experimental investigations for the stationary vertical, the stationary inclined, and the rotating closed thermosyphon, with water and mercury as working fluid, and gave dimensionless correlations of the measurements. The results suggest that, in addition to the commonly used Grashof number based on gravity acceleration, a dimensionless centrifugal acceleration term also has a marked influence on the Nusselt number of the cylindrical tube under investigation.

3.2 Film Cooling of Hot-End Components

An analysis of film cooling physics for any practical design of turbine blades, end wall elements, stators or combustor and afterburner liners is not yet feasible.

No wonder that an increasing amount of research work is being done. The following table gives a survey of film cooling work reported on.

Author/Ref.	Paper	Configurations	Range of Thermodyn. Parameters	Comments
J.F.Louis	(28)	angular injections for flat plate streamwise angles 10°, 20°, 30°, crosswise angles 0°, 30°, 50°, 70°, 90°	Ma_0 = 0,5 T_0 = 556 K T_c = 122 . . . 278 K $\dot{m}$ = 0,1 . . . 1,6	shock tunnel with about 10 ms steady flow test time $\dot{m} = \frac{\rho_c W_c}{\rho_0 W_c}$
		blade profile with various film-cooling ejections	exit Mach number = 0,6 T_0 = 450 K T_c = 293 K	
B.E.Richards	(34)	flat plate with injection through double row of holes with 30° stream-wise injection angle	Ma_0 = 0,6 T_0 = 382 K T_c = 267 . . . 365 K $\dot{m}$ = 0,5 . . . 1,5	short duration wind tunnel operating with single-stroke light piston compression
J.Francois	(5)	turbine casing; end wall "MINOS" turbine rig conditions		
H.Kruse	(8)	turbine blade leading edge film cooling flat plate	T_0 = 400 K T_c = 293 K $\dot{m}$ = 0,5 . . . 2,0	single blade model tests
R.Best	(17)	slot configuration inside tube	Ma_0 = 0,1 . . . 0,16 T_0 = 453 . . . 500 K T_c = 293 K W_c/W_0 = 0,5 . . . 1,9	variation of coolant side Tu
E.Le Grives	(36)	single and multiple row of holes with various stream-wise and crosswise angles	wide range of blowing parameter; thermo-dynamic data not all given explicitly	flat plate experiments; comparison of test results with new analytical prediction method presented by the author

J.F.Louis (28) reported about a very comprehensive experimental program performed at MIT on film-cooling configurations mainly of single and double line holes for different streamwise and crosswise angular injection. The importance of these experiments becomes clear when it is considered that most of the practical application in turbines make use of injection holes rather than continuous blowing out of slots. Substantial research work on film cooling with various injection hole configurations was performed about one decade ago at the University of Minnesota, as reported by E.R.G.Eckert at the 1970 AGARD PEP Meeting, and at Arizona State University by D.E.Metzger et al. These investigations were made for very low mainstream Mach numbers and in some cases in the transonic range. The temperature ratio between coolant and mainstream was close to 1.0. At the same conference C.Liess reported about measurements at VKI downstream of inclined injection holes which were taken at elevated Mach numbers of 0,4 . . . 0,6 but still with only small temperature differences. The present shock tunnel tests at MIT cover nearly the full range of thermodynamic parameters which occur in advanced turbines. The overall correlation used is essentially based on equivalent slot width, the square root of momentum ratio to the 1.35th power and the coolant Reynolds number to the 0.25th power. It must be noted that this correlation describes fairly well the experimental results of individual injection hole arrangements. However, the attempt to describe the isothermal efficiencies of the very different geometric configurations by such an overall correlation parameter leads to a rather wide scatter of data and therefore

is still unsatisfactory. It is interesting to note that Louis can align the effectiveness of hole and slot configurations by a simple geometric "mixing area" correction.

The very high potential of presently available test equipment becomes evident from the presentation by D.L.Schultz (31) and D.E.Richards (34) on tests with the so-called Isentropic Piston Tunnel at Oxford and VKI, respectively. Film cooling experiments using a double row of holes with a 30° injection angle were reported on by Richards. The test results show similar trends to the previous investigations by Eriksen and Goldstein, which were performed under incompressible flow conditions. So far, the results indicate that there is obviously no strong influence of increased Mach numbers. It must be borne in mind, however, that primarily, these tests should prove experimentally the linear relationship between "overall heat transfer coefficient" (based on difference of mainstream and wall temperature) and a non-dimensional coolant temperature. Furthermore, of course, Richards demonstrates the capabilities of the transient test technique based on single-stroke isentropic compression rather than performs any systematic study on film cooling configurations.

As far as continuous blowing is concerned some different analytical methods are already available. In his paper J.F.Louis (28) refers to Demirjian, whose mathematical modelling for angular injection predicts quite well the film behavior in the region near the slot injection and up to blowing rates at which boundary layer lift off occurs and consequently the cooling effectiveness is reduced.

For injection through discrete holes, a new analytical technique was presented by E.Le Grives (36). It must be appreciated that this paper already demonstrates impressive progress in theoretical methods for describing interaction between mainstream and single jets and array of jets by means of the dilution theory. The paper provides valuable references to previous publications by other authors and points out that the future work of the authors will be focussed on curvature effects.

Generally speaking, more fundamental experimental data are obviously needed in order to develop computational methods for the highly complex three-dimensional flow situation in the case of film cooling with hole injection configurations which are aimed at improved cooling effectiveness. Furthermore, this future work will have to simulate more closely engine environmental conditions, in order to study the effect of hot gas mainstream flow characteristics prevailing in turbines behind engine combustors.

In his paper (17) R.Best draws attention to the velocity profiles and turbulence distribution of the coolant flow in the plane just before entering the mainstream boundary layer, which he measured for different slot widths and for a wide range of blowing rates. He shows that there is an adverse effect of the entering coolant turbulence upon film cooling effectiveness. This effect is more pronounced for coolant to mainstream velocity ratios $W_c/W_0 = 1$. His semi-empirical model fairly well describes the observed experimental phenomena of this type of tangential slot film cooling.

Rather little is known about the interaction of film cooling jets with the mainstream boundary layers of turbine blade or vane leading edges, which have to withstand the highest thermal loading. H.Kruse (8) reported about boundary layer measurements using a minature temperature probe in the vicinity of a turbine blade leading edge simulated by a single airfoil mounted in a small tunnel with adjustable flexible walls. From these investigations, it becomes evident that, for differently angled injection hole arrangements, there is a strong influence of the coolant blowing rate upon the local cooling effectiveness. Furthermore, it is shown that any changes in the stagnation point severely affect the cooling performance when there is only one row of holes near the leading edge.

3.3 Transpiration Cooling

L.S.Han (11) presented a paper on the analytical studies being conducted at Ohio State University on the influence of transpiration cooling on turbine blade boundary layers. The authors described a method by which the external boundary layer and heat transfer distribution can be calculated.

The experimental and theoretical work by F.J.Bayley (10) reported on at this meeting confirmed again the very high cooling effectiveness of transpiration cooled turbine vanes and blades compared with other cooled blade configurations. He also pointed out the excellent correlation of the heat transfer aspects pertaining to the design of transpiration cooled components. In his paper A.W.H.Morris (12) reported on the experimental evaluation of a transpiration cooled nozzle guide vane. The test program was conducted to evaluate the thermal design of the NGV and to determine the influence of the transpiring flow on stage efficiency. Cascade tests and a single stage high temperature turbine test rig were utilized in this program. The vanes used in this evaluation consist of a POROLOY porous metal airfoil, diffusion bonded to the main structural element. The cascade and engine test results demonstrated again the uniformity in airfoil metal temperatures and the high effectiveness of transpiration cooled blades and vanes. On the mechanical aspects of transpiration air cooled blades, the authors, on the basis of the single stage rig tests, conclude that the uniformity in airfoil metal temperatures possible with transpiration cooled blades and vanes will result in reduced thermal stresses and propensity to thermal cracking. Their test results lead them to believe that pore blockage of the transpiration cooled airfoil structure is not a significant problem. In addition, inadvertent exposure of the turbine to foreign object damage showed extensive maltreatment of the transpiration cooled blades could be tolerated without disastrous consequences. All the above mechanical characteristics of transpiration cooled blades, confirm the test

results noted earlier by another author and presented at the 36th PEP Meeting in Florence, Italy, in 1970. In noting the quality of the transpiration cooled vanes of the current paper and the quality of the vanes of the earlier reported work, it is obvious that significant strides have been made, over the past seven years, on the fabrication aspects of transpiration cooled structures.

As regards the performance aspects, the authors presented cascade data on profile loss coefficient versus coolant flow ratios on fully transpiration cooled nozzle guide vanes (NGV), as well as for transpiration air cooled vanes with various percentages of the suction surface blocked. Using these data and test results from the testing of the vanes in a single stage turbine test rig, the authors then conducted engine cycle studies comparing the sfc and thrust relationships of a transpiration cooled NGV configuration with a conventionally cooled NGV. On the basis of this study, the authors concluded that direct substitution of transpiration cooled NGV offered no significant performance advantages over the higher coolant flow usage of a conventionally cooled NGV turbine stage. In their assessment of turbine efficiency when using transpiration air cooled NGV's the authors, in applying their cascade results to the cycle studies, have defined turbine efficiency according to the method outlined by L.Y.Goldman of NASA. Consequently, the derived turbine-stage thermodynamic efficiency decreases markedly with increasing coolant flow. The simple application of this efficiency correlation on engine cycle studies, however, appears to be inconsistent with the findings of other investigators. Additional research and engine development testing is indicated to clarify the situation.

3.4 Rotating Disc Heat Transfer

In order to meet the requirements of advanced analytical techniques in the structural design of compressor and turbine discs, improved prediction methods for steady-state and transient temperature distributions are necessary. The solution of the basic heat-conduction equations for any geometrical configuration appears to be no longer a problem and several mathematical routines are available which tend to use effective finite-element methods. This was also indicated in the paper by M.Caprili (39). It gives, however, details of a different mathematical approach to disc temperature calculation in the case of prescribed surface heat transfer coefficients. Furthermore, the paper demonstrates, in a parametric study, the effect of disc heat transfer coefficient and coolant mass flow on radial temperature distributions in a typical turbine disc.

In a general comment, it must be stated that, for several rotating disc arrangements, the analytical methods for calculation of the heat transfer boundary conditions are often based on rough empirical methods. It can be said that past progress in this field of heat transfer research has not kept pace with fast heat conduction solution procedures which are nowadays being widely used. Therefore, it must be appreciated that one paper by J.M.Owen (14) was devoted solely to the very problem of heat transfer from turbine and compressor discs. Whereas several previous publications have already dealt with different rotating disc and cavity arrangements, this paper in particular presents heat transfer measurements for

(a) the situation of central axial throughflow and

(b) the situation of radial outflow of coolant

between co-rotating discs.

The experiments reveal strong vortex breakdowns for the situation (a) and identify different heat transfer regimes for the situation (b). Judging from the present results, the author's concluding view must be shared that much more research work is necessary for establishing theoretical or even empirical prediction methods.

4. EFFECT OF TURBINE COOLING ON AERODYNAMIC PERFORMANCE

From the angle of aerodynamic losses, the most attractive blade profile position for ejection of cooling air is seen to be the trailing edge of the blade. O.Lawaczeck (30) presented cascade wake flow measurements in a wide range of downstream subsonic to supersonic flow conditions. The experimental results provide basic turbine design data in terms of downstream flow angles and loss coefficients for this type of coolant ejection.

The evaluation of the effects of film-cooled vanes and blades on turbine aerodynamic performance and the effect on overall cycle thermodynamic efficiency was the subject of the paper presented by J.D.McDonel (29). The testing was done on a single-stage turbine test rig which featured five independent coolant supplies for independent variations of coolant-to-mainstream temperature ratios, pressure ratios, and mass flow ratios. The program included five test configurations, including two different film cooling designs, and three combinations of film-cooled and solid airfoils. Test results were presented showing the effects of the individual and combined vane and blade cooling air flow ratios on overall stage efficiency. These results were then compared with previously reported analytical methods, and the correlation was quite good. Using the results of the turbine rig, McDonel conducted a cycle analysis study program on a typical high temperature high-performance core engine to demonstrate the effects of cooling air utilization on overall engine performance. The base line turbine inlet temperature of the core engine was 1478 K (2200° F).

The results of this study were presented in parametric form, showing how engine output and efficiency varied with cooling air flow usage for various increases in turbine inlet temperature. This paper clearly demonstrates the potential cycle performance gains resulting from increases in engine cycle temperatures. In addition, it also points out

that, if the cooling is inefficient, the increased coolant flow rates and film injection losses can erode the potential cycle performance gains very rapidly. Curves were presented which showed specific limits which must be placed on the coolant flow rate for specific temperature increases. These results should be helpful to designers in establishing coolant flow limits during engine preliminary design studies. This paper was most timely, since film cooling of vanes and blades is now well established in modern aircraft engines.

Small turbines are generally accepted "to be different" and to have their own problems. During the last 10 to 15 years the small, cooled, axial-flow turbine has been the subject of several research programs. H.F.Due (4) presented a very useful review paper on the special aspect of the aerodynamic performance of the small turbine. The author presented several experimental results of various US-industry and government-sponsored investigations and concluded that considerable efforts are still necessary in order to improve turbine design methods, with special emphasis on prediction of coolant effects.

Besides the author's statement, it is believed that the expected better understanding of aerodynamic losses will guide new approaches to cooled turbine designs which offer still further potential for reduction of losses owing to adverse interaction between turbine mainflow and discharging cooling air.

5. COMBUSTORS AND AFTERBURNERS

Investigation of different liner cooling configurations of combustors and afterburners of aero engines was the general subject of the paper presented by M.Buisson (15). It presents rig measurements of cooling effectiveness by means of the gas analysis technique and the application of thermal paints and outlines the basic features of a simplified analytical approach which is being used for predicting the wall temperature of combustors and afterburners. Furthermore the advantage of combustor liner sandwich design, which employs effective convection cooling before coolant ejection takes place, is emphasized.

J.Winter (16) discussed various practical solutions for combustor cooling problems typically associated with a reverse-flow annular combustor and with a cylindrical flame tube combustor operating in a regenerative gas turbine engine. This paper is mostly devoted to the very typical development problems combustion engineers are faced with, when component life has to be increased or more potential for engine uprating is necessary. The subject of this paper is seen to be very suitably placed in this "High Temperature Problems" conference, the intention of which is, on the one hand, to cover the wide scope of present scientific research work and, on the other hand, to deal with application problems which influence the direction of future research work.

A topical area of combustor-related research work is the development of analytical models which describe exhaust species concentrations as well as overall combustor performance. The paper of W.P.Jones (40) et al., presented by C.H.Priddin, dealt with measurements of species concentrations and velocities in a small-scale research combustor, these being compared with predictions of their mathematical model of chemically reacting flow which uses finite-difference equations. The present status of this model describes the profiles of fuel/air ratios and UHC concentrations quite well, but exhibits shortcomings in the prediction of CO concentrations along the combustor axis. The authors discuss possible approaches to overcome the present limitations in future developments in the model. Without doubt, some of these improvements can be easily incorporated into the existing mathematics as, for instance, a modified probability function or an additional reaction mechanism for NOX formation.

The authors regard the introduction of adequately prepared fuel breakdown physics, with model capabilities to describe ignition and extinction limits, as a rather more longterm development. Hesitation may, therefore, be justified in sharing the optimism expressed in the authors' concluding statements which suggest that only a little further development is necessary.

Alternative aviation fuels under consideration for future aircraft engines will influence especially the combustor system design. The paper by L.Martorano (18) deals with H_2-air combustion in a coaxial-stream cylindrical combustor up stream of a small single-stage research turbine featuring variable nozzle guide vanes.

The primary zone air loading of the combustor can be varied by movable inlet baffles and testing has been done over a wide range of fuel/air ratios, but no specific details of combustor measurements are given. It can be expected that the impact of alternative fuels on engine combustor design, as well as on cooling techniques, will attract increasing interest in future high temperature turbines. In this sense, the subject of this paper is believed to be also of considerable importance for future High Temperature conferences.

The last paper of the combustion session was devoted to the severe problem of low-frequency combustion in mixed-flow afterburners known as rumble or chugging. F.N.Underwood (19) categorised the several possible mechanisms which are normally seen to cause or regulate this special phenomenon. The paper gives a status report on a research project which is aimed at developing a reliable empirical and analytical model to aid afterburner design.

The experimental rig test data presented identify airflow dynamics and fuel distribution as main rumble contributors and the overall mathematical model of the augmentor system is shown to already predict typical rumble conditions.

Improvements by incorporation of a more adequate combustion model are necessary and were announced by the author.

6. HIGH TEMPERATURE MATERIALS AND COATINGS

Six papers were given, discussing the properties, characteristics, and selection of materials for use in hot section components operating at high turbine inlet temperatures. G.M.Ault (3) presented a very comprehensive survey on the status, progress, and future potential of advanced processes, materials, and coatings currently under development by the gas turbine community for advanced high temperature engines. As noted in previous papers (12, 29), significant payoff in engine performance can be achieved by minimizing the amount of cooling air used. Thus, the development of advanced materials and coatings, together with the development of improved cooling techniques are keys to realizing the full performance benefits of the high temperature gas turbine. In his paper, Ault (3) also predicted that pre-alloyed, powder-metallurgy-processed super alloys will afford increased strength and fabrication cost benefits, especially for turbine discs. Oxide dispersion strengthened alloys for use in vanes and combustor components show at least 90°C (160°F) higher use temperature potential than conventional sheet materials. Ceramics offer the highest use potential, in the order of 1400°C (2600°F), of all materials. Good progress in solving some of the problems inherent in ceramic components is reported on SiC and SiN_4 materials. Directional structures offer a major improvement potential over the best conventionally cast super alloys. D.S. eutectic alloys appear to offer as much as 80°C (150°F) use temperature advantage. Refractory fiber-reinforced super alloys afford potentially the highest use temperature capability of current super alloys. The advances in the development of more effective coatings for advanced super alloys were presented, comparing the effectiveness of aluminide coatings with the more advanced PVD, Co, Cr, Al, Y, aluminized Ni, Cr, Al, Si and the Pt-Al systems. Tailoring the coating to the substrate is vital for optimum effectiveness. Such tailoring can most readily be achieved with the PVD* process. Insulating refractory coatings show potential in providing an effective thermal barrier on blades and vanes. Ceramic coatings in the order of 0.25 mm (.010 in.) thick on a typical core engine study showed an eightfold reduction in cooling air flow and a 110°C (220°F) reduction in vane metal temperatures. Furthermore, the predictions are that a thermal-barrier-coated, convection cooled blade would be as effective as a full coverage film cooled blade in view of the reduced aerodynamic losses. Naturally, many problems involving cost, fabrication, and material property characteristics must be solved before these advanced materials and concepts can be used in the hot section of engines.

In outlining the trends toward improved high temperature materials, Ault (3) also stressed the potential improvements in material properties afforded by directionally solidified composites. H.Bibring (20) reviewed the progress of the ONERA developed family of refractory D.S. materials. Material properties of COTAC 74 are compared with similar properties of IN 100 material, showing the improved high temperature characteristics of the COTAC 74 over IN 100 material in the 1000 K metal operating temperature range. For increased corrosion protection, COTAC 74 can be protected by the coating DE 77 presented by Ph. Galmiche (22). Progress on the development of COTAC 74 has been sufficient to justify testing blades in an actual engine. On the basis of the work done so far, the authors claim that the increased temperature properties of COTAC 74 can be immediately exploited in the field of uncooled turbine configurations. However, more development efforts are required to apply this material to air-cooled blade configurations.

A very interesting paper was presented by A.D.Davin (23) on the development and experience of overlay coatings for the protection of cobalt-based alloys from hot corrosion. He points out the limitation of diffusion-type coatings in providing good oxidation protection, but stated these coatings lack the ability to adequately control sulphidation or hot corrosion. Furthermore, diffusion coatings applied to directionally solidified or oxide-dispersion-strengthened metals may alter the alloy properties. The overlay coatings, of the Co/Ni Cr-Al-Y type, eliminate most of the disadvantages of the diffusion coatings, and have shown exceptional corrosion resistance in service. The Co/Ni-base overlay coatings were shown to provide increased protection from oxidation and corrosion in high temperature turbine applications. The individual constituents of the overlay alloy can be optimized as a function of ductility requirements or coating process.

The prediction of the corrosion behavior of super alloys exposed to combustion gases is a very difficult task. The paper by U.Ducati (21) deals with the effects of sulphates, chlorines, and mixtures of them on the corrosion behavior of typical commercial nickel super alloys. In addition, some experimental alloys and a Co-base super alloy, together with a few typical impregnation coatings are reported on. The results of this work confirm the observation of Billingham (1973) on the influence of thermal treatment on corrosion behavior of super alloys; the hypothesis of intervention of electrochemical steps in hot corrosion has been advanced and justified.

The evaluation of a ceramic combustion chamber for a small gas turbine engine was the subject of G.Sedgwick's paper (27). The combustor was fabricated from hot pressed silicon nitride and flame sprayed reaction bonded silicon nitrate. The design of the combustor was tailored to take account of the lack of ductility of the ceramic material, by utilizing stacked rings for the flame tube and a low stressed reverse flow disk. Twelve ceramic components were utilized in making up the combustor assembly. Combustion testing in excess of 1200 K (2250°F) turbine inlet temperature was accomplished. Seven of the components survived the seven combustion tests of approximately 5 hours' duration. The greatest number of failures occurred on the two most complex components, namely the head

* Physical vapour deposition.

plate and rear disc. The failures of these components continued even after redesign to very low stress levels, and indications were that a major contributing factor was material inhomogenity.

Ph. Galmiche (22) presented a very informative paper on the ONERA developed coating process, which permits the application of a pack coating on both the external and internal surfaces of the blades and vanes. Mr. Galmiche presented micro-photographs of the wide application of this new coating process to conventional super alloys, as well as to advanced D.S. alloys such as COTAC 74 previously described by Bibring (20). Especially interesting were the results of the DE 77 coating applied to COTAC-74 D.S. material, which showed no distress after 500 hours of cyclic testing to 1130°C (2070°F). The coating method is applicable to new parts, as well as to parts which have been previously coated by thermochemical, chemical or PVD methods. This latter point is important from a maintenance standpoint, since blades which show coating distress during the overhaul process may be reprocessed by this coating technique.

7. REMARKS ON OVERALL ENGINE DESIGN AND PERFORMANCE ASPECTS

Two papers were addressed to some overall engine aspects as seen from the engine manufacturer's point of view. The paper presented by J.L.Price (24) dealt with different structure technology advancement areas that are dictated by the current trend of high thrust-to-weight engines. Furthermore, the author described details of a systematic time-phased development plan, which included the implementation of a sophisticated computerized structural analysis method. Mission-related stress analysis of static and rotating components and tip clearance control of rotor blades, for instance, are covered as important problem areas for advanced engines, and prospects are given for expected trends of major turbine design parameters over the next decade.

The paper presented by E.A.White and M.J.Holland (1) dealt with the influence of aircraft engine mission profile and engine rating on the service life of air-cooled high pressure turbine rotor blades, in particular. This paper also illustrated computerized analytical techniques available for assessment of critical engine components with respect to their life consumption. The authors presented some interesting results of a parametric study for a military aircraft engine operating with an assumed 1600 to 1800 K turbine stator outlet temperature. Some specific problems of small turbine technology were mentioned by Belaygue (2) who addressed also some aspects of overall engine performance with respect to increasing turbine temperatures.

Although these papers gave some trends of turbine design requirements, it is unfortunate that, generally, fairly little data was presented on the overall engine performance aspects, both theoretical and practical, of high temperature gas turbines. It is understandable that the engine manufacturers are reluctant to discuss the overall status of, and experience with, their current or advanced high temperature engines, because of commercial or proprietory considerations. Nonetheless, the conference would have benefitted if such a survey had been presented to set the stage for the ensuing discussions.

8. CONCLUSIONS

In summary, it appears that the following major conclusions can be drawn:

(1) This conference on high temperature problems in gas turbines resulted in a successful interchange of much valuable technical information regarding status on the design aspects of high temperature components, and the potential of new concepts in testing, cooling, design, materials and coating technology required to obtain further improvements in performance, cost, reliability and maintenance aspects of advanced engines. It is believed that NATO member nations participating in this meeting were able to develop a realistic assessment of the overall current state of the art, as well as the future potential approaches for the attainment of further increases in turbine inlet temperatures.

(2) There was agreement among the speakers and those who participated in the discussions that efficient utilization of the cooling air used to maintain proper metal temperatures is of paramount importance. Futhermore, it appears that further increases in turbine inlet temperatures, in the near term, will result from improvements in cooling concepts and configurations, combined with new or improved higher use temperature metals and coatings.

(3) Improved film cooling techniques with adequately developed design methods are seen as an important factor for future progress in high temperature turbines. It is believed that improved testing facilities, together with new measuring and analysis methods, can have considerable influence on further progress.

(4) Transpiration cooling of blades and vanes was shown to be very effective in maintaining low metal operating temperatures with very low cooling air flows. However, before the full performance benefits afforded by transpiration cooled blades can be realized, further improvements must be made on the allowable operating temperatures of porous materials. In addition, a critical review is required of the assumptions used in defining stage efficiency for cycles incorporating a transpiration cooled turbine. The methods presented at this conference appear to be overly pessimistic and in conflict with earlier published engine test results.

(5) Better understanding of the effect of engine-typical cooling air injection methods on turbine aerodynamics and overall engine performance is needed in order to focus research work on the reduction of performance losses.

(6) The selection of conference papers dealing with combustor-related problems appears to highlight the main fields for future development of this engine component: liner cooling techniques, application of ceramic materials, improved combustor analytical models and the use of alternative fuels with inherent engine design modifications. The last subject is believed to deserve additional attention in future conferences on high temperature turbines.

(7) Since the last AGARD meeting on high temperature turbines, progress has been demonstrated in fabrication technology for hot section components, as evidenced by the sophisticated film cooled blades, the diffusion bonded transpiration cooled blades, and the coated hardware examples presented in some papers during the course of this meeting.

(8) Much progress has been demonstrated in achieving the performance benefits of high technology in small gas turbines; however, further efforts are required to reach the higher performance levels demonstrated in high technology large engines.

(9) The successful interchange of much valuable technical information from the meeting, hopefully, will lead to some degree of standardization of terminology and, hence, result in an improvement of communications between the technical workers in this important, though somewhat specialized field.

9. RECOMMENDATIONS

(1) This meeting provided a measure of the progress made in technology of high temperature gas turbines since the last meeting, and provided useful and timely opportunities for the exchange of ideas and information on advanced concepts between the gas turbine specialists of the NATO countries.

It is recommended that a future meeting on high temperature turbines be held in 4-5 years. Using the present meeting as a base, it could evaluate the progress made in the intervening time. It appears that materials, cooling and coatings technology have progressed to the point that a significant step in operating temperatures of engines will take place in the next few years.

(2) A change in format of the meeting to include one or two half-day, round-table discussion sessions on a specific subject, problem area or theory, would enhance the technical interchange aspects of the meeting.

(3) As a final recommendation, it would be desirable, at a future assemblage of this eminent group of specialists, that a keynote overall survey paper be given by an engine manufacturer or government technical organization outlining the specific benefits in cycle performance or aircraft mission performance afforded by operating at high turbine inlet temperatures.

PROJECT OPTIMISATION OF MILITARY GAS TURBINES WITH RESPECT TO TURBINE LIFE

E.A.White – Assistant Chief Engineer, Advanced Projects, and
M.J.Holland – Assistant Chief Engineer, Combustion and Air Systems
Rolls-Royce Limited
Aero Division
Filton
Bristol
UK

SUMMARY

Parametric studies for the otpimisation of an aero engine for a particular type of military requirement have generally, in the past, been heavily biased in the direction of best performance with some recognition of thrust = weight trends. In practice this led to a specific choice of Aero/Thermodynamic cycle and this clearly required that some choice about the engine rating had to be made. It can be shown that the way an engine is rated and controlled can have at least as much, if not considerably more, influence on its performance levels and characteristics as its choice of cycle. However, if the engine's ratings are being changed then, of course, so is its service life, particularly in respect of the critical hot-end components.

Any engine optimising process that takes place should recognise that engine life is of great importance. The availability of better techniques for engine and aircraft 'packaging' and turbine life analysis has made it possible to process a considerable amount of inter-related data to assist in the choice of engine for a specific aircraft task. How that engine would suit other roles, how its service life would then be affected and how its ratings could be adjusted to compensate are all very interesting questions which are now becoming answerable in a short enough timescale to influence major policy decisions.

This paper describes some of the techniques and analytical processes now in use for the definition of future engine projects and gives examples of the results for a range of military aircraft considered in terms of the turbine life and cooling requirements they pose.

1. INTRODUCTION

Traditionally engine manufacturers have done their best to produce a design with a long, reliable life but it has frequently been the case that the end result has been a design that is "unbalanced." That is to say, many components, particularly those towards the front of the engine where the operating temperatures are relatively low, will last virtually indefinitely, whereas the critical high temperature components, and especially the high pressure turbine, need regularly replacing over short intervals at considerable expense.

In all probability this situation will always obtain to some extent since we are dealing with a very wide spectrum of technological difficulty. However, there is no doubt that the problems have been compounded by three gaps in our knowledge. Firstly, a basic lack of detailed understanding of how engines are actually handled in day-to-day service operation. Secondly, a genuine appreciation of how engines should be rated so that their thrust characteristics match the requirements of the aircraft in all flight conditions and, thirdly, the computerised analytical techniques for examining the characteristics of high pressure turbine blades under the various stresses of operation.

These three gaps are being, or have been plugged. The first is being met by the use of flight data recordings on a range of U.K. military aircraft in the E.U.M.S. programme (Engine Usage Monitoring System). This is a subject which would require a paper on its own account and is not dealt with in detail here. The last two are coming about by developments in the state-of-the-art and by an increasing awareness of what are the more appropriate ingredients for the specification of a new military aircraft so that the best overall cost-effective weapon system is more likely to be procured.

This paper illustrates these developments in analytical procedures with regard to air-cooled H.P. turbine rotor blade service lives in various hypothetical future combat aircraft fulfilling several roles. It does not presume to cover the whole field.

2. PREDICTION OF H.P. TURBINE BLADE LIFE

The life prediction method described is commonly used during the early stages of project investigations. It consists of empirical correlations of the turbine blade lives experienced on various Rolls-Royce engines during bench endurance tests and service operation. The form of the correlations was originally obtained from rig or laboratory testing and theoretical analysis.

Three modes of failure are considered:

1. Creep based on average blade section stress and temperature

2. Low cycle fatigue (LCF) based on both average and local blade temperatures during the 'hot hold' part of the cycle together with allowance for actual blade dimensions.

3. Coating based on local blade hot spot temperature.

The life consumed for each failure mode is calculated for every phase of the mission and summed by means of the simple linear accumulation of damage assumption (Miner's Law). The actual calculation routines were programmed and carried out on a C.D.C. Cyber 74 Computer. The study reported here took one technical engineer 3 days and required 90 runs totalling 2½ minutes on the computer.

3. ASSUMPTIONS

The following data were assumed constant over the whole range of conditions considered for this paper.

Turbine details:

Single stage transonic turbine.
Relative hot gas temperature = 0.88
Stator outlet temperature.
Combustion radial temperature distribution factor = 0.1
Cooling air temperature
Compressor delivery temperature = 1.0

Blade details:

Precision cast blade in IN 100 nickel base alloy
Pack Aluminised coating
Mean cooling effectiveness = 0.6
Minimum cooling effectiveness = 0.5
Shroudless design with combination of internal convection and external film cooling.

Maintaining all the above details constant reduced the number of variables involved and enabled us to concentrate on those quantities of direct interest for the present study i.e., engine rating and mission profile. Even so it was necessary to examine the results from 45 engine rating/mission combinations each of which was run at two L.C.F. frequencies,

Blade stress and size were varied from engine to engine as shown in Table 1. During each mission stresses were assumed to vary in proportion to the square of the H.P. spool speed.

The assumption of constant cooling effectiveness implies a fixed blade design scaled from one engine to another by the linear scale factor given in Table 1. Local blade metal thickness was also scaled and allowance was made for the effect of wall thickness on creep and L.C.F. life.

4. MISSION PROFILES

It is a statement of the obvious, but only when it has been made, that the service life requirement for a warplane applies, in fact, to peace-time operation, which is the norm. We therefore have to contemplate the possiblity of a somewhat paradoxical situation where the aircraft specification defines a war-time capability in which the rate of engine usage may be less severe than in peace-time practice missions. This is because the operational sortie will generally contain a proportion of throttled-back engine operation with low life consumption in the phases of cruise to and from the FEBA*. Peace-time training missions can often be of shorter duration and contain a larger proportion of high engine ratings which consume life. In addition, more than one simulated operational manoeuvre may be made in one training mission so that the degree of difficulty is compounded. Hence, any examination of engine service life must consider the peace-time case where cost effectiveness is of great importance and in war-time we may reasonably assume that operational effectiveness takes precidence over all other factors.

* Forward edge battle area

For the purpose of this paper five mission profiles have been examined, three in war-time and two corresponding ones in peace-time. The details of these are given in Table 3. Each mission is broken up into phases of flight which define a period of operation at a certain value of engine inlet total temperature (T_1). This parameter is a key factor in determining the level of turbine entry temperature** at which the engine is operating. Certain missions contain a proportion of the time which is neither at maximum engine rating nor is it throttled back far enough so as to be non life-consuming. In these cases, this part of the flight time has been converted into an equivalent time which is of the same total duration but is made up of operation at maximum rating plus operation at non life-consuming ratings.

In general the peace-time sorties tend to be shorter and quite substantial differences are exhibited between peace-time and war-time in the proportion of high life-consuming engine ratings. Air superiority can represent a more arduous role in peace-time than in war and ground attack can be the opposite. The interceptor mission is probably the most arduous of all.

Although the missions for the various aircraft roles can be fixed with some confidence, the L.C.F. frequency requirements for the various missions are less certain. We therefore decided to include two frequencies, namely 2 and 6 major cycles per hour, and ignored minor cycles.

5. ENGINE RATINGS

In order to illustrate the differences in life predictions that can occur with different ways of rating a given engine or with different engine cycles a suitable range of engine data has been examined for the paper. These data are by no means exhaustive and omit a consideration of how a method of rating and/or choosing the most appropriate thermodynamic cycle of an engine will actually fit the precise thrust requirements of a given aircraft. This is a very complicated subject in its own right and involves quite subtle considerations of the relative merits of various important factors. For example, if the war-time performance requirements of a very high capability fighter aircraft are met or even, perhaps, exceeded then in peace-time such an aircraft may spend a great deal of time of low engine throttle settings and may therefore have a longer life than if the original specification was only partly met. We thus enter into an initial cost versus replacement parts cost argument.

Suffice to say that the data used will illustrate certain important trends within the constraint of a manageable total of actual numbers used. The data are given in Table 2 for the various engines and ratings shown in Figure 1. Basically we are trying to show the effect of rating a given engine referred to as engine "Z" in five different ways with either constant S.O.T. operation above $T_1 = 288^{\circ}K$ or rising S.O.T. above $T_1 = 288^{\circ}K$ such that S.O.T.: T_1 remains constant, subject to an absolute maximum cut-off limit. In addition four other new engine cycles have been selected simply to illustrate the effect of some $200^{\circ}C$ difference in peak S.O.T. at constant overall compression ratio together with the effect of reducing compression ratio from 28 to 16 at essentially constant S.O.T. For the purpose of this paper these four engines have been rated in a similar way i.e., S.O.T. rising with inlet temperature subject to a maximum cut-off value. Any slight difference in these rules is accounted for by the fact that the engine data were drawn from existing information. The differences are so small, in any case, so as not to invalidate the overall conclusions.

6. RESULTS OF THE STUDY

The combination of 9 engine ratings, 5 missions and 2 L.C.F. frequencies generated a large volume of computer output in terms of service life predictions for the three failure modes. In what follows we have therefore concentrated on the more important trends which emerged.

6.1 Blade Temperatures

Turbine blade life is very sensitive to blade temperatures which are in turn determined by the values of cooling effectiveness assumed.

Figures 2 and 3 show the variation of blade temperatures with stator outlet temperature (S.O.T.) and compressor delivery temperature (T_3). Figure 2 gives the blade peak or hot spot temperature while Figure 3 gives the mean blade temperature. Each engine rating is identified as a single line on each figure.

It can be seen that the slopes of the lines of constant S.O.T. and T_3 are of similar magnitude, implying that blade temperatures are equally sensitive to compressor delivery and stator outlet temperatures. This is due to the assumption of cooling effectiveness values around the 0.5 region.

** The term 'turbine entry temperature' has in the past been used to denote both the combustion chamber exit temperature and the H.P. turbine stator outlet temperature, which could be about $50^{\circ}K$ lower. To avoid confusion in this paper we will hereafter use the term 'Stator outlet temperature' (S.O.T.)

As might be expected, the 1800°K engine has the highest blade temperature and the 1600°K engine the lowest. The relatively low blade temperature for the low pressure ratio engine are worthy of note, they stem from the low compressor delivery temperature (T_3).

6.2 Effect of Engine Rating on Life

A fixed engine Z was employed to study the effect of varying the rating method. Five ratings were investigated and are identified as Z1 to Z5. The variation in blade temperature for the various ratings (Figures 2 and 3) produces a marked variation in life in all three failure modes. This is shown on Figure 4 for the chosen war-time air superiority mission for all five ratings.

The effect of varying S.O.T. for a fixed method of rating was investigated by analysing three different engines identified as "1800, 1700 and 1600". A fourth variant engine "1800 LPR" was included to indicate the importance of overall cycle pressure ratio. Again a marked variation in life is found between these 4 engines and this is illustrated in Figure 5 for the chosen war-time air superiority mission.

Figures 4 and 5 both show blades lives falling exponentially with increase in the peak S.O.T. value. The LCF lives are lowest indicating that this would be the failure mode predicted for engines spending all their time flying this particular mission, irrespective of the rating method adopted.

Comparing Figures 4 and 5 it can be seen that creep life falls more rapidly on the former, this is due to the significant increase in H.P. spool speed and blade stress that occurs with the increasing S.O.T. for the Z engine. For the engines "1800, 1700, 1600 and 1800 LPR," blade stresses are very similar at the high S.O.T. levels where creep life consumption is greatest.

The general similarity between Figures 4 and 5 indicates that for the chosen war-time air superiority mission blade life is sensitive mainly to peak S.O.T. on the S.O.T. vs. T_1 rating curves (Figure 1) and not so sensitive to the actual shape of the curve. This result holds for all three war-time missions examined and also the peace-time ground attack mission. Only the chosen peace-time air superiority mission is sensitive to the shape of the rating curve. This latter mission is the only one to spend a significant proportion of its flight time consuming life at low T_1 ratings. The former four missions exhibit the common feature that their maximum life consumption occurs at high T_1 values where the S.O.T. vs. T_1 rating curves are all relatively flat.

Thus our selection of mission profiles has in most cases nullified the weaker effect of the shape of the engine rating curve and blade life has become primarily a function of peak S.O.T.

The increase in life for the low pressure ratio engine "1800 LPR," shown in Figure 5 is most marked for the creep failure mode. The lower LCF lives however, make this large creep improvement academic. The relatively long coating lives shown in Figures 4 and 5 will in practice be considerably shortened by erosion, a potential failure mode for long life blades which has been ignored in this study. The low pressure ratio engine thus offers a modest but useful improvement in LCF life.

6.3 Effect of Mission on Life

The results obtained showed that for all three failure modes the effect on blade life of varying the mission was broadly similar for all engine ratings. This is shown in Figures 6 and 7.

To isolate the effects of varying mission the lives of these two figures have been normalised by expressing the lives for each failure mode relative to the life of that same mode for the war-time air superiority mission. Note however, that the actual lives for this latter mission do vary considerably with S.O.T. and engine ratings as shown earlier in Figures 4 and 5.

Figure 6 combines the results for all engine ratings having similarly shaped rating curves (Z3 to Z5, "1800, 1700, 1600 and 1800 LPR"). Figure 7 contains just the two ratings Z1 and Z2 which are much flatter than the other rating curves in Figure 1.

Figures 6 and 7 both show that whereas mission exerts a strong effect on creep and coating lives the effect on the more important LCF lives is much weaker.

The war-time interceptor mission gives the shortest creep and coating lives. Life consumption for these two modes depends on time at temperature and the war-time interceptor mission produces the most adverse combination of time vs. T_1 and hence also vs. S.O.T. and T_3 for all engine ratings. This drop in creep and coating life for the war-time interceptor means that these two failure modes become limiting for this mission.

Table 4 shows how the life limiting failure mode depends upon the particular combination of mission and engine rating. Except for the war-time interceptor mission LCF is the dominant failure mode. The major importance of LCF emphasises the need to be able to define the cycle frequency requirements for the various missions much more precisely than we can at present. Current lack of knowledge in this area impairs the ability to predict service life for turbine blades.

The relative insensitivity of LCF life to mission shown in Figures 6 and 7 is attributed to our assumption of constant LCF frequency plus the fact that at 6 cycles per hour the bulk of the LCF cycles are experienced at high T_1 where the rating curves are all relatively flat. This effect is further reinforced in Figure 7 by the flatness of the Z1 and Z2 rating curves over most of the T_1 range.

The major difference between Figures 6 and 7 centres on the peace-time air superiority mission. This mission spends a larger proportion of life consuming time at the lower T_1 ratings. This mission therefore shows a significant fall in relative life for the flatter rating curves Z1 and Z2 of Figure 7 when compared with Figure 6.

6.4 Effect of Improved Cooling on Life

The major interest here is in increasing the LCF life since this is likely to be the most common failure mode. LCF failures have been assumed to occur at the blade hot spot, increasing the cooling effectiveness here by 0.1 would give around a ten-fold increase in blade life provided of course that the creep mode does not then become limiting. An increase of this size in the local cooling effectiveness would represent a drop in blade hot spot temperature of around 70°C and an increase in cooling air flow of 0.5-1% of the turbine mass flow. Thus the benefits of increased life would have to be weighed against a possible loss of engine performance.

7. ENGINE COMPARISON

Leading parameters for all the four engines studied are listed in Table 5. Most of the data is expressed in relative terms with engine "1600" as datum. All engines were in fact sized to meet common requirements.

Although it is not the object of this paper to recommend the optimum engine solution it can be seen that the benefits of reduced engine size and weight that come with high S.O.T. are obtained at the cost of a severe drop in H.P. turbine life.

8. CONCLUSIONS

This paper has concentrated on the effect of engine rating method and mission on H.P. turbine blade life as an illustration of the type of techniques now available for use in project studies to investigate the effect of numerous engine parameters on life.

The following conclusions relate to the particular conditions selected for this paper:

1. For aircraft missions which spend the largest proportion of time at high T_1, the failure mode is either creep or coating.

2. For aircraft missions which spend relatively less time at high T_1 the failure mode is LCF.

3. The most common failure mode is LCF and in this mode life is relatively insensitive to the mission flown at the higher cycling frequencies which are more likely to be typical of actual operation.

4. Our current lack of knowledge regarding the number of LCF cycles experienced during the various aircraft missions limits our ability to predict blade service life.

5. Blade life is highly dependent on peak S.O.T. on the rating curve. The actual shape of the curve is relatively unimportant for most missions since life consumption is dominated by the flat rated high inlet temperature cases.

6. Blade life is highly dependent on cycle pressure ratio for creep life, but less so for the more common LCF failure mode.

9. ACKNOWLEDGEMENTS

The authors wish to thank their colleagues in Rolls-Royce Limited for assistance in the preparation of this paper. They also wish to thank Rolls-Royce Limited for permission to publish this paper but would emphasise that the views expressed are their own and not necessarily those of the Company.

TABLE 1

H.P. TURBINE BLADE STRESS AND SIZE

ENGINE	1800	1700	1600	1800 LPR	Z
Stress at 100 % H.P. spool speed					
MN m^{-2}	192.9	189.0	188.9	188.9	199.3
Tons.in^{-2}	12.49	12.24	12.23	12.23	12.90
Blade relative linear scale	0.889	0.871	1.02	0.847	1.0

TABLE 2 ENGINE PERFORMANCE DATA

T_1 °K	ITEM	DIFFERENT WAYS OF RATING THE SAME ENGINE					EFFECT OF S.O.T. AT CONSTANT OVERALL PRESSURE RATIO			EFFECT OF OVERALL PRESSURE RATIO
		Ƶ1	Ƶ2	Ƶ3	Ƶ4	Ƶ5	"1800"	"1700	"1600"	"1800 LPR"
280	S.O.T.°K	1610	1635	1560	1560	1610	1634	1543	1454	1619
	T_3°K	800	810	780	780	800	795	795	794	668
	N_H	0.971	0.980	0.956	0.956	0.971	0.946	0.946	0.946	0.943
288	S.O.T.°K	1650	1675	1600	1600	1650	1688	1594	1501	1684
	T_3°K	816	826	797	797	816	822	822	820	695
	N_H	0.982	0.988	0.969	0.969	0.982	0.964	0.964	0.964	0.964
300	S.O.T.°K	1650	1675	1655	1655	1655	1743	1646	1549	1743
	T_3°K	822	832	824	824	824	849	849	847	720
	N_H	0.986	0.993	0.986	0.986	0.986	0.981	0.981	0.981	0.981
320	S.O.T.°K	1650	1675	1700	1750	1750	1793	1694	1600	1790
	T_3°K	831	841	853	872	872	878	878	878	755
	N_H	0.988	0.995	1.001	1.018	1.018	0.994	0.994	0.997	0.998
330	S.O.T.°K	1650	1675	1700	1750	1750	1784	1686	1592	1790
	T_3°K	836	846	857	877	877	878	878	878	760
	N_H	0.989	0.996	1.002	1.018	1.018	0.990	0.990	0.992	0.999
340	S.O.T.°K	1650	1675	1700	1750	1750	1774	1677	1584	1790
	T_3°K	841	851	862	880	880	878	878	878	765
	N_H	0.990	0.997	1.003	1.018	1.018	0.984	0.984	0.986	1.000

S.O.T. H.P. turbine stator outlet temperature, T_3 = H.P. Compressor delivery temperature, N_H = Relative H.P. spool Rotational speed.

TABLE 3

MISSION PROFILES

FLIGHT CONDITION	MISSIONS				
	WARTIME			PEACETIME	
	AIR SUPERIORITY	GROUND ATTACK	INTERCEPTOR	AIR SUPERIORITY	GROUND ATTACK
HIGH RATINGS, LIFE CONSUMING PROPORTION OF TIME %	3.5	26	35	25	15
LOW RATINGS, NON LIFE CONSUMING PROPORTION OF TIME %	96.5	74	65	75	85
RELATIVE TOTAL MISSION TIME	3.0	2.0	1.0	1.0	1.5

TABLE 4

H.P. TURBINE BLADE LIFE LIMITING FAILURE MODES

LCF FREQUENCY - 6 CYCLES PER HOUR

ENGINE RATING	MISSION				
	WARTIME			PEACTIME	
	AIR SUPERIORITY	GROUND ATTACK	INTERCEPTOR	AIR SUPERIORITY	GROUND ATTACK
Z1	LCF	LCF	(COATING (+ (LCF	LCF	LCF
Z2	LCF	LCF	(COATING (+ (LCF	LCF	LCF
Z3	LCF	LCF	(COATING (+ (LCF	LCF	LCF
Z4	LCF	CREEP	CREEP	LCF	LCF
Z5	LCF	CREEP	CREEP	LCF	LCF
"1800"	LCF	LCF	(CREEP (+ (LCF	LCF	LCF
"1700"	LCF	LCF	(COATING (+ (LCF	LCF	LCF
"1600"	LCF	COATING	(COATING (+ (LCF	LCF	LCF
"1800 LPR"	LCF	LCF	LCF	LCF	LCF

Where two failure modes are shown the life of the second is very close to the life of the first or primary failure.

TABLE 5 ENGINE COMPARISON

PARAMETER	ENGINE			
	"1800"	"1700"	"1600"	"1800 LPR"
DESIGN BYPASS RATIO	1.5	1.1	0.72	1.45
DESIGN S.O.T. ^{o}K	1800	1700	1600	1800
DESIGN OVERALL PRESSURE RATIO	28	28	28	16
RELATIVE THRUST AT 0.9M SL ISA REHEATED	0.913	0.952	1.0	0.992
RELATIVE S.F.C. AT 0.9M SL ISA REHEATED	1.022	1.014	1.0	0.990
RELATIVE ENGINE WEIGHT	0.757	0.884	1.0	0.730
RELATIVE FAN INLET DIAMETER	0.946	0.973	1.0	0.936
RELATIVE H.P. TURBINE BLADE LIFE FOR SAME COOLING SYSTEM for all missions dominated by high T_1 operation	0.078	0.286	1.0	0.169

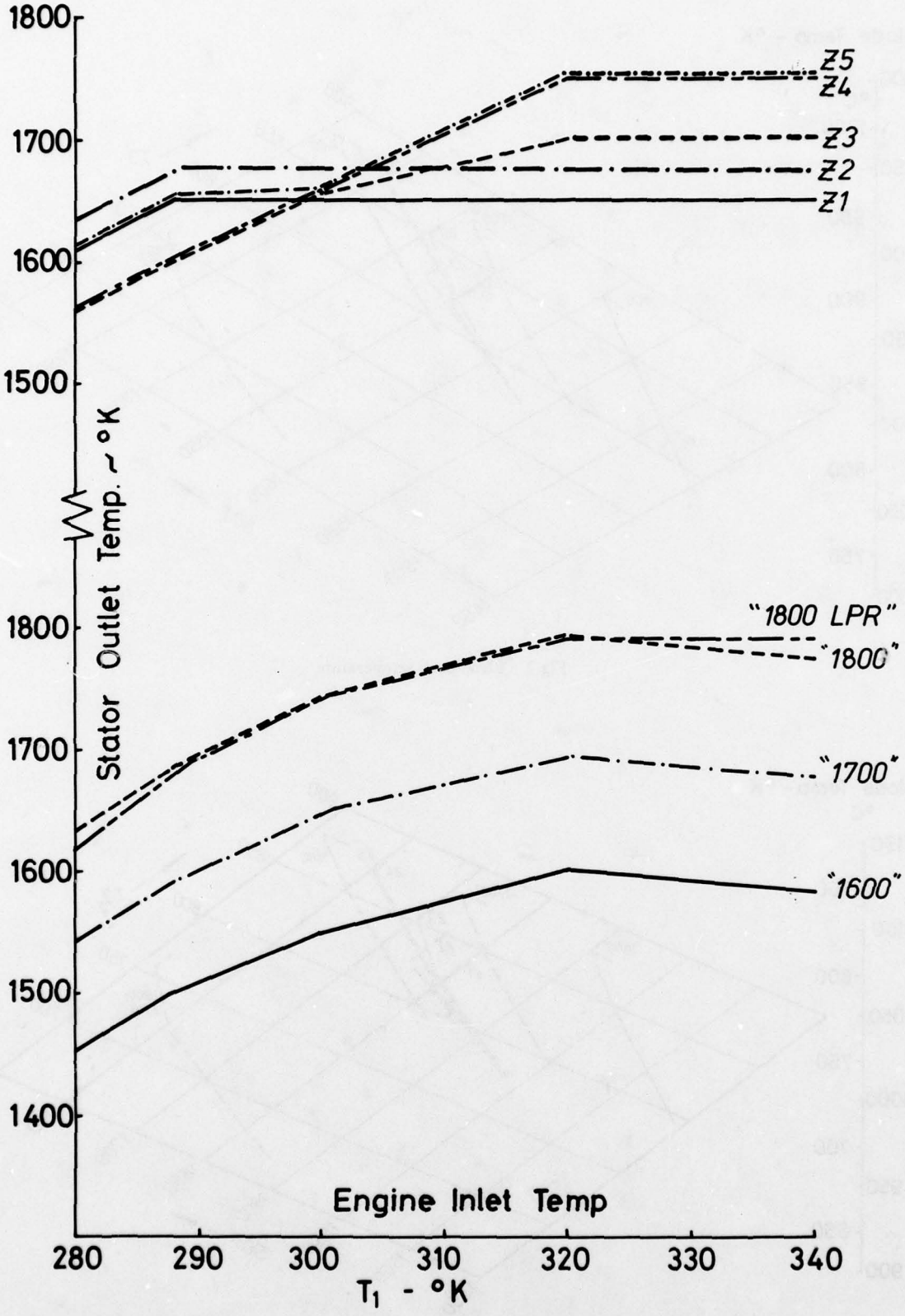

Fig. 1 Rating curves

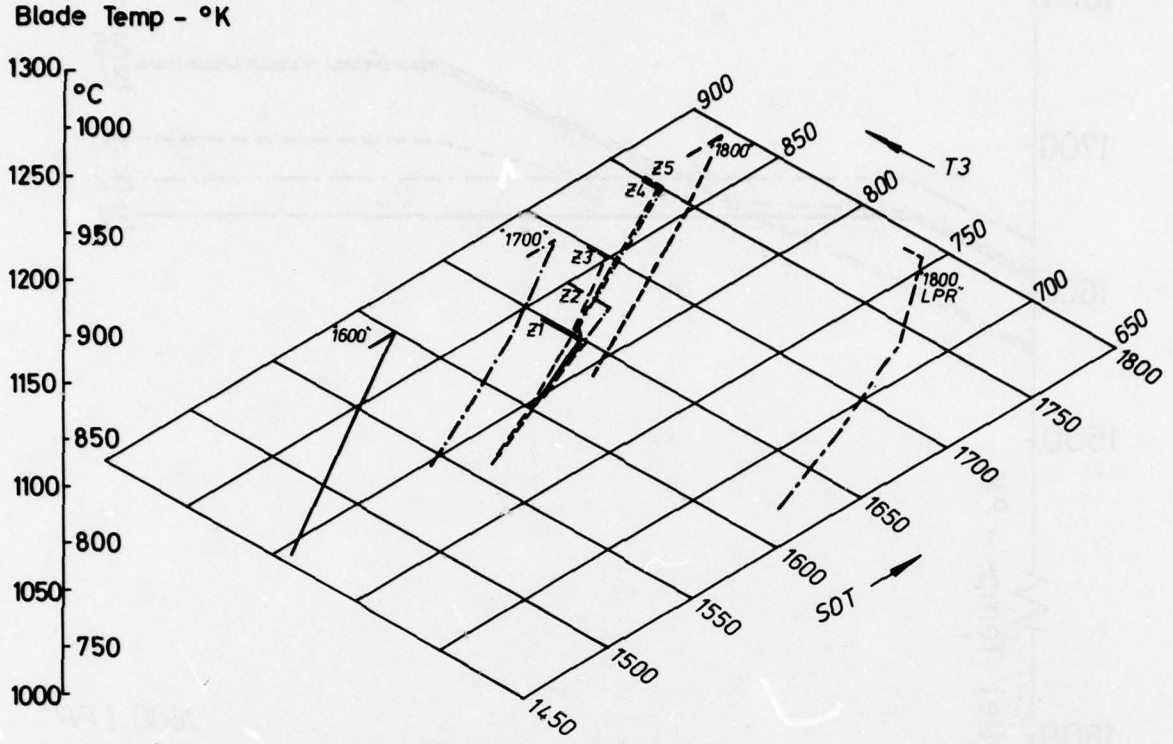

Fig.2 Blade peak temperature

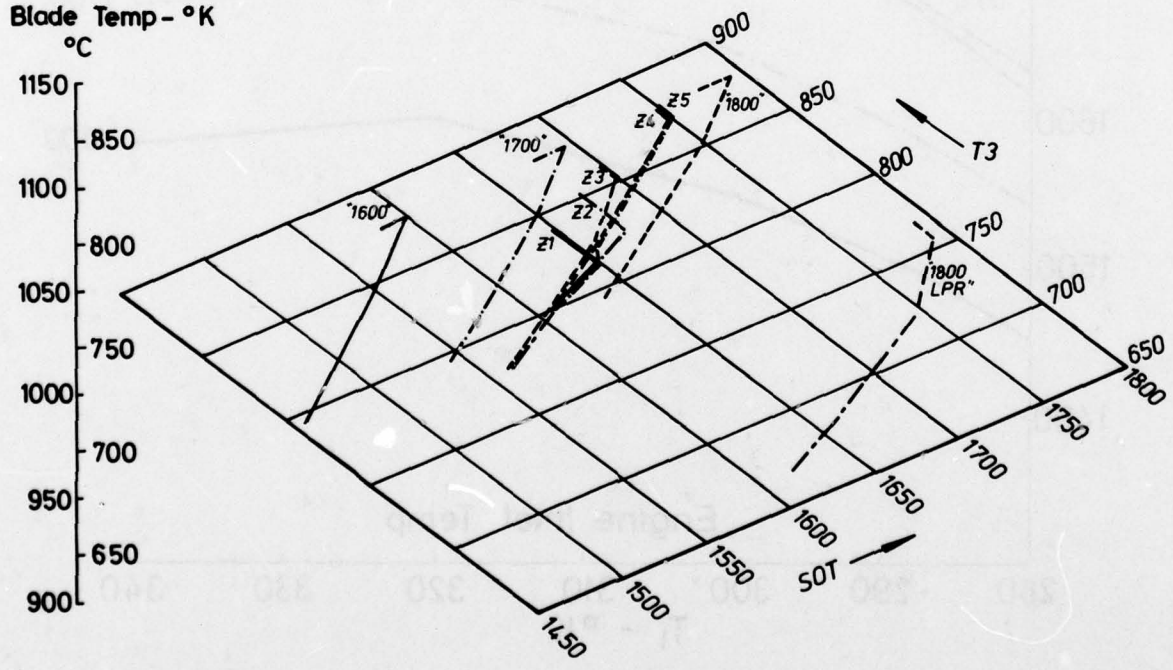

Fig.3 Blade mean temperature

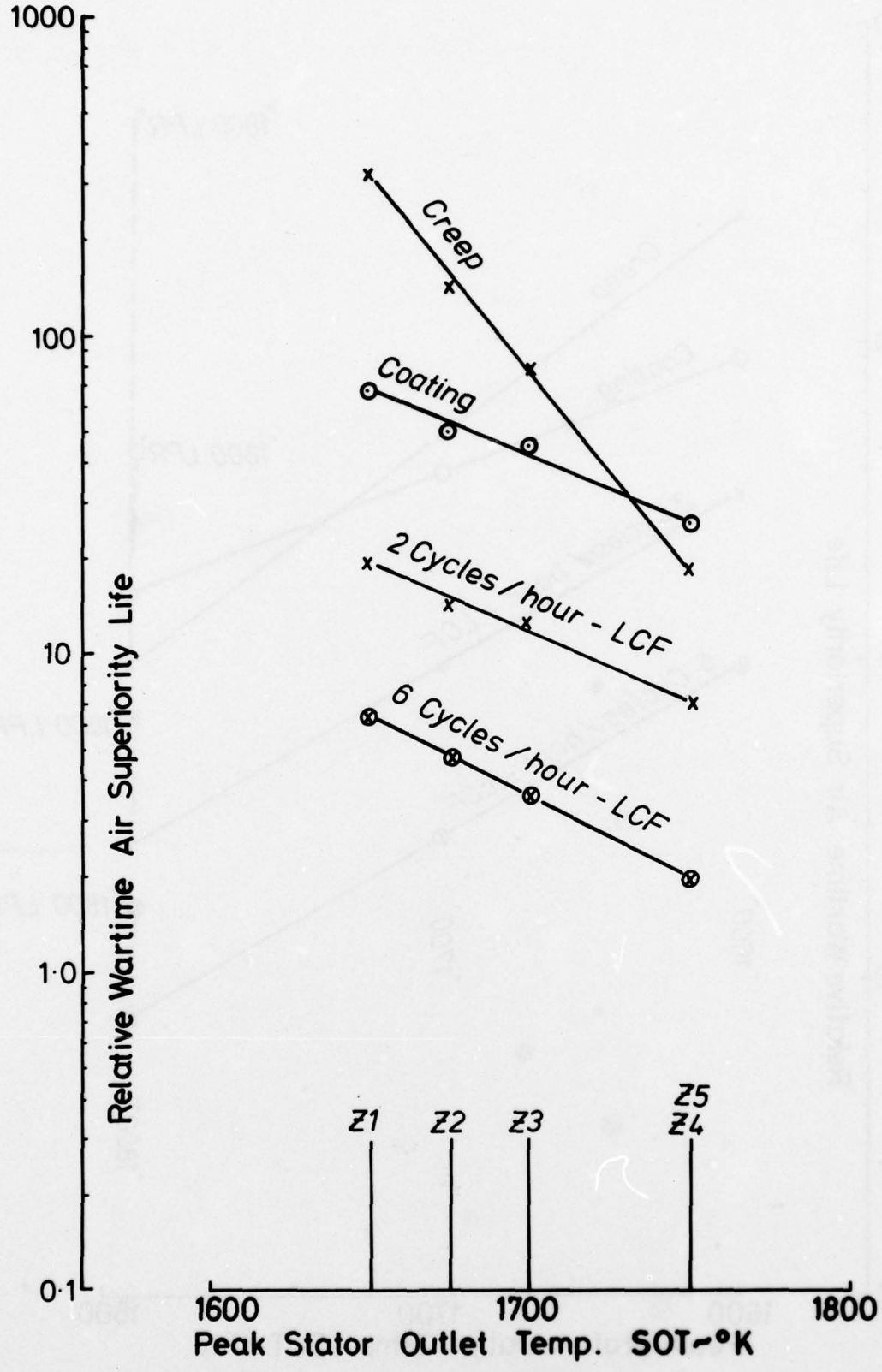

Fig.4 Wartime air superiority life vs peak S.O.T.
Effect of engine rating method

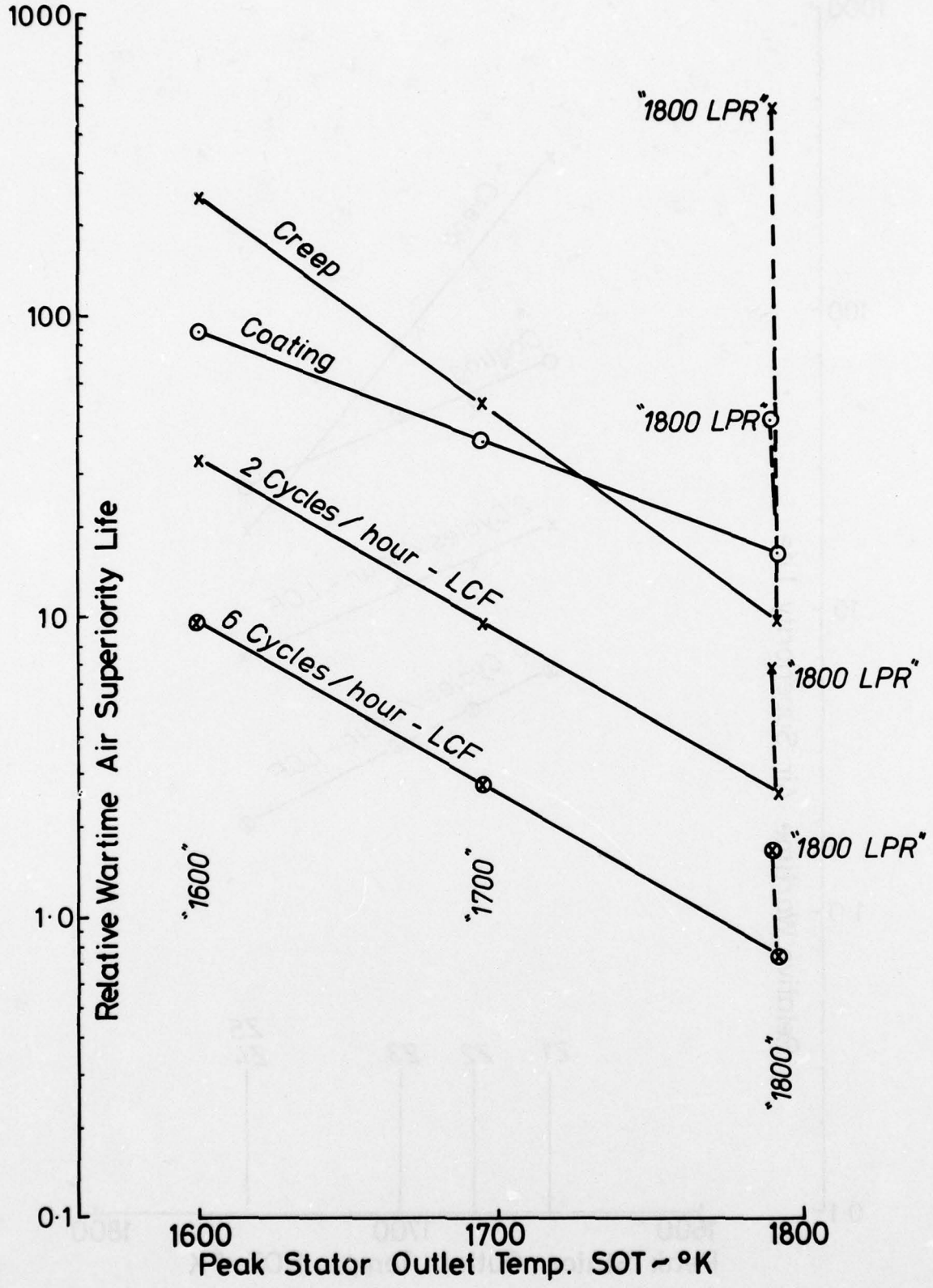

Fig.5 Wartime air superiority life vs peak S.O.T.
Effect of overall pressure ratio

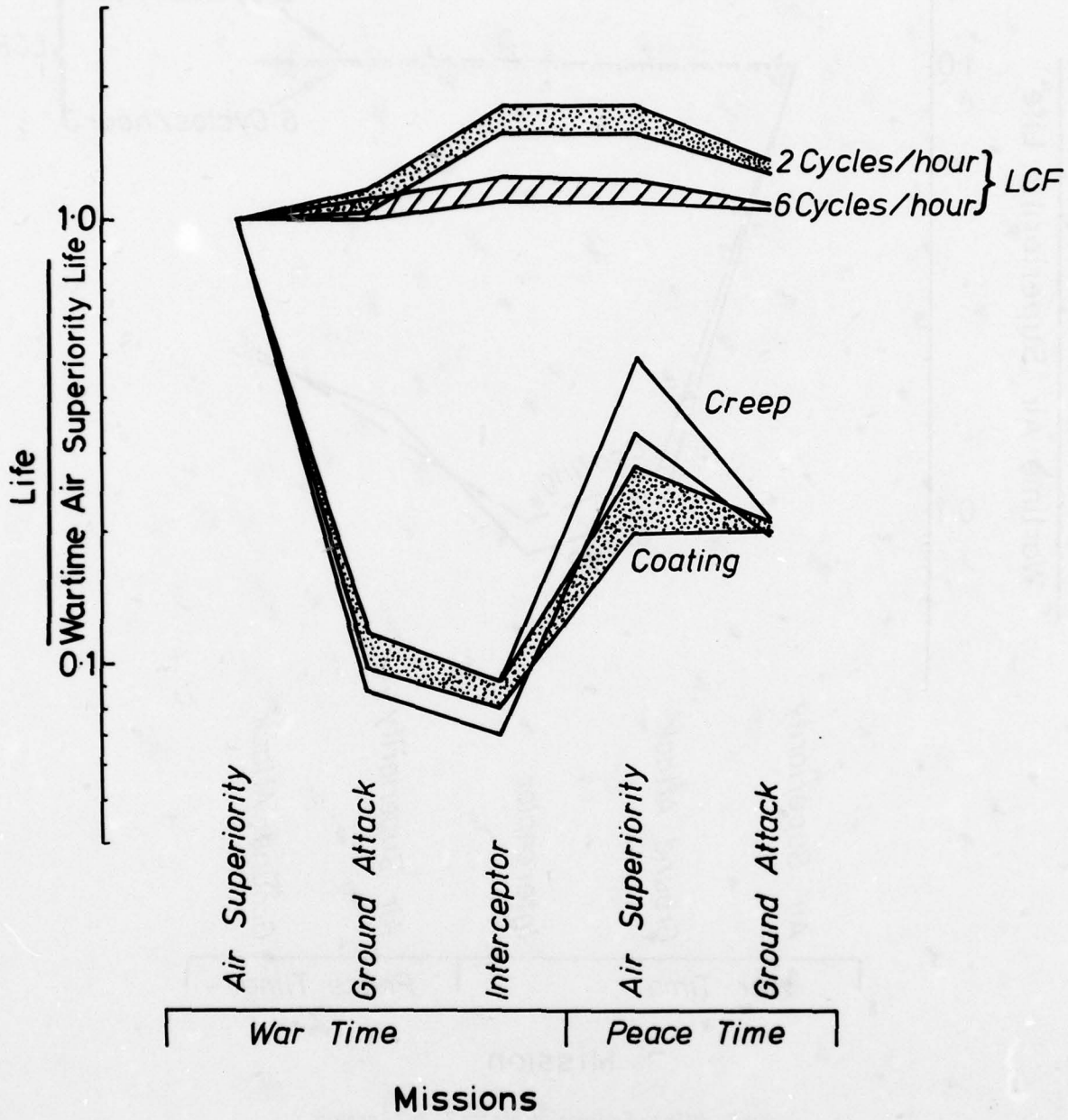

Fig.6 Effect of mission on life for
Z3–Z5, "1800, 1700, 1600, & 1800LPR" engines

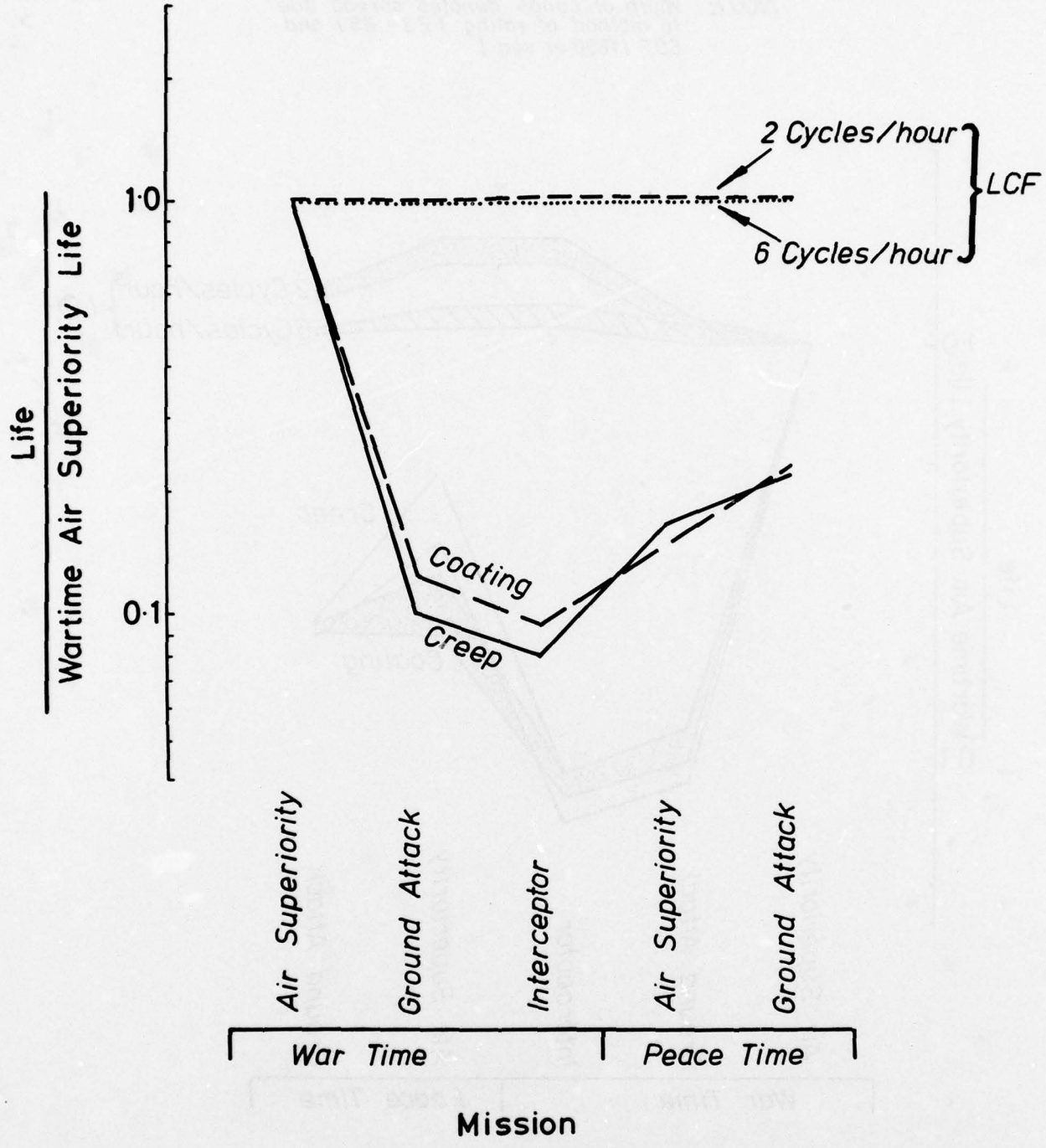

Fig.7 Effect of mission on life for Z1 & Z2 engines

DISCUSSION

E.E.Covert, US

The authors are to be congratulated for a sharp delineation of the effects of mission profile on engine life. I hope our customers can be made aware of the consequences of the change in mission upon the spare parts and maintenance requirement of engines. I wish them well in communicating with our military customers.

I would like to ask the authors if they used methods of fracture mechanics in estimating LCF life or coating life?

Author's Reply

Whilst there is interest in methods of fracture mechanics for possible future use, such methods are not currently used by us in estimating the lives of turbine blades.

PROBLEMES DES HAUTES TEMPERATURES DANS LES PETITES TURBOMACHINES

par
P. BELAYGUE
TURBOMECA
64320 Bizanos
France

RESUME

Aprés avoir précisé le domaine de puissance des petites turbomachines aéronautiques et rappelé les objectifs de développement des moteurs de cette taille, l'auteur présente les répercussions de l'augmentation de la température à l'entrée de la turbine.

Cette augmentation de température qui s'accompagne d'un accroissement du rapport de pression,concerne tous les composants, aussi bien le compresseur que la chambre de combustion et la turbine.

Mais cette évolution, souhaitée pour l'amélioration des performances,comporte des limitations ; non seulement métallurgiques et technologiques mais aussi aérodynamiques et thermodynamiques. Elles sont analysées en fonction des faibles dimensions des composants.

GENERALITES

On désigne par petite turbomachine, une turbomachine de faible puissance, en général inférieure à 1500 kW.

La puissance d'une turbine à gaz est définie par les quatre paramètres suivants :

- le débit d'air,
- le taux de compression,
- la température à l'entrée de la turbine,
- le rendement des divers composants.

Le débit réduit à l'entrée de la turbine, fonction à la fois du débit d'air, de la température à l'entrée de la turbine et de la pression maximale de cycle, est donc représentatif du niveau de puissance d'une turbomachine.

La hauteur de pale du distributeur du premier étage de turbine,directement fonction du débit réduit à l'entrée de la turbine donne une bonne idée de la véritable taille d'une turbomachine.

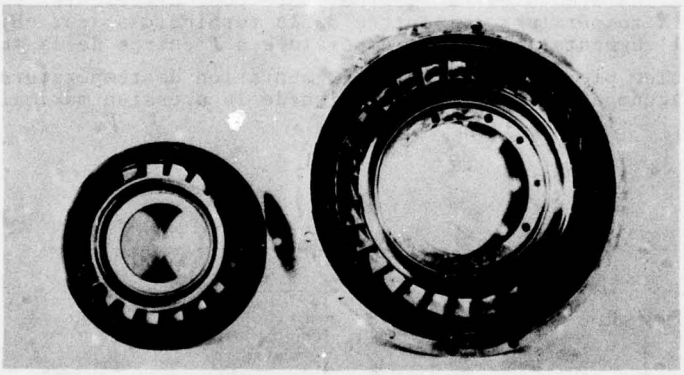

DISTRIBUTEUR HP ARRIEL
h = 14 mm
ϕ_i = 130 mm

DISTRIBUTEUR HP MAKILA
h = 20.5 mm
ϕ_i = 212 mm

Figure 1

La figure 1 donne deux exemples de distributeurs de turbine Haute Pression.

- le distributeur HP du turbomoteur à turbine libre ARRIEL de 480 kW de puissance sur l'arbre dont la hauteur de pale est de 14 mm.
- le distributeur HP du turbomoteur à turbine libre MAKILA de 1325 kW de puissance sur l'arbre dont la hauteur de pale est de 20,5 mm.

Ces deux machines situent les limites inférieures et supérieures de la gamme de puissance qui nous concerne.

DEVELOPPEMENT DES TURBOMACHINES

Les objectifs de tous les constructeurs sont :

- l'augmentation des puissances spécifiques (puissance fournie par unité de débit),
- la diminution des consommations spécifiques,

avec évidemment le souci permanent de réduire la masse des moteurs et d'améliorer les durées de vie.

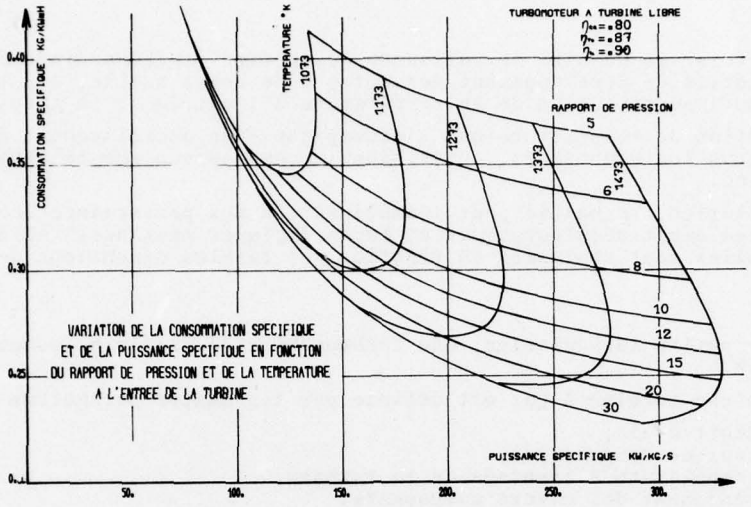

Figure 2

Comme le montre le diagramme (figure 2) donnant la consommation spécifique et la puissance spécifique d'un turbomoteur à turbine libre pour différentes valeurs du taux de compression et de la température à l'entrée de la turbine, ces deux objectifs de développement imposent l'augmentation de la température à l'entrée de la turbine.

Mais pour bénéficier pleinement de cette augmentation de température, il est nécessaire que celle-ci s'accompagne d'une augmentation de la pression maximale de cycle.

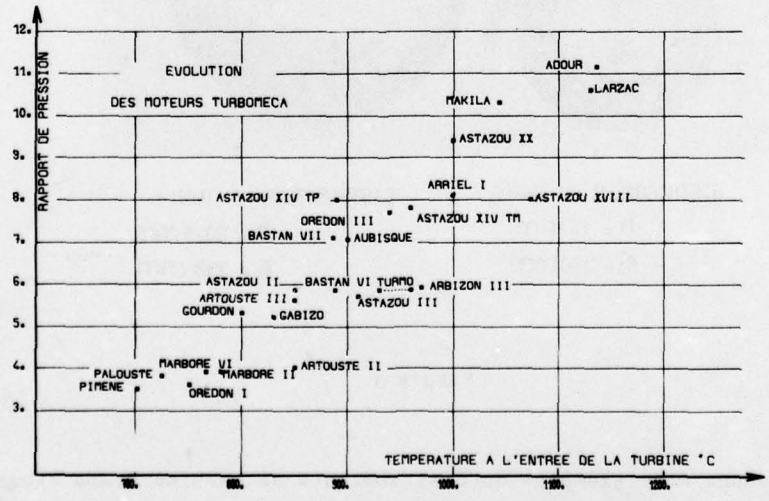

Figure 3

Ceci est bien connu et c'est l'évolution qui s'est produite chez tous les constructeurs. La figure 3 donne l'évolution du rapport de pression et de la température à l'entrée de la turbine de l'ensemble des moteurs TURBOMECA. Cette évolution simultanée des deux paramètres tend à suivre la ligne des optima dans le diagramme de la figure 2, minimum de consommation spécifique pour un maximum de puissance spécifique.

Sur le diagramme de la figure 2 on constate que si l'accroissement de puissance spécifique reste important au fur et à mesure que la température à l'entrée de la turbine augmente, au delà de 1473 °k, l'abaissement de consommation spécifique qui en résulte devient minime et à ce niveau de température le rapport de pression optimum se situe entre 12 et 14.

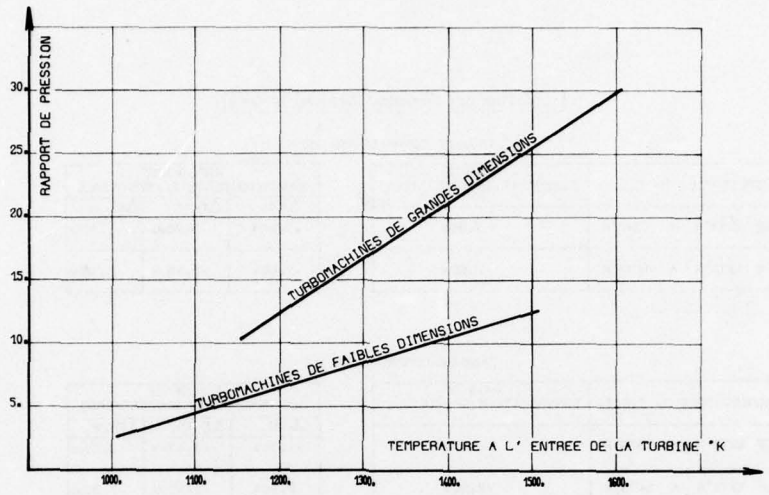

Figure 4

Dans le cas des grosses turbomachines aéronautiques, le niveau des optima n'est pas le même et l'évolution a été différente comme le montre la figure 4. Le rapport de pression optimum se situe au delà de 20 et la température souhaitée à l'entrée de la turbine est supérieure.

On peut dire que les problèmes rencontrés dans une machine ayant un débit d'air de 20 kg/s et un taux de compression de 20/1 sont analogues à ceux d'une machine de 10 kg/s avec un taux de compression de 10/1, mais comme dans le domaine de puissance qui nous concerne les débits d'air sont seulement de 1 à 4 kg/s et le taux de compression de l'ordre de 10/1, les différents problèmes que nous allons évoquer sont pour la plupart liés aux faibles dimensions géométriques de la machine.

Et ceci d'autant plus que l'évolution simultanée de la pression maximale de cycle et de la température à l'entrée de la turbine rend une "petite" turbomachine encore plus"petite".

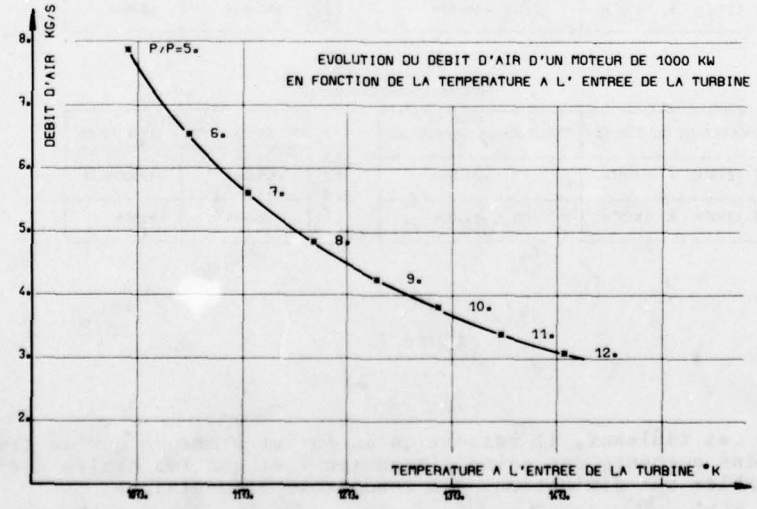

Figure 5

La figure 5 donne l'évolution du débit d'air d'une machine de 1000 kW compte-tenu de l'évolution présentée figure 3. Lorsque la température à l'entrée de la turbine passe de 1123 °k à 1473 °k, le débit d'air de la machine est divisé par 2.

Le diagramme donnant les évolutions de puissance spécifique et de consommation spécifique présenté figure 2, a été établi en supposant les rendements de tous les composants constants.

Les tableaux présentés figure 6 et figure 7 relatifs aux gains de consommations spécifique et de puissance spécifique que l'on peut attendre d'une augmentation de la température, font apparaitre également les variations des rendements élémentaires et les pertes thermodynamiques susceptibles de réduire ou d'anihiler ces gains.

EVOLUTION DES CONSOMMATIONS SPECIFIQUES

TAUX DE COMPRESSION: 10

AUGMENTATION DU T.E.T.	GAIN DE CONSOMMATION SPECIFIQUE	INFLUENCE DES RENDEMENTS ELEMENTAIRES		
		Δ CS	$\Delta\eta$ TG	$\Delta\eta$ CR
DE 1273°K A 1373°K	-3.80%	+3.80%	-3.20pts	-3.35pts
DE 1373°K A 1473°K	-2.60%	+2.60%	-2.65pts	-2.75pts

TAUX DE COMPRESSION: 12

AUGMENTATION DU T.E.T.	GAIN DE CONSOMMATION SPECIFIQUE	INFLUENCE DES RENDEMENTS ELEMENTAIRES		
		Δ CS	$\Delta\eta$ TG	$\Delta\eta$ CR
DE 1273°K A 1373°K	-4.50%	+4.50%	-3.45pts	-3.65pts
DE 1373°K A 1473°K	-2.90%	+2.90%	-2.70pts	-2.90pts

Figure 6

EVOLUTION DES PUISSANCES SPECIFIQUES

TAUX DE COMPRESSION: 10

AUGMENTATION DU T.E.T.	GAIN DE PUISSANCE SPECIFIQUE		INFLUENCE DES RENDEMENTS ELEMENTAIRES	
			$\Delta\eta$ TG=-5 PTS	$\Delta\eta$ CR=-5 PTS
DE 1273°K A 1373°K	+21.70%	Δ PUISSANCE SPECIFIQUE	+14.30%	+11.50%
DE 1373°K A 1473°K	+18.00%		+12.00%	+9.60%

TAUX DE COMPRESSION: 12

AUGMENTATION DU T.E.T.	GAIN DE PUISSANCE SPECIFIQUE		INFLUENCE DES RENDEMENTS ELEMENTAIRES	
			$\Delta\eta$ TG=-5 PTS	$\Delta\eta$ CR=-5 PTS
DE 1273°K A 1373°K	+23.50%	Δ PUISSANCE SPECIFIQUE	+15.20%	+12.00%
DE 1373°K A 1473°K	+19.00%		+12.60%	+9.90%

Figure 7

De l'examen de ces tableaux, il ressort qu'au fur et à mesure que la température à l'entrée de la turbine augmente les gains s'amenuisent et que les cycles deviennent de plus en plus vulnérables aux diminutions des rendements élémentaires.

Or, comme nous le verrons, dans le cas d'une augmentation simultanée des pressions et des températures, les causes de diminution des rendements des composants sont nombreuses.

REPERCUSSIONS DE L'AUGMENTATION DE TEMPERATURE SUR LES DIVERS COMPOSANTS

L'accroissement de température devant turbine affecte le dimensionnement de tous les composants de la machine, la turbine bien sûr mais aussi le compresseur et la chambre de combustion. Ceci pour deux raisons essentielles :

- d'une part, parce que l'augmentation de température s'accompagne d'une augmentation du taux de compression et pour une puissance donnée d'une diminution du débit d'air,
- d'autre part, parce qu'on cherche dans les turbomachines à utiliser la totalité des possibilités des matériaux dans toutes les parties de la machine.

Le compresseur.

Contrairement aux grosses turbomachines aéronautiques qui utilisent des compresseurs axiaux multiétages, dans les petites turbomachines, la configuration qui prévaut pour les compresseurs est celle qui consiste à utiliser un étage de compression centrifuge et n étages axiaux, le nombre d'étages axiaux allant en augmentant avec le taux de compression.

Les justifications de ce choix sont les suivantes :

- diminution du nombre de composants
- impossibilité, dans ces petites dimensions, d'obtenir un rendement meilleur d'un compresseur axial multiétages.

A titre d'exemple, pour une machine de 1000 kW la figure 8 donne en fonction du taux de compression les domaines respectifs des configurations : 1 centrifuge seul, 1 axial + 1 centrifuge, 2 axiaux + 1 centrifuge, 3 axiaux + 1 centrifuge... et l'évolution des rendements qui en résulte.

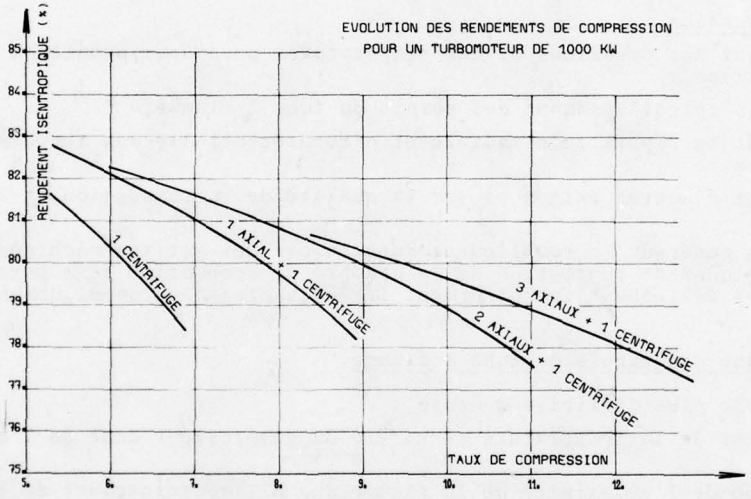

Figure 8

Cette répartition des domaines relatifs aux diverses configurations peut être différente suivant la conception générale de la machine. Par exemple, pour un matériau donné et une durée de vie fixée, les vitesses périphériques admissibles pour le compresseur centrifuge sont supérieures dans le cas des moteurs qui ne nécessitent pas un arbre coaxial pour la transmission du mouvement. D'où, la possibilité dans ce cas là d'augmenter le rapport de pression du compresseur centrifuge et donc de reculer l'adjonction d'un étage de compresseur axial supplémentaire.

La figure 9 donne les limites approximatives des vitesses périphériques admissibles, pour différents matériaux, dans les deux configurations de moteur.

On constate que pour une puissance donnée, malgré l'adjonction d'étages de compression supplémentaire, le rendement isentropique global a tendance à diminuer.

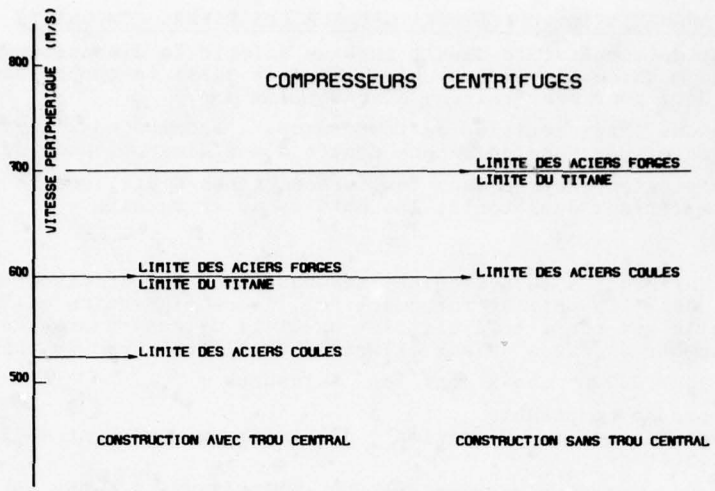

Figure 9

La chambre de combustion.

L'accroissement des pressions et des températures pose deux problèmes pour les chambres de combustion :

- l'optimisation du refroidissement des parois du tube à flamme,
- l'optimisation de la répartition radiale et circonférentielle des températures à la sortie de la chambre

auxquels s'ajoutent d'autres exigences sur la qualité de la combustion et le niveau de pollution.

Ces problèmes généraux se compliquent dans le cas des petites machines soit pour des raisons spécifiques de conception de la chambre de combustion soit parce que les solutions habituelles deviennent techniquement irréalisables ou économiquement inconcevables.

Tenue thermique des parois du tube à flamme.

Elle est rendue plus difficile à cause :

. de l'accroissement de la température en sortie du compresseur donc de l'air de refroidissement
. de l'augmentation de l'émissivité de la flamme due à l'accroissement de la formation de particules de carbone consécutive à l'élévation de pression
. de l'accroissement de l'apport de chaleur dans la chambre (croissance plus rapide de la température à l'entrée de la turbine que de la température en sortie du compresseur).

Bien que le volume de la chambre de combustion et donc la surface à refroidir diminue le débit d'air utilisable pour le refroidissement des parois est plus faible pour de multiples raisons comme :

. la diminution du débit d'air global
. la nécessité d'avoir pour des critères de pollution (oxydes d'azote en particulier) une zone primaire pauvre avec excès d'air
. la nécessité de disposer d'un débit d'air suffisant dans la zone de dilution pour contrôler le profil de température.

La présence d'un compresseur centrifuge qui conditionne en partie le maitre couple et la nécessité de réduire la longueur de l'arbre entre le compresseur et la turbine imposent des types de chambre différents des chambres annulaires des gros moteurs.

Le refroidissement de ces tubes à flamme est rendu plus difficile par leur petite taille, les faibles vitesses de l'air et le chemin tortueux qu'il parcourt entre le tube à flamme et les carters.

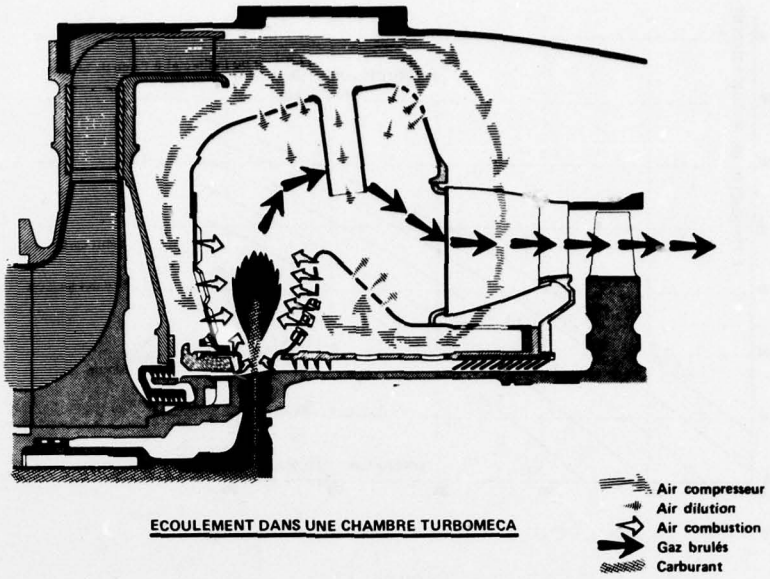

ECOULEMENT DANS UNE CHAMBRE TURBOMECA

Figure 10

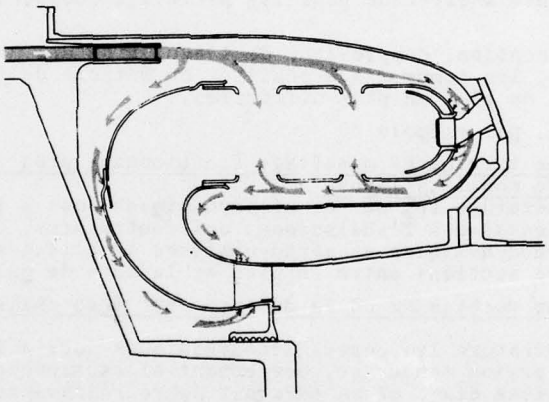

CHAMBRE DE COMBUSTION A FLUX INVERSE

Figure 11

Champ de température en sortie de chambre.

Le profil radial de température sur une petite turbomachine est fortement affecté par le film d'air utilisé pour le refroidissement des parois du tube à flamme qui occupe en sortie du distributeur un pourcentage important de la hauteur de veine et a tendance à donner un profil de température bombé.

L'homogénéité circonférentielle nécessaire pour éviter les déformations excessives des enveloppes et pour contrôler le jeu en bout d'aube est limitée par le nombre des injecteurs déterminé par la taille minimum réalisable.

Le principe d'injection centrifuge TURBOMECA permet de résoudre ce problème et donne une excellente homogénéité circonférentielle sur les parties fixes mais pose celui des tolérances de fabrication sur la roue d'injection pour ne pas engendrer de points chauds sur les parties mobiles.

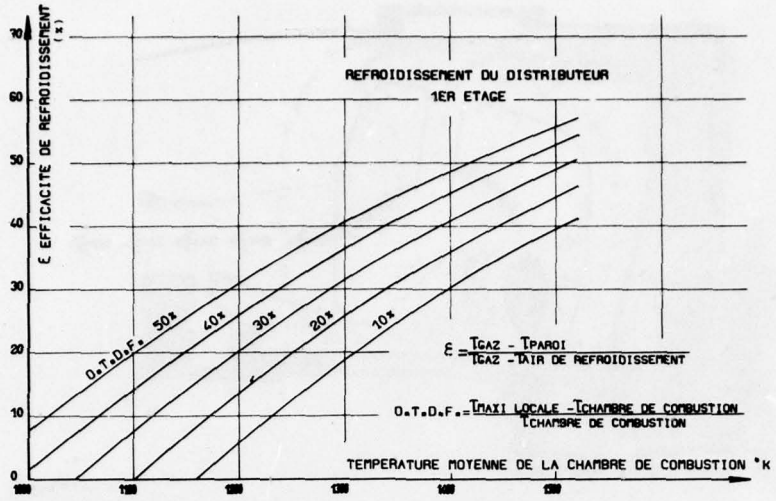

Figure 12

Néanmoins, même si les valeurs de RTDF et de OTDF sont conservées lorsque la température à l'entrée de la turbine augmente, comme le montre la figure 12, les efficacités de refroidissement à réaliser sur les turbines sont de plus en plus importantes.

La turbine.

Suivant le niveau de puissance, de température à l'entrée de la turbine et de taux de compression, la détente s'effectue pour les petites turbomachines dans 2, 3 ou 4 étages de détente.

Au stade de la conception, compte-tenu de l'évolution des matériaux et des techniques de refroidissement, les compromis à réaliser en matière de turbine doivent être revus fréquemment et sont de plus en plus difficiles.

Ces compromis sont, par exemple :

- Dans le cas d'une turbine HP monoétage fonctionnant près de la limite où le refroidissement de la roue mobile s'impose :
à partir de quelle température les pertes aérodynamiques dues à l'épaississement relatif du pied de la pale, nécessaire à l'abaissement des contraintes, deviennent-elles supérieures aux pertes thermodynamiques et aérodynamiques associées au refroidissement d'une pale ayant un rapport de sections entre le pied et la tête de pale plus faible ?

- Dans le cas d'une turbine HP où la détente peut être envisagée avec un ou deux étages de turbine :
à partir de quelle température les pertes aérodynamiques dues à l'augmentation de charge aérodynamique dans la version monoétage, deviennent-elles supérieures à celles dues au refroidissement du deuxième étage et au surcroit de refroidissement du premier étage dans la version à deux étages ?

- Dans le cas d'une turbine HP de deux étages, dont le deuxième étage fonctionne près de la limite où le refroidissement de la roue mobile deuxième étage est nécessaire :
à partir de quelle charge aérodynamique sur le premier étage, dont l'augmentation vise à éviter le refroidissement du deuxième étage, les pertes deviennent-elles supérieures à celles dues au refroidissement du deuxième étage dans le cas d'une répartition des travaux entre les deux étages plus favorable au rendement de l'ensemble ?

On peut dresser à partir de ces considérations une liste des difficultés que l'on rencontre dans l'étude aérodynamique et thermique de ces turbines ; difficultés liées aux faibles dimensions et aux hautes pressions et hautes températures dont elles doivent être capables.

• L'optimisation des paramètres de définition de la turbine en vue de faciliter la résolution des problèmes thermiques, que ce soit par exemple l'augmentation de la charge aérodynamique ou la diminution de degré de réaction qui permettent de diminuer la température totale relative à l'entrée de la roue mobile, n'est pas en général favorable à l'amélioration ou au maintien des performances. Bien sûr des progrès en aérodynamique sur la maitrise des écoulements transsoniques et la réalisation de déviations plus importantes dans les aubages permettent et permettront d'augmenter la charge des turbines. Et ces progrès peuvent être mis à profit pour réduire la température des pales.

• Mais cette augmentation de charge, lorsqu'elle est possible, s'accompagne d'une réduction de la hauteur des pales. Or la faible hauteur de la pale donne de plus en plus d'importance aux jeux en sommet d'aube et ce d'autant plus que la charge est grande. Pour ces petites machines où les aubes à talon sont en général inapplicables, une augmentation de 1 % du jeu relatif en sommet d'aube entraine une chute de rendement de 1,5 point. Et pour la turbine haute pression d'un turbomoteur de 1000 kW, 1 % de jeu relatif ne représente que 0,15 mm.

Le bon contrôle des dilatations des parties fixes et mobiles pour maintenir un jeu minimum dans toutes les conditions de fonctionnement devient donc essentiel.

• La faible hauteur de veine rend aussi très difficile la maitrise du profil de température qui en cas de détérioration peut affecter profondément la durée de vie des aubages. Or les fuites entre chambre de combustion et distributeur, ou entre distributeur et anneau de roue, ou les débits nécessaires pour éviter l'entrée de gaz chauds à l'intérieur de la machine, dégradent le profil de température.

A titre d'exemple, la figure 13 montre la déformation du profil de température qu'entraine une fuite de 1 % du débit compresseur en tête de pale et de 1 % en pied de pale, ces fuites restant localisées sur 20 % de la hauteur de la veine. Il en résulte pour une même température moyenne, une augmentation de la température totale à l'entrée de la roue mobile de 15 degrés.

Ces débits de ventilation interne sont souvent conditionnés par des jeux de labyrinthe dont le contrôle dans toutes les conditions de fonctionnement devient lui aussi impératif mais dont la valeur minimale n'évolue pas comme la taille de la machine. Ils prennent donc davantage d'importance dans une petite machine.

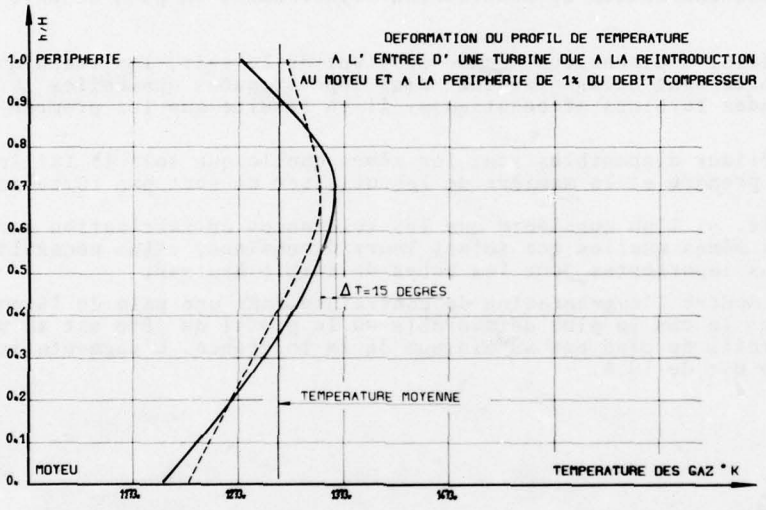

Figure 13

• Les difficultés d'introduction des techniques de refroidissement des parties mobiles dans les petites turbomachines et la relative modération des objectifs de température font que jusqu'à présent la majorité des moteurs construits en série n'ont pas de refroidissement des pales de la turbine haute pression, la température à l'entrée de la turbine étant limitée aux environs de 1325 °k. Néanmoins, la prochaine génération de petites turbines, pour accroitre les puissances spécifiques, aura des températures à l'entrée des turbines de l'ordre de 1425 °k à 1475 °k. A ces températures, un refroidissement des pales mobiles est nécessaire.

Les contraintes que cela impose sont nombreuses et toutes préjudiciables au rendement de la turbine.

Dans le cas du refroidissement par convection à l'intérieur de canaux radiaux, l'épaisseur minimale de paroi à respecter et le diamètre minimum réalisable pour les passages d'air de refroidissement sont des paramètres presque indépendants de la taille du moteur. Pour les pales de petites dimensions, ceci est très pénalisant.

Pour les longueurs de corde inférieures à 20 mm la section totale des passages d'air tend à devenir négligeable et la longueur non refroidie du côté du bord de fuite très importante.

La nécessité de refroidir les aubes impose donc des cordes longues d'où un nombre de pales plus faible, des épaisseurs relatives importantes et des bords de fuite épais, contraintes qui ne répondent pas exactement aux souhaits des aérodynamiciens.

D'autre part, sous peine d'accroitre les contraintes de façon prohibitive, on ne peut augmenter la hauteur de pale dans les mêmes proportions que la corde, on atteint des rapports hauteur de pale/corde défavorables. Ceci tend à accroitre les pertes secondaires

et à dégrader le rendement de détente.

● A ces pertes aérodynamiques imposées par la nécessité de refroidir les pales s'ajoutent les pertes thermodynamiques et aérodynamiques associées aux débits d'air de refroidissement.

.. Pertes thermodynamiques : tout air de refroidissement réintroduit dans la veine à une pression plus basse qu'au niveau du prélèvement est évidemment moins apte à fournir du travail dans la turbine. D'où pour une même température à l'entrée, une diminution de la puissance et une augmentation de la consommation spécifique.

Pour le refroidissement du distributeur HP, quelle que soit la configuration de la chambre de combustion, il est nécessaire de prélever l'air en sortie du compresseur. Par contre, pour les éléments suivants, puisque les pressions statiques vont en diminuant on peut prélever l'air à des pressions plus basses. Deux avantages à cela : travail de compression plus faible et température plus basse de l'air de refroidissement.

Cependant, dans bien des cas et plus particulièrement pour les petites turbomachines pour des raisons de simplicité de construction et de commodité, on utilise pour tous les refroidissements la même source en sortie du compresseur, ce qui tend à augmenter les pertes thermodynamiques.

.. Pertes aérodynamiques : les pertes liées aux réintroductions des débits de refroidissement dans la veine dépendent beaucoup de l'endroit où ils sont réintroduits.

Si les performances de la turbine ne sont pas trés sensibles aux réintroductions au niveau du distributeur, il n'en est pas de même pour les réintroductions sur les pales mobiles surtout lorsqu'elles ont lieu sur l'extrados ou en sommet de pale avec des aubes sans talon.

Les pertes dues aux débits de ventilation réintroduits en pied de pale sont aussi trés élevées.

Du fait des faibles dimensions, comme on vient de le voir, les techniques de refroidissement applicables sont nécessairement moins sophistiquées que celles largement répandues dans les grandes turbines aéronautiques. Il en résulte que les progrés à attendre sont plus limités.

● Si les matériaux disponibles sont les mêmes quelle que soit la taille du moteur, les précautions à prendre et la manière de les utiliser ne sont pas forcément identiques.

.. Par exemple, si l'on considère que les tolérances de fabrication sur l'épaisseur des aubes sont les mêmes quelles que soient leurs dimensions, elles nécessitent de prendre des marges plus importantes pour les aubes de faible hauteur.

La figure 14 montre l'augmentation de contrainte dans une pale de 15 mm de hauteur qui se produit dans le cas le plus défavorable où le profil de tête est au maximum de la tolérance et le profil de pied est au minimum de la tolérance. L'augmentation de contrainte en pied de pale est de 10 %.

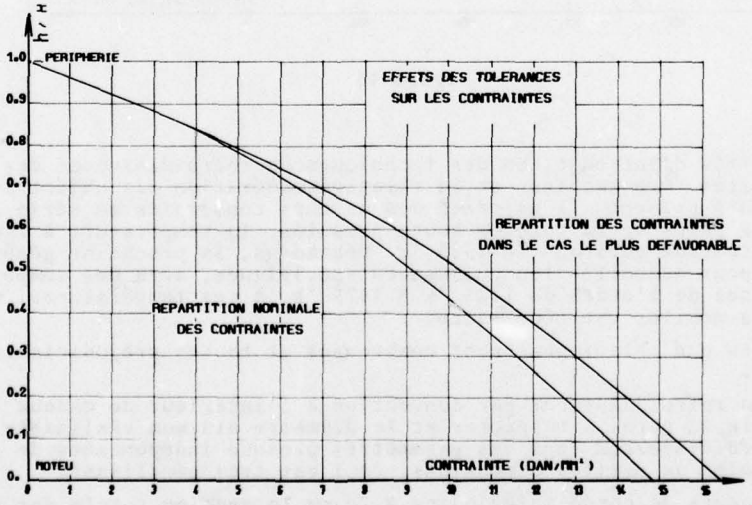

Figure 14

.. Un autre aspect bien spécifique des petites turbomachines concerne l'utilisation dans certains cas de roues de turbine monobloc.

Si l'on compare la technique du "monobloc" avec celle des pales rapportées, généralisée dans le cas des grosses turbomachines, elle présente les avantages et les inconvénients suivants :

- elle est généralement moins couteuse,
- elle est avantageuse pour le devis de masse, car elle n'exige pas de renforcement du disque comme dans le cas des pales rapportées,
- elle ne permet pas de séparer les fonctions "pales" de celles des "disques", pièces soumises à des conditions de sollicitation très différentes, et d'adopter les techniques de refroidissement possibles avec les pales rapportées,
- elle impose le changement complet de la roue dans le cas de rupture d'aube.

Ce sont les deux premiers arguments économique et technique qui justifient l'introduction, lorsque cela est possible, de la technique "monobloc".

L'augmentation croissante des températures élimine progressivement la solution monobloc forgée dans les parties les plus chaudes, les matériaux de forge étant limités en température, au profit de la solution monobloc coulée.

Néanmoins, le problème de l'application de la fonderie de précision à une roue de turbine est délicat. En effet, une telle pièce est soumise selon la zone considérée à des conditions de sollicitation très différentes : (figure 15) fatigue oligocyclique dans le moyeu, fatigue thermique et fluage dans la jante, fluage à haute température dans la pale.

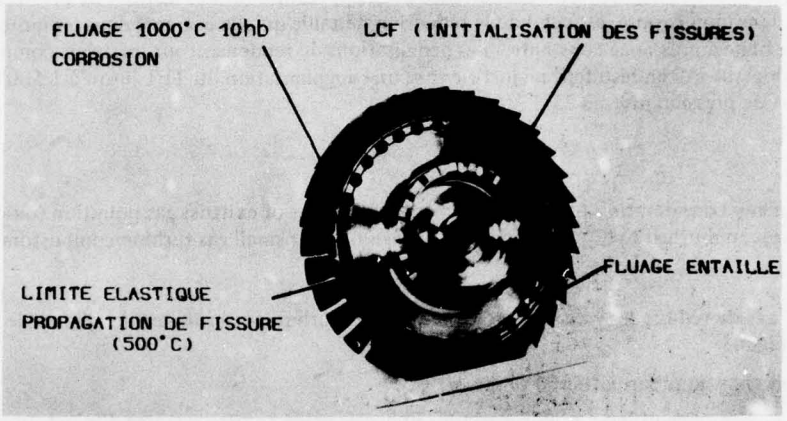

ROUE DE TURBINE : SOLLICITATIONS PRINCIPALES

Figure 15

En particulier, pour une petite machine, en raison du fort gradient thermique à la jante, les problèmes de fatigue thermique sont particulièrement aigus pour une roue monobloc. Pour les diminuer, on est amené à réaliser dans les interpales des fentes radiales se terminant par des trous (figure 15).

Par suite de ces impératifs, le choix du matériau est limité aux superalliages à base de Nickel. Or, compte-tenu de la géométrie particulière d'une roue de turbine et de la tendance à la cristallisation grossière de ces alliages de fonderie dans les parties épaisses, on peut s'attendre à obtenir une structure à gros grains dans le moyeu, où les problèmes de fatigue oligocyclique sont les plus sévères et un grain fin dans les pales, zones pour lesquelles la résistance au fluage est prépondérante. Cette situation est d'autant plus accusée, que la partie du disque est plus épaisse et que les pales sont plus nombreuses, plus longues et plus fines.

D'autre part, les microretassures sont également plus probables dans les zones massives donc au niveau du moyeu, là où elles sont le plus difficile à détecter lors du contrôle radiographique et où leur effet risque d'être le plus nocif (résistance à la fatigue oligocyclique).

CONCLUSION

Après ce tour d'horizon des problèmes liés à l'augmentation de température dans les petites turbomachines, on peut conclure en disant :

- que pour les futures machines qui fonctionneront à des températures et des pressions plus élevées un soin tout particulier doit être apporté à la réduction des pertes de toutes sortes si l'on veut que des gains sensibles soient enregistrés et que ce souci doit devenir un des facteurs prédominants au stade de la conception

- qu'il existe une température au-delà de laquelle il n'est pas souhaitable de fonctionner, la complexité technologique et par conséquent le prix étant considérablement accrus, et la fiabilité pouvant être affectée

- que le niveau de température ne doit pas être le seul critère de jugement du degré de perfectionnent atteint, qu'il faut plutôt considérer le rendement effectif obtenu sur l'arbre pour une température donnée avec une durée de vie convenable.

DISCUSSION

N.F.Rekos, US

What do you consider to be the major technical problems that prohibit using the very high temperature (1500°C) and the very high pressures (25 atmos.) common to large gas turbine engines to small gas turbine engines?

Author's Reply

Le problème essentiel de l'augmentation simultanée des températures et des niveaux de pression, comme j'ai essayé de le montrer dans mon exposé, est celui de la réduction de taille qu'elle entraine dans les moteurs de petite puissance, si on raisonne à puissance constante. Les pénalisations de rendement sur les divers composants et la complexité technologique qui en résultent ne justifient ni une augmentation du TET jusqu'à 1 500°C, ni une augmentation du rapport de pression jusqu'à 25/1.

N.F.Rekos, US

Have you given any consideration to the environmental problems of exhaust gas pollution (oxides of nitrogen, carbon monoxide, unburned hydrocarbons) in the design of your small gas turbine combustors?

Author's Reply

Nous avons essayé de réduire les émissions de CO et d'hydrocarbures imbrûlés en améliorant le rendement de combustion à bas régime.

Les résultats obtenus nous permettent d'observer:

(a) Un niveau extrêmement bas en hydrocarbures imbrulés grâce à notre système d'injection centrifuge (indice d'émission $< 0{,}5$ sur des moteurs récents au régime de ralenti).

(b) Un niveau trés bas en monoxyde de carbone (indice d'émission de l'ordre de 25 au régime de ralenti).

(c) Un niveau acceptable en oxydes d'azote (indice d'émission de l'ordre de 10 au régime de décollage).

Malheureusement, ce niveau a tendance à croître sur les moteurs récents compte-tenu:

- de l'accroissement des températures à l'entrée de la chambre
- des modifications de la chambre destinées à diminuer les émissions de CO et d'hydrocarbures imbrulés.

Nous envisageons un programme de recherche pour réduire les Nox sur nos futurs moteurs.

Nota: Les indices d'émission donnent le rapport de la masse en g de polluant émis à la masse en kg de carburant consommé.

PROGRESS IN ADVANCED HIGH TEMPERATURE TURBINE MATERIALS, COATINGS, AND TECHNOLOGY

by
John C. Freche
Associate Chief, Materials and Structures Division
and
G. Mervin Ault
Director of Energy Programs
National Aeronautics and Space Administration
Lewis Research Center
21000 Brookpark Road
Cleveland, Ohio 44135,U.S.A.

SUMMARY

Advanced materials, coatings, and cooling technology are the keys to achieving improved performance via high cycle operating temperatures, lighter structural components, and adequate resistance to the various environmental factors associated with aircraft gas turbine engines. Significant progress has recently been made in many high temperature material categories, in providing coating protection against oxidation, hot corrosion and erosion, and in turbine cooling technology by the industrial community, DOD and NASA. The material categories include metal matrix composites, superalloys, directionally solidified eutectics, and ceramics. These material categories as well as coatings and recent turbine cooling developments are reviewed, the current state-of-the-art identified, and an assessment, when appropriate, of progress, problems, and future directions is provided.

INTRODUCTION

The keys to improved aircraft turbine engine performance are the development of advanced high temperature materials, the coatings required to protect them adequately against the oxidation, corrosion, and erosion encountered in the gas turbine environment, and improved cooling technology to achieve higher cycle operating temperatures. Consideration of the various turbine components indicates the nature of the improvements that are needed and the specific benefits that can result (Fig. 1). Thus, by increasing the strength of intermediate temperature materials that are used for turbine disks, increased rotor speeds and fewer turbine stages can be achieved with resultant reductions in turbine engine weight and cost. Similarly, increases in allowable turbine blade and stator vane temperatures will permit operation at higher cycle temperatures or with reduced cooling air. The resultant benefits are increased power output, decreased fuel consumption, and/or decreased maintenance cost.

An important new emphasis in high temperature materials technology is the development of coatings. This takes on a greater degree of importance today than before. In part, environmental protection has become more difficult to provide because such significant strides are being made in increasing the high temperature strength of materials. Unfortunately such strength increases usually go hand in hand with decreased oxidation resistance. In addition, there is the requirement for petroleum conservation and the increasing cost of petroleum products. Aircraft gas turbine engines typically use a clean kerosene-type fuel. But the cost of such fuels is increasing dramatically, by a factor of 3 in the past 4 years. It may become necessary to use cheaper cuts from petroleum or even residuals. The impurities present in such fuels can lead to severe corrosion and erosion of turbine materials and to tolerate such fuels will necessitate greatly improved coatings for turbine vane and blade materials. Thus, the coatings problem takes on added significance.

It must be emphasized that extremely high costs are involved in bringing a new material from the laboratory stage to engine usage. For example, it has been estimated by one engine manufacturer that approximately $15 million are required to bring a DS eutectic system to the point where it can be incorporated as a turbine blade in an aircraft engine. Thus, it becomes of paramount importance that the most advantageous choices be made in selecting the engine component and material to be addressed. To do this requires that careful benefit-cost analyses be made. Several NASA-sponsored benefit-cost studies (1,2,3,4) quantify the gains that can be achieved by increasing material capability for aircraft gas turbines. An example of the economic benefits of material improvements for specific engine components for a fleet of 500 subsonic commercial transport aircraft with a 3000 nautical mile range, and a load factor of 55% of the total passenger capacity of 180 is provided by the benefit-cost studies (3,4). The benefits (including return on investment and direct operating cost) over the life of the aircraft assuming the following advanced materials could be employed, would be $45 million for prealloyed powder metallurgy disks, $90 million for directionally solidified eutectic blades, and $200 million for ceramic vanes.

In this paper, the authors review the state-of-the-art of high temperature materials, coating technology, and recent turbine cooling developments as well as assess future trends, utilizing critical turbine components as a framework for discussion.

MATERIALS FOR INTERMEDIATE TEMPERATURE APPLICATION - DISKS

Prealloyed powder processing (5,6,7) holds promise for providing superalloys with increased strength for turbine disk applications. Although current PM disk alloy development is principally concerned with existing alloys such as Rene' 95 (8) and IN-100 (9), work is underway with more advanced alloys which show significant improvements in strength (Fig. 2). Even further strength increases are anticipated over the next decade. For example, for powder metallurgy processing, alloys can be specifically designed to accommodate larger quantities of strengtheners without encountering the segregation which would occur if they were cast. In this way, the feature of greater structural homogeneity resulting from the prealloyed powder process can most effectively be utilized.

Fig. 2 shows the 650°C (1200°F) yield strengths of promising candidate PM disk alloys such as AF 115 (10), IIB-7 (11), and AF2-1DA (12). These can be processed to have 650°C (1200°F) yield strengths in excess of 1380 MN/m^2 (200 ksi). Since in some advanced turbine designs consideration is being given to still higher maximum disk temperatures, it is interesting to see how the 650°C (1200°F) yield strength is affected when the PM alloys AF 115 (13), AF2-1DA (14), and IIB-11E (15)are processed to give maximum 760°C (1400°F) strength. For the first two, lower 650°C (1200°F) strengths result. This would presumably also occur for IIB-11E were data available. Thus, adequate PM disk alloy strength over a range of temperatures requires that a suitable compromise in a processing heat treatment selection be made.

In addition to improved short time strength compared to conventional forged alloys, improvements in long time creep rupture strength are also required to make PM alloys viable candidates for disks, particularly for high temperature disk applications. Significant improvements have already been obtained (Fig. 3). An important aspect to be noted, however, is that the relatively large grain size needed for high creep rupture strength calls for higher solution treatment temperatures than would be used to achieve the greater short time tensile strength. Since mechanical working effects are then annealed out, this will reduce the tensile strength. Therefore, the development of optimum processing and heat treating steps is a most important key to the development of advanced PM disk alloys.

Although significant increases in static strength are possible with PM disk alloys, further research is required to insure that advanced prealloyed powder alloys also have cyclic life improvements commensurate with their static strength improvements. It is important that early in the research for new materials-process combinations, realistic disk test cycles be used in evaluating cyclic crack initiation and crack growth behavior. It is unfortunate that we do not have available a simple low cost screening test for this purpose. However, the fluidized bed type of thermal fatigue testing which is being used extensively to rate materials with regard to thermal fatigue resistance (16) can be used to provide some measure of the relative resistance to crack initiation and measurement of crack growth rate. But the actual engine cycles cannot be reproduced in such facilities.

Decreased life cycle cost represents the greatest objective for gas turbine disks. Reductions in initial cost can be achieved by prealloyed powder processing. Fig. 4 compares this process schematically with the conventional casting and forging process. It is apparent that less starting material, fewer operational steps, and less machining is required to reach the final disk shape. For a commercial turbine disk, currently produced in large volume by forging and costing $10,000 per disk, the savings in both raw material and machining could be $2,000 (17). Of the process variations, the greatest cost reduction opportunity exists for the as-hot isostatically pressed (HIP) to near net shape approach, with a smaller cost opportunity possible for the extruded or HIP plus warm work approaches.

MATERIALS FOR HIGH TEMPERATURE APPLICATION

Low Stress - Vanes, Combustors

Several key turbine power plant components must withstand very high temperatures, but the stresses to which they are subjected are relatively low. The most promising materials for several of these applications are discussed in the next sections.

ODS alloys.- For use as turbine stator vanes, the oxide dispersion strengthened (ODS) alloys offer a significant improvement over both currently used and the most advanced conventional cast superalloys (Fig. 5). Their metal use temperature ranges up to 1230°C (2250°F) and they should see service as stator vanes within the next five years. Several of the more promising, HDA8077 (a NiCrAl with Y_2O_3), MA 754 (a NiCr with Y_2O_3) and YD-NiCrAl (a NiCrAl with Y_2O_3) are shown on the figure.

The melting point of these materials is about 1370°C (2500°F). This high melting point and the greater microstructural stability of these materials provide additional pluses compared to conventional cast superalloys for vane use. The advantage of greater overtemperature capability may be seen in Fig. 6, in which a conventionally cast MAR M-509 and a TD-NiCr vane are compared (18). These vanes were subjected to overtemperature while being tested in the same nozzle assembly of an experimental engine. The cast vanes, although cooled, melted. The uncooled TD-NiCr vanes remained essentially undamaged. Another advantage of ODS alloys for vane application is their greater thermal fatigue resistance. Some ODS alloys have shown up to 10 times greater resistance to cracking under simulated vane operating conditions than conventionally cast superalloys (18).

Combustors also fall into the category of high temperature, low stress applications where ODS alloys afford significant potential. Combustor components require formable, weldable, as well as oxidation, distortion, and thermal fatigue resistant sheet alloys. For service temperatures near 980°C (1800°F) the conventional cast and wrought alloys, Haynes Alloy 188, Inconel 617 and the developmental MERL 72 show good potential (19, 20). However, the ODS NiCrAls have a potential for a 90°C (160°F) higher temperature capability than conventional sheet materials. Manufacture of an ODS-NiCrAl sheet product has been demonstrated (21) but there are no commercial sources for sheet at present. Once the advantageous role of ODS-NiCrAl vanes is established, it is expected that attention will be focused on the manufacture of ODS-NiCrAl sheet products.

There are a number of problem areas with ODS materials which must be noted, however. Foremost is the historical one of high alloy cost (about 5 times that of conventional superalloys). Another, the low oxidation resistance of the NiCr base has largely been solved. As in virtually all instances where there is a pronounced directionality of grain structure, transverse ductility may be a problem. But this can probably be adequately handled by trading off some longitudinal strength for increased transverse ductility by process control treatments that reduce the grain structure directionality. Another problem is the creep-behavior of ODS sheet alloys for such applications as combustor components. With the increased diffusion rates at the higher temperatures for which these alloys are intended, diffusional type creep could be the major contributor to the creep process. In ODS sheet alloys, such as TD-NiCr, diffusional creep has been observed and the creep-damage by this process was shown to be severe (22), although there appears to be a threshold stress below which significant diffusional creep does not occur. This factor must be taken into consideration in engine component designs where zero creep may be required.

The problem of high cost is being addressed by the development of improved powder manufacturing techniques such as mechanical alloying (23) and current activities to scale-up for large production quantities promise substantial reductions in the cost of these materials. Simpler recrystallization techniques can be employed substituting furnace recrystallization for the more time-consuming gradient annealing. Finally, further cost reductions are anticipated by use of near-net-shape fabrication techniques such as are currently under development in a NASA-sponsored program (24). This program includes extension and forging of consolidated preforms to provide a vane geometry that requires minimal machining to final shape.

The problem of low cyclic oxidation resistance observed in the early ODS-NiCr alloys has effectively been eliminated as may be seen from Fig. 7 by changing to a NiCrAl base that includes 4 to 5 weight % aluminum. The figure shows that essentially no weight loss occurred with the NiCrAls after severe cyclic testing (r.t. to 1200°C (2200°F)) in a Mach 1 burner. Hot corrosion resistance was also significantly improved (25). The NiCrAls form an aluminum containing oxide scale which provides excellent oxidation resistance. For long time service (e.g., at least 3000 hours) however, the ODS NiCrAls may require a protective coating as will be discussed later.

Directionally solidified superalloys. -

The promising nature of the ODS alloys notwithstanding another approach, one that employs directionally solidified conventional superalloys for vanes, also shows considerable potential. As shown in Fig. 8, significantly improved thermal fatigue resistance can be achieved by directional solidification of superalloys. These results taken from (16) show orders of magnitude increases in cycles to the first observable crack for two typical high temperature, gamma prime strengthened nickel base superalloys (Mar-M 200 and NASA TAZ-8A) when they are directionally solidified as compared to their random polycrystalline form. The fluidized bed test technique previously referred to was employed in this study and the results shown are representative of those obtained with a wide variety of superalloys.

A direct comparison of the thermal fatigue resistance of directionally solidified superalloys and ODS materials was also shown (16). This indicates that TD NiCr has approximately the same thermal fatigue resistance as many of the conventionally cast (random polycrystalline structure) superalloys. The comparison must be considered as inconclusive due to the limited ODS material available for test in that study. Further evaluations are underway to provide a more definitive ranking. However, the clearly excellent thermal fatigue resistance of directionally solidified conventional superalloys suggests that such materials afford great potential for relatively early application to aircraft turbine engine stator vanes, although their current use is for high stressed turbine blades.

Ceramics. -

As shown in Fig. 5, ceramics offer the highest use temperature potential of all materials for stator vanes, on the order of 1400°C (2600°F).

Currently, the most promising ceramics appear to be Si_3N_4 and SiC. Extensive screening studies of some 35 different ceramics in the NASA Lewis Mach 1 burner (26,27) have shown them to have the most favorable thermal shock resistance. Other investigators (28-31) have also shown the superiority of Si_3N_4 and SiC. These ceramics also have excellent high temperature creep rupture properties as may be seen from Fig. 9. Commercial hot pressed Si_3N_4 (32) has substantially higher use temperature capability (approximately 1320°C (2400°F)) at stresses of approximately 50 MN/m^2 (7 ksi) which are typical of those encountered in stator vanes, than the strongest known conventionally cast vane alloy, WAZ-16 (33). It also shows about a 100°C (200°F) advantage over the ODS alloys.

Both Si_3N_4 and SiC are under development and significant improvements in high temperature strength are being achieved as shown in Fig. 9. Work is underway under NASA sponsorship (34) to improve creep-rupture strength by decreasing the alkali metal content from approximately 2500 to less than 400 ppm and by lowering O_2 content to less than 1%. The intent is to limit the amount of strength reducing second phase formation at the grain boundaries which results from the reaction of such impurities with densification additives such as MgO and Y_2O_3. Further strength improvements are possible with these ceramics by improving processing procedures such as powder handling, sintering, and hot pressing. Although no creep rupture data are yet available, another promising Si_3N_4 base material is the class known as SiAlONs. These are solid solutions of Al_2O_3 in Si_3N_4. Demonstrated advantages are that the SiAlONs do not require sintering to reach high density (94%) and that they appear to have outstanding thermal shock resistance (35).

It should be noted that ceramics for turbine application have become the center of much effort in recent years. For example, there is the ARPA program (36). The program which began in July 1971, is intended to demonstrate that ceramics can be applied successfully as stator vanes, turbine blades, and disk, combustor and nose cone components in a 1370°C (2500°F) gas temperature automotive turbine power plant. Another phase of this program seeks to demonstrate the effectiveness of ceramic first stage stator vanes for a 1370°C (2500°F) gas temperature 30 megawatt ground power turbine installation. It is expected that the vehicular unit combustors, ducts and stators will meet the 1978 goal of 200 hours of operation at a maximum turbine inlet temperature of 2500°F. Major effort is going into the most demanding application of ceramics, the vehicular turbine rotor. Although the ARPA program is intended to demonstrate the successful application of ceramics in automotive and electric ground power turbines, much of what is being learned will be of great value in the development of ceramics for aircraft gas turbine applications as well.

High Stress - Turbine Blades

For high stress applications such as turbine blades, substantial increases in use temperature can be expected by means of directional structures of several types (Fig. 10). Initial advances were made with conventional nickel base alloys such as PWA 664 (37) in which grains were aligned parallel to the direction of the major stress axis by means of directional solidification. Further increases can be expected from monocrystals (38). The directionality concept is also being applied to eutectic systems with considerable success. Directionality of structure is also the key to the ODS+γ' systems and tungsten fiber superalloy composites.

Directionally solidified eutectics. - Major research and development effort is being expended in industry and government to exploit eutectic systems. Figure 11 provides a comparison of the 1000 hour creep rupture properties (39,40) of the major eutectic systems currently under study and directionally solidified MAR M-200 + Hf. At turbine blade operating conditions, the DS eutectics now afford about a 30-80°C (50-150°F) use temperature advantage, or a 40-60% increase in creep rupture strength.

Figure 12 shows the microstructure of the two major types of eutectic systems, a typical rod or fiber reinforced system, HAFCO, and a typical lamellar reinforced system $\gamma/\gamma'-\delta$. The matrix has been etched away to bring into relief the two types of reinforcing phases. In both systems a relatively ductile matrix is reinforced by a brittle phase. Most rod or fiber (not all are perfect rods as may be seen from the figure) reinforced systems utilize some type of carbide fibers (Hf carbide in HAFCO and TaC in both CoTaC and NiTaC) ranging from 5 to 15 volume percent (41). The matrices are generally complex. For example, the matrix of the NiTaC systems consists of a γ' precipitate within a γ nickel solid solution containing Cr and Al to provide oxidation resistance and precipitation strengthening. Additions of W or Mo can be made to provide additional solid solution strengthening. The $\gamma/\gamma'-\delta$ alloy (Ni-20Cb-6Cr-2.5Al) is typical of the lamellar reinforced systems. The δ (Ni_3Cb) lamellae make up approximately 40 volume percent and this contributes to very low transverse ductility at low and intermediate temperatures, as will be discussed subsequently. The matrix consists of a γ' precipitate within a complex γ nickel solid solution.

A number of problem areas exist which must be solved before eutectic systems can be effectively utilized. Foremost, and common to all systems is the slow growth rate directionally solidified eutectics require in their manufacture, typically less than 3 cm/hr (40,42). Work is being directed toward achieving more acceptable rates from a blade fabrication standpoint.

Another potential problem with some eutectics is that of thermal instability upon thermal cycling. A visual example of this is shown for the CoTaC system in Fig. 13 (43). It may also be seen that by suitable compositional changes such instabilities can be overcome. The thermal instability demonstrated (Figs. 13(a) and (b)) upon cycling 2000 times between 425 and 1100°C (797 and 2012°F) could have been caused by a number of factors whose individual roles have not as yet been well defined -- thermal coefficient of expansion mismatch between fibers and matrix, fiber solubility in matrix, fiber surface energy of formation, and imperfections of reinforcing fiber phase (41,43,44). Figures 13(c) and (d) show that by substituting HfC for TaC fibers instability during thermal cycling was totally eliminated (45). A better understanding of the importance of the role of the individual factors that can contribute to such thermal instability must be obtained, but it is apparent that the problem is not insurmountable.

A further area of considerable concern with some eutectic systems is that of low transverse ductility at the intermediate temperatures. This poses fatigue problems in the

blade. Another problem is design of the blade root because of normally imposed shear and bending stresses. The solution to the latter problem will require modified (lower stress) root designs or superalloy bonded roots for advanced "high work" blades (46). Figure 14 shows the transverse tensile fracture strain for representative eutectic systems compared to a currently used directionally solidified superalloy DS MAR M-200. The rod or fiber reinforced systems (NiTaC and CoTaC (40,47)) have reasonably good room and intermediate temperature transverse ductility which compares well with DS MAR M-200 + Hf (42). However, the lamellar γ/γ'- δ system has relatively low transverse ductility at these temperatures. Attempts are being made to alter the deformation mechanism of the high (40 volume percent) brittle intermetallic phase (δ , Ni_3Cb). Recent efforts have improved 760°C (1400°F) transverse fracture strain from ~ 0.2 to 0.9%. This was achieved (42) by obtaining a fully lamellar structure by decreasing growth rate from 3 to 2 cm/hr and by the addition of 0.06% C. Heat treatments (870°C, 1600°F) also appear to provide some improvement although the mechanism is as yet unknown.

A very recent development is the γ/γ'- α eutectic alloy. The α phase consists of molybdenum fibers that act to reinforce the γ/γ' matrix phase. Preliminary results indicate that this alloy has about a 17°C (30°F) higher use temperature for 1000 hour stress-to rupture life than the γ/γ'- δ alloy together with significantly improved transverse ductility and shear strength (48,49).

Despite the problems cited, eutectic systems are promising candidates for high stress turbine applications and it is expected that some eutectic systems will see at least limited engine service as aircraft turbine engine blades within the next 10 years.

ODS + gamma prime alloys. - Recent advances in the production of oxide dispersion strengthened alloys have introduced ODS superalloys as possible contenders for advanced turbine blade applications. For this use, the high strength of a gamma prime (γ') strengthened alloy (needed at the blade root) is combined with the elevated temperature strength derived from dispersion strengthening (needed in the airfoil). At 1100°C (2000°F) the creep-rupture life of experimental ODS superalloys such as ODS WAZ-D (50) and the very recently developed "Alloy D" (51) compare favorably with conventionally cast random polycrystalline γ' strengthened alloys and directionally solidified eutectic alloys. As shown in Fig. 15, these alloys have use temperatures in the range of 1150°C (2100°F) for 1000 hour life at a stress of 102 MN/m^2 (15 ksi). "Alloy D" developed by The International Nickel Company has demonstrated improved rupture ductility (~ 3%) compared to previous ODS superalloys (~ 1% for ODS WAZ-D); it has also demonstrated good oxidation and excellent corrosion resistance in comparative tests with conventional superalloys. An added advantage of the ODS alloys is their higher incipient melting temperature derived from the compositional uniformity inherent in processing by powder metallurgical techniques.

The ODS superalloys are relative newcomers to the scene and only sketchy data exist. Thus, their potential for blade application remains largely unchartered except for their outstanding strength. A potential problem area may be low transverse rupture ductility which is expected to be less than the longitudinal ductility. However, it is anticipated that the interest generated by this class of materials will shortly result in a more definitive evaluation of their potential.

Composites. - Of all the directional metallic systems, tungsten fiber reinforced superalloys afford potentially the highest use temperature capability for turbine blades, but their application to service is also furthest down the road (Fig. 10). These materials combine the high temperature strength of W wires with the ductility, toughness, and oxidation resistance of a superalloy matrix. Although the technology for these composites is not as advanced as for the DS eutectics (in-situ composites) considerable research is underway in this area (52 to 57). The significant strength advantage of W fiber reinforced superalloys over DS eutectics (up to 2 1/2 times) and current superalloys (up to 5 times) is apparent from Fig. 16 which shows a comparison of their 1090°C (2000°F) 1000-hour density normalized data. The actual composite data (solid lines) were obtained with a uniform reinforcement of 70 volume percent tungsten fibers along the length of the specimens. For an average 30 volume percent reinforcement with varying fiber content along the blade span, calculated results (dotted lines) are shown which take into account potential composite degradation due to fiber matrix interaction over 1000 hours exposure. Because of improvements in compatibility since the data were obtained, some of the calculated results are even more favorable. To make the 30 volume percent of reinforcing fibers a viable concept, the fibers have to be suitably distributed along the blade span to accommodate spanwise variation in blade centrifugal force. A 30 volume percent of reinforcement would result in composite blades of approximately the same weight as those of current superalloy blades. This would be accomplished by taking advantage of the greater stiffness and strength of the composite to reduce blade thickness and taper.

A major breakthrough in making these composite systems viable candidates for turbine blade application has been the successful development of a monolayer tape fabrication process shown in Fig. 17. Two techniques, one using powder cloth, the other alloy foils, are shown. It is envisioned that the latter will be more efficient for volume production and that turbine blade fabrication costs should approach those for current turbine engine titanium fan blades (58).

Major problem areas associated with the application of W fiber reinforced superalloys to turbine blades are fiber-matrix interaction (interdiffusional effects reduce wire strength) during fabrication and service exposure, and resistance to thermal and mechanical fatigue caused by turbine operational modes. The former problem has been greatly reduced by development of the monolayer tape fabrication process and by making appropriate

adjustments to the matrix compositions. It now appears that the fiber-matrix interaction factor should not be a deterrent to composite use in turbine blade application. The thermal fatigue problem stems from the large thermal mismatch between the superalloy matrix and the W fibers. Only limited thermal fatigue data have been obtained to date but the most recent results obtained at NASA-Lewis and by other investigators suggest that this problem also is much nearer the solution stage. Fig. 18 shows some encouraging results for a W-1ThO_2/FeCrAlY specimen subjected to 1000 cycles from room temperature to 1200°C (2200°F) by direct-resistance-heating in a Naval Air Systems Command program conducted at TRW. No matrix or fiber cracking occurred. However, considerable research remains to be done before W fiber reinforced superalloys can be used as turbine blades.

Ceramics. - The ultimate in potential use temperature capability for turbine blade application resides in ceramic materials. As shown in Fig. 10, use temperatures on the order of 1200 to 1370°C (2200 to 2500°F) can be expected. In addition to the potentially low cost of ceramics (about 1/10 that of superalloys), their low density (about 1/3 that of superalloys) together with their high strength-to-density ratios, make ceramics particularly desirable for rotating turbine blades where the primary stresses result from centrifugal forces. However, it is not reasonable to expect the characteristics of essentially no ductility and very low impact resistance to be circumvented to the extent necessary to permit the use of ceramics as aircraft engine turbine blades much before the last decade of this century. There is a much greater likelihood that ceramic turbine blades will see service in ground power installationns or automobiles considerably before this.

Although it is not feasible to achieve ductile ceramics, considerable effort is being expended to improve their impact resistance. Modest, although not consistently obtainable, improvements in impact strength have been obtained to date. Figure 19 shows in chronological order the increases in both room temperature and 1315°C (2400°F) impact strength achieved with Si_3N_4 by various investigators. Increasing the purity of δ -phase Si_3N_4 powders (59), application of a lithium aluminum silicate layer (60), and carburization to create a compressive layer (61) have each provided an increase in impact strength. The last mentioned approach resulted in one J (10 in-lb) impact strength, a factor of ten increase over as-received Si_3N_4. More impressive improvements in impact strength of Si_3N_4 have resulted (62,63,64) from reinforcing hot pressed Si_3N_4 with 25 v/o Ta wire of 25 mil diameter. Drawbacks to this approach are the more than doubled density of the Si_3N_4-Ta product over the monolithic Si_3N_4 body (6.55 g/cc vs. 3.2 g/cc) and the possibility of catastrophic oxidation of any exposed Ta when the product is placed in service. Most recently, with work still in progress (65), the energy absorbing surface layer approach for improving the impact strength of Si_3N_4 has given encouraging results. Use of silica-zircon layers has resulted in Charpy impact strengths of about 20 in-lbs. And, in very preliminary work, porous reaction sintered silicon nitride layers on dense Si_3N_4 have provided impact strengths of 10 in-lbs. Further improvements in impact resistance, particularly as regards reproducibility are anticipated, although much higher values of impact strength are not likely to be achieved.

In order to use ceramics for turbine blades, the designer must tailor his design philosophy to effectively deal with materials of essentially no ductility. Very early work by the authors (66,67) recognized the need to accommodate the lack of ductility of ceramics by designs that employed cushioning interfaces between blades and disk and generous radii on the blade roots. Figure 20 illustrates some early attempts that were partially successful (67). The interface materials acted to further distribute the stress in the root attachments. Porous or screen material interfaces were especially beneficial. Interestingly, as was the case in the early NACA work, recent investigations (68, 69) have shown that the use of ductile inter-layer materials such as platinum is highly desirable. These serve to distribute the stresses and to prevent chemical reaction between the ceramic blades and metal disks. Utilizing these methods, full-scale (4" span) blades were operated 20 years ago for as long as 240 hours at continuous full engine power without root failures. This was accomplished at a time when these engines were qualified for military service with a 150 hour test. The brittle airfoils could not withstand the impact of typical foreign objects, however.

The early attempts to use ceramics and cermets as turbine blades were handicapped by relatively weak materials, rather immature ceramic processing procedures and very crude stress analysis techniques. Fortunately, designers today have far superior materials (SiC and Si_3N_4) to work with as well as design procedures based on fracture mechanics and 3D finite-element stress analyses made possible by use of computers. The 3D finite-element stress analysis permits determination of local principal stresses throughout the component so that the designer can pin-point critical stress conditions which may result from stress concentrations.

Fracture mechanics can be used to determine the crack growth characteristics of the materials under design loads. Since the strength of ceramic materials is determined by initial flaw size and distribution, and since essentially no ductility is available to arrest crack growth, the careful application of fracture mechanics to ceramics is even more important than in the design of highly stressed metallic systems. The ceramic materials must be characterized by determining the sustained load subcritical crack growth and cyclic load crack growth. Fortunately, a good basis for this work has been established by the National Bureau of Standards, and others (70, 71, 72) working with glass, Al_2O_3, SiC and Si_3N_4. However, it must be noted that for the ceramic data obtained to date, direct quantitative comparisons with K_{Ic} values for metals can be misleading because of differences in the fracture toughness specimen sizes involved. Thus, relatively large specimens (inches in thickness) are used for metals whereas the specimen thickness of the ceramic specimens has typically been on the order of 30 mils. A rough indication of the relative fracture toughness of these materials is that a heat treated steel has 30 to 50

times the fracture toughness of hot pressed Si_3N_4.

Despite the difficulties and limitations, however, the tools available to the designer today make designing around the ceramic ductility problem appreciably more likely than in the past. Nevertheless, the challenge is to learn how to effectively utilize these materials. Their extreme brittleness makes them far more sensitive to internal flaws inherent in their manufacture and to surface flaws resulting from accidental damage than has been true for any materials used heretofore in critical high stress applications such as blades.

HIGH PRESSURE TURBINE SEALS

An important way of enhancing aircraft gas turbine engine performance is by reducing and preserving turbine airfoil tip clearances. Increases in these clearances with engine operation result in decreased turbine efficiency with attendant loss of thrust and increased fuel consumption. It has been estimated that the turbine efficiency penalty can be as much as 1% for a .025 cm (0.010 in) increase in first stage turbine blade tip clearance. Significant advances are being made in the development of shroud materials which act to preserve the airfoil tip clearance during engine operation. To be more effective, shroud materials must have improved resistance to oxidation and erosion. At the same time, they must have the quality of abradability. That is, their response to rubbing by the airfoil tip must be such that this can occur without material removal from the blade. Figure 21 schematically illustrates the effect of airfoil/seal rub interaction on tip clearance. An abradable seal minimizes the clearance increase caused by rubbing of the airfoil tips against the shroud. Most rub clearances can be reduced by 70% with abradable seals.

Figure 22 (73) dramatically illustrates the results of a CF6-50C ground-engine test of shroud segments of a newly-developed GE-NASA-Seal material (Genaseal) and of the current Bill-of-Material. The Genaseal shroud segments (porous NiCrAlY alloy optimized for resistance to the engine enrivonment) are numbered 11 and 14. The Bill-of-Material shroud segments are numbered 9,10,12 and 13. All were subjected to 1000 engine test cycles equivalent to a typical take-off, cruise, and landing engine condition. The superiority of the Genaseal shroud segments is clearly evident. These results indicate that marked improvement is possible in this critical engine performance area by alloy development designed to achieve improved resistance to severe engine environments. Continued efforts in this area should be pursued in order to further enhance turbine engine performance.

ENVIRONMENTAL PROTECTION

All of the metallic systems discussed for turbine stator vanes and blades require surface protection in order to realize their high use temperature potential for long service times. The turbine combustion gas poses problems of oxidation and hot corrosion which range in severity depending upon the type of fuel used and the atmospheric environment. In addition, turbine cyclic operational modes cause thermal fatigue cracking. Considerable progress has been made in developing conventional coatings, thermal barrier coatings, and in alloying techniques to provide good resistance to these various failure mechanisms. In addition, research on fuel additives is also underway to reduce the harmful effects of impurities.

Coatings for oxidation, hot corrosion, and thermal fatigue. - Significant advances have been made in the development of coatings for advanced superalloys in the past several years. The importance of this aspect of high temperature materials research cannot be over emphasized in view of the requirements for petroleum conservation which dictate the use of dirty fuels. Even greater effort is needed in this area to establish tolerance limits for materials and coatings and to provide improved coating protection for turbine blades and vanes so that such fuels can be used without lowering turbine operating temperatures. Figure 23 provides a summary of fuel costs as well as the impurity contents that contribute to hot corrosion and erosion in various grades of fuel. Associated with desirable reductions in fuel cost, are impurity content increases of several orders of magnitude which contribute to increased hot corrosion and erosion.

Figure 24 shows the effectiveness of some of the most advanced coating systems on two representative high strength nickel base alloys subjected to a cyclic operational mode in the LeRC Mach 1 burner facility. The cycles consisted alternately of 1 hour at 1090°C (2000°F) and 3 minutes at room temperature. Shown are cycles to first thermal fatigue crack and cycles to first observed weight loss. The results are displayed from left to right in chronological order with the most recent development at the extreme right. Improvements over commercial aluminide coatings in cycles to first crack by a factor of almost eight have been obtained. The advanced coating systems displayed are described (74,75,76) for the PVD CoCrAlY, the aluminized NiCrAlSi and the Pt-Al systems, respectively. Figure 24 clearly shows a difference in coating performance for the two alloys. This emphasizes the necessity for tailoring the coating to the substrate. Such tailoring can most readily be achieved with the PVD process, since virtually any desired coating composition can be achieved simply by evaporation from a molten pool.

Figure 25 shows the hot corrosion behavior of these coating systems on the same two alloy substrates under cyclic operation in the Mach 1 burner. The cycle imposed consisted of 1 hour at 900°C (1650°F) and 3 minutes at room temperature. In this instance, 5 PPM salt was introduced into the combustion gas stream to simulate sulfidation conditions. Again, the same coating systems were not best for both alloy substrates. Also, the coating thatprovided the greatest oxidation protection was not necessarily the one that gave the

best sulfidation protection for a particular substrate. It is apparent that the coating system must also be tailored to the substrate to achieve the most effective sulfidation protection.

For the future, coatings must be developed for long life protection for the advanced temperature ODS systems, the DS eutectics, and the W fiber reinforced superalloy systems. Although the ODS NiCrAls do not require coatings for short time use (500 hours) they may require coating protection for long time service (thousands of hours). Significant progress is being made in this area. Thus, 1000 cycles (1 hr at 1090°C (2000°F), 3 min. at R.T.) in the LeRC Mach 1 burner facility were run with PWA 267 (a PVD NiCrAl coating) as well as NASCOAT 70M (an aluminized PVD NiCrAl coating) on a TD-NiCrAl substrate without significant weight loss. This represents a 25 to 30% life improvement over uncoated TD-NiCrAl. In the area of advanced eutectics, excellent isothermal oxidation resistance has been achieved at 1090°C (2000°F) with the $\gamma/\gamma'-\delta$ eutectic by means of a NiCrAlY plus Pt overlay coating (77). The coating also provides some improvement in resistance to thermal fatigue cracking. However, coating modifications are needed to increase coating ductility so as to further improve thermal fatigue resistance.

Because the overlay coating method is not dependent upon diffusion with the substrate, it affords the opportunity for applying a wide variety of coating compositions. Because of this versatility, the method has great appeal to the coating designer. However, the high cost of the PVD method (currently the most common method of applying overlay coatings) makes development of alternative low cost overlay coating processes of considerable importance. Finally, coating the increasingly complex internal cooling configurations of high temperature turbine blades and vanes poses an even more severe problem. Further work is needed to provide economically as well as physically, viable techniques to meet this growing challenge.

In addition to the need for further development of coating techniques, there is a major requirement for developing reliable methods to predict coating life. Recent work at NASA (78,79) is directed toward developing a better understanding of the two primary coating degradation mechanisms associated with turbine blade and vane applications. These are: (1) inter-diffusion of key elements from the coating into the metal substrate and, (2) oxidation and spallation. Equations are proposed for a first-approximation oxidation attack parameter applicable to NiCrAl coating systems. Experimental verification studies under long time exposure conditions are currently being conducted.

Alloy design for oxidation protection. - Another promising approach (80) for increasing environmental protection is by compositional alterations to the substrate. Figure 26 shows how the cyclic oxidation resistance of a high γ' content nickel base alloy was increased by small additions (0.5 wt. %) of silicon. Negligible weight loss was observed after 300 cycles (1 hour at 1090°C (2000°F) followed by 3 minutes at room temperature) in the LeRC Mach 1 burner facility. Alloy performance was as good as with a commercial aluminide coating. Long time creep rupture properties were not degraded by the silicon addition when suitable heat treatments were applied. This approach should be exploited as a means of increasing the totality of environmental protection rather than as a substitute for coatings.

Fuel additives. - The introducton of additives into the turbine fuel affords another means for reducing hot corrosion attack. Some progress has already been made in this area (81). Typical results obtained from cyclic burner tests with representative superalloys, IN-100, and IN-792, are shown in figure 27. A commercial chromium-based fuel additive was used. Exposure cycles consisted of 1 hour at 900°C (1650°F) followed by 3 minutes of forced air cooling. Five PPM sea salt was injected into the gas stream and the soluble salts were washed off the specimens after every 10 cycles. The specific weight change after each wash was determined and a comparison is provided for the same alloys evaluated in oxidation only (no additive, no sea salt), in hot corrosion (sea salt, no additive), and in hot corrosion with the fuel additive. The figure shows that the fuel additive reduced material weight loss by about a factor of two. This was also generally the case for all the alloys investigated regardless of their chemistries. However, considerable hot corrosion attack was still observed. It should be emphasized therefore that the fuel additive approach should be considered primarily as a valuable adjunct to the protective coatings approach and not as a substitute for minimizing hot corrosion in gas turbine engine components.

Thermal barriers. - Recent advances (82) have been made in providing insulating refractory oxide coatings on the order of .25 mm (.010 in.) thick which provide effective thermal barriers on cooled turbine vanes and blades. The payoff consists of large reductions in both coolant flow and metal temperatures. For example, core engine turbine vanes coated with a 0.51 mm (.010 in) ceramic thermal barrier could have both an eightfold reduction in coolant flow and a 110°C (200°F) reduction in vane metal temperature compared to an uncooled vane (82). Figure 28 illustrates the concept and indicates some of the results obtained in cyclic burner facility tests and full-scale J-75 engine ground tests at NASA-Lewis. The most favorable results have been obtained to date with 12% Y_2O_3 and 3% MgO stabilized ZrO_2 coatings .25 mm (.010 in) thick placed over a 0.1 mm (.004 in) NiCrAl layer, plasma sprayed onto the blade surface. Fiture 29 shows the tested fully bladed J-75 turbine wheel after 500 cycles from 1370°C (2500°F) to flame out (83). No cracking of the oxide was observed. The thermal barrier concept appears very promising, particularly for ground power applications, in which coating failures if they do occur are not so potentially dangerous. This approach may afford a way of extending the upper use temperature for turbine blades with current superalloy materials without the radical technology change required by substituting a new class of materials such as the DS eutectics.

TRENDS IN TURBINE COOLING TECHNOLOGY

Interest in improving gas turbine cycle performance by increasing turbine inlet temperature places a continuing emphasis on the development of more efficient and flexible turbine cooling systems. As inlet gas temperatures increase, a departure from the simpler convection-cooled configurations toward more complex airfoil cooling systems involving combinations of impingement/convection cooling and surface film cooling are required. Figure 30 (from ref. 84) illustrates this dramatically in terms of calculated cooling flow requirements. As gas temperature and pressure increase, convection cooling requirements rise sharply. Use of a more sophisticated cooling system, full-coverage film cooling, can substantially decrease the cooling flow required at current gas temperatures and pressures. Furthermore, it can permit operation at much higher gas temperatures and pressures without the need for exorbitant cooling flows. Figure 30 also shows the potential benefit of applying a thermal barrier coating such as has been described previously to a convection cooled configuration. This combination could reduce the coolant flow requirement to that of the full-coverage film cooled configuration. There would of course be concomitant advantages in this combination in that the complex processing procedures associated with the provision of drilled film cooling holes could be avoided. In addition, the tendency toward more complex thermal stress patterns, together with greater stress amplification factors would be reduced. Although aerodynamic penalties would be associated with the thicker trailing edge resulting from the application of the thermal barrier coating (85), these losses are expected to be considerably less than with ejection of air from the multiplicity of holes in full coverage film cooled airfoils and platforms.

Extensive research is underway in the United States to investigate advanced turbine cooling concepts, both in industry and government installations such as NASA. To effectively do such work requires advanced facilities such as one-vane tunnel hot tests, two dimensional vane cascade tests, flat plate heat-transfer measurements, and flow visualization with neutrally bouyant helium bubbles. Figure 31 (taken from ref. 84) illustrates a hot turbine facility under construction at the NASA Lewis Research Center which is expected to be operational in 1978. It will provide pressures up to 40 atmospheres and temperatures to 2480 K. Vane, blade, and wall temperatures with advanced cooling methods will be measured during turbine operation at design conditions with its very high heat fluxes. This facility and its full capabilities are described in reference 86.

Of course, in addition to providing the means for experimental verification of advanced cooling techniques more sophisticated analytical tools are needed. These must deal with predictions of complex combustion gas and coolant flows (particularly those at the turbine passage end-walls) and the associated local steady-state and transient-metal temperature. Improved methods must also be developed for life prediction of turbine components such as blades and vanes since they are subjected to complex loading cycles at temperatures where both fatigue and creep mechanisms are active. One of the more recently developed and promising approaches for handling the fatigue-creep problem is the method of Strainrange Partitioning (87). This method is currently under investigation under the auspices of the NATO AGARD Structures and Materials Panel. A specialists meeting is scheduled for the spring of 1978 at which 19 participating laboratories from 5 nations will present the findings of their independent assessment of the method's capabilities for characterizing the high temperature low cycle creep-fatigue behavior of high temperature engineering alloys. Each laboratory will be testing a material that is of interest to their own organization. Approximately 2/3 of the materials are high temperature gas turbine materials. It should also be noted that within the past year a number of advancements have been made in extending the capability of Strainrange Partitioning to a number of practical design problems. Reference 88 describes in detail techniques for utilizing Strainrange Partitioning under conditions of multiaxiality at high temperatures. Techniques are also now under development for applying the method to the nominally elastic fatigue regime and its applicability for treating simulated thermal fatigue problems is delineated in detail (89).

Finally, in order to most effectively apply turbine component life prediction methods, the most accurate possible knowledge of the local transient temperatures and strains is required. Preliminary work at NASA indicates that advanced experimental methods such as infra-red image enhancement afford promise as a means of establishing the time temperature history of simulated airfoil applications. These can then be used together with finite element analysis to establish local critical strain conditions.

SUMMARY

Significant payoffs in turbine engine performance can be achieved by providing advanced materials, coatings, and cooling technology. Significant improvements are envisioned for intermediate and high temperature gas turbine components such as the disks, combustors, stator vanes, and turbine blades. Before such payoffs can be realized in engine service, formidable problems must be overcome in bringing materials and turbine cooling capability to the level needed. These are, of course, the challenges faced by the technologist.

For disks prealloyed powder superalloys are expected to afford both increased strength as well as reduced fabrication cost. For low stressed, high temperature components such as combustors and stator vanes, ODS alloys have a 90oC (160oF) higher use temperature potential than conventional sheet materials. Ceramics afford the highest use temperature potential, on the order of 1400oC (2600oF), of all materials for stator vanes with SiC and Si_3N_4 being the most promising. For high stressed, high temperature

components, such as the turbine blades, directional structures afford major improvements over the strongest conventional cast superalloys. The DS eutectic systems presently appear to offer as much as an 80°C (150°F) use temperature advantage. Although the technology for tungsten fiber reinforced superalloys is not as advanced as that for DS eutectics, these composites afford potentially the highest use temperature capability of all the directional metallic systems with strengths as much as five times greater than current superalloys. The ultimate in use temperature capability for turbine component applications resides in ceramics with potential use temperatures as high as 1370°C (2500°F). To successfully apply ceramics to the high stressed turbine blades and disks, however, the designer will have to tailor his design philosophy to deal with these materials of essentially no ductility by utilizing fracture mechanics concepts and advanced 3D finite-element stress analysis techniques. Early applications will probably need to operate at relatively low average stresses because of the low ductility.

The problem of providing environmental protection to turbine vanes and blades assumes an even greater importance than heretofore. The economic necessity for using dirty fuels containing greater quantities of impurities that contribute to hot corrosion and erosion demands that improved substrate/coating combinations be developed. This concept must be embodied in future advanced metallic system designs for high temperature turbine components.

Finally, advanced turbine cooling concepts such as impingement/convection cooling are required in order to improve gas turbine cycle performance by permitting increased turbine inlet gas temperatures. More sophisticated analytical methods must be developed to deal effectively with predictions of complex combustion gas and coolant flows. In addition, improved methods such as Strainrange Partitioning are under development for life prediction of turbine components that are subjected to complex loading cycles where both fatigue and creep mechanisms are active.

REFERENCES

1. G. L. Brines, Studies for Determining the Optimum Propulsion System Characteristics for Use in a Long Range Transport Aircraft, PWA-4449, East Hartford, Connecticut, Pratt & Whitney Aircraft, July 1972; also NASA CR-120950.

2. Propulsion System Studies for an Advanced High Subsonic, Long Range Jet Commercial Transport Aircraft, R72-AEG-296, Cincinnati, Ohio, General Electric Co., Nov. 1972; also NASA CR-121016.

3. J. W. Bisset, Cost/Benefit Study of Advanced Materials Technologies for Aircraft Turbine Engines, PWA-5073, East Hartford, Connecticut, Pratt & Whitney Aircraft, Oct. 1974; also NASA CR-134701.

4. E. W. Ross, R. P. Johnston, and R. E. Neitzel, Cost Benefit Study of Advanced Materials Technology for Aircraft Turbine Engines, Cincinnati, Ohio, General Electric Co., Nov. 1974; also NASA CR-134702.

5. J. B. Moore, J. Tequesta, and R. L. Athey, Fabrication Method for the High Temperature Alloys. U. S. Patent 3,519,503, July 7, 1970.

6. J. C. Freche, W. J. Waters, and R. L. Ashbrook, Method of Forming Superalloys. U. S. Patent 3,702,791, Nov. 14, 1972.

7. J. C. Freche, W. J. Waters, and R. L. Ashbrook, Method of Forming Articles of Manufacture from Superalloy Powders. U. S. Patent 3,775,101, Nov. 27, 1973.

8. Private communication with E. Kerzicnik, General Electric Co., Cincinnati, Ohio.

9. Private communication with Marvin M. Allen, FR&DC, Pratt & Whitney Aircraft.

10. Private communication with E. Kerzicnik, General Electric Co., Cincinnati, Ohio.

11. Private communication with W. B. Kent, Universal Cyclops, Bridgeville, Pennsylvania.

12. D. J. Evans, Evaluation of Powder Metallurgy Superalloy Disk Materials, PWA-5263, East Hartford, Connecticut, Pratt & Whitney Aircraft, Aug. 1975; also NASA CR-134865.

13. J. L. Bartos, Development of a Very High Strength Disk Alloy for 1400° F Service, Cincinnati, Ohio, General Electric Co. (AD-A001937; AFML-TR-74-187), Nov. 1974.

14. M. M. Allen, B. E. Woodings, and J. A. Miller, Advanced Wrought Nickel-Base Alloy Turbine Disk Evaluation Program, PWA-FR-6035, East Hartford, Connecticut, Pratt & Whitney Aircraft (AFML-TR-73-271; AD-916496L), 1973.

15. R. V. Miner, Jr., and W. B. Kent, An Experimental Wrought Superalloy for Advanced Temperature SErvice Fabricated from Prealloyed Powder. Submitted to ASM Metals Engineering Quarterly, 1977.

16. P. T. Bizon and D. A. Spera, Comparative Thermal Fatigue Resistance of Twenty-Six Nickel and Cobalt Base Alloys. NASA TN D-8071, Washington, D. C., National Aeronautics and Space Administration, Oct. 1975.

17. H. R. Gray, Turbine Materials and Life Prediction. Aeronautical Propulsion, NASA SP-381, Washington, D.C., National Aeronautics and Space Administration, May 1975, pp. 201-288.

18. P. G. Bailey, Proceedings of the Sixth National Technical Conference for Materials on the Move, Soc. Advancement of Mater. and Process Eng., 1974, pp. 208-217.

19. J. W. Semmel, Jr., Proceedings of the Sixth National Technical Conference for Materials on the Move, Soc. Advancement of Mater. and Process Eng., 1974, pp. 154-167.

20. W. F. Simmons, Current and Future Materials Usage in Aircraft Gas Turbine Engines, MCIC-73-14, Columbus, Ohio, Battelle Columbus Labs., June 1973.

21. L. J. Klingler, et al., Development of Dispersion Strengthened Ni-Cr Alloy Sheet for Space Shuttle Vehicles, Baltimore, Md., Fansteel, Inc., Dec. 1972; also NASA CR-121164

22. J. D. Whittenberger, Relation of Structure to Mechanical Properties of Thin Thoria Dispersion Strengthened Nickel-Chromium (TD-NiCr) Alloy Sheet. NASA TN D-7988, Washington, D. C., National Aeronautics and Space Administration, May 1975.

23. J. S. Benjamin, Metall. Trans. 1 (1970), p. 2943.

24. Low Cost Fabrication of ODS Alloy Vanes, General Electric Co., NASA Contract NAS3-19710 (in process).

25. D. L. Deadmore, C. E. Lowell, and G. J. Santoro, High Gas Velocity Oxidation and Hot Corrosion Testing of Oxide Dispersion-Strengthened Nickel-Base Alloys. NASA TM X-71835, Washington, D. C., National Aeronautics and Space Administration, Nov. 1975.

26. W. A. Sanders and H. B. Probst, Evauation of Oxidation Resistant Nonmetallic Materials at 1204°C (2200°F) in a Mach 1 Burner. NASA TN D-6890, Washington, D. C., National Aeronautics and Space Administration, Aug. 1972.

27. W. A. Sanders and H. B. Probst, Behavior of Ceramics at 1200°C in a Simulated Gas Turbine Environment, Paper No. 740240, New York, Society of Automotive Engineers, 1974.

28. C. G. Nessler, Gas Turbine Ceramic Vane Testing, Paper No. 740235, New York, Society of Automotive Engineers, 1974.

29. A. N. Holden, S. E. Mumford, and C. R. Booker, Jr., Testing of Ceramic Stator Vanes to 2500° F (1371° C), Paper No. 75-GT-103, New York, American Society of Mechanical Engineers, 1975.

30. R. J. Beck, Evaluation of Ceramics for Small Gas Turbine Engines, Paper No. 740239, New York, Society of Automotive Engineers, 1974.

31. A. F. McLean, Ceramics for High Performance Applications, Brook Hill Pub. Co., 1974, pp. 9-36.

32. A. F. McLean, E. A. Fisher, and R. J. Bratton, Brittle Materials Design, High Temperature Gas Turbine, Dearborn, Michigan, Ford Motor Co. (AMMRC-CTR-74-26; AD-920691), Apr. 1974.

33. W. J. Waters and J. C. Freche, A Nickel-Base Alloy, NASA WAZ-16, with Potential for Gas Turbine Stator Vane Application. NASA TN D-7648, Washington, D. C., National Aeronautics and Space Administration, June 1974.

34. T. Vasilos, Improving the Toughness of Refractory Compounds. AVSD-0108-76-RR, Lowell, Mass., Avco Corp., Nov. 1975; also NASA CR-134813.

35. K. H. Jack and W. J. Wilson, Nature Phys. Sci., 238 (1972), pp. 28-29.

36. A. F. McLean and R. R. Baker, Brittle Materials Design, High Temperature Gas Turbine, Dearborn, Mich., Ford Motor Co. (AMMRC-CTR-76-31; AD-C-015331), Oct. 1976.

37. B. J. Piearcey and F. L. VerSnyder, A New Development in Gas Turbine Materials. The Properties and Chracteristics of PWA 664, PWA 65-007, East Hartford, Conn., Pratt & Whitney Aircraft, Apr. 1965.

38. B. Piearcey and F. VerSnyder, Monocrystaloys, - A New Concept in Gas Turbine Materials. The Properties and Characteristics of PWA 1409, PWA 66-007, East Hartford, Conn., Pratt & Whitney Aircraft, Feb. 1966.

39. E. R. Thompson and F. D. Lemkey, Composite Materials, Vol. 2, L. Brontman and R. Krock, eds., Academic Press, 1973, pp. 101-157.

40. C. A. Bruch, Eutectic Composite Turbine Blade Development, General Electric Co., Mar. 1976.

41. R. L. Ashbrook, Directionally Solidified Composite Systems under Evaluation. NASA TM X-71514, Washington, D.C., National Aeronautics and Space Administration, Apr. 1974.

42. K. D. Sheffler, R. H. Barkalow, and A. Yuen, Alloy and Structural Optimization of a Directionally Solidified Lamellar Eutectic Alloy, PWA-5300, East Hartford, Conn., Pratt & Whitney Aircraft, May 1976; also NASA CR-135000.

43. F. M. Dunlevey and J. F. Wallace, Metall. Trans. 5 (1974), pp. 1351-1356.

44. M. Gell, Specialists Meeting on Directionally Solidified In-Situ Composites, E. R. Thompson and P. R. Sahm, eds., AGARD-CP-156, France, Advisory Group for Aerospace Research and Development, 1974, pp. 117-128.

45. Y. G. Kim, Structure and Thermal Cycling Stability of a Hafnium Monocarbide Reinforced Directionally Solidified Cobalt-Base Eutectic Alloy. NASA TM X-71751, Washington, D.C., National Aeronautics and Space Administration, 1976.

46. K. D. Sheffler and J. J. Jackson, STress Analysis, Thermomechanical Fatigue Evaluation and Root Subcomponent Testing of Gamma/Gamma Prime-Delta Eutectic Alloy. PWA-5472, East Hartford, Conn., Pratt & Whitney Aircraft, Dec. 1976; also NASA CR-135005.

47. H. Bibring, Conference on In Situ Composite. Volume II - Papers on Mechanical Properties, NMAB-308-II, National Materials Advisory Board, 1973, pp. 1-69.

48. M. R. Jackson, J. L. Walter, and M. F. Henry, Evaluation of Directionally Solidified Eutectic Superalloys for Turbine Blade Applications. CR-135151, 1977.

49. F. D. Lemkey, Development of Directionally Solidified Eutectic Nickel and Cobalt Alloys, UTRC-R75-912046-4, East Hartford, Conn., United Technologies Research Center (AD-A024420; NADC-76115-30), Dec. 1975.

50. T. K. Glasgow, An Oxide Dispersion Strengthened Ni-W-Al Alloy with Superior High Temperature Strength. NASA TM X-71888, Washington, D.C., National Aeronautics and Space Administration, 1976.

51. Y. G. Kim, L. R. Curwick, and H. F. Merrick, Development of an Oxide Dispersion Strengthened Turbine Blade Alloy by Mechanical Alloying. NASA CR-135150, 1977.

52. A. V. Dean, The Reinforcement of Nickel-Base Alloys with High Strength Tungsten Wires, Rept. R-266, England, National Gas Turbine Establishment, Apr. 1965.

53. R. H. Baskey, Fiber Reinforcement of Nonmetallic Composites, Cleveland, Ohio, Clevite Corp. (ASD-TDR-63-619); AD-417390), July 1963.

54. D. W. Petrasek, R. A. Signorelli, and J. W. Weeton, Refractory Metal Fiber-Nickel Base Alloy Composites for Use at High Temperatures. NASA TN D-4787, Washington, D.C., National Aeronautics and Space Administration, Sept. 1968.

55. D. W. Petrasek and R. A. Signorelli, Preliminary Evaluation of Tungsten Alloy Fiber-Nickel Base Alloy Composites for Turbojet Engine Applications. NASA TN D-5575, Washington, D.C., National Aeronautics and Space Administration, Mar. 1970.

56. I. Ahmed, et al., Metal Matrix Composites for High Temperature Applications, WVT-7155, New York, Watervliet Arsenal (AD-734304), Oct. 1971.

57. R. A. Signorelli, Review of Status and Potential of Tungsten Wire/Superalloy Composites for Advanced Gas Turbine Engine Blades. NASA TM X-2599, Washington, D.C., National Aeronautics and Space Administration, Sept. 1972.

58. R. A. Signorelli, Metal Matrix for Aircraft Propulsion Systems. NASA TM X-71685, Washington, D.C., National Aeronautics and Space Administration, Mar. 1975.

59. W. H. Rhodes and R. M. Cannon, High Temperature Compounds for Turbine Vanes, AVSD-0336-72-CR, Lowell, Mass., Avco Corp., Sept. 1972; also NASA CR-120966.

60. H. P. Kirchner and J. Seretsky, Improving Impact Resistance of Ceramic Materials by Energy Absorbing Surface Layers, State College, Pa., Ceramic Finishing Co., Mar. 1974; also NASA CR-134644.

61. H. P. Kirchner, Strengthening of Oxidation Resistant Materials for Gas Turbine Applications, State College, Pa., Ceramic Finishing Co., June 1974; also NASA CR-134661.

62. J. J. Brennan and M. A. Decrescente, Fiber Reinforced Ceramic Matrix Composites, M911294-4, East Hartford, Conn., United Aircraft Corp. (AD-757063), Jan. 1973.

63. J. J. Brennan, Development of Fiber Reinforced Ceramic Matrix Composites, UARL-N911647-4, East Hartford, Conn., United Aircraft Corp. (AD-778651), Apr. 1974.

64. J. J. Brennan, Development of Fiber Reinforced Ceramic Matrix Composites, UARL-R911848-4, East Hartford, Conn., United Aircraft Corp. (AD-A009360), Feb. 1975.

65. J. J. Brennan, Development of Si_3N_4 and SiC of Improved Toughness, United Technologies Research Center, NASA Contract NAS3-19731 (in process).

66. J. C. Freche, Further Investigation of Gas Turbine with NBS Body 4811C Ceramic Rotor Blades. NACA RM-49L07, Washington, D.C., National Advisory Committee for Aeronautics, Mar. 1950.

67. G. C. Deutsch, A. J. Mayer, and G. M. Ault, A Review of the Development of Cermets, AGARD-185, Paris, Advisory Group for Aeronautical Research and Development, 1958.

68. B. Walker, Design, Fabrication, and Evaluation of Gatorized Ceramic-Wrought Alloy Attachment Concepts, SR-6, East Hartford, Conn., Pratt & Whitney Aircraft, July 1974 - Dec. 1975.

69. G. Calvert, Ceramic Blade - Metal Disk Attachment, East Hartford, Conn., Pratt & Whitney Aircraft, NASA Contract NAS3-19715 (in process).

70. A. G. Evans, L. R. Russell, and D. W. Richerson, Metall. Trans. A., 6A (1975), pp. 707-716.

71. R. W. Davidge, J. R. McLaren, and G. Tappin, J. Mater. Sci., 8 (1973), pp. 1699-1705.

72. R. C. Bradt, D. P. H. Hasselman, and F. F. Lange, eds., Fracture Mechanics of Ceramics, Plenum Press, 1974.

73. R. C. Schwab, Improved High Pressure Turbine Shroud, Sixth Quarterly Technical Progress Report, July 19, 1976, General Electric Co., NASA Contract NAS3-18905 (in process).

74. F. P. Talboom, R. C. Elem, and L. W. Wilson, Evaluation of Advanced Superalloy Protection Systems, PWA-4055, East Hartford, Conn., Pratt & Whitney Aircraft, Dec. 1970; also NASA CR-72813.

75. M. A. Gedwill and S. J. Grisaffe, Met. Eng. Q., 12 (1972), pp. 55-61.

76. Platinum Met. Rev. 16, (1972), p. 87.

77. T. E. Strangmen, E. J. Felten, and R. S. Benden, Refinement of Promising Coating Compositions for Directionally Cast Eutectics, PWA-5441, East Hartford, Conn., Pratt & Whitney Aircraft, Oct. 1976; also NASA CR-135103.

78. S. R. Levine, Reaction Diffusion in the NiCrAl and CoCrAl Systems. NASA TN D-8383, Washington, D.C., National Aeronautics and Space Administration, 1977.

79. C. A. Barrett and C. E. Lowell, Resistance of Nickel-Chromium-Aluminum Alloys to Cyclic Oxidation at 1100° and 1200°C. NASA TN D-8255, Washington, D.C., National Aeronautics and Space Administration, June 1976.

80. R. V. Miner, Jr., and C. E. Lowell, Effects of Silicon Additions on Oxidation and Mechanical Behavior of the Nickel-Base Superalloy B-1900. NASA TN D-7989, Washington, D.C., National Aeronautics and Space Administration, June 1975.

81. C. E. Lowell, S.J. Grisaffe, And S. R. Levine, Toward More Environmentally Resistant Gas Turbines. Progress in NASA-Lewis Programs. NASA TM X-73499, Washington, D.C., National Aeronautics and Space Administration, 1976.

82. C. H. Liebert and F. S. Stepka, Potential Use of a Ceramic Coating as a Thermal Insulation on Cooled Turbine Hardware. NASA TM X-3352, Washington, D.C., National Aeronautics and Space Administration, Feb. 1976.

83. C. H. Liebert, et al., Durability of Zirconia Thermal-Barrier Ceramic Coatings on Air-Cooled Turbine Blades in Cyclic Jet Engine Operation. NASA TM X-3410, Washington, D.C., National Aeronautics and Space Administration, Sept. 1976.

84. T. P. Moffitt, F. S. Stepka, and H. E. Rohlik, Summary of NASA Aerodynamic and Heat Transfer Studies in Turbine Vanes and Blades. NASA TM X-73518, Washington, D.C., National Aeronautics and Space Administration, 1976.

85. R. G. Stabe and C. H. Liebert, Aerodynamic Performance of a Ceramic-Coated Core Turbine Vane Tested with Cold Air in a Two-Dimensional Cascade. NASA TM X-3191, Washington, D.C., National Aeronautics and Space Administration, 1975.

86. R. P. Cochran, J. W. Morris, and R. E. Jones, A High-Pressure, High Temperature Combustor and Turbine-Cooling Test Facility. NASA TM X-73445, 1976.

87. M. H. Hirschberg and G. R. Halford, Use of Strainrange Partitioning to Predict High-Temperature Low-Cycle Fatigue Life. NASA TN D-8072, 1976.

88. S. S. Manson and G. R. Halford, Multiaxial Rules for Treatment of Creep-Fatigue Problems by Strainrange Partitioning. 1976 ASME-MPC Symposium on Creep-Fatigue Interaction. MPC-3, ASME, 1976, pp. 299-322.

89. G. R. Halford and S. S. Manson, Life Prediction of Thermal-Mechanical Fatigue Using Strainrange Partitioning. Thermal Fatigue of Materials and Components, ASTM STP 612, D. A. Spera and D. F. Mowbray, Eds., Amer. Soc. for Testing and Mat., 1976, pp. 239-254.

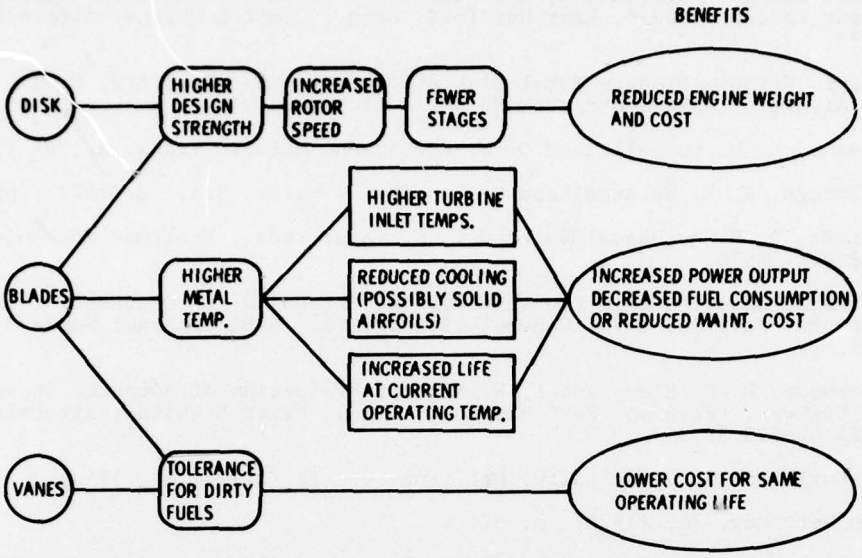

Fig. 1. - Turbine engine payoffs from advanced materials

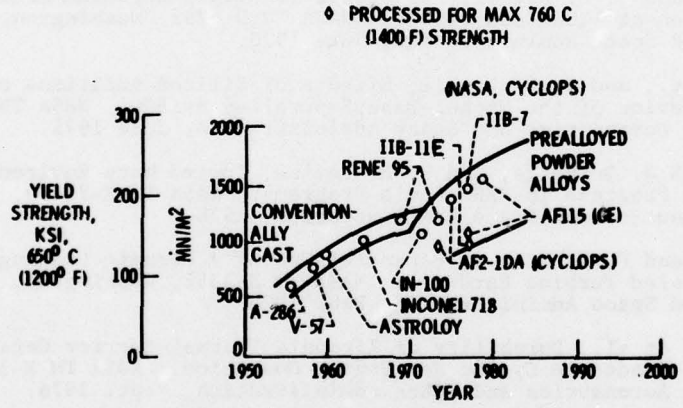

Fig. 2. - Increased yield strength projected for prealloyed powder alloys

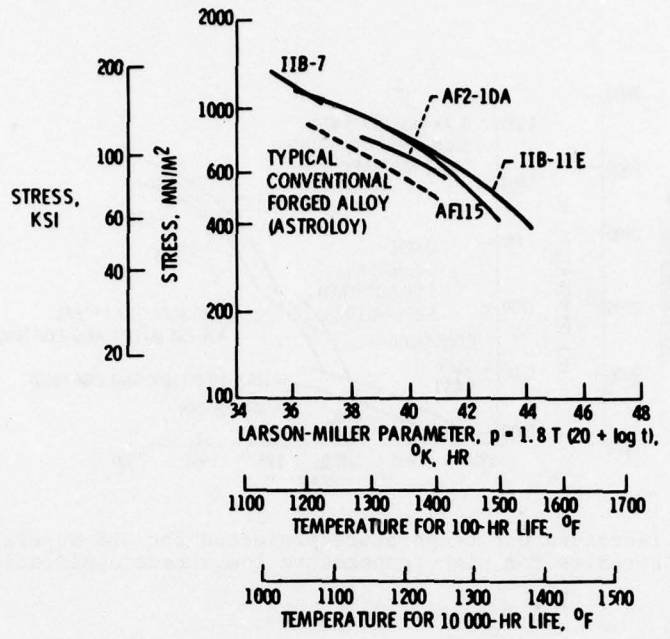

Fig. 3. - Prealloyed powder alloys superior to currently used conventional cast and forged alloy in stress to rupture

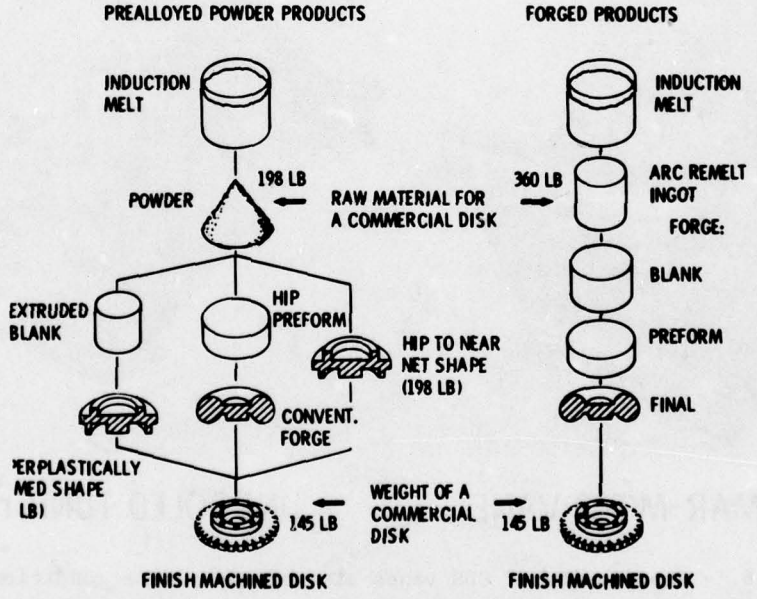

Fig. 4. - Prealloyed powder process permits reduced costs in disk fabrication compared to conventional forging process

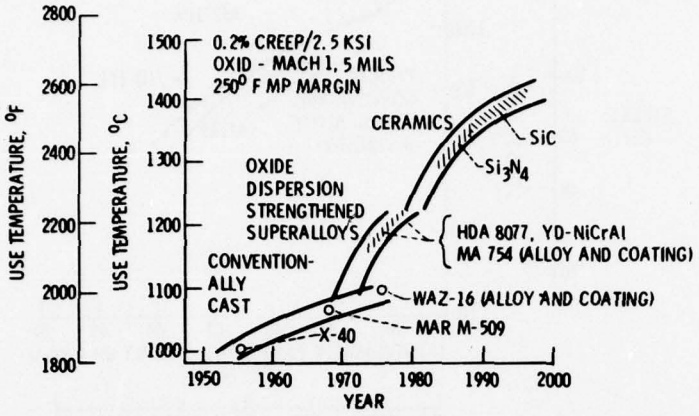

Fig. 5. - Increased use temperature projected for ODS superalloys and ceramics for high temperature low stress applications

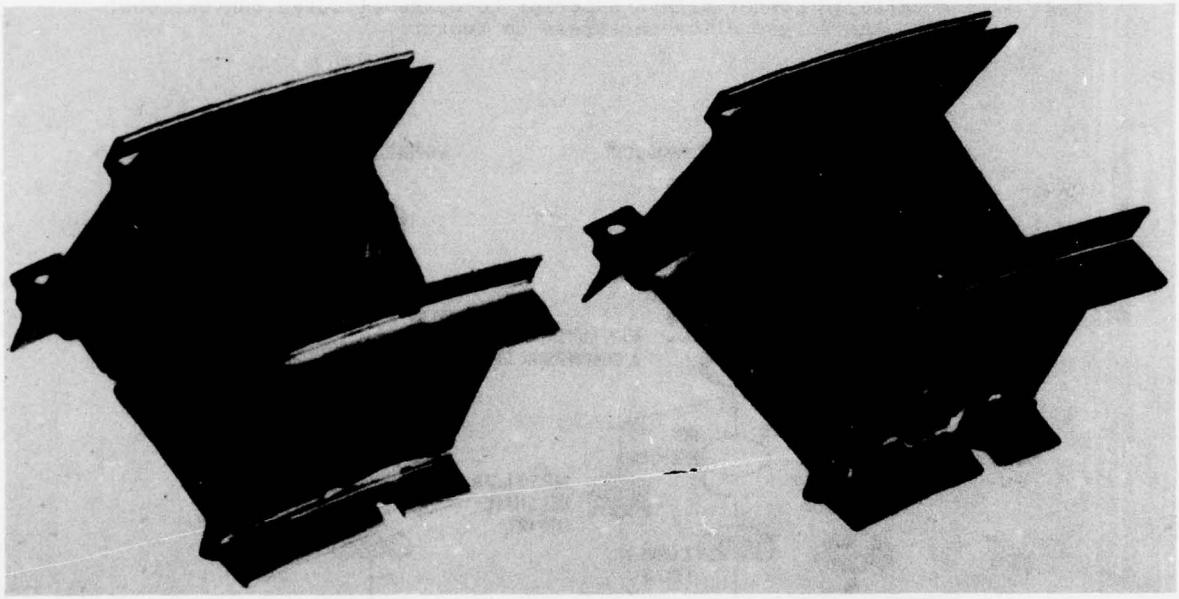

Fig. 6. - Superiority of ODS vanes at overtemperature conditions

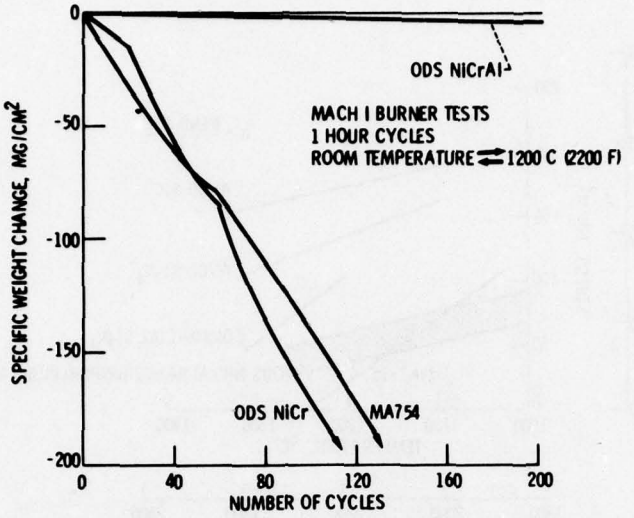

Fig. 7. - Changing to NiCrAl base affords substantial improvement in cyclic oxidation resistance of ODS alloys

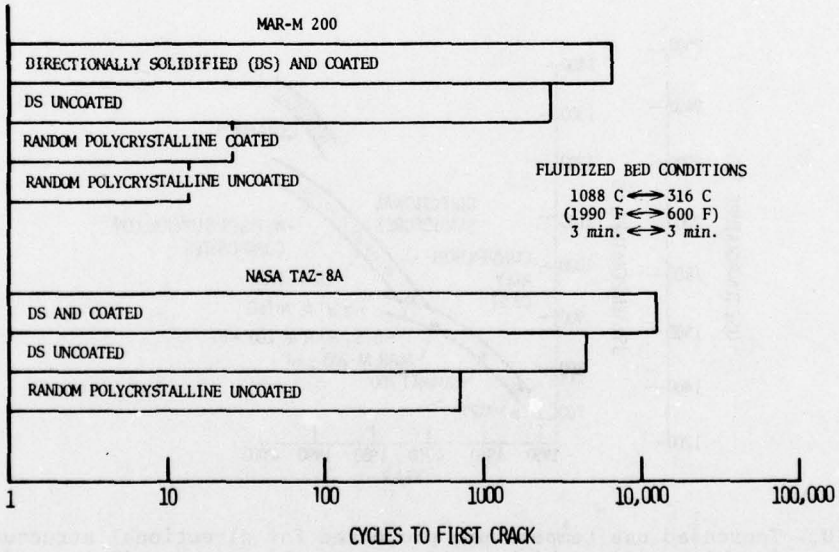

Fig. 8. - Directional solidification increases thermal fatigue resistance of superalloys

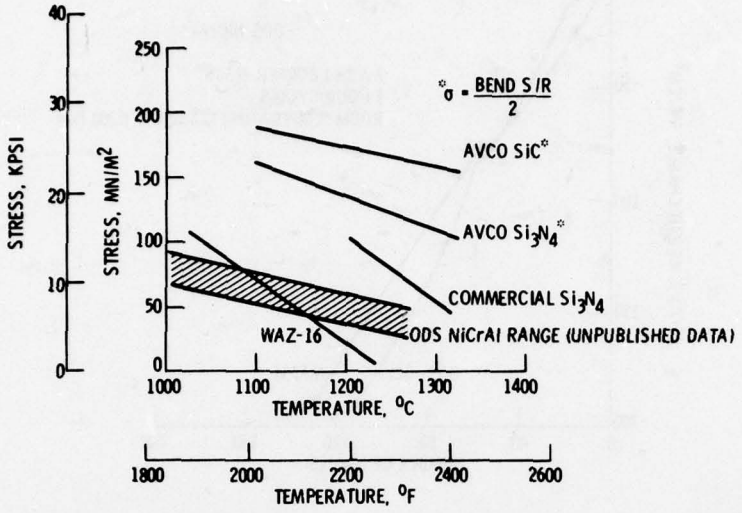

Fig. 9. - Ceramics show significant stress rupture strength increase over metallic vane materials

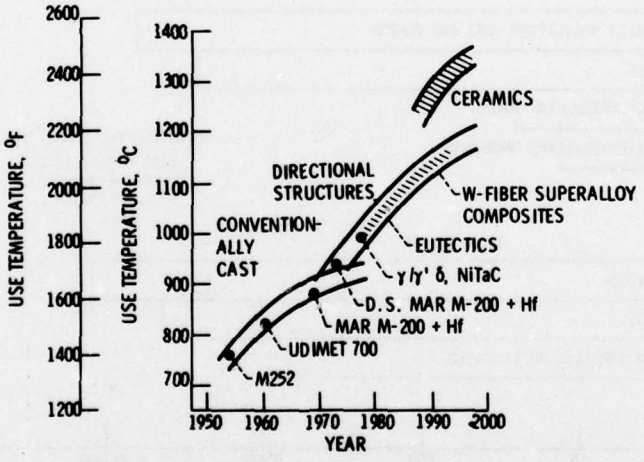

Fig. 10.- Increased use temperature projected for directional structures for high-stress, high-temperature applications. (Test condition, 30 ksi, 5000 hours.)

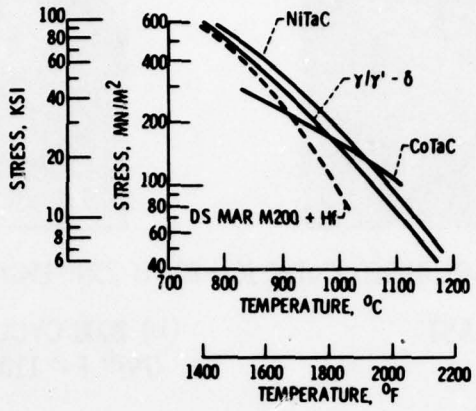

Fig. 11.- Directionally solidified eutectic alloys for blade application show significant advantage over conventional superalloy in 1000 hour stress-rupture.

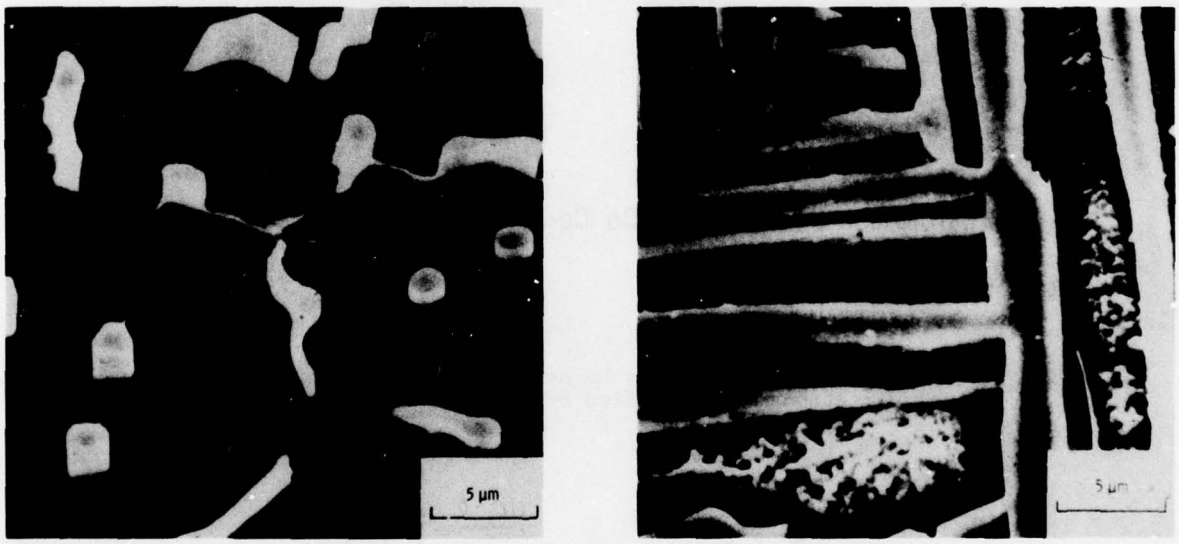

ROD HfC; HAFCO

LAMELLAR Ni_3Cb; γ/γ'-δ

Fig. 12.- Two types of DS eutectics

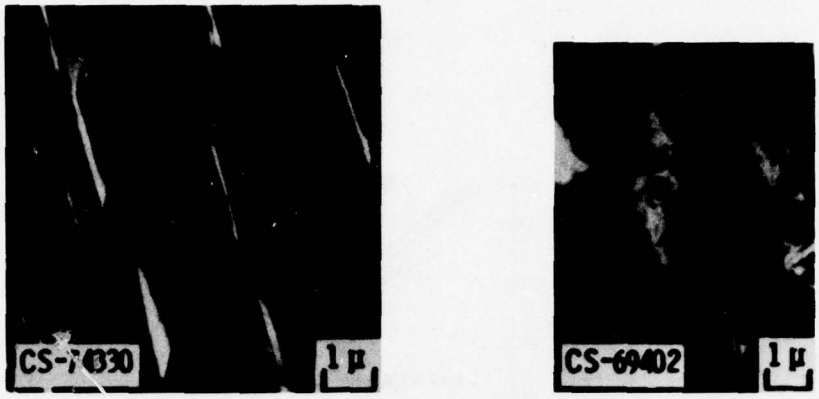

DIRECTIONALLY SOLIDIFIED CoTaC (Co-20 TO 25Ni-15Cr-12Ta-0.8 C)

(a) AS-CAST

(b) 2000 CYCLES, 425° C (797° F ≠ 1100° C (2012° F)

DIRECTIONALLY SOLIDIFIED HafCo (Co-20 TO 25Ni-15Cr-10.5 Hf-0.7 C)

CS-76753 (c) AS-CAST

(d) 2500 CYCLES, 425° C (797° F) ≠ 1100° C (2012° F)

Fig. 13.- Compositional change may be needed to insure thermal stability of directionally solidified eutectics

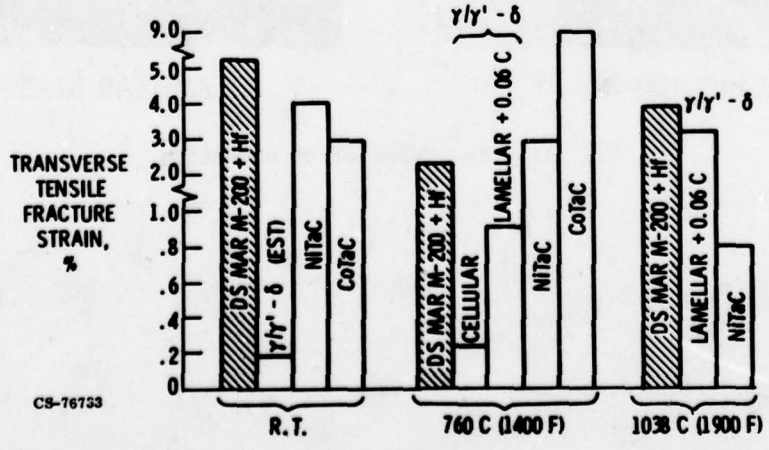

Fig. 14.- Transverse ductility problem with some DS eutectics

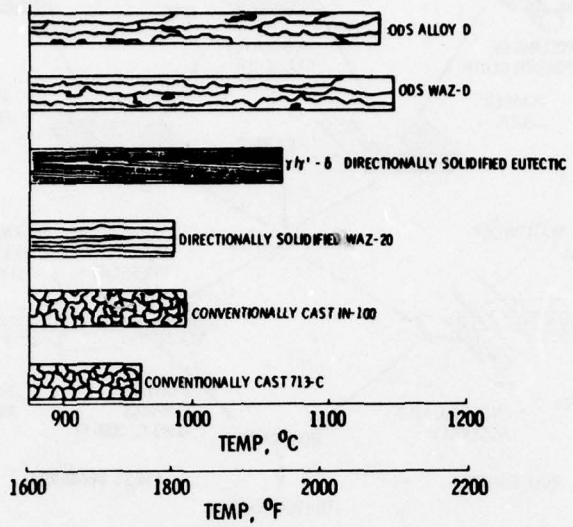

Fig. 15.- Oxide dispersion strengthening plus gamma prime strengthening provides large use temperature increases over conventionally cast and directionally solidified alloys: test conditions: 103 MN/M^2 (15KS1), 1000 hour life

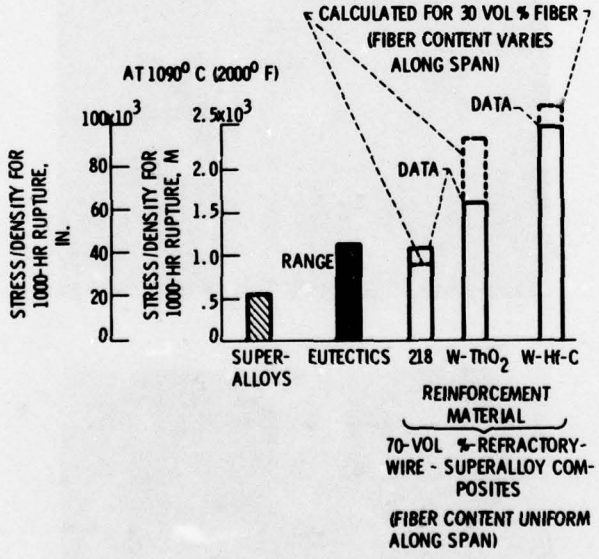

Fig. 16.- Refractory metal fiber reinforced alloys show potential advantage over advanced blade materials

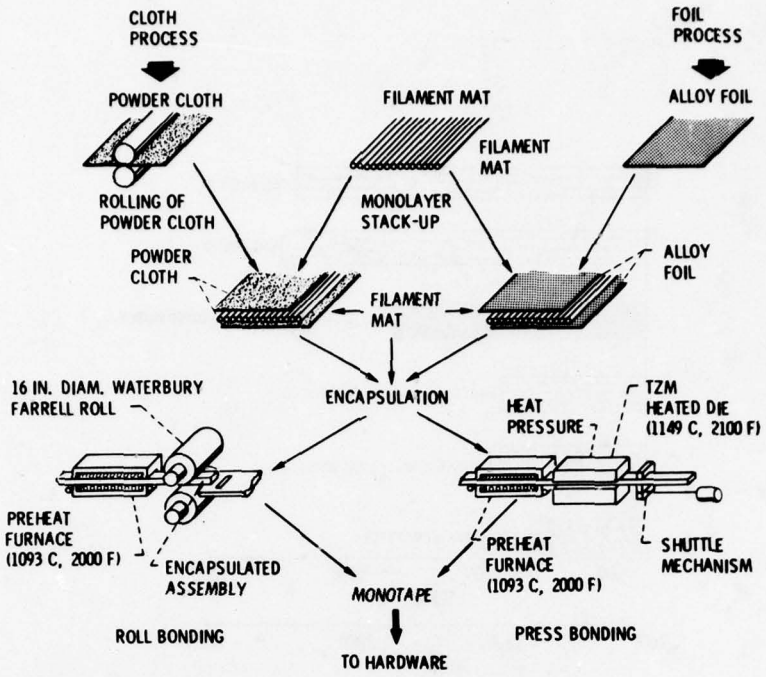

Fig. 17.- Flow diagram of diffusion bonding techniques for the manufacture of tungsten fiber-Ni alloy matrix monotapes

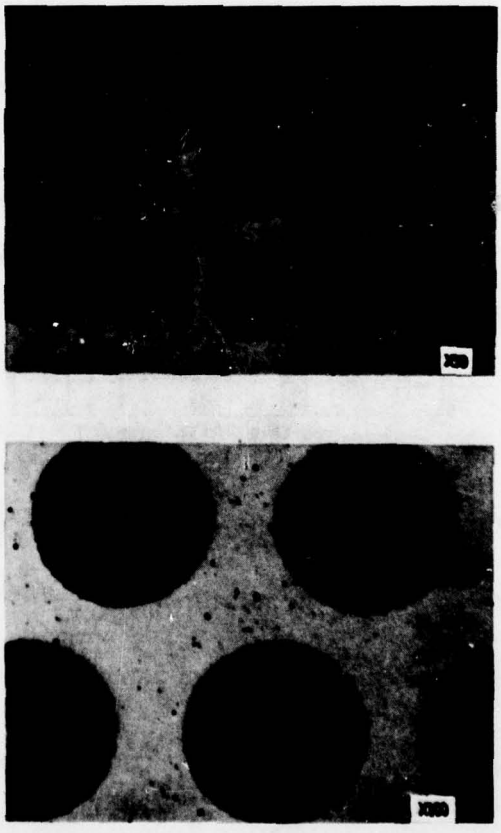

1000 CYCLES 30-1200°C (85-2200°F)

Fig. 18.- Thermally cycled tungsten wire reinforced superalloy composite promises acceptable thermal fatigue resistance (W-1 ThO_2/FeCrAlY)

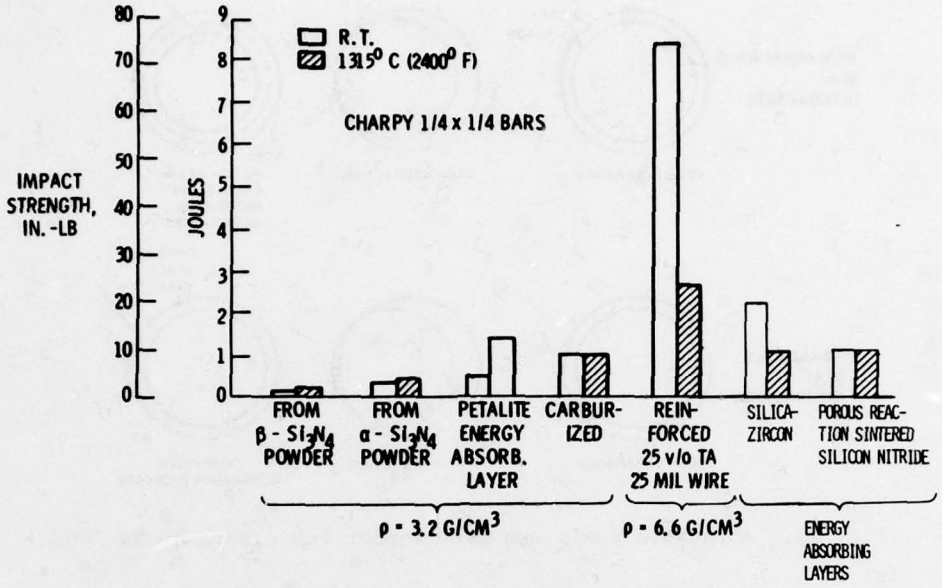

Fig. 19.- Impact strength improvements in Si_3N_4 ceramic

TYPE ROOT	MAXIMUM LIFE, HR	TEST RESULTS
	3	BENDING IN ROOT
	21	BENDING IN ROOT
	68	BENDING IN ROOT
	59	BENDING IN ROOT
	[a]242 (ALSO 108 CYCLES)	COMPRESSION IN ROOT CAUSED PIN TO LOOSEN. NO ROOT FAILURES
	[a]150	AIRFOIL (NO ROOT FAILURES)

[a]RUN DISCONTINUED - BLADES DID NOT FAIL.

Fig. 20.- Early efforts to handle problem of low ductility of ceramic blades

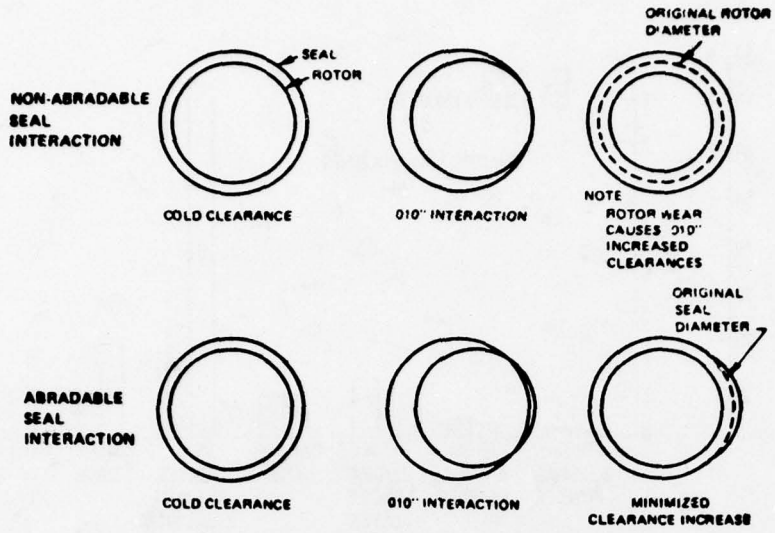

Fig. 21.- Abradable seals can reduce post rub clearance by 70%

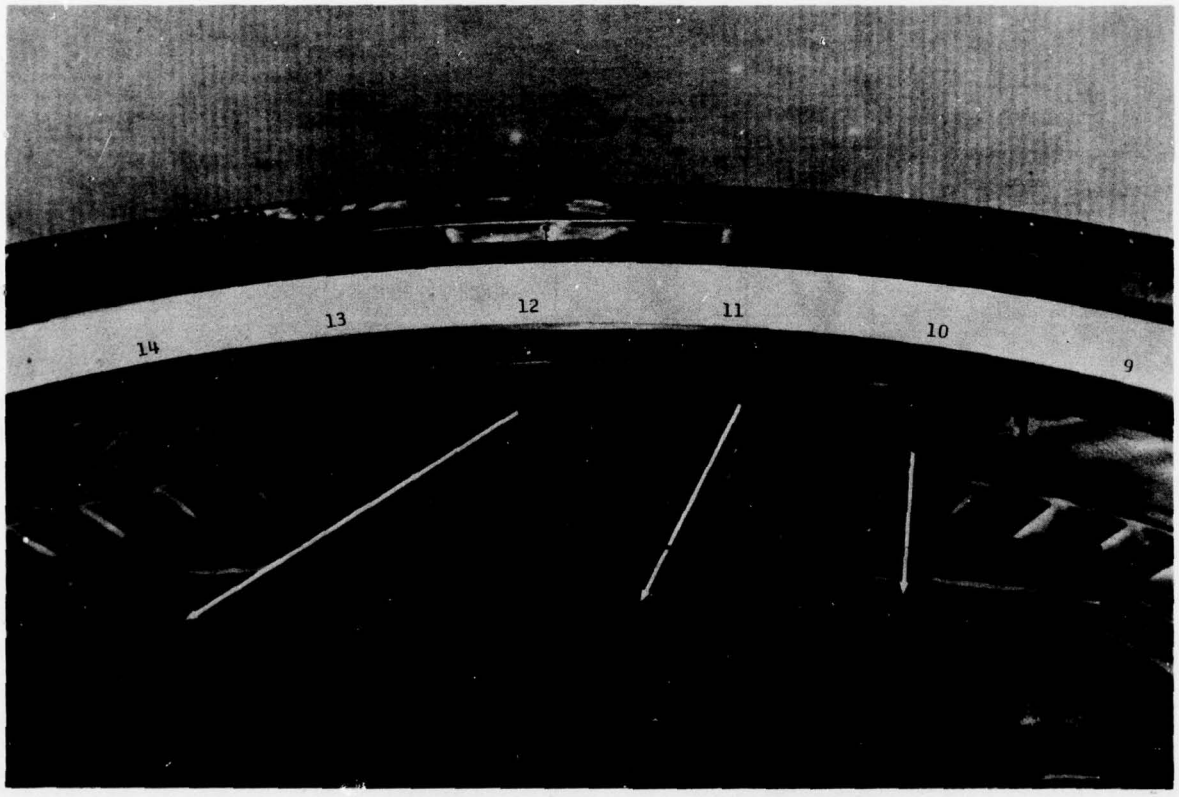

Fig. 22.- Advanced abradable porous NiCrAlY (Genaseal) shows improvement over current seal material after 1000 test/cycles in CF6-50C engine ground tests. Genaseal numbers 11 and 14; Bill of material seal numbers 9, 10, 12, 13

FUEL TYPE	IMPURITIES CONTRIBUTING TO HOT CORROSION				IMPURITIES CONTRIBUTING TO EROSION		COST
	V, (PPM)	Na+K, (PPM)	Pb, (PPM)	S (%)	ASH (PPM)	FILTERABLE DIRT %	$/10^6 BTU
KEROSENE	0.1	0.1	---	0.1	---	.002	2.80
NO. 1GT[a]	0.5	0.5	0.5	LEGAL EPA REQT.	100	.002	2.60
H-COAL[b]	2.0	5.0	---	0.5	2000	----	2.25 (CALC)
RESIDUAL OIL (NO. 4 GT)[a]	500	10.0	5.0	2.7	300	.2	2.00

INCREASING HOT CORROSION ↓ (V, Na+K, Pb, S)

INCREASING EROSION ↓ (ASH, FILTERABLE DIRT)

INCREASING COST ↑ ($/10^6 BTU)

[a] ASTM 2880-76

[b] REF. ECAS TASK II (IN PRINT) - COAL DERIVED LIQUID FUEL

CS-76730

Fig. 23.- Dirty gas turbine liquid fuels cost less than kerosene but increase hot corrosion and erosion

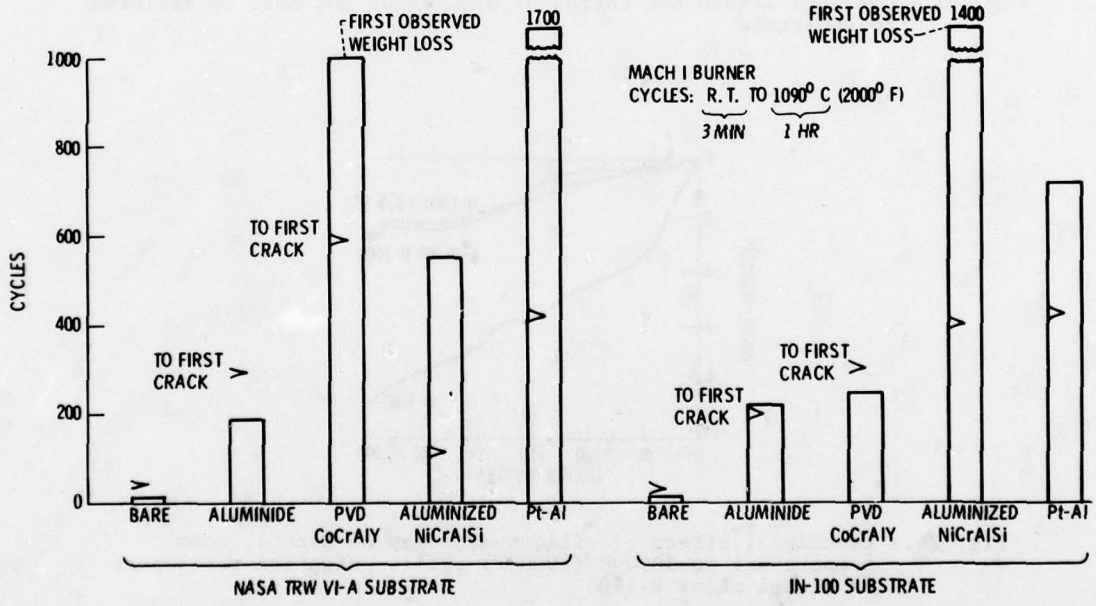

Fig. 24.- Coatings offer oxidation and thermal fatigue protection but must be tailored to substrate

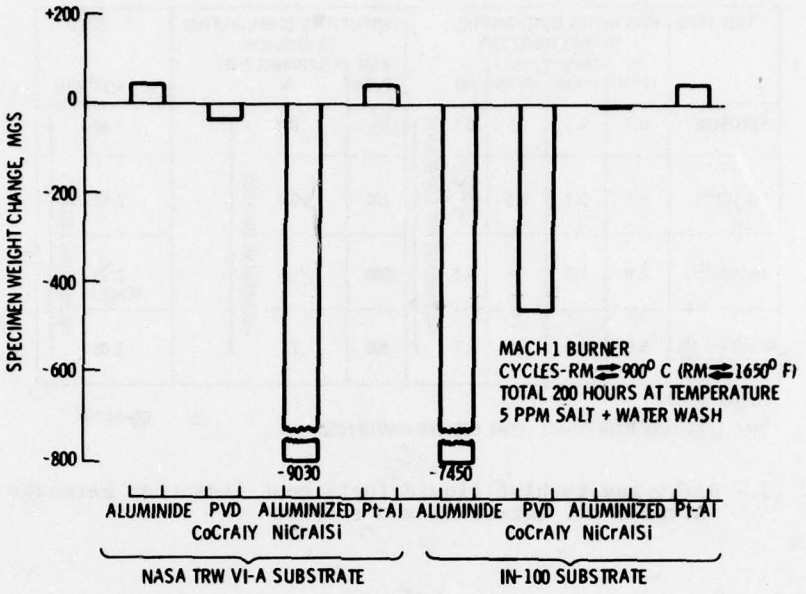

Fig. 25.- Coatings afford hot corrosion protection but must be tailored to substrate

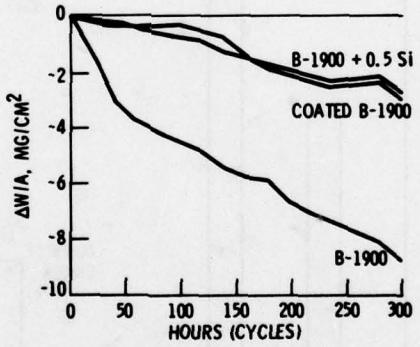

Fig. 26.- Beneficial effect of silicon addition on Mach 1, room temperature to 1090°C (2000°F) cyclic oxidation resistance of nickel alloy B-1900

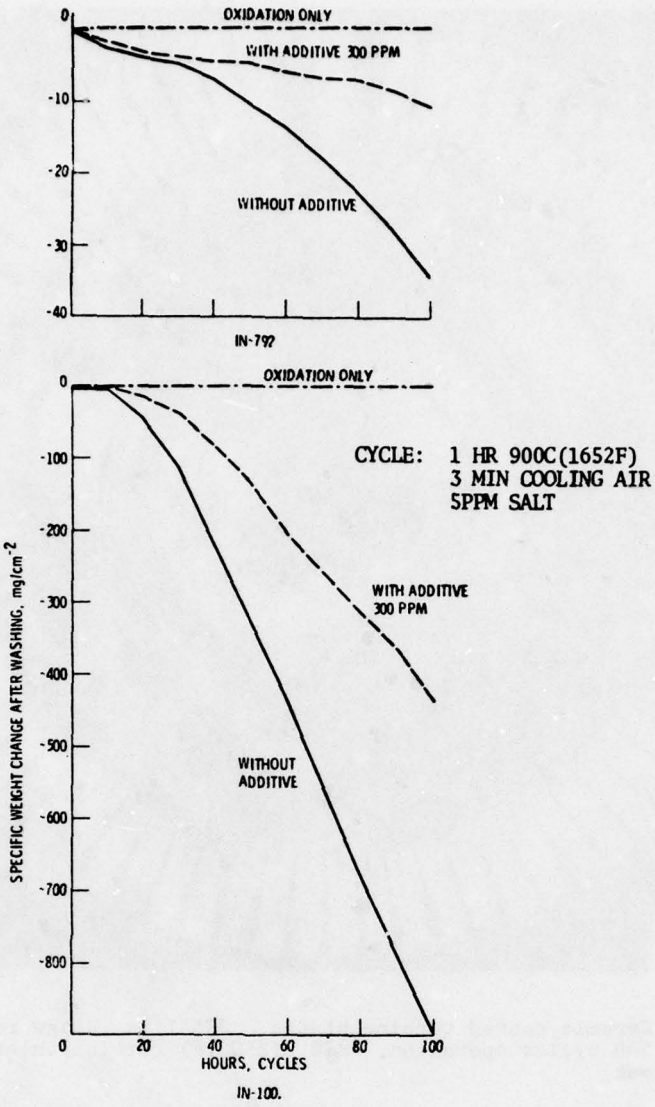

Fig. 27.- Chromium fuel additive reduces hot corrosion attack

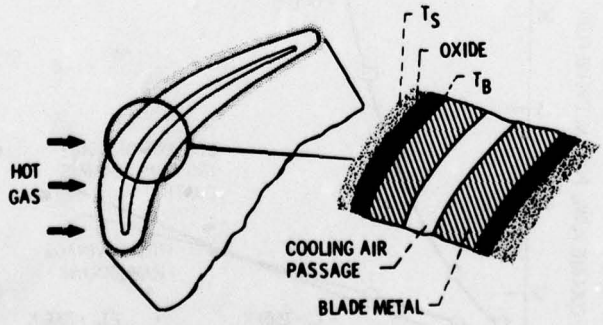

M 0.3 RIG - 182, 1-HR CYCLES
T_S = 1425° C (2600° F) T_B = 925° C (1700° F) ΔT = 480° C (900° F)

J 75 ENGINE TEST - 500, 1-MIN (AT MAX TEMP) CYCLES
T_S = 1060° C (1950° F) T_B = 900° C (1650° F) ΔT = 150° C (300° F)

Fig. 28.- Thermal barrier concept - coatings insulate turbine blades

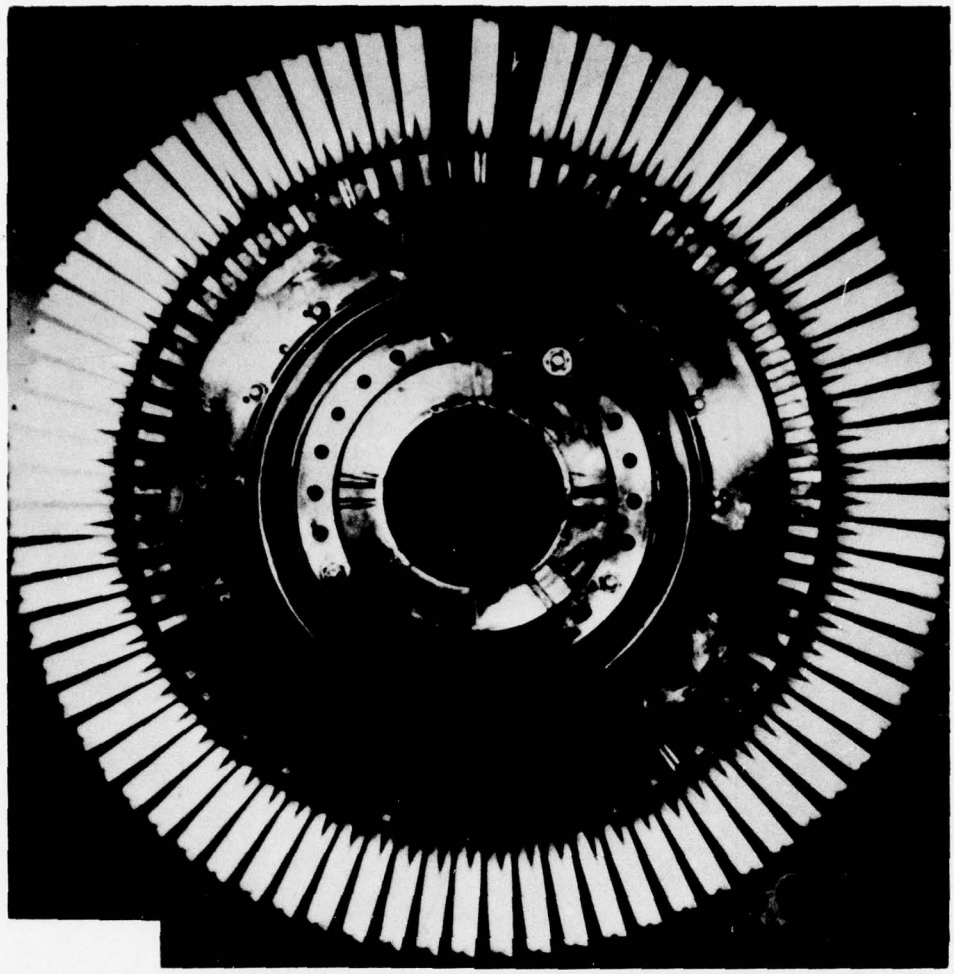

Fig. 29.- Ceramic coated turbine blades. J75 first stage rotor after 500 cycles operation, 1370 C(2500 F) turbine inlet to flame out

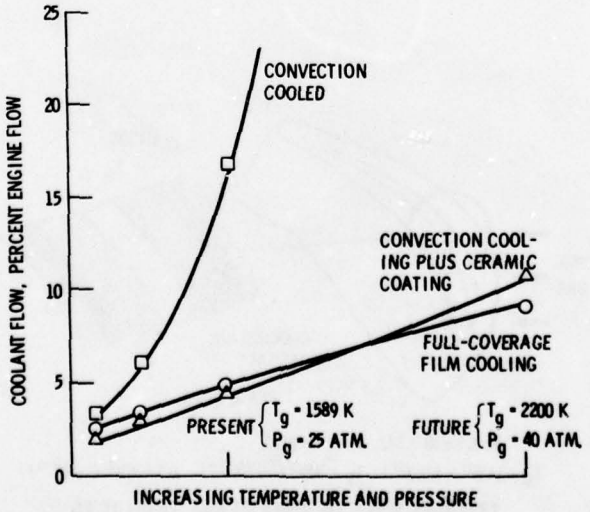

Fig. 30.- Cooling requirements for several cooling methods

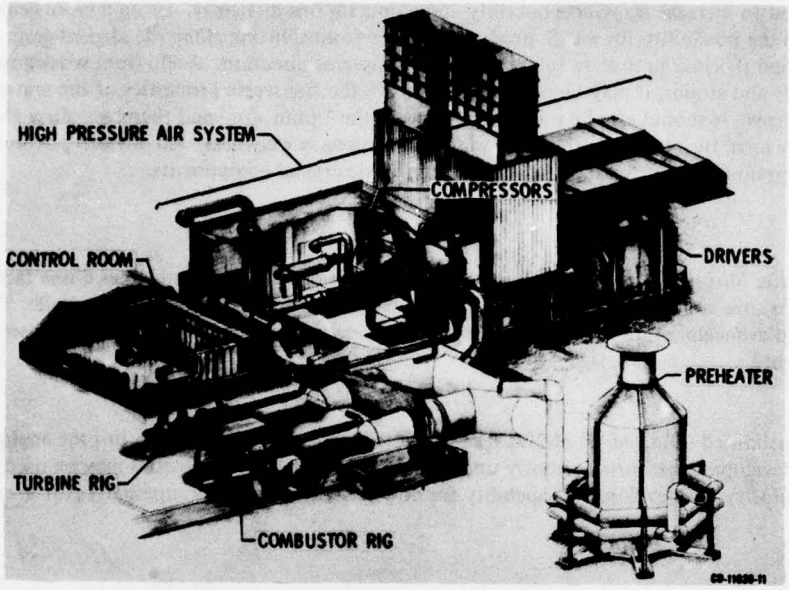

Fig. 31.- High pressure facility

DISCUSSION

A.W.H.Morris, UK

You have presented a very interesting paper and I would like to make one comment concerning tungsten wire reinforcement. The NGTE has done a considerable amount of work in this field and I would not share your optimism for this material for rotor blades in an aero engine.

My question concerns directionally solidified blades in which not only are grain boundaries longitudinal to the blade but also the grain strength. In a blade one has a complex stress pattern including transverse and high local stress perturbations. I believe there is evidence of the longitudinal grain boundary "unzipping" in D.S. blades. Can you please comment and offer any solution to the problem.

Author's Reply

During casting of D.S. blades cracking or "unzipping" was sometimes observed along grain boundaries. The addition of Hf was found to increase transverse ductility and eliminate this difficulty. From a more general point of view, there is always the possibility for a D.S. product to suffer from splitting along the aligned grain boundaries if the applied loads and thermal strains are too great in the transverse direction. Aside from redesigning to reduce the transverse loads and strains, it may be possible to improve the transverse properties of the material by slight chemistry changes. It should also be possible to increase the "grain size" and thereby reduce the total transverse grain boundary area, thus reducing the basic source of transverse weakness. An obvious possibility is to eliminate the transverse grain boundaries altogether by growing single crystal components.

A.Mihail, France

Je tiens à féliciter Monsieur Ault pour son exposé qui a fait le point de ces problèmes d'une façon remarquable. J'aurais les questions suivantes à lui poser: Vous avez parlé de la solidification directionnelle. Peut-on savoir quel est l'état d'avancement de ce problème sur le plan industriel proprement dit et quand il sera disponible pour l'emploi courant?

Author's Reply

Directionally solidified (D.S.) MAR M-200 + Hf has been used for several years in turbine engines. Industry and Government development efforts currently under way indicate that D.S. eutectics may be used in turbine engines in 2–3 years. Industry has developed a capability for directionally solidifying superalloys for use as turbine blades.

A.Mihail, France

Vous avez parlé des fibres, mais vous n'avez pas mentionné les fibres de carbone et de bore (boranes). Quelle est votre opinion sur ces types de fibres?

Author's Reply

Superalloy matrix composites reinforced with fibers other than tungsten have merit and are being studied at NASA and other laboratories. Other refractory metal alloy fibers, molybdenum, tantalum, niobium as well as carbide, oxide, and nitride fibers in superalloys, have been identified as systems with excellent potential for high temperature components. The tungsten/superalloy composite represents one of the stronger first generation systems and employs readily available fibers. Further, the plastic deformation tolerance of tungsten wire at composite fabrication temperatures is desirable in developing process techniques. It should be noted, however, that more refractory, and more brittle non-metallic fibers have greater strength-density potential for future development.

In our paper, we confined our discussion of fiber reinforced materials to turbine blade applications. Both carbon and boron fibers are primarily associated with low temperature applications such as fan or compressor blades. The use of carbon or boron fibers as reinforcements for superalloy matrix turbine blades would pose very significant problems due to fiber-matrix interaction. This would occur not only during fabrication but also during high temperature service. The question also makes reference in parenthesis to boranes, presumably the boranes referred to are the earlier boron fibers made from the diborane. These fibers were of generally poor quality. Current boron fibers are made by a boron-chloride-hydrogen process.

A.Mihail, France

Vous avez fait mention de l'utilisation de nouveaux matériaux dont les céramiques. Ces derniers posent, je crois, des problèmes du point de vue élasticité et résistance aux chocs thermiques. Que pouvez-vous nous dire sur ce dernier point et quelle est l'expérience en la matière?

Author's Reply

The problems associated with the application of ceramics to turbine components are considerable and our paper deals with a discussion of ceramics for potential high temperature, low stress applications (pp.6-7) as well as potential high temperature, high stress applications (pp.11 and 12). Rather extensive screening of many ceramics has been conducted in burner tests in which ceramic wedge-shaped specimens have been alternately subjected to a

hot and cold gas stream. In this way it has been possible to determine the more favorable ceramics from a thermal shock resistance standpoint. Both Si_3N_4- and SiC base materials are particularly outstanding in this regard and have a combination of properties which make them superior in thermal stress resistance to the oxide ceramics considered for turbine application in the past. These properties are high strength (σ), relatively high thermal conductivity (K), and low thermal expansion coefficient (α). These properties along with Young's modulus (E), are used to determine the widely used parameters

$$R_1 = \frac{\sigma}{E\alpha} \quad \text{and} \quad R_2 = \frac{\sigma K}{E\alpha}$$

which define for brittle materials the relative thermal stress resistance for an instantaneous surface temperature change and for steady-state heat flow, respectively. Si_3N_4- and SiC-base materials have high R_1 and R_2 values compared to most oxide based ceramic materials. The work at NASA-Lewis and at other organizations has clearly demonstrated the superiority of SiC and Si_3N_4 base materials over other classes of ceramics from the standpoint of thermal shock resistance.

Question from a UK participant

What do you think are the potentials of single crystals?

Author's Reply

Preliminary data indicate that single crystal alloys designed for turbine blade applications may have use temperature potential approximately equivalent to first generation D.S. eutectics, that is 25° to 55°C (50° to 100°F) greater than D.S. MAR M-200 + Hf. A substantial amount of research and development is still needed to fully define the characteristics and use temperature capability of single crystal alloys. It is not anticipated that single crystal turbine blades will be in service before the end of this decade.

M.J.Holland, UK

In connection with thermal barrier coatings, could you confirm that you are working with Zirconia rather than zirconate, also do you find coating adherence worse on the sharp radius of curvature leading edge region than on other parts of the aerofoil?

Author's Reply

Thermal barrier coatings offer an attractive near-term technology for improving the performance and/or durability of gas turbines. Preliminary analysis of current high bypass subsonic engines indicates that if a thermal barrier coating is applied so that turbine inlet temperature can be increased 80°C and cooling air flow reduced 40 percent, and 18 percent increase in thrust, a four-fold increase in life, and a two percent decrease in fuel consumption can be achieved with current blade and vane alloys. These coatings also have good retrofit potential. Benefits can be taken in terms of combinations of performance improvement as well as life improvements. Current efforts are aimed at gas turbine readiness demonstrations in the mid 1980 time frame.

THE STATUS OF SMALL, COOLED, AXIAL-FLOW TURBINES

H. F. Due, Teledyne CAE, 1330 Laskey Rd., Toledo, Ohio 43612
A. E. Easterling, U. S. Army AMRDL, Eustis Directorate, Ft. Eustis, Va.
J. E. Haas, U.S. Army AMRDL, Lewis Directorate, Cleveland, Ohio

SUMMARY

In the past ten years, a number of government and industry programs have been conducted with the objective of identifying and quantifying solutions to aid the turbine designer faced with the problem of designing small, cooled, axial-flow turbines. The problem is two-fold: one is achieving a preselected aerodynamic performance and structural life; the other lies in defining the flowpath and cycle variables necessary to satisfy the performance problem.

The small turbines addressed, fall in the 1-to-5-pounds-per-second airflow class with gas foil heights of less than 1 inch. The primary variables include blade height and chord, stagger angle blade thickness, flowpath curvature, blade curvature, cooling-flow injection, inlet turbulence, number of blades and spacing, and turbine work level.

Inability to consistently and accurately predict losses, flow conditions, operating velocity triangles, and thus stage matching has made the design development process a time-consuming, trial and error, and hence, costly procedure.

The efforts expended to develop accurate design techniques appear to reach agreement in only a few general areas. In many cases, differences in turbine hardware result from the application of different design systems attempting to satisfy the same problem statement.

This paper presents the findings of several programs which addressed the small, cooled, axial-flow turbine design problem to achieve preselected performance levels investigating the flowpath variables which affect turbine performance.

INTRODUCTION

Historically, the one gas turbine engine component which has presented few problems and concerns has been the turbine. The design of this component was considered to be relatively straightforward, yielding efficiencies in the 88% to 91% range. However, requirements for higher specific power, lower specific fuel consumption, longer life, and reduced weight dictated turbines with higher pressure ratios, and higher turbine inlet temperatures. These requirements, particularly for small engines, forced the turbine designer toward small, stubby, low-aspect-ratio, high-work blade designs for which empirical design correlations were nonexistent. The unavailability of accurate methods to predict losses, flow conditions, operating velocity triangles and thus stage matching has resulted in consistently optimistic performance predictions and has made the design development process an expensive and time-consuming trial-and-error procedure.

In 1964 two programs were sponsored to advance the technology of small, high-work, high-temperature, axial-flow turbines. Both programs successfully demonstrated the feasibility of advanced cooling concepts, but failed to achieve turbine efficiency goals. One program (1)* investigated the feasibility of utilizing a closed loop fluid (steam) thermosiphon cooling system. The predicted efficiency of the turbine was 86.7 percent. However, the demonstrated total-to-total efficiency was only 81 percent. The other program (2) investigated the feasibility of utilizing a transpiration cooling system. The demonstrated performance was approximately eighteen percentage points below the design prediction. The predicted performance of each design was based on existing techniques and correlations. However, while these prediction procedures had been substantiated in the past, they were derived from correlations of data from large, uncooled, axial-flow turbines.

Additional effort (3) was performed to investigate two potential areas of performance loss in small axial turbines: aspect ratio and blade-tip clearance. It was concluded from this effort that the performance of a small axial-flow turbine deteriorates rapidly with decreasing aspect ratios and increasing blade clearances.

During the period from 1968 to 1972, various studies of the problems associated with small, axial-flow turbines were conducted by the government and private industry. In general, it was concluded that the degradation of efficiency in small, axial-flow turbines relative to large, axial-flow turbines is a result of the three-dimensional end-wall flows in the small turbine and the increase in losses in small, axial-flow turbines associated with blade tip clearance. It was also concluded that the data required to establish the magnitude of the losses associated with small, axial-flow turbines is severely lacking.

In 1972, a program was conducted (4) to investigate various parameters which affect losses and to provide the advanced-technology small, axial-flow turbine designer with empirically-derived techniques to improve their accuracy in predicting losses, flow conditions, and velocity triangles, and in design point matching.

Several recent programs (5, 6, 7, 8, 9) were directed at investigating the aerodynamic penalties incurred from injecting cooling air from the gasfoil surface into the main stream.

A program initiated in 1974 (Low-Aspect-Ratio Turbine Technology Program) has the objective of synthesizing the losses in a turbine stage and developing an analytical model which could be used for design prediction.

Of the many investigations completed, none has indicated that it is possible to analytically predict the flow conditions and losses in a highly loaded, small, cooled turbine stage very accurately. The favored design approach still remains overly empirical, and the design goals are achieved by trial-and-error testing in test-rig environments.

Survey of Loss Prediction Methods

A widely used procedure to estimate turbine efficiency is to relate turbine blade loss characteristics to turbine mean-section velocity diagrams, Stewart (10) and Smith (11). An alternate approach still using mean-line parameters is to consider a breakdown into individual losses, such as profile, secondary, trailing-edge wakes, Reynolds and Mach numbers, and incidence, and to correct for annulus and tip-clearance effects. Ainley (12, 13), Balje' (14, 15) and Cooke (16) give extensive data on this approach.

Cold-flow rig test evaluation of a fluid-cooled, high-temperature, gas generator turbine provided observations on aerodynamic problems unique to small, cooled turbines (1). A turbine was designed by a conventional approach to yield an efficiency of over 85 percent, yet which tested to only a peak of 82 percent. Deterioration of performance was attributed to high secondary losses arising from short, thick blading, low aspect ratios, and end-wall effects. Schlichting and Das (17) suggest that blading with an aspect ratio of less than 2.0 will have losses mainly comprised of end wall or secondary flow type. Test data on aspect ratio and tip-clearance effects of the turbine of (1) suggest a tradeoff of increased hub work for longer blading to produce performance similar to a turbine with higher rim speeds but shorter blading (18, 19).

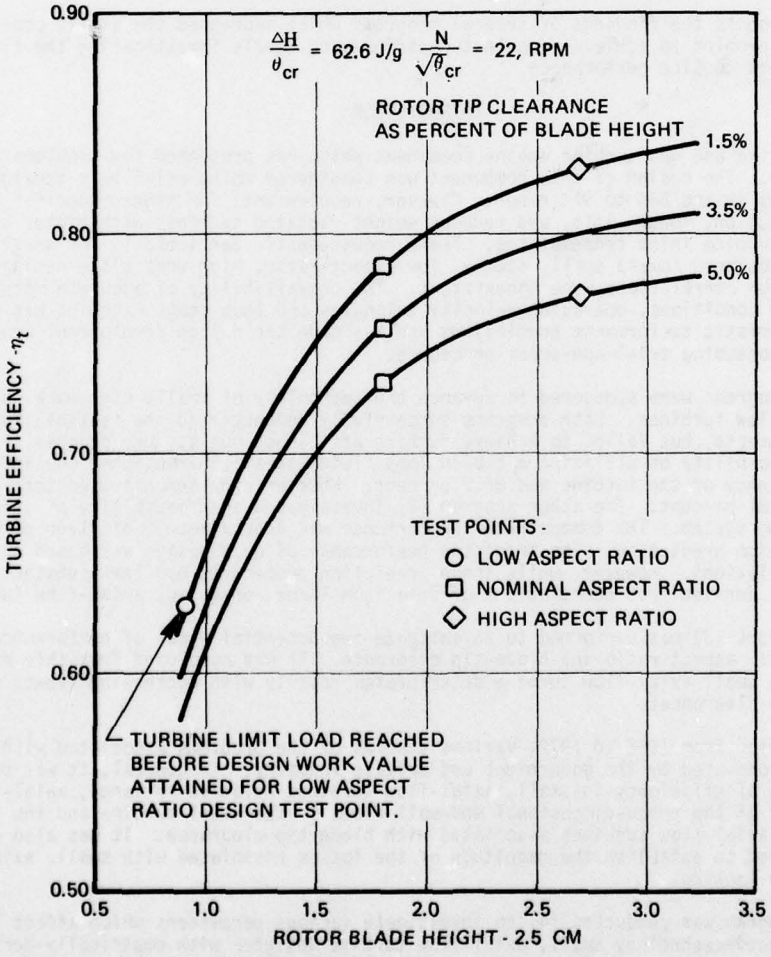

FIGURE 1. TURBINE EFFICIENCY VERSUS ROTOR BLADE HEIGHT AT 1.5, 3.5, AND 5.0-PERCENT HEIGHT CLEARANCE

Figure 1 summarizes the results of the uncooled turbine aspect-ratio testing reported in (18 and 19) and indicates a strong correlation of efficiency with aspect ratio. The addition of cooling-injection flows compounds the situation, because higher percentages of engine airflow are required for small turbines compared to large turbines.

Dunham and Came (20) made improvements to the Ainley-Mathieson prediction technique to better account for secondary and tip losses, and Figure 2 shows a comparison of predictions with the test results of (19). Burrows (21) also did extensive testing and correlated data on the low aspect ratio stator of (19) for improvements in efficiency prediction.

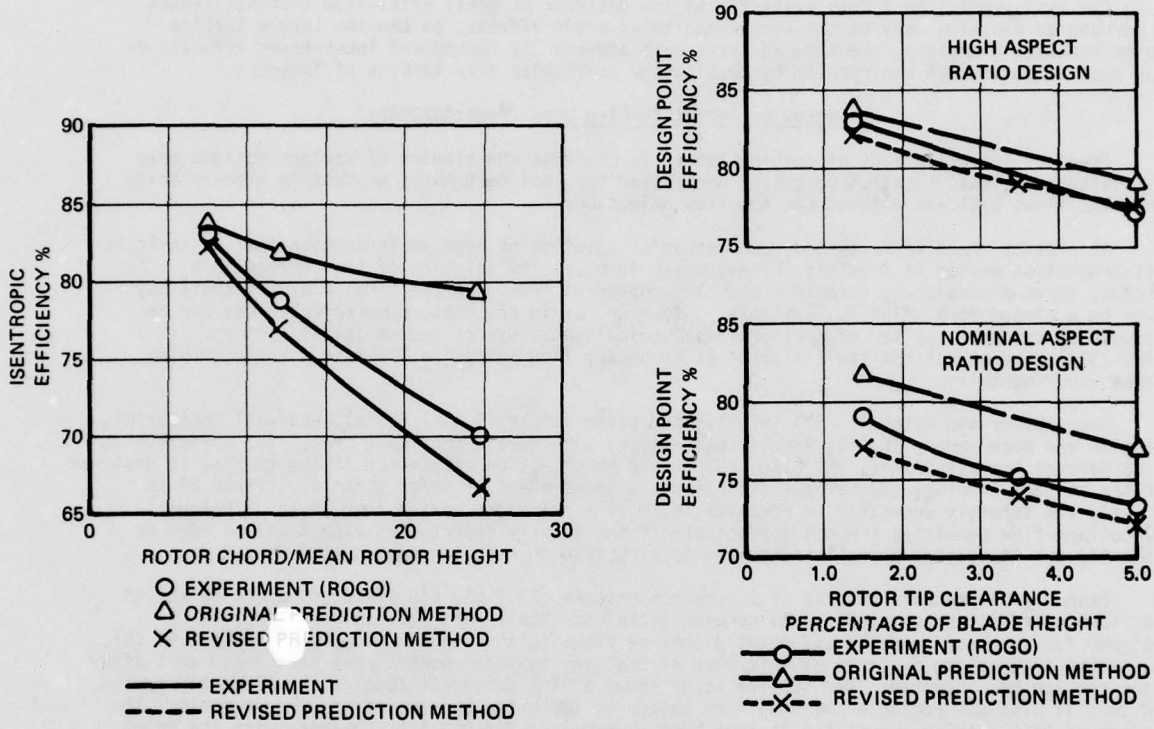

FIGURE 2. DUNHAM & CAME TURBINE EFFICIENCY PREDICTION VS. TEST DATA

Carter and Lenherr (22) performed cascade testing on the same family of turbines as Burrows tested. They chose a rectilinear cascade and concluded that the short blades of (19) were more efficient. However, the data also showed that small irregularities in flowpath and small leakages increased total loss coefficients by as much as a factor of 5. The method of defining the loss coefficients from a simple survey can also lead to inaccuracies in interpreting experimental results which makes the data of (23) suspect.

Several investigators (24, 25, 26, 27) have shown that cooling flow and location, amount, and type of injection influence aerodynamic losses; however, no universal agreement has been reached as to the method of loss prediction.

Boundary-layer and end-wall effects have been examined theoretically and semi-empirically (28, 29, 30, 31, 32, 33). Agreement between test and theory was reported difficult to achieve when addressing three dimensional flows, blade row interactions, and high Mach number effects. Inlet boundary layer and distortion effects under adverse pressure gradients in small channels have been mentioned as loss precipitators; however, data is scarce. Launder (30) presents data showing that laminarization of the boundary layer inside a stator passage is essentially independent of the boundary layer entering the cascade.

The design of the highly loaded turbine of (34, 35, 36) employed boundary layer analysis to define the blade and wall shapes, and tests were run to demonstrate the performance capabilities. The blading incorporated high aspect ratios, thin trailing edges and thin airfoils characteristic of the large, uncooled turbofan turbine and could not be scaled for use in a "small" cooled machine. The approach showed potential, but application of a simple free vortex turbine in the same flowpath and with the same mean velocity triangles was estimated to produce the same efficiency as the tested forced vortex turbine of (34).

Reference (37), reported on fundamental cascade and full-round testing on a high-work turbine using vortex flow generators, tandem blading, tangential blowing, and jet flaps. It was shown that the jet flap has a significant potential for improving performance of cooled and uncooled configurations (38).

Turbulence intensity and Reynolds number effects on cascade losses (39, 40) reported that stator losses increased with increased turbulence, whereas rotor losses decreased. The decrease in rotor losses was attributed to a reduction in off-design incidence.

A number of the referenced investigations were performed to experimentally determine the effects of various flow disturbances on the turbine performance and then to establish a model to enable prediction. It would be of value to the designed if he could quantitatively assess the effects of flow disturbances using the preliminary or detail phase of turbine design.

The loss prediction models available to the designer of small axial-flow turbines cannot be derived by dropping many of the second-and third-order effects, as can the larger turbine design models. Therefore, the flow analysis must address the second-and lower-order effects, or they must be dealt with empirically by testing the particular size turbine of interest.

Survey of Recent Turbine Loss Investigations

Previous investigations of turbine losses in cascades and blading of various designs have stimulated additional research to better understand the loss mechanisms present in high-velocity turbulent flows with and without cooling-flow injection.

At present there is no agreed-upon method of solution or even an indication that an analytic loss-prediction method is feasible. The problem involves the solution of the compressible, viscous, three-dimensional, turbulent and time-dependent flow. In the final analysis there may never be a closed form solution available. However, as in the past, some correlations can be employed to produce a system of semi-empirical guidelines. Several recent investigations (1970-1976) have approached the treatment of secondary flow losses in low-aspect ratio turbine stages experimentally.

Ewen, Huber and Mitchell (41) investigated blade height (1.45-1.65 cm), end-wall contouring, reaction and Mach number in a 25.3-cm (tip-diameter) turbine and concluded that: (1) efficiencies of 85 percent are attainable, (2) blade height has no effect on efficiency if the turbine is designed for the correct annulus, (3) turbine efficiency is independent of stage work level (from 24 to 50 J/g), and strongly dependent on reaction (mean line reactions varied from 26 to 39 percent), (4) cooling-flow penalties are not appreciable if the flow is injected at vane trailing edge or blade tip and (5) stator endwall contouring is effective in reducing secondary flow losses.

Okapuu (42) presents results of a research program (22.7 cm, tip diameter) where he stated that turbine efficiencies of 88 to 89 percent (total-to-total) were indicated by turbines designed for supersonic nozzle and rotot discharge flows (blade heights of approximately 2.90 cm). One of the interesting features of this work is that the turbine reaches peak efficiency well after rotor choking has occurred. The turbine stage shows a high degree of loss in the blade tip region, and this is also the region of maximum work output as indicated by temperature measurements. The blading of this turbine was stated to have been compromised for cooling; however, with the rotor trailing edge radius of 0.023 cm, it would be difficult to accommodate cooling passages with today's state of the art in manufacturing of cooling passages, using either casting, EDM or drilling operations. In contrast to the results of (41), Okapuu showed that the peak efficiency occurs at substantially lower reactions (approximately 22 percent) at the design point pressure ratio. The accuracy of the estimated peak efficiency is subject to question since the efficiency calculations were based on measured temperatures.

Fruchtman (43) described the limit-load phenomenon which turbines experience as they operate beyond the design pressure ratio. A procedure was presented to estimate the boundary layer separation pressure ratio. The simple approach should be welcomed by many turbine designers.

The Department of Defense (the Army, the Navy, the Air Force and the NASA) have supported continuing efforts toward the better understanding of the flow in small, cooled, axial-flow turbines. Several investigations, recently completed, are discussed in the next section.

Some Results of Recent Experimental Studies

The performance of cooled turbine vanes and blades in actual production gas turbine hardware have been investigated using production hardware in addition to hardware designed specifically for research.

One of the studies investigated the aerodynamic penalty incurred when cooling air was injected to cool the GE-12 demonstrator engine's turbine vanes. The performance of the cooled vanes was compared to that of the uncooled and to cooling penalty predictions. The vanes are shown in Figure 3. It can be noted that two rows of cooling holes are present on both the pressure and the suction sides and that they are in close proximity to the maximum curvature on the suction side. The vanes have an annular end-wall height of 1.75 cm and a vane aspect ratio of 0.5.

During the experimental investigation the vanes were tested over a range of main flow to coolant temperature ratios from 1.0 to 2.08 and pressure ratios from 1.0 to 1.4 coolant flows. They resulted in a cooling flow range from 3.0 to 10.7 percent of the main flow.

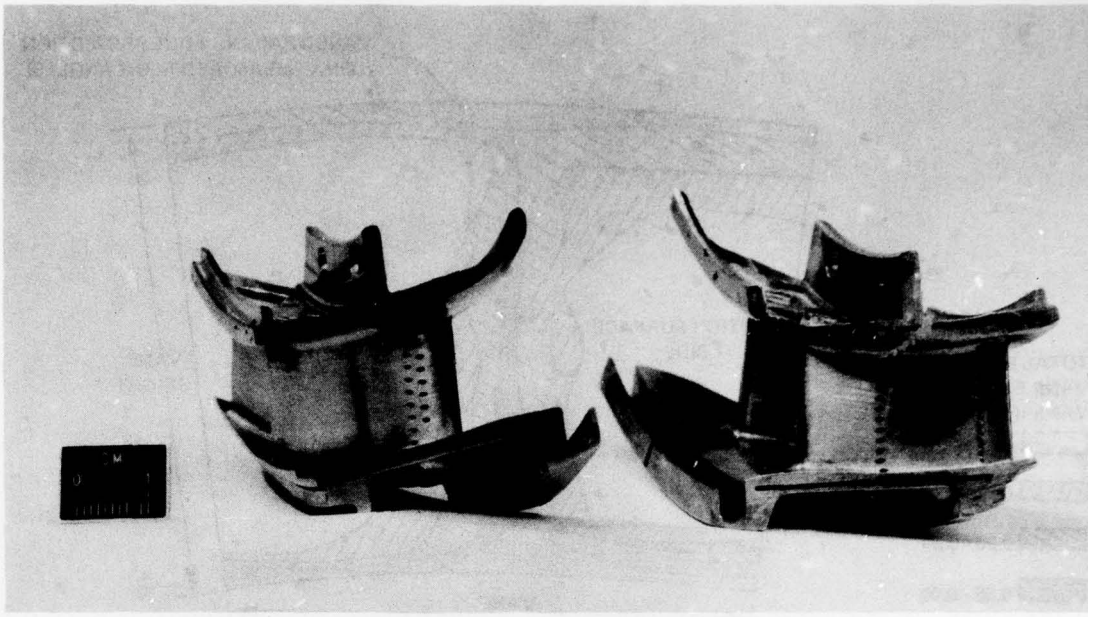

FIGURE 3. STATOR VANE SEGMENTS USED IN ANNULAR CASCADE STUDY

The performances of the cooled vanes are show in Figure 4. An efficiency of 92.9 percent was obtained for the uncooled vanes at the design point pressure ratio. The figure illustrates parametically the effects of the cooling flow ratio and the cooling temperature ratio on efficiency.

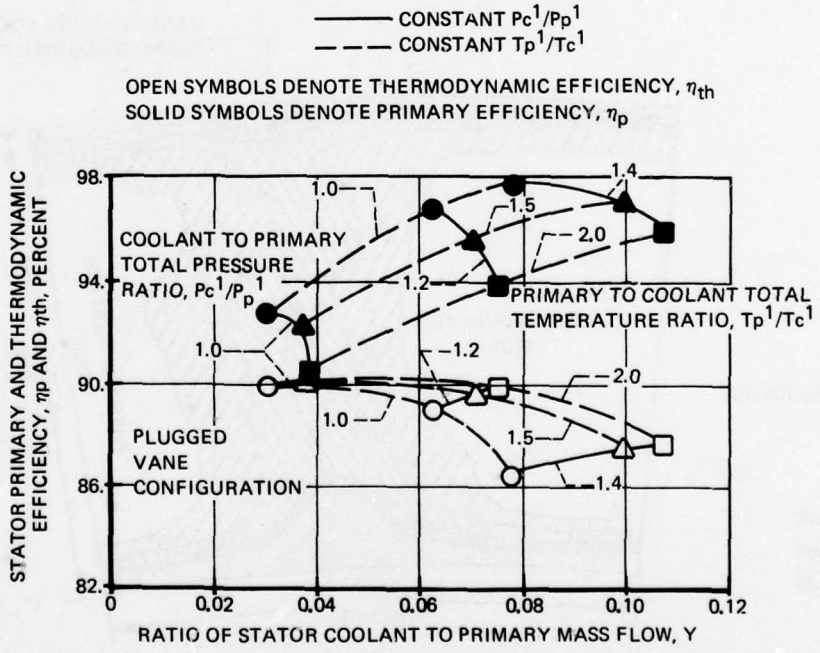

FIGURE 4. VARIATION OF PRIMARY AND THERMODYNAMIC EFFICIENCY WITH COOLANT TEMPERATURE AND PRESSURE RATIO

Pressure loss contours for the cooled and the uncooled vanes are shown in Figures 5 and 6 fo the condition of 10.7-percent cooling flow. It is readily seen that the coolant flow injection caused considerable thickening of the trailing-edge wakes. The effects of cooling flow injection on turbine efficiency was estimated using the technique of Goldman (9), and reasonable agreement was obtained (Figures 7 and 8).

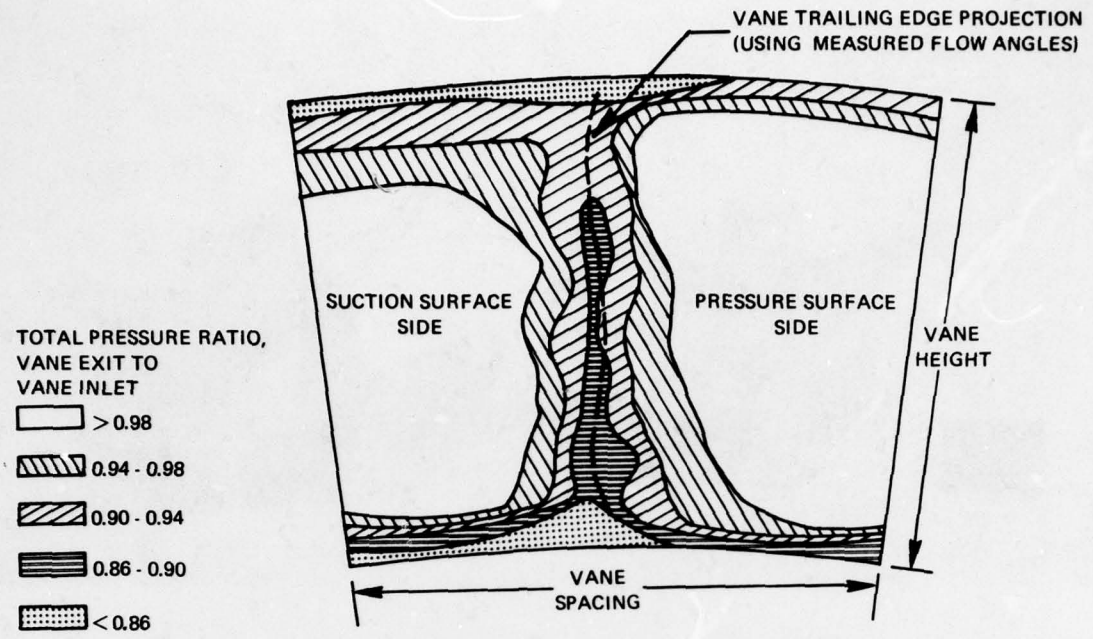

FIGURE 5. TOTAL PRESSURE RATIO CONTOUR PLOT FOR PLUGGED STATOR VANE CONFIGURATION

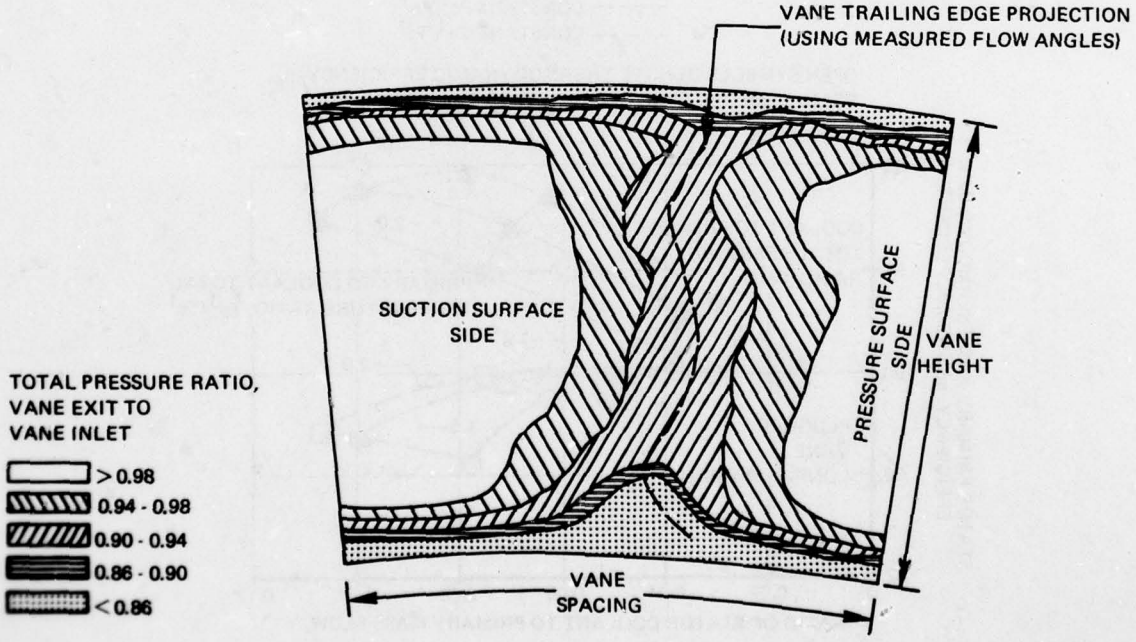

FIGURE 6. CONTOURS OF TOTAL PRESSURE AT SURVEY PLANE. DATA FOR COOLANT TO PRIMARY TOTAL PRESSURE RATIO OF 1.4 AND PRIMARY TO COOLANT TOTAL TEMPERATURE RATIO OF 1.98. (COOLANT FLOW EQUAL TO 10.7% OF THE PRIMARY FLOW)

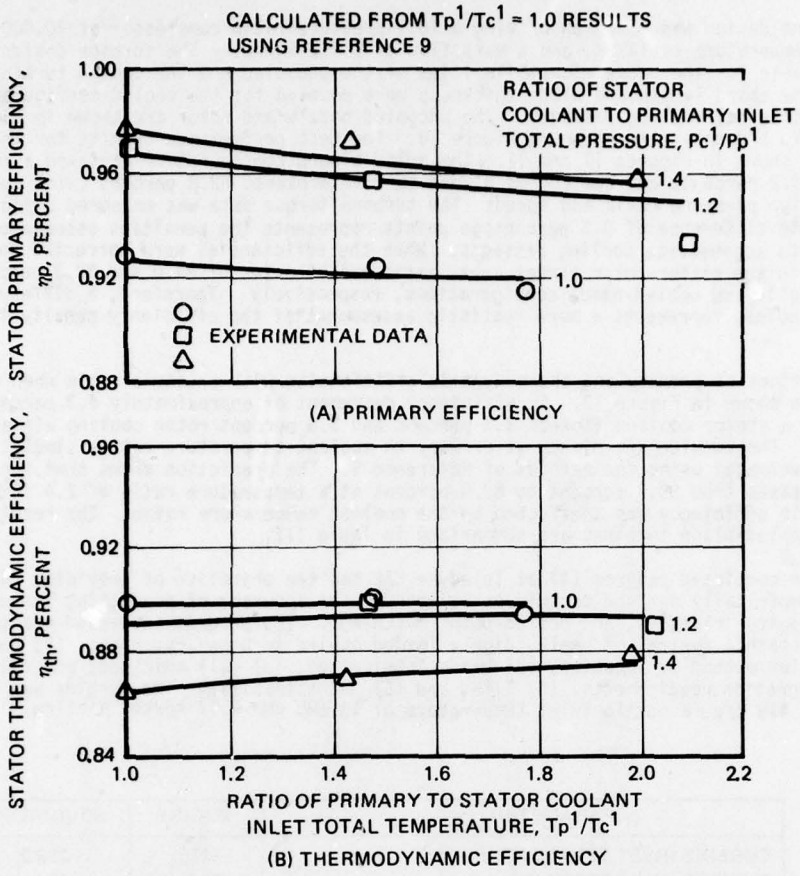

FIGURE 7. COMPARISON OF CALCULATED AND MEASURED PRIMARY AND THERMODYNAMIC EFFICIENCIES

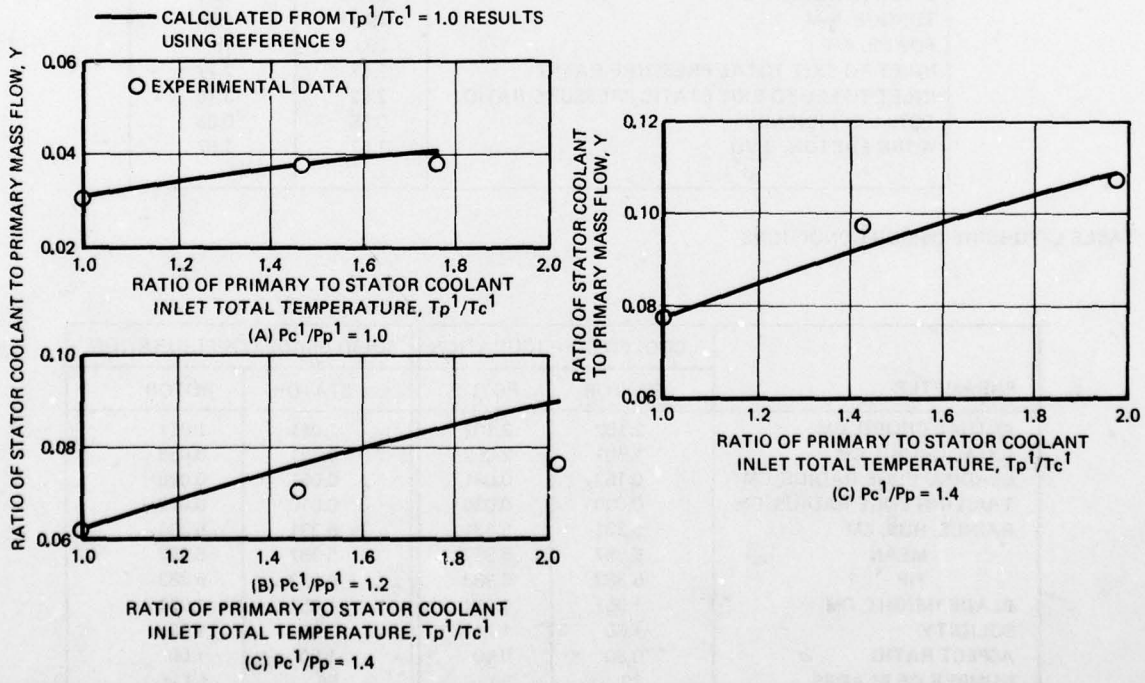

FIGURE 8. COMPARISON OF CALCULATED AND MEASURED COOLANT TO PRIMARY MASS FLOW FRACTIONS

Another program conducted was the 12.7 cm axial turbine program (5, 6, 7, 8). The objective of this program was to determine the baseline level of achievable efficiency and evaluate the aerodynamic penalty due to cooling air.

The turbine design was based on driving a 10:1-pressure-ratio compressor at 70,000 RPM, a turbine inlet temperature of 1478K, and a mass flow of 0.952 kg/sec. The turbine design conditions are listed in Table I. The geometric similarities of the uncooled and the cooled turbines are given in Table II. The chord length and blade thickness were doubled for the cooled configuration to allow for sufficient internal cooling passages. The uncooled nozzle and rotor are shown in Figure 9, and the cooled nozzle and rotor are shown in Figure 10. The test performance results for the two configurations are shown in Figures 11 and 12. The solid bladed configuration achieved a total-to-total efficiency of 83.2 percent, and the cooled bladed turbine achieved 82.8 percent (with cooling holes plugged) at design pressure ratio and speed. The turbine torque data was measured using an air dynamometer. The difference of 0.5 percentage points represents the penalties associated with larger blading to accommodate cooling passages. When the efficiencies were corrected to account for mismatches in the stator-rotor throat area, ratio efficiencies of 84.0 and 82.3 percent were estimated for solid-and cooled-blade configurations, respectively. Therefore, a difference of 1.7 percentage points represents a more realistic assessment of the efficiency penalty for geometric differences.

The variations of primary and thermodynamic efficiencies with pressure ratio when cooling flow was injected are shown in Figure 13. An efficiency decrement of approximately 4.3 percentage points was observed at a stator cooling flow of 3.3 percent and 3.6 percent rotor cooling air at design pressure ratio. The turbine efficiency at primary to coolant temperature ratios simulating an engine condition was estimated using the methods of Reference 9. The prediction shows that the primary efficiency decreases from 83.7 percent to 82.0 percent at a temperature ratio of 2.4 (Figure 14). The thermodynamic efficiency was uneffected by the coolant temperature ratio. The results of the solid-and the cooled-blade turbines are summarized in Table III.

A recently completed program (4) at Teledyne CAE had the objective of providing the turbine designer with empirically derived techniques to improve the accuracy of predicting losses, flow conditions, velocity triangles, and design-point matchings. The program addressed practical mechanical constraints typical of small, highly loaded cooled turbines, such as: (1) cooling system type and injection method or location, (2) blade fabrication, (3) wall thickness and tolerances, (4) engine integration requirements, (5) life, and (6) maintainability. The turbine was designed for a work level of 419 J/g, a nozzle inlet temperature of 1316°C and 2.17 kg/sec airflow.

PARAMETER	ENGINE	EQUIVALENT
TURBINE INLET TEMPERATURE, K	1478	288.2
TURBINE INLET PRESSURE, N/cm^2	92.1	10.1
MASS FLOW RATE, KG/SEC	0.952	0.246
ROTATIVE SPEED, RPM	70,000	31,460
SPECIFIC WORK, J/G	307.3	62.1
TORQUE, N-M	39.91	4.64
POWER, KW	293	15
INLET TO EXIT TOTAL PRESSURE RATIO	2.57	2.77
INLET TOTAL TO EXIT STATIC PRESSURE RATIO	2.92	3.16
TOTAL EFFICIENCY	0.85	0.85
WORK FACTOR, $\frac{\Delta VU}{U}$	1.67	1.67

TABLE I. TURBINE DESIGN CONDITIONS

	COOLED CONFIGURATION		SOLID BLADE CONFIGURATION	
PARAMETER	STATOR	ROTOR	STATOR	ROTOR
ACTUAL CHORD, CM	2.102	2.102	1.051	1.051
AXIAL CHORD, CM	1.607	2.062	0.721	0.968
LEADING EDGE RADIUS, CM	0.152	0.081	0.051	0.028
TRAILING EDGE RADIUS, CM	0.080	0.036	0.010	0.018
RADIUS, HUB, CM	5.331	5.331	5.331	5.331
MEAN	5.357	5.357	5.357	5.357
TIP	6.383	6.383	6.383	6.383
BLADE HEIGHT, CM	1.051	1.051	1.051	1.051
SOLIDITY	1.60	1.71	1.60	1.68
ASPECT RATIO	0.50	0.50	1.00	1.00
NUMBER OF BLADES	28	30	56	59
RADIUS RATIO	0.835	0.835	0.835	0.835

TABLE II. COMPARISON OF TURBINE PHYSICAL PARAMETERS

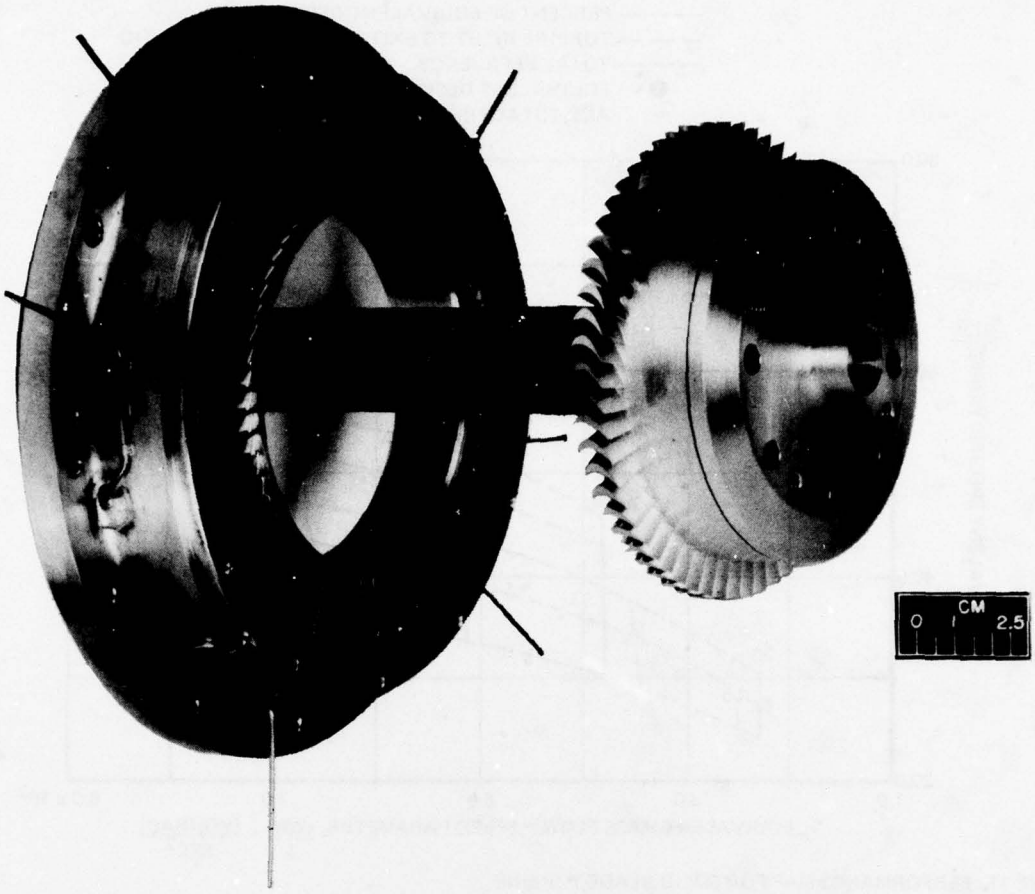

FIGURE 9. SOLID BLADE TURBINE CONFIGURATION

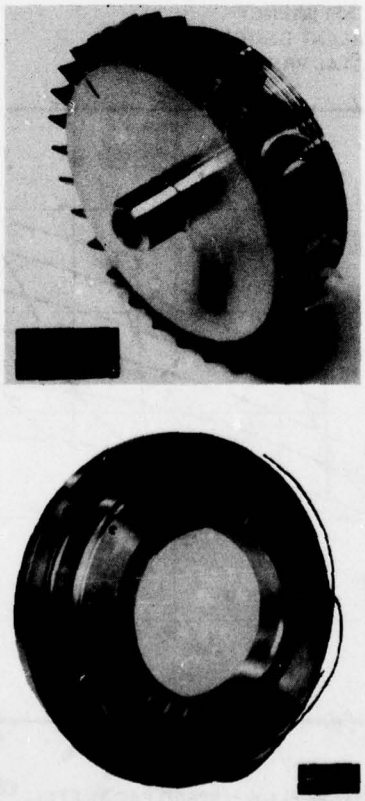

FIGURE 10. COOLED BLADE TURBINE CONFIGURATION

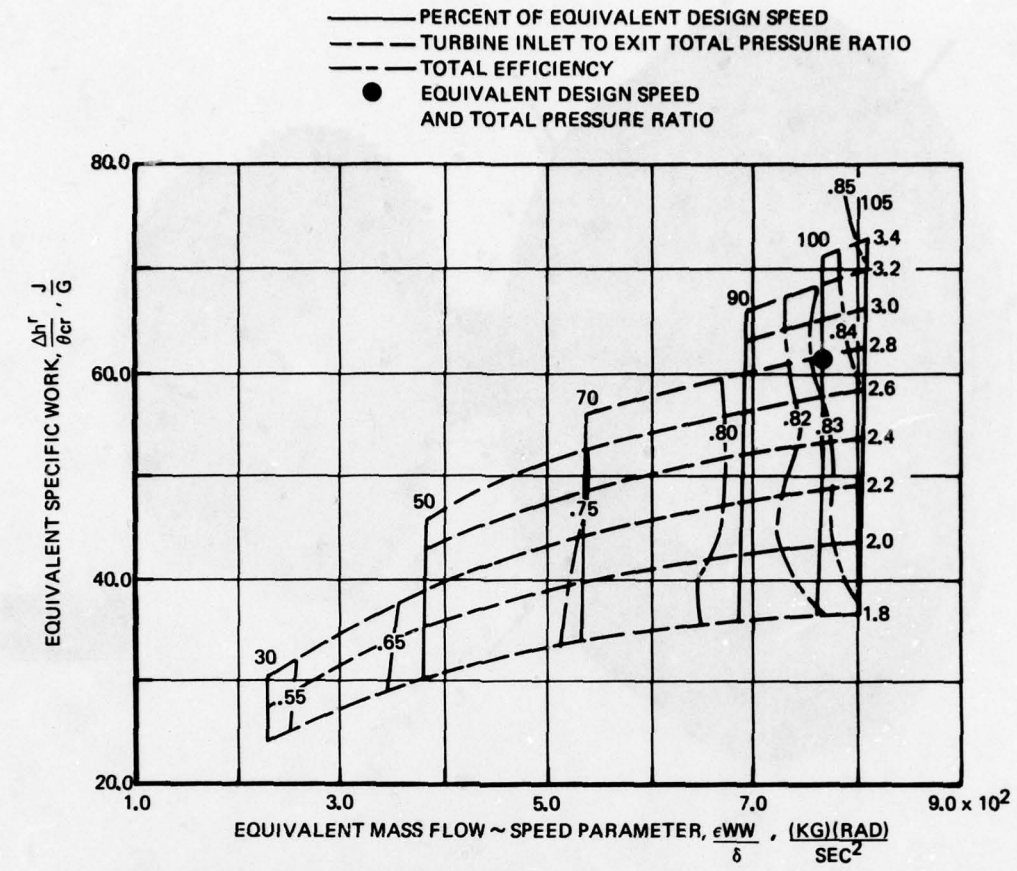

FIGURE 11. PERFORMANCE MAP FOR SOLID BLADE TURBINE

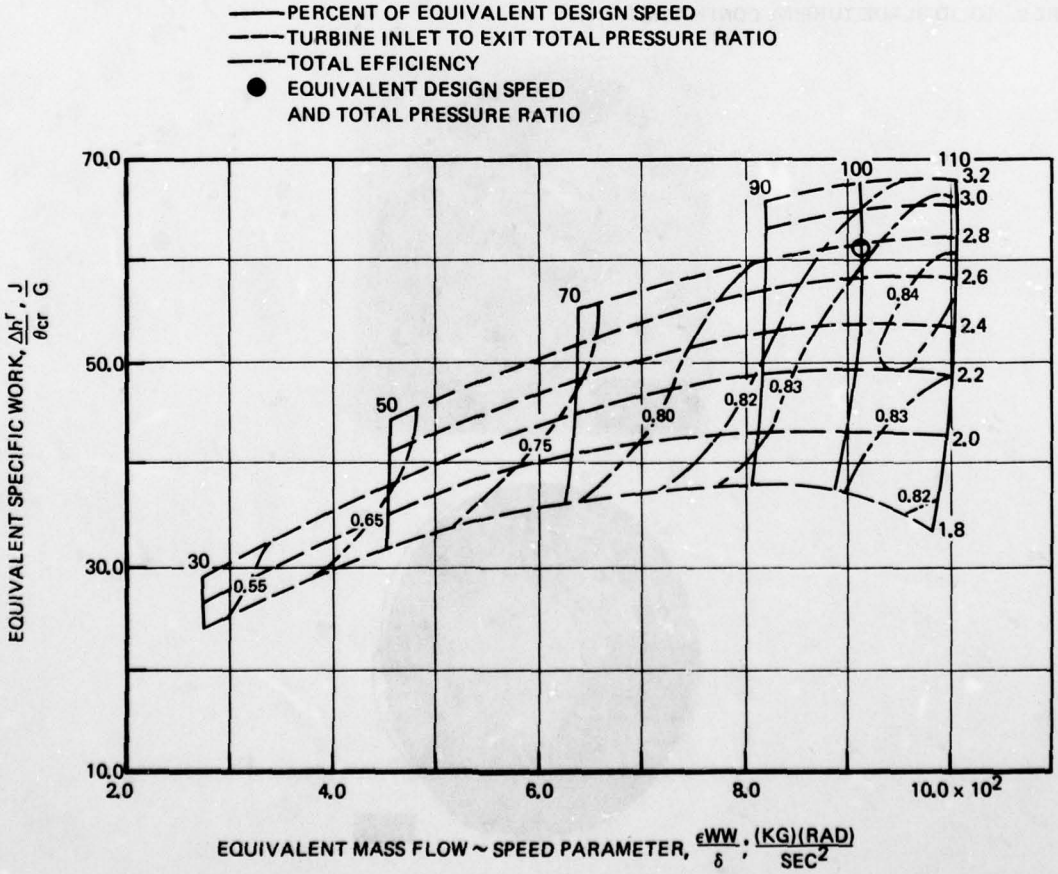

FIGURE 12. PERFORMANCE MAP FOR COOLED BLADE TURBINE

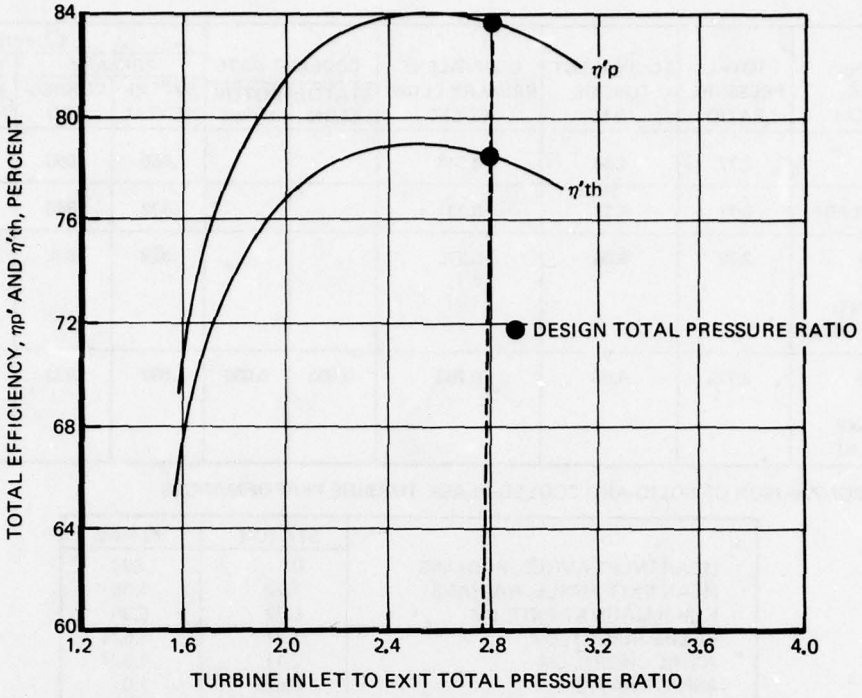

FIGURE 13. VARIATION OF PRIMARY AND THERMODYNAMIC EFFICIENCY WITH PRESSURE RATIO. (DATA AT 100% EQUIVALENT DESIGN SPEED WITH 3.3% STATOR COOLING AIR AND 3.6% ROTOR COOLING AIR)

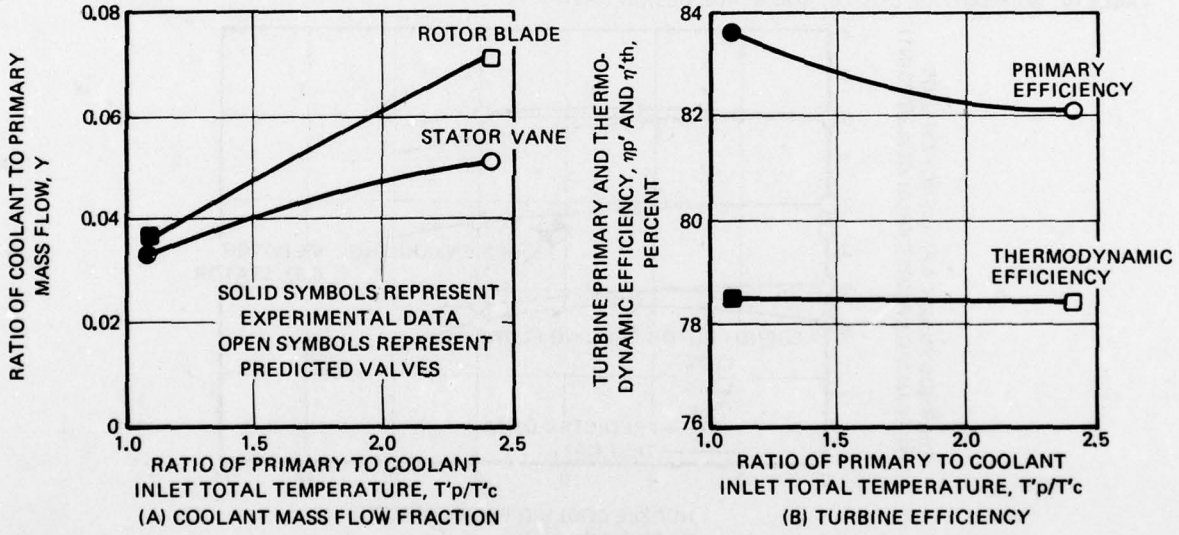

FIGURE 14. PREDICTION OF COOLANT MASS FLOW FRACTIONS AND TURBINE EFFICIENCY AT A PRIMARY TO COOLANT TOTAL TEMPERATURE RATIO OF 2.4 FROM REDUCED TEMPERATURE RATIO RESULTS

The overall program was arranged to isolate the variables which affect turbine flow and to develop both empirical data and design judgement criteria which can be incorporated into a design technique. The program was conducted in five phases.

The Phase-I effort was directed toward establishing a turbine design to meet the geometry objectives stated above for a high-performance turboshaft engine environment. The physical size of the turbine is given in Table IV.

In Phase-II, various turbine configurations were tested in a cold flow annular sector cascade. The configurations were obtained using the Phase-I turbine aerodynamics for the baseline design and varying nozzle end wall contours, inlet-flow field distortion and nozzle cooling injection. The cascade performance was determined on an average basis using a momentum transfer device, and detailed exit surveys were performed using traversing probes.

The Phase-III effort consisted of determining the turbine performance in a stage configuration. The baseline aerodynamics of the Phase-I turbine design were modified based on the results for the Phase-II testing. The effects of inlet-flow field distortion, blade loading, leakage, and nozzle and rotor cooling on performance were also investigated in the Phase-III stage configuration.

TURBINE CONFIG-URATION	TOTAL PRESSURE RATIO	EQUIVALENT TORQUE, N-M	EQUIVALENT PRIMARY FLOW, KG/SEC	COOLANT RATE		EFFICIENCY			
						PRIMARY		THERMODYNAMIC	
				STATOR Kg/sec	ROTOR Kg/sec	EXPERI-MENTAL	CORREC-TED	EXPERI-MENTAL	CORREC-TED
1. DESIGN	2.77	4.64	0.246			.850	.850	.850	.850
2. SOLID BLADE	2.77	4.27	0.231			.832	.840	.832	.840
3. COOLED BLADE (COOLANT) HOLES PLUGGED)	2.77	5.06	0.275			.828	.828	.828	.823
4. COOLED BLADE (COOLANT HOLES OPEN)	2.77	4.93	0.263	0.033	0.036	.837	.832	.785	.780

TABLE III. COMPARISON OF SOLID-AND COOLED-BLADE TURBINE PERFORMANCES

	STATOR	BLADE
MEAN INLET ANGLE, RADIANS	0	.809
MEAN EXIT ANGLE, RADIANS	1.22	1.05
HUB RADIUS AT EXIT, CM	6.77	6.35
BLADE HEIGHT, CM	1.21	1.524
AXIAL CHORD, CM	2.11	1.524
ASPECT RATIO	0.576	1.0
MEAN LEADING EDGE RADIUS, CM	.178	.076
TRAILING EDGE RADIUS, CM	.038	.038

TABLE IV. SUMMARY OF STATOR AND BLADE DESIGN DATA

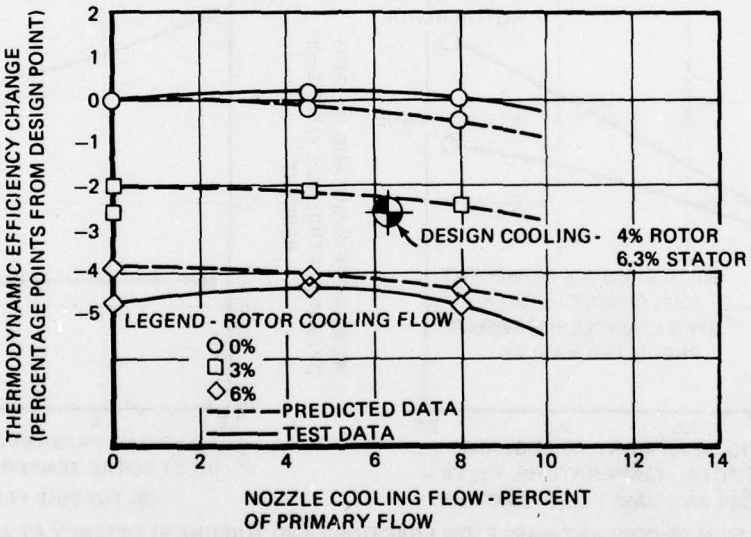

FIGURE 15. EFFECT OF STATOR AND ROTOR COOLING FLOW ON TURBINE STAGE EFFICIENCY

The results of Phases II and III were combined to provide the basis for a design technique modification in Phase IV. The turbine was modified to yeild a performance increase using the developed semi-empirical model. The turbine modification consisted of a stator throat area variation with the intended purpose of shifting the radial distribution of flow toward the inner flowpath region.

Phase-V consisted of the experimental verification of the turbine's performance. Tests were performed to determine the stator loss distribution and the turbine stage performance for two rotor blade loadings: one which favored the suction side and another which favored the pressure side. The results showed that the average stator loss had increased (relative to the Phase III result) however, the stage efficiency was improved by one percent on both rotor configurations, and the predicted performance level was achieved.

The results of the cooling flow investigations conducted in Phase III of the program are shown in Figure 15. It was observed that the injection of the stator cooling flow from the pressure side of the stator had little effect on efficiency; however, the rotor blade cooling flow had a considerable effect. The rotor blade cooling flow was also injected from the pressure surface at spanwise locations upstream of the throat. The design-point cooling flows of 6.3 percent for the stator and 4 percent for the rotor resulted in an efficiency decrement of approximately two and one-half points.

PARAMETER OR EFFECT OF:	CONFIGURATION AND CHANGE	FLOW		EFFICIENCY		EFFICIENCY
		PERCENT CHANGE FROM BASELINE	PERCENT DIFF. FROM DESIGN	POINTS CHANGE FROM BASELINE	POINTS DIFF. FROM DESIGN	
NONE-DESIGN	DESIGN	——	——	—— •	——	NOZZLE 90.1 STAGE 80.2
COOLING FLOW ON NOZZLE	NOZZLE ALONE: COOLING FLOWS OF 0 AND 1.8 PERCENT	——	-6.4, -4.6	0, -0.1	2.4/2.3	92.5/92.4
DISK WINDAGE BEARING AND COOLING PUMPING LOSSES	NOZZLE PLUS BLADELESS DISK ASSEMBLY	STAGE EFFICIENCY LOSS IN POINTS @ P = 1 ATMOS.		(A) DISK WINDAGE AND BEARING = 3.4 (B) DISK WINDAGE, BEARING WITH 1.8% ROTOR COOLING = 4.2		
NONE - BASELINE PLR	PLR STAGE: NO COOLING	0	-6.4	0	-3.7	76.5
COOLING FLOW ON PLR STAGE	PLR-STAGE WITH COOLING, W_{CN} = 4% W_{CR} = 2%	+2.0	-4.6	-2.2	-5.9	74.3
ROTOR BLADE LOADING	SLR STAGE: NO COOLING	0	-6.4	+2.3	-1.4	78.8
NOZZLE BYPASS FLOW ON SLR STAGE PERFORMANCE	SLR STAGE WITH W_{BP} = 4%	+4.0	-2.6	-2.6 *	-4.0	76.2
NOZZLE BYPASS FLOW ON PLR STAGE PERFORMANCE	PLR STAGE WITH W_{BP} = 4%	+4.0	-2.6	-1.6	-5.3	74.9
INCREASED NOZZLE/ ROTOR AXIAL SPACING ON PERFORMANCE OF SLR TURBINE	SLR STAGE WITH INCREASED NOZZLE/ROTOR AXIAL SPACING FROM 0.25 TO 0.45 IN.	0	-6.4	-3.2	-4.6	75.6
INCREASED NOZZLE/ ROTOR AXIAL SPACING ON PERFORMANCE OF SLR TURBINE WITH NOZZLE BYPASS FLOW	SLR STAGE WITH 0.2 IN. INCREASED NOZZLE/ ROTOR AXIAL SPACING AND W_{BP} = 4%	+4.0	-2.6	-3.7	-5.1	75.1
INCREASED BOUNDARY LAYER ON BOTH WALLS	PLR-STAGE: 8% ANNULUS BLOCKAGE PLATES ON ID AND OD WALLS 40 x 40 x 0.012 SCREEN	0	-6.4	-1.2	-4.9	75.3
INCREASED OUTER WALL VELOCITY GRADIENT	PLR-STAGE: 24% ANNULUS BLOCKAGE PLATE ON ID 12 x 12 x 0.020 SCREEN	0	-6.4	0	-3.7	76.5
DECREASED ROTOR SOLIDITY ON PERFORMANCE OF PLR TURBINE	PLR BLADING WITH 22% REDUCED SOLIDITY	0	-6.4	-3.7	-7.4	72.8
REYNOLDS NUMBER ON PERFORMANCE OF PLR TURBINE	PLR STAGE AT NR/N_P DESIGN = 0.41	0	-6.4	-2.7	-6.4	73.8
REYNOLDS NUMBER ON PERFORMANCE OF SLR TURBINE	SLR STAGE AT NR/N_P DESIGN = 0.41	0	-6.4	-2.5 *	-3.9	76.3

* BASELINE IS SLR STAGE WITH NO COOLING, TEST 5.

TABLE V. SUMMARY OF PHASE III TEST RESULTS AT DESIGN SPEED AND WORK

A summary of the many flow perturbations investigated in Phase III and their effects on performance are given in Table V. The PLR and SLR stages referred to in the table denote two rotors of different design loadings, one favoring the pressure side (PLR) and the other favoring the suction-side (SLR). The design-point efficiency of both stages was 80.2 percent and both were designed to the same velocity triangles. Reference (4) will provide a more detailed description of the design and test parameters described in Table V.

The Phase IV analysis identified a stator modification which had the effect of decreasing the hub incidence and increasing hub reaction. The results of Phase V are compared to Phase III in Table VI.

	PHASE V		PHASE III		DESIGN
	PLR	SLR	PLR	SLR	
REFERRED SHAFT SPEED, % DESIGN	100%	100%	100%	100%	100%
PRESSURE RATIO (TOTAL-TO-TOTAL)	4.0	4.0	4.0	4.0	4.0
REFERRED WORK, $\Delta H/\theta_{cr}$, J/G	73.5	75.6	72.6	74.9	77.7
EFFICIENCY, (TOTAL-TO-TOTAL)	77.8	79.9	76.8	79.1	80.2
ROTOR REACTION, HUB	0.044	0.072	0.012	0.046	0.11
ROTOR REACTION, MEAN	0.094	0.130	0.101	0.139	0.17
ROTOR REACTION, TIP	0.145	0.188	0.190	0.233	0.24

Both stage configurations (SLR and PLR) responded favorably to the stator modification. Rotor blade incidence was reduced, and hub reaction through the rotor increased as expected to yeild an approximately 1.0-point improvement in stage efficiencies. The SLR performance approached to within 0.3 points of the design goal efficiency of 80.2 percent. As a result of the stator cutback, air deflection angles were reduced through the stator cascade.

The relative performance between the two rotor configurations was the same as in Phase III testing, with the suction surface loaded configuration yielding superior performance by 2.1 points in efficiency. This was attributed in part to the more favorable near-hub rotor incidence and reaction of the SLR configuration.

Comparisons of Recent Small-Turbine Investigations

A comparison of some of the various parameters affecting turbine efficiency should suggest correlations. The turbine investigations discussed in the previous section are compared in Table VII. The parameters listed include important physical dimensions and design-point aero-thermo quantities. Also; listed are the design (as available) and test values of total - total adiabatic efficiencies at design-point pressure ratio and equivalent speeds. The physical dimensions of the turbine vary with the cycle/engine requirements and with the design methodology used to meet the cycle requirements. For example, the designer has a choice of a wide range of speeds, turbine diameters and blade heights to meet a particular flow rate and work requirement. Constrained somewhat by compressor speed requirements and structural limitations at turbine operating temperatures, the designer still has the freedom to design several turbines differing widely in blading and flowpath to fit the same application. The final constraint however is optimum performance. Each turbine design will produce different operating characteristics. Of the turbines discussed in the previous section and compared in Table VII, all are classified as small, high-work, cooled turbines, and yet, there is a wide variation of physical and aero-thermo parameters.

One of the most significant turbine efficiency correlating parameters is the stage work coefficient. Figure 16 shows efficiency - stage work coefficient correlation for the turbines in Table VII. Correlations of some previous investigations are also shown as taken from Horlock (44). It is readily apparent that the trend of decreasing efficiency with increasing work coefficient has been consistent throughout the years. It can also be noted that the level of efficiency has decreased with decreasing turbine size. Of the turbines shown in Figure 16 only number 4 does not fit well with the correlation. However, it can also be noted that the blade height of that turbine is twice that of most others in the comparison and that the aspect ratio is 1.81 compared to the others of around 1.0. In addition the rotor trailing-edge radius is significantly less for that turbine which could also be a factor contributing to its higher efficiency. In drawing conclusions from comparisons and

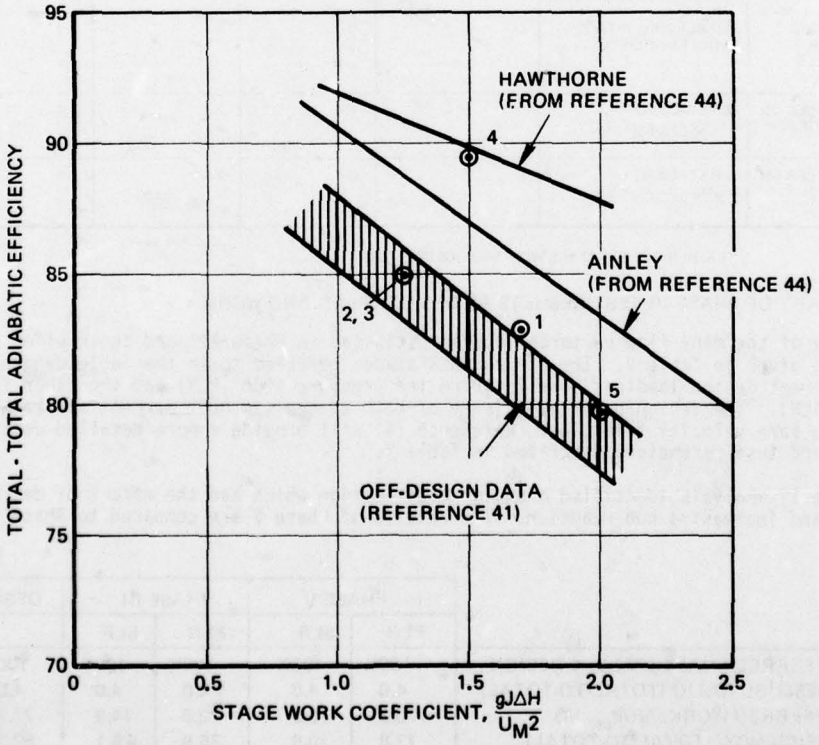

FIGURE 16. TURBINE EFFICIENCY CORRELATIONS WITH STAGE WORK COEFFICIENT

SOURCE	ROTOR TIP DIAMETER CM	TIP CLEARANCE CM	ROTOR BLADE HEIGHT CM	AXIAL ASPECT RATIO (ROTOR)	AXIAL SOLIDITY (ROTOR)	STAGE LOADING $\Delta H/\theta_{cr}$ J/G	STATOR T.E.R CM	ROTOR T.E.R. CM	EQUIVALENT ROTOR TIP SPEED M/SEC	STAGE WORK COEFFICIENT $\frac{gJ\Delta H}{U^2}$ (MEAN)	TURBINE STAGE EFFICIENCY TOTAL-TOTAL	
											DESIGN	TEST
1. NASA	12.76	0.0254	1.051	0.50	1.71	62.1	0.080	0.036	210.3	1.66	85.0	82.8
2. P&W	25.3	0.0254	1.65	1.0	0.94	44.2	0.051	0.032	205.9	1.18		85.0
3. P&W	24.9	0.0254	1.45	0.77	0.93	71.6	0.063	0.070	260.2	1.18		85.0
4. UACL	22.76	0.048	2.9	1.81	1.21	83.6	0.047	0.023	292.0	1.49		89.7
5. T/CAE	15.75	0.035	1.524	1.0	1.36	75.6	0.038	0.038	214.5	1.49	80.2	79.9

TABLE VII. COMPARISON OF SMALL TURBINE INVESTIGATIONS

correlations of this type one must always consider all of the geometric and aero-thermo differences between one turbine and another in addition to those previously mentioned, such as flowpath curvature, vane and blade profile curvature, vane-to-rotor axial spacing, disk front-face leakage, vane or blade lean angle, and inlet turbulence intensity and velocity profile, just to mention a few.

It should be accepted that specialized correlations of turbines designed and tested by a variety of sources are susceptible to errors for a number of reasons. The generalized trend, however, remains fairly true to that illustrated in Figure 16.

CONCLUSIONS

As pointed out by Benstein (45), the design of turbines for high-performance applications with their attendant small blade heights, high stage loadings, and intricate cooling passages has not come about without a great deal of anguish for the designer. The investigations delving into quantifying the secondary flows and effects on turbine losses have been directed toward specific applications, and their results are tempered by the basic design technique used to initiate the investigation. A partial solution to further quantify losses is therefore an iterative process whereby many redesigns are tested using the type of approach followed in Reference 4, whereby a number of perturbations on the flow field are produced in a systematic manner and the net effect is observed.

If the data shown in Figure 16 describes a reasonable efficiency-work relationship for small turbines which address the tip clearance, trailing edge thickness, low aspect ratio, and small blade height then a relatively simple criteria can be developed to satisfy the aero-thermo, structural, and cost requirements for a particular engine application. A loading approach of this type, simplistic as it may be, satisfies the needs of most designs, at least during the preliminary analysis. More detailed approaches can be applied to estimate the sensitivity of performance to other parameters, such as described in (4) using a modified Ainley model, however, the variation from the trend level of Figure 16 will not be greater than two percentage points. Further detailed flow analysis approaches at this point in time have not yeilded demonstrated results, however, the USAF-APL-sponsored low aspect ratio program now in progress may provide them.

With regards to cooling flows, the data of various industry, and government-sponsored investigations agrees relatively closely and follows fairly closely the simple mixing loss analysis (9). As pointed out in (41) front-face turbine leakage flow can produce significantly higher losses than vane or blade injected flows. This effect was also observed in the reference (4) turbine, as shown in Table V.

In conclusion, it can be stated that the design techniques presently available for small, cooled axial flow turbines are not yet adequate for meeting the requirements of high performance gas turbine engines without relying heavily on semi-empirical relationships. The efficiencies which can be expected range from 80 to 86 percent depending on stage loading with an additional penalty of 2 to 4 percentage points caused by cooling air. The payoff of increasing the efficiency to an average of 87 compared to 83 percent would be realized in higher specific power and lower fuel consumption.

1. Gabel, R.M. and Tabby, A.J., USAAVLABS, Advancement of High-Temperature Turbine Technology for Small Gas Turbine Engines, January 1969, Technical Report 68-65.

2. Franklin, W., Heilbron, J., and Moskowitz, S., USAAVLABS, Small Gas Turbine Engine Component Technology - Turbine, Volume II, August 1968, Technical Report 68-50B.

3. Rogo, C., and Marshall, R., USAAVLABS, Experimental Investigation of Low Aspect Ratio and Tip Clearance on Turbine Performance and Aerodynamic Design, February 1968, Technical Report 67-80.

4. Due, H.F., et al, USAAMRDL, Advanced Small Turbine Technology, May 1977, Final Final Report, TR-77-1.

5. Haas, Jeffrey E., and Kofskey, Milton, G., Cold - Air Performance of a 12.766 - Centimeter - Tip - Diameter Axial - Flow Cooled Turbine I - Design and Performance

5. Haas, Jeffrey E., and Kofskey, Milton G, NASA, Cold - Air Performance of a 12.766 - Centimeter - Tip - Diameter Axial - Flow Cooled Turbine I - Design and Performance of a Solid Blade Configuration, 1975, TND-7881.

6. Haas, Jeffrey E., and Kofskey, Milton, G., Cold-Air Performance of a 12.766 - Centimeter - Tip - Diameter Axial - Flow Cooled Turbine, II - Fffect of Air Ejection On Turbine Performance. To Be Published.

7. Haas, Jeffrey E., and Kofskey, Milton, G., NASA, Effect of Coolant Flow Ejection On Aerodynamic Performance of Low Aspect-Ratio Vanes, I - Performance With Coolant Ejection Holes Plugged, 1976, TMS-3395.

8. Haas, Jeffrey E., and Kofskey, Milton G., Effect of Coolant Flow Ejection on Aerodynamic Performance of Low Aspect-Ratio Vanes, II - Performance With Coolant Flow Ejection at Temperature Ratios Up To 2. To Be Published.

9. Goldman, Louis J., NASA, Cooled-Turbine Aerodynamic Performance Prediction From Reduced Primary to Coolant Total-Temperature Results, 1976, TND-8312.

10. Stewart, W.L., ASME, A Study of Axial-Flow Turbine Efficiency Characteristics In Terms Of Velocity Diagram Parameters, November 1961, Paper No. 61-WA-37.

11. Smith, S.F., A Simple Correlation Of Turbine Efficiency, Journal of the Royal Aeronautical Society, Vol. 69, p. 467-470, July 1965.

12. Ainley, D.G., Aeronautical Research Council, An Approximate Method For The Estimation Of The Design Point Efficiency Of Axial Flow Turbines, C.P. 30, 1950.

13. Ainley, D.G. and Mathieson, G.C.R., Aeronautical Research Council, An Examination Of The Flow Of Pressure Losses In Blade Rows Of Axial Flow Turbines, 1955, R&M 2891.

14. Balje, O.E.R.L. Binsley, Axial Turbine Performance Evaluation. Part A - Loss Geometry Relationships, Paper No. 68-GT-13.

15. Balje, O.E.R.L. Binsley, Axial Turbine Performance Evaluation. Part B - Optimization With and Without Constraints, Paper No. 68-GT-14.

16. Cooke, D.H., U.S. Army Aviation Material Laboratories, Fort Eustis, Virginia (USAAVLABS TR-68-34), A Study Of High-Mach-Number, High-Temperature Application Of A Small, Single-Stage, Axial-Flow Gas Turbine, June 1968, AD 676184.

17. Schlichting, H., Das, A., ASME, Recent Research On Cascade Flow Problems, July 1965, Paper No. 65-FE-A.

18. Rogo, C., SAE, Experimental Aspect Ratio and Tip Clearance Investigation On Small Turbines, 1969, Transaction Paper 6800448.

19. Rogo, C., and Marshall, R., USAAVLABS, Experimental Investigation Of Low Aspect Ratio and Tip Clearance On Turbine Performance and Aerodynamic Design, Task Im125901A01409, Contract DA-44-177-AMC-447 (T), Technical Paper 67-80, February 1968.

20. Dunham, J., and Came, P.M., Improvements To The Ainly-Mathieson Method Of Turbine Performance Prediction, Paper No. 70-GT-2.

21. Burrows, L., AGARD, Investigation Of The Design And Performance Of Small Axial Flow Turbines, 1968, Report on Advanced Components for Turbojet Engines Part 2, AD 687774.

22. Carter, A.F., and Lenherr, F.K., USAAVLABS, An Investigation Of Efficiency Limits For Small, Cooled Turbines, August 1970, Technical Report 70-14.

23. Provenzale, G.E. and Thirumalaisamy, S.N., ASME, Experimental Investigation Of The Effects Of Transpiration Cooling On Turbine Stator Blade Aerodynamics, Paper No. 69-GT-39.

24. Moffitt, T.P. and Prust, H.W., Jr., Szanca, E.M., NASA, Summary Of Cold Air Tests Of A Single-Stage Turbine With Various Stator Cooling Techniques, TM X-52968.

25. Hartsel, J.E., AIAA, Prediction Of Effects Of Mass-Transfer Cooling On The Blade-Row Efficiency Of Turbine Airfoils, January 1972, Paper No. 72-11.

26. Anderson, L.R. and Heiser, W.H., ASME, Systematic Evaluation of Cooled Turbine Efficiency, Paper No. 69-GT-63.

27. Barnes, J.F. and Came, P.M., ASME, Some Aerodynamic Aspects of Turbine Blade Cooling, Paper No. 69-GT-15.

28. Dring, R.P., United Aircraft Corp., Pratt & Whitney Aircraft Division, East Hartford, Conn., A Momentum-Integral Analysis of the Three-Dimensional Turbine End-Wall Boundary Layer.

29. Turner, J.R., An Investigation of the End-Wall Boundary Layer of a Turbine-Nozzle Cascade, Phillipsburg, N.J.

30. Launder, Brian E., MIT, Laminarization of the Turbulent Boundary Layer by Acceleration, November 1964, Report No. 77.

31. Horlock, J.H., Boundary Layer Problems in Axial Turbomachines, CUED/A - Turbo/TR11.

32. Mellor, G.L., and Wood, G.M., An Axial Compressor End-Wall Boundary Layer Theory, Paper No. 70-GT-80.

33. Associated Electrical Industries (Manchester) Limited, A New Method of Prodiling the Guide Cascades of Stages with Small Ratios of Diameter to Length, 18 July 1963, Translation No. 3277.

34. Welna, H., and Dahlberg, D.E., and Heiser, W.H., AFAPL, Investigation of a Highly Loaded Two-Stage Fan-Drive Turbine, December 1969, TR-69-92, Volume I.

35. Welna, H., and Dahlberg, D.E., and Heiser, W.H., AFAPL, Investigation of a Highly Loaded Two-Stage Fan-Drive Turbine, December 1969, TR-69-92, Volume III.

36. Welna, H., and Dahlberg, D.E., and Heiser, W.H., Teledyne CAE, Investigation of a Highly Loaded Two-Stage Fan-Drive Turbine, December 1969, T-71-27, L-3665, Volume II.

37. Lueders, H.G., NASA, Experimental Investigation of Advanced Concepts to Increase Turbine Blade Loading, May 1970, CR-1580.

38. Bettner, J.L., NACA, Design and Experimental Results for a Turbine with Jet Flap Stator and Jet Flap Rotor, May 1973, CR3344.

39. Zysina-Molozien, L.M., Vannik, I.D., Korotkov, M.A., and Medvedeva, M.A., UDC, Effect of Turbulence and the Reynolds Number on Flow Through Blade Cascades, 621.165.533.6.

40. Elsner, J., and Porochnicki, J., NASA, Influence of Flow Turbulence on the Efficiency of Heat Turbine Blade Systems, TT-F-13, 180, Accession No. N70-37524.

41. Ewen, J., Huber, F., and Mitchell, J., ASME, Investigation of the Aerodynamic Performance of Small Axial Turbines, April 1973, Paper No. 73-GT-3.

42. Okapuu, U., ASME, Some Results from Tests on a High Work Axial Gas Generator Turbine, April, 1974, Paper No. 74-GT-81.

43. Fruchtman, I., ASME, The Limit Load of Transonic Turbine Blading, April, 1974, Paper No. 74-GT-80.

44. Horlock, J.H., Axial Flow Turbines, Butterworth, London, 1966, p. 115.

45. Benstein, E.H., AIAA, Small Flying Engines Are Different, October 1974, Paper No. 74-1185.

ADAPTATION D'UN BANC DE TURBINE

AUX RECHERCHES POUR LES HAUTES TEMPERATURES

J. FRANCOIS SNECMA-VILLAROCHE

Y. LE BOT ET J. MICHARD ONERA CHATILLON

P. DEGUEST CEPr SACLAY

1 - INTRODUCTION

Les turboréacteurs modernes sont caractérisés par des températures et corrélativement des pressions élevées devant turbines afin de réduire leur consommation spécifique. Parallèlement on demande à leurs composants et notamment à la turbine des rendements plus élevés et des durées de vie plus longues.[1]

Pour atteindre ces objectifs il a fallu diversifier les techniques de refroidissement en améliorant la convection d'abord, en ayant recours à la protection par film ensuite.

L'augmentation des niveaux de pression, dont résulte un accroissement des flux de chaleur, a rendu les aubes plus sensibles aux problèmes de fatigue. Leur tenue est donc devenue de plus en plus un problème de températures locales et non plus de températures moyennes.

Une bonne connaissance des conditions extérieures, coefficients d'échange et températures, est donc maintenant primordiale. Le rôle de l'environnement moteur devient alors important, les hétérogénéités de pressions et de températures, le niveau de turbulence, les sillages et la centrifugation pouvant modifier les coefficients d'échange et les efficacités de film.

Le rendement de la turbine installée sur le moteur peut être, lui aussi, fortement affecté par cet environnement moteur, les débits de refroidissement émis sur les pales ou les plates-formes, les fuites, les jeux et les sillages pouvant le dégrader de façon notable.

C'est pourquoi, après avoir développé les méthodes de calcul et les essais partiels de laboratoire dans les différentes disciplines concernées, il a paru indispensable de concevoir un moyen d'essais reconstituant le mieux possible les conditions de l'environnement moteur tout en permettant des mesures de qualité.

L'objectif n'est pas seulement de prouver la bonne tenue d'un aubage et d'en évaluer le rendement dans des conditions proches de celles du moteur, il est surtout de caractériser ces conditions de fonctionnement pour comprendre l'influence des différents paramètres et valider les méthodes de calcul.

C'est compte tenu de ces objectifs que les services officiels (Direction des Recherches et Moyens d'Essais en liaison avec la Direction Technique des Constructions Aéronautiques) ont associé un motoriste, la SNECMA, un office de recherche, l'ONERA, et un centre d'essais spécialisé, le CEPr, dans le projet MINOS (Montage Inter ONERA-SNECMA).

2 - PLACE DU MINOS DANS UN PROGRAMME D'ETUDES SUR LES TURBINES HAUTE TEMPERATURE

Les mesures détaillées souhaitables pour toute analyse fine des performances des différents composants d'une turbine sont généralement impossibles sur banc moteur par suite de la compacité des machines expérimentées et des conditions d'environnement sévères rencontrées (niveaux de températureset de pressions élevés, vibrations). De plus, des interférences entre différentes disciplines (aérodynamique, thermique, métallurgie, mécanique) ne permettent souvent d'acquérir que des résultats trop globaux pour être transposés aisément à un autre type de turbine.

Ainsi la validation des méthodes de calcul de dimensionnement et de prévision des performances d'un prototype, développées à partir d'études en laboratoire, conduit à la définition d'un montage probatoire intermédiaire entre les bancs thermiques statiques, destinés aux essais partiels, et les moteurs proprement dits. Ce montage probatoire doit obligatoirement présenter des dispositifs de contrôle du fonctionnement de la turbine suffisamment souples et nombreux pour permettre de faire varier indépendamment les paramètres influençant les phénomènes à analyser dans un environnement comparable à celui rencontré sur moteurs. Son équipement en instrumentation doit, de plus, être suffisamment complet pour autoriser des mesures aussi détaillées que celles effectuées sur bancs d'essais partiels.

MINOS a été défini afin de répondre à ces objectifs. Sa place comme moyen d'essais dans un programme d'études sur les turbines haute température est rappelée dans le tableau I. La position charnière qu'il occupe par rapport à l'expérimentation sur moteurs, aux essais sur bancs partiels et aux études sur montages élémentaires destinés aux recherches à caractère fondamental y apparaît nettement. Les résultats acquis sur MINOS doivent permettre en particulier d'orienter les essais sur bancs partiels et réciproquement, traduisant ainsi la parfaite complémentarité de ces deux types d'installations.

TABLEAU I

Place du MINOS comme moyen d'essais dans un programme d'études sur les turbines haute température

	AVANTAGES	INCONVENIENTS
Expérimentation sur moteurs	. Conditions d'essais moteur	. Complexité et manque de souplesse des essais . Interférences entre paramètre . Difficultés de mesures détail . Difficultés de transposition des résultats à un autre type de moteur . Coût élevé
Essais sur bancs partiels	. Etudes de performances globales d'éléments séparés . Simplicité relative des montages d'essais . Etudes paramétriques relativement aisées et rapides . Conditions d'essais variées . Coût relativement modéré . Conclusions directement utilisables pour la mise au point d'un moteur	. Reproduction plus ou moins fidèle des conditions d'essai moteurs . Résultats souvent trop globau pour permettre une analyse détaillée des phénomènes élémentaires
Etudes sur montages élémentaires	. Analyse détaillée de phénomènes élémentaires . Finesse et précision des mesures effectuées . Liaison étroite théorie - expérience . Recherche fondamentale : objectifs à court, moyen et long terme	. Conditions d'essais parfois éloignées de celles rencontré sur moteurs
Synthèse des recherches fondamentales	. Développement de méthodes de calcul d'une turbomachine	. Difficultés pour tenir compte dans les hypothèses de calcul de la complexité des phénomèn réels dans les moteurs . Difficultés de validation des méthodes de calcul dans les conditions d'essais moteurs
Montage probatoire MINOS	. Validation des méthodes de calcul de performances et de dimensionnement de turbines haute température en présence d'un environnement moteur . Montage intermédiaire entre les bancs d'essais partiels et les bancs d'essais moteurs (possibilité de mesures détaillées, souplesse du contrôle des paramètres de fonctionnement) . Liaisons étroites avec les essais moteurs, les essais sur bancs partiels et les recherches fondamentales	. Contraintes technologiques da la conception du banc d'essai imposées par les mesures à effectuer . Difficultés d'équipement du b en instrumentation de mesures

3 - OBJECTIFS

L'objectif général du MINOS, qui est l'étude de tous les paramètres influant sur les performances et la tenue d'aubes de turbine refroidies, sera atteint par la réalisation des étapes suivantes :

- vérification du bon fonctionnement aérodynamique
- caractérisation de l'environnement : mesure du niveau de turbulence, des fluctuations de température, analyse des sillages
- étude des coefficients d'échange
- étude de l'efficacité des films de protection
- essais de fatigue thermique
- essais d'aubes capables de hautes températures
- étude de technologies particulières, plates-formes, anneaux, abradables....

La vérification du bon fonctionnement aérodynamique est un point important, les résultats thermiques ne pouvant être correctement interprétés sans une bonne connaissance des répartitions de vitesse autour des profils.

La caractérisation de l'environnement permettra d'évaluer les différences entre moteur et banc statique, elle sera faite dans les différents plans de la turbine.

L'étude des coefficients d'échange et de l'efficacité des films sera faite avec les mêmes méthodes de mesure et les mêmes aubes sur banc statique et sur MINOS. On essaiera d'abord des aubes avec des films simples au bord d'attaque, à l'extrados ou à l'intrados, puis des combinaisons de ces films. On déterminera non seulement l'efficacité thermique, mais aussi la varia-

AD-A052 845 ADVISORY GROUP FOR AEROSPACE RESEARCH AND DEVELOPMENT--ETC F/G 21/5
HIGH TEMPERATURE PROBLEMS IN GAS TURBINE ENGINES.(U)
FEB 78

UNCLASSIFIED AGARD-CP-229 NL

3 OF 7
AD A052845

HEAT TRANSFER CHARACTERISTICS OF THE CLOSED THERMOSYPHON SYSTEM

Prof. R.W. Stuart Mitchell & drs. J. Andries
Laboratorium voor Verbrandingsmotoren en Gasturbines
Technische Hogeschool Delft, Mekelweg 2, Delft, The Netherlands.

SUMMARY

The work reported herein forms part of a research programme aimed at the development of a closed thermosyphon system of gas turbine blade cooling, using liquid metals and a secondary cooling circuit in a blade root. Experimentally determined heat transfer characteristics are presented for a 10.6 mm diameter cylindrical closed thermosyphon with a length diameter ratio 11.6 : 1 and a heated-to cooled-length ratio of 1 : 1 using water and mercury under a uniform heat flux, hot wall boundary condition. Results have been obtained with the thermosyphon stationary and variously angled to the vertical between 0^o and 45^o and mounted in a rotating arm apparatus at rotational speeds between 500 r.p.m. and 1000 r.p.m. The results from the stationary vertical thermosyphon agree with existing data for water and mercury. The results from the rotating experiments have been correlated using a Grashof Number based on the gravitational acceleration, whilst the centrifugal acceleration is included in a third dimensionless parameter. Comparison of the results from the stationary and rotating experiments shows that angling the stationary thermosyphon to the vertical does not simulate the heat transfer in the rotating thermosyphon.

LIST OF SYMBOLS

a	acceleration, used in definition of non-dimensional groups
$\underline{a}_{Coriolis}$	Coriolis acceleration
$\underline{a}_{centrifugal}$	centrifugal acceleration
C_p	specific heat at constant pressure of fluid
D	inside diameter
$\underline{g}$	gravitational acceleration
g	value of gravitational acceleration
k	thermal conductivity of fluid
l	length, used in definition of non-dimensional groups
L	tube length of open thermosyphon or half length of closed thermosyphon
L_c	cooled length of closed thermosyphon
L_H	heated length of closed thermosyphon
$\underline{r}$	distance to rotation axis
r_m	mean distance to rotation axis
R	inside tube radius
T_C	mean temperature of cooled wall
T_H	mean temperature of heated wall
T_{CL}	temperature of fluid entering the open thermosyphon
T_{LE}	uniform leading edge temperature (see refs. 7, 8, 9)
T_{TE}	uniform trailing edge temperature (see refs. 7, 8, 9)
T_{wx}	local wall temperature at distance x from closed end in open thermosyphon
$\underline{v}$	velocity of fluid element relative to frame of reference fixed to thermosyphon
β	coefficient of thermal expansion of fluid
Θ	angle of inclination
μ	dynamic viscosity of fluid
ϕ	total heat flow in thermosyphon
ρ	density of fluid
$\underline{\omega}$	angular velocity
ω	value of angular velocity

A bar under a symbol means that the symbol represents a vector. The sign x means a vectorial multiplication.

NON-DIMENSIONAL GROUPS

Gr Grashof number = $\frac{\beta \rho^2 . \Delta T}{\mu^2} . a.l^3$

j "non-dimensional centrifugal acceleration" = $\frac{\omega^2 r_m}{g}$

Nu Nusselt number = $\frac{hl}{k} = \frac{\phi l}{2\pi R L_H \Delta T k}$

Ra Rayleigh number = GrPr

Pr Prandtl number = $\frac{\mu C_p}{k}$

t "non-dimensional temperature = Gr.Pr. $\frac{l}{L_H}$

SUBSCRIPTS (used in Gr, Nu, Ra and t)

D based on diameter (l = D)

R based on radius (l = R)

SUPERSCRIPTS (used in Gr, Ra and t)

none based on g (a = g)

' based on gcosΘ (a = gcosΘ)

" based on $\omega^2 r_m$ (a = $\omega^2 r_m$)

NOTE: Gr, Nu, Ra or t without a subscript means that no definition is given in the considered publication.

1. INTRODUCTION

One system of turbine blade cooling is that called the free convection thermosyphon arrangement, wherein each turbine blade is hollow and filled with liquid. In a "closed" thermosyphon, the hollow turbine blade, filled or partly filled, with liquid or gas is closed and sealed at each end. The working fluid in this closed system is heated at one end and cooled at the other, as shown in fig. 1A. In an "open" thermosyphon, the fluid filled cavity is sealed at one end and at the other communicates with an open surface fluid reservoir. The cavity is heated along the whole of its length and the heat is extracted from the reservoir, as shown in fig. 1B.

2. BODYFORCES IN STATIONARY AND ROTATING THERMOSYPHONS

Heat transfer by convection occurs because of motion in a fluid. When the motion in the fluid is due to temperature gradients, with corresponding differences in fluid density, the convection is "free". If the motion is due to induced pressure differences e.g. using a pump, then the greater part of the heat transfer is by "forced" convection. In a stationary thermosyphon test rig the bodyforces result from the uniform gravitational acceleration $\underline{g}$. In a rotating thermosyphon, in addition to the gravitational acceleration there are the centrifugal acceleration and the Coriolis acceleration (see fig. 2). In this case the accelerations are:

$$\underline{a}_{centrifugal} = -\underline{\omega} \times (\underline{\omega} \times \underline{r})$$

$$\underline{a}_{Coriolis} = -2\underline{\omega} \times \underline{v} \quad \text{and} \quad \underline{g}.$$

The bodyforce which a fluid element experiences is due to the resultant of these three accelerations.

The centrifugal and Coriolis accelerations are not uniform. The former acceleration is proportional to the radius from the axis of rotation and is in a direction approximately along the axis of the thermosyphon. The latter acceleration is proportional to the velocity of the fluid-element and in a direction perpendicular to it. For the considered rotational speeds the centrifugal and Coriolis accelerations will be large compared with the gravitational acceleration. The last can then be neglected.

3. SIMULATION OF ROTATION BY INCLINATION OF THE THERMOSYPHON

Several research workers have claimed that the heat transfer in a rotating thermosyphon can be simulated qualitatively in a stationary thermosyphon by inclining the latter to the vertical, see fig. 3. This was first put forward by Eckert and Jackson (1) and Alcock (2). The component of the gravitational acceleration, perpendicular to the axis of the thermosyphon then simulates the Coriolis acceleration.

Between the rotating and the stationary inclined thermosyphons, there exist the following differences:

a) The direction of the Coriolis acceleration is dependent on the direction of motion of the fluid-element. Thus fluid streams in opposite directions are subject to corresponding opposite direction Coriolis accelerations, see fig. 4. In a stationary inclined installation, each fluid element experiences a uniform acceleration, the direction of which is independent of the direction of motion.

b) The magnitude of the Coriolis acceleration is dependent on the velocity of the fluid-element. In the stationary inclined installation, the component of the gravitational acceleration, perpendicular to the axis of the thermosyphon is everywhere constant.

c) The centrifugal acceleration is dependent on the radial distance from the axis of rotation. In the stationary inclined installation, the component of gravitational acceleration, parallel to the axis of the thermosyphon is everywhere constant.

4. LITERATURE REVIEW

There have been several investigations on the subject of the heat transfer characteristics of the stationary thermosyphon inclined to the vertical. On the other hand, the number of investigations on the rotating thermosyphon, details of which have been published, is very limited.

Outstanding reviews of the published literature have been given by Bayley and Martin (3) and Japikse (4). In the following sections, the published literature is very briefly reviewed.

4.1 THE OPEN THERMOSYPHON

Hartnett, Welsh and Larsen (5) have published the results of an investigation on an inclined open thermosyphon with L/D = 10.5, water and mercury as the fluid and a uniform heat flux through the wall. They presented their results in the form:

$$Nu_R = f(Ra'_R \cdot Nu_R)$$

where Nu_R and Ra'_R were based on $\Delta T = T_{wx} - T_{CL}$.
The fluid properties were evaluated at the local wall temperature T_{wx}. For mercury they found that for a given value of $Ra'_R.Nu_R$ Nu_R increased by about 100% when the thermosyphon was inclined at 30% to the vertical. Larsen and Hartnett (6) using the same apparatus and a similar shorter one with L/D = 7.3 presented their results in the form:

$$Ra_R = f(Ra'_R \cdot Nu_R)$$

where Nu_R and Ra'_R were based on $\Delta T = T_{wx} - T_{CL}$.
They evaluated the fluid properties at T_{CL}. For the short thermosyphon they found that Ra'_R at a given $Ra'_R Nu_R$ value decreased with increasing inclination for both water and mercury.
For water the decrease was about 30% when the thermosyphon was tilted 5^o. On further tilting, Ra'_R continued to decrease but less rapidly. For mercury, Ra'_R decreased approximately linearly with tube inclinations between 0^o and 45^o. They found for the larger thermosyphon that Ra'_R for a given $Ra'_R Nu_R$ decreased about 50% for tube inclinations up to 30^o.

Martin and Cresswell (7), Martin (8) and Cresswell (9) made some measurements on an inclined open thermosyphon with L/D = 7.5 and a uniform wall temperature. As thermosyphon fluids the following were investigated: glycerine, rape-seed oil, ethylene glycol and water. At each angle of inclination two measurements were made, one whereby a uniform temperature (T_{LE}) was maintained along the leading edge of the thermosyphon and the other, similarly for the trailing edge (T_{TE}). They presented their results in the form:

$$Nu_R = f(Ra'_R)$$

where Nu_R and Ra'_R were both based on $\Delta T = T_{LE} - T_{CL}$ and $\Delta T = T_{TE} - T_{CL}$ respectively and the fluid properties were similarly evaluated at T_{LE} and T_{TE}.
For glycerine and rape-seed oil they found that Nu_R for a given Ra'_R and increasing angle at first decreased until at an angle of 6^o to the vertical it started to increase again. At an angle of 45^o to the vertical the value of Nu_R exceeded the value measured in the vertical case. At 51.5^o the increase in Nu_R was 56% for glycerine and 58% for rape-seed oil at $Ra'_R = 10^{5.75}$. In the case of water Nu_R increased sharply to begin with but then levelled off to an approximately constant value at $\Theta = 22^o$. Compared with the vertical case, Nu_R increased by about one third at the leading edge and by about two thirds at the trailing edge for $Ra'_R = 10^{7.75}$. On the basis of a calculation of the ratio of the Coriolis acceleration to the centrifugal acceleration in a turbine blade, it was concluded, that an angle of inclination somewhere between 0^o and 11^o, simulated the Coriolis effect, which was induced in actual practice.

Leslie (10), in an analytical solution of the heat transfer in an inclined open thermosyphon, for laminar flow, at small angles of inclination Θ, showed that the rate of heat transfer increased with increasing values of Θ.

There have been a number of not very successful experimental blade cooling systems, incorporating an open thermosyphon with water. (Schmidt (11), Friedrich (12), Freche and Diaguila (13) and Ivanov (14)).

4.2 THE CLOSED THERMOSYPHON

Japikse, Jallouk and Winter(15), Jallouk (16) and Japikse (17) have published the results of an investigation on the heat transfer in an inclined closed thermosyphon, with L/D = 4, water as the operating fluid and a uniform wall temperature. The angle with the vertical was varied, whilst the heat input was held constant. Nu_D, at first increased rather quickly, with increasing values of the angle of inclination Θ but later levelled off (see fig. 10(b)).

Brown (18) and Colclough (19) have investigated the heat transfer conditions in a rotating closed thermosyphon, filled with a liquid metal. This research was carried out in connection with the PAMETRADA cooled gas turbine project. This latter is the only known project, involving the building of a turbine, the blades of which were cooled by means of a closed thermosyphon. Brown (18), found

$$Nu \propto (Gr".Pr^2)^{2/13}$$

No definitions were given for Nu, Gr" and Pr.
Colclough (19) concluded that for a rotating closed thermosyphon of variable cross sectional area

$$Nu_D = \left(\frac{L_C}{L_H}\right)^{0.66} \cdot \left(\frac{D}{L_T}\right)^{2.4-8D} \cdot \left(Gr"Pr^2\right)^{1.7D+5.35}$$

where $L_T = L_H + L_C$ + length of the midsection spacer in inches.

D = diameter in inches.

No definitions were given for Nu_D, Gr" and Pr.

Ogale (20) investigated a rotating closed thermosyphon in which the cooled section had a larger cross-sectional area than the heated section. The working fluid was a eutectic mixture of sodium and potassium. For a thermosyphon with the heated section of circular cross-section, Ogale quoted:

$$Nu_D = 0.325(Gr"_D P_r^2)^{0.13}$$

where D was diameter of heated section, whilst, when the heated section was in the form of an aerofoil blade cross-section, the corresponding relationship was:

$$Nu_D = 0.6038(Gr"_D.P_r^2)^{0.09}$$

where D was hydraulic diameter of heated section. In both formulae Gr_D was based on $\Delta T = T_H - T_C$. The fluid properties were evaluated at $(T_H + T_C)/2$.

Le Grivès and Genot (21) investigated a rotating closed thermosyphon, with a rectangular cross-section, filled with sodium potassium and rotating up to 6,500 r.p.m. The rate of heat transfer increased with increasing rotational speed up to 3,500 r.p.m. Above this speed, the rate of increase was very much reduced. They evaluated:

$$Nu_D \propto (Gr"_D Pr^2)^{0.2}$$

where Gr_D was based on $\Delta T = T_H - T_C$. The fluid properties were evaluated at $(T_H + T_C)/2$.

Uskov and Tseitlin (22) have given the results of measurements made on a sodium filled rotating closed thermosyphon at rotating speeds up to 710 r.p.m. and $3 < \frac{L}{D} < 20$. They found:

$$Nu_D = 14.1 \left(\frac{Gr_D Pr^2}{1 + Pr}\right)^{-1.15} \cdot \left(\frac{\omega^2 r_m}{g}\right)^{0.32} \cdot \left(\frac{D}{L}\right)^{1.43}$$

The fluid properties were evaluated at the fluid temperature on the axis of the thermosyphon.

Zysina-Molodjen, Jablonic, Poljak, Uskov and Tkachenko (23) have given results for a rotating closed thermosyphon filled with air and water. For $4.3 < \frac{L}{D} < 30$ they quoted:

$Nu \propto (Gr".Pr)^{0.25}$ for the laminar flow regime and

$Nu \propto (Gr".Pr)^{0.50}$ for the turbulent flow regime.

No further definitionsof Nu, Gr" and Pr were given.

Tkachenko (24) reported an investigation on a rotating closed thermosyphon, but gave no heat transfer results.

4.3 SUMMARY

The results of the experiments on rotating thermosyphons are in all cases, except by Uskov and Tseitlin (22), expressed in terms of the Grashof number, in which the centrifugal acceleration is used in place of the acceleration due to gravity. For stationary inclined thermosyphons, the component of the gravitational acceleration, along the axis of the thermosyphon is incorporated in the Grashof number.

From the foregoing it can be stated that for the rotating thermosyphon increase in the rotational speed does increase the rate of heat transfer as does increase of inclination to the vertical for the stationary thermosyphon

In what follows in this paper, describing the authors' own research, it is discussed, in how far the heat transfer characteristics of the rotating thermosyphon can be simulated quantitatively by inclining a stationary unit.

5. AN EXPERIMENTAL TEST-RIG

Figs. 5, 6 and 7 show the test-rig, originally built by Ogale (20) and after some modifications used for the present experimental investigation on the cylindrical closed thermosyphon. The thermosyphon used, comprises a stainless steel cylinder, closed at both ends, 124 mm long inside x 16 mm outside diameter and 10.65 mm inside diameter. One half of the thermosyphon is heated electrically by means of a 1.8 mm diameter electric resistance rod winding in an external spiral groove on the cylinder. The other half of the thermosyphon is cooled by water, pumped at constant temperature and mass flow, through a cooling water jacket. The thermosyphon wall temperatures are measured by means of 33 chromel-alumel thermocouples, which are fitted into the cylindrical wall at 0.5 mm below the surface. The thermocouples are mounted in groups of 4, in 8 rectangular cross-sections of the cylinder; one thermocouple is fitted in the base of the cylinder. The thermosyphon is mounted in a rotating arm, which is driven by an electric motor, the speed of which is variable. The heated part of the thermosyphon is surrounded by glass-wool, for insulation, to limit as much as possible any radial heat loss. The electrical input is supplied and measured, under rotation, using two copper slip rings. The thermocouple outputs, under rotation, are recorded, on punched tapes, via silver slip rings and a data acquisition system.

6. AN EXPERIMENTAL PROGRAMME

6.1 DETERMINATION OF THE HEAT FLOW

A part of the heat input does not pass through the working fluid of the thermosyphon but rather, directly through the wall of the thermosyphon, in the axial direction, to be given up to the cooling water and the surroundings. In order to estimate this loss, the thermosyphon was filled with glass-wool, so that all the supplied heat input had to pass through the wall. The temperature difference, between the two sections, on either side of the change over from hot to cold, was measured as a function of the electrical input. On the assumption, that the same relationship existed, when the thermosyphon was filled with fluid, the nett heat flow, through the primary working fluid could be determined.

6.2 MEASUREMENT OF THE WALL TEMPERATURES

For a given angle of inclination for a stationary unit, or a given rotational speed of the test-rig, respectively, the electrical input was established. After the mean temperature had become stabilised, all temperatures were taken, successively, with an interval of one second between each reading. This was repeated ten times and a mean temperature, for each thermocouple was determined. These mean temperatures, in conjunction with the radial heat flow through the thermosyphon wall, enabled the temperature conditions of the inside wall to be estimated.

6.3 DIMENSIONLESS REPRESENTATION OF THE EXPERIMENTAL RESULTS

To enable the results of various investigations to be compared with one another, the experimental data must be expressed in the form of relationships between dimensionless numbers, viz.:

The Nusselt number Nu_D

The Prandtl number Pr

A dimensionless temperature number t_D and a number given by the formula $Gr_D Pr^2$

For the inclined and the rotating closed thermosyphons, in addition to the variables incorporated in the above dimensionless numbers, the angle of inclination to the vertical, Θ and the rotational speed ω, respectively, influence the heat transfer. The experimental results can be expressed most clearly by means of the additional dimensionless numbers, viz. - $\tan \Theta$ and $j = \frac{\omega^2 r_m}{g}$ respectively. The fluid properties were evaluated at $\frac{T_H + T_C}{2}$. They were calculated using polynomial approximations from references (25) and (26).

For the stationary thermosyphon with water as the working fluid, the experimental results are expressed as:

$$Nu_D = f(t_D, \tan \Theta)$$

and with mercury as fluid:

$$Nu_D = f(Gr_D Pr^2, \tan \Theta)$$

For the rotating thermosyphon the corresponding expressions are:

$$Nu_D = f(t_D, j) \quad \text{and} \quad Nu_D = f(Gr_D Pr^2, j), \text{ respectively.}$$

7. RESULTS

7.1 WATER, AS THE WORKING FLUID

Fig. 8 is a plot of the results of the authors' experiments for the vertical stationary closed thermosyphon, filled with water, together with comparable results taken from the published literature. Although the fluid properties have been calculated at different temperatures and the wall conditions differ, (see fig. 8), there is reasonable agreement between the various results. For low values of t_D a laminar impeded flow regime operates, which at $\log_{10} t_D = 5.6$ changes into laminar boundary flow. In the region of laminar impeded flow, there is a linear relationship between Nu_D and $\log_{10} t_D$. The change-over to laminar boundary flow is rather abrupt as is evident from a change of slope in the Nu_D v. $\log_{10} t_D$ curve (see fig. 9) and a sudden increase in T_C, following increasing electrical input to the thermosyphon. Fig. 9 shows the corresponding heat transfer curves for the stationary closed thermosyphon, inclined at an angle to the vertical, over a range of angles of inclination. It can be seen, that the curves of the inclined and of the vertical thermosyphons are of basically the same shape, thus providing qualitative agreement between the two systems. Fig. 10(a) based on the data of fig. 9 shows, for the inclined closed thermosyphon with water, the Nusselt number Nu_D plotted against tan Θ with t_D constant. There is good qualitative agreement with similar curves, previously obtained by Jallouk (16) as indicated in fig. 10(b). Nu_D increases quite rapidly up to an angle of inclination of about 25^o. Thereafter, the rate of increase of Nu_D progressively falls off.

Fig. 8 shows also the results of an experimental investigation, on the rotating closed thermosyphon, filled with water. Nu_D is increased very considerably, with respect to the stationary case. There is no unique relationship between Nu_D and t_D, which is valid over the considered range of rotational speeds. Also shown in fig. 8 are the same rotating thermosyphon results, plotted as $\log_{10} Nu_D$ v. $\log_{10} t_D$". Again there is no unique relationship apparent between Nu_D and t_D". Fig. 10(c), for the rotating closed thermosyphon, with water, is based on fig. 8 and shows the Nusselt number Nu_D plotted versus j with t_D held constant.

7.2 MERCURY, AS THE WORKING FLUID

Fig. 11 is concerned with the heat transfer, in the stationary vertical, the stationary inclined and the rotating, closed thermosyphons when filled with either mercury or sodium-potassium eutectic. The results are analysed in the form of $\log_{10} Nu_D$ plotted versus $\log_{10} Gr_D Pr^2$. The authors' investigations with mercury, for the vertical installation are compared with similar results published by Pucci and Gerretsen (25) and it can be seen, that there is good agreement, between the two sets of data. The same figure also shows Nu_D for the stationary inclined closed thermosyphon, over a range of angles of inclination. Based on the data from fig. 11, the Nusselt number Nu_D is plotted in fig. 12(a) as a function of tan Θ, with $Gr_D Pr^2$ held constant. Nu_D increases with increasing angle of inclination Θ, the rate of increase which is small between 0^o and 5^o (even negative for $\log_{10} Gr_D Pr^2 = 3.30$) increases at larger angles. There is no levelling off at larger angles.

The experimental results, of the rotating closed thermosyphon, with mercury are also shown in fig. 11. There is no unique relationship, between the Nusselt number Nu_D and the dimensionless parameter $Gr_D Pr^2$ which is valid over the range of rotating speeds investigated. Also shown in fig. 11 are the same rotating thermosyphon results plotted as $\log_{10} Gr"_D . Pr^2$. It can be seen, that at high values of $Gr"_D Pr^2$, the Nusselt number Nu_D decreases with increasing rotational speed. This is in contradiction with the situation for the inclined thermosyphon, where for increasing angle of inclination Nu_D increases. In fig. 12(b), for the rotating closed thermosyphon, with mercury, the Nusselt number, Nu_D is plotted as a function of j with $Gr_D Pr^2$ held constant.

8. CONCLUSIONS

Our experimental results, for the stationary vertical closed thermosyphon are in good agreement with those previously published in the literature. The laminar impeded flow regime noted by us for water conforms with that reported by Bayley and Lock (28) for glycerine.

The influence, on Nu_D, of inclining the stationary thermosyphon to the vertical, is not such as to simulate the effect of rotation, for the range of rotational speeds investigated. For the rotating closed thermosyphon Nu_D is dependent on both the Grashof number based on acceleration due to gravity and the dimensionless centrifugal acceleration. A Grashof number, based on centrifugal acceleration is not, by itself, satisfactory for the prediction of the heat transfer characteristics of the thermosyphon. This latter, for the higher rotational speeds, requires the establishment of a relationship between the Nusselt number and the dimensionless centrifugal acceleration.

REFERENCES

1. Eckert, E.R.G. and Jackson, T., "Analytical Investigation of Flow and Heat Transfer in Coolant Passages of Free Convection Liquid Cooled Turbines", NACA R.M., E50D25, 1950.

2. Alcock, J.F. "General Discussion on Heat Transfer", Proc. Inst.Mech.Eng., A.S.M.E (London) Conf.Proc., 1951, p. 378.

3. Bayley, F.J. and Martin, B.W. "A Review of Liquid Cooling of High Temperature Gas Turbine Rotorblades", Proc. Inst.Mech.Eng. 1970-1971, Vol. 185, no. 18, pp. 218-227.

4. Japikse, D. "Advances in Thermosyphon Technology", Advances in Heat Transfer, Vol. 9, 1973, pp. 1-111.

5. Hartnett, J.P., Welsh, W.E. and Larsen, F.W. "Free Convection Heat Transfer to Water and Mercury in an Enclosed Cylindrical Tube", Chem. Engng. Progress Symp Series-Nucl.Engng, Vol. 55, no. 23, 1959, pp. 85-91.

6. Larsen, F.W. and Hartnett, J.P., "Effect of Aspect Ratio and Tube Orientation on Free Convection Heat Transfer to Water and Mercury in Enclosed Circular Tubes", J. Heat Transfer, Vol. 83, 1961, pp. 87-93.

7. Martin, B.W. and Cresswell, D.J., "Influence of Coriolis Forces on Heat Transfer in the Open Thermosyphon", The Engineer, Vol. 204, no. 4, 1957, pp. 926-930.

8. Martin, B.W., "Free Convection Heat Transfer in the Inclined Open Thermosyphon", Proc. Instn.Mech. Engnrs., London, Vol. 173, no. 32, 1959, pp. 761-777.

9. Cresswell, D.J., "The Influence of Coriolis Forces on Free Convection Heat Transfer in the Open Thermosyphon", M.Sc. Thesis, University of Durham, 1959.

10. Leslie, F.M., "Free Convection in the Tilted Open Thermosyphon", J. Fluid Mechanics, Vol. 7, 1959, pp. 115-127.

11. Schmidt, E., "Heat Transmission by Natural Convection at High Centrifugal Acceleration in Water-cooled Turbine Blades", Proc. Inst.Mech.Eng., A.S.M.E (London), Conf.Proc., 1951, pp. 361-363.

12. Friedrich, R., "Eine Gasturbine mit Gekühlten Schaufeln für Gastemperaturen über 1000^{o}C", Brennst.-Waerme-Kraft, Vol. 14, 1962, pp. 368-373.

13. Freche, J.C. and Diaguila, A.J., "Heat Transfer and Operating Characteristics of Aluminium Forced Convection and Stainless Steel Natural Convection Water Cooled Singlestage Turbines", NACA R.M. E50D03A, 1950.

14. Ivanov, V.L., Manushin, E.A. and Lapin, Yu.D., Izv.Vuz.Aviats.Tekhn., Vol. 9, no. 2, 1966, pp. 143-150, also Sov. Aeron, 1966, pp. 87-91.

15. Japikse, D., Jallouk, P.A. and Winter, E.R.F., "Single Phase Transport Processes in the Closed Thermosyphon", Int. J. Heat Mass Transfer, Vol. 14, no. 7, 1971, pp. 869-887.

16. Jallouk, P.A., "Experimental Investigation of Heat Transfer in a Closed Thermosyphon", M.Sc. Thesis, Purdue University, Lafayette, Indiana, 1969.

17. Japikse, D., "Heat Transfer in Open and Closed Thermosyphons", Ph.D. Thesis, Purdue University, Lafayette, Indiana, 1969.

18. Brown, T.W.F., "Development of the Longlife Marine Gas Turbine", CIMAC Congr., Zürich, 1957, pp. 443-484.

19. Colclough, C.D., "Measurement of Rotor Blade Temperatures in a Liquid Cooled Gas Turbine", B.S.R.A. Rep. N.S.2, Mar.Eng. Rep. no. 2, 1963.

20. Ogale, V.A., "On the Application of the Semi-closed Thermosyphon System to Gas Turbine Blade Cooling", Dr. Thesis, University of Technology Delft, The Netherlands, 1968.

21. Le Grivès, E. et Genot, J., "Refroidissement des aubes de turbines par les metaux liquides", AGARD CP no. 73, 1971.

22. Uskov, I.B. and Tseitlin, L.M., "Heat Transfer in Rotating Closed Straight Cylindrical Channels Filled with Sodium", Teploenergetira, Vol. 17, no. 1, 1970, pp. 56-58, also Therm.Eng., Vol. 17, no. 1, 1970, pp. 80-83.

23. Zysina-Molodjen, L.M., Jablonic, R.M., Poljak, M.P., Uskov, I.B. and Tkachenko, G.M., "The Investigation of the Heat Transfer in the Mass Force Field", Proc. Int. Heat Transfer Conf., 4th, Paris Versailles, Paper no. 4.7, 1970.

24. Tkachenko, F.M., "Flow Mechanism of a Liquid Coolant in Closed Rotating Passages", Izv.Vuz.Energ., Vol. 6, 1970, pp. 61-65 also, Heat Transfer - Sov. Res., Vol. 2, no. 6, 1970, pp. 48-52.

25. Coulson, J.M. and Richardson, J.F., "Chemical Engineering", Vol. 1, Fluid Flow, Heat Transfer and Mass Transfer, Third Impression, Pergamon Press, London, 1956.

26. Lyon, R.N. ed., "Liquid Metals Handbook", Second ed. (revised), Atomic Energy Commission and the Dept. of the Navy, Washington, D.C. 1954 .

27. Pucci, P.F. and Gerretsen, J.C.R., "Heat Transfer Characteristics of a Liquid Metal Filled Closed Thermosyphon", A.S.M.E Gas Turbine and Fluids Eng. Conf. San Fransisco, Paper 72-GT-36, 1972.

28. Bayley, F.J. and Lock, G.S.H., "Heat Transfer Characteristics of the Closed Thermosyphon", J. Heat Transfer, Vol. 87, no. 1, 1965, pp. 30-40.

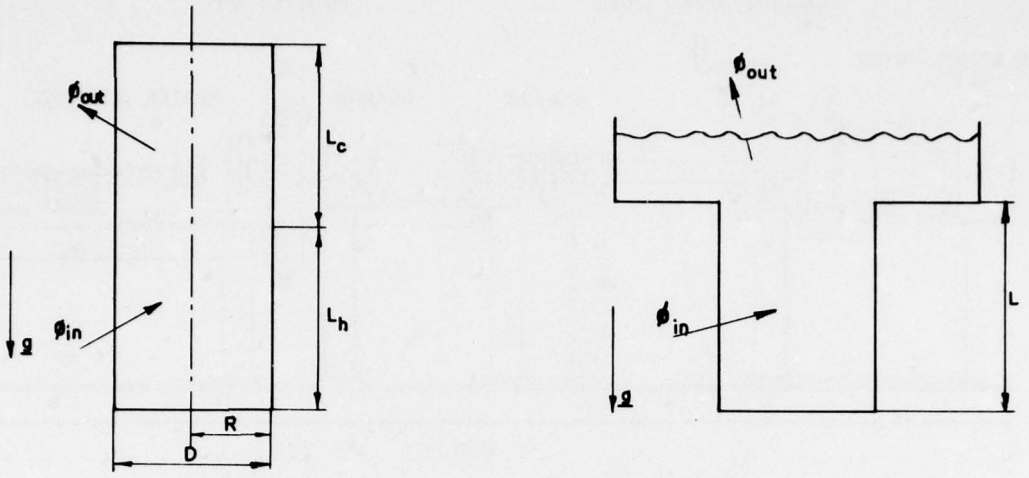

(A) CLOSED THERMOSYPHON (B) OPEN THERMOSYPHON

FIG. 1 THERMOSYPHON SYSTEMS

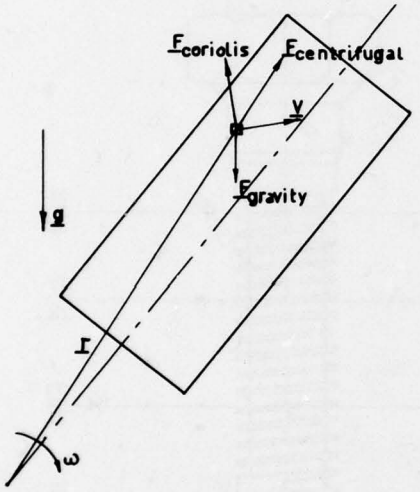

FIG. 2 FORCES IN A ROTATING SYSTEM

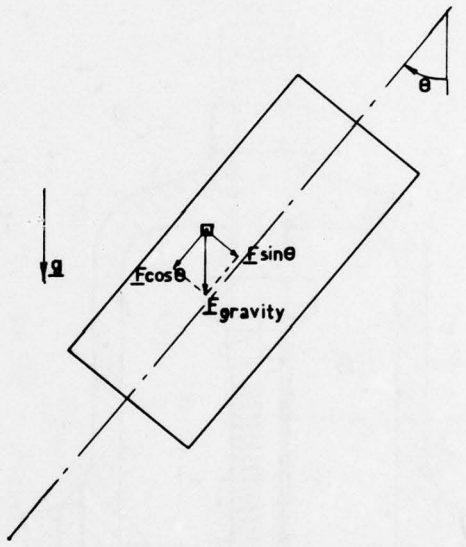

FIG. 3 FORCES IN A STATIONARY INCLINED SYSTEM

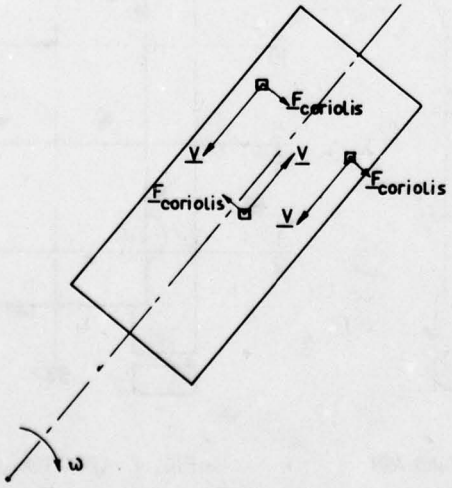

FIG. 4 CORIOLIS FORCES ON FLUID ELEMENTS MOVING IN OPPOSITE DIRECTIONS

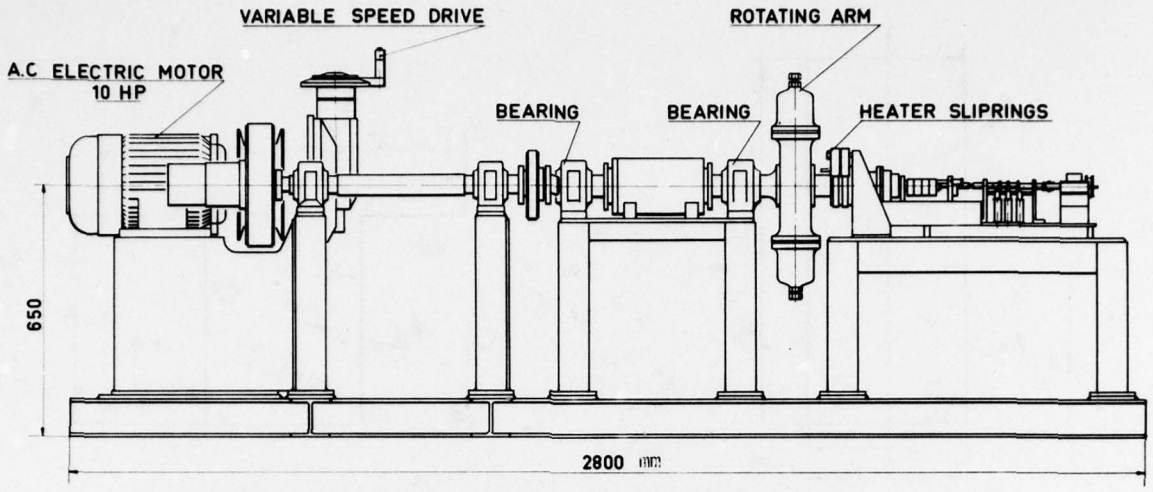

FIG. 5 SCHEMATIC ARRANGEMENT OF THE ROTATING TEST-RIG

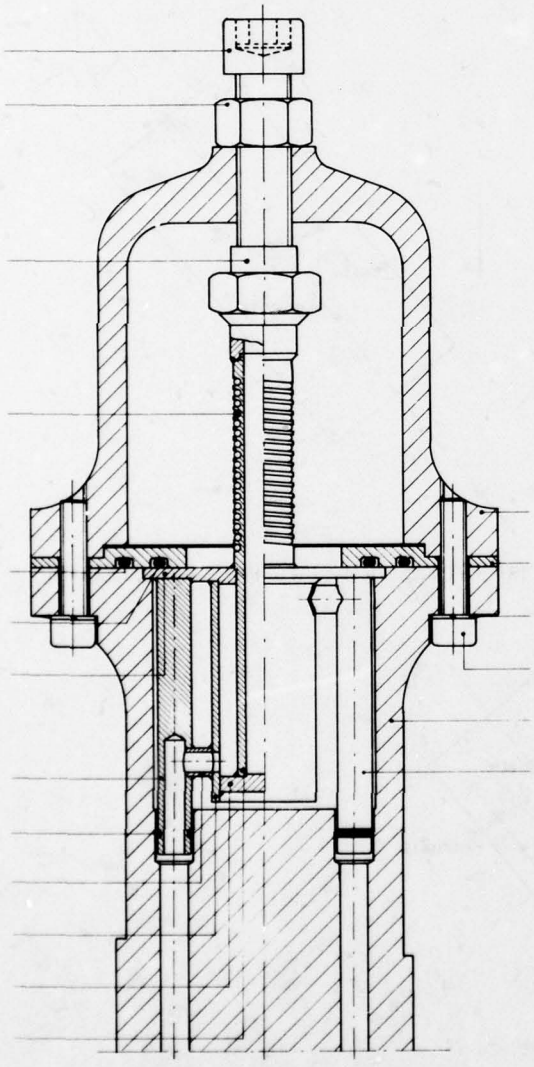

FIG. 6 CLOSED THERMOSYPHON IN ROTATING ARM

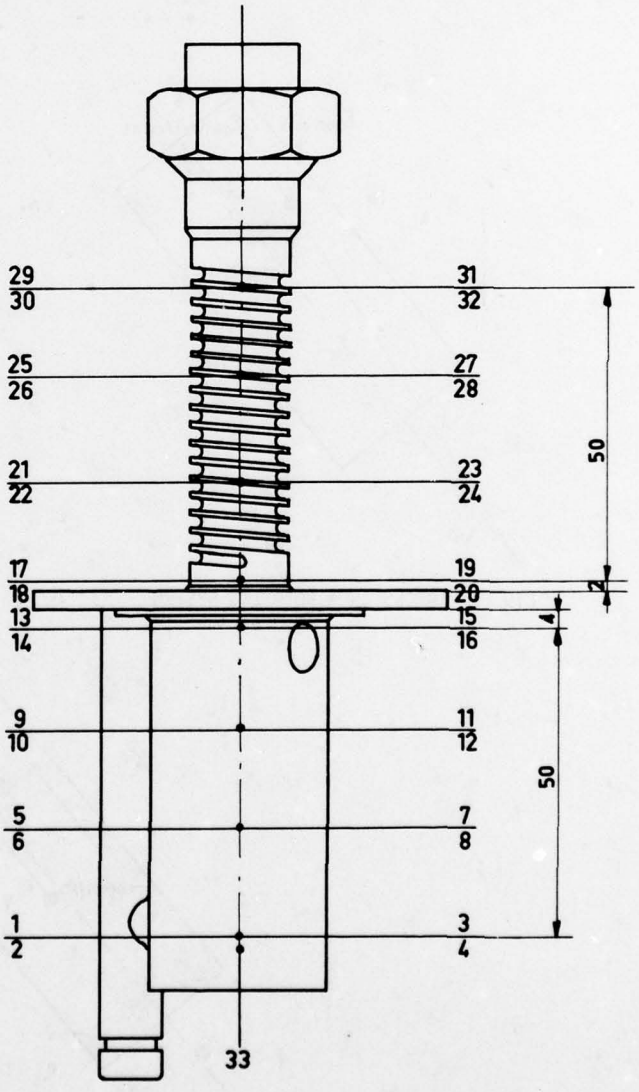

FIG. 7 LOCATION OF THERMOCOUPLES

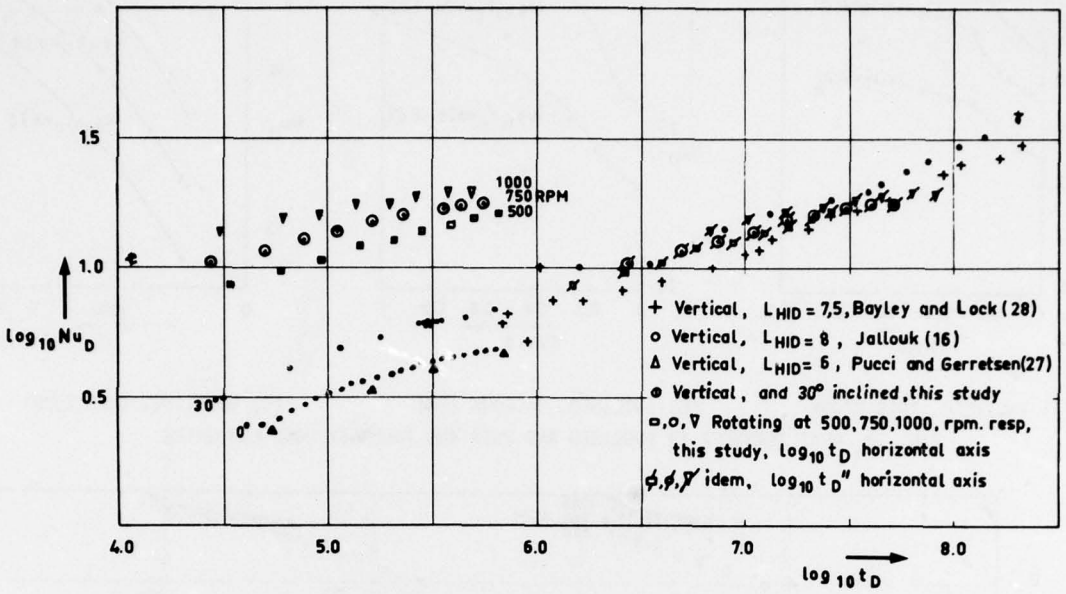

FIG. 8 HEAT TRANSFER IN THE CLOSED THERMOSYPHON FOR WATER, $L_H/L_C = 1$
NOTES: +, O FLUID PROPERTIES AT T_H, UNIFORM WALL TEMPERATURE;
Δ FLUID PROPERTIES AT $(T_H + T_C)/2$, UNIFORM HEAT FLUX

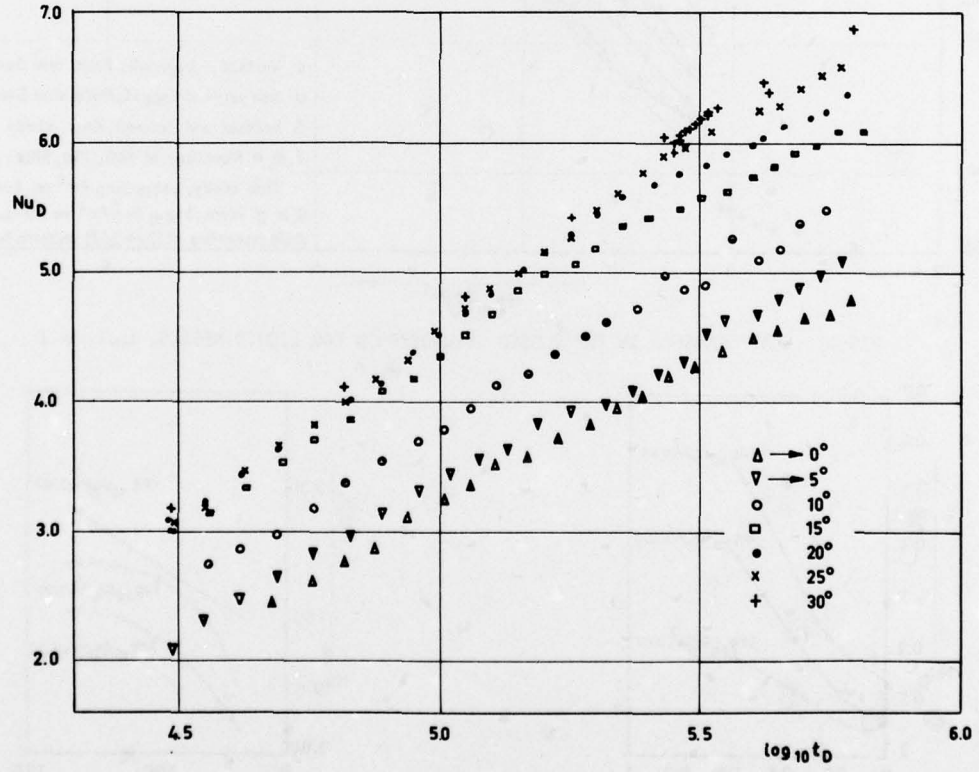

FIG. 9 HEAT TRANSFER IN THE STATIONARY INCLINED CLOSED THERMOSYPHON

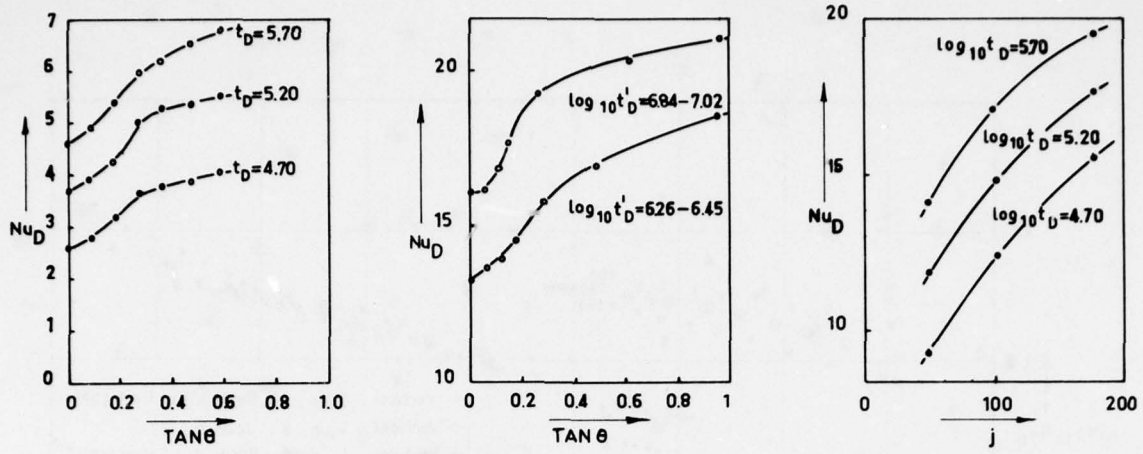

(A) INCLINED, THIS STUDY (B) INCLINED, JALLOUK (26) (C) ROTATING, THIS STUDY

FIG. 10 HEAT TRANSFER IN INCLINED AND ROTATING THERMOSYPHONS FOR WATER

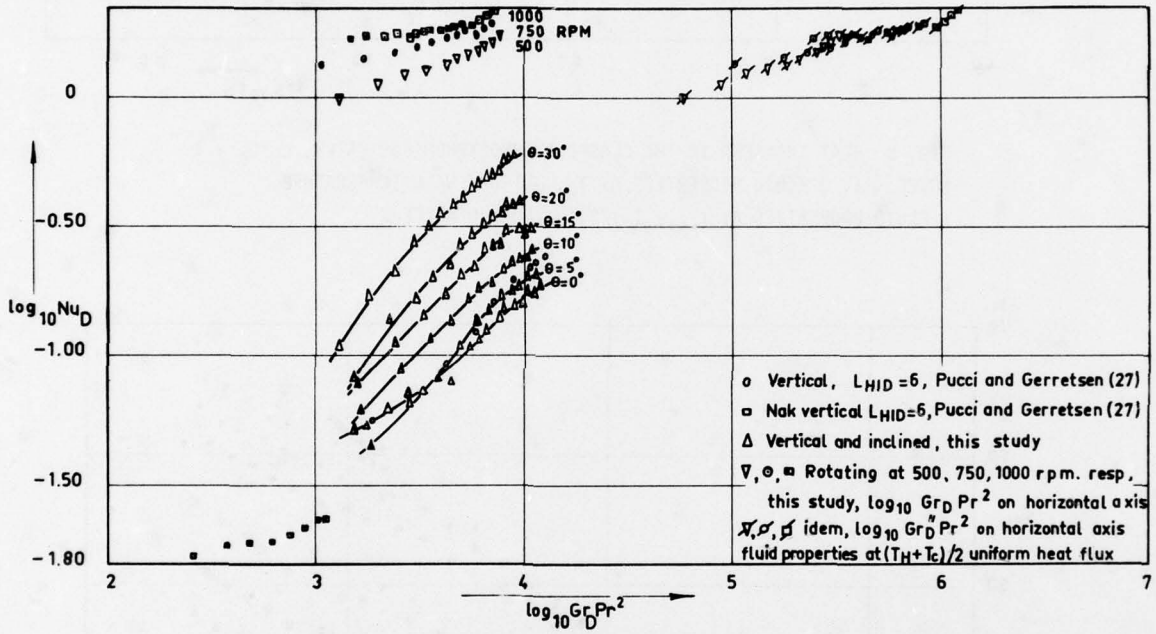

FIG.11 HEAT TRANSFER IN THE CLOSED THERMOSYPHON FOR LIQUID METALS, L_H/L_C = 1

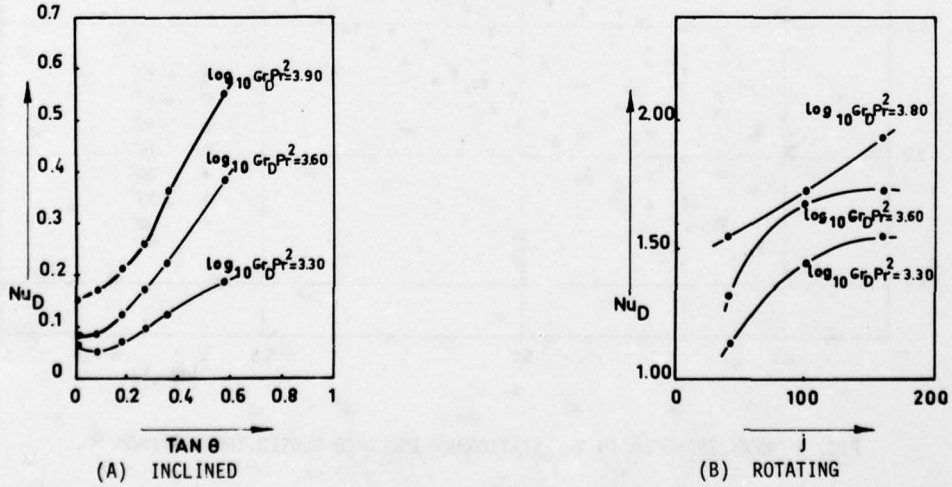

(A) INCLINED (B) ROTATING

FIG. 12 HEAT TRANSFER IN INCLINED AND ROTATING THERMOSYPHONS FOR MERCURY

DISCUSSION

E. Le Grivès, France

Lors de la précédente réunion AGARD sur les turbines à haute température (Florence, 1970), une communication sur le refroidessement par cycle à métal liquide (Na-K), par cycle de thermosiphon ou par cycle évaporatif a été présentée par E. Le Grivès et J.Génot.

Les résultats exposés avaient été obtenus sur un montage à grande vitesse de rotation (jusqu'à 8000 tpm) réalisé par la SNECMA et avec des flux thermiques comparables à ceux qui sont réalisés sur turbine réelle. Je suis surpris que vous n'en ayiez pas fait mention dans votre présentation, vos résultats se situant dans un domaine d'accélération centrifuge et de valeur du paramètre $Gr\,Pr^2$ très inférieur à celui d'une turbine à gaz industrielle ou aéronautique.

D'autre part, pourriez vous fournir des précisions concernant:

(1) la distribution radiale de température sur la partie chauffée de votre éprouvette d'essai;

(2) l'abaissement du niveau de température moyenne de cette partie par rapport à la température athermane (éprouvette non refroidie par convection interne)?

Author's Reply

(1) The radial temperature distribution in the heated section was quite flat in the stationary vertical thermosyphon.

In the angled case the thermocouples along the 'leading edge' became relatively colder.

A typical value for the mercury-filled thermosyphon at an angle of 30° to the vertical was about 10% lower than the temperature along the 'trailing edge'.

For water the effect was somewhat smaller.

In the rotating case we saw the same effect and also that the relative temperature levels in the cooled section become much higher.

(2) We didn't make a comparison between the temperature levels in a massive uncooled cylinder and a hollow cooled cylinder.

W.D.Morris, UK

The use of an acceleration ratio to account for the fact that rotation cannot be uniquely correlated in terms of a buoyancy effect implies that this is an additional centrifugal effect. It is more physically likely that this is a Coriolis effect. Thus it might be better for present data and those of other workers to be compared using a non-dimensionless group which reflects this Coriolis interaction. This group could typically have the mathematical structure of a conventional Reynolds number but which uses a measure of peripheral speed as the characteristic velocity required.

Author's Reply

I agree with you that it is more logical to use a non-dimensional group which reflects the Coriolis acceleration. The use of j was only a provisional way to include the rotational speed in the correlations and to make a comparison with published rules possible.

D.K.Hennecke, Germany

I would like to make a general comment. Aero engines will continue to use air cooling of the turbine blades for some time to come. However, cooling engineers should be people of vision and also look at new, even exotic cooling methods. Therefore, we have included your paper in the program. And I am glad we did because you have shown the very high Nusselt numbers which you can achieve with your thermosyphon. In an engine they would be even higher owing to the larger rotational speed.

Yet one should not forget the problems one will encounter when this system is to be applied in an engine. There, the hot end of the thermosyphon would be in the turbine blade while the cold end would be located within the blade root or the disc. Therefore, one would be faced with the task of removing the large amount of heat flowing into the blade at the blade root or the disc. So it appears that one has shifted the problem from one location to another without solving it.

Thus, the applicability of a system like yours will depend on the fact if one is able to remove the heat at the new location easier than it was to air-cool the blade. And this will be a challenging task because, in order to remove the heat at the blade root or disc, one would have to achieve large heat transfer coefficients that are comparable to the extremely high values at the blade, or to provide large surface areas for the heat transfer or have a very low coolant temperature. All of this is not readily done in an engine.

Author's Reply

I agree with your comment. Providing a solution to the problem of removing the heat from the blade root will be a formidable task. The study on which this paper was based only considered the heat transfer in the closed thermosyphon itself without considering the problems you mentioned.

HEAT TRANSFER FROM TURBINE AND COMPRESSOR DISCS

Dr J.M. Owen
Lecturer
School of Engineering & Applied Sciences
University of Sussex
Falmer
Brighton
BN1 9QT
England.

SUMMARY

Mean and local Nusselt numbers have been determined for three different rotating disc configurations. Heat transfer measurements are presented for:

(1) a single disc rotating close to a stator with a radial outflow of coolant, representing the flow between an air-cooled turbine disc and a casing;

(2) a rotating cavity with a central axial throughflow of coolant, representing the flow between corotating compressor discs;

(3) a rotating cavity with a radial outflow of coolant, representing the flow between corotating air-cooled turbine discs.

Results are presented for a range of axial gaps, coolant flow rates and rotational speeds, and the similarities and differences between the three cases are discussed. In particular, it is shown that vortex breakdown, which can occur in case (2), dramatically alters the flow and heat transfer.

LIST OF SYMBOLS

C_w	mass flow coefficient ($C_w \equiv \dot{m}/\mu r_o$)
f	frequency of jet precession
G	gap ratio ($G \equiv s/r_o$)
k	thermal conductivity
$\dot{m}$	coolant mass flow rate
Nu	local Nusselt number ($Nu \equiv qr/k(T_o - T_{o,ad})$)
$\overline{Nu}$	mean Nusselt number ($\overline{Nu} \equiv q_{av}\, r_o/k(T_o - T_{o,ad})_{av}$)
Pr	Prandtl number
q	heat flux normal to disc surface
r, r_I, r_o	radial coordinate, inlet radius, disc radius
Re_φ	rotational Reynolds number ($Re_\varphi \equiv \Omega r_o^2/\nu$)
Re_z	axial Reynolds number ($Re_z \equiv 2\overline{W}\, r_I/\nu$)
s, s_c	axial clearance between the two discs, axial clearance between rotating disc and shroud.
T	temperature
V_φ	tangential component of velocity
$\overline{W}$	bulk average velocity in the inlet pipe
z	axial coordinate
α	local Nusselt number parameter
ϵ	Rossby number ($\epsilon \equiv \overline{W}/\Omega r_I$)
ν	kinematic viscosity
ρ	density
Ω	angular velocity of disc
μ	absolute viscosity

SUBSCRIPTS

ad	adiabatic
av	radially-weighted average
fd	free disc
min,max	minimum, maximum
o	pertaining to the rotating disc

1. INTRODUCTION

A plane rotating disc can be used to examine the fluid dynamics and heat transfer that occurs in more complex turbine and compressor disc geometries. A single disc rotating near a stator, with or without a peripheral shroud, as shown in Fig. 1(a), provides a useful model of an air-cooled turbine disc rotating close to a stationary casing. A radial outflow of air is used to cool the turbine disc and to prevent the radially inward leakage of hot gas over its surface.

A rotating cylindrical cavity, in which two corotating discs are joined at their periphery, provides a simple model for the examination of the flow and heat transfer between adjacent turbine or compressor discs. With an axial throughflow of air, as shown in Fig. 1(b), the model can represent discs in a high-pressure compressor rotor through the centre of which coolant passes on its way to the turbine cooling system. With a radial outflow of air, as shown in Fig. 1(c), the model can represent corotating air-cooled turbine discs.

In the past, more attention has been paid by research workers to the single rotating disc case than to the more complex problem of the rotating cavity. Apart from Hennecke et al (Ref.1) and Pustolov & Sparrow (Ref.2), who obtained numerical solutions of the Navier Stokes and laminar-energy equation for the respective cases of a heated cylindrical cavity with and without axial throughflow, Sparrow and his co-workers (Refs 1-7) have been principally concerned with heat transfer from a single rotating disc. A number of experiments were conducted on rigs with $r_I/r_o = 0.11, G \leq 2$ (where $G \equiv s/r_o$), $Re_z \leq 5 \times 10^4$ (where $Re_z \equiv 2\overline{W}r_I/\nu$, $\overline{W}$ being the bulk average velocity in the inlet pipe) and $Re_\varphi \leq 10^6$ (where $Re_\varphi \equiv \Omega r_o^2/\nu$). The main differences in these experiments were in whether the coolant entered through the centre of the stator or the centre of the rotor, and whether it left between the stationary disc and shroud or between the rotating disc and shroud.

Like Sparrow, Owen and his co-workers (Refs 8-11) have been principally concerned with heat transfer from shrouded and unshrouded single rotating discs. Measurements were made on a rig similar to the schematic drawing of Fig. 1(a) with $r_I/r_o = 0.13$, $G \leq 0.18$, $C_w \leq 5 \times 10^4$ (where $C_w \equiv \dot{m}/\mu r_o$) and $Re_\varphi \leq 4 \times 10^6$. More recently Owen and Bilimoria (Ref. 11) obtained heat transfer measurements for cylindrical cavities (similar to those shown in Figs 1(b) and 1(c)), with either an axial throughflow or a radial outflow of coolants, for a rig with $r_I/r_o = 0.10$, $G \leq 0.4$, $Re_z \leq 1.8 \times 10^5$ and $Re_\varphi \leq 2.5 \times 10^6$.

A knowledge of the flow and heat transfer behaviour in the configuration shown in Fig. 1 is a necessary prerequisite for the calculation of temperature, stress, expansion rate and life of a gas turbine rotor. In this paper, the experimental apparatus used to measure the heat transfer rates will be described and the principal experimental results will be discussed.

2. EXPERIMENTAL APPARATUS AND MEASUREMENT TECHNIQUES

2.1 The single rotating disc rig

The rotating disc was made from mild steel of radius $r_o = 381$ mm and could be rotated up to 4000 rev/min, by an 11 kW electric motor, at axial distance, s, from 3.8 to 230 mm from the stator, which was the same diameter as the disc. A coolant flow rate of up to 0.7 kg/s was supplied (at a temperature of approximately 20°C) from a centrifugal blower through a pipe of 100 mm diameter opening into, and coaxial with, the centre of the stator. The stator was fitted with an adjustable cylindrical shroud allowing axial clearances, s_c, from 1.3 mm to the full stator to rotor clearance.

The outer face of the rotating disc was radiantly heated from a bank of electrical heater bars, which had a maximum output of 22 kW (the maximum disc temperature was limited to 100°C). The rotor and stator were instrumented with embedded thermocouples enabling their surface temperatures to be measured. Traverse units, fitted with total-

head and total-temperature probes, were located on the coolant inlet pipe and on the stator periphery, thus allowing the coolant inlet and outlet velocity and temperature profile to be measured. The signals from the thermocouples on the rotating disc (taken out through slip ring assemblies), and those on the stator and probes, were measured by means of a Fenlow DVM (with a resolution of 10μV) and an MBM data logger.

Mean Nusselt numbers for the rotating disc were calculated in two independent ways. In the 'conduction solution' method, Laplace's equation was solved numerically using the measured surface temperatures as boundary conditions, and the heat flux was computed from the calculated temperature field. The 'enthalpy change' method was used to calculate the total heat flow through the rotating disc from the difference between the outlet and inlet enthalpy of the cooling air. The disc work term was included (from separate disc windage torque measurements), and the heat loss through the stator (which was maintained sensibly adiabatic by guard heaters) was neglected. The agreement between the mean Nusselt numbers determined from these two methods was good, but neither method was suitable for the calculation of local Nusselt numbers (owing to the small temperature difference involved in the 'conduction solution', and to the fact that only mean values were determined from the 'enthalpy change'). Ref. 9 includes more details of the apparatus and calculation procedures, whilst Ref. 10 contains details of how the local Nusselt numbers were calculated from the mean values.

2.2 The rotating cavity rig

A general view of the rotating cavity is shown in Fig. 2. The assembly downstream of the cavity itself is the same as that used with the single rotating disc.

The cylindrical cavity comprised two stainless steel discs of radius r_o = 381 mm and a perpheral shroud which was either impermeable, for the axial throughflow tests, or contained thirty equi-spaced holes of 28.6 mm diameter, for the radial outflow tests (as shown in Fig.2). The axial gap between the two discs was variable up to a maximum of s = 203 mm, and the whole system could be rotated up to 2500 rev/min. Cooling air (at approximately 20°C) entered the cavity at the centre of one disc (the 'upstream disc') through a tube of 38 mm radius at flow rates up to 0.23 kg/s. The air could leave the cavity either axially through a tube of 38 mm radius at the centre of the second disc ('downstream disc') or through the holes in the shroud. The two discs were driven by a drive shaft, of 25 mm diameter, which passed through the centre of the cavity. The air entered the upstream rotating tube through four ports and, for the axial throughflow tests, it left the downstream rotating tube through four ports and a volute.

The outer face of the downstream disc was radiantly heated (to a maximum temperature of 100°C) from a bank of electrical heater bars, which had a maximum output of 22 kW. Both surfaces of each disc were instrumented with embedded thermocouples, which were brought out through separate slip ring assemblies. For the axial throughflow tests, the inlet and outlet coolant temperature was measured by means of total-temperature probes immediately upstream and downstream of the rotating cavity. The thermocouple signals were measured by the same DVM and data logger as used for the single disc experiments.

Owing to the relatively low thermal conductivity of the discs in the cavity (compared with the mild steel used in the single disc rig), the temperature differences across the downstream heated disc enabled both local and mean Nusselt numbers to be determined by the 'conduction solution'. However, as the enthalpy rise of the cooling air in the axial throughflow tests was relatively small, (and the heat loss through the shroud and upstream disc difficult to quantify), and as it was not practicable to measure the coolant outlet temperature for the radial outflow tests, the 'enthalpy balance' was not used to determine mean Nusselt numbers.

More details of the experimental apparatus for the rotating cavity tests can be found in Ref. 11

3. HEAT TRANSFER FROM AN AIR-COOLED DISC ROTATING CLOSE TO A STATOR

Heat transfer from a free disc (a disc rotating in an infinite environment) has been extensively investigated (Refs 9, 12, 13, 14). For turbulent flow ($Re_\varphi \geq 2 \times 10^5$) over a disc with a quadratic temperature rise, Owen and Haynes (Ref. 9) obtained the empirical correlation for the mean Nusselt number for the free disc, $\overline{Nu}_{fd}$ where

$$\overline{Nu}_{fd} = 0.0171\, Re_\varphi^{0.814} \qquad (3.1)$$

which is valid for air (Pr = 0.72) up to $Re_\varphi \approx 4 \times 10^6$.

The presence of a stator close to a rotating disc (as shown in Fig. 1(a)) can result in either an increase or a decrease in heat transfer, compared with the free disc, depending on the gap ratio and coolant flow rate. This is illustrated in Fig.3, and theoretical and experimental corroboration can be found in Ref. 9. For the case of zero coolant flow rate, $C_w = 0$, the heat transfer reaches a minimum (approximately 50% of the free disc value) at $G = G_{min}$ where

$$G_{min} = 0.23\ Re_\varphi^{-0.2} \tag{3.2}$$

For $G < G_{min}$, Couette flow starts to occur and $\overline{Nu}$ increases; for $G > G_{min}$, $\overline{Nu}$ increases until $G = G_{max}$ where

$$G_{max} = 1.05\ Re_\varphi^{-0.2} \tag{3.3}$$

after which the stator does not influence the disc and the free disc level is reached.

A certain minimum coolant flow rate, $C_{w,min}$, is necessary to ensure that $\overline{Nu} \geq \overline{Nu}_{fd}$ if $G \leq G_{max}$. This flow rate is considered to be the same as that entrained by a free disc, so that

$$C_{w,min} = 0.22\ Re^{0.8} \tag{3.4}$$

For $G \leq G_{max}$, the above flow rate should prevent an inflow over the stator; for $G > G_{max}$, a peripheral shroud is required to prevent inflow. For a shrouded system, with $G_c << G$ (where $G_c \equiv s_c/r_o$), the minimum flow rate required to seal the system $C^1_{w,min}$, is (according to Ref. (15))

$$C^1_{w,min} = 0.61\ G_c\ Re_\varphi \tag{3.5}$$

In order to achieve turbulent flow over the entire disc, Kreith et al (Ref. 16) suggest that for a radial outflow of coolant

$$C_w/2\pi G > 5000 \tag{3.6}$$

If eqn (3.4) is used for C_w and eqn (3.3) for G, then eqn (3.6) reveals that the flow will be turbulent if $Re_\varphi > 1.5 \times 10^6$, which is consistent with the free disc transition criterion.

Owen and Haynes (Ref.10) obtained a correlation for the mean Nusselt numbers, obtained from the rig described in Section 2.1, based on two asymptotic values, $\overline{Nu}_1$ and $\overline{Nu}_2$, for small and large gap ratios (or low and high rotational speeds). For $G << C_w/Re_\varphi$

$$\overline{Nu}_1 = 0.0145\ (C_w/G)^{0.8} \tag{3.7}$$

and for $G > G_{max}$ (and $Re_\varphi > 2 \times 10^5$)

$$\overline{Nu}_2 = \overline{Nu}_{fd}\ (1 + 0.22\ (r_o/r_I)^2\ C_w/Re_\varphi) \tag{3.8}$$

where $\overline{Nu}_{fd}$ is given by eqn (3.1). Using these two equations, the following correlation was produced

$$\overline{Nu} = (\overline{Nu}_1^6 + \overline{Nu}_2^6)^{1/6} \tag{3.9}$$

and was compared with the experimental results and numerical solutions of the boundary layer equations for $0.01 \leq G \leq 0.18$, $1.4 \times 10^4 \leq C_w \leq 9.8 \times 10^4$ and $Re_\varphi \leq 3.9 \times 10^6$. Examples of the results are shown in Fig. 4 for a small gap ratio ($G \doteq 0.02$) and in Fig. 5 for large gap ratios ($G \geq 0.08$). Eqn (3.9) is only valid for turbulent flow for a rotating disc with a quadratic temperature rise and care should be exercised in applying it to geometries or conditions different to those over which it has been tested. Ref. 10 contains modifications for the effect of shroud clearance ratio and suggested corrections for other Prandtl numbers and disc temperature distribution as well as formulae for the frictional moment coefficient on air-cooled rotating discs. Gosman et al (Refs 17 & 18) also describe numerical methods that have been applied successfully to single rotating disc problems.

Local Nusselt numbers can be derived from eqn (3.9) using the definitions of the local Nusselt number

$$Nu \equiv qr/k\ (T_o - T_{o,ad}) \tag{3.10}$$

(where T_o is the disc temperature and $T_{o,ad}$ the adiabatic disc temperature)
and the mean Nusselt number

$$\overline{Nu} \equiv q_{av}\ r_o/k\ (T_o - T_{o,ad})_{av} \tag{3.11}$$

(where av refers to the radially-weighted average value) such that

$$Nu = \overline{Nu} + \left\{\frac{1}{T_o - T_{o,ad}} \int_o^r (T_o - T_{o,ad})rdr\right\} \frac{d}{dr}\left(\frac{\overline{Nu}}{r}\right) \tag{3.12}$$

For the case of a quadratic temperature rise over the disc (where $(T_o - T_{o,ad}) \propto r^2$) eqns (3.7), (3.8), (3.9) and (3.12) give

$$Nu = \left\{ \alpha_1 \overline{Nu}_1^6 + \alpha_2 \overline{Nu}_2^6 \right\} / \overline{Nu}^5 \qquad (3.13)$$

where $\alpha_1 = 0.75$

and $\alpha_2 = 1 + (0.157 - 0.0205\ (r/r_I)^2\ C_w\ Re_\varphi^{-1}) / (1 + 0.22 (r/r_I)^2\ C_w\ Re_\varphi^{-1})$

As stated in Section 2.1, local Nusselt numbers were not determined experimentally. However, Fig. 6 shows a comparison between Nu calculated from eqn (3.13) and values obtained from numerical solution of the turbulent boundary layer equations. It would therefore appear reasonable to use eqn (3.13) for design purposes, subject to the limitation stated above.

4. HEAT TRANSFER IN A ROTATING CAVITY WITH AN AXIAL THROUGHFLOW OF COOLANT

In comparison with the single disc case, heat transfer in a rotating cavity with an axial throughflow (see Fig. 1(b)) is difficult to understand and even more difficult to predict. Experiments conducted on the experimental rig described in Section 2.2 showed that small changes in axial flow rate or rotational speed could, under certain conditions, cause very large changes in heat transfer rates. In order to investigate what caused these step-changes in behaviour, a half-size isothermal version of the main heat transfer rig* was constructed using perspex discs (380 mm diameter), and flow visualization and laser doppler anemometry, LDA, (full details of which are contained in Ref. 19) were used to obtain details of the flow inside the cavity.

Flow visualization on the perspex rig revealed that transition from laminar to turbulent flow inside the cavity coincided with transition in the central axial jet. Owing to the approach conditions (a calming section and 16:1 area-ratio contraction was used), fully-turbulent flow could be delayed to $Re_z \approx 2 \times 10^4$. Alternatively, by 'tripping' the flow downstream of the contraction, it was possible to cause transition at $Re_z \approx 2 \times 10^3$ (the 'traditional' pipe Reynolds number associated with transition).

Under laminar flow conditions, it was not possible to obtain an axisymmetric flow. A temperature difference of 0.1^oC between the incoming air and the cavity walls was sufficient to create buoyancy effects and, for a stationary cavity, instead of achieving the anticipated patterns (for G = 0.53) shown in Fig. 7(a), the asymmetric patterns of Fig. 7(b) were observed. By contrast, the secondary flow inside the cavity under turbulent conditions was powerful enough to assure the axisymmetry illustrated in Fig. 7(c). The turbulent toroidal vortex, which was centred at $r/r_o \approx 0.8$ and $z/s \approx 0.5$, could result in recirculating mass flow rates up to three times that of the axial throughflow (although only a few percent of the throughflow was actually entrained into the cavity!)

In laminar flow, the initial effect of rotation was to reduce the strength of the secondary flow. This resulted in a weak quasi-axisymmetric toroidal vortex which reduced in radial extent with increasing rotational speed. The shrinking of the vortex towards the centre is illustrated in Fig. 7(d), and this process continued until the Rossby number, ϵ ($\epsilon \equiv \overline{W}_z / \Omega r_I$) was of order unity. For $0.7 \lesssim \epsilon \lesssim 3.6$, the central jet became unstable, as shown in Fig. 7(e), and oscillated with a frequency half that of the rotational frequency of the cavity. This effect was attributed to vortex breakdown (Ref. 19) and for turbulent flow the effects were even more dramatic. Under turbulent conditions, the central jet began to oscillate intermittently at $\epsilon \approx 100$, and as the Rossby number was reduced (by either increasing the rotational speed or decreasing the flow rate) the jet began to precess violently about its own axis, as illustrated in Fig. 7 (f). This effect, attributed to spiral vortex breakdown, built up in intensity to reach a peak at $\epsilon \approx 21$. If the Rossby number was further reduced, the jet would resume its central passage through the cavity in a quasi-axisymmetric fashion with pulsations of the jet boundaries. Spectral analysis of the jet oscillations revealed that during the spiral vortex breakdown ($21 \lesssim \epsilon \lesssim 100$) the jet oscillated at a frequency, f, proportional to the axial velocity ($fr_I/\overline{W} \approx 3.8 \times 10^{-3}$), whereas during the quasi-axisymmetric breakdown ($\epsilon \lesssim 21$) the jet pulsated with a fundamental frequency (equal to the rotational frequency of the cavity) together with a large number of higher harmonics.

The precise boundary between the turbulent spiral and quasi-axisymmetric vortex breakdown was difficult to determine accurately owing to hysteresis effects (a change from spiral to axisymmetric breakdown occurred at a lower Rossby number than the reverse change).

* Footnote It should be pointed out that there was in fact a difference between the perspex rig and the heat transfer rig. In the former, the two discs were independently driven from a lay-shaft, hence neither the central drive shaft nor the ports (described in Section 2.2) were necessary.

Fig. 8 shows the observed regimes of vortex breakdown for both laminar and turbulent flow at G = 0.53. The region of laminar breakdown was delineated from rms levels of the tangential components of velocity measured by the laser anemmometer; the transition from turbulent spiral to quasi-axisymmetric breakdown was found by flow visualization (and corroborated by step changes in the pressure drop across the cavity, step changes in the tangential velocity, and step changes in the frequency of the jet fluctuations). The start of spiral breakdown was difficult to establish by visual means and the limit at $\epsilon \approx 100$ was inferred from slope discontinuities in the axial pressure drop measurements. All physical observations were consistent with a gradual start of spiral breakdown, at $\epsilon \approx 100$ and a sudden end, at $\epsilon \approx 21$.

The observation of vortex breakdown on the perspex rig is consistent with the thermal discontinuities found on the heat transfer rig. Local Nusselt numbers, measured at G = 0.4 on the heated downstream disc, are shown in Fig. 9 for $Re_z = 0.18 \times 10^5$ and 0.9×10^5. For both flow rates, very high 'peaky' profiles occur in the spiral breakdown range, $21 \lesssim \epsilon \lesssim 100$. The fact that the minimum value of Nu occurs at $r/r_o \approx 0.8$ is also consistent with fluid dynamics measurements in the perspex rig (in which the toroidal vortex was centred at $r/r_o \approx 0.8$, and LDA measurements revealed that $V_\varphi/\Omega r \leq 1$ for $r/r_o \gtrsim 0.8$).

Subsequent flow visualization in the heat transfer rig at G = 0.4 (using a transparent polycarbonate shroud) revealed that (despite the presence of a central drive shaft) vortex breakdown occurs in the isothermal and the heated cavity at approximately the same flow conditions. Whilst the demarcation between spiral and quasi-axisymmetric breakdown is less precise in the heat transfer rig than in the perspex rig, it does appear to occur at $\epsilon \approx 21$.

Flow visualization in the perspex rig at smaller gap ratios has revealed that turbulent spiral breakdown is present at G = 0.38 but appears to be absent at G = 0.25. At the latter gap ratio, counter-rotating toroidal vortices occur when the cavity is stationary. The initial effect of rotation is to suppress the outer, weaker, vortex and to shrink the inner vortex towards the centre of the cavity. At $\epsilon \lesssim 21$ (where the quasi-axisymmetric breakdown occurs at the larger gap ratios) the core suddenly 'explodes' outwards with a dramatic increase of turbulence inside the cavity. Further increase of rotational speed causes the core to shrink inwards again until, at $\epsilon \approx 1$ (where vortex breakdown occurs in laminar flow) it again moves outwards. Whilst it has not yet been possible to reduce the Rossby number below a value of $\epsilon \approx 0.8$, it is believed that the core will continue to shrink until, at $\epsilon \ll 1$, there is no isothermal circulation inside the cavity. Under those conditions, buoyancy effects must dominate the flow and heat transfer inside the cavity.

Although heat transfer measurements have been made at G = 0.4, 0.267 and 0.133, owing to the effects described above, no clear patterns for the influence of flow rate and rotational speed on the mean Nusselt numbers have been determined. It can be said, however, that the average level of heat transfer from the downstream disc is consistently less than that for the single rotating disc under similar conditions. Work is continuing on the heat transfer rig to establish the effect of inlet and exit conditions on the heat transfer; and on the perspex rig detailed measurements of the flow in the cavity at a number of gap ratios is continuing. A new rig is also being built in which it will be possible to measure simultaneously heat transfer and fluid dynamics data.

It is worth noting that Yu et al (Ref. 3) who conducted experiments in a system where the coolant entered axially through the centre of the heated rotating disc and left through a clearance between the shroud and the stator, observed a flow behaviour similar to the spiral breakdown described above. From examination of their results, for $0.44 \leq G \leq 2$, it appears that the central jet precessed about its axis for $1 \leq \epsilon \leq 12$.

5. HEAT TRANSFER IN A ROTATING CAVITY WITH A RADIAL OUTFLOW OF COOLANT.

For the case of radial outflow (see Fig. 1(c)) the half-size perspex rig, mentioned in Section 4 and modified by the inclusion of thirty holes of 13 mm diameter in the shroud, was used for flow visualization. Fig. 10 illustrates the flow patterns observed at a gap ratio of G = 0.53; the cross-hatching represents regions where the smoke was observed to penetrate.

Fig. 10(a) shows a stationary cavity with $Re_z \approx 600$ which results in a laminar central jet, a laminar wall jet (on the downstream disc) and laminar recirculation. At low rotational speeds ($Re_\varphi \lesssim 2500$), the laminar central jet oscillates shedding vorticity into the cavity, via the wall jet, which induces a turbulent core of recirculating fluid. At higher speeds ($Re_\varphi \gtrsim 6000$), the turbulent core shrinks radially inwards, as shown in Fig.10(b)

and Ekman layers (in which all of the radial outflow occurs) appear on each disc. For higher rotational speeds ($Re_\varphi \gtrsim 5 \times 10^4$), the core shrinks towards the centre of the cavity, as shown in Fig. 10(c), leaving thin Ekman layers on the discs. This observation is consistant with the laminar source flow model of Hide (Ref. 20).

By increasing Re_z, it is possible to produce a turbulent radial wall jet before the central jet becomes turbulent, and the flow in the cavity becomes progressively more turbulent as Re_z is increased from 10^3 to 2×10^4. Under stationary turbulent conditions, the flow in the cavity, see Fig. 10(d), is similar to that observed with an axial throughflow. Although spiral vortex breakdown was observed with a radial outflow over a similar range of Rossby numbers to that in the axial throughflow case, its effect is far less dramatic. An effect that is marked is the shrinking of the turbulent core with increasing rotational speed. After a critical value of Re_φ, the radius of the core, r_c, decreases with increasing rotational speed, as shown in Fig. 10(e). There appears to be a minimum radius to which the core shrinks, and the size of this radius (and the critical value of Re_φ at which the core begins to shrink) increases with increasing Re_z. As for the laminar flow case, Ekman layers appear on both discs, and between these layers (where the fluid rotates at a speed slower than the discs) smoke only penetrates slowly by diffusion rather than by convection. For all gap ratios tested ($0.125 \leq G \leq 0.53$), the turbulent core starts to shrink at virtually the same value of Re_φ (for a given value of Re_z) and reduces in size to approximately the same minimum radius.

The Nusselt numbers obtained from the heated downstream disc on the full-size heat transfer rig described in Section 2.2 were consistent with the flow visualization observations. The variation of mean Nusselt number with Re_φ, for a range of Re_z, is shown in Fig. 11. At small values of Re_φ, rotational speed has little influence on heat transfer; this is the core-dominated regime. At a critical value of Re_φ, which increases with increasing Re_z, $\overline{Nu}$ increases with both Re_z and Re_φ; this is the shrinking-core, or developing Ekman layer, regime. At still higher values of Re_φ, the mean Nusselt numbers begin to 'flatten off' again and show a reduced increase with increasing Re_φ; this is considered to be the region of the fully-developed Ekman layer, or the fully-shrunk core.

In the core-dominated regime heat transfer is controlled by the radial mass flow rate; in the shrinking core regime, heat transfer increases as the Ekman layer grows in radial extent with increasing Re_φ; in the fully-developed Ekman layer regime, increase in heat transfer with increasing Re_φ is attributed to thinning of the Ekman layer. It can also be seen that the extent of the second (shrinking core) regime is reduced with increasing Re_z. This is consistent with the observation that the value of Re_φ at which the core begins to shrink, and the minimum radius of the core, increases with increasing Re_z. Referring to Fig. 11, it is probable that at a sufficiently high value of Re_z ($Re_z > 5 \times 10^5$) the core will not shrink and the three regimes will merge into one. Other gap ratios tested ($G = 0.267, 0.133$) provide results very similar to those obtained at $G = 0.4$.

Fig. 12 shows the radial distribution of local Nusselt numbers for $G = 0.4$ and $Re_z = 5 \times 10^5$. The rotational Reynolds number has little influence on the level or distribution of Nu until $Re_\varphi \gtrsim 9.5 \times 10^5$, which is consistent with the mean Nusselt numbers shown in Fig. 11. It should be noted that, owing to the definitions of Nu and $\overline{Nu}$ used (see eqns 3.10 and 3.11), it is possible for the mean Nusselt number to exceed the maximum local Nusselt number.

6. CONCLUSIONS

Heat transfer measurements have been obtained for a single disc rotating close to a stator (with gap ratios $0.01 \leq G \leq 0.18$, radial outflow rates of $C_w \leq 10^5$ and rotational speeds of $Re_\varphi \leq 4 \times 10^6$) and for the downstream disc of a rotating cavity with either an axial throughflow or a radial outflow of coolant (with $0.13 \leq G \leq 0.4$, $Re_z \leq 5 \times 10^5$ and $Re_\varphi \leq 2.5 \times 10^6$).

For the single rotating disc case, if the gap ratio exceeds a maximum value ($G_{max} = 1.05\, Re_\varphi^{-0.2}$) the presence of the stator no longer affects heat transfer from the rotating disc. If $G < G_{max}$, a minimum flow rate ($C_{w\,min} = 0.22\, Re_\varphi^{0.8}$) is necessary to prevent inflow and to ensure that the heat transfer exceeds that of a free disc. Empirical correlations are presented for the variation of mean and local Nusselt numbers with gap ratio coolant flow rate and rotational speed.

For a rotating cavity with an axial throughflow of coolant, heat transfer is strongly affected by vortex breakdown. At $G = 0.4$, spiral vortex breakdown occurs over a range of Rossby numbers $21 \lesssim \epsilon \lesssim 100$ causing a 'peaky' distribution of local Nusselt numbers. Although the mean Nusselt numbers show erratic changes with Re_φ and Re_z, the general level

is considerably lower, under equivalent conditions, than for the single rotating disc case (the latter being typically of order three times higher).

For a rotating cavity with a radial outflow of coolant, three regimes of heat transfer have been identified. At relatively low rotational speeds, a turbulent core-dominated region exists where $\overline{Nu}$ is only weakly affected by Re_ϕ but increases with increasing Re_z. At intermediate speeds, the core shrinks, Ekman layers begin to develop on the discs and $\overline{Nu}$ increases strongly with Re_ϕ and Re_z. At high speeds, the core reaches a minimum radius, the Ekman layers become fully-developed and heat transfer increases only weakly with Re_ϕ. For large values of Re_z, there is evidence to suggest that the central turbulent core does not shrink, and the three regimes are expected to merge into one. The average level of heat transfer is, under equivalent conditions, lower than that for the single rotating disc but much greater than that obtained with axial throughflow.

It is considered that heat transfer from a single rotating disc is reasonably well understood and can be predicted (numerically and empirically) with satisfactory accuracy over a wide range of conditions. For a rotating cavity with an axial throughflow of coolant, the heat transfer behaviour is (owing to vortex breakdown) difficult to understand and even more difficult to predict. It is quite possible that a numerical method could be devised to either determine the onset of vortex breakdown or to calculate heat transfer rates when breakdown is absent; but it is unlikely that a method will be developed in the near future to do both! By contrast, the rotating cavity with a radial outflow of coolant appears easier to understand, and it should be possible to predict (numerically and/or empirically) heat transfer rates. It is clear that more experimental and theoretical research is necessary before temperature distributions in corotating turbine or compressor rotors can be determined with any accuracy.

REFERENCES

1. Hennecke, D.K. Sparrow, E.M. and Eckert, E.R.G., 'Flow and heat transfer in a rotating enclosure with axial throughflow', Warme-und Stoffubertragung, 4, 1971, p. 222.

2. Pustalov, V.N. and Sparrow, E.M., 'Natural convection in a closed rotating cylinder', Int. J. Heat Mass Transfer, 17, 1974, p. 1623.

3. Yu, J.P., Sparrow, E.M. and Eckert, E.R.G., 'Experiments on a shrouded parallel disk system with rotation and coolant throughflow', Int. J. Heat Mass Transfer, 16, 1973,p.311.

4. Sparrow, E.M., Buszkiewicz, T.C. and Eckert, E.R.G., 'Heat transfer and temperature field experiments in a cavity with rotation, recirculation and coolant throughflow', J. Heat Transfer, Trans. ASME, Series C, 97, 1975, p.22.

5. Sparrow, E.M. and Goldstein, L.G., 'Effect of rotation and coolant throughflow on the heat transfer and temperature field in an enclosure', J. Heat Transfer, Trans. ASME, Series C, 98, 1976, p. 387.

6. Sparrow, E.M., Shamsundar, N. and Eckert, E.R.G., 'Heat transfer in rotating cylindrical enclosures with axial inflow and outflow of coolant', J.Eng. Power, Trans ASME, Series A, 95, 1973, p. 278.

7. De Socio, L.M.,Sparrow, E.M. and Eckert, E.R.G., 'Analysis of rotating recirculating turbulent flow and heat transfer in an enclosure with fluid throughflow', Int. J. Heat Mass Transfer, 19, 1976, p. 345.

8. Haynes, C.M. and Owen, J.M., 'Heat transfer from a shrouded disk system with a radial outflow of coolant', J. Eng. Power, Trans ASME, Series A, 97, 1975, p. 28.

9. Owen, J.M., Haynes, C.M. and Bayley, F.J. 'Heat transfer from an air-cooled rotating disk', Proc. R. Soc. Lond. A, 336, 1974, p. 453.

10. Owen, J.M. and Haynes, C.M.,'Design formulae for the heat loss and frictional resistance of air-cooled rotating disks', Improvements in fluid machines and systems for energy conversion, 4, Hoepli, Milan, 1976, p. 127.

11. Owen, J.M. and Bilimoria, E.D., 'Heat transfer in rotating cylindrical cavities', J. Mech. Engng. Sci. To be published.

12. Cobb, E.C. and Saunders, O.A., 'Heat transfer from a rotating disk', Proc. R. Soc. Lond. A, 236, 1956, p. 343.

13. Dennis, R.W., Newstead, C. and Ede, A.J. 'Heat transfer from a rotating disc in cross-flow', Heat Transfer 1970, 4th Intl. Heat Transfer Conference, Versailles, III, 1970, F.C.7.1.

14. McComas, S.T. and Hartnett, J.P., 'Temperature profiles associated with a single disc rotating in still air', Heat Transfer 1970, 4th Intl. Heat Transfer Conference, Versailles, III, 1970, F.C.7.7.

15. Bayley, F.J. and Owen, J.M. 'The fluid dynamics of a shrouded disc system with a radial outflow of coolant', J. Eng. Power, Trans ASME, Series A, 92, 1970, p. 335.

16. Kreith, F., Doughman, E. and Kozlowski, H., 'Mass and heat transfer from an enclosed rotating disk with and without source flow', J. Heat Transfer, Trans ASME, Series C, 85, 1963, p. 153.

17. Gosman, A.D., Lockwood, F.C. and Loughhead, J.N. 'Prediction of recirculating swirling turbulent flow in rotating disc systems', J. Mech. Engng, Sci., 18, 1976, p. 142.

18. Gosman, A.D. Koosinlin, M.L., Lockwood, F.C. and Spalding, D.B., 'Transfer of heat in rotating systems', ASME Gas Turbine Division, Paper 76-GT-25, 1976.

19. Owen, J.M. and Pincombe, J.R., 'Vortex breakdown in a rotating cylindrical cavity', Mech. Eng. Report No. 76/Me/79, School of Engineering & Applied Sciences, Univ. of Sussex. 1977.

20. Hide, R., 'On source-sink flow in a rotating fluid', J. Fluid Mech., 32, 1968, p. 737.

ACKNOWLEDGEMENTS

The author wishes to thank Rolls Royce (1971) Limited and the Science Research Council for sponsoring the work.

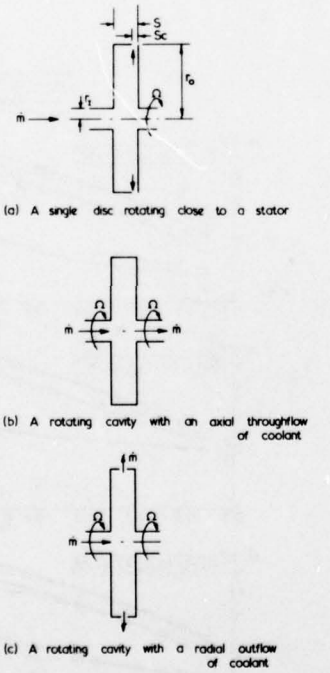

FIG. 1 SCHEMATIC DIAGRAM OF ROTATING DISC SYSTEMS

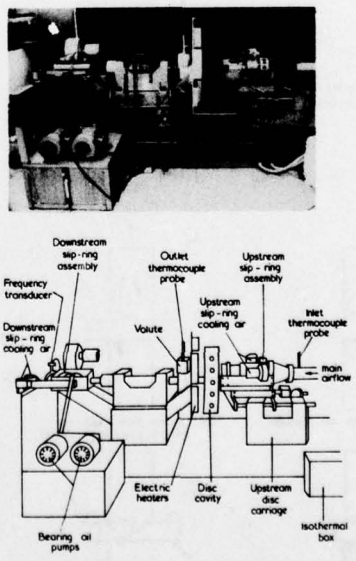

FIG. 2 GENERAL VIEW OF THE HEAT TRANSFER APPARATUS

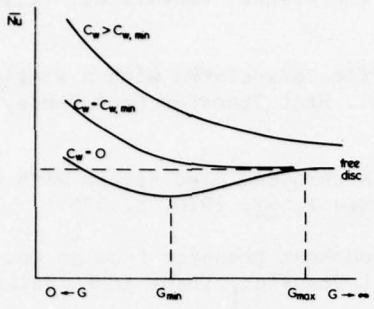

FIG. 3 VARIATION OF MEAN NUSSELT NUMBER WITH GAP RATIO

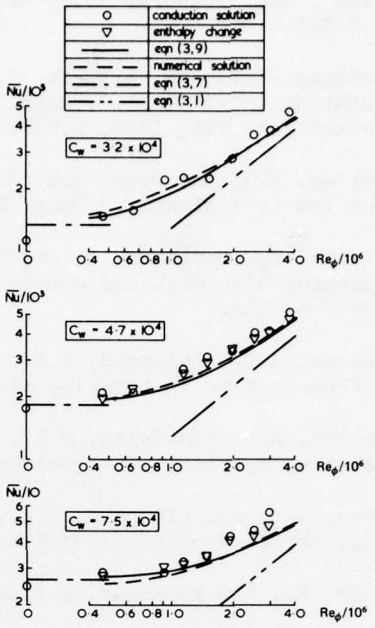

FIG. 4 MEAN NUSSELT NUMBERS FOR AN AIR-COOLED DISC AT A GAP RATIO OF G = 0·02

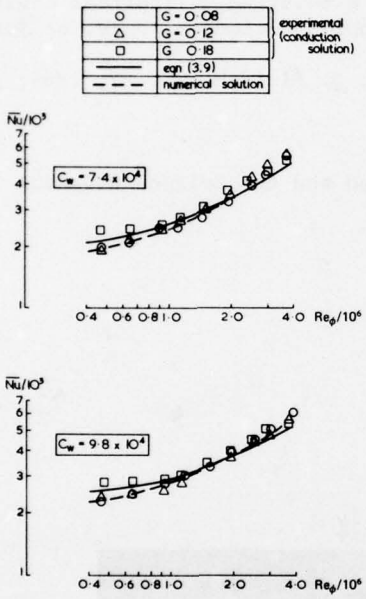

FIG. 5 MEAN NUSSELT NUMBERS FOR AN AIR-COOLED ROTATING DISC AT LARGE GAP RATIOS

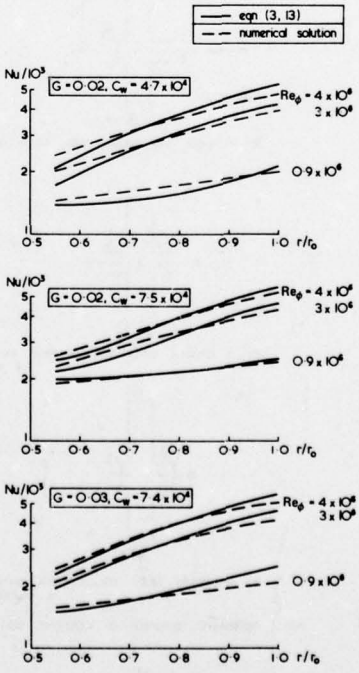

FIG. 6 LOCAL NUSSELT NUMBERS FOR AN AIR-COOLED ROTATING DISC

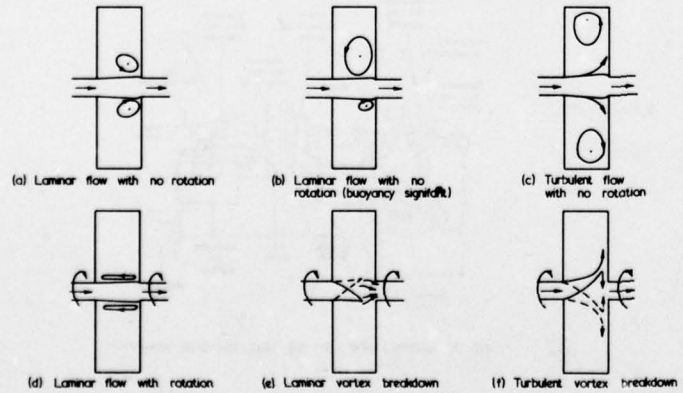

FIG. 7 VISUAL IMPRESSIONS OF THE FLOW PATTERNS INSIDE A CYLINDRICAL CAVITY WITH AXIAL THROUGHFLOW

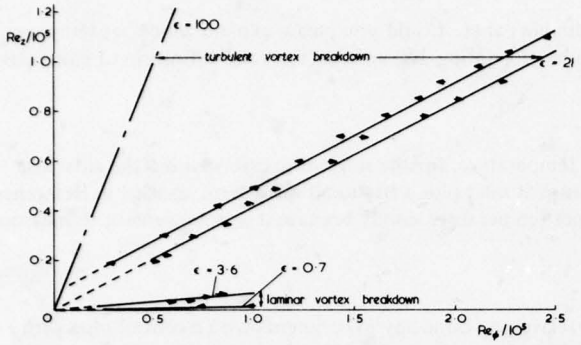

FIG 8 REGIMES OF VORTEX BREAKDOWN IN A CYLINDRICAL CAVITY WITH AXIAL THROUGHFLOW, G = 0·53

← Re_ϕ increasing → Re_ϕ decreasing

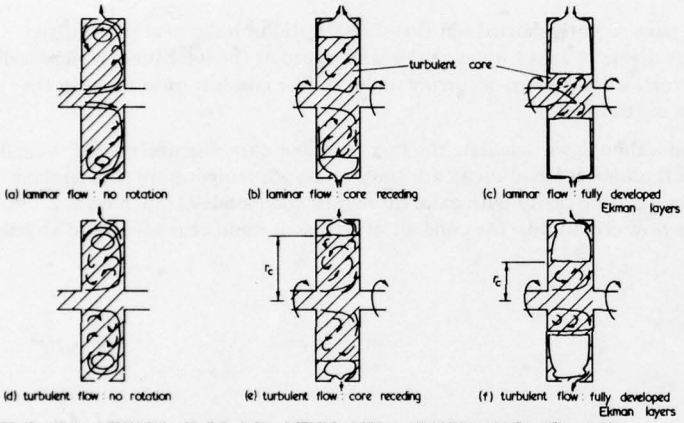

FIG 10 VISUAL IMPRESSIONS OF THE FLOW PATTERNS INSIDE A CYLINDRICAL CAVITY WITH RADIAL OUTFLOW AT G = 0·53

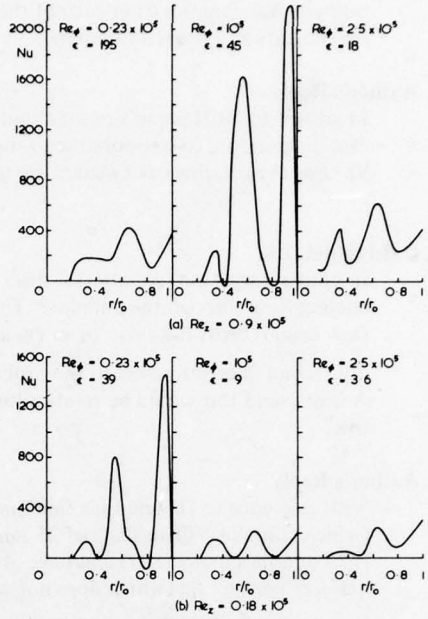

FIG 9 LOCAL NUSSELT NUMBERS FOR A ROTATING CYLINDRICAL CAVITY WITH AXIAL THROUGHFLOW, G = 0·4, $\beta\Delta T$ = 0·27

Symbol	$Re_z/10^5$	$C_w/10^3$
○	0·18	0·28
△	0·45	0·71
●	0·90	1·4
▲	1·8	2·8
▼	3·48	5·4
▽	5·04	7·8

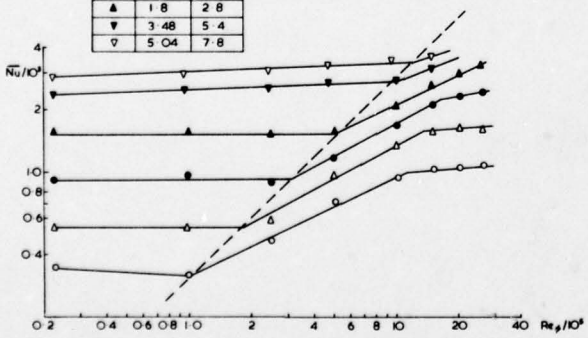

FIG 11 MEAN NUSSELT NUMBERS FOR RADIAL OUTFLOW AT G = 0·4 (DOWNSTREAM DISC HEATED, $\beta\Delta T \simeq 0·27$)

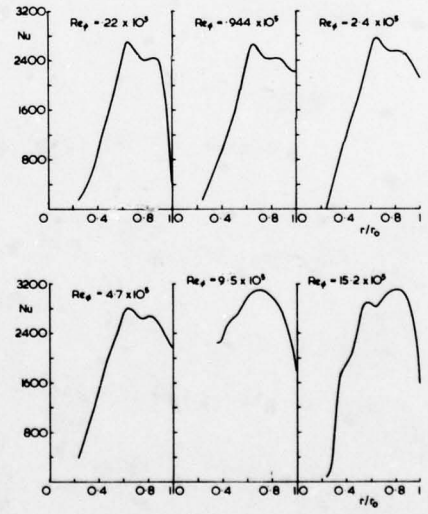

FIG 12 LOCAL NUSSELT NUMBERS FOR A ROTATING CYLINDRICAL CAVITY WITH RADIAL OUTFLOW, G = 0·4, Re_z = 5·0 x 10^5, $\beta\Delta T \simeq 0·27$

DISCUSSION

M.J.Holland, UK

I would first like to compliment the author on a very valuable paper. Could you please explain which gas temperature you have employed in each of the three configurations of rotating disc systems for your definition of convective coefficients and Nusselt numbers.

Author's Reply

In answer to Mr Holland's point about the reference gas temperature, for the single disc case we used the adiabatic disc temperature (corresponding to the coolant temperature at inlet plus a frictional work term, as used in Reference 9). For the rotating cavity cases, we used the coolant inlet temperature simply because it was convenient to measure.

C.H.Priddin, UK

In your second case (compressor discs with throughflow) have you done any experiments with a central pipe with cooling flow through the annulus? The vortex breakdown mechanism you describe may not be so significant if the flow cannot cross the axis. In an engine situation it is likely that there will be a shaft through the center.

My second question refers to the problem of definition of heat transfer coefficient raised in a previous question. A way round this would be to abandon the coefficient and use the actual heat flux in correlations – have you tried this?

Author's Reply

With reference to Dr Priddin's first query, we have recently carried out flow investigation on the heat transfer rig (which contains a drive shaft of 25 mm outside diameter that rotates at the same speed at the inlet tube, which itself is 75 mm inside diameter) and have observed vortex breakdown occurring under similar conditions to those in the half-size perspex rig (which does not contain a central shaft).

I agree with Dr Priddin's second comment, and although we calculate the flux from our experimental results, we still (out of convention!) present our data as Nusselt numbers based on an arbitrary reference temperature (the coolant inlet temperature). As the heat transfer for the rotating cavity with axial throughflow depends as much on the thermal boundary conditions as it does on the flow conditions, the concept of a Nusselt number is somewhat archaic!

REVUE DES TECHNIQUES DE PROTECTION THERMIQUE DES PAROIS DES FOYERS PRINCIPAUX ET DE RECHAUFFE DES TURBOREACTEURS

M. BUISSON
J.P. GAILLAC
B. DEROIDE

DEPARTEMENT COMBUSTION-POLLUTION-RECHAUFFE
CENTRE DE VILLAROCHE - 77 550 - MOISSY-CRAMAYEL (France)

RESUME

L'évolution du cycle des turboréacteurs qui se traduit par une augmentation du niveau de pression et de température en amont des foyers, et la nécessité d'accroître la sécurité de fonctionnement, exigent de la part des constructeurs un effort particulier concernant la protection des parois de la chambre de combustion et du canal de réchauffe.

Ce problème technique est analysé en tenant compte de ses différents domaines d'application, et en soulignant les difficultés résultant des contraintes qu'impose le bon fonctionnement du moteur. Une étude critique des solutions classiques (convection forcée, refroidissement par film etc..), conclut à la nécessité de l'utilisation de procédés plus élaborés. De tels procédés sont proposés ; des calculs simplifiés sont menés en vue de les caractériser et leurs résultats confrontés à ceux de l'expérience.

SYMBOLES et indices

a	facteur d'absorption
C_{CO_2}	concentration en CO_2
C_p	capacité calorifique
C_D	coefficient de débit = débit réel/débit théorique
d	diamètre des perçages en multiperforation
Dh	diamètre hydraulique
e	facteur d'émissivité
h	coefficient de transfert convectif
H	hauteur du tube à flamme
k	conductibilité thermique
l	longueur moyenne de rayonnement ($1{,}2\ H < l < 1{,}7\ H$)
L	facteur de luminosité
m	taux de soufflage $m = \frac{(\rho V)f}{(\rho V)_g}$ (film classique)
	(multiperforation $= \frac{(\rho V)perc}{(\rho V)_g}$
p	pas (intervalle entre orifices)
P	pression (bar)
Pe	Nombre de Peclet = $V_i d/\alpha t$
Pr	Nombre de Prandtl = $\mu Cp/k$
dQ	flux de chaleur
r	rapport de mélange air-carburant
Re	nombre de Reynolds = $\rho VDh/\mu$
s	hauteur de fente
S	distance entre deux rangées d'orifices (multiperforation)
t	température °C
T	température °K
V	vitesse
x	abscisse
X	paramètre de corrélation de film = x/ms

αt	diffusivité turbulente
δ	épaisseur de paroi
η	efficacité
θ	angle film à alvéole
μ	viscosité dynamique
ρ	masse spécifique
σ	perméabilité (%)
σ_s	Constante de Stefan Boltzmann
φ	richesse = r/r Stoechiométrique
ϕ	diamètre (au niveau du film considéré)

ad	adiabatique
c	convection
cart	carter
cond	conduction
e	externe
f	film
perc	perçage
F	flamme
g	gaz (brûlés ou chauds)
i	interne
p	paroi
r	rayonnement

unités SI (sauf spécifications contraires)

1. INTRODUCTION

L'évolution du cycle du turboréacteur d'aviation orientée vers la recherche de l'amélioration du rendement thermique conduit à accroître le taux de compression, ce qui se traduit par des températures à l'entrée et à la sortie des chambres de combustion en constante augmentation. Il en résulte une plus grande difficulté pour l'obtention d'une tenue mécanique satisfaisante des tubes à flamme, compte tenu des températures atteintes et des contraintes dues à la pression et aux gradients thermiques. Les progrès réalisés à ce jour doivent beaucoup à la métallurgie, à l'évolution des techniques de fabrication mais aussi à un meilleur contrôle de l'aérodynamique interne des foyers et des techniques de refroidissement de paroi.

Cet exposé a pour but de passer rapidement en revue les différentes techniques de refroidissement de foyers de turboréacteurs, d'essayer de montrer leurs limites et leurs possibilités de développement pour l'avenir. Les procédés de protection contre l'oxydation et les matériaux réfractaires (par exemple : céramique, matériaux frittés ...) ne seront pas traités dans cette étude.

Les parois des foyers de réchauffe appelées "chemises de protection thermique" font appel aux mêmes techniques quant au refroidissement des parois. La réchauffe est utilisée sur avion militaire ; dans le cas d'une utilisation sur un avion civil, telle que par exemple, la combustion dans le flux froid d'un avion supersonique, la fiabilité demandée serait du même ordre de grandeur que pour la chambre principale.

2. ETUDE CRITIQUE DES SOLUTIONS UTILISABLES POUR LE REFROIDISSEMENT DES PAROIS

L'évolution technique des turboréacteurs a conduit le constructeur à mettre en oeuvre des procédés de protection thermique de plus en plus élaborés, tenant compte d'impératifs thermiques aussi bien que mécaniques et thermodynamiques. L'importance relative de ces différents facteurs ayant varié au cours du temps, les choix qui en ont découlé ont eux mêmes été très divers. Nous nous proposons de les passer en revue depuis les solutions les plus anciennes jusqu'à des techniques qui en sont encore au stade expérimental, en distinguant les domaines d'application : foyer principal d'abord, réchauffe ensuite.

2.1. Chambres de combustion principales

Préliminaires

Le rôle de la chambre principale est d'élever l'enthalpie totale de l'écoulement issu du compresseur, tout en obéissant à certains impératifs :

- utiliser le carburant de façon optimale, c'est-à-dire, avoir un rendement de combustion maximal avec une plage de fonctionnement stable la plus large possible.
- fournir à la turbine des gaz chauds dont la répartition de température soit compatible avec la fiabilité demandée
- dégrader le moins possible l'énergie de l'écoulement, donc, générer une perte de charge minimale.
- assurer une tenue mécanique satisfaisante, en particulier, limiter la température des parois à une valeur maximale dépendant de l'alliage réfractaire utilisé (ordre de grandeur actuel 850 à 900°C).

Rappelons qu'on distingue classiquement trois types de chambre : tubulaire, tubo-annulaire et annulaire (fig.1). Actuellement, la géométrie annulaire pure se généralise pour des raisons de poids et de performances (en particulier sur le plan de la tenue thermique, puisque le rapport surface de paroi/volume du tube y est minimal). Cependant, quel que soit le type de chambre, la conception doit tenir compte de certains principes fonctionnels :

- le tube à flamme doit réaliser la distribution de l'air en une zone primaire (où s'effectue la combustion vive dans des conditions quasi stoechiométriques)et une zone secondaire où se fait le mélange avec l'air frais pour réaliser le niveau de température voulu.
- il doit aussi générer la turbulence nécessaire à la stabilisation de la combustion ainsi qu'à l'obtention de rendements élevés et d'une répartition de température suffisamment uniforme.
- il joue enfin un rôle important de protection thermique des carters. Il est donc, par nature, soumis à des transferts importants d'énergie thermique, par rayonnement, convection et conduction.

Ces principes étant posés, il existe néanmoins une grande variété de solutions selon les contraintes technologiques existantes et les objectifs prioritaires choisis (stabilité de combustion, rendement, répartition de température, pollution, etc...). Ces solutions correspondent à des caractéristiques fort différentes, en particulier quant à la vitesse et à la turbulence, des écoulements interne et externe au tube à flamme. On comprend dans ces conditions, que les techniques de refroidissement se soient diversifiées et mettent en jeu une quantité d'air variant de 25 à 50% du débit total, cet air ayant, en plus de la fonction refroidissement, un rôle en dilution, voire en combustion. Nous exposerons brièvement, ci-dessous, les fondements de ces techniques.

Convection forcée

Cette solution bien qu'ancienne, est à la base de nombreuses techniques. Elle consiste à exploiter la capacité calorifique importante de l'air introduit en zone secondaire en lui transférant par l'intermédiaire des couches limites, les flux issus de l'intérieur de la chambre. Cette solution a été employée en particulier sur les chambres de type ATAR (fig.2) et les chambres à retour. Ses avantages sont évidents : emploi rationnel de l'air de dilution, simplicité de conception conduisant à des prix acceptables et une bonne sécurité d'emploi.

Cette technique intéressante pour des moteurs peu comprimés, à température d'entrée turbine basse, est difficilement extrapolable pour des conditions plus sévères. Elle conduit en effet, pour augmenter les coefficients d'échange, à accroître les vitesses entre tube et carter, donc à diminuer les sections de passage. Ceci entraîne un risque technologique (pour le positionnement), une pénalisation du cycle quant à la perte de charge, et une difficulté d'alimentation des orifices du tube.

Il est bien évident par ailleurs que ces procédés s'appliquent difficilement à certaines parties aval du tube.

Refroidissement par film pariétal

La convection externe avait pour but d'absorber le flux de chaleur transféré par les gaz chauds à la paroi. Le procédé de film pariétal se propose de diminuer ce flux convecté par les gaz chauds en interposant entre eux et la paroi une lame d'air froid. Pour agir efficacement, un film pariétal doit répondre à certaines spécifications :

- il doit être le plus homogène possible en vitesse, à l'introduction dans la chambre.
- il doit être dimensionné de façon à ce que la lame d'air froid se mélange le plus lentement possible aux gaz chauds, sans que la quantité d'air introduit de cette manière soit prohibitive.
- il doit être généré par une pièce mécaniquement saine, participant d'ailleurs à la tenue de l'ensemble du tube, mais fiable et de prix de revient minimal.

On trouvera dans le chapitre 5 différents moyens technologiques pour fabriquer des films réalisant plus ou moins bien ces objectifs. Cependant, si le film joue un rôle d'écran vis-à-vis de la convection des gaz chauds sur la paroi, il ne protège pas du rayonnement. De plus, le flux qu'il peut absorber par convection à la paroi est nécessairement limité par la quantité d'air utilisée et la vitesse d'introduction relativement basse.

Dans la pratique, on est donc conduit à associer à l'effet de film, la convection externe. C'est ce qui est fait dans un grand nombre de chambres de combustion actuelles (fig. 3).

Solutions faisant l'objet de recherches pour les chambres futures

L'objectif étant d'utiliser plus rationnellement l'air de refroidissement, c'est-à-dire de l'introduire dans la chambre à une température proche de celle de la paroi, divers procédés sont envisageables pour améliorer les transferts de chaleur entre l'air froid et les parois :

- on peut augmenter les échanges convectifs en accroissant les surfaces d'échange (ailettes), ou en agissant au niveau des couches limites par de petits obstacles (pontets, etc...).
- on peut aussi utiliser l'effet, local mais important,de l'impact des jets sur une paroi, pour améliorer le coefficient d'échange. Cet effet sera employé pour des pièces de petites dimensions fortement sollicitées thermiquement, comme les fonds de chambre.
- on peut faire travailler l'air en convection dans une double paroi avant de l'introduire en film. C'est par exemple le cas des films à retour, en matériau sandwich (fig.4). Ces dernières solutions se heurtent cependant à des problèmes de tenue mécanique, en particulier à l'implosion.
- on pourrait enfin utiliser le procédé bien connu de transpiration, mais là encore les problèmes de tenue mécanique ne peuvent être résolus par la technologie actuelle. Par contre, les progrès des techniques d'usinage (perçage par bombardement électronique) permettent de réaliser une multiperforation des parois qui cumulent une convection intense à l'intérieur de la tôle et un effet de film du côté chaud. Cette technique, déjà utilisée pour combattre les surchauffes locales, fait actuellement l'objet de recherches à la S.N.E.C.M.A.

2.2. Chambres de réchauffe

Le refroidissement des parois des chemises de protection thermique des canaux de réchauffe fait appel aux mêmes principes que celui des foyers principaux. Les niveaux de pression ($P \leqslant 4$ bars) sont cependant moins élevés, la nature et l'échelle de turbulence différentes ; par contre, les canaux sont généralement longs et de grand diamètre et les vitesses de gaz élevées. Les zones de rencontre des fronts de flamme avec les parois sont très sollicitées. On rencontre d'importantes hétérogénéïtés circonférentielles de température, par suite de la non homogénéïté de l'écoulement des gaz qui alimentent le foyer de rechauffe (sillages chauds). On est conduit de ce fait à sur-dimensionner le refroidissement des parois au risque de se pénaliser du point de vue des performances de la réchauffe.

On distinguera les réchauffes des moteurs monoflux, de celles des moteurs double flux. Les premiers ont généralement des chemises dites à convection forcée, les seconds, disposant d'air frais, utilisent souvent le refroidissement par films d'air successifs, l'air des premiers films participant à la combustion. Ces films sont généralement réalisés par emboutissage avec liaison par rivets ou soudure,afin de diminuer les prix de revient et de donner une certaine souplesse en atténuant de ce fait les contraintes thermiques. La difficulté réside dans la réalisation de films donnant un écoulement d'air homogène et qui ne se déforment pas dans les zones de gradients thermiques élevés dus aux sillages chauds.

Des chemises en matériau sandwich à l'intérieur duquel l'air servant à former le film travaille par convection forcée, sont susceptibles de donner d'excellents résultats. Leur prix de revient est actuellement un obstacle important au développement de telles formules. L'utilisation de la multiperforation, soit seule, soit en complément du film semble être une technique très intéressante car elle réduit considérablement les gradients thermiques.

3. METHODES DE DIMENSIONNEMENT DES FILMS CLASSIQUES ET A MULTIPERFORATION

3.1. Cas du film pariétal classique

On se référera, pour la formulation du problème, aux notations définies sur la figure 5.

Considérons donc un élément de paroi refroidi par film d'air, de longueur dx, d'épaisseur δ et de largeur unité. On supposera que les phénomènes aérodynamiques et thermiques mis en jeu sont permanents et bidimensionnels, ce qui revient à supposer négligeables les flux de chaleur selon Oz. Pour l'élément de paroi en question, de volume $\delta .dx$, supposé en équilibre thermique, le bilan de chaleur s'écrit :

(1) $$dQ_{ir} + dQ_{ic} + dQ_{er} + dQ_{ec} + dQ_1 + dQ_2 = 0$$

Dans cette expression figurent, en plus des flux convectés et rayonnés, les flux dQ_1 et dQ_2 conduits à travers les frontières amont et aval de l'élément considéré. Le flux thermique conduit entre les faces interne et externe de la paroi, au point d'abscisse x, s'exprime quant à lui par :

(2) $$dQ_{cond,i\to e} = h_p \frac{dx}{\delta} (T_{pi} - T_{pe})$$

Pour estimer le flux de chaleur rayonné par les gaz chauds, nous avons été amenés, afin de tenir compte de l'hétérogénéïté des zones fortement réactionnelles, à définir une température de rayonnement T_F qui peut être supérieure à la température de convection interne T_g.

Avec ces notations, nous pouvons écrire à partir des lois de Stefan Boltzmann pour le rayonnement :

(3) $$dQ_{ir} = \sigma_s \left(\frac{1+e_p}{2}\right)\left(e_F T_F^4 - a_F T_{pi}^4\right) dx$$

Cette formulation simplifiée du problème complexe que posent les échanges radiatifs à l'intérieur de la masse gazeuse et avec les parois, exige la connaissance des facteurs d'émission et d'absorption.

Pour le premier, e_F, nous avons utilisé l'expression proposée par Reeves [2] , qui traite l'émission totale de la flamme comme celle des constituants gazeux (essentiellement CO_2 et H_2O) en lui affectant un facteur de luminosité L pour tenir compte de la présence de particules de carbone, non négligeable pour les carburants d'aviation :

(4) $$e_F = 1 - exp\left(-2.86.10^4\ P_L\ (r\ell)^{0.5}\ T_F^{-1.5}\right)$$

on en déduit le coefficient d'absorption a_F par la formule suivante [1] :

(5) $$\frac{a_F}{e_F} = \left(\frac{T_F}{T_{pi}}\right)^{1.5}$$

en limitant toutefois la valeur de a_F à 1 dans les cas où un gros écart entre T_F et T_{pi} conduirait à une valeur supérieure.
D'autre part le rayonnement de la face externe de la paroi sur les carters, dans l'hypothèse où $T_{carter} = T_e$, s'exprime par :

(6) $$dQ_{er} = \sigma_s\ e_{eff} \left(Tpe^4 - Te^4\right) dx$$

où e_{eff} est l'émissivité effective de la paroi de chambre qui, dans le cas d'une géométrie annulaire, s'exprime en fonction des émissivités de la paroi et du carter par :

(7) $$e_{eff} = \frac{1}{1 + \left(\frac{1}{e_p} - 1\right) - \frac{\phi_{pe}}{\phi_{cart}} \left(\frac{1}{e_{cart}} - 1\right)}$$

Pour évaluer le flux échangé par convection sur la face externe de la paroi, nous avons mis à profit une visualisation de l'écoulement dans cette zone montrant le développement d'une couche limite turbulente à partir du point d'arrêt A. Dans ces conditions, naturellement schématiques, le coefficient de transfert de chaleur peut s'écrire selon la formulation de COLBURN pour une plaque plane :

(8) $$\frac{h_{ex}}{h_e} = 0.024\ Re_x^{0.8}\ Pr^{0.33}$$

les grandeurs caractéristiques (Re, Pr) étant évaluées à une température T* définie par [3] :

(9) $$T^* = 0.5\left(Tpe - Te\right)$$

Le coefficient d'échange de chaleur convectif dans le film (côté gaz de combustion) est défini par analogie avec une couche limite classique à partir de la notion de température adiabatique de paroi T_{ad} selon :

(10) $$h_i = \frac{dQ_{ic}}{(T_{ad} - T_{pi})\,dx}$$

Cette température adiabatique est localement accessible par la mesure de l'efficacité adiabatique

(11) $$\eta_{ad} = \frac{T_g - T_{ad}}{T_g - T_e}$$

qui est connue si on fait l'analogie entre les profils de température et de concentration dans la couche de mélange. Pour caractériser l'évolution de l'efficacité adiabatique, on fait très souvent appel à un paramètre adimensionnel X introduit de la façon suivante :
le mélange entre les films et les gaz chauds est essentiellement lié à la grandeur de la fluctuation turbulente de vitesse V' de ces derniers. On peut écrire que le débit des gaz chauds pénétrant dans le film est proportionnel à $(\rho V')_g$, donc à $(\rho V)_g\ dx$ si l'on suppose la turbulence isotrope, c'est-à-dire $\left(\frac{V'}{V}\right)_g$ = cte.

Si l'on rapporte ce débit à celui du film, on pourra définir le terme différentiel

$$dX = \frac{(\rho V)_g \, dx}{(\rho V)_f \, \delta}$$

qui s'intègre en (12) $$X = \frac{(\rho V)_g . x}{(\rho V)_f . \delta} = \frac{x}{m . \delta}$$

Pour pouvoir résoudre numériquement l'équation (1) nous avons recherché une expression littérale de η_{ad} faisant intervenir X . Diverses corrélations sont proposées par la littérature. Elles sont généralement empiriques et établies pour des films ayant un fonctionnement aérodynamique peu différent de la fente pure.

Une revue de ces principales corrélations a été présentée par M.A. Paradis [8] . Les premiers travaux présentaient η_{ad} en fonction du seul paramètre X, mais étaient d'une application restreinte au domaine de température et pression concerné. Par la suite, le nombre de Reynolds de la fente et le niveau relatif de température du film et de l'écoulement principal ont été pris en compte. L'expression de η_{ad} présentée par la relation (13) a été proposée par KUTATELADZE et LEONT'EV [4]. Nous l'avons adoptée pour notre calcul de température de parois, car elle recoupait de façon correcte nos mesures d'efficacité : on constate en effet sur la figure 11, où X est le paramètre de représentation, un bon accord entre cette formule générale et nos essais effectués dans des conditions bien déterminées.

(13) $$\eta_{ad} = (1 + 0.249\,\beta)^{-0.8}$$

ou $$\beta = X \left(Re_f \frac{\mu_f}{\mu_i} \right)^{-0.25}$$

Pour en revenir au calcul de la convection interne, nous avons tenté de tenir compte de la non adiabaticité de la paroi en remplaçant T_{ad}, qui ne décrivait que le phénomène de mélange, par T_{eff} qui intègre les échanges de la paroi avec les gaz. Avec ces hypothèses, on peut évaluer la convection interne par une expression du type de celle de COLBURN :

(14) $$\frac{h_i \, x}{k_i} = 0.032 \, Re_x^{0.8} \, Pr^{0.33}$$

les divers paramètres étant évalués à la température :

(15) $$T^{**} = 0.5 \, (T_{eff} + T_{pi})$$

3.2. Cas de la multiperforation

Le cas de la multiperforation est traité de façon identique. Les mesures de température effectuées ont montré la validité de l'hypothèse de la formation d'un film d'air perpétuellement régénéré à la paroi. Les paramètres nécessaires à l'évaluation de l'efficacité adiabatique de ce film sont d, p, m, S. Les divers résultats obtenus sur plaques multiperforées ont été corrélés par l'expression (16) introduite en [6] et utilisée par MAYLE et CAMARATA [5] :

(16) $$\eta_{ad} = 1 - \exp\left(- \frac{\pi^{0.5}}{4} \frac{d}{p} \, m \, Pe^{0.5} \sum_{k=0}^{n-1} \left(\frac{x}{d} - k \frac{S}{d} \right)^{-0.5} \right)$$

La méthode des traceurs exposée au paragraphe 4 est mal adaptée à la mesure des efficacités adiabatiques en multiperforation. En fait seules les mesures de température de paroi permettent actuellement d'accéder à ce paramètre. Dans le cas de la multiperforation, au bilan thermique écrit en (1), il faut adjoindre l'échange thermique convectif dans l'épaisseur de la tôle qui, pour un orifice s'exprime par :

(17) $$dQ_{perc.} = \pi \, d \, \delta \, h_{perc} \, (T_{pm} - T_e)$$

avec $$T_{pm} = 0.5 \, (T_{pi} + T_{pe})$$

(18) $$h_{perc.} \, d / k_e = K \, Re_{perc.}^{0.8} \, Pr^{0.4}$$

en régime établi K = 0.023 selon [3] mais compte tenu des faibles δ/d des orifices, K = f[Re, δ/d], selon [9] et [10].

3.3. Déroulement du calcul

La méthode numérique employée résoud pas par pas l'équation (1) par tranches de longueur dx en négligeant dans un premier temps les termes dQ_1 et dQ_2. La conduction longitudinale est prise en compte au cours des traitements suivants. La convergence est obtenue lorsque le dT_{pi} est négligeable pour tout x entre deux traitements successifs.
Par ailleurs, les termes dQ_1 et dQ_2 sont négligés dans le cas de la multiperforation, où ils sont (sauf à l'origine de la zone multiperforée) faibles par rapport au terme dQ_{perc} exprimé en (17).
Il faut noter que la tridimensionnalité de l'écoulement n'a pas été envisagée : l'interaction des jets issus des orifices équipant les tubes à flamme, avec les films pariétaux ou les éléments de parois multiperforées n'est pas prise en compte dans le schéma étudié.

Certains paramètres sont encore connus avec peu de précision : telles les valeurs exactes du coefficient de luminosité L, intervenant dans (5). Il est fonction du type de kérosène, du mode d'injection du carburant, et évolutif le long de l'axe de la chambre (de 2.4 en zone primaire à 1 en zone de dilution). Il faut aussi noter que les différentes expressions du coefficient de transfert de chaleur utilisées pour la résolution numérique peuvent être insuffisantes dans certains cas particuliers, notamment dans le cas de la multiperforation, où l'effet d'entonnement de l'air dans les orifices peut se traduire par une augmentation des échanges thermiques au voisinage de la paroi, côté externe. Du côté interne, le processus d'échange convectif reste lui aussi assez mal connu. De même, dans les orifices, nous avons essayé de prendre en compte l'effet de non-établissement des couches limites sur les échanges de chaleur par une correction préconisée par Mac Adams [3] d'après les travaux de Latzko. La correction proposée par Ermolin [10] est plus importante et sans doute plus réaliste.

Quant au film pariétal, la présence de carburant liquide près de la paroi, dans certaines conditions de fonctionnement, permet le développement d'une combustion dans la zone de mélange, rendant hasardeuse l'estimation des échanges dans cette zone.

4. MOYENS D'ESSAIS DE CARACTERISATION DES TECHNIQUES DE REFROIDISSEMENT

4.1. Introduction

L'écoulement dans les chambres de combustion et de réchauffe étant généralement très hétérogène et turbulent (orifices sur les parois servant à créer des recirculations ou une dilution, sillages, etc...) il est apparu nécessaire d'essayer les différents types de refroidissement dans des installations d'essais partiels, garantissant une bonne fidélité dans les comparaisons, et une mise en oeuvre rapide et peu coûteuse, les recoupements devant cependant être faits sur chambres complètes au banc d'essai partiel ou sur moteur.

4.2. Méthode utilisée pour comparer les différents types de refroidissement

Dans le cas d'un refroidissement par film d'air pariétal, l'écoulement de gaz chauds est généré par une chambre de combustion disposée de façon à obtenir une très grande homogénéïté des températures, car le CO_2 qu'il contient va servir de traceur. A partir du moment où l'homogénéïté est suffisante, on injecte de l'air de refroidissement. Au lieu de mesurer la température de paroi, ce qui suppose une paroi parfaitement isolée thermiquement, et beaucoup de soin dans la mesure des températures, on mesure le degré d'avancement du mélange en utilisant le CO_2 comme traceur. Aucune isolation thermique de la paroi n'est nécessaire. Les thermocouples sont remplacés par les prises de gaz en statique et les échantillons ainsi prélevés sont analysés dans un analyseur classique CO_2. Le prélèvement des gaz est fait très lentement de façon à avoir une valeur moyenne du CO_2 à une très faible distance de la paroi.

A la distance x mesurée depuis la sortie du film, l'efficacité adiabatique que l'on mesure est :

$$\eta_{ad} = \frac{C_{CO2\ initial} - C_{CO2}(x)}{C_{CO2\ initial}} = \frac{Tg - Tad}{Tg - Te}$$

L'approximation est valable si l'on peut assimiler les profils de concentrations aux profils de température, c'est-à-dire, si le nombre de LEWIS est égal à 1. Or, pour l'air Le $\simeq$ 1. Cette méthode présente l'avantage sur la méthode directe par température de dissocier les phénomènes de rayonnement et de convection. Ce type d'installation est représenté sur la figure 6. Dans le cas de la réchauffe, on a voulu juger le comportement du film attaqué par un front de flamme à haute température, les gaz étant en cours de réaction. Le CO_2 ne pouvant plus servir de traceur, on peut, soit utiliser un traceur tel que l'Hélium injecté de façon homogène dans le circuit de refroidissement, soit comparer les températures réelles des tôles en utilisant des peintures thermosensibles à virages multiples. Cette dernière méthode bien qu'assez imprécise permet cependant une comparaison simple et rapide de diverses configurations. Cette technique est utilisée en particulier pour le refroidissement par multiperforation. Le schéma de cette installation est présenté figure 7.

4.3. Installations d'essais

Le schéma de la figure 6 représente une veine d'essai bidimensionnelle à paroi circulaire ; une deuxième installation, tout à fait analogue dans son principe, a également été utilisée permettant d'essayer des parois planes.

Les schémas de la figure 8 montrent quelques uns des types de films qui ont été essayés dans ces installations. Ils sont décrits au § 5-1.

Un écoulement externe peut être réalisé, il est nécessaire pour certains films, compte tenu de la position de leurs orifices d'alimentation. Le banc à paroi circulaire conduit à une installation plus homogène, ne posant pas de problème d'étanchéité ; de plus, il n'y a pas d'effet de paroi parasite. La réalisation du film à essayer est cependant nettement plus coûteuse.

Dans les essais effectués, les conditions d'écoulement du flux chaud ont été les suivantes :

P = 1.2 bar

t_g = 500°C

V_g = 35 $m.s^{-1}$ (parfois 108 $m.s^{-1}$ et 260 $m.s^{-1}$)

Les conditions d'alimentation du film ont varié par l'intermédiaire de la perte de charge créée à travers le film ($\Delta P/P$).

Les ordres de grandeur des paramètres que l'on a fait varier sont les suivants :

$\Delta P/P$	de	2	à	8%	(et jusqu'à 16% quand $V_g = 260\ m.s^{-1}$)
s	de	2.8	à	8.5	mm
x	de	0	à	200	mm

Le schéma de la figure 7 représente une installation pour l'étude du refroidissement des chemises de réchauffe dans laquelle on a créé un sillage chaud local à l'aide d'un stabilisateur de réchauffe. La veine d'essai est de section rectangulaire mais le dispositif à étudier est implanté sur une tôle ayant une courbure pour améliorer le comportement mécanique compte tenu des gradients de température élevés. La température de réchauffe au voisinage de la paroi à protéger est de 1300°C environ. La combustion se continue tout le long de la plaque. Le débit spécifique des gaz chauds est constant : $(\rho V)_g \simeq 85\ kg.s^{-1}.m^{-2}$. Le paramètre vitesse n'est pas d'un accès aisé compte tenu de l'évolution de la combustion. Le refroidissement externe par convection peut être réglé à la valeur voulue ainsi que la perte de charge à travers le film ou la multiperforation.

Le schéma de la figure 9 montre les températures des parois atteintes sur une plaque essayée en n'utilisant que le refroidissement par convection forcée externe (simulation de l'écoulement entre chemise et canal). Ces installations d'essais permettent évidemment la mesure du coefficient de débit global du film ou de la multiperforation ainsi que le calcul de tous les paramètres aérothermodynamiques moyens de l'écoulement.

5. TECHNIQUES ETUDIEES ET RESULTATS

5.1. *Choix d'une technique et principaux types de films essayés*

On a vu au paragraphe 2-1 que l'ingénieur qui fait le choix et le dimensionnement d'un type de film de refroidissement pariétal doit :

- chercher à créer un écoulement homogène le long de la paroi à protéger.
- s'assurer que le mélange se fera le plus lentement possible avec les gaz chauds (problème de mélange turbulent). Il doit de plus faire en sorte que ces caractéristiques ne soient pas dégradées par des déformations en fonctionnement (contraintes mécaniques, dilatations ou gradients thermiques locaux).

Cet élément participe aussi à la tenue mécanique du tube à flamme soumis à d'importantes contraintes statiques et vibratoires. La fente pure, représentée sur le schéma 1 (fig. 8) serait à priori la solution idéale du point de vue homogénéité, mais elle n'est malheureusement pas réalisable. Même les essais au banc partiel sur une paroi plane n'ont pas été satisfaisants par suite de variation de la hauteur de la fente s. On est donc, en général conduit à calibrer l'entrée du film par des orifices, la hauteur de fente étant choisie si l'échelle le permet pour créer l'écoulement optimal, compte tenu des caractéristiques des gaz chauds. L'homogénéité du film d'air frais dépendra en définitive de la disposition des orifices et de la longueur de la languette (contradictoire avec une bonne tenue thermique). L'épaisseur de cette dernière δ doit être également faible, car elle génère une turbulence parasite par effet de culot.

Le résultat final du dimensionnement sera un compromis entre la tenue thermique et l'homogénéité caractérisée par l'efficacité adiabatique. Les premiers films qui sont apparus sur les chambres ont été réalisés à partir de tôles formées par emboutissage et assemblées par rivetage, brasage ou soudage. Ce type de technologie est représenté sur les schémas 4, 5, 6 (fig.8). Dans certains cas l'effet de refroidissement par impact de l'air du film sur la languette a été recherché.

La disposition 6 (fig.8) à deux rangées d'orifices quinconcées sur une paroi inclinée ($\sim 18°$) permet d'engendrer un film continu, avec une languette de longueur raisonnable. Ce type de film est utilisé à la S.N.E.C.M.A.

Le film correspondant au schéma 2 (fig.8) à liaison par ondulé est d'une réalisation simple, mais d'un emploi peu souple car il ne permet pas d'agir séparément sur les paramètres débit et vitesse.

La tendance actuelle est de remplacer les films réalisés en tôle par des films usinés dans la masse. En effet, des pincements de la languette peuvent se produire localement malgré certains perfectionnements tels que des pontets entre languette et paroi. Les films usinés deviennent de plus en plus nécessaires par suite de l'augmentation des niveaux de pressions et de températures dans les chambres. Les schémas 7, 8, 9, 10 (fig.8) donnent quatre exemples d'une telle conception. Il a été nécessaire de procéder à de nombreux essais pour définir des technologies susceptibles de donner un écoulement homogène. Pour un film tel que celui schéma 10 (fig.8) (double élargissement), les paramètres géométriques sur lesquels on peut jouer sont nombreux. La réalisation de tels types de films reste d'un prix plus élevé que celle des films en tôle.

Le schéma 3 (fig.8) montre un film constitué en matériau sandwich, l'écoulement de l'air générateur se faisant dans les canaux. On a vu dans le paragraphe 2.1 que cette conception permet d'allier un effet de convection interne au matériau à l'effet de film. Le calibrage du débit peut se faire par exemple par écrasement des canaux au niveau de l'alimentation (schéma fig. 14). Cette technologie est actuellement réalisable mais très coûteuse, un gain de poids peut cependant être obtenu. L'expérience de cette technologie est encore limitée (tenue aux vibrations par exemple).

5.2. Principaux résultats obtenus par la mesure de l'efficacité adiabatique

Les efficacités adiabatiques η_{ad} sont portées en fonction de X (voir paragraphe 3.1).

Fente pure et matériau sandwich

Les essais avec fente pure n'ayant pas donné de résultats cohérents par suite de variation de la hauteur de la fente s, nous avons jugé préférable de prendre comme référence un film constitué en matériau sandwich (schéma 3 fig. 8) réalisé en tôles très fines. La figure 10 présente l'influence du taux de soufflage $m = \frac{(\rho V)f}{(\rho V)g}$ pour 3 vitesses des gaz chauds : 35, 108 et 260 $m.s^{-1}$. On voit que pour le domaine d'utilisation des films dans les chambres de foyers principaux ($X \leqslant 20$) les efficacités sont très élevées. Dans le cas de la réchauffe, la valeur maximale de X est plus élevée (s est bornée inférieurement par la technologie et supérieurement par le débit disponible), l'efficacité peut atteindre des valeurs assez basses en fin de virole même avec ce film très homogène. On notera que l'optimum d'efficacité se trouve réalisé pour $m \simeq 1$.

Comparaison des différents types de film

La figure 11 présente plusieurs types de films essayés dans les mêmes conditions expérimentales. Cette planche ne prétend pas présenter que des films optimisés dans chaque technologie, elle a pour but de montrer les écarts que l'on peut obtenir entre films. Les numéros de la figure renvoient aux schémas de la figure 8. Les films en tôle sont généralement assez bons, le film usiné à double élargissement (repère 10) utilisé à la S.N.E.C.M.A. a fait l'objet d'une optimisation géométrique poussée. La figure 12 montre à titre d'exemple pour ce film, la dispersion des résultats d'essais lorsque l'on a fait varier la hauteur de fente de 3 à 8,5 mm à perte de charge donnée et géométrie optimisée. Le bon comportement mécanique et thermique de ce film a été par ailleurs vérifié sur moteur.

5.3. Résultats obtenus sur un banc simulant un foyer de rechauffe

Essais de divers types de films avec peinture thermosensible

La figure 13 présente à titre d'exemple une plaque équipée d'un film à simple élargissement muni de deux rangées d'orifices quinconcées (fig. 8 schéma 6). La courbe présente le recoupement entre les valeurs mesurées et calculées. Ce film de conception et de réalisation simple se comporte dans ces conditions de façon satisfaisante. Les hypothèses faites pour le calcul semblent suffisamment précises pour permettre une prévision correcte des températures de paroi.

Des plaques planes munies de matériau sandwich ont également été essayées. Un programme de calcul d'échanges thermiques dans les matériaux à multicanaux a été employé pour prévoir les températures de paroi. Les répartitions de température présentées (fig. 14) concernent une plaque en matériau de ce type sans film d'air entre gaz chauds et paroi et une convection externe très faible. Les calculs effectués sont compatibles avec l'essai. Il est à souligner que la température de la plaque est en tout point inférieure à 450°C. Dans les mêmes conditions expérimentales, une plaque refroidie par convection s'équilibre à 880°C.

La répartition des flux de l'écoulement du matériau sandwich repéré sur la coupe C(fig.14) est présentée ci-dessous en pourcentage du flux fourni côté gaz chauds.

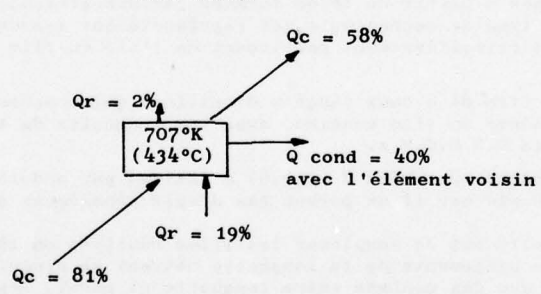

Le gain de 400°K obtenu (par rapport à une plaque pleine refroidie par convection externe) est supérieur à ce que pourrait permettre une technique de film pariétal classique dans les mêmes conditions.

Essais de tôles multiperforées

Il s'agit de tôles perforées d'une multitude de petits trous disposés dans le cas de nos essais, en rangées de manière à former des triangles équilatéraux. On a fait varier les diamètres des orifices de d = 0.3 à 1.4 mm et les perméabilités σ de 0.5 à 5.7%.

σ rapport de la section totale des orifices à la surface de tôle intéressée par la multiperforation s'exprime par :

$$\sigma = \frac{\pi}{2\sqrt{3}} \left(\frac{d}{p}\right)^2$$

p est le pas ; c'est-à-dire la distance entre deux orifices.

L'objectif est de répartir régulièrement l'air utilisé auparavant dans les films de façon discontinue, le refroidissement de la tôle se fait alors d'une part par convection dans l'épaisseur de la tôle, d'autre part par effet de film le long de la paroi.

Nous présenterons ici quelques uns des résultats obtenus, la comparaison des différentes configurations essayées se faisant à même débit de refroidissement. L'écoulement externe correspondant à celui entre paroi du foyer et carter a également été simulé.

Influence du diamètre de perçage des orifices à perméabilité σ donnée et débit constant à travers les trous (perçage normal à la tôle d'épaisseur 1.2 mm)

Sur la figure 15 correspondant à une perméabilité σ = 1 %, on constate que le refroidissement est d'autant plus efficace que le diamètre et le pas des orifices sont faibles. C'est dans ce cas que l'on a la plus grande surface de contact avec l'air frais à travers la plaque, la vitesse dans les trous étant sensiblement constante. La même expérience a été faite pour une perméabilité σ = 3% correspondant à d = 0.3, 0.52, 0.73 mm pour des pas respectifs de 1.65, 2.85, 4 mm. Les résultats thermiques sont très voisins pour ces trois configurations ainsi que les coefficients de débit.

Influence du pas des orifices de diamètre d = 0,3 mm (perçage normal à la tôle)

La figure 16 présente l'évolution du coefficient de débit qui passe par un optimum vers σ = 1% et les résultats thermiques qui font également apparaître un optimum vers σ = 1 à 1.5%. Le meilleur résultat n'est donc pas obtenu lorsque la surface d'échange avec l'air frais à travers la tôle est la plus grande. Par contre, c'est dans ces conditions que l'effet de film est le plus important, ce que l'on constate par l'observation de la partie aval non perforée de la plaque d'essai. La vitesse de l'air frais dans les orifices varie de façon inversement proportionnelle à la surface mouillée comme le montrent les mesures de perte de charge. Ce résultat inexpliqué par notre calcul mérite cependant une réserve : le niveau de pression de l'air qui alimente les orifices évolue légèrement tout au long de la plaque ce qui, aux fortes perméabilités (faibles ΔP) peut se traduire par une hétérogénéïté d'alimentation difficile à prendre en compte.

D'autres paramètres ont été étudiés, comme par exemple, l'inclinaison des perçages (α = 0 trous normaux, 30° et 45°). Ces essais ayant été faits à σ = 1% et d = 0.3 mm, le gain probablement faible que l'on peut escompter de ces configurations n'a pas pu être mis en évidence sur cette installation d'essai.

La figure 17 concerne les résultats obtenus pour trois plaques multiperforées comparés aux températures calculées. Les trois plaques ont des perméabilités et des diamètres de perçage différents. L'imprécision due à l'emploi des peintures thermosensibles limite actuellement l'optimisation de la méthode de calcul. Ce calcul ne permet pour le moment que de classer les différentes configurations.

Ces premiers essais montrent bien l'intérêt de la multiperforation pour le refroidissement des parois, un effet presque instantané peut en être attendu si l'on choisit bien la configuration de perçage en fonction du ΔP disponible. Des applications sur moteur ont confirmé les résultats obtenus au banc partiel. Nous avons acquis dès à présent une certaine connaissance des coefficients de débit nécessaire au dimensionnement, mais des expériences systématiques devront être envisagées, si on veut mieux analyser, dans le fonctionnement thermique, la part due à l'efficacité du film d'air continuellement régénéré le long de la paroi.

5.4. Résultats sur chambre complète et sur canal de rechauffe

Des bancs d'essais pouvant recevoir des chambres complètes ou des secteurs de chambre dans des conditions moteur (jusqu'à une pression de 25 bars et une température entrée chambre de 500°C) ont permis la validation des dispositifs de refroidissement dans des conditions de fonctionnement réelles.

La figure 18 présente un exemple de recoupement entre les valeurs des températures de paroi prévues par le calcul et les valeurs obtenues par peinture thermosensible. Il s'agit ici d'une chambre complète et le film concerné est un film massif à double élargissement (schéma 10 fig.8). Cet exemple a été choisi surtout dans le but de montrer les influences respectives des deux principaux paramètres de l'écoulement, à savoir : pression et température à la sortie du compresseur, qui sur moteur varient corrélativement. Le recoupement entre les valeurs mesurées et calculées est satisfaisant, l'influence prépondérante de la température d'entrée chambre Te apparaît sur cette figure.

Les différents types de refroidissement essayés au banc partiel ont pu être utilisés sur canal de rechauffe moteur. Les résultats obtenus confirment ceux du banc partiel, aussi bien en ce qui concerne les techniques classiques (film pariétal) que les techniques nouvelles (multiperforation, matériau sandwich).

6. CONCLUSION

On a vu que l'évolution du cycle thermodynamique des turboréacteurs pose des problèmes pour la tenue mécanique et thermique des parois des foyers. Signalons que la nécessité de concevoir maintenant des chambres peu polluantes, conduit à modifier les techniques d'injection, voire même l'architecture générale du foyer (chambre à deux têtes, à deux modules ...), ce qui se répercute le plus souvent par un accroissement des surfaces. Dans cette optique, des travaux sont en cours.

../..

Après une optimisation du refroidissement par film pariétal, des résultats très intéressants ont été obtenus avec les matériaux sandwich et la multiperforation, techniques envisageables grâce aux progrès de la fabrication. Des études et des essais seront cependant encore nécessaires pour appréhender avec plus d'exactitude les nombreux paramètres intervenant dans les calculs thermiques.

REFERENCES

1. A.H. LEFEBVRE — "Radiation from flames in gas turbine and rocket engines" 12 th Symposium on Combustion P. 1247 - 1253

2. D. REEVES — "Flame radiation in an industrial gas turbine combustion chamber" N.G.T.E. Memo N° M 283

3. Mc. ADAMS — "Heat transmission" Chemical Engineering Series Mc Graw Hill 3rd edition

4. S.S. KUTATELADZE, A.I. LEONT'EV — "The heat curtain in the turbulent boundary layer of a gas". High Temperature N° 1 1963 P. 250 - 258

5. R.E. MAYLE, F.J. CAMARATA — "Multihole cooling film effectiveness and heat transfer" ASME P. 534 - 538 November 1975

6. R.J. GOLDSTEIN, E.R.G. ECKERT, V.L. ERIKSEN, J.W. RAMSEY — "Film cooling following injection through inclined circular tubes" NASA CR 72 612 November 1969

7. J. CARUEL — "Le développement des chambres de combustion annulaires à hautes températures à la S.N.E.C.M.A." 1er Symposium sur les Moteurs Aerobies Marseille 19-23 Juin 1972

8. M.A. PARADIS — "Film cooling of gas turbine blades : A study of the effect of large temperature differences on film cooling effectiveness". Journal of Engineering for Power April 1976

9. W.M. ROHSENOW, J.P. HARTNETT — "Handbook of heat transfer" Mc Graw Hill 1973 Section 7

10. V.K. ERMOLIN — "Local and average heat transfer coefficients of an airstream in a tube with a pointed inlet ". International Journal of Heat and Mass Transfer. 23 - 1960 - P. 147

REMERCIEMENTS

Les auteurs tiennent à remercier les membres du département Combustion de la S.N.E.C.M.A. grâce auxquels ce travail a pu être effectué et en particulier Mademoiselle S. COUTOR.

DIFFERENTS TYPES DE CHAMBRES

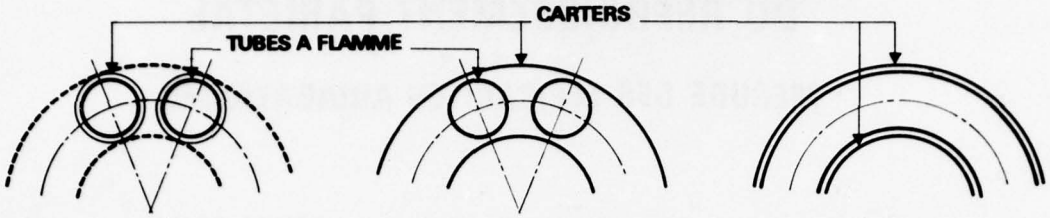

fig. 1

CHAMBRE "ATAR"

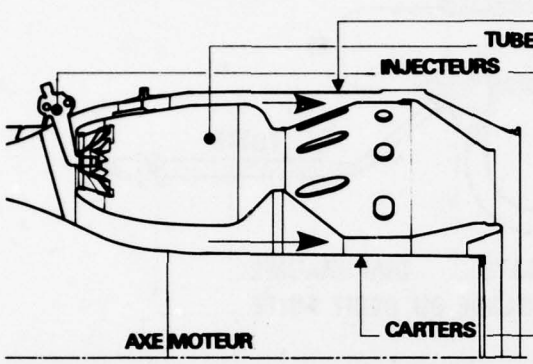

REFROIDISSEMENT PAR CONVECTION FORCEE

fig. 2

CHAMBRE CLASSIQUE A FILM

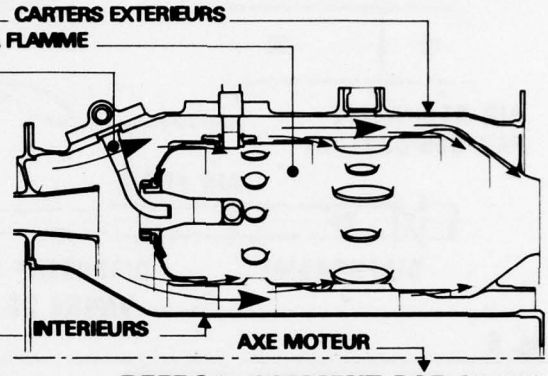

REFROIDISSEMENT PAR FILMS ET CONVECTION FORCEE

fig. 3

PRINCIPE DU FILM A RETOUR EN MATERIAU SANDWICH

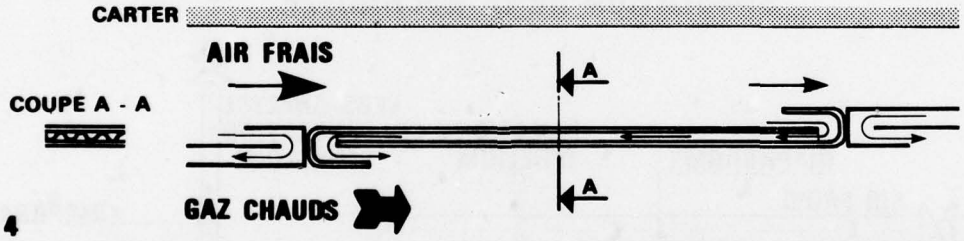

fig. 4

MODELE THERMIQUE ET AERODYNAMIQUE D'UN FILM PARIETAL

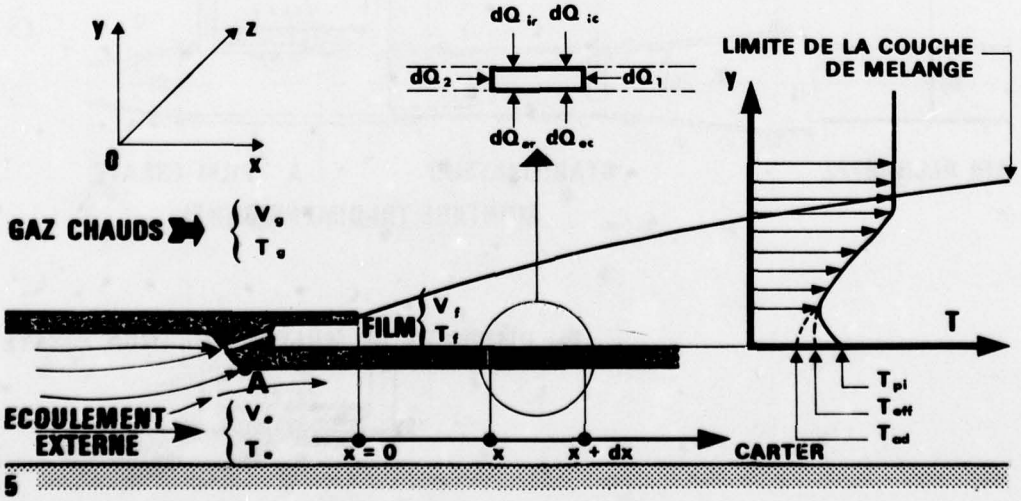

fig. 5

SCHEMA D'UN BANC D'ETUDE DU REFROISSEMENT PARIETAL

MESURE DES EFFICACITES ADIABATIQUES

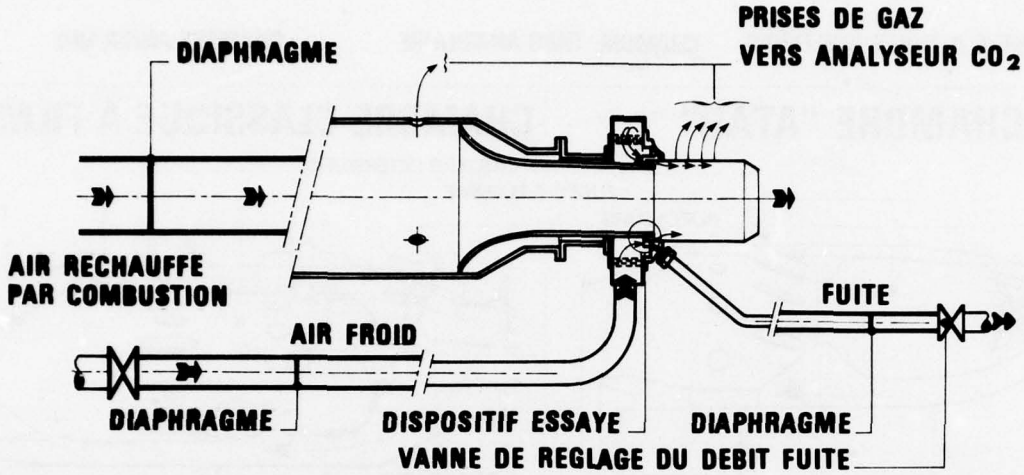

fig. 6

SCHEMA D'UN BANC D'ETUDE DU REFROIDISSEMENT PARIETAL

SIMULATION DE LA RECHAUFFE

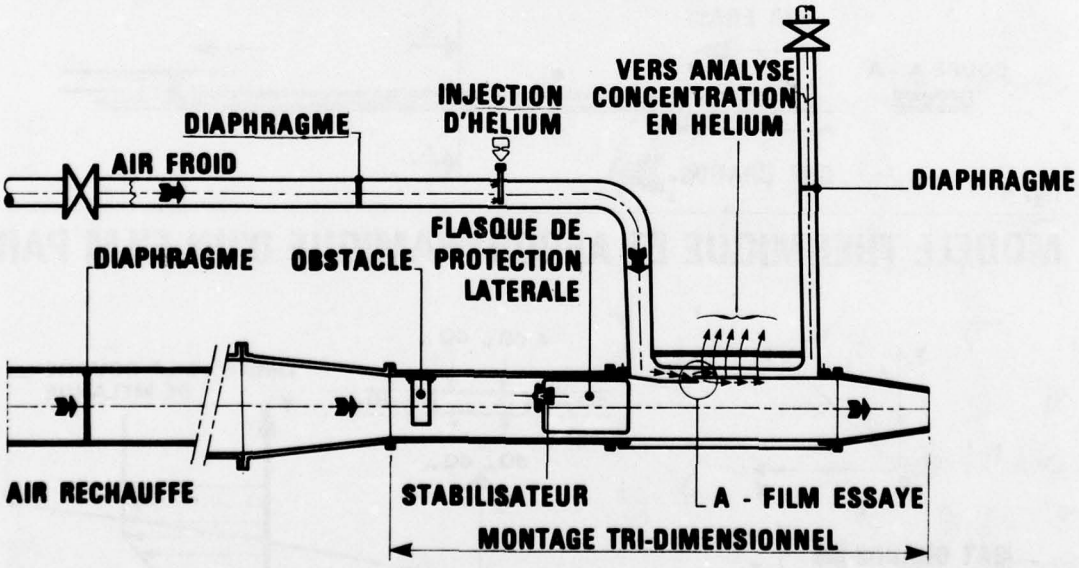

B - DISPOSITIF DE MULTIPERFORATION ESSAYE

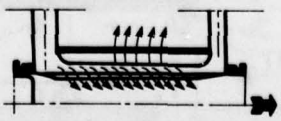

fig. 7

DIFFERENTS TYPES DE FILMS PARIETAUX

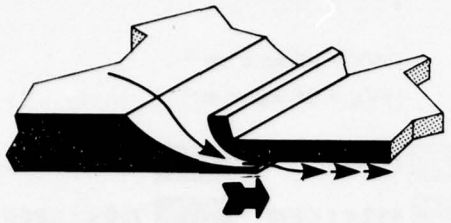

• FENTE PURE 1

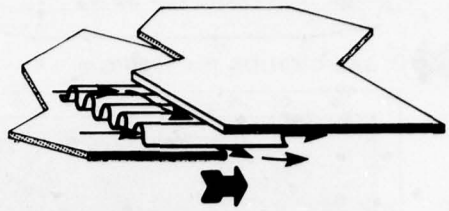

• FILM A LIAISON PAR ONDULE 2

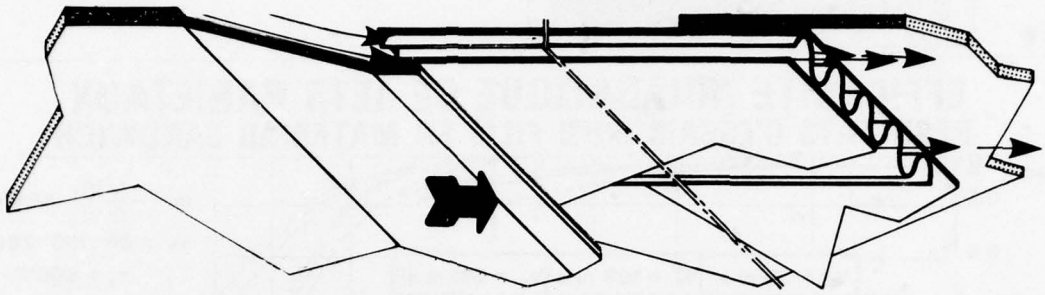

• FILM EN MATERIAU SANDWICH 3

FILMS CHAUDRONNES (EN TOLES ASSEMBLEES)

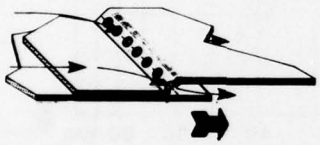

• AVEC EFFET D'IMPACT 4

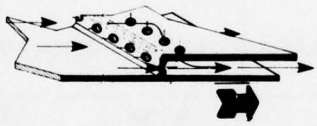

• A DOUBLE ALIMENTATION 5

• AVEC EFFET D'IMPACT
• DEUX RANGEES D'ORIFICES 6

FILMS USINES DANS LA MASSE

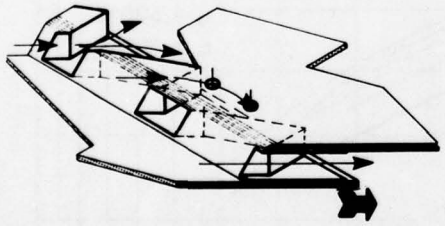

• A ALVEOLES α = 60°
• DOUBLE ALIMENTATION 7

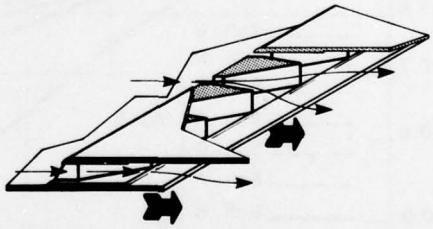

• A ALVEOLES α = 20°
• SIMPLE ALIMENTATION 8

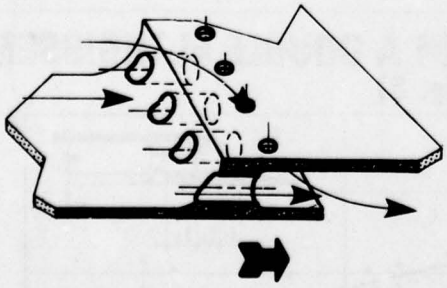

• A SIMPLE ELARGISSEMENT
• EFFET D'IMPACT
• DOUBLE ALIMENTATION 9

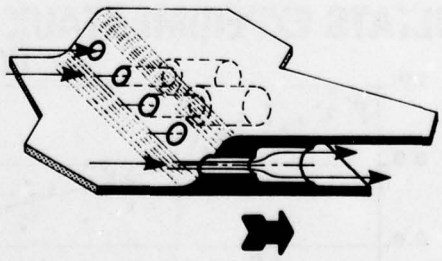

• A DOUBLE ELARGISSEMENT 10

fig. 8

PLAQUE PLEINE REFROIDIE PAR CONVECTION PURE

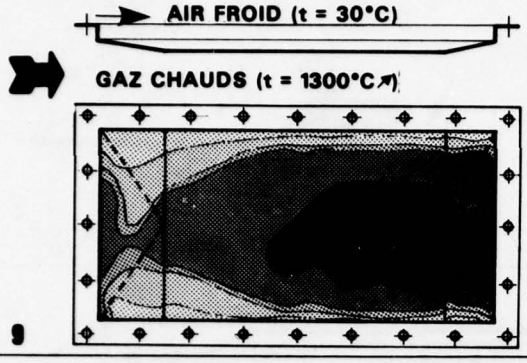

$(\rho V)_e$ = 112 kg.s^{-1}.m^{-2}
$(\rho V)_g$ = 85 kg.s^{-1}.m^{-2}

t < 482	606 < t < 760
482 < t < 570	760 < t < 850
570 < t < 606	850 < t < 908

fig. 9

EFFICACITE ADIABATIQUE DE JETS PARIETAUX
RESULTATS D'ESSAIS D'UN FILM EN MATERIAU SANDWICH

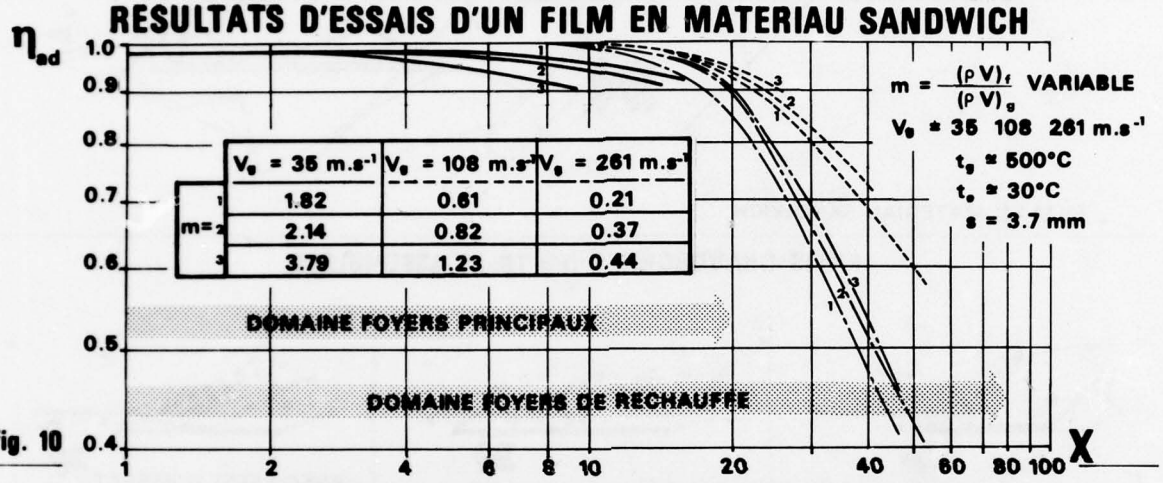

m=	V_g = 35 m.s^{-1}	V_g = 108 m.s^{-1}	V_g = 261 m.s^{-1}
1	1.82	0.61	0.21
2	2.14	0.82	0.37
3	3.79	1.23	0.44

fig. 10

COMPARAISON DE DIVERS TYPES DE FILMS

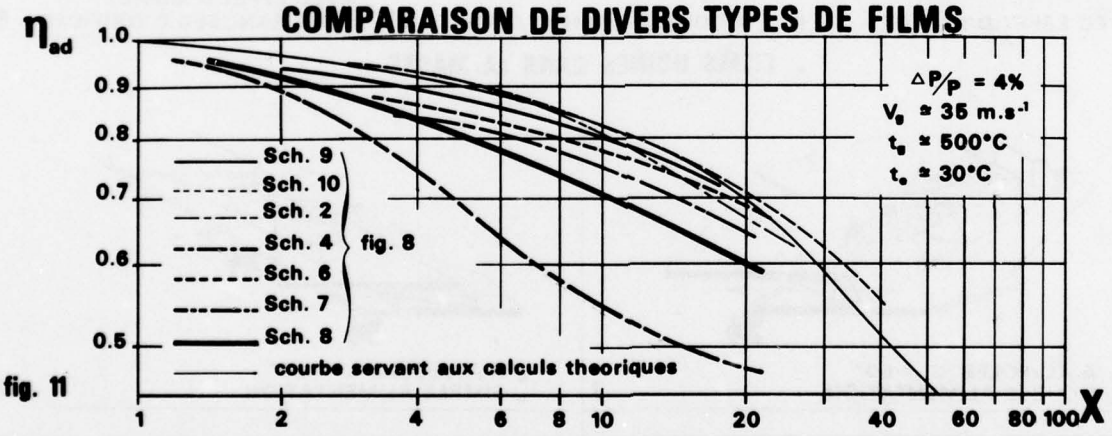

fig. 11

RESULTATS EXPERIMENTAUX DU FILM A DOUBLE ELARGISSEMENT
TYPE 10 (fig. 8)

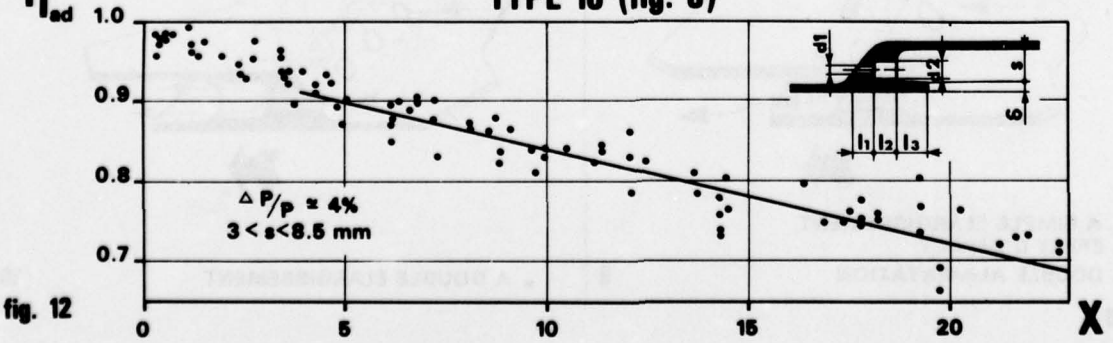

fig. 12

EVOLUTION DES TEMPERATURES SUR PLAQUE MUNIE D'UN FILM TYPE 6 (fig 8)

COURBE PREVUE PAR LE CALCUL

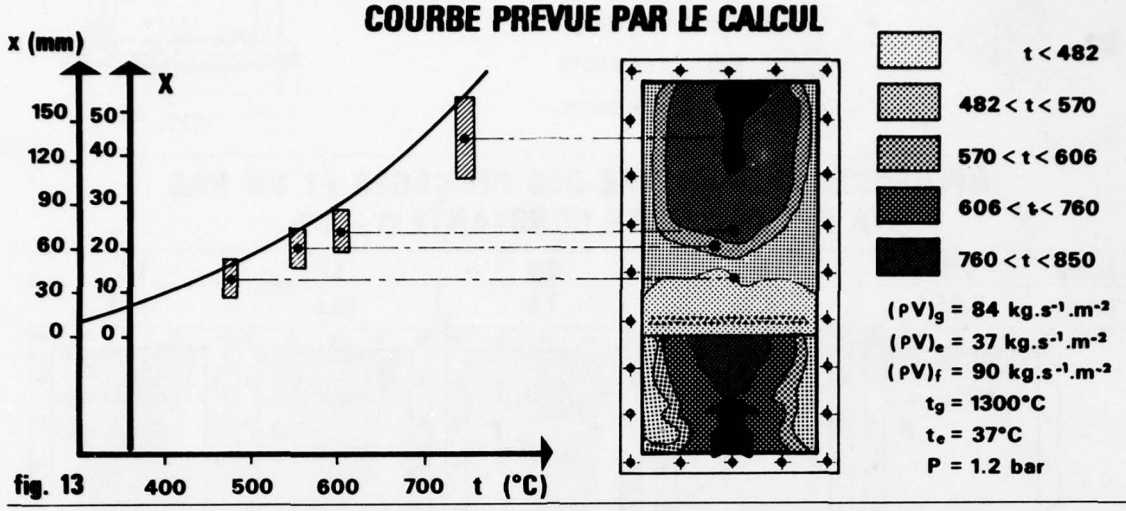

fig. 13

REPARTITION DE TEMPERATURES DANS UN ELEMENT DE PAROI EN MATERIAU SANDWICH

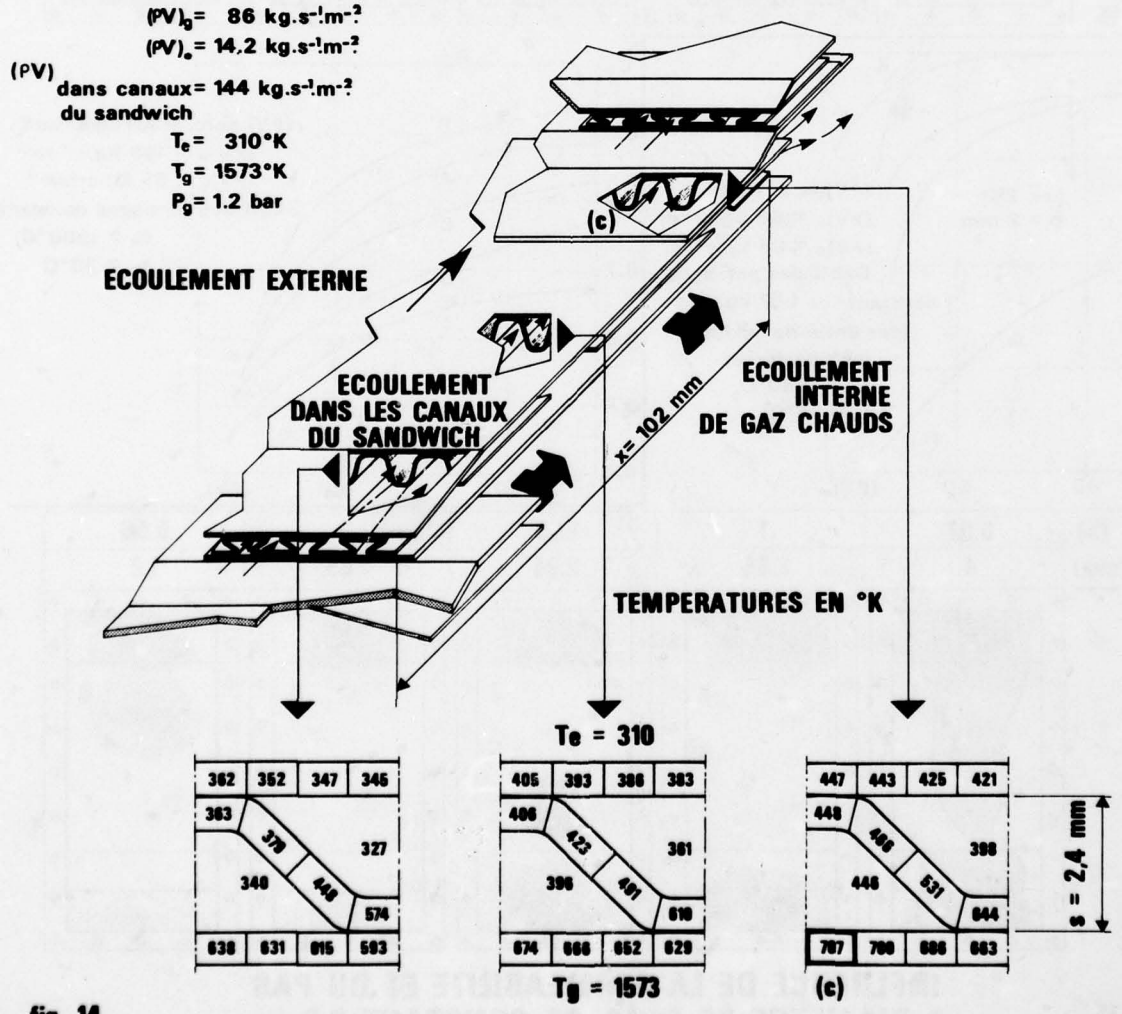

fig. 14

MULTIPERFORATION

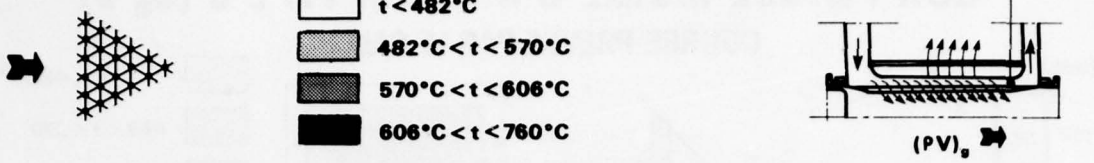

INFLUENCE DU DIAMETRE DES PERÇAGES ET DU PAS A PERMEABILITE CONSTANTE σ = 1 %

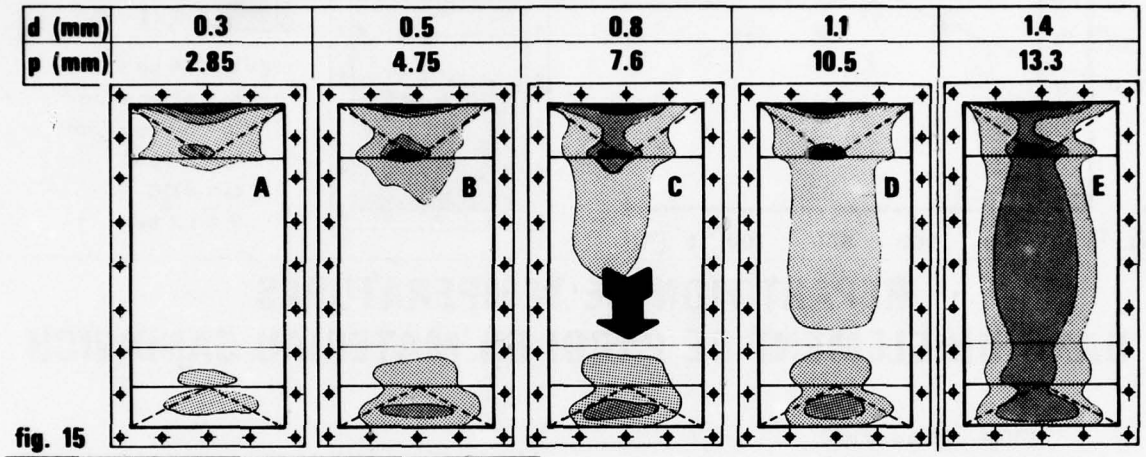

fig. 15

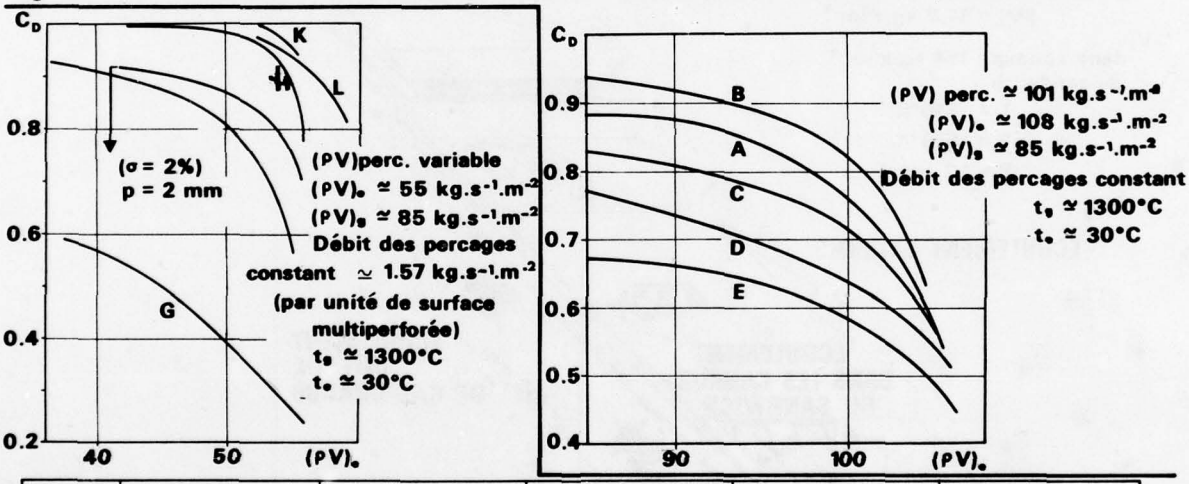

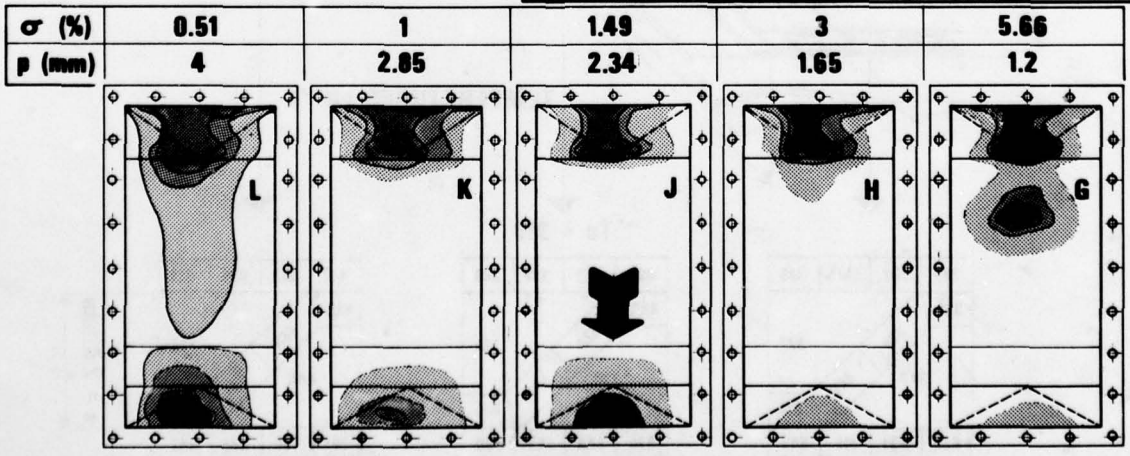

fig. 16

INFLUENCE DE LA PERMEABILITE ET DU PAS A DIAMETRE DE PERÇAGE CONSTANT 0.3 mm

MULTIPERFORATION

COMPARAISON A MEME DEBIT DE REFROIDISSEMENT DE PLAQUES MULTIPERFOREES A PERMEABILITE ET PAS VARIABLES

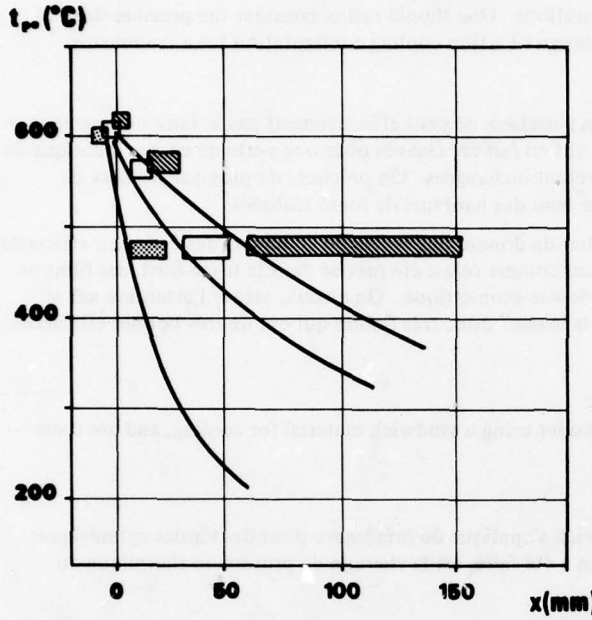

$(\rho V)_o$ = 87±2 kg.s^{-1}.m^{-2}

$(\rho V)_o$ = 105±5 kg.s^{-1}.m^{-2}

P= 1.5 bar

t_o= 1300°C

t_e= 30°C

p (mm)	7.6	4.75	1.65
d (mm)	0.8	0.5	0.3
σ (%)	1	1	3
$(\rho V)_{perc.}$ (kg.s^{-1}.m^{-2})	101 ±3	101 ±3	55 ±1

fig. 17

RESULTATS OBTENUS SUR CHAMBRE COMPLETE PAR PEINTURE THERMOSENSIBLE. RECOUPEMENT AVEC LES EVOLUTIONS PREVUES POUR UN FILM TYPE 10 (fig. 8)

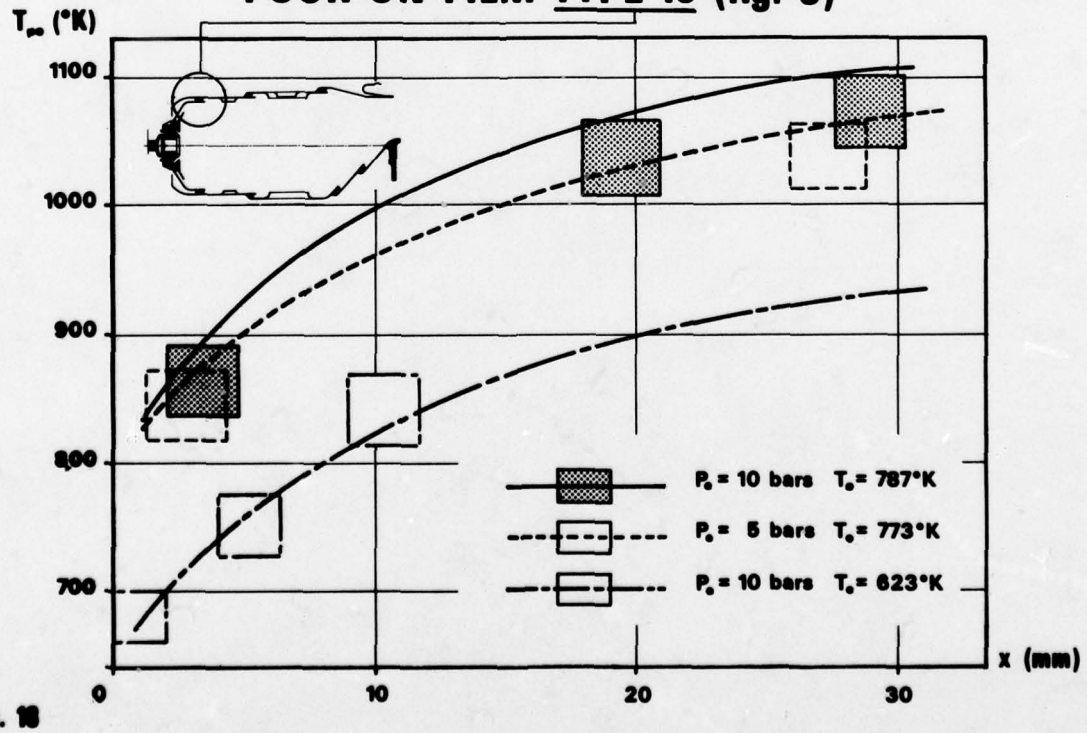

fig. 18

DISCUSSION

D.K.Hennecke, Germany

I would like to caution you about using the customary way of employing the parameter $X = x/ms$ for the comparison of the film cooling effectiveness of configurations such as you have shown. Those configurations are not ideal slots but are characterized by a large number of holes and a lip. Thus the various configurations have different flow areas, discharge coefficients, etc. It has been our experience that a comparison solely on the basis of x/ms may lead to the wrong conclusions as to the most effective configurations. One should rather consider the pressure drop as well since that is a parameter which is prescribed in the design of a film cooling configuration for a combustor.

Author's Reply

La comparison des efficacités de différents types de films pariétaux ne peut effectivement pas se faire uniquement en fonction du seul paramètre X. Tous les films présentés ont en fait été essayés pour une perte de charge identique de l'ordre de 4%, les condition d'écoulement du flux chaud étant inchangées. On précisera de plus que les taux de soufflage sont peu différents (m a varié de 1 à 2) compte tenu des hauteurs de fente réalisées.

La planche de comparison de cet exposé a surtout pour but de donner des ordres de grandeurs des écarts en efficacité que l'on peut rencontrer entre différentes technologies, car comme cela a été précisé dans le texte écrit, ces films ne sont peut-être pas tous parfaitement optimisés du point de vue géométrique. On a voulu attirer l'attention sur le fait qu'il a été possible de réaliser des films "usinés dans la masse" donc très fiables qui ont de très bonnes efficacités.

C.H.Priddin, UK

On which parts of a combustion chamber would you consider using a sandwich material for cooling, and are there any regions where this could not be used?

Author's Reply

Par suite des impératifs de fabrication, le matériau sandwich s'applique de préférence pour des viroles cylindriques ou tronconiques. Une application très intéressante qui en a été faite, est la chemise de protection thermique du canal de réchauffe.

En ce qui concerne la chambre principale, certaines régions à forte courbure ne pouvaient pas être traitées de cette façon. Il reste toujours un problème délicat à la fonction de ce matériau avec une tole classique. Le développement de ce matériau pour cette utilisation est actuellement freiné pour des questions de prix de réalisation.

PRACTICAL SOLUTIONS TO THE COOLING OF COMBUSTORS OPERATING AT HIGH TEMPERATURES

by
J Winter - Research Manager
H Todd - Senior Development Engineer
Lucas Aerospace Limited, Fabrications Division
Lucas Laboratories, Burnley
England

SUMMARY

Two experimental investigations are described, both having demonstrated improved flame tube life potential for small gas turbine engine applications where high temperature operating conditions occurred.

A small annular reverse flow combustion chamber has been evolved which utilises an unconventionally high proportion of the incoming air for wall film cooling purposes, prior to some of these films being redirected to produce the required combustor flow pattern. The concept is shown to minimise the cooling difficulties encountered on conventional small annular chambers particularly when operating at elevated turbine entry temperatures.

The high combustor air inlet temperatures associated with regenerative gas turbine engines pose severe metal temperature problems. The use of conventional wall film cooling techniques promotes metal temperature gradients, and hence stress levels, and reduces the quantity of air directly available to the combustion process. The development of a simplified low cost combustor employing impingement cooling techniques is described.

1. INTRODUCTION

During the design and development of combustion equipment by the Lucas Laboratories at Burnley for aero, industrial and vehicular gas turbine engines, certain applications have created special problems in the achievement of acceptable combustor metal temperatures. These have usually been due either to unfavourable combustor geometry, or demanding operating conditions. Two examples are described in which different methods are employed to reduce such problems.

The first part of the paper describes the performance of a small annular reverse flow combustor which utilises an unconventionally high proportion of the incoming air for wall film cooling purposes prior to the redirection of some of the cooling air for combustion and mixing.

The second part describes the work carried out on a combustor for a vehicular regenerative gas turbine engine where impingement cooling liners were employed to overcome problems of high metal temperatures on a low cost unit.

2. SMALL ANNULAR REVERSE FLOW COMBUSTOR

2.1. Review of Problem

One of the design problem areas associated with small annular reverse flow combustion chambers is the large surface to volume ratio. This means that when using conventional cooling techniques, a significant proportion of the available air has to be used for flame tube wall cooling purposes e.g. in the case of the standard combustor for the Rolls Royce Gem-2 engine approximately 55% of the incoming air is used for wall cooling.

Even using these relatively large quantities of cooling air, the flame tube wall temperatures of the standard Gem-2 although acceptable for current performance requirements are such as to make difficult major uprating of the system using the same design concept. Thus either more efficient wall cooling techniques must be employed or if additional air is used to reduce wall temperatures, more effective use must subsequently be made of this air in the combustion process after it has completed its initial use for cooling purposes. The evolution of a means of achieving this latter objective is described.

2.2. Combustor Design Concept

The flame tube arrangement is shown in Figure 1. The evolutionary flow pattern studies were carried out using Perspex models, employing a water analogy flow visualisation technique. The primary and secondary recirculations were generated by using two annular baffles to deflect the air flow from opposed cooling devices, the air flowing over each baffle face serving additionally as baffle coolant. To allow controlled efflux from the recirculations the baffles were castellated (2 rectangular castellations per vaporiser) with flow deflectors fitted below the castellations on one side of each baffle.

The directions of rotation of the recirculations were arranged to be compatible with the desired primary/secondary flow distribution. Since the secondary zone of the flame tube admitted the major part of the combustion air flow, the secondary recirculation was arranged to rotate in the same direction as the adjacent air annuli flows so that total pressure air feeds could be used. Consequently the primary recirculation, which rotated in the opposite direction, was generated by reverse splash cooling air. A sketch of the flow pattern obtained on a flow visualisation rig is shown in Figure 1.

The chamber was designed for an overall chamber pressure loss of 2.5% of the inlet total pressure.

Fuel injection was by means of 17 equispaced vaporiser tubes of the type shown in Figure 1 and similar to those used in the standard Gem-2 combustor.

The single torch igniter, situated in the outer primary zone wall, consisted of a high energy spark plug operating from a 12 Joule supply and a 0.2 flow number fan spray fuel injector. The torch was only in operation during the ignition phase of each test.

2.3. Combustion Test Equipment

2.3.1. Test rig

A photograph of the test rig arrangement is given in Figure 2. The test facility enabled preheated unvitiated air to be supplied at pressures up to a maximum of approximately 830 kPa.

2.3.2. Instrumentation

Exhaust temperature distributions were obtained using an instrument fitted with eight platinum v platinum - 13% rhodium thermocouples. In order to minimise the radiation loss from the thermocouples to the duct walls, double walled platinum radiation shields surrounded each thermocouple. The instrument was rotated in increments of $4\frac{1}{2}^{o}$ and the eight exhaust thermocouples were arranged in two groups of four such that a complete traverse grid of 80 x 4 points could be covered by 180^{o} rotation.

The traverse instrument also housed exhaust total pressure probes and a hot-water (423K) cooled exhaust gas sampler which required 360^{o} rotation of the instrument to obtain full traverses. A photograph of the instrument is shown in Figure 3.

The inlet wall static pressure and inlet temperature were measured using fixed instrumentation, the inlet total pressure being deduced from a calculated value of inlet kinetic pressure and the measured static pressure.

2.4. Test Conditions

The combustion calibration was carried out at two conditions relevant to the Rolls Royce Gem-2 engine plus one uprated turbine entry condition relevant to a future small engine requirement. Due to rig facility limitations the true engine pressures could not be obtained at the higher power conditions and these tests were undertaken at scaled pressure conditions, while maintaining the correct inlet temperature and reference casing Mach No. (i.e. by scaling the air mass flow).

The test rig operating conditions are given in Table I.

TABLE I

RIG TEST CONDITIONS
ENGINE CONDITIONS SHOWN IN PARENTHESIS

	Cruise	Pressure Simulated Intermediate Contingency Rating	Pressure Simulated Uprated Condition
Air Inlet Pressure kPa	827	827 (1200)	827 (1320)
Air Inlet Temperature K	580	657	674
Air Mass Flow kg/s	2.3	2.0 (2.9)	2.0 (3.2)
Air/Fuel Ratio	66.4	51.8	41.0
Mean Exhaust Temperature K (Assuming 100% combustion efficiency).	1130	1340	1500

All tests reported used kerosine (Avtur) fuel.

2.5. Combustor Performance

2.5.1. Flame tube metal temperatures

Flame tube metal temperatures were assessed using temperature indicating paint at the above conditions and typical results for the experimental combustor, illustrated by photographs, are shown in Figure 4, the code for the temperature levels corresponding to the colour changes in the paint being given on the Figure.

At the Cruise conditions, (not illustrated) approximately 75% of the flame tube surface did not exceed 788K, and maximum temperatures, occurring on the outer primary zone wall and on the outer discharge

bend, were below 1087K.

At the simulated Intermediate Contingency Rating, Figure 4a, approximately 50% of the flame tube surface did not exceed a temperature of 788K whilst peak temperatures on the outer primary wall and on the outer discharge bend, were limited to 1133K or below.

Generally speaking the levels of metal temperature for the experimental chamber showed a significant improvement on those of the Gem-2 combustor and also the temperature gradients were less severe. For example data from a standard Gem-2 combustor operating at the simulated Intermediate Contingency Rating indicate that approximately 75% of the flame tube area is above 788K with local hotter patches mainly on the inner primary zone wall.

Thus the potential for uprating the experimental chamber to the higher Turbine Entry Temperature conditions was demonstrated.

For the test at the uprated conditions, Figure 4b, approximately 35% of the flame tube surface did not exceed 788K whilst temperature patches in excess of 1133K appeared only on the outer discharge bend and in small localised areas on the outer primary wall. Visual and dimensional flame tube examinations showed that, following tests of approximately one hour duration at each operating condition, the flame tube was mechanically sound and free from distortion; furthermore the mechanical baffles and the vaporisers were shown to be satisfactorily cooled.

2.5.2. Exhaust temperature distribution

The exhaust temperature distribution can be defined in terms of the O.T.D.F. (Overall Temperature Distribution Factor) and the R.T.D.F. (Radial Temperature Distribution Factor) where:

$$\text{O.T.D.F.\%} = \frac{\text{Peak Exhaust Temperature} - \text{Mean Exhaust Temperature}}{\text{Mean Temperature Rise Through Combustor}} \times 100$$

$$\text{R.T.D.F.\%} = \frac{\text{Peak Mean Radial Temperature} - \text{Mean Exhaust Temperature}}{\text{Mean Temperature Rise Through Combustor}} \times 100$$

Figure 5 illustrates the exhaust temperature distribution at the simulated uprated condition, a value of 25.6% being obtained for the O.T.D.F. The radial temperature distribution showed a relatively flat profile, cooler at the turbine tip, the value of R.T.D.F. being 2.6%. Values of 23.1% and 26.4% were obtained for the O.T.D.F. at the Cruise and simulated Intermediate Contingency conditions respectively, whilst the corresponding values for the R.T.D.F. were 2.0% and 2.7%.

2.5.3. Combustion performance

Exhaust gas analysis at the simulated Intermediate Contingency Rating and at the uprated conditions gave combustion efficiencies of 99.8% in both cases.

The internal appearance of the flame tube after test at each of the conditions was mainly clean and bright. Minor carbon formations included thin soot films on the vaporiser tubes following each test and small patches of soot between some vaporiser outlets on the inner primary wall cooling skirt.

A smoke value of 4.4 $\mu g/l$ (equivalent to an E.P.A. smoke no. of approximately 30) was obtained using a gravimetric method of analysis from a sample collected in the exhaust duct some 1200 mm downstream of the unit during test at the uprated conditions.

Exhaust NO_x concentrations, measured by a chemiluminescence technique, were of the order of 120 p.p.m. (vol.).

2.6. Comments on Achieved Performance

A flame tube design exhibiting generally lower metal temperatures than those associated with the Gem-2 combustor has been evolved without apparently compromising the performance in other aspects. The potential for operating this design of combustor at higher turbine entry temperatures has been demonstrated.

3. REGENERATIVE ENGINE COMBUSTOR

3.1. Review of Problem

Gas turbine engines with exhaust heat recovery can impose very high air inlet temperatures on the combustor, some 200K higher than the maximum inlet temperatures of current high compression ratio aero engines.

The problems associated with such high air temperatures were experienced during the development of combustion equipment for the British Leyland 270 kW (350 h.p.) regenerative gas turbine engine. At the specified combustor air inlet temperatures which varied between 990K and 1080K dependent on the engine load, metal temperatures greater than 1300K could be anticipated presenting problems of material thinning due to oxidation and mechanical damage resulting from the inability of the reduced strength material to withstand the stress levels produced by temperature gradients. It was appreciated that the use of wall film cooling techniques would increase the cost, promote metal temperature gradients and high stress levels and reduce the quantity of air directly available to the combustion process. The potential of impingement cooling to overcome these limitations made this technique attractive and a simplified low cost combustor was developed and successfully operated on engine trials.

3.2. Initial Design Concepts

3.2.1. Engine installation

Considerations of engine layout, servicing and assessibility resulted in the adoption of a reverse flow pipe chamber combustor mounted on the engine vertical centre-line with air transference from the twin heat exchangers via kidney shaped ducts positioned on opposite sides of the combustor as shown in Figure 6. The combustor exhausted into a volute connected to the turbine nozzle assembly.

3.2.2. Temporary film cooled combustor

To cater for the early engine running programme during the rig development of the low cost combustor, a number of more expensive film cooled units were employed based on a well proven Lucas design used in a variety of non-regenerative industrial gas turbine applications.

Although the relatively weak operating air/fuel ratio permitted the use of a greater percentage of the air flow for film cooling than in normal non-regenerative engine applications, this design proved to have a limited life requiring repairs to the flare, primary and dilution walls on average within 100 hours of engine operation. Whilst some improvements could have been made, the major effort was devoted to the design and development of a low cost combustor.

3.2.3. Initial low cost combustor

From the outset a simple cylindrical combustor flame tube was adopted with a conical primary baffle, both manufactured from NIMONIC ALLOY 75*. This arrangement shown in Figure 6 minimised welding in possible regions of high temperature gradients and permitted the use of thicker than normal material 3.25 mm (0.128 ins) to provide a robust construction and an allowance for material thinning due to oxidation.

A relatively high air flow was introduced over the edge of the conical baffle (approximately 25%) to cool the flame tube wall. Primary air recirculation was promoted by the introduction of slots approximately halfway down the flame tube wall, the air through which provided a pneumatic baffle to deflect the major proportion of the cooling air towards the centre of the chamber for primary combustion. Final mixing was provided by four large dilution holes positioned downstream of the slots. Following early tests, a radially inward flow swirler was introduced at the baffle to maintain freedom from carbon and 4 trimming holes were positioned between the dilution holes to improve the exhaust temperature distribution. The air admission ports were sized to limit the overall pressure loss to 3% of the inlet air pressure.

A further consideration in the adoption of a simple cylinder design was the desire to be able to maintain features which could be readily produced in ceramic, since in the long term it was felt that this would prove to be the best combustor material for long life and low cost.

Atomisation of the diesel oil fuel was provided by a pressure jet sprayer with air assistance. Ignition was by high tension spark.

Although it was appreciated that this simple approach would probably require development and additional features to meet the specification, initial testing was undertaken to assess its potential and explore possible low cost improvements.

3.3. Combustion Test Equipment

3.3.1. Test rig

The test unit simulated the engine geometry local to the combustion chamber which exhausted via water cooled pipework to a silencer stack.

Air at the correct pressure was raised to the required inlet temperature by an in line preheater. Oxygen replenishment of the inlet air was carried out to minimise the effect of vitiation on combustion performance. Since this development programme was completed, an indirect heat exchanger test facility has been installed with the capability to provide unvitiated air at the high inlet temperatures of the regenerative type of engine.

3.3.2. Instrumentation

Inlet temperature was measured by Chromel/Alumel thermocouples, and exhaust temperatures, total pressures and gas samples were obtained at the annular plane of the turbine nozzle guide vanes by means of a rotatable water cooled instrument similar to that described previously for the annular combustor tests.

Metal temperature measurements were made by Chromel/Alumel thermocouples welded to the flame tube, supported by data from thermal sensitive paints. It was found that the latter were useful in indicating the regions of high temperature to enable the positioning of the thermocouples but due to the high level of vitiation combined with the high inlet air temperature the different colours and shades were indistinct and incapable of precise interpretation.

3.4. Test Condition

During the development programme testing was undertaken on the rig at the engine full load, 50% speed and idling conditions given in Table II.

* Registered trade mark of Henry Wiggin and Company Limited

TABLE II

ENGINE AND RIG OPERATING CONDITIONS

		Full Load	50% Speed	Idling
Air Inlet Pressure	kPa	390	151	148
Air Inlet Temp.	K	993	1080	720
Air Mass Flow	kg/s	1.63	0.47	0.73
Air/Fuel Ratio		100/1	244/1	428/1
Mean Exhaust Temp. (Assuming 100% comb. effy.)	K	1341	1222	809

Although the air inlet temperature at the full load condition was lower than at the tabulated part load condition, the higher combustion loading and richer air/fuel ratio of the full load condition produced the highest flame tube temperatures and the most severe temperature gradients.

3.5. Performance of Low Cost Combustor

3.5.1. Initial arrangement

The initial design of combustor provided a satisfactory combustion performance at full load but exhibited high metal temperatures particularly towards the edge of the primary baffle and in the region of the air slots where temperatures in excess of 1420K were indicated by thermal sensitive paint and local temperatures approaching 1500K were measured by thermocouple. These high temperature levels resulted in some distortion and local burning of the combustor flame tube and primary baffle within a few hours of operation at full load conditions.

3.5.2. Combustor with impingement cooling

Faced with these high metal temperatures and rapid mechanical deterioration it was apparent that unless some simple means of cooling could be employed, it would not be feasible to proceed with this design of low cost combustor.

Cooling of flame tube

Following examination and analysis of the results the evidence indicated that a satisfactory solution would be achieved by the addition of a concentric cylinder containing a holing arrangement to provide impingement cooling.

Although the engine manufacturers agreed that an additional pressure loss of 1% of the combustor inlet pressure could be tolerated across the concentric cylinder to provide the necessary impingement velocity, it was expected that there would be scope during subsequent development to reduce this back to the original specification. In order to achieve the maximum cooling effect all the combustor air was routed through the wall of the impingement cooling cylinder.

The need to provide quickly an acceptable design imposed limitations on the number of arrangements which could be tested and on the range of measurements taken, which after initial examination were restricted to the full load operating conditions. (Figure 7).

An initial test with a local impingement cooling cylinder with 5.1 mm (0.2 ins) dia holes positioned over the rear section of the flame tube demonstrated a significant reduction in metal temperature with a maximum measured value of 1298K.

Further tests were carried out using commercially available stainless steel sheeting perforated uniformally with 4.7 mm (0.187 ins) dia holes and 9.5 mm triangular pitch and with an impingement cooling cylinder with relatively large holes (25.4 mm - 1 in dia) positioned to direct the cooling air over local areas of maximum temperature. The maximum measured temperatures and the corresponding pressure loss across the impingement cooling cylinder for these arrangements, shown plotted on Figure 7 confirmed the influence of pressure drop as a major factor and indicated that for a given pressure drop there is scope for improvement by ensuring good impingement in the areas requiring maximum cooling.

The impingement cooling cylinder with large diameter holes shown in Figure 8 and the initial arrangement with local cooling gave the best results but the former was preferred as it was considered to offer a cheaper more reliable arrangement and to be more suitable for future development.

A much improved flame tube metal temperature distribution was obtained with the introduction of impingement cooling as shown by the Figure 9 and during subsequent engine operation the modified combustor showed no significant signs of distortion or oxidation. Calculations showed that the differences in metal temperature between the initial and impingement cooled flame tubes had produced a ten fold increase in the external convective heat transfer coefficient.

Cooling of primary baffle

The introduction of an impingement cooling skin upstream of the primary baffle as shown on Figure 10(a) did not give immediate relief from the high temperature level of approximately 1500K occurring towards the baffle outer diameter. A number of different holing arrangements were investigated on the combustion and flow visualisation rigs with all the primary baffle air passing initially through the impingement cooling skin. The baffle tip diameter was reduced to maintain a constant effective area and allow most of the total pressure loss to occur across the cooling skin impingement. Flow studies showed that most of the air passing through the cooling skin did not impinge on the baffle but turned sharply through 90° to form a flow stream parallel to the baffle face.

Baffle temperatures were eventually reduced to an acceptable level of less than 1300K by the introduction of holes in the baffle face out of line with the impingement cooling holes as shown on Figure 10(b). The presence of the baffle holes ensured that the cooling air discharged from the cooling skin and impinged at right angles onto the rear of the baffle before passing through it. The resulting arrangement therefore could be considered as a combination of impingement and effusion cooling. It was not possible to isolate the relative cooling effect of each factor but it is worth noting that during one test which was carried out with a series of small holes (2.5 mm - 0.1 ins) drilled in the baffle and no impingement cooling skin, there was no apparent reduction in the temperature of the baffle. On the final arrangement, 3.5% of the total air flow was used for baffle cooling which contrasts with the unsuccessful initial arrangements where attempts to employ the total baffle airflow of more than 20% failed to reduce significantly the temperature level.

3.5.3. General performance

The final impingement cooled combustor shown on Figure 11 gave a satisfactory general performance at full load conditions with an overall total pressure loss of 3.6% and an O.T.D.F. of 12.8%. Measurements undertaken on the engine showed the exhaust pollutant levels to be within the U.S.A. requirements for heavy duty vehicle engines as indicated by Table III.

TABLE III

ENGINE EXHAUST EMISSION LEVELS

	Brake specific emissions for 13 mode cycle (gm/B.H.P. - hour)			
	CO	UHC	NO_x	NO_x + UHC
Engine Test with Impingement Cooled Combustor *	1.4	0.1	2.8	2.9
1977 Californian Requirements	25	-	-	5
Proposed Federal Requirements for 1979	25	1.5	-	10

* Based on five operating conditions from idle to full load.

3.6. Comments on Derived Design

A significant reduction in both the level of temperature and the thermal gradients was achieved by the use of impingement cooling. Simultaneously the manufacturing price of the combustor was reduced to approximately one third of the price of the conventional film cooled unit. The effectiveness of the cooling on this combustor design was probably enhanced by the particular holing arrangement on the flame tube wall which, in general, enabled short flow paths between the impingement cooling liner and flame tube thus reducing the possibility of annulus cross flows deflecting the impinging jets. It is estimated that more than 90% of the total air flow would have an unopposed flow path from the cooling cylinder to the flame tube. The use of relatively large holes provided a high local momentum of the impinging air to offset any opposing annulus disturbances, and the unusually thick material (3.25 mm) gave sufficient conduction between impingement holes to avoid excessive temperature gradients.

It is apparent, however, that even with careful cooling provisions, the limit of operation for metallic combustors at the described level of operating temperatures was being approached. In general, maximum wall temperatures can be expected to be not less than 300K higher than the inlet air temperature and although improved high temperature alloys will help to extend the operating range, the stage has now been reached where ceramics will need to be employed to permit any further increases in engine cycle temperatures.

ACKNOWLEDGEMENTS

Thanks are due to the Directors of Lucas Industries Limited for permission to publish the paper, and also to the Ministry of Defence (U.K.) and British Leyland on whose behalf the described test programmes were carried out. Thanks are also due to Rolls Royce Limited for permission to refer to the Gem-2 engine. The authors wish also to thank colleagues for their support during the test programmes and in the preparation of the paper.

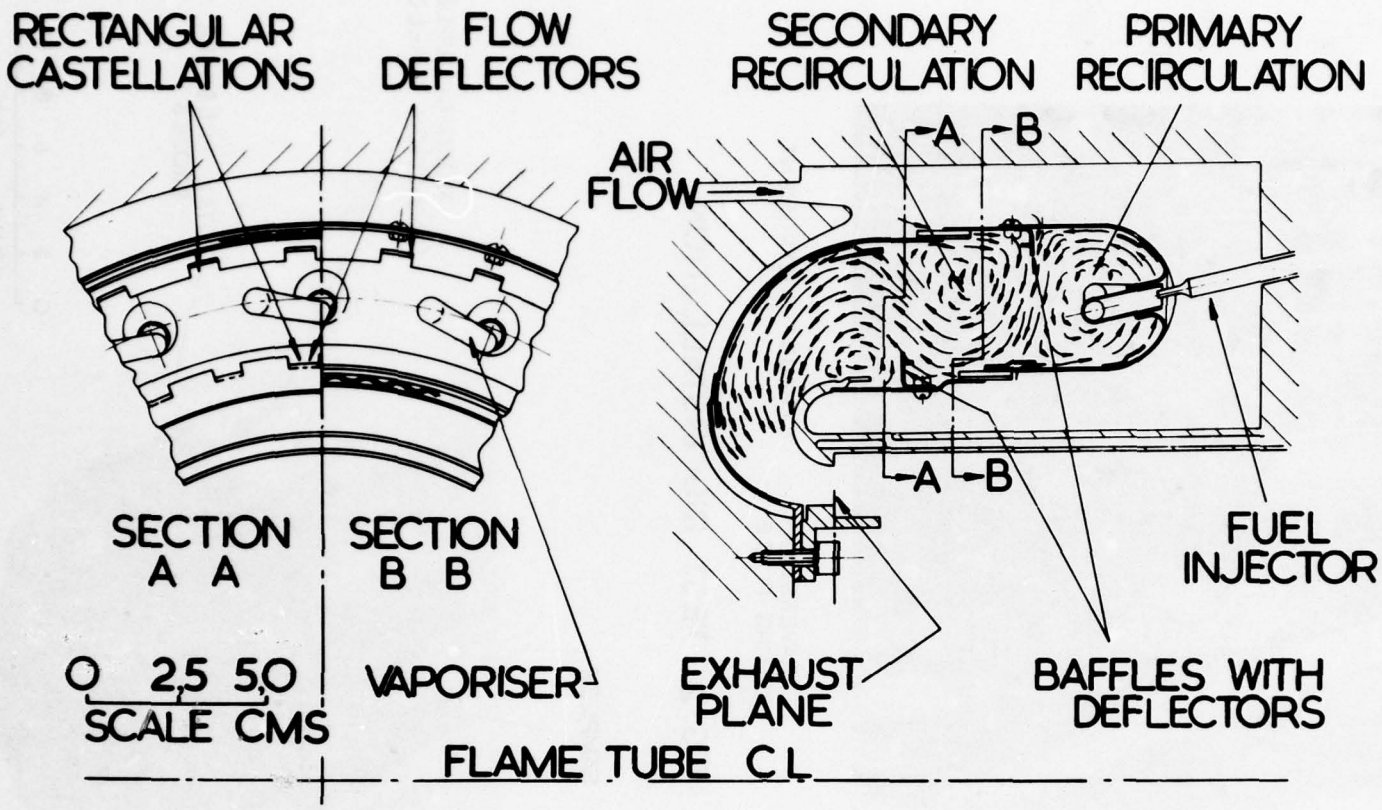

FIG. 1. SMALL ANNULAR TEST UNIT.

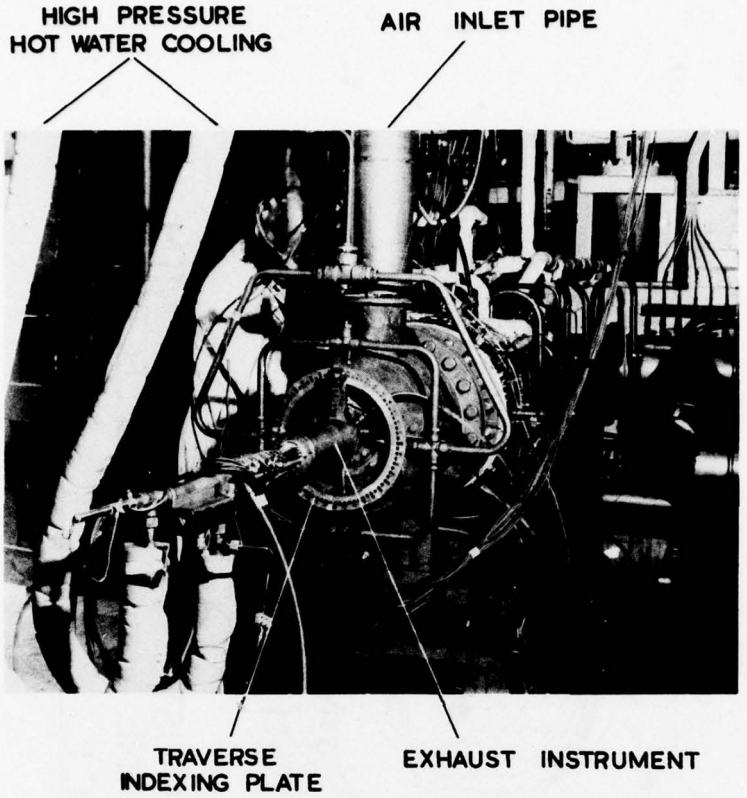

FIG. 2. TEST RIG INSTALLATION.

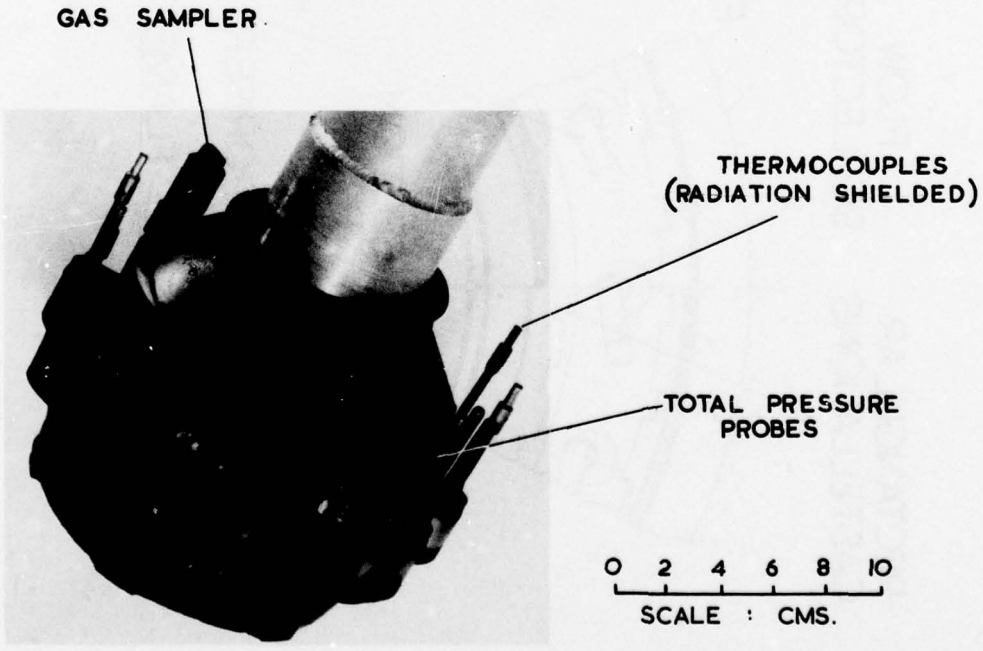

FIG. 3. EXHAUST INSTRUMENT.

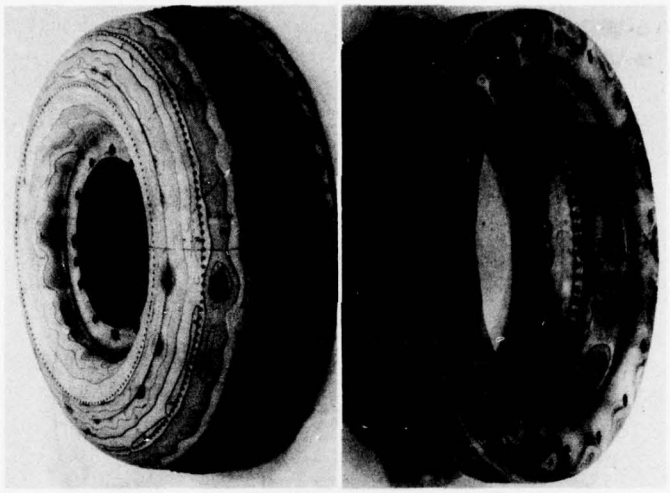

a. INTERMEDIATE CONTINGENCY CONDITIONS

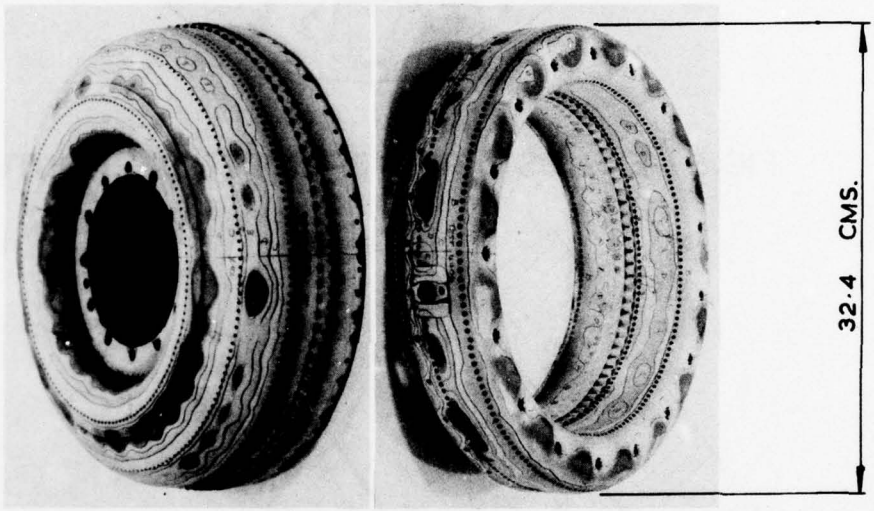

b. UPRATED CONDITIONS

CODE LETTER	TEMP K
B	BELOW 788
C	788 – 815
D	815 – 968
E	968 – 1087
F	1087 – 1133
G	ABOVE 1133

FIG. 4. FLAME TUBE METAL TEMPERATURES.

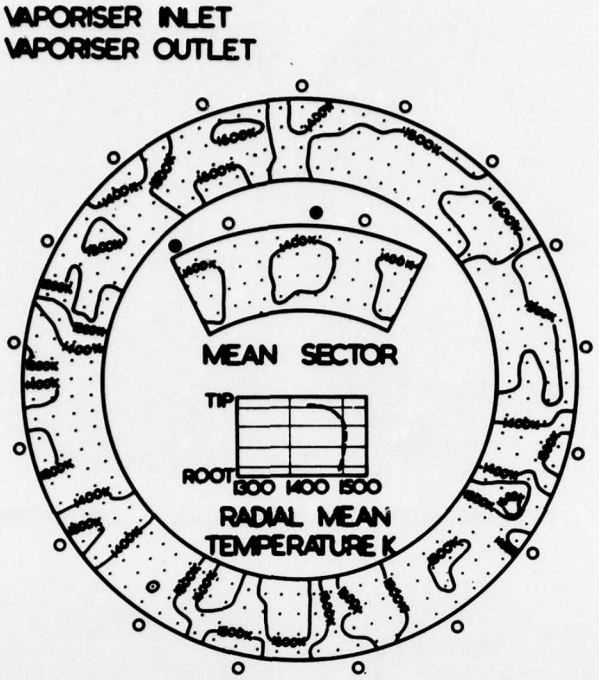

FIG.5. EXHAUST TEMPERATURE DISTRIBUTION.

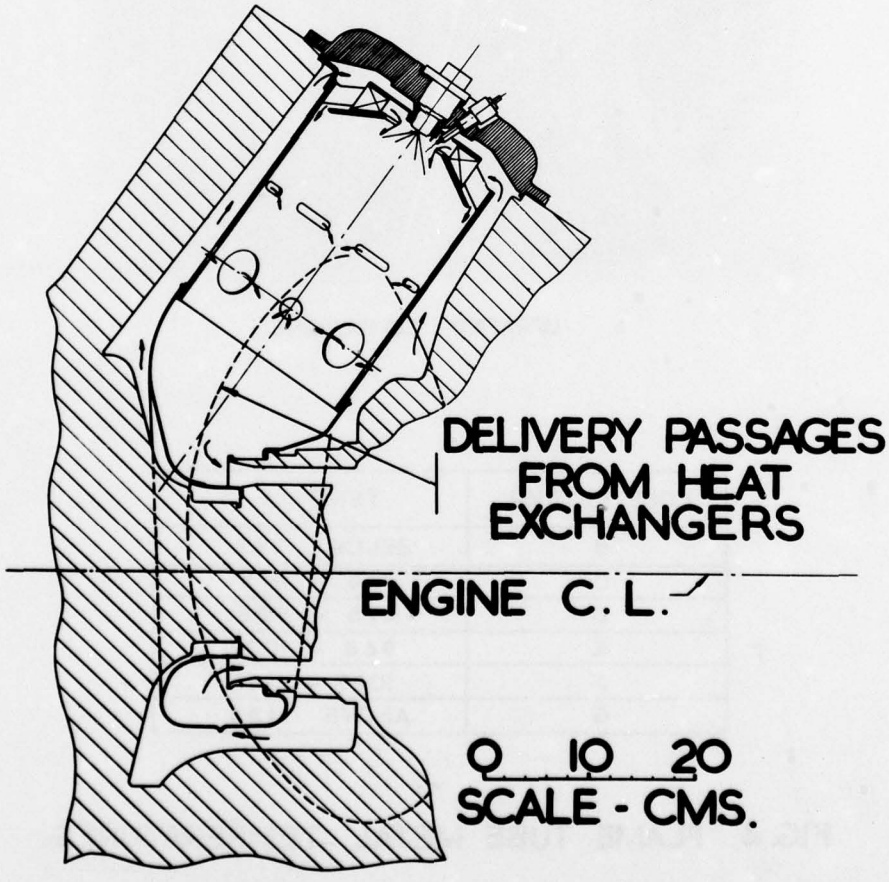

FIG. 6. INSTALLATION OF VEHICLE ENGINE COMBUSTOR.

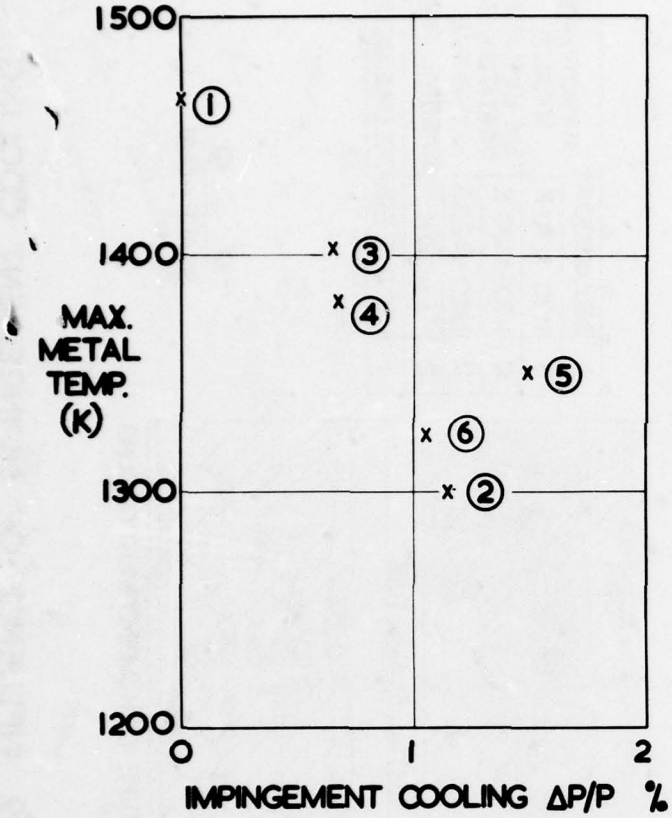

①	NO IMPINGEMENT COOLING 47mm I/D
②	BLANKS 5.1mm I/D HOLES DISC 8mm 47mm I/D
③	4.7mm I/D HOLES 8mm 53mm I/D
④	4.7mm I/D HOLES 8mm 53mm I/D
⑤	AS 4 WITH BLANKS OPPOSITE FLAME TUBE HOLES
⑥	25.4mm I/D HOLES 8mm 47mm I/D

FIG.7. IMPINGEMENT COOLING ARRANGEMENTS.

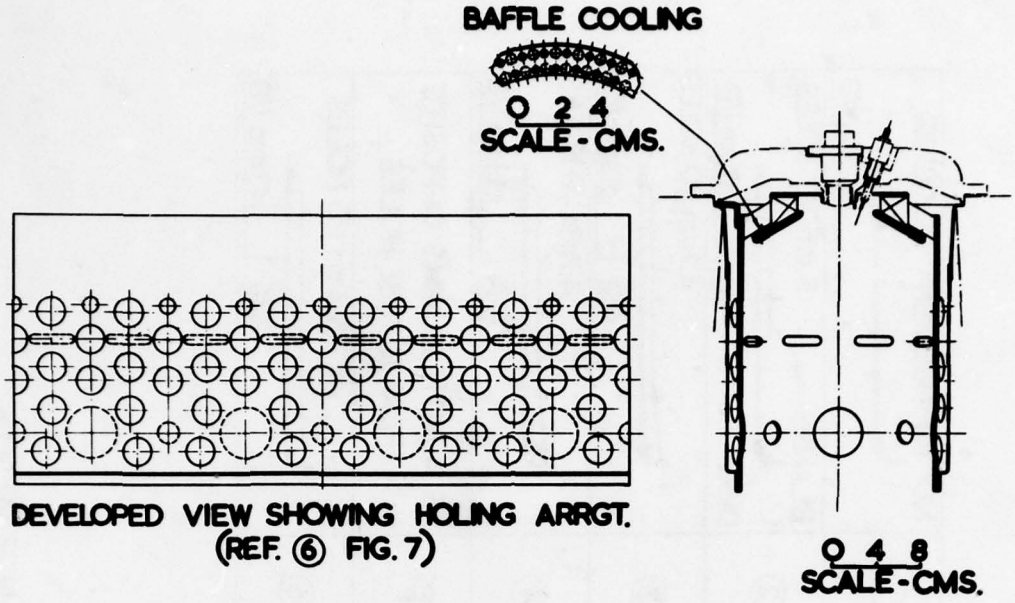

FIG. 8. FINAL COOLING ARRANGEMENT.

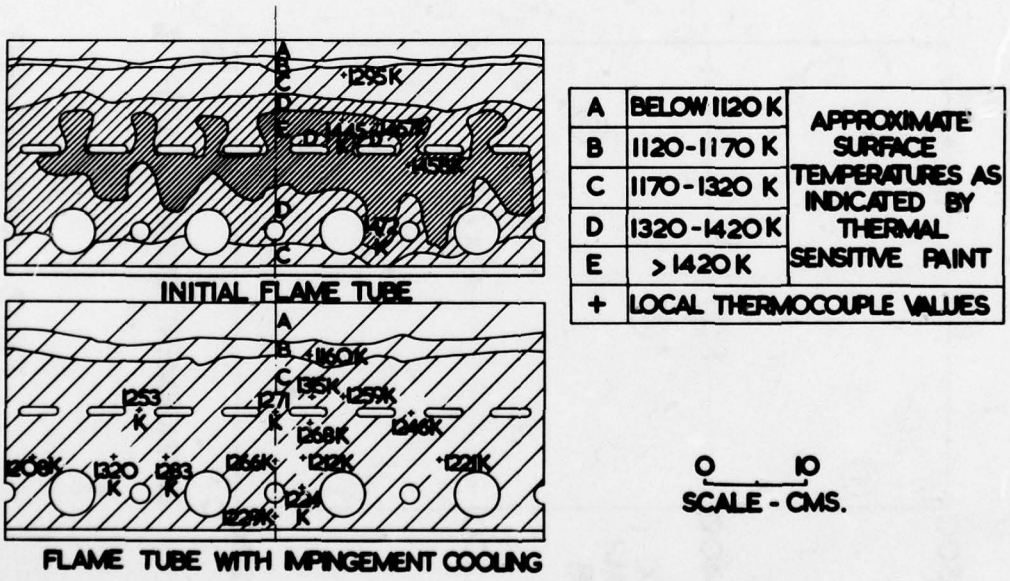

FIG. 9. INFLUENCE OF IMPINGEMENT COOLING.

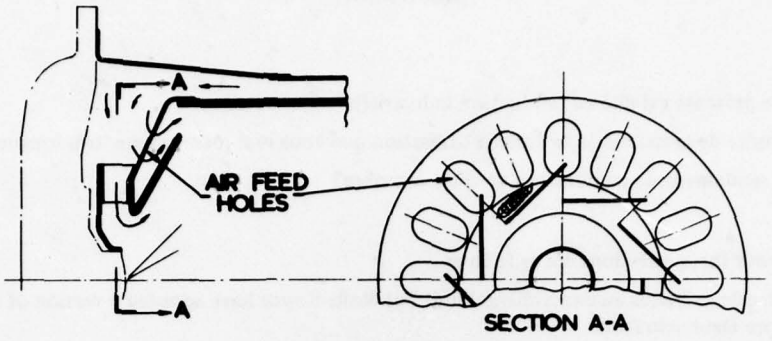

a) BAFFLE AIR DIRECTED TOWARDS UPSTREAM FACE OF BAFFLE

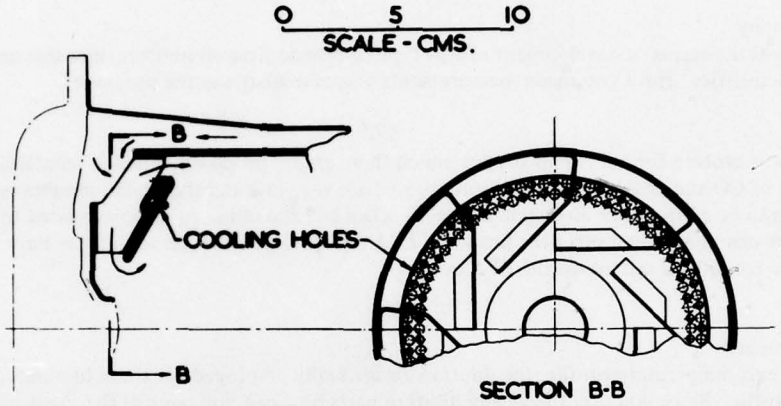

b) IMPINGEMENT / EFFUSION COOLING OF BAFFLE

FIG. 10. PRIMARY BAFFLE COOLING ARRANGEMENTS.

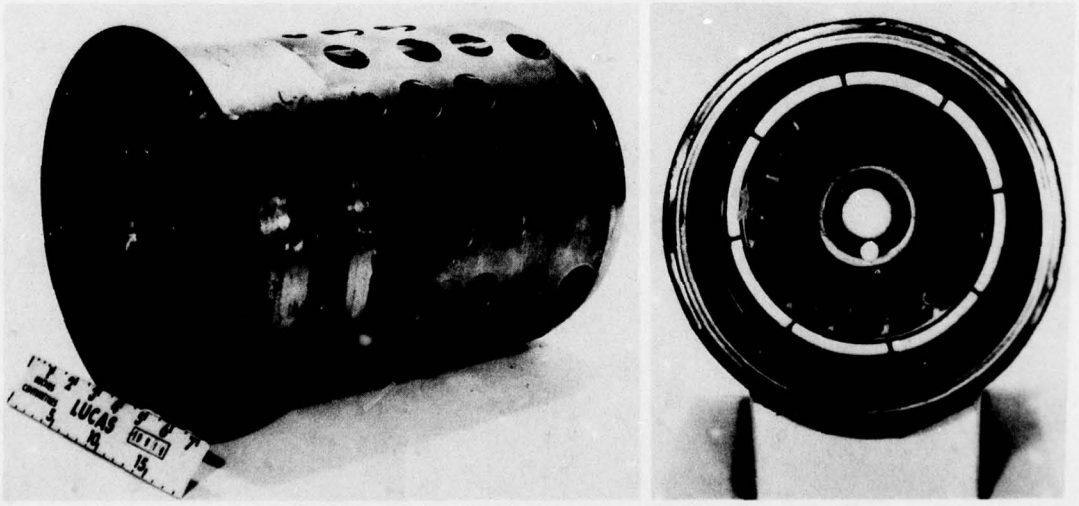

FIG. 11. DEVELOPED COMBUSTOR.

DISCUSSION

A.Mihail, France

(1) La chambre présente est-elle en production industrielle?

(2) Quel est l'ordre de grandeur de la durée d'utilisation que vous indiquez comme 'très longue durée'?

(3) Quel est le rendement de combustion de cette chambre?

Author's Replies

My answers to your three questions are as follows:

(1) The chamber described is an experimental unit but Rolls-Royce have adopted a version of it for their High Pressure Core Demonstrator.

(2) This type of chamber is not yet in practical use on an engine but we should get life and cycling experience on the High Pressure Core Demonstrator.

(3) The combustion efficiency for the tests quoted was better than 99.8%.

R.Eggebrecht, Germany

In order to assess the status of development of this type of reverse flow combustor, it is also necessary to discuss the emission characteristics. Have you made measurements yet, and what was the outcome?

Author's Reply

The chamber was evolved for helicopter use for which there are no proposed emission regulations. However, the emission levels of CO and UHC at the conditions quoted are very low and the smoke number is below 30. If the combustor was to be adopted for an engine in the P_1 class and the idling conditions related to 5% engine power, then I think the chamber would meet the proposed EPA regulations, although to date we have not made measurements at all the conditions relative to the EPA cycle.

D.K.Hennecke, Germany

Regarding the exit temperature profile, the dilution air is usually employed for the achievement of an optimal radial temperature profile. Since you don't have any dilution parts how can you control the shape of the profile?

Author's Reply

We have shown that the radial profile can be modified by varying the air distribution to the cooling devices and also by the inclusion of dilution holes on the downstream side of the secondary baffle.

THE INFLUENCE OF COOLANT TURBULENCE INTENSITY ON FILM COOLING EFFECTIVENESS

by
R. Best
Institut für Technische Thermodynamik
Technische Hochschule Darmstadt
Petersenstrasse 30
6100 Darmstadt
Germany

SUMMARY

In pipe flow experiments cold air was injected tangentially to the tube wall of the test section through an annular slot into a hot fully developed turbulent pipe flow. The adiabatic wall temperature was measured along the pipe length for different velocity ratios, injection slot heights and degrees of turbulence of coolant and main streams. Simultaneously the velocity and the temperature profiles as well as the distribution of the turbulent fluctuation velocities were measured. The measurements indicate that an increasing turbulence intensity of the coolant can significantly reduce film cooling effectiveness. By means of turbulent fluctuation velocity measurements and a physical model the film cooling effectiveness can be calculated. The derived correlations reveal the best cooling effectiveness for a velocity ratio near unity and a decrease of the cooling effectiveness with increasing turbulence. There is a good agreement between experiments and theoretical predictions.

LIST OF SYMBOLS

A_τ	turbulent momentum exchange coefficient
A_q	turbulent heat exchange coefficient
c_p	specific heat at constant pressure
K	constant
l_d	lip thickness
Ma	Mach number
$\dot{m}$	mass flow rate
$\dot{Q}$	heat flow rate
$\dot{q}$	heat-flux rate
R	test section radius
Re	Reynolds number
R_o	mainstream inlet radius
r	radial coordinate
s	slot height
t	temperature
$\overline{w}$	time and area averaged velocity
$\overline{w'}$	short expression for the root-mean-square-value of the velocity fluctuation $\sqrt{\overline{w'^2}}$
z	axial coordinate along the tube axis
φ	azimuthal angle
η	film cooling effectiveness
λ	heat conductivity
μ	dynamic viscosity
ρ	density

SUBSCRIPTS

aw	adiabatic wall
max	maximum value
z	in direction of the coordinate z
o	mainstream
2	coolant stream

1. INTRODUCTION

In the film cooling of combustion chambers it is desirable to keep the amount of air used as small as possible. For this reason it is necessary to have an exact knowledge of the cooling process. In the past numerous experiments of film cooling were performed and wall temperatures were measured downstream of the injection point. The dependence of the most important parameters such as injection velocity, density, slot height, lip thickness, axial pressure gradient and injection angle were determined.
A review of the numerous investigations is given by Goldstein [1] and Schultz [2]. The main objective of the studies was to determine the adiabatic wall temperature variation t_{aw}, for example, the dimensionless adiabatic wall temperature, the so called cooling effectiveness,

$$\eta = \frac{t_{aw} - t_o}{t_2 - t_o} \tag{1}$$

where t_o is the temperature of the hot mainstream gas and t_2 is the temperature of the cooling medium at the point of injection. The experimental results were partly presented in terms of empirical formulae or described in terms of semiempirical models. The numerical solution of the differential boundary layer equations employing initial conditions and turbulent diffusivities result in more or less good agreement with the measurements. Up to now, the influence of turbulence on the film cooling and particularly the turbulence of the cold stream has scarcely been investigated. The present work is concerned with the experimental study and mathematical description of this effect. The knowledge of turbulence mechanism can result in a more complete understanding of turbulent exchange processes in the vicinity of the wall between combustion products and the cooling film. Of particular importance is the optimization of the coolant mass flow rate which has been experimentally observed by many authors that results in maximum effectiveness for a given coolant injection velocity. Since no models exist in the literature to describe such a maximum in cooling effectiveness an analysis is presented to calculate the temperature distribution of a film cooled wall accounting for the influence of tubulence and other film cooling parameters.

2. TEST SECTION

For the study of the fundamental relations in film cooling the phenomena in a combustion chamber can be geometrically simulated by tube flow with slot injection (Fig. 1).

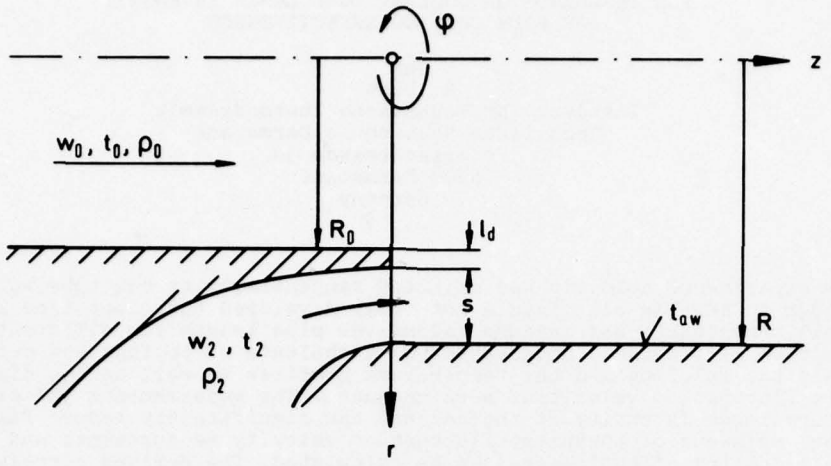

Fig. 1: Sketch of film cooling in a tube

The primary objective of the work is to investigate the influence of turbulence on film cooling, and the secondary objective is to prove that film cooling on a flat plate is similar to that in an annulus and to determine if the wall curvature has a strong influence on the cooling process. In Fig. 1, z denotes the coordinate in the flow direction, e. g. the tube axis, r is the radial coordinate and φ is the azimuth, s is the height of the coolant injection slot, l_d is the lip thickness and R is the tube radius. The velocities of the streams are denoted by w_0 and w_2, the temperatures by t_0 and t_2 and the densities by ρ_0 and ρ_2. These quantities are the time and cross-section averaged values at the point of injection (z=0). The subscripts o and 2 denote the hot and the cold gas streams, respectively.

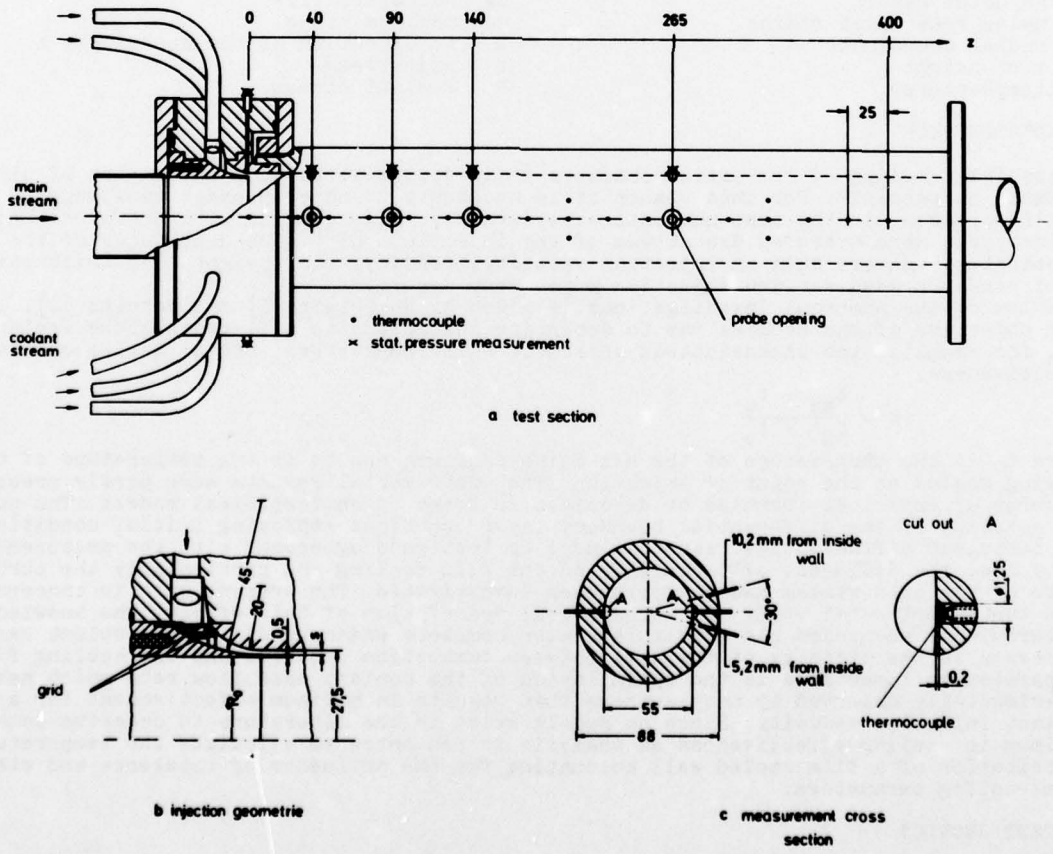

Fig. 2: Schematic presentation of the test section

The main parts of the experimental system employed is an open wind channel [3] for producing fully developed hot tube flow (mainstream: 50 m/s < w_o < 70 m/s; 180 °C < t_o < 230 °C; $7 \cdot 10^4$ < Re_o < $1.1 \cdot 10^5$; 0.1 < Ma_o < 0.16), a second flow channel which delivers the cold gas and a test section. The experiments were performed with air. The test section (Fig. 2a) consists essentially of a flow tube with an annular mixing nozzle for injection of a cooling medium through a tangential slot. The cooling medium is introduced through 12 rationally symmetric individual tubes into the annular chamber of the mixing nozzle. The cold stream is bent 90° and accelerates up to the slot exit. In order to vary the turbulence in the cold air stream a set of holes (72 holes with 2 mm inside diameter were placed circumferentially) with grids is introduced into the annular chamber (Fig. 2b). The distribution of the cold stream into 12 individual streams produces relatively strong vortices and turbulent eddies in the annular chamber of the mixing nozzle. By flowing through the tight grid structure, depending on the number and size of the grid, the turbulence is reduced. The highest level of turbulence of the cold stream in the present experimental set-up results in the absence of holes and grid. The grids used have a wire diameter from 0.1 mm up to 0.16 mm and a mesh size from 0.14 mm up to 0.29 mm. Various slot heights s can be produced with annular nozzles of different diameter. Experimental measurements were performed with slot heights of s = 0.8 mm, 1.5 mm and 2.5 mm. The connected test section is a thick-walled, adiabatic, insulated teflon tube of 55 mm inside diameter. The inside wall temperature of the teflon tube and therefore the adiabatic wall temperature is measured with 40 thermocouples at 16 cross sections in a length of 40 cm.
At 5 locations along the test section a combined thermocouple - pitot tube probe is used for determining the radial temperature and velocity distributions as well as a hot-wire-anemometer for measuring the radial distribution of the longitudinal fluctuation velocity. The openings for the probes are located at distances z=0, as well as 40, 90, 140 and 265 mm from the injection point.
The experimental data were recorded with a digital data system and then stored on a tape for evaluation on computer at a later time. With the experimental arrangement the adiabatic wall temperature and therefore the cooling effectiveness for a large number of velocity ratios w_2/w_o, for different temperatures t_2 and t_o, for varying slot heights and varying turbulent intensities of the cold stream were measured along the tube length.

3. EXPERIMENTAL RESULTS

3.1 DISTRIBUTION OF THE LONGITUDINAL VELOCITY FLUCTUATIONS

Fig. 3 illustrates the experimentally measured root-mean-square-value of the longitudinal velocity fluctuations $\sqrt{\overline{w_z'^2}}$ (denoted simply as $\overline{w_z'}$) for the mainstream gas plotted as a function of radial coordinate r obtained with a hot-wire-probe. The turbulent mainstream flow is fully developed at the point of injection (z=0). Illustrated are the fluctuations $\overline{w_{zo}'}$ for three different mainstream velocities w_o. In the center of the channel there exist relatively low fluctuations which depend on the flow velocity and increase as the wall is approached. In the vicinity of the wall there is a maximum in the longitudinal velocity fluctuation and decreases sharply until it reaches a value of zero at the wall. Similar distributions were, for example, given by Laufer [4] and also by Perry and Abell [5] for tube flow and by Klebanoff [6] and Blom [7] for flow over a flat plate. It shows that the turbulent fluctuating motion $\overline{w_z'}$ depends on the average flow velocity as well as on the distance from the wall.

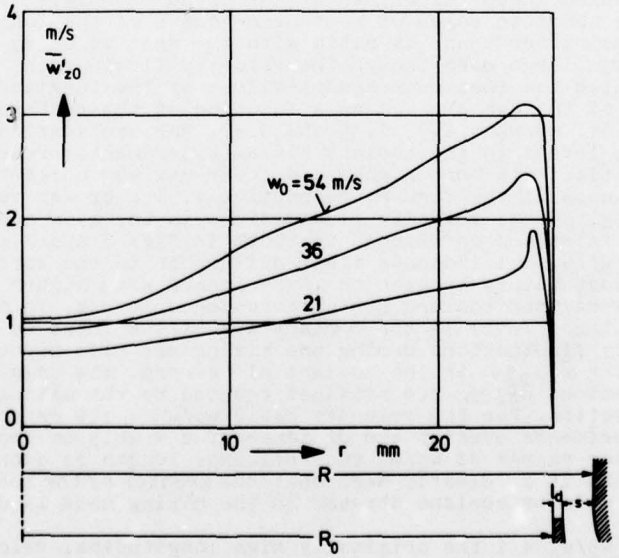

Fig. 3: Root-mean-square-value of the longitudinal velocity fluctuation $\overline{w_{zo}'}$ of the main stream across the inlet test section radius R_o

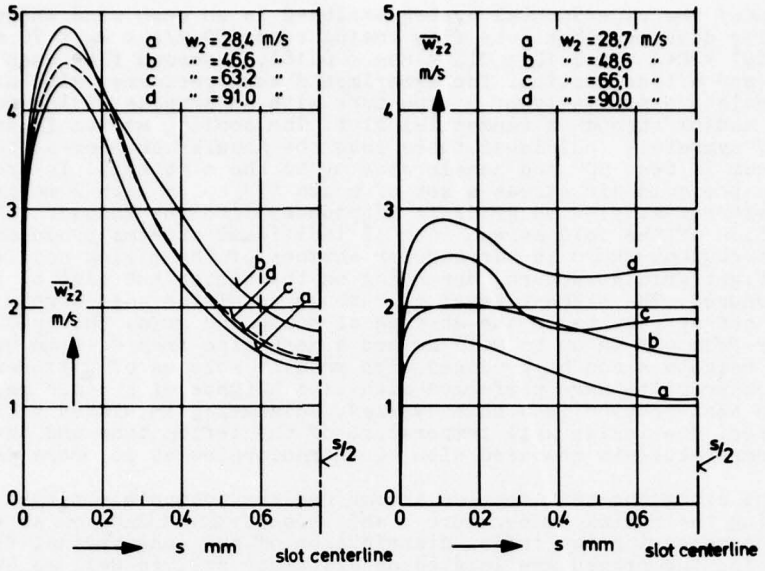

Fig. 4: Distribution of the root-mean-square-value of the longitudinal velocity fluctuation $\overline{w'^2_{z2}}$ of the coolant stream across the slot height s. left part: experiments with a higher maximum fluctuating motion; right part: experiments with a lower maximum fluctuating motion.

Different turbulent intensities of the coolant were obtained through the installation of grids in the annular chamber discussed earlier (Fig. 2b). Fig. 4 shows the distribution of the longitudinal coolant velocity fluctuations $\overline{w'^2_{z2}}$ (root-mean-square-value) plotted against the slot height. As an example, here are given measurements with the slot height s = 1.5 mm for four cold stream velocities. The left part of the figure shows experiments with high maximum longitudinal velocity fluctuations which were obtained without the grid structure shown in Fig. 2b. With the grid (Fig. 4, right part of figure) the maximum of the fluctuating motion is strongly decreased, but the turbulence in the center of the slot, however, increases somewhat. Downstream of the injection point the intensity of the heat exchange between the two streams depends strongly, for a short distance, on the value of the fluctuations near the slot wall facing the mainstream. Therefore, the maximum value of the fluctuations is important. The magnitude of the fluctuations in the center of the slot is of secondary importance for film cooling. Since the velocity fluctuations depend not only on the flow velocity but show also a radial distribution therefore to characterize the magnitude of turbulence the maximum longitudinal velocity fluctuations of the measured profile of the main and cooling streams are given at the entrance of the test section. The mainstream turbulence $\overline{w'^2_{z0\,max}}$ corresponds to that of a fully developed turbulent pipe flow and was not changed in the experiments. The turbulence level in the present work is characterized by the absolute value of root-mean-square of the longitudinal turbulent velocity fluctuations rather than its ratio with the mean velocity since the ratio at low mean velocities becomes large even though the velocity fluctuations remain small.
In Fig. 5 are presented the root-mean-square-values of the longitudinal velocity fluctuations during mixing of the two streams as a function of the test section radius for different velocity ratios, w_2/w_0 = 1.9, 1.35 and 0.57. For explanation of the influences of different turbulence levels in the coolant stream experimental results are presented for the same velocity ratios with both higher and lower maximum coolant turbulence levels in the left and right parts of the figure, respectively. The broken curves give again the variation of the longitudinal velocity fluctuations in the main and coolant streams at the test section inlet and correspond to those in Fig. 3 and Fig. 4.
The velocity ratios $w_2/w_0 > 1$ indicate clear difference in the variation of the longitudinal velocity fluctuations between the experiments with higher (left part) and smaller (right part) maximum coolant stream turbulence levels. In the experiments with higher maximum turbulence level in the coolant air at the inlet to the test section, the longitudinal velocity fluctuations during the mixing are also higher than in the experiments with the smaller $\overline{w'^2_{z2\,max}}$ in the coolant air stream. The originally high coolant air velocity fluctuations $\overline{w'^2_{z2\,max}}$ are somewhat reduced by the mixing but extend over a larger flow cross section. For the velocity ratio w_2/w_0 = 1.9 one can note a difference between the two experiments even at the distance of z = 26.5 cm from the point of injection. For smaller values of w_2/w_0 the influence length is decreased.
From these experiments it is clearly seen that the greater of the longitudinal velocity fluctuations of the main or coolant streams in the mixing zone is dominating for short distances.
For velocity ratios $w_2/w_0 < 1$ the originally high longitudinal velocity fluctuations of the coolant air stream decrease very rapidly so that with decreasing velocity ratio the turbulence of the coolant wir stream entering the test section becomes always of smaller influence. For w_2/w_0 = 0.57 one can observe a small influence of turbulence only up to a distance of z = 14 cm.
This comparison makes it clear how the turbulence introduced with the coolant stream in the test section influences the distribution of the longitudinal velocity fluctuations.

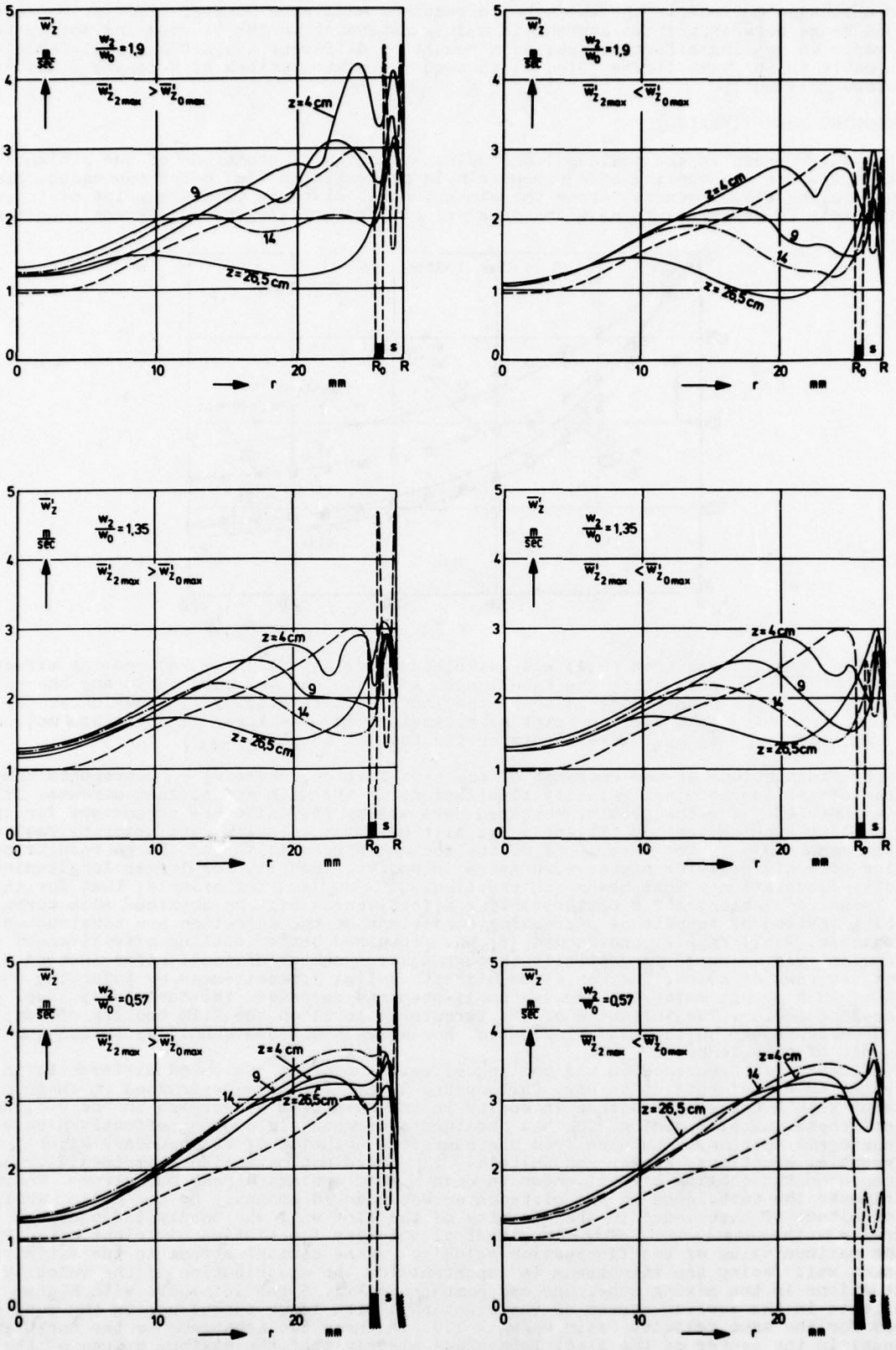

Fig. 5: Influence of different root-mean-square-values of longitudinal velocity fluctuation of the coolant stream at the test section inlet (---z=0) on the distribution of the velocity fluctuations during the mixing of the main and coolant streams for different distances z from the point of injection and velocity ratios w_2/w_0 = 1.9 to 0.57. The left column shows experiments with higher coolant air turbulence and the right column shows experiments with lower turbulence. The maximum longitudinal fluctuating motion of the mainstream is nearly constant $\overline{w'_{z0\,max}}$ = 3 m/s.

The fluctuating motions in the two other directions will show similar effects. Since the heat exchange between the two streams is mainly dependent on the fluctuating motion the difference in cooling effectiveness, as a result of different coolant air turbulence, is explainable in the next figure (Fig. 6) through the distributions of velocity fluctuations discussed previously.

3.2 COOLING EFFECTIVENESS

How the differences in the maximum longitudinal velocity fluctuations of the coolant stream influence the cooling effectiveness η is presented in Fig. 6 for two cases. Plotted is the cooling effectiveness versus the dimensionless distance from the point of injection. The two sets of measurements have the same velocity ratio w_2/w_o but different longitudinal

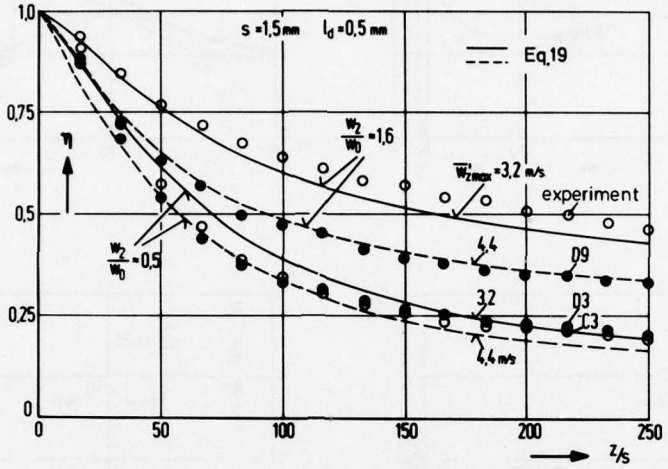

Fig. 6: Measured (o,●) and calculated from Eq. (19) (—,--) cooling effectiveness along the tube length z/s with the velocity ratio and the root-mean-square-value of the longitudinal velocity fluctuation at the test section inlet as parameters (o —— lower fluctuating motion $\overline{w'_z}_{max}$; ● ----- higher fluctuating motion $\overline{w'_z}_{max}$).

velocity fluctuations at the entrance of the test section, where $\overline{w'_z}_{max}$ represents the greater of the longitudinal velocity fluctuations in the main and coolant streams. It is implied here that for the results compared here all of the influence parameters for the film cooling such as the lip thickness l_d, slot height s, density- and velocity rations are the same and only the turbulence of the coolant stream is varied. There results poorer cooling effectiveness for higher turbulence intensity, that is, for larger longitudinal velocity fluctuations. This means in practical applications, for example, that for the same amount of coolant air a better cooling effectiveness will be obtained when turbulence reducing instead of turbulence increasing conditions at the injection are constructed. For example, Wahl, Kappler and Schmid [8] have obtained better cooling effectiveness when the coolant was injected tangentially through a large number of small holes instead of one or two rows of holes. They obtained highest cooling effectiveness by injecting cooling air through a porous material, because small openings decreased the turbulence level of the coolant medium. The influence of the turbulence level on the film cooling effectiveness depends though on the mass flow ratio. For $w_2/w_o < 0.5$ one cannot establish any influence of turbulence.
The influence of turbulence on the cooling effectiveness was evaluated differently in the few existing experiments up to now. Carlson and Talmor [9] have determined in their experiment with a higher turbulence intensity in the mainstram a decrease in the cooling effectiveness. Also, Spalding [10] has obtained a decrease in cooling effectiveness with increasing mainstream turbulence from the numerical solution of the boundary layer differential equations. Kacker and Whitelaw [11] could not establish experimentally any influence on the cooling effectiveness through higher coolant stream turbulence. In their experiments the turbulence in the slot center was changed probably by the grids, while the magnitude of turbulence in the vicinity of the slot wall was hardly influenced. According to the measurements of the longitudinal velocity fluctiation distribution in Fig. 5, the maximum value of the fluctuation velocity of the coolant stream in the vicinity of the slot wall facing the mainstream is important for the distribution of the velocity fluctuations in the mixing zone. One can compare in Fig. 5 the left part with higher turbulence in the cooling stream to the right part with lower turbulence in the cooling stream for the same velocity ratio $w_2/w_o = 1.9$. In these two measurements the turbulence is equal in the center of the slot. This shows clearly that the maximum values of the longitudinal velocity fluctuations influence the turbulence during the mixing of the two streams.
In Fig. 7 are presented experimental data for three runs with approximately the same mass flow ratio $\dot{m}_2/\dot{m}_o = 0.19$ but different slot heights s and therefore different velocity rations w_2/w_o. The experimental measurements clearly establish that for equal mass flow ratio the maximum cooling effectiveness is independent of the slot height s for this run for which the velocity ratio is $w_2/w_o \approx 1$. Only for short distances from the injection point the heat protection of a thicker cooling film, as a result of higher slot height (s = 2.5 mm) between the hot mainstream and the wall, is of greater influence than the

velocity ratio $w_2/w_o = 1$. Smaller cooling effectiveness are obtained for those measurements for which the velocity difference between the main and the coolant stream $|w_2/w_o - 1|$ is large and through it more intensive momentum and heat exchange is produced. For very large distances z from the point of injection the three set of results approach the same value of cooling effectiveness. The run with the largest value $|w_2/w_o - 1|$ reached this condition at the smallest distance z.

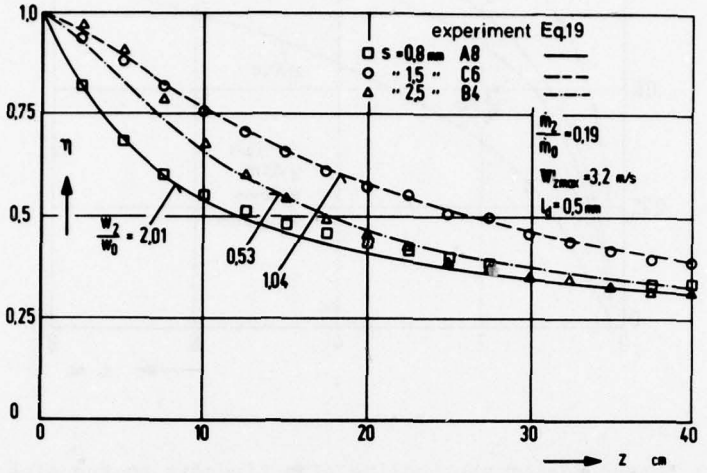

Fig. 7: Comparison of measured and calculated (from Eq. (19)) cooling effectiveness along the tube length z/s for equal mass flow ratios but different slot height s and velocity ratios.

In Fig. 8 are presented experimentally determined cooling effectiveness for five distances from the point of injection as a function of the velocity ratio w_2/w_o. In agreement with the experiments of Pai and Whitelaw [12] and Nicoll and Whitelaw [13], the results show an increase in cooling effectiveness with an increase in the coolant injection velocity. In the neighbourhood of the velocity ratio $w_2/w_o = 1$ there is obtained a maximum cooling effectiveness. An increase in the ratio up to $w_2/w_o > 1$ gives for shorter distances no further improvement in cooling effectiveness. The explanation of this trend is the reduced momentum exchange between the two streams when the coolant and main stream velocities approach each other; therefore, the mixing is not as intense as in the case of higher velocity differences, and hence the cooling effectiveness is better. For higher velocity ratios the cooling effectiveness hardly decreases in spite of further increase in momentum exchange since the mass of coolant injected increases accordingly.

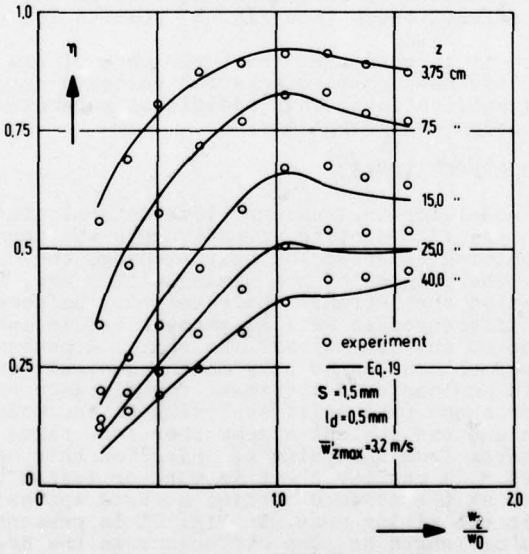

Fig. 8: Comparison of measured (o) and calculated (———) cooling effectiveness as a function of the velocity ratio with the distance z from the injection point as parameter.

The dependence of the cooling effectiveness on the slot height s is given in Fig. 9 for two different velocity ratios and distances from the point of injection as parameters. For smaller values of the slot height an increase of the slot height results in greater improvement of the cooling effectiveness as for the larger ones. In practice this means that an average cooling effectiveness can be achieved with relatively small slot heights.

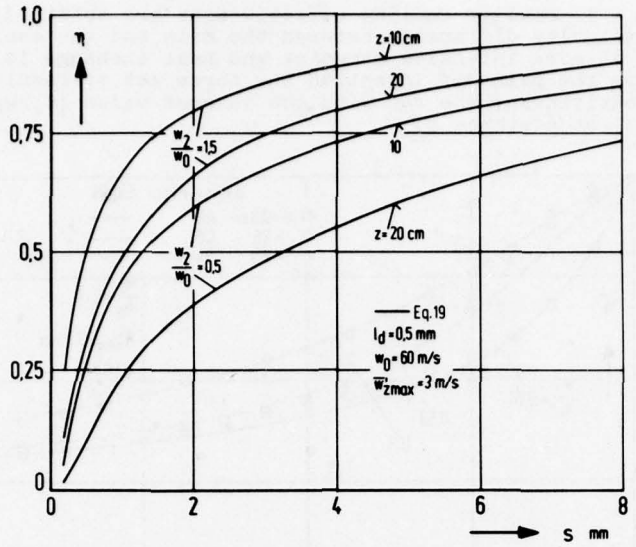

Fig. 9: Dependence of the cooling effectiveness on the slot height s with the velocity ratio and the distance from the point of injection as parameters.

3.3 TEMPERATURE AND VELOCITY DISTRIBUTIONS

Fig. 10 shows the temperature and velocity profiles in the test section for different distances z from the point of injection and for four different velocity ratios of the coolant and the mainstream. For large velocity ratios a slow decrease of the wall jet and at the same time a heating of the coolant are observed. The velocity difference between the wall jet and the mainstream promotes the momentum- and heat exchange. The increase in w_2/w_o and therefore a greater velocity difference compensates the effect of the greater heat sink which results from an increase in coolant mass flow. This is the explanation why there is no further rise in the cooling effectiveness with the increase in $w_2/w_o > 1$ (see Fig. 8). For small velocity ratios the same two mechanisms mentioned above are in effect. But through the lower coolant mass flow rates the resulting heat sink effect is smaller. For velocity ratios $w_2/w_o \approx 1$ the momentum- and heat exchange between the two streams caused by the velocity difference is small. The injected cold air mass and therefore the heat sink effect produced is sufficient so that in the vicinity of this velocity ratio an optimum cooling effectiveness (see Fig. 8) results for short distances z from the injection point.
From the results presented it is seen that the turbulence of the coolant air influences strongly the cooling effectiveness particularly for velocity ratios $w_2/w_o \geq 1$ which are of interest for practical applications. This additional parameter on film cooling must therefore be taken into design considerations.

4. CALCULATION OF COOLING EFFECTIVENESS

The following simplified model for the semiempirical determination of the influence of the coolant air turbulence on the film cooling effectiveness was developed. Through turbulent mixing motion and the resulting momentum and heat exchange the hot mainstream gives up heat to the coolant film. The origins of the mixing motion are, in addition to the turbulence of the two streams at the entrance their velocity difference $|w_o - w_2|$, their temperature and density differences as well as geometrical influences. In order that the processes could be considered one-dimensional the radial dependence of the temperature and the velocity are therefore considered only on the control surface (see Fig. 11, surface B-B) between the main and the cold stream at the distance of the slot height plus half lip thickness away from the tube wall. According to the model the turbulent heat exchange between the main and the coolant stream therefore takes place on this control boundary. For short distances from the point of injection this assumption fully is justified. For larger distances z in reality there is more or less a thicker mixing zone. This means that the restriction at the assumed control surface approximates an average value in the radial direction in the mixing zone. In Fig. 11 is presented a heat balance on an element of coolant stream of length dz. The difference in the heat flow rates $\dot{Q}_b - \dot{Q}_a$, between outflow and inflow, is equal to the heat transport from the mainstream $\Delta\dot{Q}_c$. As a consequence of an adiabatic wall there is no heat conduction through the wall, and one has that

$$\dot{Q}_b - \dot{Q}_a = \Delta\dot{Q}_c \qquad (2)$$

As a result of the heat transport (at approximately constant velocity) there is heating of the coolant element,

$$\dot{Q}_b - \dot{Q}_a = \dot{m}_2 \, c_{p2z} \, \frac{\partial t_{2z}}{\partial z} \, dz \qquad (3)$$

Here $\dot{m}_2$ denotes the mass flow rate of the coolant medium and t_{2z} represents the tempera-

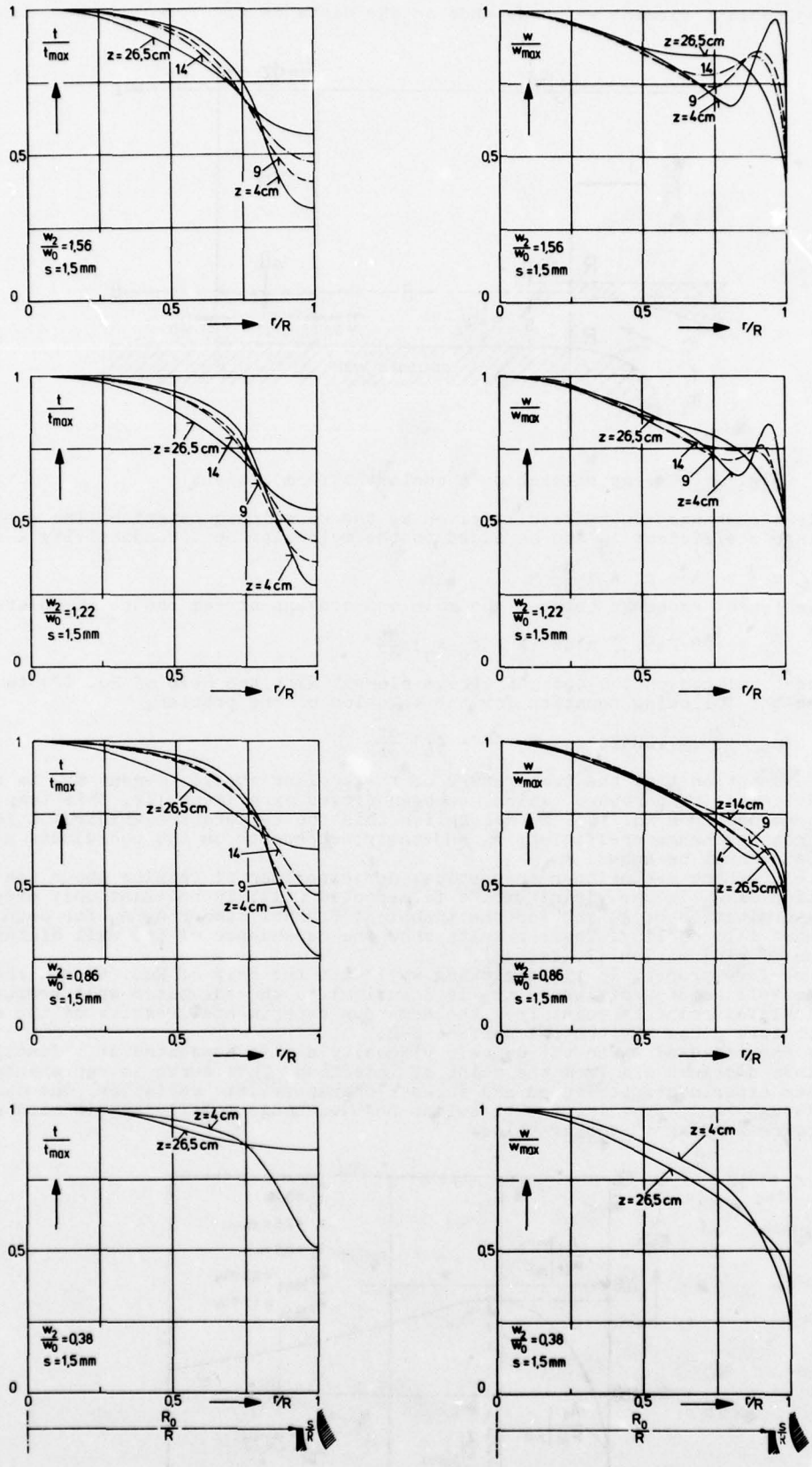

Fig. 10: Temperature and velocity profiles after the mixing of the main and coolant streams for different distances z from the point of injection and different velocity rations w_2/w_0.

ture of the coolant element which depends on the distance z.

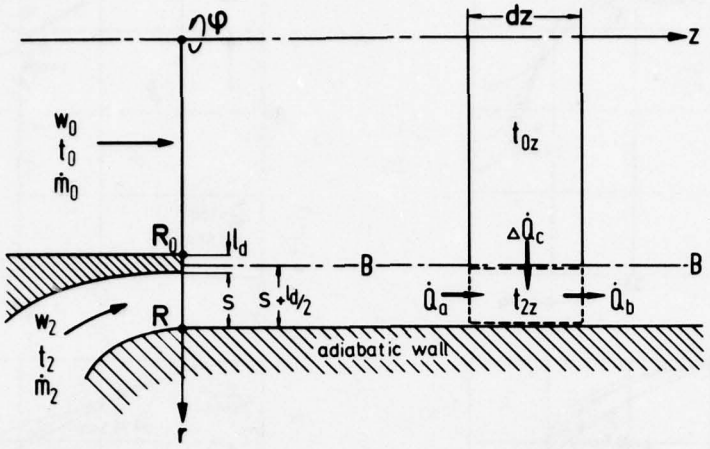

Fig. 11: Energy balance on a coolant stream element

The turbulent exchange can be readily given by the Boussinesq relation. The turbulent heat exchange coefficient A_q can be added to the molecular heat conductivity λ such that

$$\dot{q} = - (\lambda + c_p A_q) \frac{dt}{dr} \tag{4}$$

The turbulent heat exchange between the main and coolant stream can be calculated by

$$\Delta\dot{Q}_c = (2R-2s-l_d) \pi \, dz \, (\lambda + c_p A_q) \frac{dt}{dr} \tag{5}$$

From the heat balance on the coolant stream element with the help of Eq. (2) to (5) there is obtained the following equation for the solution of the problem,

$$\dot{m}_2 \frac{dt_{2z}}{dz} = (2R-2s-l_d) \pi \left(\frac{\lambda}{c_p} + A_q\right) \frac{dt}{dr} \tag{6}$$

Under the assumption that the temperature of the coolant stream element t_{2z} is equal to the adiabatic wall temperature which has been proved experimentally, this temperature can be determined from Eq. (6). To accomplish this the temperature gradient dt/dr and the turbulent heat exchange coefficient A_q and their dependence on the coordinate z in the flow direction must be known.
Unfortunately, there are neither theoretical nor experimental results about the magnitude and variation of A_q in the vicinity of a film-cooled wall. There exist only experiments for the determination of A_q and for the turbulent Prandtl number A_T/A_q for boundary layer flows without film cooling. These results show the dependence of the wall distance and also of the flow direction [7, 14, 15].
One can therefore proceed in the following way: With the help of Eq. (6) and the knowledge of dt/dr as well as dt_{2z}/dz, where t_{2z} is identical to the adiabatic wall temperature, A_q was calculated point by point from the numerous experimental results of the adiabatic wall temperature along the control surface B-B.
In Fig. 12 the ratio of A_q to the dynamic viscosity μ_{02} is presented as a function of dimensionless distance z/s from the point of injection. This curve is representative of the numerous experiments performed and shows a characteristic variation. One can readily see that $A_q/\mu_{02} >> 1$, that is, the turbulent heat exchange coefficient is much greater than the corresponding molecular value.

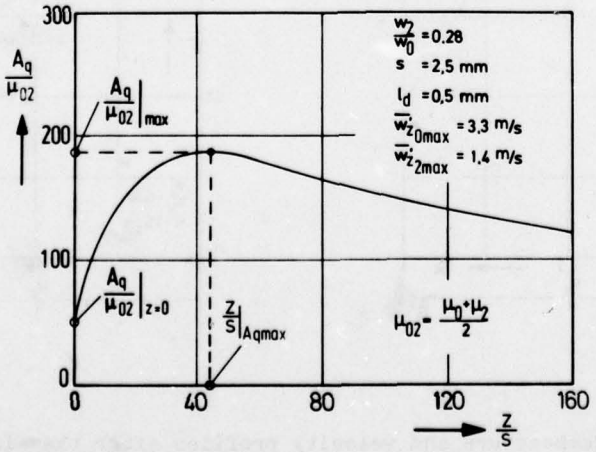

Fig. 12: Dimensionless turbulent heat exchange coefficient as a function of z/s.

Similar orders of magnitude have been observed by others [16, 17]. As can be further seen, A_q goes through a maximum downstream from the coolant air injection point and then decreases with increasing distance z/s. As an approximation, the variation of A_q with the dimensionless tube length z/s could be expressed by

$$\frac{A_q}{\mu_{o2}} = K_1 + \frac{K_2 z/s}{(K_3+z/s)^3} \tag{7}$$

The constants K_1, K_2 and K_3 depend on the injection geometry and on the flow parameters. These constants were evaluated from experimental data with the help of the π-theorem of dimensionless analysis [18]. Three characteristic points were utilized along the A_q curve, namely the value of A_q at the point of injection and the position of the maximum of A_q in determining the constants. At the point of injection (z = 0) the turbulent heat exchange between the main and coolant streams A_q is proportional to the velocity difference between the two streams $|w_2 - w_o|$, the fluctuation velocity $\overline{w'_z}_{max}$, and to the ratio of the lip thickness l_d to the slot height s,

$$\left.\frac{A_q}{\mu_{o2}}\right|_{z/s=o} = 1+1.4\cdot10^4 \left[(1+\frac{|w_2-w_o|}{w_o}) \frac{\overline{w'_z}_{max}}{w_o} (\frac{l_d}{s})^{0.25}\right]^2 \tag{8}$$

Also, the maximum value of A_q,

$$\left.\frac{A_q}{\mu_{o2}}\right|_{max} = 5\cdot10^3 \frac{s}{R} (\frac{l_d}{s})^{0,6} + 6.5\cdot10^4 (\frac{\overline{w'_z}_{max}}{w_o})^{2.5} \frac{w_2}{w_o} \tag{9}$$

and the distance of the maximum from the point of injection,

$$\left.\frac{z}{s}\right|_{A_q\,max} = 15 \frac{R}{s} e^{-\left|\frac{w_2}{w_o} - 1\right|(\frac{R}{s})^{0.25}} \tag{10}$$

show the dependence on the flow characteristics and geometry. For $\overline{w'_z}_{max}$ the greater of the two longitudinal velocity fluctuations of the main and coolant streams at the point of injection is used,

$$\frac{\overline{w'_z}_{max}}{w_o} = Max\ \{\frac{\overline{w'_z}_{omax}}{w_o}, \frac{\overline{w'_z}_{2max}}{w_o}\} \tag{11}$$

The reason for this is that the turbulent heat exchange is promoted by the velocity difference between the two streams and also through the maximum fluctuating motion which is carried into the mixing zone from the main or the coolant stream (see Fig. 5).
The constants K_1, K_2 and K_3 can be expressed through the relation (8) to (10) by

$$K_1 = \left.\frac{A_q}{\mu_{o2}}\right|_{z/s=0} \tag{12}$$

$$K_2 = \frac{27}{4} (\left.\frac{A_q}{\mu_{o2}}\right|_{max} - K_1)\ K_3^2 \tag{13}$$

$$K_3 = 2 \left.\frac{z}{s}\right|_{A_q\,max} \tag{14}$$

In this work the lip thickness was held constant at l_d = 0.5 mm for all measurements. In order to take into account the influence of the lip thickness on the cooling effectiveness experimental results of Ballal and Lefebvre [19], Kacker and Whitelaw [11, 20] and Sivasegaram and Whitelaw [21] were utilized.
The variation of A_q/μ_{o2} and therefore the dependance of all film cooling parameters as a function of the tube length z/s can be calculated from Eqs. (7) through (14).
The temperature gradient dt/dr on the control surface was determined from the temperature profile measurements (Fig. 10) and was expressed functionally [3] with the help of a, so called, mixing thickness and the mass flow ratio of the two streams. After the introduction of the dimensionless coordinates z/s and r/s the following dependence is obtained,

$$\frac{dt}{d(\frac{r}{s})} = \frac{t_o + K_4\ t_2 - (K_4+1)\ t_{2z}}{K_5\ (K_6 + z/s)} \tag{15}$$

Where the constants are given by

$$K_4 = \frac{\dot{m}_2\ c_{p_2}}{\dot{m}_o\ c_{p_o}} \tag{16}$$

$$K_5 = 0.0425 \tag{17}$$

$$K_6 = \frac{0.004 + 0.00475\ e^{-11.5\ \dot{m}_2/\dot{m}_o}}{s\ K_5} \tag{18}$$

With the knowledge of the functional dependence of A_q and the temperature gradient, Eq. (6) can be integrated after separating the variables. After some rearrangements the

dependence of the cooling effectiveness η on the dimensionless distance from the point of injection z/s can be expressed as

$$\eta = \frac{1}{K_4+1}\left[K_4 + \left(\frac{K_6+z/s}{K_6}\right)^{-K_8} \left(\frac{K_6(K_3+z/s)}{K_3(K_6+z/s)}\right)^{-K_{10}} e^{-K_{11}+\frac{K_{12}}{K_3+z/s}+\frac{K_{13}}{(K_3+z/s)^2}}\right] \tag{19}$$

The new constants are given by,

$$K_7 = \frac{(2R-2s-l_d)\,\pi\,(\mu_o + \mu_2)}{2\,\dot{m}_2\,K_5} \tag{20}$$

$$K_8 = (K_4 + 1)\,K_7\,K_1 \tag{21}$$

$$K_9 = \frac{(K_4 + 1)\,K_2\,K_7}{K_3 - K_6} \tag{22}$$

$$K_{10} = \frac{K_9\,K_6}{(K_3 - K_6)^2} \tag{23}$$

$$K_{11} = \frac{K_9}{K_3}\left(\frac{K_6}{(K_3 - K_6)} + \frac{1}{2}\right) \tag{24}$$

$$K_{12} = \frac{K_9\,K_6}{(K_3 - K_6)} \tag{25}$$

$$K_{13} = \frac{K_9\,K_3}{2} \tag{26}$$

The molecular quantities do not appear in the above equation since they are negligibly small in comparison to A_q. Eq. (19) gives the dependence of the cooling effectiveness for tube flow on z/s, where for z/s → o the effectiveness η approaches unity. The equation is also approximately applicable for film cooling on a flate plate when small changes are made in the relations [3].
In the following, some characteristic influence parameters, representative of the experimental results will be compared with the calculations.
As Fig. 6 shows the influence of the maximum longitudinal velocity fluctuation $\overline{w_z'}_{max}$ is relatively well described by Eq. (19). The solid lines give the calculated cooling effectiveness for small $\overline{w_z'}_{max}$ and the dashed lines the calculated variation for the higher values of $\overline{w_z'}_{max}$. With Eq. (19) the influence of turbulence on film cooling for the first time can also be described in terms of the maximum longitudinal velocity fluctuation of the main and coolant streams.
Also, the influence of the various slot heights s and different velocity ratios of the coolant and main streams can be described with the derived expression. The curves in Fig. 7 give again the calculated cooling effectiveness for three measured data sets at different slot heights s for equal mass flow ratio of the coolant and main streams.
In Fig. 8 experimentally determined cooling effectiveness are presented for five distances z from the point of injection as a function of the velocity ratio w_2/w_o and compared with the values calculated from Eq. (19) (solid line). The essential result of this presentation is that the derived equation describes a maximum cooling effectiveness for $w_2/w_o \approx 1$ at small distances from the injection point. This maximum was not given by any earlier theoretical or semiempirical relations even though it has been always observed experimentally.
The experimental results are described relatively well by the equation. The differences between measurements and calculations amount less than 10 % for all experimental conditions.

5. CONCLUSION

The investigation shows that the turbulence of the main and coolant streams, characterized by the maximum longitudinal velocity fluctuation $\overline{w_z'}_{max}$, has the same influence on film cooling effectiveness as, for example, velocity ratio and slot height especially for velocity ratios of coolant and main stream $w_2/w_o \geq 1$. The turbulence in both streams must also be taken into account in film cooling problems as other parameters.

6. REFERENCES

1 Goldstein, R. J.
"Film cooling"
Advances in Heat Transfer, Academic Press, New York, London, 7 (1971) 321/379

2 Schultz, D. L.
"A survey of film cooling theory and experiment"
v. Karman Inst. Fluid Dyn., Turb. Blade Cool. Conf., Lecture Ser. 83 (1976)

3 Best, R.
"Einfluß der Turbulenz auf den Wärmeaustausch an einer filmgekühlten Rohrwand"
Dissertation, TH Darmstadt, 1977

4 Laufer, J.
"The structure of turbulence in fully developed pipe flow"
NACA Report 1174 (1954), 417/434

5 Perry, A. E. and C. J. Abell
"Scaling laws for pipe-flow turbulence"
J. Fluid Mech. 67 (1976), 257/271

6 Klebanoff, P. S.
"Characteristics of turbulence in a boundary layer with zero pressure gradient"
NACA Report 1247 (1955)

7 Blom, J.
"An experimental determination of the turbulent Prandtl number in a developing temperature boundary layer"
Thesis, Tech. Univ. Eindhoven, Niederlande (1970)

8 Wahl, D. and G. Kappler, J. Schmidt
"Messung des Wärmeübergangs an filmgekühlten Flammrohrwandelementen"
Brennst.-Wärme-Kraft 27 (1975) 5, 201/205

9 Carlson, L. W. and E. Talmor
"Gaseous film cooling at various degress of hot-gas acceleration and turbulence levels"
Int. J. Heat Mass Transfer 11 (1968) 1695/1713

10 Spalding, D. B.
"Boundary-layer theory applied to film-cooling processes"
Progress in Heat and Mass Transfer IV, Pergamon Press (1971) 279/296

11 Kacker, S. C. and J. H. Whitelaw
"The effect of slot height and slot-turbulence intensity on the effectiveness of uniform density, two-dimensional wall jet"
J. Heat Transfer 90 (1968) 4, 469/475

12 Pai, B. R. and J. H. Whitelaw
"The influence of density gradients on the effectiveness of film cooling"
Aeron. Res. Council London, Paper 29928, H. M. T. 182 (1968)

13 Nicoll, W. B. and J. H. Whitelaw
"The effectiveness of the uniform density, two-dimensional wall jet"
Int. J. Heat Mass Transfer 10 (1967) 623/639

14 Ludwieg, H.
"Bestimmung des Verhältnisses der Austauschkoeffizienten für Wärme und Impuls bei turbulenten Grenzschichten"
Z. Flugwiss. 4 (1956) 1/2, 73/81

15 Reichardt, H.
"Die Grundlagen des turbulenten Wärmeübergangs"
Arch. f. Wärmetechn. 2 (1951) 129/142

16 A. Quarmby and R. Quick
"Measurements of radial and tangential eddy diffusities of heat and mass in turbulent flow in a plain tube"
J. Heat Mass Transfer 15 (1972), 2309/2327

17 T. Mizushina, R. Ito and F. Ogino
"Eddy diffusivity distribution near the wall"
Preprints of papers, 4th Int. Heat Transfer Conf., Paris - Versailles 1970, Vol. II, FC 2

18 J. Pawlowski
"Die Ähnlichkeitstheorie in der physikalisch-technischen Forschung"
Springer-Verlag, Heidelberg-New York (1971)

19 Ballal, D. R. and A. H. Lefebvre
"A proposed method for calculating film-cooled wall temperatures in gas turbine combustion chambers"
ASME Paper 72-WA/HT-24 (1972)

20 Kacker, S. C. and J. H. Whitelaw
"An experimental investigation of the influence of slot-lip-thickness on the impervious-wall effectiveness of the uniform-density, two-dimensional wall jet"
Int. J. Heat Mass Transfer 12 (1969) 1196/1201

21 Sivasegaram, S. and J. H. Whitelaw
"Film cooling slots: The importance of lip thickness an injection angle"
J. Mech. Engng. Sci., 11 (1969) 22/27

7. ACKNOWLEDGEMENT

This work was performed under the advice of Professor Dr.-Ing. H. Beer, Institut für Technische Thermodynamik, TH Darmstadt. Thanks are due to Professor Dr. R. Viskanta for

his help in editing. This work was supported by the Deutsche Forschungsgemeinschaft.

DISCUSSION

D.K.Hennecke, Germany

I want to compliment you on your interesting paper. You show that the turbulence of the coolant stream has a very large influence on film cooling effectiveness. And this, to my knowledge, has not been investigated before.

In the light of your results one may perhaps more easily understand why the various film cooling configurations that Mr Buisson showed earlier this afternoon display quite different effectiveness. Depending on the geometry of the configuration, the turbulence of the coolant at the end of the lip may be different and influence the film cooling effectiveness.

HIGH TEMPERATURE H_2-AIR VARIABLE GEOMETRY COMBUSTOR AND TURBINE: TEST FACILITY AND MEASUREMENTS

by
L. Martorano and D. Dini
Centro per l'Automatica E. Piaggio
56100 Pisa, ITALY

SUMMARY

A new design concept for gas turbine H_2-Air combustor is presented and its potential verified by experimental data. In developing the test facility and program, performance parameters variation have been considered. In such a high temperature flow, reactions approach rapidly to chemical equilibrium.

The research has been largely concerned with investigation into the combustor performance with a view to the use of H_2-Air in conventional variable geometry gas turbines.

Proposals and development for varying and controlling the air flow distribution characteristics appear feasible and worthy of further research work.

Encouraging results are given by the first high temperature tests carried out on variable geometry combustor and turbine blading.

LIST OF SYMBOLS

T = static temperature, °R
v = specific volume, cubic ft/lb
p = static pressure, psia
t = running time, seconds
P = weight, lb
$\dot{P}$ = weight flow, lb/sec
w = air speed, ft/sec
W = power, HP
u = peripheral blade speed, ft/sec
μ = equivalence ratio
ψ = air-fuel ratio
f = fuel-air ratio
Δw = peripheral change of flow speed, fl/sec
c = nozzle exit speed, ft/sec
550 lb-feet = 1 HP
1545.6/25.4 • 144 = gas constant, ft/°R
Q = Hydrogen heat of combustion, BTU/lb
c_p = constant pressure specific heat, BTU/lb °R
ϵ = combustion efficiency
η = expansion efficiency
n = polytropic exponent
m = molecular weight
g = gravity acceleration ft/sec^2

SUBSCRIPTS

1 = air in the storage system
2 = air downstream the regulating valve
3 = combustion conditions
4 = static nozzle exit
g = gas

INTRODUCTION

The use of H_2-Air combustion mixtures as a possible operating fluid for aircraft gas turbines has been considered for a number of years. Among the many problems associated with the use of this mixture are those of efficient burning under a variety of conditions.
Of the common fuel-oxidant systems, the H_2-Air system is probably the simplest, the one about which much of the chemistry is known, and the one about which there is the greatest likelihood of learning more.
One of the main problems in gas turbine combustors is the assurance of stable combustion of the H_2-Air mixture during the process of free turbulent mixing of high speed axial gas flows and chemical reactions in the mixing zone. To extend the domain of stable combustion, it is necessary to assure such concentrations of the intermediate reaction products in the stream being mixed as would "catalyze" the reaction, assuring its rapid and stable progress; this expecially under conditions at which spontaneous ignition do not occur.

This investigation, for a large variety of equivalent ratios (H_2-Air ratio divided by stoichiometric H_2-Air ratio mixture composition), could be carried out experimentally by a pre-mixed variable area combustor, supplied by fuel-oxidant mixture in a wide field of temperature and pressure levels. In order to do that conveniently from the point of view of exercise expenses, an existing intermittent blow-down wind tunnel, associated to an ejector, was used for collecting air and gaseous hydrogen into the combustion chamber. High pressure exhaust gases could reach atmospheric level by expansion in an action single stage variable geometry turbine. Turbine power was driving an hydraulic dynamometric brake.

Due to the small power turbine, in the field of 150 - 350bhp, it was possible to operate with relatively small combustor and air supply. Moreover, investigation could be carried out with different kinds of tur-

bine blading, simply using each time the same rotor. Heat transfer to the blades was limited by the short duration blowdown discharge.

The authors are expert in designing H_2-Air supplied reciprocating engines, and aircraft and missile gas turbine engines.

TEST FACILITY FOR VARIABLE GEOMETRY H_2-AIR COMBUSTOR AND TURBINE

Our variable combustor and turbine assembly is supplied by an existing intermittent blowdown wind tunnel, that can run steadily only for a limit period of time, 100 ÷ 200 seconds, because of the capacity system, figure 1, used for the air supply. In this blow-down tunnel, the air is stored in containers at high pressure (no more than 50 atmospheres) and discharged across the connecting high pressure pipe to a pressure control system, before operation in the combustion chamber and exhaust to the atmosphere through the turbine.

Operating flexibility is such that mass flow, pressure and temperature, both for air and gaseous hydrogen, as well as combustor and turbine variable geometry, may be changed as wanted. This occurs because of: a discharge variable nozzle to the atmosphere downstream the air pressure control system; an air heat transfer; and an axisymmetric air and gaseous hydrogen free turbulent mixing through an ejector system.

The test running time can vary, depending on the pressure level and capacity of the containers used (4, 8, 12, 16 or 20 cylindrical containers, 63.5 cubic feet each as volume) and on the weight flow per second supplying the turbine. After each run the containers are brought back to the conditions existing before the run by means of compressors with aftercoolers, water and oil separators, and dryers.
The pressure and the temperature of the air inside the containers vary during the run, because of the expansion of the air and the heat transmitted from the walls.
The pressure regulating valve in the control system is adjusted manually before each run according the average pressure wanted in the combustor. Therefore, weight flow per second, pressure and temperature vary downstream this control system. That is the reason because in a run lasting more minutes, only 100 ÷ 200 seconds may be considered steady for the test in progress. A lot of flexibility is offered by the turbine and hydraulic dynamometric brake in absorbing variable combustion gas power during initial and final running time.
A capacity heating system absorbing heat from the atmosphere is not sufficient, as the mixing temperature in front of the combustion chamber has to be higher than atmospheric. Heating is performed in a separate hot gas plant, installed in the main line between the pressure control valve and the gaseous hydrogen mixing zone.

By reason of the physical properties of liquid hydrogen, a superinsulated vessel is used, in which heat flow of radiation between internal and external surfaces is reduced by interposing shields of aluminium foils and thin layers of fibre glass. A centrifugal pump, designed for fully submerged operation, operates for delivering liquid hydrogen in a linear heat exchanger, from which the gaseous hydrogen forms an annular coaxial stream with the central air stream, before turbulent mixing in different equivalence ratio at the entrance of the combustor.

The combustor has been designed to meet the requirements of variable geometry combustion.

Turbine flow capacity can be changed restricting the annulus area.

The test facility has shown the necessary flexibility to carry out a complete set of experimental data on H_2-Air combustion for modern gas turbines.

THERMODYNAMIC DESIGN OF THE TEST FACILITY

The air storage system in figure 1 is suitable for steady combustion tests in the range of pressure from 14.696 psia to 285 psia. Constant mass flow may be lasting 60 seconds as minimum for the highest pressure.

Air flow is started by opening a pneumatic geared actuator gate valve, through which a given weight flow at any given stagnation pressure is delivered to a control system which connects the storage system to the combustion chamber and turbine exhaust system in the atmosphere. The pressure and the temperature of the air inside the storage cylindrical containers vary during the run. Downstream of the control system, the pressure is kept at a wanted constant value by means of a manually operated pressure-regulating valve (one for each required weight flow), sensitive to the pressure in the combustion chamber. The valve open gradually during the run. The temperature in the storage containers decreases because of the expansion of the air and decreases across the pressure regulating valve bacause of the Joule-Thomson effect. The initial temperature of the air and of the flasks is equal to or close to atmospheric. During the expansion process, heat is transmitted from the walls of the containers and pipes to the air. The heat transmission from the walls and the Joule-Thomson effect, which decreases when the pressure in the storage tanks decreases, tend to decrease the drop of the temperature of the air to the mixing zone of the combustion chamber.
For our low rates of weight flow, the relative stagnation temperature varies very slowly or remains about constant with time. Therefore, no control temperature is required. The heating system is required to keep the stagnation temperature constant for larger rates of weight flow.

Applying thermodynamic laws and heat balances to a weight air flow from a 1.181 inches exit diameter regulating valve, downstream of a four container vertical row for the total internal capacity of 254.25 cubic feet (one of the rows on figure 1), in which air is supplied at 734.8 psia and delivered downstream at 44.088 psia, one obtains:

- 528°R, as initial static temperature in the containers;
- 934.88 lb, as initial air weight in the containers;
- 0.272 cubic feet/lb, as initial air specific volume;
- air in the containers during running time t: specific volume v_1, static temperature T_1, static pressure p_1, weight P;
- air at the exit of the regulating valve: weight flow $\dot{P}$, specific volume v_2, static temperature T_2, static pressure p_2, air speed w_2;
- during the time, flow parameters are changing as in the following Table:

t	0	30	60	90	120	150	180	210	240	270	300
v_1	0.272	0.293	0.320	0.344	0.376	0.414	0.462	0.520	0.597	0.691	0.814
T_1	528.0	508.0	490.2	475.8	457.8	439.8	409.8	390.0	368.4	345.9	323.4
p_1	734.8	662.3	584.3	527.7	465.5	405.8	348.5	295.3	243.2	197.7	156.9
P	933.88	869.5	804.4	739.9	675.9	612.7	550.1	488.9	426.5	368.0	311.7
$\dot{P}$	--	2.175	2.150	2.135	2.108	2.084	2.042	2.023	1.949	1.871	1.773
v_2	--	3.51	3.99	3.31	3.23	3.15	3.06	2.94	2.83	2.72	2.59
T_2	--	401	391	383	373	362	342	330	317	303	290
p_2	--	44.088	44.088	44.088	44.088	44.088	44.088	44.088	44.088	44.088	44.088
w_2	--	1004	958	928	896	863	820	804	725	669	604

In a running time of five minutes, the weight flow is decreasing only 18.5%. But, for thermodynamic measurements, constant flow may be considered during one minute of discharge; for instance, from 30" to 90", the weight flow is decreasing 1.84%, with exit temperature T_2 about constant ($\Delta T_2 = 10°R$). Expansion is computed by the expression pv^n = constant, where n = 1.0955 (corresponding to an expansion efficiency $\eta = 0.3$).

The pressure recovery, due to kinetic energy drop at the combustion chamber entrance, is about lost in the mixing process with gaseous hydrogen.

Using an equivalence ratio, $\mu = (H_2/Air)/(H_2/Air)_{stoich} = f/f_{stoich} = 0.4$ (where f is fuel-air ratio) = $= \psi_{stoich}/\psi$ (where ψ is air-fuel ratio), we obtain, because of combustion

$$\Delta T = \varepsilon Q/c_p(1 + \psi) \simeq \varepsilon Q(f_{stoich}\cdot\mu)/c_p(f_{stoich}\cdot\mu + 1) \qquad (1)$$

in which, Q, ε and c_p are, respectively, hydrogen heat of combustion, combustion efficiency and specific heat at constant pressure.

Introducing the numerical values

$$Q = 51{,}590\ \text{BTU/lb},\ \varepsilon = 0.96,\ c_p = 0.378\ \text{BTU/lb°R}\ f_{stoich} = 0.029156$$

the combustion temperature and the exhaust speed c_4 from an expansion nozzle to atmosphere become, approximately

$$T_3 = T_2 + \Delta T = 390 + 1510 = 1900°R$$

$$c_4 = 0.95\sqrt{2g\cdot n\cdot 1546.6\cdot 1900\left|1 - (14{,}696/44.088)^{(n-1)/n}\right|/(n-1)m + w^2} = 2540\ \text{ft/sec}$$

with n = 1.35, w = 164 ft/sec, g = 32.2 ft/sec^2 and m = 25.4 = molecular weight

Referring to figure 2 and 3, we get, for a single stage action turbine, having the following characteristics:

- blade tip diameter 0.944 feet
- blade hub diameter 0.708 feet
- blade peripheral speed u = 984 feet/sec

$$\Delta w = 2930\ \text{ft/sec}$$

$$v_3 = 1545.6\cdot 1900/25.4\cdot 44.088\cdot 144 = 18.21\ \text{ft}^3/\text{lb}$$

$$v_4 = v_3(44.088/14.696)^{1/m} = 41.09\ \text{ft}^3/\text{lb}$$

$$\dot{P}_g = \pi\left|(0.472)^2 - (0.354)^2\right| c_4\ \text{sen}\ 20\cdot 0.33/v_4 = 2.135\ \text{lb/sec}$$

(where 0.33 is the nozzle arch of blading periphery)

$$W = \dot{P}_g \cdot \Delta w \cdot u/g \cdot 550 \approx 347.6 \text{ HP}$$

This power is provided by such a single stage action turbine, about 60 second from the opening of the actuating gate valve.

If the same single stage action turbine is supplied by eight of the containers in figure 1, with a total air capacity of 508.5 cubic feet at 734.8 psia, the temperature T_1 and pressure p_1 drops are quite less (curves 1 in figure 4) and a constant weight flow may be obtained for a double running time.

Referring now to figure 5, we get, for a single stage reaction turbine, supplied by sixteen of the containers in figure 1, with a total air capacity of 1017 cubic feet at 734.8 psia, the temperature T_1 and pressure p_1 drops shown (curves 3) in figure 4.
With a reaction degree of 0.5, the flow is undergoing an expansion in the static nozzles, along the total periphery from 44.088 to 26.453 psia, and another expansion, in the dynamic nozzles along the rotating blades from 26.453 to 14.696 psia, figure 5.

$$c_4 = 2540/\sqrt{2} = 1801 \text{ feet/sec}$$

$$\Delta w = 2398 \text{ feet/sec}; \qquad v_3 = 18.21 \text{ cubic feet/lb}$$

$$\dot{P}_g = \pi\left|(0.457)^2 - (0.354)^2\right| \cdot 1801 \cdot \text{sen } 20° / v_4 \; 6.08 \text{ lb/sec}$$

$$W = (6.08 \cdot 2398 \cdot 984)/32.2 \cdot 550 = 810 \text{ HP}$$

For testing purposes, the same turbine assembly was used. Only the stator vanes and the rotor blading were changed and manufactured according the very short test duration.
The weight flow supplied by the 1.181 inches diameter regulating valve was varying from initial 6.18 to 5.72 lb/sec after 6 minute running time. In the same period of time, the temperature and velocity are decreasing from $T_2 = 413°R$ to 320°R and from w = 997 ft/sec to 705 ft/sec.
Constant conditions may be accepted during the running time from 30 to 120 seconds, in which, downstream weight flow, temperature and velocity, range, respectively, from 6.18 to 6.07 lb/sec, 405 to 377°R, and 997 to 935 ft/sec.

Referring to figure 6 (modified free discharge Wright turbine), we carried out, for a single stage action turbine, supplied by four of the containers in figure 1, with a total air capacity of 254.25 cubic feet at 734.8 psia, the temperature T_1 and pressure p_1 drops shown (curves 2) in figure 4, according a 0.738 inches exit diameter regulating valve.
During the combustion tests, the hydraulic dynamometric brake took up 139 HP of power, according the turbine mechanical design. Weight flow, downstream temperature and velocity, could be considered at the constant values of 0.841 lb/sec, 400°R and 1000 ft/sec.
In the same conditions of figure 2 and page 3, we got (0.13 as nozzle arch blading periphery)

$$\dot{P}_g = \pi\left|(0.472)^2 - (0.354)^2\right| \cdot c_4 \text{ sen } 20 \cdot 0{,}13/v_4 = 0.841 \text{ lb/sec}$$

$$W = \dot{P}_g \cdot \Delta w \cdot u/g \cdot 550 = 136.9 \text{ HP}$$

Experimentation was conducted for the above mentioned lean mixture ratio (equivalence ratio $\mu = 0.4$) corresponding to combustion temperature $T_3 = 1900°R$ at $p_3 = 44.088$ psia. Operation is possible for higher and lower values of μ, T_3 and p_3.

Hydrogen handling - By reason of physical properties of liquid hydrogen, high efficiency thermal insulation must be adopted. Our small 5.3 cubic feet superinsulated storage vessel, figure 7, contains a reflecting layer type insulation together with a hard vacuum in the double jacket interspace. Radiation between the two coaxial surfaces is reduced by interposing n shields. The stainless steel inner vessel is suitable for a working pressure of 73.50 psia.

Figure 7 shows a general schematic diagram of the hydrogen system from the vessel Ref. 4. In the vaporizing circuit, firstly, a route I was tried, and liquid hydrogen flowed in the heat exchanger by gravity.
As the heat exchanger was located under the floor, and it had a sufficiently large heating surface, it was expected to vaporize the liquid hydrogen, and its temperature was to rise near the ambient air in a very short time. Then, the warmed hydrogen gas was expected to return to the tank and promote the vaporization so that to raise the pressure in the system soon.
In practice, however, when the liquid level in the tank was lower than about a half, the rate of the vaporization became so slow as to be insufficient for the combustion chamber operation.
Secondly, a gas pumps was incorporated to flow the hydrogen by force in the opposite direction.
Effort was made to rise the temperature of hydrogen gas as warm as possible at the entrance of the combustion chamber intake port. Therefore, hydrogen was conducted through a not insulated tube to the intake port. In practical running, the average temperature of the compressed hydrogen gas was about 400°R. Hydrogn-air mixing was at constant pressure and temperature.

Hydrogen has often been used as a fuel in combustion with air, because of its high burning velocity, wide

flammability range, high heating value per unit weight, and great flame stability.

From the relation between equivalence ratio μ and volume-percent hydrogen for H_2-Air mixtures, we have

μ = 0.2	H_2 in aria, by volume	= 8%
μ = 0.4	" " " " "	= 14%
μ = 0.6	" " " " "	= 20%
μ = 0.8	" " " " "	= 25%
μ = 1.0	" " " " "	= 29%

Figure 8 is a schematic representation of the flow situation encountered, with the prediction of the axisymmetric free turbulent mixing and combustion between a central cold hydrogen jet and coaxial air-stream. To assure conditions for the self-ignition of the hydrogen escaping from the central nozzle, the air is heated because of combustion of a small quantity of hydrogen in the pre-chamber.
The flammable range is widened by heating the unburned mixtures. That is, because the lean limit occurs at lower concentrations and the rich limit at higher concentrations as the mixture temperature is increased. For μ = 0.4 (14% by volume of H_2 in air) and mixture initial temperature T_2 = 400°R, the theoretical flame temperature at 44.088 psia is around 1980°R.

Combustion takes place in the inner mixing region between the two streams where oxygen and hydrogen are brought together at a temperature which is higher than the self ignition temperature.

The liquid-gaseous hydrogen fuel system in figure 7 has been designed, considering heat exchanges from an external high temperature source before the hydrogen pump and from the atmosphere temperature along the tube connecting the hydrogen vessel and the central cylindrical nozzle in figure 8.
The governing equations for the coaxial mixing of two dissimilar gases including heat release by chemical reactions in the mixing region were approximately applied in designing the flow field with combustion on figure 8. The Navier-Stokes equations of motion, the conservation of mass, the conservation of species, and the energy equation for a compressible flow were considered in the instantaneous form, assuming that the potential core region and the outer jet region consisted of chemically frozen, inviscid, and steady axisymmetric flow with body forces.

Variable geometry combustion chamber - The combustion has been designed to meet the requirements of a pre-mixed variable geometry chamber, including the possibility of operation in a wide field of equivalence ratios, pressures and temperatures.
The combustor may be considered as comprising three zones, primary, secondary and dilution. The air admitted in the primary zone is controlled by the movement of the baffle; the remaining air ports (secondary holes, dilution holes, film cooling devices) have constant cross-sectional areas. For varying and controlling the air flow distribution characteristics a vortex has been applied to a short diffuser, Ref. 1 and 2, requiring a small fraction of the main stream air to be bled from the vortex chamber to maintain stability.
Even though the hydrogen and air are premixed, an intermediate zone is required to prevent abrupt quenching of any partially completed reactions of the gases emerging from the primary zone.
The dilution zone is entirely conventional and requires no further comment.

Variable geometry turbines - With variable geometry, the off design behaviour can be influenced to a degree exceeding the limit set by the RPMs of the controlled rotor.
Figure 9 depicts a schematic view of an adjustable turbine stator.
The stator variable geometry is being used to improve the fuel consumption. As turbine inlet temperature is modified, the turbine nozzle area can be changed to allow (in the complete engine) the compressor to remain at its design point.

With fixed geometry turbines, there is only one flow-peripheral speed relationship. It is desiderable to change this relationship in order to improve the performance, or to use different kind of bladings on the same rotor disk for our testing purposes. Turbine flow capacity can be changed by restaggering the stator blades, allowing the flow to be increased above nominal, or by restricting the stator blades.
Restricting the annulus area is possible by mechanically introducing an obstruction into the flow, for instance by attaching wedges to the casing inside the blade passages, or by introducing an obstruction into the flow through air injection in annular grooves both ahead of and behind the stator and in slot at the stator throat.

With better materials technology, variable geometry in the hot parts of gas turbines appears feasible, and development of variable turbine advanced gas generators have been initiated by manufactures of regenerative gas turbines, because of operation at a practically constant specific fuel consumption. Varying the power turbine capacity permits a free selection of the gas generator operating point. This can be used to ensure sufficient surge margin for all operating conditions. The handling improvement obtained by this means can eliminate the necessity for variable compressor geometry or air bleeding, Ref. 3.
A variable geometry turbine must have a range of some 60° through which the vanes can be turned, in order to meet all engine requirements. This range provides, figure 10, continuous coverage from the smallest throat area up to the neutral position with the largest throat area.

An axial one stage variable geometry action turbine was designed, and its operating characteristics were

investigated by means our test facility on figure 1. The flow upstream of the test turbine was generated by means of the H_2- Air combustion chamber, for the above mentioned short blowdown running time.
In a series of tests, torques, efficiences and weight flows were measured at various vane turning angles, as a function of specific work at different peripheral speeds, comparing results with predicted performances.
A further special feature of variable nozzle guide vane geometry is the changing spacing between vane trailing edges and rotor blade leading edges, in order to study the possibility of resonance excitation.

Special instrumentation, capable of high response as well as steady-state outputs, is being experienced. The parameters of primary interest are pressures, temperatures, and vibrations. Dynamic sensing requires at least one sensing probe, figure 11, for each parameter being measured.
For pressure measurements, strain gauges are used, capable of measuring to within 0.05 percent over the full instrument range.
For temperature measurements, fluidic sensors, Ref. 6, operate on the principle of an edge-tone resonator. Turbulent flow entering the inlet of the sensor generates a tone with a frequency that is proportional to the acoustic velocity and the length of the acoustic path.

Glass fibre reinforced materials for testing turbine blading - Composite materials as used in gas turbine static structures are being used for turbine blades and their joint rings, undergoing high temperature gas flow for a very short duration (less than 200 seconds). In this way, it is possible to build inexpensive stator and rotor turbine bladings, each time applied on the same disk, in order to carry out a large variety of turbine tests, according the previous purposes to gain experience on H_2-Air combustion mixtures at different pressures and temperatures.
There are a number of materials which have greatly enhanced strengths when they are produced in a fine filament form. The most important fibre materials at present available are glass fibre, carbon fibre, and boron fibre. An application of special interest, using plastic materials reinforced by glass fibres, is the air intake duct for the engine T.64 installed in the FIAT G222 aircraft.

In our case, the material operating temperatures have no time to reach critical values. Therefore, the use of present synthetic resin plastic matrix material is not restricted. As it is known, in order to make use of glass fibres, they have to be embedded in a suitable matrix, so that the product can have rigidity and accuracy of form.
The structure of the blade ring containment must be provided with reinforcement in the plane of the stator or rotor disk able to support the vanes or blades detached in case of failures.

H_2-AIR VARIABLE GEOMETRY COMBUSTION CHAMBER

For varying the air flow distribution characteristics during combustion, in order to have different gas mixture equivalence ratios and temperatures, a vortex flow control device was used, Ref. 1 and 2.
To retain a stable vortex and to have the required variation in primary zone flow, by recircolation from the secondary zone, an air bleed-off was provided. A vortex controlled diffuser was described in Ref. 7, which relied solely on the aerodynamic design of cusps in the diffuser walls to locate vortices in a manner as shown in figure 12. By the air-bleed system, air is extracted from a port, entered the actuator assembly and passed through a filter to the atmosphere. A small portion of this air is bled through an orifice to an external line which directs it to a slide valve located on the hydrogen regulator housing.

In this way it was possible to carry out H_2-Air combustion tests with equivalence ratios $\mu = 0.4$ to $\mu = 0.8$. Figure 13 is showing a schematic view of the combustion chamber.

To determine analitically the local values of the average flow field parameters, a computational model was developed which includes the numerical solution of the conservation equations for the boundary layer. The governing equations are reduced to the boundary layer type form by assuming the negligibility of diffusion in the axial direction and of energy transfer by conduction in the axial direction, and the dependence of viscous shear stresses primarily in the radial gradient of axial velocity.
The numerical method of solution for computing the lines of constant flow quantities in the mixing zone, figure 8, is provided by Ref. 8.
A comparison between the computation and the results of experimental investigation shows that the location of the visible flame boundary is closer to the nozzle exit.

The first steps of our test facility were concerning setting up of the main components for handling hydrogen, from liquid to gaseous state, solving a lot of complex problems introduced by the high temperatures of combustion, even though at low equivalence ratios. As a first approach, the flame temperatures increase almost linearly with initial mixtures temperature. As the composition approaches stoichiometric, however, dissociation becomes more important, and flame temperature less dependent on initial mixtures temperature.

In high temperature combustion, the approach to chemical equilibrium is rapid. When the gas undergoes an expansion, as in turbine nozzles, the chemistry is initially near to equilibrium. The fall in temperature consequent upon the acceleration of the flow induces changes in chemical composition which attempts to follow the changing position of chemical equilibrium.

Hydrogen-fueled gas turbines offer worthwhile environmental gains: emissions of carbon monoxide, carbon dioxide, hydrocarbons and smoke, are virtually eliminated.
Hydrogen provides for a much wider fuel/air ratio operating range than conventional thermal engine fuel. Because of this, hydrogen fuel brings with it the potential for theoretical reductions in nitric oxide

formation of about two orders magnitude for the same primary zone dwell time. Dwell time is a measure of the time the combustion products remain at full temperature prior to air dilution and/or expansion in turbine, usually the order of millisecond or so. A second significant route to lower oxides of nitrogen production is much higher "space heating rates" of the hydrogen; this giving the possibility to considerably shorten engine combustor length and associated dwell times.

At the moment, the only well-developed water-splitting process we have is electrolysis. Solar energy may some day power hydrogen generation. And hydrogen may prove a better medium than electricity.

Projecting to the last decade of this century, and beyond, hydrogen may be, as a consequence of recent events on the energy front, the "ECONOMIC FUEL" of the future.

REFERENCES

L. R.C. Adkims, "A Short Diffuser with Low Pressure Loss", ASME/CSME Conference, Montreal, Canada, May, 1974

2. R.S. Fletcher and R.C. Adkins, "The Variable Geometry Combustor", 48th PEP Meeting, AGARD Conference, Paris, September, 1976

3. J. Hourmouziadis, K. Hagemeister, O. Rademacher and H. Koblen, "Experience with One Stage Variable Geometry Axial Turbine", 48th PEP Meeting, AGARD Conference, Paris, September, 1976

4. L. Martorano, "Trasformazione di un Motore Automobilistico per il Funzionamento ad H_2", 32nd Congresso Nazionale ATI, Roma, 1977

5. D. Dini, "Performance Characteristics of Turbo-Rockets and Turbo-Ramjets Using High Energy Fuel", 48th PEP Meeting, AGARD Conference, Paris, September, 1976

6. D. Dini and M. Santochi, "Fluidic Sensors for Turbojet Engines", 44th PEP Meeting, AGARD, Ustaoset, Norway, September, 1974

7. F. O. Ringleb, "Flow Control by Generation of Standing Vortices and the Cusp Effect", Aeronautical Engineering Report N_o. 317, Princeton University, July, 1953

8. H. Rörtgen, "Theoretical Analysis of Non-equilibrium Hydrogen Air Reactions between Turbulent Supersonic Coaxial Streams", 43rd PEP Meeting, AGARD, Liege, April, 1974

9. R. Lazzeretti, G. Nardi and D. Dini, "Fabrication Techniques of Compact Fluidics Control Equipment for Aerospace Engines", 35th PEP Meeting, AGARD, London, April, 1970.

ACKNOWLEDGEMENTS

The authors wish to gratefull acknowledge the contribution made by Mrs G. Cei and Mr S. Fiorini in typewriting and drawing the present Paper and further development studies.

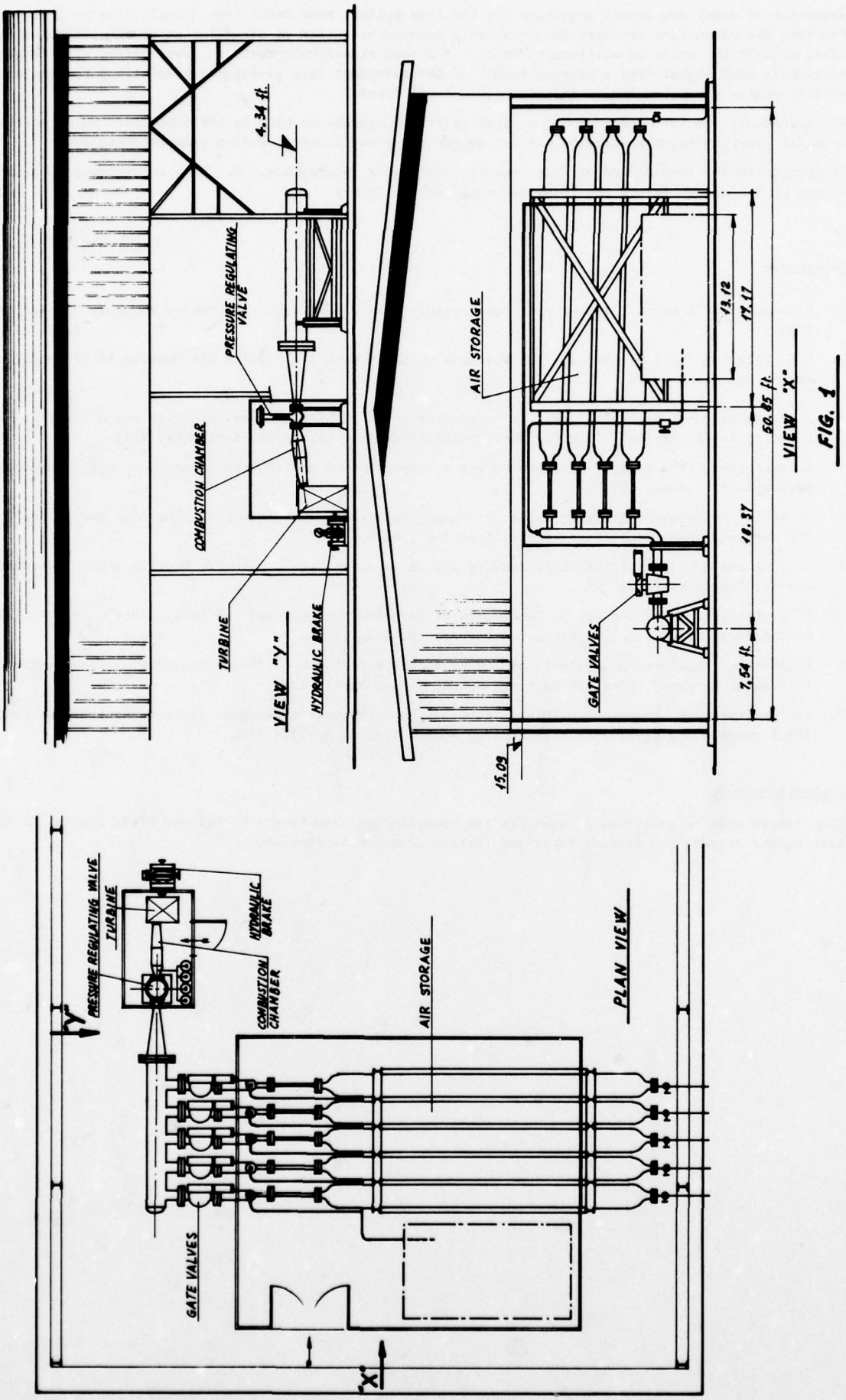
4.34 ft.
PRESSURE REGULATING VALVE
COMBUSTION CHAMBER
TURBINE
HYDRAULIC BRAKE
VIEW "Y"
AIR STORAGE
GATE VALVES
13.12
17.17
18.37
7.54 ft.
60.85 ft.
15.09
VIEW "X"
PRESSURE REGULATING VALVE
TURBINE
HYDRAULIC BRAKE
COMBUSTION CHAMBER
AIR STORAGE
GATE VALVES
PLAN VIEW
Y
X

FIG. 1

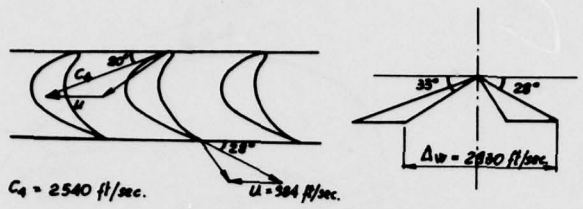

Fig. 2

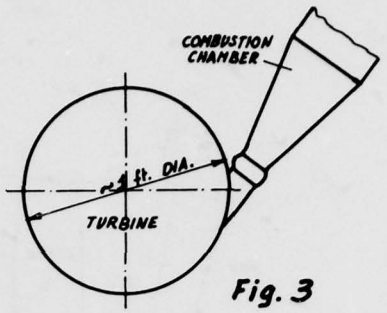

Fig. 3

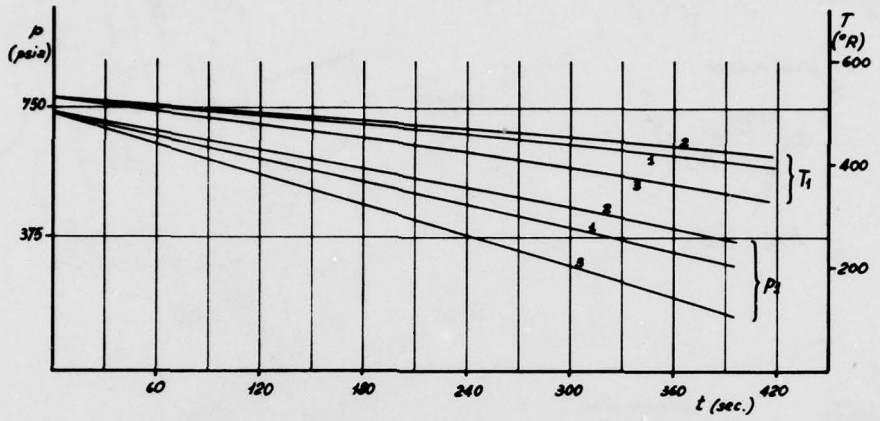

Fig. 4

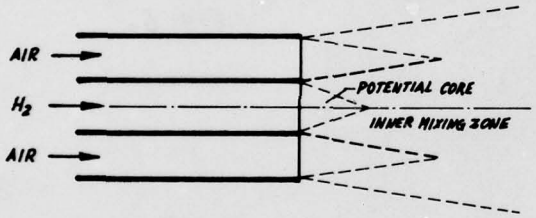

Fig. 8

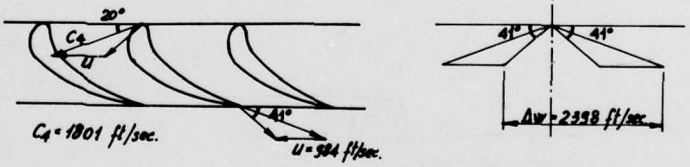

Fig. 5

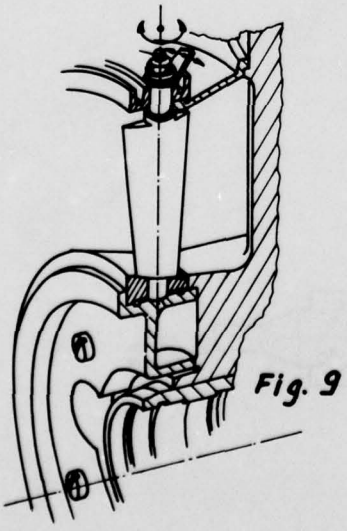

Fig. 9

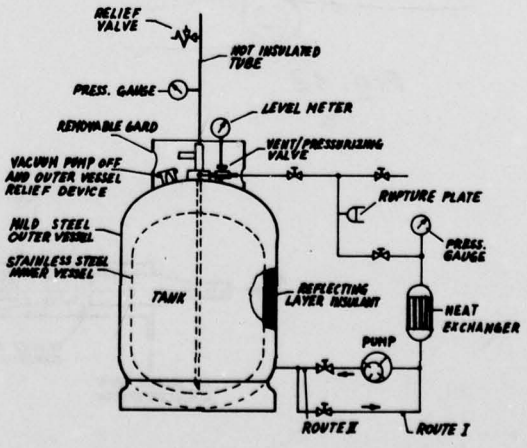

Fig. 7

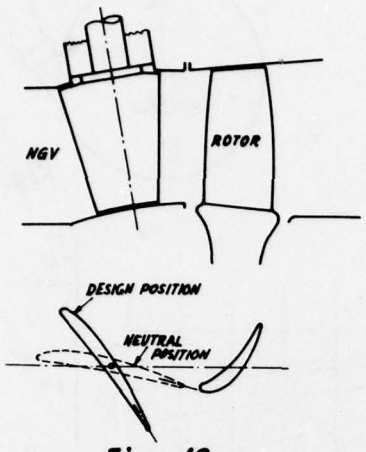

Fig. 10

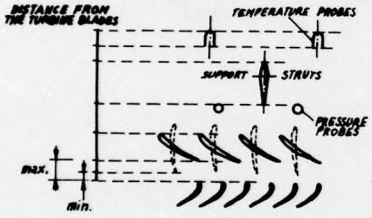

Fig. 11

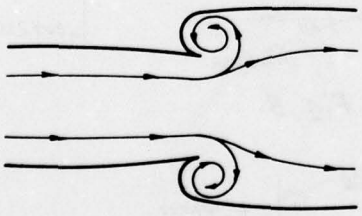

Fig. 12

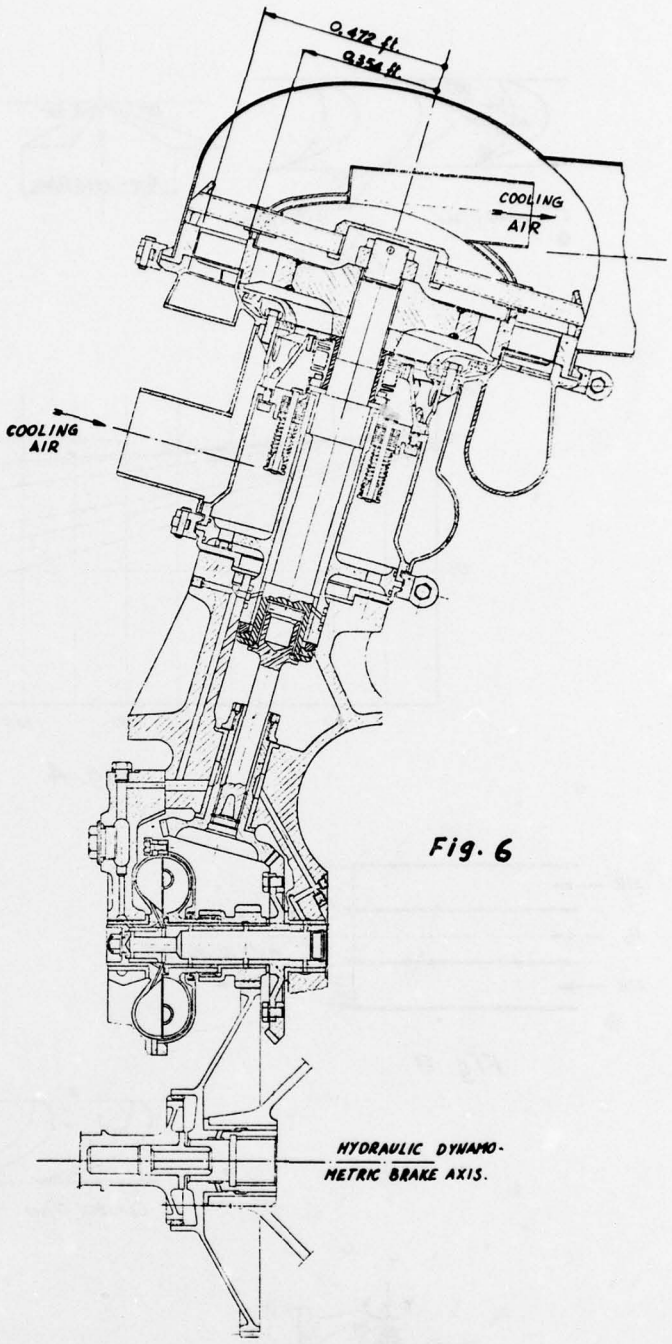

Fig. 6

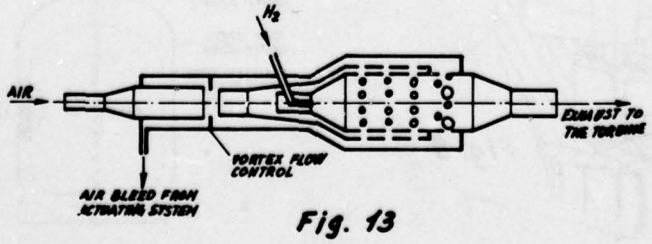

Fig. 13

LOW FREQUENCY COMBUSTION INSTABILITY IN AUGMENTORS

by

F.N.Underwood
Air Force Aero Propulsion Laboratory, Wright-Patterson AFB, Ohio, USA

and

J.P.Rusnak, R.C.Ernst, E.A.Petrino, P.L.Russell and R.Murphy, Jr
Pratt & Whitney Aircraft, Government Products Division
West Palm Beach, Florida, USA

SUMMARY

With the advent of the mixed-flow afterburner in turbofan engines, a type of low-frequency combustion instability known as rumble or chugging has become a serious problem. "Cut-and-try" methods during engine development have been partially successful, but very expensive. To aid the development engineer in designing afterburners that are free from this low-frequency instability, an analytical model has been formed. The model has evolved in conjunction with and checked by an experimental program. Rumble mechanisms investigated in this study include the system airflow dynamics, combustion efficiency oscillations, fuel vaporization, recirculation wake energy, and turbulence upstream of the flameholders. Comparisons of the model predictions with experimental data have been good.

NOMENCLATURE

C	speed of sound
FA	fuel/air ratio
K_1	wake recirculation coefficient
ℓ	axial lengths between stations
M	Mach number
N	flameholder width
p	pressure
q	volumetric heat release rate
s	entropy or Laplace transform variable
T	temperature
T_i	ideal temperature rise
t	time
u	internal energy
V	velocity or volume of combustion zone
X	axial location
W	mass flow rate
β_1	pre-flameholder vaporization coefficient
β_2	fuel collection coefficient
β_3	surface vaporization coefficient
η	augmentor efficiency
θ	overall fuel-air ratio, or term as defined
ϕ	wake fuel-air ratio
ρ	density
ψ	stability parameter
w	frequency

$\bar{}$ superscript denoting steady-state value

Δ change in a variable from its steady-state

$'$ change in a variable divided by its steady-state

I. INTRODUCTION

While the phenomenon of combustion instability has plagued all types of high heat release combustors, the problem has been most severe in flight propulsion systems where weight considerations require highly efficient structures. In turbojets, ramjets, and rockets, the pressure, vibration, and heat loads resulting from combustion instability, superimposed on the normal loading, are usually destructive.

In the early 1950's high frequency combustion instability (screech) presented problems in airbreathing engines. Engineers sought solutions through mathematical modeling and analytical studies, but unfortunately the computer technology and analytical techniques of twenty years ago proved inadequate. Engine manufacturers turned to "cut-and-try" empirical approaches involving changes in flameholders, combustion chamber shape, fuel injection, velocity profiles, and flame piloting. They tested fuel additives and combustion chamber baffles. Although some of these approaches, notably baffles, produced marginal improvement, the problem was not solved until damping devices in the form of acoustical absorbers (screech liners) were introduced. Screech liners are used routinely and high frequency instability is no longer regarded as a problem.

With the advent of the mixed-flow afterburner in turbofan engines, a type of low frequency instability known as rumble or chugging became a serious problem. Rumble is a periodic afterburning combustion instability (pressure oscillations fed by the combustion process) occurring usually at high fuel/air ratios at flight Mach numbers and altitudes when low duct inlet air temperatures and pressures exist. This instability usually leads to afterburner blowout and/or fan surge and engine stall. The frequency of oscillation usually lies between 30 and 200 Hz. This occurrence of instability at lower frequencies makes use of screech liners of conventional design inappropriate. For adequate damping, the absorbing devices are designed so that the resonant frequency corresponds to the expected frequencies of pressure oscillations. Since the required cavity volume for the liner is inversely proportional to the square of the resonant frequency, the liners of large cavity volumes required for low frequencies would necessitate an unacceptable increase in engine weight.

Data from engine programs and early rumble investigations suggest several possible mechanisms which regulate or cause low frequency combustion instability in afterburners. They can be summarized under the following categories:

1) Longitudinal system dynamics.

2) Pressure disturbances at the fuel injector

3) Combustion efficiency oscillations

4) Insufficient and/or non-uniform fuel vaporization

5) Low recirculation wake energy

6) Turbulence upstream of the flameholder.

Even subtle changes in flameholder designs have altered the rumble characteristics of a turbofan engine. With some experience at hand, the design engineer has successfully produced "fixes" for unstable conditions. Redistribution of the fuel-to-air mixture ratio has worked, and deriching the fan duct has lessened rumble problems in the past. However, complete understanding of this combustion/dynamics problem has been inadequate to design rumble-free mixed flow afterburners with confidence.

The purpose of this research project is to devise a reliable empirical and analytical model that will aid afterburner designers. The approach used began by isolating mechanisms thought to contribute to rumble. As the major mechanisms were being investigated, a mathematical model that could predict unstable conditions and that could be extended to innovative designs was carefully developed.

This research is being conducted by the Government Products Division of Pratt & Whitney Aircraft under United States Air Force contracts F33615-76-C-2023 and F33615-76-C-2024.

II. MATHEMATICAL MODEL

The trial-and-error, "cut-and-try" method used so extensively by turbine engine manufacturers to correct unstable combustion problems in the afterburners of turbofans is expensive and time consuming. Ideally, the development engineer should design the afterburner free from rumble at the outset. This has not been the case in the past. We undertook this research program not only to learn more about rumble (or chugging), but we began this effort to give the designer tools with which he can develop stable burning augmentors. For the tools to be practical, however, the mathematics must be rigorous enough to model the physics accurately, yet simple enough to be used by engineers other than the originator. For this reason, and because of the current state of the art, we pursued a linear analysis of this combustion problem.

The mathematical model of the augmentor system was developed using linearized continuity, momentum, and energy equations for one dimensional time variant flow. The equations describe the interrelationship of pressure waves traveling downstream at the speed of sound plus throughflow velocity and upstream at the speed of sound minus the throughflow velocity. Laplace transform techniques were used to obtain a distributed parameter solution in the frequency domain relating pressures, temperatures, and velocities at the fan exit, flameholder, and nozzle exit plane to the heat release rate and location within the augmentor.

The system stability was assessed using standard control theory techniques. The open loop frequency response technique used is shown schematically in Figure 1. In this method of stability assessment, the linearized heat addition rate q is forced to vary sinusoidally at an amplitude A and frequency w. The linearized system equations are simultaneously solved for pressure, temperature, and velocity perturbations throughout the system. System instability is predicted whenever the forced heat release q_{in} and the predicted heat release q_{out} are in phase, and in addition, the amplitude of q_{out} is equal to or greater than q_{in}. Physically, this means the system becomes unstable when a perturbation in flameholding conditions produces a heat release perturbation in phase with and equal to or greater than the initial disturbance.

The augmentor model geometry, shown schematically in Figure 2, was a long pipe fed by a choked inlet orifice. In a turbojet augmentor, station (1) would represent the turbine discharge and station (9) the upstream face of the exhaust nozzle. In a turbofan duct augmentor, station (1) would represent the fan discharge.

Fuel was supplied through spraybars at station (4). The resulting fuel-air mixture flowed over a set of flameholders between stations (5) and (6). For some tests, a screen was inserted upstream of the spraybars between stations (2) and (3) to generate turbulence in the air stream.

The flameholders divided the augmentor into a cold upstream section and a hot downstream section. The cold section was at uniform pressure and temperature except in cases of a small pressure drop which occurred when the turbulence screen was in place.

Based upon the empirical correlation of Ref 1, shown in Figure 3, the hot section was divided into three zones. Between stations (6) and (7) the flameholder wake ignites the fuel-air mixture with little heat being released and with a small temperature rise. At station (7) temperature begins to rise sharply as the ignited mainstream mixture begins burning. Between stations (7) and (8) the majority of combustion takes place. The locations of the beginning and the end of the combustion zone and the temperature rise were computed from the efficiency correlation of Figure 3 and the ideal temperature rise correlation of Figure 4.

For any section of augmentor with rigid walls and constant cross-sectional area through which an inviscid fluid flows, the one-dimensional continuity, momentum, and energy equations are:

$$\frac{\partial P}{\partial x} + \rho V \frac{\partial V}{\partial x} + \rho \frac{\partial V}{\partial t} = 0$$

$$\rho \frac{\partial V}{\partial x} + V \frac{\partial \rho}{\partial x} + \frac{\partial \rho}{\partial t} = 0 \qquad (1)$$

$$q + \frac{PV}{\rho}\frac{\partial \rho}{\partial x} + \frac{P}{\rho}\frac{\partial \rho}{\partial t} = \rho V \frac{\partial u}{\partial x} + \rho \frac{\partial u}{\partial t}$$

For an ideal gas non-linear wave equations may be written:

$$(V+C)\left[\frac{1}{P}\frac{\partial P}{\partial x} + \frac{\gamma}{C}\frac{\partial V}{\partial x}\right] + \left[\frac{1}{P}\frac{\partial P}{\partial t} + \frac{\gamma}{C}\frac{\partial V}{\partial t}\right] = (\gamma-1)\frac{q}{P}$$

$$(V-C)\left[\frac{1}{P}\frac{\partial P}{\partial x} - \frac{\gamma}{C}\frac{\partial V}{\partial x}\right] + \left[\frac{1}{P}\frac{\partial P}{\partial t} - \frac{\gamma}{C}\frac{\partial V}{\partial t}\right] = (\gamma-1)\frac{q}{P} \qquad (2)$$

$$V\left[\frac{1}{P}\frac{\partial P}{\partial x} - \frac{\gamma}{\rho}\frac{\partial \rho}{\partial x}\right] + \left[\frac{1}{P}\frac{\partial P}{\partial t} - \frac{\gamma}{\rho}\frac{\partial \rho}{\partial t}\right] = (\gamma-1)\frac{q}{P}$$

The wave equations are linearized by the small perturbation substitutions for P, ρ , C, V, and q:

$$P(x,t) = \bar{P}(x) + \Delta P(x,t) \qquad (3)$$

Second order terms are neglected. It is further assumed that mean values of the steady-state parameters $\bar{P}(X)$, $\bar{V}(X)$, $\bar{C}(X)$ can be chosen so that $\bar{P}$, $\bar{V}$, $\bar{C}$ can be considered constants. That is:

$$\frac{d\bar{P}(x)}{dx} = \frac{d\bar{V}(x)}{dx} = \frac{d\bar{C}(x)}{dx} = 0 \tag{4}$$

To simplify notation, the following substitutions are made which normalize the change in each variable with its steady-state value

$$P' = \frac{\Delta P}{\bar{P}}, \; V' = \frac{\Delta V}{\bar{V}}, \; \rho' = \frac{\Delta \rho}{\bar{\rho}}, \; q' = \frac{\Delta q}{\bar{q}} \tag{5}$$

For zero initial conditions, the solution of equations (2) from a station (1) at X = 0 to a station (2) at X = ℓ, written in terms of the Laplace transorm of each normalized variable, is

$$\begin{aligned}
P_2' + \gamma\bar{M}V_2' &= [P_1' + \gamma\bar{M}V_1']e^{\frac{-\ell S}{\bar{C}(1+\bar{M})}} + \theta_1 \\
P_1' - \gamma\bar{M}V_1' &= [P_2' - \gamma\bar{M}V_2']e^{\frac{-\ell S}{\bar{C}(1-\bar{M})}} + \theta_2 \\
P_2' - \gamma\rho_2' &= [P_1' - \gamma\rho_1']e^{\frac{-\ell S}{\bar{C}\bar{M}}} + \theta_3
\end{aligned} \tag{6}$$

Where

$$\begin{aligned}
\theta_1 &= \frac{(\gamma-1)}{\bar{C}(1+\bar{M})} \int_0^{\ell} \left(\frac{\bar{q}}{\bar{P}}\right) q'(x,s)\, e^{\frac{-(\ell-x)S}{\bar{C}(1+\bar{M})}}\, dx \\
\theta_2 &= \frac{(\gamma-1)}{\bar{C}(1-\bar{M})} \int_0^{\ell} \left(\frac{\bar{q}}{\bar{P}}\right) q'(x,s)\, e^{\frac{-xS}{\bar{C}(1-\bar{M})}}\, dx \\
\theta_3 &= \frac{(\gamma-1)}{\bar{C}\bar{M}} \int_0^{\ell} \left(\frac{\bar{q}}{\bar{P}}\right) q'(x,s)\, e^{\frac{-(\ell-x)S}{\bar{C}\bar{M}}}\, dx
\end{aligned} \tag{7}$$

In equations (6) the first equation describes downstream running waves of the form $P' + \gamma \bar{M}V'$, traveling at sonic speed plus throughflow velocity. The second equation describes upstream running waves of the form $P' - \gamma \bar{M}V'$, traveling at sonic speed minus throughflow velocity. The third equation describes entropy waves, $P' - \gamma\rho'$, drifting downstream at throughflow velocity.

Figure 5 describes the model used for the development of the combustion equations. Taking into consideration particle drift times, ideal temperature rise, fuel/air ratio, combustion efficiency, and the stability parameter, equations for heat release in terms of the Laplace transform of each normalized variable can be written:

$$q_6' = W_6' - \left[\frac{\overline{FA}}{\overline{Ti}}\frac{\partial Ti}{\partial FA} + \frac{\overline{FA}}{\bar{\eta}}\frac{\partial \eta}{\partial FA}\right] W_4' \, e^{\frac{-\ell_4 S}{\bar{V}_4}} + \frac{\bar{\psi}}{\bar{\eta}}\frac{\partial \eta}{\partial \psi}\psi' \qquad (8)$$

$$q_7' = q_6' \, e^{\frac{-\ell_4 S}{\bar{V}_4}}$$

$$q'(x,s) = q_7' \, e^{\frac{-xS}{\bar{V}_s}}$$

Terms $\frac{\overline{FA}}{\overline{Ti}}\frac{\partial Ti}{\partial FA}$ and $\frac{\overline{FA}}{\overline{M}}\frac{\partial M}{\partial FA}$ are defined from the ideal temperature rise curve, Figure 4, and the efficiency curve, Figure 3.

The solution technique is based upon the Nyquist stability criterion, and consists of determining whether the time response of the system to a small disturbance would display oscillatory behavior with a growing amplitude. A physical interpretation of the solution technique can be gained by reference to Figure 6. A sinusoidal disturbance oscillation in combustion heat release, q_{in}, produces an oscillation in pressure, velocity, and density throughout the augmentor, which in turn produces an oscillation in combustion heat release, q_{out}. If the "feedback" heat release is in phase with the disturbance, and has greater amplitude, the system will be unstable. A typical open loop transfer function is plotted in Figure 7 which indicates an instability at 56 Hz.

III. EXPERIMENTAL TESTING

The experiments were conducted in a combustion tunnel in which the pressures, temperatures, and gas flows of an augmentor were simulated. The circular cross-sectional rig was designed so that various configuration changes, including flameholders, spraybars, and distances between reflective points, could be made easily. Figure 8 shows a drawing of the test rig.

A. INSTRUMENTATION

The instrumentation monitored the airflow, fuel flow, rig inlet total pressure and temperature, combustor exit total pressure, combustor-pressure oscillations, fuel temperature, flowrate, and pressure, velocity changes in the duct, temperature changes in the combustor, pilot burner and acetylene flow rates, and the flameholder skin temperature. Most of the data were recorded by an automatic data recording system and were reduced with the use of an IBM 370/168 computer. The combustor was instrumented with six (6) high-response Kistler Model 606A pressure transducers to determine both the frequency and the type of wave occurring during combustion instability. The phase relationship and relative amplitude of the oscillations provided the necessary information to identify wave pattern and amplitude gains during rumble. An oxy-acetylene pilot torch was mounted in the recirculation zone of the center flameholder to provide continuous ignition and simulated piloting by wake heat addition. The center flameholder position was instrumented with two skin thermocouples.

Two four inch diameter vycor glass viewing ports were located 180° apart at the training edge of the primary flameholder so that high-speed motion pictures could be made.

The primary purpose of the first series of tests, was the determination of the rumble characteristics of the rig. The first series also was used to evaluate the rig hardware and its instrumentation. With a successful completion of these initial tests, the rest of the experiments could be run. Figure 9 details the experimental testing schedule.

B. ANALYSIS AND RESULTS

During rumble (chugging) pressure amplitudes were recorded as a function of time. Typical amplitudes occurring prior to blowout are shown in Figure 10. The plots indicate the presence of more than one frequency with amplitude of the higher frequency varying with time. To distinguish phase and amplitude relationships between various Kistler probes, all of the pressure amplitude data recorded on magnetic tape in the second series of tests were electronically processed in transfer function form; that is, they were expressed as the amplitude ratio and the phase difference between two pressure readings as a function of frequency. The flameholder Kistler probe served as the base for comparison. Approximately 100 different combinations of inlet pressure, temperature, airflow, fuel-air ratio, choked and unchoked nozzles were investigated investigated in the first test phase for two different flameholder blockages. Fuel distribution and exhaust nozzle conditions were found to have a significant effect on rumble amplitudes and blowout characteristics. Fuel distribution is shown in Figure 11 to affect both rumble amplitude and blowout fuel air ratio. The lowest pressure amplitudes and the widest blowout limits are obtained with uniform fuel distribution. Fuel distribution also affects stability at high fuel-air ratios.

Testing the effect of nozzle conditions on the stability of combustion was initiated with an unchoked nozzle and then the nozzle was choked. The nozzle area was closed holding a constant fuel-air ratio and nozzle discharge pressure. In another method, nozzle discharge pressure was reduced at a constant

nozzle area and fuel-air ratio. Both methods resulted in rig blowout.

(1) Baseline

The instability pressure amplitudes recorded during the baseline configuration testing are shown in Figure 12 to be primarily a function of fuel-air ratio and to a smaller extent a function of the blowout parameter, $\frac{V}{NPT^{1.7}}$. The trends depicted in this figure are representative of most of the configurations tested. The baseline rumble frequencies encountered ranged from 50 to 70 Hz.

(2) Airflow Dynamics

The system airflow dynamics are dependent on pressure waves which, reflected between different axial surfaces, cause a change in the combustion process. These combustion changes initiated by any disturbance can feed an oscillation until its amplitude grows until augmentor blowout or engine stall occurs. Different duct lengths from the upstream reflecting surface to the spraybars were tested. Figure 13 shows that this length change, and consequently, airflow dynamics, contribute to rumble.

(3) Fuel Vaporization

Poor fuel vaporization increases the flameholder wake mixture ratio above freestream value. In fact, it is possible for the flameholder wake to have a stoichmetric fuel-air ratio with a lean freestream. Further increases in fuel flow creates an overly rich flameholder wake, reducing wake efficiency, which lowers the overall combustion efficiency.

Any change in airflow will change the fuel distribution between the wake and the freestream, affecting combustion efficiency. Gaseous methane and JP4 caused high amplitude rumble oscillations for equivalence ratios between 0.9 and 1.2. Since rumble occurs at a higher fuel-air ratio with the gaseous fuel than with the liquid fuel, it appears that vaporization has a significant effect on rumble. However, these results are somewhat clouded because of the possibly different fuel distributions of the JP4 and the methane tests (Figure 14).

Another check on vaporization effects was made by moving the spraybar away from the flameholders. Figure 15 does not confirm the suspicion that extra flameholder-to-spraybar distance will improve stability. Fuel distribution apparently affects the results. Although we could not completely isolate the effect of fuel distribution as a rumble mechanism, we did show that the effect of fuel distribution on the fuel-air ratio in the flameholder wake is very important in the stability of the augmentor system, and it, in fact, may be the overriding consideration in determining augmentor stability.

(4) Turbulence

The mechanisms through which turbulence affects augmentor stability involves the rate of addition of unburned fuel-air mixture to the flameholder recirculation region, specifically the residence time of a particle in the flameholder wake. Too much mainstream turbulence can reduce the wake efficiency thereby generating a combustion heat release perturbation, which could interact dynamically with the augmentor-fan duct system. On the other hand, turbulence generators add stiffness in the system which can affect airflow dynamics.

Screens with two and three percent pressure loss were placed in the duct upstream of the flameholders and spraybars. From data presented in Figure 16 one concludes that the screens improve the system stability at low values of blowout parameter, but they have little effect on stability at higher values of blowout parameter.

IV. COMBUSTION/FLAMEHOLDER MODEL

In the current study a general data correlation (see Figures 3 and 4) provides combustion information for the system model. However, another investigation is underway to model combustion in the afterburner. After that study is complete, it will be incorporated into the system model to produce a more comprehensive model of rumble.

This flameholder stability model describes the combustion process response of wake efficiency and turbulent flame speed as functions of inlet pressure and temperature, flameholder blockage and geometry, fuel-air ratio, fuel vaporization, and inlet dynamics (pressure and velocity changes as well as turbulence level). The physics begins with the injection of liquid fuel through a spraybar upstream of the flameholder. While some fuel vaporizes immediately, some fuel as droplets accelerate with the airstream toward the flameholder, vaporizing concurrently. At the flameholder's leading edge droplets impinge on the surface forming a liquid film. Some liquid is vaporized by the heat flux from the hot wake through the flameholder surface, and it enters the recirculation zone through the shear layer, providing fuel vapor for the wake reaction process. Some fuel is lost to the recirculation as it detaches from the flameholder and is carried downstream by the flow. Through an iteration procedure, wake fuel-air ratio, wake reaction level, and wake temperature are calculated. Figure 17 is a schematic for the model with fuel-air ratio being treated by the following equation:

$$\frac{\phi}{\theta} = \beta_1 + (1-\beta_1)\frac{\beta_2\beta_3}{K_1}$$

where $\emptyset$ is the wake vapor phase fuel-ratio, θ is the approach fuel-air ratio, β_1 is fuel vaporization, β_2 is fuel droplet collection rate, β_3 is the gutter surface fuel vaporization and K_1 is vapor recirculation.

The impact of the flameholder occurs as turbulence generation and flow acceleration. These conditions in turn affect the recirculation zone where the combustion occurs in a well-stirred chemical reactor volume. Combustion efficiency is evaluated by integration of the spread of the turbulent flame speed, which is a function of fuel-air ratio and approach conditions.

V. CORRELATION WITH DATA

The math model underwent continued refinement as test results from the rig became available. Mathematical descriptions were based on physical reality and their ability to track test data. Comparisons between test and analysis were good, but adjustments in the math have improved the model's capability of simulating experiment. Some examples of comparison follow.

Rig test results generally show a rising rumble amplitude as fuel-air ratio increases above stoichometric (Figure 18). Model predictions display a rapid movement from the stable to the unstable operating region as fuel-air ratio increases (Figure 19). The model also predicts rumble as fuel-air ratio is lowered, but in this test case lean blowout usually occurs with little rumble amplitude.

The model also indicates that, in addition to fuel-air ratio management, rumble can be controlled by damping oscillations in the spraybar-to-flameholder region. A turbulence screen with a low pressure drop (5% $\Delta P/P$) was placed 40 inches upstream of the flameholder. There was no dramatic reduction in rumble amplitudes, although some runs showed some reduction. Since the experimental results of damping were not major, we infer that the math model was overly sensitive to the addition of damping. The source of the damping was identified as the temperature gradient of the combustion zone in the wave equations.

An estimate of the influence of the gradient on airflow dynamics was made by modeling the gradient as two step changes, one at the beginning and the other at the end of the combustion zone. The spacing between the two steps had limited the checkout to frequencies up to about 60 Hz. A system resonance at 30 Hz, which the model previously failed to predict, was now predicted. Also, a resonance at 70 Hz was now predicted to be lower in amplitude at a fuel-air ratio of .10 and higher in amplitude at a fuel-air ratio of 0.06. Airflow dynamics were affected enough to necessitate an accounting of temperature gradient.

Preliminary stability predictions for the rig with a long duct and with a short duct (duct length upstream of the flameholder reduced from 80" to 40") using the two-step approximation for the temperature gradient were made. The strong stabilizing trend of shortening the duct length observed in rig data was predicted by the model as a reduction in amplitude ratio of the open-loop transfer function for the short duct.

In general, the results of the test rig data agree well with the analytical model. The brief discussion in this section typifies the kind of analysis that has helped modify the model to improve its prediction capability. The research effort described in the Combustion/Flameholder Section of this paper which is to be incorporated into this sytem model is expected to improve the model's capabilities.

VI. CONCLUSIONS

Low frequency combustion instability (rumble or chugging) is a system problem in which the airflow dynamics couple with the combustion process. Several general comments can be made. Experimental rig test data identify airflow dynamics and fuel distribution as rumble contributors. Increased wake heat addition, decreased wake fuel-air ratio through flameholder geometry, increased turbulence level, and increased fuel vaporization help reduce rumble. The distance between the fuel injectors and flameholders should be short. The system model predicts rumble conditions well, but will be improved with the addition of an improved flameholder/combustion section that currently is being developed.

VII. REFERENCES

1. Petrien, R. J. Longwell, J. P., and Weiss, M. A., "Flame Spreading from Baffles," Jet Propulsion, February 1957, p. 81.

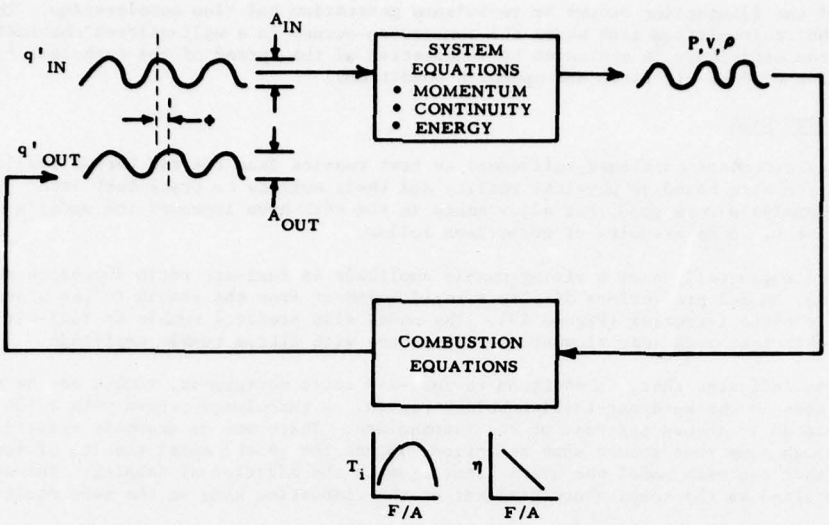

• UNSTABLE IF AT SOME FREQUENCY: $A_{OUT} \geq A_{IN}$ AND $\Phi = 0$

Figure 1. Condition for Rumble

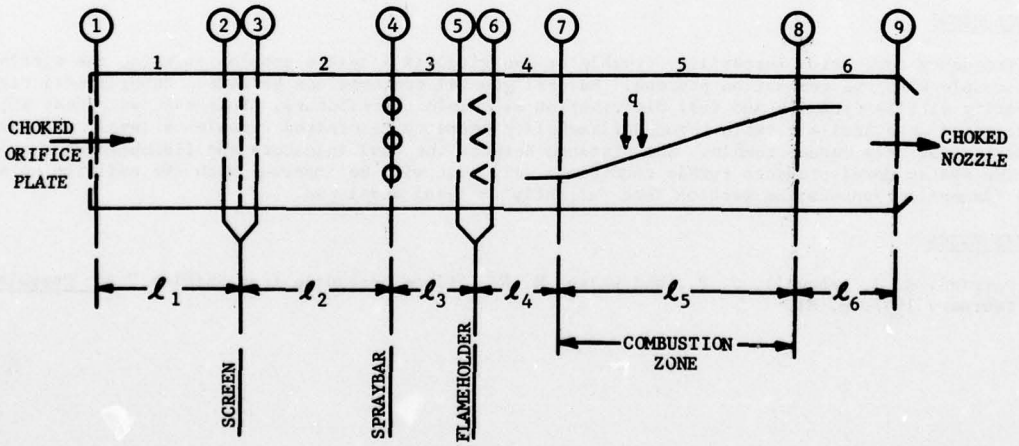

Figure 2. Augmentor Rig Math Model Schematic

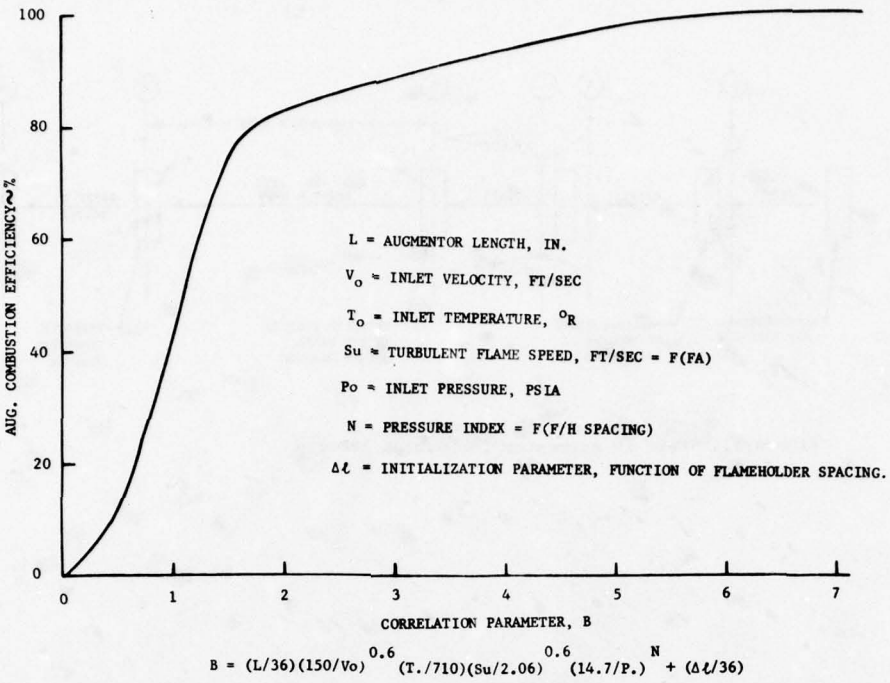

Figure 3. Augmentor Efficiency Correlation . Reference 1

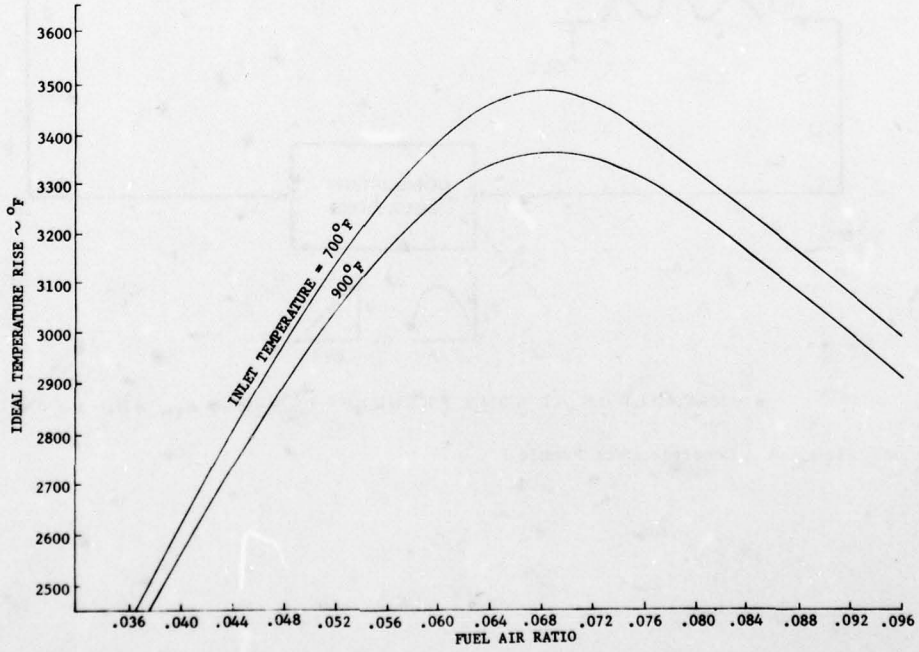

Figure 4. Ideal Temperature Rise for Constant Pressure Combustion of Hydrocarbon Fuels

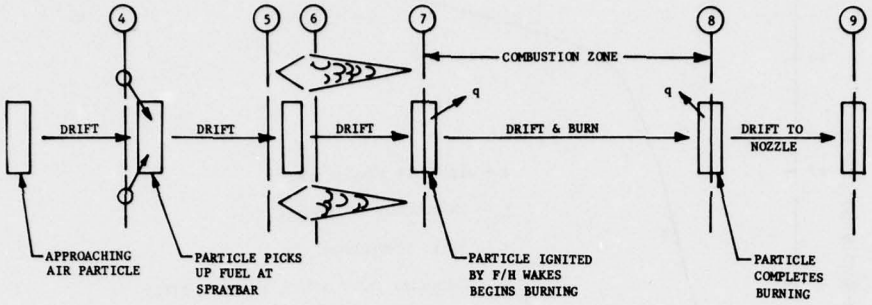

Figure 5. Steps in Augmentor Combustion Process

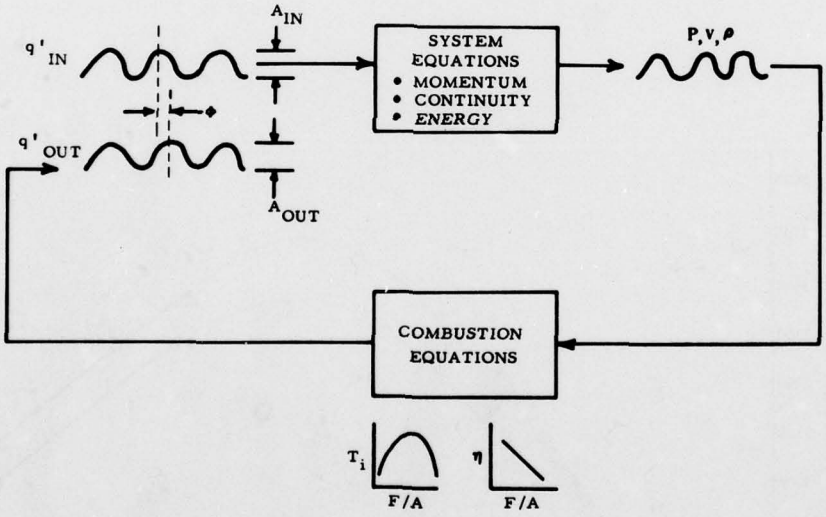

• UNSTABLE IF AT SOME FREQUENCY: $A_{OUT} \geq A_{IN}$ AND $\Phi = 0$

Figure 6. Condition For Rumble

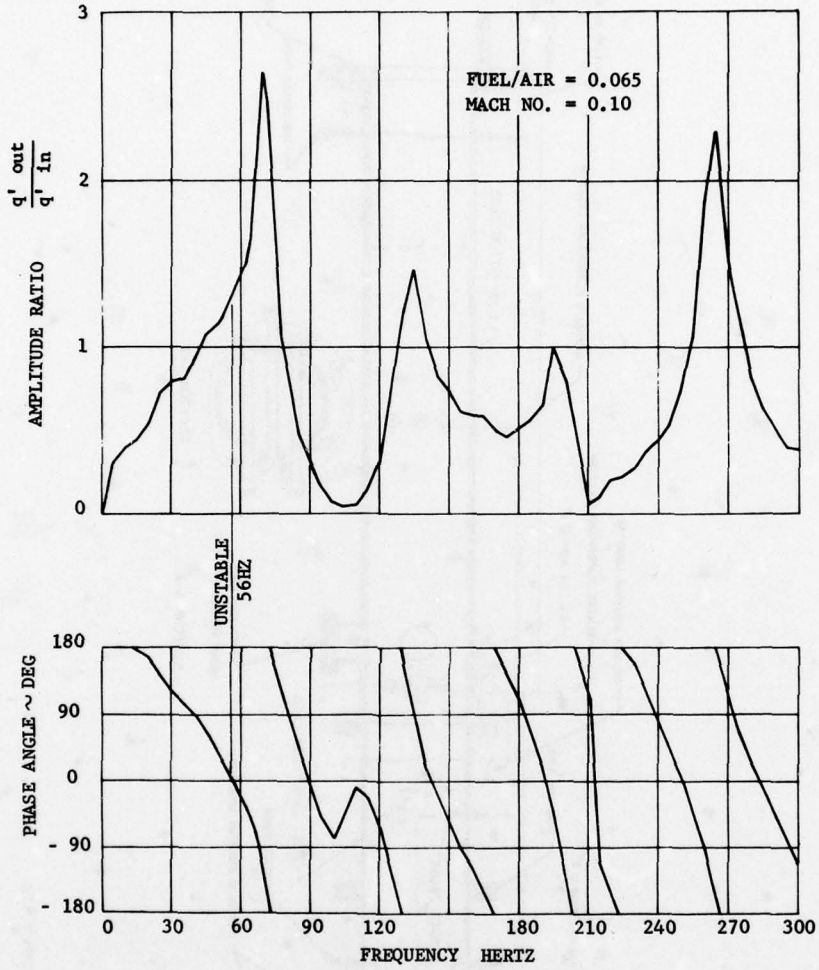

Figure 7. Open Loop Transfer Function Baseline Configuration

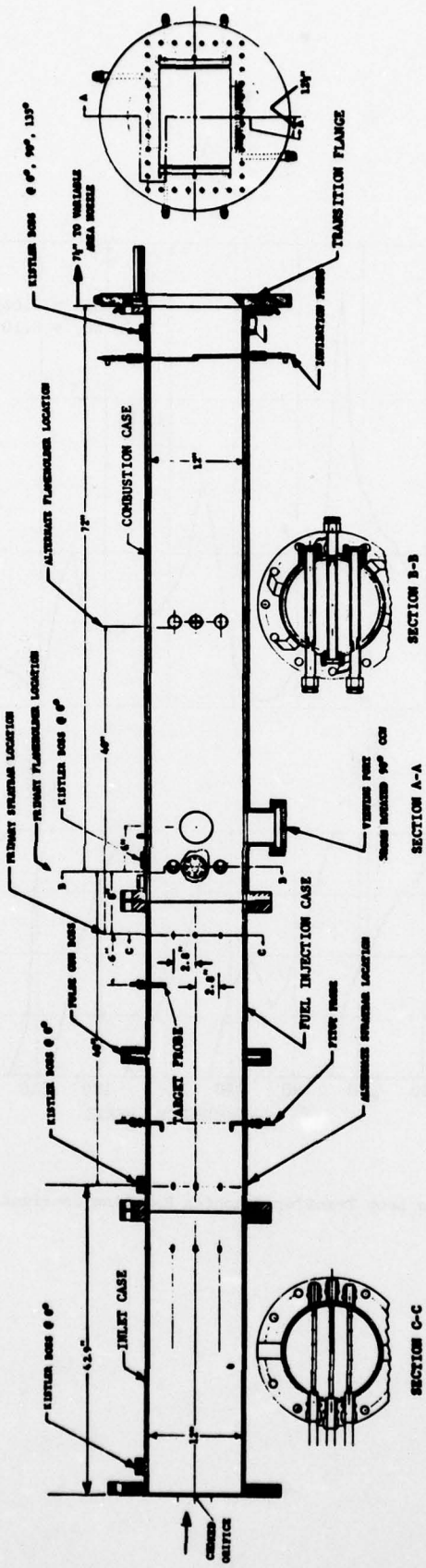

Figure 8. System Instability Study Test Rig

Series	Test Cond. No.	Flameholders			Fuel Type	Orifice to Nozzle Distance	Spraybar to Flameholder Distance	Flameholder to Nozzle Distance	Test Conditions				Test Purpose
		Number	Width	Blockage					Inlet Pressure	Inlet Temp.	Inlet Mach No.	Fuel/ Air Ratio	
			in.	%		in.	in.	in.	PSIA	°F			
I	1	3	1.2	35	JP-4	163	9	78	6.5	200	0.12-0.25	.065-.15	Map system low frequency stability characteristics of the experimental apparatus. High speed motion pictures will be filmed during "rumble".
	2	3	1.2	35	JP-4	163	9	78	10	400	0.12-0.25	.065-.15	
	3	3	1.2	35	JP-4	123	9	78	30	1300	0.12-0.25	.065-.15	
	4	3	1.8	52	JP-4	163	9	78	6.5	200	0.12-0.25	.065-.15	
	5	3	1.8	52	JP-4	163	9	78	10	400	0.12-0.25	.065-.15	
	6	3	1.8	52	JP-4	123	9	78	30	1300	0.12-0.25	.065-.15	
II	7	3	(1)	(1)	JP-4	163	42	78	(2)	(2)	(2)	(2)	Determine the effect of fuel vaporization on system stability.
	8	3	(1)	(1)	JP-4	163	42	78	(2)	(2)	(2)	(2)	
	9	3	(1)	(1)	CH_4	163	42	78	(2)	(2)	(2)	(2)	
	10	3	(1)	(1)	CH_4	163	42	78	(2)	(2)	(2)	(2)	
III	11	3	(1)	(1)	JP-4	123	9	78	(2)	(2)	(2)	(2)	Determine the effect of system length on system stability.
	12	3	(1)	(1)	JP-4	123	9	78	(2)	(2)	(2)	(2)	
IV	13	3	(1)	(1)	JP-4	123	9	78	(2)	(2)	(2)	(2)	Determine the effect of turbulence at the flameholders and spraybars on system stability. (3)
	14	3	(1)	(1)	JP-4	163	9	78	(2)	(2)	(2)	(2)	
	15	3	(1)	(1)	JP-4	163	9	78	(2)	(2)	(2)	(2)	
	16	3	(1)	(1)	JP-4	163	9	78	(2)	(2)	(2)	(2)	
V	17	3	(1)	(1)	JP-4	163	9	78	(2)	(2)	(2)	(2)	Determine the effect of injection point ΔP on system stability. (4)
	18	3	(1)	(1)	JP-4	163	9	78	(2)	(2)	(2)	(2)	
VI	19	3	(1)	(1)	JP-4	163	42	41	(2)	(2)	(2)	(2)	Determine the effect of combustion efficiency oscillations on system stability.
	20	3	(1)	(1)	JP-4	163	42	41	(2)	(2)	(2)	(2)	
VII	21	3	(1)	(1)	JP-4	163	9	78	(2)	(2)	(2)	(2)	Determine the effect of flameholder recirculation wake energy on system stability. (5)
	22	3	(1)	(1)	JP-4	163	9	78	(2)	(2)	(2)	(2)	

NOTES:

(1) Geometry of test conditions 7 through 22 will be based on the stability limits determined in test conditions 1 through 6.

(2) Exact test conditions will depend on stability limits determined during test conditions 1 through 6.

(3) Two different screens will be tested. Both screens will be 123 inches from the nozzle.

(4) Two different spraybar Δp's at the same flowrate will be tested.

(5) Energy will be added by use of an Oxy-Acetylene burner at the flameholder.

Figure 9. Lo-Frequency Augmentor Instability Investigation Test Matrix

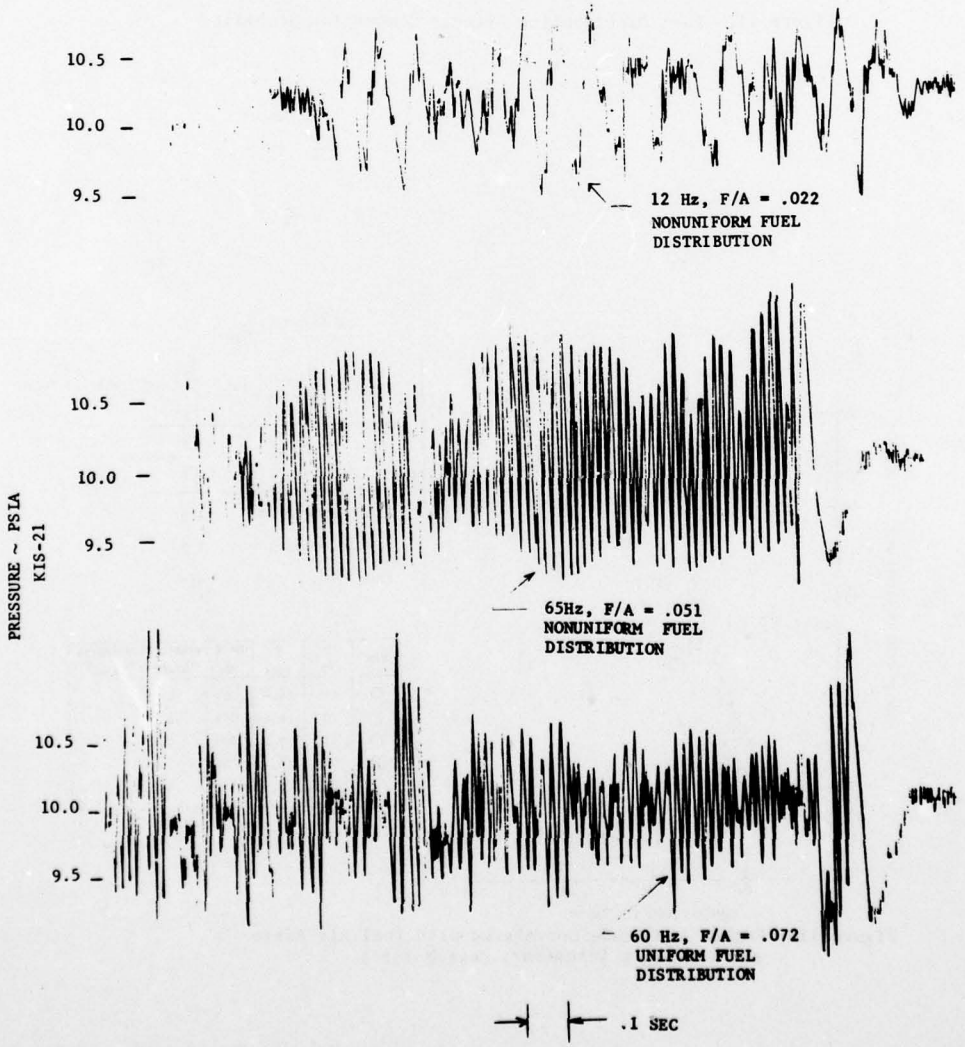

Figure 10. Typical Rumble Induced Blowout O-Graph Traces (50% Flameholder Blockage))

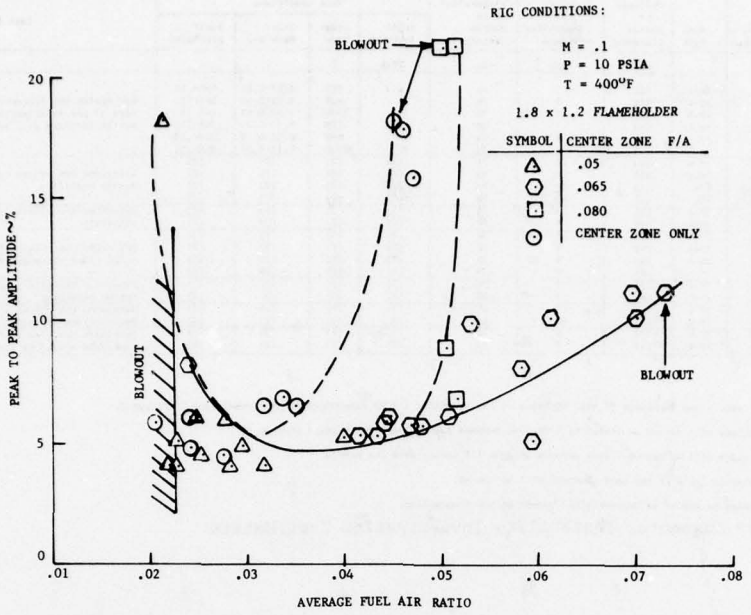

Figure 11. Fuel Distribution Affects Combustion Stability

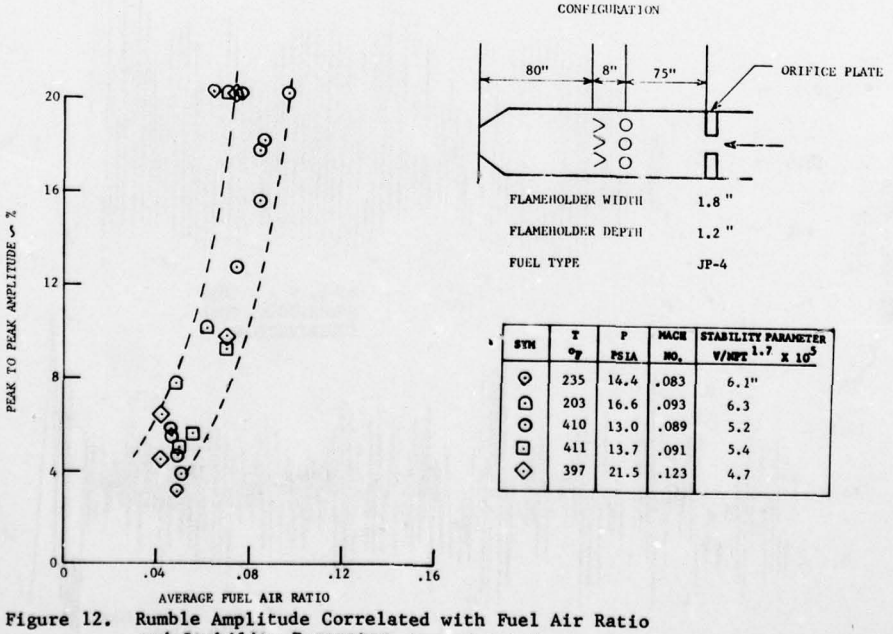

Figure 12. Rumble Amplitude Correlated with Fuel Air Ratio and Stability Parameter, Test Point 1

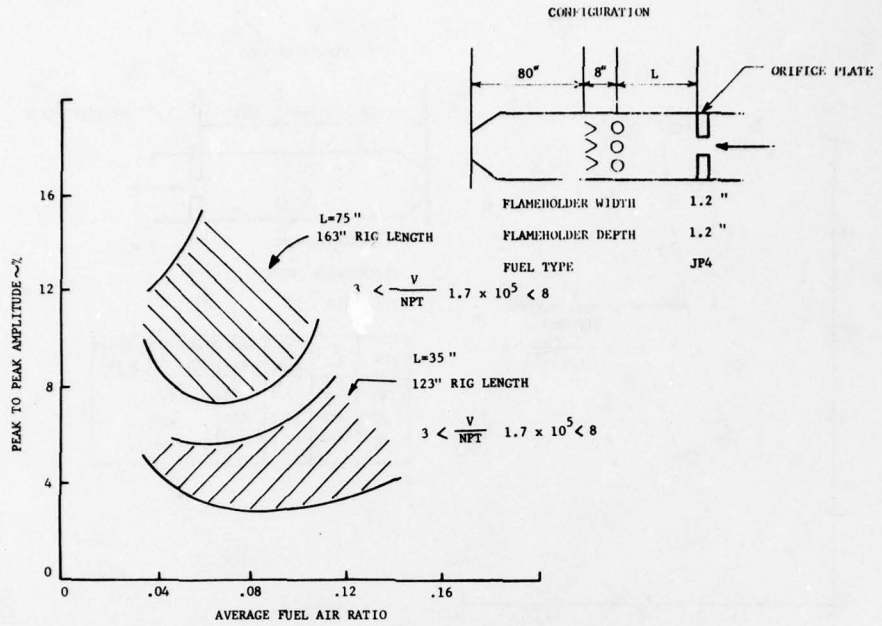

Figure 13. Effect of Cold Duct Length on Stability. Comparison of Test Point 11 and Test Point 3.

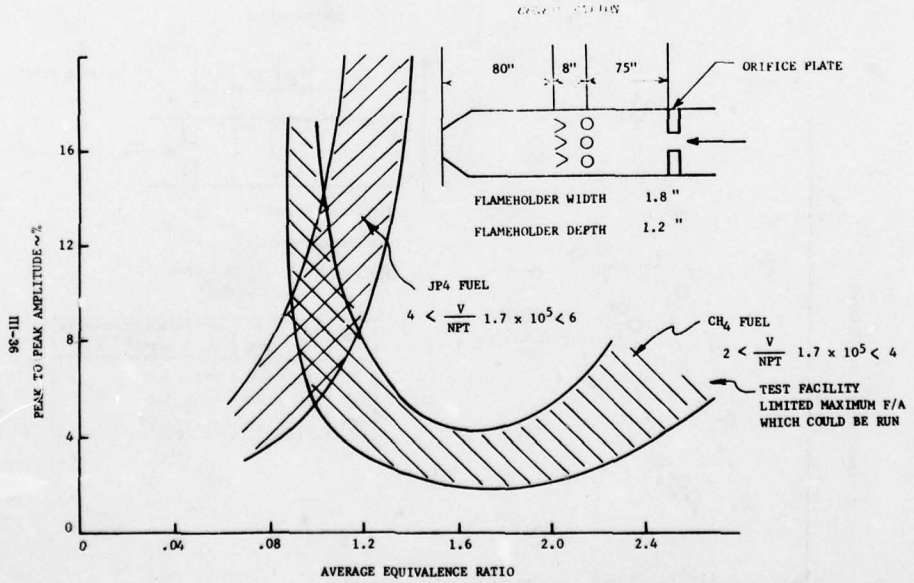

Figure 14. Comparison of Liquid JP4 Test Point 1 Fuel and Gaseous Methane Test Point 2 with Same Test Configuration

AD-A052 845 ADVISORY GROUP FOR AEROSPACE RESEARCH AND DEVELOPMENT--ETC F/G 21/5
HIGH TEMPERATURE PROBLEMS IN GAS TURBINE ENGINES.(U)
FEB 78

UNCLASSIFIED AGARD-CP-229 NL

4 OF 7
AD A052845

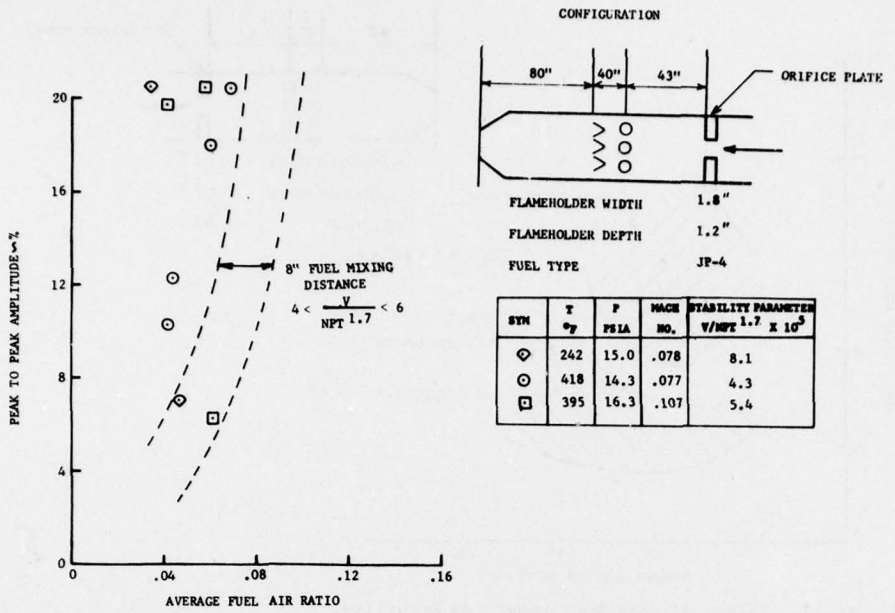

Figure 15. Effect of Increased Injector to Flameholder Length. Comparison of Test Point 9 with Test Point 1.

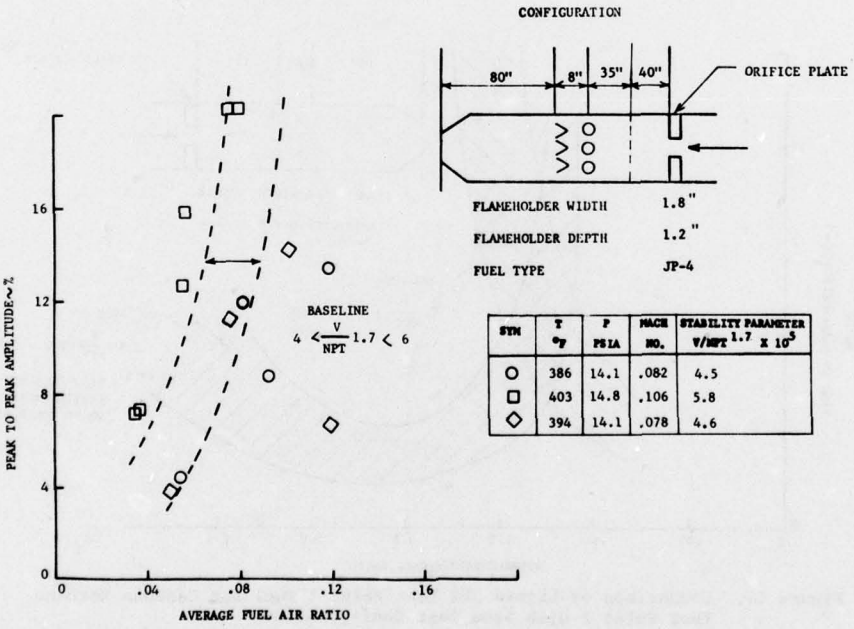

Figure 16. Effect of Turbulence Screen on Stability. Comparison of Test Point 7 with Test Point 1.

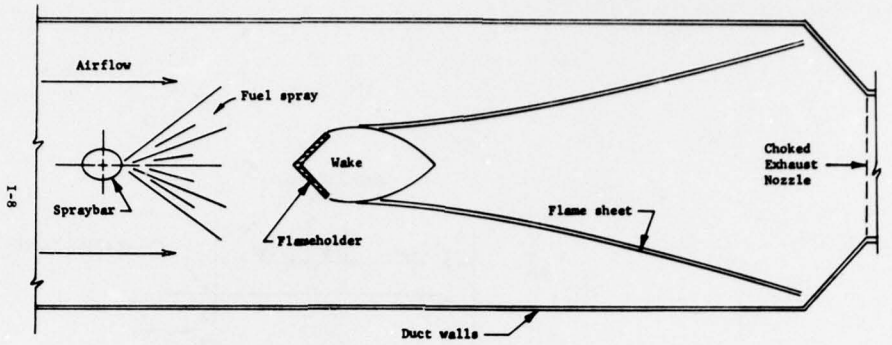

Figure 17. Basic Two-Dimensional Ducted Flame Model

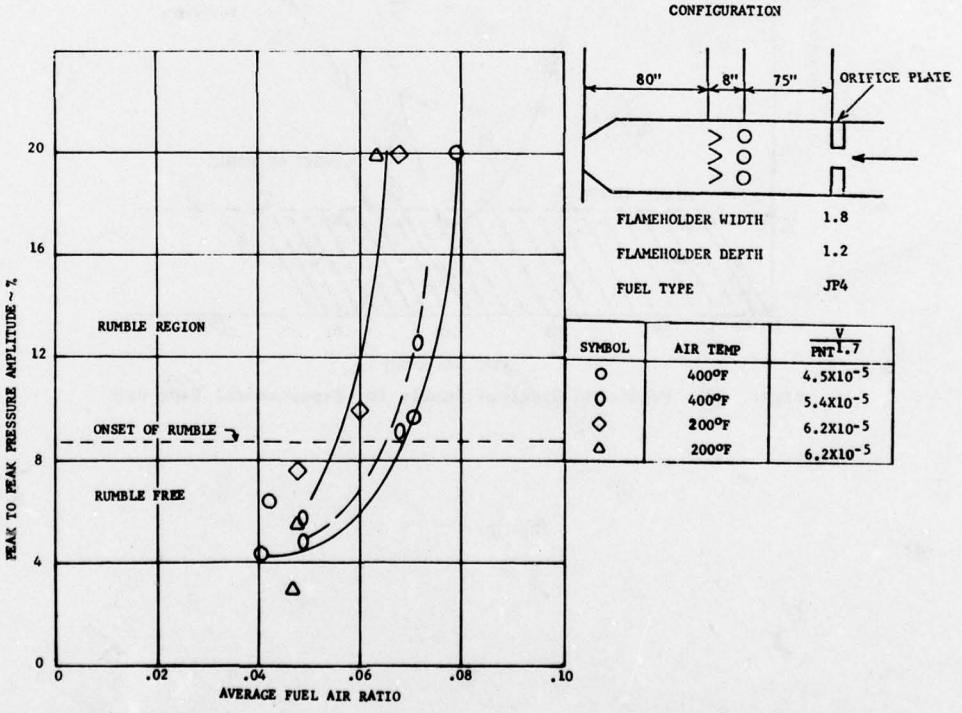

Figure 18. Rumble Amplitude Correlates with Blowout Parameter and Fuel Air Ratio

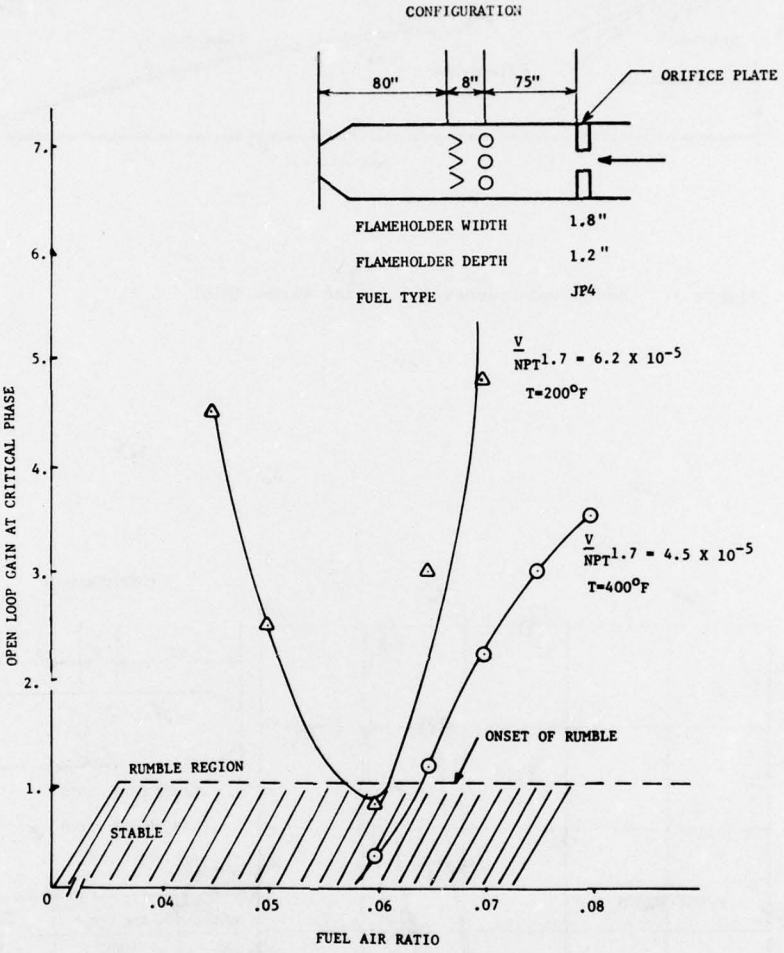

Figure 19. Predicted Onset of Rumble for Experimental Test Rig

DISCUSSION

M.Buisson, France

(1) Vous avez dit que ce problème de 'rumble' se produisait sur les moteurs 'turbofan'. Est-ce un problème plus spécifique de la combustion dans le flux froid ou cela se produit-il sur les deux flux?

(2) Y a-t-il une influence du niveau de pression de la veine sur ce phénomène de vibration basse fréquence?

(3) Quel est le mode principal des vibrations que vous appelez rumble? (transverse, radial, longitudinal)

(Translation)

(1) You reported that the "rumble" problem occurs in turbofan engines. Is it more specific of combustion in the cold flow, or does it occur in both flows?

(2) In this low-frequency vibration phenomenon influenced by the pressure level in the airflow?

(3) What is the main vibration mode which you call "rumble"? (transverse, radial, or longitudinal).

Author's Reply

(1) "Rumble" occurs in both cold and hot flows, but the airflow dynamics (system acoustical "softness") of the fan duct and the poor combustion efficiency of the cold flow make the cold flow the critical portion of the afterburner. Rumble rarely occurs in a turbojet.

(2) Low-frequency vibration phenomenon is not strongly affected directly by pressure level in the augmentor under typical operating conditions. However, the pressure level in the afterburner can slightly affect fuel vaporization which, in turn, can change local fuel-air ratios, combustion efficiencies, and, therefore, "rumble".

(3) "Rumble" is a longitudinal wave phenomenon.

MATÉRIAUX D'AVENIR POUR TURBINES A HAUTE TEMPÉRATURE
Les composites ONERA face aux problèmes d'aubes

par Hervé BIBRING

Office National d'Etudes et de Recherches Aérospatiales (ONERA)
92320 Châtillon - France

Le problème des turbines à gaz plus performantes, sollicitées à plus haute température, nous renvoie immédiatement à la question : existe-t-il des matériaux nouveaux capables d'assurer une telle réalisation ?

Les composites réfractaires ONERA répondent à cette question. Ces matériaux ne constituent pas une découverte de laboratoire pour laquelle on chercherait une application ; au contraire, ils sont l'aboutissement d'une recherche de matériaux nouveaux destinés précisément à améliorer les performances et la fiabilité des turbines de demain.

On confronte les exigences requises d'un matériau pour aubes de turbomachines haute température avec les performances enregistrées sur les composites de solidification orientée Cotac. En particulier, après avoir précisé la structure et les propriétés des nuances 74 et 741, on évalue leur stabilité structurale à haute température, la tenue en fatigue thermique et mécanique, la résistance à l'oxydation et l'aptitude à la protection superficielle. L'importance du gain de température montre l'avantage immédiat d'utilisation de ces composites pour la confection d'aubes pleines non refroidies. Le problème d'aubes refroidies est également discuté.

●

NEW MATERIALS FOR HIGH TEMPERATURE TURBINES
ONERA'S DS COMPOSITES CONFRONTED WITH THE BLADE PROBLEMS

The problem of advanced aircraft turbines operating at higher temperature does immediately raise the question : are there new materials available required for such a realization ?

ONERA's refractory DS composites answer the question. These materials are not a laboratory invention looking for an eventual application ; on the contrary, they represent the outcome of a research work directed precisely to new materials for better and more reliable turbine blades in advanced aircraft engines.

The needs required for a blade material in aircraft turbines operating at higher temperatures are compared with the actual performance as found on Cotac DS composites testing. The paper specifies the structure and the properties of the more fully developed 74 and 741 types. In particular, the high temperature structural stability, the impact of thermal and mechanical fatigue, the oxidation resistance and the coating capability are more thouroughly evaluated. The great benefit in operational temperature of these materials can be immediately exploited in the field of uncooled solid blades. The problem of cooling passages in DS eutectic blades is also outlined.

INTRODUCTION -

Quand on analyse le développement des turbomachines on a coutume de privilégier l'amélioration des performances assurées par l'élévation de la température de la source chaude. De fait, en l'espace des vingt dernières années, la température d'entrée de turbine est passée d'environ 1 100 K à plus de 1 500 K dans les moteurs civils, près de 400 K de plus dans les moteurs militaires et les objectifs très prochains (1980) prévoient la montée à 1 600 et 2 100 K respectivement. Cependant, pas moins significative est la tendance à augmenter les contraintes : pour ne prendre que les cinq dernières années, la résistance demandée aux aubes de turbine s'est accrue de près de 30 % et la vitesse de cette progression ne semble devoir se ralentir dans la décennie à venir.

Une telle escalade n'aurait pas été envisageable sans le progrès parallèle dans le domaine des matériaux : recherche métallurgique débouchant sur des alliages structuralement plus stables, mieux durcis, offrant un gain de température d'utilisation et de résistance ; solidification unidirectionnelle permettant l'obtention des pièces coulées plus fiables, débarrassées du risque de rupture prématurée par décohésion intergranulaire ; techniques de protection diversifiées et mieux adaptées ; progrès technologiques et industriels dans la conception et la réalisation des pièces. De surcroît, l'approfondissement des lois d'écoulement et des transferts thermiques a permis l'optimisation des circuits de refroidissement : la différence entre la température d'entrée turbine et la température maximale de l'aube peut atteindre et dépasser 500 K.

Les turbomachines d'avenir nécessiteront des matériaux aux performances encore accrues. Les systèmes de refroidissement ont atteint un tel degré de sophistication que la technologie d'agencement de circuits pourra difficilement suivre cette voie sans pénalisation prohibitive en coût et en rendement, à moins que des conceptions révolutionnaires ne puissent assurer un gain encore imprévisible. Les thermiciens seuls peuvent s'y hasarder. Mais, pour ce qui concerne la science des matériaux, on ne prend guère de risques en affirmant qu'un bond supplémentaire de 50 K ou de 30 % en résistance n'est pas envisageable par l'amélioration des superalliages actuels à base de Co ou de Ni.

En revanche, les composites réfractaires élaborés par solidification unidirectionnelle représentent une classe de matériaux métalliques capables d'assurer la relève. Le mode d'élaboration, les caractéristiques et les possibilités d'application de tels composites ont été largement analysés dans les conférences spécialisées (1, 2) ou des réunions AGARD (3, 4) pour ne citer que les synthèses les plus complètes. Les nuances réfractaires destinées à la confection d'aubes de turbomachines sont des composites fibreux ou lamellaires, c'est-à-dire des matériaux essentiellement biphasés, bien qu'élaborés à partir de systèmes multiconstitués (nombre de constituants plus grand que le nombre de phases). La matrice complexe, à base de Co ou de Ni, est renforcée par des fibres de carbures réfractaires de grande résistance (5) ou par des lamelles alternées de phases intermétalliques (6). En fluage à très haute température, ces composites apportent un gain spectaculaire de résistance et de température d'utilisation, étape que l'on ne pouvait espérer franchir par l'amélioration des alliages actuels.

Pour important qu'il soit, le gain en fluage haute température ne suffit pas pour promouvoir un matériau nouveau à la confection des pièces chaudes dans les turbomachines de demain. Pour être accepté, un matériau nouveau doit d'abord satisfaire à l'ensemble de caractéristiques que le motoriste avait déjà coutume de manier dans le calcul de ses prévisions, mais aussi, certaines particularités moins habituelles des matériaux composites peuvent-elles conduire le motoriste à un changement de conception et d'analyse qui nécessiteront, à leur tour, la vérification expérimentale des propriétés nouvelles. Il s'agira d'examiner ici comment les matériaux composites conçus par l'ONERA pour améliorer les performances et la fiabilité des turbines de demain répondent aux interrogations des motoristes.

PROPRIETES COURANTES DU COTAC 74.

Structure : les composites réfractaires ONERA, actuellement au stade de développement, appartiennent à la famille désignée Cotac 74 (*) (7). La matrice est un superalliage de cristallisation orientée à base de Ni, Co, Cr, durcie à la fois en solution solide par une forte teneur en W et par précipitation cohérente d'une phase de composition complexe de type $\gamma' Ni_3 Al$ assurée par addition d'aluminium ; les fibres de renforcement sont des monocarbures réfractaires NbC, de même structure cristallographique CFC que la matrice. Solidifié sous fort gradient thermique (150 à 200 K cm^{-1}) à vitesse relativement lente ($\leq$ 2,4 cm h^{-1}) le système s'organise d'emblée, dans des conditions proches d'équilibre thermodynamique, en composite orienté à fibres dont la figure 1 montre la structure métallographique observée sur coupe transversale au microscope électronique à balayage.

(*) Composition nominale : Ni - 20 Co - 10 Cr - 10 W - 4 Al - 4,9 Nb - 0,6 C

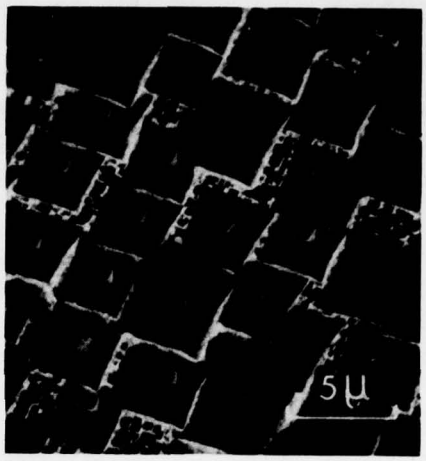

Fig. 1

Avec ses précipités, la matrice rappelle ici la microstructure de meilleurs superalliages à base de Ni. De fait, comme les nuances modernes les plus performantes élaborées par solidification dirigée, le composite est exempt de joints de grains transversaux ce qui améliore la fiabilité à haute température pour des sollicitations principales dirigées dans l'axe de la cristallisation. De plus, l'orientation unique de l'ensemble des grains de la matrice suivant une direction cristallographique à faible module d'élasticité permet de minimiser les contraintes thermiques. Le renforcement est assuré par des fibres réfractaires NbC, filaments monocristallins parfaits (whiskers) de très grande longueur et d'environ 0,8 µm de diamètre, dont l'extraordinaire résistance mécanique approche de valeurs théoriques.

Propriétés : Bien que renforcé par fibres pratiquement indéformables, le composite n'en garde pas moins une parfaite ductilité en traction (figure 2) comme au choc (tableau I) dans tout le domaine de température. Remarquons, en passant, la relative insensibilité à l'entaille : l'énergie de rupture au choc d'éprouvettes entaillées est supérieure à celle de l'alliage commercial IN-100 (*). Malgré l'anisotropie de comportement, les propriétés transversales du composite paraissent satisfaisantes : à la température du pied de pale, par exemple, le travail de rupture au choc en travers reste supérieur à 8 J cm^{-2} tandis qu'en traction travers la déformation est de 2,5 %.

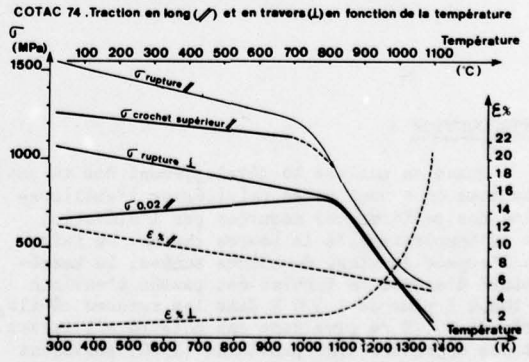

Fig. 2

(*) Composition nominale : Ni - 15Co - 10 Cr - 5.5 Al - 4,7 Ti - 3 Mo - 1 Ti - 0,18 C - Zr

Tableau I - Travail de rupture comparé en flexion par choc (J cm^{-2})

Température (°C)	Eprouvettes lisses COTAC 74	Eprouvettes lisses IN 100	Eprouv. entaillées COTAC 74	Eprouv. entaillées IN 100	Eprouv. travers COTAC 74 entaillé*
20	77 - 110	57 - 120	25 - 31	14 - 28	6 - 7
700	37,5 - 40	43	21 - 23	12	8,3 - 8,7
1000	48 - 50	25	25 - 26	111	13 - 14

* *Entaille parallèle aux fibres.*

En fluage, pour une durée de vie de 1 000 heures, le Cotac 74 dépasse l'IN- 100 au dessus de 900° C (figure 3).

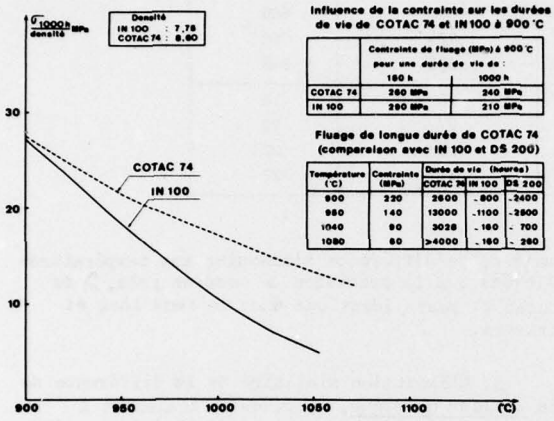

Influence de la contrainte sur les durées de vie de COTAC 74 et IN100 à 900 °C

	Contrainte de fluage (MPa) à 900 °C pour une durée de vie de : 150 h	1000 h
COTAC 74	260 MPa	240 MPa
IN 100	290 MPa	210 MPa

Fluage de longue durée de COTAC 74 (comparaison avec IN 100 et DS 200)

Température (°C)	Contrainte (MPa)	Durée de vie (heures) COTAC 74	IN 100	DS 200
900	220	2800	- 800	- 2400
950	140	13000	- 1100	- 2800
1040	80	3028	- 160	- 700
1080	80	>4000	- 160	- 280

Fig. 3

On voit que malgré le handicap de densité, le gain en contrainte spécifique est de plus de 30 % à 950° C, 40 % à 980° C et de 60 % à 1 000° C ; à contrainte spécifique égale, le gain en température est de 40 à 80 K. Pour des durées plus longues, une augmentation de contrainte de 30 à 40 % correspond à un gain de température de 100 K et l'amélioration en durée de vie atteint un facteur de l'ordre 20. Il faut cependant remarquer que le composite est moins intéressant en fluage à température moyenne et aussi plus sensible aux variations de contrainte que l'alliage équiaxe : à 900° C, pour passer d'une durée de vie moyenne de 150 à 1 000 heures, il faut abaisser la contrainte de fluage de l'IN 100 de plus de 25 % alors qu'une faible réduction de contrainte -inférieure à 10 %- suffit à gagner le même temps de rupture dans le Cotac 74.

Pour une aube de turbine, l'association des caractéristiques de fluage, et la répartition des contraintes σ et de la température T le long de la pale permet déjà l'estimation des possibilités du matériau en durée de vie par la localisation du point critique où les courbes (σ, T) le long de l'aube rencontrent la courbe de durée de vie correspondante du matériau. Dans les superalliages usuels, on trace généralement la famille de courbes de 300, 1 000 ou 2 000 heures de durée à la température admissible, fonction de la contrainte, pour provoquer une déformation de 1 % ; cependant, en ce qui concerne le composite Cotac 74, les ruptures en fluage se font avec des déformations relativement faibles, de l'ordre de 1,2 - 1,5 %; il faut donc prendre en compte ici non pas tant une déformation limite mais la durée de vie du matériau affectée d'un coefficient de correction. Pour l'alliage IN 100, par exemple, les résultats expérimentaux montrent que le temps à déformation 1 % correspond sensiblement à la demi-durée de vie en fluage rupture ; pour le calcul du Cotac 74 on prend habituellement la durée de vie, minorée et divisée par deux, ce qui laisse une bonne marge de sécurité puisque la déformation de 1 % est près de la durée totale. La figure 4, par exemple, compare les possibilités des matériaux pour la confection d'une aube non refroidie, basse pression, c'est-à-dire dont la pale est soumise à des contraintes centrifuges relativement faibles : la température maximale admissible, provoquant dans les superalliages IN 100 et DS 200 une déformation de fluage de 1 % en 2 000 heures est comparée ici à une durée de 5 000 heures du composite Cotac 74.

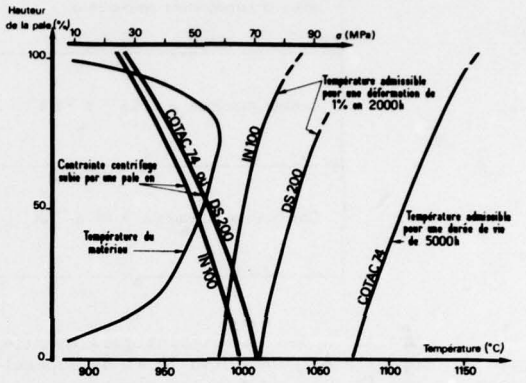

Fig. 4

Une telle représentation a l'avantage de montrer la possibilité d'emploi du composite pendant de longues durées, sous contrainte modérée. Dans les turbomachines à double flux de la prochaine génération dont les étages basse pression travailleront à des températures supérieures à 1 000° C, le Cotac 74 paraît particulièrement intéressant pour la fabrication d'aubes pleines, évitant ainsi les complications technologiques fâcheuses pour des circuits de refroidissement supplémentaires.

Cependant, à côté des propriétés déterminées en fluage, c'est-à-dire en fonctionnement stabilisé, restent les problèmes thermiques et les sollicitations vibratoires lesquels, avec l'oxydation et la corrosion sèche, constituent les facteurs principaux de la durée de vie et de la fiabilité des aubes. Nous allons passer en revue chacun de ces points.

PROBLEMES THERMIQUES -

De densité équivalente à celle de la plupart de superalliages à base de Ni (DS 200, X-40, René 120), plus léger que les alliages à base de Co (MAR- M 509, L- 605, WI-52), le Cotac 74 se trouve cependant pénalisé par l'exceptionnelle légèreté de l'alliage IN - 100 auquel nous le comparons ici (tableau II), en ce qui concerne notamment la diffusivité thermique. En revanche, le gain en température de fusion commençante est notable. C'est là, assurément, un avantage sérieux -en particulier pour les aubes directrices- avantage que l'on paye, cependant, en difficultés technologiques : plus la température de fusion du matériau est élevée, plus les difficultés d'élaboration s'accumulent. Ajouté à la nécessité de forts gradients thermiques et de faibles vitesses de cristallisation orientée du composite, ceci constitue un handicap dont il faudra tenir compte dans l'évaluation du coût.

Tableau II - Propriétés physiques

Propriétés \ Matériaux		Cotac 74 orienté		IN 100
		en long //	en travers ⊥	équiaxe
Densité, ρ (10^3 kg m^{-3})		8,6		7,8
Température de fusion commençante (K)		1605		1535
Dilatation thermique linéaire moyenne, α (10^{-6} K^{-1}) entre la température ambiante et	1000 K	13,7	14,6	14,6
	1100 K	14,3	15,3	15,5
	1200 K	15,2	16,3	16,3
	1300 K	16,2	17,8	17,4
Chaleur massique, e_p(J kg^{-1} K^{-1}) à	1000 K	625		525
	1100 K	675		660
	1200 K	725		760
	1300 K	800		845
Conductivité thermique, λ (W m^{-1} K^{-1}) à	1000 K	26		18
	1100 K	27 5		20
	1200 K	29,5		23,5
	1300 K	31 5		27

La comparaison des caractéristiques thermiques du composite orienté Cotac 74 et du superalliage équiaxe IN 100, appelle les remarques suivantes :

1. La dilatation thermique, α, de deux matériaux est de même ordre de grandeur ; les différences du comportement du composite en long et en travers sont faibles.

2. La conductivité thermique, λ, du Cotac 74 est supérieure à celle de l'alliage du commerce mais cette différence s'amenuise aux températures élevées ; à la précision de mesures près, λ du Cotac 74 reste identique dans le sens long et travers.

3. L'évolution similaire de la différence de la chaleur massique, c, conduit finalement à une faible incidence sur la diffusivité thermique $\lambda/c\rho$.

Tableau III - Diffusivité thermique comparée.

T^{re} (K)	λ_{Cot}	λ_{IN}	$\frac{\lambda_{Cot} - \lambda_{IN}}{\lambda_{IN}}$	$c_{p\,Cot}$	$c_{p\,IN}$	$\frac{c_{p\,Cot} - c_{p\,IN}}{c_{p\,IN}}$	$\frac{\lambda/c\rho\ Cot - \lambda/c\rho\ IN}{\lambda/c\rho\ IN}$
875	24,3	15,5	0,57	585	390	0,50	− 0,05
1225	30,5	24,2	0,26	745	785	− 0,05	0,20

On peut donc dire que le changement de matière consistant à remplacer dans une aube refroidie l'alliage IN 100 par le composite Cotac 74 ne modifie pas sensiblement le champ de température (8) :

- en régime permanent, l'augmentation de λ entraîne une diminution des gradients de température ce qui a un effet favorable sur la tenue de l'aube ; toutefois, la température moyenne de l'aube sera pratiquement inchangée ;

- en régime transitoire,

(a) à faible température (roulage au sol → plein gaz) l'augmentation de λ, et la diminution relative de $\lambda/c\rho$ entraînent une augmentation des gradients de température ; cependant, les températures de métal étant basses cet effet n'est pas dangereux ;

(b) à haute température (plein gaz → ralenti) l'augmentation simultanée de λ et de la diffusivité entraîne des gradients thermiques très réduits : le champ de température doit être peu affecté.

FATIGUE THERMIQUE -

Superposé aux contraintes de fluage (sollicitation centrifuge) et de fatigue (impulsions vibratoires de haute fréquence) le phénomène de fatigue thermique, c'est-à-dire l'application répétée, en un point localisé de la pale, de contraintes mécaniques et thermiques combinées, est de ceux qui peuvent le plus fâcheusement dégrader la durée de vie d'une aube. Cependant, l'étude des lois de superposition fluage-fati[illegible] n'en est qu'à son début (9,10) ; les matériaux sont caractérisés par des essais de laboratoire, généralement en sollicitation unidirectionnelle. Mais le mécanisme de rupture d'une aube dépend de la combinaison de contraintes complexes, parmi lesquelles il faut prioritairement prendre en compte les sollicitations liées aux régimes transitoires. Il faut donc déterminer le nombre de cycles de vol dont l'aube sera capable et cette détermination exige la connaissance du spectre contrainte et température (σ , T) lors d'un cycle. Bien entendu, le cycle de vol-type comme le nombre de cycles est différent suivant qu'il s'agisse d'un avion commercial, moyen ou long courrier ou d'un intercepteur, par exemple.

Tableau I - Travail de rupture comparé en flexion par choc (J cm^{-2})

Température (°C)	Eprouvettes lisses COTAC 74	Eprouvettes lisses IN 100	Eprouv. entaillées COTAC 74	Eprouv. entaillées IN 100	Eprouv. travers COTAC 74 entaillé*
20	77 - 110	57 - 120	25 - 31	14 - 28	6 - 7
700	37,5 - 40	43	21 - 23	12	8,3 - 8,7
1000	48 - 50	25	25 - 26	111	13 - 14

* *Entaille parallèle aux fibres.*

En fluage, pour une durée de vie de 1 000 heures, le Cotac 74 dépasse l'IN- 100 au dessus de 900° C (figure 3).

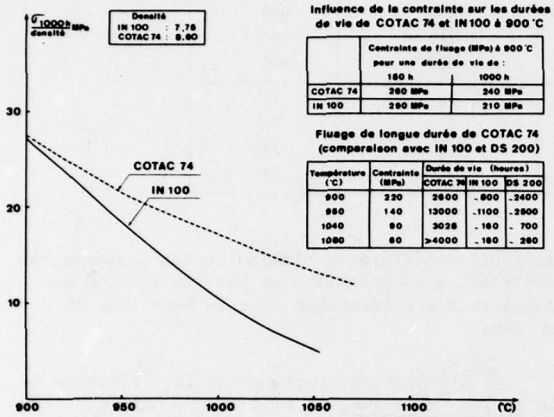

Fig. 3

On voit que malgré le handicap de densité, le gain en contrainte spécifique est de plus de 30 % à 950° C, 40 % à 980° C et de 60 % à 1 000° C ; à contrainte spécifique égale, le gain en température est de 40 à 80 K. Pour des durées plus longues, une augmentation de contrainte de 30 à 40 % correspond à un gain de température de 100 K et l'amélioration en durée de vie atteint un facteur de l'ordre 20. Il faut cependant remarquer que le composite est moins intéressant en fluage à température moyenne et aussi plus sensible aux variations de contrainte que l'alliage équiaxe : à 900° C, pour passer d'une durée de vie moyenne de 150 à 1 000 heures, il faut abaisser la contrainte de fluage de l'IN 100 de plus de 25 % alors qu'une faible réduction de contrainte -inférieure à 10 %- suffit à gagner le même temps de rupture dans le Cotac 74.

Pour une aube de turbine, l'association des caractéristiques de fluage, et la répartition des contraintes σ et de la température T le long de la pale permet déjà l'estimation des possibilités du matériau en durée de vie par la localisation du point critique où les courbes (σ, T) le long de l'aube rencontrent la courbe de durée de vie correspondante du matériau. Dans les superalliages usuels, on trace généralement la famille de courbes de 300, 1 000 ou 2 000 heures de durée à la température admissible, fonction de la contrainte, pour provoquer une déformation de 1 % ; cependant, en ce qui concerne le composite Cotac 74, les ruptures en fluage se font avec des déformations relativement faibles, de l'ordre de 1,2 - 1,5 %; il faut donc prendre en compte ici non pas tant une déformation limite mais la durée de vie du matériau affectée d'un coefficient de correction. Pour l'alliage IN 100, par exemple, les résultats expérimentaux montrent que le temps à déformation 1 % correspond sensiblement à la demi-durée de vie en fluage rupture ; pour le calcul du Cotac 74 on prend habituellement la durée de vie, minorée et divisée par deux, ce qui laisse une bonne marge de sécurité puisque la déformation de 1 % est près de la durée totale. La figure 4, par exemple, compare les possibilités des matériaux pour la confection d'une aube non refroidie, basse pression, c'est-à-dire dont la pale est soumise à des contraintes centrifuges relativement faibles : la température maximale admissible, provoquant dans les superalliages IN 100 et DS 200 une déformation de fluage de 1 % en 2 000 heures est comparée ici à une durée de 5 000 heures du composite Cotac 74.

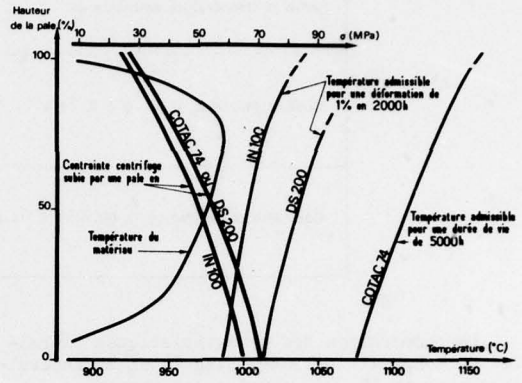

Fig. 4

Une telle représentation a l'avantage de montrer la possibilité d'emploi du composite pendant de longues durées, sous contrainte modérée. Dans les turbomachines à double flux de la prochaine génération dont les étages basse pression travailleront à des températures supérieures à 1 000° C, le Cotac 74 paraît particulièrement intéressant pour la fabrication d'aubes pleines, évitant ainsi les complications technologiques fâcheuses pour des circuits de refroidissement supplémentaires.

Cependant, à côté des propriétés déterminées en fluage, c'est-à-dire en fonctionnement stabilisé, restent les problèmes thermiques et les sollicitations vibratoires lesquels, avec l'oxydation et la corrosion sèche, constituent les facteurs principaux de la durée de vie et de la fiabilité des aubes. Nous allons passer en revue chacun de ces points.

PROBLEMES THERMIQUES -

De densité équivalente à celle de la plupart de superalliages à base de Ni (DS 200, X-40, René 120), plus léger que les alliages à base de Co (MAR- M 509, L- 605, WI-52), le Cotac 74 se trouve cependant pénalisé par l'exceptionnelle légèreté de l'alliage IN - 100 auquel nous le comparons ici (tableau II), en ce qui concerne notamment la diffusivité thermique. En revanche, le gain en température de fusion commençante est notable. C'est là, assurément, un avantage sérieux -en particulier pour les aubes directrices- avantage que l'on paye, cependant, en difficultés technologiques : plus la température de fusion du matériau est élevée, plus les difficultés d'élaboration s'accumulent. Ajouté à la nécessité de forts gradients thermiques et de faibles vitesses de cristallisation orientée du composite, ceci constitue un handicap dont il faudra tenir compte dans l'évaluation du coût.

Le plus simple est de calculer le cycle de déformation mécanique subi par chaque élément d'aube au cours de la période transitoire et comparer le résultat à des cycles répétés au laboratoire. Si, pour simplifier, on suppose que les sections d'aubes restent planes et parallèles à elles-mêmes du fait de l'intensité du champ centrifuge, le niveau de contrainte thermique locale σ sera, dans le domaine élastique, du type

$$\sigma = E\,\alpha\,(T_{moy} - T_{locale})$$

Superposé aux sollicitations centrifuges, le niveau de contraintes ainsi calculé dépasse facilement le domaine élastique. Cependant, moyennant l'hypothèse simplificatrice ci-dessus et si l'on connaît les lois du comportement du matériau, le calcul reste possible, aussi bien pour la phase arrêt → plein gaz que pour la sollicitation dans le passage instantané inverse (NB. Dans le cas PG → arrêt, chaque cycle diffère du précédent car dans le domaine plastique du matériau chaque élément d'aube possède déjà une déformation mécanique propre. Cependant, l'expérience montre que les cycles de déformation convergent rapidement vers un cycle stabilisé ce qui permet d'effectuer des essais sur éprouvettes simples au laboratoire, représentatifs du cycle subi par chaque élément de l'aube).

Sur le plan expérimental, deux types d'essais ont été faits sur le composite Cotac 74. D'une part des essais de cyclage thermique destinés à définir la stabilité structurale du matériau lors des cycles chauffage -refroidissement répétés et leur incidence sur les propriétés mécaniques ; d'autre part, des essais de fatigue thermique proprement dite sur éprouvettes coin dans des conditions simulant le processus de fissuration des bords de fuite d'aubes de turbine.

Cyclage thermique -

La différence des coefficients de dilatation thermique des fibres et de la matrice peut introduire dans le composite de fortes contraintes internes lors des chauffages et des refroidissements répétés. Si ces contraintes dépassent le domaine élastique de la matrice, l'équilibre thermodynamique entre les phases est détruit et l'accumulation de déformations plastiques répétées peut provoquer une dégradation de la phase de renforcement entraînant une baisse des caractéristiques du matériau. Il a donc été décidé de rechercher pour les composites Cotac 74 des matrices fortement durcies, à limite élastique élevée, de manière à assurer au composite une durée de vie en fluage cyclé équivalente ou la plus proche possible du fluage isotherme (11). C'était le sens du choix des matrices à base de Ni, avantageusement durcissables en solution solide et par précipitation cohérente de la phase ordonnée γ'.

Les essais sous contrainte appliquée comportaient généralement des cycles de 30 minutes dont 28 minutes de maintien à température maximale (800 à 1 100° C) suivi d'un refroidissement rapide à 250° C environ. Dans ces conditions l'incidence du cyclage thermique sur la stabilité des fibres et les performances du composite Cotac 74 sont nulles à température modérée (par exemple, non rupture en 5 000 h de fluage cyclé -plus de 10 000 cycles- entre 800 et 250° C sous une contrainte de 400 MPa) ; aux températures maximales de 1 100° C, la fatigue thermique provoque une légère dégradation des caractéristiques : pour obtenir en fluage cyclé une durée de vie équivalente à celle du fluage isotherme la contrainte doit être réduite d'environ 10 % (7).

Fissuration en fatigue thermique -

Ces essais, dont l'objectif est l'étude de la formation et de la croissance de fissures dans des conditions représentatives de la fissuration réelle des bords de fuite d'aube de turbine, ont été réalisés sur des éprouvettes coin, à bord mince (r = 0,25 mm) par chauffage au chalumeau à propane en 60 secondes jusqu'à 1 100° C et refroidissement au jet d'air forcé en 20 secondes jusqu'à environ 100° C (figure 5).

Fatigue thermique du COTAC 74

Schéma de l'éprouvette et du cycle

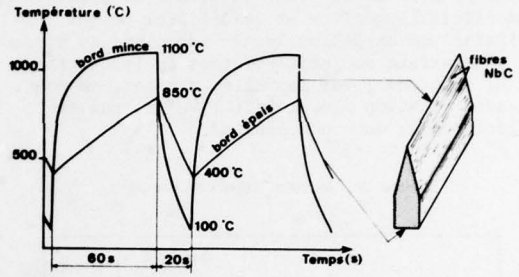

Fig. 5

Aux fins de comparaison, les essais ont été poursuivis dans des conditions identiques sur le composite Cotac 74 et sur deux superalliages, l'IN 100 à base de Ni et MAR-M 509 à base de Co (*). Les trois matériaux ont subi une protection superficielle préalable. Comme le chauffage et le refroidissement s'effectuent par l'attaque directe de l'arête mince, ceci conduit à l'établissement des isothermes sensiblement parallèles au bord, aux fibres de renforcement et aux joints de grains du composite. Dans ces conditions, des fissures apparaissent sur le bord mince des éprouvettes. La figure 6 compare la propagation de la plus longue fissure de chaque matériau en fonction du temps (nombre de cycles).

Fatigue thermique

Evolution de la plus longue crique en fonction de la température

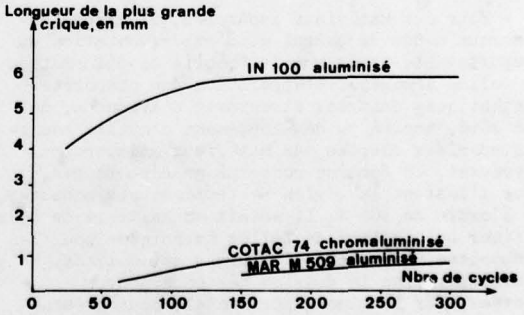

Fig. 6

On constate que la tenue du composite Cotac 74, nettement meilleure que celle du superalliage IN-100, reste très proche de l'alliage MAR-M 509 à base de Co, connu pour sa bonne tenue en fissuration thermo-mécanique (12). L'analyse plus fine de l'essai permet de mettre en relief les différences du mécanisme de fissuration de ces

(*) MAR-M 509, composition normale :
Co-23 Cr - 10 Ni -7 W 3,5 Ta -0,6C- Zr, Ni

deux matériaux. Dans l'alliage MAR-M 509, on remarque d'abord la formation de petites fissures de l'ordre de 0,5 mm qui se propagent lentement mais continuellement jusqu'à atteindre 5 à 10 mm de long. Dans le Cotac 74, en revanche, les petites criques se stabilisent à une longueur de 0,5 à 1,5 mm, ce qui correspond à la distance entre le bord mince et le premier joint de grain. Cependant, si les fissures ne progressent pas vers l'intérieur, leur nombre augmente avec le nombre de cycles et peut atteindre une densité de 20 fissures par cm. Bien que les fissures de fatigue thermique n'évoluent plus dans le Cotac 74 après quelques centaines de cycles, certains essais ont été poursuivis bien au-delà : après 4 500 cycles on peut voir la couche de protection superficielle gonfler et se décoller, ce qui entraîne une oxydation locale accentuée au niveau de l'interface composite-protection (protection Cr Al standard ; les nouvelles protections dont il sera question plus loin (13) n'ont pas été expérimentées dans ces essais).

Tableau IV - Modules d'élasticité comparés.

		Cotac 74 //	Cotac 74 ⊥	IN 100
Module d'élasticité dynamique (GPa) à	300 K	158	171	218
	1000 K	122	137	175
	1200 K	106	118	158

Par rapport à l'alliage équiaxe IN-100, la progression de fissures plus lente s'explique ici, d'une part, par la plus faible valeur du module élastique du composite, ce qui permet la formation d'une zone plastique en tête de la fissure. (Dans ce matériau hautement anisotrope, le module transversal est d'environ 8 % plus élevé ; il faut cependant noter que le module spécifique E/ρ reste plus faible et ceci conduit, dans des pièces de même géométrie, à des fréquences propres 20 % plus basses). D'autre part, l'absence de joints de grains perpendiculaires au bord de fuite est apparemment aussi favorable à la bonne tenue en fatigue thermique.

ESSAIS MOINS COURANTS -

Pour des matériaux isotropes, il existe de nombreux modes de calcul et d'expérimentation du comportement, basés sur la théorie de déformation du solide homogène. L'apparition des composites synthétiques dans les structures d'avions a, de son côté, incité au développement d'outils analytiques mieux adaptés aux matériaux anisotropes. Cependant, le domaine concerné ne dépasse pas, pour l'instant, la région de températures modestes, de l'ordre de 500 K. Il serait souhaitable de voir affiner aujourd'hui de telles techniques pour les composites réfractaires naturels qui doivent travailler dans le domaine de températures élevées. Sur le plan expérimental, nous présentons ici un certain nombre de résultats d'essais moins conventionnels, tels que fluage en flexion, fluage entaillé ou encore fluage par cisaillement, pour la caractérisation de la tenue du pied de la pale (14).

Fluage en flexion -

Il s'agissait de vérifier comment la déformabilité relativement faible du composite en fluage-traction à haute température s'accentue ou s'atténue lorsque la contrainte n'est pas uniforme dans toute la section de l'éprouvette. A titre de comparaison, ces essais ont été poursuivis parallèlement sur le Cotac 74 et sur l'IN 100, à la température de 900 et 1 050° C.

Les éprouvettes sont sollicitées dans un montage de flexion en trois points, distance entre appuis 40 mm, à 900 comme à 1 050° C. Les déformations de fluage correspondent aux flèches mesurées sur les enregistrements 0,25 h avant la rupture.

Tableau V - Fluage en flexion.

Température (°C)	Charge (kg_p)	IN 100 $t_{rupt.}$ (h)	IN 100 flèche (mm)	Cotac 74 $t_{rupt.}$ (h)	Cotac 74 flèche (mm)
900	90			1273	11
	105	150	6	116,4	11
	126	49,5	7,8	76	11
1050	27	332	9,8	600	1,0
	35	124	4,5	163	2,3
	40	35	5,6		
	45	21	5,2	28,5	2,7

On remarque (tableau V) que les durées de vie en fluage augmentent rapidement lorsque la charge décroit alors que les déformations de ruptures restent sensiblement constantes. A 900° C le composite ne présente pas de fragilité particulière : la plasticité est confortable, supérieure à celle mesurée sur le superalliage de commerce pour des durées de vie comparables. A 1 050° C, on note pour le composite des capacités de déformation plastique relativement faibles, bien que, pour une charge identique, les temps de rupture du Cotac 74 restent plus longs que les durées de vie de IN 100.

Fluage sur éprouvettes entaillées (K_t = 3,4) -

Les éprouvettes de Cotac 74 ont été prélevées parallèlement à l'axe de fibres de renforcement. La figure 7 permet de comparer les durées de vie en fluage sur éprouvettes lisses et sur éprouvettes entaillées (K_t = 3,4) en Cotac 74, sous différentes contraintes à 800, 1 000 et 1 050° C.

Durée de vie comparée en fluage lisse et en fluage entaillée sur COTAC 74 (K_t : 3,4)

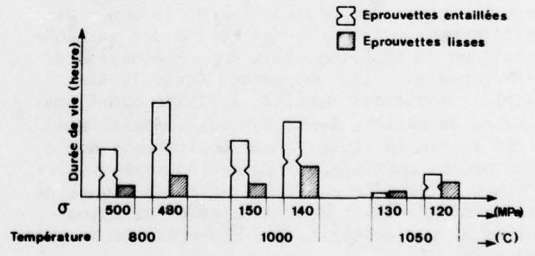

Fig. 7

On peut remarquer que la présence d'une entaille K_t = 3,4 n'a pas d'effet dommageable sur la tenue en fluage du composite. Les durées de vie d'éprouvettes entaillées restent équivalentes à celles déterminées sur éprouvettes lisses, à 1 050° C ; à 1 000° C elles augmentent d'un facteur 2,5 à 4,1 et à la température de 800° C (pied de la pale) la présence de l'entaille améliore le temps de rupture d'un facteur 4 à 4,3.

Fluage en cisaillement (pied de sapin) -

Ces essais ont pour objectif de soumettre le composite à des contraintes de cisaillement exer-

cées parallèlement aux fibres, type de sollicitation qui se rencontre dans les dents de l'attache des aubes au disque de la turbine. Des essais comparatifs ont été exécutés sur le composite Cotac 74 et sur l'alliage IN 100, à la température de 700° C sous une contrainte de 400 MPa (charge rapportée à la surface théorique de cisaillement dans le sens de l'effort appliqué). Par analogie avec le comportement de composites synthétiques on pouvait craindre qu'un effort de cisaillement parallèle aux fibres ne provoque de rupture prématurée sous faible contrainte le long des interfaces matrice-fibres. C'est la raison du choix des conditions particulièrement sévères avec contraintes de cisaillement relativement élevées, compte tenu des sollicitations réelles subies par le pied de la pale.

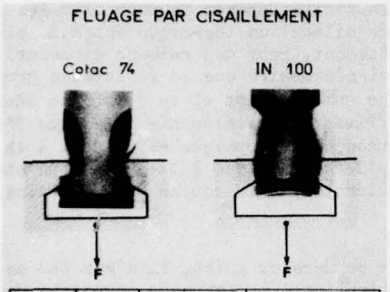

Temp (K)	Force (N)	Contrainte (MPa)	Temps de rupture (h)	
			Cotac 74	IN 100
973	9960	400	90,8	1,3

Fig. 8

On remarque (figure 8) que dans ces conditions (973 K/400 MPa) la rupture du composite se fait bien en fluage par cisaillement parallèle aux fibres, alors que dans les mêmes conditions l'alliage équiaxe IN 100 rompt rapidement par décohésion en traction. Compte tenu de la grande différence des durées de vie enregistrées dans cet essai il semble que la tenue du pied de sapin d'aubes en Cotac 74 ne doive pas inspirer de crainte particulière.

FATIGUE OLIGOCYCLIQUE (PIED DE LA PALE) -

Afin de compléter la caractérisation du comportement de l'attache de l'aube en Cotac 74, des essais de fatigue oligocyclique ont été effectués à la température de 923 K. Par suite de la combinaison de contraintes thermiques et mécaniques, la pièce subit des sollicitations vibratoires de basse fréquence, sollicitations qui atteignent des niveaux les plus élevés en régime transitoire lors d'une accélération ou, une décélération rapide du moteur.

Les essais ont été effectués en traction répétée à la fréquence d'un cycle par minute. Chaque cycle comportait une mise sous contrainte rapide (10 s) suivie d'un palier de maintien à σ_{max} pendant 20 secondes ; la décharge (10 s) était à son tour suivie d'un palier de maintien de 20 secondes à σ_o (figure 9).

Fatigue oligocyclique comparée à 923 K sur éprouvettes entaillées (K_t = 2,4)

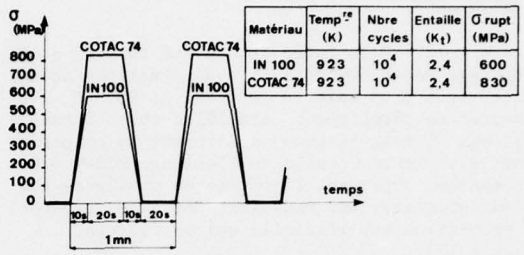

Matériau	Temp.re (K)	Nbre cycles	Entaille (K_t)	σ rupt (MPa)
IN 100	923	10^4	2,4	600
COTAC 74	923	10^4	2,4	830

Fig. 9

Sur éprouvettes plates, entaillées d'un côté (K_t = 2,4) la comparaison des résultats d'endurance à 10^4 cycles montre une nette supériorité du Cotac 74 -près de 40 %- par rapport à l'alliage du commerce.

FATIGUE HAUTE FREQUENCE -

De façon générale, en fatigue haute fréquence, la limite d'endurance des composites naturels est supérieure à celle des superalliages conventionnels (15). Pour le Cotac 74, les résultats sont indiqués dans le tableau VI . La tenue en fatigue dans le sens travers se situe encore à 75 % du résultat en long et, en ce qui concerne l'influence de la protection superficielle, les limites d'endurance déterminées en flexion rotative indiquent une baisse minime, de l'ordre de 2 %. L'examen de surfaces en fractographie montre qu'environ 70 % de la section est du type rupture en fatigue.

Tableau VI - Fatigue haute fréquence sur Cotac 74.

Température (K)	Eprouvette	Sollicitation		$\sigma_{non\ rupt.}$ en 10^7 cycles (MPa)
		Type	Fréquence (Hz)	
293	Torique, // aux fibres	Flexion rot.	49	± 400
293	Torique, ⊥ aux fibres	Flexion rot.	49	± 310
973	Torique, // aux fibres	Traction répétée	87	20 - 680
1073	Torique, // aux fibres	Traction répétée	87	20 - 520

Ces résultats ne doivent pas faire oublier que les ruptures relèvent souvent des mécanismes, plus complexes, par exemple, superposition des sollicitations stationnaires aux phénomènes vibratoires de haute fréquence. Il faudra veiller également au risque d'entrée en résonance avec la fréquence propre de l'aube, signalé plus haut.

IMPACT BALISTIQUE -

Dans ces essais, de type technologique, on compare l'évolution des dommages à haute température provoqués par des projectiles tirés à différentes vitesses. Un projectile de 3 g. à bout tronconique, vient frapper des plaquettes-cibles

30 x 70 mm, de 2,5 mm d'épaisseur, encastrées à une extrémité. Les cibles sont portées à la température de 800, 950 ou 1 100° C au moyen d'un chalumeau oxyacétylénique et les températures sont contrôlées sur la face opposée, au niveau de l'impact, par deux couples thermoélectriques. Les essais faits sur éprouvettes du composite Cotac 74 et des alliages IN 100 et MAR-M 509 permettent de constater qu'aux températures et conditions de tir, c'est le composite qui a la meilleure tenue à l'impact (14).

A 800° C, à endommagement comparable, le gain de vitesse de tir sur Cotac 74 est de 20 m s^{-1} par rapport à l'IN 100 et de 30 m s^{-1} par rapport au MAR-M 509.

A 950° C, le gain sur l'IN 100 est de 40 à 50 ms^{-1} et, par rapport aux cibles en MAR-M 509, de 25 à 30 ms^{-1}.

A 1 100° C, le Cotac 74 n'a été comparé qu'à l'alliage MAR-M 509 seul. Les déformations apparentes sont plus faibles qu'à 800 et 950° C, les fissures se développent parallèlement et normalement aux fibres, la tenue à l'impact du composite reste supérieure à celle de l'alliage MAR-M 509. On remarque cependant (éprouvettes protégées par Cr Al standard) une mauvaise adhérence du dépôt de protection superficielle qui se fissure (figure 10).

Fig. 10

CORROSION SECHE, OXYDATION ET PROTECTION DU COTAC 74 -

A côté des dommages accidentels occasionnés par l'injection de corps étrangers ou par déréglage du moteur, les pièces chaudes subissent en fonctionnement une dégradation progressive de leurs propriétés par rapport aux caractéristiques d'origine et cela tant à cause de l'évolution structurale du matériau qu'à la suite de l'agression en surface par le milieu ambiant. En ce qui concerne la stabilité structurale (problèmes de diffusion thermique accélérée, apparition de phases indésirables, coalescence etc...), les résultats d'essais de longue durée sur le Cotac 74, rapportés plus haut, montrent abondamment que ce point reste l'objet de l'attention vigilante des physiciens du métal. Reste le problème de l'incidence d'une exposition prolongée du composite à une atmosphère hautement oxydante, aggravée aux températures plus modérées par l'attaque sulfurante en milieu salin. Nous l'abordons ci-après.

Le rapport comburant / carburant contient un grand excès d'air et les gaz de combustion attaquent toujours les aubes à haute température avec une flamme oxydante. D'autre part dans les moteurs d'avions qui utilisent pourtant du kérosène raffiné, les gaz de combustion n'en contiennent pas moins des impuretés comme le soufre ou le sel qui peuvent provenir aussi bien du combustible que de l'air.

Comme il n'existe pas d'alliages métalliques pouvant satisfaire à la fois aux multiples conditions mécaniques requises à haute température et doués en même temps d'une parfaite inertie devant l'agression du milieu ambiant, on choisit le matériau en fonction du premier critère (haute résistance mécanique et thermique), à condition, bien entendu, qu'il ait au moins une aptitude à la protection superficielle par un revêtement approprié. De fait, quel que soit le matériau métallique choisi, les aubes de turbine reçoivent toutes un gainage protecteur.

Les qualités protectrices du gainage (attaque chimique, érosion, stabilité) doivent s'accompagner d'une bonne adhérence au substrat, d'une stabilité relative par rapport à celui-ci de manière à minimiser les échanges par diffusion, d'une plasticité capable de compenser les différences de dilatation thermique entre la pièce et son revêtement. Pour des raisons de sécurité il est aussi nécessaire que la résistance propre de l'alliage en oxydation et en corrosion sèche soit déjà suffisante pour éliminer le risque d'une dégradation catastrophique conduisant à la destruction rapide de la pièce à la suite d'un endommagement accidentel de la couche de protection.

Sur ce dernier point, il n'y a pas de problèmes particuliers. La tenue du composite Cotac 74 non protégé en corrosion sèche ou en oxydation à haute température est généralement du même ordre sinon meilleure que celle de la plupart d'alliages actuellement utilisés, en particulier l'IN 100. En attestent de nombreux essais d'oxydation et de corrosion directe du Cotac 74 nu ainsi que les essais de fluage de longue durée et de fatigue dans l'air sur éprouvettes avec et sans protection. En revanche, le problème de protection du composite se révèle plus délicat.

Il y a d'abord le fait que, si le composite doit assurer un gain en température d'utilisation, le revêtement protecteur devra, lui aussi, pouvoir résister à des températures au moins 40 à 60 K plus élevées que n'en demandaient les ailettes en alliages commerciaux actuels. De surcroit, il est vrai, les composites anisotropes biphasés n'ont pas la même aptitude au revêtement que les alliages homogènes.

Le développement des méthodes de protection ONERA a permis de trouver une solution efficace qui consiste à interposer entre le matériau composite et le gainage superficiel une couche de diffusion intermédiaire constituée d'un alliage Ni-Cr type 80/20 avec additions stabilisantes. Ce point sera développé plus loin (référence 13). Qu'il suffise de dire ici que les revêtements réalisés, dénommés DE 77, sont relativement ductiles et assurent une protection efficace du composite, aussi bien contre l'oxydation à haute température que contre la corrosion saline en essais de cyclage sur roue expérimentale. L'épaisseur régulière du gainage, prédéterminée avec précision, n'évolue pratiquement pas au cours de maintien prolongé à haute température.

L'incidence du gainage DE 77 sur les propriétés mécaniques du Cotac 74 sont examinées en détail. Jusqu'à 900° C, les essais de fluage donnent des résultats identiques sur éprouvettes protégées et sur éprouvettes nues ; à température plus élevée (1 000 et 1 070° C), une certaine perte en contrainte pourrait être estimée à environ 10 %. Des déterminations plus précises sont en cours.

CONCLUSIONS -

Nous avons dressé un bilan de caractéristiques du composite naturel Cotac 74, matériau destiné à la confection d'aubes de turbomachines de demain. Plus résistant, capable d'un gain en température et en contrainte par rapport aux performances des alliages actuels, le composite n'en constitue pas moins un matériau inusuel, hautement anisotrope, élaboré par des techniques spéciales. Il n'est pas évident, à priori, que ses propriétés exceptionnelles mesurées parallèlement aux fibres suffisent à provoquer l'adhésion spontanée du motoriste, même si les performances dans les autres directions nous paraissent rassurantes. Le Cotac 74 est un matériau nouveau et son utilisation éventuelle dépend moins de l'appréciation de ceux qui l'élaborent que de l'intérêt de ceux qui doivent l'appliquer. Aussi, plutôt que de porter un jugement de qualité, nous sommes-nous limités à comparer ses caractéristiques, courantes et moins courantes, avec les propriétés de meilleurs matériaux métalliques d'aujourd'hui pour voir dans quelle mesure le Cotac 74 offre la possibilité de satisfaire aux exigences de la technologie des moteurs de demain. La question reste ouverte et les éléments de réponse devront être cherchés dans un échange suivi avec les futurs utilisateurs.

Pour notre part, les résultats satisfaisants déjà acquis sur le Cotac 74 ne nous cachent pas l'importance du travail qui reste à accomplir. Il nous faut approfondir les problèmes fondamentaux de solidification, diminuer progressivement le nombre d'hypothèses simplificatrices pour mettre à la disposition des industriels une méthode d'élaboration élégante et simple, permettant l'obtention des pièces en composites aux propriétés requises et à coût réduit. Il nous faut améliorer la prévision par calcul thermodynamique des diagrammes des systèmes plus complexes, évitant erreurs et tâtonnements.

C'est la voie que nous poursuivons. Si nous nous sommes limités ici à la présentation du Cotac 74 sur lequel la caractérisation a été la plus poussée en essais de laboratoire comme au banc moteur, des raffinements de composition nous ont déjà permis d'élargir la famille Cotac 74 aux nuances 741 et 742, plus résistantes, plus réfractaires, plus fiables en durée. Des méthodes d'élaboration nouvelles, actuellement expérimentées, permettent l'élaboration directe d'aubages de forme finie et le programme de calcul à l'étude devra permettre son extension à la solidification industrielle simultanée de grappes d'aubes orientées. Mais des progrès doivent être réalisés dans le domaine de céramiques pour la confection des noyaux de bonne cohésion et faciles à éliminer.

Le perçage des canaux de refroidissement transversaux dans les aubes en Cotac 74 peut être obtenu par usinage électrochimique, avec des électrolytes et des électrodes relativement simples, mais adaptés au matériau ; de grandes vitesses de perçage ont été réalisées par électroérosion. Des résultats encourageants par soudage- diffusion ou par brasage- diffusion indiquent la possibilité de réaliser par cette technique des aubes creuses, procédé qui pourrait entrer en compétition avec la technique de noyaux céramiques trop difficiles à éliminer.

Les résultats d'essais travers et de fluage en cisaillement du Cotac 74 sont rassurants et ne paraissent pas devoir entraîner des modifications dans la conception du pied de la pale. Mais une analyse plus fine -par exemple, le calcul tridimensionnel complet par la méthode des éléments finis de l'état de contrainte de l'attache de l'aube- dira mieux si, compte tenu des contraintes élastiques du Cotac 74, la forme du pied actuel peut être conservée.

Dans le stade actuel du développement, le progrès nécessaire à l'emploi des composites naturels dans les turbomachines ne pourra s'accomplir que par une collaboration serrée entre les chercheurs des matériaux, les thermiciens et les motoristes. C'est la voie où nous nous sommes engagés et nous ne pouvons que féliciter les organisateurs de la Conférence d'avoir facilité ici une telle confrontation.

REFERENCES BIBLIOGRAPHIQUES

[1] - Proceedings of the Conference on In-Situ Composites, (Lakeville), National Academy of Sciences, Washington, D.C., NMAB- 308- I, II, III, Jan. 1973.

[2] Conference on In-Situ Composites - II (Lake George), Xerox Individualized Publishing, Lexington, Mass, May 1976.

[3] Impact of Composite Materials on Aerospace Vehicles and Propulsion Systems, AGARD Conf. Proc. n° 112, Toulouse, Sept. 1972.

[4] Directionaly Solidified In-Situ Composites, AGARD Conf. Proc. n° 156, Washington, D.C., April 1974.

[5] H. BIBRING, G. SEIBEL et M. RABINOVITCH, Nouveaux développements dans l'étude des superalliages à fibres obtenus par solidification dirigée, Mém. Sc. Rev. Mét. 69 (1972), 341 ; TP ONERA 1137.

[6] F.D. LEMKEY, G. Mc CARTHY, Quaternary & Quinary Modifications of Eutectic Superalloys Strengthened by Ni_3 Nb Lamellae and Ni_3 Al Precipitates, Rpt n° NASA CR 134678, Febr. 1975.

[7] H. BIBRING, T. KHAN, M. RABINOVITCH and J.F. STOHR , Development and Evaluation of New Industrial D.S. monocarbide reinforced composites for turbine blades, 3rd Intern. Symposium on Superalloys, Seven Springs, Pa, Sept. 1976; TP ONERA 1976-22.

[8] SNECMA, Dir. Techn. Rpt. YOTM 3- n° 31529, Juin 1975.

[9] J. LEMAITRE et J.L. CHABOCHE, A non-linear model of creep-fatigue damage cumulation and interaction, Symp. IUTAM, Göthenburg, Suède, Sept. 1974 ; TP ONERA 1394.

[10] J.L. CHABOCHE, Viscoplastic constitutive equations for the description of cyclic and anisotropic behaviour of metals, Bull. Ac. Pol. des Sciences, série Sc. Techn., Vol. XXV, n° 1, p. 33, 1977.

[11] J.F. STOHR, T. KHAN, M. RABINOVITCH et H. BIBRING,
Stabilité thermique des fibres de monocarbures de métaux de transition dans les composites réfractaires élaborés par solidification unidirectionnelle,
4 th Int. Conf. Strength Met. and Alloys, ICSMA- 4, Nancy, Sept. 1976 ; TP ONERA 1976-62.

[12] C.A. RAU , Jr, A.E. GEMMA and G.R. LEVERANT, Thermal-Mechanical Fatigue Crack Propagation in Ni- and Co- base superalloys under various strain-temperature Cycles, Fat. at Elev. Temp., ASTM STP 520, p. 166, Aug. 1973.

[13] P. GALMICHE, Protection d'aubes refroidies à structure interne complexe, AGARD Symp. on high temperature problems in Gaz Turbine Engines, ce volume, Ankara, Sept. 1977.

[14] SNECMA, Dir. Techn. Rpt. YOTM 3-31780, Février 1977.

[15] H. BIBRING, Mechanical Behavior of Unidirectionally Solidified Composites, ref. 1 ci-dessus, vol. II p. 1 à 69 ;
TP ONERA 1147.

DISCUSSION

A.W.H.Morris, UK

How complex is the cooling system which you can produce in your Cotac 74?

Author's Reply

Although the directional solidification is associated to the general foundry family techniques, one must admit that the direct manufacturing of cooled Cotac 74 blades does not offer the same possibilities as those of cast commercial alloy blades with complex cooling passages. It would not be advisable, for example, to introduce in the molten metal horizontally disposed ceramic parts which could hinder the growth of the composite with aligned fibers. Hence, only cores for hollow blades or for channels parallel to the fibers should be envisaged. To achieve this end it is necessary to have reliable and high strength cores capable of resisting any reaction with the liquid metal during many hours and which can be easily eliminated after solidification. No satisfactory solution has been found as yet.

However, all techniques used to achieve cooling configurations identical to those currently in practice in wrought superalloy blades (drilling, electrochemical machining, spark discharge and electron bombardment) can be applied right now for Cotac 74 blades. These various possibilities are described in the written version in your hands.

A.W.H.Morris, UK

You mentioned stresses generated by the mismatch of matrix and fibre coefficients of expansion, clearly this is important in thermal fatigue but in a real blade one has additional localised stresses. Have you done any thermal fatigue tests on representative cooled specimens?

Author's Reply

The existence of cooling passages in the turbine blades creates high transverse thermal gradients which may cause structural instabilities (Soret effect) and localised thermal stresses. We have been able to check the two points:

(i) firstly, laboratory tests showed that transverse thermal gradients of 100 K/mm have no adverse effect on the structural stability of Cotac 74 under the envisaged utilization conditions i.e. up to a maximum temperature of 1370 K (Scripta Met, 10,1976, 729; TP ONERA 1976-119 and also Reference 11 of this paper);

(ii) secondly, simultaneous static bench tests up to 1150°C currently in progress, comprising Cotac 74, IN 100 and DS 200 cooled blades mounted on the same wheel confirm that in conditions generating localised thermal stresses on real Cotac 74 blades the composite is superior to the two other commercial materials.

A.W.H.Morris, UK

You say that in thermal fatigue cracks in Cotac 74 stabilise at a short length. This is precisely what one would expect in a composite where the fibres act as crack stoppers and absorb energy along the fibre matrix interface. What concerns me is the effect the presence of these cracks has on properties such as shear, creep, tensile strength. Have you submitted thermally cycled specimens to tests evaluating such properties?

Author's Reply

As you mentioned, I showed that the thermal fatigue cracks originating at the trailing edge do not progress over a small length corresponding to a distance where they come across the first fibre or the longitudinal grain boundary; moreover, I also showed the experimental evidence that Cotac 74 is relatively insensitive to notches (Fig.7). Under these conditions, we did not find it useful to build intricate set-ups in order to perform tensile, creep or shear tests on either tapered thermal fatigue specimens or on previously cracked blades since this kind of initial damage would probably not have any other effect except a small reduction in the useful cross-section of the specimen.

Dr Siva, UK

Can you use this alloy for casting cooled blades, if so do you get homogeneous properties such as same U.T.S. through the section and no porosity?

Author's Reply

As I explained in answering the first question of Dr Morris, if one can find good ceramic cores it is perfectly conceivable to cast cooled Cotac 74 blades, provided the shape of the ceramic does not hinder the alignment of the reinforcing phase during the directional solidification. In these conditions, the composite blade will display faultlessly homogeneous structure and properties throughout the section: each square millimeter will comprise the same number of fibres, say 60 000 or 85 000 depending upon the solidification rate (1.2 or 1.6 cm/hour) and the U.T.S. will be similar in each solid element of the blade, for example 1 500 MPa (fifteen hundred megapascals) at room temperature. On the other hand, our experience confined to sintered alumina ceramics for longitudinal straight holes did not show any porosity in Cotac 74 components thus obtained. As a matter of fact, DS components generally display more sound structures and lesser porosity as compared to the conventionally cast parts.

Dr Siva, UK

Due to the matrix structure do you get anisotropic effect in the material?

Author's Reply

DS composites possesses a twofold anisotropy:

(i) the reinforcement is constituted by unidirectionally aligned fibres and

(ii) both the fibres and the matrix have a unique crystallographic orientation.

Your question relates to the second point and involves the matrix. In Cotac 74, the face centred cubic matrix growth axis is parallel to the crystallographic direction ⟨100⟩. This leads to elastic moduli values which are at once relatively low (advantage in thermal fatigue) and unequal ($E_{/\!/} < E_{\perp}$ and also the Poisson's ratio $\nu_{/\!/} < \nu_{\perp}$). Apart from this point, the anisotropy of a free structure is in fact not pronounced enough so as to produce a marked effect on the physical and mechanical properties of the material.

Dr Siva, UK

Compared with IN 100 alloy Cotac 74 is superior in fatigue strength but do you get the same order improvement in U.T.S.?

Author's Reply

For materials designed to operate at high temperature and extended service life, I think that the U.T.S. values are not very informative. In fact, you seem to share my opinion as it appears from your question that a better behaviour in fatigue or in creep does not necessarily mean a higher tensile strength.

When you compare the U.T.S. of Cotac 74 with that of IN 100 one notes that the commercial alloy is superior by 20% at 1000°C; around 800°C the U.T.S.'s of the two materials intersect; going further down, Cotac 74 progressively becomes superior and at room temperature it shows an increase in tensile strength of about 50% over IN 100.

HIGH TEMPERATURE CORROSION OF Ni-BASE FOR TURBINE BLADES ALLOYS IN SULPHATE-CHLORIDE CONTAINING ENVIRONMENTS

U. DUCATI[x], G. LECIS COCCIA[x], P. CAVALLOTTI[xx], F. BORILE[xxx]

[x] Istituto di Chimica Fisica, Politecnico di Milano

[xx] CNPM, Politecnico di Milano

[xxx] LTM, Cinisello Balsamo (Milano)

Summary

A number of commercial and experimental alloys have been submitted to various heat treatments and to corrosion tests by applying thermobalance, salt dip and electrochemical techniques. An hypothesis is advanced on hot corrosion triggering agents.

1. Introduction

The prediction of corrosion behaviour of nickel or cobalt superalloys, exposed to combustion gases in service, is a very difficult task, because even the behaviour of known materials is often peculiar of the single case.

The detrimental effect of salt contamination due to combustion ashes is currently recognized. In particular sulphate, chloride and vanadate salts are usually considered to be responsible for catastrophic corrosion.

This study deals with the effect of sulphates, chlorides and their mixtures on the corrosion behaviour of some commercial Ni base superalloys. For comparison, some experimental alloys and a Co base superalloy has been considered, as well as a few typical impregnation coatings.

A lot of papers have been published on the subject, many of which have brought valuable contributions to enlight special features related to the problem.

Two main trends can be distinguished in the literature:

i) the chemical approach (1-4), dealing with chemical thermodynamic and kinetic aspects, in which phase equilibria, solubility and diffusion processes play the main role;

ii) the electrochemistry oriented one (5-6) assuming that electrochemical reactions uniformly occur on the surface.

These studies are of fundamental type and consequently their prediction content is, generally speaking, low. A technological approach is often considered the most useful one (7). In this approach, burners, contamined oil and full scale turbine components are involved and the rig test is supposed to give the needed informations. Although these tests are valuable to verify the behaviour of the materials in those particular conditions, they do not appear to give sufficiently detailed informations on process mechanisms and on actual corrosion rates.

The literature is lacking for what concerns the relative role of chemical and electrochemical reactions in the corrosion resistance of the materials, and their mutual interactions.

According to us, this point should be considered with particular care.

Special features, like as incubation time, the early period of firing, during which the corrosion does not appear to operate, substantiate the important role of the above mentioned interactions.

We submitted a number of materials to different heat treatments and corrosion measurement techniques, in order to characterize the triggering agents for hot corrosion.

2. Experimental methods

The chemical composition of the materials, which have been tested, is given in Table 1. Most of these are nickel superalloys which exhibited Cr base scale formation, except for IN-100 which forms Al-base scale.

The behaviour of a single cobalt superalloy has been studied for comparison. CRG 2 and CRK 4 are conventional names of two experimental alloys, specially designed to give rise to known γ'-phase volume fractions dispersed in a matrix of given composition: namely CRG 2 contains 19% and CRK 4 4% γ'-phase volume fraction (at 800°C).

The tests have been performed on untreated samples and on samples submitted to various heat treatments specifyed for solubilization, aging and grain growth, as it is hereafter described.

TABLE 1

Element / Alloy	C	Cr	Co	Mo	Ti	Al	Nb	Zr	S	B	Ni	Other
IN 100	0.18	10	15	3	4.7	5.5	-	0.06	-	0.014	bal	1.0 V
U 500	0.08	18	18.5	4.0	2.9	2.9	-	0.05	-	0.006	bal	-
U 700[x]	0.08	15	18.5	5.2	3.5	4.3	-	-	-	0.030	bal	-
EPK 57	0.05	24.3	19.7	1.5	3.0	1.4	0.95	0.05	-	0.0125	bal	-
CRK 4	0.009	24.1	19.8	1.55	1.29	0.7	0.48	0.05	0.004	0.012	bal	-
CRG 2	0.007	24.15	19.9	1.53	2.66	1.34	0.93	0.05	0.006	0.011	bal	-
X 45	0.25	25.5	bal	-	-	-	-	-	0.04	0.01	10.5	Si < 1
												Mn < 1
												W 7.5
												Fe 2

[x] This composition can be considered to be representative of Astroloy alloy also.

To check the behaviour of the most corrosion-resistant components of the alloys, pure chromium metal, as well as aluminium layers have been studied; Cr-Al diffusion layers have been also tested for purpose of comparison.

Thermogravimetric runs have been performed at 900°C in still air by a Cahn 100 thermobalance on samples contamined by small amounts of the following salts: Na_2SO_4, NaCl, and Na_2SO_4 + 10 w/o NaCl mixture. About 2 mg/cm^2 salt have been deposited on the previously polished surface, by immersion in a saturated aqueous solution of the salts followed by drying in an oven at 200°C. Of course, this procedure did not produce a completely anhydrous salt layer, but it is our opinion that this is not a drawback, because water is always contained in the environment to which the material is exposed in service.

The sample weight and surface area ranged respectively 3 – 6 g and 5 – 15 cm^2. The specimens were held within an alumina pan suspended by a Pt-Rh 10% wire.

We tested also the corrosion resistance of the same materials dipped in oxygen-saturated Na_2SO_4 + + 10 w/o NaCl fused salt mixture.

In this case only the weight variation at the end of the test has been measured. The most important information drawn from this test concerned the possible modification of scale composition in respect to the one obtained in thermobalance runs.

Such test were carried out by melting the salt mixture in an alumina crucible under continuous oxygen bubbling, which had also moderate stirring effect, and simply dipping the samples.

Electrochemical measurements of corrosion rates have also been adopted. In this part of experimental work, fused quartz glass or alumina cells have been used, whose schematical diagram is shown in Fig. 1 a). As long as possible, the criteria were followed of a) carefully defining the electrode working area, b) assuring a uniform current density (c.d.) distribution on the electrode.

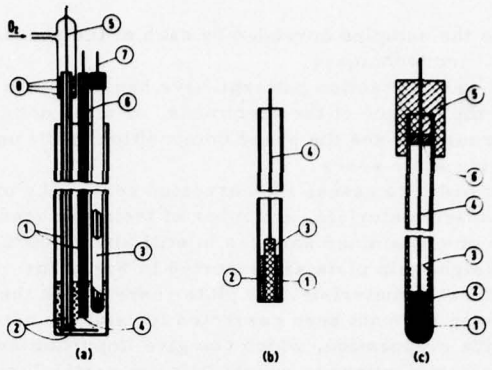

Fig. 1 - Cell for electrochemical measurement. a) 1. Sintered Al_2O_3 tubes; 2. Pt foil and wire; 3. Sintered zirconia R.E.; 4. Working electrode; 5,6,7. Leads; 8. PTFE gasket. b) 1. Sintered Al_2O_3 tube; 2. BN gasket; 3. Working electrode; 4. Lead. c) 1. Stabilized zirconia sintered tube; 2. Ni + NiO powder mixture; 3. Electroless Ni flash; 4. Lead; 5. Epoxy cast sealing; 6. PTFE plug.

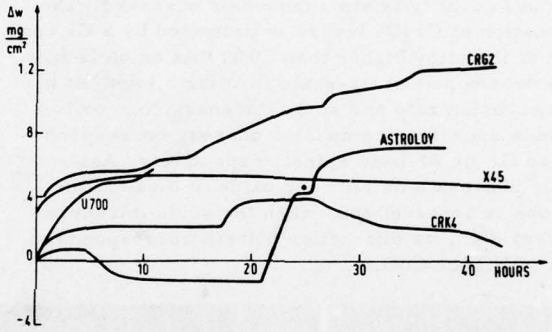

Fig. 2 - Weight change plots for heat treated materials. T = 900°C 2 mg/cm^2 Na_2SO_4 + NaCl 10 w/o . Still air.

The electrode was cylindrically shaped and the lateral surface was enrobbed by an hot rolled BN lining keyed in an outer alumina tube, so that only the lower base of the electrode was exposed (see Fig. 1 b).

The Pt/O_2 counterelectrode was placed on the bottom of the cell, so that it directly faced the working electrode.

The electrode tension was measured against an oxygen reference electrode (R.E.), which currently consisted of a stabilized zirconia sintered tube containing a mixture of Ni and NiO with a Ni lead, and sealed at the top with epoxy resins (Fig. 1 c).

Being the bath saturated in respect to oxygen, the R.E. potential could be considered as unaffected by slight changes in bath composition during the measurement time.

Electrical feeding and measurements have been as follows:

i) current recording at steadily increasing voltage;
ii) current recording at given constant applied voltage;
iii) voltage recording at steady current, and voltage transients recordings at current steps.

The working electrode has been acted always as an anode, at c.d. in the range 0 – 200 mA/cm^2, against a Pt/O_2 counterelectrode at 920°C.

Conventional metallographic procedures, X ray diffraction and electron microprobe analysis have been used to charac-

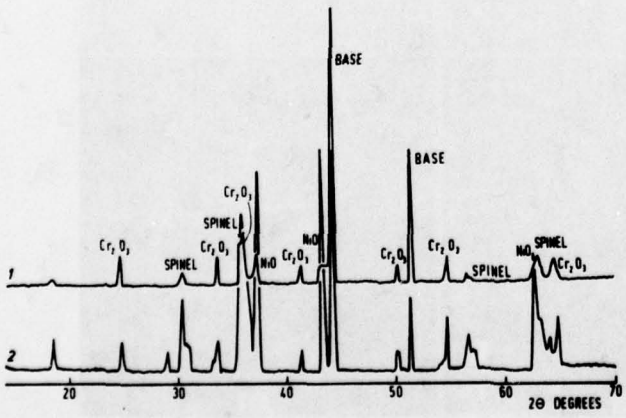

Fig. 3 - X-ray diffraction patterns of a Cr scale forming sample. 1: after abrasion : 2: as oxidized.

terize the samples corroded by each of the above-mentioned techniques.

X-ray diffraction patterns have been obtained from the surface of the specimens, or after delicate abrasion to see the phase composition of the underlying scale zones.

In order to assess the corrosion resistance of the chosen materials, a number of tests has been made on contamined samples in still air at 900°C.

Weight gain plots are reported in Fig. 2 for heat treated materials. The plots, here and in the following, have not been corrected for salt or metal oxide evaporation, which can give important negative contributions to weight gain, in particular when Al and Ti contents are low. From the reported results a fairly good corrosion resistance is observed for several materials.

X-ray diffraction patterns of the scale show the mean structural composition of the outer layer.

When the corrosion rate and the scale thickness is low, an hexagonal oxide of trivalent metal ions, corresponding to the Cr_2O_3 X-ray diffraction pattern, is mainly observed. In some cases, rutile in a small quantity is simultaneously observed. The formation of Cr_2O_3 layers is promoted by a Cr content of the alloy higher than 20%; this oxide is firstly developped on Cr-scale forming alloys. At high corrosion rate and scale thickness, one or two spinels appear as companion phases, corresponding to Cr-or Al-base spinel respectively. Aside these phases, a definite fcc oxide of divalent metal ions is observed too, when the scale thickness is very high; its diffraction pattern corresponds to that of NiO or CoO.

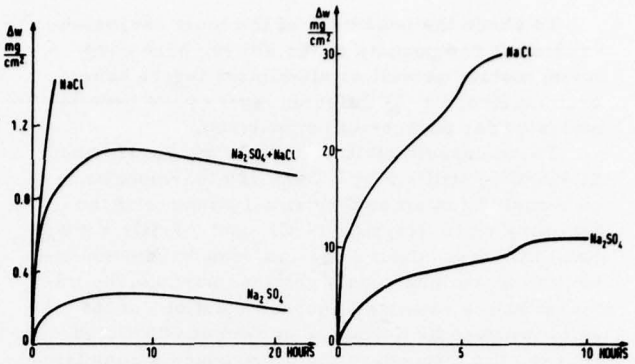

Fig. 4 (left) and 5 (right) - Influence of contaminant on corrosion rate of CRG 2 alloy samples. Left: heat treated. Right: as extruded. T = 900°C. 2 mg/cm^2 salt contamination. Still air.

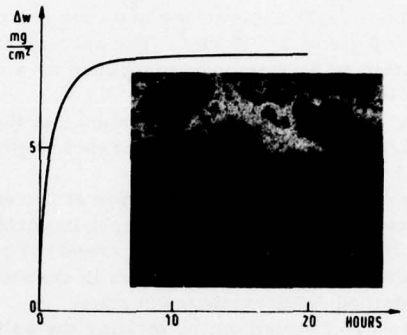

Fig. 6 - Weight gain and macrographic picture (× 7 approx.) of an IN 100 alloy sample. T = 900°C. 2 mg/cm^2 Na_2SO_4 + NaCl 10 w/$_o$ salt contamination still air.

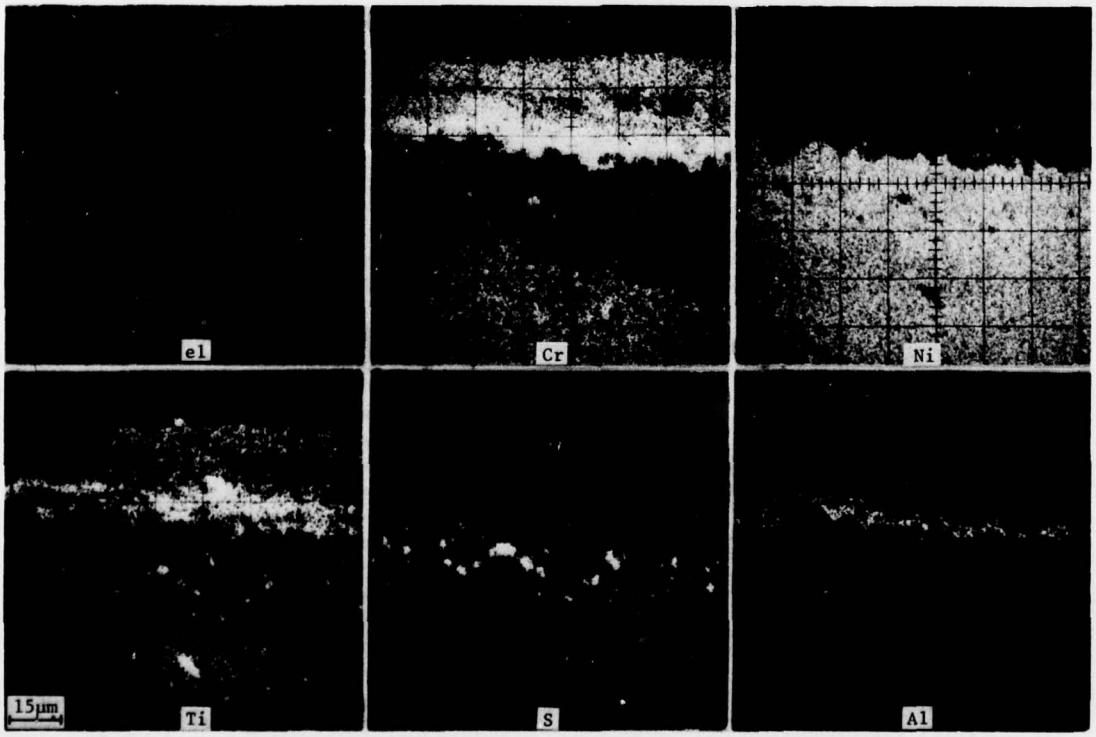

Fig. 7 - Electron and X-ray emission images of a section of an untreated CRG 2 alloy sample corroded at 900°C in still air. 2 mg/cm^2 Na_2SO_4 + + NaCl 10 w/$_o$ salt contamination.

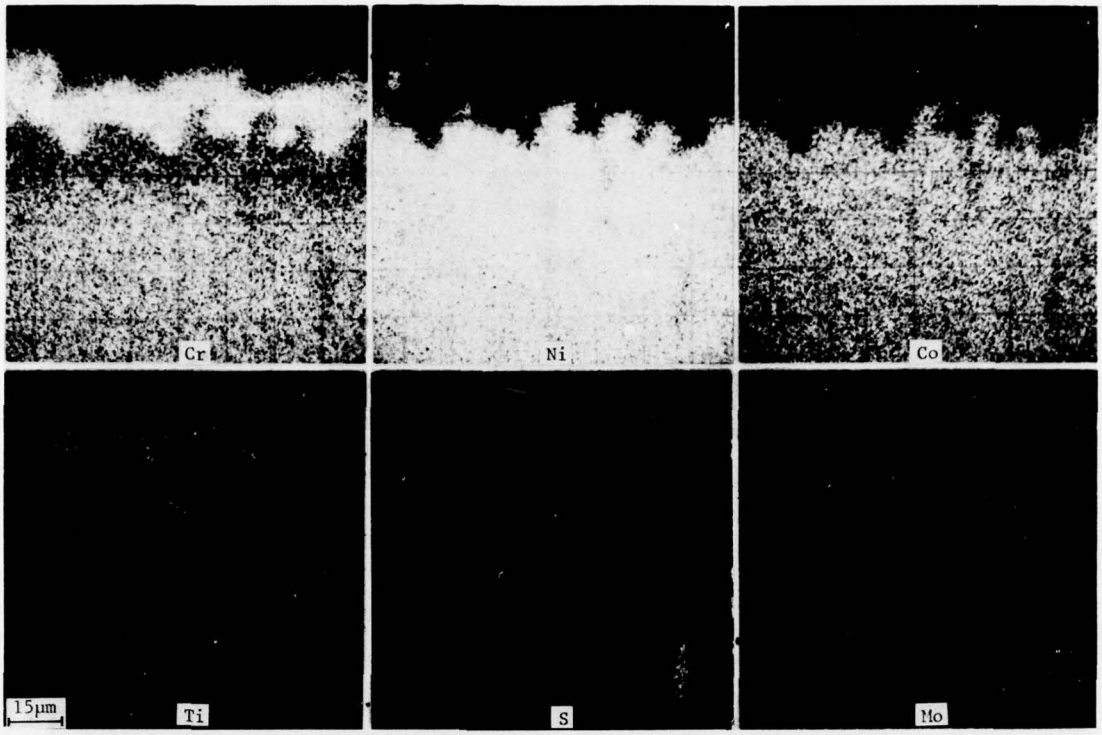

Fig. 8 - X-ray emission images of a section of an untreated U 700 alloy sample in conditions as above.

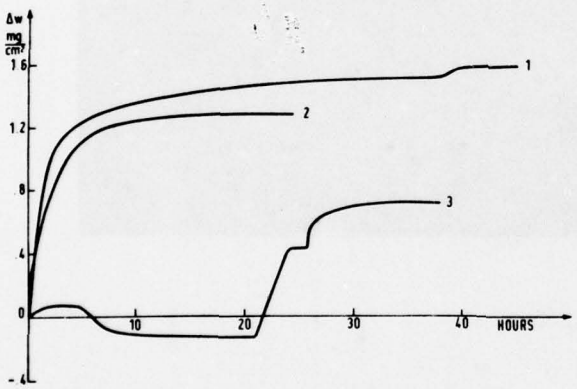

Fig. 9 - Weight change curves for variously heat treated hipped Astroloy alloy samples. T = 900°C. 2 mg/cm^2 Na_2SO_4 + NaCl 10 w/o salt contamination. Still air. 1. As hipped: 2. 4 h heat treated at 1190°C plus 16 h aged at 790°C; 3: 50 h heat treated at 1190°+ plus 16 h aged at 790°C.

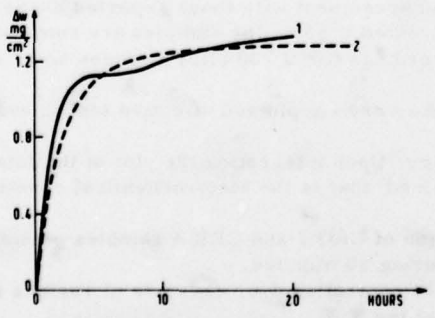

Fig. 10 - Weight change curves for equally treated U 700 alloy (1) and hipped Astroloy alloy (2) samples corroded in conditions as above.

By gradually abrading the surface layer, the diffraction patterns exhibited by the samples are changed as it is shown in Fig. 3. The NiO peaks rapidly disappear, the Cr spinel peaks decrease, whilst the Al spinel peaks, if any, are relatively enhanced as well as the Cr_2O_3 ones.

The influence of the nature of the contaminant on the corrosion rate is reported in Fig. 4.

In the Fig. 5, the corresponding diagrams for materials not submitted to thermal treatments are reported, and the rise of the corrosion rate for untreated alloys is evidenced.

In Fig. 6 the macrographic appearence of an untreated IN 100 corroded sample is shown, as well as its oxidation curve.

Fig. 7 and 8 shows the electron and X-ray emission images for samples of CRG 2 and U 700 in the untreated conditions.

To throw light on the influence of the grain size on the corrosion rate, hot isostatically pressed (hipped) samples obtained from Astroloy powders (whose composition is very close to that of U 700 alloy) have been tested after different times of heat treatments at 1190°C, followed by a standard ageing at 790°C for 16 h. The results are presented in Fig. 9, and compared to the weight gain of an as-hipped specimen. A comparison between U 700 and Astroloy alloys behaviour after identical heat treatment is shown in Fig. 10.

In Fig. 11 the microscopic and microanalytical images are shown for U 700, and in Fig. 12 the same features related to 50 h heat treated Astroloy are presented.

Dipping the samples in oxygen-saturated Na_2SO_4 + + 10% NaCl salt mixtures, at 920°C, gives rise to formation of a scale which is currently thicker than

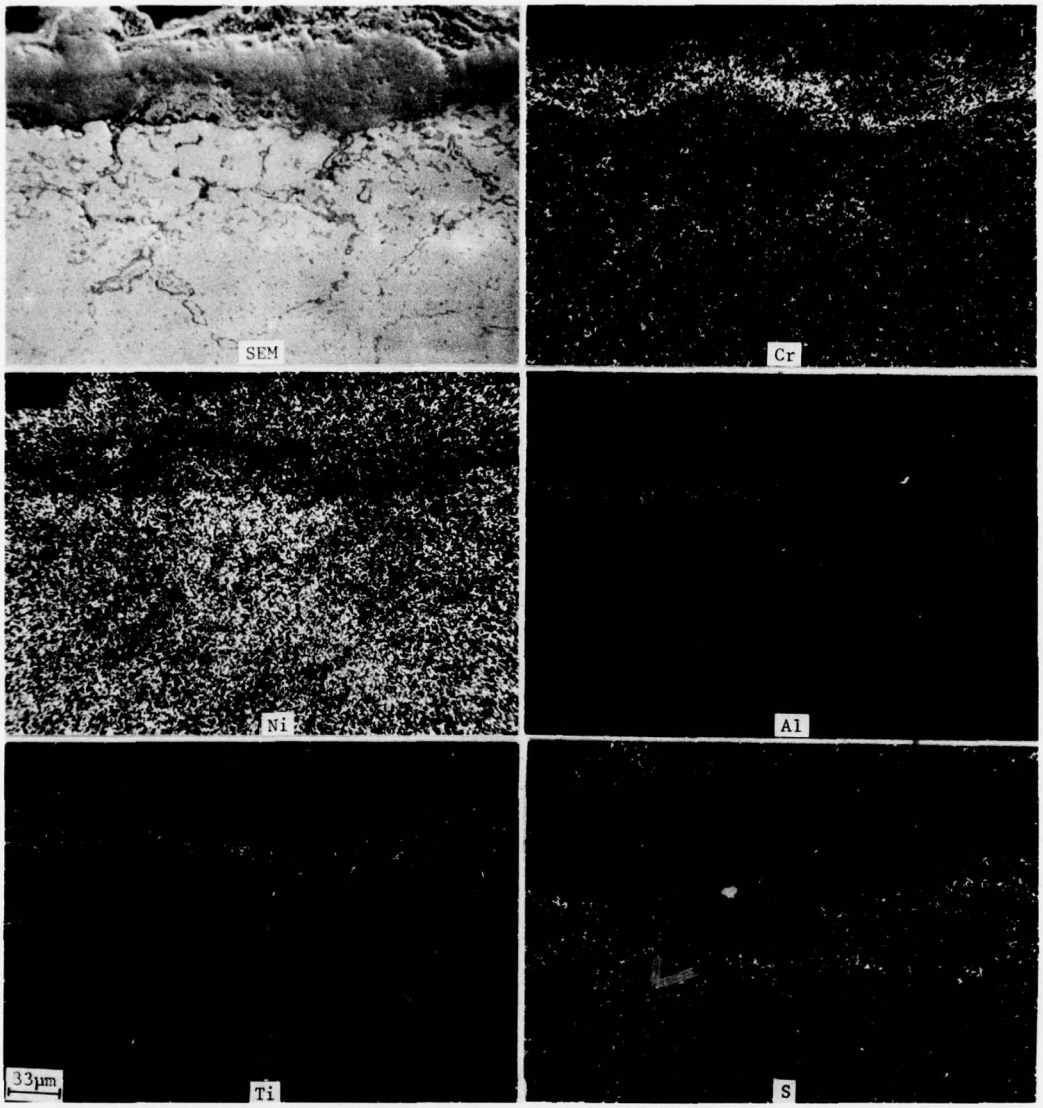

Fig. 11 - Electron and X-ray emission images of a section of U 500 alloy sample of Fig. 10.

that obtained in thermobalance tests of salt contamined samples.

X-ray diffraction patterns show scale constitution not too different from that of salt contamined samples corroded in still air. Nevertheless the presence of α-Al_2O_3 in the scale of IN - 100 samples and higher Cr_2O_3 contents in the scale of the other alloys are peculiar features.

In Fig. 13, the X-ray emission images of a section of a thick scale, grown on an as-extruded CRG 2 alloy sample are shown.

Electrochemical corrosion tests displayed behaviour in good agreement with those reported above.

The results of potentiodynamic experiments on differently treated U 500 alloy samples are summarized in Fig. 14. Figs. 15 and 16 reported the corresponding recordings for U 700 alloy samples and the behaviour of Cr, Al, and Cr-Al respectively.

Measurements of current intensity in potentiostatic mode is a very simple and effective tool to evaluate the corrosion rate in a controlled accelerated way.

Such recording are shown in Fig. 17 for untreated U 500 alloy. Upon integration, the plot of the total circulated charge versus time, at co nstant overvoltage, is obtained: that is the electrochemical counterpart of weight change vs. time plot.

Fig. 18 and 19 show the microanalytical images of the section of CRG 2 and CRK 4 samples potentiostatically corroded at 920°C in Na_2SO_4 + NaCl 10% mixtures during 30 minutes.

In amperostatic mode operations the material is submitted to controlled d.c. currents of various intensities and the total electrode overvoltage is measured against the R.E.

By imposing transitients of current during electrolysis, the overvoltage components, conventionally

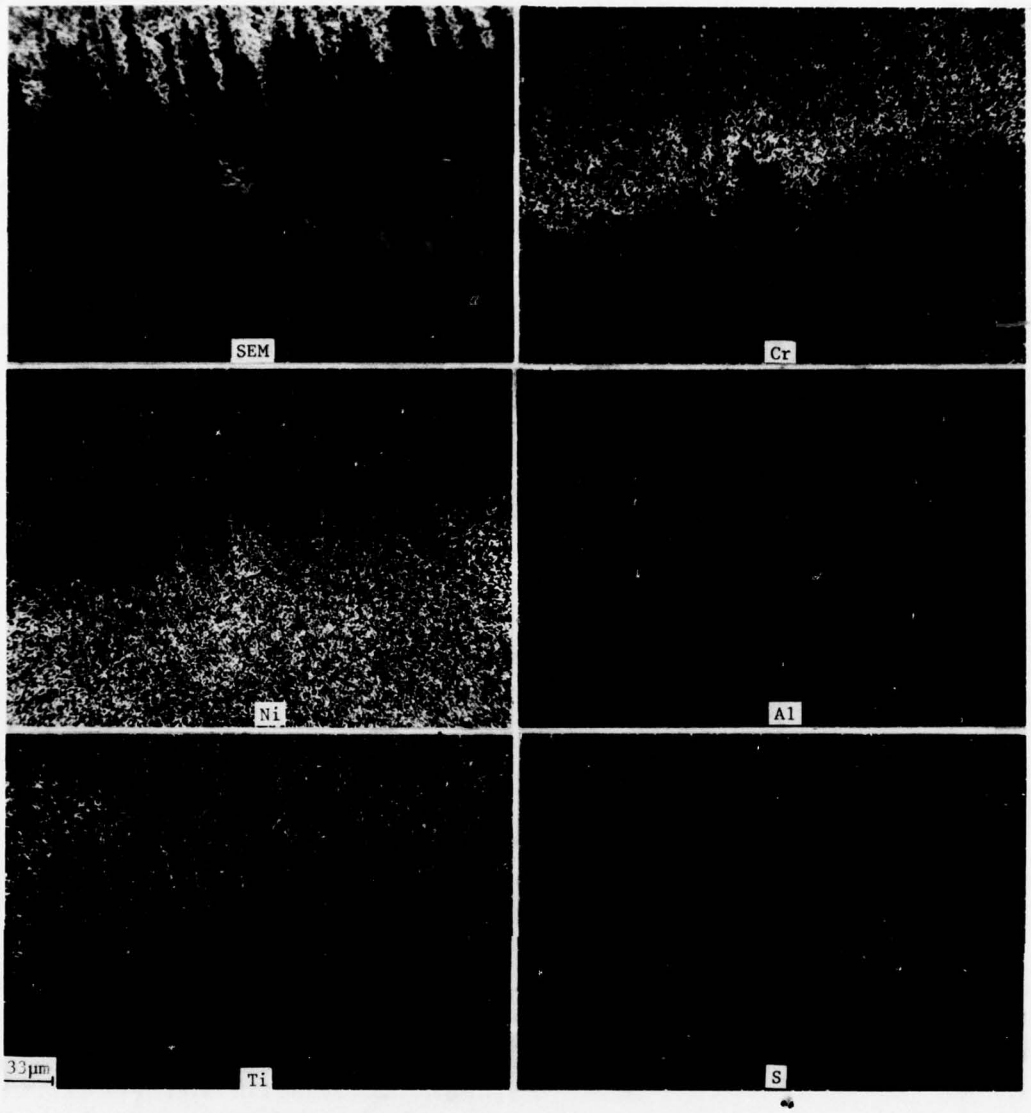

Fig. 12 - Electron and X-ray emission images of a section of the hipped Astroloy alloy sample of Fig. 2, 3.

specified as follows:

i) ohmic drops;

ii) ion-exchange overvoltage;

iii) concentration polarization (c.p.) both in the salt bath and in the scale;

can be split on the base of the related relaxation times and evaluated.

Both oscillographic and fast pen recording have been obtained.

In Fig. 20 a) the voltage vs. time characteristic and its variation with electrolysis time is reported for a sample of U 500 alloy, and the corresponding curves are shown in Fig. 20 b) for a CrAlY impregnation layer obtained by slurry techniques on IN 738 LC samples. The variations in electric characteristics are evident: when the electrolysis is switched on, the ohmic component is high and the c.p. one is rapidly set up.

At high circulated charges, ohmic drop becomes very low, whilst high c.p. overvoltages are typically affected by the porous scale.

Discussion of the results and conclusion

The analysis of the weight gain plots vs. time does not substantiate any simple hypothesis on regular time dependence of the scale thickness, with the possible exception of the low rate range of the curves to which uniform corrosion processes can be associated by sample inspection.

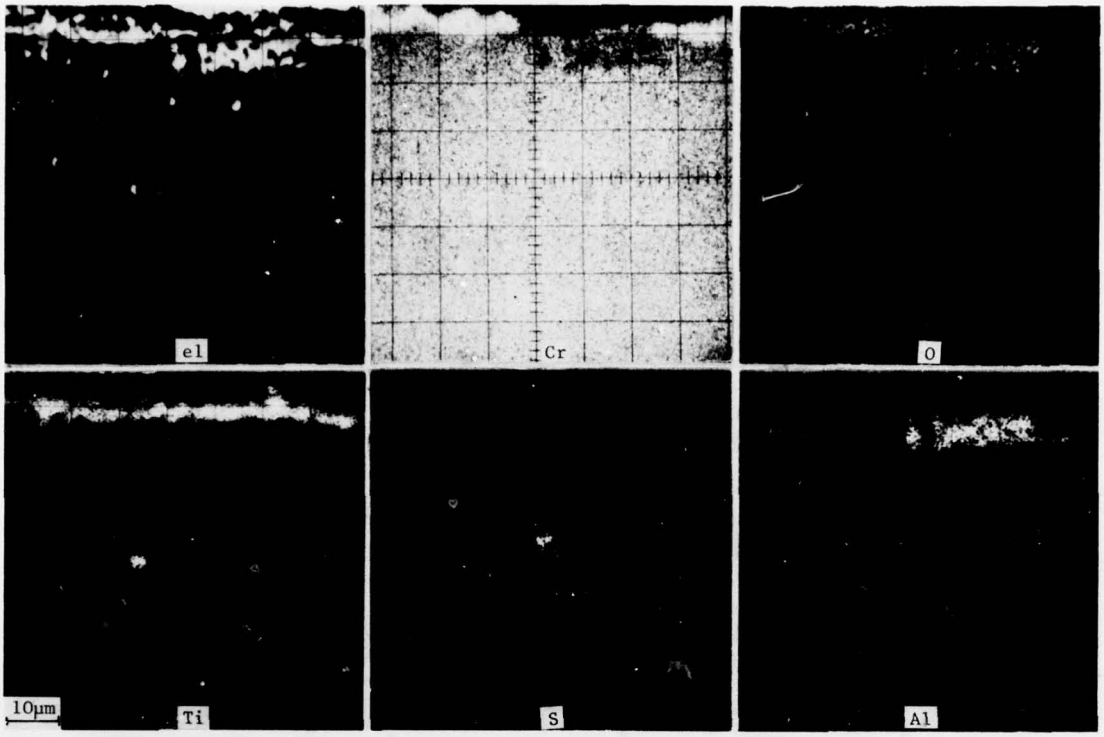

Fig. 13 - Electron and X-ray emission images for an as-extruded CRG 2 alloy sample corroded by the salt dip test. Oxygen saturated Na_2SO_4 + + NaCl 10 w/$_o$ molten salt mixture. T = 920°C. 16 h.

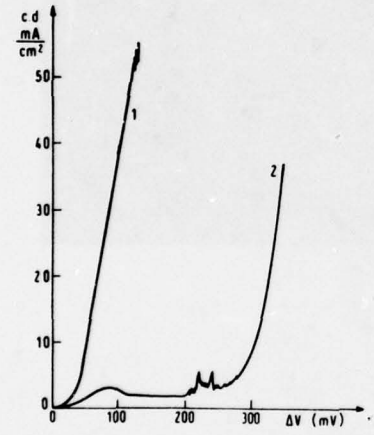

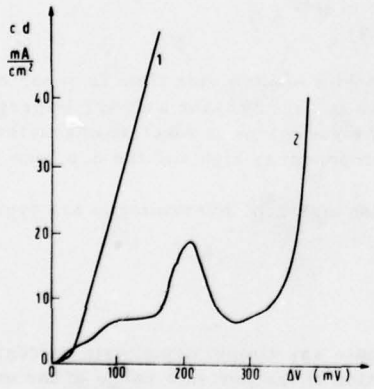

Fig. 14 (upper) and 15 (lower) - Potentiodynamic curves for U 500 alloy (upper) and U 700 alloy (lower) samples. 1. Untreated; 2. 8 h heat treated at 1150°C and 16 h aged at 750°C. Na_2SO_4 + NaCl 10 w/$_o$ molten salt mixture. T = 920°C.

Sudden slope variations and quasi-plateau features of the diagrams need more complex hypothesis to be advanced for mechanism interpretation.

When catastrophic corrosion is observed, we suggest that two main mechanisms contribute to the total observed weight change:

i) an uniform (chemical) attack, due to the reaction between the metal and environmental oxygen, possibly promoted by the salt layer, which causes an even and dense scale to grow;

ii) a localized (electrochemical) attack at preferred sites, with sulphur injection in the matrix (cathodic areas) and formation of an oxide scale which is prous because of the extremely high rate of growth (anodic areas).

Cracks, porosities and other inhomogeneities in the scale or in the metal may be considered to be responsible for this type of corrosion.

Inspection of the thermogravimetric results, indeed, shows that the differences in behaviour exhibited by the same base material submitted to various heat treatments are greater than those among different materials submitted to equal heat treatments, the worst behaviour being observed for untreated, as-cast samples.

This result stresses the role of inhomogeneities, both structural and of chemical composition. Macroscopic variations of local chemical composition have a greater effect on the corrosion rate than the microscopic ones, as one can deduce from the minor but revealing difference in corrosion rate between CRK 4 and CRG 2 (the letter exhibiting a higher volume fraction of γ'-phase precipitates). In absence of thermal treatments, the macroinhomogeneities, such as uneven Cr distribution, give a dramatically enhanced corrosion rate of the material, in respect to the one

due to γ'-phase precipitation, as it is clearly shown by comparison of Figs. 2, 4, 5 and 9.

The same general behaviour is displayed regardless the nature of contaminants, although pure chloride salts appeare to be the most aggressive ones.

The study of hipped Astroloy samples has been carried out in order to check the role of inhomogeneities such as chemical composition variations inside the grain and grain boundaries on corrosion rate.

Fig. 9 can be interpreted as follows:

i) the steepest curve, related to as-hipped samples, displays the corrosion rate of a highly inhomogeneous material, affected by uneven chemical composition, small grain size, and, possibly, cold work;

ii) in the intermediate curve, some of these disturbances have been removed by the heat treatments, probably cold work and chemical composition gradients inside the grain, whose size too has been possibly extenden by the heat treatment;

iii) the very low curve shows the beneficial effect of the grain growth obtained by a 50 hours heat treatment at 1180°C, as well as the effect uniform γ'-phase precipitation, subsequent to ageing at 790°C for 30 hours. In this curve, the incubation period, usually not exceeding 20'−30', is lasting some 20 hours.

The simultaneous examination of X-ray diffraction patterns and electron and X-ray emission images shown in Fig. 12 enlights the phase constitution of the scale grown on samples of this alloy.

The exagonal oxide of trivalent metal ions, which is observed at the early stages of growth, is comp-

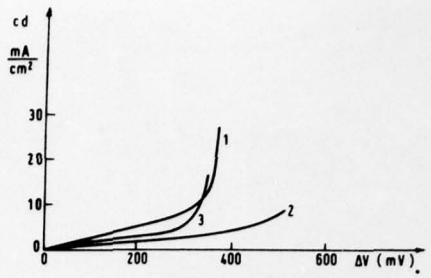

Fig. 16 - Potentiodynamic curves for Cr metal (1) electroplated Al layer on U 500 alloy not submitted to diffusion (2); CrAl impregnation coating (3). Conditions as above.

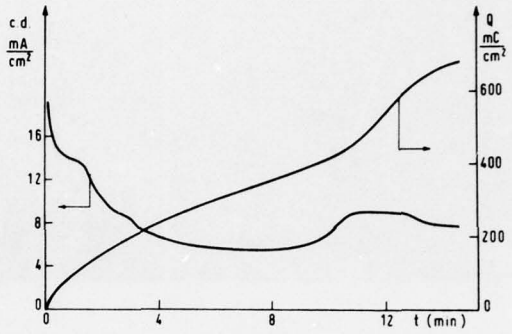

Fig. 17 - Potentiostatic curve for untreated U 500 alloy sample Na_2SO_4 + NaCl 10 w/o molten salt mixture. T = 920°C. ΔV = 100 mV.

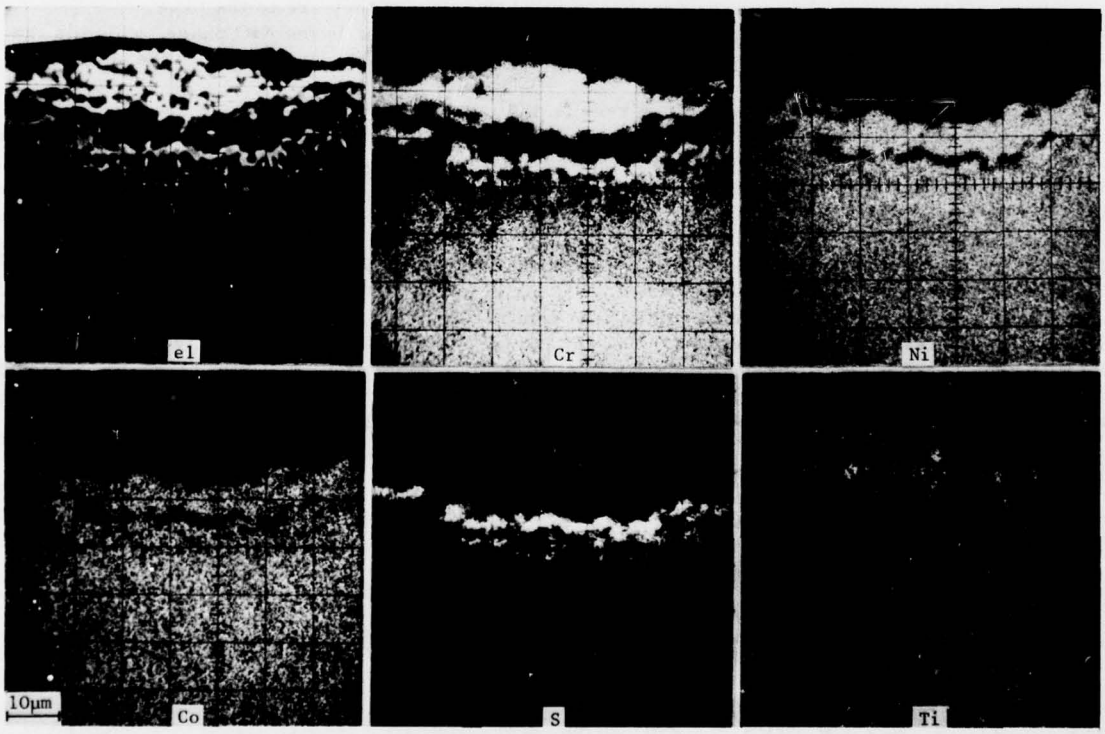

Fig. 18 - Electron and X-ray emission images of a section of a CRG 2 alloy sample submitted to potentiostatic corrosion. Conditions as above.

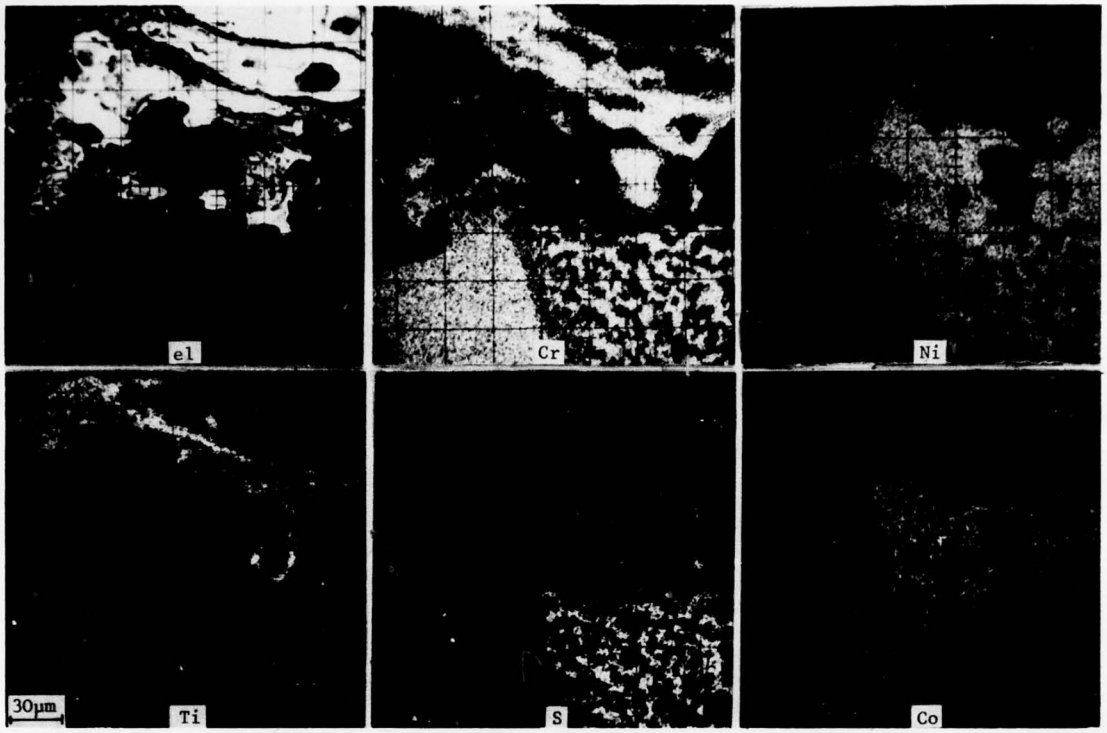

Fig. 19 - Electron and X-ray emission images of a section of a CRK 4 alloy sample. Conditions same as above.

act and adherent to the metal base, which comes out Cr-depleted in the outer layer. The spinel phases are usually formed subsequently and they are richer in Al the closest they are to the base.

These phases are less coherent than the Cr_2O_3 one, and even softer is the NiO phase, which is the last one which appears. The lack of coherence is related to the reconstructive nature of the transformation from the hexagonal oxide to the fcc one.

Electrochemical methods do confirm these results and moreover by means of high speed tests. No discrepancy is evident in respect to the informations drawn from long term tests such as thermogravimetry or from fast, electrochemical methods; and the information content of the latters is higher.

This conclusion is supported by the microanalytical images and X-ray diffraction patterns of the scale, and it is, in our opinion, related to the abovementioned hypotheses on hot corrosion mechanism of Ni base superalloys.

The presence of localized corrosion processes responsible for Sulfur penetration is clearly stated by Figs. 13 and 19.

In the first one, the border line between Cr-base and Al base scale is copied, inside the matrix, by the S-rich precipitates; the scale appears to grow inward the metal at Al-rich sites outward at Cr-ones.

Fig. 19 shows a sharp splitting of the matrix in a cathodic area, dotted by sulfides, and in an anodic, sulfur free, one. A crack in the scale is probably responsible for such an effect, giving rise to a gradient of oxygen potential at the metal-scale interface in respect to the zones coated by uncraked scale,

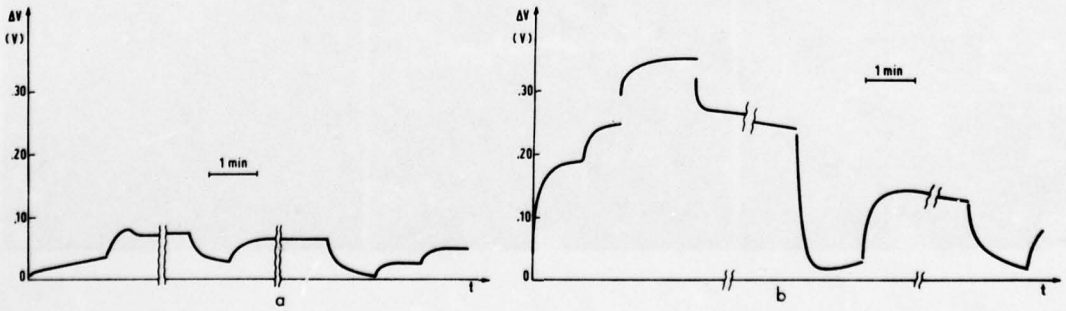

Fig. 20 - Voltage transients at current steps. $i = 5\ mA/cm^2$. T = 920°C. Na_2SO_4 + NaCl 10 w/o molten salt mixture. a) untreated U 500 alloy sample; b) CrAlY impregnation coated IN 738 LC alloy.

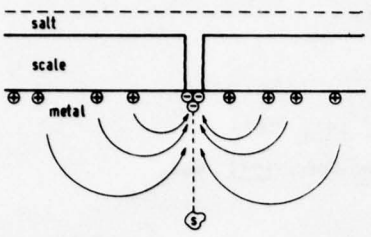

Fig. 21 - Schematic diagram of electron trails inside the metal being corroded in the case of large anodic areas and restricted cathodic ones.

that is to a galvanic concentration cell. The related emf.s and the consequent current circulation in the metal beneath the scale account also for the observed absence of sulphur spreading inside the matrix.

Should the matrix be in equipotential conditions, the probability of finding a single sulphur precipitate inside the metal would be uniform in an hemisphere of radius r related to sulphur (or sulphide) diffusion coefficient and to the time elapsed after SO_x^{2-} (x = 3, 4) reduction. If, on the contrary, charge circulation paths are supposed like as those schematically drawn in Fig. 21, the most likely trail of sulphide precipitates, which require very high electron activity for their stability, is the dotted one.

The model is clearly oversimplified, nevertheless it is, in our opinion, revealing.

In Fig. 14, for instance, the cross section of the sulphide rich zone is decreasing with the depth of penetration, indicating a costraint to the sulphide diffusion direction.

A very suggestive support to the intervention of electrochemical steps in hot corrosion is, moreover supplied by Fig. 6, in which the upper, uncorroded zones, are surrounded by heavily corroded ones.

Should the process be chemical in nature, that is solely related to the short range environment of the metal atoms, such a result would never occur, in as much as in studies on hot corrosion no alloy compositions show complete resistance to oxidation. Thus, long range, that is electrochemical effects, must be accounted for in this case, and in the abovementioned ones. In the early stages of corrosion via contaminants, or by fused salts dip, the cathodic reaction product may be hydrogen coming from residual water or from OH^- ions. This is why the upper zones of the metal surface shown in Fig. 6 appear to be bright.

Then, due to changes in local composition, the cathodic zones may migrate, so that the whole metal surface eventually appears to be covered by oxidation products.

Only at this stage the electrochemical process is in such conditions as to give sulfur and sulphides as cathodic reaction products. That is, when the scale at the cathodic sites is sufficiently thick to effectively screen the metal in respect to diffusion of highly oxidizing species from the atmosphere, SO_x^{2-} (x = 3, 4) is thus reduced at cathodic sites.

The oxidation rate is completely changed by this effect. The process is, on the one hand, stopped by the filling of the active cracks and pores by reaction products. On the other hand, it is promoted by the formation of new cracks, produced by shear stresses induced in the scale by the uneven growth. The latter effect eventually exceeds the former, so that the weight gain curve assumes the characteristic stepwise feature. The main difference between salt contamination plus air oxidation tests and the electrochemical ones seems to be in the higher rate of the process of uniform scale growth that is found in the latter. Sulphur deposition is any way due to local corrosion cells.

The same is, moreover, true if burner test and salt contamination thermobalance runs are compared, in our opinion. When the metal is thoroughly heat treated, two types of inhomogeneities are still found: grain boundaries and γ'-phase precipitates. The effect of the former ones is clearly displayed by Fig. 11. where sulphur precipitation at the grain boundaries is evident. The effect of the latter is shown by Fig. 2, in which the weight gain of a metal containing about 20% precipitate (CRG 2) is corroded at higher rate than one containing 4% precipitate (CRK 4).

Among the electrochemical results, the most interesting one, in view of its information and prediction content, appears to be that given by intensiostatic techniques.

Fig. 20 clearly cut the scenario of dissipative contributions at the electrode and enables to schematize the requirements for an high corrosion resistance, as follows:

i) high ohmic drops (that is compact scale) through out the electrolysis duration;
ii) rapidly releasing c.p. components (that is impervious scale);
iii) absence, or at least tardy and scarcely prominent maxima in polarization curves (that is straigtforward oxidation mechanism, absence of complex processes).

The same informations are contained, in a less explicit forme, in all electrochemical experimental results, and a one can draw up a self-consistent picture of the process with the aid of other corrosion measurement techniques, and moreover of microanalitical, X-ray diffraction and morphological results.

In conclusion, we confirmed the observation of Billingham et al. (1973) on the influence of thermal treatment on corrosion behaviour of superalloys. The hypothesis of intervention of electrochemical steps in hot corrosion has been advanced and justified.

Literature

(1) M.A. DE CRESCENTE, N.S. BORNSTEIN - Proc. Air Force Mat. Lab. Conference on Corr. of Mil. and Aerospc. Equipmts. 1967.

(2) H.T. SHIRLEY - J. Iron and Steel Inst., 1956, 144.

(3) G. BOMBARA, G. BAUDO, A. TAMBA - Corrosion Sci., 1968, 393.

(4) Y. BOURHIS, C. ST. JOHN - Oxidation of metals, 1975, 507.

(5) A. RAHMEL - Werkstoffe u. Korrosion, 1968, 750.

(6) J. BALAJKA - Werkstoffe u. Korrosion, 1973, 961.

(7) N.S. BORNSTEIN, M.A. DE CRESCENTE - Metall. Trans., 1971, 2875.

(8) J. BILLINGHAM, J. LAURIDSEN, R.E. LANVIN - Corrosion Sci., 1973, 623.

Aknowledgments: we are indebted to dr. Antona and Mr. Carughi who prepared the hipped Astroloy alloy specimens and CrAlY impregnation coatings.

DISCUSSION

A.Mihail, France

Existe-t-il du Vanadium dans les alliages présents et si oui quelle est l'influence des sels qui en résulte?

Author's Reply

Only one alloy contains Vanadium: IN 100. We have not made extended experimentation on this alloy, we have only studied it for comparison.

We think that vanadate presence poses a very difficult and interesting problem; and we intend to study it in the near future.

PROTECTION D'AUBES REFROIDIES A STRUCTURE INTERNE COMPLEXE

par Philippe GALMICHE

Office National d'Etudes et de Recherches Aérospatiales (ONERA)
92320 Châtillon - France

Résumé

Le problème d'actualité relatif à la protection générale ou localisée d'aubes refroidies présentant une structure interne complexe a pu être résolu d'une façon à la fois simple et fiable.

La méthode correspondante développée récemment à l'ONERA, technique SF, permet d'assurer, le plus souvent au cours d'une seule opération, aussi bien la protection des surfaces externes des pièces que la protection de leurs surfaces internes ou des surfaces d'orifices d'éjection d'air de refroidissement éventuels, quelle que puisse être la finesse de diamètre de ces derniers.

La méthode SF est appliquée le plus souvent dans le cas de traitements de protection en « pack » ; son utilisation peut être envisagée, d'une part dans le cas de pièces initialement vierges, d'autre part dans le cas de pièces préalablement revêtues par voie thermochimique, chimique ou P.V.D.

D'une façon générale, l'épaisseur des gainages externes et l'épaisseur des gainages internes peuvent être établis initialement avec précision, aucune particule parasite ne pouvant se trouver inclue à l'intérieur des pièces protégées, après application des traitements SF.

Les résultats obtenus jusqu'à présent par application de la méthode ONERA-SF sont illustrés par la présentation et l'examen de pièces très diverses de turbo-machines avancées, qui ont été remises pour traitements suivis de mise en essais ou en service par différents motoristes et par des Compagnies Aériennes.

PROTECTION OF COOLED BLADES OF COMPLEX INTERNAL STRUCTURE

Summary

The problem of the general protection of cooled blades of complex internal structure has been solved in a simple and reliable manner.

The corresponding method recently developed at ONERA, called SF technique, permits the realization in a single operation of the protection of both external and internal surfaces, as well as those of the orifices of cooling air, whatever their diameter. The SF method is most offen applied in the case of pack process, at controlled or high activity ; its use can be envisaged for previously uncoated parts, but also for pieces already coated by a thermochemical, chemical or PVD method. In a general way, the respective thickness of external and internal coatings may be precisely predetermined, no parasitic particle being liable to remain inside the parts after application of the protecting treatment.

Results obtained to date by application of the ONERA-SF method are illustrated in the paper by the presentation and examination of quite various parts of advanced turbomachines, which were handed over for treatment, followed by tests or operational use, by engine manufactures or airlines.

INTRODUCTION

L'accroissement incessant du rendement ou de la poussée des turbo-machines, au cours de ces dernières années a été et reste lié à un relèvement permanent des températures d'entrée devant turbine. Les facteurs essentiels qui ont conduit à obtenir de telles améliorations sont, d'une part la mise en oeuvre de superalliages réfractaires présentant des caractéristiques de tenue mécanique à chaud particulièrement élevées, d'autre part le développement de nouvelles configurations de pièces refroidies qui permettent désormais d'envisager des températures d'entrée de turbine sensiblement supérieures aux points de fusion des matériaux constituant les étages les plus avancés de la turbine chaude des moteurs.

D'une façon très générale, l'amélioration de la qualité de tenue mécanique à chaud des superalliages réfractaires, directement liée à des modifications de leur composition chimique, ainsi que la définition de nouveaux systèmes perfectionnés de refroidissement ont eu tendance, en contrepartie, à se traduire par une aggravation considérable des problèmes de dégradation des pièces sous l'influence des phénomènes de corrosion en service à haute température plus particulièrement oxydation et sulfuration sous cyclage thermique (1 à 4).

Les raisons principales de l'aggravation actuelle des problèmes de corrosion à haute température sont les suivantes :

a) réduction nécessaire de la teneur en chrome des matériaux dans le cas des superalliages réfractaires à base de nickel évolués, qui constituent presque exclusivement les aubes mobiles, permettant l'accroissement de la phase durcissante gamma prime.

b) Réduction de l'épaisseur des parois des pièces refroidies et accroissement de la complexité de géométrie intérieure correspondant aux configurations internes les plus efficaces.

c) Apparition de phénomènes de corrosion et de fissuration internes, parfois imprévisibles, particulièrement marqués dans le cas d'aubes refroidies constituées par les superalliages réfractaires les plus évolués.

La recherche et la mise au point de revêtements protecteurs permettant de réduire, sinon d'éviter complètement, les effets de dégradation par corrosion des pièces chaudes de turbo-machines ont été l'objet, depuis une vingtaine d'années, de nombreux travaux. Des méthodes efficaces ont pu être développées, initialement pour la protection de pièces classiques ; elles ont été améliorées sans cesse, puis parallèlement étudiées ou modifiées en vue de leur application pour la protection de pièces refroidies.

L'objet essentiel de l'exposé est la présentation des bases générales et des résultats de la nouvelle méthode ONERA SF, dont l'étude a été entreprise dans le but d'assurer une protection très efficace de pièces refroidies contre la corrosion et contre la fissuration interne, quelle que puisse en être la complexité de géométrie intérieure. Cette méthode, qui présente un caractère d'adaptation très général et dont l'application ne necessite l'utilisation d'aucun appareillage spécial a pu être étudiée, mise au point et transposée sur pièces réelles de turbo-machines, dans les meilleures conditions et dans un délai relativemenr bref, en raison même de l'intérêt qu'elle a suscité dès son apparition ; de nombreux motoristes français ou étrangers ainsi que d'importantes Compagnies Aériennes ont en effet mis à la disposition du laboratoire, pour essais ou traitements, des pièces refroidies très diverses de turbo-réacteurs avancés ainsi que de turbines à gaz de puissance, sur lesquelles l'expérimentation a été menée et sur lesquelles des résultats favorables ont été obtenus.

1 - BASES GENERALES DES METHODES ACTUELLES DE PROTECTION DES SUPERALLIAGES REFRACTAIRES.

Les procédés actuels de protection des pièces chaudes de turbo-machines font appel le plus souvent à deux types de méthodes, méthodes par voie thermo-chimique et méthodes par P.V.D., dont les principes fondamentaux et surtout les conditions d'application sont très différents. L'ensemble des méthodes correspond cependant de façon générale à la formation de revêtements riches en aluminium, qui assurent une protection efficace des pièces traitées contre la corrosion à chaud en raison de la formation d'un film superficiel très mince mais continu et auto-régénérable d'oxydes réfractaires très stables.

Les méthodes de protection par voie thermo-chimique, le plus souvent méthodes "à la poudre", sont essentiellement basées sur l'apport en milieu halogéné et la diffusion d'un ou de plusieurs éléments métalliques ; elles peuvent être appliquées, soit en une seule opération effectuée à haute température, 1 000 à 1 100°, méthodes à activité contrôlée, soit en deux opérations successives indépendantes ; apport à la température modérée, 750° à 900°C, suivi de rediffusion hors pack à la température plus élevée, méthodes à haute activité. La protection par voie thermo-chimique peut faire également appel à une diffusion successive, correspondant à des opérations différentes, de plusieurs éléments protecteurs, par exemple diffusion initiale de chrome et de tantale apportés en quantités contrôlées, suivi de diffusion d'aluminium selon méthode à activité contrôlée ou à haute activité ;elle peut d'un autre côté être appliquée sur des pièces initialement revêtues par voie électrolytique de dépôts minces de métaux nobles tels que le platine ou le rhodium.

La réalisation d'alliages de diffusion complexes a de toutes façons pour but l'obtention finale de revêtements protecteurs présentant une résistance à la corrosion améliorée, éventuellement une meilleure ductilité, comparativement à la tenue de gainages obtenus par seule aluminisation.

Les méthodes de protection par P.V.D. ou "overlay" correspondent au dépôt par voie physique : pulvérisation cathodique, ion-plating, plasma .... d'alliages complexes spéciaux, contenant en général un élément à caractère dispersoïde tel que l'yttrium, dont la composition est pratiquement indépendante de la nature du substrat qui est revêtu ; les revêtements réalisés par P.V.D., dont la dénomination générique est M-CrAlY, correspondent essentiellement à la combinaison en diverses proportions des éléments aluminium, chrome et yttrium avec un ou plusieurs métaux de base, le plus souvent nickel et cobalt.

Les méthodes de protection par voie thermo-chimique sont actuellement les plus utilisées (5, 6) ; la plupart de ces méthodes présentent en effet l'intérêt d'avoir un prix de revient relativement peu élevé, de permettre l'obtention de gainages protecteurs d'épaisseur régulière et prédéterminable avec une grande fiabilité, tout en n'influençant que faiblement les caractéristiques de tenue mécanique à chaud des matériaux traités. Il en est ainsi de façon générale dans le cas des méthodes de protection par voie thermo-chimique développées à l'ONERA (7), méthodes dont les principes et les caractéristiques d'ensemble sont schématisées dans le tableau 1. Un ensemble technique pour leur application est présenté figure 1.

Les techniques de protection par chromaluminisation, tancralisation et sylcralisation, dont l'une des caractéristiques communes est, outre la mise en oeuvre de masses d'apport "inusables", l'établissement in situ d'une barrière de rediffusion en service, sont actuellement bien connues. La méthode DE 77, beaucoup plus récente et n'ayant pas donné lieu jusqu'à présent à publication, correspond essentiellement à l'établissement initial, sur des pièces devant être protégées finalement de façon classique (par chromaluminisation à activité contrôlée, aluminisation à haute activité ...), d'un prégainage ductile de composition moyenne nickel-chrome 82/18 à 80/20, plus additions (en particulier traces d'éléments lourds). Le prégainage dont l'épaisseur très régulière est le plus souvent comprise entre 10 et 25 microns,est obtenu par dépôt chimique de nickel-bore en solution aqueuse, suivi d'une opération de déboruration-prédiffusion effectuée vers 850° de façon simple en atmosphère halogénée, puis d'un traitement de transformation en alliage au chrome par voie thermo-chimique (chromisation modérée, dopée aux lanthanides).

La technique de protection DE 77 présente un caractère d'application très général ; elle convient aux superalliages réfractaires, eutectiques orientés, alliages à phase dispersée, ... Elle permet d'obtenir finalement des gainages ductibles, d'épaisseur prédéterminable et très régulière, stable en utilisation et présentant une résistance particulièrement élevée à l'oxydation et à la sulfuration à haute température sous cyclage thermique. Aucune des opérations correspondant à l'application de la méthode DE 77 n'étant appliquée à température supérieure à 1 050°C, sauf cas particuliers, l'influence du traitement sur les caractéristiques de tenue en fluage des pièces peut être considérée comme le plus souvent négligeable.

Tableau 1 : Caractéristiques générales des techniques thermo-chimiques ONERA de protection des superalliages réfractaires.

TECHNIQUE	PRINCIPES GENERAUX	MATERIAUX PROTEGEABLES	COMPATIBILITE AVEC METHODE SF	RESULTATS D'ENSEMBLE
CHROMALUMINISATION (activité contrôlée)	DIFFUSION EN UNE ETAPE D'ALUMINIUM ET DE CHROME	SUPERALLIAGES à base de nickel ou de cobalt.	SANS PROBLEME	Très bonne tenue à l'oxydation et à la sulfuration.
ALUMINISATION HA (haute activité)	APPORT D'ALUMINIUM EN PRESENCE DE CHROME + REDIFFUSION HORS PACK.	SUPERALLIAGES à base de nickel	POSSIBLE, mais non générale	Bonne résistance à l'oxydation
SYLCRALISATION ET TANCRALISATION	TRAITEMENTS "DUPLEX" a)chromisation ou tantalichromisation modérées, en présence de lanthanides (5 à 30 microns) b)Chromaluminisation+ ou aluminisation°	SUPERALLIAGES à base de nickel	SANS PROBLEME, si opération terminale "à activité contrôlée"	Très bonne tenue à l'oxydation ; résistance accrue à la sulfuration.
DE 77	TRAITEMENT "TRIPLEX" Dépôt chimique de nickel-bore, déboruré par voie thermo-chimique (5 à 30 microns en général), puis Sylcralisation ou Tancralisation	SUPERALLIAGES à base de nickel ou de cobalt EUTECTIQUES ORIENTES ALLIAGES A PHASE DISPERSEE	SANS PROBLEME, si opération terminale à "activité contrôlée"	Excellente tenue à l'oxydation et à la sulfuration ; stabilité et ductilité des gainages particulièrement élevées.
	+ e.g. méthode à activité contrôlée ° e.g. méthode à haute activité.			

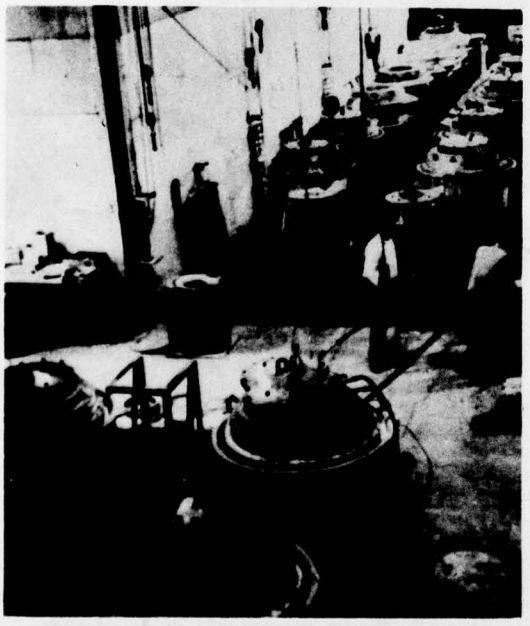

Figure 1 : Type d'installation permettant l'application de l'ensemble des techniques thermo-chimiques ONERA de protection ou d'assemblage (vue partielle) - Alloy Surfaces-Wilmington.

Les résultats obtenus par application de la méthode DE 77 peuvent être mis en évidence par l'examen des figures 2 à 4, qui se rapportent à un problème d'actualité, particulièrement délicat et jusqu'à présent imparfaitement résolu, en l'occurrence la protection d'eutectiques orientés renforcés par fibres de carbures type COTAC.

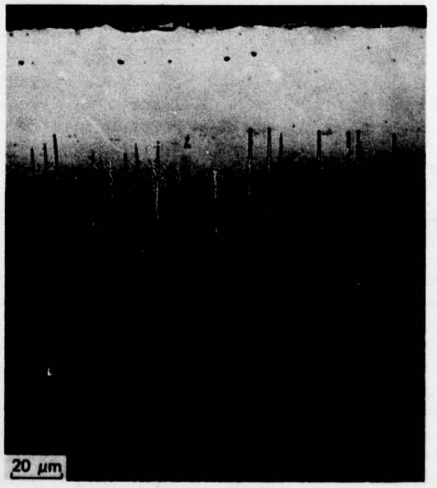

Figure 2 : Structure de la base d'accrochage caractéristique du traitement de protection DE 77 : exemple COTAC 74 - sens perpendiculaire aux fibres

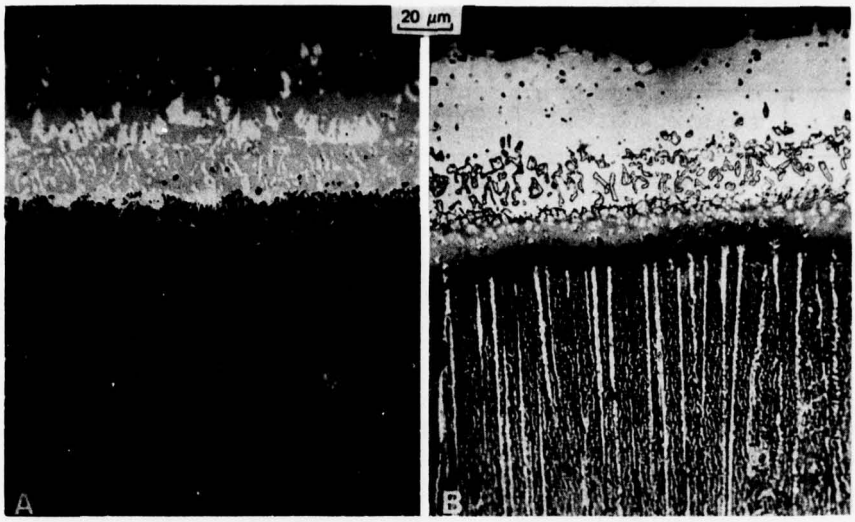

Figure 3 : Structure d'un gainage DE 77 appliqué sur COTAC 74 : 3A - sens parallèle aux fibres, 3B - sens perpendiculaire aux fibres

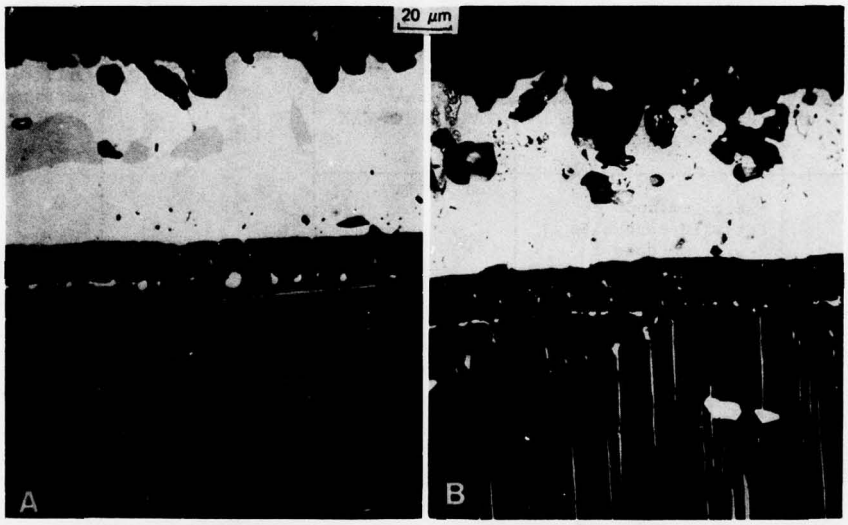

Figure 4 : Structure d'un gainage DE 77 appliqué sur COTAC 74 après essai d'oxydation sous cyclage thermique violent de 500 heures à 1 130°C dans l'air : 4A - sens parallèle aux fibres, 4B - sens perpendiculaire aux fibres ; noter l'absence pratique d'évolution de l'épaisseur initiale du gainage.

Les méthodes de protection par P.V.D. permettent d'établir à la surface des pièces à protéger des revêtements dont l'épaisseur n'est en principe pas limitée ; la composition des gainages est homogène et peut être adaptée à celle de matériaux complexes présentant une résistance inégalée à la corrosion à haute température (8,9). En contre-partie, les méthodes de protection par P.V.D. présentent plusieurs inconvénients majeurs ; ces inconvénients sont, outre un prix de revient très élevé, un faible pouvoir de pénétration et une ductilité en général imparfaite, une tendance à la rediffusion en service à haute température susceptible de se traduire par un abaissement sensible de la tenue en fluage des pièces protégées (10).

L'efficacité et plus particulièrement la stabilité des revêtements protecteurs réalisés par P.V.D. peuvent être sensiblement améliorées en associant une telle méthode de protection avec une opération initiale de gainage effectuée par voie thermo-chimique, telle que diffusion des quantités limitées de chrome, d'aluminium et de chrome ou de chrome et de tantale (11), un revêtement initial général de l'ensemble des surfaces des pièces à protéger pouvant alors être obtenu. La base d'accrochage particulière type nickel-chrome 80/20 + additions qui correspond à la caractéristique essentielle de la méthode DE 77, ainsi que des gainages d'épaisseur faible mais régulière pouvant être finalement obtenus en fin d'application de la méthode, se présentant a priori comme des types de pré-revêtements particulièrement efficaces dans le cas de pièces devant être protégées par P.V.D.

L'application terminale d'un traitement de gainage complémentaire par voie thermo-chimique, tel que la chromalunimisation, sur des pièces protégées essentiellement par P.V.D. est, d'un autre côté, bien connue ; elle permet, dans différents cas particuliers, aussi bien d'améliorer la qualité et l'homogénéité des zones superficielles des gainages que d'assurer le revêtement et par suite la protection de zones des pièces n'ayant pu être atteintes lors de l'application du traitement de recouvrement par P.V.D. (12)

2 - PRINCIPE, DISPOSITIONS ESSENTIELLES ET CONDITIONS D'ENSEMBLE D'APPLICATION POSSIBLE DE LA METHODE ONERA-SF.

A - Principe.

Le principe et le but de la méthode SF correspondent à la possibilité d'assurer de façon simple et fiable, le plus souvent avec une seule opération par voie thermo-chimique, la protection de l'ensemble des surfaces externes et des surfaces internes de pièces refroidies (en général ailettes mobiles ou aubages redresseurs), soumises aux effets de la corrosion ou de la fissuration en milieu corrosif, quelle que puisse être la complexité de la géométrie interne des pièces à revêtir ; un autre objectif est la définition de traitements permettant d'établir des revêtements protecteurs d'épaisseur prédéterminable suivant chaque zone particulière des pièces, sans aucun risque d'obturation des orifices d'écoulement de fluide de refroidissement, si fin soient-ils, ou de réduction intempestive des dimensions de tels orifices.

L'application de la méthode SF apparaît principalement justifiée dans le cas de la protection de pièces refroidies constituées par des superalliages très sensibles à l oxydation ou à la sulfuration tels que l'IN 100 ou le B 1900, surtout quand le refroidissement des pièces est assuré, au moins en partie, par des orifices d'éjection d'air de très faible diamètre ou par des canaux longs et étroits : refroidissement par convection, film impact ... ou association simultanée de plusieurs de ces méthodes.

B - Dispositions essentielles.

La méthode SF correspond à deux dispositions caractéristiques essentielles, dont la mise en oeuvre unitaire ou l'association peuvent être envisagées, en fonction de chaque cas particulier :

a) séparation initiale des pièces à protéger du milieu de traitement, au moins suivant des zones d'arrivée ou d'éjection d'air de refroidissement, à l'aide de capots ductiles à très forte porosité, dont la forme peut être exactement adaptée à celle des zones des pièces qu'elles doivent recouvrir : disposition SF figure 5.

b) Introduction initiale, à l'intérieur des pièces à protéger, de matériau protecteur apporté en quantités prédéterminées, suivant une disposition permettant d'en assurer une utilisation à la fois progressive et totale au cours du traitement de gainage ; disposition SF +.

Les capots de séparation sont constitués par de la feuille mince et parfaitement ductile de feutre de nickel présentant une porosité ouverte à la fois très élevée et très fine, transformée par voie thermo-chimique en duplex, en feutre également très poreux et ductile d'alliage nickel-chrome-aluminium ; le matériau possède une porosité entièrement ouverte de l'ordre de 90 % et son épaisseur est généralement de l'ordre de 0,3 à 0,4 millimètre.

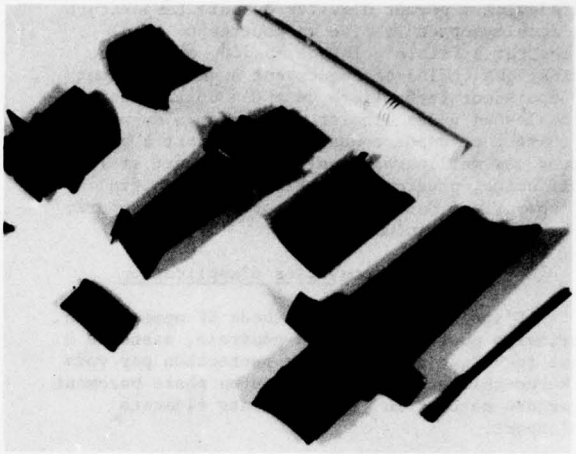

Figure 5 : Aubes mobiles refroidies diverses et capots de séparation correspondants pour protection SF.

Le matériau poreux qui peut être mis en forme sans difficultés, soit initialement, soit après transformation par voie thermo-chimique préalable par chromisation modérée, ne présente aucune réponse élastique sensible, se révèle pratiquement neutre sur le plan thermo-chimique et ne peut adhérer finalement à la surface des pièces protégées, correspond de ce fait à un type de séparation particulièrement satisfaisant. Les caractéristiques particulières du matériau et plus particulièrement sa porosité ouverte à la fois très élevée et très fine permettent, d'une part d'éviter toute pénétration de particules, si fines soient-elles, à l'intérieur des pièces à revêtir, d'autre part d'accentuer les mouvements de convection assurant la circulation des vapeurs d'halogénures vecteurs des métaux d'apport émises à partir de la charge de traitement. Une densification locale, partielle ou complète, du matériau, qui peut être effectuée initialement par simple écrasement permet d'un autre côté d'assurer si nécessaire une réduction contrôlée ou, à la limite, la suppression des courants de convection ; cette dernière disposition peut être utilisée, soit pour obtenir des gainages d'épaisseur notable sur certains compartiments déterminés seulement de pièces refroidies particulières, soit pour participer à la réalisation de réserves de protection, aussi bien internes qu'externes.

L'incorporation initiale éventuelle d'une quantité prédéterminée et entièrement consommable d'éléments protecteurs d'apport à l'intérieur des pièces à protéger, nécessaire dans différents cas pour assurer un rôle de relais des vapeurs d'halogénures métalliques émises à partir de la charge de traitement proprement dite, met en jeu le plus souvent un matériau (type "sandwich") à base d'aluminium-chrome. Ce matériau est constitué en général, suivant les cas, soit par des sections de feuille mince, soit par des sections de fil fin d'aluminium, revêtues de chrome déposé le plus souvent par électrolyse pour un rapport en poids chrome sur aluminium bien défini et qui sont introduites à l'intérieur des pièces à protéger en quantités correspondant au résultat finalement recherché. Il est également possible, dans certains cas au moins, de mettre en oeuvre des particules d'aluminium chromé électrolytiquement ou oxydées anodiquement qui sont alors injectées initialement à l'aide de pâtes ou de gels éliminables à chaud sans formation de résidus nocifs.

Le dépôt initial de chrome à la surface de

l'aluminium permet d'éviter à haute température l'écoulement et la mise en gouttes du métal substrat à faible point de fusion, et empêche ainsi que celles-ci conduisent à un revêtement d'épaisseur irrégulière ou à des corrosions locales en phase liquide des surfaces du matériau traité ; ce dépôt conduit d'autre part à assurer dans les meilleures conditions l'apport et la diffusion, progressives mais totales en fin d'opération, des éléments protecteurs d'apport, chrome et aluminium.

C - Conditions possibles d'application

L'application de la méthode SF apparaît en principe possible de façon générale, associée à une technique quelconque de protection par voie thermo-chimique à la poudre ou en phase purement gazeuse mettant en jeu différents éléments d'apport.

En fait, l'utilisation de la méthode SF apparaît la plus intéressante et se révèle la plus efficace dans le cas des procédés de protection à activité contrôlée, faisant intervenir au moins en partie l'aluminium comme élément diffusant protecteur, par exemple chromaluminisation ONERA ou Co-Dep de General Electric.

La méthode SF,associée éventuellement à la disposition complémentaire décrite ci-dessus, peut être appliquée sans modification de principe aux traitements de protection proprement dits, d'une part dans le cas de pièces initialement vierges, d'autre part dans le cas de pièces initialement revêtues par voie électrolytique, thermo-chimique, ou P.V.D.

Dans le cas de protections correspondant à des revêtements particuliers obtenus par application successive d'au moins deux opérations analogues ou différentes, certaines dispositions spéciales de préparation des pièces apparaissent le plus souvent nécessaires.

Ainsi, la protection par seule voie thermo-chimique, type chromaluminisation par exemple, d'ailettes mobiles dont le refroidissement doit être assuré par la présence d'un grand nombre de perforations très fines et dont la protection doit correspondre respectivement à des gainages de forte épaisseur suivant les surfaces externes des pièces et à des gainages plus minces suivant la surface des orifices de refroidissement et des surfaces intérieures pourra nécessiter des traitements successifs ; la perforation des pièces dans de pareils cas pourra être effectuée après application des premiers traitements, chromaluminisation ou sylcralisation par exemple, qui correspondent en eux-même pratiquement à l'obtention du gainage externe de forte épaisseur et peuvent être réalisés de façon en soi classique, le traitement complémentaire de protection interne nécessitant alors seulement la mise en oeuvre d'une au moins des dispositions SF.

Un processus analogue de perforation interposée suivi de traitement complémentaire de protection par voie thermo-chimique suivant la méthode SF peut être envisagé de même, dans le cas de pièces revêtues initialement par P.V.D. au lieu d'être protégées par diffusion.

D'un autre côté, l'application d'au moins une disposition SF permet d'assurer, dans le cas de certains types de pièces refroidies, un prégainage général ou seulement interne destiné à améliorer finalement la qualité de tenue à la corrosion d'aubes dont la protection des surfaces externes est essentiellement prévue par application de méthodes P.V.D. La limitation initiale d'un prégainage à base d'aluminium aux seules surfaces internes de pièces refroidies et aux surfaces d'orifices d'éjection d'air éventuels peut être assurée de façon simple en utilisant la disposition SF correspondant à l'introduction d'éléments associés consommables, type aluminium chromé : les pièces à traiter peuvent alors, selon le cas et le but recherché, être chauffées soit en phase purement gazeuse, soit dans un milieu pulvérulent neutre ou actif, par exemple, dans ce dernier cas, cément de chromisation modérée assurant lors de la même opération l'établissement d'un gainage enrichi en chrome suivant les surfaces externes des pièces à recouvrir.

D'une façon très générale, il apparaît essentiel de préciser que la réalisation de revêtements protecteurs suivant les surfaces internes des pièces creuses ou perforées se traduit inévitablement par une surépaisseur, régulière et prédéterminable, qui correspond à la moitié environ de l'épaisseur de gainage proprement dite ; une telle surépaisseur, en elle-même facile à compenser initialement, peut être éventuellement mise à profit pour obtenir des perforations très fines à partir de perforations de diamètre initialement plus élevé et de ce fait plus faciles à réaliser.

3 - ANALYSE DE QUELQUES RESULTATS OBTENUS PAR APPLICATION DES DISPOSITIFS SF.

Les figures 6 et 7 représentent différents types de pièces d'étages avancés de turbo-machines protégées par seule voie thermo-chimique ou par association de méthodes de protection différentes, avec mise en oeuvre de la méthode SF : pièces refroidies par convection, film, impact ... ; elles permettent de méttre en évidence la grande diversité des cas qui ont déjà pu être étudiés, aucune configuration interne particulière des pièces ne semblant en elle-même poser de problème insurmontable.

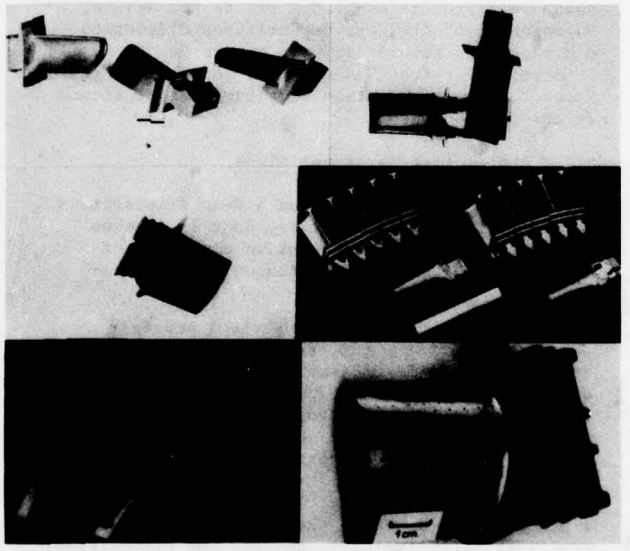

Figure 6 : Pièces refroidies diverses de turboréacteurs protégées par méthode SF.

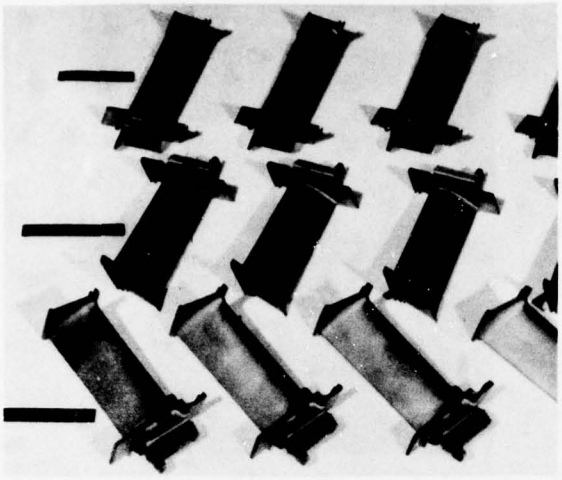

Figure 7 : Aubes mobiles refroidies de turbine industrielle de puissance protégées par méthode SF (alliage réfractaire IN 100 : protection chromaluminisation, sylcralisation ou DE 77).

L'examen des micrographies qui correspondent aux figures 8 à 14, permet de son côté d'illustrer les résultats qui ont pu être obtenus dans différents cas de façon désormais prédéterminée et fiable.

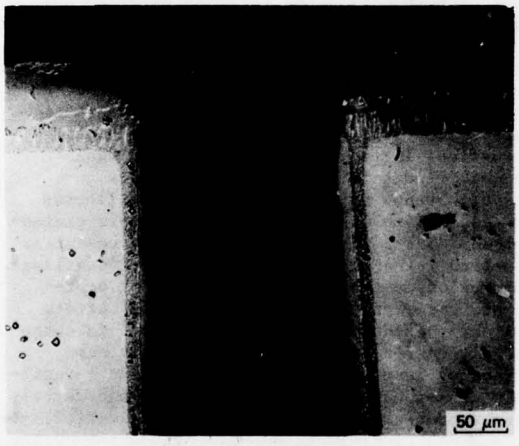

Figure 8 : Structure du gainage d'une aube mobile refroidie en B 1900 protégée par chromaluminisation SF, pour gainage d'épaisseur différente suivant les surfaces externes de la pale et les surfaces des orifices d'éjection d'air de refroidissement

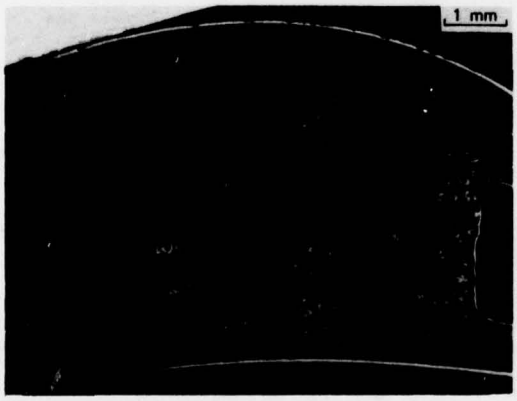

Figure 9 : Structure du gainage externe et du gainage interne d'une aube mobile refroidie en MAR 002 protégée par chromaluminisation SF+ - section à mi-hauteur.

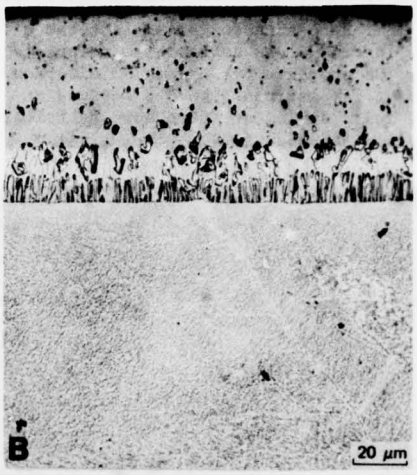

Figure 10 : Structure du gainage externe et du gainage interne d'une aube mobile refroidie en Nimonic 108 protégée de façon générale par chromaluminisation SF+ ; 10 A : vue d'ensemble, 10 B : détail de la structure du gainage externe, 10 C : détail de la structure du gainage interne section à mi-hauteur.

Figure 11 : Structure du gainage externe et du gainage interne d'une aube mobile refroidie en Nimonic 108 protégée par chromaluminisation SF suivant compartiments bord d'attaque et bord de fuite seulement. Côté bord de fuite, section à mi-hauteur (12).

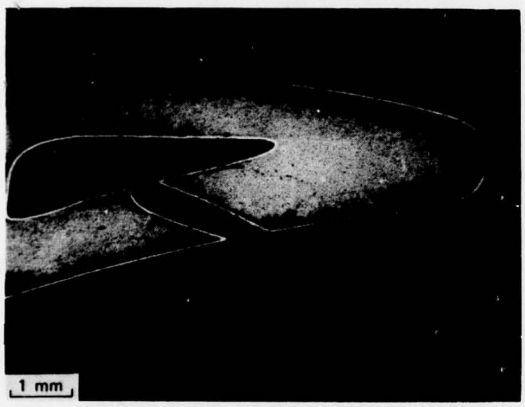

Figure 12 : Structure du gainage externe et du gainage interne d'une aube mobile refroidie en Nimonic 108 protégée par sylcralisation SF - section à mi-hauteur.

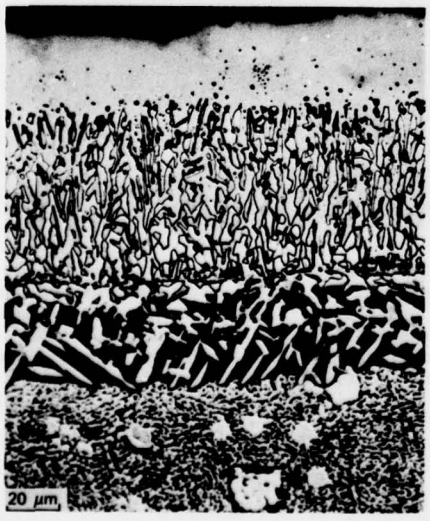

Figure 13 : Structure des zones superficielles du gainage externe obtenu sur une aube refroidie en B 1900 protégée initialement par P.V.D. (Cocraly de P.WA.) puis chromaluminisation SF

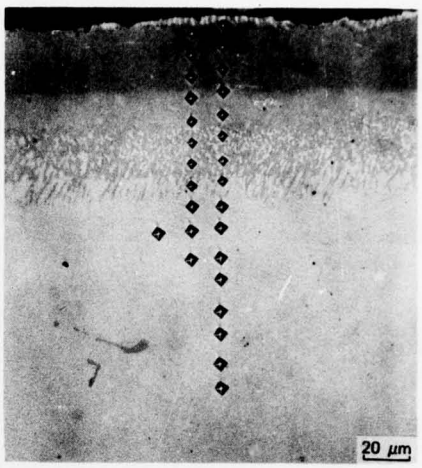

Figure 14 : Structure des zones superficielles d'une éprouvette d'IN 100 protégée par chromaluminisation SF après dépôt électrolytique très mince de platine

D'une façon générale, l'épaisseur des gainages internes de pièces refroidies réalisés suivant application de la méthode SF se trouve le plus souvent comprise entre une dizaine et une trentaine de microns ; l'épaisseur des revêtements devant assurer la protection des surfaces externes des pièces est de son côté habituellement comprise entre trente et cent microns. Si l'on se rapporte à une unité d'épaisseur de gainage correspondant à une valeur déterminée, par exemple vingt microns, la qualité de résistance à la corrosion à haute température sous fatigue thermique des revêtements des surfaces internes apparaît au moins égale à la qualité des revêtements des surfaces externes obtenus par application des meilleures méthodes classiques de protection par voie thermochimique ; les revêtements internes ne présentent en particulier aucune susceptibilité à l'écaillage en milieu oxydant à haute température et protègent efficacement le substrat contre les effets de la fatigue thermique. La résistance à la corrosion particulièrement élevée des revêtements internes et leur absence de sensibilité à l'écaillage s'expliquent aisément par le fait que de tels gainages protecteurs sont constitués essentiellement par des aluminiures sub-stoechiométriques par rapport à la définition exacte M-Al, les alliages de diffusion correspondants contenant par ailleurs du chrome selon toute leur épaisseur et se trouvant dans un état de compression a priori favorable.

L'examen des figures 8 à 14 ne semble pas justifier de commentaires détaillés, de tels commentaires ne pouvant que recouper des indications déjà présentées.

La figure 15, par contre, se rapporte à un cas spécial, en l'occurrence la protection contre la corrosion et surtout contre le colmatage de rampes d'injection de post-combustion. Dans un pareil cas, qui nécessite seulement de façon générale la disposition SF complémentaire, la présence du revêtement interne permet en particulier, sinon d'éviter complètement, du moins de réduire considérablement, l'apparition et le développement de phénomènes de dépôt et de croissance de sites de germination de suies à base de carbone qui peuvent se traduire finalement par l'obturation locale ou générale des injecteurs.

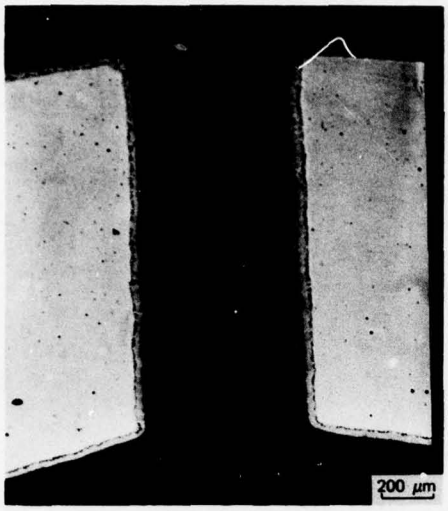

Figure 15 : Structure des zones superficielles d'une perforation de rampe de post-combustion en Inconel protégée par chromaluminisation SF+

CONCLUSIONS.

Les résultats qu'a déjà permis d'obtenir sur pièces réelles l'application de la technique de gainage SF, dans le cas d'éléments refroidis présentant une géométrie interne particulièrement complexe, semblent pouvoir apporter une contribution intéressante au développement et à la sécurité d'emploi de turbo-machines avancées, caractérisées essentiellement par des températures d'entrée de turbine très élevées.

La collaboration très positive qui s'est établie entre le laboratoire de l'ONERA et différents constructeurs ou utilisateurs est de toutes façons l'une des raisons primordiales qui ont conduit la méthode SF à dépasser rapidement le stade de l'application initiale sur éprouvettes ou maquettes homothétiques, permettant de ce fait d'en assurer une transposition et une mise au point effectives susceptibles dès maintenant de se traduire par une application en production de série.

REFERENCES

(1) P. Esslinger and A.Huff : Development of materials used in gas turbine engines. Rev. Int. Htes Temp., 1976 (12), pp 172-185.

(2) J. Stringer : Hot Corrosion in Gas Turbines. N.T.I.S. Contract F 33615-71-C-1067, June 1972

(3) F.W. Armstrong : To Morrow Power. Flight International, Janvier 1977, pp 113-117.

(4) C.G. Mac Greath : The Role of Injected Salts in Hot Corrosion. T.I.M.E. (G.B.), 1976 (88), pp 145-149

(5) V.S. Moore, W.D. Brentnall and A.R. Stetson : Evaluation of coating for cobalt and nickel base superalloys. N.A.S.A. - CR-72714, Juillet 1976

(6) R.P. Seelig : High Temperature Resistant Coatings of Superalloys. Congrès de Reutte (Autriche), mai 1977, (preprint) (en cours d'édition).

(7) P. Galmiche : Applications en Construction Aérospatiale des Techniques Thermo-chimiques ONERA. L'Aéronautique et l'Astronautique, 1973 (41), pp 33-42.

(8) D.H. Boone : Overlay Coatings for High Temperature Applications. AIRCO TEMESCAL, January 1976.

(9) D.L. Deadmore : Oxidation of Cocraly and aluminized coatings in high velocity gases. N.A.S.A.-TN-D-6842-E 6809-July 1972

(10) W. Betz, H. Huff, W. Track : Zur Bewertung von Schutzschichten gegen Heib Gaskorrosion and Gasturbinenschaufeln. Z.F. Werkstofftechnik (J. of Materials Technology),1976, Heft 5, pp 161-L96

(11) P. Galmiche : The ONERA thermo-chemical techniques. Metal Forming, 1968 (3)

(12) P. Galmiche : Sulla corrosionne delle superleghe refractrie esposte ai gaz di combustione ad alta temperatura. Trattamenti dei Metalli, 1973 (6), pp 27-35.

COBALT-BASE ALLOYS FOR HOT CORROSION PROTECTIVE COATINGS.*

A. Davin, J.M. Drapier, D. Coutsouradis, L. Habraken**
C.R.M., Abbaye du Val Benoit, Liège (Belgium)

ABSTRACT

In the field of gas turbine applications, the severe requirements of extended operation in marine environments or an increase in the inlet temperature, limit the life of the diffusion aluminide base coatings for nickel and cobalt superalloys.

During the last few years, new protective "overlay" coatings such as Co/Ni-Cr-Al-Y-Ta have been developed in order to satisfy the requirements of the gas turbine designers and have shown an exceptional hot corrosion resistance. They were even optimized to obtain an acceptable compromise between hot corrosion and thermal shock resistance .

The present paper aims at summarizing the experience gained so far with the development of such cobalt base and particularly Co-Al-Cr-Ta-Ni-Y alloys and the evaluation of corresponding coatings by various techniques.

1. INTRODUCTION

Diffusion coatings have been widely used during the last years to protect gas turbine blades. The majority of diffusion-coating system contain aluminide compounds which interact with the base metal to form a diffusion layer rich in Ni Al, or Co Al as protective layer. These intermetallic compounds have an excellent oxidation resistance but their sulphidation or hot corrosion resistance is weak. Under the latter conditions their protective action ceases and the material itself is attacked. Furthermore, for the newer engines, which use alloys such as directionally-solidified or the oxide dispersion-strengthened alloys, the diffusion coatings result in a weakening of the alloy (1). New coatings are needed to satisfy the requirements of the designers.

They must be free of elements such as W, Nb, Mo, V which affect detrimentally the hot corrosion resistance as shown by recent studies. On the contrary they must contain aluminium and chromium, the principal scale-forming elements in order to provide adequate hot corrosion and oxidation resistance. Overlay coatings were developed during the last years in order to meet these requirements. Among these the Co/Ni-Cr-Al-Y developed by Pratt and Whitney Arcraft and S 57 developed by CRM have shown an exceptional corrosion resistance.

The present paper aims at summarizing the experience gained so far with this type of overlay coatings and particularly with the S 57 series of cobalt base alloys.

2. M-Cr-Al-Y OVERLAY COATINGS

The basic features of this type of coatings will be briefly described in this section. Coatings of this type developed by Pratt and Whitney contain typically about 12%Al, 30%Cr, 0.5%Y, M representing Co or Co + Ni.

Fig. 1 compares the microstructure of a typical Co Cr Al Y overlay coating to that of diffused aluminide on a nickel base alloy. The comparison illustrates the difference in depth of interdiffusion between the two systems.

Fig. 2. compares the hot corrosion resistance of M Cr Al Y-type coatings to that of aluminide coatings. The oxidation resistance of the M Cr Al Y coatings is due to the formation of protective Al_2O_3. Following Pettit and Giggins (2) chromium assists in Al_2O_3 formation during the transient oxidation period. Improved resistance to Al_2O_3 spallation under thermo-cyling conditions is due to the presence of Y_2O_3 which forms micro-pigs at grain boundaries and within grains and improves the adherence of Al_2O_3 on the alloy surface.

The hot corrosion of the M Cr Al Y alloys derives from two factors (3), namely the presence of adherent Al_2O_3 which retards the basic fluxing initiation stage and the presence of significant amounts of chromium which retards the basic fluxing-sulfide oxidation propagation stage. It has been observed that the Co-Cr-Al-Y are more resistant in hot corrosion than the corresponding Ni-Cr-Al-Y alloys.

Concerning the mechanical properties of the coatings, the Al concentration plays a major role as regards the ductility of the coating. The compositions which give rise to a matrix phase of CoAl or NiAl with a dispersed solid solution phases or pure Co Al or Ni Al exhibit brittle-ductile transition behavior similar to that observed for the aluminide coatings (Fig. 3). Nevertheless significant ductility can be obtained by a decrease in aluminium content at the expense, however of the oxidation and hot corrosion resistance.

* Research carried out under the auspices of the Institut pour l'Encouragement de la Recherche Scientifique dans l'Industrie et l'Agriculture (I.R.S.I.A.).

** Respectively, Chercheur Principal, Chef de Service Adjoint, Ingénieur en Chef and Directeur Adjoint at CRM and Professeur at the University.

The coatings were optimized to obtain an acceptable compromise between hot corrosion and thermal shock resistance (1).

Many methods of processing, including diffusion bonding, powder sintering or melting, plasma spraying and physical vapor deposition including sputtering were evaluated for the application of the overlay coatings. Of these, physical vapor deposition, involving evaporation of a continuously fed ingot with a high voltage electron beam and condensation of the vapor on parts appropriately rotated in the vapor cloud has been shown the most promising for the application of the M Cr Al Y type alloys. This process operates now on a large scale (Fig. 4).

3. DEVELOPMENT OF S 57

3.1. Introduction

The effect of various alloying elements on the dry corrosion behaviour of Co-Cr binary and more complex cast alloys was determined in previous works (4, 5, 6).
The results showed that additions of Cr, Ta and Al contribute significantly to the oxidation, sulphidation and hot corrosion resistance of cobalt alloys. Moreover, yttrium additions improve the adhesion of the oxide scale during thermal cycling and decrease the penetration of internal sulphides and oxides.

These systematic investigations led to the development of S-57, a cast or wrought cobalt-base alloy containing nominally 25%Cr-10%Ni, 5%Ta, 3%Al and 0.5%Y. Nickel was included as it is normally incorporated in cobalt base alloys to stabilize the f. c. c. structure. The chromium content was limited to 25% so as to limit the risks of σ phase formation and because a chromium content of this level appeared, from previous experience, satisfactory for adequate corrosion resistance.

The S 57 alloy is particularly resistant to oxidation in still air and to hot corrosion in combustion gases contaminated with sulphur and alkali metal salts and is far superior to current superalloys. Fig. 5 compares the mass-gain curves for S 57 at 1095°C in still air with those for various cobalt-base superalloys (7) : the S-57 alloy appears even more resistant than FSX 414 which, on account of its 30%Cr content, already possesses good oxidation resistance. Similarly, Fig. 6 confirms the good hot corrosion behaviour of S 57 as compared with other nickel-and cobalt-base superalloys.

The isothermal oxidation kinetics of S 57, Co-35Cr, TD-Co and related commercial alloys X 40, WI 52, Haynes 1002 and alumina-forming dispersion-strengthened alloys have been compared at Battelle Columbus Laboratories (8).

Table I gives the test conditions and the weight increases for the different alloys. The results show that the alumina-forming alloys(Co-20Cr-6Al and S-57) have the best oxidation resistance; they are followed by the alloys forming protective chromia scales (Co-35Cr, X-40 and HA-1002) and then by the WI-52 alloy forming a cobalt rich oxide scale.

The good resistance of S-57 to hot corrosion has been further confirmed in studies carried out at Battelle (8) or at the Nasa Lewis Research Center (9).

3.2. Coating studies.

Because of its excellent resistance in corrosive environments the application of S 57 as a protective coating appeared of particular interest. To this end, S 57 prealloyed powders, sheets and wires were prepared for coating or for making parts by different techniques.

The S 57 powders intended for coating parts by plasma-torch spraying were obtained by water or inert gas atomization or by the Coldstream process and then screened within the 37-88 μm and <37 μm size ranges.

Figs. 7 to 9 illustrate the morphology and the dendritic microstructure of such powders. A typical size distribution of water atomized powders as obtained by Quantimet analysis is given in Fig. 10. Most of the plasma-spraying tests were made with the 37-88 μm water atomized powders with Ar, Ar + 8%H_2 or N_2 + 10% H_2 as plasma gas. Homogeneous S 57 coatings with good density and bonding could be readily obtained on various substrates. The bonding of the S 57 deposits with the substrate was evaluated by a qualitative method used in aeronautical gas turbine construction (10, 11). Sheet specimens were coated over one face and submitted to a deep drawing Erichsen-type test from the uncoated face. The tests were made on 18/8 stainless steel sheets with deposits 0.15 to 0.2 mm thick subjected to 5 and 7.6 mm deep deformation.

The ductility and the bonding of the S 57 deposits with thickness up to 0.2 mm appears quite good. S-57 coatings made on IN 738 substrates performed under a protective atmosphere to prevent the oxidation of the powders, with Ar or Ar + 8%H_2 as plasma gas, have shown that the porosity in the deposit was least with Ar + 8%H_2 as plasma gas and that heat treatment under vacuum for 4 h at 1065°C improves the density of the deposits and promotes a precipitation reaction leading to higher microhardness.

Plasma spraying tests were also performed on experimental cobalt alloys containing 10%Cr as well as on the nickel base alloy IN-713. A diffusion treatment for 21 h at 1100°C in an inert atmosphere was applied to the speciments which were then subjected to hot corrosion tests at 950°C in combustion gases contaminated with sulphur and sodium with cooling to room temperature every 48 h. In such tests, uncoated samples of the Co-10%Cr and IN 713 alloys become heavily corroded already after some 100 h.

The S 57 coating improves their life by a factor of 10.

Sheet specimens (45 x 75 x 1 mm) of Inconel 600 were coated on one face with S 57 prealloyed powders. Other S 57 coatings on a stainless steel substrate have been prepared by the low pressure plasma spray process. The coating was applied either on a cold or a preheated (815°C) surface and the average coating thickness was about 170 μm. Figs. 11 and 12 illustrate the microstructure of the different coatings in the as received condition (12). Unmelted prealloyed particles, characterized by their dendritic structure, are embedded in the different coatings.

Hot corrosion were performed on these specimens in combustion gases contaminated with sulphur (1%) and sodium (5 ppm) with cooling to room temperature every 48 hours. Fig. 13 gives the microstructure of the coatings on the different specimens after an exposure time of 1000 hours and 2000 hours at 950°C. In all cases no complete corrosion and no penetration in the substrate material were observed.

A few plasma-spraying tests were also performed with the argon atomized S-57 powders on actual gas turbine parts. The coated components are being tested under service conditions.

It is worth mentioning that the S 57 alloy can also be processed into sheet or wire form. Thicknesses and diameters down to 0.25 and 0.15 mm respectively have been obtained on a laboratory scale. Fig. 14 shows the temperature dependence of the tensile properties of hot-rolled S-57 sheet material (10).

TIG-welding tests without filler metal or preheating of the hot rolled sheets have shown that homogeneous and sound welds can be obtained provided the weld root is properly shielded with the protective gas, preferably argon. The welded material retains an ultimate tensile strength of 765 MN/m^2, i.e. about 80% of the strength of the hot rolled material.

The S 57 sheet material may be used to make coatings by various techniques such as explosive welding, cladding, hot isostatic gas pressure bonding, or sputtering. Prelimineray experiments have shown that sputtered S 57 deposits are characterized by a homogeneous distribution of the alloying elements, including yttrium and tantalum, as opposed to the as-cast or wrought material (13).

3.3. Optimization of the hot corrosion resistant alloy S-57

Protective coating applications, in particular for coatings produced by plasma spraying, do not necessarily require powders of alloys of such high formability as S 57.
Therefore an optimization of the S 57 composition has been undertaken aiming at increasing further its hot corrosion resistance at the least expense of its formability. Several cast experimental grades derived from the S 57 composition by modifying the Ta and Al contents were prepared and tested under hot corrosion conditions (Table II).

Some of the 10%Al alloys appear very brittle and were heavily cracked during cooling after casting. Specimens of 25 x 25 x 5 mm^3 were prepared by electrospark machining and tested under cyclic hot corrosion conditions at 870°C and 950°C in combustion gases contaminated with sulphur and alkali salts.
The sulphur content of the fuel was adjusted to 1% by addition of carbon sulphide and the amount of sodium was 5 ppm of the total air consumed. Fig. 15 gives the decrease in thickness observed on the different alloys after exposure of about 2000 h at 950°C. These results confirm the good behaviour of the S 57 alloy and show that the highest corrosion resistance is exhibited by the S 67 grade containing 25%Cr, 10%Al, 10%Ta, 10%Ni and 0.5%Y. On the other hand, the tantalum-free (S 65) and aluminium-free (S 66) alloys exhibit the largest decrease in thickness.

It must be pointed out that the observed improvement of hot corrosion resistance over the basic S 57 alloy was achieved at a large expense of the material's ductility due to the increase in Al and Ta contents. This factor is to be kept in mind for coating applications, even by plasma-spraying, since the mechanical behaviour of the coating depends on the sprayed material's ductility.

The alloys with intermediate composition in Al and Ta, between S 57 and S 67 present a poor machinability but no cracks appeared after casting (alloys S 69 to S 78).

For these alloys the cyclic hot corrosion tests were performed at 950°C and 870°C in combustion gases heavily contaminated with sulphur (1%S) and alkali salt (100 ppm Na). Figs. 16 A-B give respectively the average and maximum decrease in thickness for the different alloys after exposure of about 2000 hours at 950°C.

All the alloys containing at least 5%Al present the best behaviour. The effect of tantalum on the hot corrosion resistance is less marked. However, a slight improvement of the hot corrosion resistance is observed by increasing the tantalum content from 5% to 7% or 10%. Among the alloys which showed the best hot corrosion resistance, it seems that the alloys containing 5%Ta-5%Al (S 76) or 5%Ta-7%Al (S 77) present the best compromise between ductility and hot corrosion resistance.

3. CONCLUSION.

Co-Ni base overlay coatings were shown to provide adequate answer to the oxidation and corrosion problems in high performance gas turbines. Their content in Cr, Al, Ni and Ta can be optimized as a function of ductility requirements or coating process. Among the latter, physical vapour deposition and plasma spraying are likely to become increasingly important in coating technology.

REFERENCES.

1. G. GOWARD
Properties of high temperature alloys.
Electrochemical Society, Proceeding 77-1, pp. 806-823

2. F.S. PETTIT and GIGGINS
J. Electroch. Society 118, 1782 (1971)

3. J.A. GOEBEL and F.S. PETIT
Report ARL TR 75-0235, June 1975

4. A. DAVIN, D. COUTSOURADIS
Cobalt n°17, p. 23, 1962

5. A. DAVIN, D. COUTSOURADIS, L. HABRAKEN
Cobalt n°35, p. 69, 1967

6. A. DAVIN, D. COUTSOURADIS, L. HABRAKEN
Cobalt n°57, p. 175, 1972

7. A. BELTRAN
Cobalt n°46, p. 3, 1970

8. I.G. WRIGHT, B.A. WILCOX, R.I. JAFFEE
Final Report "Oxidation and hot corrosion of Ni-Cr and Co-Cr base alloys containing rare earth oxide dispersions".
(May 8, 1975), contract N 62269-74-C-0291, Naval Air development Center.

9. G. J. SANTORO
Hot Corrosion of S-57, a cobalt-base alloy
(Sept. 9, 1976), Internal NASA Report.

10. J.M. DRAPIER, A. DAVIN, D. COUTSOURADIS
High Temperatures-High Pressures, 1974, vol. 6, p. 301-312

11. C. JUST, M. VILLAT,
Sulzer Brothers (Winterthur, Switzerland)
Private Communication.

12. A. MESSBACHER, MTU-Germany
Private Communication.

13. R. PICHOIR, Onera, Chatillon-sous-Bagneux, France
Private Communication.

TABLE I - Isothermal oxidation details (8)

Alloy	Temp (°C)	Time (hrs)	Weight gain (mg/cm^2)
Co-20Cr-6Al-2Y_2O_3	950		0.0490(*)
	1100	51	0.1874(*)
	1100	59	4.3390
	1100	63	2.3370
Co-20Cr-6Al-10W-2Y_2O_3	1100	51	3.2800
	1100	52	0.5720
	1100	65	0.1195(*)
	1200	52	4.0360
	1200	102	-1.1071
Co-20Cr-6Al-10Ta-2Y_2O_3	1100	92	-0.0491
Co-20Cr-6Al-10Ta-2Y_2O_3	1100	112	-0.9530
Co-20Cr-6Al-0.5C-2Y_2O_3	1100	103	0.0001
Co-20Cr-6Al-2Y_2O_3	1100	69	0.4165
	1200	72	-1.5307
X 40 Co-25Cr-10Ni-7.5W-1.5Fe-0.5Mn-0.5Si-0.5C	1100	98	386.780
	1200	47	
WI52 Co-21Cr-1Ni-11W-2Nb-2Fe-0.5Mn-0.5Si-0.45C	1100	49	-20.8990
Haynes 1002 Co-22Cr-16Ni-7W-3.7Ta-1.5Fe-0.7Mn-0.4Si-0.2Ti-0.3Al-0.6C-0.04La	1100	97	1.6136
	1200	68	-15.5745
S 57(**)	1100	100	0.3400
Co-25Cr-10Ni-5TA-3Al-0.5Y	1100	138	0.3675
	1200	121	0.0287

(*) specimens preoxidized in impure hydrogen, 18h, 1050°C
(**) Alloy hot rolled to 1.75 mm, cold rolled to 1 mm; with intermediate anneals, used in cold rolled, and pickled and polished condition.

TABLE II - Nominal composition of experimental alloys

	Co	Cr	Al	Y	Ta	Ni
S 65	bal	25	10	0.5	-	10
S 66	bal	25	-	0.5	10	10
S 67	bal	25	10	0.5	10	10
S 68	bal	25	10	-	-	10
S 69	bal	25	3	0.5	7	10
S 70	bal	25	3	0.5	10	10
S 71	bal	25	5	0.5	7	10
S 72	bal	25	5	0.5	10	10
S 73	bal	25	7	0.5	7	10
S 74	bal	25	7	0.5	10	10
S 75	bal	25	10	0.5	7	10
S 76	bal	25	5	0.5	5	10
S 77	bal	25	7	0.5	5	10
S 78	bal	25	7	0.5	5	10

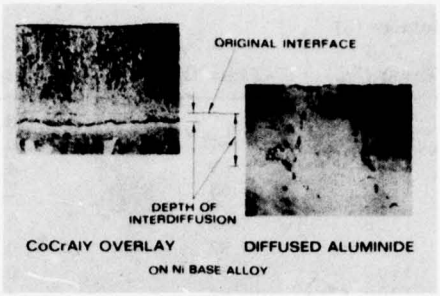

Fig. 1. Overlay versus diffusion coating (Airco Temescal)

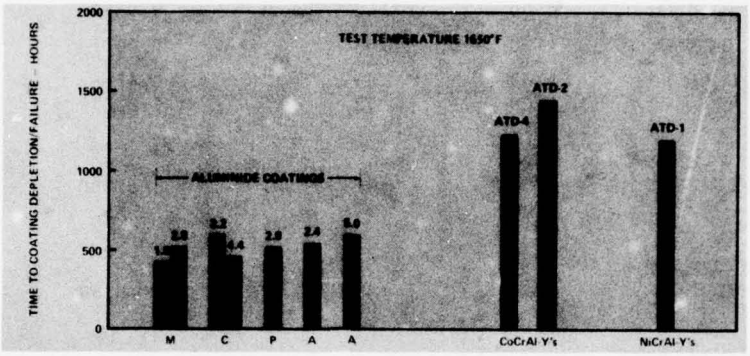

Fig. 2. Sulfidation /Hot corrosion rig testing of CoCrAlY and production aluminide coatings. Cobalt base substrate, 35 ppm salt (Airco Temescal)

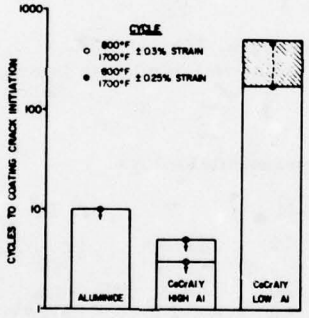

Fig. 3. Thermal mechanical fatigue behavior of brittle and ductile coatings (1)

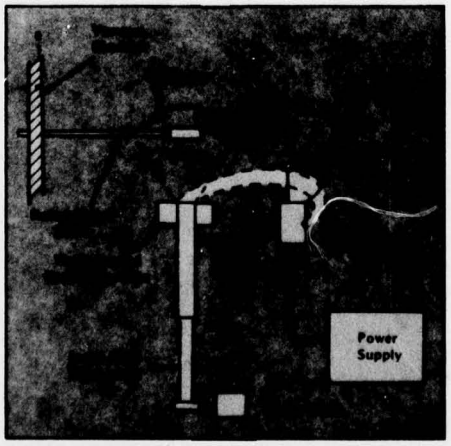

Fig. 4. Electron beam evaporation (Airco Temescal)

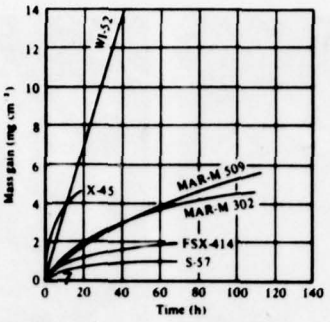

Fig.5. Oxidation of S-57 and current-cobalt-base superalloys in still air at 1095°C. Data on the commercial superalloys from (7)

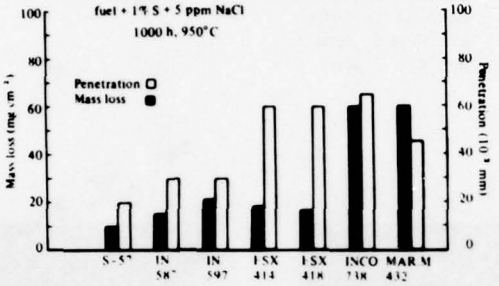

Fig.6. Hot-corrosion resistance of S-57 alloy and of commercial nickel-and cobalt-base alloys. 1000-hour exposures at 950°C in combustion gases contaminated with sulphur (1%) and sodium (5ppm), with cooling to room temperature every 48 hours (6)

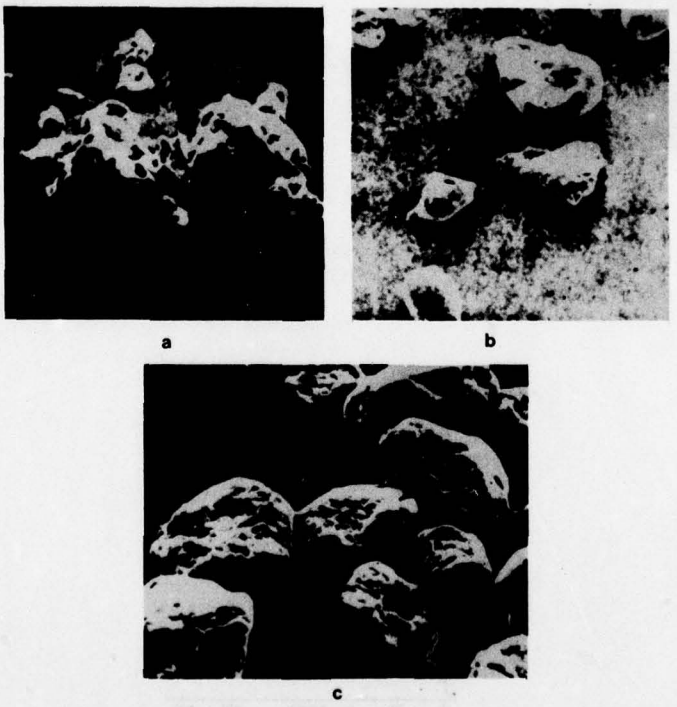

Fig.7. Scanning-electron micrographs of S-57 prealloyed powders (x 400)
(a) water-atomized (37-88 μm)
(b) water-atomized (< 37 μm)
(c) Coldstream (37-88 μm)

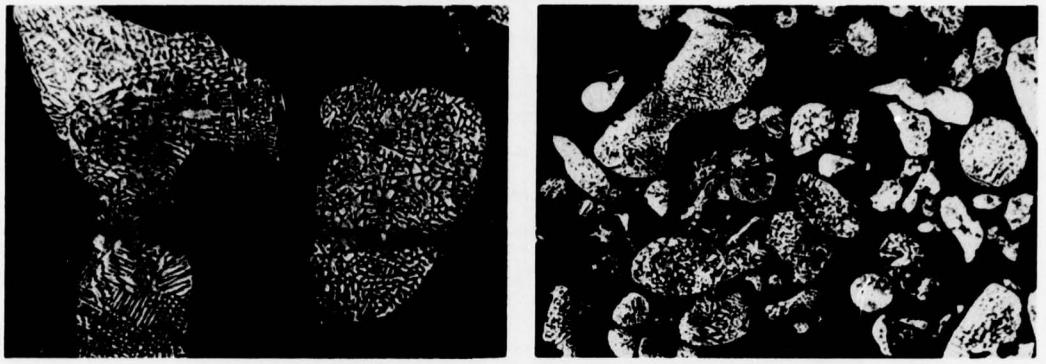

a b

Fig. 8. Optical microstructure of water-atomized S 57 powder (x 400).
a : 37-88 μm
b : < 37 μm

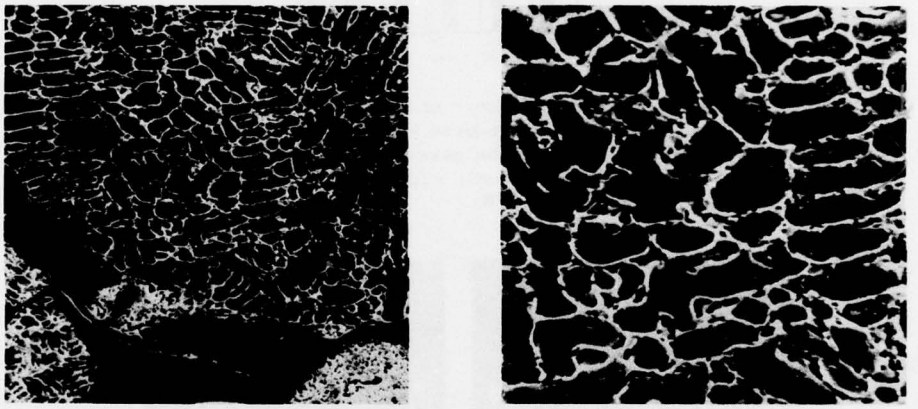

x 1600 x 4000

Fig. 9. Morphology of argon atomized S-57 powders

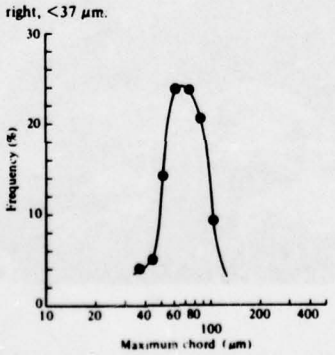

Fig. 10. Frequency-size distribution of the screened 37-88μ water atomized S 57 powders

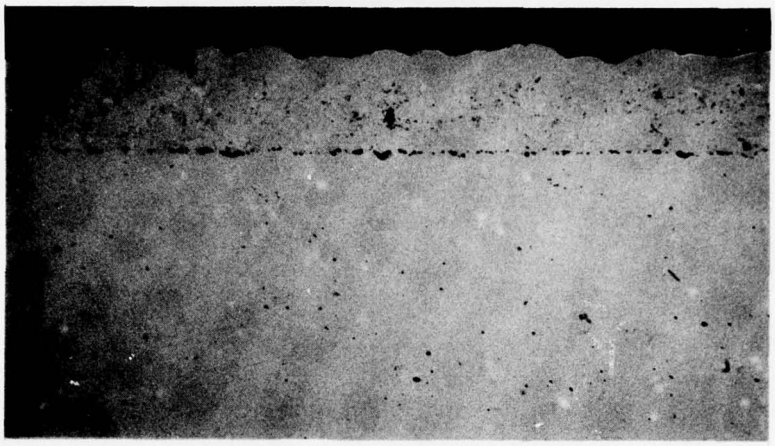

x 100

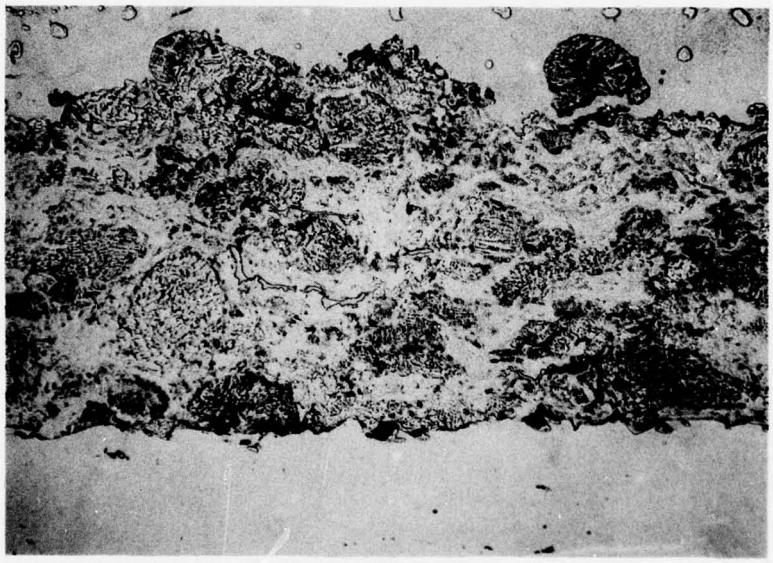

x 500

Specimen A - LPPS process - cold material

Fig.11. Microstructure of the S 57 coating on stainless steel substrate (12)

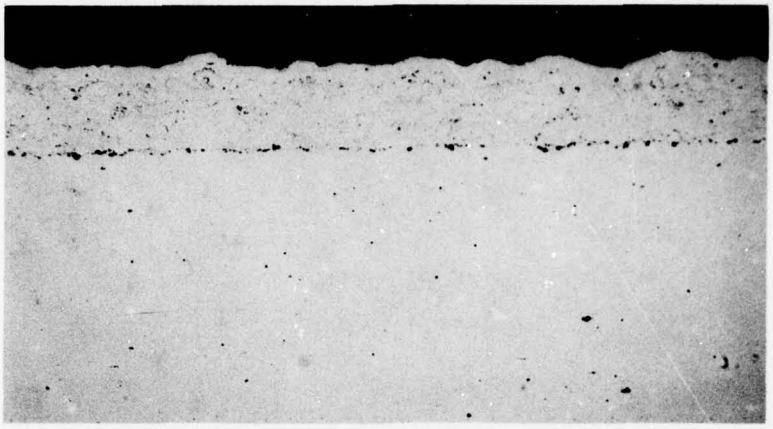

x 100

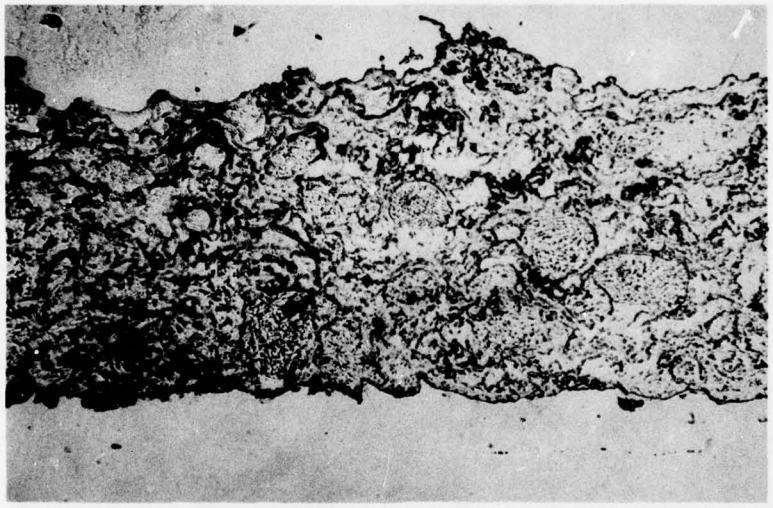

x 500

Specimen C - LPPS process-preheated material

Fig. 12. Microstructure of the S 57 coating on stainless steel substrate.(12)

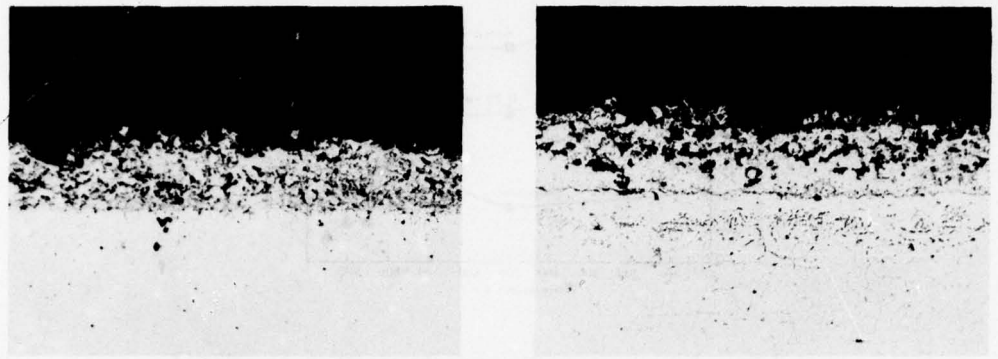

1000 H 2000 H

x 100

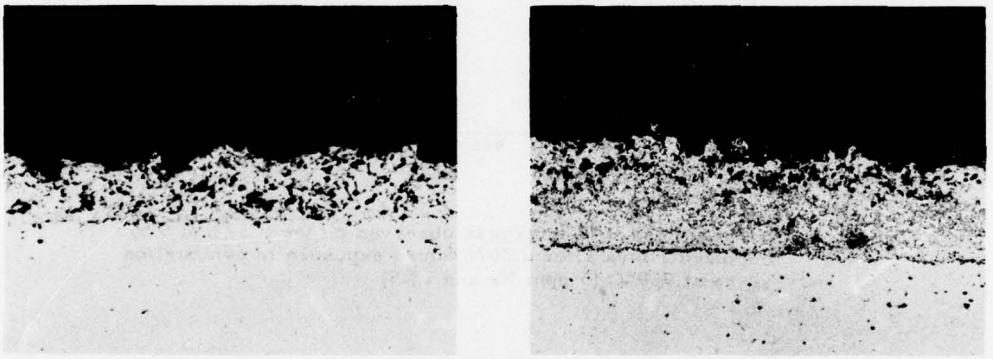

1000 H 2000 H

x 100

Fig. 13. Aspect of the S 57 coating on stainless steel after a hot corrosion test in combustion gases polluted with 1 %S and 5 ppm Na at 950°C during 1000 and 2000 hours of exposure

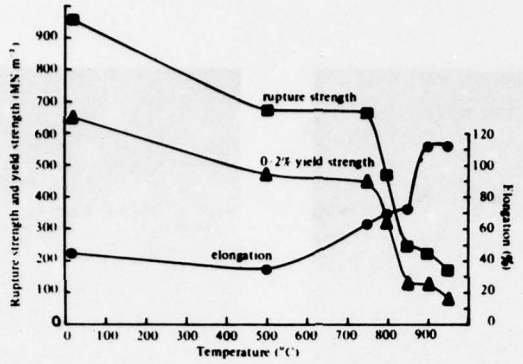

Fig.14. Temperature dependence of the tensile properties of hot-rolled, 2 mm thick, S-57 sheet material (10)

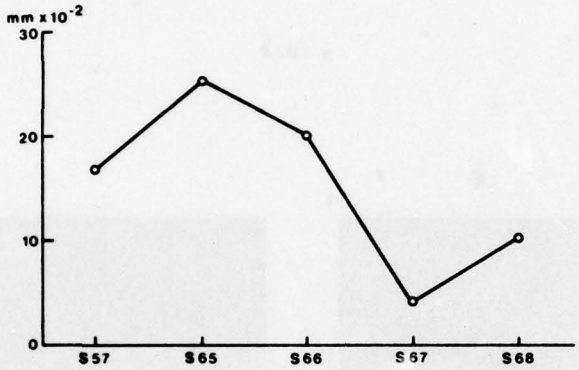

Fig.15. Average losses in thickness observed on the S 57 and S 57 modified alloys after a 2076 hours exposure in combustion gases at 950°C (5 ppm Na and 1 %S)

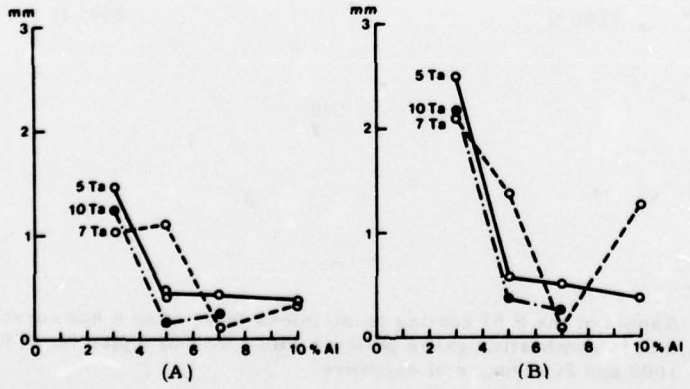

Fig.16. Average (A) and maximal (B) losses in thickness observed on the S-57 and S-57 modified alloys after a 2076 hours exposure in combustion gases at 950°C. (100 ppm Na and 1 %S).

TRENDS OF FUTURE TURBINE LIFE PREDICTION; TIME PHASED AUTOMATED ANALYSIS AND TEST VERIFICATION

J. L. Price
Manager Structures Technology
Government Products Division
Pratt & Whitney Aircraft Group
West Palm Beach, Florida 33402

I. J. Gershon
Technical Area Manager
Propulsion Branch
Air Force Aero-Propulsion Laboratory
Wright Patterson AFB, Ohio 45433

SUMMARY

The development of gas turbine engines has been keyed primarily to increases in thrust-to-weight ratio and to greater demands for structural durability. In fewer than 20 years, the thrust-to-weight ratio of turbine engines has doubled, as demonstrated by the F100-PW-100 engine compared to the J75. In this same period, the required design life for turbine engines increased by a factor of 40, as demonstrated by changes in the Government Turbine Engine Military Design Specification (MIL-E-5007) for the period. Also, a new engine life parameter, low cycle fatigue, was recognized. This new parameter, results from stress variations in the engine hardware during thrust level excursions and is now included in the latest engine Military Specification (MIL-E-5007D). Both the increased thrust-to-weight and life requirements were successfully accomplished by effective implementation of improvements in structural analysis techniques, increases in aerodynamic performance, utilization of higher strength materials and reductions in component allowable stress margins.

Unfortunately, the high strength material and reduced stress margins, which were required to realize the low engine weight and which allowed achievement of this thrust-to-weight improvement, make the modern turbine engine more susceptible to structural distress and high development cost than its predecessors. Since current projections of propulsion systems for the next decade show a continuing trend of increases in thrust-to-weight ratio and required durability, highly sophisticated structural design and verification techniques are being developed to insure that the risk of structural distress and "high-costs" during development and after deployment are minimized.

The techniques that are being developed (Ref. 1) to insure attainment of this minimum risk concept include both implementation of economical computerized structural analysis techniques, which are highly automated to reduce design iteration time, and implementation of a time-phased development methodology, which will insure elimination of inadequate structural and material concepts at the lowest possible level of the development process.

These techniques will be of prime importance in the design and development of turbines for future propulsion systems. In the past, the hot environment and high strength materials utilized in the turbine section of these high performance propulsion systems have established the turbine as the prime structural distress area. Since the projected characteristics of future high performance turbines continue to show substantial increases in wheel speed, stage loading and combustor exit temperature, the turbine is assured of maintaining its established position. Thus, the techniques being developed to ensure minimum risk for structural distress will have a primary application in the turbine section.

The following discussion presents a review of the most significant design parameters affecting turbine durability, and the structural analysis and verification techniques which are being developed for identification of structural inadequacies early in the propulsion system development cycle.

LIST OF SYMBOLS

APSI	-	Advanced Propulsion Subsystem Integration
ATEGG	-	Advanced Turbine Engine Gas Generator
IFR	-	Initial Flight Release
FFR	-	Full Flight Release
ISR	-	Initial Service Release
OCR	-	Operational Capability Release
JTDE	-	Joint Technology Demonstrator Engine
2-D	-	Two-dimensional
3-D	-	Three-dimensional
Mil.	-	Military
A/B	-	Afterburner
PP	-	Part power
Max	-	Maximum
DS	-	Directional solidified
psi	-	Pounds-per-square-inch
ksi	-	Thousand-pounds-per-square-inch
BIE	-	Boundary integral equations
No.	-	Number
AMT	-	Accelerated mission test
deg	-	degrees
LCF	-	Low Cycle Fatigue
HFF	-	High Frequency Fatigue

ΔK_{th}	-	Threshhold stress intensity
FMEA	-	Failure Mode and Effect Analysis
B/H	-	Bolthole
K_{Ic}	-	Threshold stress intensity factor

INTRODUCTION

The criteria for structural design of turbines for propulsion systems prior to a decade ago were primarily a direct function of total time spent at long-time cruise conditions and the total number of throttle excursion from idle-to-maximum power and back to idle. The take-off and climb time defined the creep growth and coating erosion requirements, and the throttle excursions defined the cyclic life requirements (low cycle fatigue, LCF). Blade and vane vibration analysis considered blade-alone natural frequencies, with disk coupling effects estimated in later designs, to prevent integral order-resonances within the engine operating range. Airfoil dampers were effectively utilized to maintain non-integral order excitation, from combustion process vibratory forces, within the materials endurance limit. Airfoil tip-to-case and interstage seal clearances were primarily a function of the dimensional stability (creep growth) of the parts within a particular stage. Overall system effects on these clearances (such as compressor shaft deflection under surge conditions) were insignificant, and were not considered in the design.

In today's propulsion system, the turbine designer is confronted with a complex interactive structural design task. The high thrust-to-weight configurations utilize high strength and low toughness materials, complex airfoil cooling schemes and a flexible rotor and rotor support structure. When these structural configurations are coupled with the modern aircrafts complex mission/duty cycle requirements (and the high performance turbine characteristics of high stage loading, high wheel speeds, and high thermal environments) a reliable life prediction becomes very difficult, time consuming, and expensive to achieve. Furthermore, the lightweight structural components of today are much more flexible than their counterparts in prior engines, and interactive effects with mating parts have become paramount design considerations.

Simultaneous evaluation of the combined effects of all design parameters has required the development of highly specialized automated computer analysis systems. These computer systems are especially tailored to accept structural configuration and load environments typical of propulsion system hardware. The automated features allow an accurate evaluation of complex structural shapes subjected to multiple load points within the mission profiles. These evaluations can now be accomplished in days, instead of months as required for past designs. Thus, the modern propulsion system design and development process represents a substantial increase in analytical complexity. An indication of the degree of increase is readily illustrated by the comparison (shown in Figure 1) of the number of mathematical calculations required to process a system from conception to production release, in today's design, compared to other systems over the past 30 years. In the 1950's era, designs such as the J48 and J57 required 2 to 12 million calculations, respectively. These calculations were primarily performed with manually operated desk calculators and no automated computer solutions were used. Todays system requires 4 trillion calculations and they are almost solely executed at remote terminals of sophisticated automated computer systems. (It is significant to note that the calender time required to implement a propulsion system has decreased.)

This trend to automated analysis capability is expected to continue to accelerate to meet the projected requirements of the future propulsion systems. The turbine performance projections for the next ten years, as shown in Figure 2, show a continuing trend of increases in design parameters which increase thrust-to-weight ratio. A 25% increase in combustor exit temperature and a 50% decrease in turbine blade tip clearance are the more significant performance parameters which effect the structural design. As for durability, in todays ever-increasing inflationary economic environment, the cost of weapons system development and ownership is expected to place heavy demands on minimizing structural distress and extending fleet operational capability. Thus, more sophisticated structural design and evaluation techniques will be required to evaluate the unique structural concepts and operational conditions anticipated for turbines of future high performance propulsion systems. The overall goals of these techniques will be to eliminate all potential structural distress prior to a weapons system deployment.

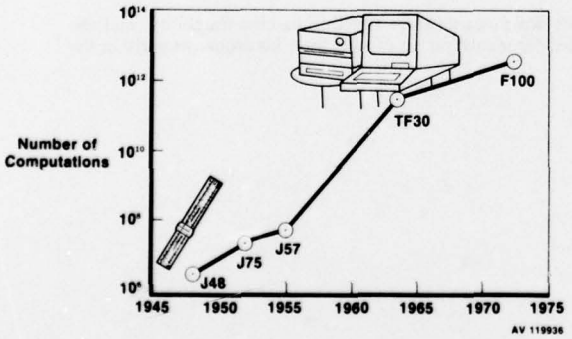

Figure 1. An Increased Number of Calculations are Required to Complete a Propulsion System Design Compared to 20 Years Ago

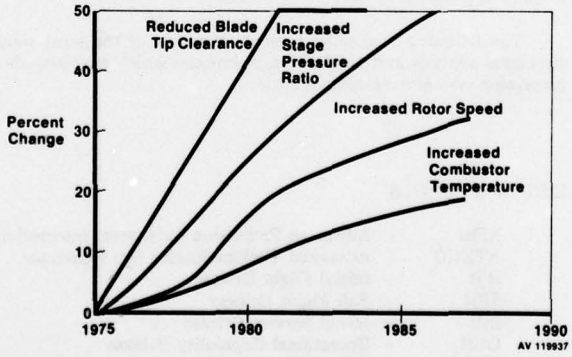

Figure 2. Projected Trends Over the Next Decade for Major Turbine Design Parameters

The design process evolves through three discrete development phases, Exploratory, Advanced and Engineering development as shown in Figure 3. Each phase exercises configuration control and closed loop life management concepts to ensure the optimized propulsion system is maintained after fleet deployment and the component design life requirements are validated by limited fleet experience, prior to committing the weapons system to full deployment. However, effective accomplishment of the overall goals requires both improvements in structural analysis prediction techniques and the development of a methodology to assure that structural inadequacies are identified at the earliest possible development stage. This methodology will allow early identification of critical life-limited parts of the turbine and continually monitor these parts from engine conceptional stage through final design, full-scale development, qualification, deployment and fleet management. A brief review of the more important features of the analysis technology and the methodology for identifying structural inadequacies is presented in the following discussion.

A. Structural Analysis Technology

The primary structural technology advancement areas that are dictated by the current trend of high thrust-to-weight, durable engines (particular to the turbine section) can be catagorized into four areas: (1) mission related stress analysis, (2) thin walled cooled blade life analysis, (3) disk life analysis, (4) airfoil tip clearance control.

1. Mission Related Stress Analysis

In contrast to prior turbines, which had to pass simple cyclic tests at long-time load conditions, future turbines will be required to meet real-time mission loads for specific flight usage. The F100-PW-100 and recent upratings of the TF30 engine are probably the first propulsion systems to be fully impacted by these requirements. Limiting stress conditions are almost always set by transient engine acceleration and deceleration speeds, where steady stresses and thermal gradient stresses combine with high frequency flow induced vibratory stress to produce minimum structural margins. Identification of this limiting stress condition requires a continual tracking of the resultant stresses in each part throughout each mission to be flown by the aircraft. Thus, to adequately account for all design parameters, the stress and metal temperature predictions for turbine blades, vanes and disks have become very complex.

To obtain sufficient accuracy in the predicted stresses for the local stress concentration areas of the blades, vanes and disks, two-dimensional (2-D) and, in most cases, three-dimensional (3-D) finite element analysis techniques, including nonlinear effects, is required. Automated computer systems (Ref. 2) have been generated to allow execution of this analysis in a timely manner. These allow a practical application of the analysis during an initial configuration selection effort for a part. Automated systems, now available for all critical turbine parts, cover vibratory response, as well as steady stress predictions. A typical example of one fully-automated design system is the stress prediction for turbine airfoils. Once an airfoil inner and outer shape is selected by the aerodynamic and heat transfer requirements, the stress analysis is initiated by a four card instruction routine to the computer. The computer automatically accesses the aerodynamic system, picks the airfoil inner and outer contours, selects the type of element and nodal breakup, which varies from the outer tip of the airfoil to the disk attachment, displays that selection on computer interactive graphics for an engineer to review before initiating the stress analysis. On the "go" signal it completes the analysis. A typical element breakup is shown in Figure 4 for a hollow turbine blade. This system reduces the turnaround time from 3 weeks to one day for a complete airfoil stress analysis.

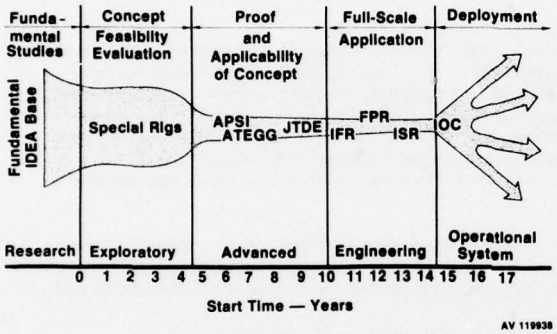

Figure 3. The Propulsion System Evolves Through Three Major Development Phases Prior to Full Deployment of the Weapons System

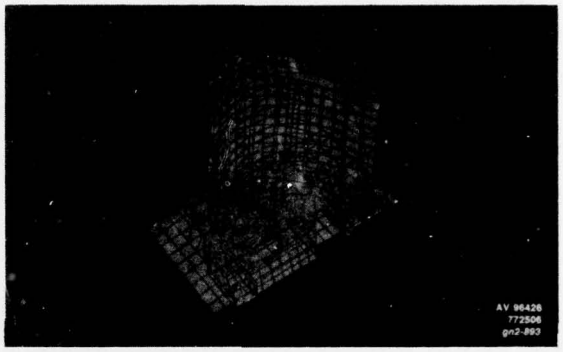

Figure 4. Typical Turbine Airfoil Finite Element Breakup for Stress Analysis

A similar system for vibratory mode shape and frequency prediction is shown in Figure 5. This system utilizes a technique called cyclic symmetry to reduce the amount of computation time. This technique allows elimination of all structure except one pie-shaped segment which contains one blade. It then predicts the vibratory characteristics of the bladed disk assembly, including coupling effects between stages.

The economical design analysis turnaround time achieved by these systems allows investigation of part stress distributions for a multitude of mission related flight points. These stress surveys of each design mission are utilized to determine the fractional life damage occurance for each mission. The resultant fractional lives are then added appropriately to reflect the aircraft mission mix for obtaining the total mission related part life.

Over the past decade the full impact of the effects of this fractional life damage has become apparent. The success of future propulsion system design efforts will be very dependent on accurate descriptions of all required operational missions early in the initial design effort.

A review of the increases in mission requirements that have occurred for the TF30 weapon systems illustrates the importance of the mission related design parameters. The original versions of these systems were designed to withstand the MIL-E-5007C specification cyclic and long hot time conditions. From 1972, when the first preoperational estimates of aircraft flight cycles were obtained from simple paper missions, to 1977, when the aircraft mission was more established and on-board flight recording of power lever positions became available, the operational conditions and cyclic requirements have escalated as shown in Figure 6. Prior to delivery of production aircraft, the primary mission planned for the weapons system indicated a need for only two full throttle excursions to maximum power per three hours of flight time. In 1974, after substantial flight experience, the primary mission became better defined and the throttle excursions to maximum power increased to 10, with 5 excursions to military power. By 1977 onboard flight recorder data indicated only one excursion to maximum power but 26 excursions from low power to maximum. Part of this change was attributable to a redefinition of the actual missions being flown. As more experience was gained in actually flying simulated missions, improved flight profiles emerged and the intended use of the weapon system matured. Also, as new threats arise, new missions are added to respond to these threats. Thus, the design requirements for the propulsion system requires constant updating to assure realistic monitoring of critical hardware part-lives. This update allows timely recommendation of new limits for critical parts, which are essential for the propulsion system user logistics and operational readiness.

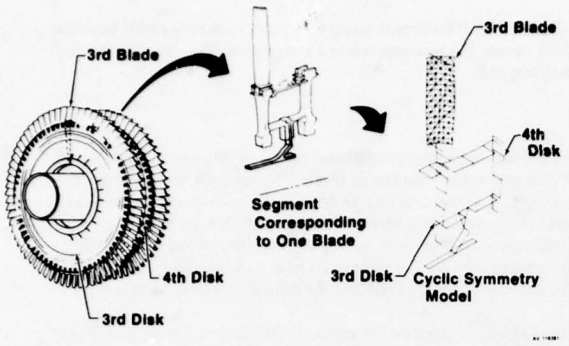

Figure 5. Cyclic Symmetry Finite Element Model

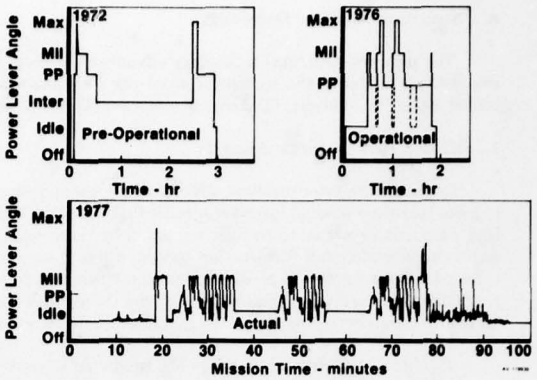

Figure 6. Throttle Excursion vs Development Time for High Usage Mission of a Current Weapons System

Figure 7 presents a summary of the changes which evolved in this instance of introducing this propulsion system into fleet usage. It includes the proper mix of different missions flown; such as, training, ferry, interdiction, etc. Of major significance to the tabulated results is, for each 1000 hours of usage, the time spent at military power more than doubled, full cycles increased by over a factor of 2, and partial cycles increased by a factor of 4. These changes required a significant design re-evaluation and some hardware modification. The automated design systems are essential to keep pace with these maturity changes which occur in a weapons system development cycle.

2. Thin Walled Cooled Airfoil

The complex cooling schemes of pins, baffles holes and slots, which are necessary to provide optimum cooling for the blades and vanes, result in many inherent local stress concentrations requiring structural evaluation. Each of these areas becomes a potential location for the initiation of a crack. Furthermore, these thin walled configurations are more sensitive to environmental temperature changes and stage pressure loading. Fast changes in environmental temperatures result in high thermal gradients between the fast responding thin sections and the slower responding platform and thick attachment sections. The high stage pressure loading makes the designs more susceptible to blade/vane deflection and interstage metal contact under off design loads, such as surges. The brittle coatings, utilized on the airfoils to provide erosion protection, degrade the life of the base airfoil material due to microscopic cracks in the coating.

The basic stress analysis technique used for these airfoil designs evaluates the stress concentration areas, thermal stresses, stage loading and vibratory frequency, and mode shapes for both blades and vanes. In prior turbines, the design analysis stopped with this static and vibratory analysis. However, recent and all future turbines will require an evaluation of crack tolerance and production tolerance effects on blade frequency.

Blade fatigue crack growth behavior is now predictable using advanced fracture mechanics techniques (Ref. 3). These predictions include variables such as, LCF-HFF interaction, temperature and mechanical load profile changes, and localized geometry influences. Crack growth behavior for cracks originating from impingement holes in the case of showerhead airfoil designs, can also be treated. Failure is established as the linkup of two colinear cracks growing between adjacent holes. Crack growth material characteristics for airfoils, under simulated airfoil thermal-fatigue loading, is usually obtained by subscale specimen testing. However for complex grain-structured, thin walled, coated airfoils like those shown in Figure 8, the primary test specimen is the actual blade or vane. The metallurgical micro-structure in the airfoils is unique to the part fabrication process and is not reproducible in the specimen shape which is required for crack growth measurements. Thus, correlations between the specimen test results and actual airfoil failure data are required to provide allowable cyclic stress design curves. Once these properties are characterized over the stress and temperature range expected, they can be utilized to estimate the part life under the actual engine stress and temperature environment. The usual fracture mechanics stress intensity relationships are converted to strain intensity terms for correlating airfoil strain with specimen crack growth data.

	Exposure Per 1000 Hours (Mission)		
	1972	1976	1977
Military time - hr	80	160	175
No. Full Cycles (Shutdown - Mil)	400	560	650
No. Partial Cycles (Idle - Mil)	140	325	7,500
(Part power - Mil)	540	3,400	1,650
No. A/B Lights	540	2,275	2,170

AV 119940

Figure 7. Typical Aircraft Mission Profile Summary

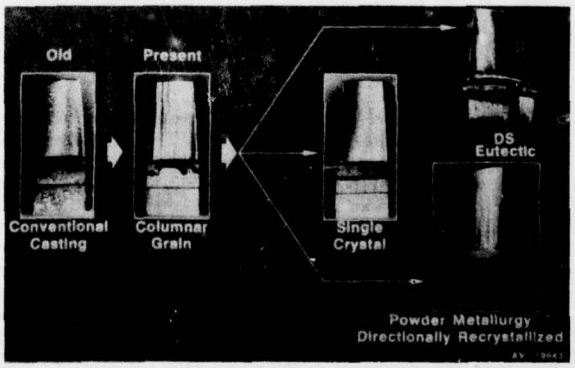

Figure 8. Turbine Airfoil Casting Material Trends

The trend in airfoil shapes has been toward low aspect ratio, long chord designs to minimize the number of airfoils-per-stage. This trend has resulted in the first natural bending frequency of the blade being very close to the overall bladed/disk coupled mode frequency, as shown in Figure 9. This condition results in a very high blade vibratory response in the most closely coupled blade of the stage. This condition is usually referred to as the tuned absorber or mistuning effect. To alleviate this potential failure mode, future turbines will require efficient vibratory damper systems or the exercise of close control of blade manufacturing tolerances to ensure that blade frequencies do not occur close to the coupled frequency. In either case, it requires substantial improvement in our capability to predict individual blade responses when the blade is coupled with a disk system and forced by main stream flow wakes. A schematic of this mistuning prediction system is shown in Figure 10.

The system basically utilizes a Monte Carlo technique to combine blade manufacturing (shape) tolerances with nonuniform airfoil damping to predict the degree of mistuning in a given wheel design.

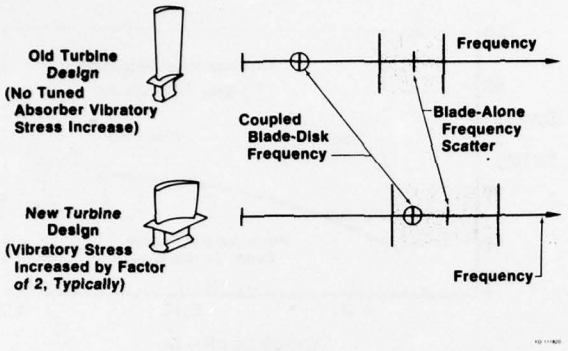

Figure 9. Comparison of Coupled Bladed Disk Frequency and Blade Alone Frequency for Old and and New Turbine Designs

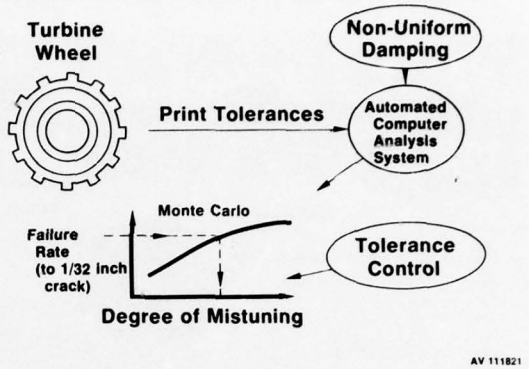

Figure 10. Statistical Analysis of Resonant Stresses in Mistuned Rotors

3. Disk Life Analysis

In the past, low to medium strength turbine disks operating in, or near, the creep region were tolerant to local yielding and stress redistribution in the local notched regions; such as, snap corners, cooling holes and boltholes. Conventional notch theories were utilized to adequately predict the life of the part. However, the increased strength disk material and reduced operating stress margins, which allowed attachment of the light-weight modern turbine designs, have made these components more sensitive to design tolerances, undetectable internal material defects, engine operational variations, and manufacturing tolerances. As shown in Figure 11, typical turbine disk nominal operational stresses have increased from 70,000 psi in 1960 to 120,000 psi in 1977. This increase resulted in the stress margin, relative to the ultimate strength of the material, of 35% as compared to 50% for engines of a decade ago.

Under the high stress and high temperature environment of the high performance turbines, the high strength alloys exhibit localized microscopic grain boundary fracture instead of redistribution when the surface stress yield allowables are exceeded. Conventional notch theory is not sufficient to characterize this local fracture condition.

Modern turbine development programs have initiated development of analysis techniques to predict these fractures and to evaluate their effect on component life. (Ref. 3, 6). However, future lightweight designs will need improved, faster turnaround prediction methods to insure application of these techniques during the initial design stage. These techniques require an accurate prediction of the local strain distribution in the part. To obtain sufficient accuracy, either 2-D or 3-D finite element, or boundary integral equation (BIE) methods are required. A typical example of a 3-D element breakup required for a typical disk rim with a radial cooling hole is shown in Figure 12. Definition of the surface elements for preliminary analysis is a simple task. Selection of element shapes and defining connecting points into the depths of this complex shape such as a local hole in disk run is impossible for any practical application of an analysis of this type. Figure 12 shows an example of the breakup required for a rim hole. This analysis is conducted by modeling only a local area of the hole and applying boundary conditions to the exterior modes as determined from the preliminary analysis model. Automated systems, which accomplish this task from simple outside contour input, are required if these techniques are to be applied effectively during a design. Crack initiation and propagation characteristics are then possible and are accomplished to establish the fatigue capability of the particular geometry.

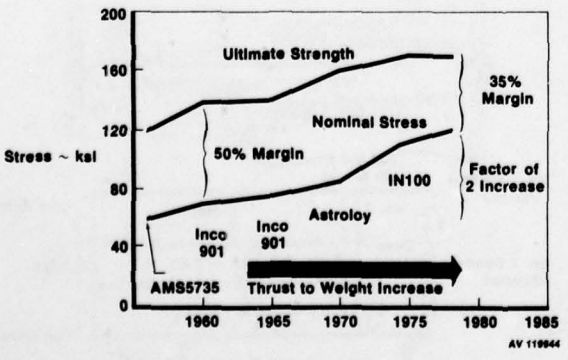

Figure 11. Nominal Disk Stress Increase Over the Past Decade

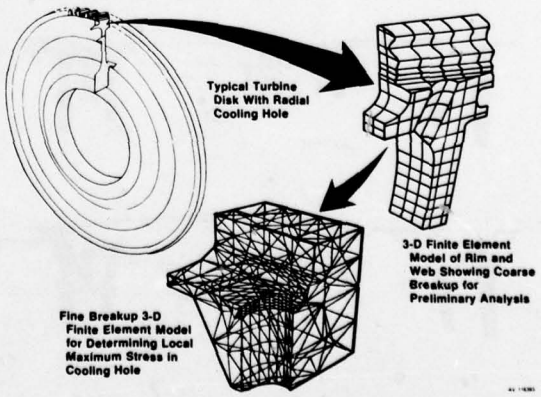

Figure 12. Typical Element Break-Up for a Turbine Disk Rim With a Radial Cooling Hole Feature

Most turbine disks have local notch areas in the creep region of the disk. Nonlinear finite element methods are used for these conditions. Creep laws of time hardening and strain hardening rules are used for the creep rate calculation. The method used to apply uniaxial creep data to evaluate the creep increment under multiple stress excursions is essentially identical to the plastic strain increment in the plasticity theory. The predominate life of these alloys is found in crack initiation and crack growth up to inspectable crack sizes of approximately 1/32 inch. Life exhibited beyond the sizes are usually very small, due to a higher crack growth rate of the high strength alloys as compared to that of prior medium strength alloys.

Techniques have been developed to predict crack propagation life after the inspectable size and these techniques are in various stages of verification and calibration for implementation into design systems. One example verification test disk is shown in Figure 13. This disk was cyclically spun to failure in a spin pit. Failure occurred after 25,000 cycles from a crack initiated at a bolt hole. The crack propagated from the corner of the hole, through the disk to the opposite side, then radially through the disk web until rupture, as illustrated in the figure. The predicted life included K variation, stress variation across the bolt hole, crack size changes, and crack path hardware thickness changes. The test cyclic life, as shown in Figure 14, agreed with the predicted life, within 10%.

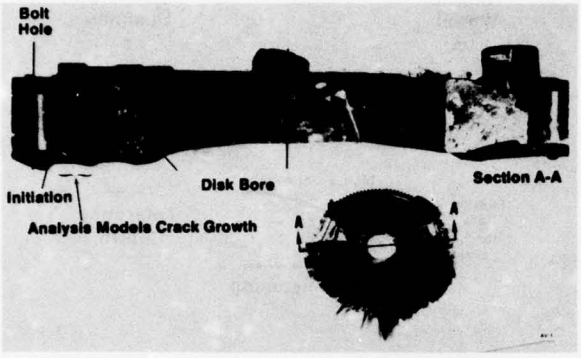

Figure 13. Verification Test Disk Cyclic Failure Crack Area

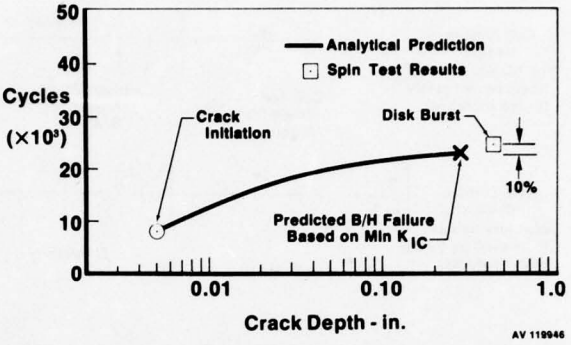

Figure 14. Agreement Between Prediction and Test for the Disk Test Shown in Figure 13

Advanced numerical methods and computer systems such as NASTRAN and MARC are used to determine local crack tip stress intensity relations. Crack tip singularity methods such as those developed by Barsoum (Ref. 4) are contained in these program capabilities. However, automated, economical design systems, which include improved crack propagation models that include life below the 1/32 inch type, are required to fully impact future designs.

4. Airfoil Tip Clearance Control

The lightweight design concepts, which have evolved from the trend towards higher thrust-to-weight ratios, has probably caused more change in the design activity for controlling the dynamic characteristics of the rotating portion of the propulsion system, than any other aspect of the design process. The weight reductions imposed on the propulsion system have made the rotor and the static support structure much more flexibile than for previous systems. This inherent flexibility causes the rotor and case longitudinal bending modes to couple together and occur within the engine speed range. The engine response, or "shake," at these low frequency coupled modes is usually controlled by oil film dampers at the bearing locations. Normally, the rotor system characteristics are of no concern for the turbine designer. However, with high thrust-to-weight ratio concepts, a requirement for very close radial clearances at the turbine blade tip and interstage seals was included for performance improvement. These clearances in prior engines were primarily a function of the thermal and radial growth of components within each stage. In the flexible, light-weight modern designs these clearances are a function of the overall system dynamic response. Rotors are usually thought of as being round and straight but today they are dynamic systems that are deflected as they rotate, as shown in Figure 15. Cases exhibit similar deflections but have an additional radial degree of freedom. Under normal operation, the effects of these deflections are usually well within the running clearances. But under abnormal operation, such as compressor surge, the relative case-to-blade tip clearance change usually defines the propulsion systems' required design running clearances. These resultant clearances set the maximum performance capability of the turbine. Therefore, today's turbine design must be an integral part of the overall rotor system design effort. A typical schematic of the analytical model used to represent a propulsion system for a response analysis is shown in Figure 16. It includes all masses, springrates and damping features of the total system, including the airframe mount springrate and damping. Resultant deflected shapes, as shown in Figure 17, are utilized to evaluate turbine clearance changes.

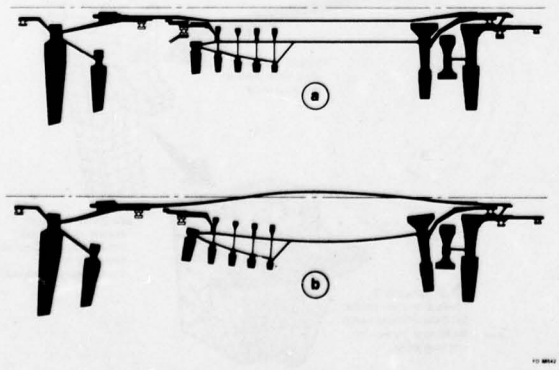

Figure 15. Engine Rotors are Thought of as Round and Straight (View a) but They are Actually Deflected as Shown in (View b)

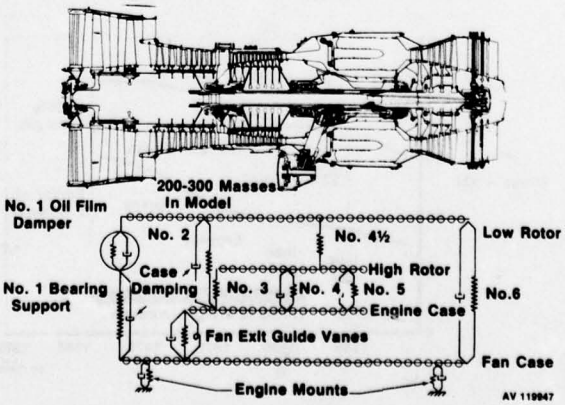

Figure 16. Typical Analytical Model Used for Critical Speed and Forced Response Analysis Showing the Model Representation Areas in the Engine

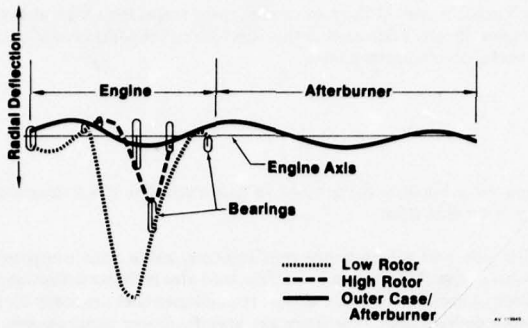

Figure 17. Typical Rotor and Case Deflection Modes

Control of these clearances in future propulsion systems will be even more demanding. Performance projections for these systems require a 50% reduction in clearances relative to todays designs, as previously shown in Figure 18. More effective rotor response dampers and development of structural concepts which are "stiff" and insensitive to transient rotor forces will be required.

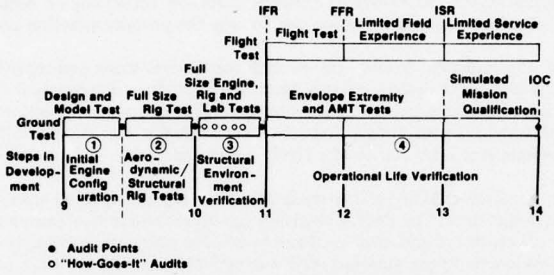

Figure 18. The Engineering Development Phase Block Diagram for the Propulsion Development Process Showing Pertinent Structural Audit Points

B. Methodology For Structural Development of Advanced Turbine Components

The methodology for integration of advanced structural and material concepts into advanced turbine engines attempts to eliminate structural risks at the lowest possible development level. In this approach a systematic time-phased development plan is employed to ensure that a particular concept progresses systematically, in stages of increasing complexity, from conception of the idea to maturity (deployment). At each stage, the concept must successfully demonstrate the structural margins required for a high confidence that the next higher development stage will be successful, and that the ultimate goals can be attained. If the basic development model provided by this method was completely implemented, it could theoretically provide a no risk development program; however, the actual degree of compliance with the basic model will in reality, depend on funding and schedule constraints imposed by the goals of each specific program. Thus, this model is intended to provide a basis for identifying areas of noncompliance relative to the optimum. This information provides the data required to quantitatively evaluate the risk of accomplishing the overall goals of the program and identifying critical life-limited parts which will require formal monitoring throughout the development effort. This assessment is performed at preselected stages within a development phase. The final assessment at the end of the phase would define the risk of continuing the concept to the next higher phase of development.

The methodology consists of four fundamental techniques: (1) an activity network which sequentially orders the significant technical tasks within a development phase, (2) audit check points and associated checklists for formally reviewing and recording technical status at critical design stages, (3) an error band analysis method for determining data accuracy and sufficiency, and (4) a risk assessment procedure to quantitatively assess the structural risk for a new concept in progressing to the next higher stage of development.

The methodology organizes each of the major development phases (exploratory, advanced and engineering development) into activity networks. Each activity network is a time-phased block diagram which represents, in sequential order from left to right, the significant technical effort or evaluation that should be accomplished prior to committing activity to the next higher development step within each respective development phase, as well as to the next higher development phase. A typical activity network for an engineering development phase is shown in Figure 18. There are four steps of development indicated for this phase, 1) initial engine design, 2) aerodynamic and structural rig tests, 3) structural environmental verification and 4) operational life verification. Similar networks are utilized in exploratory and advanced phases.

At critical times within this effort, such as completion of initial design or completion of major design modifications resulting from test, audit blocks are specified on the networks to indicate the optimum points for formal evaluation of the program technical accomplishment. Required modifications are identified, and the remaining activities are redirected for optimum program advancement. To facilitate the execution of these audits, the methodology includes checklists to ensure that all required analyses and test verifications are identified, and the acceptability of the results are compared to a specified experience based criteria. An error band analysis procedure is provided to ensure that proper consideration is given to the accuracy of each analysis and test. All tolerances affecting the results are considered in this analysis. These tolerances are statistically evaluated to determine the probable inaccuracy in the results and the probability of meeting the criteria. A statistical risk assessment method is provided to aid in quantitatively assessing all results with their respective error potential. This assessment method is fundamentally an opinion poll. It utilizes qualified engineers, from the particular development field, to evaluate the technical maturity of the program and to identify the risk of not being able to meet the program goals. This method is based on a technique recommended by the United States Air Force Academy (Ref. 2).

A discussion of the activities which exist in each of the four development steps, for a typical blade development effort, in the engineering phase follows. Although not specifically addressed in this discussion, the same type of activities, audits, and checklists are used for both exploratory and advanced development phases.

Steps in Engineering Development

Step No. 1 — Initial Engine Design

The basic structural configuration for a blade is determined in this step. The block diagram in Figure 19 highlights the sequential activities which are significant for this effort.

The design duty cycle description, life and maintenance requirements, along with component performance data for the optimum engine configuration, establish a design information base. This base also includes definition of design techniques based on previous experience, and an identification of component and material technologies that are ready for advancement from Advanced Development. With knowledge of previous development experience and specific design requirements, the structural design criteria are also developed.

With this design information base and material characterization data, the design and analysis of an initial engine configuration is accomplished. The resultant configuration is based primarily on analytical stress, internal flow, heat transfer and aerodynamic computer simulations. Some subcomponent testing may be required in this step to optimize particular details or processes for the specific configuration. Also, during this period special attention is given to those parts which, based on analysis, are projected to be critical in the remainder of the development effort. Critical parts are identified as, either those parts which have minimum structural margins and would cause major program delays (if proven to be inadequate in the future), or those particular hardware configurations that historical experience shows to be problem prone. These critical parts should receive a detailed analysis review and verification testing in an environment that as closely as possible simulates actual engine conditions. Possible alternative configurations for these parts should also be evaluated for future use, in case the primary selection proves undesirable.

Based on this initial design and subcomponent testing, design modifications are made and retested, if required, for improved confidence. It should be noted that the number of design and test iterations throughout development must be preplanned in order to define a program cost and schedule. Iterations beyond the planned number are not to be accomplished without modifying downstream activities to remain within the planned budget and schedule. Normally, this should only be done during a program audit where a risk assessment of alternate strategies can be effectively performed.

A system failure mode and effects analysis (FMEA) will be initiated in this step and updated in subsequent development stages to reflect the latest configuration and design data. The FMEA identifies significant and critical failure modes and the design action that will reduce risk of failure or provide control of undesirable effects on mission capability and safety of flight. Initially, historical data derived from previous engine development programs and service experience are used to define possible modes of failure and associated consequences. As detailed design data becomes available, specific failure modes and probabilities of occurrence can be defined and evaluated. Coupled with FMEA, fault-tree analyses can also be conducted for inflight shutdown and engine fire.

The first structural audit is conducted prior to proceeding with aerodynamic and structural rig tests. Since the engine design at this point is based primarily on unverified analyses, the main purpose of this audit is to assess the risk that the analyses can be verified in the scheduled activities. However, if design problems can be identified with confidence, the risk of solving them later in development should also be assessed. It should be realized at this audit that if the risk of continuing with the existing program is considered too great, alternative strategies must be developed and evaluated. Historically, there has always been a great reluctance at this early development stage to change a program direction drastically. However, if the quantified risk assessment procedure shows a minor change will significantly improve the probability of success, then serious consideration should be given to modifying the program accordingly.

Step 2 — Aerodynamic and Structural Rig Tests

Proceeding to this step indicates that the structural design has been judged to be sufficiently sound to permit design and procurement of full-scale rig hardware. There are two sequential series of rig tests in this step, as shown in Figure 20. The first series emphasizes aerodynamic performance, and the second evaluates the structural aspects of the finalized aerodynamic designs.

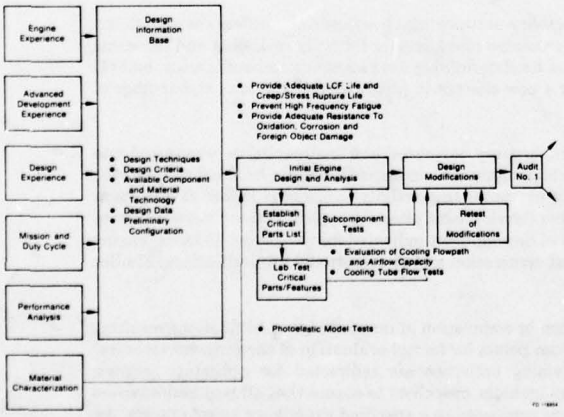

Figure 19. Blade Detail Block Diagram for Initial Engine Design Step in Engineering Development Phase

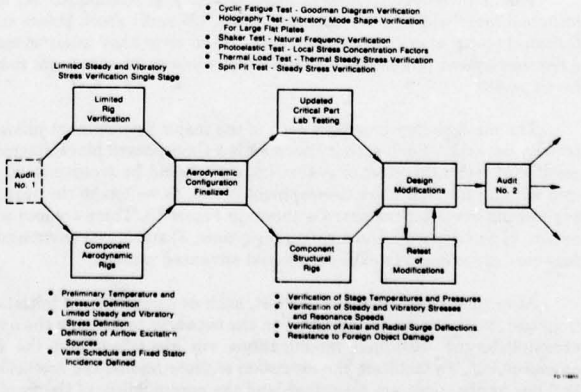

Figure 20. A Blade Detail Block Diagram for Aerodynamic and Structural Rig Test Step of Engineering Development Phase

The aerodynamic testing is accomplished on full-scale module level components incorporating a significant amount of boilerplate hardware. Therefore, structural evaluation is limited to only those parts which are flight-type. Furthermore, aerodynamic testing is normally of short duration, limiting structural evaluation to high frequency vibration and assembly anomalies.

The finalized aerodynamic configuration is then subjected to structural rig tests which provide a complete documentation of steady stress and vibratory conditions. Although the internal flows, pressures, and temperatures from these tests do not represent exactly the engine conditions, the data will be sufficient for updating the structural design system. In addition, wear rigs and laboratory testing of containment, proof and burst pressures may also be conducted. The critical parts list may change as a result of both the final aerodynamic configuration and the results of the structural testing. Critical parts should continue to receive special tests and analytical treatment. As in the previous step, design modifications are made as a result of this testing. Retesting of modifications may also be required to increase confidence in the design.

The second structural audit is concerned with ensuring that the design is sufficient for commitment to full-scale complete engines with a low risk of completing the planned program. Confidence in the design should be considerably greater than in audit No. 1, since subsequent rig testing has verified the design system. Therefore, any major structural problem appearing at this point can result in significant configuration changes and iteration to any of the previous development steps even as far back as to definition of mission and duty cycle. Again, a risk assessment of alternate strategies will point the way to any program redirection.

Step No. 3 — Structural Environmental Verification

The purpose of this step is to verify that the engine has sufficient structural life qualities to permit flight testing and operational verification. This verification is achieved by core and full-scale engine testing as shown in Figure 21. These tests subject the individual components, for the first time, to an engine environment which includes the coupling effects between sub-components, such as turbines and compressors. The environment includes actual secondary flows, heat transfer conditions and system dynamics. These engines will be heavily instrumented to obtain structural data on internal flows, temperatures, strains, overspeeds and vibrations. The engine tests will be supplemented with laboratory tests of those components expected to be limited by low cycle fatigue and creep. These laboratory tests, such as spin pit and ferris wheel tests, are employed to evaluate long-lived parts without requiring time consuming engine tests. When the design system is updated with this environmental and component life data, the analysis of the engine structural elements can be updated and necessary design modifications incorporated with a "how-goes-it" audit of the test results after completion of each significant full-scale engine test.

Following the completion of all redesign and associated test verification, the final structural audit for step No. 3 is conducted. This audit is a summation of all the "how-goes-it" audits and should concentrate on assessing whether the engine life has been sufficiently verified so that the engine can be fully qualified for flight testing and operational verification. Since the preceding life verification tests should have uncovered any remaining major structural problems in the system. This should be the last audit wherein decisions concerning significant program redirection are required.

Step No. 4 — Operational Life Verification

The objective of this step is to verify that the engine structure is satisfactory for field usage and meets expected life requirements. The activities include the flight test program, limited field experience, limited service evaluation, accelerated mission tests (AMT), flight-envelope extremity tests in a simulated altitude test facility and the final preproduction qualification simulated mission test, as shown in Figure 22.

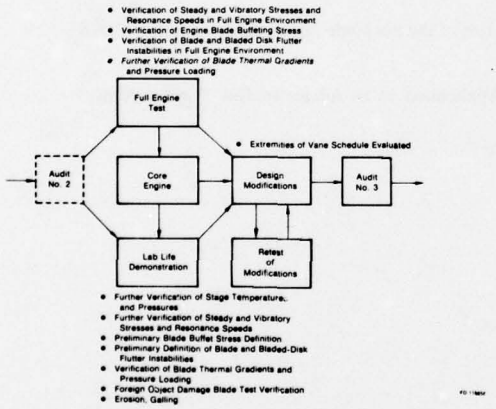

Figure 21. A Blade Detail Block Diagram for Engine Structural Environment Verification Step of Engineering Development Phase

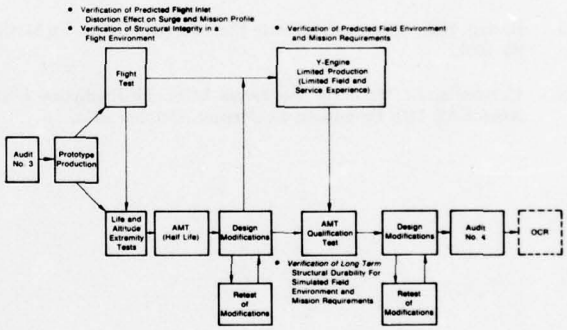

Figure 22. A Blade Detail Block Diagram for Engine Operational Life Verification Step of Engineering Development Phase

Flight testing provides confirmation of engine functional suitability through maneuver and envelope extremity tests and operational usage simulations. The real environment evaluation of the components is expanded in flight testing to include actual airframe/engine interface loads and actual transient aerodynamics. Structural data that could be obtained during flight testing include blade vibratory stresses, engine vibration measurements, and transient internal pressures and temperatures.

Simultaneously with the flight test program, expanded ground testing of complete engines is conducted. The extremes of the flight envelope are explored in ground facilities prior to flying in these regions. Accelerated mission tests (AMT) are conducted to evaluate the life potential of the engine. The AMTs are conducted in sea level and altitude test facilities as required to simulate the operational usage. The engine is subjected to the total operating time at rated temperature and the total number of LCF cycles at the correct altitudes and Mach numbers. The steady-state, low power portions of the operational usage are reduced in the AMT because they do not contribute to creep, erosion, or LCF damage. For practical and economic reasons, these tests would normally evaluate only a portion of the predicted life; an approximate half-life is considered a reasonable objective.

Following the flight test and ground life testing, design modifications may be required. In addition to vibration and environmental data from flight and engine testing, this redesign effort also considers results of inspection of parts taken from engines during teardown. These modifications are then incorporated into a small number of engines for limited fleet evaluation. In this evaluation, the aircraft are operated by the user organization in a manner that is expected to characterize full deployment conditions. This provides supplemental flight test data and guidance in planning the preproduction qualification test.

The simulated mission qualification test that leads to production is a full-life test that verifies the engine capability to meet fleet readiness life and performance requirements. This testing is tailored to simulate the optimized mission mix and duty cycle defined by the parallel limited fleet evaluation. The modifications required prior to full production committal are incorporated into the design. This fleet evaluation, prior to final production, ensures that the final design will satisfy the real fleet usage as described by the TF30 example in Figure 7.

The fourth structural audit verifies that the engine is ready for production. It is expected that all critical life problems have been solved prior to this audit; thus the audit is no longer concerned with development risk. Instead, it considers the state of structural maturity and the remaining minor problems in term of the risk of meeting required operational readiness requirements and operating costs. It may further assess possible engineering change programs aimed at improving readiness and costs.

The closed loop management and configuration control does not stop with the production release. Special engines will be maintained with accelerated, fleet operational hours greater than any deployed propulsion system. These special engines will be lead-the-force systems and will be used for early identification of any potential fleet problem. This technique again allows user command, logistics and operational readiness projection updates.

CONCLUSIONS

Continuation of the trend in turbine design towards higher thrust-to-weight ratios and for increased durability will require substantial improvements in structural analysis methods and the implementation of a time-phased systematic development system. Reliable methods to predict new weapons systems mission requirements and flight profiles are required to reduce propulsion system configuration changes during development. Reliance on sophisticated automated structural analysis design systems will be required to effectively consider all required design parameters.

REFERENCES

1. Air Force Aero Propulsion Laboratory Final Report AFAPL-TR-76-104 "Development of Turbine Engine Structural Design Criteria," Air Force Wright Aeronautical Laboratories, Air Force Systems Command, Wright-Patterson Air Force Base, Ohio.

2. Joint Faculty Project United States Air Force Academy, Colorado, "Final Report of the USAF Academy Risk Analysis Study Team," August 1971.

3. Price, J.L., "Practical Application of Fracture Mechanics to Turbine Engine Rotor," Twenty-Second Sagamore Army Materials Research Conference Proceedings, September 1975.

4. Barsoum, R.S., "Application of Quadratic Isoparametric Finite Elements in Linear Fracture Mechanics," Int. J. Num. Meth. Engrg. 10, 551 (1976).

5. Barten, H.J., "Automated Finite Element Grid Break-Up Method; Verification of the Six Node Averaging Approach," NASA SP-390L.

6. Hurchalla, J., "Fracture Mechanics LCF Life Prediction System With Application to an Advanced Gas Turbine Alloy," AIAA/SAE 11th Propulsion Conference, October 1975.

DISCUSSION

Dr Siva, UK

I must congratulate the authors on the excellent paper on life prediction. This subject is a very difficult one to deal with without a lot of service record. How did you obtain sufficient temperature boundary condition to solve a 3D problem on rotor disc and blade?

Author's Reply

We use a separate thermal analysis, which could be either 2D or 3D, depending on the complexity required to predict the temperature of the hardware. This analysis is conducted at enough flight points to assure that the worst transient thermal gradients are identified. The thermal analysis is the major cost item of the total analysis (all accelerations and decelerations are investigated).

Dr Siva, UK

Can you explain why you need rig tests as well as engine tests? Are you able to simulate the engine condition on the rig? Is the rig a back up for your mathematical model.

Author's Reply

Engine tests almost always have instrumentation limitations, either in quantity of measuring devices or accessibility. It is easier and cheaper to obtain a large volume of data which includes 'off-design' conditions to determine operating margins from rigs. Full scale engine data is required to ensure that the 'rigs' are truly reproducing engine characteristics and are not identifying problems associated to the rig itself and are not real engine problems. The rigs do duplicate engine condition. The rigs are used to evaluate the accuracy of mathematical models to predict engine stress and thermal state. These data are an integral part of determining error bands and risk assessment.

M.J.Holland, UK

Concerning Figure 2 of your paper, could you please clarify whether the timescale refers to the year in which the engine is designed or when it is first deployed in service?

Author's Reply

Generally, they refer to deployment or release of an engine for service use.

FINITE ELEMENT ANALYSIS OF SOME PROBLEMS ARISING IN COOLED TURBINE BLADES

P. Beckers
First Assistant

G. Sander
Associate Professor

M. Hogge
Assistant

University of Liège
Institut de Mécanique
75, Rue du Val-Benoît
4000, Liège, Belgium

SUMMARY

The finite element method has been applied successfully to a large number of engineering problems.

The present paper summarizes the main approaches to some problems of heat transfer and stress computation that arise in the analysis of turbine blades.

The introduction of non linear boundary conditions and temperature dependent material properties is considered in the heat transfer analysis. Various non linear effects are also taken into account in the static and dynamic stress analysis. It includes centrifugual forces, initial stresses, temperature dependent properties and elasto-plastic behaviour.

Different situations concerning turbine blades and rotors are analysed to illustrate the capabilities that are part of a general purpose program developped by the University of Liège.

1. INTRODUCTION

The finite element method has had its first applications in structural mechanics [1,2] ; it is nowadays a wide spread procedure for the evaluation of stresses in many areas of engineering. The method has also been used for field problems [2,3,4,5] where its properties of generality, simplicity in presence of several materials and complex boundary conditions have often overcome particular methods or the well-known difference method.

The problem of heat transfer and (associated) thermal stresses in solids is precisely one for which the finite element method may add to these advantages by a unique way of treating the two problems.

These analyzes will be undertaken within the frame of uncoupled thermoelasticity [6]: the thermal and structural problems are separate ones and one can seek first for thermal fields and solve afterwards the elastic boundary value problem resulting from this thermal field; in other words the work of the applied loading is achieved so slowly that it does not produce heat enable to disturb the initial thermal configuration. This hypothesis is quite reasonable in most of the practical cases if one avoids situations such as welding [7].

The paper is therfore divided into two main parts: sections 2 to 4 deal with the thermal field determination problem by means of temperature discretizations; the problem may be either linear or non-linear and both steady-state and transient cases are examined. The second part of the paper covers the thermal stresses determination in elastic solids by use of structural displacement models (sections 5 and 6).

2. BASIC EQUATIONS FOR THERMAL FIELDS

The heat conducting body occupies a region R bounded by a surface ∂R, the outward normal is represented by the unit vector n*.
Let $\theta(x,\tau)$ be the instantaneous temperature distribution referred to cartesian coordinates x. The temperature gradient is denoted by

$$e = d\theta \tag{1}$$

where the operator d is defined as $d^T = \left[\frac{\partial}{\partial x_1} \quad \frac{\partial}{\partial x_2} \quad \frac{\partial}{\partial x_3} \right]$ (2)

The heat flow vector is related to it by Fourier's law

$$q = - He \tag{3}$$

H is the symmetric matrix containing the heat conductivity coefficients; they may be temperature-dependent. Energy conservation related to heat transfer is expressed by the thermal balance equation

---

* Matrix formulation is used for simplicity: a greek letter denotes a scalar, a small letter a column vector and a capital letter a matrix; the super scriptes ^{T} and $^{-1}$ denote the transpose and inverse operations respectively.

$$\kappa \frac{\partial \theta}{\partial \tau} = \psi_R - d^T q \quad \text{in } R \tag{4}$$

where κ denotes the heat capacity of the solid (it may be temperature - dependent) and ψ_R the prescribed internal heat sources, both quantities being referred to the unit volume.

Boundary conditions may be expressed in the general equation

$$n^T q = \alpha(\theta^m - \theta_e^m) - \psi_e \qquad \text{on } \partial R \tag{5}$$

which relates the heat flux at the boundary to a function of the boundary temperature θ and of the prescribed environment temperature θ_e by an exchange coefficient α (eventualy temperature-dependent). A surface prescribed heat source distribution ψ_e may also be present.

This general expression may easily be particularized to the usual cases of

- prescribed temperature distribution ($\psi_e = 0, \alpha \to \infty$)

$$\theta = \theta_e \qquad \text{on } \partial R_1 \tag{6}$$

- prescribed surface heat sources ($\alpha = 0$)

$$n^T q = -\psi_e \qquad \text{on } \partial R_2 \tag{7}$$

- convective heat transfer ($\psi_e = 0$, m=1)

$$n^T q = \alpha_c(\theta - \theta_e) \quad \text{on } \partial R_3 \tag{8}$$

-radiative heat transfer ($\psi_e = 0$, m=4)

$$n^T q = \alpha_r(\theta^4 - \theta_e^4) \text{ on } \partial R_4 \tag{9}$$

The formulation of the problem is finally completed by the knowledge of the initial temperature distribution

$$\theta(x,0) = \theta^* (x) \tag{10}$$

This general problem will be subdivised into steady-state case, for which every function is only spatially varying, and the transient case.

In each of these cases, we shall pay attention to the linear problem first for which the material properties (H, κ) and prescribed data (α, ψ_R, ψ_e) are temperature-independent and the power m of exchange law (5) is equal to one; we shall afterwards treat the general non-linear problem.

3. STEADY-STATE THERMAL FIELDS

Using the Finite Element Method the first task to implement is the search for integrated forms of the problem since, by definition, the goal of the method is to deduce approximate global relations for a finite domain. According to this it has been early recognized that the steady-state problem with temperature-independent properties; like other similar field problems, can receive a true variational formulation. The latter states that the functional

$$\begin{aligned} \mathcal{J}(\theta) = \frac{1}{2} \int_R e^T H e \, dR - \int_R \psi_R \theta \, dR \\ - \int_{\partial R_2} \psi_e \theta \, d\partial R + \int_{\partial R_3} \alpha_c \, \theta \left(\frac{\theta}{2} - \theta_e \right) d\partial R \\ + \int_{\partial R_4} \alpha_r \, \theta \left(\frac{\theta^4}{5} - \theta_e^4 \right) d\partial R \end{aligned} \tag{11}$$

is stationary under small perturbations $\delta\theta$ of the temperature field subject to the constraint

$$\delta\theta = 0 \qquad \text{on } \partial R_1 \tag{12}$$

Indeed performing such a variation and expressing the stationarity of (11) we find after an integration by parts on the first term

$$\begin{aligned} \delta\mathcal{J}(\theta) = - \int_R d^T(He) \, \delta\theta \, dR - \int_R \psi_R \, \delta\theta \, dR + \int_{\partial R_3} \alpha_c(\theta - \theta_e) \delta\theta \, d\partial R + \int_{\partial R_4} \alpha_r(\theta^4 - \theta_e^4) \delta\theta \, d\partial R = 0 \\ + \int_{\partial R} n^T H e \, \delta\theta \, d\partial R - \int_{\partial R_2} \psi_e \, \delta\theta \, d\partial R \end{aligned} \tag{13}$$

Because of the constraint (12) the boundary term on ∂R generates contributions on ∂R_2, ∂R_3 and ∂R_4 only and we obtain as Euler-Lagrange equation and natural boundary conditions a steady state version of equations (3,4,7,8,9).

The main advantage of formulating the global problem in that manner is that the functional (11) may be proved to reach a minimum value for the temperature field satisfying exactly this set of equations [2] .

Besides, in absence of radiative exchange, a complementary minimum variational principle can be expressed in termes of the dual variable of heat conduction: the heat flow vector [8] . Advantage may then be taken of this situation to obtain a numerical estimate of the convergence to the true solution by upper and lower bounds to a characteristic functional of the boundary value problem: the dissipation function. This aspect will not be described here but may be found detailed in reference [1,5] .

3.1. Finite Element Linear Analysis

3.1.1. General Formulation

The variational formulation (13), related to the application of a GALERKIN type approximation to the initial differential system, is used, but the non-linear radiative term is dropped.
The linear temperature models that we will derive are well known [2,5] : they are based on a continuous piecewise differentiable temperature field θ discretized as

$$\theta(x) = w^T(x)\ t \qquad \text{in } E \tag{14}$$

within the domain E of the finite element. The components of w are the shaping functions or interpolation functions of the temperature field.
To organize interelement continuity of the temperature field, it is possible to define the unknowns t, as local values of the temperature field itself, or as temperature average to build pure temperature, hybrid or delincuent models [9] .
The temperature gradient field is written as

$$e = d\ \theta(x) = d\ w^T\ (x)\ t = G(x)\ t \tag{15}$$

The stationarity condition (13) is finally expressed in terms of the local temperature degrees of freedom at the element level by

$$\begin{aligned}\delta \mathcal{J}(t) = {} & \delta t^T \left[\int_E G^T(x)\ H(x)\ G(x)\ dE\right] t \\ & + \delta t^T \left[\int_{\partial E_3} \alpha_c(x)\ M(x)\ d\partial E\right] t \\ & - \delta t^T \left[\int_E \psi_R(x)\ w(x)\ dE\right] - \delta t^T \left[\int_{\partial E_2} \psi_e(x)\ w(x)\ d\partial E\right] \\ & - \delta t^T \left[\int_{\partial E_3} \alpha_c(x)\ \theta_e(x)\ w(x)\ d\partial E\right] = 0\end{aligned} \tag{16}$$

with $M(x) = w(x)\ w^T(x)$
The variations δt being arbitrary except for the constraint (12), equation (16) yields the following linear system at the element level

$$[K + K_c]\ t = f + g + g_c \tag{17}$$

where

$$K = \int_E G^T(x)\ H(x)\ G(x)\ dE \tag{18}$$

is the main conductivity matrix of the element, H(x) standing for the matrix of heat conductivity coefficients

$$K_c = \int_{\partial E_3} \alpha_c(x)\ M(x)\ d\partial E \tag{19}$$

is the convective part of the conductivity matrix;
The second member of (17) groups all the generalized fluxes due to prescribed sources or convective exchanges :

$$f = \int_E \psi_R(x)\ w(x)\ dE \tag{a}$$

$$g = \int_{\partial E_2} \psi_e(x)\ w(x)\ d\partial E \tag{20 (b)}$$

$$g_c = \int_{\partial E_3} \alpha_c(x)\ \theta_e(x)\ w(x)\ d\partial E \tag{c}$$

The system (17) can now be extended to its structural dimension by assembling the finite elements following classical procedures [1] .

Once the linear system is built up, it has to be solved. Well-known techniques, such as the frontal solution technique [10,11] , are available to this effect.

Finally the wear quantity attached to the temperature models, i.e. the heat flow vector, may be derive α element by element as

$$q(x) = - H(x)\ e(x) = - H(x)\ G(x)t$$
$$= T(x)\ t \qquad (21)$$

3.1.2. Typical linear finite element [5]

According to these theoretical developments several particular elements have been devised.
They are able to deal with one -, two- and three dimensional heat transfer in solids in a very general way: possibility of anisotropic thermal conductivity, variable geometric data (thickness, cross-section) and account taken of the three types of boundary conditions (internal or surface heat sources plus convection).

3.1.3. Numerical examples

Those capabilities are included in the general purpose computer program SAMCEF [11] that has been used to perform the two numerical examples that we shall now present to illustrate the effectiveness of the models.

a) Steady-state thermal fields in a turbine blade

The cross-section of the blade is represented figure 1 and the thermal characteristics of the problem are the following :
- homogeneous isotropic material of constant conductivity (k = .183 w/cm.°c)
- convective exchange at the blade outer surface with a hot fluid (θ_e = 690°c) including variable convection coefficients α_c (figure 2).
- convective exchange at the fifteen internal cooling ducts with fluids different temperatures and with different constant coefficients (figure 2).

The discretization of the cross-section comprizes 351 triangular elements for 249 nodes. Several analyzes were performed involving linear, quadratic and cubic local fields, that is 249, 863 and 1477 degrees of freedom respectively. The associated computer costs were 71, 100 and 163 CPU seconds on the IBM 370/158 of the University of Liège. The results are plotted on figures 3 and 4 in the form of isothermal curves and heat flow patterns, for quadratic and cubic discretizations.

b) Analysis of a gas turbine rotor

This second example involves a three-dimensional body that can be reduced to an axisymmetric-type of structure by replacing the blade effect by modified exchange coefficients at the outer surface of the rotor core (figure 5). It is then sufficient to analyze an axial section of this core; it is made of four different parts and materials. The thermal properties of each material are taken to be isotropic and constant.
The boundary conditions are of three types :

- prescribed temperature for the rotor around the supporting oil bearings (P).
- convective exchange at the outer surfaces of the wheels (C) with varying exchange coefficients and gas temperatures.
- adiabatic surfaces elsewhere. (A).

The contacts between the differnet parts of the rotor are supposed by perfect, i.e. there is no thermal resistance at the joints. The discretization of the core has been made by use of triangular axisymmetric volume elements (figure 6): 876 elements for 552 nodes. The results presented in figures 7 and 8 correspond to an analysis involving 1994 degrees of freedom and quadratic local fields. The greatest temperature gradients appear in part I of the rotor and the maximum temperature is around 600°c. These results have been partly confirmed by a finite difference analysis of part I of the rotor (figure 9,10). Advantages of the finite element method are obvious: different materials, complex boundary conditions and shapes are easily taken into account.

3.2. Finite element non-linear analysis

3.2.1. General formulation

Once radiative exchange appears at the boundary or in case of temperature dependent thermal data or prescribed heat sources, the linear system (17) does not hold any longer. It must be replaced by

$$[K(\theta) + K_c(\theta) + K_r(\theta)]\ t = f(\theta) + g(\theta) + g_c(\theta) + g_r(\theta) \qquad (22)$$

where the new conductivity matrix K_r and the additional fluxes g_r are deduced from elementary values given by

$$K_r = \int_{\partial E_4} \alpha_r\ (x,\theta)\ \theta^3(x)\ M(x) \qquad d\partial E\ . \qquad (a)$$
(23)

$$g_r = \int_{\partial E_4} \alpha_r(x,\theta)\ \theta_e^4(x)\ w(x)\ d\partial E \qquad (b)$$

The other dependences on the temperature vector, expressed in (22), are due to the possible variation of the thermal data (H,α_c) and of the prescribed values (ψ_R,ψ_e) with the temperature. The proposed solution technique for (22) is the so-called "tangential conductivity" |17, 5 |, which is quite close to the Newton-Raphson technique: for each element, the non linear system is analyzed in the neighbourhood of the solution θ_o, or t_o in terms of generalized temperatures

$$K\ (\theta_o + \Delta\theta)\ (t_o + \Delta t) = g(\theta_o + \Delta\theta) \qquad 24)$$

where K an a g stand for the detailed matrices of (22). The following linearization is then applied

$$K(\theta_o)(t_o+\Delta t)+ \int G^T \frac{\partial H}{\partial \theta}\ G\ (t_o+\Delta t)\Delta\theta\ dR = g(\theta_o)+ \frac{\partial g}{\partial \theta}\ \Delta\theta \qquad (25)$$

If one only retains the first order terms in the temperature increment $\Delta\theta$, it yields

$$|K(\theta_o) + \int\{ G^T \frac{\partial H}{\partial \theta}\ G\ t_o\ w^T - \frac{\partial \psi}{\partial \theta} R\ \ M\}\ dR - \int_{\partial R} \frac{\partial \psi}{\partial \theta}\ M\ d\partial R\ |\ \Delta t = g(\theta_o)-K(\theta_o)t_o \qquad (26)$$

The variable ψ represent the term $\alpha_c(x)\theta$ for the convective boundary and the term $\alpha_r(x)\ \theta^4(x)$ for the radiative boundary. Expression (26) furnishes the required increment to apply from a gess value t_o, given the temperature dependence of the conductivity and of the generalized fluxes. The solution can be written

$$\Delta t = K_T^{-1}\ (t_o)\ |g(t_o) - K\ C(t_o)\ t_o| \qquad (27)$$

where

$$K_T\ (t_o) = K(t_o)+ \int \{ G^T \frac{\partial H}{\partial \theta}\ \ G\ t_o\ w^T - \frac{\partial \psi_R}{\partial \theta} M\}\ dR - \int_{\partial R} \frac{\partial \psi}{\partial \theta}\ M\ d\partial R \qquad (28)$$

is the "tangential conductivity" matrix.

Unfortunately the second term of equation (28) produces a matrix which is not symmetric. This fact yealds more computer storage and cost. However it is intersting to notice that the non linearities due to convection or in general due to the imposed fluxes produce symmetric matrices in the expression of the tangential conductivity matrix.

3.2.2. Numerical example

As an illustration of the procedure we shall analyze the steady-state situation of the turbine blade previously examined (section 3.1.3a). Nothing has changed as far as thermal input is concerned but the isotropic conductivity is now temperature-dependent
The guess solution was the linear one and the process required 3 iterations to converge. The results are plotted on figure 11 a. They are compared to the linear ones on figure 11 b, and exhibit only slight differences (5%) . Those are mainly located around the trailing edge where the mean temperature differs markedly from the 300°C corresponding to the constant conductivity of the linear analysis.

4. TRANSIENT THERMAL FIELD

No true variational principle exist for the transient problem of heat transfer even in the linear case [12] : all direct attempts to derive integral functionals suitable for finite element idealization proceed from restricted or quasi-variational principles. Sometimes preliminary modifications such as convolution enable a true variational treatment [3] . In addition it has been shown [12] that all these approaches are equivalent to a direct application of the Galerkin procedure to the set of equations (3,4,6,7,8,9) in the realm of piecewise linear spatial approximations to the unknown function. Finally various attempts based on finite elements in time and space [4,13] have shown no advantage on the separate treatment of the problem into space and time coordinates. That is the reason why we shall analyze the problem in the standard way, that means:
- spatial discretization through Galerkin procedure,
- time integration of the resulting differential system.

Previous to this second step a modal analysis [5,14] may be performed in the linear case: the idea is to analyze the initial temperature distribution θ^* and the forcing terms f and g into natural thermal modes of the problem. The differential system is then reduced to a set of uncoupled ordinary differential equations and all the computational work is transferred to the eigenvalue problem. The method is particularly well suited for long range solutions in time for which only few modes are required [14] .
In this paper we shall concentrate on the direct integration procedure which allows for non-linear situations. The integrated form suitable for finite element spatial discretization results from the Galerkin formulation

$$\delta\tilde{J}(\theta,\tau) = \int_R e^T\ H\ \delta e\ dR + \int_R K\ \frac{\partial \theta}{\partial \tau}\delta\theta\ dR - \int_R \psi_R \delta\theta dR - \int_{\partial R_2} \psi_e \delta\theta d\partial R + \int_{\partial R_3} \alpha_c(\theta-\theta_e)\delta\theta d\partial R$$
$$+ \int_{\partial R_4} \alpha_r\ (\theta^4-\theta_e^4)\delta\theta\ d\partial R = 0 \qquad (29)$$

The only difference with equation (13) is the presence of the temperature time derivative and the possibility for all prescribed functions ψ_R, ψ_e and θ_e to be time-dependent.

4.1. Finite element linear analysis

4.1.1. General formulation

We turn back to the matrix formulation of section 3.1. and consider first the linear case. The temperature field is discretized spatially as in (14) :

$$\theta(x,\tau) = w^T(x)\ t(\tau) \tag{30}$$

By analogy with the developments of section 3.1 we find by substitution of (30) into (29) the generalization of the steady state system (17), which is after assembling the elements

$$[K + K_c]\ t(\tau) + C\ \frac{\partial t(\tau)}{\partial \tau} = f(\tau) + g(\tau) + g_c(\tau) \tag{31}$$

The only new matrix is the capacity matrix C which is obtained from its elemental contributions

$$C = \int_E \kappa(x)\ M(x)\ dE \tag{32}$$

in the same way as the conductivity one.
The differential system (31) is completed by the initial condition deduced from (10) :

$$t(o) = t^* \tag{33}$$

4.1.2. Direct time integration through finite differences formulae [5,13] .

For time integration purposes we shall only consider one step direct schemes for which the time derivative at a particular time of the interval $(\tau, \tau + \phi\Delta\tau)$:

$$\tau_\phi = \tau + \phi\ \Delta\tau \qquad \phi \in [0,1] \tag{34}$$

is approximated by the finite ratio

$$\left.\frac{\partial t}{\partial \tau}\right|_{\tau_\phi} = \frac{t(\tau+\Delta\tau) - t(\tau)}{\Delta\tau} = \frac{\Delta t}{\Delta\tau} \tag{35}$$

This allows the system (31) to be written

$$\left|\frac{C}{\Delta\tau} + \phi K\right|\ \Delta t = g(\tau_\phi) - K\ t(\tau) \tag{36}$$

where K and g stand for $K + K_c$ and $f+g+g_c$ respectively. This scheme furnishes the temperature vector change Δt within a time step $\Delta\tau$, given the knowledge of the temperature at the beginning of the time step and of the forcing function at the particular time τ_ϕ.
This family of methods is implicit except for $\phi = 0$ (explicit Euler scheme); in particular the case $\phi = 1/2$ corresponds to the well-known trapezoidal rule, $\phi = 2/3$ to the so-called Galerkin scheme while $\phi = 1$ stands for the fully implicit scheme.
The main problem related to those schemes is accuracy since they are unconditionnaly stable for $\phi \geq 1/2$.
The conclusions of the theoretical accuracy analysis are the following [5] : among unconditionnaly stable schemes the choice is between the trapezoidal rule, the Galerkin scheme and the fully implicit scheme; each of them corresponds to some optimal point of view: lowest truncation error, best solution in the weighted residual sense or no approximation on the applied loading respectively. The scheme $\phi = 1$ is only valuable if large time steps are required. The scheme $\phi = 1/2$ interesting for all cases where the higher modes do not play an important role - i.e. long time solution - or problems with no fast varying boundary conditions; otherwise the Galerkin scheme is to be favored due to its better short-time accuracy [15] .

4.1.3. Numerical example

Several situations have been analyzed to compare those direct schemes and to confirm the theoretical conclusions . Work has also been done to compare this direct approach to the modal superposition [14] . The example we shall present here is devised to illustrate the procedure in a typical situation using the best suited technique. It concerns the transient analysis of the turbine blade cross-section already analyzed twice in steady-state conditions (figure 1). The transient behaviour is governed by the evolution laws to gas temperatures (fig. 12) which are rather severe. The effective thermal characteristics are temperature-dependent but are taken constant in the frame of linear heat transfert:

$$k = .1893\ w/_{cm.°c} \qquad \alpha_c = 4.1928\ J/_{cm^3.°c}$$

The same discretization as for the steady-case is used (249 degrees of freedom). Due to fast varying boundary conditions we choose the particular member $\phi = 2/3$ within the family of one step-method (36). Time steps are chosen according to the piecewise linear time variation of the given data and the results are plotted figure 13 for one mode located at the thermal gauge position 12 (figure 1). On this figure are also plotted the results of a mod al analysis. Both finite element solutions differ from test results but are very near to each other. The differences observed were only partly explained by the limits of linear analysis in a non-linear situation : it has been established afterwards that understimated hot gas temperatures and escapes in the cooling system occured during the tests.

Both phenomenons have effects in the observed sense but is has not been possible to update the data to rerun the problem.

4.2. Finite element non-linear analysis

4.2.1. General formulation

Use of discretization (30) into functional (29) where thermal data and prescribed functions may be temperature-dependent yields the non-linear differential system

$$K(t)\ t(\tau) + C(t)\ .\ \frac{dt(\tau)}{d\tau} = g(t,\tau) \qquad (37)$$

where $K(t)$ stands as in (22) for $K(t) + K_c(t) + K_r(t)$ and $g(t,\tau)$ in a similar way for $f(t,\tau) + g(t,\tau) + g_c(t,\tau) + g_r(t,\tau)$.
The signification of all the particular matrices is the same as before (sections 3.2.1 and 4.1.1).
Most of the proposed schemes for the solution of this problem are iterative incremental schemes [7,16] .
However it is possible to extend the proposed technique of tangential conductivity to the transient case |5| : this yields the incremental system within the time interval $(\tau,\tau+\Delta\tau)$:

$$\left\{\frac{C\ |t(\tau)|}{\Delta\tau} + \phi K_T\ |t(\tau)| \ - \ \phi\frac{dg}{dt}\right\}\Delta t = g\ |t(\tau)| - K\ |t(\tau)|\ t(\tau) \qquad (38)$$

It is free of iterations during a time step since it implies only the knowledge of the non-linear matrices at the beginning of the time interval. The presence of the tangential conductivity matrix (28) and of temperature-dependent thermal forces in (38) results in a non-symmetric matrix to be inverted as in (27) .
The choice of a particular φ will be guided by the conclusions of the linear analysis though one must be careful in such an extension.

4.2.2. Typical finite elements for non-linear transient analysis

Finite elements suited for non-linear transient problems simply combine the characteristic matrices built in sections 3.2 and 4.1.

4.2.3. Numerical example

As a final example of thermal fields determination we shall analyze the most general situation for the blade: the temperature - dependent data are in the case of the blade, the thermal conductivity and capacity of the material. Their non-linear behaviours are approximated by quadratic temperature polynomials suitable for the buiding of K_T and C in (38) . Time steps have been chosen identical to those of the linear analysis (section 4.1.3.) and the Galerkin scheme $\phi = 2/3$ has still been retained. Compared linear and non-linear results are presented on figure 14 for the thermal gauges node 12 . The benefit of the non-linear analysis is mainly to exhibit a better capacity behaviour : full power temperatures are lower and slow motion temperatures greater than the linear ones.

5. BASIC EQUATIONS FOR THERMAL STRESSES [5]

The uncoupled quasi-static theory of thermoelasticity that we consider allows to seek for displacement and stress fields in elastic solids given a prescribed temperature distribution [16] . The governing equations of the problem are then the following

- compatibility relations for small deformations
- Duhamel - Neumann constitutive relation in presence of a prescribed thermal field. The tensor of isothermal moduli is defined at the reference temperature.
- the boundary value problem is completed by the usual boundary conditions: prescribed displacements or surface tractions .

6. FINITE ELEMENT TREATMENT USING DISPLACEMENT MODELS [5,11]

6.1. General formulation

The integrated forms suitable for finite element discretizations are this time true variational principles: they constitute either the generalization of the principle of minimum total potential or that of the principle of minimum complementary energy [5] .

The presence of a temperature field results simply, for displacement elements, in the presence of additional generalized forces and stresses, in a way similar to the well-known Duhamel method of equivalent forces [1,5] . The integrations required to compute these forces are usually made on the basis of a linear interpolation between the known nodal values of the temperature field.

6.2. Typical displacement elements for thermal stresses [5]

Many already available, structural displacement finite elements [11] have been provided with the appropriate terms to enable the analysis of thermal stress problems. The structural shapes and functions implemented are the bars, membranes, thin plates, flat shells, axisymmetrical membranes, shells and solids, and the general three-dimensional solids (tetrahedron or "brick"-element).

6.3. Numerical example

As an illustration we shall perform the subsequent step of the analysis of section 3.1.3.b, which is to compute the thermal stresses in the rotor under the determined temperature field. The kinematical boundary conditions are the following:

- the rotor may exhibit free dilatations along the axial direction
- the outer surface is free of tractions when the rotational effect is not taken into account .

The different materials are provided with thermal expansion coefficients and the same discretization as for the thermal problem has been used: 878 axisymetric solid elements. The local displacement fields were quadratic and defined 3642 degrees of freedom. The total execution time of the problem was 1070 CPU seconds. The results obtained are displayed on figure 15 for the most important part of the rotor.

REFERENCES

1. FRAEIJS de VEUBEKE B., SANDER G. and BECKERS P. (1972)
   Dual Analysis by Finite Elements : Linear and Non-linear Applications, AFFDL-TR-72-93, 1972.

2. ZIENKIEWICZ O.C. and CHEUNG Y.K. (1967)
   The Finite Element Method in Structural and Continuum Mechanics, Mc. Graw Hill, London, 1967.

3. WILSON E.L. and NICKELL R.E. (1966)
   Application of the Finite Element Method to Heat Conduction Analysis, Nucl. Eng. Des., Vol. 4, 276-286, 1966.

4. DONEA J. (1973)
   Méthodes Variationnelles appliquées à l'analyse de problèmes mécaniques et thermiques posés par la technologie nucléaire, Doctoral Thesis, Univ. Liège, Belgium, 1973.

5. HOGGE M. (1975)
   Transfert de chaleur et contraintes thermiques dans les structures par la méthode des éléments finis, Doctoral Thesis, Univ. Liège, Belgium, 1975.

6. BOLEY B.A. and WEINER J.H. (1960)
   Theory of Thermal Stresses, J. Wiley, N.Y., 1960.

7. HIBBITT H.D. and MARCAL P.V. (1973)
   A Numerical Thermo-mechanical model for the welding and subsequent loading of a fabricated structure, Comp. and Str., Vol. 3, 1145-1174 , 1973.

8. FRAEIJS de VEUBEKE B.M. and HOGGE M.A. (1972)
   Dual Analysis for Heat Conduction Problems by Finite Elements, Int. Jnl. Num. Meth. en Engng., Vol. 5, 65-82, 1972.

9. SANDER G. and BECKERS P. (1976)
   The influence of the choice of connectors in the finite element method,Proc. of the meet. on math. aspects of finite element methods, Roma, Dec. 1975.

10. IRONS B.M. (1970)
    A Frontal Solution Program for Finite Element Analysis, Int. Jl. Numerical Meth. Engng. 2, 5-32, 1970.

11. SANDER G. et al. (1972-1975)
    SAMCEF User's Manual, LTAS, Univ. Liège, Belgium

12. FINLAYSON B.A. and SCRIVEN L.E. (1967)
    On the Search for Variational Principles.
    Int. Jnl. Heat and Mass. Transfer, Vol. 10, 799-820, 1967.

13. FRIED I. (1969)
    Finite Element Analysis of Time Dependent Phenomena
    AIAA Jnl., Vol. 7, n°6, 1170-1173, 1969.

14. HUCK A. (1976)
    "Méthodes numériques en réponse dynamique avec amortissements structural"
    Doctoral Thesis, LTAS Report VF-30, Univ. Liège, Belgium, 1976.

15. DONEA J. (1974)
    On the Accuracy of Finite Element Solution to the Transient Heat Conduction Equation
    Int. Jnl. Num. Meth. in Engng., Vol. 8, 103-110, 1974.

16. WILSON E.L., BATHE K.J. and PETERSON F.E. (1973)
    Finite Element Analysis of Linear and Non-linear Heat Transfer, 2nd SMIRT Conf., Berlin Sept. 73, Paper L1/4.

17. NYSSEN Cl. and BECKERS P. (1977)
    Dual Analysis in Plasticity ; to be presented at the conference on Finite elements in non linear solid and structural mechanics. GEILO, NORWAY, AUGUST 1977.

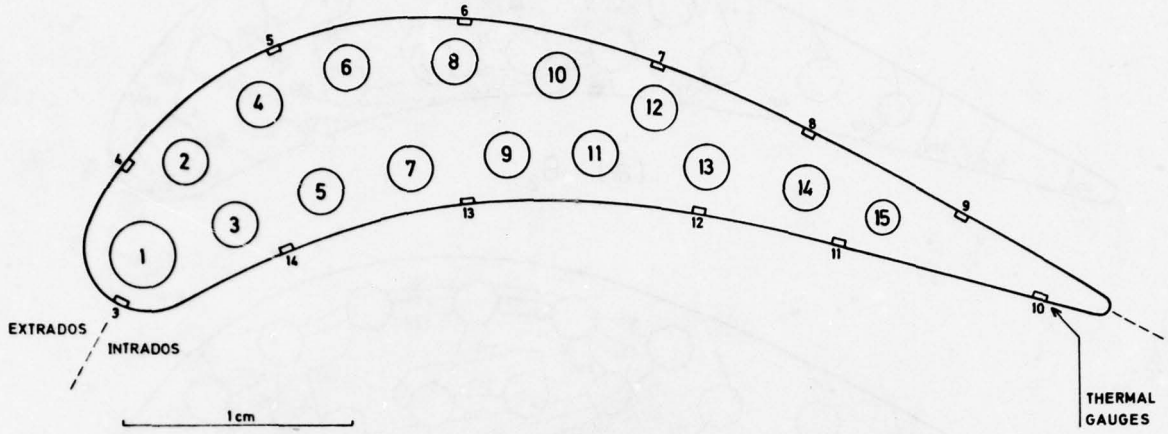

FIG. 1 TURBINE BLADE CROSS SECTION

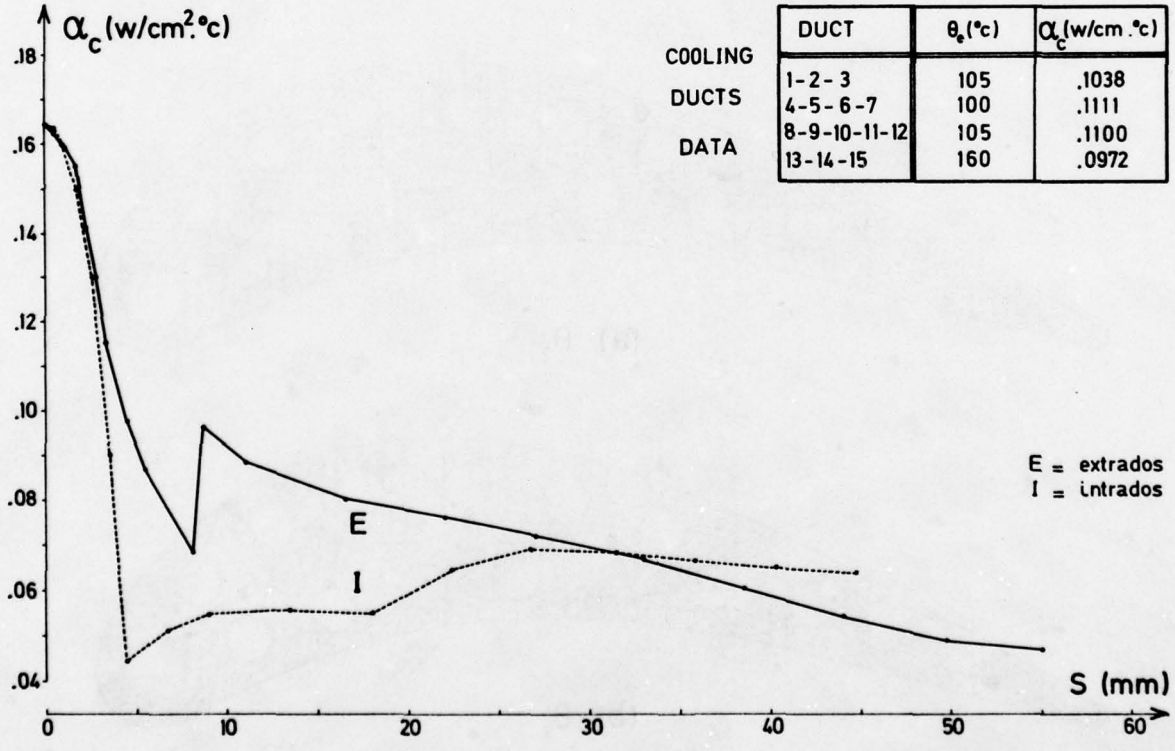

COOLING DUCTS DATA	DUCT	θ_e (°c)	α_c (w/cm .°c)
	1-2-3	105	.1038
	4-5-6-7	100	.1111
	8-9-10-11-12	105	.1100
	13-14-15	160	.0972

FIG. 2 BLADE EXTRA - AND INTRADOS EXCHANGE COEFFICIENTS

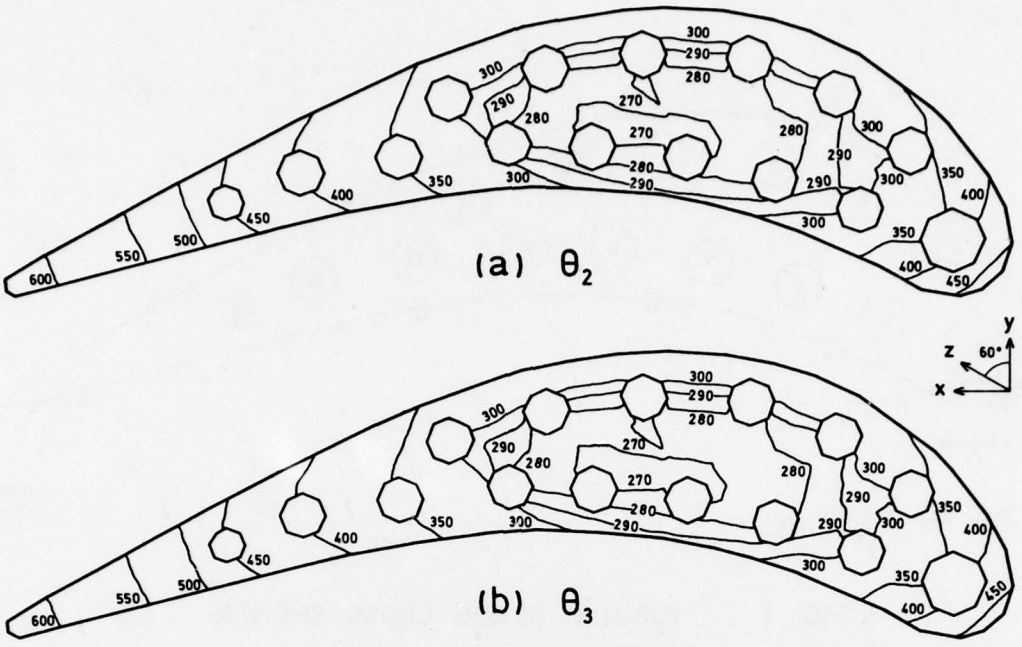

FIG. 3 ISOTHERMAL CURVES FOR THE BLADE

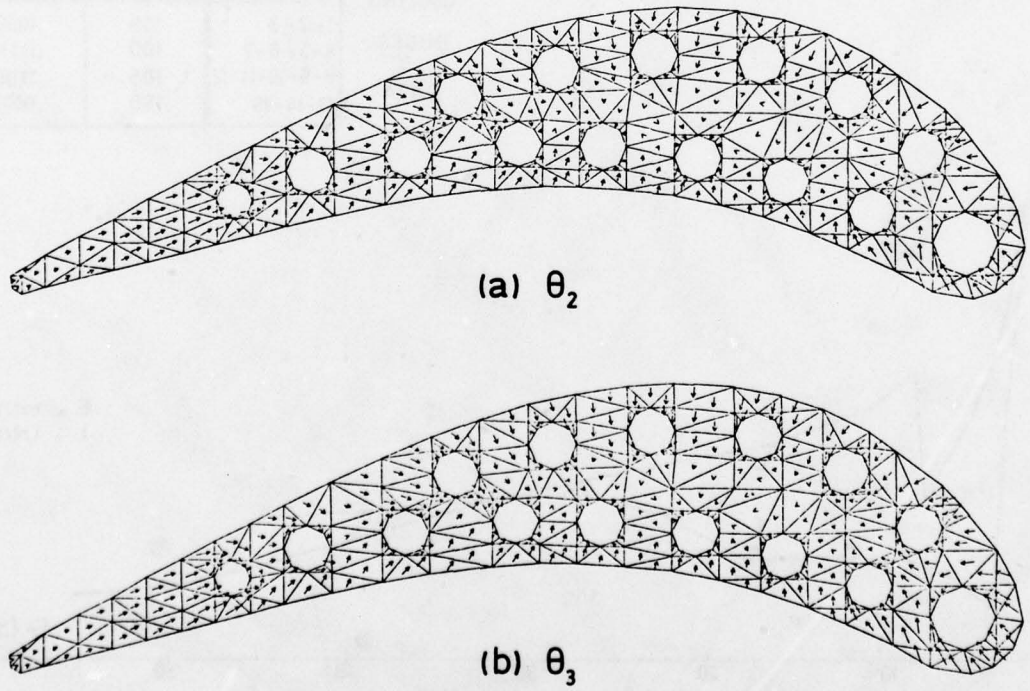

FIG. 4 HEAT FLOW PATTERNS FOR THE BLADE

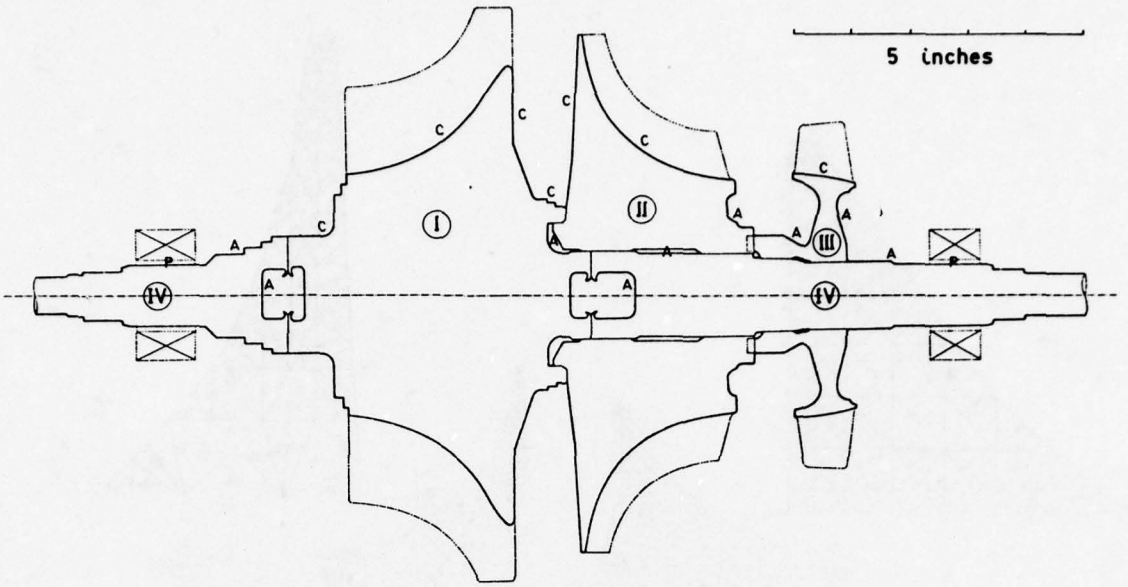

FIG. 5 ROTOR CORE

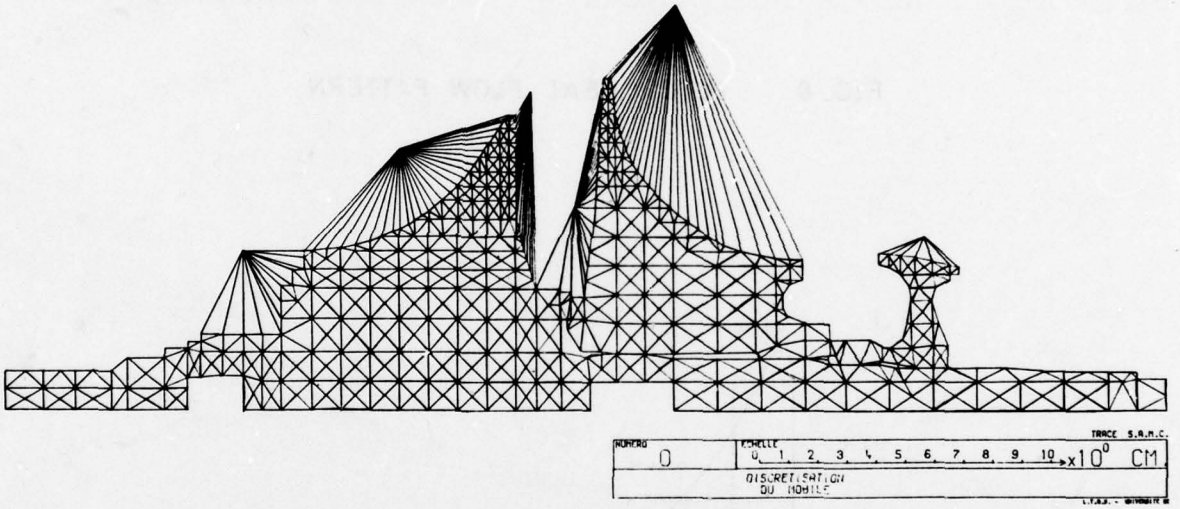

FIG. 6 ROTOR CORE DISCRETIZATION

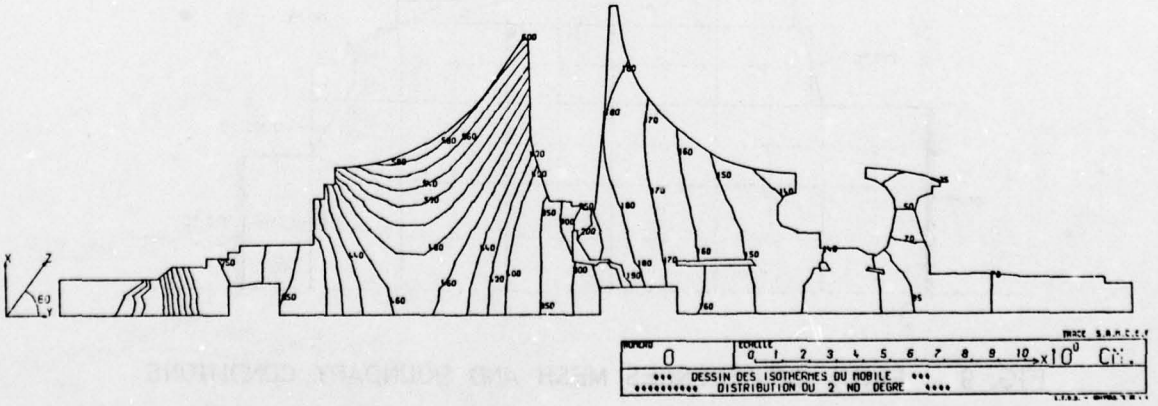

FIG. 7 ROTOR ISOTHERMAL CURVES

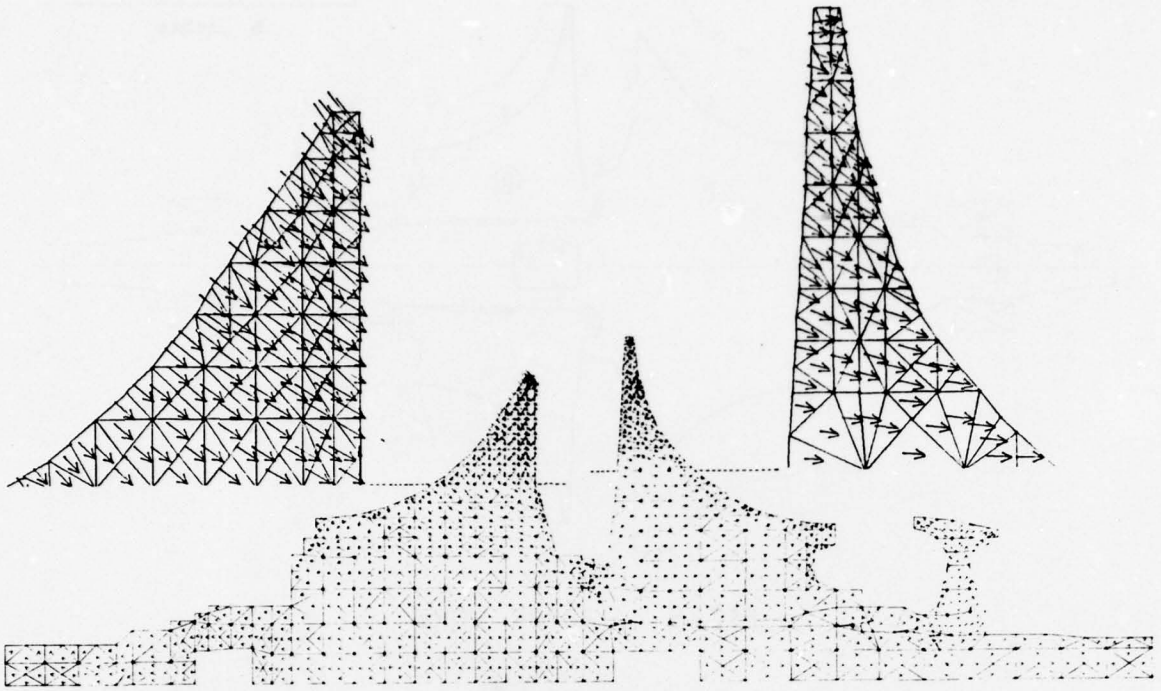

FIG. 8 ROTOR HEAT FLOW PATTERN

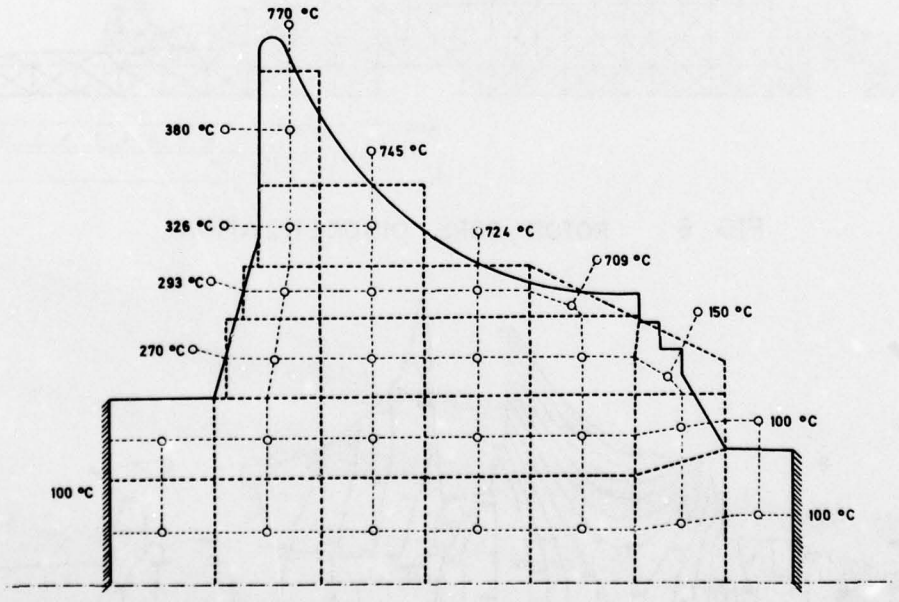

FIG. 9 FINITE DIFFERENCES MESH AND BOUNDARY CONDITIONS

	480 540					
	453 474	533 546				
	422 420	500 505	569 561	585 537		
	391 386	466 475	514 522	495 509	358 415	
180 —	343 366	431 445	469 485	441 469	343 404	
175 —	316 361	403 427	434 462	394 412	277 402	148 —

A FINITE DIFFERENCES

B FINITE ELEMENTS

FIG. 10 COMPARISON OF RESULTS FOR PART I

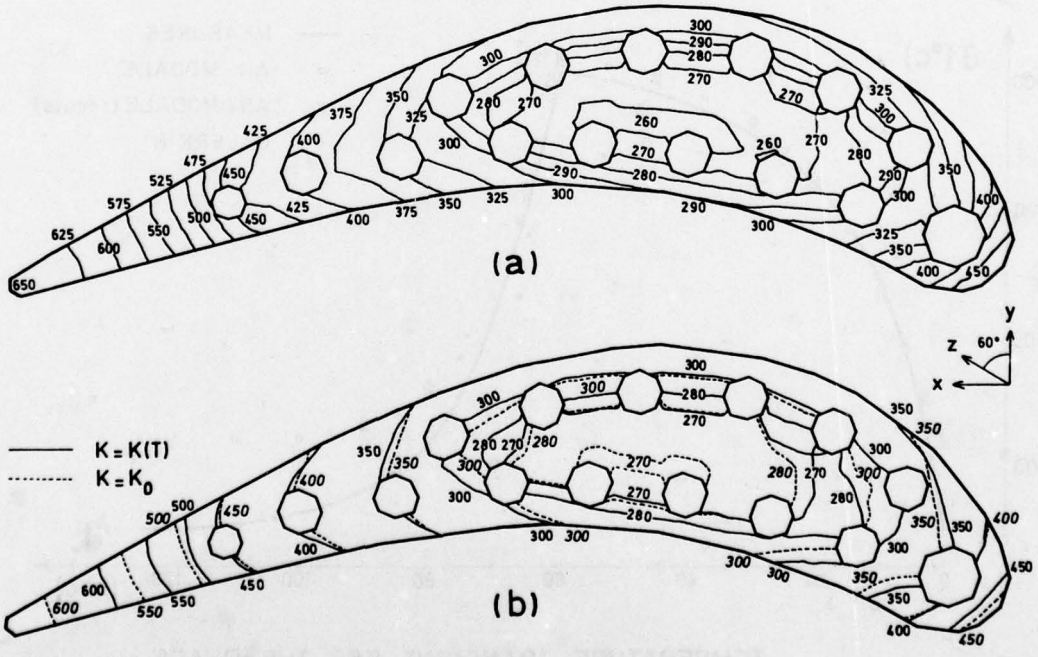

FIG. 11 COMPARISON OF LINEAR AND NON LINEAR STEADY - STATE TEMPERATURE

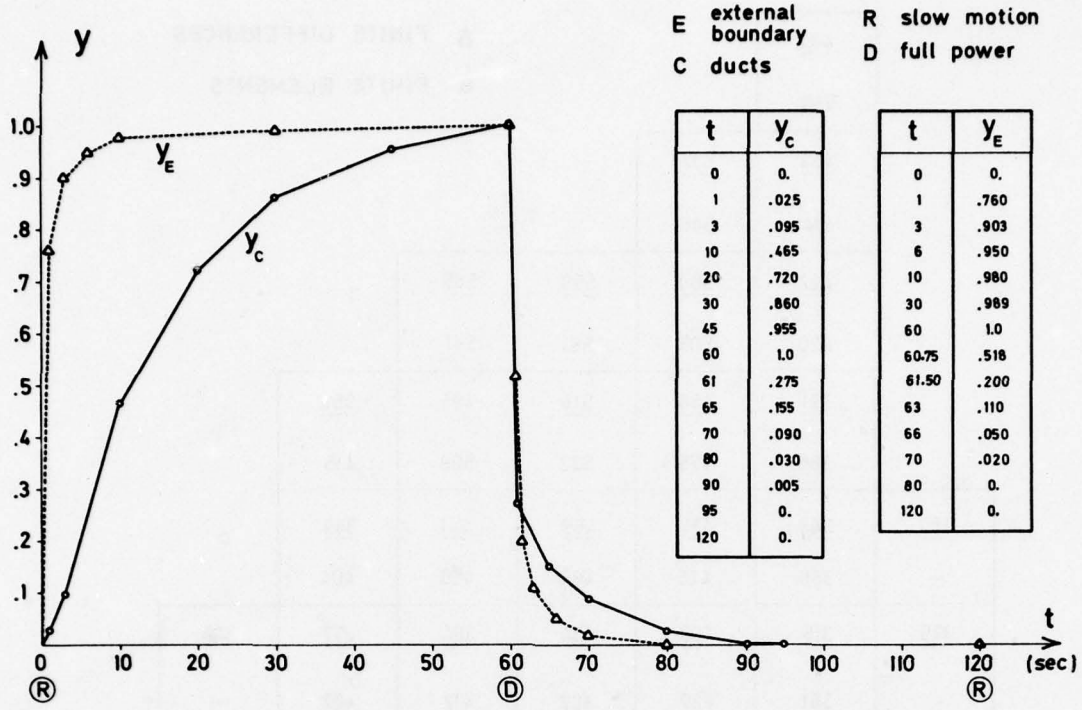

t	y_C
0	0.
1	.025
3	.095
10	.465
20	.720
30	.860
45	.955
60	1.0
61	.275
65	.155
70	.090
80	.030
90	.005
95	0.
120	0.

t	y_E
0	0.
1	.760
3	.903
6	.950
10	.980
30	.989
60	1.0
60.75	.518
61.50	.200
63	.110
66	.050
70	.020
80	0.
120	0.

FIG. 12 EVOLUTION LAWS FOR FLUID TEMPERATURES

$$y(t) = \frac{\theta(t) - \theta_R}{\theta_D - \theta_R}$$

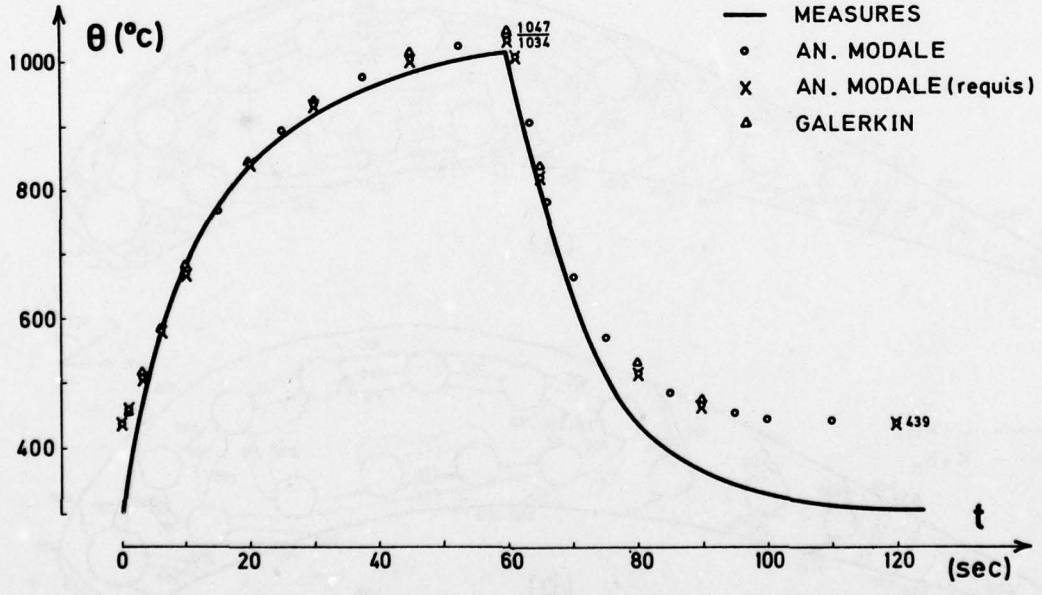

FIG. 13 TEMPERATURE TRANSIENT FOR THE BLADE THERMAL GAUGE 12

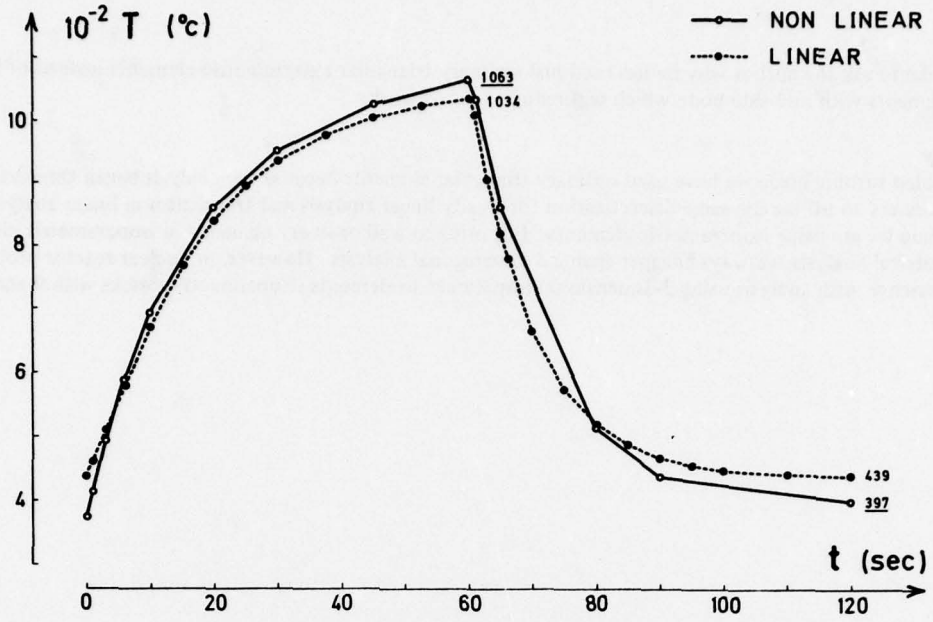

FIG. 14 NON LINEAR TEMPERATURE TRANSIENT FOR THE BLADE THERMAL GAUGE 12

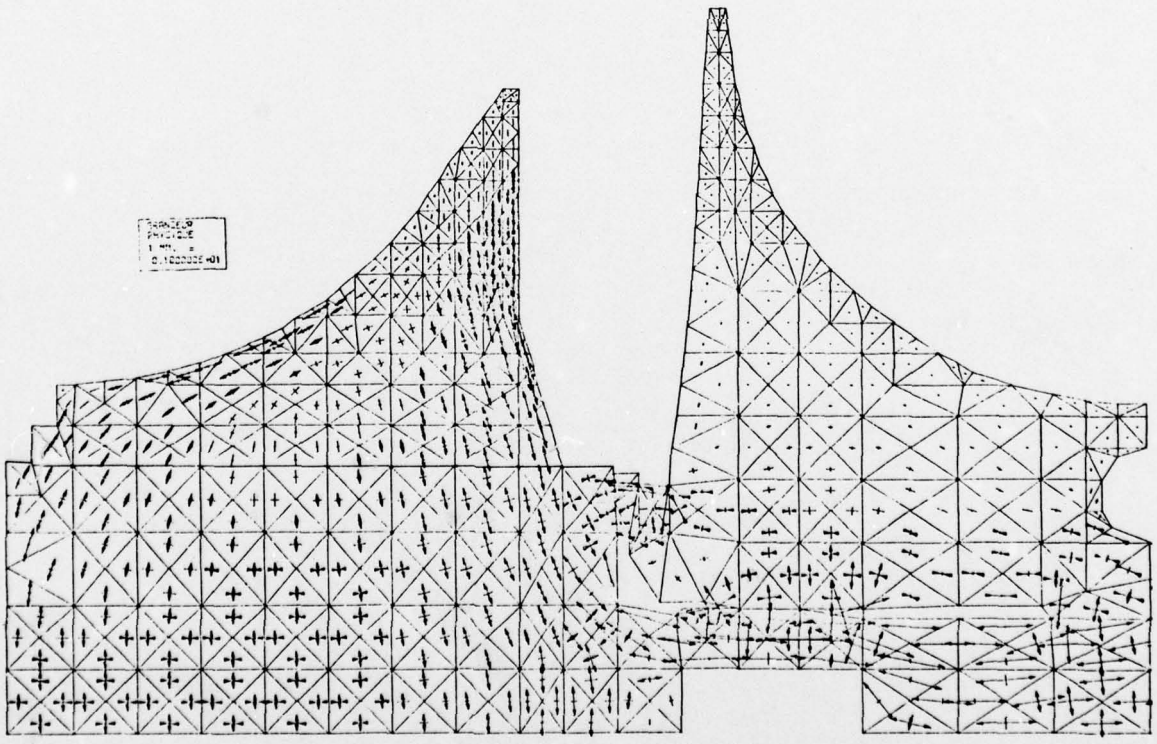

FIG. 15 ROTOR THERMAL STRESSES PATTERN

DISCUSSION

Dr Siva, UK

I would like to ask the author why he has used just ordinary triangular axisymmetric elements instead of isoparametric elements with mid-side node which will reduce a lot of work.

Author's Reply

In the cooled turbine blade we have used ordinary triangular elements because the analysis began three years ago and it was necessary to utilize the same discretization for steady linear analysis and transient non linear analysis. At the present time we are using isoparametric elements. But using as well ordinary elements as isoparametric elements an axisymmetrical analysis is always cheaper than a 3-dimensional analysis. However, in nuclear reactor problems we have experience with analysis using 3-dimensional isoparametric elements (isoparametric bricks with 9 and 20 nodes).

EVALUATION OF A CERAMIC COMBUSTION CHAMBER FOR A SMALL GAS TURBINE ENGINE

By
G Sedgwick - Project Designer
Lucas Aerospace Limited, Fabrications Division
Lucas Laboratories, Burnley
England

SUMMARY

Description is presented of the design, component evaluation and combustion testing of a reverse flow annular combustion chamber in silicon nitride. Heat transfer assessments were made of the temperature levels which components would reach during combustion testing and a thermal test programme was formulated which enable thermal loadings well in excess of those estimated for the actual flame tube environment to be imposed upon specimen components. Thermal stress and probability of survival values were obtained using the method based on a Weibull statistical analysis using the "weakest link" volume critical flaw assumption. Finite element and brittle failure analyses were carried out on both thermal stress test specimens and the components making up the flame tube.

The programme of seven combustion tests carried out on a pressure rig culminated in operation at a turbine entry temperature in excess of 1500 K.

1. INTRODUCTION

The Ministry of Defence is sponsoring work at the Lucas Aerospace Limited Engineering Laboratories at Burnley, England, to evaluate ceramic combustion chambers for small gas turbine engines.

The work falls into two areas:-

(i) The demonstration of the suitability of silicon nitride for potential use in small gas turbine engines as an aid to increasing specific power, using a small annular combustion chamber.

and (ii) The demonstration of the advantages to be gained in the reduction of emission levels by the operation of an uncooled ceramic flame tube.

This paper is concerned with the former investigation.

2. GENERAL CONSIDERATIONS

A reverse flow annular combustion chamber was chosen as a test vehicle for this investigation, such a configuration being consistent with the general requirements of the chosen cycle associated with a small main or auxiliary power unit.

At the start of the programme (1972) it was considered unlikely that the published strength of silicon nitride would be sufficient to withstand the thermal stresses which would be imposed on a monolithic construction and consequently, of a number of alternatives considered, two main concepts were pursued.

(i) A tile concept which would minimise both axial and circumferential stresses.

(ii) A stacked ring construction which would minimise axial stresses.

For the original programme it was considered impracticable and unduly expensive to use unconventional flame tube arrangements since these would require combustion development to obtain a basic performance. Such designs were therefore eliminated in favour of configurations on which experience existed on developed metallic designs. It was felt that the tile and ring constructions warranted more detailed investigation and, following stress analysis, typical components were manufactured in hot pressed silicon nitride (HPSN) and flame sprayed route (FSR) reaction bonded silicon nitride (RBSN), and subjected to thermal stress testing.

3. THERMAL STRESS TESTS

3.1 Temperature Assessments

Heat transfer assessments were made of the temperature levels which components would reach during combustion testing to a chamber exit temperature of 1500°C, using Lucas computer programmes developed specifically for this purpose. Primary zone mean wall temperatures thus estimated are given in Table I, together with radial gradients through the material, and the peak temperatures associated with local hot spots.

TABLE I

PRIMARY ZONE WALL TEMPERATURES

	Mean Temperatures		Local Hot Spot Temperatures	
	Wall Temp.	Gradient	Wall Temp.	Gradient
Outer F/T	870°C	68°C	1115°C	104°C
Inner F/T	820°C	77°C	1055°C	115°C

Stress distributions, based on the temperature conditions in Table I, were established which showed peak tensile stresses in inner and outer elemental rings to be 113 MPa (16380 lbf/in^2) and 161 MPa (23350 lbf/in^2) respectively (1).

To give an increased severity factor for the component tests, however, a radial gradient of 150°C (302°F) was adopted and the superimposition of local hot spots, such as would occur in a practical combustion chamber, imposed additional thermal stress on the test specimens up to a level of 236 MPa (34210 lbf/in^2) on an inner ring.

In practice the inner faces of components were heated by a ring burner using an oxygen enriched air/gas mixture, whilst the outer faces were cooled by cold air jets from a ring manifold. A hot spot was applied by means of an oxy-hydrogen flame at a single point on each specimen.

3.2 Flame Sprayed Route Reaction Bonded Silicon Nitride (FSR RBSN) Rings

A statistical approach to brittle failure analysis based on the "weakest link" hypothesis (2) was applied to the FSR RBSN rings, a volume critical flaw distribution being used to predict the probability of failure under the applied loading. Values of material strength and Weibull modulus were obtained from test bars produced at the same time as the test components.

Six rings of inside diameter 200 mm (7.9 in), length 32 mm (1.26 in), and of differing thickness were tested, the performance of each is given in Table II.

Measurements of Material Strength and Weibull modulus taken from the above components fell short of those used in the stress analysis which had not predicted failure at the applied stress level.

3.3 Hot Pressed Silicon Nitride (HPSN) Rings

Initial trials were carried out using a ring which contained castellations along one edge tc permit ingress of air into the annular chamber for combustion purposes. Failure occurred when mean temperatures of 860°C (1580°F) and 760°C (1400°F) were imposed on the inner and outer faces respectively, and when the superimposed peak temperature had reached 1200°C (2192°F). Fracture originated at the root of a castellation within the hot streak. A further castellated ring, with a small radius introduced at the edges, and plain rings were tested to mean temperatures of 790°C (1454°F) and 640°C (1184°F). A hot streak was superimposed on each specimen, the temperature being increased incrementally from 1050°C to 1250°C (1922°F to 2282°F). X-ray examination showed no cracks in any of these specimens which had been subjected to conditions giving peak tensile stresses of the order of 240 MPa (34800 lbf/in^2).

3.4 Hot Pressed Silicon Nitride (HPSN) Tiles

The plain inner faces of each of six specimens was heated to a mean temperature of 890°C (1634°F) whilst the outer faces were cooled generally to 800°C (1472°F). Hot streaks were superimposed in steps from 900°C to 1350°C (1652°F to 2462°F). No failures were induced in any component. Gradients through the tile thickness were quite severe since, when the inner face was at 1350°C (2462°F), the outer face was at 1050°C (1922°F) i.e. 300°C (572°F) over 7,6 mm (0.3 in).

TABLE II

THERMAL TEST RESULTS ON FSR RBSN RING SPECIMENS

Specimen	Ring Thickness mm (ins)	Temperature Differential thro' mtl. Thickness		Peak Stress Applied MPa (lbf/in^2)	Failure Stress MPa (lbf/in^2)
		Withstood Without Failure	Failure Condition		
1	7,6 (0.3)	125°C (257°F)	As differential was being increased to 150°C (302°F)	61.2 to 73.4 (8875 to 10640)	61.2 to 73.4 (8875 to 10640)
2	7,6 (0.3)	150°C (302°F)+ hot spot of 1250°C (2282°F)	On removal of hot spot with differential maintained, at 90° to where hot spot was applied	142 (20590)	73.4 (10640)
3	7,6 (0.3)	125°C (257°F)	As differential was being increased to 150°C (302°F)	61.2 to 73.4 (8875 to 10640)	61.2 to 73.4 (8875 to 10640)
4	5,1 (0.2)	100°C (212°F)+ broad hot spot of 1200°C (2192°F)	On retest as differential was being increased from 125°C (257°F) to 150°C (302°F)	118.7 (17210)	61.2 to 73.4 (8875 to 10640)
5	5,1 (0.2)	100°C (212°F)+ hot spot of 1100°C (2010°F)	As hot spot was being increased to 1200°C (2192°F)	127 (18415)	127 (18415)
6	5,1 (0.2)	100°C (212°F) + hot spot of 1250°C (2282°F)	On retest with hot spot in new position	120 (17400)	120 (17400)

4. DESIGN STANDARD

Whilst proving tests on both rings and tiles in HPSN showed both to be capable of withstanding thermal conditions more severe than those anticipated in service, the stacked ring concept was preferred for the following reasons:-

(a) The potentially lower manufacturing cost.

(b) The elimination of the sealing problems inherent with the tile construction.

(c) The simpler mounting to the engine pressure casing.

(d) The elimination of the flame tube annulus blockage present in the tile design.

Consequently a prototype stacked ring type annular flame tube was constructed for combustion testing on a pressure rig (Figure 1).

Concentric stacks of HPSN rings (Items 2 to 6 and 8 to 12 inclusive in Figure 2) formed the inner and outer walls of the flame tube. The head ring (Item 1) has holes for Lucas fan sprayers. The rear disc (Item 7) is butted to the outer ring stack and has a ceramic piston ring sealing joint to the inner casing. These latter components were tested in both FSR RBSN and a "low calcium" form of HPSN.

The design accommodates differential thermal expansion between the ceramic flame tube and the metal casing by means of an intersecting interface principle, the success of which had been shown on earlier work at Lucas on a monolithic pipe chamber. Transient temperature casing conditions are accommodated by the

inclusion of constant load spring washers in a cooler area of the arrangement. By slippage at the interface a sensibly constant clamping pressure can be maintained throughout the temperature range.

Consequently, the compression mounting load merely needs to be of sufficient magnitude to ensure that the components are kept in position during vibration and mechanical shock loading. Such movement can be minimised in the case of stacked rings by angling the faces in contact. An additional advantage is gained with angled faces in the event of a ring cracking in service, the radially inward component of the end load tends to hold the cracked ring in position.

Since the head ring (Item 1) is a slide fit within the first outer ring (Item 2) compressive end loading can be independently introduced to both ring stacks, thus facilitating assembly.

The combustion chamber volume and casing geometry was chosen to give a conservative combustion intensity and allow flexibility of design in silicon nitride. Established parameters in the design of small annular chambers were used within the constraints imposed by the preference to introduce air into the flame tube through slots at the edges of rings. Based on experience with other designs the required flow pattern was achieved by introducing the primary air through the outer wall of the flame tube (Item 3, Figure 2), and to use an opposed dilution-hole system (Items 5 and 11, Figure 2) to achieve the desired exhaust temperature distribution. The arrangement was compatible with the use of fan-spray fuel injectors of the type developed by Lucas for this type of small annular chamber.

5. COMBUSTION TESTING

5.1 Operating Conditions

The target full load operating conditions, corresponding to sea level static ISA conditions included a turbine entry temperature of at least 1473 K (2192°F) at an inlet pressure approaching that of an engine with a 4:1 compression ratio.

5.2 Description of Tests and Results

Seven combustion tests were carried out occupying a total running time of 5 hours 20 minutes, the operating conditions and the duration of each test is given in Table III, test 7 achieving the target operating conditions.

In all tests a combustion preheater, upstream of the flame tube under test, was operated for sufficient time to allow the temperature of the arrangement to reach the operating inlet temperature of 473 K (392°F) before ignition within the ceramic flame tube was attempted.

TABLE III

TEST OPERATING CONDITIONS

Test No.	Air Mass Flow kg/s (lb/s)	Fuel Flow kg/s (lb/s)	Air/Fuel Ratio	Inlet Pressure kPa (lbf/in²abs)	Chamber Exit Temp K (°F)	Duration Mins.
1	0,904 (1,99)	0,01 (0.02)	90,4:1	393 (56.9)	950 (1250)	30
2	0,703 (1.55)	0,008 (0.017)	87,9:1	241 (34.9)	800 (980)	25
3	0,590 (1.30)	0,008 (0.017)	73,7:1	207 (30.0)	-	30
4	0,987 (2.17)	0,019 (0.04)	51,9:1	395 (57.3)	1143 (1598)	55
5	1,02 (2.25)	0,025 (0.055)	40,8:1	397 (57.6)	1273 (1832)	60
6	1,01 (2.22)	0,027 (0.059)	37,4:1	396 (57.4)	1200 (1700)	30
7	0,997 (2.20)	0,033 (0.073)	30,4:1	397 (57.6)	1515 (2267)	90

Tests 1 to 4 inclusive were terminated when flame colour-changes indicated ingress of air through cracks. In each case the rear disc (Item 7, Figure 2) was found to be fractured. Extensions to the programme of brittle failure analysis were now available for application to these failures and pieces of the rear disc from Test 4 were used to establish material strength. The stress analysis programme was applied to this

component revealing high thermal circumferential stresses on the periphery of the components, particularly at full load conditions - Figure 3.

A brittle failure analysis at the test 4 failure conditions showed failure stress ratios, defined as:-

$$\frac{\text{Predicted Maximum Stress for 50\% Probability of Survival}}{\text{Estimated Maximum Stress at Test Failure Condition}}$$

at Weibull moduli of 10 and 15 to be 0,95 and 1,08 respectively. Material property data established from the failed component showed mean values of Modulus of Rupture between 255 and 390 MPa (36975 and 56550 lbf/in^2) with Weibull modulus between 5 and 17. This analysis is consistent with the failures experienced and clearly indicated the need for design revision.

Meanwhile tests 5 and 6 were carried out using a skin cooled Nimonic rear disc and higher chamber exit temperatures were achieved although failures of the head ring (Item 1, Figure 2) were now experienced. Details of the test duration and condition of each ceramic item are given in Table IV.

Examination of the effect of slotting the rear disc from the inside, showed sufficiently high stresses in the outer periphery to still predict component failure. The critical failure stresses consist predominantly of hoop stresses on the outer periphery, and since these would certainly be eliminated by slotting from the outside, both rear disc (Item 7) and head ring (Item 1) components were produced to this design in FSR RBSN for test 7.

In this test a chamber exit temperature of 1515 K (2267^{o}F) was achieved for 30 minutes during a total running time of 1 hour 30 minutes. The temperature quoted is the mean of readings taken from thermocouples, situated in the exhaust gases, which gave readings from 1482 K to 1548 K (2208^{o}F to 2327^{o}F). Strip down revealed that the rear disc had cracked in a number of places and one piece, of maximum dimension 42 mm (1.65 in), had become detached. The fracture pattern was such that the remainder of the disc was retained in place until the strip down was carried out.

Subsequently test bar controls nitrided with the disc were shown to have a strength of only 151 MPa (21900 lbf/in^2) and microstructure examination showed extensive thick skins of silicon carbide/silicon oxynitride material in components and bars. The presence of such a skin has been shown to drastically reduce the strength of components (4).

Of the remaining 11 ceramic components, 9 were undamaged and 2 were found to be cracked. The first outer ring (Item 2, Figure 2) had one longitudinal crack emanating from a mounting pad cut-out, and the head ring (Item 1, Figure 2) had radial and circumferential cracks for two thirds of its circumference.

6. SUMMARY OF TEST RESULTS

A total of 5 hours 20 minutes combustion testing was carried out on a pressure rig in the full programme of seven tests. Of the 12 ceramic components making up the flame tube assembly, seven were used in all tests without showing signs of deterioration.

The initial failures experienced in the head ring and rear disc (Items 1 and 7, Figure 2) were attributable to excessive circumferential hoop stress, and the re-design of these components reduced the maximum predicted stress levels to the order of 10 MPa and 13,8 MPa respectively (1450 lbf/in^2 and 2000 lbf/in^2). The subsequent failures of these re-designed components showed that even these low stress levels were greater than the components' "large-volume" strength which had been reduced by the presence of silicon carbide/silicon oxynitride.

Three failures (Items 2 and 3, Figure 2) resulted when cracks propogated from areas of potentially higher stress in regions where local machining features give rise to stress raisers. Two of these failures were on "low calcium" HPSN material which had been shown to have regions of lower strength due to pressing cracks.

7. CONCLUSIONS

7.1 A silicon nitride flame tube has been designed, and combustion tested to a turbine entry temperature in excess of 1500 K (2240^{o}F), operating for 30 minutes at the design condition.

7.2 Seven of the 12 components making up the flame tube assembly survived the total of seven combustion tests of 5 hours 20 minutes duration. These components were all in fully machined hot pressed silicon nitride produced by Lucas Group Research Centre.

7.3 The greatest number of failures occurred on the two most complex components, namely the head ring (four failures) and the rear disc (five failures). Subsequent re-design reduced the stress levels in these components to trivial levels but failures again occurred which were directly attributable to material inhomogeneity.

7.4 Simulated structural bench tests undertaken in this programme were useful in highlighting local design features acting as stress raisers and these were largely eliminated in the design which was combustion tested.

7.5 The programme revealed the requirement for manufacturing development of all but the simplest type of components. However the work carried out in this programme provides a valuable basis for future comparison with improved ceramic materials and different manufacturing routes.

7.6 The programme has demonstrated that, however valuable material coupon tests are in broadly characterising materials, it is essential that actual components should be manufactured and exposed to the combustion chamber environment if a realistic assessment is to be made.

7.7 Providing consistent material properties and manufacturing techniques for silicon nitride can be developed this programme demonstrates that the design of a specific ceramic combustion chamber for a typical present generation small gas turbine is a practical possibility.

8. REFERENCES

1. Waring B, Hicks B — Investigation into the use of Silicon Nitride for Small Gas Turbine Combustion Chambers. Combustion Sub-Committee - A R C June 1974.

2. Sivill A D — Thermodynamic Stress Analysis of Silicon Nitride Components. Department of Mechanical Engineering, University of Nottingham 1974.

3. Sedgwick G — Annular Combustion Chamber Studies. Autumn Meeting T T C P - P2 Panel 1975.

4. Godfrey D J — Ceramics for Gas Turbines: Engineering Philosophy and Material Property Considerations. 3rd US/UK Conference - Gas Turbine Materials in a Marine Environment September 1976.

ACKNOWLEDGEMENTS

Thanks are due to the Directors of Lucas Industries Limited for permission to publish the paper, and also to the Ministry of Defence (U.K.) on whose behalf the described programme was carried out.

The author also wishes to thank colleagues for their support during the design and test programmes and in the preparation of the paper.

TABLE IV

TEST DURATION AND CONDITION OF CERAMIC COMPONENTS AFTER TEST

	Component	Material/Supply	Running Time	Description of Failure	Observations
1 (a)	To original design	Low calcium HPSN	2 hrs. 2 mins.	1 crack through material	Excessive thermally induced circumferential hoop stress.
(b)	To original design	Low calcium HPSN	3 hrs. 30 mins. (inc. above test)	Second crack appeared	"
(c)	To original design	Low calcium HPSN	30 mins.	Broken into 7 pieces	"
(d)	To new design	Flame sprayed RBSN/AML	1 hr. 30 mins.	Broken into 8 pieces with circumferential cracks	Inhomogeneous material
2 (a)		HPSN/GRC	3 hr. 20 mins.	Broken into 2 pieces	Thermal stress at local stress raisers
(b)		Low calcium HPSN	1 hr. 30 mins.	1 crack through material	Failure at local stress raiser
3		HPSN/GRC	3 hrs. 50 mins.	1 crack through material	"
4		HPSN/GRC	5 hrs. 30 mins.	NO FAILURE	
5		HPSN/GRC	5 hrs. 20 mins.	NO FAILURE	
6 (a)	To original design	HPSN/GRC	3 hrs. 50 mins.	NO FAILURE	Subsequently modified to suit metallic rear disc.
(b)	Modified form	HPSN/GRC	1 hr. 30 mins.	2 cracks through material from same point	Special component for use with metallic rear disc. Shape resulted in additional bursting load being applied.
7 (a)	To original design	Flame sprayed RBSN/AML	30 mins.	Multiple cracks & breaks	Excessive circumferential hoop stress
(b)	To original design	Flame sprayed RBSN/AML	25 mins.	Multiple cracks & breaks	"
(c)	To original design	Low calcium HPSN	30 mins.	Crack & breaks retainable by spring fingers	"
(d)	To original design	Low calcium HPSN	1 hr. 25 mins. (inc. above test)	Multiple cracks & breaks	"
(e)	To new design	Flame sprayed RBSN/AML	1 hr. 30 mins.	Multiple cracks & breaks	Inhomogeneous material
8		HPSN/GRC	5 hrs. 20 mins.	NO FAILURE	
9		HPSN/GRC	5 hrs. 20 mins.	NO FAILURE	
10		HPSN/GRC	5 hrs. 20 mins.	NO FAILURE	
11		HPSN/GRC	5 hrs. 20 mins.	Longitudinal crack from castellations	Failure at local stress raiser
12		HPSN/GRC	5 hrs. 20 mins.	NO FAILURE	This component is in two parts comprising L.H. & R.H. half rings.

A.M.L. - Admiralty Materials Laboratory
G.R.C. - Lucas Group Research Centre

(Component numbers refer to Figure 1)

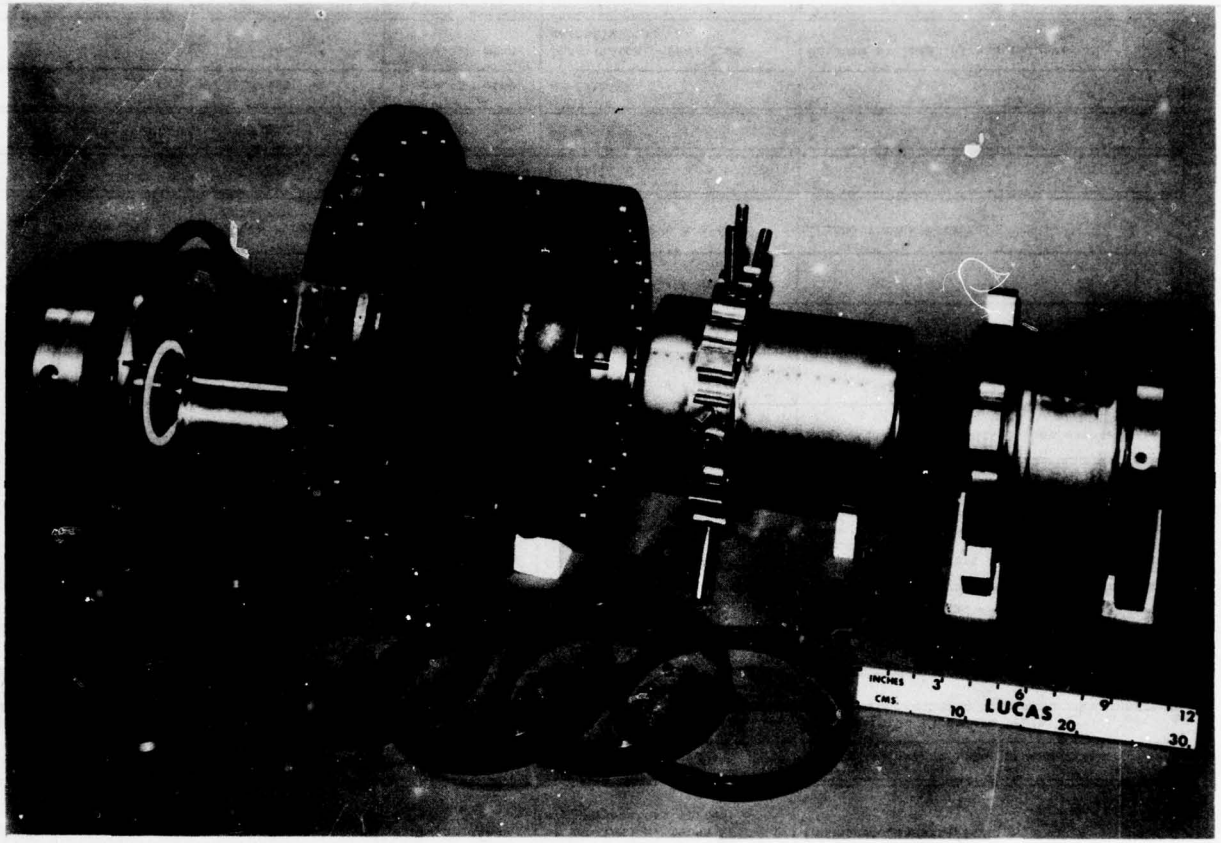

FIG. I. COMBUSTION RIG CASING AND CERAMIC COMPONENTS.

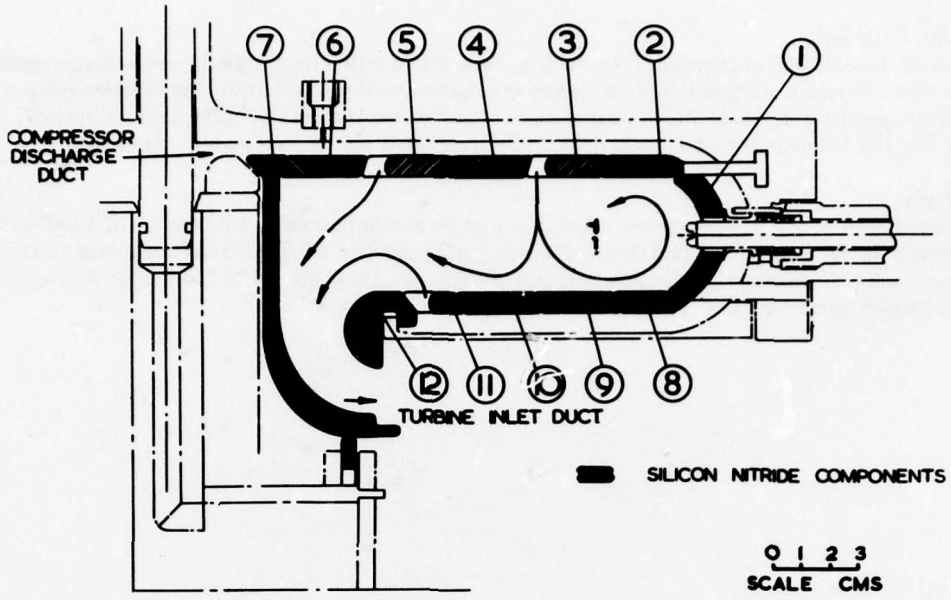

FIG.2. STACKED RING ANNULAR FLAME TUBE.

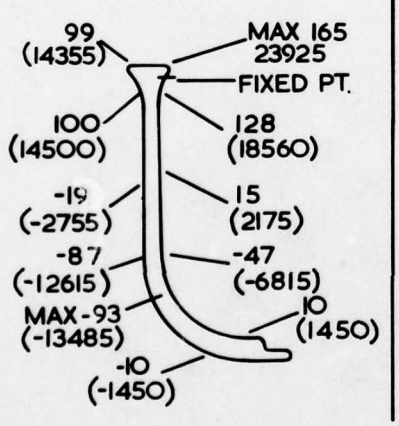

STRESSES CORRESPONDING TO TEST 4 OPERATING CONDITIONS

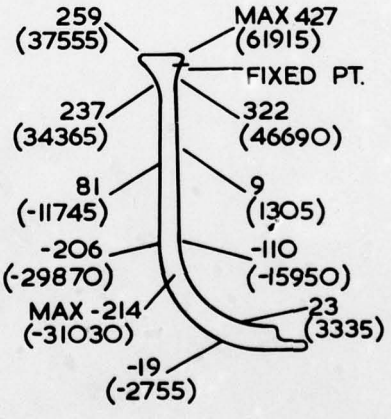

STRESSES CORRESPONDING TO FULL LOAD OPERATING CONDITIONS

STRESS VALUES IN MPa WITH lbf/in^2 IN PARENTHESIS

FIG.3. HOOP STRESS DISTRIBUTIONS ON REAR DISC.

DISCUSSION

R.Eggebrecht, Germany

First of all, I would like to comment that you have presented a very interesting engineering design approach for application of ceramic materials for this type of annular reverse flow combustor. My question refers to the rear disc failure you have shown in one of your pictures. Can you explain the test cycle you have applied? It is right to say that this failure occurred under mainly steady state conditions as your presentation suggests?

Author's Reply

In an attempt to achieve the first prime target of operation at a turbine entry temperature of 1200°C the test cycles consisted of increases in air and fuel flows, after ignition, to increase T.E.T. Consequently, rear disc failures occurred under conditions when temperatures were increasing. Those quoted in Table III of the paper are the TET levels at which failure occurred.

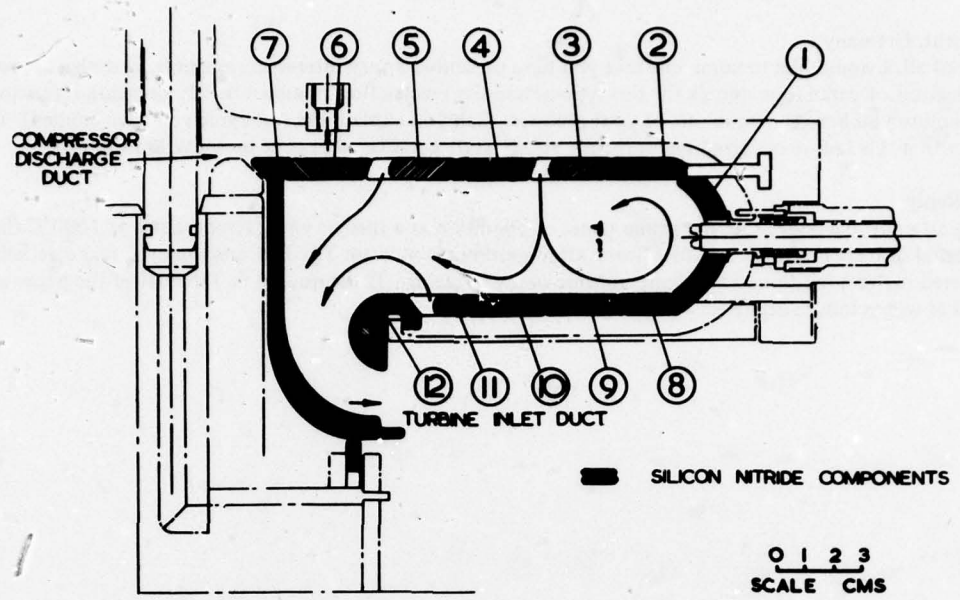

FIG.2. STACKED RING ANNULAR FLAME TUBE.

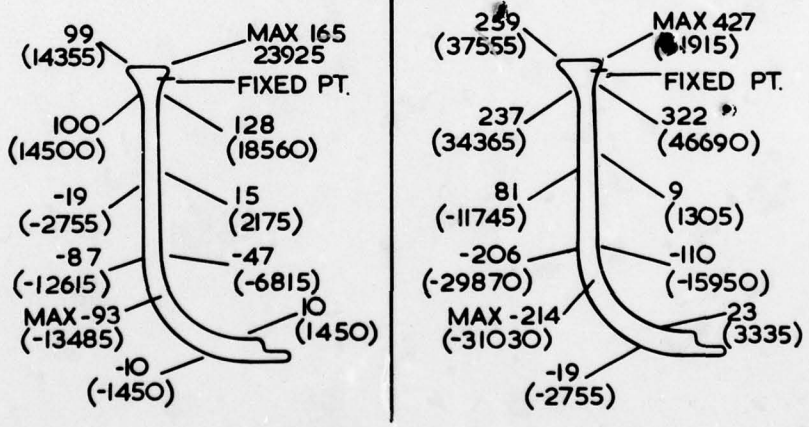

STRESSES CORRESPONDING TO TEST 4 OPERATING CONDITIONS

STRESSES CORRESPONDING TO FULL LOAD OPERATING CONDITIONS

STRESS VALUES IN MPa WITH lbf/in^2 IN PARENTHESIS

FIG.3. HOOP STRESS DISTRIBUTIONS ON REAR DISC.

Systematic Studies of Heat Transfer and Film Cooling Effectiveness

J. F. Louis*

Massachusetts Institute of Technology
Cambridge, Massachusetts U.S.A. 02139

ABSTRACT

A review is given of studies in heat transfer and film cooling effectiveness at MIT. The purpose of these studies is to develop an in-depth understanding of heat transfer and film cooling in gas turbines. A common experimental procedure is described for heat transfer measurements under isothermal wall conditions using fast response heat transfer gauges in tests conducted in a shock tunnel and a blow-down facility. The tests were conducted at flow and thermodynamic conditions modeling the operating conditions of advanced gas turbines. The configurations under study were single slot, single line of holes, double line of holes on a flat plate, and double line of holes on an airfoil.

I. Introduction

High performance gas turbines require high turbine inlet temperatures while maintaining the skin of exposed components at relatively low temperature for long life expectancy.

This low skin temperature can be obtained by a combined use of internal convection cooling and of an external thermal barrier in the form of a film of cool air, covering the skin of exposed components. The design of such turbines requires detailed information on the heat transfer distribution and aerodynamics of highly-loaded stages, and on the effectiveness of the film thermal barrier. This film can be obtained by blowing air through a porous surface, a slot, or an array of holes. The first technique, transpiration cooling, requires relatively small cooling flows. The momentum of the blown air is negligible compared to the main stream momentum and boundary layer theory can be applied to determine the thermal effectiveness of the film. However, the technological implementation of transpiration cooling has met severe difficulties, and the second technique of film cooling has found many applications in advanced gas turbines. Since the air is injected through a limited number of orifices, often at an angle to the wall, momentum of the injected flow is not negligible compared to the main flow and boundary layer theory cannot be applied to this case. New analytical and experimental information is therefore needed to determine the effectiveness of the film thermal barrier obtained by a wide variety of injection configurations.

Engine performance optimization depends critically on the selection of an effective cooling configuration and a detailed understanding of heat transfer to turbine components. A systematic study of relevant heat transfer and film cooling effectiveness is described in this paper, which covers (1) analytical and experimental studies of a wide variety of film cooling configurations, (2) experimental and analytical predictions of heat transfer over highly-loaded profiles, and (3) film cooling effectiveness over a subsonic profile. Short duration studies using a shock tunnel and hot blow-down facilities[1] provide a practical and flexible means to acquire the necessary experimental information while providing good modeling of the flow and temperature fields.

II. Experimental Approach

A. Adiabatic and Isothermal Wall Heat Transfer

Heat transfer measurements are conventionally referred to adiabatic conditions. The determination of heat transfer rate requires the knowledge of film coefficient and of an adiabatic wall temperature (T_{ad}). The heat transfer coefficient is determined for the case of no injection and a well-developed boundary layer. An adiabatic wall effectiveness is defined as

$$\eta_{ad} = \frac{T_{ad} - T_\infty}{T_c - T_\infty}$$

where T_∞ and T_c are the main stream and coolant temperatures. This adiabatic approach is correct when the ratio of the main stream to film temperatures is close to one. In advanced gas turbines, heat diffusion brings metal temperatures closer to an isothermal temperature distribution rather than an adiabatic one. In the presence of angular injection and high main flow to coolant temperature ratios, and in close vicinity to the injection point where large gradients of flow properties exist, the validity of using adiabatic wall information to determine heat loads to the cooled surfaces is in doubt, thus requiring the investigation of heat transfer phenomena by directly measuring heat transfer under correctly modeled turbine conditions. This need provides the justification to refer the data to isothermal conditions. Under these conditions, the heat transfer rate is

$$Q/A = h(T_w - T_\infty)$$

*Professor of Aeronautics and Astronautics

where T_w is the temperature of the isothermal wall and the isothermal effectiveness is defined

$$\eta_{iso} = 1 - Q_c/Q_o$$

where Q_c is the heat transfer with cooling and Q_o is the heat transfer at the same condition without cooling. The isothermal effectiveness represents the capacity of the thermal barrier provided by the film to reduce the heat transfer.

Adiabatic and isothermal effectivenesses are related by

$$\eta_{iso} = 1 - h_c/h_o \left(1 + \eta_{ad} \frac{T_c - T_\infty}{T_\infty - T_w} \right)$$

when h_c and h_o are the film coefficients with and without cooling.

B. Experimental Techniques

Unsteady heat transfer measurements under steady flow conditions provide the advantages of relatively simple heat transfer measurements of short duration, and of flexibility in modeling actual gas turbine operating conditions. To model gas turbines, one needs a high enthalpy flow for the mainstream and a low enthalpy flow for the coolant. By scaling the temperatures of these flows and the skin temperature from the actual turbine conditions and matching Reynolds, Mach and Prandtl numbers, a fairly representative model can be obtained for the heat transfer and cooling problems.

The experimental technique used is to establish the high and low enthalpy flows concurrently in a stepwise fashion for a duration short enough to render wall temperature changes minimal so that heat fluxes can be measured.

The short duration necessitates the use of fast response instrumentation such as thin-film gauges, calorimetric gauges, and Kistler pressure transducers.

C. Apparatus

A shock tunnel and a blow-down facility[1] are used for these tests. The shock tunnel is used to obtain basic data on film cooling effectiveness over flat and curved plates. The blow-down facility can be used either in conjunction with a cascade or with a rotating turbine rig to determine distribution of heat transfer rates and film cooling effectiveness over blade profiles, end walls, and turbine shrouds.

The shock tunnel[1] (Figure 1) is attached to a 3" shock tube through an accelerating nozzle. At the downstream end of the plexiglass, constant area (2 in x 7/8 in) tunnel, a choked nozzle controls the Mach number. The steady flow test time is approximately 10 ms, whereas the time to establish flow is 1 ms. For those short durations tests of the order of 10 ms, the plexiglass walls have large enough thermal inertia to limit their temperature rise to less than 7°F, thus not offsetting the isothermal wall boundary. Various configurations of coolant holes (or slots) on the tunnel walls are connected to a coolant flow supply plenum. The location of the holes (or slots) provides a local flow Reynolds of 3×10^5. The coolant flow is prepurified nitrogen, which is cooled by passing it through a copper coil immersed in a bath of liquid nitrogen. The introduction of the coolant is synchronized with the rupture of the shock tube diaphragm. Arrays of thin-film gauges are located downstream of the injection point to determine the heat transfer rate as a function of distance.

The Hot Blow-down Facility[1] (Figure 2) consists of air supply system storing 400 lbs of air at 2400 psi, dome-loading type pressure regulators, a 6 ft long and 1.5 ft diameter pebble bed heater filled with 3500 lbs of stainless steel balls and a filter trap. The facility has two legs, each consisting of a diaphragm section, a metering throat, a pressure reducing section utilizing of a supersonic nozzle and diffuser, and a transitional piece leading in one leg to the turbine rig and in the other leg to the cascade. The tests are typically less than 1 s, whereas steady flow is established after 0.15s. The heat transfer rate is measured by calorimetric gauges, a thin aluminum or copper disc (0.5 mm thick) embedded in a teflon cap with a thermocouple joined to its back.

E. Similarity Laws

The flow modeling used in the above facilities can easily be determined. The short operating time makes it reasonable, first, to assume an isothermal wall model, and, second, to scale down the operational temperature of the metal surface, T_{op}, to room temperature, T_R, by the temperature scaling factor, $S = Top/T_R$.

Matching up experimental Reynolds and Mach numbers to those of the actual engine conditions, one obtains

$$\frac{\rho_R V_R L_R}{\mu_R} = \frac{\rho_{op} V_{op} L_{op}}{\mu_{op}}$$

where L is the scale length, and

$$V_R/(\gamma_R R_R T_R)^{1/2} = V_{op}/(\gamma_{op} R_{op} T_{op})^{1/2}$$

if the Prandtl numbers of the two conditions are the same.

Assuming

$$\frac{\mu_{op}}{\mu_R}\left(\frac{\gamma_R}{\gamma_{op}}\cdot\frac{R_{op}}{R_R}\right)^{1/2}=\left(\frac{T_{op}}{T_R}\right)^{n}$$

where n is a number like Ø.5 to Ø.7, one obtains

$$\frac{P_{op}}{P_R}\cdot\frac{L_{op}}{L_R}\approx\left(\frac{T_{op}}{T_R}\right)^{n+1/2}=(S)^{n+1/2}$$

The scaling implies that if room temperature is used to model turbine components, temperatures which are as high as 1650°F, the temperature scaling factor would be 4. If the length scale is kept the same and n = Ø.64, the pressure would be reduced by the ratio, $p_{op}/p_r = S^{1.14} = 4.86$. For the tests with film cooling, the temperature of the coolant is reduced by the ratio S = 4.

III. Film Cooling Effectiveness

As mentioned before, engine designs geared to long life do not presently use transpiration cooling, seldom use injection parallel to the mainstream and, in most cases, use injection at an angle to the mainstream. As a reference, however, the state of understanding of parallel injection will be reviewed briefly..

A. Parallel Injection

When the film is injected parallel to the main flow, turbulent mixing dominates the interaction between the two streams. Downstream, the mixed layer is dominated by the wall shear stress, therefore, by suitable balance of both energy and mass for the mixed streams, Stollery and El Ehwany[2], and Leontev and Kutateladze[3] have derived the following relation:

$$\frac{T_{ad}-T_\infty}{T_\infty-T_c}\approx A\left(\frac{ms}{x}\right)^{0.8}\left(R_{ec}\frac{\mu_c}{\mu_o}\right)^{0.2}$$

applicable for x>>s, where s is the slot height, with a = 3.Ø3 in reference 2, and a = 3.1 in reference 3, where R_{ec} is the Reynolds number based on coolant conditions.

This theoretical relationship compares favorably with the test results[4][5][6] for data obtained far downstream, but the scatter becomes appreciable in the region closer to the injection point. In the vicinity of the injection point, the mixing is dominated by the local vorticity field and this local phenomenon is not included in the above theoretical formulation.

B. Film Cooling with Angular Injection

When a film is injected at an angle to the mainstream from a well to provide a thermal barrier over a section of wall, it undergoes two determining processes: a viscous interaction and a pressure interaction. The viscous interaction results in the turbulent mixing of the two streams. The pressure interaction exists since the momentum of the injected flow normal to the wall is commensurable with the main stream momentum. The pressure gradient normal to the wall near the injection point is significant and boundary layer theories are no longer applicable.

Further, for values of the injection parameters normal to the wall, the boundary flow separates at the injection point and forms a separation bubble just downstream of the injection point. The evidence for the existence of the boundary layer separation at the injection point and the formation of a separation bubble are several:

1. This separation is theoretically expected when the criterion determined by Kutateladze and Leontev[7] is applied to the conditions of film cooling with angular injection. This criterion indicates that separation will occur when the normal mass injection parameter

$$m_y=\frac{(\rho_c U_c)_y}{\rho_\infty U_\infty}\geq 2\,C_{fo}$$

where C_{fo} is the skin friction coefficient in the absence of coolant, and y refers to the direction normal to the wall. For a flow Reynolds number at the injection point of $R_e = 3 \times 10^5$, $C_{fo} = 2 \times 510^{-3}$, and this criterion would indicate that separation is likely to occur when $m_y >> 5 \times 10^{-3}$, i.e., for a typical angle of injection of 30°, separation would occur for a value of the total mass injection parameter.

$$m=\frac{\rho_c U_c}{\rho_\infty U_\infty}\geq 0.1$$

Practical values of the injection parameter are generally appreciably larger than m = Ø.1.

2. The existence of a separation bubble downstream of 30° slot was demonstrated by dye and hydrogen bubble visualization techniques in a water tunnel[8]. The study indicated that the length of the separation bubble was proportional to the momentum ratio

$$K_o^2 = \frac{\rho_c U_c^2}{\rho_\infty U_\infty^2}$$

The flow visualization also indicated the appearance of streamwise vortices having consecutive opposite directions of rotation. This vorticity results from the coupling between the injected flow and its streamwise velocity. The vortical motion has the effect of enhancing the mixing of the coolant with the mainstream as evidenced by the presence of fluid elements in the separation bubble. The study also indicated that the vortices persisted far downstream.

3. Measurements of heat transfer coefficient (Figure 3) downstream of a 30° injection slot on a curved wall indicated that the heat transfer coefficient goes through a maximum close to the injection for a given value of the injection parameter. This maximum can be explained by the existence of the separation bubble in which hot gas is being entrained.

4. Measurements of heat transfer rate at the trailing edge of a plate indicate[9] that the isothermal effectiveness measured at the trailing edge can be severely reduced (Figure 4) by locating the coolant injection slot at a distance shorter than the reattachment joint of the separation bubble (Figure 5). The separation bubble is observed in the range of mass injection up to values of m, for which complete separation of the boundary layer occurs.

Film-Cooling Effectiveness for Angular Injection

A comprehensive experimental program[10][11][12] has been undertaken to investigate different film cooling configurations of slots, single and double line holes for different streamwise and crosswise angular injection.

Figure 6a is a representative layout of the flat plat used in the shock tunnel for the evaluation of film-cooling effectiveness. The injection scheme uses a double line of holes which make an angle α_1, with the streamwise direction and α_2 with the crosswise direction. Thin-film heat transfer gauges are located at different distances corresponding to different values of the ratio of the streamwise distance (x) to the hole diameter. These gauges provide an average local heat transfer rate, whereas the gauges located at x/D = 27 are used to measure the crosswise variation of effectiveness. Most of the tests were conducted at a stagnation temperatue of 1000°R and 10 psia stagnation pressure, which simulated the inlet conditions 4000°R and 175 psia of an advanced gas turbine. The Mach number was typically M = 0.5 and the coolant temperatures were 220°R, 310°R, 400°R and 500°R. The mass injection parameter was varied between 0.1 to 1.6. The streamwise angles used were 10°, 20° and 30° and the crosswise angles used were 0°, 30°, 50°, 70°, and 90°.

The influence of the different configuration parameters can be assessed.

1. Effect of the Crosswise Angle for Holes

The cross-stream injection angle does not affect the film cooling effectiveness over a flat plate to any great degree. Its influence is limited to the area just downstream of the injection point as indicated by the film effectiveness footprints[11], e.g., (Figure 6b), measured for α_2 = 30° and for different values of the mass injection parameter. In the region close to the hole, the coverage increases with the crosswise width of the hole.

2. Influence of the Distribution of Holes

Data of film effectiveness were correlated by using the concept of equivalent slot width, which is the width of a slot which would pass the same amount injection mass flow as the single or double line of holes.

Figure 7 gives the general correlation found for single and double lines of holes with α_2 varying from 0° to 90° using the concept of equivalent slot width in the parameter

$$A_o^* = B\, K_o^{-1.35}\, R_{es}^{-.25}\, x/S_{eq}$$

where B is a constant, K_o is the square root of the momentum ratio and R_{es} is the Reynolds number based on the injection conditions.

3. Slot versus Hole Injection

As seen in Figure 8, the film cooling effectiveness of hole injection is sharply lower than injection through a slot, corrected for equivalent coolant mass flow introduced to form the film. By observing that the mixing area for a hole is ¶ times larger per unit length of slot, the correlation parameter A was corrected by this amount for data related to holes in other words $¶^x = 1.0$ for a slot and $¶^x = ¶$ for hole injection. With this change in the correlation parameter, the hole data aligned with the slot data quite well (Figure 9). The best overall agreement is, however, obtained when the factor $¶^x$ is raised to the power 1.41.

4. Overall Correlation

With the incorporation of this parameter and the temperature ratio $\Theta = T_c/T_\infty$, the best correlation[12] is obtained for both holes and slots, with the group $m^{-1.35} \cdot \Theta^{-0.68}$, which reduces to $K_o^{-1.35}$.

The best overall correlation of slot and holes data obtained for $\alpha_1 = 20°$ (Figure 10) is, therefore, obtained against the group

$$A_2 = ¶^{*1.41}\, K_o^{-1.35}\, x/s_{eq}$$

Previous film cooling data for values of α_1 = 10, 20, 30° have indicated a dependence of the effectiveness on the parameter $(K_o \cos^2 \alpha_1)^{-1.35}$. However, more data (over a wider angular range) are needed to validate this correlation fully.

Mathematical Modeling for Angular Injection

The experiments provide a good insight in the fluid mechanics of the film with angular injection and an attempt was made to model the film downstream of a slot[10]. As shown before, the flow emerging from a slot at mass injection parameters between 0.1 and 1.0, undergo both mixing and strong dynamic effects at the injection point. The dynamic interaction results in the formation of a separation bubble. Within the bubble a circulation pattern entrains coolant near the reattachment point while some of the bubble gas is entrained by the coolant near the injection point. Further, the curved interface between the coolant and the hot gas is unstable and streamwise vortices of the Gortler type are generated.

Downstream of the injection point, both turbulent and vortical mixing occur. Because of the strong dynamic interaction in the vicinity of the injection point and of the vortical mixing downstream, the boundary layer theory cannot be applied except very far downstream of the injection point, a region of little interest in film cooling.

Consequently, a mathematical model has to use integral forms of the momentum and energy equations together with a relation describing the mixing of the main flow with the coolant. In reference 10, the mixing is modelled by an entrainment mass flow rate in

$$\dot{m}_{ent} = [A|\cos \alpha - U_c/U_\infty| + B \sin \alpha_o \sin (\alpha_o - \alpha_{eff}) e^{-K\frac{x}{s}}]\rho_\infty U_\infty$$

where the first term models entrainment due to the shear layer formed by the slip between the coolant and main stream where α is the instantaneous angle of the shear layer relative to the wall. In the second term, B describes the strength of the vortical mixing and the term $\sin \alpha_o \sin (\alpha_o - \alpha_{eff})$ describes the curvature of the separation bubble, where s/K is the characteristic length for the vorticity attentuation.

The numerical model[10] covers three consecutive regions (Figure 11). In the first region continuity and momentum relations are used to determine the angle ($\alpha_o - \alpha_{eff}$) by which the coolant is turned by the mainstream. In region (2), the continuity, streamwise and normal momentum energy equations together with the entrainment relation are used to solve the coolant curved flow over the separation bubble. In region (3), after the reattachment point, the continuity, streamwise momentum and energy equations are applied in the entrainment region. The mixing zone ($\sigma - \delta$) due to the mass entrainment is computed as a function of distance. The mathematical model can be used for both adiabatic and isothermal wall conditions.

The parameter A can be empirically derived from experiments with parallel injection using thin injection lips [4][13] and the experiments with angular injection were used to determine B and K.

Since the turbulence of two streams separated by a shear layer increases with density [15]; A is assessed to vary as $A = A_1 (\rho_c/\rho_\infty)$. It was found that

$$A_1 = A_2 \, x/L \text{ for } 0 < x < L$$
$$A_1 = A_2 \text{ for } x > L$$

where L is a length in which full mixing is developed. The mixing can be expected to depend on the momentum ration K_o^2.

A correlation of A_2 and L/s with k_o^2 was determined for the data[4][14][15]. a value of n = 1.5 was found to fit data[4] best. A value of s/K of 35 was adapted and a correlation of B dependent on both m and T_c/T_∞ was used based on data[4][14][15]. The numerical model predicted both adiabatic and isothermal effectivenesses favorably (Figures 12, 13, 14) up to the conditions of boundary lift off (Figure 13), which the model cannot handle.

The numerical model[10] is a first attempt to predict the film in the region near the slot injection point. Better description and more detailed measurements are needed for the vortical motion and improvements have to be made on the turbulent mixing term before such an analysis can be extended to the film produced by the arrays of holes.

III. Heat Transfer Over Blade Profiles

The distribution of heat transfer over exposed turbine components is critical information for the evaluation of cooling requirements. This information is particularly important for highly loaded blades, which provide a means to reduce cooling requirements per unit of turbine work.

The pressure and the heat transfer distributions around four blade profiles were determined in the range of outlet Mach number from 0.6 to 1.6 at nominal incidence. A similar investigation was carried out for one profile as a function of incidence[16]. The four blades were designed for inlet angle $\beta_1 = 32^o$ and outlet angle $\beta_2 = 65^o$, with a spacing to chord ratio g/c = 0.75. All four blades were designed from a reference Blade 1 with the same subsonic section. Differences exist downstream of the throat.

Blade 1 (Figure 15a) is the references blade with a straight suction back downstream of the throat. It has a thick trailing edge thickness of 4% (relative to the chord).

Blade 2 (Figure 15c) is almost identical to blade 1 except for a thinner trailing edge thickness of 2%.

Blade 3 (Figure 15b) has a contoured suction side downstream of the throat contoured to cancel the expansion waves originating from the opposite side of the throat. Trailing edge thickness is 2%.

Blade 4 (Figure 15d) is a convergent-divergent blade (Figure 15d) with a trailing edge thickness of 1.5%.

The supersonic sections of Blade 3 and 4 were designed by the method of characteristics. The aerodynamic performance of the blades (Figure 16) indicate the strong influence of trailing edge thickness on losses in the sonic and subsonic regime. Blade 2 has the best performance up to an outlet Mach number of 1.3. Beyond this value, losses associated with shock boundary layer interaction and shockwaves dominate and Blade 4 performance is best. In this investigation of heat transfer rates, a ratio of $T_\infty/T_w = 1.5$ was used, which corresponded to a stagnation temperature of 810°R. The measured turbulence level was 10%. The master blade was instrumented with 25 pressure taps and 25 calorimetric gauges located close to mid span. Figure 16, 17, and 18 give the distribution of the ratio of Nusselt number to the eighth power of the Reynolds number as a function of location and outlet Mach number. Very high heat transfer rates are observed at the leading edge, at the transition point near the suction point and near the trailing edge on the pressure side.

Figure 19 gives the mean Stanton number for the three blades as a function of Mach Number. Changes in incidence were found to only have a small effect on the average Stanton number[16]. In Figure 20, a comparison is made between the measured blade mean Nusselt Number [15][16] with other available data. The M.I.T. experimental data lie in the upper region which is expected as a result of the high turbulence level (10%) and of the high outlet Mach numbers.

The experimental heat transfer data were compared with the predictions given by a NASA computer program[17] using the airfoil static pressure distribution as input. This program gives the solution of the two-dimensional compressible laminar (Cohen and Reshotko's method) and turbulent (Sasman and Cresci's method) boundary layer in an arbitrary pressure gradient. A typical comparison of experimental and predicted values is shown in Figure 21, the comparison is favorable considering the fact that the numerical solution does not include surface curvature effects, surface roughness, influence of turbulence levels, and particularly shock boundary layer interaction.

IV. Heat Transfer to a Film-Cooled Blade Profile

The work outlined in the previous sections provided a basis for an experimental study of film cooled blades.

In choosing a blade profile to be film cooled, it was noted that blades 1 and 3 gave better aerodynamic performance (discounting the effect of the thicker trailing edge for Blade 1) up to an exit Mach number of 1.3 and lower average heat transfer rates. Distribution of heat transfer rates[15][16] around blade profiles indicated four regions of very high heat transfer rates: the leading edge, the transition point on the suction side of the blade and the trailing edge regions on both suction and pressure sides of the blade. It was also realized that a relatively thick trailing edge is required when film cooling is applied the trailing edge. For these reasons, the Blade 1 profile was selected and 5 zones of injection were used as shown in Figure 22.

At the leading edge, four rows of holes (D = .040 in) at a 90° injection angle cool the entire region (a). A double row of holes with an injection angle of 40° is located at the transition point (e). A double row of holes with a 20° injection angle is located halfway along the pressure side (b) to test the film cooling effectiveness near the trailing edge associated with this location. Injection upstream on both sides of the trailing edge in (c) and (d) is performed through a double row of holes with 20° injection. The flow through each coolant supply plenum (A, B, C, D) is separately metered. The location of pressure taps and heat transfer gauges is also shown. In the tests performed so far at an exit Mach number of 0.6, with a stagnation temperature of 810°R, and a coolant temperature of 528°R, the isothermal effectiveness of each injection zone has been studied for different injection mass flow parameters m.

Figure 23 shows the normalized heat transfer distributions of the cooled and uncooled blade. Injection from the leading edge with m = 1.4 is found to be effective around the profile. Injection at the transition point on the suction side is found to be very effective with a small m (m = 0.35) in the region downstream of the injection, with strong mixing reducing its effectiveness in the trailing edge region. Injection through plenums C and D also give favorable results. Figures 24 and 25 give the film data obtained with injection from plenums B and C. These data are compared with the correlation derived in Reference 1 for films injected from a double line of holes and with the overall correlation based on Figure 10, but using the parameter $(K_o \cos^2 \alpha_1)^{-1.35}$. The comparisons show derivations which underestimate the effectiveness on the suction side and overestimate it on the pressure side. Since the correlations were established for a flat plate, the discrepancy indicates that corrections should be applied for the effects of curvature and pressure gradients.

Conclusions

1. Short duration experiments provide a practical and flexible means to study problems of film cooling and heat transfer in turbines while providing good modeling of operating conditions.

2. A fairly systematic study of film cooling effectiveness with various configurations under a variety of conditions indicate that the key parameters correlating the effectiveness are K_o^2, the momentum ratio; the injection angle relative to the wall and $.x/S_{eq}$ where S_{eq} is the equivalent slot width providing the same mass flow per unit width as the single or double line of holes.

The mathematical modeling of the film has emphasized the near region downstream of the injection and is using an entrainment model for the mixing of the two streams.

3. Detailed measurements of heat transfer rates distribution, pressure distributions, and pressure losses were obtained for four profiles with high aerodynamic loading. The profile with a straight back gave good overall performance for outlet Mach numbers up to 1.3. For higher outlet Mach numbers, the profile with a contoured suction side and the profile providing a convergent and divergent section gave better performance.

4. The detailed film cooling and blade performance studies provide a very adequate basis for the study of the performance of film-cooled profiles. However, data on film cooled blades indicate that data and correlations obtained on flat plates have to be corrected for curvature and pressure gradients.

Acknowlegement:

The work described in this paper was performed under contract F33625-76-C-2018 from the Air Force Aeropropulsion Laboratory and on contract N00014-76-C-0253 from the Office of Naval Research. The data on the last three figures was obtained by A. Berenfeld.

References

1. Louis, J.F., ET AL., "Short Duration Studies of Gas Turbine Heat Transfer and Film Cooling Effectiveness", ASME, 1974-GT-131, 1974.

2. Stollery, G.L., and El-Ehwany, A.A. International Journal Heat Transfer, Vol. 8, No. 1 1965.

3. Kutateladze, S.S., and Leontev, A.I., "Thermal Physics of High Temperatures", Vol. 1, No. 2, pp 281-290 (1963).

4. Papell and Trout, NASA, TW, ND-9, 1959.

5. Hartnett, Birkebak and Eckert, Journal of Heat Transfer, ASME, Series C, Vol. 82, No. 3, 1961.

6. Seban, Trans. ASME, Ser. C, Vol, 82, No. 4, 1960.

7. Kutateladze, S.S., and Leontev, A.I., Heat-Mass Transfer and Friction in a Turbulent Boundary Layer, Energiya Press, Moscow 1972.

8. Hruby, V., "Flow Visualization Studies in a Water Channel with Slot Injection Simulating Film Cooling", M.I.T., Gas Turbine Laboratory Internal Report, 1972.

9. Amana, O.M., et al., "Aerodynamics and Heat Transfer at the Trailing Edge of Transonic Blades", ASME, 76-GT-95, 1976.

10. Demirjian, A.M., "An Analytical and Experimental Investigation of Film Cooling Effectivness over a Flat Plate", Ph.D. thesis, Department of Aeronautics and Astronautics, M.I.T. September 1975.

11. Bakos, J.H., "Film Cooling by Cross Flow Hole Injection", S.M. thesis, Department of Aeronautics and Astronautics, M.I.T. September 1975.

12. Ortiz, M., "The Effect of Geometry on Film Cooling Effectiveness", S.M. thesis, Department of Aeronautics and Astronautics, M.I.T. February 1976.

13. Chin, G.H., Skervin, S.C., Hayes, L.E., and Burgroff, V.R., Journal of Heat Transfer, ASME Ser. V, Vol. 21, No. 2, 1954.

14. Sivisagaram, S. and Whitelaw, J.H., "Film Cooling Slots: The Importance of Lip Thickness and Injection Angle", J. Mech. Eng. Sci., Vol 11, No. 1, pp 22-27, 1969.

15. Demuren, H.O., "Aerodynamic Performance and Heat Transfer Characteristics of High Pressure Ratio Transonic Turbines", D.Sc. thesis, Department of Aeronautics and Astronautics, M.I.T., February 1976.

16. Hajjar, F. G., "The Heat Transfer Characteristics of Transonic Turbine Blades as a Function of Angle of Incidence", S.M. thesis Department of Aeronautics and Astronautics, M.I.T., 1977.

17. McNally, W.D., "Fortran Program for Calculating Compressible Laminar and Turbulent Boundary Layers in Arbitrary Pressure Gradients", NASA TN D-5681, 1970.

18. Ainley, D.G., "An Experimental Single Stage Air-Cooled Turbine, Part II", Proceedings of the Institute of Mechanical Engineers, Vol. 167, pp. 351, 1953.

19. Wilson, D.G., Pope, J.A., "Convective Heat Transfer to Gas Turbine Blade Surfaces", Proceedings of the Institute of Mechanical Engineers, Vol. 134, No. 36, 1954.

20. Hodge, R.I., "A Turbine Nozzle Cascade for Cooling Studies, Parts I and II", A.R.C.C.P. Nos. 492, 293, 1960.

21. Bammert, F., and Hahnemann, H., "Heat Transfer in the Gas Surrounding Cooled Turbine Blades", Ministry of Supply, Report G.D.C. 2466, 1951.

22. Andrews, S.J. and Bradley, P.C., "Heat Transfer to Turbine Blades", A.R.C.C.P. No. 294, 1957.

23. Fray, D.E., and Barnes, J.F., "An Experimental High Temperature Turbine (No. 126) Part 2. The Cooling Performance of a Set of Extruded Air-Cooled Turbine Blades", A.R.C.C.P. and M 3405, 1965.

24. Halls, G.A., "Air Cooling of Turbine Blades and Vanes", AGARDograph 120, Supersonic Turbojet Propulsion Systems and Components, ed., J. Chauvin,, 1967.

25. Turner, A.B., "Local Heat Transfer Measurements on a Gas Turbine Blades", Journal of Mechanical Engineering Science, Vol. 13, No. 1, 1971.

AD-A052 845 ADVISORY GROUP FOR AEROSPACE RESEARCH AND DEVELOPMENT--ETC F/G 21/5
HIGH TEMPERATURE PROBLEMS IN GAS TURBINE ENGINES.(U)
FEB 78

UNCLASSIFIED AGARD-CP-229 NL

5 OF 7
AD
A052845

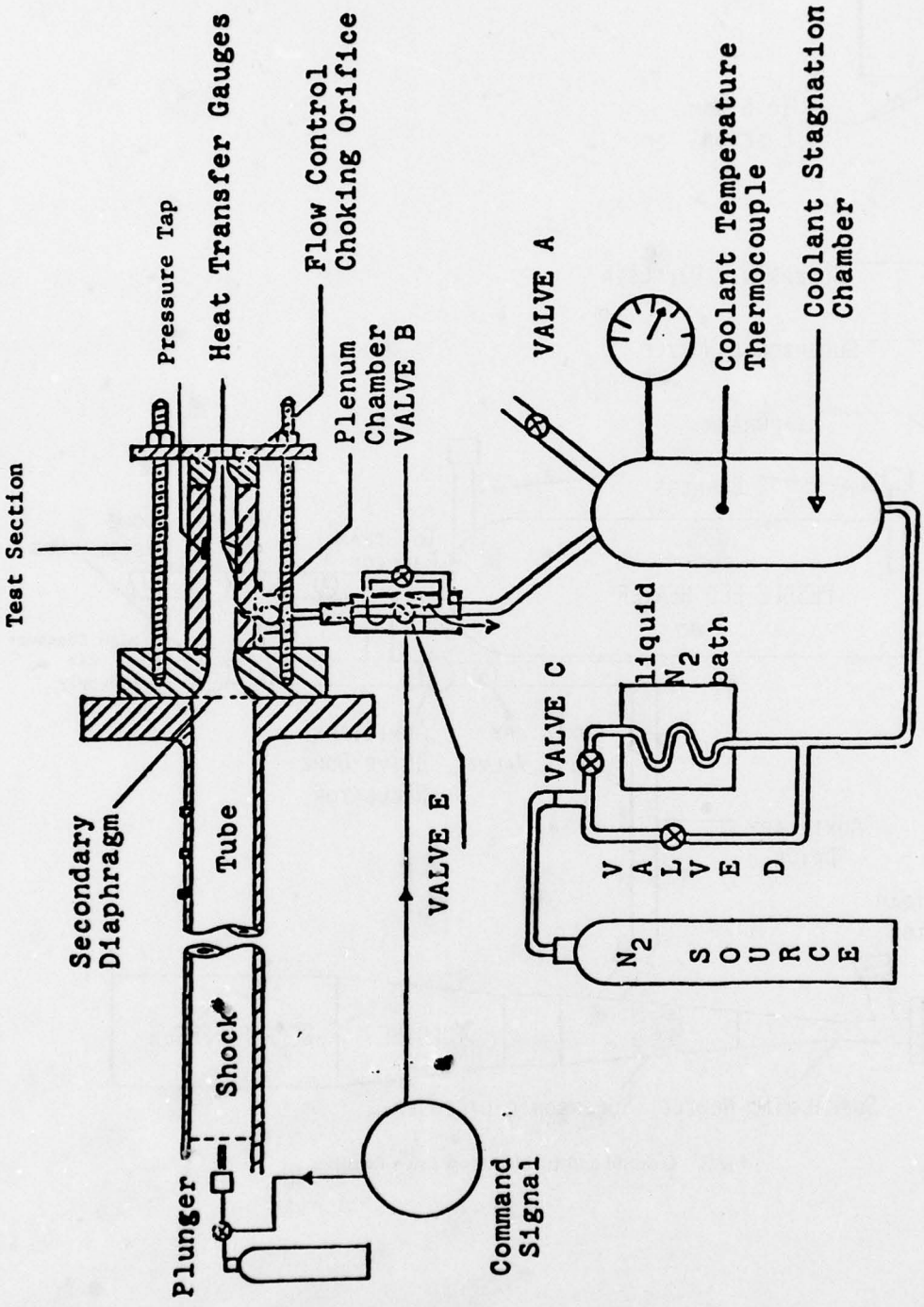

Fig. 1 Shock tunnel apparatus

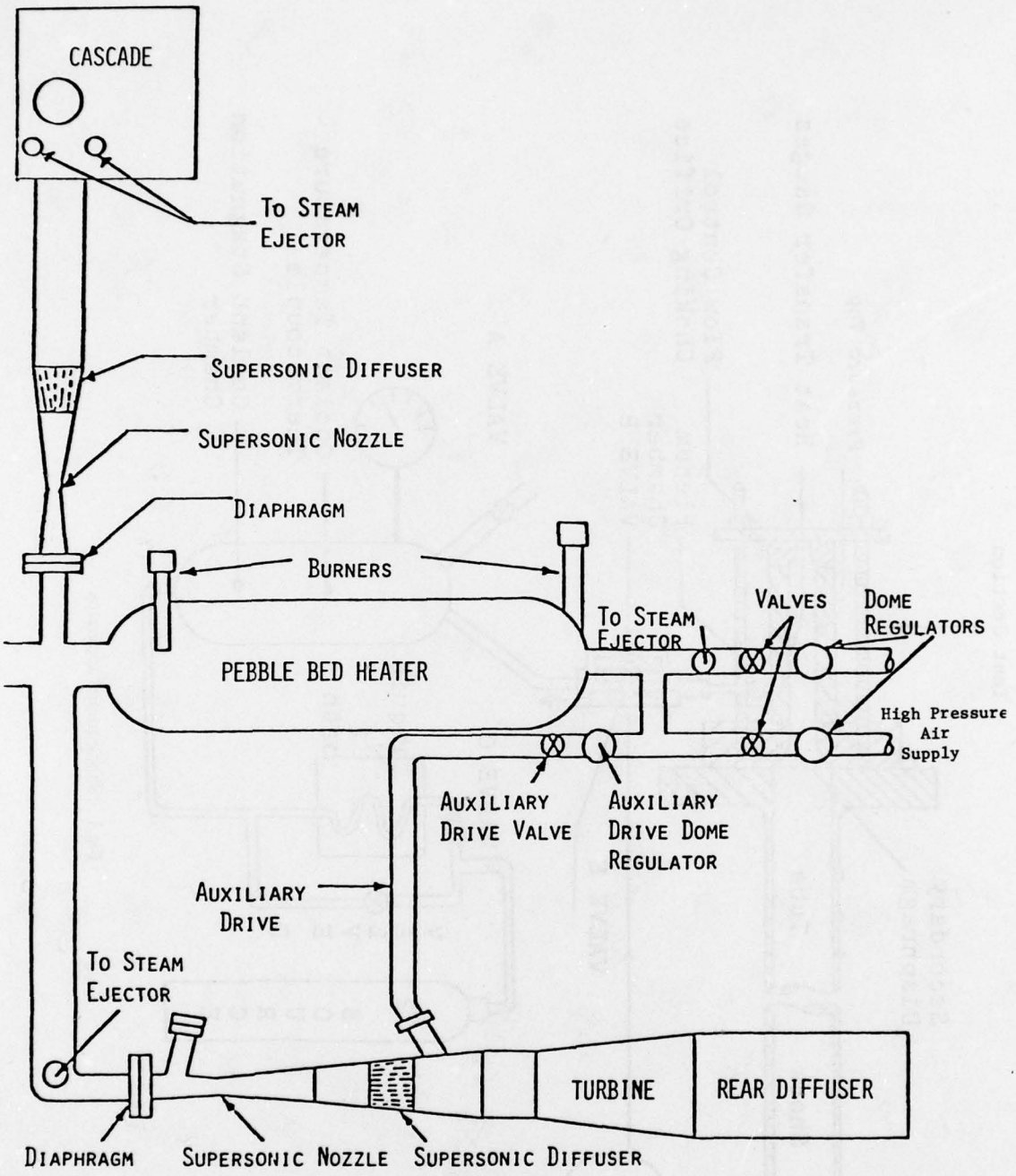

Fig.2 Cascade and turbine blowdown facilities

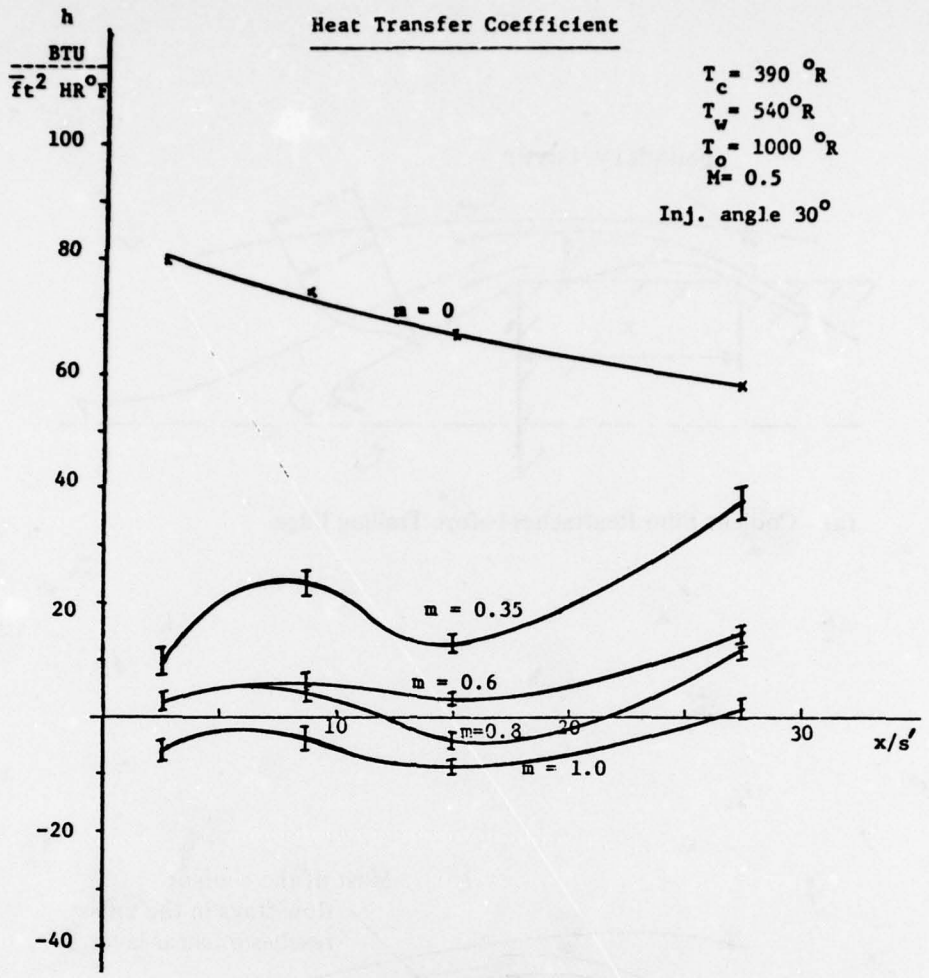

Fig.3 Heat transfer coefficients with film cooling

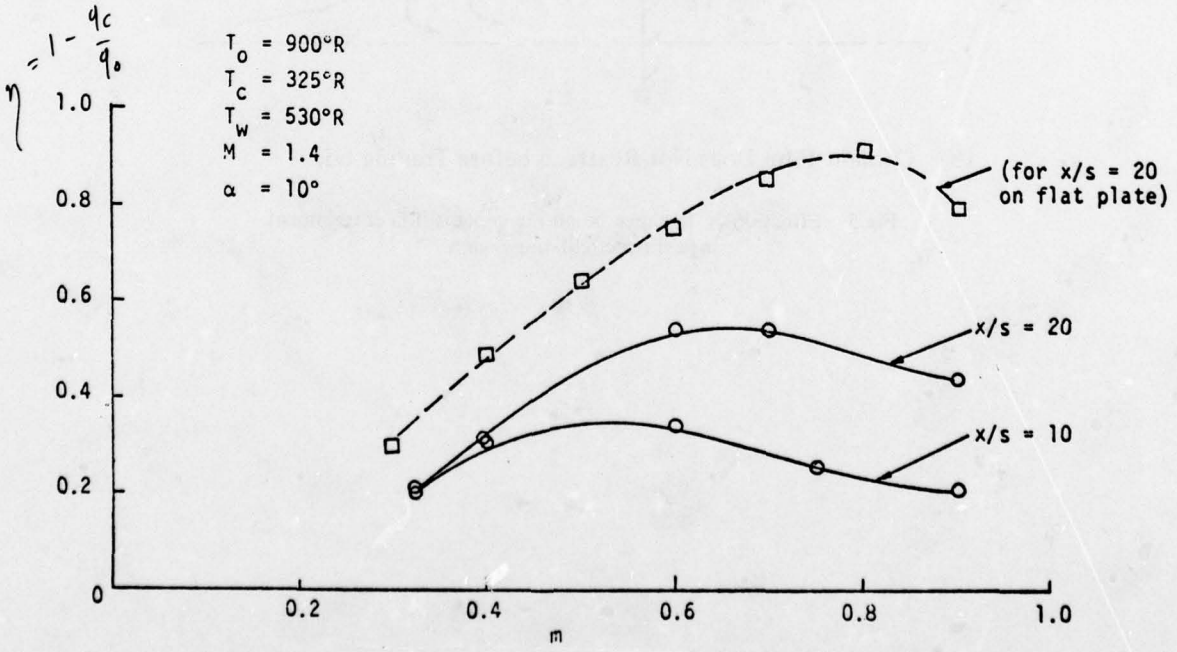

Fig.4 Variation of η with m for trailing edge. Injection from suction side only

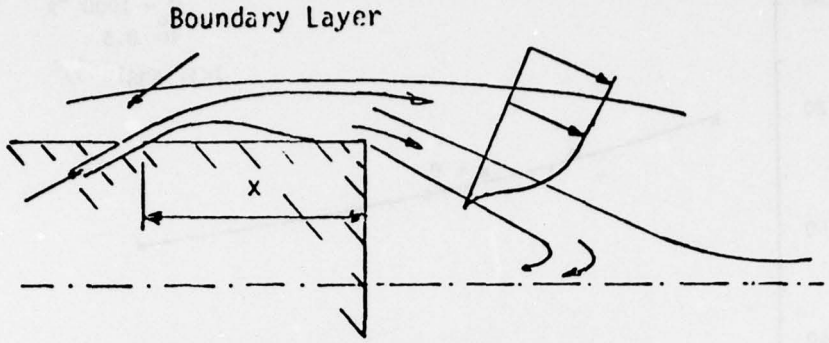

(a) Coolant Film Reattaches before Trailing Edge

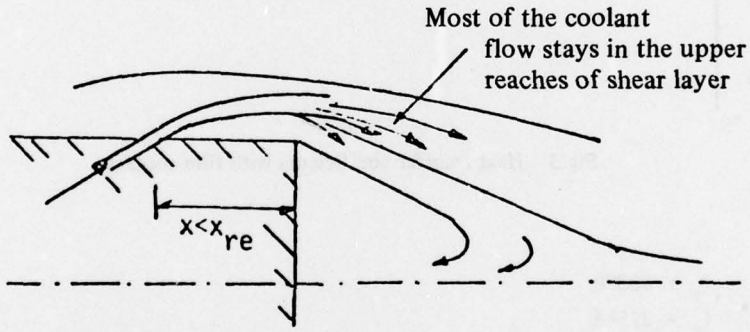

(b) Coolant Film Does Not Reattach before Trailing Edge

Fig.5 Effect of the distance x on the coolant film entrainment into the recirculating region

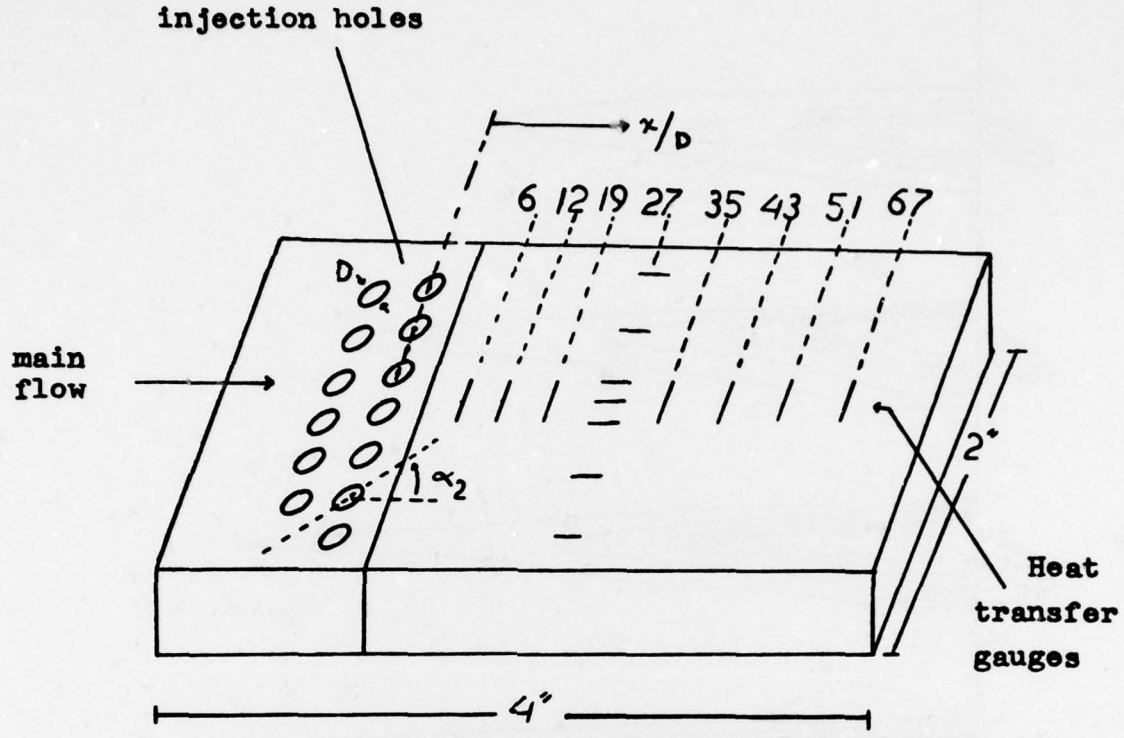

Fig.6(a) Layout of flat plate with double line of holes

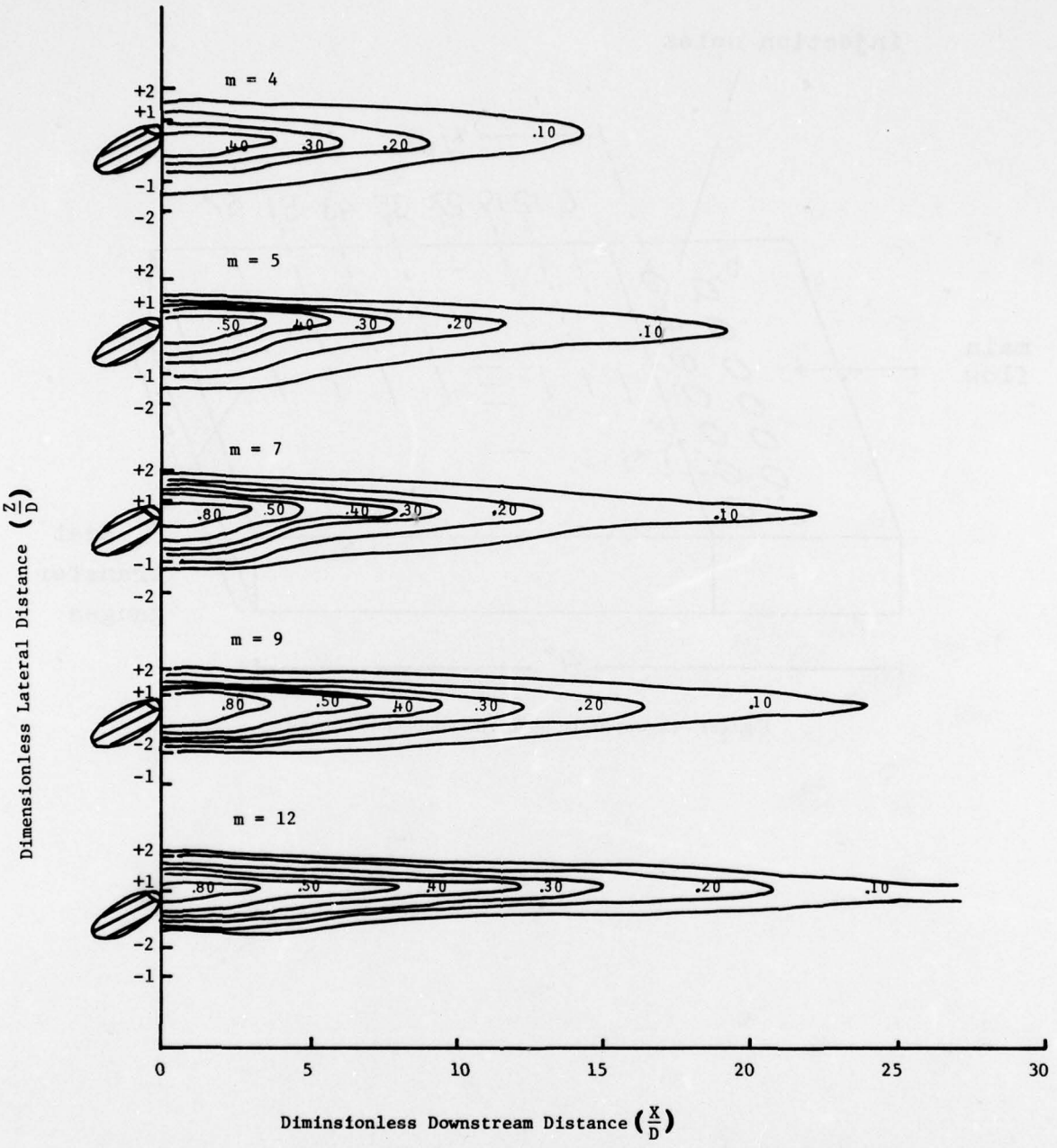

Fig.6(b) Effectiveness footprints obtained from the single hole experiments

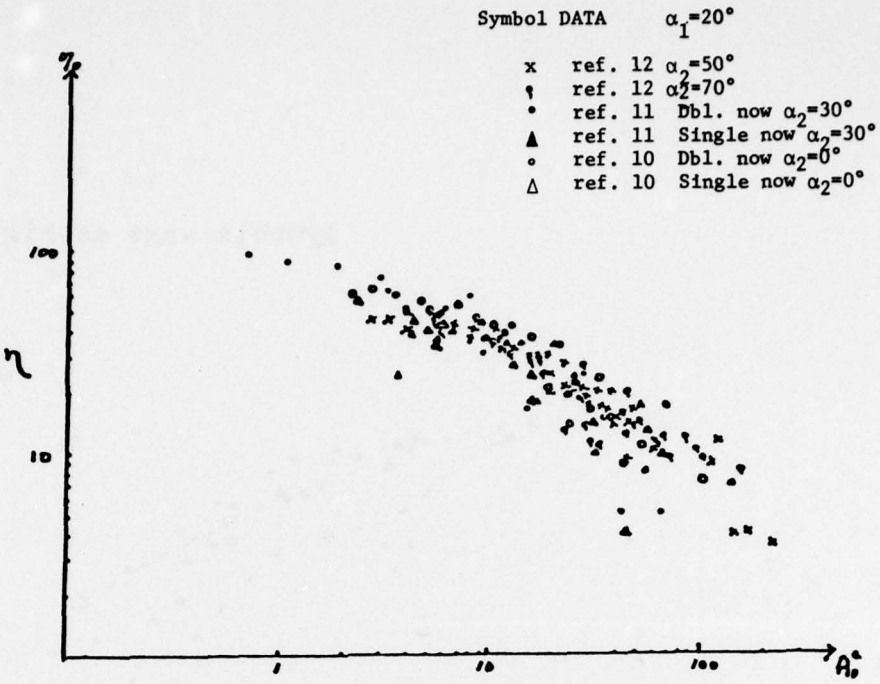

$$A_o^* = B.\ K_o^{-1.35}\ R_{es}^{-.25}\ \frac{x}{S}\ eq$$

Fig.7 Hole data correlated by using the equivalent slot width

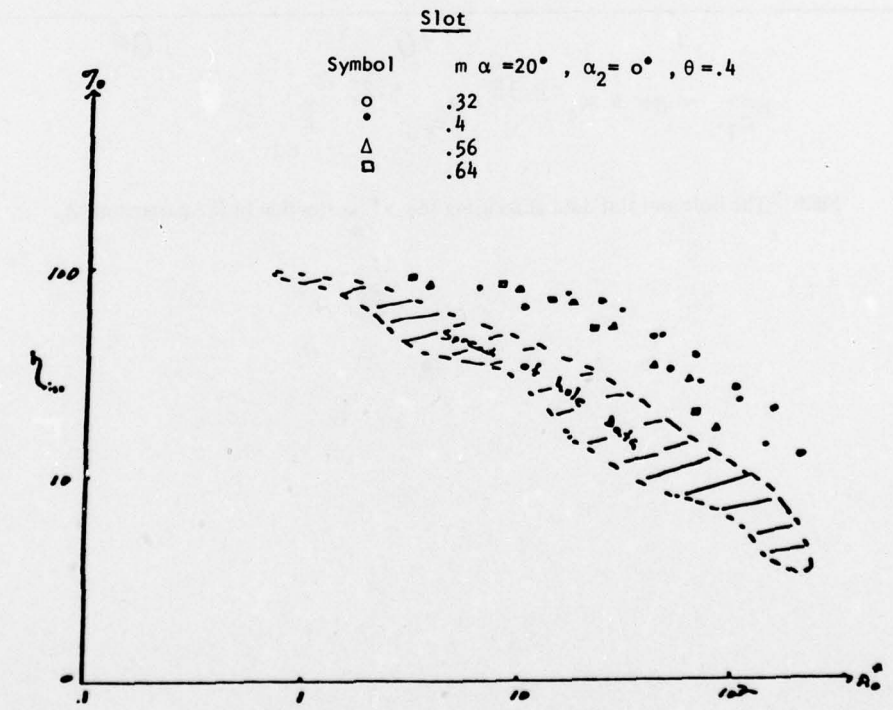

$$A_o^* = B.\ K_o^{-1.35}\ Re^{-.25}\ \frac{x}{s}$$

Fig.8 Slot data[10] compared to hole data from Figure 7

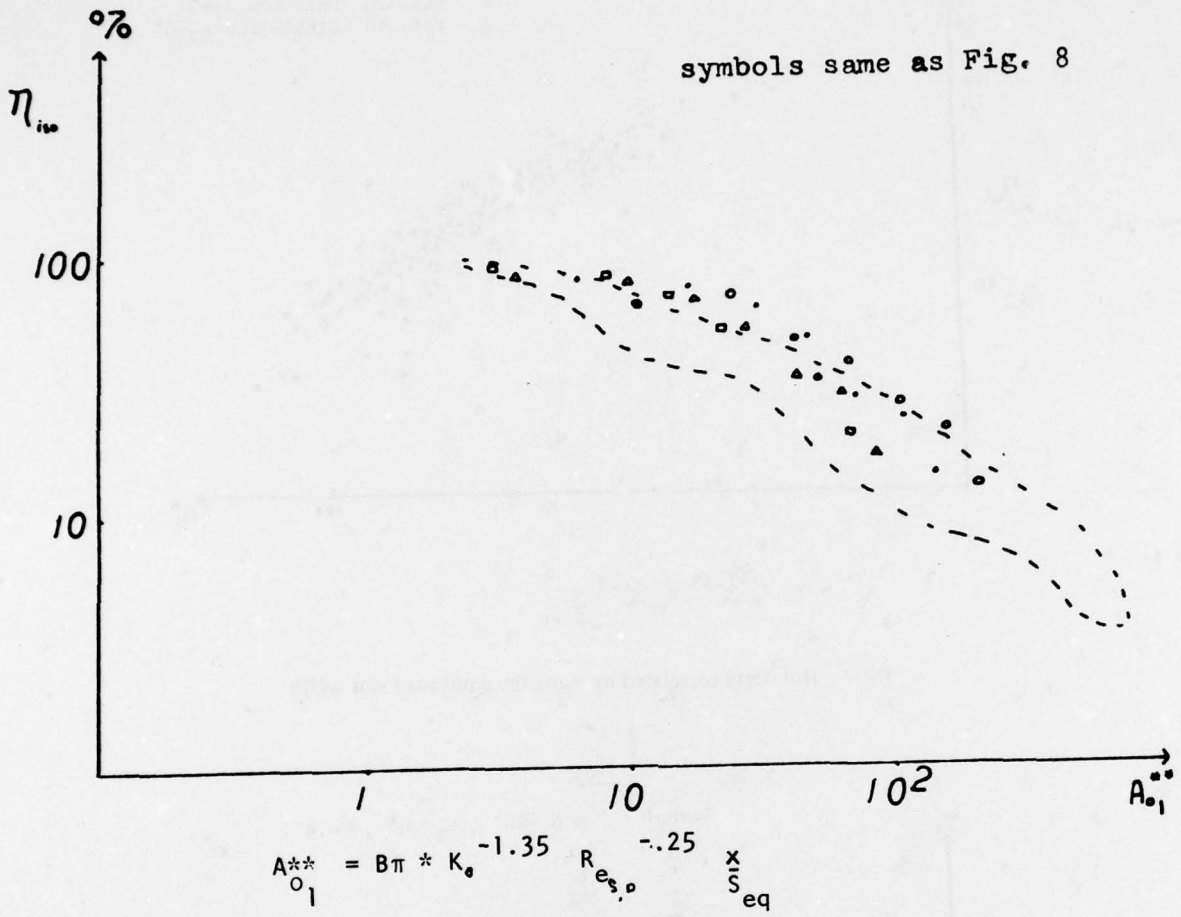

Fig.9 The hole and slot data align using the π^* correction in the parameter A_o

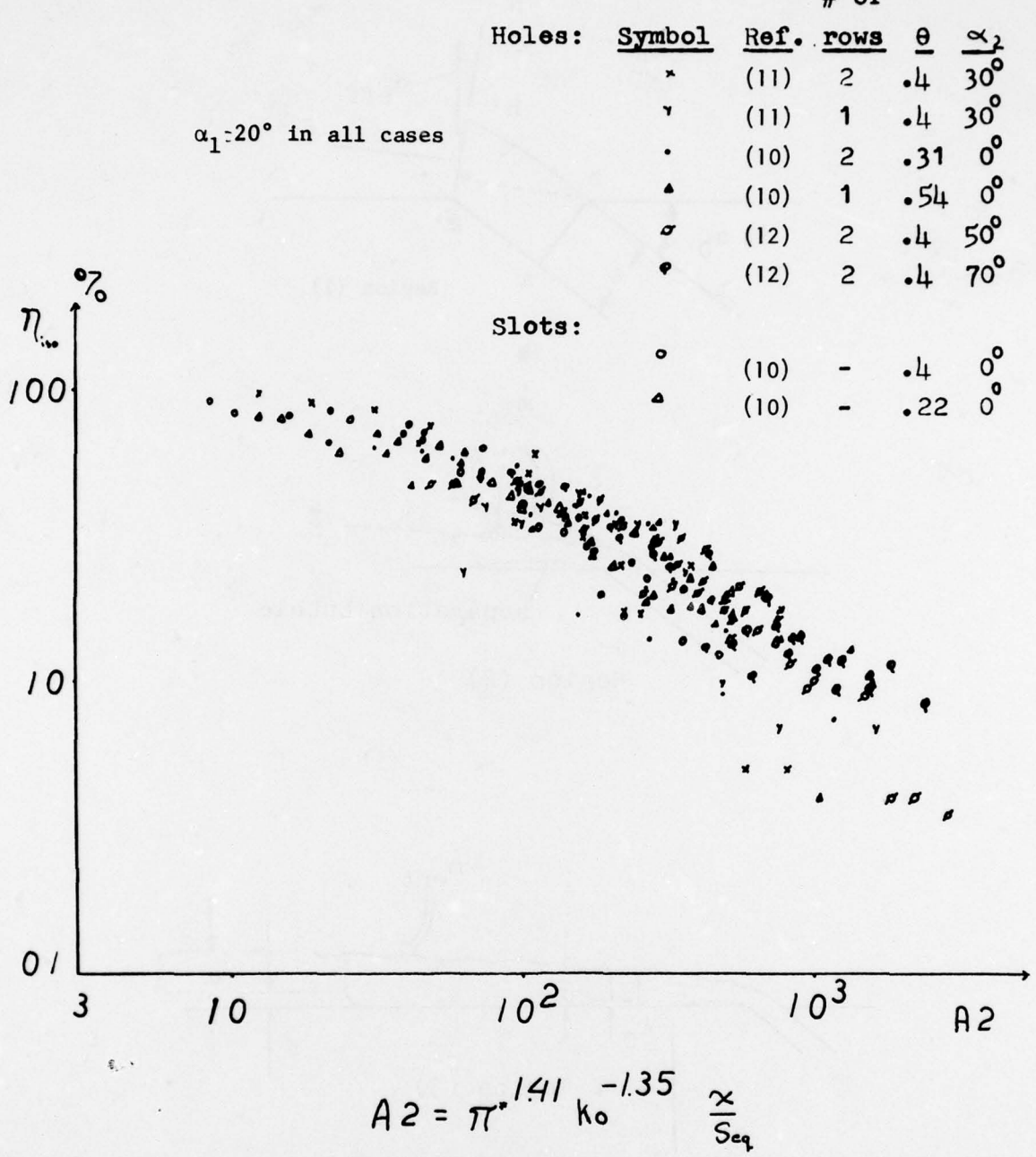

Fig.10 General correlation of film cooling data utilizing many different geometries

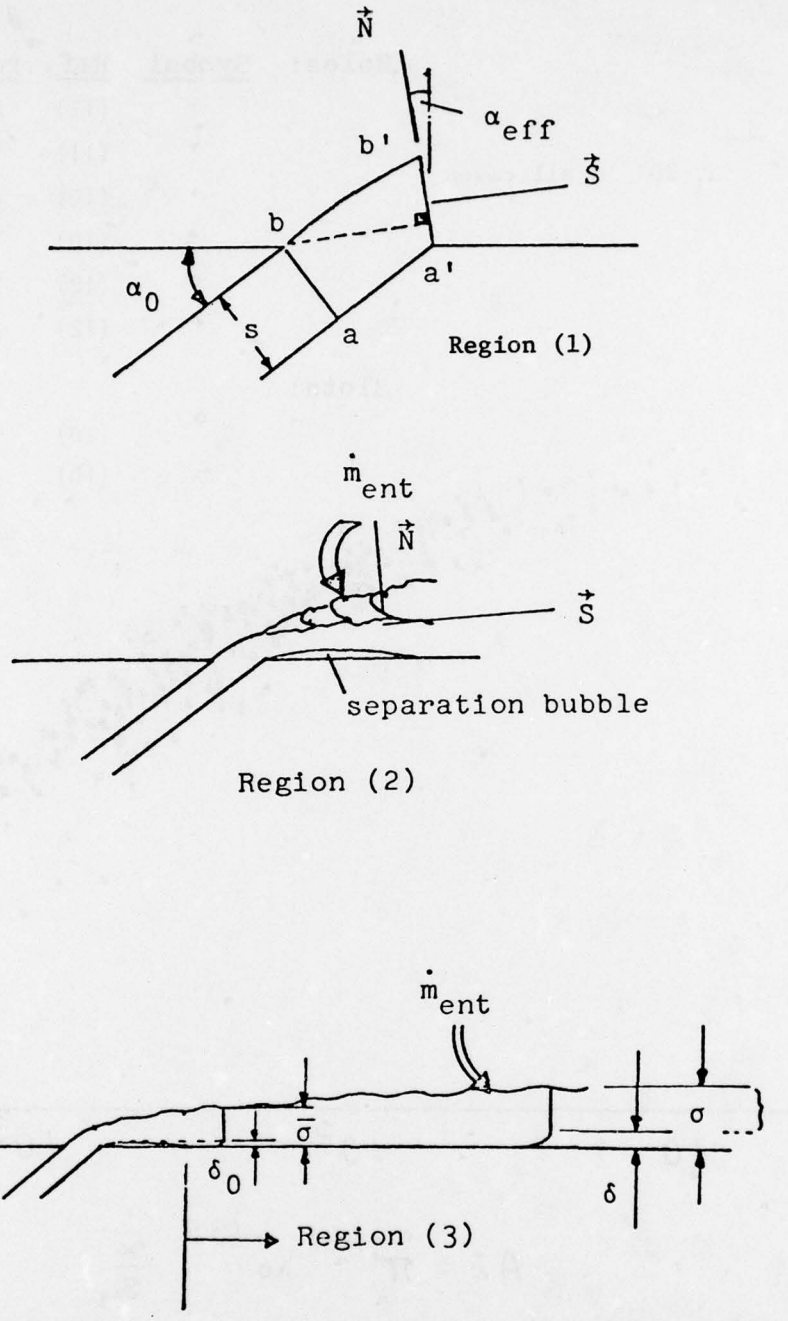

Fig.11 Structure of the flow considered in the numerical model

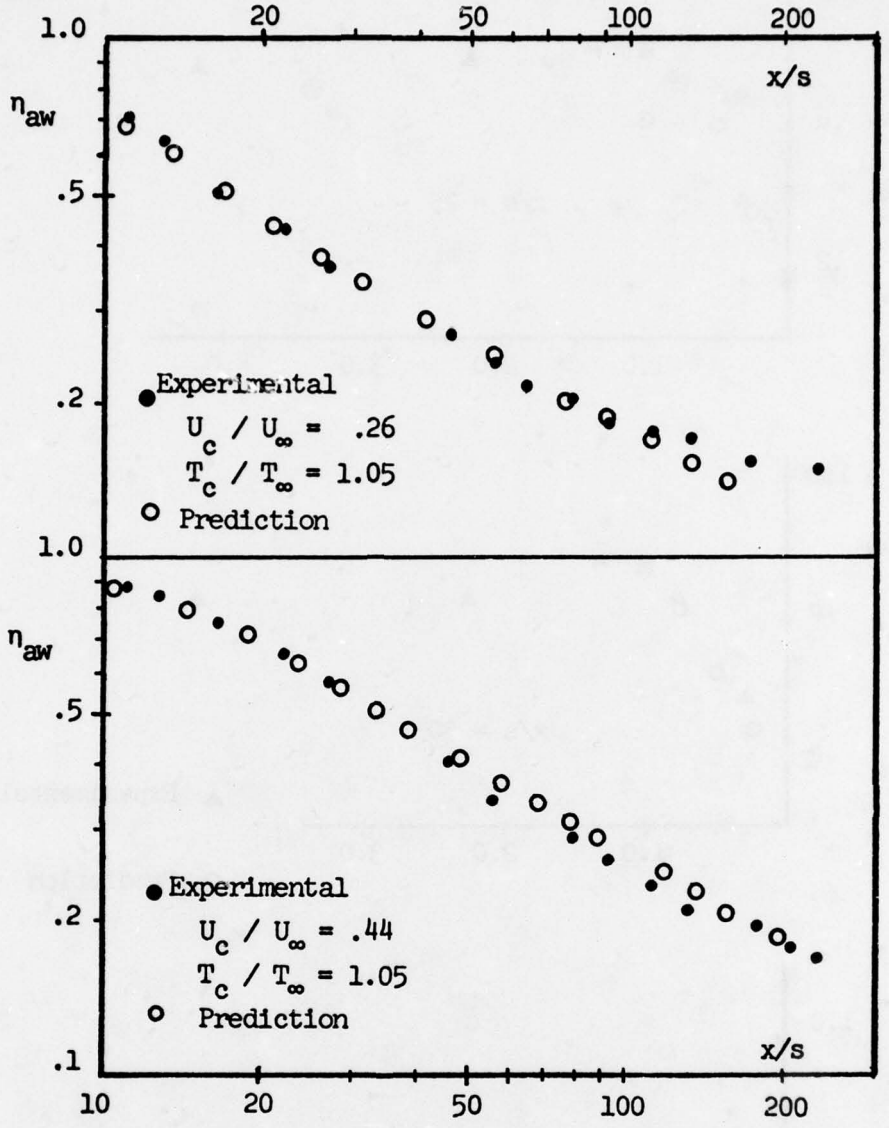

Fig.12 Prediction of experimental data of Chin et al.[13]

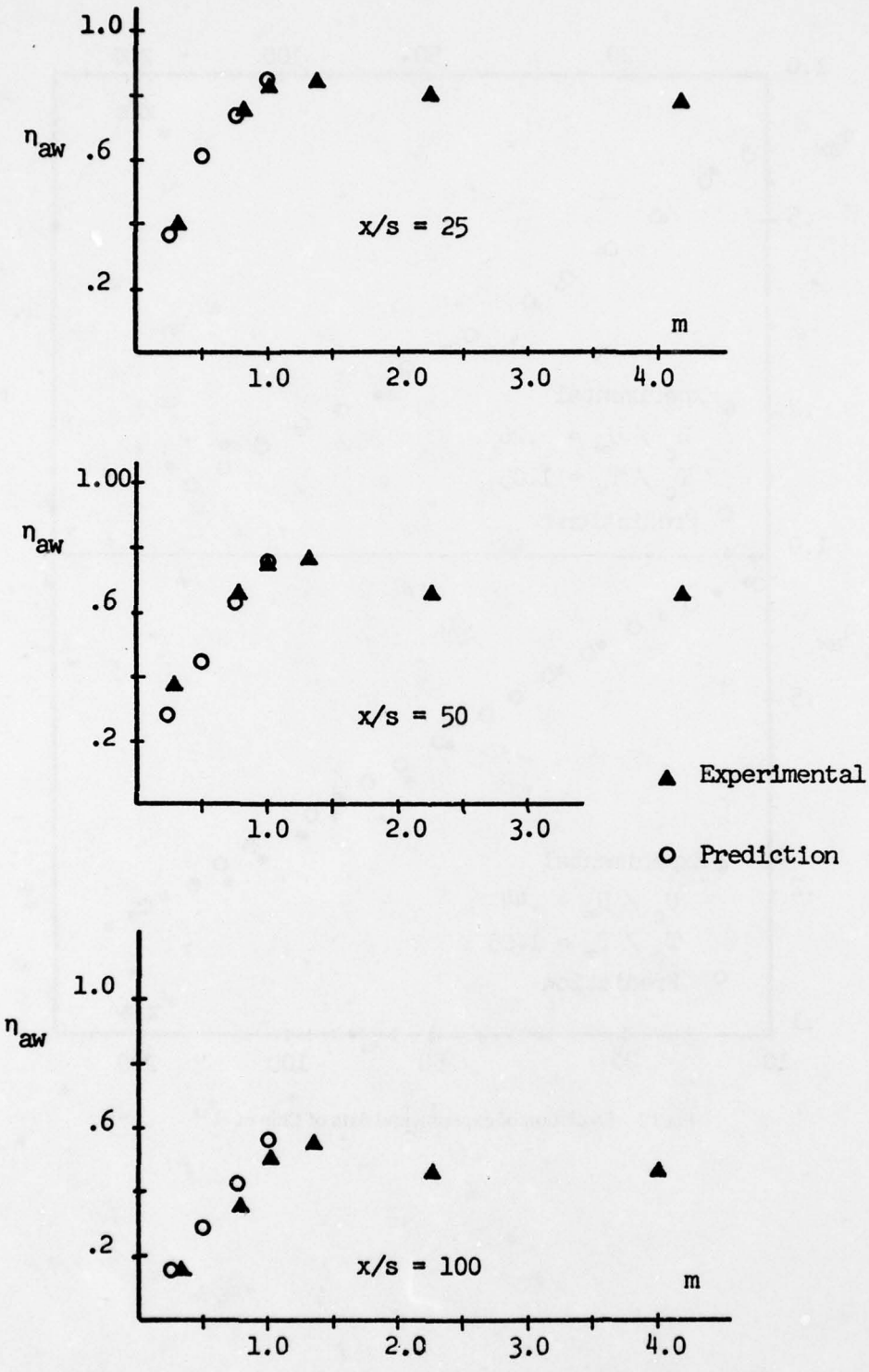

Fig.13 Prediction of experimental data of Sivisigaram and Whitelaw[14]

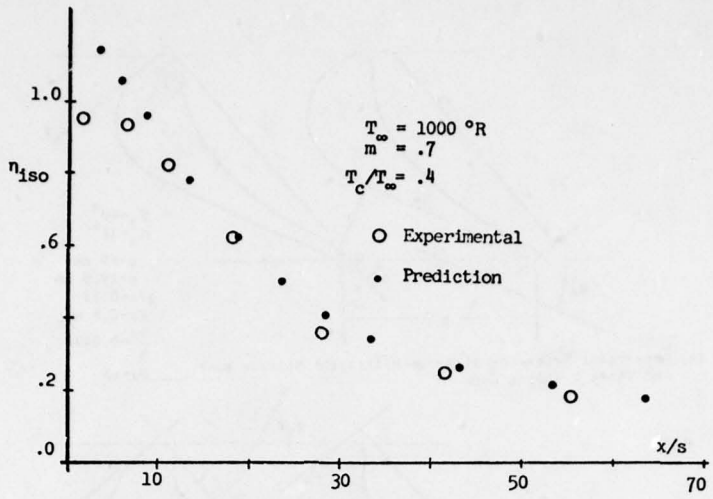

Fig.14(a) Comparison of experimental data[10] and prediction (m = .7)

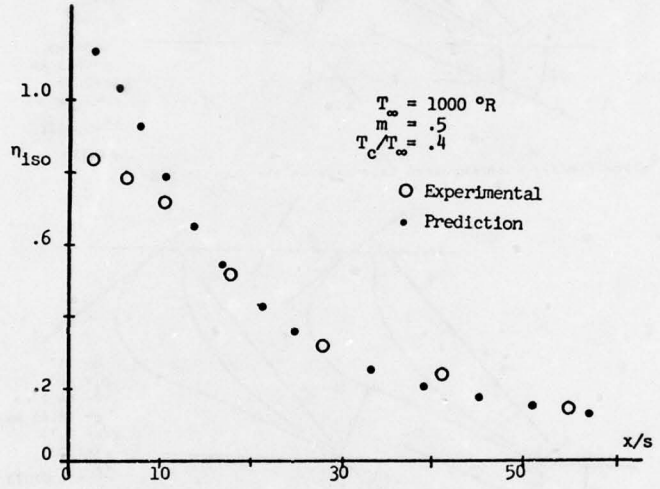

Fig.14(b) Comparison of experimental data[10] and prediction (m = .5)

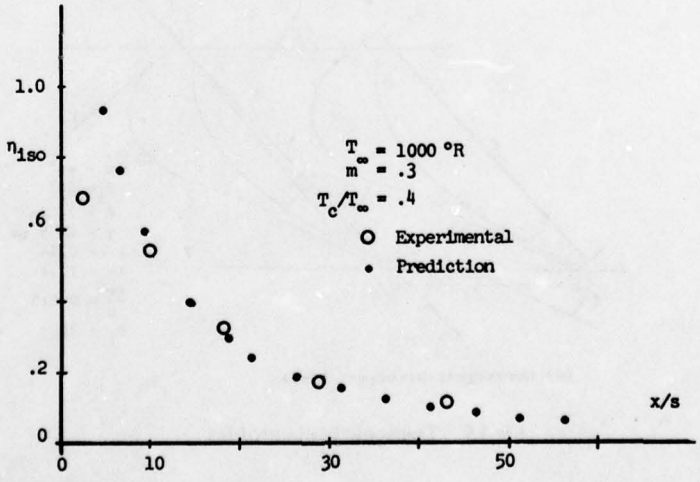

Fig.14(c) Comparison of experimental data[10] and preduction (m = .3)

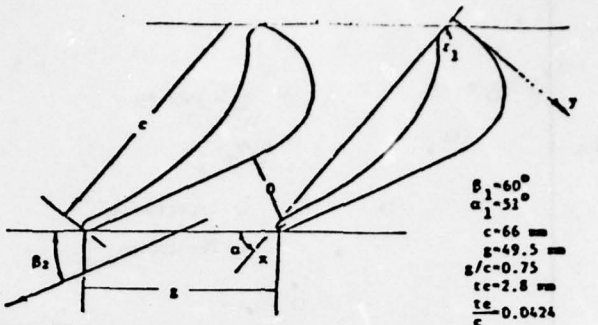

(a) Convergent Reference Blade with Straight Suction Back and Thick Trailing Edge

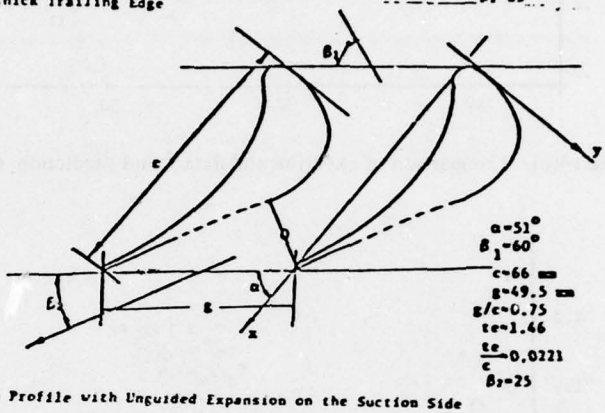

(b) Blade Profile with Unguided Expansion on the Suction Side

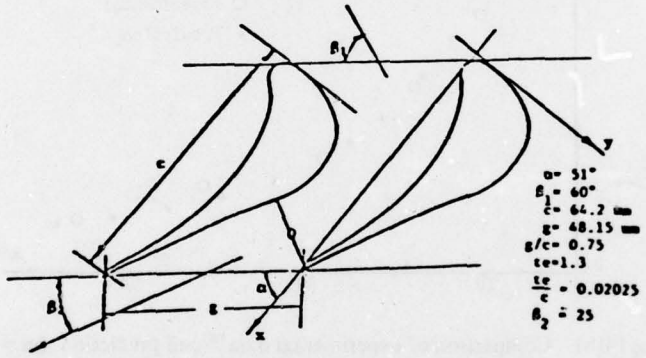

(c) Convergent Blade with Straight Suction Back but Thin Trailing Edge

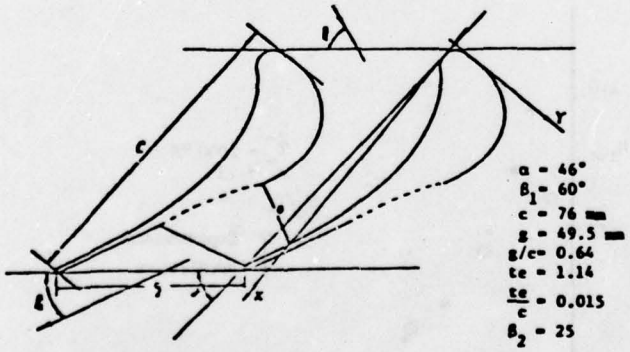

(d) Convergent-Divergent Blade

Fig.15 Transonic blade profiles

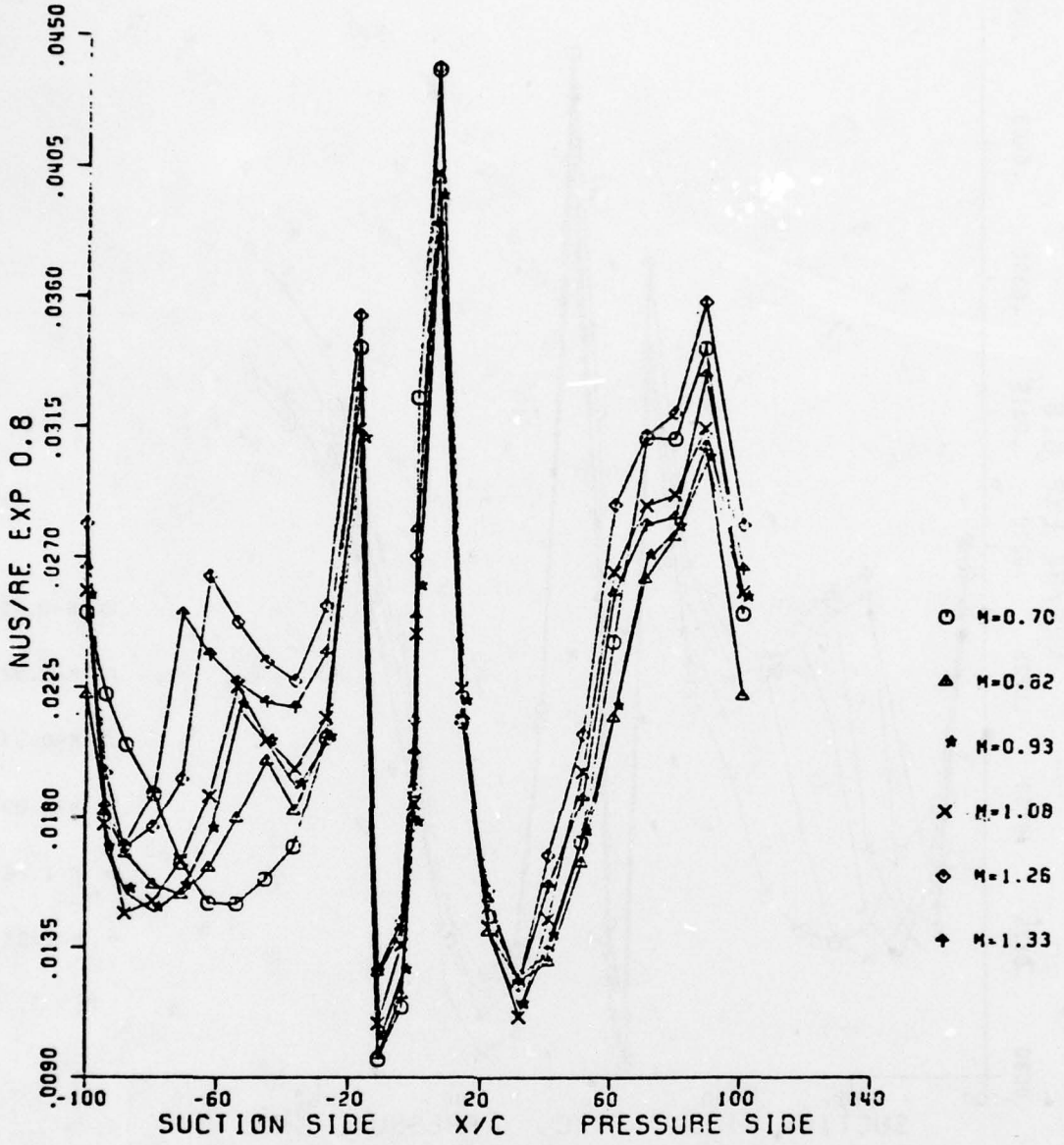

Fig.16 Blade 1 distribution of $Nu/Re^{0.8}$ over the blade surface

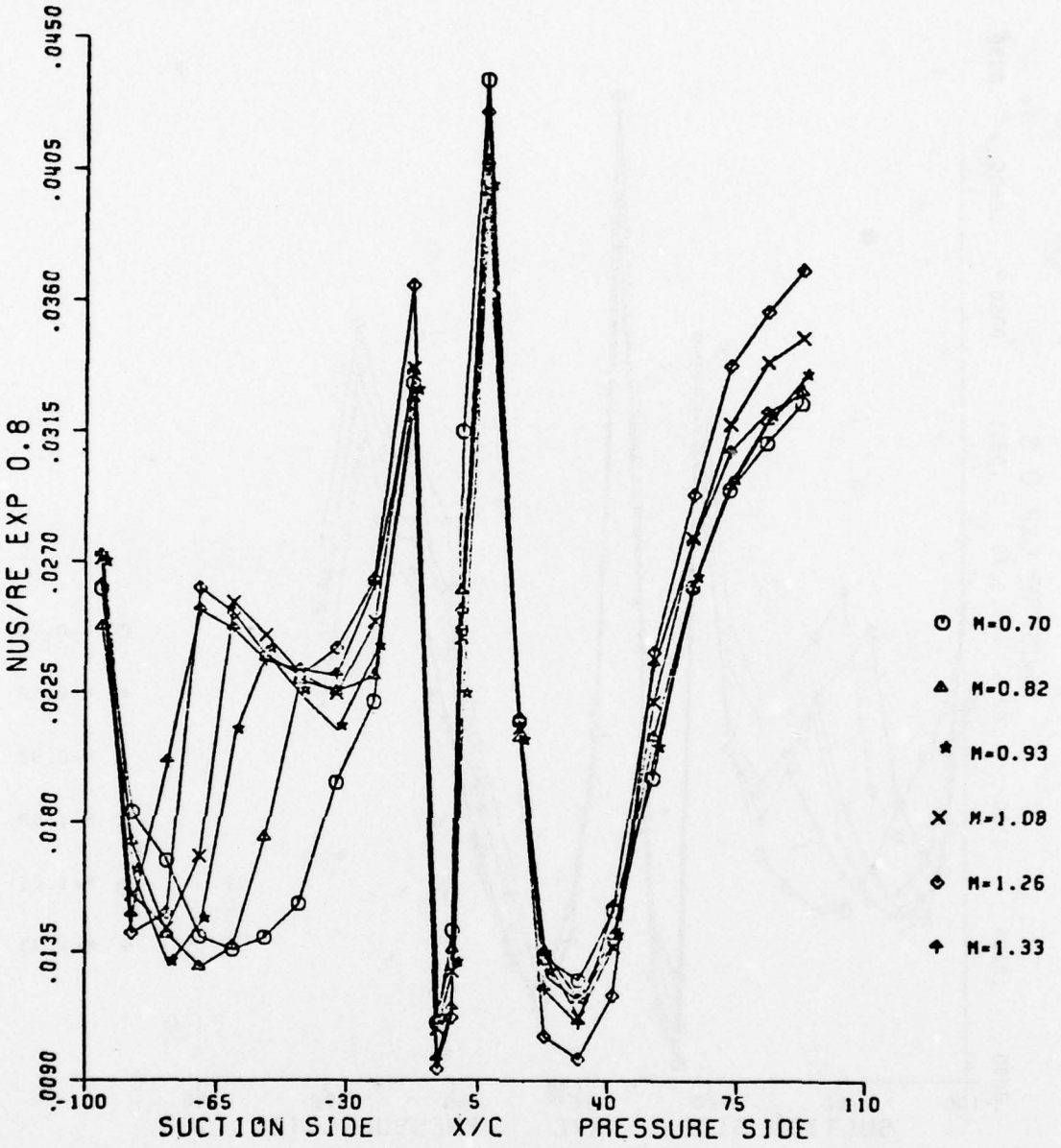

Fig.17 Blade 3 distribution of $Nu/Re^{0.8}$ over the blade surface

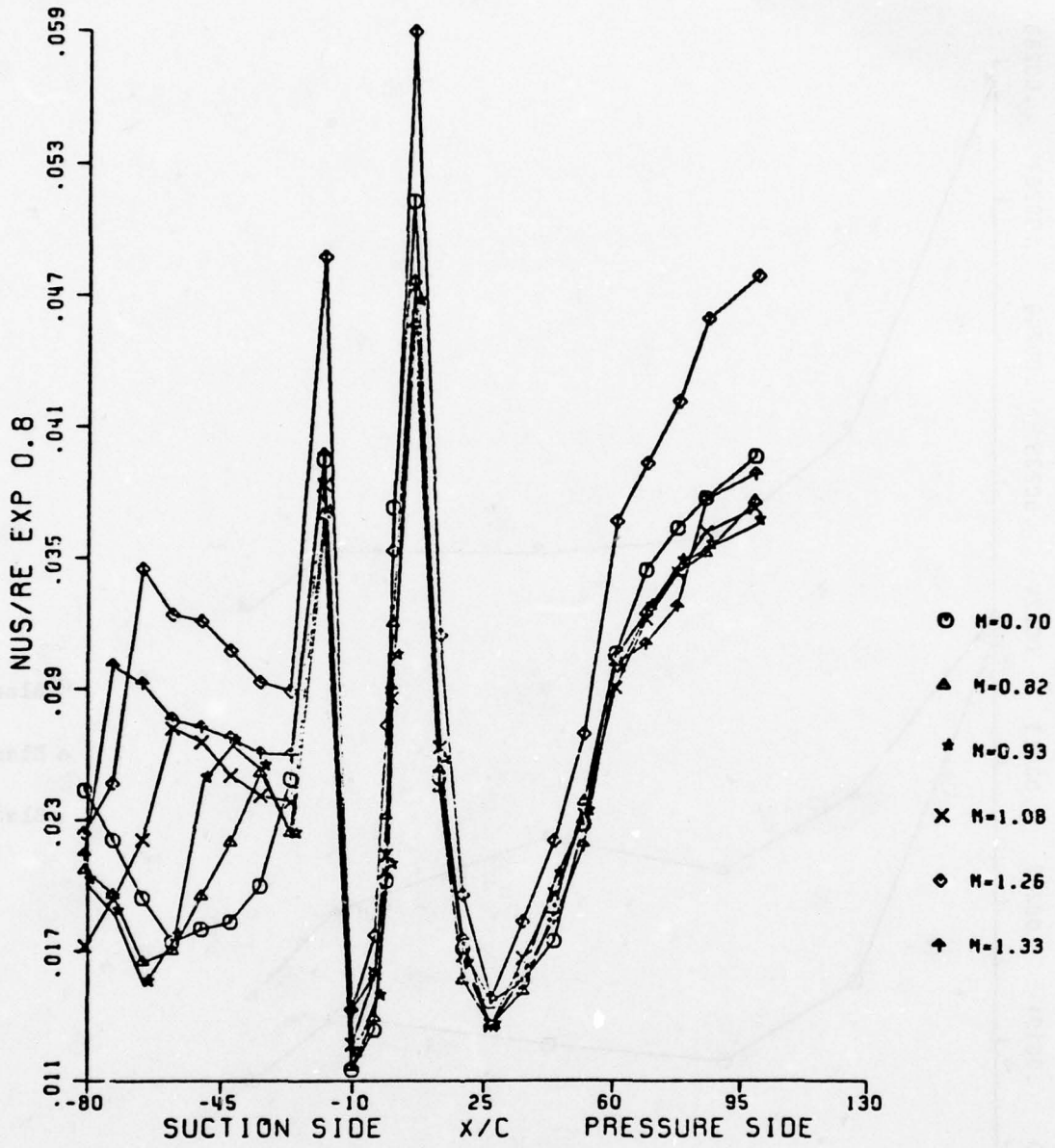

Fig.18 Blade 4 distribution of $Nu/Re^{0.8}$ over the blade surface

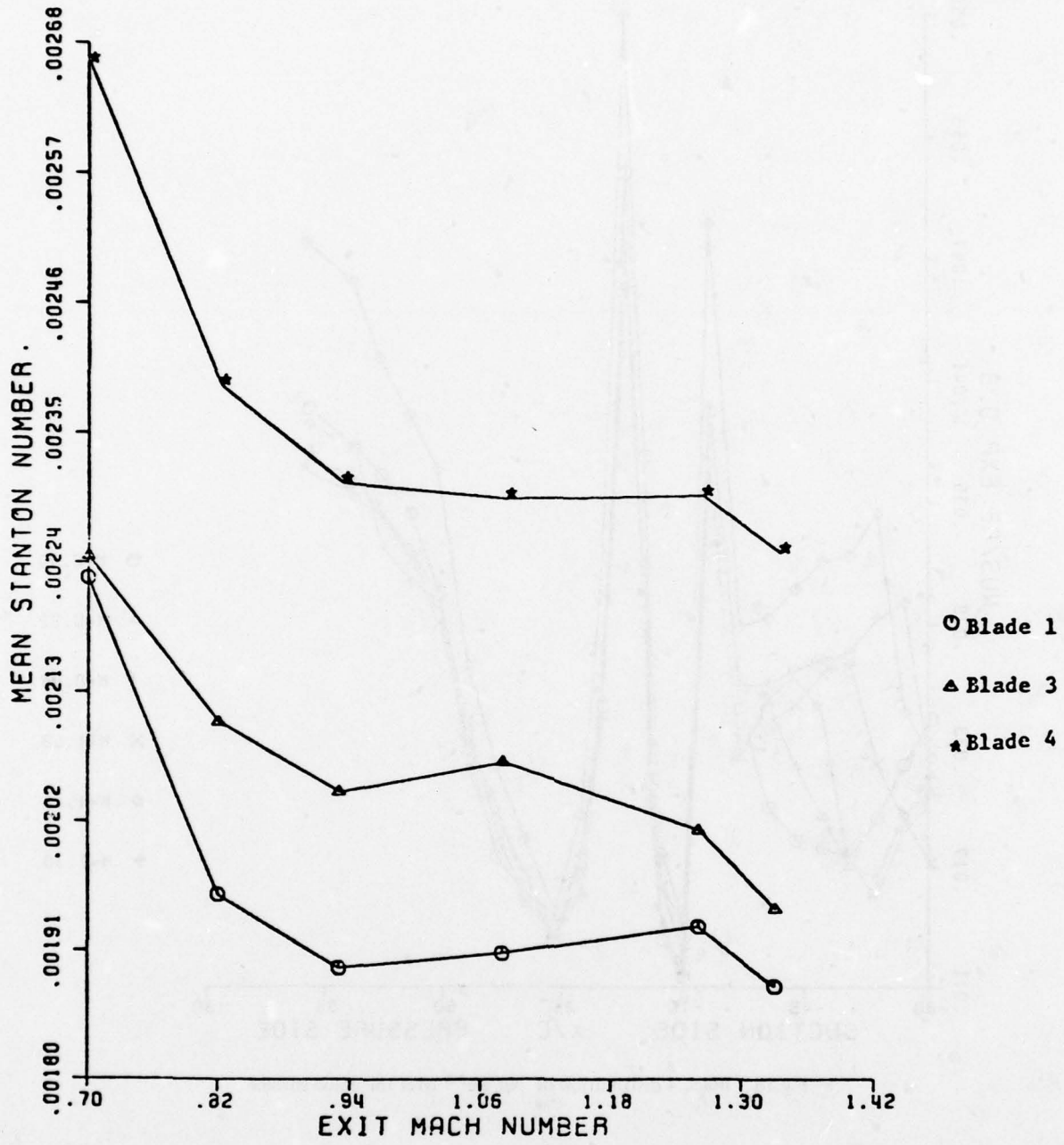

Fig.19 Blade average Stanton number versus exit Mach number

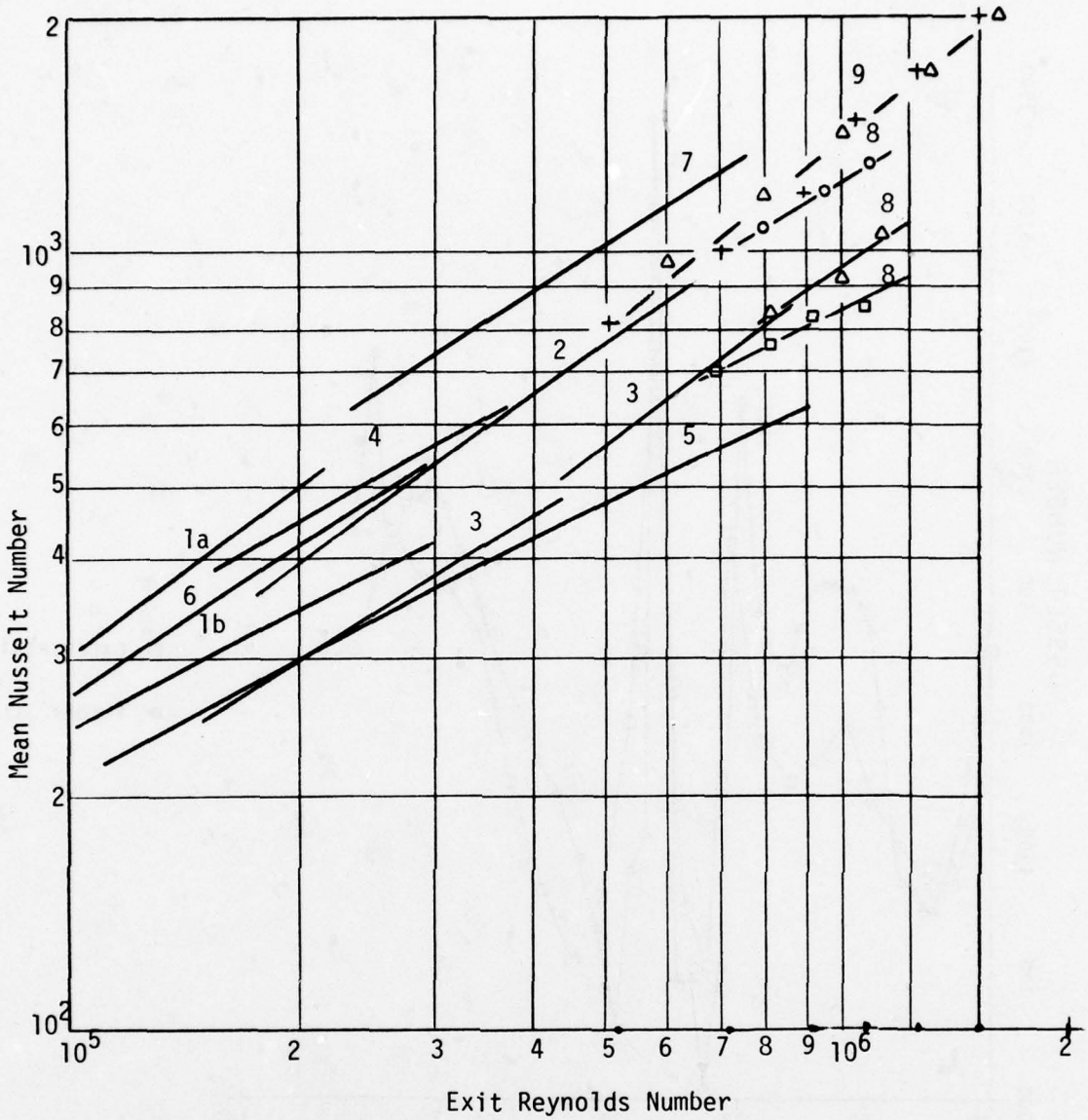

1a	Ainley turbine	(ref. 18)
1b	Ainley cascade	
2	Wilson and Pope	(ref. 19)
3	Hodge	(ref. 20)
4	Bammert and Hahnemann	(ref. 21)
5	Andrews and Bradley	(ref. 22)
6	Fray and Barnes	(ref. 23)
7	Halls	(ref. 24)
8	Turner	(ref. 25)

Symbol	Turbulence
○	5.9%
△	2.2%
□	0.45%

9 Experiment 15△, 16+ } 10%

Fig.20 Heat transfer results

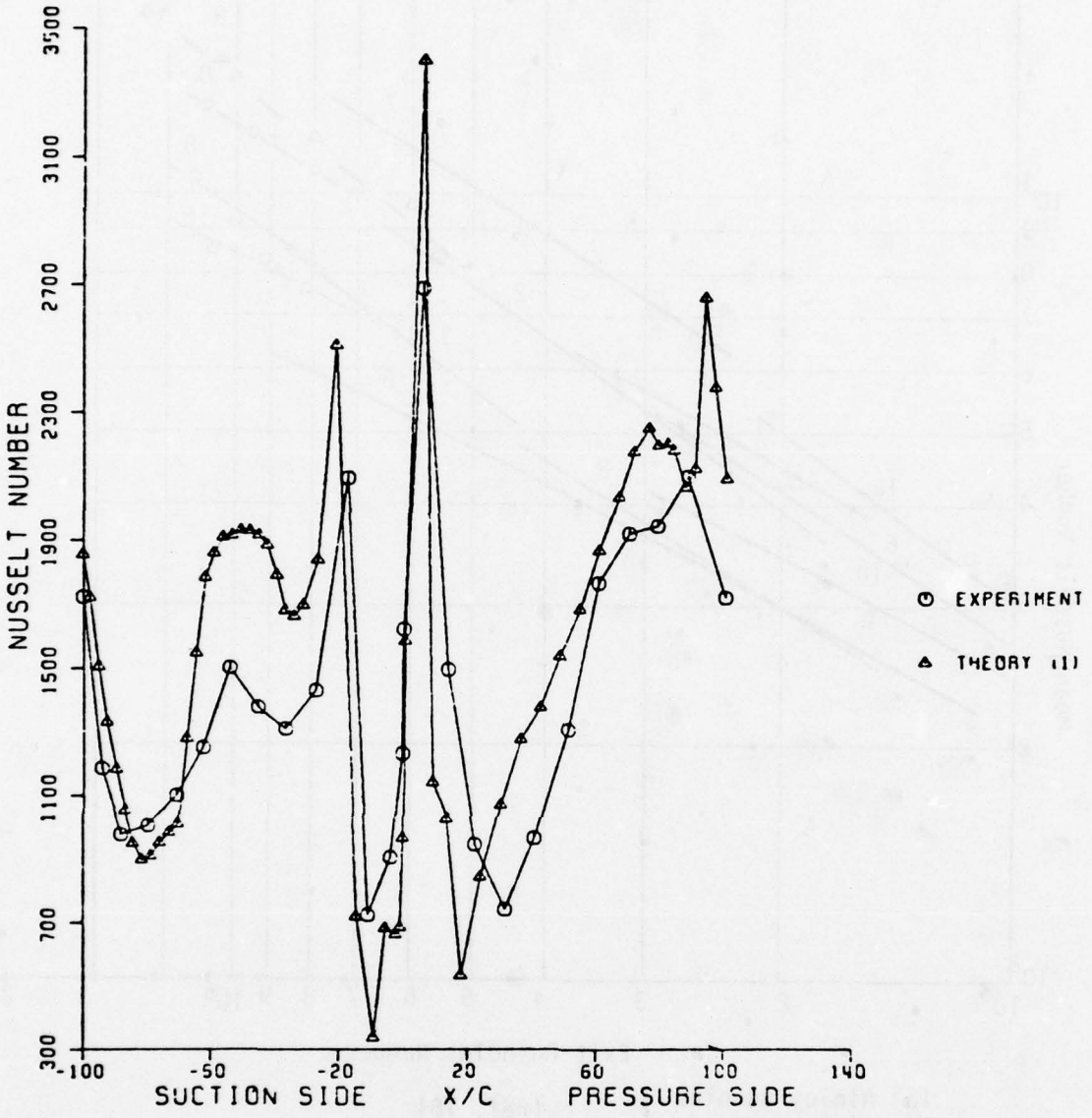

Fig.21 Comparison between $Nu_{experimental}$ and $Nu_{theoretical\ prediction}$ for blade I and M = 1.08

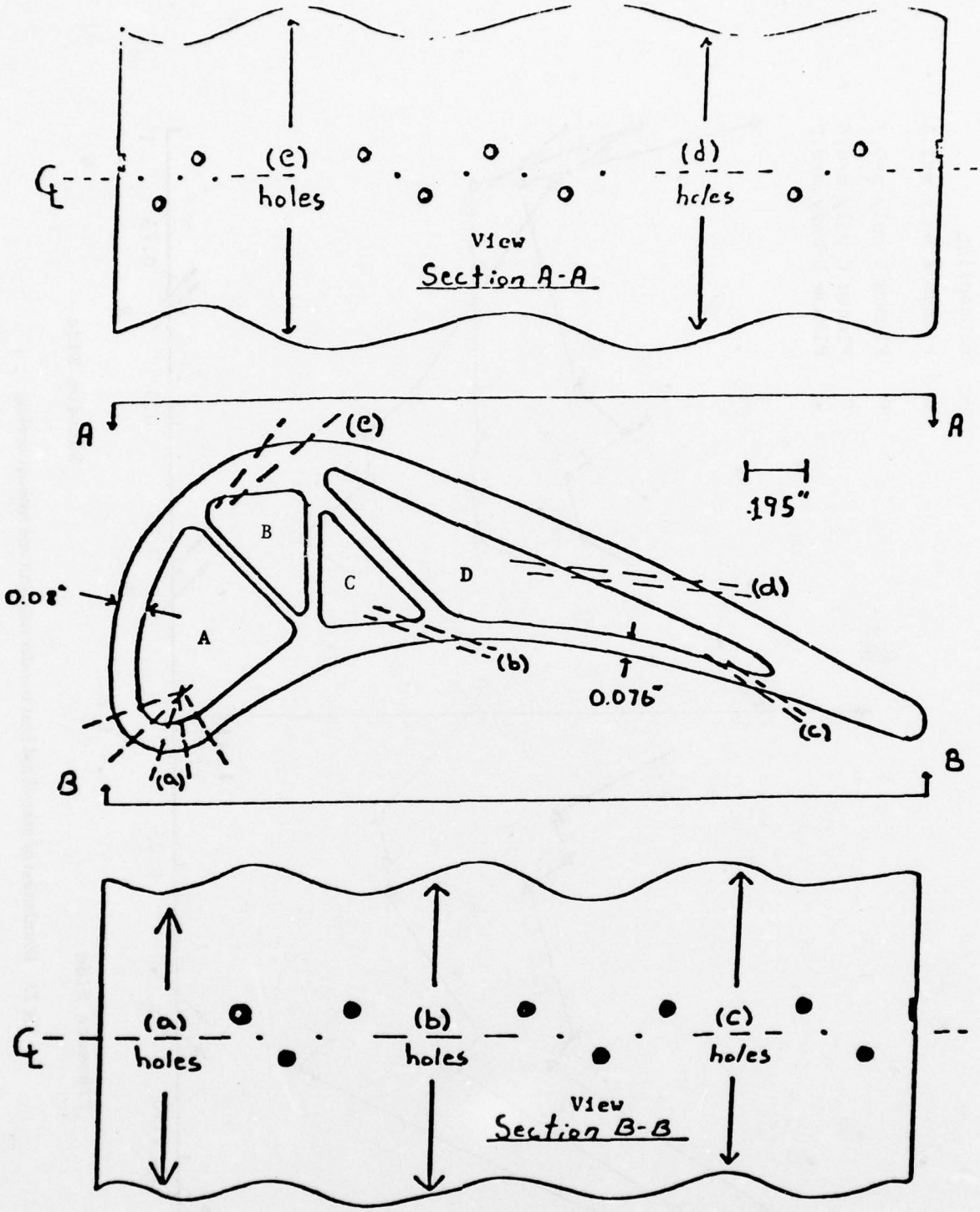

Fig.22 Dashed lines are hole center lines. All holes are 0.040" diameter.
Angles of holes $C_L\alpha_1$ to surface tangent are:
(a) $-90°$, (b) and (c) $-19°$, (d) $-20°$, (e) $-40°$
● represent heat transfer gauges • represent pressure taps

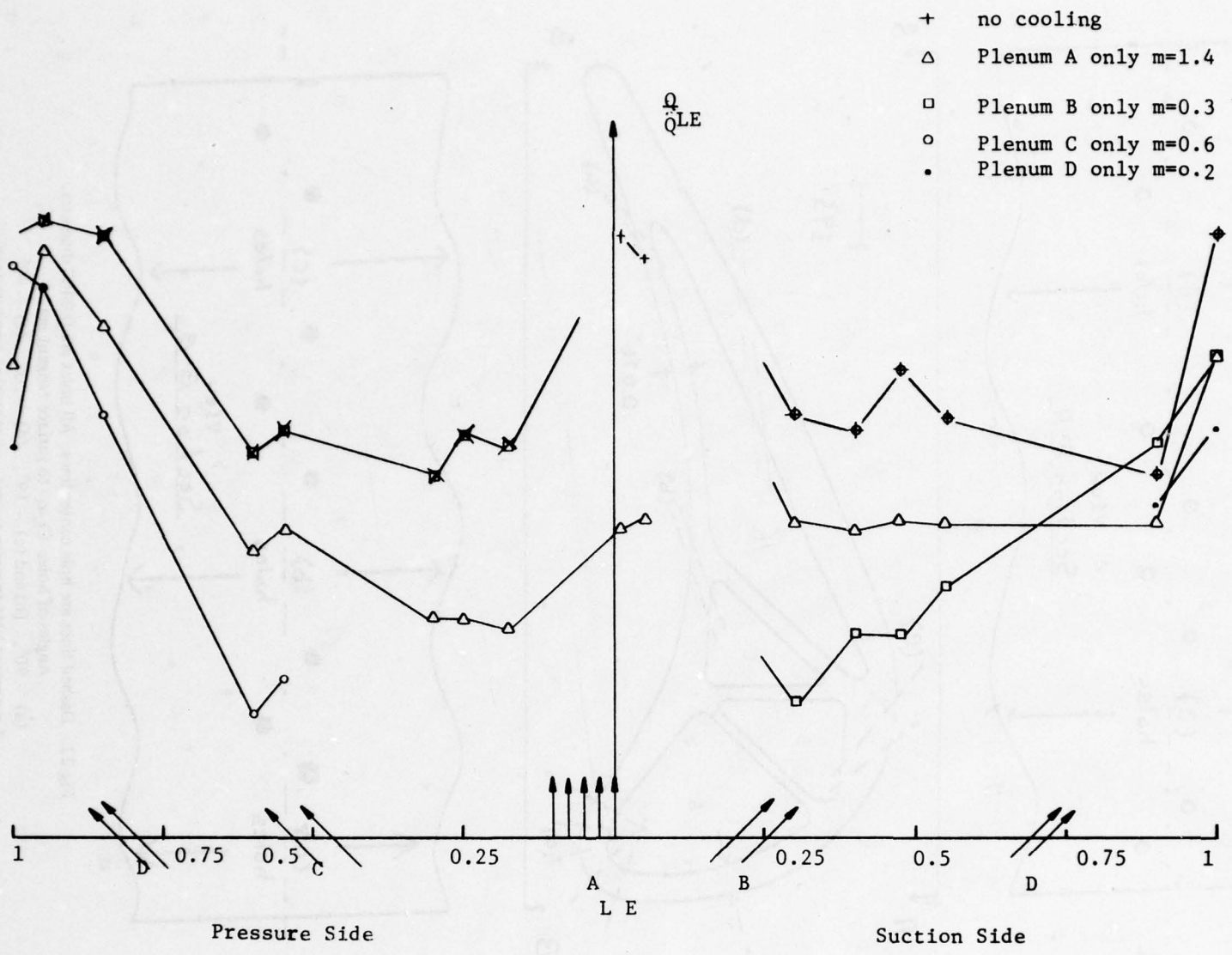

Fig.23 Distribution of normalized heat transfer rate with and without cooling

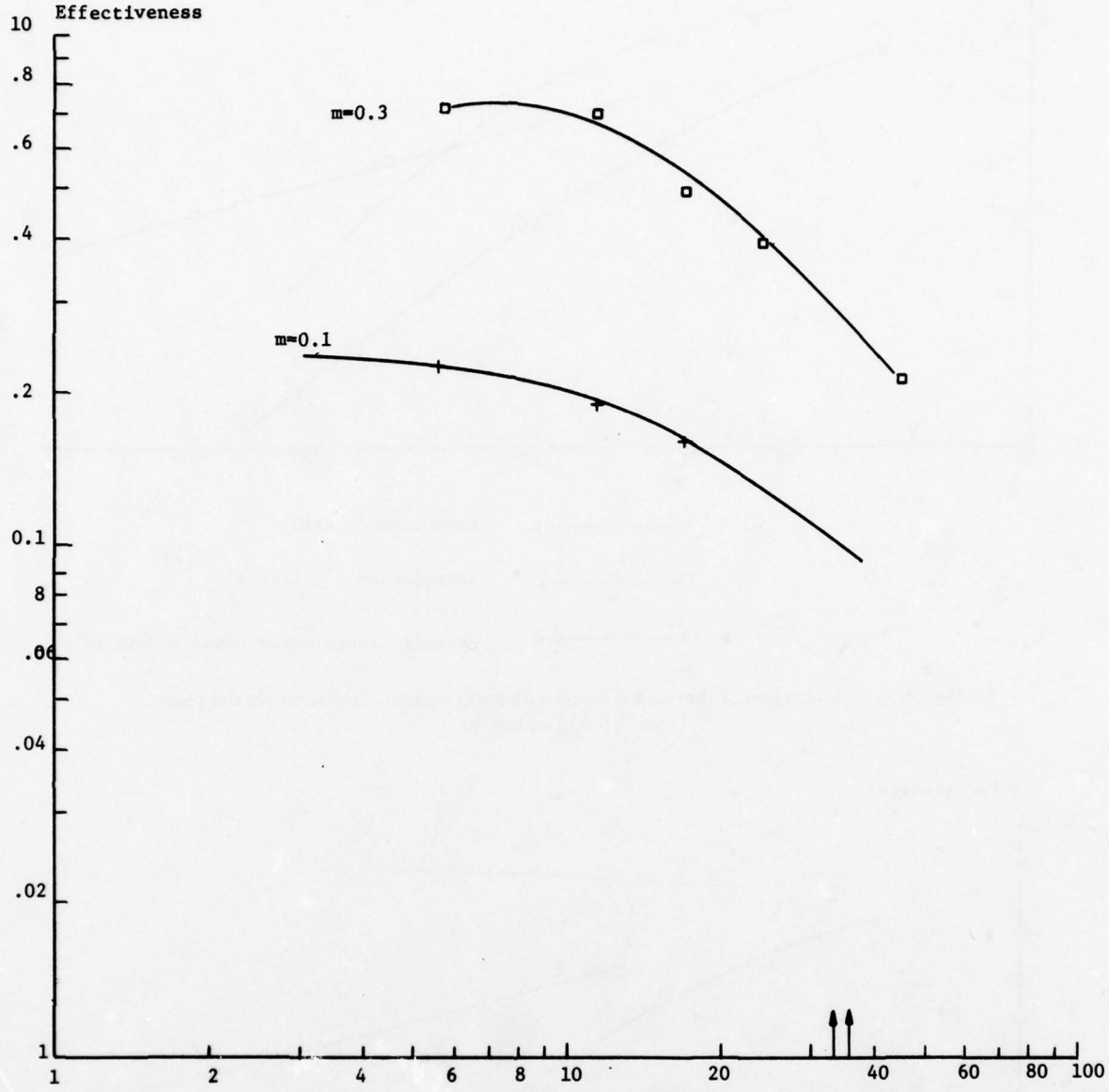

Fig.24(a) Effectiveness of film injected from plenum B on the suction side of the blade as a function of the ratio of length of hole diameter (S/D)

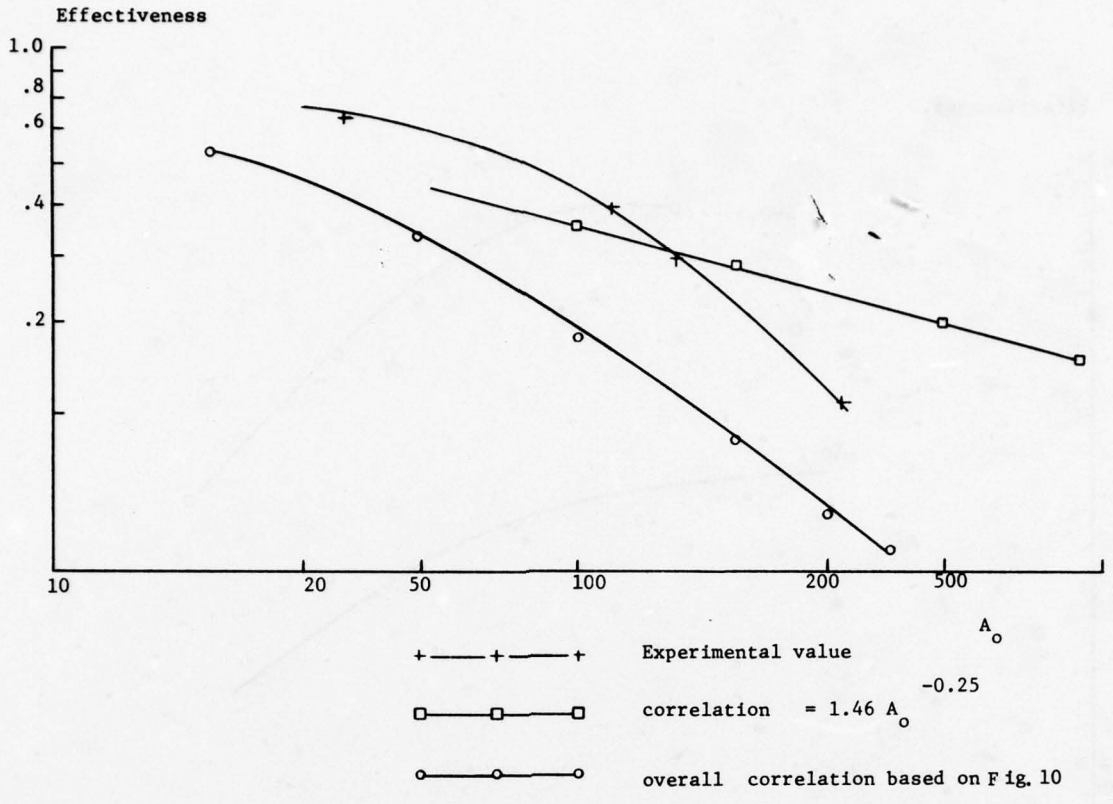

Fig.24(b) Comparison of film effectiveness with experimental correlation for flat plate (m = 0.3, plenum B)

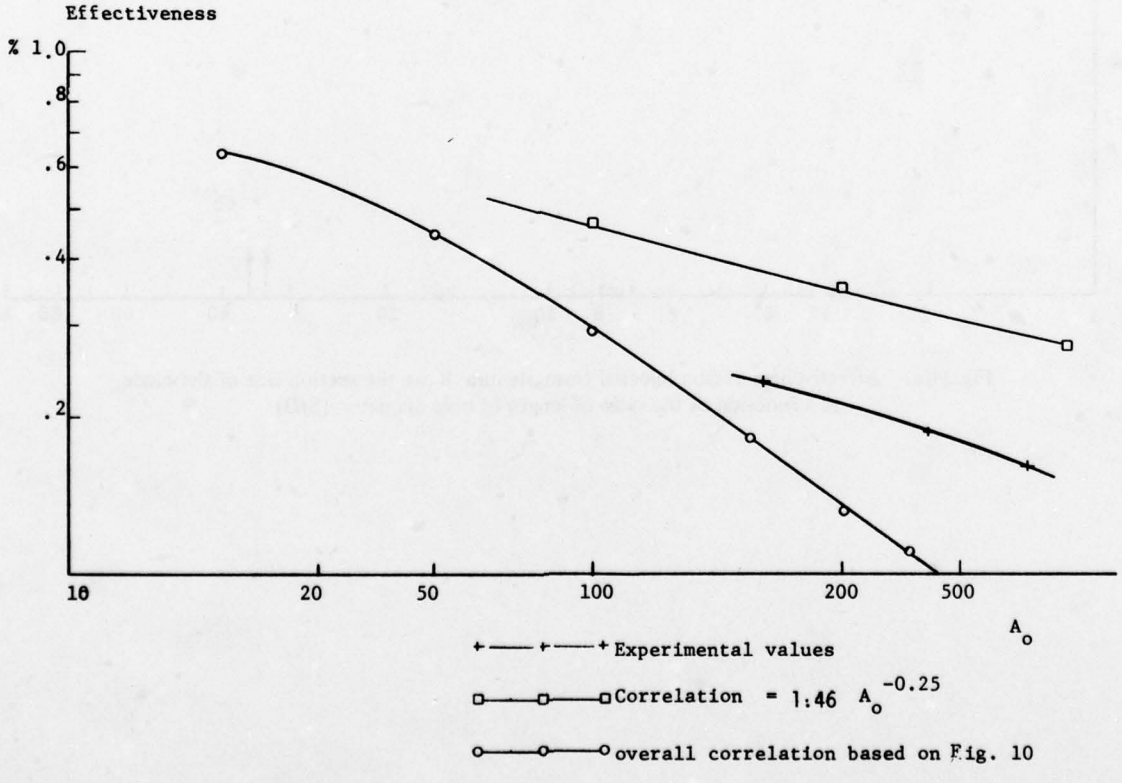

Fig.24(c) Comparison of film effectiveness with experimental correlation for flat plate (m = 0.1, plenum B)

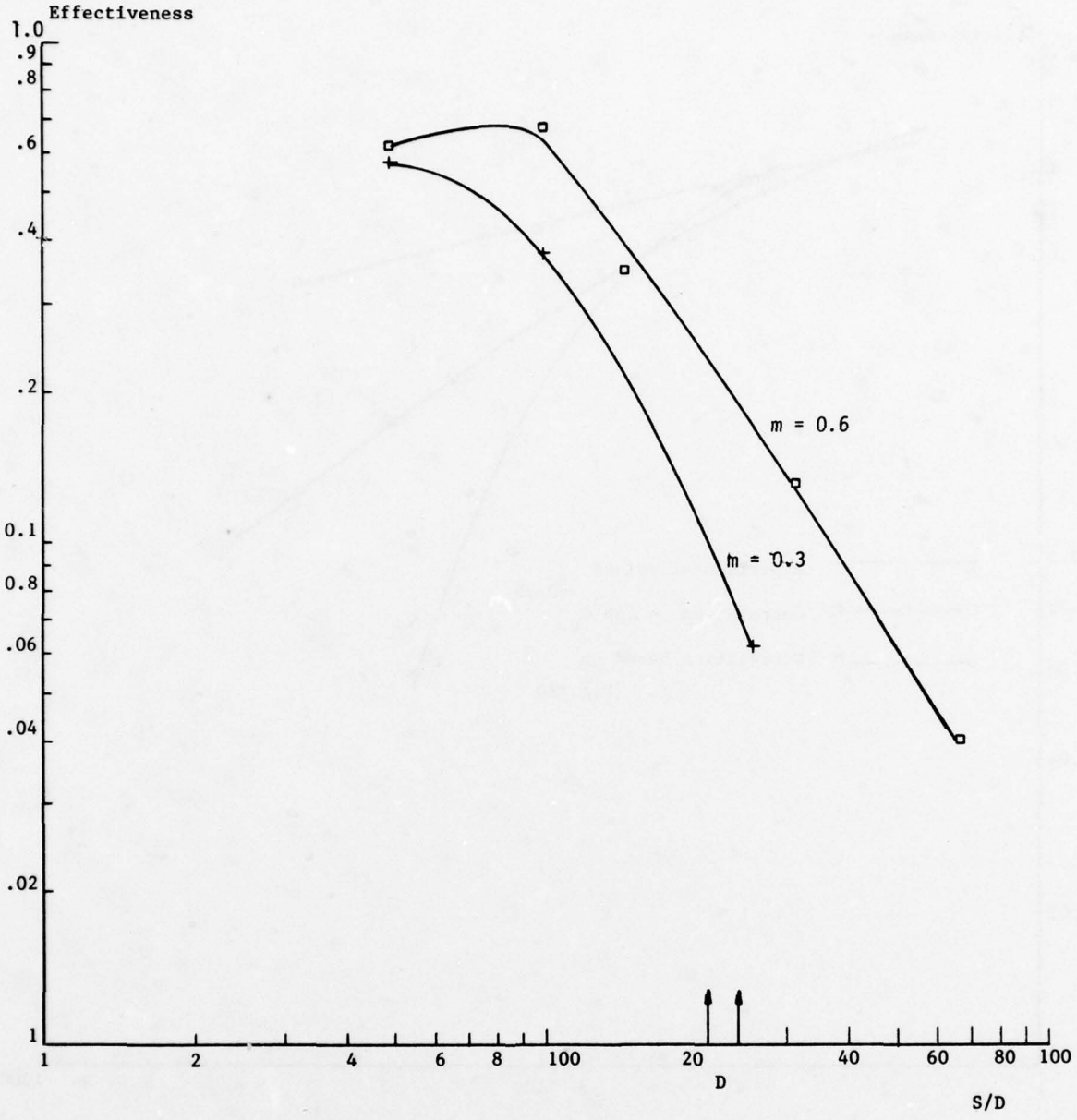

Fig.25(a) Effectiveness of film injected from plenum C on the pressure side of the blade as a function of the ratio length to diameter S/D

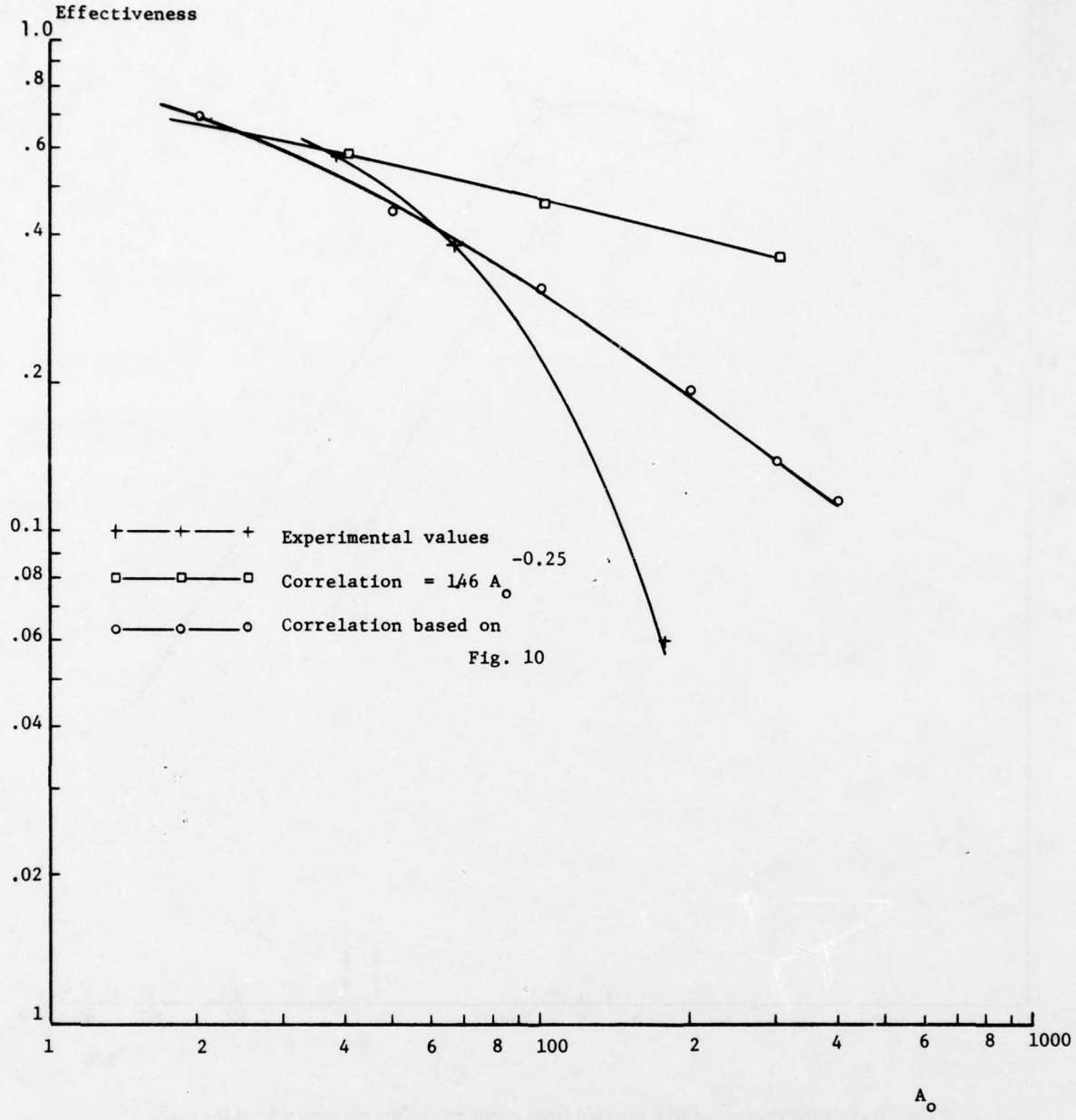

Fig.25(b) Comparison of film effectiveness with experimental correlations for flat plate (m = 0.3, plenum C)

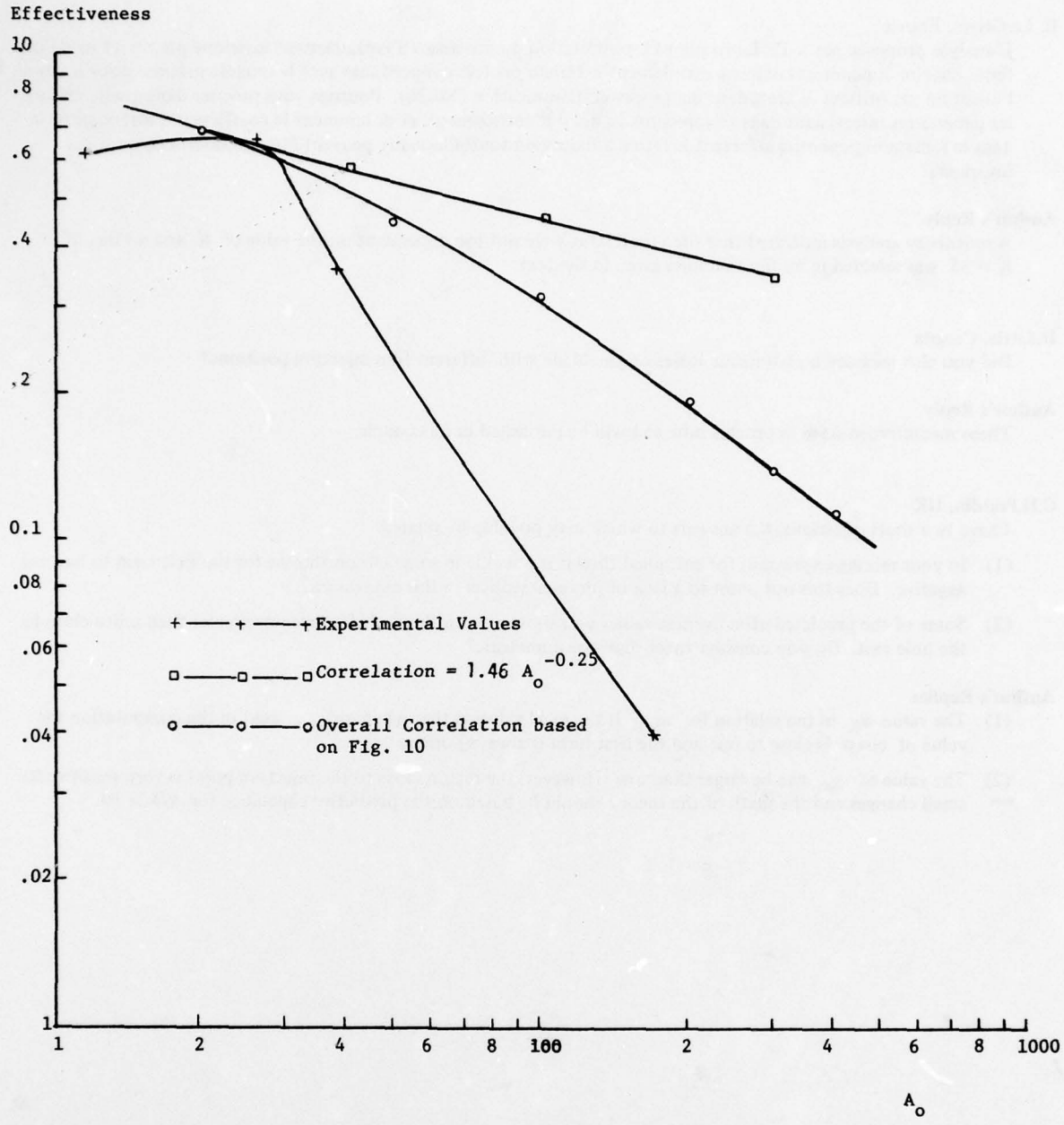

Fig25(c) Comparison of film effectiveness with experimental correlations for flat plate (m = 0.6, plenum C)

DISCUSSION

E. Le Grivès, France

L'analyse proposée par le Dr Louis pour l'interprétation du processus d'entrainement massique par un jet issu d'une fente linéaire et pénétrant dans un écoulement extérieur est très condordante avec le modèle proposé pour le cas de l'injection par orifices discrets dans ma propre communication (No.36). Pourriez vous préciser dans quelle mesure les paramètres intervenant dans l'expression du débit d'entrainment, et notamment le coefficient d'atténuation K dans le facteur exponentiel affectant le terme d'induction tourbillonnaire peuvent être considérés comme des invariants?

Author's Reply

A sensitivity analysis indicated that the predictions were not too dependent on the value of K and a value of $K = 35$ was selected in all the examples given in the text.

D.Little, Canada

Did you also measure aerodynamic losses on the blade with different film injection positions?

Author's Reply

These measurements are in process now and will be published in due course.

C.H.Priddin, UK

I have two short questions, the answers to which may possibly be related.

(1) In your mixing expression for entrained flow it is possible in some circumstances for the first term to become negative. Does this not point to a lack of physical realism in this expression?

(2) Some of the predicted effectiveness values you show have isothermal effectiveness greater than unity close to the hole exit. Do you consider this behaviour unrealistic?

Author's Replies

(1) The value α_K in the relation for $\dot{m}_{ent}$ is the local value so that when $\dot{m}_{ent}$ is used in the computation the value of $\cos\alpha$ is close to one and the first term is always positive.

(2) The value of η_{iso} can be larger than one. However, the region close to the injection point is very sensitive to small changes and the math of the theory should be based on the predictive capability for $x/\delta > 10$.

EFFECTS OF FILM INJECTION ON PERFORMANCE OF A COOLED TURBINE*

BY
JAMES D. MCDONEL
MANAGER - TURBINE COOLING DESIGN
AND
JAMES E. EISWERTH
ENGINEER - TURBINE COOLING DESIGN
GENERAL ELECTRIC COMPANY
AIRCRAFT ENGINE GROUP
EVENDALE, OHIO 45215
USA

SUMMARY

Tests have been conducted on a 20-inch (.508 m.) diameter single-stage air-cooled turbine designed to evaluate the effects of film cooling air on turbine aerodynamic performance. A previous paper reports the results of five test configurations, including two different cooling designs and three combinations of cooled and solid airfoils. A comparison is made of the experimental results with a previously published analytical method of evaluating film injection effects on turbine performance.

The results of these tests are used to determine the effects of film cooling on overall engine performance for selected cycle conditions. These engine performance studies are used to show the cycle benefits of increased gas temperature at various coolant flow rates.

LIST OF SYMBOLS

g	Gravitational constant
h_1	Turbine inlet enthalpy (BTU/lbm), (J/kg)
h_{1c}	Coolant inlet enthalpy
h_{3p}	Turbine discharge ideal enthalpy of primary flow
h_{3c}	Turbine discharge ideal enthalpy of coolant
J	Mechanical equivalent of heat
P_{t1}	Turbine inlet total pressure (psia),(N/m^2)
P_{t3}	Turbine discharge total pressure
$T_{4.1}$	Turbine rotor inlet total temperature (^oR),(^oK)
T_{t1}	Turbine inlet total temperature
T_{tr}	Turbine rotor relative total temperature
T_{tc}	Coolant inlet total temperature
U_m	Rotor blade velocity at turbine flowpath mean radius (ft/sec),(m/sec)
U_c	Rotor velocity at cooling inducer radius
V_{uc}	Tangential component of rotor coolant velocity at inducer discharge
$\dot{W}_{4.1}$	Turbine rotor inlet mass flow rate (lbm/sec), (kg/sec)
$\dot{W}_p$	Turbine inlet mass flow rate
$\dot{W}_c$	Coolant mass flow rate
$\dot{W}_v$	Vane coolant mass flow rate
$\dot{W}_b$	Blade coolant mass flow rate
γ	Ratio of specific heats
η_t	Uncooled turbine efficiency
η_{th}	Turbine thermodynamic efficiency

BACKGROUND

There have been many technology advancements in recent years which have led to the development and production of modern high performance turbojet and turbofan aircraft engines. Some of the most dramatic gains have resulted from advancements in turbine cooling technology which permit increased cycle temperatures and the resulting improvement in cycle thermodynamic efficiency. Technology advances have led from early cooling systems which employed mainly simple convection cooling to the current highly sophisticated schemes which combine more effective convection systems with film cooling systems. However, the gain in cycle performance which results from increased cycle temperature is not realized unless the quantity of air used to cool the turbine and the aerodynamic mixing losses resulting from injection of coolant in the form of film on the flowpath surfaces are minimized. There are many technology development programs aimed at maintaining turbine metal temperatures at the desired values for a minimum expenditure of coolant. However, if the coolant injection losses are to be minimized, a more complete understanding of the relationship between cooling and aerodynamics is needed, including detailed knowledge of how coolant injection influences aerodynamic performance.

Recent tests have been undertaken to determine the effects of coolant injection on turbine performance. These results have been summarized in Reference 1 and were compared with an analytical technique developed for predicting coolant injection effects. The present paper will review the results of these tests, the analytical prediction method, and the comparison of results. However, the primary objective of this paper is to relate the important results of Reference 1 to the effects of turbine cooling on overall cycle thermodynamic efficiency. This objective will be obtained by utilizing the analytical prediction technique, shown to give excellent agreement with test results in Reference 1, to calculate incremental changes in turbine thermodynamic efficiency for various incremental changes in coolant flow rate for a typical single stage high pressure turbine matched to drive a modern, core engine compressor. The incremental changes in turbine thermodynamic efficiency and incremental changes in cycle temperature will be used to estimate the changes in overall core engine performance by simple cycle analysis techniques.

*The model turbine tests described in this paper were sponsored by The NASA Lewis Research Center. (Contract NAS3-16732)

TEST PROGRAM

The effects of turbine cooling flows on turbine performance have been experimentally evaluated in a warm air turbine test rig. This test rig features five independent coolant supplies for independent variation of coolant-to-mainstream temperature ratio, pressure ratio, and/or mass flow ratio for different cooling circuits. This permitted simulation of engine values of the appropriate coolant-to-mainstream ratios for the stator vane, stator inner band, stator outer band, rotor blade and rotor stationary shroud cooling systems. The results of tests conducted with the stator vane and rotor blade coolant flow rate variable, while the band and shroud coolants were maintained fixed at design values, have been examined in detail and are presented in Reference 1.

The air turbine design conditions for this experimental program are presented in Table 1 and a schematic of the test rig with station designations is shown in Figure 1. The vane and blade airfoils are constant section, untwisted designs. The meanline vector diagram of this 20 inch (.508m) tip diameter turbine is the meanline vector diagram of a 30 inch (.762 m) tip diameter turbine which was previously tested.[2] The turbine is typical of a moderately loaded first stage, of a two stage group, with subsonic relative velocities throughout.

Table 1 Nominal Air Turbine Test Parameters

Turbine Inlet Total Temperature, T_{t1}	950°F (783°K)
Turbine Inlet Total Pressure, P_{t1}	56.5 psia (3.90 x 10^5 N/m^2)
Turbine Inlet Mass Flow, W_p	24.6 lb/sec (11.2 kg/sec)
Rotative Speed (100%)	10,146 rpm
Tip Diameter	20.0 inches (.508 m)
Hub to Tip Radius Ratio	0.85
Number of Stages	1
Number of Vanes	36
Number of Blades	64
Stage Total to Static Pressure Ratio	2.14
Work Output Corrected to Standard Sea Level Conditions	17.0 btu/lb (3.95 x 10^4 J/kg)

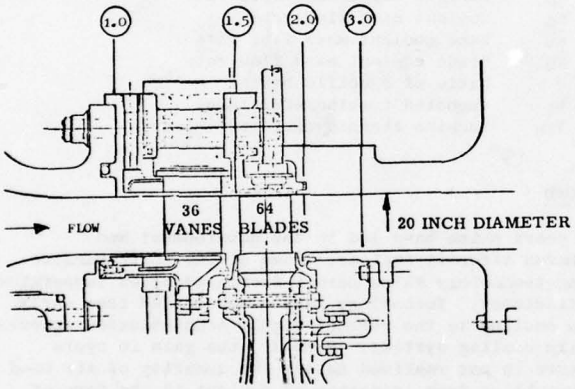

FIGURE 1 Schematic of air turbine with station nomenclature.

The air turbine components were designed to simulate high pressure turbine cooling systems typical of advanced high temperature designs. Stator inner and outer band cooling designs utilize impingement and film systems, where the spent impinged coolant is discharged to the flowpath through discrete rows of film holes. The rotor stationary shroud is a transpiration cooled system.

Two stator vane and rotor blade cooling systems were designed at identical operating conditions. The first blade and vane design, called "full film", consists of an impingement and film system in which spent impinged coolant is discharged to the flowpath through many small diameter holes drilled in the airfoil shells. The small diameter film holes are oriented in the direction of the mainstream flow on the airfoil surface.

The second vane and blade designs, called "discrete film", also consist of impingement/film systems. In the "discrete film" system the number of film holes and rows has been greatly reduced, (approximately 1/3 as many as the "full film") by selectively locating rows of larger diameter film holes such that cooling is maximized by an improved film blanket.

In addition to the above cooled stator vanes and rotor blades, a solid airfoil design was also manufactured for the purpose of obtaining uncooled baseline performance. The same constant section, untwisted airfoil contours were used for both of the cooled designs and for the solid design.

The air turbine experimental program consisted of several series of tests in which coolant flows were varied for each turbine cooling circuit by adjusting the coolant to mainstream pressure ratio in that circuit. Coolant inlet temperature was approximately 60°F (289°K) for all circuits and at design coolant flow rates the coolant-to-mainstream pressure ratio was representative of engine conditions. The five test configurations consisted of the "full film" design, the "discrete film" design, and three configurations in which the "discrete film" airfoils and the solid airfoils were substituted for each other. These combination configurations were solid vanes and "discrete film" blades, "discrete film" vanes and solid blades, and the solid vanes and solid blades. In all tested configurations the stator inner and outer bands, and the rotor stationary shroud were unchanged. The test data presented in Reference 1 and discussed herein were all obtained with the turbine speed, total-to-static pressure ratio, inlet temperature, and inlet pressure maintained constant at the design values.

DATA REDUCTION

The results of the test program were presented in Reference 1 in terms of a thermodynamic efficiency which was defined to reflect cooled turbine performance as installed in a typical gas turbine engine. This type of definition permits easy evaluation of various cooling concepts with regards to overall engine performance. The definition can be written as;

$$\eta_{th} = \frac{\text{Net Turbine Power Output}}{\text{Isentropic Available Gas Power}} \qquad (1)$$

The net turbine power output accounts for the work required to accelerate the rotor coolant from coolant tangential velocity at rotor entry to the blade meanline velocity. For purposes of determining the coolant tangential velocity at rotor entry, a cooling air expander (inducer) was assumed which accelerates the coolant in the direction of rotation, at the rotor entry radius. The assumed expander total-to-static pressure ratio is the turbine inlet gas stream total pressure divided by the turbine blade dovetail supply pressure required for design blade coolant flow. This type of rotor blade coolant supply system is typical of many modern aircraft gas turbines. The isentropic available gas power of equation (1) includes the expansion of the primary gas and all coolant from turbine inlet total pressure to turbine discharge total pressure utilizing the measured inlet temperature for primary and each individual coolant supply. The turbine inlet pressure was chosen as the source pressure for evaluating the ideal available gas power of all the coolant based on the assumption that if the turbine were uncooled the coolant could be mixed with the combustion products in the combustor and expanded through the turbine. Thus equation (1) becomes;

$$\eta_{th} = \frac{\text{Gross Turbine Power-Blade Coolant Pump Power}}{\dot{W}_p \left[h_1 - h'_{3p}\right] + \sum \dot{W}_c \left[h_{1c} - h'_{3c}\right]} \qquad (2)$$

wherein;

$$\text{Blade Coolant Pump Power} = \dot{W}_b \left[\frac{U_m^2 - U_c V_{uc}}{gj}\right] \qquad (3)$$

$$\left[h_1 - h'_{3p}\right] = f(T_{t_1}, P_{t_1}/P_{t_3}) \qquad (4)$$

$$\left[h_{1c} - h'_{3c}\right] = f(T_{tc}, P_{t1}/P_{t3}) \qquad (5)$$

The "Gross Turbine Power" term in the numerator of equation (2) was determined from the observed torque and speed with corrections for turbine rig rotor coolant pumping and bearing losses.

ANALYTICAL PREDICTIONS

Analytical predictions were made of the changes in turbine performance anticipated as a result of coolant injection for the stator vane and rotor blade cooling configurations tested. These predictions are based on the method of Hartsel[3] which was used to determine the effects of coolant injection on cascade performance. This result was then applied with an energy accounting procedure consistent with the efficiency definition of equation (2).

The cascade efficiency losses based on Hartsel's method give the mixing losses which result from injecting relatively low momentum coolant into the primary stream. This procedure essentially determines an "average" total pressure of the mixed gas stream. The effect of this reduced cascade efficiency on stage efficiency is easily determined by any of several methods; however, the coolant, having been "mixed" with the primary stream, expands through the remainder of the stage producing power. Thus, the "available expansion energy" of the coolant must be determined in order to determine the full effect of the coolant on stage performance.

The calculation of cascade mixing loss vs. vane or blade coolant flow rate was performed for two separate methods of flow variation. The first calculations were performed assuming that the flow rate is modulated by varying the coolant pressure with constant film hole geometry. These calculations are representative of the way the coolant flow variation tests were conducted and therefore should be directly comparable to data from these tests. The second calculations were performed assuming that the coolant pressure is maintained constant at design value and the coolant flow is modulated by varying the film hole geometry (variable film hole size). These latter calculations are thus representative of a series of design points where coolant pressure is constant and the coolant flow is varied by using various numbers and diameters of holes to achieve desired levels of coolant effectiveness at different design conditions. The results of these calculations were used to compare test data of cooled and solid configurations. The two methods yield identical results at design coolant flow which occurs at design coolant pressure.

The available expansion energy of the vane coolant is assumed to be the same as the primary gas output corrected for reduced source temperature. This assumption is consistent with the defintion of total pressure mixing loss described by Hartsel.

The method of predicting the available expansion energy of rotor blade coolant is different from the method used for vane coolant. The coolant expansion energy is assumed to be the energy transfer calculated from the change in angular momentum of the fluid from the point of rotor entry to its point of discharge. For the purposes of this calculation, the coolant entry angular momentum must correspond to the inducer discharge

conditions assumed in data reduction. The coolant angular velocity at the rotor discharge is calculated by assuming that the coolant expands off the rotor blade at the primary gas stream Mach number but at reduced velocity due to lower temperature.

For multiple stage turbines, the expansion of the vane coolant and rotor blade coolant of the initial stages through subsequent stages must also be included. This expansion energy is assumed to be the same as the primary gas output corrected for reduced inlet temperature, which corresponds to coolant source temperature less energy extracted in initial stages.

RESULTS

The results of the five test configurations are shown as Figures 2, 3, 4, and 5 and are shown compared with analytical predictions as in Reference 1. The analytically determined efficiencies in these figures were made to coincide with the experimental values at the design coolant fraction. The effects of coolant were calculated from these base conditions. Figure 2 contains experimental data from three of the five configurations plotted as thermodynamic efficiency vs. vane coolant fraction. The data show the variation in thermodynamic efficiency as the vane coolant was modulated by changing the coolant source pressure for the "discrete film" design. Two independent variations are presented, one of which was with solid blades in the rotor and the other with the "discrete film" blades where the blade flow was constant at design value. In addition, the performance of the solid vane/solid blade configuration is shown. The calculated variation in turbine performance with varying coolant pressure, described earlier, is shown as solid lines which are referenced to the test data at the design flow rate of 5.0%. The dashed lines present the results of the constant coolant pressure variable film hole geometry calculations and thus represent a series of turbines designed for various coolant flow rates at the design coolant pressure. These can be extrapolated to zero flow rate to predict solid airfoil performance. The difference between the solid blade/cooled vane efficiency and the cooled blade/cooled vane efficiency is noted to be 2.2 percentage points. The difference between the solid blade/cooled vane design flow efficiency and the solid blade/solid vane efficiency is 1.15 percentage points.

The test data shown in Figure 3 are from the vane coolant variation portion of the "full film" cooled test. The blade coolant flow rate was held constant at design value for this portion of the test. Calculated changes in turbine performance for both the variable coolant pressure (solid line) and constant coolant pressure (dashed line) methods of coolant variation are shown as described for Figure 2. These curves have been referenced to the test data at the design vane coolant value of 5.3%.

Figure 4 again contains experimental data from three of the test configurations plotted as thermodynamic efficiency vs. blade coolant fraction. The data show the variation in thermodynamic efficiency as the blade coolant was modulated by changing the coolant source pressure for the "discrete film" design. The two independent variations of blade coolant shown are for the solid vane configuration and the "discrete film" vanes with the vane flow held constant at design value. The performance of the solid vane/solid blade configuration is again shown. The calculated turbine performance vs. flow results are shown as solid and dashed lines as in the previous figures and are referenced to the test data at the design rotor blade flow rate af 8.15%. The difference between the solid vane/cooled blade efficiency and the cooled vane/cooled blade efficiency is noted to be 1.1 percentage points. The difference between the solid vane/cooled blade efficiency at design blade flow rate and the solid vane/solid blade value is 2.25 percentage points.

The test data shown in Figure 5 are from the blade coolant variation portion of the "full film" cooled test and were obtained with the vane coolant maintained at design value. Calculated changes in turbine performance for the design and off-design flow variation cases are shown as dashed and solid lines as in the previous figures.

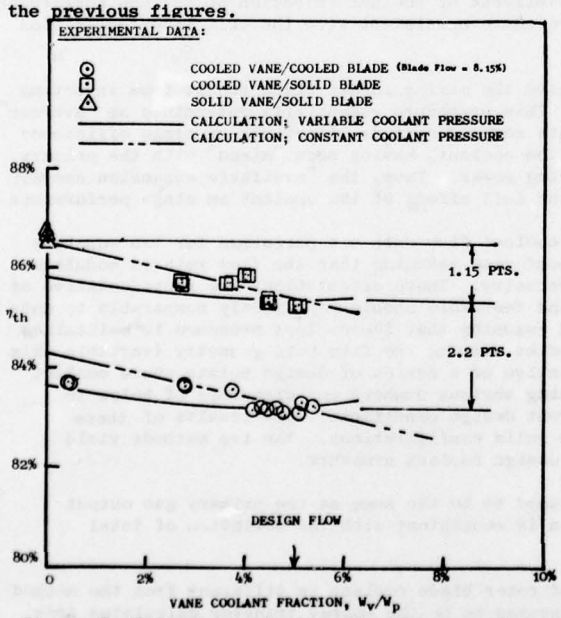

Figure 2 Measured variation of turbine performance with vane coolant flow compared with calculated, "discrete film" configuration.

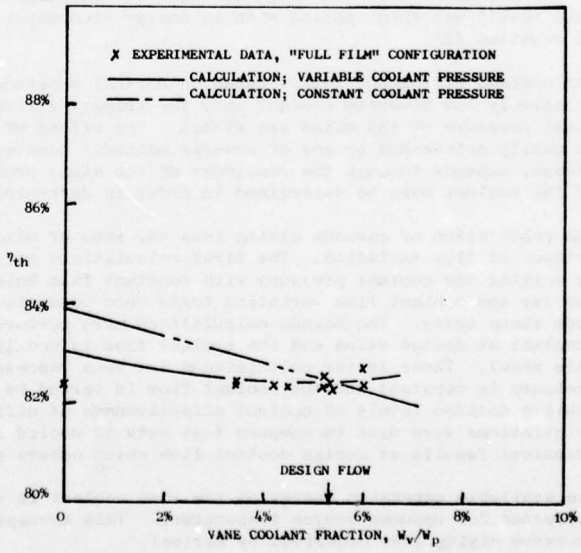

Figure 3 Measured variation of turbine performance with vane coolant flow compared with calculated, "full film" configuration. (Blade Flow = 8.45%)

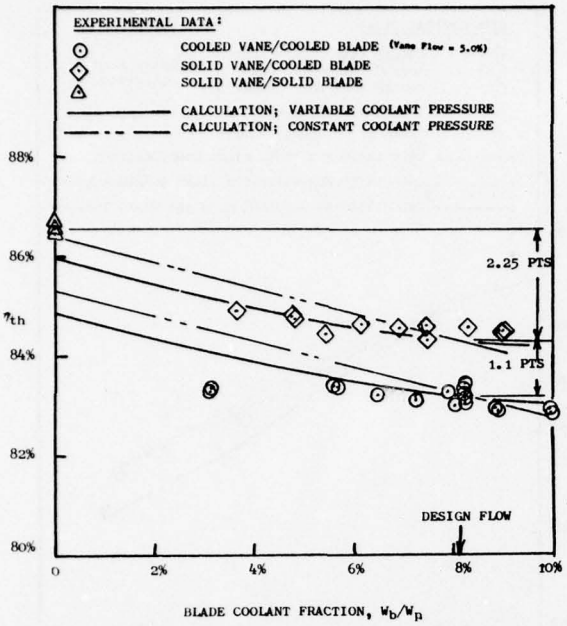

Figure 4 Measured variation of turbine performance with blade coolant flow compared with calculated, "discrete film" configuration.

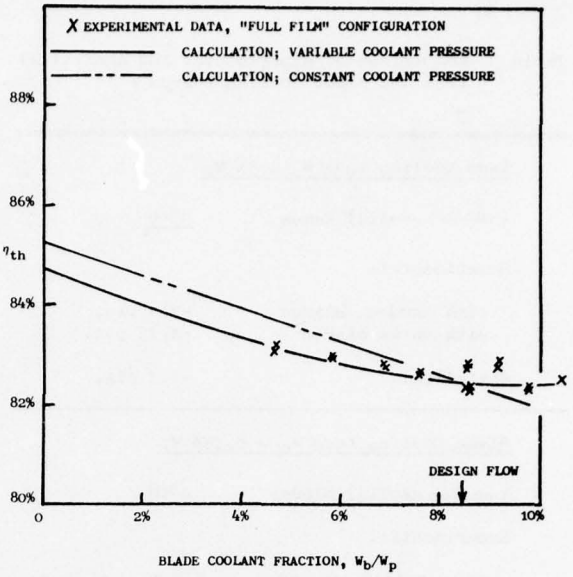

Figure 5 Measured variation of turbine performance with blade coolant flow compared with calculated, "full film" configuration. (Vane Flow = 5.3%)

DISCUSSION OF RESULTS

Evaluation of the analytical prediction technique with coolant variation test data is accomplished by comparing the off-design flow test data of Figures 2, 3, 4, and 5 with the solid lines which were calculated for variable coolant pressure. This comparison shows considerable scatter of the test data from the prediction in some cases and good agreement in other cases. The result is not too surprising considering that the analytical technique did not consider removal of boundary layer flow in calculating the recirculatory flow losses.

A better evaluation of the analytical prediction technique is obtained by comparing the performance differences between the five test configurations evaluated at design coolant flow rates. For this comparison, the problems associated with primary gas recirculation losses at reduced coolant supply pressures are eliminated. The experimental increments for this comparison were noted on Figures 2 and 4 and are listed in Table 2 along with the values calculated for the "discrete film" designs using the analytical prediction technique for constant coolant pressure. For the "full film" design, the comparison of individual vane and blade flow effects cannot be made. However, the overall effects can be compared using the solid vane/solid blade performance and the "full film" design point performance which is then compared with the calculated losses for that configuration.

The comparison made in Table 2, in addition to the "full film" comparison, is shown graphically in Figure 6 by plotting the design point thermodynamic efficiency of each of the five configurations. The efficiency is plotted vs. total turbine coolant fraction including stator outer band, stator inner band and stationary rotor tip shroud flows which were held constant at a total value of 3.6% for these tests. The analytical variations shown are the dashed lines of Figures 2, 3, 4, and 5 but are referenced to the solid vane/solid blade test point for this comparison.

Excellent agreement between the test data and analytical predictions is seen for all test configurations. The performance of the "discrete film" configuration is approximately three-fourths of a percentage point greater than the "full film" configuration at their respective design flow rates. However, the "full film" design flow rate was greater than the "discrete film" value. For purposes of comparing mixing losses alone, the results should be compared at constant flow rate. When this correction is made, the "discrete film" configuration performance is found to be one-half of a percentage point better than the "full film".

Calculations were made of the performance losses which would be attributed to the band and shroud coolant. These results were used to extrapolate the experimental data to an all solid turbine efficiency as shown on Figure 6. This value is slightly greater than 87%. However, no correction was made for the roughness of the transpiration shroud material. A correction for smooth shrouds raises the extrapolated all solid turbine efficiency to approximately 87.5%.

Table 2 Comparison of experimental and analytical vane and blade cooling losses.

Vane Cooling Loss; W_v = 5% W_p	
(cooled -solid) Vanes	$\Delta\eta_{th}$
Experimental:	
with cooled blades	-1.1 pts.
with solid blades	-1.15 pts.
Analytical:	-1.1 pts.

Blade Cooling Loss; W_b = 8.15% W_p	
(cooled -solid) Blades	$\Delta\eta_{th}$
Experimental:	
with cooled vanes	-2.2 pts.
with solid vanes	-2.25 pts.
Analytical:	-2.1 pts.

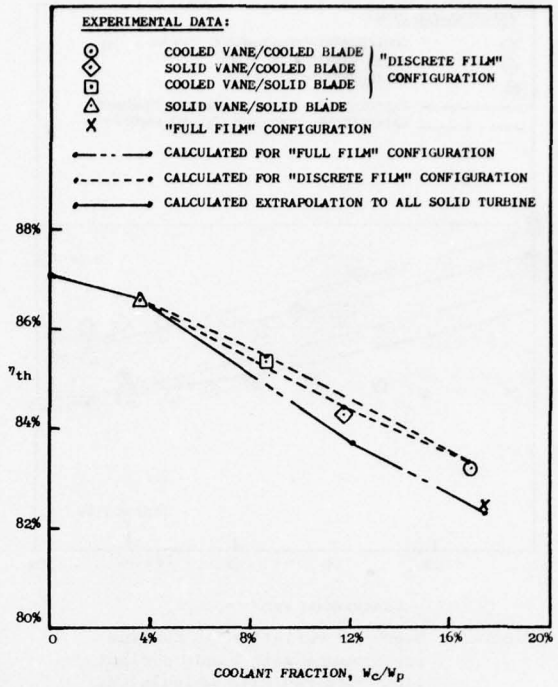

Figure 6 Comparison of measured design point efficiencies with calculated values.

The relative slope of the various line segments shows that the blade coolant has a slightly greater effect on performance than the vane coolant. This is shown graphically in Figure 7 where coefficients of thermodynamic efficiency loss with respect to rotor blade and stator coolant are compared. The rotor derivative shown is based on the experimental loss for the discrete film cooled blade. The stator derivative shown is based on the experimental loss for the discrete film cooled vane plus the calculated losses of the band and shroud coolants.

Further insight into the results are gained by examining the elements of the losses calculated by the analytical methods described. Figure 8 graphically shows the total coolant loss for the discrete film configurations divided into four elements. The total vane coolant loss is mixing loss as described by Hartsel because the coolant was assumed to be extracted from compressor discharge and injected forward of the rotor. The rotor coolant loss, however, is divided into the mixing loss and the throttling loss plus available energy combination shown. The mixing losses are functions of mass flow rate, coolant injection pressure, primary gas Mach number - squared, injection angle and coolant injection temperature. However, the throttling loss and available energy term is a linear function of mass flow rate and the coolant source only.

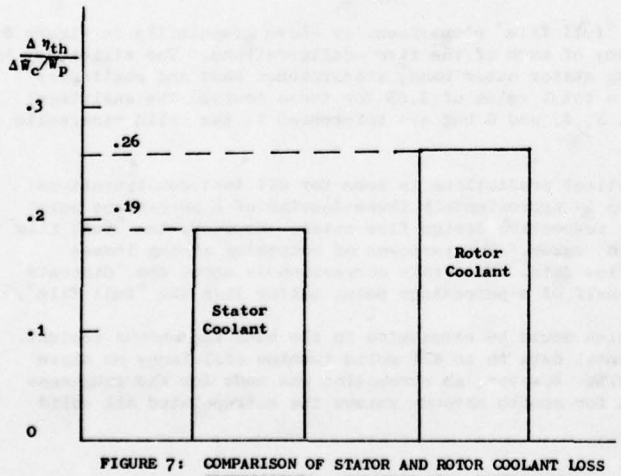

FIGURE 7: COMPARISON OF STATOR AND ROTOR COOLANT LOSS COEFFICIENTS. DISCRETE FILM CONFIGURATION.

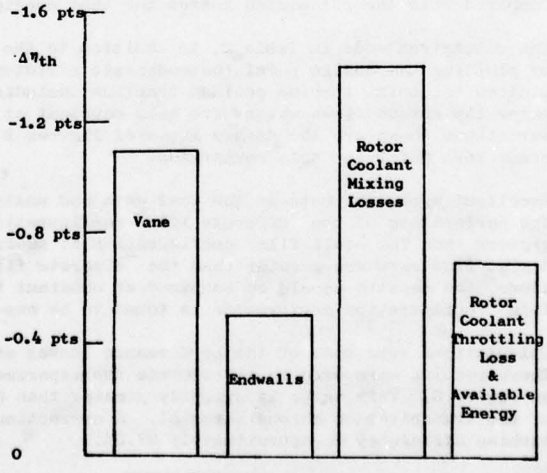

FIGURE 8: COOLANT LOSSES FOR DISCRETE FILM COOLED CONFIGURATION.

CALCULATION OF OVERALL ENGINE CYCLE PERFORMANCE BASED ON EXPERIMENTAL RESULTS

Increases in turbine coolant flow rate and film injection losses can erode the potential cycle performance gains resulting from increases in engine cycle temperatures. In order to estimate the magnitude and possible limits of coolant flow rates for increases in cycle temperature, a core engine cycle was selected for analysis. The cycle is representative of a core of a modern turbofan engine operating with inlet conditions corresponding to the discharge conditions of a low pressure compressor. Table 3 presents the selected cycle and single stage turbine parameters assumed in this study.

For the study cycle, the baseline average turbine rotor inlet temperature, $T_{4.1}$, was selected to be 2200°F (1478°K), because at cycle temperatures below this value convection cooling dominates, whereas at temperatures above this value film cooling is usually introduced. The experimental turbine, described in the previous sections and in Reference 1, is the first stage of a two stage turbine with a combined power output sufficient to drive the compressor of the study cycle. Since most modern turbofan engines utilize single stage core turbines, it was desired to analyze changes in cycle performance for variations in cooling flows of a single stage turbine. Thus the single stage turbine of the study cycle is of considerably higher pressure ratio, corrected tip speed and corrected work extraction then the experimental stage. The interstage relative discharge velocities for the study cycle turbine are supersonic, whereas the experimental turbine had subsonic velocities throughout. Therefore, the experimental stator and rotor coolant loss coefficients shown in Figure 7 could not be used for this calculation of cycle performance. However, the analytical method described in previous sections was used to determine similar coolant loss coefficients for the high work extraction stage of Table 3.

Calculations of stator and rotor coolant loss coefficients have been made for a stage with characteristics as shown in Table 3 and the results are shown as Figure 9. It is observed that the stator coefficient has decreased relative to Figure 7 and the rotor coefficient has increased. This change can be explained qualitatively by noting that for the high work stage, the stator inlet Mach number is considerably lower than for the lesser work stage and that considerable coolant film is injected on the vane and stator endwalls in the stator inlet region. The high work stage also is lower in reaction than the lower pressure ratio stage. These two factors serve to reduce the relative mixing losses of the stator and increase the rotor. However, from a quantitative standpoint, the absolute loss for the high work stage is much greater for an identical value of loss coefficient, as defined, since one percentage point in thermodynamic efficiency represents considerably more energy.

Simple cycle calculations have been made for the core engine at the baseline conditions of Table 3 and for a matrix of operating conditions where the turbine rotor inlet temperature, $T_{4.1}$, and the coolant flow rate were varied. For these calculations, the compressor inlet conditions, compressor mass flow rate, compressor pressure ratio, and combustor pressure drop were held constant. The coolant flow was assumed to be extracted at compressor discharge and split equally between stator and rotor. The baseline calculation was made at $T_{4.1}$ = 2200°F (1478°K), η_{th} = 89% and with a nominal convection coolant flow rate. For the remainder of the calculations, the thermodynamic efficiency was varied in accordance with the additional coolant flow rates, the coolant loss coefficients of Figure 9, and the assumed coolant split between stator and rotor. For each calculation case the core turbine discharge total temperature, total pressure, and mass flow rate were determined. In addition the gas stream was assumed to expand through a low pressure turbine of sufficient power to compress the core engine mass flow from ambient to core inlet conditions. Low pressure turbine expansion efficiency was assumed to be 91.5%. Finally the remaining turbine discharge ideal gas power was determined based on an isentropic expansion of the gas from low pressure turbine discharge conditions to ambient pressure. This is then the ideal gas power available to compress the bypass air in a turbofan engine, produce jet thrust in a turbojet engine, or produce shaft power for a turboshaft engine. Any additional turbine stages required for these configurations could be combined with the low pressure turbine and bypass fan stages can be combined with the low pressure compressor.

The performance comparison for the various cases was calculated in terms of ideal core gas power output divided by fuel flow rate. The results are presented in Figure 10 which shows performance gains available for various increments of cycle temperature and cooling flow rate. This plot shows the increases available in energy output per unit fuel burned for increased cycle temperature if the additional coolant flow required is maintained at reasonable values. The same information is shown on Figure 11 which shows the tradeoff necessary in limiting coolant flow as cycle temperature increases to obtain the potential performance improvement.

Another aspect of the increase in cycle temperature is the core engine ideal gas power output per unit core engine inlet airflow. Figure 12 shows the impact of cycle temperature, $T_{4.1}$, and additional coolant flow rate on the gas power output per unit core engine inlet airflow. Increases in this parameter permit reduction in core engine size, for a given application, thus reducing overall engine weight and cost. Reduction in engine weight can be converted into fuel savings, aircraft weight, aircraft payload or range depending on the aircraft and mission.

The parametric studies shown above are first order analyses and do not reflect second order effects. For example, changes in mixing losses and uncooled turbine efficiency as the turbine pressure ratio changes due to variations in turbine inlet temperature and coolant flow rate are not included. In addition the analytical method has been found to give excellent agreement with experimental data for a subsonic stage, however, it is applied herein to a transonic stage without consideration for coolant injection/shock interaction losses. Nevertheless these results are expected to give a good indication of the effects of film cooling on the potential payoff of increased cycle temperature.

TABLE 3: CORE ENGINE CYCLE PARAMETERS FOR OVERALL PERFORMANCE CALCULATIONS (Ambient Inlet Conditions)

Overall Cycle Pressure Ratio	26:1
Core Compressor Pressure Ratio	11:1
Core Compressor Inlet Pressure	34.7 psia (2.39×10^5 N/m^2)
Core Compressor Inlet Temperature	265°F (403°K)
Turbine Rotor Entry Temperature, $T_{4.1}$ (Baseline)	2200°F (1478°K)
Turbine Work Output Corrected to Standard Sea Level Conditions (Baseline)	38.7 $\frac{BTU}{LB.}$ (9.0×10^4 J/Kg)

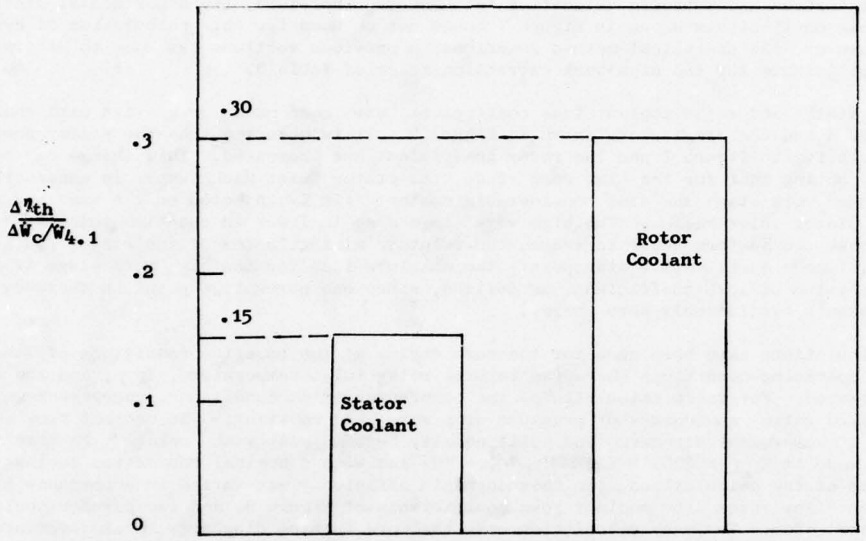

FIGURE 9: CALCULATED STATOR AND ROTOR COOLANT LOSS COEFFICIENTS. HIGH WORK EXTRACTION STAGE.

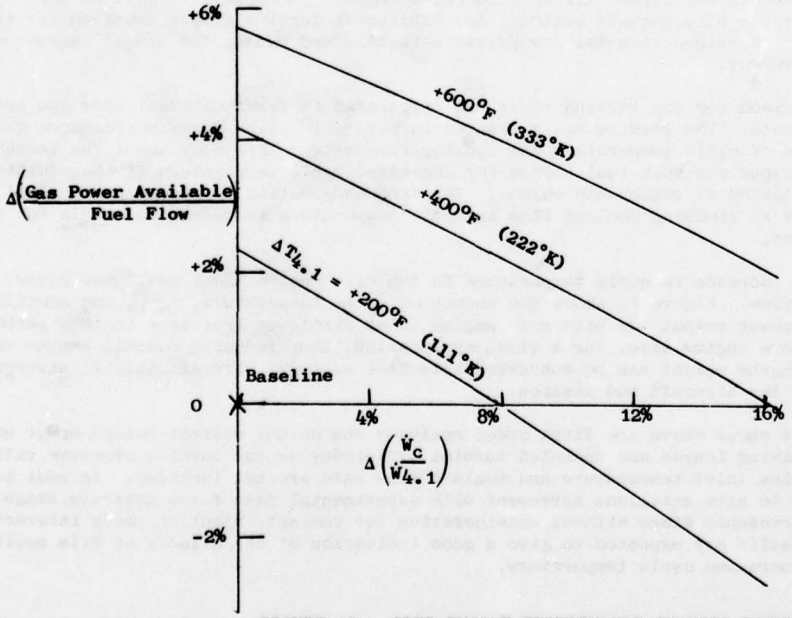

FIGURE 10: CORE ENGINE PERFORMANCE CHANGES RESULTING FROM CYCLE TEMPERATURE INCREASE FOR VARIABLE COOLANT FLOW RATES.

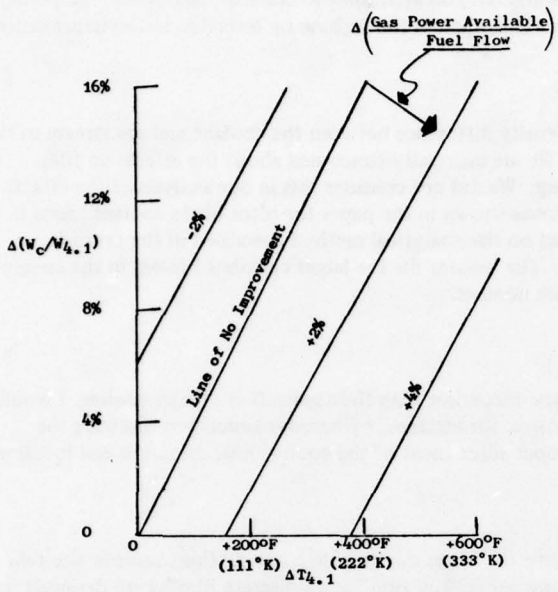

FIGURE 11: RELATIONSHIP BETWEEN CYCLE TEMPERATURE INCREASES AND COOLANT FLOW RATES FOR LEVELS OF CORE ENGINE PERFORMANCE IMPROVEMENT.

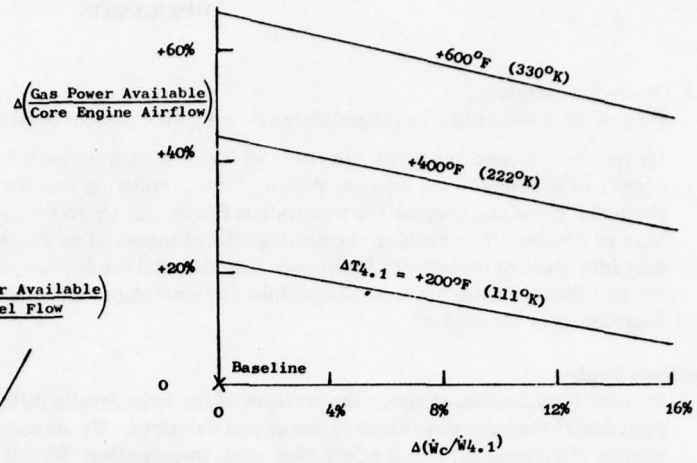

FIGURE 12: CORE ENGINE POWER INCREASES FOR INCREASES IN CYCLE TEMPERATURE FOR VARIABLE COOLANT FLOW RATES.

CONCLUSIONS

Excellent agreement has been shown between the experimental data and calculation procedure for determining effects of film injection on turbine stage performance which permits the use of this method for predicting cooled turbine performance.

It is a well known fact that increases in turbine coolant flow rate and film injection losses can erode the potential performance gains resulting from increases in cycle temperature. The results of this study show the limits which must be placed on coolant flow rate for specific cycle temperature increases. These curves can be useful to the designer in establishing coolant flow limits during engine preliminary design studies.

REFERENCES

1. McDonel, J.D., Eiswerth, J.E.; "Measured Effects of Coolant Injection on the Performance of a Film Cooled Turbine", AIAA Paper 77-946, July 1977.
2. Whitney, Warren J., Szanca, Edward M., Moffitt, Thomas P., Monroe, Daniel E., "Cold-Air Investigation of a Turbine for High Temperature Engine Application, "NASA TN D-3751, 1967.
3. Hartsel, J.E.; "Prediction of Effects of Mass-Transfer Cooling on the Blade-Row Efficiency of Turbine Airfoils" AIAA Paper 72-11, January, 1972.

ACKNOWLEDGMENTS

The authors wish to acknowledge the contributions of Messrs. Warren J. Whitney and Edward M. Szanca of the Lewis Research Center who have served as Projects Managers for the experimental program and Mr. Thomas P. Moffitt of Lewis Research Center for his continued interest and support of this program.

DISCUSSION

D.K.Hennecke, Germany

First of all, I would like to congratulate you on your excellent presentation.

My question is concerned with the effect of film injection on rotor blades. The fluid in the film may have twice the density of the fluid in the host gas stream. Now considering that the centrifugal acceleration may be several ten thousand g one can imagine the tremendous forces that try to throw the cooling film radially outward. This may have an adverse effect both on the cooling effectiveness and on the aerodynamic performance. Does your analysis take into account this effect? From your experimental results, can you quantify the order of magnitude? Is, perhaps, the fact that the rotor blade had larger losses in your engine runs than in the turbine rig tests due to the larger centrifugal forces in the engine?

Author's Reply

We have been concerned about the problem of the large density difference between the coolant and gas stream in the presence of the large centrifugal forces as you described. We are especially concerned about the effects on film cooling effectiveness. This is a field that needs investigating. We did not consider this in our analysis of the effects of coolant on aerodynamic performance. However, the curves shown in the paper for rotor blade coolant losses in an engine are not experimental, but were calculations based on the analytical method described in the previous sections that compared well with the turbine rig test data. The reasons for the larger calculated losses in the engine are due to differences in stage reaction and gas stream Mach number.

D.K.Hennecke, Germany

After having seen the large aerodynamic losses that one may encounter with the application of film cooling, I would like to know if you can see some ways of reducing these losses, for instance, by aerodynamically optimizing the blade profile taking film cooling into account and by a proper adjustment of the cooling hole direction and location, without compromising the cooling, of course.

Author's Reply

There certainly are ways that the turbine designer can reduce the losses due to film cooling. For example, the two cooling designs which were examined in the early part of the paper "full film" and "discrete film" were designed for the same cooling performance but the latter was specifically aimed at reduced cooling losses. The results show that this was successful. There are more design variations which we have successfully applied to reduce the aerodynamic losses of film cooling which cannot be discussed in this paper. An important point; in order to design with low cooling losses, the initial design of the aerodynamic flowpath, airfoil passages and stage vector diagrams must all include the coolant.

A.R.Stuart, UK

The tests referred to in the paper were carried out at a stage loading

$$\frac{\Delta H}{2U^2} = 0.8$$

I would like you to comment upon the effect of turbine loading and Zweifel coefficient? In addition, how much of the coolant flow was ejected from the rotor blade suction surface, and how much was ejected from the suction surface downstream of the throat?

Author's Reply

Turbine loading and Zweifel coefficient do affect the film cooling losses. The loading affects the relative velocities and thus is accounted for by the analytical method. The Zweifel coefficient affects the cooled surface area in addition to relative velocities, thus this effect is reflected in both the quantity of coolant and the mixing losses.

Approximately 3% W_c/W_p coolant was injected as film on the blade suction surface for the two test configurations. Of this approximately 1/2%–1% was injected downstream of the throat.

A.W.H.Morris, UK

Your method was developed from subsonic flow data but in your example of its application you have transonic flow in which losses might be expected to be different. Would you please comment.

Author's Reply

Other test results indicate that the analytical method is valid for transonic flow.

A.W.H.Morris, UK

In your application example you cite a 50–50 split of cooling flow between stator and rotor. Clearly on the rotor at the high blades speed the relative gas temperature is lower and hence less cooling air should be required. I would have expected more coolant on the stator than rotor. Can you comment?

Author's Reply

The choice of a 50–50 split of coolant for the example calculation was entirely arbitrary. The actual split is a function of many things, including:

- Vane and blade materials,
- Vane and blade life,
- Stage reaction,
- Blade stress,
- Vane and blade Zweifel coefficients.

A.W.H.Morris, UK

What influence does the variation of Tg/Tc have on losses and is there any evidence of influence from the absolute level of Tg?

Author's Reply

There is no evidence that gas temperature level affects coolant losses directly, however, the coolant-to-gas temperature ratio is an important parameter and the effects can be predicted by the present method.

THE INFLUENCE OF JETS OF COOLING AIR EXHAUSTED FROM THE TRAILING EDGES OF A SUPERCRITICAL TURBINE CASCADE ON THE AERODYNAMIC DATA *)

Dr.-Ing. Ortwin Lawaczeck

DFVLR

Bunsenstraße 10

D - 3400 Göttingen

Summary

In a case of a stator cascade the influence of jets of coolant air on the aerodynamic behaviour was tested. The jets exhaust from the trailing edges of four blades. By the evaluation of wake flow measurements over two pitches the losses and the downstream flow angle were determined. In addition schlieren-pictures were taken. The downstream velocity was varied from a subsonic over a transonic up to a supersonic flow. The rate of the coolant air with respect to the primary air running through two adjacent blades was changed from zero to four percent. The measurements were carried out in the wind tunnel for two-dimensional cascades of the DFVLR-AVA Göttingen.

Symbols

a	velocity of sound	w	velocity
c	chord length (fig. 1)	Δi_s	difference of enthalpy at constant entropy
c_m	mass flow rate (eq. (1))	β	flow angle (fig. 1)
g	pitch length (fig. 1)	γ_s	stagger angle (fig. 1)
h	blade height	ζ	energy loss coefficient (eq. (6))
$M = \frac{w}{a}$	Mach number	η_p	primary efficiency (eq. (8))
m	mass	η_t	thermodynamic efficiency (eq. (4))
p_0 , p	stagnation-, static pressure	γ	ratio of specific heat
$Re = \frac{w \cdot c}{\nu}$	Reynolds number	ν	kinematic viscosity
T_0 , T	total, static temperature		

Indices

1	homogeneous flow upstream
2	homogeneous flow downstream
2'	local flow values downstream
c	coolant
is	isentropic

*) The investigations were sponsored by Kraftwerk-Union AG., Mülheim/Ruhr, Germany

1. Introduction

The efficiency of gas turbines increases with increasing turbine inlet temperature. This temperature today is high enough, that the turbine blading must be cooled to avoid excessive stress and oxidation of currently available materials. The general method for cooling the blading is to bleed air from the compressor, direct it through the turbine blades for cooling, and then discharge it from the blade into the main gas stream. There are different procedures of cooling: (1) the coolant flow discharges from rows of coolant holes on the suction surface of the blade, (2) coolant flow is ejected from a particular trailing edge slot more or less parallel to the main stream, and (3) coolant flow is ejected over the complete blade surface at an angle normal to the blade surface (Ref. [1] to [12]). In general the second method, significantly increases the turbine work output [8] . The energy of the coolant, guided into the wake increases the energy of the boundary layers of the suction and pressure sides. It is also possible that the structure of the wake changes: the vortex streets, shedding from the trailing edges of the blades may be suppressed, which in turn may lead to a reduction of profile losses. That applies especially to transonic exit flow conditions, since in the transonic velocity region the vortex streets are considerably thickened [13, 14] . On the other hand, it is possible that the methods (1) and (3) lead to certain aerodynamic penalties, because the boundary layers are getting thicker.

In any case it is necessary to investigate the behaviour of turning angle and losses, if a coolant flow is ejected from the blade. To determine the influence of a coolant flow, ejected from the trailing edges of the blades, on the aerodynamic data of a stator cascade, some experiments were carried out in the two-dimensional cascade wind tunnel of the DFVLR-AVA Göttingen. The total temperatures of the primary air and of the coolant air were equal and atmospheric air was used for the two flows. The tests were conducted at sub-, trans- and supersonic exit flow velocities. The rate of coolant air to primary air mass flow varied from zero to four percent.

2. Cascade Geometry and Wind Tunnel

The cascade consisted of stator blades with a chord length of $c = 52$ mm. The cascade geometry was defined by a pitch chord ratio of $g/c = 0.83$ and a stagger angle of $\gamma_s = 50^\circ$. The profiles used and the cascade geometry are given in fig. 1.

The cascade wind tunnel of the DFVLR-AVA is a suction type tunnel. A detailed description of the facility is given in Ref. [15] . The test section can accomodate 8 - 15 blades of a high deflection geometry and nearly 20 blades of low deflection geometry. In general the blade chord, c, is 50 to 60 mm and the height, h, is 125 mm. Thus the height chord ratio, h/c, is greater than two.

A survey of the usually taken data is given in fig. 2. The total pressure and the total temperature are measured in the settling chamber. The distribution of the static pressure in front of the cascade is obtained from pressure taps at the side wall. In the same plane the flow angle, β_1, is controlled. The local values of the downstream flow, p_{02}, , p_2, and β_2, are measured with a wedge type probe, specially developed for the use in transonic velocities [16] . The distance of the probe from the exit plane can be varied. For schlieren-pictures the blades are usually fixed within the glass-walls with the aid of two pins at each side of the blade. The tunnel has a rectangular nozzle upstream of the cascade and either a free jet or a tail-board downstream.

The coolant air was taken from the settling chamber and led to the blades passing a venturi-nozzle for measuring the mass flow and a throttling valve for control of the mass flow. It is sufficient to supply four blades of the cascade with coolant air (fig. 3). The air supply to each of the four blades is done from both sides of the cascade to ensure a constant flow ejection along the height of the blade trailing edge. The way of the coolant flow within one blade is shown in fig. 4. There are provisions for measuring the total pressure, p_{0c}, within the blade and the static pressure, p_c, near the trailing edge.

3. Test Program and Evaluation of the Measurements

The coolant mass flow is related to the primary flow, passing through two adjacent blades:

$$(1) \qquad c_m = \frac{m_c}{m_1}$$

This relative mass flow was varied from zero to four percent in the following steps:

$$c_m = 0 \; ; \; 0.5\,\% \; ; \; 1\,\% \; ; \; 2\,\% \; ; \; 3\,\% \; ; \; 4\,\%$$

The downstream flow Mach numbers were changed from $M_2 = 0.5$ to 1.4 . The upstream flow angle was $\beta_1 = 90^\circ$. The local flow values were measured by traversing over two pitches, to check, whether the flow was periodic. The probe was mounted in a distance of 60 mm normal to the exit plane. Fig. 5 shows the cascade in the wind tunnel together with the probe and the window for schlieren-pictures. The schlieren-pictures are taken with a spark light source with a flash duration of about $20 \cdot 10^{-9}$ sec.

The local flow values are transformed to a homogeneous flow far downstream which is obtained by application of the equations of conservation for mass, momentum and energy across the controle volume II in fig. 2 . This method is described in Ref. [17] .

In the present paper the following characteristic data of the cascade are given:

- the downstream flow Mach number, M_2
- the downstream flow angle, β_2 [°]
- the energy loss coefficient, ξ
- the primary efficiency, η_p

The energy loss coefficient is in general defined for a cascade as follows:

$$\xi = 1 - \frac{\frac{w_2^2}{2} \cdot (m_1 + m_c)}{\left(\Delta i_{s1} + \frac{w_1^2}{2}\right) \cdot m_1 + \left(\Delta i_{sc} + \frac{w_c^2}{2}\right) \cdot m_c} \tag{2}$$

Assuming, at first, that the total temperatures of the upstream flow, T_{01} , of the coolant flow, T_{0c} , and of the downstream flow, T_{02} , are different (fig. 6), eq. (2) can be written in the form:

$$\xi = 1 - \frac{(T_{02} - T_2)(1 + c_m)}{(T_{01} - T_{2is}) + (T_{0c} - T_{cis}) \cdot c_m} \tag{3}$$

This definition can be related to the thermodynamic efficiency of Ref. [2] :

$$\xi = 1 - \eta_t \tag{4}$$

In the tests described in this paper the total temperatures were equal to each other:

$$T_{01} = T_{02} = T_{0c} \tag{5}$$

Taking into acc ount eq. (5), the eq. (3) can be transformed to:

$$\xi = 1 - \frac{\frac{\gamma - 1}{2} M_2^2 \quad (1 + c_m)}{\frac{\gamma - 1}{2} M_2^2 + \left[1 - \left(\frac{p_{02}}{p_{01}}\right)^{\frac{\gamma - 1}{\gamma}}\right] + \left(\frac{\gamma - 1}{2} M_2^2 + \left[1 - \left(\frac{p_{02}}{p_{0c}}\right)^{\frac{\gamma - 1}{\gamma}}\right]\right) \cdot c_m} \tag{6}$$

In addition to the energy loss coefficient, ξ , in the literature the primary efficiency is used, which relates the actual kinetic energy of the total flow to the ideal energy of only the primary flow and is expressed in general as

$$\eta_p = \frac{m_1 (T_{02} - T_2) + m_2 (T_{0c} - T_2)}{m_1 (T_{01} - T_{2is})} \tag{7}$$

If eq. (5) is valid, the eq. (7) can be transformed to:

$$\eta_p = (1 + c_m) \frac{\frac{\gamma - 1}{2} M_2^2}{\frac{\gamma - 1}{2} M_2^2 + \left[1 - \left(\frac{p_{02}}{p_{01}}\right)^{\frac{\gamma - 1}{\gamma}}\right]} \tag{8}$$

The primary efficiency can reach values greater than one. That may be useful in such cases, where the coolant air, bleeding from the compressor, is treated as a loss in the energy balance of the whole gas turbine.

4. Results and Discussion

To show the aerodynamic influence of the coolant air on the characteristic cascade data, the following values are presented:

fig. 7	downstream flow angle versus downstream Mach number
fig. 8	energy loss coefficient versus downstream Mach number
fig. 9	primary efficiency versus downstream Mach number
fig. 10	energy loss coefficient versus relative coolant mass flow

In addition the results of the pressure measurements within the blade are plotted

fig. 11 total pressure ratio p_{02}/p_{0c} versus downstream Mach number

fig. 12 pressure ratio p_c/p_{0c} versus downstream Mach number

fig. 13 pressure ratio p_c/p_2 versus downstream Mach number

Finally three schlieren-pictures (figs. 14, 15, 16) are presented showing the influence of the coolant mass on the flow field in the sub-, trans- and supersonic exit flow. The upper blade in these pictures has no coolant ejection whereas the two lower blades are provided with slots for the coolant air.

Looking first to the results of the investigated cascade without ejection, one can see, that the losses in the subsonic region are more or less constant (fig. 8), but on approaching transonic flow, the losses increase rapidly with increasing Mach number. The downstream flow angle (fig. 7) shows a corresponding tendency. The schlieren-pictures give an obvious explanation for the increase of losses. In the high subsonic flow there is only a small separation at the suction side of the blade. This separation becomes severe in the transonic exit flow case. The separation point is moving upstream. The wakes are broadening and are growing together just immediately behind the cascade. With a further increase of the Mach number up to supersonic exit flow the wakes decrease slightly and the separation point moves downstream. The reason for the separation in trans- and supersonic exit flow lies in the fact, that behind the throat the suction side is curved. This causes an overexpansion, which is terminated by a normal shock leading to separation (fig. 15).

The schlieren-pictures (fig. 16) show that the boundary layer separation is of the laminar type, the separation occurs tangentially. The maximum test Reynolds number, based on chord length and on downstream flow conditions, is $Re_2 \approx 7 \cdot 10^5$, whereas the Reynolds number for the fullscale gas turbine is ten times greater. But, when using a tripping wire to induce transition, the loss rise between $M_2 \approx 0.9$ to $M_2 \approx 0.95$ is shifted only slightly. The maximum loss is not affected.

The coolant flow has no influence on the critical Mach number (figs. 8 and 9), but in all other cases there is a remarkable influence of the coolant on the losses and on the downstream flow angle. Prior to the discussion of this influence, some remarks should be made on the measurements and their evaluation. The local flow values are measured over two pitches, the upper and the lower pitch of fig. 5, to check, whether there are periodic flow conditions for the two blades in the middle of the cascade. The evaluation for both pitches results in the same downstream flow values (see in the figs. 7, 8, 9 the values of $c_m = 0$ and $c_m = 2\,\%$).

Except for the critical Mach number, there is a remarkable influence of the coolant mass flow on the downstream flow values. This is shown in fig. 10 for two discrete subsonic and two discrete supersonic downstream Mach numbers. The losses have a minimum at $c_m \approx 3\,\%$. This is true for the subsonic as well as for the supersonic flow. But it should be regarded, that the total pressure of the coolant in the blade changes with the downstream Mach number (fig. 11). In order to investigate the influence of the total pressure, p_{0c}, at equal downstream Mach numbers and equal coolant flow rates, and in order to find out, whether the tendency for the influence of the coolant on the losses can be generalized, further experiments are planned. The velocity of the coolant, when leaving the blade was subcritical in all cases investigated (fig. 12).

The schlieren-pictures show the influence of the coolant on the flow field (figs. 14, 15, 16). In sub- and transsonic flow there is only a small change in the wake, but at supersonic exit Mach numbers a distinct change of the flow field in the exit area is visible. Without coolant flow the expansion fan at the trailing edge is stronger than with coolant flow for the same pressure drop over the cascade (see fig. 16, the upper blade without coolant and the two other blades with coolant air). Obviously the wake is energetically enriched so that there is no need for the expansion fans at the trailing edges to be as strong as in cases without coolant air. This may explain the lower losses when coolant air is ejected from the trailing edges of the cascade.

5. Summary

Investigations, carried out in the wind tunnel for two-dimensional cascades of the DFVLR-AVA Göttingen, show the influence of a coolant flow, ejected from the trailing edges of stator blades on the downstream flow values, i.e. flow angle and losses. The coolant flow rates, based upon the primary mass flow, were changed from zero to four percent in a downstream Mach number region of $M_2 = 0.5$ to 1.4. In the sub- and supersonic exit flow cases the losses are decreased with an increasing coolant flow rate up to $c_m \approx 3\,\%$. With a further increase of the coolant air the losses increase again. The critical Mach number, at which the losses increase - due to separation - suddenly, was not affected by the coolant mass flow. The influence of the jet on the turning was comparatively small.

Literature

[1] Whitney, W. J.; Szana, E. M.; Behning, F. P. — Cold-Air Investigation of a Turbine with Stator Blade Trailing-Edge Coolant Ejection I - Overall Stator Performance NASA TM X-1901 (Oct. 1969)

[2] Prust, H. W.; Behning, F. P.; Bider, B. — Cold Air Investigation of a Turbine with Stator Blade Trailing Edge Coolant Ejection II - Detailed Stator Performance NASA TM X-1963 (1970)

[3] Moffit, T. P.; Prust, H. W.; Szana, E. M.; Schum, H. J. — Summary of Cold Air Tests of a Single Stage Turbine with Various Stator Cooling Techniques NASA TM X-52968 (Apr. 1971)

[4] Prust, H. W.; Helon, R. M. — Effect of Trailing Edge Geometry and Thickness on the Performance of Certain Turbine Stator Blading NASA TN D-6637 (Jan. 1972)

[5] Stabe, R. G.; Dengler, R. P. — Experimental Investigation of Aerodynamic Performance of Cooled Turbine Vanes at Gas- to Coolant-Temperature Ratios up to 2.75 NASA TM X-2733 (March 1973)

[6] Brown, D. B.; Helon, R. M. — Cold Air Aerodynamic Study in a Two-Dimensional Cascade of a Turbine Stator Blade with Suction Surface Film Cooling NASA TM X-2685 (Jan. 1973)

[7] Prust, H. W.; Bartlett, W. M. — Cold Air Study of the Effect on Turbine Stator Blade Aerodynamic Performance of Coolant Ejection from Various Trailing-Edge Slot Geometries NASA TM X-3000 (March 1974)

[8] Moffitt, T. P.; Prust, H. W.; Bartlett, W. M. — Two-Dimensional Cold-Air Cascade Study of a Film-Cooled Turbine Stator Blade I - Experimental Results of Pressure-Surface Film Cooling Tests NASA TM X-3045 (May 1974)

[9] Goldman, L. J. — Cooled Turbine Aerodynamic Performance Prediction from Reduced Primary to Coolant Total-Temperature-Ratio Results NASA TN D-8312 (Oct. 1976)

[10] Mukherjee, D. K. — Experimentelle Untersuchung zur Bestimmung des aerodynamischen Verhaltens einer Turbinenschaufel mit verschiedenen Sekundärluft-ausblasungen zur Kühlung der Hinterkante Turboforum 3/1973, S. 129-134

[11] Mukherjee, D. K. — Pressure Loss Coefficient of Impingement Cooled Leading Edge System of a Turbine Blade Trans ASME, Ser. A, J. Eng. Power 98, No. 4 (1976), p. 554-556

[12] Mukherjee, D. K. — Film Cooling with Injection Through Slots Trans ASME, Ser. A, J. Eng. Power 98, No. 4 (1976), p. 556-559

[13] Lawaczeck, O.; Heinemann, H.-J. — Von Karman Vortex Streets in the Wakes of Subsonic and Transonic Cascades 'Unsteady Phenomena in Turbomachinery' AGARD-CP No. 177 (1976), p. 28-1 - 28-13

[14] Lawaczeck, O.; Bütefisch, K. A.; Heinemann, H.-J. — Vortex Streets in the Wakes of Subsonic and Transonic Turbine Cascades Symposium IUTAM sur l'Aeroelasticite dans les Turbomachines Rev. Francaise de Mecanique, Numero special (1976)

[15] Lawaczeck, O. — Der Prüfstand für ebene Schaufelgitter der Aerodynamischen Versuchsanstalt Göttingen DFVLR-AVA-Bericht 70 A 46 (1970)

[16] Amecke, J.; Lawaczeck, O. — Aufbau und Eichung einer neuentwickelten Keilsonde für ebene Nachlaufmessungen, insbesondere im transsonischen Geschwindigkeitsbereich DLR-Forschungsbericht 70 - 69 (1970)

[17] Amecke, J. Anwendung der transsonischen Ähnlichkeitsregel auf die Strömung durch ebene Schaufelgitter
VDI-Forschungsheft 540, (1970), S. 16-28

List of Figures

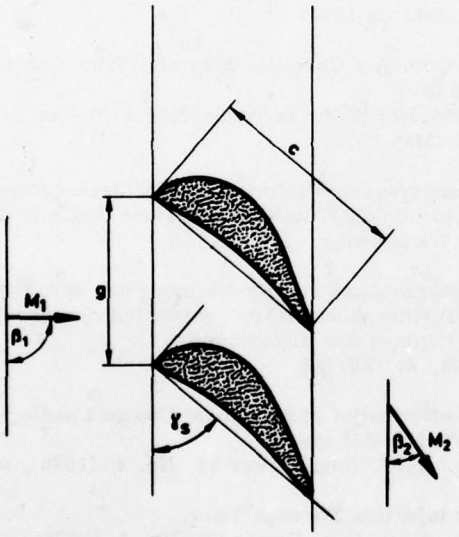

Figure 1

Cascade geometry

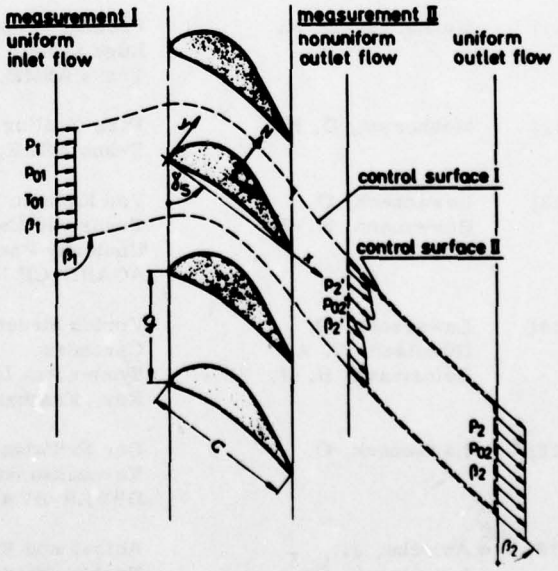

Figure 2

Testing of two-dimensional cascades

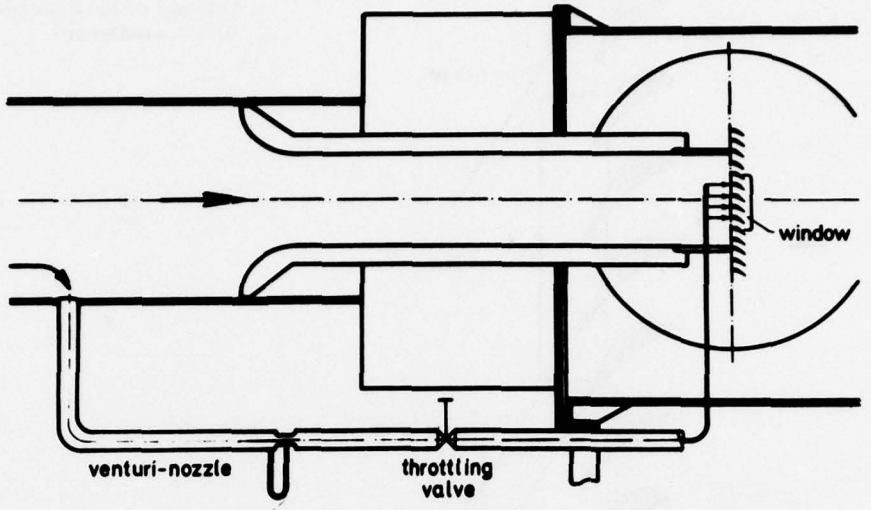

Figure 3 Scheme of the primary and of the coolant flow

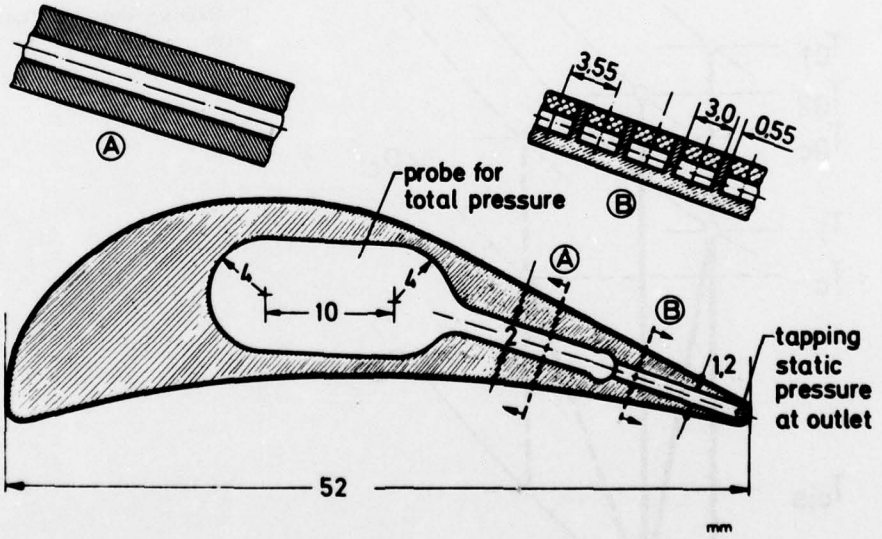

Figure 4 The way of coolant flow within the blade

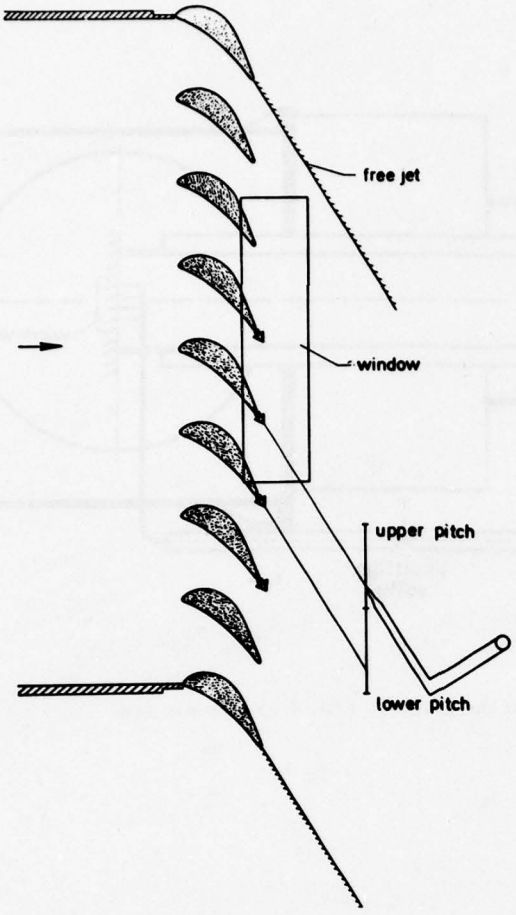

Figure 5

Scheme of the cascade
in the windtunnel

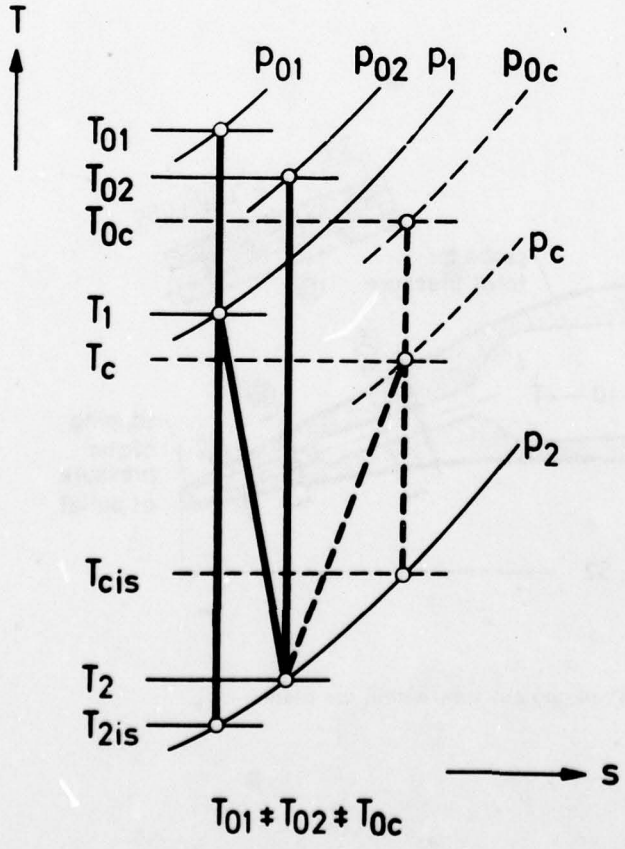

Figure 6

T-S-Diagram for a cascade
with coolant flow

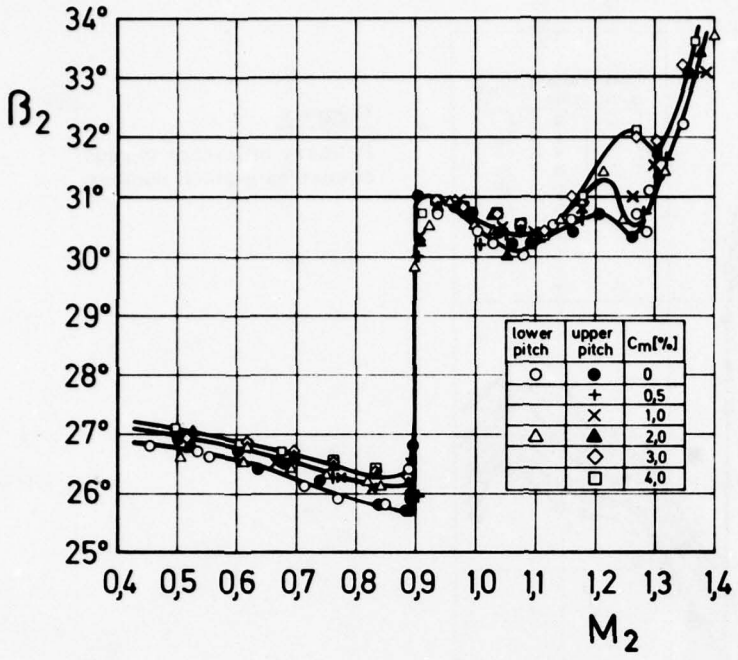

Figure 7

Downstream flow angle versus downstream Mach number

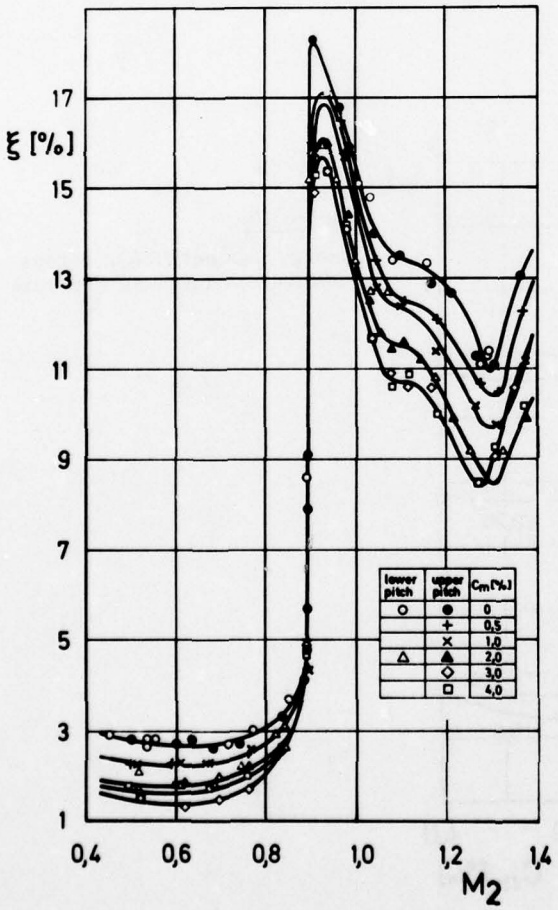

Figure 8

Energy loss coefficient versus downstream Mach number

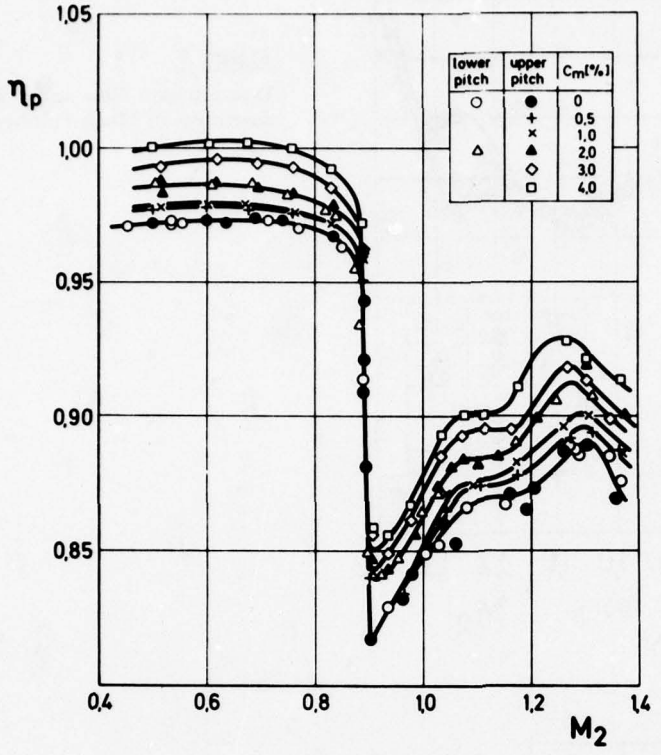

Figure 9

Primary efficiency versus downstream Mach number

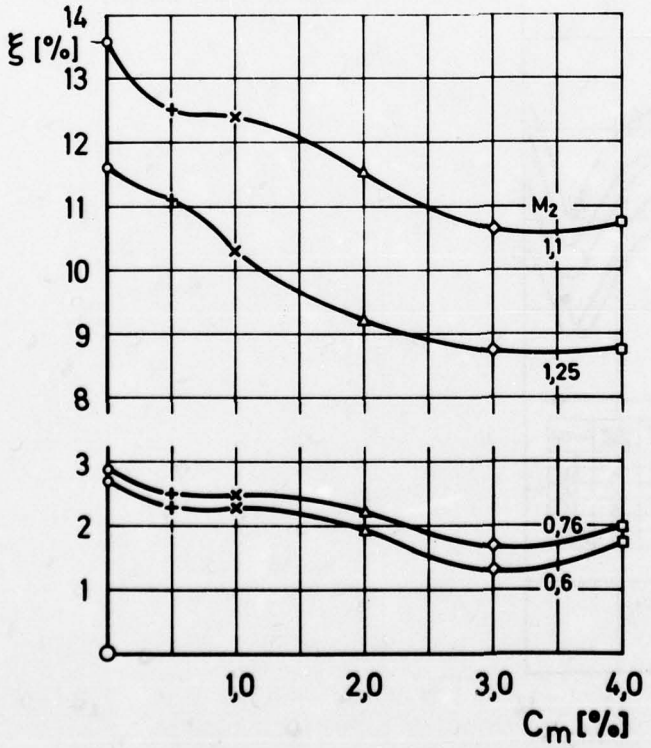

Figure 10

Energy loss coefficient versus relative coolant mass flow rate

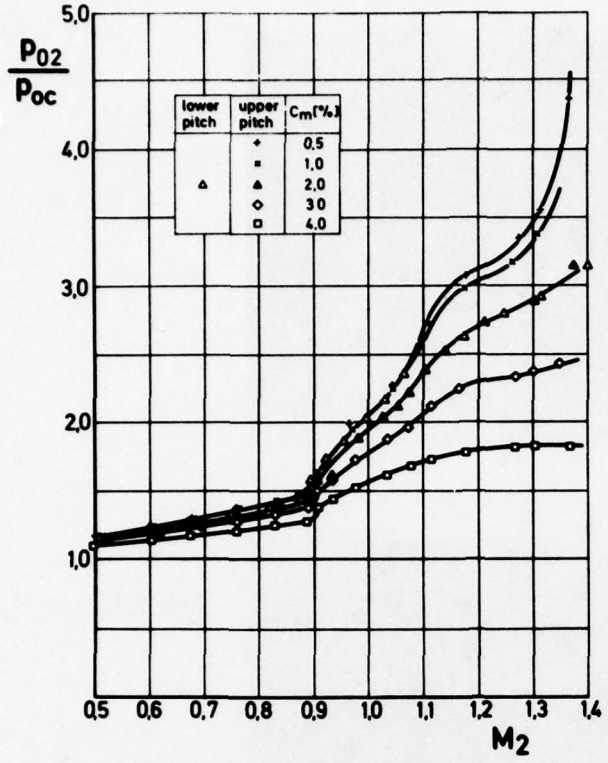

Figure 11
Total pressure ratio p_{02}/p_{0c} versus downstream Mach number

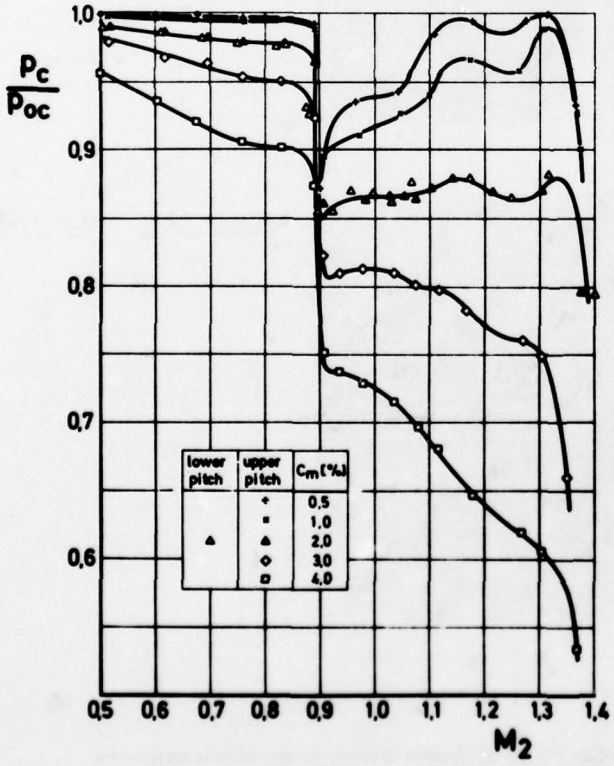

Figure 12
Pressure ratio p_c/p_{0c} versus downstream Mach number

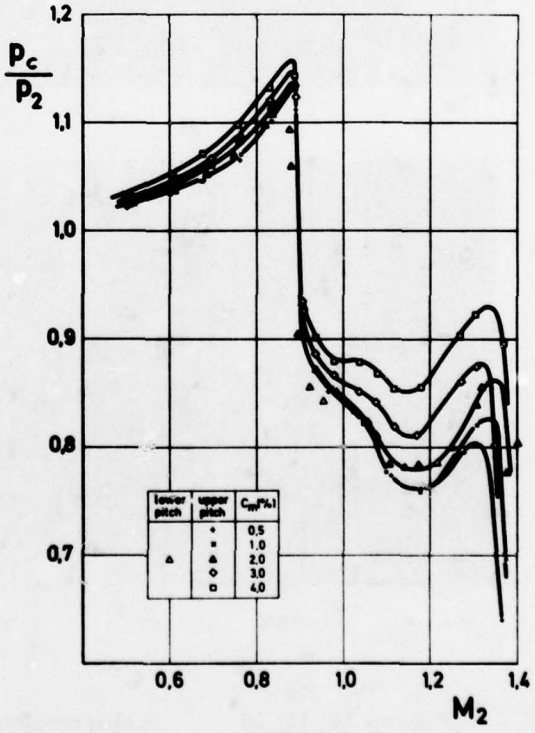

Figure 13
Pressure ratio p_c/p_2 versus downstream Mach number

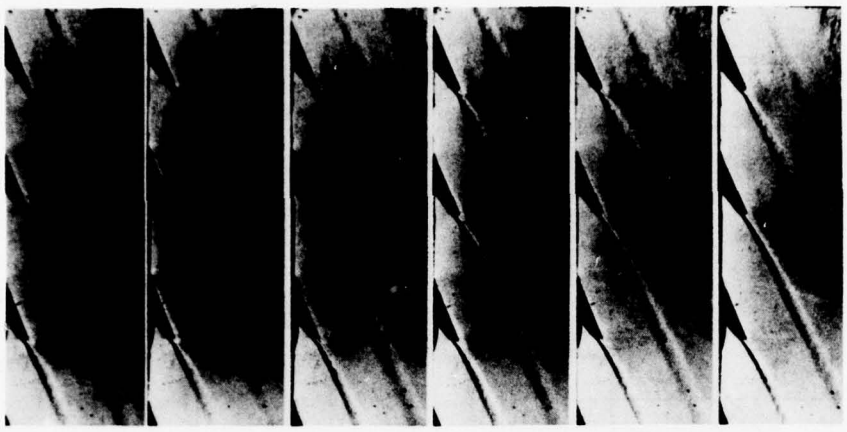

Figure 14 $M_2 = 0.7$

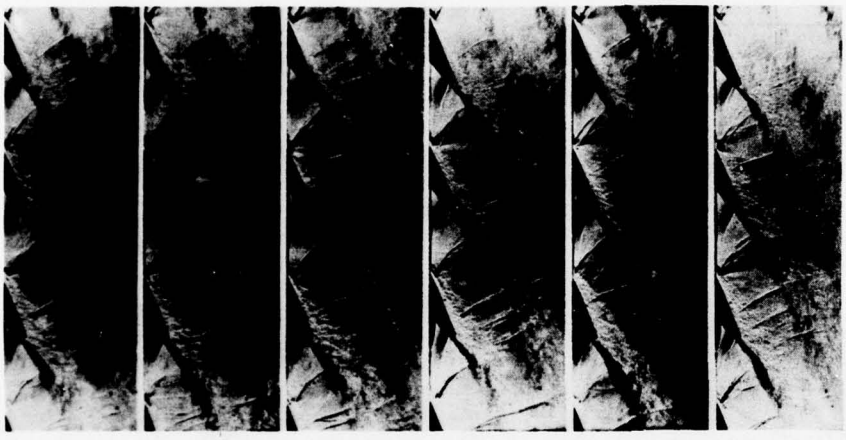

Figure 15 $M_2 = 0.925$

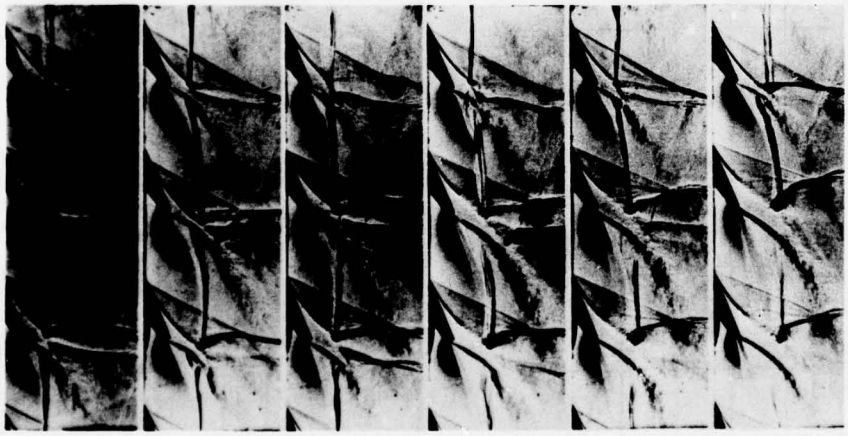

Figure 16 $M_2 = 1.36$

Figures 14, 15, 16 Schlieren-pictures for three different downstream Mach numbers and the different coolant flow rates

DISCUSSION

D.Little, Canada

(1) How large was the suction surface turning downstream of the throat?

(2) What was the o/s ratio?

(3) What was the trailing edge thickness/pitch ratio?

Author's Reply

(1) The suction surface turning downstream of the throat was nearly 20°.

(2) The throat o here is defined as the shortest distance between two adjacent blades; s is the pitch length. The o/s ratio was 0.406.

(3) The ratio $\frac{\text{trailing edge thickness}}{\text{pitch length}}$ was 0.06.

A NEW TRANSIENT CASCADE FACILITY FOR THE MEASUREMENT OF HEAT TRANSFER RATES

D.L. Schultz, T.V. Jones, M.L.G. Oldfield and L.C. Daniels
Department of Engineering Science, Oxford, U.K.

Summary: A new type of transient cascade has been developed for testing turbine blades and nozzle guide vanes at full scale engine Reynolds and Mach numbers. It is based on a free piston compressor capable of producing uniform flow conditions for periods between 0·3 and 1·0 secs. Heat transfer rate measurements are made using thin film surface resistance thermometers deposited onto insulating substrates such as quartz or machinable glass ceramic. Pressure distributions may also be obtained using conventional model techniques. Flow visualisation using schlieren and holographic techniques has also been employed and typical results from rotor blades will be presented. The principle of operation of the cascade is described together with the basis of its mechanical design and the predicted performance compared with experimental observations. The technique is shown to have advantages both in cost and effectiveness over continuous running cascades.

Nomenclature

W	Pump tube volume
A	cross sectional area of pump tube
A*	throat area
a	sound speed
τ_{tube}	time for gas in tube to be expelled through blade throat
τ_{run}	flow duration
M	Mach number
$\bar{P}$	"matching" pressure
Po	initial pressure in pump tube
Re	Reynolds number
T	Temperature
$\dot{m}$	mass flow rate
V	volume of driver cylinders
L	length of pump tube
M	Piston mass
u	piston velocity
u/U	turbulence level
α	thermal diffusivity
$\dot{q}$	heat transfer rate
ρ	density
c	specific heat of substrate
k	thermal conductivity of substrate
s	Laplace transform variable
H	Heaviside step function

Subscripts

r	reservoir (high pressure)
b	blade
o	initial pump tube conditions
s	surface

1. Introduction: The development of high temperature gas turbines is dependent upon facilities which are necessarily expensive in terms of capital cost and direct operating costs so that research aimed at new engine designs may be handicapped if it is conducted in an operating engine rig. The basic tool of much turbine aerodynamic research is the cascade, but even this reduction in scale can lead to demands for large air compressors in the case of cold aerodynamic studies on compressor blades, nozzle guide vanes and turbine rotor blades. For studies of the heat transfer rate to rotor blades it is common practice to utilise a segment of an existing engine combustion system, to supply this with compressed air from a central plant and to test blades fabricated from high temperature alloys. In the latter case it is possible to achieve full scale engine stagnation temperatures but the expense of producing special blades for research purposes can inhibit thorough investigation of, for instance, various internal and external (i.e. film) cooling systems. As an example of the power requirements for such heat transfer studies it can be shown that a cascade with an inlet area 25cm x 7·5cm, operating at 2·75 MN/m^2 stagnation pressure, 1600K stagnation temperature with inlet Mach number 0·3 has an effective inlet power of 12 megawatts. Clearly the direct operating costs of such a facility reduce the scope of any investigation to essential measurements. There exists, therefore, a requirement for a facility which will operate at full scale engine conditions but in a transient mode so that although the power flow is correct, the total energy demand is substantially reduced. This feature of transient facilities is especially advantageous to university research laboratories where the capital and running costs of continuous running high performance heat transfer cascades effectively prohibits research under realistic conditions. Much valuable blade cooling research has been done in low speed facilities but finally the theories must be tested at the correct Mach and Reynolds number, pressure gradient, surface curvature and the obvious solution is to resort to an actual blade profile.

Such a transient facility should be capable of attaining and exceeding full scale blade Reynolds numbers, Mach numbers and gas-to-wall temperature ratios. If blade film cooling is to be investigated it should be possible to initiate the coolant flow and to monitor it during the test. Ideally it should be possible to measure the same quantit-

ies as those familiar to blade designers, i.e. heat transfer rate, static pressure distribution and blade loss coefficients.

When transient techniques are employed it is possible to start the test with the model cold. Even with the very high heat transfer rates associated with high pressure turbine stages, the rise in blade temperature during a short run is such that materials such as aluminium may be used for model construction. If the gas-to-wall temperature ratio is taken as the parameter for the modelling of heat transfer processes through the boundary layer it will be seen that a stagnation temperature of approximately 520K will simulate, with a room temperature model at 288K a gas total temperature of 1600K and blade temperature of 1100K.

Gas temperature of this magnitude can readily be obtained in a transient mode by single stroke isentropic compression and a compression ratio of 3·71 would suffice to reach a final temperature of 420K starting from 288K. Isentropic compression is not very well suited to the attainment of temperatures much in excess of about 600K, starting from ambient, because of the high pressure ratios required but such a temperature with a model initially at 288K would give a gas-to-wall temperature ratio of 2·08, above that required to simulate future engine operating conditions.

An additional advantage in operating with models initially at ambient temperature and gas total temperatures around 450 to 600K is the marked increase of unit Reynolds number. For example, Reynolds number per metre per Pascal increases from 6·17 at M =0·2 to 25·93 with a decrease in total temperature from 1620K to 450K - a gain of just over four times in Reynolds number.

The research described in the present paper is largely concerned with the use of a novel form of free piston compressor which meets many of the requirements for blade simulation in a transient cascade but the original turbine related heat transfer studies at O.U.E.L. were made in a shock tunnel, Ref.1. Shock tubes have been employed for heat transfer research for many years, largely associated with hypersonic vehicle problems and the Mach numbers attained have generally been in excess of 5 to 7 although the reservoir temperatures and pressures have been 2000 to 3500K and 100 to 200 Atm, Ref.2. The flow conditions in a turbine are of course far removed from these but it has been possible to operate a reflected shock tunnel in a subsonic mode by locating the throat downstream of the working section, Ref.3. The flow Mach number is in this case, as in the hypersonic nozzle, a function of throat to working section area ratio although the starting time is longer because the conventional nozzle diaphragm used to establish the flow in the working section is now some way upstream of the throat. Flow durations of between 5 and 10 milliseconds were obtained at high Reynolds numbers (15×10^6/metre) and Mach numbers (0·2 to 0·8) in the shock tunnel described in Ref.3 and similar studies have been reported by Louis et al, Ref. 4.

2. Design Requirements for Transient Cascade Facilities: Although there is a wide range of operating conditions to be found in modern gas turbines a cascade should be capable of operating up to and beyond the most stringent found in advanced engine designs. This implies that rotor blade Reynolds numbers around 10^6 based on true chord inlet conditions, inlet Mach numbers between 0·2 and 0·8 and gas-to-wall temperature ratios up to 2 should be attainable. Conventional cascades generally provide for a large number of blades to ensure that exit static pressures are constant across the rear plane of the central instrumented blades. While this is a desirable target it represents a considerable wastage of power in a transient facility and provision for a limited number of blades, say 5 to 8, is acceptable provided care is taken to check the constancy of inlet and exit conditions. The aspect ratio of the blades should preferably be large also to reduce the effect of secondary flows. Span to throat aspect ratios of 3 or greater are generally aimed at in conventional cascades although values as low as 1·5 or 2 have been used. Reduction of the aspect ratio makes the task of instrumenting a blade section simpler but care must be taken to ensure that measurements are not made in regions which are influenced by secondary flow unless attention is directed especially at this phenomenon.

The single most important characteristic of a transient cascade facility is the flow duration and the influence which this has on the parameters which can be measured. One of the prime advantages of transient techniques is that it is much easier to measure heat transfer rates in such facilities than in continuously operating devices. The use of thin film heat transfer gauges whereby the temperature of the model's surface of known thermal properties is measured, enables heat transfer rates ranging up to $1 kw/cm^2$ to be determined with good accuracy , Ref. 5. Since the model surface temperature will only rise a few tens of degrees C in times up to, say, 1 second the model can be fabricated from readily machinable materials such as aluminium although current practice is still to mount thin film gauges on quartz , Pyrex or machinable glass ceramic* subtrates machined to match the contour of the model. The measurement of static pressure distribution about a blade can be made using externally mounted pressure transducers provided the rise time of the connecting hypodermic tubing is short. In order to retain the techniques normally encountered in conventional cascades it should be possible to fill lengths of up to 25cm of 0·5mm bore hypodermic tubing in the running time of the transient cascade.

* Corning MACOR.

High accuracy, at least to 1% is generally sought in such pressure measurement so that the transducer itself should be capable of rapid response and have a stable calibration factor. These requirements are met by quartz pressure tranducers coupled to modern charge amplifiers. More recently integrated circuit semiconductor tranducers have been used with good results.

Finally the transient cascade should itself have flow properties which are closely repeatable from run to run and which are constant during the flow duration. It will be seen that all of the above features of cascade operation and instrumentation are met in the isentropic free piston cascade which provides an economic and convenient facility for turbine aerothermodynamic research and development. The following sections in this paper describe the principles of operation and the design features of the large O.U.E.L. cascade. A pilot study of the free piston compressor principle was made in 1970 and reported in Ref. 6 and subsequently a larger prototype was built (ref. 7) to enable more detailed measurements to be made of flow duration, properties and constancy as a prelude to the design of the larger cascade.

3. The Free Piston Compressor (a) Principle of operation: The operation of the device may be explained with reference to Figs. 1 and 2 (a general view of the cascade is shown in Fig 2(b)) The system comprises a high pressure reservoir connected via a valve and throat to a pump tube which in turn discharges through the working section nozzle into a dump tank. A piston runs freely in the pump tube which is bored and honed to within ± 75μm to provide a smooth passage for the piston which commences its travel at the high pressure reservoir end of the pump tube. A fast acting gate valve isolates the pump tube from the working section during the compression stage of the cycle. With the piston in its initial retracted position the reservoir valve is opened and air from the high pressure reservoir flows through the reservoir throat, driving the piston down the pump tube and compressing the test gas ahead of it. When this gas has been compressed to a specified pressure, determined by a pressure transducer, the fast acting gate valve is opened and the test gas flows into the working section. If the areas of the reservoir throat and the blade throats are arranged so that the volumetric flow rate out of the pump tube into the working section is equal to the flow rate coming into the region behind the piston from the reservoir then the test gas conditions will remain constant until the piston reaches the nozzle entrance. With this condition satisfied the cascade is said to be operating in a "matched" mode. A comprehensive theory for the operation under these conditions is given in Ref. 6.

A simple theory repeated here for convenience from Ref.6 may be established for the performance of the system if it is assumed that the piston is light so that the pressures on either side of it are equal. The time scale of operation must therefore be long in comparison with the transit time of a sound wave down the tube. It is further assumed that the compression process is adiabatic and that piston friction may be neglected. If further the piston velocity is much less than the local speed of sound then the kinetic energy of the gas within the cylinder may also be neglected. Departures from ideal behaviour caused by finite piston mass are included later in the analysis as is the effect of a finite high pressure reservoir volume.

With these simplifying assumptions it is possible to determine, from the energy equation, the gas conditions within the tube.

If the gate valve connecting the pump tube to the working section were opened at the same instant as the valve between the reservoir and pump tube the gas within the tube would be expelled in a time, called the "tube time" found from simple continuity considerations.

$$\tau_{tube} = \frac{W}{\beta a_o A_b^*} \quad , \quad \beta = \left(\frac{2}{\gamma+1}\right)^{\frac{\gamma+1}{2(\gamma-1)}} \tag{1}$$

The actual running time is less than this because the volume of test-gas is reduced by the compression required to heat the gas to the desired temperature.

Thus
$$\tau_{run} = \tau_{tube}\left(\frac{P_o}{\bar{P}}\right)^{\frac{\gamma+1}{2\gamma}} \tag{2}$$

The matching temperature is then obtained from the isentropic relationship

$$\frac{\bar{T}}{T_o} = \left(\frac{\bar{P}}{P_o}\right)^{\frac{\gamma-1}{\gamma}} \tag{3}$$

Substituting eqn (3) in (2) gives

$$\tau_{run} = \left(\frac{T_o}{\bar{T}}\right)^{\frac{\gamma+1}{2(\gamma-1)}} \times \tau_{tube} \tag{4}$$

Equations (4) and (1) may be combined to give a direct relationship between the pump tube volume W required to produce a given run time τrun at a given total temperature $\bar{T}$ commencing with an initial gas temperature of To (which in turn determines ao).

$$W = \tau_{run}\,\beta\, a_o\, A^*\left(\frac{\bar{T}}{T_o}\right)^{\frac{\gamma+1}{2(\gamma-1)}} \tag{5}$$

These equations are presented in nomographic form in Fig. 3 for an initial gas temperature To of 300K. Also shown on the nomogram is the standard relationship between working section area, Mach number and throat area such that from the former the throat area may be found, together with the necessary tube volume W. Referring to the nomogram which is designed to cover a wide range of working section Mach numbers; the method of employing the nomogram is as follows:

(1) Enter the chart from the bottom with the required working section Mach number and read off the nozzle throat area for a given working section area. The example shown is actually for M=5 so that for a working section area of 100cm^2 a nozzle throat area of 3·5cm^2 would be required.
(2) Entering the chart from the top at the desired stagnation temperature, 900K in the example, a tube time τ of 2·8 secs is read off if the desired flow duration is 1 second.
(3) The line joining the nozzle throat area A* to the tube time intercepts the central scale at the pump tube volume, 1·5m^3 in the example.

It will be seen from equation (3) that there is a substantial advantage in having an initial tube temperature To higher than 300K since the isentropic process requires a pressure ratio of 11·31 to attain a final temperature of 600K starting from 300K but only 4·13 if the initial pump tube temperature is raised to 400K. The potential gain in running time with a preheated pump tube is shown in Fig.4. Equally there is a gain in running time if the total temperature for a given total pressure is reduced. But this potential gain must be considered in conjunction with the aim of correct temperature ratio simulation. The high compression ratio required to reach temperatures much above 600 to 700K makes the device more suited to operation below these total temperatures, but this still enables gas-to-wall temperature ratios in excess of 2 to be obtained for correct engine simulation.

The time for the compression process to be completed can be calculated from the equation

$$P = P_o + (\gamma \dot{m}_r R T_r / W) t \qquad (6)$$

derived by considering the gain in energy of the gas within the tube to be equal to that lost by the high pressure reservoir gas. Thus from equations (6) and (1), and "matching"

$$(dP/dt)_c = \gamma \dot{m} R T_r / W$$
$$= \frac{\gamma}{\tau_{tube}} \left(\frac{\bar{P}}{P_o} \right)^{\frac{\gamma-1}{2\gamma}} \cdot \bar{P}$$

The time for the gas to reach $\bar{P}$ from Po may be approximated by

$$\tau_c \doteq \bar{P} \Big/ \left(\frac{dP}{dt} \right)_c \qquad (7)$$

$$\text{i.e.} \quad \tau_c \doteq \frac{\tau_{tube}}{\gamma} \left(\frac{P_o}{\bar{P}} \right)^{\frac{\gamma-1}{2\gamma}}$$

or in terms of the temperature ratio

$$\tau_c = \frac{\tau_{tube}}{\gamma} \left(\frac{T_o}{\bar{T}} \right)^{\frac{1}{2}} \qquad (8)$$

The compression time may be read off the nomogram in Fig. 3 using the scales on the right for $\bar{T}$. This time would be of concern if it were so long that the compression process ceased to be adiabatic but there is no evidence of this departure from ideal behaviour in the measurements made in the Oxford facilities where the compression times are typically less than 1 second.

3(b) Design target for the Oxford University transient cascade: The experience gained with the prototype free piston compressor indicated that in most respects a simple first order theory was adequate to explain the main features of its performance. The compression process, "matching" of reservoir and working section throat areas, flow duration and constancy of flow conditions were all predicted well, Ref. 7, although the duration of 'hot' flow was found to be about 25% less than the total flow duration. This was found to be due to the doughnut vortex rolled up in front of the piston. Consequently the size and shape of the transient cascade was based on the testing requirements of two typical sets of blades. One such set was a nozzle guide vane row with the total throat area of 58cm^2 operating at high pressure, 0·83 MN/m^2, total temperature of 450K and the other set was a high-pressure rotor row with a total throat area 96cm^2, total pressure of 0·43 MN/m^2. With a temperature ratio of 2·04 as an upper limit the ratio τrun/τtube is obtained from equation (4) since for air with γ=1·4 this reduced to:

$$\frac{\tau_{run}}{\tau_{tube}} = \left(\frac{T_o}{\bar{T}} \right)^3 = 0.1178$$

Thus for a run time of 0·1 secs the tube time τtube must be 0·85secs. From equation (1) the tube volume W may then be derived for each of the requisite throat areas A_a*

	blade nozzle area A*		pump tube volume W	
	in^2	cm^2	ft^3	m^3
Case 1	15	96·8	57·39	1·63
Case 2	9	58·0	34·43	0·975

Taking the larger of the two blade nozzle areas as the maximum it is seen that a pump tube volume of about 57ft^3 will be required and will give running times of 0·167 seconds with the smaller of the two working section nozzle areas at $\bar{T}$ = 450K. The pump tube design was therefore based on the larger value and the internal diameter and length determined by the available machining capacity of firms expert in honing large cylinders. A bore of 24" (60·96cm) and a length of 18ft (5·486m) could be accomodated in a suitable industrial honing machine and thus the value of W was fixed at 56·55 ft^3 (1·60m^3), slightly below the target figure of 57·39ft^3. The expected flow duration of the pump tube is shown as a function of nozzle throat area and total temperature in Fig. 5. The tube diameter has to be large in comparison with the nozzle entrance area so that the rarefaction wave, formed when the fast acting outlet value opens, does not become a significant fraction of the total pressure. The magnitude of this pressure disturbance is given by

$$\frac{\Delta P}{\bar{P}} = 2\beta\gamma\left(\frac{A^*}{A}\right) \simeq 1.62\left(\frac{A^*}{A}\right) \qquad (9)$$

with A*=15in^2(95·8cm^2) and A=πft^2(2918cm^2) the value of $\Delta P/\bar{P}$ is 5·25%, an acceptable level. The pump tube was stressed for a maximum working pressure of 500 psia (5·51 MN/m^2). The tube was fabricated by rolling and welding 1·25 in thick (3·175cm) plate followed by boring and honing. The bore is true to ± 0·004 in (0·1016mm) over its length and departures from circular cross section do not exceed 0·005in (0·127mm). The circularity and constancy of the bore are regarded as essential for the attainment of constant flow properties.

3(c) High pressure reservoir requirements: In the simplified analysis presented in section 3(a) it was assumed that the pressure in the high pressure reservoir did not fall during the compression process, i.e. it had an infinite volume and allowance must be made for the effect of finite reservoir volume. It can be shown, Ref. 6, that the fall in pressure Δp in total pressure due to a finite reservoir volume can be expressed in the form

$$\frac{\Delta p}{\bar{P}} = \frac{\gamma(3\gamma-1)}{4}\frac{W\bar{P}}{V_r P_r}\left(\frac{P_o}{\bar{P}}\right)^{2/\gamma} \qquad (10)$$

Clearly the higher Pr is to start with the lower the fall in total pressure during the running time. Starting with the value of W=56·55ft^3(1·6m^3) for the pump tube, curves showing the value of PrVr as a function of $\Delta p/\bar{P}$ may be prepared with $\bar{P}$ as an independent variable. Examples of these are shown in Fig. 6 for the case $\bar{P}/Po$=12·29 i.e. a total temperature of 600K and an initial tube temperature of 293K. The five storage cylinders available for use on the facility had a total volume of 10·55ft^3(0·30m^3) and it can be seen that the fall in stagnation pressure due to the finite reservoir volume is 1·66% at $\bar{P}$ = 200 psi (1·38 MN/m^2). Operation at higher total pressures results in larger values of $\Delta p/\bar{P}$ and additional storage would be desirable. Operation of the storage cylinders at 2000 psi (13·8 MN/m^2) gives a PrVr product of 21,100 psi x ft^3, 4 MNm. It is interesting to note from Eqn 10 that operation at lower values of $\bar{T}$ requires a larger reservoir volume for a given tolerance on $\Delta P/\bar{P}$ than operation at higher values of $\bar{T}$.

Air compressors are also available whose operating pressure are 150 atmospheres (2200 psi, 15·2MN/m^2) and these are also extensive ranges of ball valves, and flexible hoses with safe working pressures of 150 atm. All of these factors contribute to the selection of 2000 psi, 136 atm, as a convenient design pressure for the high pressure reservoir. The reservoir is charged from a diaphragm compressor (Corblin A34C 150) which is remotely controlled and supplied from the main laboratory low pressure air system at 25 atm. The inlet throat must be of such a cross sectional area that the volumetric flow rate from the high pressure reservoir into the region behind the piston matches the flow rate through the working section. If the reservoir is large it can be assumed, for design purposes, that the gas temperature remains at approximately the ambient value. If the total temperature and pressure of the compressed gas is $\bar{T}$ and $\bar{P}$ and the reservoir Tr and Pr, then the ratio of the throat areas to achieve this balance of volumetric flow is:

$$\frac{A^*_r}{A^*_b} = \left(\frac{\bar{T}}{T_r}\right)^{\frac{1}{2}}\left(\frac{\bar{P}}{P_r}\right) \qquad (11)$$

In the design of the cascade it was found preferable from the operational point of view to fix the reservoir pressure Pr, since this also influenced the fall $\Delta p/\bar{P}$ in total pressure during the run, and to adjust A*r for different operating levels of $\bar{P}$.

3(d) Piston Design: The piston naturally plays an essential part in the overall performance of the cascade and its design merits close study. Ideally the piston should be of the minimum mass so that it acts as a barrier between the gas flowing into the pump tube from the reservoir and the gas ahead of it, the compressed test gas. It should move freely in the bore of the pump tube and provide an effective seal between the two gases. Considerations of structural rigidity, so that it does not deform as it accelerates down the pump tube, and diaphragm stresses in the face, which arise when it strikes the end of the pump tube, result in a piston design whose mass is non-negligible. At the end of the compression phase of the cycle the piston is travelling at a low velocity as illustrated in Fig. 7. Immediately the gate valve opens the test gas ahead of the piston accelerates to a high velocity which is determined by the tube/working section area ratio. This velocity is higher than piston velocity at the instant of valve opening and the piston, being of finite mass, cannot instantaneously adjust to the

velocity of the test gas. The pressure ahead of the piston thus falls, see Fig. 7, and subsequently the piston oscillates at a frequency and with an amplitude which depend on the piston mass and the mass of the gas within the pump tube. It can be shown (Ref.6) that the periodic time of piston oscillations is given by

$$T = \frac{2\pi}{\gamma^{1/2}} \left(\frac{P_o}{\bar{P}}\right)^{1/2\gamma} \left\{1-\left(\frac{P_o}{\bar{P}}\right)^{1/\gamma}\right\}^{1/2} \left(\frac{LM}{A\bar{P}}\right)^{1/2} \qquad (12)$$

and that the relative amplitude of the pressure fluctuations is:

$$\frac{\Delta P}{\bar{P}} = \frac{T\gamma}{2\pi} \left\{ \frac{1}{\tau_{tube}} \left(\frac{\tau_{tube}}{\tau_{run}}\right)^{\frac{\gamma-1}{\gamma+1}} - \frac{1}{\tau_{run}} \right\}^{1/2} \qquad (13)$$

The amplitude of pressure fluctuations is thus a function of (piston mass)$^{\frac{1}{2}}$ and is inversely proportional to (total pressure)$^{\frac{1}{2}}$. Oscillations in pressure are therefore likely to be more serious at low operating pressures and at the higher stagnation temperatures since τ_{run} is reduced under these conditions. A parametric design study was made to determine the mass of a piston which would be strong enough to withstand the diaphragm stresses which arise when the piston comes to rest over the openface of the test section inlet but which would give acceptably low amplitudes of pressure fluctuations under the operating ranges expected for total pressure. Values of $\Delta P/\bar{P}$ as a function of the piston mass M are shown in Fig. 8 for a particular operating level of $\bar{P}$ which represents the design level for one of the initial blades tested in the cascade. This blade was regarded as representative of H.P. rotor blades in general. The total temperature $\bar{T}$ is employed as an independent variable. It is apparent from Fig. 8 that the amplitude of pressure fluctuations is quite sensitive to total temperature and that piston masses below about 10kg should be aimed at for the test conditions initially set as a target for the cascade. The piston design was therefore based around a mass of 12kg which was considered to give acceptable values of $\Delta P/\bar{P}$, 2½%, for total temperatures of 400K. The initial piston design, comprising a rolled, perforated aluminium skirt, PTFE piston rings and an aluminium alloy piston face, Fig. 9 was deliberately made conservative so that piston failure was unlikely. Subsequent design employing an aluminium honeycomb reinforced piston face and lighter skirt have been made for future manufacture. A method for compensating for the finite mass of the piston has been developed and is described in section 3(f). This technique is capable of eliminating the oscillations and has so far obviated the need to fabricate a light weight piston.

3(e) Gate valve design: Accurate control of the reservoir pressure in the free piston compressor depends on precise timing of the gate valve separating the heated gas from the working section. A schematic diagram of the technique finally chosen to open the valve is shown in Fig.10. The rising ramp of pressure ahead of the piston is measured with a quartz transducer and the output from its associated amplifier is used to trigger the discharge of a large capacitor through the electrical detonator in Fig. 10. A pressure of from 3 to 7 atm, depending on $\bar{P}$, is applied to one side of the piston just prior to the run. The detonator completely destroys the Perspex tube and the piston is driven to the right opening the gate valve in approxiamtely 25 millisecs. A needle valve on the exit part of the cylinder is used to decelerate the piston and gate valve and this is adjusted by trial. The moving surfaces of the gate valve are faced with hard Nylon which slide on the polished aluminium-silicon alloy housing. A characteristic distance versus time curve for the gate valve is shown in Fig. 13 and a record of this action is taken on each run to check the timing of valve opening. The design of the valve was based on the assumption that inertial effects would dominate those of friction and this has proved to be the case in practice at least up to the operating loads of 3·5kN so far experienced.

3(f) Compensation for piston oscillations: Even with careful optimisation of the design of the piston to alleviate the effects of piston oscillations it is not possible to reduce them to below about 2% of $\bar{P}$ without compromising the structural integrity of the piston itself. These oscillations were seen to be due to the difference between the actual piston velocity at the instant of flow initiation and that needed to achieve "matching", Fig. 7. The piston is required to accelerate rapidly to maintain the total pressure constant after the gate valve opens but its finite mass prevents this. The amplitude of oscillation can be substantially reduced by arranging that the piston is actually travelling at its correct matching velocity just prior to the commencement of flow. This increased velocity may be obtained by having a reservoir mass flow in excess of that required and reducing this suddenly to the correct value when test section flow commences. The mass flow needed to achieve this condition can readily be determined.

The piston velocity during compression is (Ref.6).

$$u_p = \frac{V}{\gamma P A} \left(\frac{dP}{dt}\right)_c \qquad (14)$$

The "matching" piston velocity is given by

$$\overline{u_p} = \beta \bar{a} \frac{A^*}{A} \qquad (15)$$

and the compression rate for matching conditions is

$$\left(\frac{dP}{dt}\right)_c = \gamma \beta A^* \bar{a} \bar{P}/W \qquad (16)$$

The matching velocity may therefore be expressed as

$$\overline{u_p} = \frac{W}{\gamma A \bar{P}} \left(\frac{dP}{dt}\right)_c \qquad (17)$$

In order that the piston velocity u_p equal the matching piston velocity $\overline{u_p}$ just prior to gate valve opening i.e. when $P=\bar{P}$

$$\left(\frac{dP}{dt}\right)_c = \frac{W}{V} \overline{\left(\frac{dP}{dt}\right)_c} \qquad (18)$$

Recalling that V is the volume of the compressed gas just prior to flow commencement and using the isentropic relationship for the compression process

$$\frac{W}{V} = \left(\frac{\bar{P}}{P_o}\right)^{1/\gamma} = \left(\frac{\bar{T}}{T_o}\right)^{\frac{1}{\gamma-1}} \qquad (19)$$

Thus

$$\left(\frac{dP}{dt}\right)_c = \left(\frac{\bar{T}}{T_o}\right)^{\frac{1}{\gamma-1}} \overline{\left(\frac{dP}{dt}\right)_c} \qquad (20)$$

The rise of pressure in the pump tube is proportional to the mass flow into the tube, in fact

$$\left(\frac{dP}{dt}\right)_c = \frac{\gamma \dot{m}_r R T_r}{W} \qquad (21)$$

Thus equation (20) also relates two reservoir mass flow rates

$$\dot{m}_r = \left(\frac{\bar{T}}{T_o}\right)^{\frac{1}{\gamma-1}} \cdot \overline{\dot{m}_r} \qquad (22)$$

This ratio $\dot{m}r/\overline{\dot{m}r}$ is plotted in terms of area ratios $A^*r/\overline{A^*r}$ as a function of $\bar{T}$ for To = 288K in Fig. 11 where it will be seen, for example, that with a $\bar{T}$ value of 430K the initial mass flow rate would need to be 2·72 greater than that needed for matching. In practice the sudden change in mass flow rate is achieved by occluding part of the main reservoir throat in the assembly shown in Fig. 12(b). The main reservoir throat and compensating throat are formed by a series of holes drilled in a central tube. The main throat area is adjusted by rotating the entire central tube system, so that more or fewer holes are occluded by the flared passage through the end flange. The compensating throat, located behind the main throat orifices can be cut off by means of the sliding shuttle driven by an auxilliary 132 atm cyclinder. The maximum additional mass flow required to achieve compensation is set by the screwed stop at the rear of the assembly and the shuttle is driven against this stop (if it is not already retracted to that position by hand prior to the run). A trigger signal derived from the compression ramp of $\bar{P}$ is used to initiate flow into the region behind the shuttle thus driving the shuttle to the left and closing off the compensating flow. The improvement in the constancy of $\bar{P}$ with the compensator in use is illustrated in Fig 12(a). The correct values of compensator throat area and the main throat area are established by measuring the rate of rise of pressure just prior to gate valve opening and adjusting the compensator throat area to achieve the correct ratio required for the working total temperature, equation (22). In the example of such an adjustment shown in Fig. 12(a) the ramp of compression for $\bar{P}$ with the compensator inoperative is $4{\cdot}15 \times 10^5$ Pascals/sec and the amplitude of pressure oscillation approximately ± 5%. This amplitude of oscillation expected would be about ± 4% (Fig. 8) for the piston in use which weighed 17kg, although the form of the oscillation follows closely that sketched in Fig. 7. With the compensator in use the slope of the $\bar{P}$ record just prior to gate valve opening is $11{\cdot}37 \times 10^5$ Pascals/sec and the ratio of the two slopes is thus 2·74 compared with a target of 2·76 for a total temperature of 532K, Fig.11. Quite small variations in ambient temperature affect the increased mass flow required to achieve perfect compensation but general practice is to leave the compensation mass flow fixed since small run-to-run variations in $\bar{P}$ also occur and the final temperature ratio ($\bar{T}$/To) varies. Since the compensator setting required varies at the 2·5 power of this ratio it is not realistic to attempt too fine a 'tuning' of the compensator. The effectiveness of the compensation system is, however, clear from the improvement in constancy of $\bar{P}$ seen in Fig 12, and it has been found possible to maintain this degree of flow steadiness. The lubrication of the piston rings has been found to be quite important. For instance, if there is any initial 'stiction' as the piston commences its travel oscillations in pressure occur during the compensation process and persist during the run since they are not eliminated by the compensator. One suitable lubricant has been Esso 'Estan O' which is not skimmed from the bore by the piston rings.

4. Cascade performance: The performance of the cascade has proved to be very close to that predicted using the first order analysis presented in Ref. 6 and in section 3(a) of this report. The measured flow durations for the range of blade throat areas so far tested are in good agreement with theoretical values. There is a loss of 'hot' running time caused by a cooled 'doughnut' vortex rolled up in front of the piston and experience in this expected reduction was obtained in a prototype free piston compressor 15cm in diameter and 1·8 metres long, Ref. 7. In practice about 25% of the available flow is cooled by this vortex which is easily recognised on heat transfer records although there is no effect on pressure measurements. The total temperature has been measured with a fine wire thermocouple, Ref. 8, and with the small corrections necessary with this device a total temperature of 430K has been determined at a pressure ratio of 4·10 in excellent agreement with the isentropic compression value. Confirmation of this temperature was also obtained with a hot wire anemometer in the course of turbulence measurements.

The piston oscillations without the compensator in use, as was the case in the early phases of cascade commissioning, with a 17kg piston were between 4 and 5·5% at a total temperature of 450K, in fair agreement with the predicted value of 4·75%. A piston weight of about 12kg had been proposed but for the early tests a 6·35mm (0·25in) thick Duralumin disc was fitted to the face of the piston as a safety precaution. The oscillations in total pressure were thus greater than had been designed for, Fig.8 but acceptable in the early stages. The periodic time of oscillation was 60 millisecs compared with 66 milliseconds predicted for the actual operating conditions.

With the compensator fitted it has been possible to reduce the oscillations in total pressure to levels below 1% with careful setting of the compensator throat area and timing of the gate valve opening. A correctly compensated run is illustrated in Fig. 13 with the gate valve and compensator shuttle pressure shown in relation to the working section static and $\bar{P}$. Adjustment of the timing of the compensator shuttle closure is made with the aid of the shuttle driver pressure signal.

Surveys of upstream and downstream static pressure have been made to check the constancy of inlet and outlet conditions. From Fig. 14(a), in which the geometrical arrangements of the static pressure tappings is shown, it can be seen that the upstream static pressure distribution is reasonably uniform with a slight increasing Mach number gradient from top to bottom of the working section. At the operating conditions used the average inlet Mach number was 0.36 and the average exit value was 0.94.The initial dump tank pressure is set by trial and error so that the correct exit Mach number is obtained during the run. Calculations of boundary layer thickness at the blade inlet position are complicated by the temperature distribution. The Reynolds number at the centre blade is approximately 10^7 at the operating conditions of Fig 14(a) so that a boundary layer thickness of about 1·1cm would be expected if it were fully developed and from the few points available from a pitot traverse, Fig 14(b) it can be seen that this is a reasonable prediction.

5. Data acquisition and processing: Early cascade tunnel measurements were recorded on a 24 channel ultra violet chart recorder and processed by hand, a procedure which, in the case of multi-channel heat transfer rate measurements, could take a day per run.

If the full benefits of a transient cascade tunnel are to be realised, it is necessary to use a fast, multi-channel data acquisition system, and to process the results of a run rapidly prior to the next run. In order to reduce the processing time and to increase the number of measurements taken per run, all transducer outputs are now handled by an on-line digital computer (DEC PDP 11/10).

The computer system is designed to take up to 6400 measurements per tunnel run on up to 32 channels at a maximum rate of 2000 samples/sec from the transducers. The system is shown schematically in Fig. 15. A software system of versatile and highly interactive programs (written largely in FORTRAN) is used to prepare runsheets, acquire and process the data and output results. The raw, rather than processed, data is archived on inexpensive diskettes ("floppy disks"). This facilitates correction of processing, and accumulates a library of data for further study.

To reduce cumulative errors down the signal chain, pressure transducers are calibrated when installed in the working section using the computer. Transducer calibrations, running conditions and raw data are all stored in compact binary computer disk files, which are automatically read by the running and processing programs, and are organised such that only changes between runs need be entered via the computer terminal. The programs prompt and guide the operator through logical decision sequences and can be used by staff with little previous computing experience to print out or edit calibration and run-sheet files, to run the tunnel to read data, and to process, print out, display and plot the results of the run.

A least squares line fitting technique is used to extract mean measurement levels from selected sections of the digitised data, and these are listed, along with the statistical 95% confidence levels on the results sheets. For static pressure measurements, the local Mach number and unit Reynolds number are also calculated and listed. For heat transfer measurements using transient thin film techniques the original temperature history of the surface, is recomputed from the heat transfer rate, $\dot{q}$, derived from the analogue networks (see section 6), and a least squares line fit of the linear section of the $\dot{q}$ ~ T curve (Fig 18(c)) is used to extrapolate $\dot{q}$ back to the original isothermal blade temperature. These extrapolated heat transfer results are again listed with 95% confidence limits, so that the significance of the results is apparent.

The processing program also computes the tunnel operating conditions (Temperature, pressure, Mach number, Reynolds number) from measurements made during the run and from parameters in the runsheet file. The reading of data by the computer is triggered by the signal which fires the gate valve. The rise in static pressure upstream of the test cascade determines the nominal run start time, and all time measurements (e.g. schlieren spark firing) are referenced to this.

The complete processing and print out of results from each run takes approximately 2 minutes.

6. Examples of pressure distribution, flow visualisation studies and heat transfer rate measurements on an H.P. rotor blade: Although the cascade was designed to study heat transfer rate it was realised from the outset that flow durations greater than 0·1 seconds would be suitable for accurate pressure measurement.

Pressure distributions around typical rotor blade sections have been obtained using the data acquisition system described in section 5. In the preliminary stages of the design of the cascade the response of 25cm lengths of 0·5mm bore hypodermic tubing to step changes in pressure had been investigated. It was found that such lengths of tubing terminated by the cavity volume of conventional quartz (Kistler type 7031) transducers would have response times of about 10ms, certainly adequate for the present purposes. Subsequently semiconductor transducers with built-in integrated circuit amplifiers (National Semiconductor types LX1620D) have also been used. These transducers have a larger reservoir volume which is, in the case of differential transducers, different for the two pressure taps but they have proved equally satisfactory from the point of view of stability and linearity. Differential measurements are made wherever possible in order to improve the overall resolution of the instrumentation and in some cases a large reference volume with an accurately determined pressure is used. Alternatively a total-static difference is measured directly or a blade static tapping is read differentially to an upstream wall static pressure whose absolute pressure is also determined simultaneously.

The entire pressure measuring system is calibrated frequently "on-line" with the digital data acquisition system. In the case of transducers in the test section, the pressure in the working section and dump tank is increased in steps and simultaneously read from a precision pressure gauge. In this way reading errors are reduced to a minimum.

A set of characteristic Mach number distributions around a H.P. rotor blade is illustrated in Fig. 16 where the design and two "off-design" conditions are included. Schlieren photographs taken at the design and high exit Mach number condition are shown in Fig. 17(a) and (b). The turbulence level in the free stream in this case was less than 1%.

The pressure measurements described above are conventional in that all can be made with equal ease in continuous or intermittent cascades.

The measurement of heat transfer rate in continuous running facilities is, however, more difficult and it is in this area of instrumentation that transient devices can demonstrate their potential advantages. The instrument used for this measurement in the Oxford cascade is the thin film surface resistance thermometer. These transducers and the principle of their operation have been extensively dealt with in the literature although the discussion has been chiefly related to their use in shock tubes and other very short duration facilities. A detailed treatment of the characterisitics of thin film gauges is included in Ref. 5 where a unified theory of thin and thick film gauges is given. The use of thin film gauges for both external and internal heat transfer rate measurements on turbine blades is further described by Schultz et al, Ref 9, and Smith, Ref. 11. The technique depends on the measurement of the variation of surface temperature with time of an insulating substrate forming either part or whole of the test blade.

If the model insulating substrate may be considered semi-infinite, i.e. for the times of interest heat conduction does not raise the inner temperature by an appreciable amount, the heat conduction equation

$$\partial^2 T/\partial x^2 = \left(\frac{1}{\alpha}\right) \partial T/\partial t$$

may be solved for the heat transfer rate $\dot{q}$ at the surface where $\dot{q}_{x=0} = -(K\partial T/\partial x)x=o$ to give

$$\bar{\dot{q}} = \sqrt{\rho c k}\ \sqrt{s}\ \bar{T} \qquad (23)$$

where the $\bar{}$ symbols are the Laplace transformed variables. For the simple case that the gas to wall temperature difference remains constant and thus $\dot{q}$ is constant the surface temperature is a parabolic function of time

$$T = \frac{2\dot{q}\sqrt{t}}{\sqrt{\pi \rho c k}} \qquad (24)$$

If the heat transfer rate varies with time because the surface temperature changes, the heat transfer rate at t may be obtained from equation (23) above.

$$\dot{q}(t) = \sqrt{\frac{\rho c k}{\pi}} \left[\frac{T(t)}{\sqrt{t}} + \frac{1}{2} \int_0^t \frac{T(t) - T(\tau)}{(t-\tau)^{3/2}}\, d\tau \right] \qquad (25)$$

by inversion and integration by parts. For a quartz insert in a turbine blade instrumented with thin film gauges a substrate thickness of about 1·5 mm is sufficient to keep the temperature at that depth to 5% of the surface value after 0·5 seconds. For better thermal conductors the depth is greater. If the shallow depth proves too restricting the time of measurement may be reduced since the 'penetration depth' is proportional to $\sqrt{\alpha t}$ so that for quartz a 0·1 second flow duration produces a 5% movement in temperature at a depth of 0·7mm which is generally satisfactory even for sharply curved surface, i.e. at the trailing edge of a blade.

In most short duration facilities such as shock tunnels the gas-wall temperature difference remains sensibly constant because although the heat transfer rate may be high the flow duration is typically 10 to 20×10^{-3} secs. and the model surface does not heat

appreciably. In the transient cascade, however. the flow duration of 0·3 to 1·0 secs results in quite large model temperature rises. For instance with a constant heat transfere rate of 20 watts/cm^2 the surface of quartz would rise about 100°C in 0·5 seconds so that with constant total gas temperature in the cascade the heat transfer rate will fall during the running time. The technique adopted is to plot the surface temperature rise versus measured heat transfer rate and extrapolate to the isothermal wall, i.e. zero surface temperature rise. In practice electrical analogues of the heat conduction process are used to convert the surface temperature information to heat transfer rate. The thin film current supply system,& electrical analogue signal conditioning amplifier are illustrated in Fig (18). The one-dimensional heat conduction equation

$$\frac{\partial^2 T}{\partial x^2} = \frac{\rho c}{k}\frac{\partial T}{\partial t} \tag{26}$$

for a body with thermal properties k,c and density ρ is analogous to the equation

$$\frac{\partial^2 V}{\partial x^2} = RC\frac{\partial V}{\partial t} \tag{27}$$

for the variation of voltage with time and distance along an R-C transmission line. The transmission line must be long enough, compared with the flow duration, for tne line to appear semi-infinite and there is then a direct analogue between input voltage and surface temperature on one hand and input current and surface heat transfer rate on the other. The first element at the commencement of the line must have a short time constant so that it can mirror rapid fluctuations in heat transfer rate and this time constant is approximately R_1C (Fig 18(a)). The duration for which a uniform transmission line will reproduce a step function in heat transfer rate for a surface temperature varying as $\sqrt{t}$ is approximately $t=0{\cdot}2n^2\ R_1C$ where n is the number of sections. For long running times it is sometimes more convenient to 'taper' the transmission line. Complete details of the construction and calibration of such analogue circuits is given in Ref. 5. It is the relative ease with which the thin film temperature signal can be used to give a direct measurement of heat transfer rate which makes the transient technique so useful. In order to plot T surface versus $\dot{q}$ the voltage signals from the input to the analogue are plotted against the voltage output from the current-to-voltage amplifier. Alternatively the derived heat transfer rate signal may be used to recover the surface temperature history. This is computationally more straight forward than using the temperature signal to derive the heat transfer rate signal (see for instance Schultz & Jones, Ref.5). The method adopted at OUEL is to digitise and store the analogue heat transfer rate signal and to recover the surface temperature by computation. If it is assumed that the heat transfer rate itself can be approximated by the summation of a series of ramps, it may be expressed in the form

$$\dot{q} = \sum_n H(t-t_n)\,a_n(t-t_n) \tag{28}$$

where a_n = slope of the n^{th} ramp function H = Heaviside function (=1 for t>tn, = 0 for t<tn). In general, for a semi-infinite substrate the Laplace transformed surface temperature is from equation (23)

$$\bar{T} = \left(\bar{\dot{q}}/\sqrt{\rho ck}\right)\left(1/\sqrt{s}\right)$$

Thus

$$\bar{T} = \frac{1}{\sqrt{\rho ck}}\sum_n a_n e^{-t_n s}\cdot\frac{1}{s^{5/2}} \tag{29}$$

and

$$T = \frac{1}{\sqrt{\rho ck}}\sum_n a_n \frac{4}{3\sqrt{\pi}}(t-t_n)^{3/2} \tag{30}$$

also

$$-a_n = \frac{\dot{q}_n-\dot{q}_{n-1}}{\tau} - \frac{\dot{q}_{n+1}-\dot{q}_n}{\tau} = \frac{2\dot{q}_n-\dot{q}_{n-1}-\dot{q}_{n+1}}{\tau}$$

Thus

$$T(t) = \frac{4}{3\sqrt{\pi\rho ck}}\sum\left(\frac{2\dot{q}_n-\dot{q}_{n-1}-\dot{q}_{n+1}}{\tau}\right)(t-t_n)^{3/2}H(t-t_n) \tag{31}$$

This is a readily computable function and has been found to give excellent agreement between actual measured surface temperatures and values obtained from heat transfer rate signals from the electrical analogues. An example of recorded $\dot{q}$ and T traces and a plot of $\dot{q}$ versus T is shown in Fig.18(b) and (c), reproduced from the graphical output system of the on-line computer. Examples of heat transfer rate distribution over an H.P. rotor blade are shown in Fig. 19(a) (b) and (c). Figs 19(a) and (b) illustrate the heat transfer distribution at lower and higher than the blade's design point Reynolds number with a free stream turbulence level of ≃ 4% ($u'/\bar{U}$ = 4%, $\Delta To/\bar{To}$ = 0·2%) produced by a grid while Fig. 19(c) shows the effect of free stream turbulence on the heat transfer rate at the nominal blade Reynolds number. The turbulence level has been measured with a constant temperature hot wire anemometer, see section 7. Varying the wire over-heat enables both velocity fluctuations and total temperature fluctuations to be reduced and the level of $u'/\bar{U}$ is confirmed by measurements of heat transfer rate to the stagnation line of a circular cylinder placed just upstream of the blade row. The turbulence level of 4% is not regarded as high enough to model the turbulence at the inlet to guide vanes or rotor blades and other systems are being considered to enhance this level.

The heat transfer rate distribution shown in Fig.19 were obtained on light alloy blades with quartz inserts optically polished to conform to the original blade contours, Fig. 20, and this technique was used extensively in the original studies. More recently heat transfer blades have been made from machinable glass ceramic (Corning MACOR). The same technique for depositing thin film guages is employed as in the case of quartz sub-

strates but there are obvious advantages in using a substrate which allows a complete blade section to be made from one material.

7. Turbulence levels in the working section: From the relatively smooth geometry of the inlet contraction and the fact that the test gas is set in motion by a moving boundary it would be expected that the turbulence level at the cascade entrance would be low. This has proved to be the case and in the undisturbed free stream a value less than 1% has been determined with a laser anemometer. In order to increase this value towards that expected in the engine environment a turbulence generator was installed just downstream of the gate valve. This generator comprised a single array of horizontal rods 12·7mm (0.5ins) diam. spanning the working section with a pitch of 31·10mm (1·5ins) 413mm upstream of the blades. In a test where the inlet Mach number was 0·32 the turbulence level was found to be $4\cdot2\% \sqrt{\overline{(\delta Re)^2}/\overline{Re^2}}$ and $0\cdot2\% \sqrt{\overline{(\delta To)^2}/\overline{To^2}}$ with a correlation coefficient of +0·5. Separation of the variables was obtained in the normal way by varying the overheat ratio of the hot wire operated in the constant temperature mode. The level of temperature fluctuations is consistent with Morkovin's hypothesis that $\delta T/\overline{T} \approx (\gamma-1)M^2 u/U$. Although the turbulence level is probably well below that in the engine it is sufficiently high to produce heat transfer rates which are significantly above the 'zero turbulence' case and which correlate well with predictions. Attempts to produce turbulence levels much above 5% usually result in a field which is neither homogeneous nor isotropic, and for the present purposes both of these criteria should, ideally, be satisfied.

8. Conclusion: The use of a transient compression process for the reservoir of a casacade has been shown to have advantages for the measurement of heat transfer rates. The flow duration obtainable with modest pump tubes is between 0·1 and 1·0 seconds for throat areas appropriate for 5 to 7 blade passages so that pressure distributions may be obtained. The relatively modest capital costs of such devices makes them a realistic facility for a university laboratory so that these organisations can conduct experimental programmes under full scale engine Reynolds and Mach number conditions. While the technique for measuring heat transfer rates with thin film gauges is not yet as widely used as the advantages merit there is now ample evidence to justify confidence in the results obtained in this manner. Extensive measurements of film cooling effectiveness have been made in the OUEL cascade using this technique and the relatively low cost of blade fabrication compared with blades made for hot flow cascades has fully justified the development of the facility.

9. Acknowledgements: The development of the transient cascade was supported by the Science Research Council under grant B/SR/89866 who also supported earlier work on shock tunnel systems. The original working section, blading and all subsequent programmes have been supported by Rolls-Royce Ltd. and M.O.D./P.E. The authors gratefully acknowledge the permission of Rolls-Royce Ltd. to include the data shown in Fig.19 and their advice and encouragement throughout the development of the cascade.

10. References:

1. Film cooling studies in subsonic and supersonic flows using a shock tunnel. T.V. Jones and D.L. Schultz. Proc. 8th Int, Shock Tube Sumposium, Ed. J.L. Stollery, A.G. Gaydon and P.R. Owen. Chapman and Hall 1971.

2. On the flow in a reflected shock tunnel. Aero Res. Council. R. and M. 3265. 1962. D.W. Holder and D.L. Schultz.

3. A study of film cooling related to gas turbines using transient techniques. O.E.L. Report 1121/70, Aero Res. Council ARC 32420, H.M.T. 261, 1970. T.V. Jones and D.L. Schultz.

4. Short duration studies of turbine heat transfer and film cooling effectiveness. A.S.M.E. 74-GT-131, 1974. J.F. Louis, A.M. Demergian, G.N. Goulios and R.F. Topping.

5. Heat-transfer measurements in short duration hypersonic facilities. D.L. Schultz and T.V. Jones. Agard AG-165, 1973.

6. On the flow in an isentropic light piston tunnel. T.V. Jones, D.L. Schultz and A.D. Henley. Aero Res. Council. R. and M. No 3731. 1973

7. Heat transfer research in short duration facilities. O.U.E.L. Report No 1126/75. April 1975. A.D. Hendley.

8. Notes on heat transfer, skin friction, total temperature and concentration measurements. pp. 63-102. T.V. Jones, In "Measurement of Unsteady Fluid Dynamic Phenomena". Ed. B.E. Richards, McGraw-Hill. 1977.

9. The measurement of heat transfer rates to film cooled external surfaces and the internal passages of turbomachine components under transient conditions using thin film gauges. O.U.E.L. Report No 1152/76. April 1976. D.L. Schultz, T.V. Jones, M.L.G. Oldfield, R.W. Ainsworth and L.C. Daniels.

10. A study of film cooling effectiveness with discrete holes and slots. O.U.E.L. Report 1100/74. 1974. M.R. Smith.

11. Film cooling effectiveness from rows of holes under simulated gas turbine conditions. O.U.E.L. Report No 1070/73. Aero Res. Council 34, 738; current paper No 1303, 1973. M.R. Smith, T.V. Jones and D.L. Schultz.

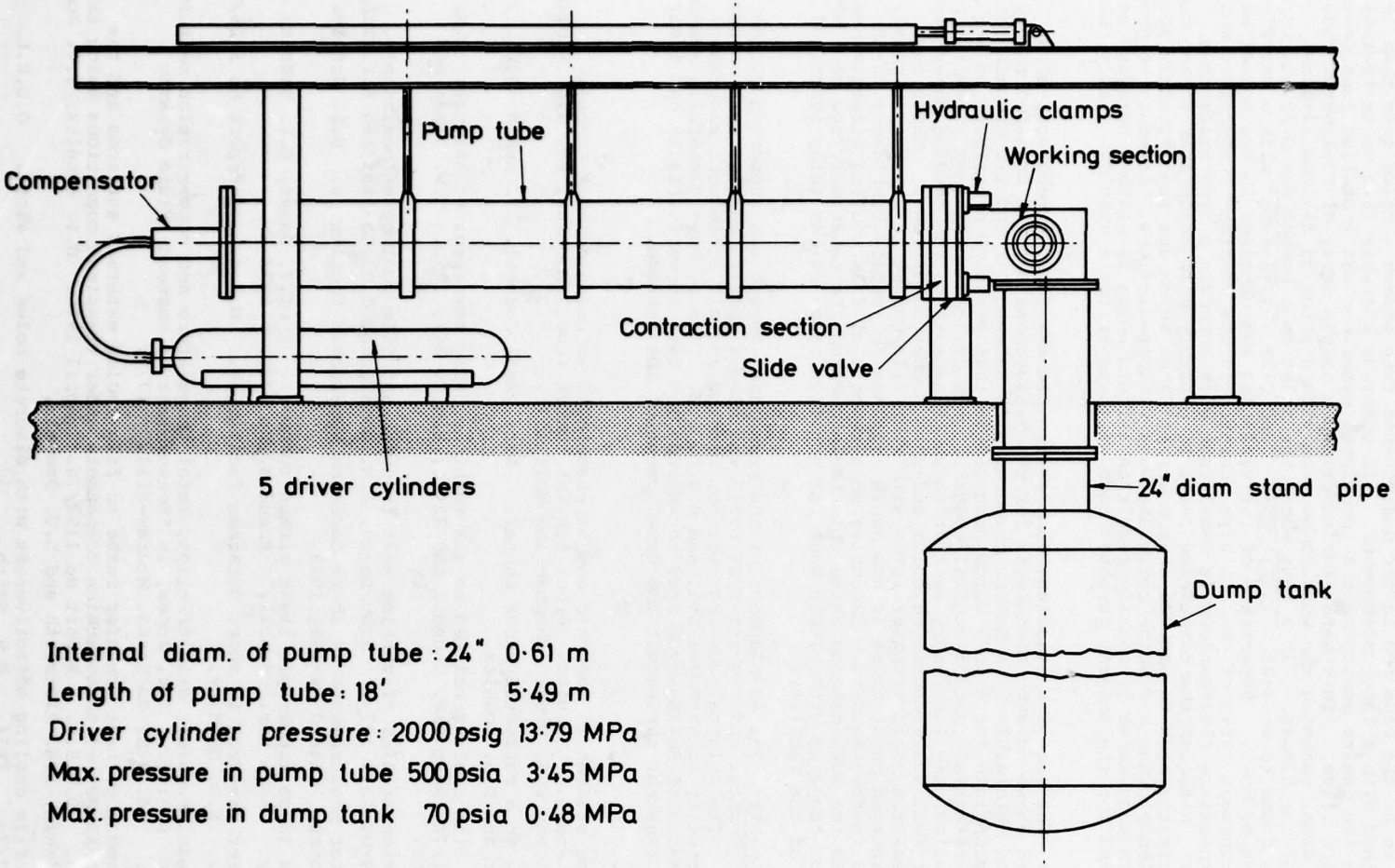

Internal diam. of pump tube : 24" 0·61 m
Length of pump tube : 18' 5·49 m
Driver cylinder pressure : 2000 psig 13·79 MPa
Max. pressure in pump tube 500 psia 3·45 MPa
Max. pressure in dump tank 70 psia 0·48 MPa

Fig. 1
General arrangement of OUEL transient cascade facility.

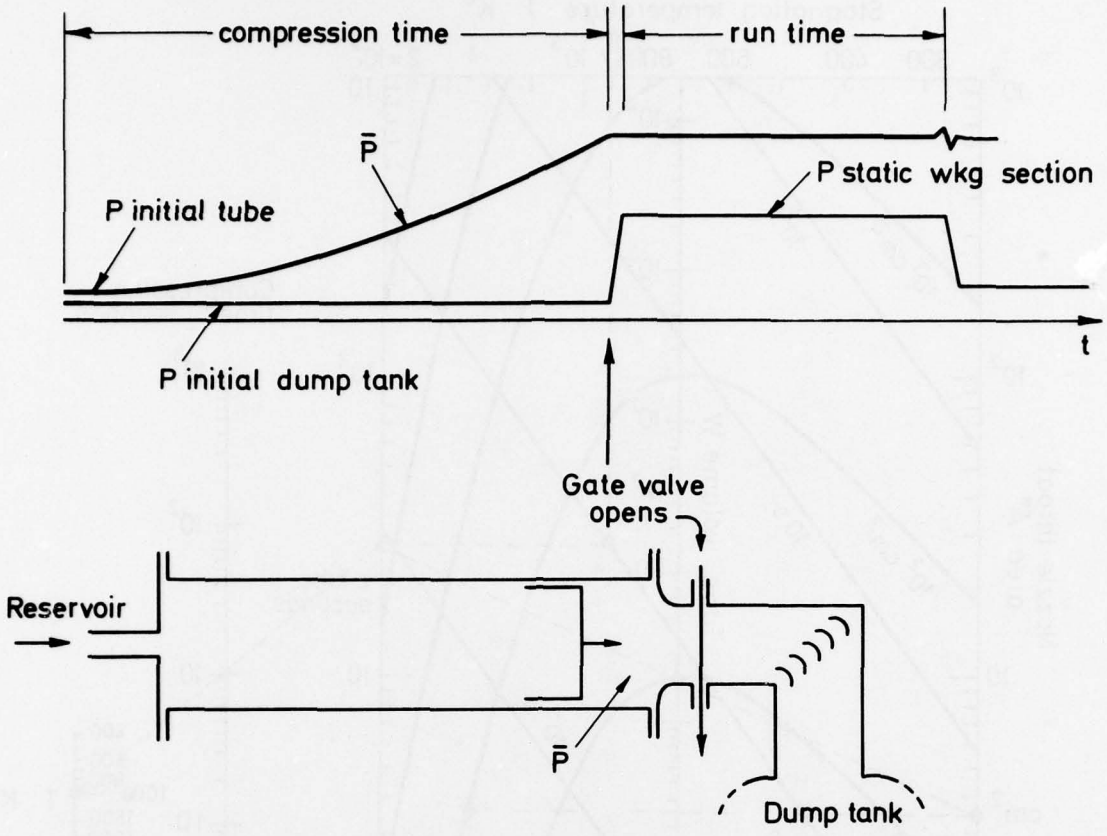

Fig. 2 (a)

Idealised pressure-time history during compression. Gate valve is opened when pressure in pump tube $\bar{P}$ reaches predetermined value.

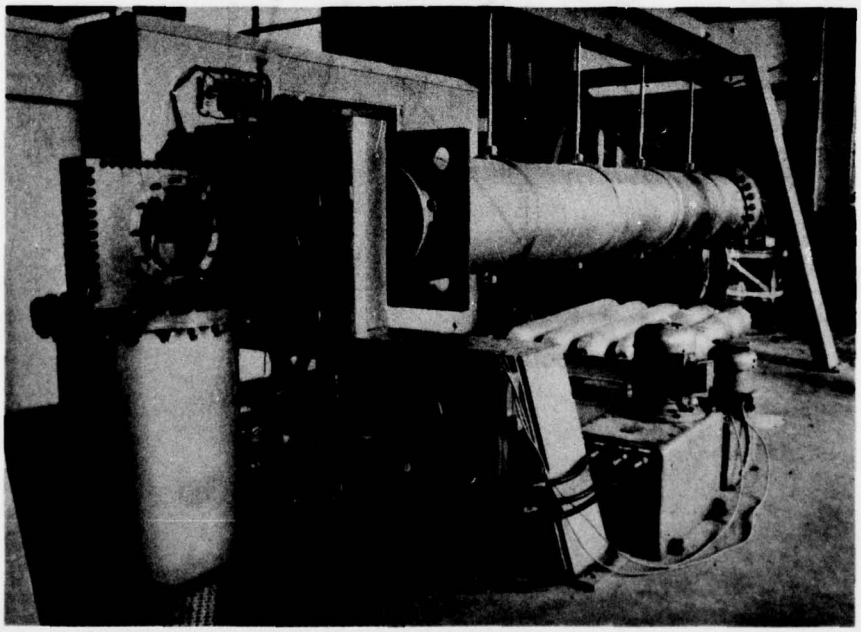

Fig. 2 (b)

The OUEL transient cascade.

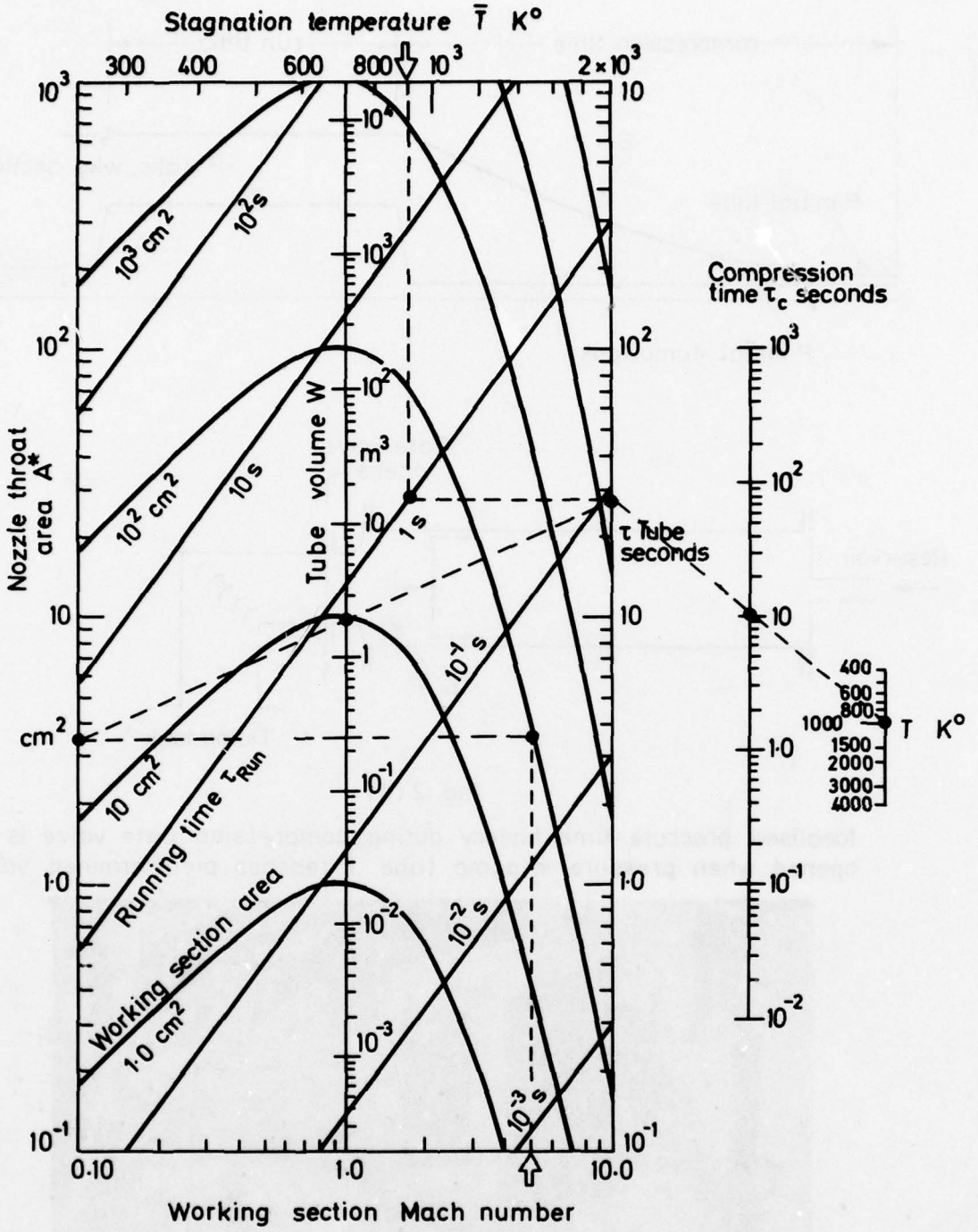

Fig. 3.
Design Nomogram for estimating performance of free piston compressors.

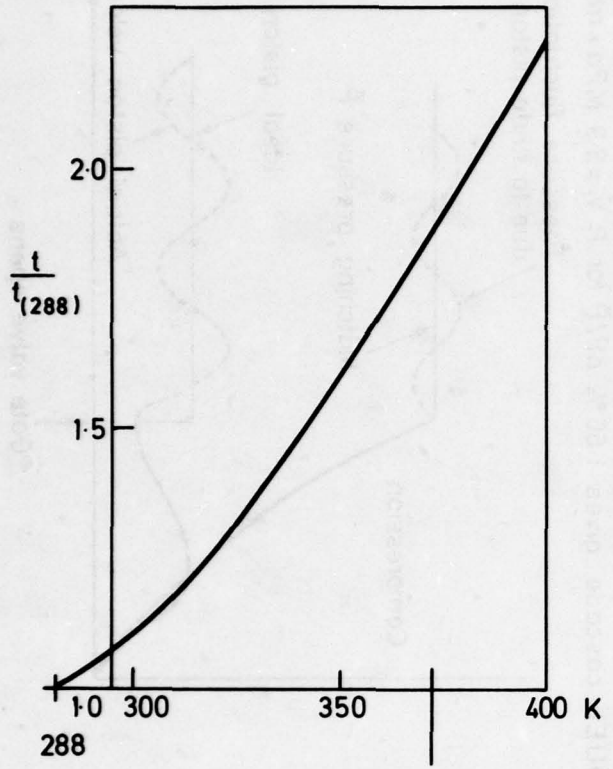

Fig. 4.
Gain in run time $t/t_{288\,K}$ with pump tube heated. For OUEL cascade.

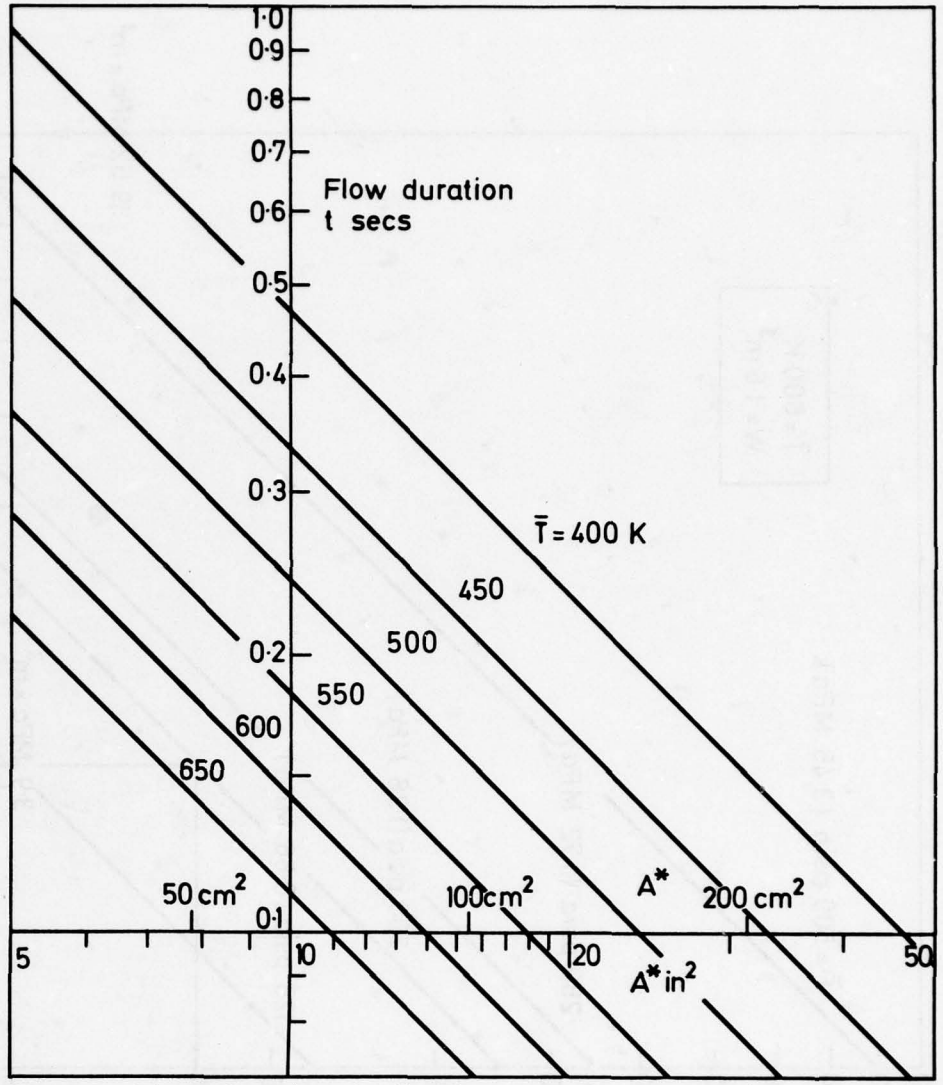

Fig. 5. Flow duration in OUEL cascade as function of throat area and total temperature.

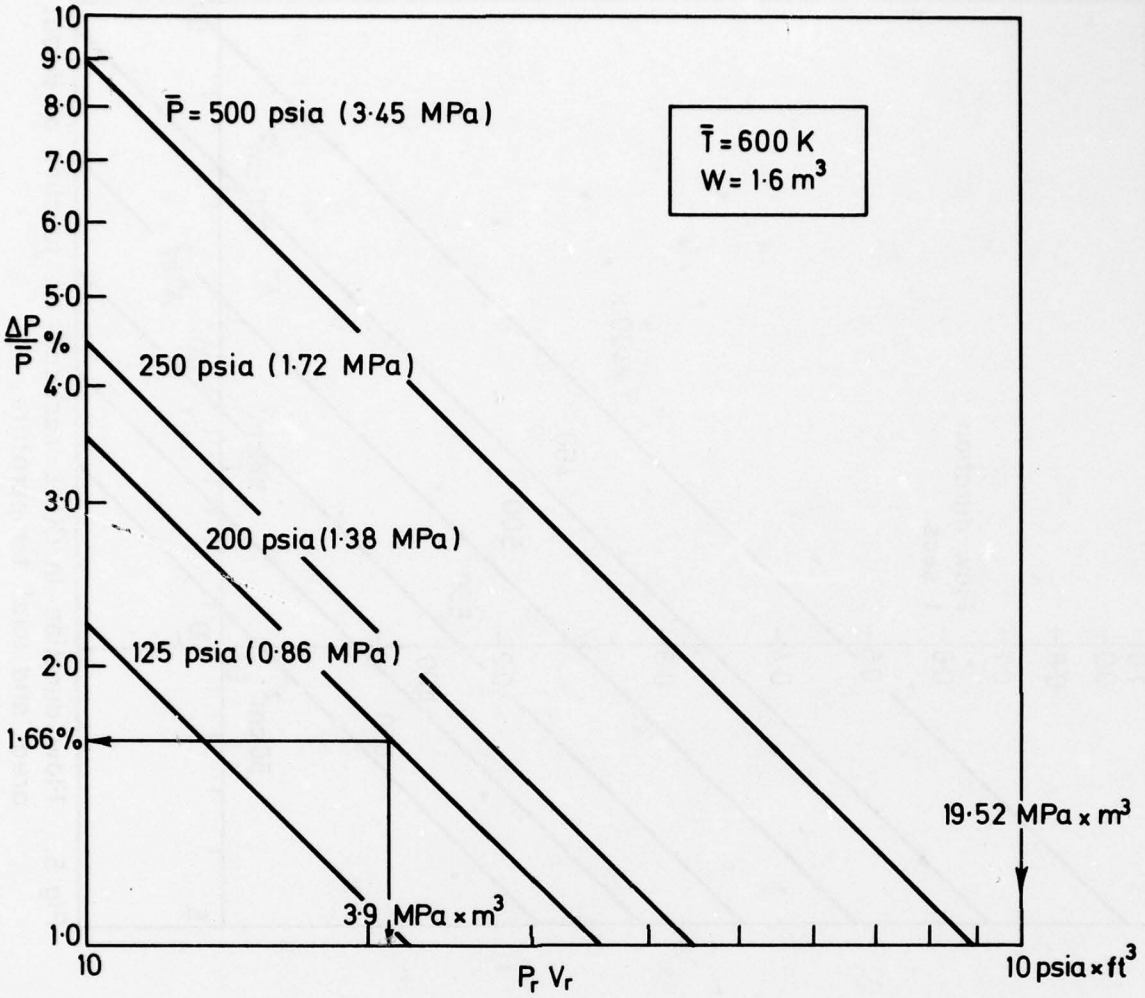

Fig. 6.

Decrease in total pressure due to finite driving reservoir volume and pressure. Total pressure as independent variable. Design point for OUEL cascade gives 1·66% $\Delta P/\bar{P}$ for $P_r V_r = 3{\cdot}9$ MPa × m³.

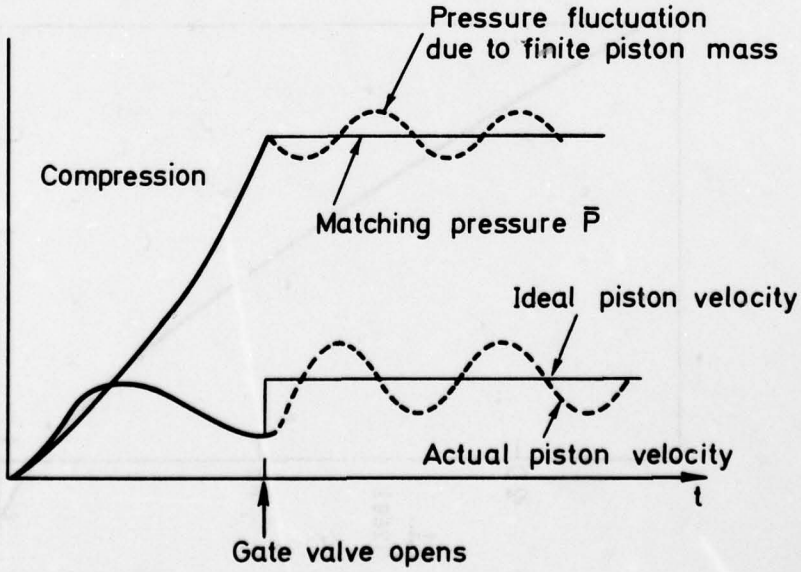

Fig. 7.

Ideal and actual piston velocity and total pressure time history. Pressure and velocity fluctuations exaggerated for clarity.

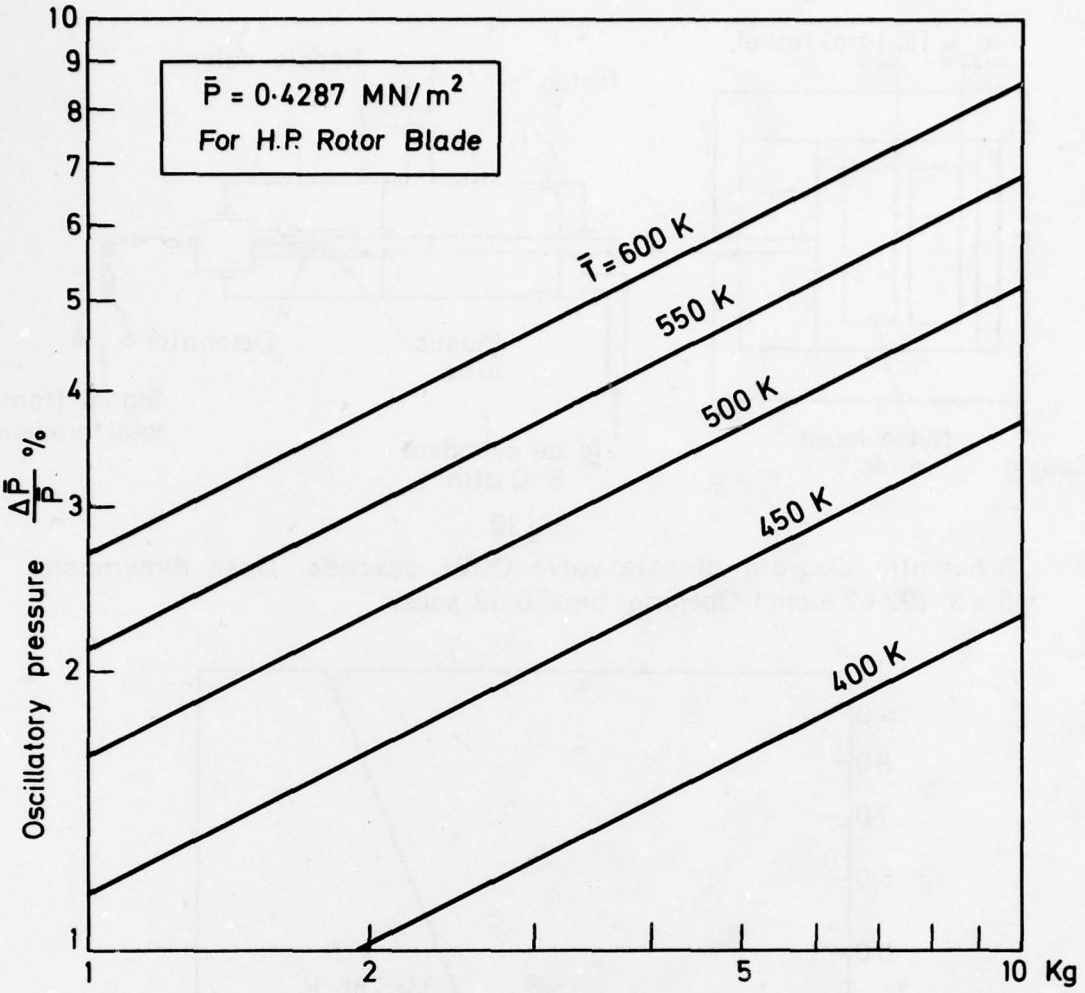

Fig. 8.

Oscillatory pressure $\Delta\bar{P}/\bar{P}$ versus piston mass for typical design case.

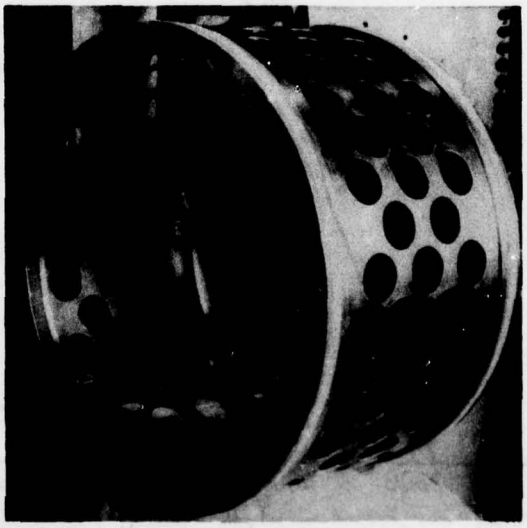

Fig. 9.

Rear view of piston.

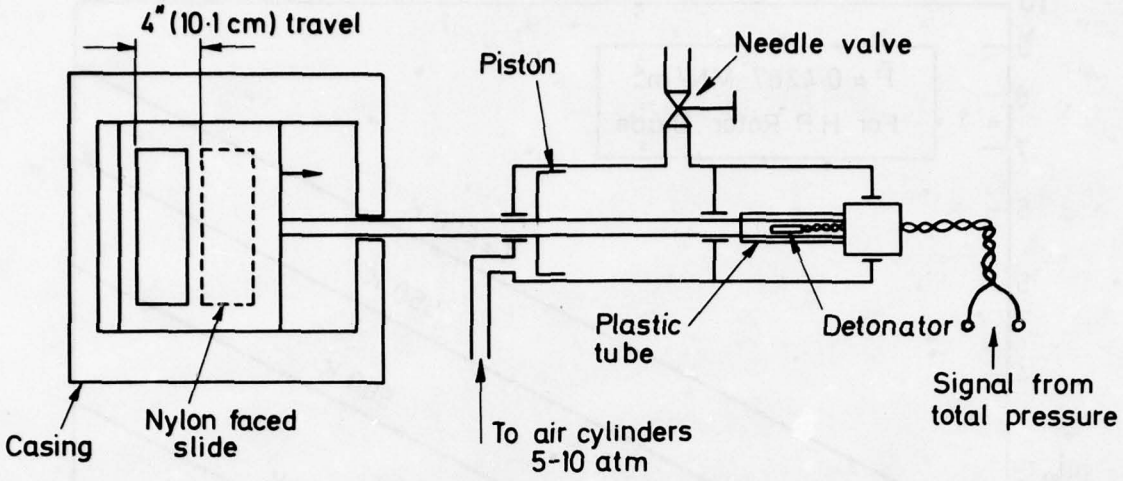

Fig. 10.

Schematic diagram of gate valve OUEL cascade. Open dimensions 9"x 3" (23 x 7·6 cm) Opening time 0·03 secs.

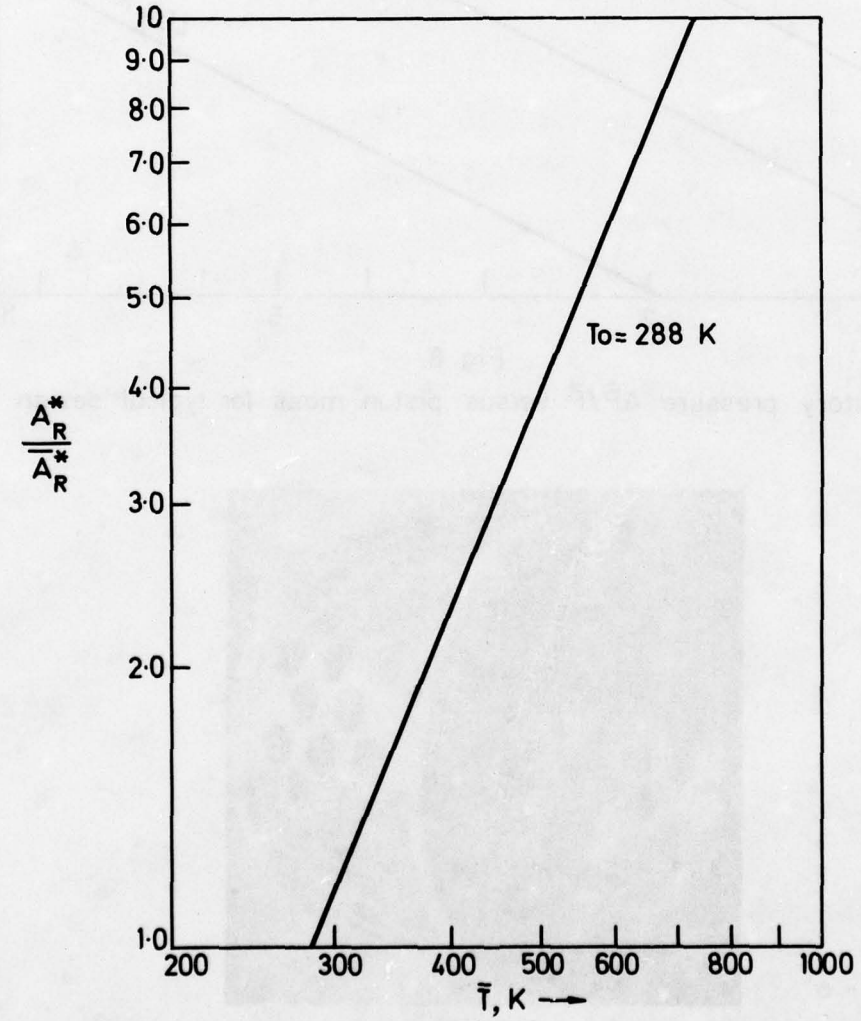

Fig. 11.

Compensating throat area required to achieve constant $\bar{P}$ as function of $\bar{T}$ for initial pump tube temperature 288 K.

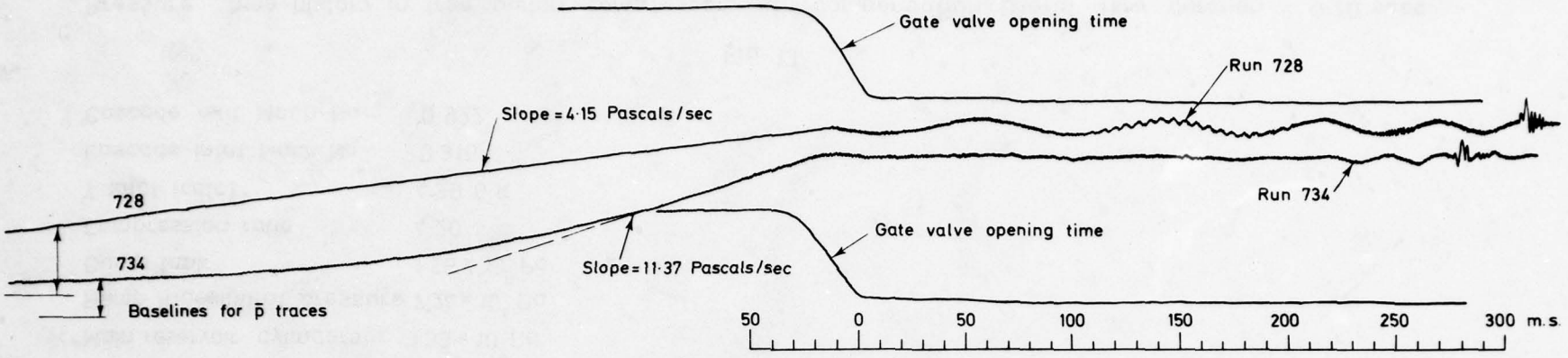

Fig. 12 (a)

Inprovement in constancy of stagnation pressure with compensator.

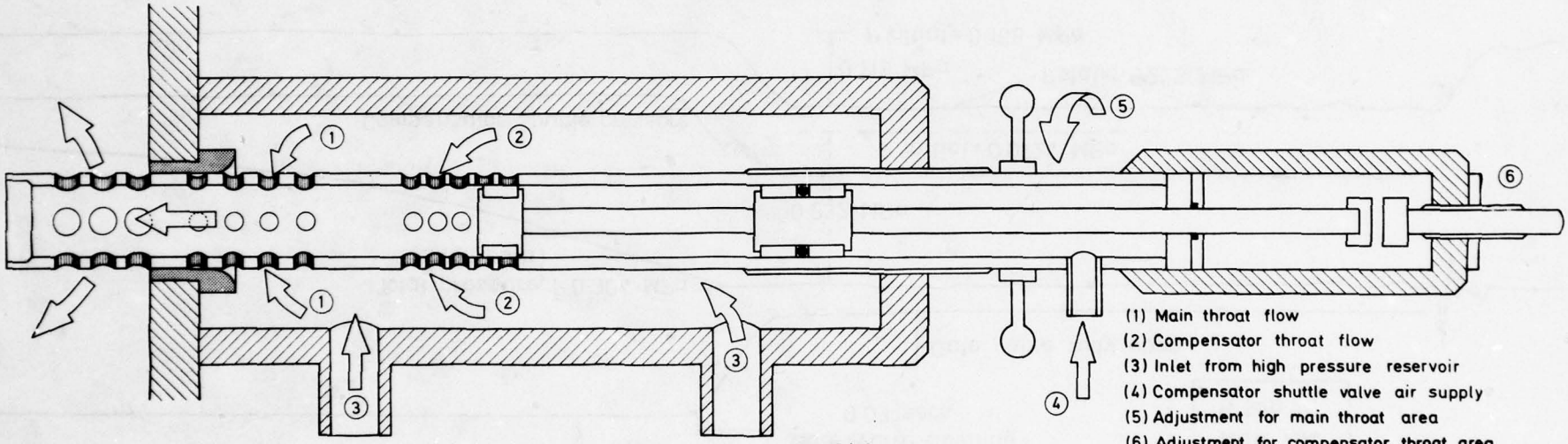

Fig. 12 (b)

Mechanical arrangement of compensator system.

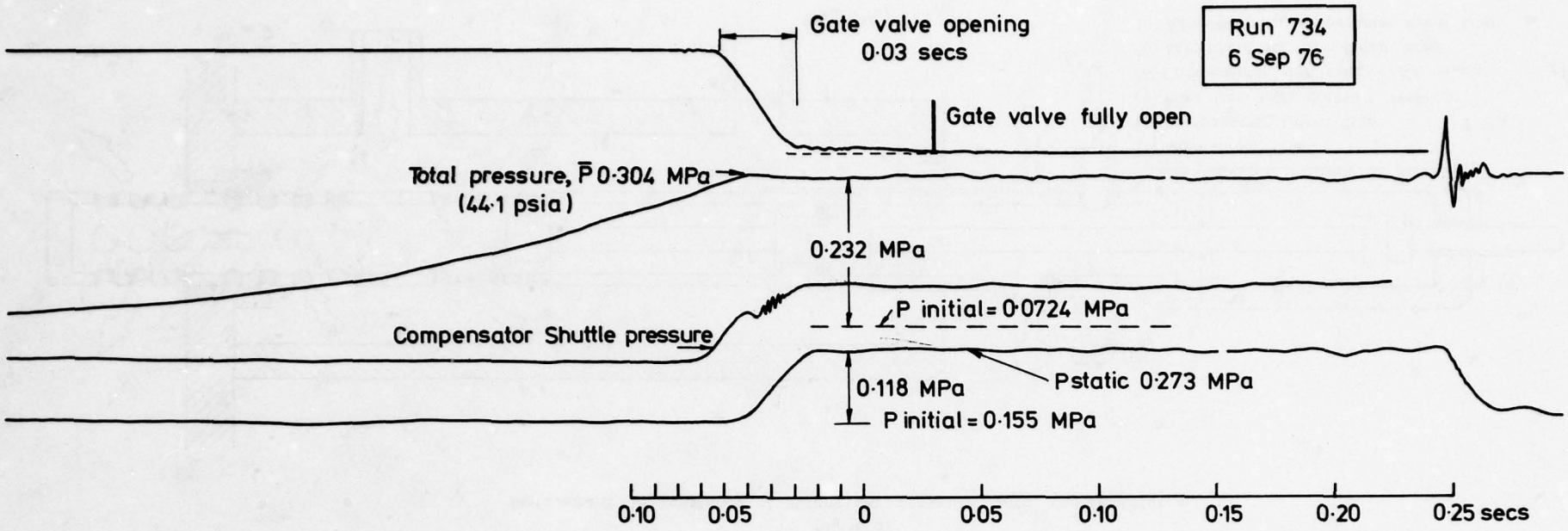

Main reservoir cylinders	$1{\cdot}39 \times 10^7$ Pa
Pump tube initial pressure	$7{\cdot}24 \times 10^4$ Pa
Dump tank	$1{\cdot}55 \times 10^5$ Pa
Compression ratio	4·20
T total (calc)	439·6 K
Cascade inlet Mach No	0·316
Cascade exit Mach No	0·922

Fig. 13.

Pressure time history in free piston compressor with compensation. Useful flow duration $\simeq$ 0·20 secs.

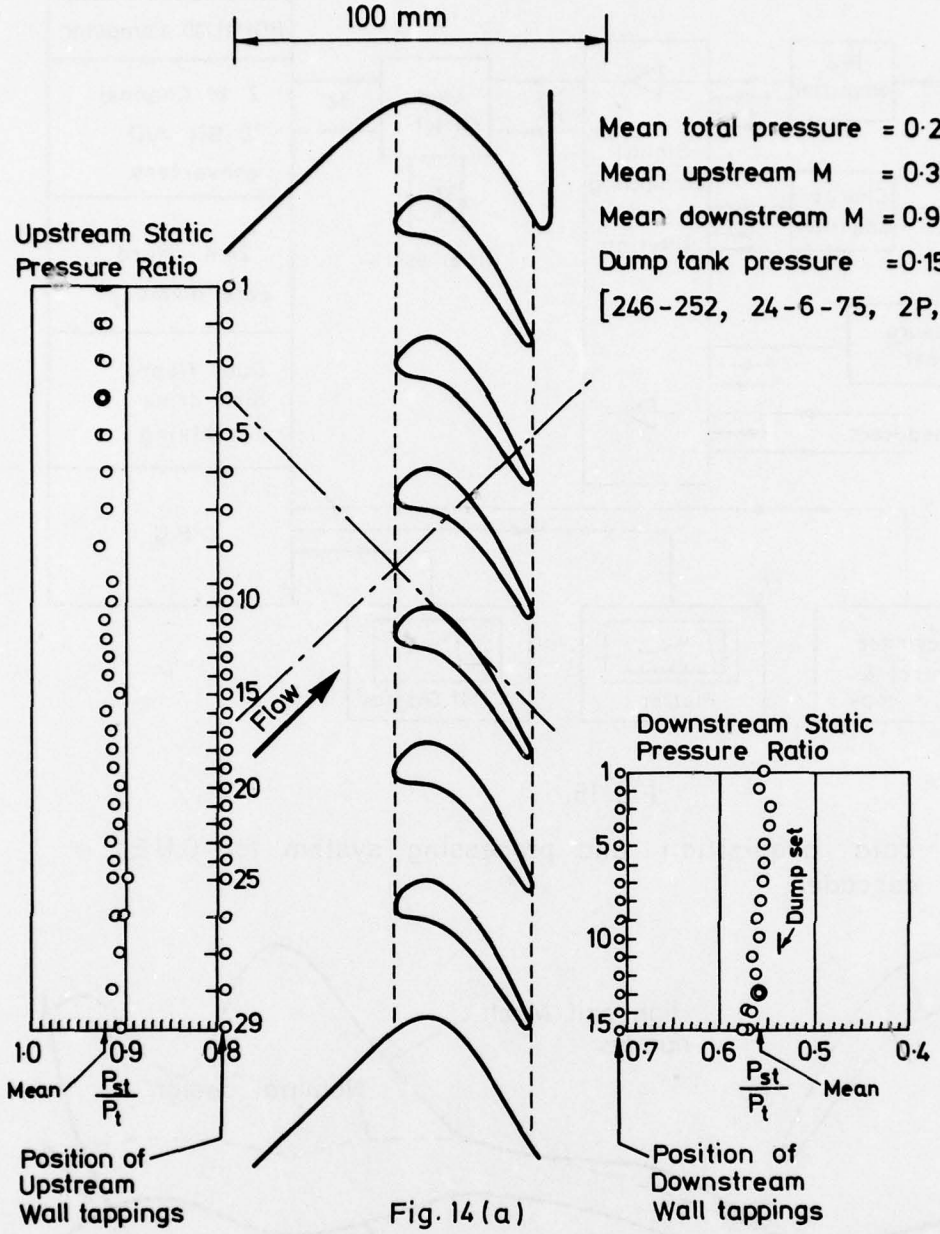

Fig. 14 (a)

Distribution of wall static pressure upstream and downstream of H.P. rotor blade cascade.

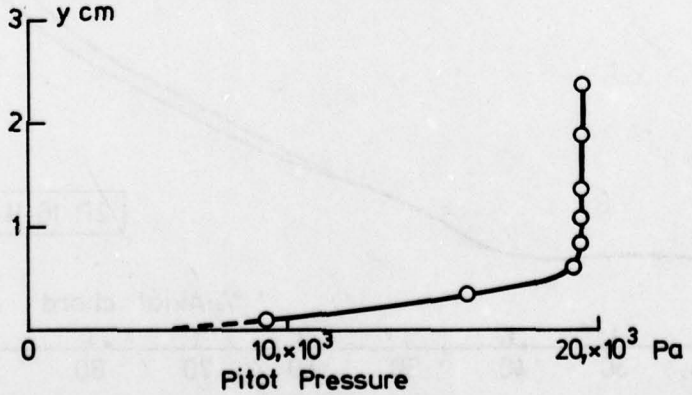

Fig. 14(b) Pitot traverse in B/L 10·15 cm upstream of centre blade. Conditions as for 14 (a)

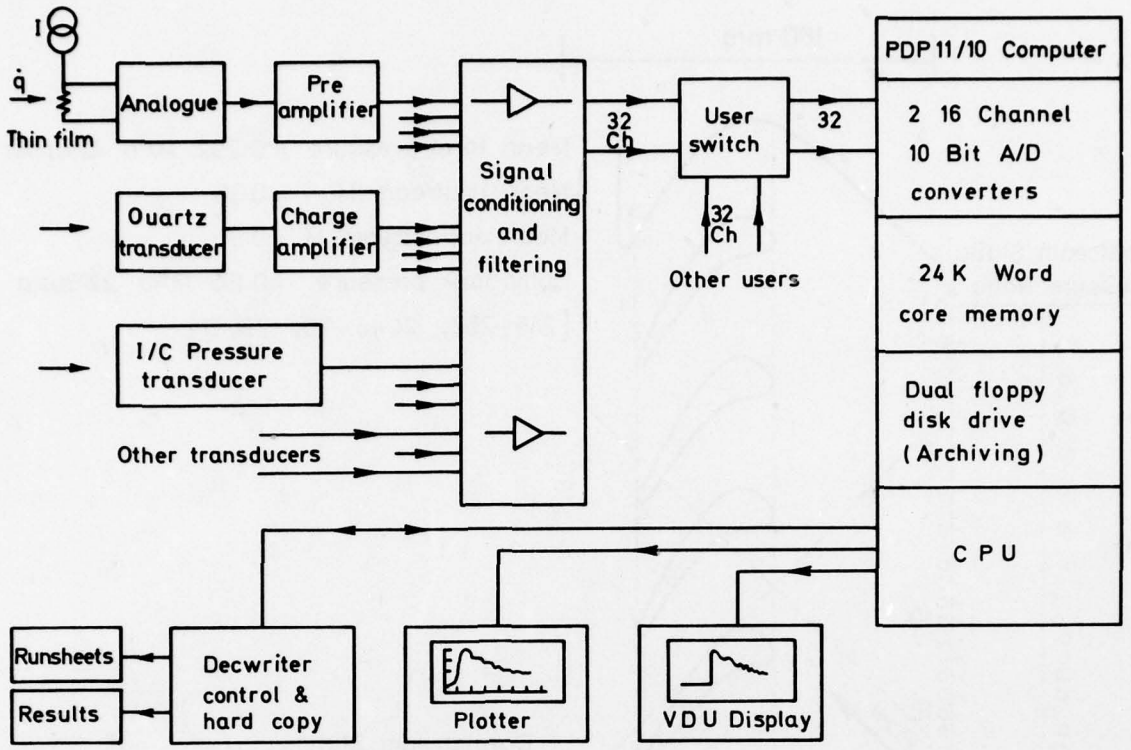

Fig. 15.

Computer data acquisition and processing system for OUEL transient cascade.

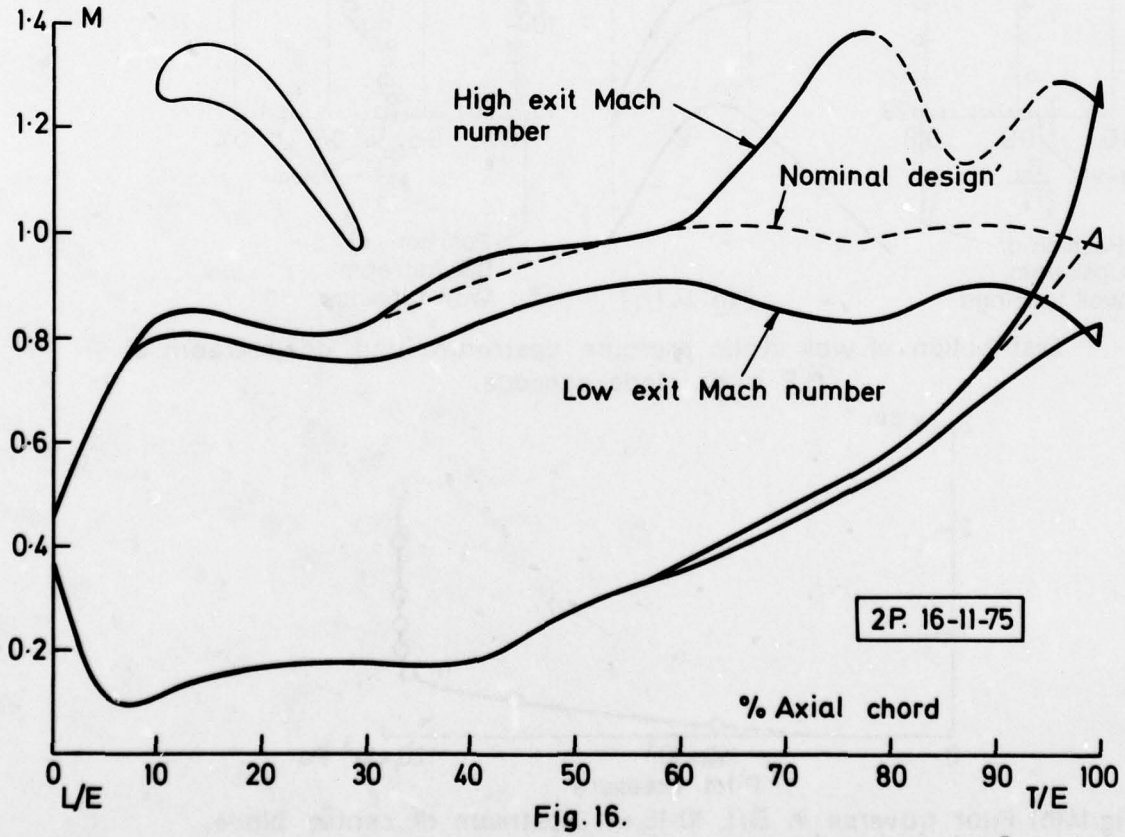

Fig. 16.

Pressure distribution on a rotor blade. Nominal $Re_x = 6{\cdot}73 \times 10^5$ (inlet M, true chord)

Fig. 17(a)

Schlieren photograph of rotor blade at nominal design conditions $M_{exit} \approx 0{\cdot}90$

Fig. 17 (b)

Schlieren at high exit Mach number $M_{exit} \approx 1{\cdot}1$

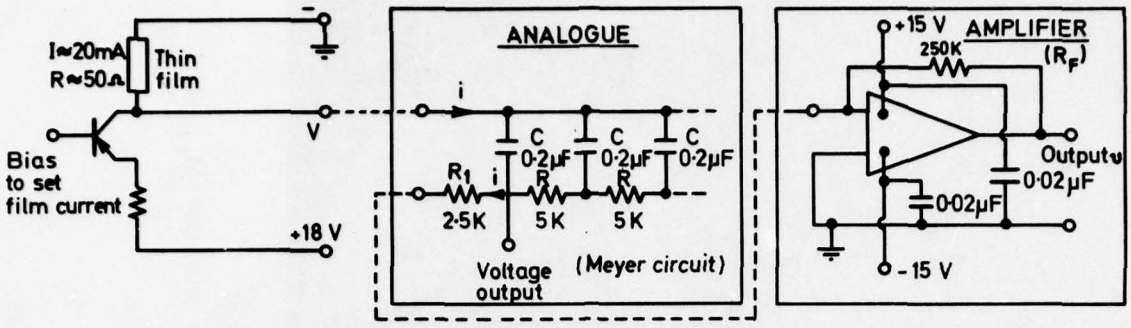

Fig. 18 (a)

Transistor constant current supply for thin film resistance thermometers, analogue circuit and current-to-voltage converter.

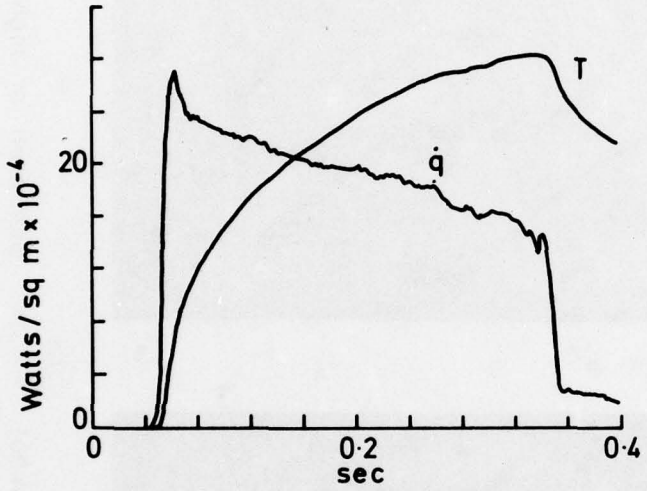

Fig. 18 (b)

Variation of surface temperature T and heat transfer rate q during run.

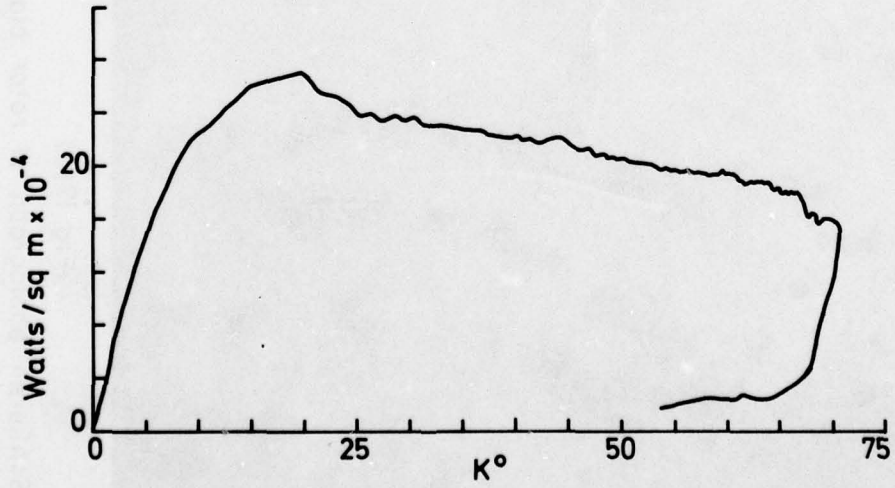

Fig. 18 (c)

Heat transfer rate versus surface temperature. Data from 18(b) Run 734

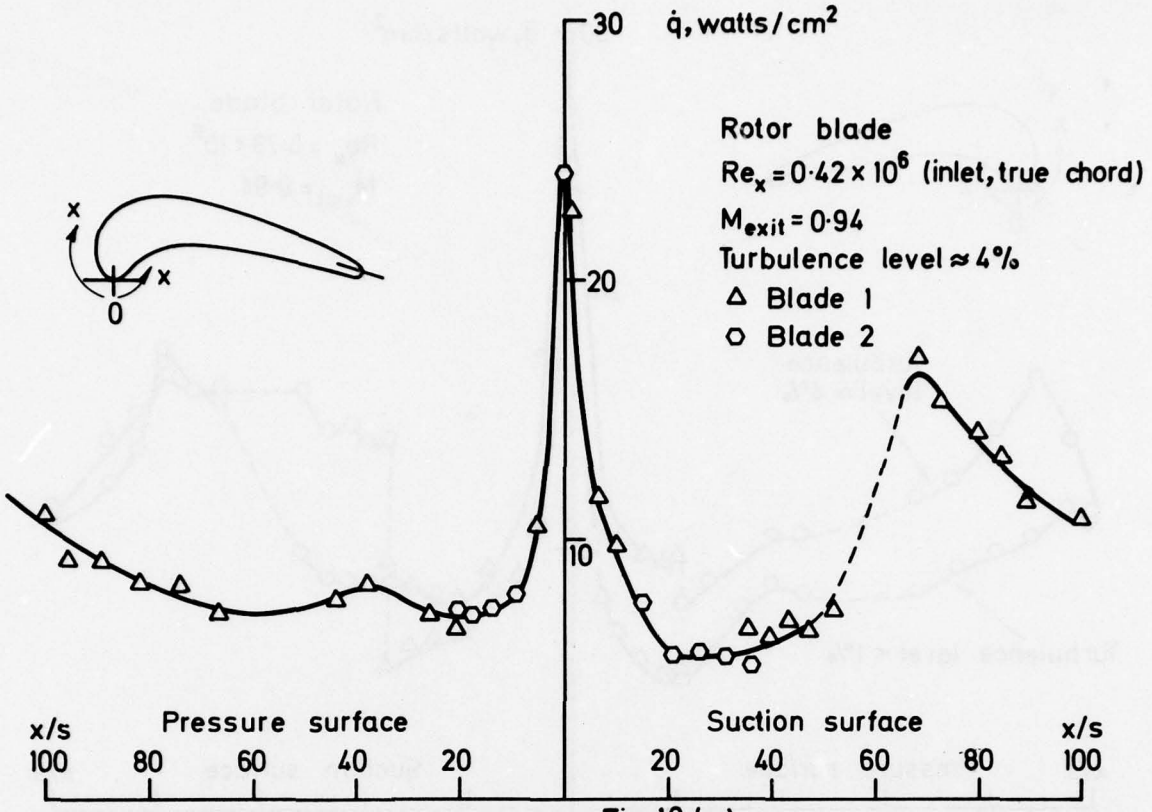

Fig. 19 (a)

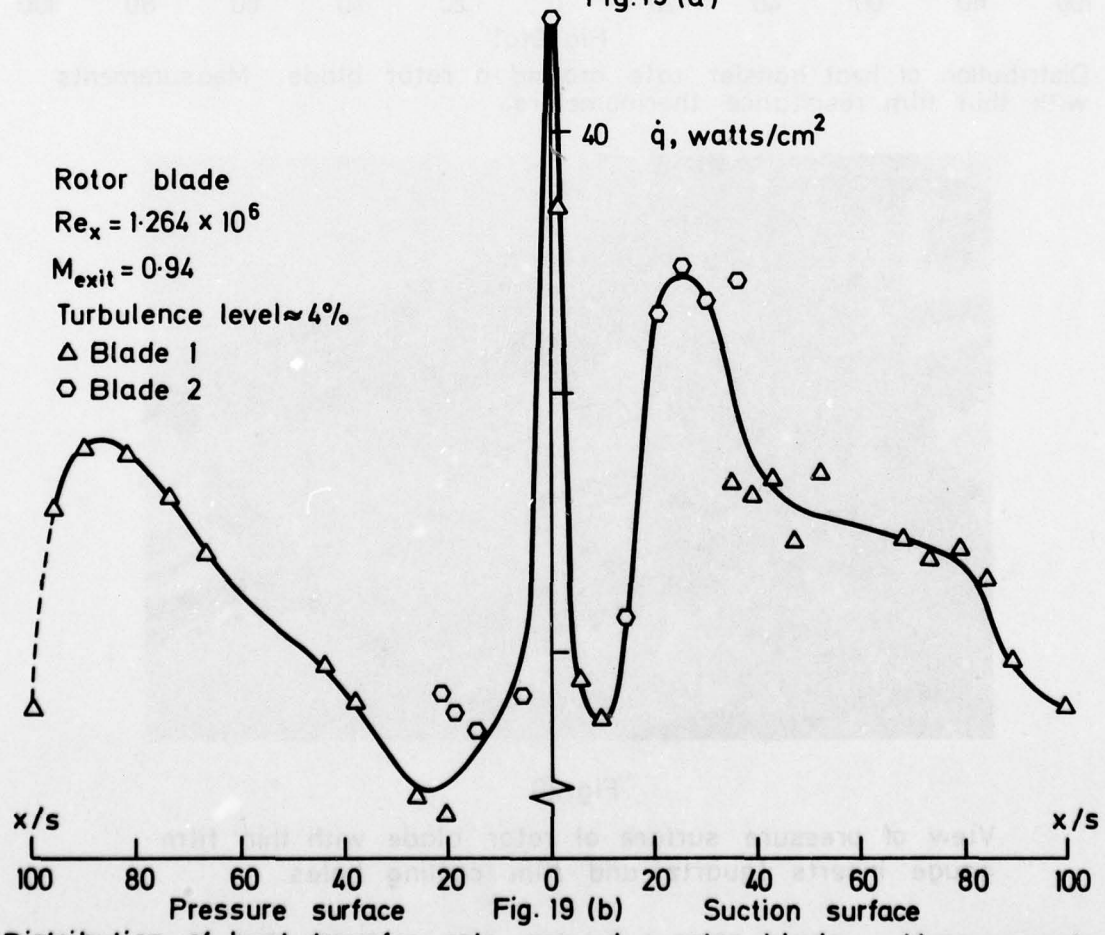

Fig. 19 (b)

Distribution of heat transfer rate around a rotor blade. Measurements with thin film resistance thermometers.

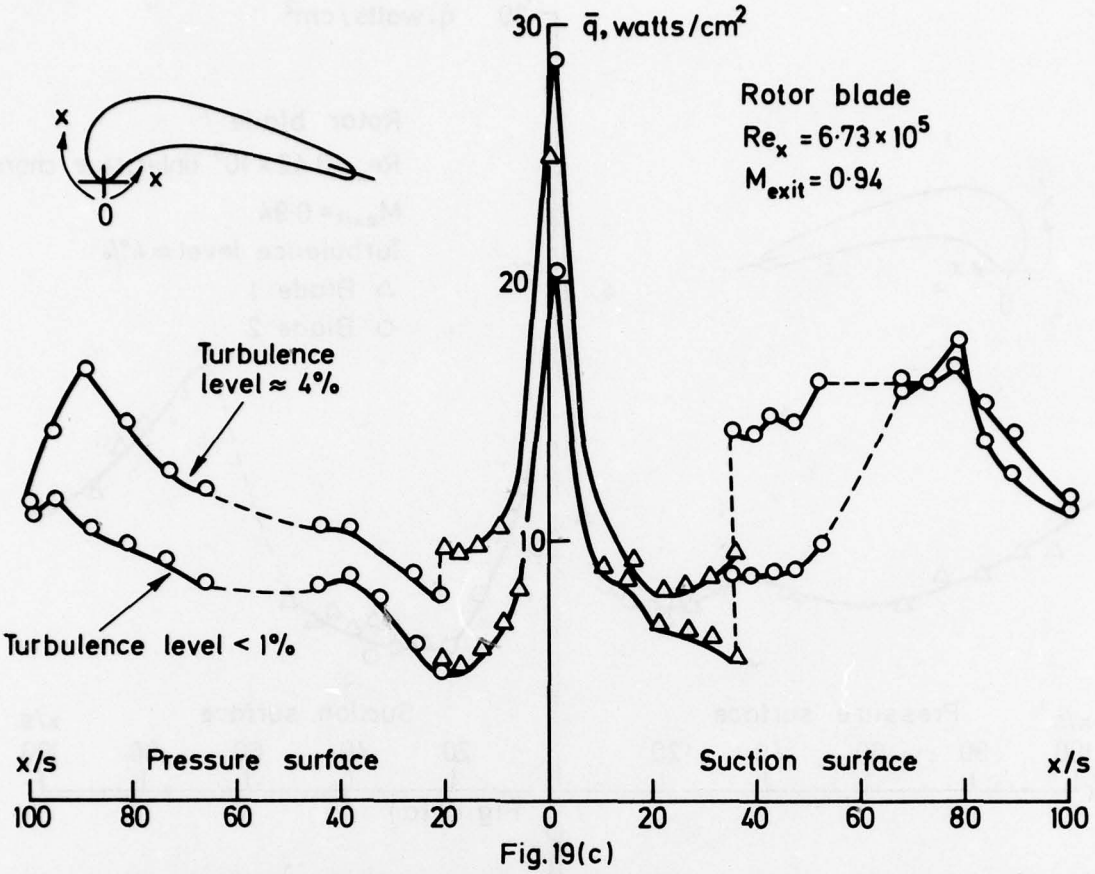

Fig. 19(c)

Distribution of heat transfer rate around a rotor blade. Measurements with thin film resistance thermometers.

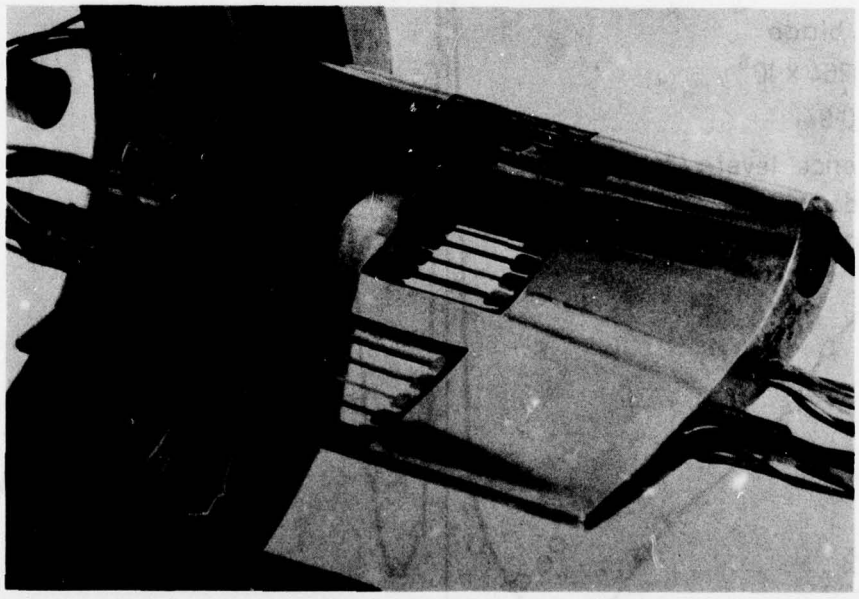

Fig. 20

View of pressure surface of rotor blade with thin film gauge inserts (quartz) and film cooling holes.

DISCUSSION

J.M.Owen, UK

Dr Schultz is to be congratulated for a clear presentation of a powerful experimental technique for the measurements of heat transfer to turbine blades. There are three questions that I should like to ask.

(1) The one-dimensional Fourier equation is solved to find the heat flux. Can the neglect of temperature variation in the streamwise direction be justified?

(2) Figure 18c shows the variation of heat flux with surface temperature. Is it not possible to calculate the heat transfer coefficient?

(3) Results have been obtained for turbulence levels up to 4%. Have you plans for the generation of high levels, and, if so, what do you intend to do?

Author's Reply

(1) The effect of streamwise temperature variations is minimised by the data reduction technique reported in the paper. The heat flux under isothermal wall conditions is deduced, otherwise the effect referred to could be important.

(2) We can determine the heat transfer coefficient from the isothermal heat transfer rates but with film cooling it would be necessary to vary the wall temperature or the coolant temperature, preferably the former, and we have not yet done this.

(3) The turbulence level of 4% was the maximum we obtained with the non-choked bar system which was chosen to give an isotropic and homogeneous structure at the blade inlet plane. Future systems may incorporate a vortex generator structure or tube bundle closer to the blade inlet.

J.F.Louis, US

How did you control the level of turbulence?

Author's Reply

An array of horizontal rods of diameter 0.5 inches spaced 1.5 inches apart (see Section 7 of the report) gave a turbulence level of $\delta Re/\overline{Re}$ of 4.2% and a $\Delta To/To$ of 0.2%. The grid was based on experimental results of Townsend and was not near choking. We have found an undisturbed free stream turbulence level about 0.2% but attempts to increase it above 5% and achieve homogeneous isotropic turbulence have not been successful.

HEAT TRANSFER TO A PVD ROTOR BLADE AT HIGH SUBSONIC PASSAGE THROAT MACH NUMBERS

B.W. Martin, A. Brown and S.E. Garrett
Department of Mechanical Engineering and Engineering Production
University of Wales Institute of Science and Technology
Cardiff CF1 3NU, United Kingdom.

SUMMARY

This paper reports heat-transfer measurements round a PVD rotor blade using a transient method. Instrumented syndanio-asbestos blades forming part of a cascade are suddenly introduced into a heated air stream, the temperature-time response of surface thermocouples attached to copper inserts in the blades then being used to determine local heat-transfer coefficients for (a) passage throat Mach numbers between 0.79 and 0.94 (b) turbulence intensities from 4.15 to 9.05 per cent (c) blade chord Reynolds numbers from 7.8×10^5 to 8.9×10^5.

Measured transition lengths on the suction surface, over which the heat transfer nearly trebles, are somewhat short in relation to other measurements. The onset of transition, which is downstream of predictions for the higher Reynolds numbers but accords with the trends of existing correlations, is little influenced by turbulence intensity variations in the above range. Over the pressure surface the heat transfer is less than for a fully-turbulent boundary layer. Comparisons with other high Mach-number measurements suggest that much further work is needed before the effects of scale of turbulence are fully understood.

LIST OF SYMBOLS

A	surface area of copper insert
B	insert Biot number = $h_i L/k_i$
Cp	pressure coefficient = $(p - p_{s2})/(p_{s1} - p_{s2})$
C_p	specific heat at constant pressure
F^p	geometrical factor specified in equation (5)
h	heat transfer coefficient
K	velocity gradient factor = $\frac{\nu}{u^2}\frac{du}{dx}$
k	thermal conductivity
L	linear dimension of copper insert = V/A
ℓ	length of transition region
Ma	mainstream Mach number
p	gas pressure
Pr	Prandtl number
Re	Reynolds number
St	Stanton number = $h/(\rho_g u C_{pg})$
T	absolute temperature
t	time
u	local mainstream velocity
u'	RMS value of fluctuation in u
u'/u	mainstream turbulence intensity
V	volume of copper insert
x	downstream distance from forward stagnation point
θ	boundary-layer momentum thickness
λ	measure of length of transition region
Λ	Pohlhausen parameter = $\frac{\theta^2}{\nu}\frac{du}{dx}$
ν	kinematic viscosity
ρ	density
τ	defined by Eq.(2)

Subscripts

b	local blade value
c	based on blade chord
g	refers to hot gas
i	insert condition
ℓ	based on length of transition
m	local mean blade value
o	initial insert condition
s	stagnation condition
t	condition at start of transition
x	based on downstream distance from forward stagnation point
λ	based on measure of length of transition
θ	based on boundary-layer momentum thickness
∞	hot gas condition
1	condition at cascade inlet
2	condition at cascade outlet

INTRODUCTION

In the last 15 years the supersession of forged and rolled gas turbine blades by high-grade castings of nickel alloys has made possible the replacement of intersecting circular arc blade profiles by those aerodynamically designed, as proposed by Lighthill (1) and Stanitz (2), to have a prescribed velocity distribution. While PVD profiles are preferable because they permit large fluid turning angles, high stage pressure ratios and maximum lift for minimum chord, they are of relatively complex shape with rapid mainstream acceleration over typically 20% of the suction surface, followed by a mainstream velocity plateau and a region of adverse pressure gradient. By contrast, circular arc profiles have little or no central region of uniform velocity and the initial favourable pressure gradient is correspondingly weaker. The negative pressure gradient over most of the pressure surface of a PVD blade leads to a steadily-increasing freestream velocity.

When strong favourable pressure gradients occur in regions of high mainstream turbulence intensity, as is likely over PVD blades in turbines, peculiarities in boundary-layer transition from laminar to turbulent flow are to be anticipated because these two influences have opposing tendencies; the former to suppress turbulence and the latter to promote it. Brown and Burton (3) observe that, over the suction surface of a PVD model blade, transition starts earlier but lasts longer than on a circular-arc blade. The extent of the transition region depends on the velocity distribution, mainstream turbulence intensity u'/u and chord Reynolds number Re_c. In such circumstances the heat-transfer measurements round the circular-arc blades of Wilson and Pope (4) and Walker and Markland (5) using electrically-heated models in a cold air stream, Turner (6) for an internally-cooled model in a heated air stream and Bammert and Hahnemann (7), Andrews and Bradley (8) and Hodge (9) using blades in cascade, offer little guidance as to the distributions to be expected round PVD blades. Turner's comparisons, which include the lower mean blade heat transfer measured by Ainley (10) in a stationary cascade than in an engine, nevertheless indicate

its direct dependence on u'/u for a particular value of Re_c.

Assuming the adequacy of heat-transfer predictions by standard flat-plate procedures for laminar or fully-turbulent boundary layers on a turbine blade (implying that surface curvature effects are not significant), the main outstanding problem in completely specifying the heat transfer round a PVD blade is identification of the onset and extent of boundary-layer transition and the heat transfer in the transition region. The bases for prediction reviewed by Brown and Martin (11) include the correlations of Hall and Gibbings (12) and Seyb (13) which both relate the onset of transition to Re_θ, u'/u and the Pohlhausen parameter Λ, though in the case of the former authors only for adverse and zero pressure gradients; for favourable pressure gradients they sketch a family of curves with u'/u as parameter based on $Re_{\theta t}$ for zero Λ and drawn parallel to the Pretsch (14) stability limit. For zero Λ they also propose a criterion to locate the end of transition which, however, appears less well founded than the correlation of Dhawan and Narasimha (15) for the extent of transition, which is related to its onset through a turbulence-spot intermittency factor. Seyb's correlation is based on the aerofoil measurements of Goldstein and Mager (16), Crabtree (17) and Hodge (9). The predictions of McDonald and Fish (18) for the location and extent of transition, which take account of the intermittency of the transitional boundary layer identified by Dhawan and Narasimha and which accord with their findings in respect of the effect of u'/u, are based on calculation of the streamwise development of a turbulent mixing length whose magnitude is governed by the turbulence kinetic energy equation.

While the above predictions and correlations are in reasonable agreement with measurements in adverse and zero pressure gradients, only Seyb's correlation (which is unconfirmed for large favourable pressure gradients and high u'/u) accords with the flat-plate transition measurements in favourable pressure gradients of Edwards and Furber (19), Buyuktur, Kestin and Maeder (20) and Junkhan and Serovy (21) at low mainstream velocities, and even this substantially overpredicts $Re_{\theta t}$ values for low u'/u observed by Dunham and Edwards (22) using aerofoil and camber line blades in cascade. Furthermore, as Brown and Martin (11) point out, the increased heat transfer in the transition region observed by the above workers usually leads to much less satisfactory heat-transfer predictions for the pressure surface than for the suction surface of non-PVD blades; apart from a proposed linear interpolation there are no heat-transfer correlations for a transition region whose extent owing to u'/u and non-zero positive Λ (or velocity gradient factor K) cannot with confidence be predicted.

Walker and Markland (5) agree with Dunham and Edwards'description of the expected laminar boundary layer on the pressure surface as 'transitional with occasional bursts of turbulence' but the latter authors find the heat transfer along the pressure surface to increase with mainstream Mach number up to 0.9; this parameter (and its relation to the scale of turbulence) may be responsible for discrepancies between $Re_{\theta t}$ values derived from their measurements and Seyb's correlation. The purpose of the present research, which is more fully reported by Garrett (23), is to investigate further the effect of high subsonic Mach number at higher u'/u than those of Dunham and Edwards using a transient method of heat transfer to a PVD blade. The throat Mach number range covered, from 0.79 to 0.94, also permits comparison with the only other reported measurements on PVD blades of Brown and Burton (3) at low mainstream velocities, which extend to lower values of u'/u.

EXPERIMENTAL APPARATUS AND PROCEDURE

Air is delivered to the cascade from a centrifugal compressor at pressures up to 4.5 bar and a maximum flow rate of 1.12 kg/s via an orifice plate, a settling chamber and a turbulence generator incorporating drilled plate grids for solidity ratios of 0.5 and 0.4 and parallel round bar grids, based on the work of Rose (24), for solidity ratios of 0.3 and 0.2. Turbulence intensity is measured just upstream of the cascade by DISA constant temperature hot-wire anemometer with a retractable probe to minimise wire breakage. Cascade entry pressures are measured by static pressure tap in the duct wall and a pitot tube which traverses from the wall to the middle of the rectangular entry section. Air delivery temperatures from 360 K to 420 K are monitored by chromel-alumel thermocouple 70 mm upstream of the turbulence generator in a region of low Mach number and measured on a Tinsley-type potentiometer. Air from the cascade is discharged to atmosphere through two silencers and a diffuser.

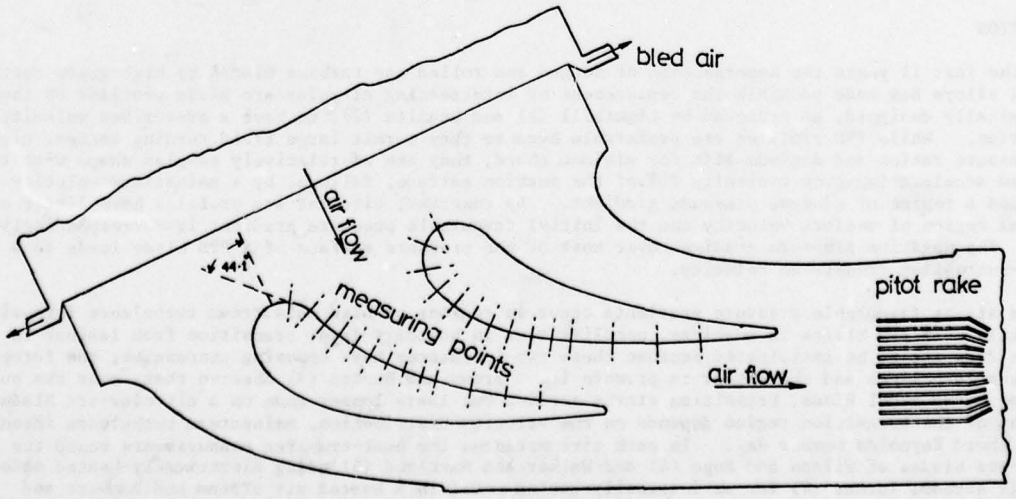

Fig.1 Cascade configuration showing measuring stations and boundary-layer bleed

The cascade shown in Fig.1 comprises two central blades between profiled top and bottom walls such that its overall height at entry is 115.5 mm and its spanwise width 34 mm; the design total throat area is 26.01 cm^2. The blades, of stagger angle 45.9°, turn the flow through 65.2°; the design angle of incidence is 44.1° as shown in Fig.1 though the measurements reported below suggest up to 15° of positive incidence in the present rig. The blade, whose suction and pressure surfaces are 58.8 mm and 49.8 mm long respectively, has a 50 mm chord; it is of the undecusped type whose relatively thick trailing edge facilitates instrumentation. Dyban and Glushchenko (25) report satisfactory correlation with predictions of cascade measurements of Mach number and temperature factor effects on heat transfer using a blade of equal chord and 40 mm span.

The suction surface of the upper blade and the pressure surface of the lower blade forming the centre channel in Fig.1 are instrumented at the stations shown, whose pitch of 5% of surface length towards the leading edge (and 10% elsewhere) takes account of the anticipated region of high streamwise acceleration. Because the small blade size renders most heat-transfer measuring techniques (except perhaps that of Turner (6)) impractical, a transient method is used which exploits the dependence of the exponential temperature-time response of a cool body initially at T_{io}, suddenly exposed to a hot fluid maintained at T_∞, on the surface heat-transfer coefficient between the two, according to

$$\frac{T_i - T_{io}}{T_\infty - T_{io}} = 1 - \exp(-t/\tau) \qquad (1)$$

where

$$\tau = \rho_i V C_{pi} / (h_i A) \qquad (2)$$

These equations assume that h_i is independent of t and transient body temperature T_i and that the latter remains uniform throughout the volume V; this is reasonable if $B = h_i L/k_i$ is small. For the cylindrical copper inserts of 2 mm diameter and length L used (with 0.51 - 0.64 mm chromel-alumel thermocouple beads crimped in holes in their sides to measure T_i) $B \approx 2.6 \times 10^{-3}$ if h_i is conservatively estimated at 0.5 kW/m^2K. According to Kreith (26), T_i then varies negligibly within the insert and the time for it to approximate T_∞ of some 40 s is well within the range of the data-recording equipment used. For h_i in kW/m^2K

$$\tau = 6.97/h_i \text{ s} \qquad (3)$$

Conduction to and between inserts, which are located flush with the blade surface at the stations shown in Fig.1, is minimised by using blades of syndanio-asbestos and by offsetting adjacent inserts spanwise by 4 mm. Thermocouple leads are embedded in slots in the blades. Sudden exposure of the inserts to the hot air is achieved by making the two central blades more than six times longer than the spanwise duct width of 34 mm so that the portions of the blades containing the inserts can be slid into the duct through holes of blade cross-section in its 6.35 mm -thick side walls; sealing is by a stuffing-box arrangement. The opposite ends of the blades incorporate 0.78 mm static pressure taps at the same stations as the inserts, as shown for the suction surface in Fig.2, and communicate through 1.6 mm embedded steel tubes with the blade ends. These are recessed in tufnol blocks to form a carriage which slides on steel rods and whose rapid motion is actuated through short tension springs by a crank mechanism.

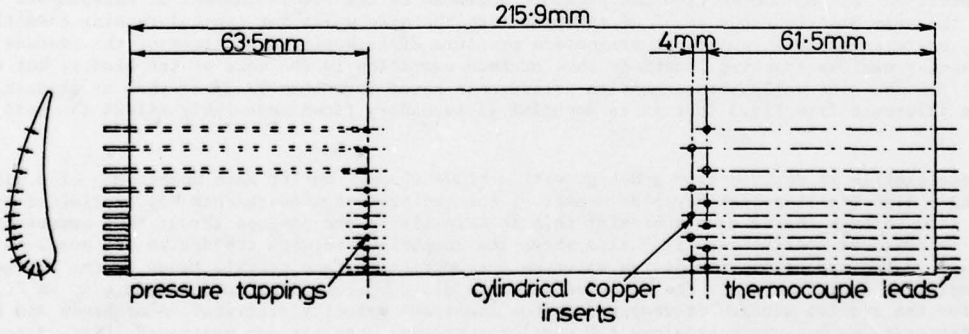

Fig.2 Instrumentation on suction surface of movable central blade

The side and profiled top and bottom walls forming the cascade body are mounted in a frame comprising two parallel plates having holes of cascade cross-section. The upstream plate is located just ahead of the leading edges and incorporates the hollow flange seen in Fig.1 through which 2 mm of the incoming boundary layer are bled round the duct periphery; the second plate is downstream of the trailing edges. The pitot comb for downstream wake measurements also shown in Fig.1 comprises twelve 0.8 mm rake tubes fanning out to 2.4 mm pitch at 31.8 mm from the 5 mm containing stem mounted normal to the plane of the comb to pass through the cascade side walls. The rake traverses the duct without influencing the extent to which the latter is blocked and also rotates in its own plane to measure vertical wake profiles through micrometer adjustment of the axial and circumferential positions of the stem. The yaw angle of the tubes to the flow is insufficient to cause measurable error. At the top and bottom of one side wall in the plane of the tips of the rake are two static pressure taps. Pressures are measured by multitube tilting manometer and photographically recorded to a resolution within 1 mm Hg. Thermocouple signals are recorded by Solartron data logger incorporating a DVM, an Addo punch tape and punch drive. The time for one complete scan of the

26 thermocouples is 8.23 s.

Derived values of h_i for the inserts are reduced to those of the adjacent blade surfaces using the procedure of Schultz and Jones (27) to account for the effect on the boundary layer of the step temperature reduction from T_b to T_i over the insert surface. Assuming the thermal conductivity of syndanio-asbestos to be that of epoxy resin, whose time-surface temperature response to various heat fluxes is presented by Schultz and Jones, the error involved in neglecting conductivity is assessed as less than 2%; the resultant instantaneous blade heat transfer coefficient may be shown from the above information, extrapolated as necessary, to be given by

$$h_b = 0.365/t^{0.517} \text{ kW/m}^2\text{K} \tag{4}$$

Elimination of t between Eqs.(1), (3) and (4), coupled with the Schultz and Jones recommendation, yields

$$\frac{h_i}{h_b} = 7.48 h_i^{0.483} \left[\ln\left(\frac{T_\infty - T_{io}}{T_\infty - T_i}\right)\right]^{0.517} = 1 + F\left(\frac{T_b - T_i}{T_\infty - T_i}\right) \tag{5}$$

where for laminar flow F ranges from 0.9 to 2.25 for inserts at 5% and 25% of the surface length and for turbulent flow from 0.27 to 0.64 for inserts at 5% and 80% of the surface length. The local mean blade heat transfer coefficient h_{bm}, on which St in Figs. 7 and 8 is based, is obtained through integration of h_b with respect to T_i over the blade temperature range $T_i \leqslant T_b \leqslant T_\infty$ i.e. $h_i \geqslant h_b \geqslant h_i/(1+F)$. Over the experimental temperature range the resultant mean values of the integral correspond within ±5% to the equation

$$\frac{h_i}{h_{bm}} = 1 + 0.458F \tag{6}$$

The uncertainty interval in deriving h_m using Eq.(2), where τ is evaluated by least-squares fit, is estimated by the procedure of Kline and McClintock (28) to average ± 9.7%.

Application of the above procedure to extended transition regions, which are most pronounced over the pressure surface and for which no validated heat-transfer predictions (on which the correction procedure depends) exist, poses particular problems of interpretation. The h_i distributions on the pressure surface are in fact corrected as for turbulent flow, since, as will be apparent below, laminar correction would result in h_{bm} distributions below the laminar flat-plate curve. There are, however, other reservations about the use of the Schultz and Jones procedure which emerge in the following discussion.

RESULTS AND DISCUSSION

It is often assumed that channels or cascades of low aspect ratio, i.e. the ratio span/chord, which in this case is 0.68, inherently have secondary flows. However, the evidence of Bardon, Moffatt and Randall (29) suggests that these can be minimised in low aspect-ratio channels by bleeding the boundary layer from all surfaces at the blade leading edges. The effect of so doing in the present cascade rig may be assessed by reference to Fig. 3 in which chordwise static pressure distribution (presented as pressure coefficient Cp) on the suction and pressure surfaces of the middle channel at midspan are compared to the same distributions at 5% of the span from the side walls for typical running conditions. Furthermore, unpresented measurements of stagnation pressure distribution downstream of the cascade using the pitot rake at various spanwise locations show maximum variation in the wake of the blades, but at 5% of the span from the side walls the stagnation pressure is never less than 92.2% of that at midspan. This supports the inference from Fig.3 that it is doubtful if secondary flows measurably affect the heat transfer results.

The blade profile is derived from a design with a blade channel outlet Mach number Ma_2 of 0.955 and a correspondingly high trailing-edge Reynolds number. For the present measurements Ma_2 is limited to 0.632 to keep the flow through the cascade subsonic; this in turn limits the passage throat Mach number to 0.94. In the form of pressure coefficient Fig.3 also shows the comparison between the design and measured velocity distributions; as Ma_2 approaches the design value so the suction surface profile tends to the design prescribed velocity distribution. The measured velocity distributions are replotted as u/u_c in Fig.4 where that for the suction surface is compared to the low-speed velocity distribution of Brown and Burton for their heat-transfer measurements along PVD suction surfaces. As already mentioned, Figs. 3 and 4 suggest some positive incidence of the blades in the present rig.

Heat transfer results for the pressure and suction surfaces are based on six experimental runs comprising three values of u'/u_c each for two values of Re_c. The distributions of St calculated from the measured heat transfer coefficient h_i are shown in Figs. 5 and 6, superimposed on which are the standard laminar and fully-turbulent local heat-transfer relationships for boundary-layer flow over a plat plate, given respectively by

$$St_x = 0.332\, Re_x^{-0.5} Pr^{-0.67} \tag{7}$$

$$St_x = 0.029\, Re_x^{-0.2} Pr^{-0.67} \tag{8}$$

Eqs. (7) and (8) are similarly superimposed in Figs. 7 and 8 which present St based on h_{bm}, where h_i is

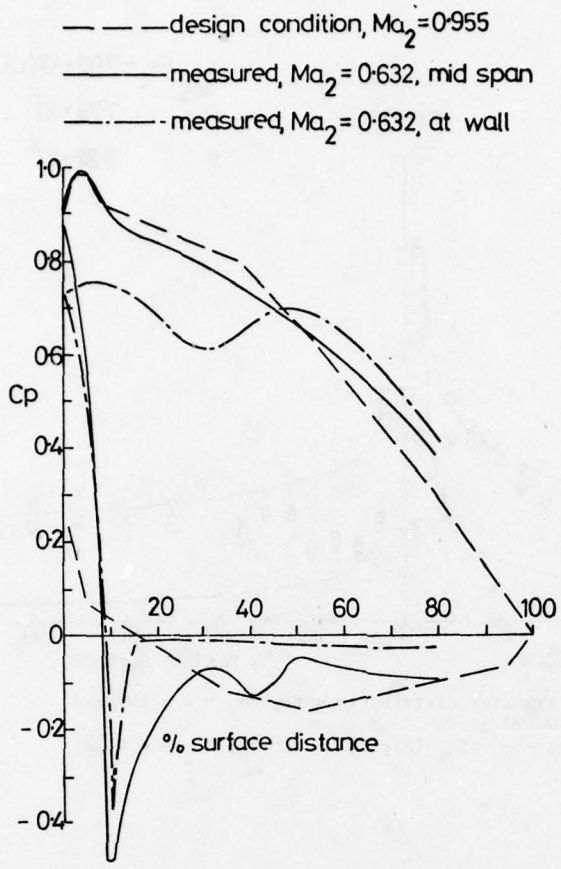

Fig.3 Comparison of measured pressure coefficients at midspan and near wall for Ma_2 = 0.632, Re_2 = 8.14 x 10^5, u'/u = 0.082 and the PVD design distribution for Ma_2 = 0.955

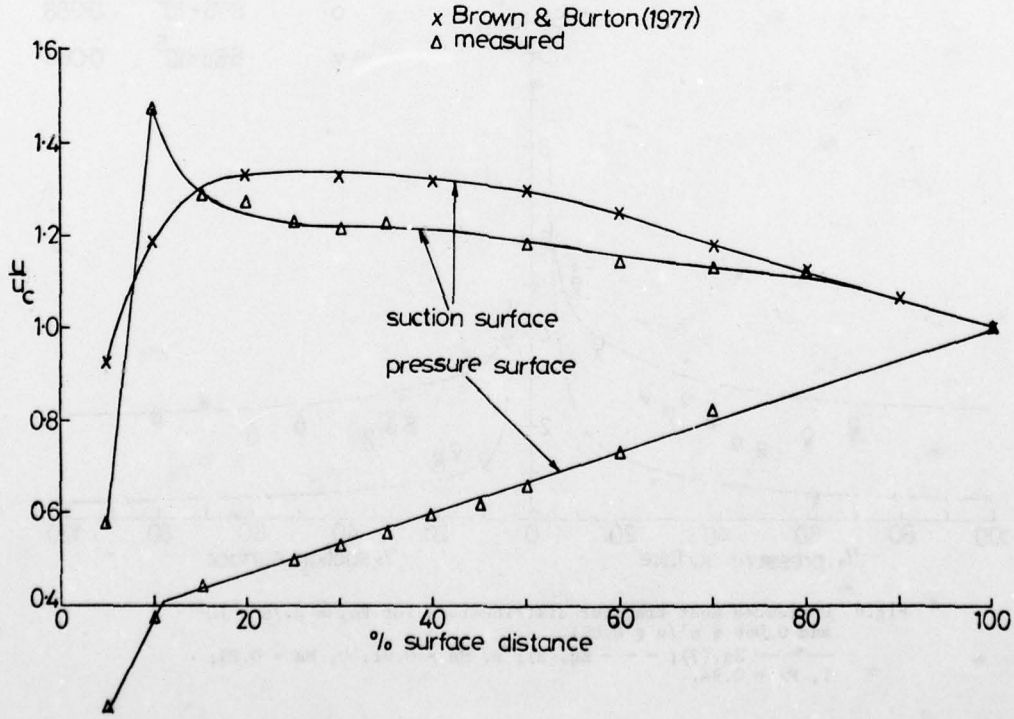

Fig.4 Measured mainstream velocity distributions and that of Brown and Burton (1977) over the suction surface only

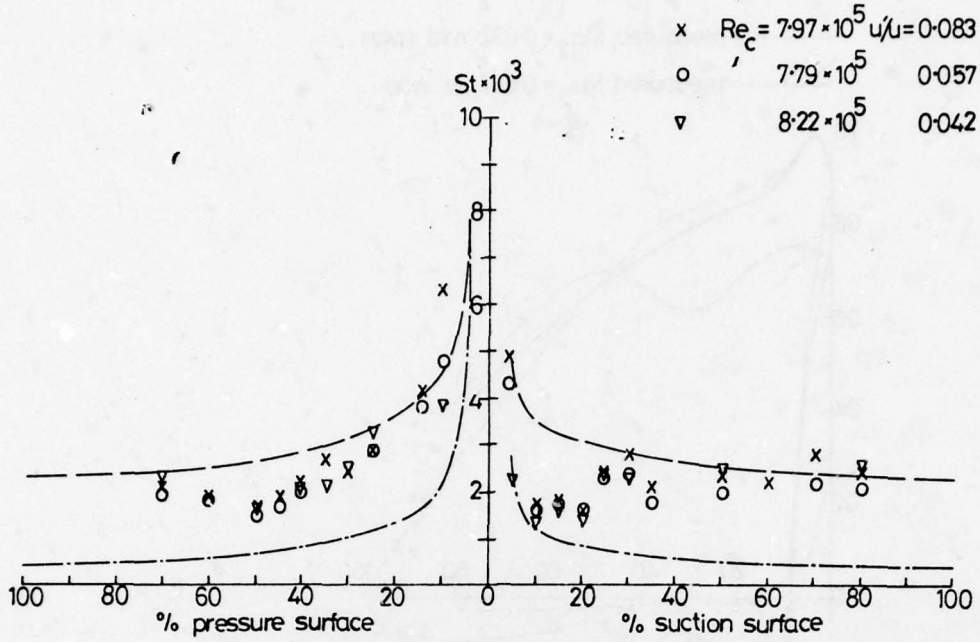

Fig.5 Unreduced heat transfer distributions for $Re_c \simeq 8 \times 10^5$ and $0.042 \leqslant u'/u \leqslant 0.083$.
— · — Eq. (7); – – – Eq. (8); x, Ma = 0.79; o, Ma = 0.82; ∇ Ma = 0.94.

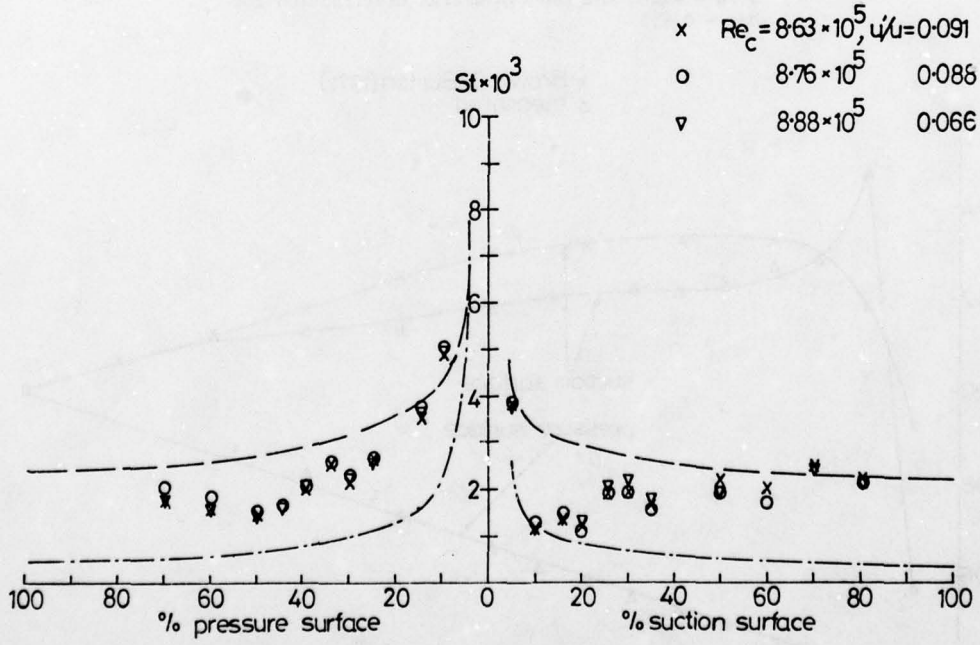

Fig.6 Unreduced heat transfer distributions for $Re_c \simeq 8.76 \times 10^5$ and $0.066 \leqslant u'/u \leqslant 0.091$.
— · — Eq.(7); – – – Eq.(8); x, Ma = 0.91, o, Ma = 0.89; ∇, Ma = 0.94.

reduced as already described by Eq.(6). Also plotted are computer predictions for the corresponding averaged Re_c and u'/u; the prediction method is basically that of Spalding and Patankar (30) which also takes account of gas pressure, temperature and local velocity, surface temperature and local radius of curvature at the points specified along the surface. The transition criterion used is that of Seyb (13) whch assumes instantaneous completion, but since the computer programme outputs data for specified points on the surface, St immediately after transition is unknown. The predicted curve is therefore smoothly joined to the next computed point.

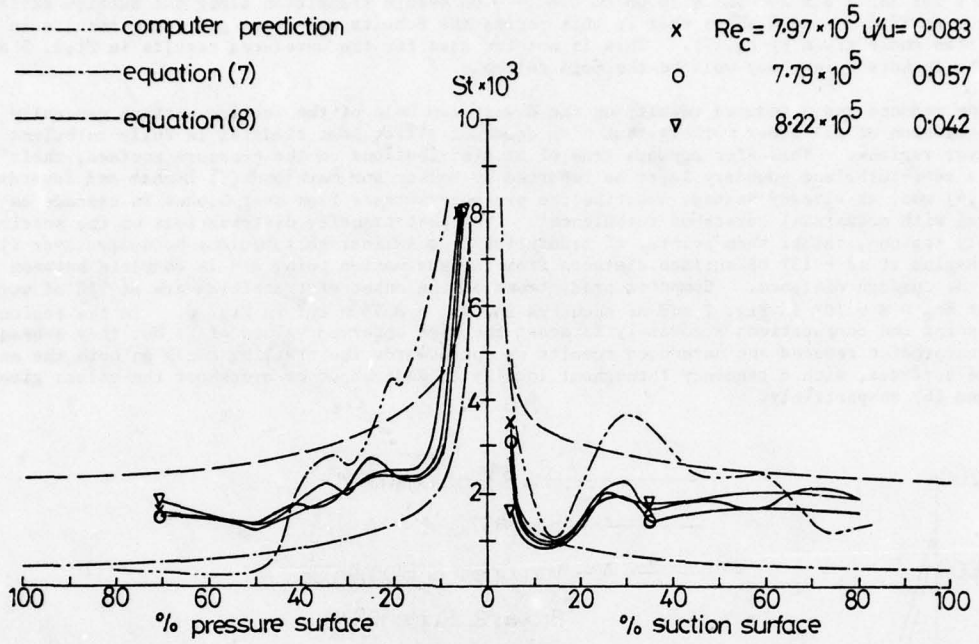

Fig. 7 Reduced heat transfer distributions for Re ≈ 8 x 10^5 and 0.042 ⩽ u'/u ⩽ 0.083.

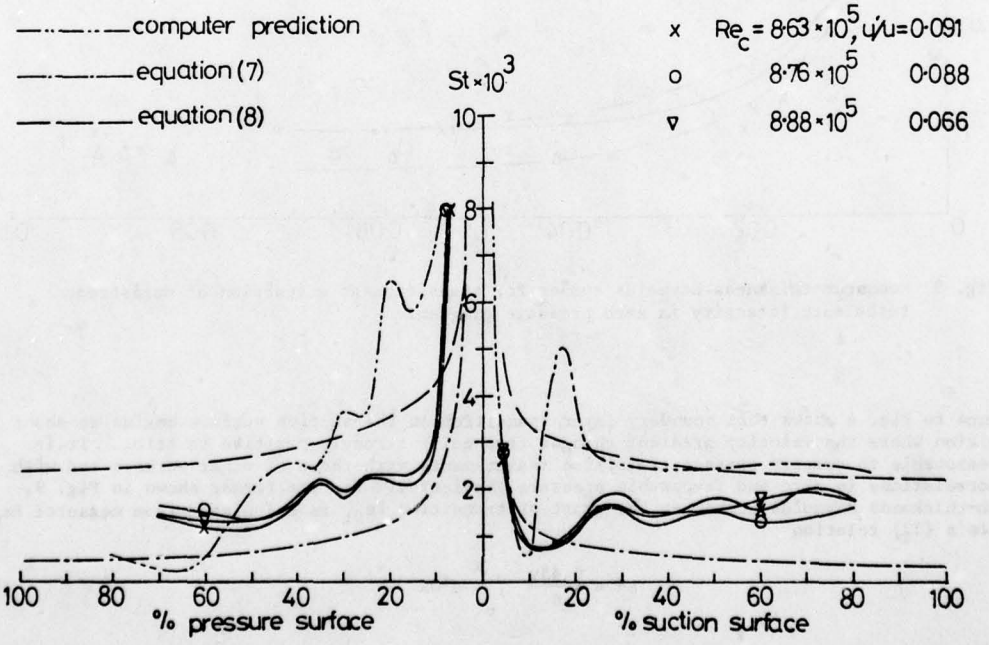

Fig. 8 Reduced heat transfer distributions for Re_c ≈ 8.76 x 10^5 and 0.066 ⩽ u'/u ⩽ 0.091.

The experience of the authors in applying the reduction procedure of Schultz and Jones leads them to believe that it overcorrects h_i. While during the transient measuring period T_i is supposedly less than T_b at the blade surface, this may not be true over the 2 mm depth of penetration of the copper insert because of the lower thermal conductivity of the neighbouring syndanio-asbestos. The temperature of the insert body may be equal to or even higher than that immediately around it. Furthermore, the Schultz and Jones procedure is based on such equations as (7) and (8) but the evidence of Kestin, Maeder and Wang (31) Buyuktur, Kestin and Maeder (20) and Brown and Burton (3) for low-speed flows is that St increases with u'/u above the value represented by Eq.(7) in laminar boundary-layer regions; this is also indicated by Figs. 5 and 7 for $Re_c \simeq 8 \times 10^5$ and u'/u up to 0.07 - 0.08 before transition along the suction surface. But reference to Figs. 7 and 8 shows that in this region the Schultz and Jones procedure results in values of St less than those given by Eq.(7). This is not the case for the unreduced results in Figs. 5 and 6 which, in the authors' view, may well be the more reliable.

Both the reduced and unreduced results on the downstream half of the suction surface generally accord with the conclusion of all other workers that u'/u does not affect heat transfer in fully-turbulent boundary-layer regions. This also appears true of St distributions on the pressure surface, their levels suggesting a semi-turbulent boundary layer as reported by Walker and Markland (5) Dunham and Edwards (22) and Turner (6) who, as already stated, describe the pressure-surface flow over blades in cascade as 'transitional with occasional bursts of turbulence'. The heat-transfer distributions on the suction surface imply regions, rather than points, of transition from laminar to turbulent boundary-layer flow; transition begins at 12 - 13% of surface distance from the stagnation point and is complete between 26% and 29% of the surface distance. Computer predictions of the onset of transition are at 14% of surface distance for $Re_c \simeq 8 \times 10^5$ in Fig. 7 and at about 9% for $Re_c \simeq 8.75 \times 10^5$ in Fig. 8. In the region of the stagnation point the computations accurately forecast the high observed values of St but they subsequently generally overpredict reduced and unreduced results except towards the trailing edges on both the suction and pressure surfaces, with a tendency throughout locally to undershoot or overshoot the values given by Eqns. (7) and (8) respectively.

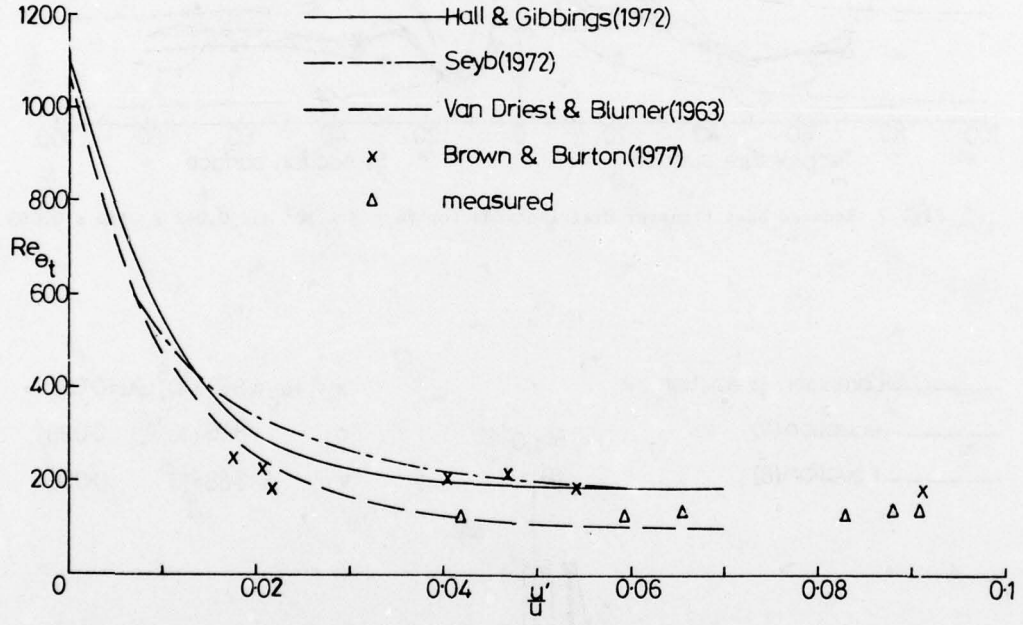

Fig. 9 Momentum-thickness Reynolds number for transition as a function of mainstream turbulence intensity in zero pressure gradient.

Reference to Fig. 4 shows that boundary-layer transition on the suction surface begins at about the surface position where the velocity gradient changes from being strongly positive to zero. It is therefore reasonable to compare present transition measurements with those of other workers and with available correlations in zero and favourable pressure gradients. For the former shown in Fig. 9, the momentum-thickness Reynolds number at the start of transition $Re_{\theta t}$ is calculated from measured Re_{xt} using Thwaite's (32) relation

$$\theta^2 = \frac{0.45\nu}{u^6} \int_0^x u^5 dx \qquad (9)$$

and is plotted against u'/u. Assuming zero velocity gradient, current measurements yield a limiting value of $Re_{\theta t} \simeq 130$ which is less than that of 190 suggested by Hall and Gibbings (12) and corroborated by the low-speed measurements of Brown and Burton; present findings do, however, accord with the correlation of Van Driest and Blumer (33).

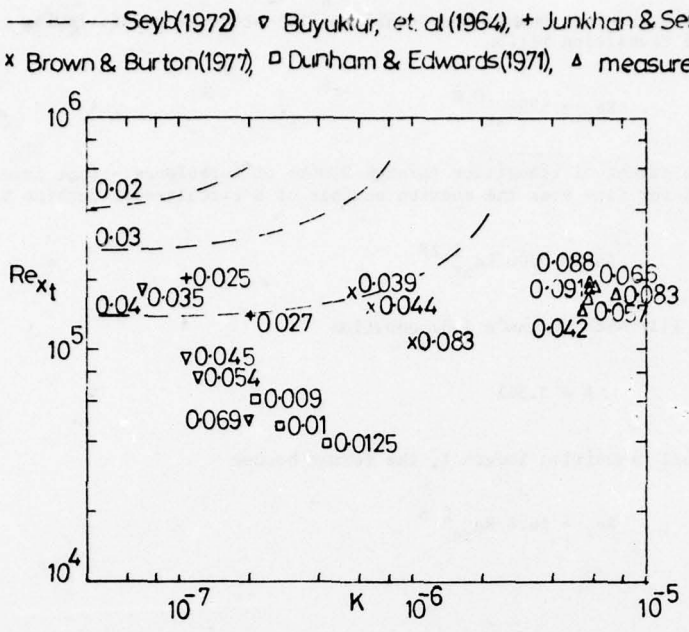

Fig. 10 Effect of mainstream turbulence intensity on length Reynolds number for transition in favourable pressure gradients.

In Fig. 10, current measurements of Re_{xt} are shown against velocity gradient factor K on the assumption that transition occurs in the strongly-favourable pressure-gradient region in Fig. 4. The numbers attached to experimental points in Fig. 10(and Fig. 11 below) are values of u'/u. Though grouped together and apparently somewhat insensitive to u'/u, present transition measurements are not unacceptable when compared to Seyb's correlation and the low-speed measurements of Buyuktur, Kestin and Maeder, Junkhan and Serovy (21) and Brown and Burton, though they represent larger K than any previously reported. However, for much the same range of high mainstream Mach numbers, current Re_{xt} values are on average four times greater than those of Dunham and Edwards at about six times their values of u'/u. These differences are difficult to explain, particularly in relation to Seyb's correlation, but if the assumption of transition in the present tests at K values of the order of 6×10^{-6} is correct, the delay in transition may arise from the suppression of turbulence generation in the boundary layer associated with laminarisation for $K > 2.5 \times 10^{-6}$. Differences between low and high-speed flow measurements for similar Re, u'/u, K and free stream velocity distributions have been discussed in terms of scale of turbulence (e.g. Brown and Burton) but the comparison of high-speed flow measurements in Fig. 10 renders such association more tenuous and the discussion more interesting.

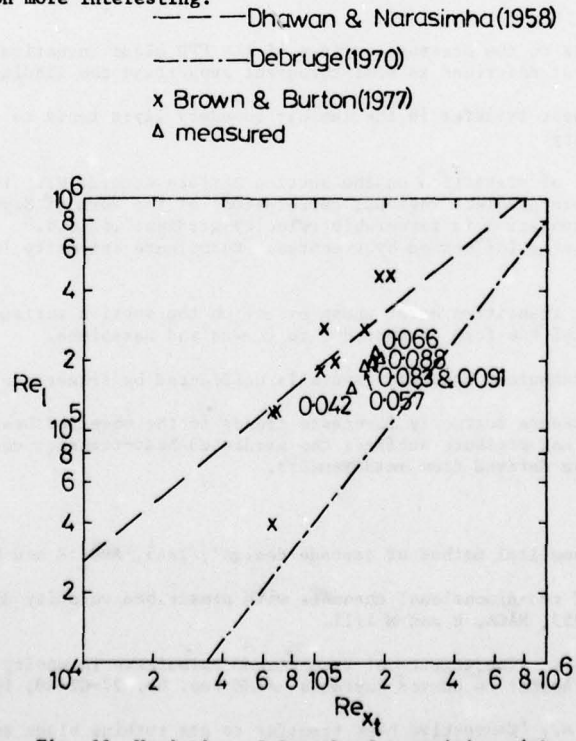

Fig. 11 Variation of length of transition with the position of start of transition.

For flow in zero pressure gradient Dhawan and Narasimha (15) proposed the following relation between the start and length of the transition region

$$Re_{\lambda} = 5\ Re_{xt}^{0.8} \tag{10}$$

where λ is a measure of the extent of transition through limits of turbulence - spot intermittency factor. Debruge (34) suggested that for flow over the suction surface of a circular-arc turbine blade

$$Re_{\lambda} = 0.005 Re_{xt}^{1.28} \tag{11}$$

By combining Eqs. (10) and (11) with Dunham's (35) equation

$$\ell = 3.36\lambda \tag{12}$$

which relates λ to the actual transition length ℓ, the former become

$$Re_{\ell} = 16.8\ Re_{xt}^{0.8} \tag{13}$$

and

$$Re_{\ell} = 0.0168\ Re_{xt}^{1.28} \tag{14}$$

Eqs. (13) and (14) are shown in Fig. 11 together with current transition measurements and those of Brown and Burton for low-speed flows over a PVD blade with the free stream velocity distribution shown in Fig. 4. The latter are scattered around the modified Dhawan and Narasimha line with the exception of the isolated point for the highest u'/u of 0.092; present measurements, which fall somewhat below this line, but well above that of Debruge, suggest a smaller Re_{ℓ} for given Re_{xt} than those of Brown and Burton.

CONCLUSIONS

The following conclusions may be drawn from the foregoing:-

(a) It is doubtful if secondary flows in the present cascade rig are sufficient to affect significantly the heat transfer results.

(b) Application of the Schultz and Jones procedure to account for step changes in blade-surface temperature appears to overcorrect the heat-transfer coefficients derived from measurements of the insert temperatures.

(c) Heat-transfer measurements on the pressure surface of the PVD blade investigated indicate that the boundary-layer flow is best described as semi-turbulent supporting the findings of other workers.

(d) On the suction surface, heat transfer in the laminar boundary layer tends to increase with free-stream turbulence intensity.

(e) The position of the start of transition on the suction surface accords with the Van Driest and Blumer correlation in zero pressure-gradient regions; correlations of the form of Seyb's may be useful in assessing the start of transition in favourable velocity-gradient regions. In both regions the start of transition is little influenced by freestream turbulence intensity in the range $0.042 \leqslant u'/u \leqslant 0.091$.

(f) Regions of boundary-layer transition exist whose extent on the suction surface is adequately predicted by an equation of the form of that due to Dhawan and Narasimha.

(g) Heat transfer in wholly turbulent boundary layers is unaffected by freestream turbulence intensity.

(h) While the prediction procedure correctly forecasts trends in the observed heat-transfer distributions, over most of the suction and pressure surfaces the predicted heat-transfer coefficients do not correspond well with those derived from measurements.

REFERENCES

1. LIGHTHILL, M.J., 'A mathematical method of cascade design', 1945, ARC. R and M 2104.

2. STANITZ, J.D., 'Design of two-dimensional channels with prescribed velocity distribution along the walls', 1953, NACA, R and M 1115.

3. BROWN, A. and BURTON, R.C., 'The effects of free-stream turbulence intensity and velocity distribution on heat transfer to curved surfaces' ASME Pap. No. 77-GT-48, 1977, pp 1 - 10.

4. WILSON, D.G. and POPE, J.A., 'Convective heat transfer to gas turbine blade surfaces', Proc. I. Mech. E. Vol. 168, 1954, pp 861 - 876.

5. WALKER, L.A. and MARKLAND, E., 'Heat transfer to turbine blading in the presence of secondary flow', Int. J. Heat Mass Transfer, Vol. 8, No. 5, 1965, pp 729 - 748.

6. TURNER, A.B., 'Local heat-transfer measurements on a gas turbine blade, J.Mech.Eng.Science, Vol. 13, 1971, pp 1 - 12.

7. BAMMERT, F. and HAHNEMANN, H., 'Heat transfer in the gas surrounding cooled gas turbine blades', 1951, Min. of Supply Rep. GDC 2466.

8. ANDREWS, S.J. and BRADLEY, P.C., 'Heat transfer to turbine blades', 1957, ARC. CP No. 294.

9. HODGE, R.I., 'A turbine nozzle cascade for cooling studies', 1960, ARC. CP 492, 493.

10. AINLEY, D.G., 'Research on the performance of a type of internally air-cooled turbine blade, Proc. I. Mech. E., Vol. 167A, 1953, pp 351 - 370.

11. BROWN, A. and MARTIN, B.W., 'A review of the bases of predicting heat transfer to gas turbine blades' ASME Pap. No.74-GT-27, 1974, pp 1 - 12.

12. HALL, D.J. and GIBBINGS, J.C., 'Influence of stream turbulence and pressure gradient upon boundary-layer transition', J. Mech. Eng. Science, Vol. 14, 1972, pp 134 - 146.

13. SEYB, N.J., 'The role of boundary layers in axial flow turbomachines and the prediction of their effects', AGARD CP 164, No. 14, 1972.

14. PRETSCH, J., 'Die stabilitat einer ebenen laminar-stromung bei druckgefalle und druckansteig', Jb. d. dt Luftfahrtforschung, Vol. 1, 1941, p. 58.

15. DHAWAN, S. and NARASIMHA, R., 'Some properties of boundary-layer flow during the transition from laminar to turbulent flow', J. Fluid Mech, Vol. 3, 1958, pp. 418 - 436.

16. GOLDSTEIN, A.W. and MAGER, A., 'Attainable circulation about aerofoils in cascade', 1950, NACA Rep. No. 953.

17. CRABTREE, L.F., 'Prediction of natural transition in the boundarylayer on an aerofoil', J.R. Aero. Soc., Vol. 62, 1958, pp. 525 - 528.

18. McDONALD, H., and FISH, R.W., 'Practical calculations of transitional boundary layers', Int. J. Heat Mass Transfer , Vol. 16, No. 9, 1973, pp 1729 - 1744.

19. EDWARDS, A., and FURBER, B.N., 'The influence of free-stream turbulence in heat transfer by convection from an isolated region of a plane surface in parallel air flow', Proc. I. Mech. E., Vol. 170, 1956, pp. 941 - 953.

20. BUYUKTUR, A.R., KESTIN, J., and MAEDER, P.F., 'Influence of combined pressure gradient and turbulence on the transfer of heat from a plate', Int. J. Heat Mass Transfer, Vol. 7, No. 11, 1964, pp 1175 - 1185.

21. JUNKHAN, G.H. and SEROVY, G.K., 'Effects of free-stream turbulence and pressure gradient on flat-plate boundary-layer velocity profiles and on heat transfer', ASME J. Heat Transfer, Vol. 89, 1967, pp 169 - 176.

22. DUNHAM, J., and EDWARDS, J.P.,'Heat transfer calculations for turbine blade design', AGARD CP 73, No. 2, 1971.

23. GARRETT, S.E., 'Heat transfer to turbine blades', M. Eng. thesis, University of Wales Institute of Science and Technology, 1976.

24. ROSE, W.G., 'Interaction of grid turbulence with a uniform mean shear', J. Fluid. Mech., Vol. 44, 1970, pp 767 - 779.

25. DYBAN, Y.P. and GLUSHCHENKO, V.G., 'Effect of the Mach number and temperature factor on heat transfer from a gas to a turbine blade', Heat Transfer - Soviet Research, Vol. 7, No. 2, 1975, pp 17 - 21.

26. KREITH, F.,'Principles of heat transfer', 2nd ed, New York, Int. Textbook Co., 1965.

27. SCHULTZ, D.L. and JONES, T.V., 'Heat transfer measurements in short duration hypersonic facilities', AGARD AG 165, 1973.

28. KLINE, S.J. and McCLINTOCK, F.A., 'The description of uncertainties in single-sample experiments', Mech. Eng., Vol. 75, 1953, pp 3 - 8.

29. BARDON, M.F., MOFFATT, W.C., and RANDALL, J.L. 'Secondary-flow effects on gas exit angles in rectilinear cascades', ASME Pap. No. 74-GT-69, 1974, pp 1 - 8.

30. SPALDING, D.B., and PATANKAR, S.V., 'Heat and mass transfer in boundary layers',London, Morgan-Grampian, 1967.

31. KESTIN, J., MAEDER, P.F., and WANG, H.E., 'Influence of turbulence on the transfer of heat from plates with and without pressure gradient', Int. Heat Transfer Conference, ASME, Pap. No. 50, 1961, pp 432 - 438.

32. THWAITES, B., 'Approximate calculation of laminar boundary layer', Aero. Quart. Vol. 1, 1949, pp 245 - 280.

33. VAN DRIEST, E.R. and BLUMER, C.B., 'Boundary-layer transition:free-stream turbulence and pressure-gradient effects', Am. Inst. Aero. and Astro. J., Vol. 1, 1963, pp 1303 - 1306.

34. DEBRUGE, L.L., 'A theoretical determination of convection heat-transfer coefficients during transition on the suction side of turbine aerofoils', AFAPL, TR-69-95, 1970.

35. DUNHAM, J., 'Prediction of boundary-layer transition on turbomachinery blades', AGARD CP 164, No. 3, 1972.

ACKNOWLEDGEMENTS

The authors acknowledge the financial support given by the Ministry of Defence of Her Britannic Majesty's Government. They also wish to thank Mrs. M.F. Read for her help in the preparation of the paper.

DISCUSSION

D.L.Schultz, UK

The correction for the effect of surface temperature discontinuities outlined in AG 165 (Ref.27) should be used with caution. It has not yet been tested systematically.

Author's Reply

As noted in our paper, we fully agree with the reservations expressed by Dr Schultz concerning the use of the surface temperature correction described in AG 165. The procedure was employed as being the best currently available but we do not wish to hide the fact that extensive extrapolation of the data in AG 165 (Ref.27) was necessary in order to cover the time scale of our measurements. This may well invalidate the use of the procedure under such circumstances.

TECHNIQUES DE MESURE DANS LES TURBINES A HAUTES TEMPÉRATURES

par Yves LE BOT, Marc CHARPENEL, Pierre-Jacques MICHARD*

Office National d'Etudes et de Recherches Aérospatiales (ONERA)
92320 Châtillon - France

La qualification des systèmes de refroidissement utilisés dans les turbines à température d'écoulement élevée a conduit l'ONERA à développer, en étroite collaboration avec la SNECMA et le Centre d'Essais des Propulseurs de Saclay (CEPr), une instrumentation permettant d'effectuer sur machines industrielles des mesures généralement limitées aux études de laboratoires. Ce sont ces mesures non classiques qui sont examinées, à savoir :

– qualification de la turbulence de l'écoulement et analyse des sillages des aubes mobiles au moyen de sondes de pression à court temps de réponse ;

– analyse des fluctuations de température d'écoulement à l'aide de sondes à thermocouple ou à fil résistant associées à une électronique de traitement du signal et par pyrométrie optique ;

– repérage des températures de surface des aubes mobiles par pyrométrie optique à court temps de réponse ;

– mesure du coefficient de transfert thermique local sur aubes de distributeurs par analyse de l'évolution en fonction du temps de la température de paroi après coupure brutale de l'air de refroidissement ;

– mesure de l'efficacité de protection thermique des parois à partir des résultats d'analyse chromatographique de prélèvements gazeux.

Les principales caractéristiques de l'instrumentation développée sont présentées et illustrées par des exemples d'application dans des bancs thermiques variés et en particulier dans un montage industriel adapté aux recherches sur les turbines à température d'écoulement élevée, installé au CEPr et appelé «Minos».

●

MEASURING TECHNIQUES IN HIGH TEMPERATURE TURBINES

With a view to qualifying cooling systems used in high temperature turbines, ONERA developed, in close cooperation with the SNECMA Company and CEPr (Propulsion Test Centre of the French Ministry of Defence) at Saclay, near Paris, an instrumentation for performing on industrial machines measurements usually limited to laboratory studies. These uncommon measurements are described :

– qualification of the flow turbulence and analysis of mobile blade wakes by short response time pressure probes ;

– analysis of the flow temperature fluctuations by thermocouple or resistor probes associated to signal processing electronics and by optical pyrometry ;

– reading of mobile blade surface temperatures by short response time optical pyrometry ;

– measurement of local thermal transfer coefficient on stator blades by analysis of the evolution in time of the wall temperature after sudden cutting off of cooling air ;

– measurement of the effectiveness of the wall thermal protection from results of a chromatographic analysis of gaseous samples.

The main characteristics of this instrumentation are presented and illustrated by examples of application on various test facilities, and in particular on an industrial set-up adapted to research on high temperature turbines, installed at CEPr and called «Minos».

1 - INTRODUCTION

La qualification des systèmes de refroidissement des turbines à température d'écoulement élevée a conduit l'ONERA à développer une instrumentation de mesure adaptée aux essais sur machines industrielles. Ces études, effectuées en étroite collaboration avec la SNECMA et le Centre d'Essais des Propulseurs, entrent dans le cadre d'un programme de recherches coordonné par les Services Officiels et particulièrement la Direction des Recherches et Etudes Techniques et la Direction Technique des Constructions Aéronautiques [1] [2].

(*) *Etude effectuée sous contrat de la DRET avec l'aide de Y. HOURS, J. WILHELM, M. IZARD, R. LARGUIER et C. d'HUMIERES.*

Une caractéristique de l'appareillage réalisé est de rendre possibles dans un environnement moteur des mesures jusqu'à présent généralement réservées aux études de laboratoire.

Le tableau I rappelle la nature de ces mesures non classiques à effectuer et l'instrumentation, ou les techniques expérimentales, retenue pour atteindre les objectifs fixés.

TABLEAU I

MESURES NON CLASSIQUES DEVELOPPEES DANS LE CADRE DES ETUDES SUR LES TURBINES A TEMPERATURE D'ECOULEMENT ELEVEE

NATURE DE LA MESURE	INSTRUMENTATION OU TECHNIQUE EXPERIMENTALE UTILISEE
Caractérisation des composantes instationnaires de l'écoulement : .Fluctuations de pression Turbulence aérodynamique .Fluctuations de température Turbulence thermique	.Sonde de pression à court temps de réponse .Sonde à thermocouple ou à fil résistant. Pyromètre optique.
Analyse des sillages des aubes mobiles.	Sonde de pression à court temps de réponse.
Repérage de la température de surface des aubes mobiles.	Pyromètre optique à court temps de réponse.
Détermination des coefficients de transfert thermique sur aubes.	Analyse de l'évolution en fonction du temps de la température de paroi des aubes en régime transitoire.
Mesure de l'efficacité de protection thermique par film gazeux.	Analyse chromatographique de prélèvements gazeux.
Caractérisation de la perméabilité d'un élément de turbine vis-à-vis de l'air de refroidissement.	Emploi d'un gaz traceur (azote ou argon) et analyse chromatographique de prélèvements gazeux.

L'appareillage de mesure développé dans le cadre de ces recherches est présenté ci-après. Ses possibilités expérimentales sont illustrées par des exemples d'applications tirés d'essais effectués dans des bancs thermiques variés et principalement dans la turbine MINOS (Montage Inter ONERA SNECMA installé au CEPr à Saclay) adaptée aux études sur les turbines à température d'écoulement élevée.

2 - MESURES DE PRESSION INSTATIONNAIRE DANS LES ECOULEMENTS A HAUTES TEMPERATURES

2.1 - Pose du problème

Les mesures de pression dans les écoulements à hautes températures sont effectuées en vue de déterminer les composantes continues et instationnaires de la pression statique et de la pression d'arrêt. Elles nécessitent la mise en oeuvre de sondes refroidies pouvant comporter un élément sensible dont la protection contre l'environnement à haute température dans des gaz souvent réactifs doit être assurée. Nous ne donnerons ici comme exemple que deux techniques de mesure particulières relatives à la détermination des fluctuations de pression et appliquées à l'étude de la turbulence aérodynamique et à l'analyse des sillages mobiles.

2.2 - Détermination de la turbulence locale de l'écoulement

Les méthodes classiques de détermination de la turbulence de l'écoulement au moyen d'anémomètres à fil ou film chaud ne peuvent plus être utilisées aux niveaux de température régnant à la sortie de la chambre de combustion ou à l'entrée de la turbine. L'anémométrie laser, technique d'avenir, n'est pas encore opérationnelle et il a fallu se rabattre sur des mesures plus classiques de la pression d'arrêt instationnaire.

Des études effectuées à température modérée ont montré que les fluctuations de pression d'arrêt, δp_i, et les fluctuations de vitesse, δV, sont reliées par la relation :

$$(1) \qquad \frac{\delta P_i}{\rho V^2} = K \frac{\delta V}{V}$$

où l'on peut prendre pour ρ et V les valeurs moyennes de la masse volumique et de la vitesse.

Le facteur de proportionnalité K peut être pris égal à 2 dans les mesures de turbulence libre [3] comme le montre la figure 1 sur laquelle sont comparées les densités spectrales énergétiques relevées avec une sonde à film chaud et une sonde de pression d'arrêt dans un écoulement à faible vitesse (M = 0,3) et température modérée (T = 340 K).

Pour des températures plus élevées des sondes spéciales ont été conçues, dans lesquelles l'élément sensible, un capteur piézoélectrique ONERA 20H47 ou 20H48 ,est plus ou moins protégé suivant la durée de vie prévue pour la sonde et la bande passante souhaitée.

La figure 2a montre le schéma d'une sonde d'arrêt de forme classique comportant un capteur affleurant. Une circulation d'eau maintient la structure de la sonde à une température convenable et une protection de la surface sensible est assurée au moyen d'un élastomère qui se carbonise progressivement. La durée de vie du capteur, variable avec les conditions d'essais, est de l'ordre de 30 minutes à 1300 K sous 4 bar. La bande passante est très élevée (300 kHz environ).

Dans le montage de la figure 2b le corps de la sonde est cylindrique et le capteur, toujours protégé par un élastomère, est placé au fond d'une cavité face à l'écoulement et ses performances sont semblables à celles de la précédente. Par contre dans la sonde cylindrique de la figure 2c l'élément sensible est placé latéralement dans une cavité refroidie [4]. Sa bande passante n'est plus que de 10 kHz mais la durée de vie semble très grande pour une température ne dépassant pas 1800 K.

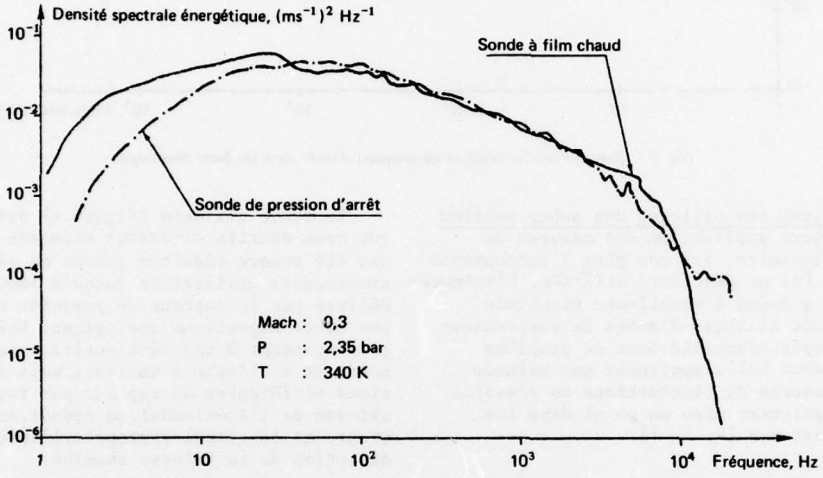

Fig. 1 — Comparaison des densités spectrales de fluctuations de vitesse d'écoulement obtenues à partir de la réponse d'une sonde à film chaud et de celles déduites des fluctuations de pression d'arrêt.

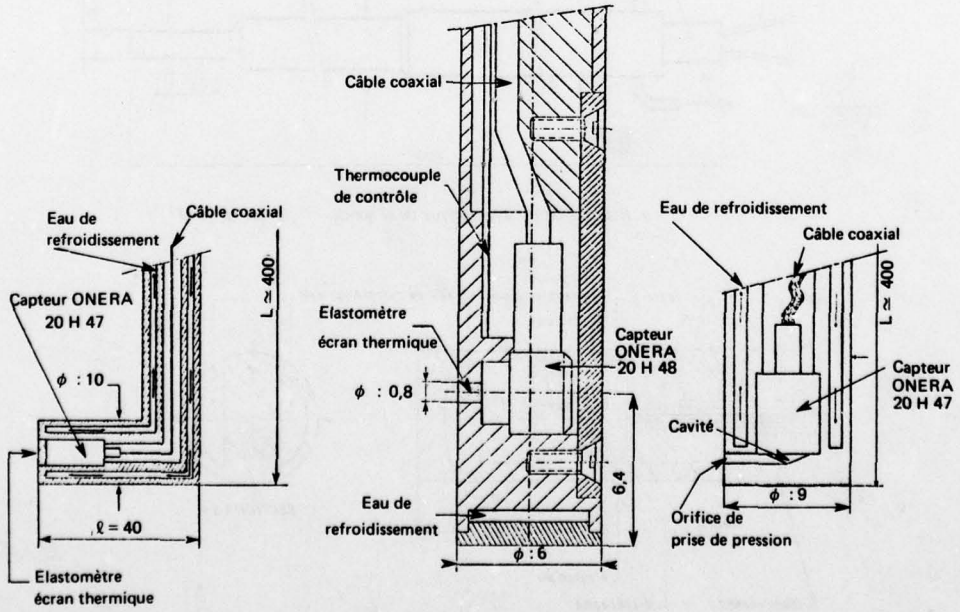

a. Sonde du type Pitot.

b. Sonde cylindrique à large bande passante.

c. Sonde cylindrique à cavité.

Fig. 2 — Représentation de trois types de sondes de pression d'arrêt à court temps de réponse utilisées pour la caractérisation de la turbulence des écoulements à température élevée. (cotes en mm).

Un exemple de répartition de densité spectrale énergétique relevée à la sortie d'une chambre de combustion est présenté sur la figure 3. La turbulence déduite des mesures était de 5 pour cent à 340 K sous 2,35 bar et de 7 pour cent à 1200 K sous 4 bar . La raie correspondant à la fréquence $F \simeq 500$ Hz est due à des instabilités induites par la combustion et est propre à l'installation.

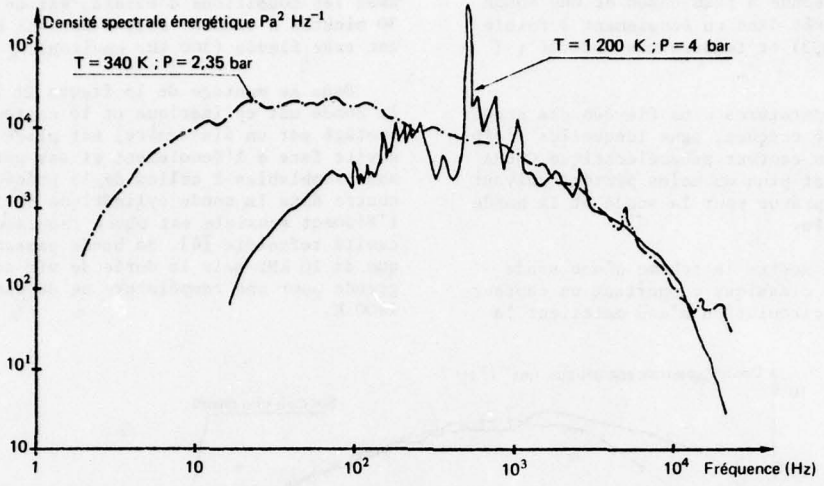

Fig. 3 – Spectres de fluctuations de pression d'arrêt dans un banc thermique.

2.3 - L'analyse des sillages des aubes mobiles constitue une autre application des mesures de pression instationnaire. Ici non plus l'anémométrie à fil chaud [4] [5] ne peut être utilisée. L'anémométrie laser, qui a donné d'excellents résultats pour les études de sillages d'aubes de compresseur [6], n'est pas opérationnelle pour ce problème non plus. Il a donc fallu appliquer une méthode basée sur les mesures de fluctuations de pression qui avait été également mise au point dans les études de compresseurs [4, 5, 7].

La sonde utilisée (figure 4) est du même type que ceux décrits ci-dessus mais ses dimensions ont été encore réduites (temps de réponse $\simeq$ 0,5 microseconde; utilisation jusqu'à 1800 K). Le signal délivré par le capteur de pression est enregistré sur bande magnétique analogique. Des indications correspondant à une même position relative de la sonde et de l'aube à analyser, mais à des orientations différentes du capteur par rapport à la vitesse de l'écoulement, on déduit, au moyen d'un programme de calcul approprié, l'intensité et la direction de la vitesse absolue.

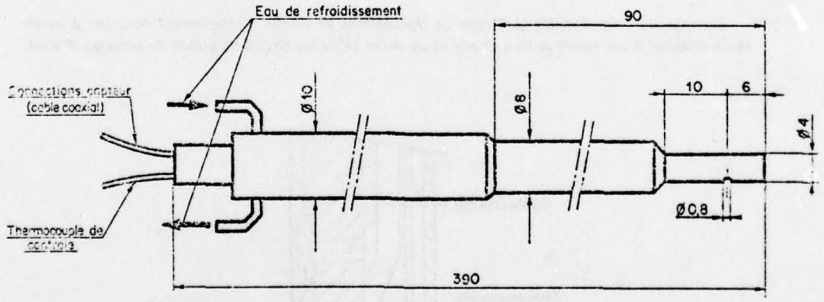

a. Représentation schématique de la sonde. (cotes en mm)

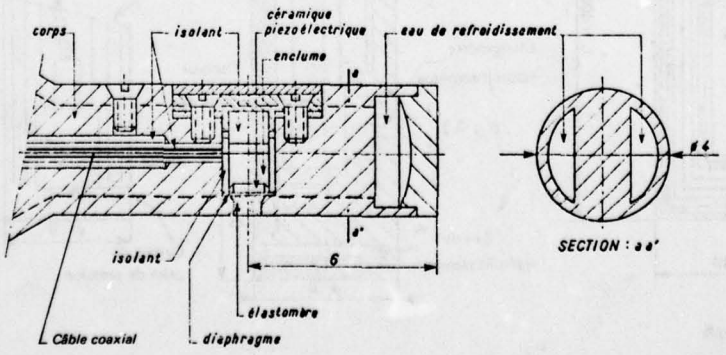

b. Détails de la tête de mesure.

Fig. 4 – Sonde de pression instationnaire haute température à tête de mesure miniaturisée développée pour l'analyse des sillages des aubes mobiles de turbine.

Au moyen d'une composition des vitesses on calcule ensuite l'intensité et la direction de la vitesse dans un système d'axes entraînés par le rotor. Un exemple d'une telle analyse à l'aval d'un rotor de turbine est présenté sur la figure 5.

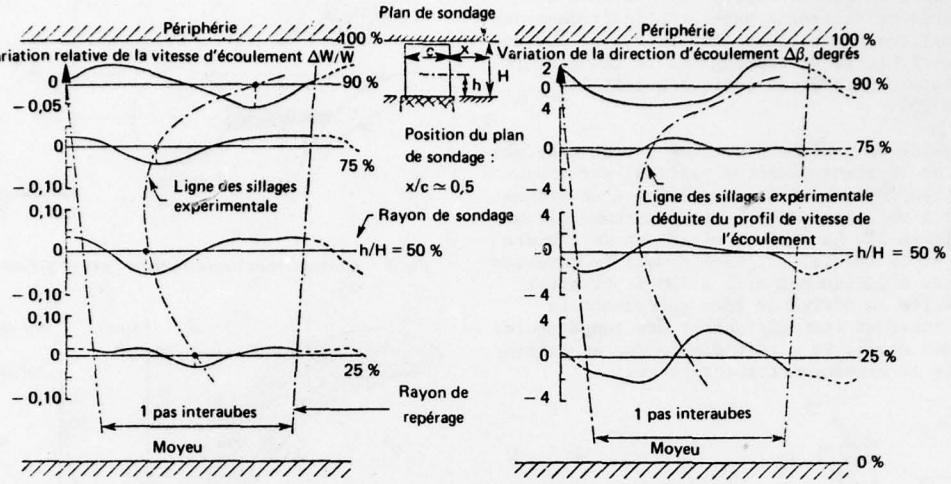

Fig. 5 – Exemple d'application d'une sonde de pression à court temps de réponse à l'analyse des sillages des aubes d'un rotor de turbine. Variations de la vitesse et de la direction de l'écoulement sur un pas interaubes, en axes liés au rotor.

3 - DETERMINATION DES TEMPERATURES

Deux types différents de mesure de températures sont effectués dans les études de caractérisation des turbines :

- les mesures de température de surface des aubes fixes ou mobiles ;
- les mesures de fluctuations de température.

Chacune de ces mesures fait appel à une instrumentation spécialisée dont le développement a été effectué au laboratoire avant application sur banc de turbine.

3.1. - Détermination de la température des aubes par thermocouples

Des thermocouples insérés dans le métal peuvent être utilisés sur des aubes fixes aussi bien que mobiles lorsqu'elles sont refroidies. La figure 6 montre un exemple d'une aube fixe munie de thermocouples. Le jeu très réduit entre chemise et aube proprement dite rend la mise en place des thermocouples très délicate. L'expérience a montré cependant que cette solution présente une grande fiabilité. La durée de vie des thermocouples s'est avérée excellente durant les cyclages successifs créés par les arrêts et les mises en fonctionnement du refroidissement interne des aubes.

Ces mesures sont essentiellement utilisées pour la détermination des coefficients de transfert décrite ci-dessous au §4.

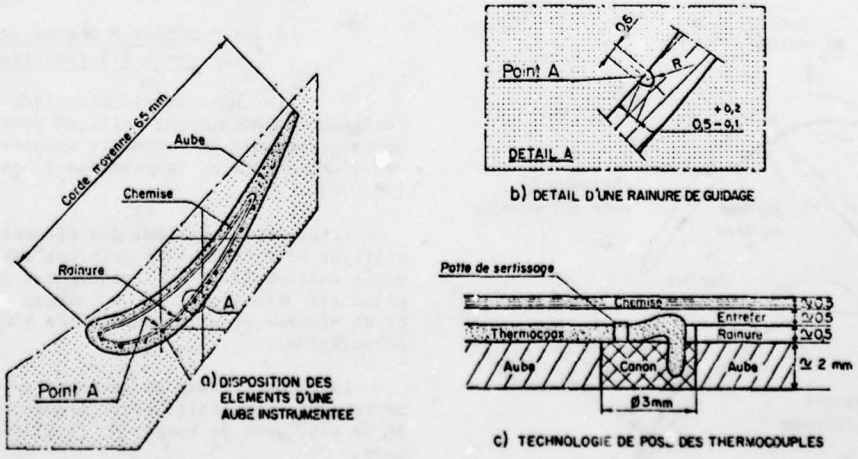

Fig. 6 – Equipement d'une aube de turbine en thermocouples de mesure.

AD-A052 845 ADVISORY GROUP FOR AEROSPACE RESEARCH AND DEVELOPMENT--ETC F/G 21/5
HIGH TEMPERATURE PROBLEMS IN GAS TURBINE ENGINES.(U)
FEB 78

UNCLASSIFIED AGARD-CP-229 NL

6 OF 7
AD A052845

3.2 - Repérage de la température de surface des aubes mobiles par pyrométrie optique

L'emploi de thermocouples est limité à des températures relativement basses. L'équipement des aubes constitue par ailleurs une amorce de rupture de celles-ci. Aussi un repérage de la température de surface par pyrométrie optique a-t-il été développé [8].

Un guide de lumière, constitué par un tube métallique de 16 mm de diamètre refroidi par circulation d'eau, est muni à son extrêmité d'un prisme de renvoi à 90° placé devant une ouverture circulaire (figure 7). La surface visée est de l'ordre de 2 mm^2 et le modulateur placé devant le détecteur à arséniure d'indium refroidi à 230 K par effet Peltier évite la dérive du zéro en coupant le faisceau incident (enregistrement des températures un tour sur deux). Un miroir dichroïque ne laisse passer que le rayonnement infra-rouge.

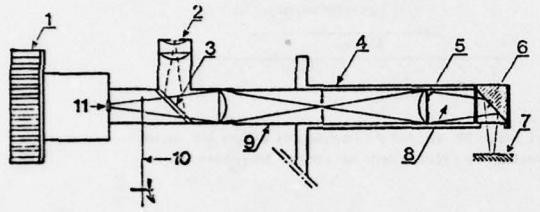

Fig. 7 – Schéma de la sonde pyrométrique à très court temps de réponse.

1. Radiateur - 2. Visée réflex - 3. Miroir semi-réfléchissant - 4. Tube refroidi - 5. Prisme - 6. Miroir à prisme - 7. Surface visée - 8. Surpression d'azote - 9. Tube coulissant - 10. Modulateur - 11. Surface sensible du détecteur.

Ce pyromètre a été étalonné pour des températures comprises entre 720 et 2100 K et a supporté des pressions de 20 bar.

Deux pyromètres identiques visent respectivement l'extrados et l'intrados des aubes (fig. 8) : le domaine visible, constitué par le voisinage du bord d'attaque et du bord de fuite, est indiqué sur cette figure. Un exemple d'enregistrement effectué à température modérée est présenté sur la fig. 9. L'interruption du signal due au passage des aubes apparaît nettement sur cette figure. Le dépouillement des mesures présenté sur la figure 10 met en évidence l'influence du débit de refroidissement sur le niveau de température de l'aube ; aux forts débits la température du bord de fuite est plus élevée que celle repérée au milieu de l'aube; aux faibles débits c'est le contraire.

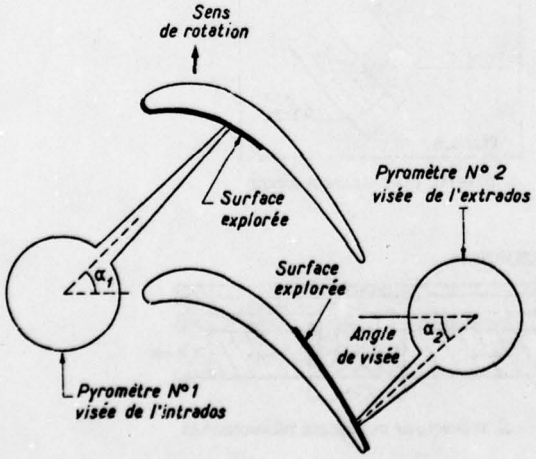

Fig. 8 – Principe de la mesure pyrométrique sur aube de turbine.

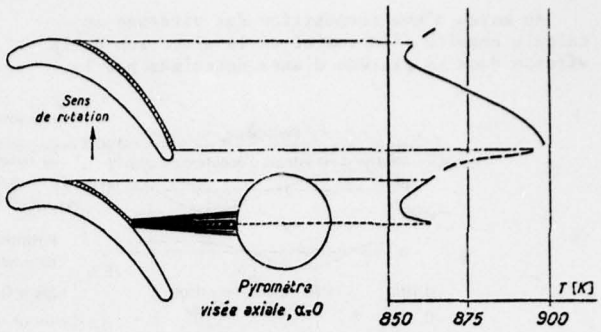

Fig. 9 – Exploration de température sur l'extrados d'une aube mobile.

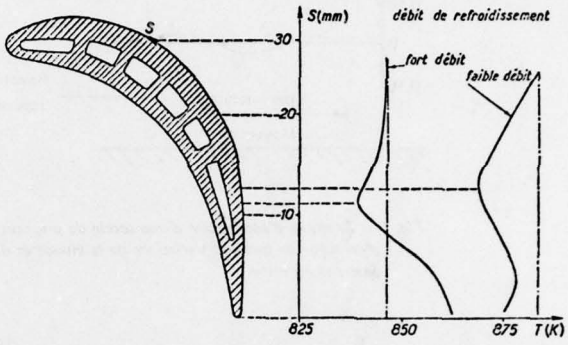

Fig. 10 – Influence du refroidissement sur le profil des températures de l'extrados.

L'utilisation du pyromètre optique a montré que cette technique présente quelques difficultés pour repérer avec précision les températures de surface en valeur absolue. C'est par contre une méthode de mesure très complète, très fiable et plus simple d'emploi que les techniques utilisant des thermocouples et son domaine d'emploi est plus étendu vers les hautes températures.

3.3 - Mesure des fluctuations de température au sein du fluide

Aux fluctuations de vitesse et de pression à la sortie d'une chambre de combustion décrites au § 2.2 sont associées des fluctuations de température dont il importe de connaître l'intensité (problème de l'oxydation superficielle des aubes sous l'effet de chocs thermiques; influence de la turbulence thermique sur les transferts de chaleur).

3.3.1 - Sondes à thermocouples et sondes à fil résistant

Le thermocouple classique ou la sonde à résistance généralement utilisés pour des écoulements permanents peuvent être adaptés à la mesure des fluctuations de température à basses fréquences [9] [10].

Le diamètre minimal des éléments sensibles à utiliser afin de leur assurer une robustesse mécanique suffisante et de limiter leur inertie thermique est directement lié au niveau de température et de vitesse et à la propreté de l'écoulement à caractériser.

La réponse brute de la sonde est corrigée au moyen d'un dispositif électronique tenant compte de la constante de temps τ de l'élément de mesure :

$$T_c = T_b + \tau \frac{dT_b}{dt} \qquad (2)$$

où T_b est la réponse brute de la sonde à l'instant t et T_c sa valeur corrigée [11]. Un exemple de signal brut et de signal traité est donné sur la figure 11.

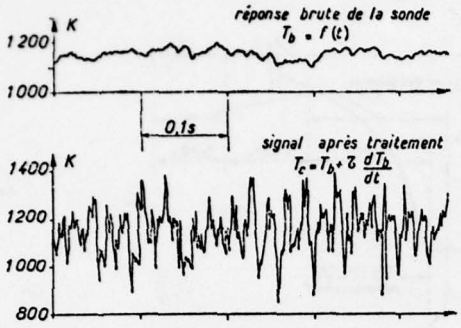

Fig. 11 – Exemple d'analyse des fluctuations de température d'écoulement au moyen d'une sonde à thermocouple à soudure sphérique (ϕ = 25/100 mm ; constante de temps, τ : 20 ms) associée à une électronique de traitement du signal brut.

3.3.2 - Pyrométrie optique

La méthode de mesure par renversement de raie mise au point à l'ONERA pour les gaz à hautes températures issus des moteurs fusée [11] [12] a été adaptée aux écoulements gazeux des bancs thermiques dont la température est inférieure à 1400 K.

Le pyromètre utilisé fonctionne dans l'infra-rouge et utilise l'absorption propre des gaz à étudier par la vapeur d'eau.

Cette méthode consiste à enregistrer le rayonnement,

a) d'une source de référence,
b) de la source de référence après traversée des gaz à étudier,
c) des gaz seuls.

Les détecteurs utilisés sont des cellules photovoltaïques à l'antimoniure d'indium refroidis à 77 K par de l'azote liquide.

Cette basse température du détecteur permet la mesure de températures de gaz jusqu'à une limite inférieure de l'ordre de 600 K. Le temps de réponse est de l'ordre de la microseconde.

La figure 12 compare les densités spectrales énergétiques mesurées à la sortie d'une chambre de combustion par une sonde à fil résistant non corrigée, l'analyse du même signal après correction et enfin l'analyse du signal délivré par le pyromètre optique. La concordance des deux dernières analyses est correcte jusqu'à une fréquence de 500 Hz environ.

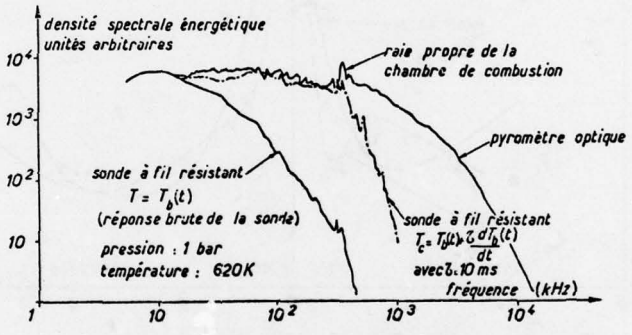

Fig. 12 – Spectres de fluctuations de température d'écoulement à la sortie d'une chambre de combustion. Mise en évidence de l'importance du traitement du signal brut pour élargir la bande passante d'une sonde à fil résistant.

A titre de comparaison nous avons porté sur la figure 13 les densités spectrales énergétiques dérivées de l'analyse des signaux délivrés par une sonde de pression d'arrêt et par une sonde pyrométrique placées à la sortie de cette même chambre de combustion. Une bonne similitude des deux courbes peut être observée.

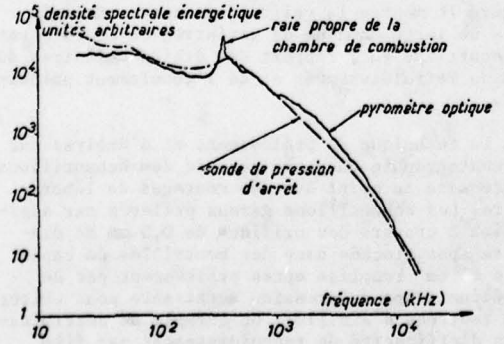

Fig. 13 – Comparaison des spectres de fluctuations de température et de pression d'arrêt à la sortie d'une chambre de combustion.

4 - TRANSFERTS DE CHALEUR

Le dimensionnement des aubes et de leurs systèmes de refroidissement est conditionné par la connaissance des coefficients d'échange et de la température d'équilibre du métal.

Des mesures de température décrites aux § 3.1 et 3.2 on peut remonter facilement à la détermination des coefficients de transfert de chaleur [14]. De l'équation de la chaleur où l'on néglige en première approximation les termes de conduction latérale :

$$(3) \qquad \alpha (T_a - T) = \rho c e \frac{\partial T}{\partial t}$$

où T est la température de paroi, T_a sa température athermane, ρ la masse volumique du métal, c sa chaleur spécifique et e l'épaisseur de la paroi, on peut déduire le coefficient d'échange α au cours d'une montée en température de la paroi

(arrêt du refroidissement). La figure 14 donne le principe de cette méthode qui s'est avérée très précise et répétable. Un exemple de dépouillement est présenté sur la figure 15. La comparaison avec les prévisions théoriques montre un assez bon accord entre expérience et calcul [15].

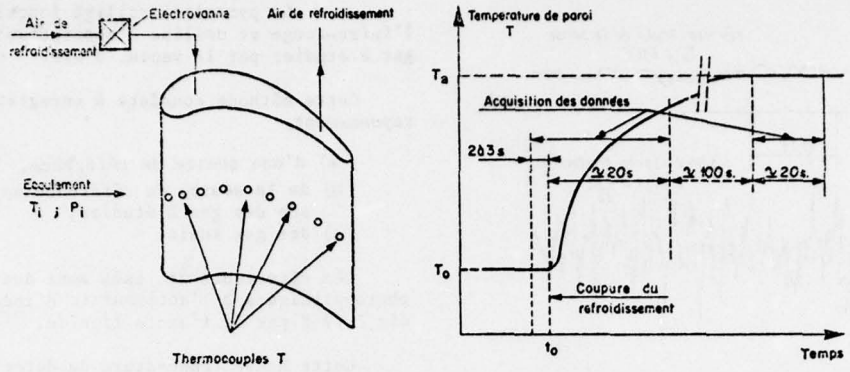

Fig. 14 – Principe de la mesure du coefficient de transfert thermique local sur aubes de distributeur.

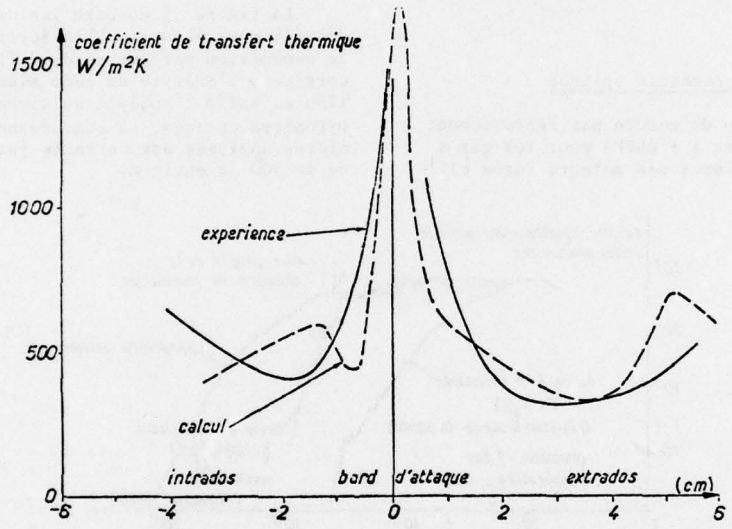

Fig. 15 – Coefficient de transfert thermique local sur aubes de distributeur.

5 - MESURE DE L'EFFICACITE DE PROTECTION THERMIQUE PAR FILM GAZEUX

Lorsque par injection à travers des évents correctement disposés sur la paroi des aubes on établit sur la surface de celles-ci des films gazeux, l'efficacité de protection thermique peut être caractérisée par le paramètre :

$$(4) \qquad \eta = \frac{T_g - T_a}{T_g - T_i}$$

où T_a est la température athermane de la paroi en présence du film, T_g la température de frottement de l'écoulement chaud et T_i la température d'injection du réfrigérant.

La température athermane locale est difficilement accessible à une détermination directe. Aussi a-t-on systématiquement utilisé l'analogie entre transfert d'énergie et transfert de masse (analogie de Reynolds) pour caractériser cette efficacité.

On peut montrer en effet [16] [17] qu'il y a équivalence entre l'efficacité thermique définie par (4) et celle déduite de :

$$(5) \qquad \eta' = \frac{\Gamma_g - \Gamma_P}{\Gamma_g - \Gamma_i}$$

où Γ est la concentration massique d'un constituant du gaz de refroidissement dont la concentration Γ_i à l'injection est différente de celle Γ_g dans l'écoulement principal. Γ_P est la concentration de ce constituant mesurée au point étudié. La figure 16 montre la validité de cette analogie dans un large domaine de variation du coefficient de soufflage m, rapport des débits unitaires du gaz de refroidissement et de l'écoulement principal.

La technique de prélèvement et d'analyse par chromatographie en phase gazeuse des échantillons a été mise au point sur des montages de laboratoire. Les échantillons gazeux prélevés par aspiration à travers des orifices de 0,3 mm de diamètre sont stockés dans des bouteilles de capacité 28 cm^3 remplies après prélèvement par de l'hélium à une surpression suffisante pour éviter des rentrées d'air [18]. Un exemple de détermination d'efficacité de refroidissement par film d'une plaque plane est présenté sur la figure 17 [19].

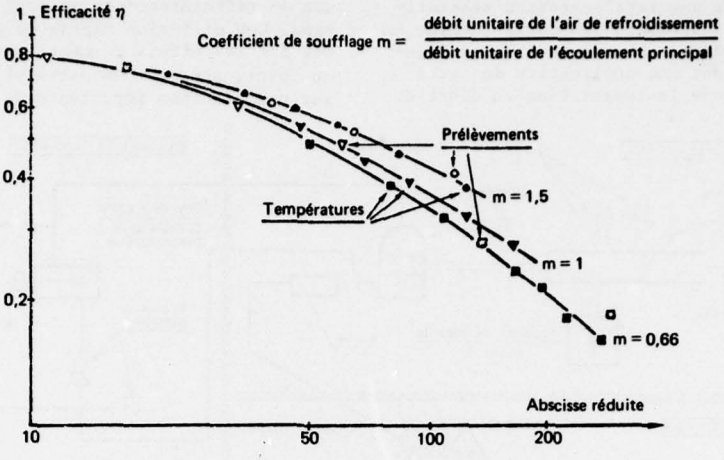

Fig. 16 – Equivalence des mesures de températures et de concentrations gazeuses pour la détermination de l'efficacité thermique de protection par film.

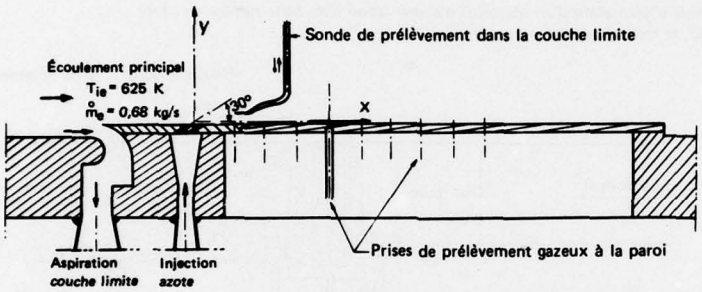

a. Détails du montage d'essai.

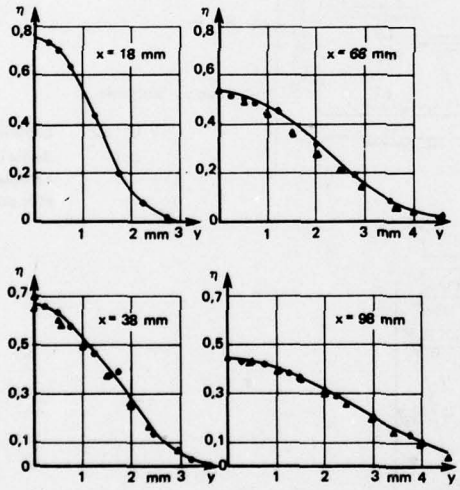

b. Comparaison des efficacités de protection thermique mesurées et calculées (coefficient de soufflage m = 1).

- *efficacité mesurée : • (concentrations)*
- *efficacité calculée : ▲(concentrations) Δ(températures)*

Fig. 17 – Exemple d'application de l'analyse chromatographique de prélèvements gazeux à la détermination de l'efficacité de protection thermique d'une paroi plane. Cas de l'émission d'un film à travers une fente de largeur 1 mm.

6 - CARACTERISATION DE LA PERMEABILITE D'UN ELEMENT DE TURBINE VIS-A-VIS DE L'AIR DE REFROIDISSEMENT. CONTROLE DU MELANGE DU GAZ DE REFROIDISSEMENT ET DE L'ECOULEMENT PRINCIPAL

Une bonne connaissance de la répartition du débit de gaz de refroidissement entre les divers éléments fixes et mobiles d'une turbine et de son mélange avec l'écoulement principal est importante afin de préciser l'influence de ces phénomènes sur les performances des diverses coupes des aubages et de permettre ensuite éventuellement d'optimiser la position des orifices d'injection au niveau des aubes et carters.

Pour contrôler le cheminement du fluide de refroidissement dans une turbine, l'injection d'air peut être remplacée par celle d'un gaz traceur, l'azote ou l'argon par exemple. L'analyse d'échantillons de gaz prélevés dans la veine permet ensuite d'aboutir, à partir des concentrations détectées, à une connaissance précise de la répartition de ce fluide traceur sur la hauteur de veine dans le plan de prélèvement retenu.

A titre d'exemple une représentation schématique d'un dispositif d'alimentation de la turbine en gaz traceur est donnée sur la figure 18. Les figures 19 et 20 illustrent une application de cette méthode pour l'étude de la répartition en débit du gaz de refroidissement en aval d'un étage de turbine. Une diffusion rapide du gaz traceur, favorisée par les effets de centrifugation à la traversée du rotor, apparaît en particulier très nettement sur une fraction importante de la hauteur de veine.

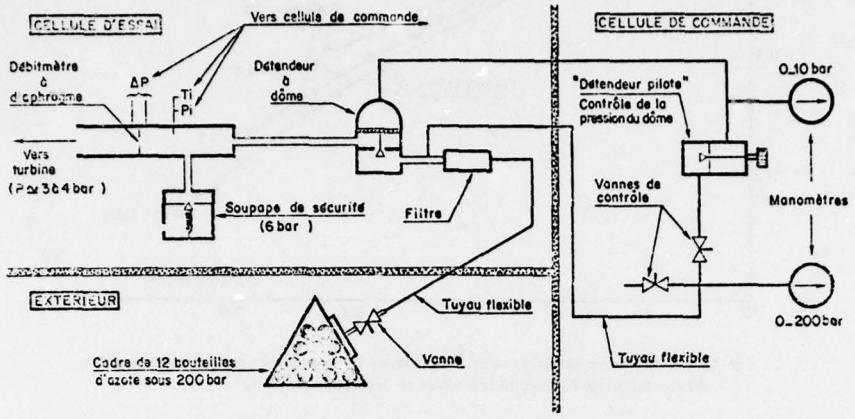

Fig. 18 – Exemple d'adaptation d'un dispositif d'alimentation d'un banc turbine en azote comme gaz de refroidissement ou gaz traceur.

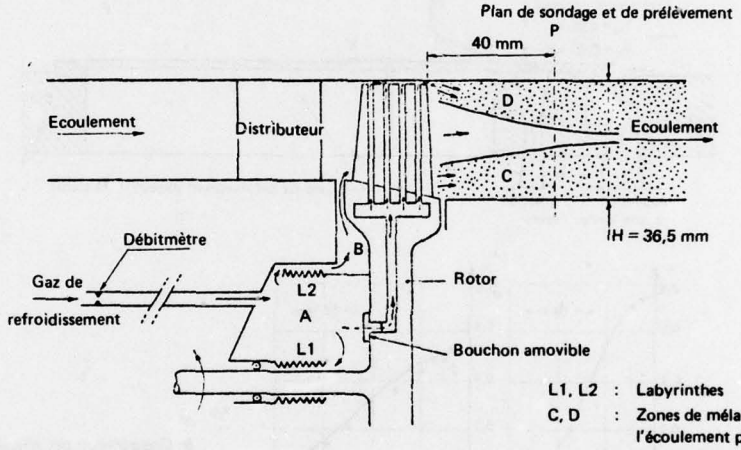

Fig. 19 – Représentation schématique de la répartition du gaz de refroidissement à la traversée d'un rotor de turbine.

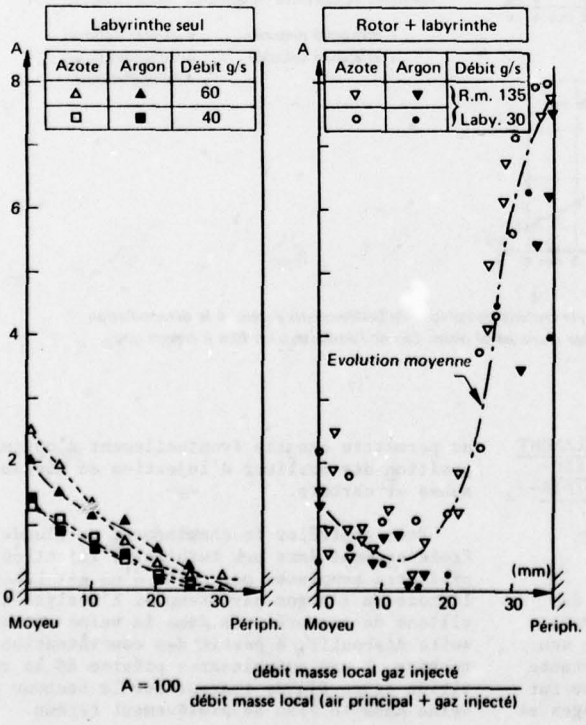

Fig. 20 – Exemple d'application de l'analyse chromatographique de prélèvements gazeux à la détermination de l'évolution radiale de la répartition du débit de gaz de refroidissement (azote ou argon) en aval d'un étage de turbine.

8 - CONCLUSION

La validation des méthodes de calcul des températures des turbines refroidies par air nécessite d'effectuer sur machines industrielles des mesures aussi nombreuses, fines et précises que celles effectuées au cours des essais sur bancs partiels.

L'instrumentation de mesure développée par l'ONERA, dans le cadre d'une étroite collaboration avec la SNECMA et le Centre d'Essais des Propulseurs, répond à ce souci. Son expérimentation dans divers bancs thermiques, en particulier au banc turbine MINOS, a permis de contrôler ses possibilités et de réaliser dans un environnement moteur des mesures généralement limitées aux études de laboratoire. La comparaison des résultats ainsi obtenus et de ceux acquis sur bancs partiels devrait permettre de mieux préciser l'influence des paramètres moteurs, comme la turbulence de l'écoulement et les effets de centrifugation dans un rotor, sur des phénomènes importants comme les coefficients de transfert thermique au niveau des parois et l'efficacité de protection thermique par film gazeux. Ces problèmes sont essentiels tant pour le chercheur et son besoin de compréhension des phénomènes rencontrés que pour le motoriste et son souci de mise au point des turbo-réacteurs.

REFERENCES

[1] - J. FOURNET
Turboréacteur de pointe, les hautes températures devant turbine.
Revue de la Défense Nationale, Déc. 76, p. 121.

[2] - J. FRANCOIS - Y. LE BOT - J. MICHARD - P. DEGUEST
Adaptation d'un banc de turbine aux recherches pour les hautes températures.
Symposium AGARD on "High temperature problems in gas turbine engines" - Ankara - sept. 77.

[3] - C. FREEMAN
The relationship between steady and unsteady spacial distorsion.
Dans "Unsteady phenomena in turbomachinery", AGARD CP n° 177, 1975.

[4] - R. LARGUIER - A. de SIEVERS
Méthodes de mesures instationnaires dans les turbomachines.
Aéronautique et Astronautique n°46 - 1974-3.

[5] - R. LARGUIER - A. de SIEVERS
Mesures instationnaires dans les turbomachines.
Rech. Aérosp. n° 1975-5, p. 267-277.
English translation. ESA TT298 (1976), p. 61-86.

[6] - A. BOUTIER - G. FERTIN - R. LARGUIER - J. LEFEVRE - A. de SIEVERS
Laser anemometry applied to research compressor.
ISL Report n° 117/1976, p. 553-565.

[7] - R. LARGUIER - C. RUYER
Méthode d'analyse expérimentale de l'écoulement instationnaire dans un compresseur aéronautique transsonique.
Rech. Aérosp. n° 1972-6, p. 353-354.

[8] - M. CHARPENEL - J. WILHELM
Pyromètre infra-rouge destiné à la mesure des températures d'ailettes de turbine.
Mesures, régulation, automatisme - Vol. 41, n° 4, Avril 1976 - p. 41-50.

[9] - R.R. DILS
Dynamic gas temperature measurements in a gas turbine transition duct exit.
ASME paper n° 73-GT-7 (1973).

[10] - R.P. BENEDICT
Fundamentals of temperature, pressure and flow measurements.
John Wiley and Sons, Inc. 1969.

[11] - P. CALVET - F. LIOUSSE
Mesures locales de températures, pressions et vitesses au moyen de capteurs thermorésistants chauffés par impulsion.
Revue Générale de Thermique n° 114 - Juin 71.

[12] - A. MOUTET - C. VERET - L. NADAUD
Méthodes optiques de mesure instantanée de la température des flammes.
Rech. Aéronautique n° 68 (Janv. Fév. 1959) p. 9-19.

[13] - A. MOUTET - J. CRABOL - L. NADAUD
Températures des gaz et des flammes.
Techniques de l'ingénieur - 6-1974 - R 2750.

[14] - J. MICHARD
Mesures de flux de chaleur sur aubes fixes de turbines.
Dans "High temperature turbines" - AGARD CP 73 (1971).

[15] - D. ARNAL - J.C. JUILLEN
Etude expérimentale et théorique de la transition de la couche limite.
Rech. Aérosp. n° 1977-2, p. 75-88.

[16] - J.J. NICOLAS - M. IZARD
Protection thermique des tuyères supersoniques par film gazeux.
Rech. Aérosp. n° 1971-4, p. 197-208.

[17] - M. BARRERE
La métrologie dans le domaine aérospatial limité aux hautes températures.
Réunion de la Société Française des Thermiciens. Toulon 20-22 mai 1974 - Edition provisoire ONERA. TP 1379 (1974).

[18] - G. LENGELLE - C. VERDIER
Prélèvement et analyse de gaz dans les phénomènes de combustion.
AGARDgraph AG n°168 (1973).

[19] - J. MICHARD - M. IZARD
Mécanismes de diffusion de masse ou d'énergie dans les couches de mélange turbulent.
Rech. Aérosp. n° 1976-1, p. 27-35.

DISCUSSION

F.J.Louis, US

What is the influence of the nature of the combustion products such as soot on the pyrometric measurements?

Author's Reply

Il est effectivement nécessaire que l'émission des gaz se trouvant entre le pyromètre et l'aube soit négligeable devant l'émission de la paroi. Cette émissivité est due: (a) soit aux gaz tels que CO_2, H_2O et il est nécessaire de supprimer les bandes d'émission les plus intenses en coupant le rayonnement infra-rouge au delà de 2,5 μm; (b) soit aux particules de suie en suspension dans les gaz. Des expériences sur bancs statique ont montré que ces particules peuvent être gênantes à haute température et haute pression (2000 K, 20 bars) mais sans influence aux températures et pressions usuelles (3 à 4 bars et 900 à 1200°C par exemple). Il faut d'ailleurs noter que le pyromètre est très près des aubes (quelques cms) et que le facteur d'émission est ainsi minimisé. Evidemment il est nécessaire d'éviter le dépot et l'accumulation de suie sur la fenêtre du pyromètre qui doit être balayé en permanence par un courant de gaz frais.

D.K.Hennecke, Germany

My question is also directed to pyrometry. Since the accuracy of this measurement technique depends much on the value and the directional dependence of the blade surface emissivity, I would like to know if you treat the blade surface in order to obtain high emissivity values and make them suitable for pyrometry.

Author's Reply

Nous n'avons pas fait subir de traitement particulier aux aubes, mais dans le cas de la turbine MINOS nous avons demandé à la SNECMA de supprimer le traitement d'aluminisation qui conduisait à des émissivités particulièrement faible, de l'ordre de 0,2. Sans ce traitement, l'émissivité de l'aube avant essai a été trouvée égale à 0.6. La comparaison avec les thermocouples pendant les essais à faible température de gaz (900°) a donné 0,74.

Des essais sur banc statique ont montré que l'émissivité des aubes aparaissait très vite pour atteindre des valeurs supérieures à 0,9 lorsqu'elles sont soumises à des gaz dont la température dépasse 1200°. Ces essais doivent être repris dans le cas où les aubes ont subi un quelconque traitement de surface.

W.Liebe, Germany

You are measuring the heat transfer in a moment when the temperature rises, if I understood well, in the front region of a hot jet. In this early stage the thermal boundary layer is not the same as in steady flow.

Author's Reply

The increase is not caused by a jet, but by decreasing the cooling flow inside the blade. The steady flow outside the blade is not disturbed.

W.Liebe, Germany

I think in the case that the increasing of wall temperature is caused by decreasing the cooling flow inside the blade, the profile of the outside thermal boundary layer will be changed. The steady flow heat transfer coefficient exists only in the beginning, at the time point "zero".

Author's Reply

La couche limite thermique externe depend effectivement de la temperature de surface de l'aube et en toute rigueur la notion de coefficient d'échange n'a de sens que pour une température de paroi constante. En conséquence, la méthode consistant à analyser l'évolution de la température de surface d'une aube sans émission après coupure brutale du refroidissement par convection interne n'est donc valable qu'en première approximation.

Pour mieux cerner cette difficulté les études expérimentales sur montages de laboratoires et sur machines industrielles sont toujours effectuées en analysant successivement plusieurs évolutions des températures de surface d'aubes en régime transitoire. Ces transitoires correspondent à des écarts de température plus ou moins importants entre les deux équilibres thermiques associés aux états 'aube refroidie' et 'aube non refroidie'. Il est apparu que la dispersion entre les coefficients de transfert thermique déduits de ces transitoires plus ou moins accentués est en général faible et la méthode utilisée peut donc être considérée comme satisfaisante en première approximation. La répartition sur l'aube du coefficient de transfert thermique ensuite retenue est une moyenne de celles obtenues au cours de ces divers transitoires successifs.

THE MEASUREMENT OF FILM COOLING EFFECTIVENESS ON TURBINE COMPONENTS IN SHORT DURATION WIND TUNNELS

J.P. Ville and B.E. Richards
Research Assistant and Associate Professor
von Karman Institute for Fluid Dynamics
72, chaussée de Waterloo
1640 Rhode-St-Genèse, Belgium

ABSTRACT

This note describes a method to measure an adiabatic wall effectiveness, η, and its associated heat transfer coefficient, h_f, of a film cooling system for turbine components in a short duration facility. Such a facility was used to provide flow conditions selected to simulate those of advanced aircraft turbines. The measurement of heat transfer rates under different coolant temperature conditions and the definition of a linear relationship between a heat transfer coefficient, h, based on mainstream recovery temperature and a non-dimensional coolant temperature, θ, leads to the evaluation of η and h_f. The measurements on a flat plate, cooled by air ejected through inclined holes at a Mach number of 0.6, unit Reynolds number of 2.4×10^7 per metre, wall to mainstream temperature ratio of 0.76, coolant to mainstream temperature of 0.70 to 0.95 and mass velocity ratio from 0.5 to 1.5 confirm the linearity of the h, θ relation and prove the ability of a short duration facility to provide useful film cooling data for blade cooling system development.

RESUME

Cette note décrit une méthode utilisée pour mesurer, dans une soufflerie à temps d'essai bref, une efficacité η, définie pour une paroi adiabatique, et le coefficient d'échange associé h_f, d'un dispositif de refroidissement par film d'air de composants de turbine à gaz. La mesure de flux thermiques pour différentes températures du gaz de refroidissement et la définition d'une relation linéaire entre un coefficient d'échange, basé sur la température de récupération de l'écoulement principal, et une température adimensionnelle θ, conduit à l'évaluation de η et h_f. Les mesures furent réalisées sur une plaque plane, refroidie par un film d'air émis par des trous inclinés, dans les conditions suivantes : Mach = 0.6, nombre de Reynolds unitaire : $2,4 \times 10^7$, rapport de température de paroi à la température de l'écoulement principal = 0.76, rapport de la température de l'air de refroidissement à celle de l'écoulement principal variant de 0.70 à 0.95. Elles confirment la linéarité de la relation $h(\theta)$ et démontrent la capacité des souffleries à temps d'essais court à produire des résultats concernant le refroidissement par film utiles pour le développement des dispositifs de refroidissement d'aubes.

LIST OF SYMBOLS

a	speed of sound
h	heat transfer coefficient of film in terms of $(T_{rm}-T_w)$ (see Eq.10)
h_f	heat transfer coefficient of film in terms of $(T_{aw}-T_w)$ (see Eq.2)
h_o	heat transfer coefficient on wall with no film cooling (Eq.1)
m	coolant mass ratio
M	Mach number
p	pressure
q	heat transfer rate
Re	Reynolds number
T	temperature
β	$(\gamma+1)/2(\gamma-1)$
γ	ratio of specific heats
η	adiabatic wall effectiveness (Eq.3)
η_q	isothermal wall effectiveness (Eq.7)
ρ	density
θ	non-dimensional coolant temperature parameter (Eq.5)

SUBSCRIPTS

aw	adiabatic wall
c	coolant
f	film
is	isentropic
m	mainstream
o	without cooling or total conditions
r	recovery
w	wall
∞	static conditions

1. INTRODUCTION

A number of researchers (Refs 1-4) are examining the effectiveness of various types of film cooling systems to cool turbine blades and components using short duration facilities instead of conventional continuous wind tunnels. The advantages of such facilities include economic testing, simple and accurate measurement techniques and accurate scaling of such important flow parameters as Mach number, Reynolds number and temperature field. This method of testing involves straight forward and accurate measurement of isothermal wall heat transfer but limitations exist in measuring the adiabatic wall temperature more conventionally selected as the main parameter of interest for film cooling in the past (e.g. Ref.5) and hence the difference in interpretation of film cooling effectiveness from these new facilities has to be considered. Testing under purely isothermal wall conditions, however, is more logical than adiabatic wall conditions for the application in mind since the present trend is for designers to mix internal convection or impingement cooling and film cooling to achieve a constant temperature blade and then adiabatic wall conditions are never achieved. Metzger et al (Ref.6) have made measurements of effectiveness using isothermal wall heat transfer data at different wall temperatures and, after a discussion of this paper by Eckert, devised a method explained in Ref.7 to obtain an adiabatic wall effectiveness, η, and associated heat transfer coefficient, h_f (which differs in value from the unblown heat transfer coefficient, h_o) from heat transfer data measured at different wall temperatures. This operation was done without directly measuring the adiabatic wall temperature. An equivalent technique, but by varying the coolant temperature, was demonstrated by Choe et al (Ref.8). All of this work was carried out in incompressible wind tunnels.

This present paper reviews and compares the different definitions of film cooling effectiveness derived from various techniques and then describes the results of experiments to determine the viability of determining an adiabatic wall effectiveness parameter and the associated heat transfer coefficient from heat transfer data obtained from experiments carried out with different coolant temperatures in the same way as Refs 7 and 8 but in the compressible flows generated in short duration wind tunnels.

2. THEORY

The heat transfer at a particular position on an impervious turbine blade is represented by the equation

$$q_o = h_o (T_{rm} - T_w) \tag{1}$$

where T_{rm} is the recovery or adiabatic wall temperature of the flow, T_w the wall temperature and h_o the associated heat transfer coefficient. If the surface is cooled by a gaseous film, then the equivalent equation is usually given by

$$q_f = h_f (T_{aw} - T_w) \tag{2}$$

where q_f is the heat transfer rate in the presence of the film, T_{aw} is the adiabatic wall temperature of the flow (and is representative of the local temperature of the film) and h_f, the associated heat transfer coefficient which has a value not too far different from h_o.

The adiabatic wall temperature, T_{aw}, is normally defined in terms of the film cooling adiabatic wall effectiveness parameter, η, given by

$$\eta = \frac{T_{rm} - T_{aw}}{T_{rm} - T_{rc}} \tag{3}$$

where T_{rc} is the recovery temperature of the coolant. Film cooling effectiveness then varies from unity, when $T_{aw} = T_{rm}$ (i.e. the film is fully effective) to zero, when $T_{aw} = T_{rm}$ which occurs so far downstream from injection that the boundary layer recovers to its undisturbed value.

Combining Eqs 2 and 3, we get

$$q_f = h_f (T_{rm} - T_w)(1 - \eta\theta) \tag{4}$$

where θ is a compressible flow version of the non-dimensional temperature parameter first introduced by Metzger et al (Ref.6) defining the level of the coolant temperature with respect to the wall temperature in terms of the mainstream temperature, i.e.

$$\theta = \frac{T_{rm} - T_{rc}}{T_{rm} - T_w} \tag{5}$$

Introducing Eq.1, we get

$$\frac{q_f}{q_o} = \frac{h_f}{h_o} (1 - \eta\theta) \tag{6}$$

Effectiveness has also been expressed in terms of the ratio of heat transfer rate with injection to that without injection (e.g. Refs 2, 3, 4) as follows

$$\eta_q = 1 - \frac{q_f}{q_o} \tag{7}$$

The relationship of this so-called isothermal wall effectiveness with the adiabatic wall effectiveness η is found by including Eq.6

$$\eta_q = 1 - \frac{h_f}{h_o}(1 - \eta\theta) \tag{8}$$

Only for the case of $h_f = h_o$ (i.e. the injection effectively causes no disturbance to the flow) and $T_{rc} = T_w$ (i.e. $\theta = 1$) does the isothermal effectiveness have the same value as the adiabatic wall effectiveness. i.e.

$$\begin{aligned} &\eta_q = \eta \text{ for } h_f = h_o \text{ and } T_{rc} = T_w \\ &\eta_q = \eta\theta \text{ for } h_f = h_o \text{ and } T_{rc} \neq T_w \\ &\eta_q = 1 - h_f/h_o(1 - \eta) \text{ for } T_{rc} = T_w \text{ and } h_f \neq h_o \end{aligned} \tag{9}$$

In order to avoid the difficulty of dealing with the adiabatic wall temperature, an alternative relation to Eq.2 is

$$q_f = h(T_{rm} - T_w) \tag{10}$$

In this relation the only parameter that can reflect the behaviour of the coolant temperature is this newly defined heat transfer coefficient h. Its effect can be seen by combining Eqs 4 and 10, i.e.

$$h = h_f(1 - \eta\theta) \tag{11}$$

which equation is plotted in Fig.1 with the heat transfer coefficients non-dimensionalised by dividing by h_o. This relation was originally developed by Metzger et al (Ref.6) who demonstrated the linearity of the expression experimentally at different values of θ, created by changing T_w. Later Metzger et al (Ref.7) defined the curve from measurements of h at different wall temperatures and then used the resulting relationship to extrapolate firstly the curve to $\theta = 0$ to obtain h_f and then to $h = 0$ to obtain $\eta = 1/\theta_{h=0}$. This provides a different method to obtain these parameters than directly measuring the adiabatic wall temperature and measuring the heat transfer rate at another wall temperature as used by Liess (Ref.5) for example. Choe et al (Ref.8) and Crawford et al (Ref.9) demonstrated on the other hand the linearity in h and θ implied in Eq.11 by changing the coolant temperature at approximately similar wall temperatures. As yet, it has not been demonstrated experimentally that the variations of h with θ using separately a change in the wall temperature or a change in coolant temperature will coincide, but the "superposition" analysis by Choe et al (Ref.8) provides reasonable confidence that this will be true for incompressible flow and small temperature differences.

These latter authors chose to display the film cooling data by providing h at θ=0 and θ=1 (obtained by changing T_{rc} from T_{rm} to T_w) giving a designer another way to obtain h at any value of θ using the relationship.

$$h = h_{\theta=0} - \theta(h_{\theta=0} - h_{\theta=1}) \tag{12}$$

This method was chosen for its appropriateness to full coverage film cooling (which has similarities with transpiration cooling in which h is normally used as the heat transfer coefficient), however for surfaces downstream of injection the same information could be used to obtain $h_f (= h_{\theta=0})$ and η (from $\eta = 1/\theta_{h=0}$) by appropriate extrapolation (see Fig.1) and then to use Eq.11 instead of Eq.12 as done by Metzger et al (Ref.7).

From this discussion arising from linearity of the temperature field implied by Eqs 4 and 11, it is seen that the film effectiveness cannot be defined just by the single parameter η_q in the same way as η, but it must be at least supplemented by an indication of the value of θ at which it is obtained. Following the arguments of Choe et al (Ref.8) considerably more flexibility can then be given to the designer by giving him η_q (or q_f or h) at another value of θ enabling him to obtain q_f at the various values of T_w and T_{rc} encountered during his design iteration. It should be remarked also that the value of η as obtained from direct measurements of adiabatic wall temperature in a steady state experiment is likely to differ slightly from that by applying the isothermal wall approach, since the upstream flow field development will be different in each case.

The assumption of linearity of the temperature field should be examined at this stage for the design case in which the total, wall and coolant temperatures may be at levels of the order of 2000K, 1200K and 600K respectively for a future projected turbine. The fluid temperature and hence the gas density gradients are so high as to suspect the

inaccuracy of an assumption concerning a constant property fluid even though the flow Mach number may be small. The conditions are also far removed from the incompressible small temperature variation flows under which the linearity of Eq.11 was proved experimentally. For example, the value of θ of 1.75 can be obtained for the design case indicated above in which $T_{rc}/T_{rm} = 0.3$ and $T_w/T_{rm} = 0.6$ as can be obtained in a typical incompressible or compressible "film heating" experiment in which $T_{rc}/T_{rm} = 1.117$ and $T_w/T_{rm} = 1.067$. This demonstrates that apart from θ, another temperature parameter should be used to define the conditions of the test e.g. T_w/T_{rm}.

No experimental information is as yet available, for the design case of compressible flow with large temperature differences, to determine the behaviour of h with θ. The achievement of linearity is not essential as long as measurements are made in the θ range of interest. This range is normally from 1.25 to 1.75 for aircraft power units.

In such a situation an assumption of linearity can be used to approximate the results to get appropriate values of h_f and η by extrapolation. Although these values may be inaccurate due to such an extrapolation, used together to determine h or q_f in the region of interest, the original measurement accuracy will be realised in a design calculation.

3. EXPERIMENTAL EQUIPMENT

3.1 Justification of using short duration wind tunnels

The importance of performing experiments on film cooling of turbine components at well simulated conditions has been explained in Section 2. However, the power levels required to achieve such conditions of high temperature at high pressure in a test rig are so large that the cost of constructing and operating a continuous facility at high power becomes prohibitive. This point is illustrated by the lack of publications available on testing at such conditions.

The main objective of short duration wind tunnels is to reduce the total energy invested in heating the working fluid by orders of magnitude whilst keeping the power level high. In such a facility, the component to be tested is at room temperature. This imposes a change in the main flow temperature level. The running time is so short that the temperature variations of the facility, test section and model are very small so that cheap conventional materials can be used. Another great advantage is that the heat transfer measurements are easy and accurate using transient temperature techniques.

If Mach and Reynolds numbers remain unchanged, Nusselt number is identical for operating and simulated conditions when the Prandtl number is unchanged. Then, temperatures and pressures levels can be scaled down by appropriate factors of proportionality. This point has been analysed by Louis et al (Ref.2).

Shock tunnels have first been adapted for subsonic and transonic flows required for turbine studies by Jones and Schultz (Ref.1). These same workers (Refs 10, 4) developed a new type of facility using a simple pure isentropic compression cycle : the isentropic light piston tunnel (ILPT) or compression tube . This ILPT is fairly well adapted for heat transfer studies under turbine flow simulation. A small pilot facility in which the present study was made has been constructed at VKI and a large version of ILPT with a test section of 300 x 100mm is now in operation for hot cascade studies.

3.2 The isentropic light piston cycle

The principle of operation of this facility is illustrated in Fig.2. The test gas contained in the tube is compressed and heated isentropically by a light free piston driven by a gas entering the tube from a high pressure reservoir. When the test gas achieves the pre-designated pressure and hence temperature, a fast operating valve (or a diaphragm) is opened allowing the test gas to flow in the test section. If the volumetric flows of the gas entering the tube from the reservoir and the gas leaving the tube through the test section are matched, the pressure and flow conditions remain constant until the piston reaches the end of the tube. The tube pressure then continues to rise until the incoming gas flow is stopped. In the test section, pressure and temperature follow a steplike variation which is most suitable for the application of a transient heat transfer measurement technique.

3.3 VKI Tunnel CT-1

The ILPT pilot tunnel of VKI was fabricated from a disused shock tube. The tube has an internal diameter of 102mm and is 3.25m long, it was connected to the main VKI air supply delivering a pressure up to 40 atm through a control valve. The various test sections have a typical throat area of 1.5 cm^2 with rectangular or axisymetric channels and are connected to a dump tank having a volume equivalent to the volume of the tube. A 60g nylon piston can move freely with a minimum of leaks inside of the tube. A fast opening shutter valve is used to start the flow in the test section. This valve is pneumatically operated and can be fully opened in less than 4 msec.

Subsonic operation can be achieved by using a throat downstream of the test section. The dump tank pressure is kept low enough to keep the flow sonic through this throat during the test.

Before firing, the tube is set to the desired initial pressure (either slightly pressurized or slightly evacuated). After presetting the instrumentation, the tunnel is set into operation by opening quickly a manually operated ball valve. The compression lasts about 1 sec and the test duration 0.1 sec. After a test, the system is brought to room pressure, the piston reset at the end of the tube ready for the next test. The turnround time for operation can be less than five minutes.

3.4 Secondary gas supply

For film cooling experiments, the secondary gas (air) is taken from a 50l reservoir precharged at a pressure up to 35 atm at room temperature. The temperature is adjusted to the desired level as the gas passes through a small regenerative heat exchanger and the mass flow controlled by a choked calibrated orifice close to the test section. A pneumatically operated ball valve then initiates the gas injection into the test section (Fig.3).

The heat exchanger is made of a stack of brass gauze screen matrices in a 25 mm diameter and 40 cm long steel tube. It has been designed to heat or cool the secondary gas at the maximum coolant mass flow rate with a temperature variation of less than 1% during the test with minimum pressure losses. The heat exchanger temperature can be adjusted between -40° and +120°C by a low pressure secondary open loop system using an electrical heater or a cooler made of an alcohol bath whose temperature can be decreased down to -70°C by addition of dry ice. After a few minutes of heating or cooling, when the required temperature is reached, the heat exchanger is isolated from the low pressure loop and connected to the high pressure reservoir ready for a test.

The calibrated orifice has been placed after the heat exchanger to minimise the volume between itself and the test section : the coolant pressure can then adjust itself to the mass flow pressure and can follow even a very small pressure fluctuation within a delay of one or two msec giving a nearly constant mass flow rate into the test section during the test. This is particularly important for small injection rates when coolant pressure is very close to main flow static pressure.

3.5 Instrumentation

All the pressures - in the tube, the test section and secondary gas supply - are measured with Validyne variable reluctance diaphragm transducers, the response time of these transducers being compatible with the relatively slow pressure variations during the test.

Heat transfer rates are measured, using a transient surface temperature technique, with standard thin film platinum resistance thermometers, brush painted and fired on quartz inserts, associated with appropriately designed analogue circuits (Ref.11).

Main flow temperature was measured in a previous series of test with a fine tungsten wire probe used as an equilibrium temperature probe. The temperature is assessed from the change in resistivity of the wire during the test and this value is corrected for conduction end losses to the wire support (Ref.12). Response times of less than 1 msec are achieved. This rapid response time enabled subtle variations in temperature to be easily detected.

For film cooling tests, the temperature of the secondary flow is measured at 2 points inside of the heat exchanger, upstream of the flow meter and in the small settling chamber just before the injection holes, using thermocouples made with 0.1mm diameter chromel alumel wires. The response time was found to be of the order of 20 msec. This slow response is due to very low gas velocity at various measurement points. Coolant pressure is also measured before the calibrated orifice and in the injection chamber.

Oscilloscopes and an u.v. oscillograph with a speed up to 256 cm/sec fitted with galvanometers with response times up to 5 kHz are used for recording the signals from the instrumentation. Galvanometer drive units were used to vary easily the recording system sensitivity and facilitate the calibration.

During operation, the various events are synchronised by a trigger and delay unit. A first triggering pulse is set off from the achievement of a "threshold voltage" by the processed signal from the transducer monitoring the tube pressure. This pulse is used to activate the valve to initiate injection and to start the u.v. recorder and, after an adjustable delay to trigger the single trace of the oscilloscopes. A second pulse, triggered in the same way as the first, activates the actuator of the fast operating shutter valve initiating the flow in the test section. The injection valve is closed and the recorder is stopped automatically after a suitable time lag to encompass the tunnel running time.

3.6 The model

The film cooled test surface is one wall of the 13.4 x 15.7 mm rectangular test channel of CT1. Typically, downstream (and on the centre line of the plate) of an injection section, 10 thin film platinum resistance gauges (with dimension of 4 mm span by 0.5 mm chord) are positioned within a length of 55 mm. These gauges average the spanwise heat transfer rate distribution across 3-4 injection holes. Only several of the gauges were selected for use in this test programme. A two dimensional spanwise slot facing upstream is installed on the test surface 30 mm upstream of the injection position to act as a

boundary layer bleed. The Mach number in the test section is fixed at 0.6 by a sonic throat of suitable area downstream of the instrumented plate.

The geometry of the coolant injection was selected as follows :

hole diameter, d	0.5 mm
spanwise spacing	1.0 mm
number of rows	2
spacing between rows	1.5 mm
injection angle	30°
injection channel length	4 mm
number of holes	25

The nominal conditions selected for study were :

Mach number	0.6
P_{om}	3.0 bar (absolute)
T_{om}	382 K (T_{is} = 401 K)
T_{oc}	267-365K
T_w	≈293K
Re	2.44 10^7/m

A drawing of the test model is given in Fig.4.

4. EXPERIMENTAL RESULTS

The aim of this part was to prove that it is possible to get repeatable and accurate heat transfer and surface temperature measurements for various secondary flow temperatures in a short duration facility and that these results, plotted in an h-θ graph (similar to Fig.1), can be used to assess the values of h_f and η.

4.1 Experimental difficulties encountered

Main flow temperature measurements indicate that this temperature is well related to the pressure variations but 5% below the isentropic temperature at the selected measurement time.

Preliminary tests with injection have shown that the secondary flow temperature was not constant during the test as illustrated by the relevant trace for the case of coolant at ambient temperature in Fig.5. Injection is initiated about 100 msec before the test to be sure that the air initially between the heat exchanger and the test section is blown out when the main flow starts. As the coolant mass flow is kept constant by the choked orifice, the pressure in the injection settling chamber (again illustrated in Fig.5) increases to its stable condition for the particular pre-test pressure in the test section. This compression is associated with a temperature rise of the order of 20°C. When the main flow starts, the settling chamber pressure suddenly rises to its nominal value controlled by the test section pressure causing a second increase of pressure and hence of temperature of the secondary gas. These "hot" gases appear to be evacuated after 20 to 30 msec for all coolant temperatures tested. To avoid taking measurements in these unstable periods, it was decided to measure heat transfer and wall temperature 32 msec after the beginning of the test. This time was also selected because the main flow pressure at that time is then equal to its mean value (nominal)(Fig.5). On the typical record presented in Fig.5, the coolant temperature variations (T_i) are smoothed because of the relatively poor response time of the thermocouple. The preliminary tests also indicate that the flow conditions upstream of the calibrated orifices were nearly constant during the test (about 0.05% change in pressure and less than 1% change in temperature). Furthermore, the pressure losses through the heat exchanger and valve were found to be negligable. In later tests pressure was then set to the required level in the H.P. reservoir and was measured only before the test. The time dependent temperature however, was measured at the same time as other parameters in all tests as illustrated in Fig.5.

4.2 Data reduction

The secondary mass flow was calculated from the area of the calibrated orifice, A^*, and the upstream flow conditions by the simple formula

$$\dot{m}_i = \beta \times \rho_{oi} \times a_{oi} \times A^*$$

where the density ρ_{oi} and speed of sound a_{oi} are defined from the measurements of P_{oi} and T_{oi}. The mass flux ratio was then obtained from this mass flow, the main flow static conditions and the injection cross sectional area A_i from :

$$m = \frac{\rho_{\infty c} V_c}{\rho_{\infty m} V_m} = \frac{\dot{m}_i}{A_i} \times \frac{1}{\rho_{\infty m} V_m}$$

The wall temperature T_w was obtained from the electrical resistance variations of the gauge and heat transfer q from the output of the analogue circuits by an appropriate calibration of the analogue, the measured temperature coefficient of resistance of the gauge and the thermal properties of the quartz on which the gauge is painted.

Heat transfer coefficient is then simply defined by $h = q/(T_{om} - T_w)$ with and without film cooling.

The results were presented as the ratio of the measured heat transfer coefficients with and without injection, h/h_o. This presentation of the results eliminates the possible small systematic error on q that may not be fully eliminated by calibration.

4.3 Results

The results of the measurements of h/h_o are first plotted against the mass velocity ratio m for a given injection temperature and the various positions selected. An example is given in Fig.6. Such a graph allows a rapid preliminary check of the results and is used to smooth the curves and to interpolate h/h_o to the desired value of m. The parameter θ is calculated, for each point, from the measured values of T_w, T_i and the main flow temperature assessed from the isentropic temperature T_{ois}. As carried out for h/h_o, θ is interpolated to the selected m when necessary. Finally, the values of h/h_o obtained by this way for a given mass velocity ratio and various secondary flow temperatures are plotted against θ.

The tests already performed with this technique for four injection temperatures give fairly good results even for "lift-off" conditions as illustrated in Fig.7. The straight lines drawn through the experimental points are extrapolated to the $\theta = 0$ and $h/h_o = 0$ axes giving the values of respectively h_f/h_o and $\theta_o = 1/\eta_{ad}$. The trend observed seems to be normal i.e. η_{ad} decreases with the distance and increases with the mass velocity ratio, and, close to injection holes (x/d = 7) h_f/h_o increase with m. Complete results of h_f/h_o and $\eta_{ad}(1/\theta_o)$ obtained by this method for x/d = 7 are plotted against m in Fig.8. The effectiveness $1/\theta_o$ increases continuously with m up to 83% for m = 0.9 and is nearly constant for m > 1.0, indicating that the lift off occurs for m = 0.9. This lift off condition is also marked by a rapid and continuous increase of h_f/h_o for m > 1. A similar trend was observed by Eriksen and Goldstein (Ref.12) but for nearly incompressible flow conditions.

These few results show that this method, is capable of providing useful measurements of film cooling effectiveness and heat transfer coefficient to the designer. The substantial difficulty of altering the coolant temperature is offset by the broadened utility of the data.

5. CONCLUSIONS

A short duration facility has been used to provide an assessment of adiabatic wall effectiveness of a film cooling system with the associated heat transfer coefficient instead of simple isothermal film cooling effectiveness as usual in short duration testing. These results were obtained by operating the experiments under different coolant temperature conditions. The reliability and repeatability of heat transfer and temperature measurement is found to be good and the hypothesis of a linear relationship between a heat transfer coefficient h and a non-dimensional coolant temperature θ, leading to the evaluation of adiabatic film effectiveness and classical heat transfer coefficient is proved experimentally. The modification of the coolant temperature, introduced complications to the normal simple techniques associated with short duration testing, but the extra effort enhanced substantially the value of these measurements taken under well simulated gas turbine flow conditions.

REFERENCES

1. Jones T.V. and Schultz D. : "Film cooling studies in subsonic and supersonic flows using a shock tunnel" in Shock Tube Research, ed. J.L. Stollery. Chapman and Hall, 1971.
2. Louis J.F., Demerijian A.M., Goulios G.N., Topping R.F. and Wiedhopf J.M. : "Short duration studies of turbine heat transfer and film cooling effectiveness" ASME Paper 74 GT 131, 1974.
3. Richards B.E., Appels C., Ville J.P., Salemi C. : "Film cooling of heated turbine surfaces at simulated conditions" AIAA Paper 77-947, July 1977.
4. Schultz D.L., Jones T.V., Oldfield M.L.G., Daniels L.C. : "A new transient cascade facility for the measurement of heat transfer rates" Paper 31, AGARD Symposium on High Temperature Problems in Gas Turbine Engines, Ankara, Turkey, Sept 1977.
5. Liess C. : "Experimental investigation of film cooling with ejection from a row of holes for the application to gas turbine blades" J. of Engineering for Power, ASME Transactions, Series A, Vol. 97, N°2 1975 pp 195-206.
6. Metzger D.E., Carper H.J. and Swank L.R. : "Heat transfer with film cooling near non-tangential injection slots" J. of Engineering for Power, ASME Transactions, Series A, Vol.90, 1968, pp. 157-163.
7. Metzger D.E., Takeuchi D.I., Kuenstler O.A. : "Effectiveness and heat transfer with full coverage film cooling" J. of Engineering for Power, ASME Transactions, Series A Vol. 95, 1973 pp 180-184.
8. Choe H., Kays W.M. and Moffat R.J. : "Turbulent boundary layer on a full coverage film-cooled surface - an experimental heat transfer study with normal injection" NASA CR-2642, January 1976.

9. Crawford M.E., Choe H., Kays W.M., Moffat R.J. : "Full coverage film cooling heat study-summary of data for normal-hole injection and 30° slant-hole injection" NASA CR-2648, March 1976.
10. Jones T.V., Schultz D.L., Hendley A.D. : "On the flow in an isentropic free piston tunnel" ARC R & M 3731, January 1973.
11. Schultz D.L. and Jones T.V. : "Heat transfer measurements in short duration hypersonic facilities" AGARDograph 165, 1973.
12. Backx E. : "The total temperature in the Longshot wind tunnel : its measurement and evaluation", VKI TN 98, 1974.
13. Eriksen L. and Goldstein R.J. : "Heat transfer and film cooling following injection through inclined circular tubes" Journal of Heat Transfer. Transactions of ASME Vol.96, Series C, N°2, May 1974 pp 239-245.

ACKNOWLEDGEMENTS

This research was made possible through the support and sponsorship of the US Government through its European Office by award of US Army Grant DA-ERO-75-G-074. The support of the dedicated technical staff of VKI is gratefully acknowledged.

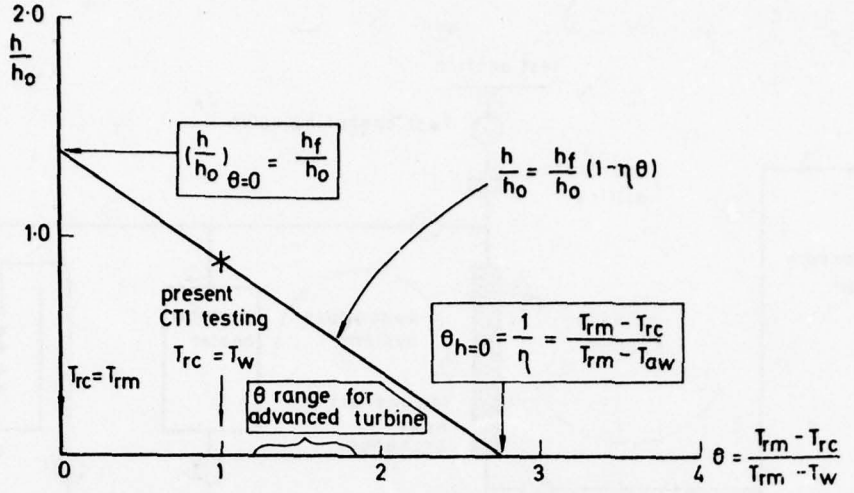

FIG. 1 VARIATION OF HEAT TRANSFER COEFFICIENT, h WITH THE COOLANT TEMPERATURE PARAMETER, θ FOR GIVEN EXTERNAL FLOW CONDITION, x, m AND HOLE GEOMETRY.

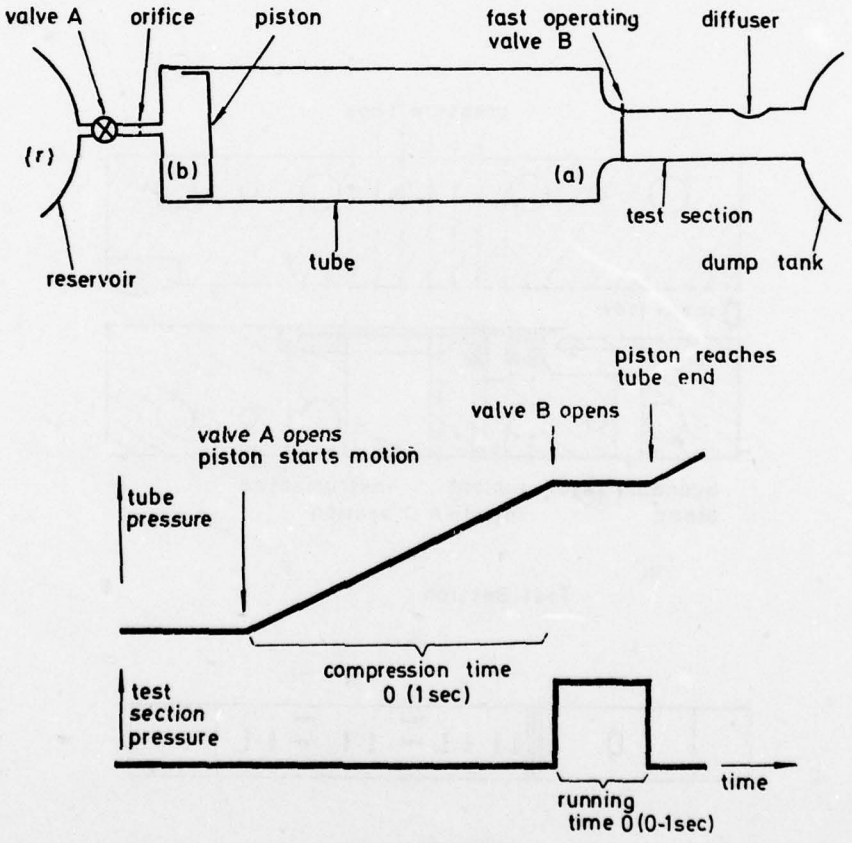

FIG. 2 SCHEMATIC AND OPERATING CYCLE OF ISENTROPIC LIGHT PISTON TUNNEL

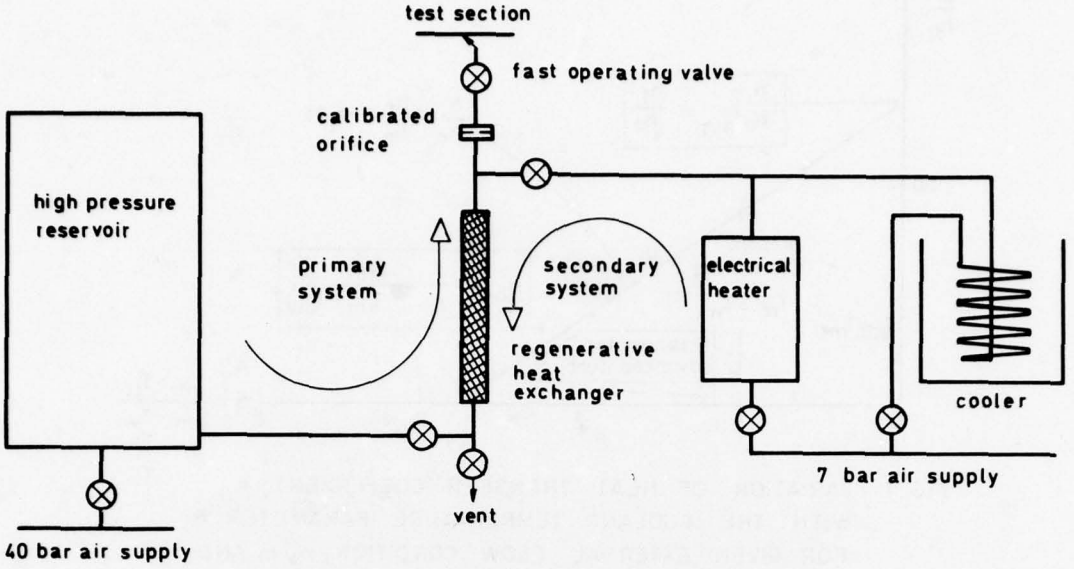

FIG. 3 SECONDARY GAS AIR SUPPLY

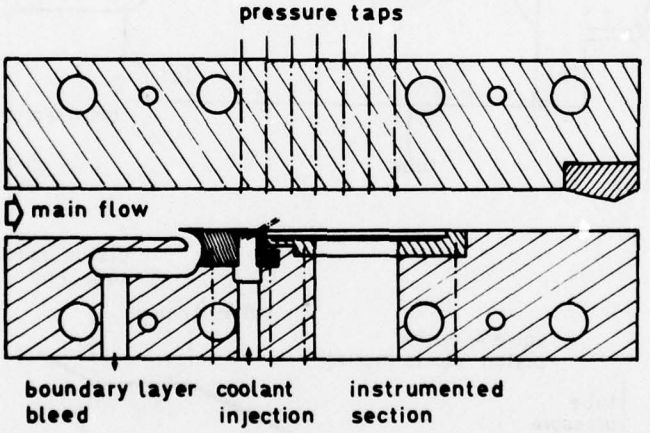

Test Section

Instrumented Plate

FIG. 4 THE MODEL

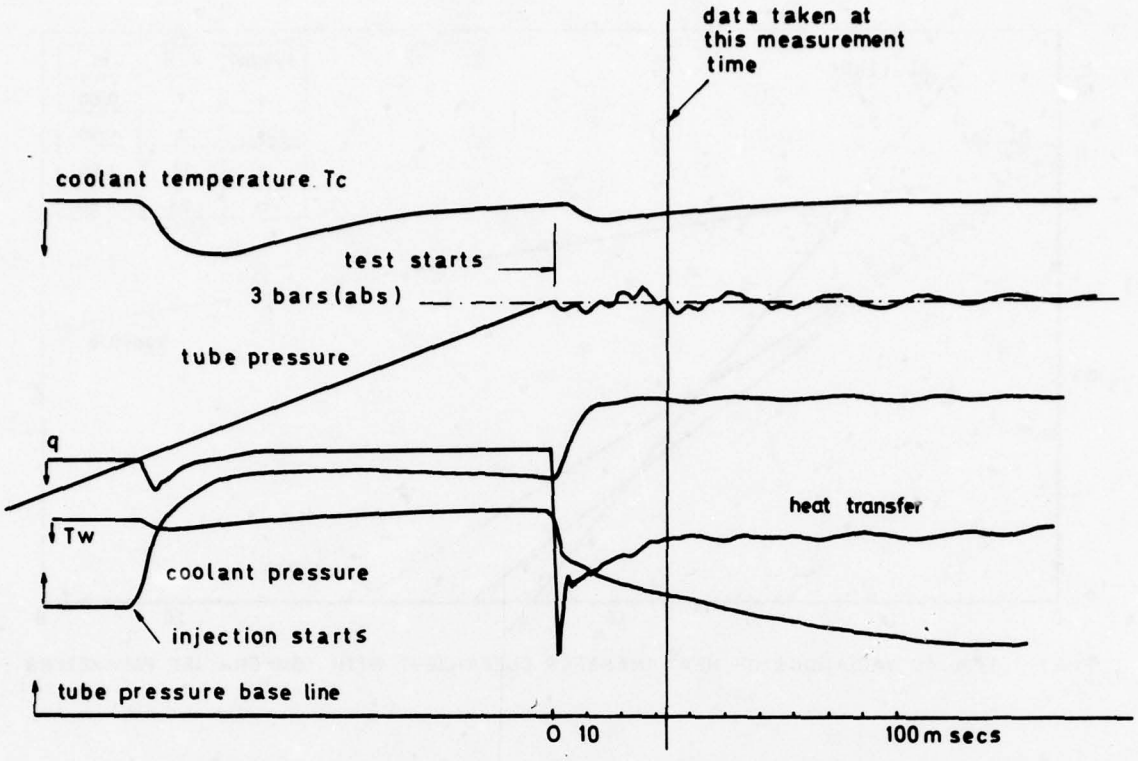

FIG. 5 TYPICAL TRACES OBTAINED (FILM AT ROOM TEMPERATURE)

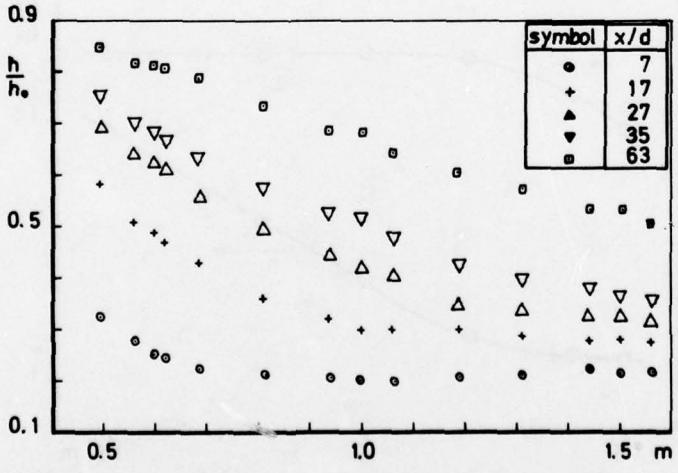

FIG. 6 HEAT TRANSFER COEFFICIENT TO FILM COOLED SURFACES
Coolant at room temperature Tc/Tom ≈ 0.77

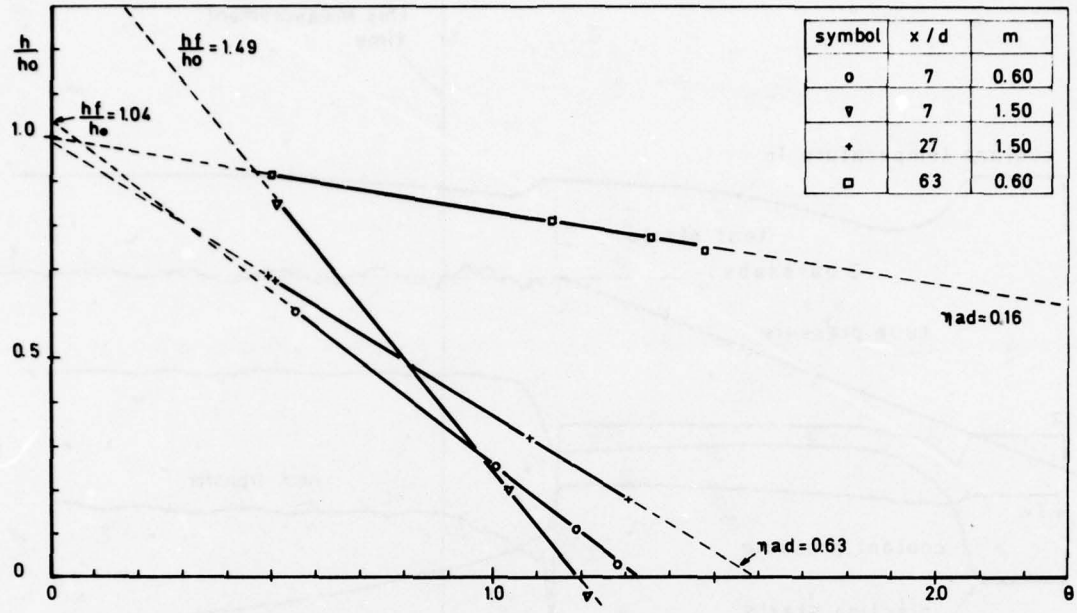

FIG. 7 TYPICAL VARIATIONS OF HEAT TRANSFER COEFFICIENT WITH TEMPERATURE PARAMETER θ

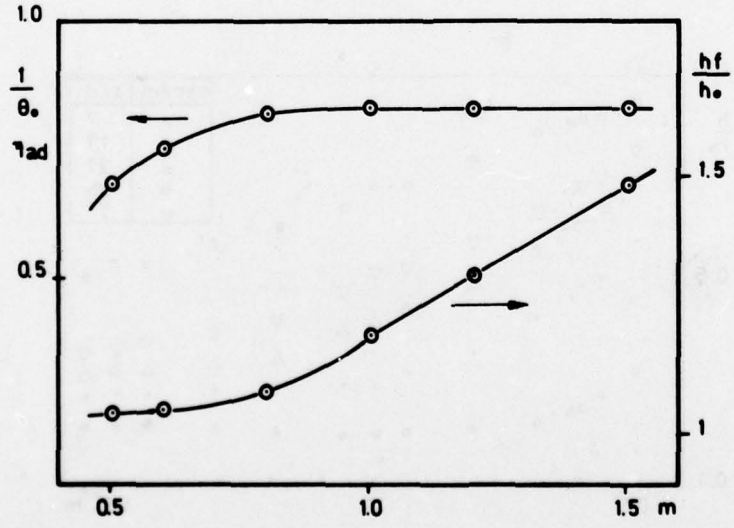

FIG. 8 RESULT OF hf/ho and 1/θe FOR x/d = 7

DISCUSSION

E.E.Covert, US

Dr Richards is to be congratulated for his exceptionally clear description of a complicated phenomena. Further, his experimental procedure (as well as those of Louis, Schultz, and of Martin that were reported in the morning session) is so arranged that it has an additional advantage. It is in the well defined temperatures. So gas and wall material properties are known accurately. This enhances the usefulness of their data. The use of the local isothermal approximation contains an implicit assumption that must be kept in mind. It is assumed the variation in the difference between the adiabatic wall temperature and the wall temperature along the length of the model is small compared to the minimum value of this difference, i.e.

$$\frac{x \dfrac{d(T_{AW} - T_W)}{dx}}{(T_{AW} - T_W)_{min}} \ll 1 .$$

When this inequality is not satisfied, the value of "h" may not be unique or accurate.

Author's Reply

I agree with Prof. Covert on the last point. This condition is indeed satisfied using the short duration techniques outlined.

C.F.Franklin, UK

The wall temperature upstream of a row of film cooling holes is often higher than that downstream of the holes. In addition there may be a wall temperature distribution downstream of the holes; the temperature increasing with increasing distance. This means that there is heat flow towards the holes and this can lead to the condition where heat flows from the blade outwards into the film.

Do you think the heat transfer coefficient ratio (h/ho) that you have shown can be used in this situation?

Author's Reply

The work described in the paper relates more to aero engines, the blades of which will be designed (through appropriate choice of both an internal convective cooling system and external film cooling) to have small changes in wall temperature to combat structural problems. The situation referred to by Mr Franklin refers to a situation more likely to occur in the power turbines of interest to Mr Franklin. Care should be taken in using the isothermal data from such short duration tunnels. However, similar care should be taken when using data taken under adiabatic wall conditions for the reasons explained in the paper. The situation of heat transfer from the upstream wall to the coolant referred to by Mr Franklin deserves some attention.

LOCAL FLAME TEMPERATURE MEASUREMENTS BY RADIATIVE METHODS

by

U.Ghezzi[+], G.Zizak[o], A.Coghe[o], F.Cignoli[o] and S.Benecchi[o]

[+] Istituto di Macchine, Politecnico; p.Leonardo da Vinci, 32. Milano. Italy.
[o] CNPM-Politecnico; via F.Baracca, 69. Peschiera Borromeo, Milano. Italy.

SUMMARY

The aim of this work is to analise the reliability of local flame temperature measurements by means of atomic fluorescence spectrometry. Conventional radiative methods give a measure averaged over the optical path through the gas. Whenever the probe volume is not homogeneous, different layers, each having an individual temperature and thickness, contribute to the measure. Results, obtained up to now, using an electronic signal processing system based on photon counting, are reported in this paper. They indicate that it is possible to obtain satisfactory space resolution and good reliability.

1. INTRODUCTION

In high-temperature combustion flows only thermocouples and spectroscopic means are available, at present, for measuring gas temperature distributions. Thermocouples are easy to use and allow local measurements, but cannot be used in flames above 2000 K and need corrections for radiative and conductive losses that are difficult to be evaluated. Spectroscopic methods such as line-reversal (Ref.1) and two-line atomic emission (Ref.2) are non perturbing, but result in line of sight averaging and, whenever the temperature profile is highly non-uniform, different layers, each having an individual temperature and thickness, contribute to the measure. Numerical procedures have been developed (Ref.3,4 and 5) through it is possible to apply Abel's inversion formula in the case of non homogeneous flames, if the simmetry is known. The radial temperature distribution can be calculated by recursive methods from the projected emission and absorption profiles. Unfortunately, numerical results obtained by this methods necessarily suffer from the fact that noise on the experimental data is amplified.

Local temperature profiles are desirable to have a better understanding of combustion processes. Recently, new non-intrusive techniques have been developed, generally based on elastic or anelastic scattering of laser radiation: Rayleigh and Raman scattering (Ref.6,7 and 8). The spectral stru-cture of Rayleigh scattered laser light exhibits simple Doppler broadening produced by molecular and atomic translational mouvements. The anelastic Raman scattering gives information on vibrational and rotational temperatures, but rotational Raman scattering do not appear promising for high-temperature combustion measurements. Unfortunately, Rayleigh and Raman scattering require high spectral resolution and sensitivity with concomitant expense and delicacy.

Another interesting method, based on atomic fluorescence spectrometry, has been proposed, which can lead to direct local temperature measurements. The temperature dependence of selected fluorescence transitions has been theoretically defined by Alkemade (Ref.9), assuming that a thermodynamic equilibrium is reached in the flame, so that a Boltzmann population distribution can be assumed. Experimentally, it has been demonstrated (Ref.10,11 and 12) that atomic fluorescence spectrometry can provide several possible ways for determining the electronic excitation temperature of flames in the range 700 to 3000 K. Moreover, taking into account the isotropy of fluorescence radiation, local measurements can be obtained if fluorescence measurements are made with the exciting source and the detector placed, for example, at an angle of 90°.

2. ATOMIC FLUORESCENCE METHOD

With the introduction of convenient metal atoms into a flame, in the presence of a radiation field, fluorescence emission can be detected. For a continuum source or a broad line source of excitation and for low atomic concentrations of the seeding atoms, assuming that thermodynamic equilibrium exists, fluorescence signal is given by:

$$B = n E_\lambda Y \gamma \Omega / 4\pi \qquad (1)$$

where:
- B radiancy (erg s^{-1} cm^{-2} Sr^{-1}),
- E_λ spectral irradiance of continuum source at wavelength λ (erg s^{-1} cm^{-2} nm^{-1}),
- n number density of metal atoms in the low absorption level,
- Ω solid angle of observation,
- γ coefficient related to system geometry and containing also some atomic constants,
- Y quantum efficiency.

At equilibrium, atomic population, n, of the low absorption level is related to that of the ground level by the Boltzmann equation:

$$n = n_o \, (g/g_o) \, \exp(-(E-E_o)/kT) \qquad (2)$$

where: g and g_o are the statistical weights of the levels.

Relations (1) and (2) give the temperature dependence of fluorescence radiation, but some parameters are not known exactly. Therefore it is more convenient to use the ratio of two fluorescence lines, Stokes and anti-Stokes:

$$(3) \qquad \frac{F_{20}}{F_{21}} = \frac{E_{\lambda 12}}{E_{\lambda 20}} \left(\lambda_{12}/\lambda_{20}\right)^5 \exp\left(V_1/kT\right)$$

where: $V_1 = E_1 - E_o$, excitation energy of the first level (erg)

F_{20}, F_{21} spectral irradiances of fluorescence emitted lines at λ_{20}, λ_{21} (erg s^{-1} cm^{-2} nm^{-1}),

E_{12}, E_{02} spectral irradiances of exicitation source at λ_{12} and λ_{02} (erg s^{-1} cm^{-2} nm^{-1}),

k Boltzmann constant (erg K^{-1}),

T_f flame temperature (K)

The equation (3) can be resolved for the flame temperature:

$$(4) \qquad 1/T_f = \left\{\frac{k}{V_1}\left(\log\frac{E_{12}}{E_{02}} + 5\log\frac{\lambda_{12}}{\lambda_{02}}\right) - \frac{k}{V_1}\log\frac{F_{20}}{F_{21}}\right\}$$

The measured spectral irradiances ratios of fluorescence and excitation source have to be corrected for the spectral response of the measuring system. For practical applications, equation (4) can be rewrite:

$$(5) \qquad T_f = 1/\left(r - \frac{k}{V_1}\log\left[\frac{F_{20}}{F_{21}}\right]_{meas}\right)$$

where the term r includes the instrumental correction factor.

With the introduction into the flame of metal atoms (for example, gallium, indium or thallium) a simple procedure for calculating flame temperatures can be applied if the spectral irradiance ratio of the excitation source is known and the ratio of direct line Stokes to anti-Stokes fluorescence is measured. Direct line fluorescence consists of excitation of an atom to a certain energy level, 2, and radiational deactivation to a metastable level, 1, above the ground state, 0. (See Fig. 2). Lifetime of a metastable state is much longer than that of a normal excited state transition 0 1 is radiatively forbidden.

In thallium, indium and gallium, metastable states $^2P_{3/2}$ can be reached by radiational deactivation of the excited levels $^2S_{1/2}$. Direct line fluorescence can be, for example, observed with thallium at 535.0 nm after excitation by 377.6 nm. Viceversa, anti-Stokes line can be observed at 377.6 nm, after excitation by 535.0 nm. The choice of thallium as seeding metal in flames is a compromise between sensitivity and accuracy requirements. (Ref. 12). Moreover, practical difficulties in the calibration of the measuring system are lowered in the range in which fluorescence transitions od thallium occur (Ref. 11).

The main problems are related to signal to noise ratio (S/N), because fluorescence signal is generally too low in comparison with thermal emission at the same spectral line. It is necessary to improve the S/N of fluorescence signal in order to lower the probe volume and to increase spatial resolution. From relation (1) it is clear that better fluorescence signal can be obtained only by increasing the spectral irradiance of the source, because the density of metal atoms is limited by auto-absorption effects. High power lasers, as exciting sources, have been used (Ref. 13), but in this way the Boltzmann equilibrium is perturbed and the time variation of atomic population out of equilibrium is not completely known.

A different approach of the problem was used in the work reported in this paper. With low power exciting source, we applied a photon counting technique to detection of fluorescence signal, instead of conventional lock-in amplifiers.

3. *PHOTON COUNTING*

This electronic signal processing system involves the digital measurements of the current pulses resulting at the anode of a photomultiplier caused by photon impact at the photocathode.

Provided that the rate of photo-electron emission and the frequency response of the electronic system are such that individual current pulses are resolved, then a direct digital analysis of the radiation intensity is performed. Photon counting is best suited to the measurements of low levels of radiation and hence its application in fluorescence spectrometry is obvious, although it has not previously been described for temperature measurements porpuses.

Further advantage of photon counting is the ability to increase the S/N by increasing count periods. In fact, if N_s is the signal count rate, N_d the back-ground count rate and τ the count period, then (Ref. 14).

$$(6) \qquad S/N = N_s \tau^{1/2} / \left(N_s + 2N_D\right)^{1/2}$$

It was assumed that:

a) the flame gives rise to emission of photons which are randomly distributed, i.e. Poisson distributed,

b) the background count rate is measured separately from the total count N_T.

The precision of measurements is the inverse of the S/N, espressed as a percentage.

In fluorescence spectrometry, the ratio $K = N_s/N_d$ is defined by experimental conditions (source power, metal atom concentration, optical geometry) and flame properties (quantum efficiency). We can rewrite relation (6):

$$(7) \qquad S/N = K\left(N_T\tau\right)^{1/2} / \left[(K+1)(K+2)\right]^{1/2}$$

where: $N_T = N_s + N_d$.

Hence, as K = const., it will be possible to improve the S/N by increasing $(N_T\tau)^{\frac{1}{2}}$; lower count periods could be used with higher count rates. In our experimental situation, as it will be shown in the next paragraph, K ranges from 10^{-3} to 10^{-2}; therefore, the relation (7) reduces:

$$(8) \qquad (S/N) = \frac{K}{\sqrt{2}} \; (N_T \tau)^{\frac{1}{2}}$$

For example, if $K = 10^{-3}$, we need $(N\tau) = 10^8$ to have (S/N) = 10 (See Fig.3).

High count rate quickly results in pulse pile-up problems (two or more unresolved pulses), but this is not a limitation if the amplifier and the pulse-height discriminator have adequate frequency response. Moreover, the frequency meter should have good frequency response and a sufficiently large register to cope with the large numbers involved in photon counting with relatively high background.

4. EXPERIMENTAL SET-UP

Two premixed laminar flames ($Ar/O_2/C_2H_2$) were investigated, produced by a burner with a multi-hole circular head (20 mm top diameter, 60 holes 1 mm diameter) or with a two-slots head (.5 ; 30 mm).The flames were not shielded to have temperature gradients. The burner system was mounted on a movable carriage allowing radial and vertical movements of the flame. The adjustement reproducibility was .10 mm in the vertical and .25 mm in the radial direction.

The seeding of metal atoms was obtained by pneumatic atomization of a water solution in a glass right-angle atomizer. In order to avoid self-absorption effects, under the present experimental conditions, the concentration of 250 μ g of thallium per ml was chosen for the solution nebulized into the flame.

The optical system for fluorescence measurements is shown in Fig.4 and was arranged in order to have good spatial resolution (about 1 mm^3), high exciting radiation power density in the probe volume and large receiving aperture to collect fluorescence radiation. For this purpose the exciting spectral lamp (OSRAM thallium metal vapour discharge) was imaged in the flame by a two quartz lenses system with magnification factor equal .1, and fluorescence emission lines were observed at 90° by a 300 mm Monochromator (HILGER-WATTS D 330). The probe volume was defined by the magnification of the receiving lens and the entrance slit dimensions. Since the receiving lens produced a double magnified image of the flame on the slit, and slit width was 1 mm and slit height was 2 mm, the probe volume dimensions resulted .5x1x1 mm^3.

A tungsten ribbon lamp with a DC power supply (H.P. type 6428 B) was mounted on axis for sodium D-line reversal measurements. The same lamp (calibrated by Metrological Institute "G.Colonnetti", Torino.Italy)was used for the calibration of the spectral response of the measuring system.

A block diagramm of the electronic set-up is reported in Fig.5 It is a background subtraction system based on an up-down counter (LABEN model 6318, 4 MHz, 8 digit display). The exciting radiation is chopped on and off by a chopper unit, so that the photomultiplier alternately sees background and fluorescence signal + background. In order to do the synchronous sampling a reference signal, derived from the chopper modulator, is sent to the sampling control unit which gates the up-down counter so that it counts up when the chopper is on and counts down when the chopper is off. Errors due to unequal or jittering chopping edges are avoided by selecting suitable duty factor. In our case, we counted for 8 ms during each 11 ms chopper window, with 1 ms delay time. The sampling time for measuring signal + background and the background only differ by less than one microsecond. The total measuring period is set by a presettable timer. In order to avoid beating effects between the chopper frequency (about 100 Hz) and the AC power supply of the thallium discharge lamp, we made a high frequency (10 kHz) power supply ($\pm$ 15 V, 1 A).

Light signal was detected by a high gain ($G = 10^8$), fast response photomultiplier (PHILIPS 56 TVP,S20 spectral response), powered by a stabilised high voltage power supply (J.FLUKE 415 B). Single photon arrival produces a current pulse that, after suitable amplification, is sent to a discriminator-pulse shaper(LABEN model FT 130) having thresholds continuously adjustable between 100 mV and 600 mV. The photomultiplier was held in water cooled housing and maintained at a temperature close to 15 °C. The dark noise was typically about 13 counts/ms. Better dark noise conditions could be obtained by cooling at lower temperatures, but in this application this is not strictly necessary, because of the high background signal (about 10^3 counts/ms). The best operational conditions were achieved with the output from the discriminator in the form of logic pulses 100 ns wide,and the dead time for the entire system was 100 ns.

Line reversal temperature measurements were performed by using the same photomultiplier in analog mode of operation by direct connection of the output to a strip-chart recorder (YOKOGAWA F type 3052).

5. EXPERIMENTAL RESULTS

From equation (5) the error in the flame temperature evaluated by fluorescence method depends upon the errors in the measurements of fluorescence emissions. In fact, we can write:

$$(9) \qquad \left|\frac{dT_f}{T_f}\right| \simeq T_f \frac{k}{V_1}\left[\left|\frac{dF_{20}}{F_{20}}\right| + \left|\frac{dF_{21}}{F_{21}}\right|\right]$$

The error in the spectral irradiance ratio and instrumental factor can be minimized (about 2%) by correct instrumental calibration and was checked by a comparison of fluorescence temperature and line reversal temperature on a flame shielded-flame, in order to avoid temperature gradients. The fundamental limit on measurement accuracy of the flame temperature arises from the random fluctuations in fluorescence irradiance. If the only significant source of error is photon statistics, then the S/N is given by equation (8) and depends on the ratio $K = N_s/N_d$ and the total count number. In practice, other sources of error can be significant; however, with care, the performance predicted by equation (8) can be approached closely.

As K = const. for any fluorescence line, and the maximum count rate is limited by frequency characte-

ristics of the electronic system, the S/N increases with the square root of the total count period.

Under the present experimental conditions, we used τ = 330 s in the measurement of fluorescence Stokes line irradiance (K = 10^{-2}) and τ = 990 s in the measurement of fluorescence anti-Stokes line irradiance (K = 10^{-3}). In this way the S/N was typically about ten for both fluorescence measurements (Stokes and anti-Stokes) with a resulting 4% error in flame temperature evaluation. Measurement accuracy was better in the inner region of the flame, because of the higher fluorescence emission. Near the fringe of the flame, lower fluorescence emission resulted in reduced total count and, hence, in reduced accuracy. A set of five to ten different measurements were performed at any position and for both fluorescence lines. The two mean values were used for temperature evaluation. In this way the random error resulted negligible, and the significant source of error was photon statistics.

Line reversal temperature measurements were performed with better accuracy (about 2%) because of the higher sodium D-line emission intensity and related S/N.

Experimental results are reported in Figs.6 to 8, in which the intensity profiles of the fluorescence lines and the corresponding temperature values are shown. In addition, for comparison, are reported temperature profiles obtained by sodium D-line reversal and, for the circular burner case, temperature profiles evaluated by the Abel inversion procedure from emission and absorption measurements of sodium D-line(Ref. 5).

Fig.6 refers to measurements made on a flame ($Ar/O_2/C_2H_2$; gas flow rates 6/1/.5 1/m) produced by a circular burner, 20 mm above the burner head. The sensible difference in temperature profiles obtained by fluorescence and line reversal methods can be explained by the integral nature of the line reversal method and the large temperature gradients near the outer regions of the flame. On the contrary, the temperature profile, evaluated by Abel inversion procedure, shows a sensible agreement with fluorescence measurements. The differences in the outer part of the flame could be a result of the imperfect reproducibility of the burner position, or of the poor S/N, because of the reduced fluorescence irradiance.

The fluorescence intensity and temperature profiles of Fig.7 refers to the same circular burner, but with a fuel-richer $Ar/O_2/C_2H_2$ flame (gas flow rates 6/1/.6 1/m).Even in this case, the temperature profile obtained by fluorescence methods differs from that of the line reversal methods, but is very close to the profile evaluated by Abel inversion. Moreover, in the outer part of the flame, it should be noted a little increase in temperature, that can be explained by the entrainment of external air and the formation of a diffusion flame front. The temperature profile obtained by the integrated line reversal method cannot show this effect directly, but presents a lower decrease than in Fig.6.

Results reported in Fig.8 were obtained by means of the two-slots burner. They refer to transversal profiles of fluorescence intensity and temperature for a $Ar/O_2/C_2H_2$ flame with the same gas flow rates of that of Fig.7. Sodium D-line reversal measurements were obtained with the two slots parallel to the line of sight (Y direction). Fluorescence measurements were obtained by illuminating the flame in the X direction and observing it along the Y direction. It should be noted that, in this case, the Abel inversion procedure cannot be applied because of the absence of symmetry in the flame geometry. The temperature values in the inner region of the flame, measured by fluorescence method, are very close to those observed in the circular burner. Moreover, the temperature profile obtained by fluorescence technique presents an increase near the outer part of the flame, like in the case of the Fig.7. The difference between the "local" and the integrated temperature measurements could be explained by the fact that longitudinal temperature profile exibits a large temperature decrease near the outer part of the flame. As a consequence, the line reversal method measure a lower average temperature. In fact, an experimental confirmation was found by measuring the line reversal temperature along the transversal direction, at Y = 0. The result, reported in the same Fig.8, is very close to fluorescence temperature and is higher than the longitudinal result, at X = 0.

6. CONCLUSIVE REMARKS

The results reported in the present paper show that it is possible to obtain local flame temperature by means of fluorescence spectrometry, at least under laboratory flame conditions and long term stability. The reliability of this technique was proved and its good spatial resolution allowed significant measurements in flame regions with non-uniform temperature distribution.

The usefulness of the photon counting technique is demonstrated by the satisfactory S/N values obtained in conjunction with a low power excitation source and good spatial resolution. It should be noted that with higher powers of the excitation source the Boltzmann equilibrium could be perturbed and the time variation of atomic population out of equilibrium is not completely known. High power lasers, as exciting sources, have been used, but it seems that reliable results can be obtained only in saturation conditions.

The minimum temperature that can be measured by fluorescence technique depends on the intensity of anti-Stokes spectral line and hence from atomic population of the level 1. Indium (V_1= .274 eV) could be used for low flame temperature from 700 K. With thallium (V_1= .966 eV) the flame temperature in the range 1500 to 3000 K can be measured.

Fluorescence measurements can be very sensitive, but can suffer from the influence of quenching by the surrounding gases. Moreover, the accuracy of the method can be greatly reduced if self-absorption of fluorescence emission or absorption of the light from the excitation source are not negligible. In fact, absorption effects could be different for the two spectral lines and hence the fluorescence ratio could be greatly altered. These effects could be remarkable in large flame systems, also with low concentration of metal atoms. However, the fluorescence method for local flame temperature measurement is of great interest because it could be used as a calibration standard for other temperature probes, in the high temperature ranges.

REFERENCES

1. Snelleman, W, 'FLAME EMISSION AND ATOMIC ABSORPTION SPECTROMETRY', J. A. Dean and T. C. Rains, Eds.(Dekker, New York, 1969) Vol. 1, Chap. 7.
2. Browner, R.F. and Winefordner, J.D., Anal. Chem. 44, 247 (1972).
3. Barr, W.L., J.O.S.A., 52, n. 8 (1962).
4. Kun, G. and Tankin, R.S., J.Q.S.R, Tr., 8, p. 1281 (1968)
5. Zizak, G.,METODO NUMERICO PER L'ANALISI DELLE CONDIZIONI LOCALI IN UNA FIAMMA PARTENDO DA MISURE OTTICHE, La Termotecnica, n. 9, 1975, p. 478.
6. Pitz, R.W., Cattolica, R., Robben, F. and Talbot, L. TEMPERATURE AND DENSITY IN A HYDROGEN-AIR FLAME FROM RAYLEIGH SCATTERING, Combustion and Flame 27, 313-320(1976)
7. Stricker, W., LOCAL TEMPERATURE MEASUREMENTS IN FLAMES BY LASER RAMAN SPECTROSCOPY, Combustion and Flame 27, 133-136 (1976)
8. Clark, R.J.H. and Hester, R.E. Editors, ADVANCES IN INFRARED AND RAMAN SPECTROSCOPY Vol. 3, Heyden, London 1977.
9. Alkemade, C.T.J., Pure Appl. Chem., 23, p. 73 (1970)
10. Omenetto, n., Benetti, P. and Rossi, G., Spectrochim. Acta, 27 B, p. 453 (1972)
11. Haraguchi, H., Smith, B., Weeks, S., Johnson, D.J. and Winefordner J.D., MEASUREMENT OF SMALL VOLUME FLAME TEMPERATURE BY THE TWO-LINE ATOMIC FLUORESCENCE METHOD, Applied Spectroscopy, 31, No. 2, 1977.
12. Benecchi, S., Coghe, A. and Zizak, G., XXVIII Congresso Nazionale ATI, Torino (1973).
13. Omenetto, N. and Winefordner J.D., Presented at 5th International Conference on Atomic Spectroscopy, Melbourne, August, 1975.
14. Jones, R., Oliver, C.J. and Pike, E.R., EXPERIMENTAL AN THEORETICAL COMPARISON OF PHOTHON-COUNTING AND CURRENT MEASUREMENTS OF LIGHT INTENSITY, Applied Optics, Vol. 10, No. 7 (1973).

ACKNOWLEDGMENT

The authors wish to thank professor Omenetto and Dr. Benetti of University of Pavia for helpful discussions and Mr. T. Ferrari and G.B. Daminelli for essential assistance in experimental work.

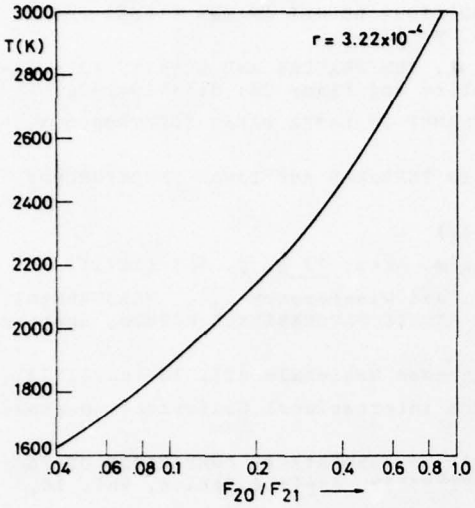

FIG. 1

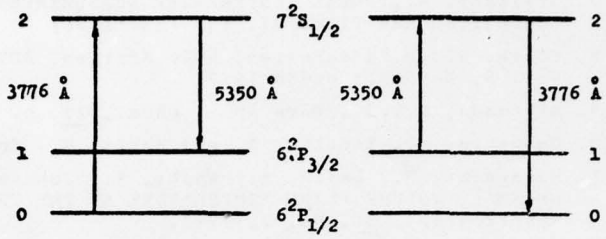

FIG. 2

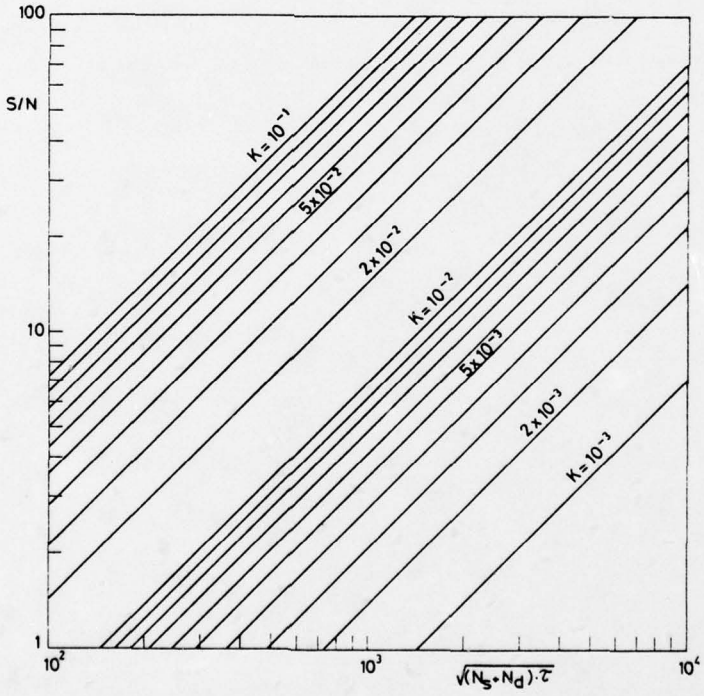

FIG. 3

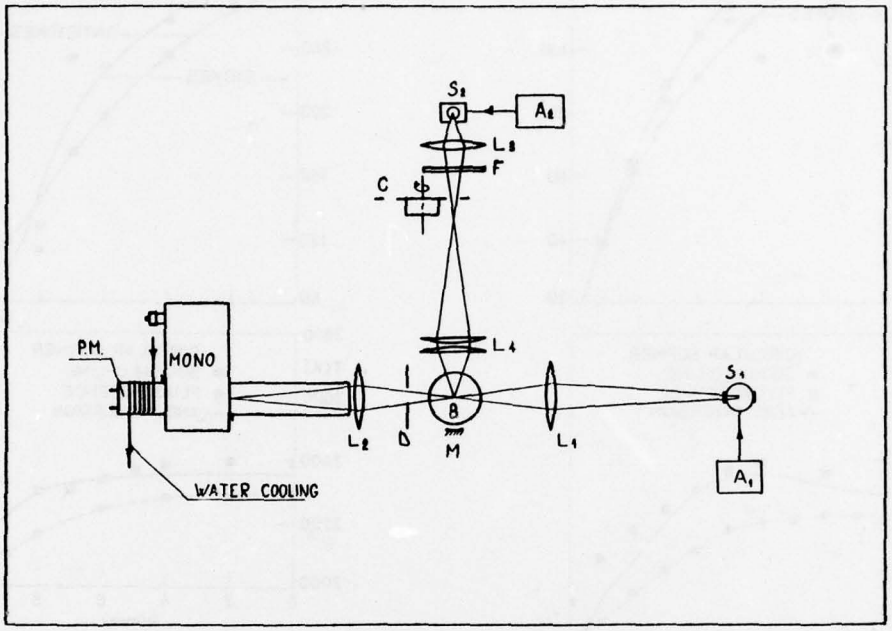
S₂
A₂
L₃
F
C
L₄
P.M.
MONO
S₁
L₂
D
B
M
L₁
A₁
WATER COOLING

FIG. 4

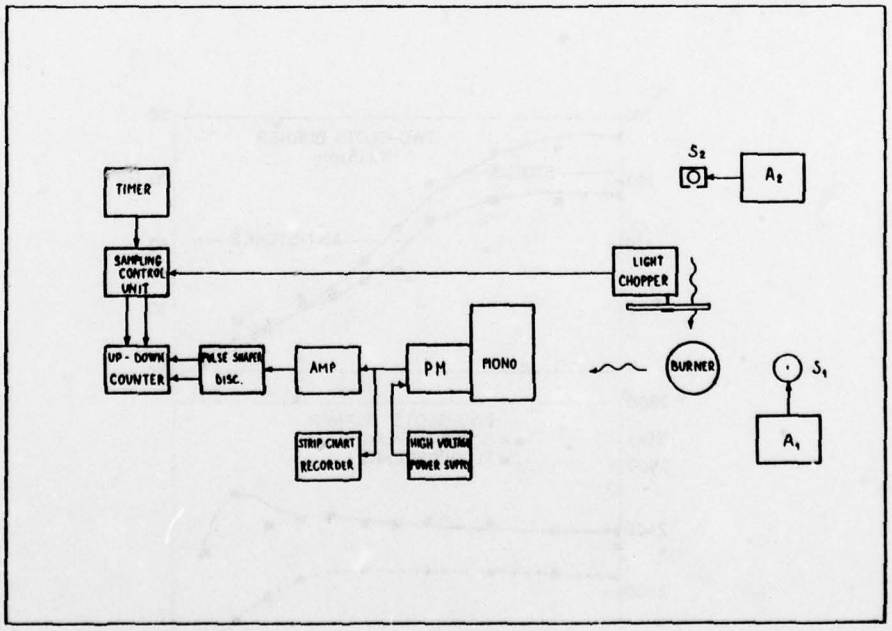
S₂
A₂
TIMER
SAMPLING CONTROL UNIT
LIGHT CHOPPER
UP - DOWN COUNTER
PULSE SHAPER DISC.
AMP
PM
MONO
BURNER
S₁
A₁
STRIP CHART RECORDER
HIGH VOLTAGE POWER SUPPLY

FIG. 5

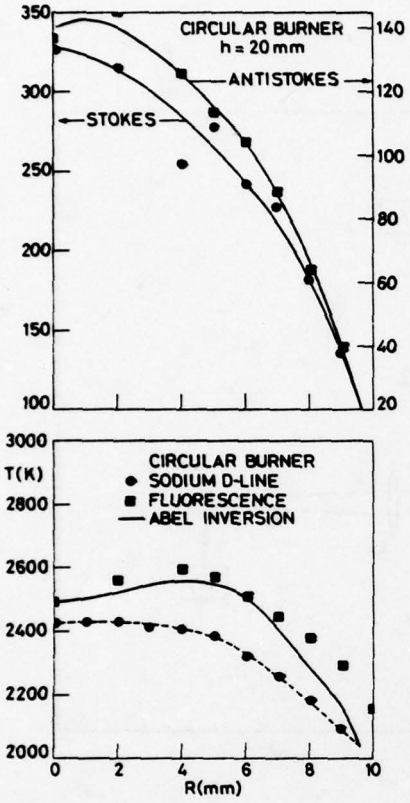

FIG. 6

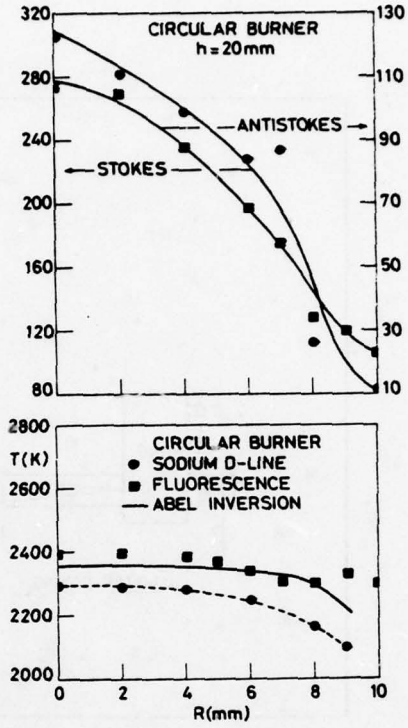

FIG. 7

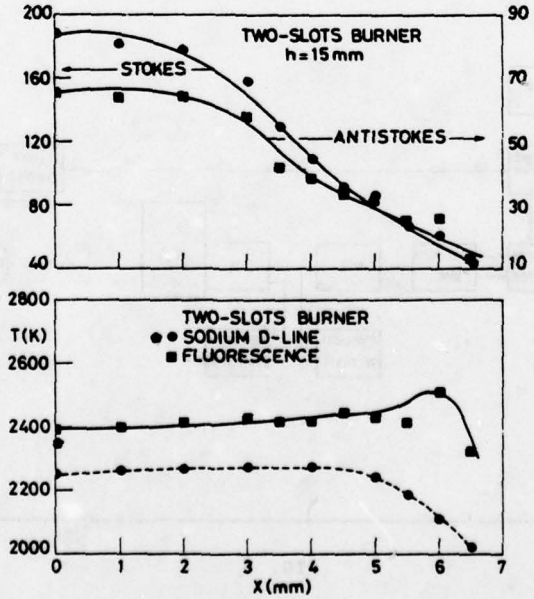

FIG. 8

MÉTHODE NOUVELLE DE CALCUL DE L'EFFICACITÉ DE REFROIDISSEMENT DES AUBES DE TURBINE PAR FILM D'AIR*

par Emile LE GRIVÈS et Jacques Jules NICOLAS

Office National d'Etudes et de Recherches Aérospatiales (ONERA)
92320 Châtillon (France)

RESUME :

Une méthode nouvelle de calcul de l'efficacité de protection par film d'air réfrigérant des aubes de turbine à gaz est proposée. Reposant sur une représentation analytique de la structure tourbillonnaire caractérisant l'aspect tridimensionnel de l'émission de film par jets discrets, cette méthode permet de prévoir la loi de mélange progressif du réfrigérant avec les gaz chauds, et d'en déduire l'efficacité adiabatique. Compte tenu des effets de dilution par diffusion turbulente et de coalescence des jets, ces prévisions se comparent favorablement avec les données d'expérience sur paroi plane.

Des règles simples de composition des efficacités de film résultant d'injections par plusieurs rangées d'orifices permettent d'étendre la validité de la méthode de calcul à une grande variété de configurations d'injection.

Les effets de la courbure des aubes, non pris en compte dans l'exposé, font l'objet de recherches consécutives.

NEW COMPUTATION METHOD OF TURBINE BLADES FILM COOLING EFFICIENCY

SUMMARY :

A new analytical technique is presented for the computation of film cooling effectiveness of gas turbine blades. It is based on a mathematical description of the counter rotating vortex structure associated with the injection of coolant through discrete holes. The transport of mass induced by these vortices plays the major part in the mixing process of hot gas with the individual jets, which defines the adiabatic effectiveness of the resulting film.

When merging of the jets and entrainment by turbulent diffusion effects are also taken into account, data from various experiments performed on flat plates are found to be in good agreement with predictions following this approach.

Simple rules for computing film effectiveness with injection through several rows of holes allow an extension of this analysis to a large variety of injection patterns.

Curvature effects not accounted for in this presentation are left for further investigations.

1.- INTRODUCTION

La technique de protection thermique des aubes de turbines à gaz par émission d'air prélevé au dernier étage du compresseur est actuellement retenue par la plupart des motoristes comme la plus apte à assurer les améliorations de performance attendues de l'accroissement de la température de sortie du foyer, et notamment une diminution de la consommation spécifique.

Afin de limiter les pénalisations qu'entraîne la mise en oeuvre de cette technique du fait des pertes énergétiques associées à l'injection du fluide réfrigérant dans l'écoulement actif, il convient de rechercher les conditions optimales d'organisation du dispositif de refroidissement interne et d'émission de film tout en minimisant la consommation d'air requise pour le maintien de la température des aubes au niveau imposé.

Parmi les diverses voies de recherches qui répondent à ces préoccupations, l'analyse de l'efficacité de la protection thermique par films émis à partir d'une ou plusieurs rangées de perforations discrètes a donné lieu à de nombreux travaux, principalement sur le plan expérimental.

Ce mode d'injection de l'air réfrigérant donne lieu généralement à un effet de pénétration des jets élémentaires, que l'on s'efforce de minimiser par des perçages d'axe aussi incliné que possible par rapport à la paroi.

Il en résulte un processus d'interaction tridimensionnelle dont l'analyse revêt une importance essentielle pour la prévision des conditions effectives de refroidissement. Un effort notable a été récemment consacré à l'élaboration de méthodes numériques de résolution basées sur les équations de Navier-Stokes pour le problème de l'écoulement dans les canaux interaubes de turbine à

* *Travail effectué sous contrat DRME.*

émission [1]. Une méthode de caractère plus analytique a été développée à l'ONERA selon une modélisation basée sur les lois physiques fondamentales qui régissent l'aspect particulier de cette interaction.

D'abord étudié au regard de motivations différentes, telles que la dilution des produits de combustion dans les foyers de turbomachines, ce processus intervient au premier chef dans le mélange progressif des jets élémentaires émis sur les parois d'aubes de turbines. Les dimensions relatives des canaux interaubes et des orifices d'émission autorisent l'application des règles reconnues dans le cas de jets pénétrant dans un écoulement semi-infini, lorsque la vitesse d'injection moyenne n'est pas trop faible devant celle de l'écoulement et lorsque l'inclinaison initiale des jets par rapport à la paroi n'est pas excessive.

Basée sur une représentation analytique de l'effet d'échappement tourbillonnaire caractérisant l'aspect tridimensionnel de cette interaction, l'approche ainsi retenue a permis, moyennant une prise en compte des effets de dilution par diffusion turbulente , de coalescence des jets et de composition des efficacités résultant de plusieurs émissions par rangées d'orifices successives, de fonder une méthode de prévision de l'efficacité adiabatique dont les résultats se comparent favorablement avec les données d'expérience sur paroi plane.

L'extension des formules proposées au cas des aubes à forte cambrure constituera le prolongement logique de ces règles prévisionnelles.

2.- METHODE DE CALCUL DE LA PENETRATION ET DU MELANGE PAR INDUCTION TOURBILLONNAIRE D'UN JET CROISANT UN ECOULEMENT SUBSONIQUE

L'étude des interactions aérodynamiques auxquelles donne lieu la pénétration d'un jet dans un écoulement subsonique a fait l'objet de plusieurs études théoriques à l'ONERA [2] [3] [4], dont les résultats essentiels seront d'abord rappelés succinctement.

En premier lieu, un modèle mathématique différant sensiblement des schémas plus anciens de représentation du processus de pénétration a été appliqué au cas général où la projection de la vitesse moyenne d'injection $\vec{v}_{j_o}$ sur le plan de la paroi est inclinée d'un angle de dérapage α_o avec la vitesse $\vec{u}$ de l'écoulement extérieur. Si l'on désigne par β_o l'angle de $\vec{v}_{j_o}$ avec le plan de la paroi, la trajectoire moyenne du jet demeure dans le plan ($\vec{v}_{j_o}$, $\vec{u}$) où l'angle ω_o que forment ces deux vecteurs est donné par

$$\cos\omega_o = \cos\alpha_o \cdot \cos\beta_o$$

La forme de la trajectoire ou ligne moyenne du jet résulte de la condition d'équilibre entre les forces appliquées à un élément de volume $\pi D^2 ds/4$ du jet, supposé rester assimilable à un cylindre circulaire (fig. 1).

Ces forces sont respectivement :

- suivant la normale à la ligne moyenne, la force centrifuge $\vec{C}$ associée à la courbure de cette ligne.
- suivant la tangente, le taux $\vec{M}$ de variation temporelle de la quantité de mouvement.
- suivant la direction opposée à celle de la vitesse relative $\vec{v}_{j_r} = \vec{v}_j - \vec{u}$, la résistance aérodynamique $\vec{T}$.

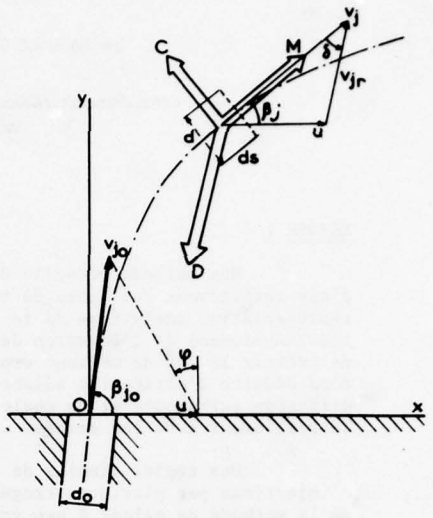

Fig. 1 – Schéma de calcul de la pénétration d'un jet dans un écoulement subsonique.

Sous forme scalaire, les intensités de ces forces s'écrivent respectivement :

$$C = \rho_j v_j^2 \frac{d\omega}{ds} \frac{\pi}{4} D^2 ds$$

$$M = \rho_j v_j \frac{dv_j}{ds} \frac{\pi}{4} D^2 ds$$

$$T = C_T \frac{\rho v_{j_r}^2}{2} \sin\delta \cdot D\, ds$$

Il est admis que le coefficient de résistance de l'élément cylindrique d'axe incliné de l'angle δ par rapport à $\vec{v}_{j_r}$ est donné par la loi dite "du cosinus".

Les équations exprimant l'équilibre de ces trois forces s'écrivent :

a) en projection sur la normale, et compte tenu des relations :

R (rayon de courbure) = $ds/d\omega$

$$\vec{v}_{j_r} \cdot \vec{n} = -\vec{u} \cdot \vec{n} = u R \sin\omega \, d\omega/ds$$

$$v_{j_r} \sin\delta = u \sin\omega ,$$

$$(1) \quad \frac{d\omega}{ds} = -\frac{2C_T}{\pi D} \frac{\rho u^2}{\rho_j v_j^2} \sin^2\omega$$

b) en projection sur la tangente

$$(2) \quad \frac{dv_j}{ds} = -\frac{2C_T}{\pi D} \frac{\rho u^2}{\rho_j v_j^2} v_j \left(\frac{v_j}{u} - \cos\omega\right) \sin\omega$$

Le diamètre D est supposé variable, à mesure que la vitesse du jet tend à s'égaliser avec celle de l'écoulement extérieur. A cet égard, l'hypothèse de conservation du débit massique à l'intérieur du tube de courant auquel est assimilé le jet a été retenue sous la forme simplifiée :

$$v_j D^2 = v_{j_o} D_o^2$$

les variations de la masse volumique ρ_j pouvant être négligées lorsque les températures génératrices des deux écoulements en présence ne sont pas trop largement différentes.

La forme des équations (1) et (2) suggère le choix de la longueur de référence

$$\bar{s} = \frac{\pi D_o}{2 C_\pi} \cdot \frac{\rho_j v_{j_o}^2}{\rho u^2}$$

et des paramètres adimensionnels

$$\nu = v_j / v_{j_o}$$
$$\lambda = v_{j_o} / u$$

Par division membre à membre de (1) par (2), l'équation sous forme réduite

$$(3) \quad \frac{d\omega}{d\nu} = \frac{\sin\omega}{\nu(\lambda\nu - \cos\omega)}$$

est obtenue indépendamment de toute hypothèse sur les valeurs ou sur l'évolution du coefficient de résistance C_π et du diamètre D ; elle peut être intégrée aisément, la solution s'écrivant par exemple :

$$(4) \quad \nu = \frac{\cos(\omega_o - \varphi)}{\cos(\omega - \varphi)}$$

où la constante φ est définie par

$$\operatorname{tg}\varphi = \frac{1 - \lambda\cos\omega_o}{\lambda \sin\omega_o} \quad , \quad \text{d'où} \quad \lambda = \frac{\cos\varphi}{\cos(\omega_o - \varphi)}$$

Le calcul de la trajectoire moyenne d'après la relation de caractère intrinsèque

$$(5) \quad \frac{d\sigma}{d\omega} = -\nu^{\frac{3}{2}} \sin^{-2}\omega \qquad (\sigma = s/\bar{s})$$

peut être mené à terme si l'on admet que le facteur d'échelle $\bar{s}$ demeure invariable, c'est-à-dire que le coefficient C_π conserve une valeur constante.

De simples quadratures permettent alors de calculer les coordonnées réduites de la ligne moyenne, dans le repère cartésien fixe par rapport à la paroi :

O centre de l'orifice, Ox parallèle à la vitesse $\vec{u}$,
Oy normale à la paroi,
Oz normale à Ox dans le plan de la paroi.

$$\xi = \frac{x}{\bar{s}} = -\int_{\omega_o}^{\omega} \left[\frac{\cos(\omega_o - \varphi)}{\cos(\omega - \varphi)}\right]^{3/2} \frac{\cos\omega}{\sin^2\omega}\, d\omega$$

$$(6) \quad \eta = \frac{y}{\bar{s}} = -\frac{\sin\beta_o}{\sqrt{1 - \cos^2\alpha_o \cos^2\beta_o}} \int_{\omega_o}^{\omega} \left[\frac{\cos(\omega_o - \varphi)}{\cos(\omega - \varphi)}\right]^{3/2} \frac{d\omega}{\sin\omega}$$

$$\zeta = \frac{z}{\bar{s}} = \sin\alpha_o \operatorname{cotg}\beta_o \cdot \eta$$

En fait, la forme de la ligne moyenne dans le repère (Ox, y, z) est bien représentée dans un domaine assez étendu à partir de l'orifice, si l'on admet dans le calcul du facteur d'échelle $\bar{s}$ la valeur $C_\pi = 2$.

Une comparaison de ces prévisions avec les résultats expérimentaux de Ziegler & Wooler [5] est présentée figure 2.

Une interprétation simple de cette valeur de C_π peut être proposée, à l'appui d'une analyse du champ aérodynamique régnant autour du jet.

Ainsi que l'a exprimé G. RUDINGER [6], le mécanisme suivant lequel l'écoulement principal s'oppose à la pénétration du jet se traduit par un échappement en apparence instationnaire de paires de tourbillons contra rotatifs. Ceux-ci décrivent en réalité des trajectoires stationnaires et participent ainsi à une structure cohérente, ce qui a permis de représenter avec une bonne approximation les vitesses induites dans le domaine d'interaction du jet avec l'écoulement externe selon l'hypothèse d'une distribution permanente d'intensité rotationnelle, répartie suivant deux trajectoires symétriques, distinctes de la ligne moyenne du jet [7].

A proximité de l'orifice d'émission, le processus d'interaction peut être assimilé d'après les observations selon les méthodes de visualisation hydrodynamique [8] à un effet de puits concentré suivant la génératrice du cylindre auquel est assimilable le jet, opposée à la ligne d'arrêt de l'écoulement amont. Dans un plan de section normale à la ligne moyenne du jet, cette modélisation conduit à représenter le potentiel complexe de l'écoulement à l'extérieur du jet sous la forme

$$(7) \quad f(z) = u\sin\omega\left(z + \frac{a^2}{z}\right) - \frac{\Gamma}{2\pi\rho}\ln\left[\frac{(z-a)^2}{z}\right]$$

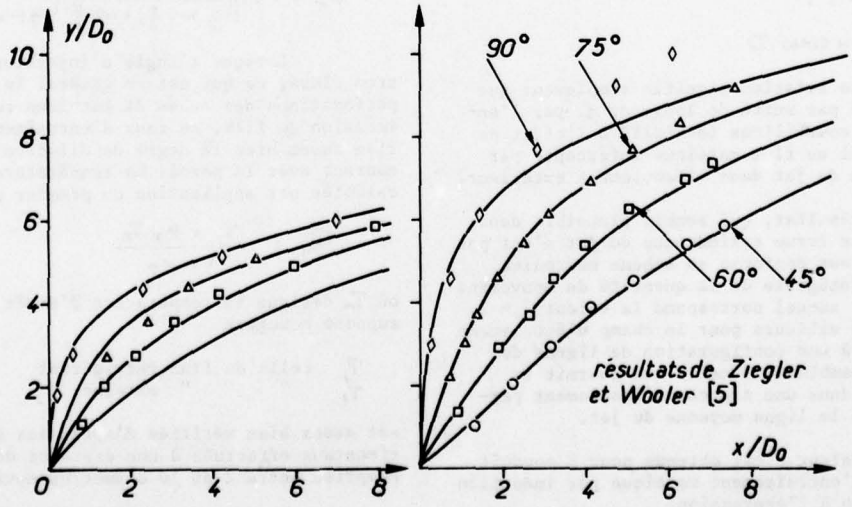

Fig. 2 – Comparaison des lignes moyennes calculées et déterminées expérimentalement.

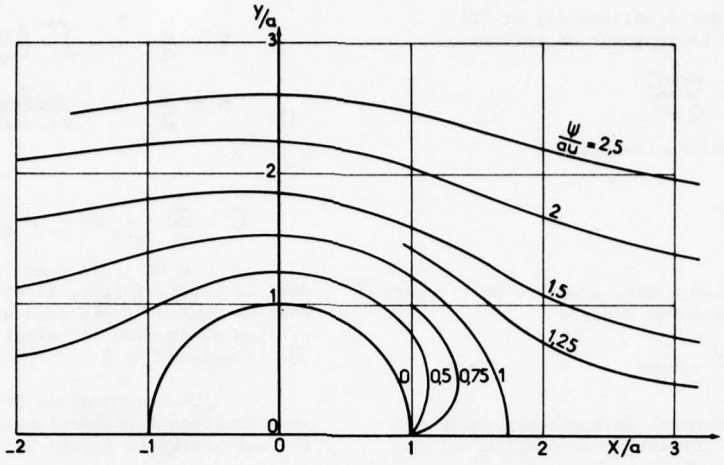

Fig. 3 – Ecoulement potentiel avec effet de puits concentré en arrière d'un obstacle cylindrique.

$Z = X + iY$ désignant la variable complexe définie suivant le schéma représenté figure 3,

a le rayon de la section circulaire du jet
E l'intensité de puits concentrée au point $Z = a$

L'expression en facteur de E prend en compte l'effet d'image du puits par rapport au cercle.

La force exercée par unité de longueur du tube de courant auquel est identifié le jet s'écrit selon la règle de Blasius :

$$\frac{dF}{d\sigma} = \frac{i\rho}{2} \int \left(\frac{df}{dz}\right)^2 dz = E u \sin\omega$$

Cette force peut s'exprimer par ailleurs en fonction d'un coefficient de résistance aérodynamique C_τ tel que :

$$\frac{dF}{d\sigma} = \frac{\rho u^2 \sin^2\omega}{2} C_\tau D$$

Il résulte de ces deux expressions de $dF/d\sigma$ que l'intensité du puits E est donnée par

$$E = \rho u \sin\omega \, D . C_\tau / 2$$

soit pour $C_\tau = 2$:

$$(8) \quad E = \rho u \sin\omega . D$$

Cette relation signifie simplement que le débit capté par unité de longueur δ par l'enroulement des tourbillons (assimilé à l'effet de puits) est égal au flux massique intercepté par la pénétration du jet dans l'écoulement extérieur.

Ce résultat, qui semble plausible dans la mesure où la forme cylindrique du jet n'est pas trop altérée, est conforme au schéma newtonien d'absorption intégrale de la quantité de mouvement du flux coupé, auquel correspond la valeur $C_\tau = 2$. Il conduit par ailleurs pour le champ d'écoulement potentiel (6) à une configuration de lignes de courant très semblable à celle que fournit la visualisation dans une tranche d'écoulement perpendiculaire à la ligne moyenne du jet.

La valeur ainsi obtenue pour E conduit pour le taux d'entraînement massique par induction tourbillonnaire à l'expression

$$(9) \quad d\mu_\tau = \frac{d\dot{m}_e}{\dot{m}_j} = \frac{4}{\pi} \frac{\rho u}{\rho_j v_{j_0}} \frac{D}{D_0} \sin\omega \frac{d\sigma}{D_0}$$

$d\dot{m}_e = E\,d\sigma$ désignant le débit massique entraîné, $\dot{m}_j$ le débit massique initial du jet, soit

$$\dot{m}_j = \rho_j v_{j_0} \pi D_0^2 / 4$$

Un modèle de représentation analytique de la structure contra rotative a été récemment proposé [4]. Il consiste à identifier le débit d'entraînement formulé suivant (8) avec celui qu'induiraient deux files rectilignes indéfinies tangentes aux trajectoires réelles des tourbillons, et conduit en ce qui concerne l'intensité de circulation, l'espacement des centres tourbillonnaires et le champ des vitesses induites à des prévisions très concordantes avec les résultats basés sur les sondages anémométriques. Cette concordance tend à confirmer la validité du modèle d'interaction du jet avec l'écoulement transversal sur lequel est basée l'équation (8).

En fonction des paramètres adimensionnels introduits dans le schéma de la pénétration, le taux d'entraînement réduit peut être mis sous la forme

$$\mu_\tau = \lambda \int_0^\sigma \nu^{-\frac{1}{2}} \sin\omega \, d\sigma = -\lambda \cos\varphi \int_{\omega_0}^{\omega} \frac{d\omega}{\sin\omega \cos(\omega - \varphi)}$$

d'où résulte la valeur explicite :

$$(10) \quad \mu_\tau = -\ln\left[\left(\frac{\operatorname{tg}(\omega - \frac{\varphi}{2}) + \operatorname{tg}\frac{\varphi}{2}}{\operatorname{tg}(\omega - \frac{\varphi}{2}) + \operatorname{cotg}\frac{\varphi}{2}}\right)\left(\frac{\operatorname{tg}(\omega_0 - \frac{\varphi}{2}) + \operatorname{cotg}\frac{\varphi}{2}}{\operatorname{tg}(\omega_0 - \frac{\varphi}{2}) + \operatorname{tg}\frac{\varphi}{2}}\right)\right]$$

Lorsque l'angle d'injection ω_0 n'est pas trop élevé, ce qui est en général le cas pour les perforations des aubes de turbines refroidies par émission de film, ce taux d'entraînement caractérise assez bien le degré de dilution du fluide en contact avec la paroi. La température de mélange, calculée par application du premier principe :

$$T_m = \frac{T_j + \mu_\tau T_e}{1 + \mu_\tau}$$

où T_m désigne la température d'arrêt du mélange supposé homogène

T_j celle du flux réfrigérant
T_e " " " externe

est assez bien vérifiée d'après les relevés expérimentaux effectués à une distance de l'orifice comprise entre 2 et 10 diamètres environ.

En plus de cet effet d'entraînement massique par enroulement des nappes tourbillonnaires, il convient de tenir compte de l'effet classique

du mélange par diffusion turbulente, auquel il se superpose sans discontinuité.

A la différence du processus macroscopique selon lequel la génération de rotationnalité est due à la composante normale $u \sin\omega$ de l'écoulement par rapport au jet, le mélange par diffusion turbulente fait intervenir la vitesse de glissement suivant la ligne moyenne, soit $(v_j - u\cos\omega)$.

Une distinction analogue a été formulée par HAWTHORNE entre les générations de rotationnalité dites par "skew" ou par "shear vorticity"; les deux effets ont été également reconnus par H. SNEL, [9], bien qu'explicités sous des formes différentes de celles du présent exposé.

Le jet étant assimilé à un tube de courant de section transversale A et de périmètre P, la densité linéaire de flux de dilution peut être exprimée sous la forme analogue à celle d'une équation de diffusion :

$$\frac{d\dot{m}_{e,D}}{d\sigma} = \frac{A}{P}\,\rho(v_j - u\cos\omega)\,\bar{E}(T_e - \bar{T}_j)$$

$\bar{E}$ désignant un paramètre adimensionnel et T la fraction massique de l'écoulement extérieur $T_e = 1$ à l'extérieur du jet et $\bar{T}_j = \frac{\mu}{1+\mu}$ en valeur moyenne dans le jet, μ désignant le taux global de dilution $(\mu_T + \mu_D)$.

Le taux de dilution par diffusion turbulente s'écrit ainsi :

$$\frac{d\mu_D}{d\sigma} = \frac{1}{\dot{m}_j}\frac{d\dot{m}_{e,D}}{d\sigma} \simeq \frac{D}{4}\cdot\frac{\rho(v_j - u\cos\omega)}{\rho_j v_{j_0}\pi D_0^2/4}\cdot\frac{\bar{E}}{(1+\mu)}$$

soit en fonction des paramètres adimensionnels précédemment utilisés :

$$\frac{d\mu_D}{d\sigma} = \frac{\lambda}{2C_T}\,\frac{D}{D_0}\,(\lambda r - \cos\omega)\,\frac{\bar{E}}{1+\mu}$$

Si l'on admet que seul l'apport de masse par diffusion turbulente contribue avec la variation de v_j/v_{j_0}, à accroître le rapport D/D_0, il vient moyennant une transformation simple, et selon l'hypothèse $C_T = 2$:

$$\frac{d\mu_D}{d\sigma} = \frac{\lambda}{4}\left(\frac{1+\mu_D}{\nu}\right)^{\frac{1}{2}}\sin\omega\,\mathrm{tg}(\omega-\varphi)\,\frac{\bar{E}}{1+\mu}$$

Une dernière approximation consiste à admettre pour le facteur $E^* = \bar{E}(1+\mu_D)/(1+\mu)$ une loi de corrélation qui a été indiquée par KEFFER & BAINES [10] :

$$E^* = 0{,}2\,\lambda^{-0{,}6}\left(\frac{\sigma}{D_0}\right)^{1{,}37}$$

Il vient ainsi sous forme intégrale et compte tenu de (4) et (5) :

$$(11)\qquad (1+\mu_D)^{3/2} - 1 = -\frac{3}{8}\cos\varphi\int_{\omega_0}^{\omega}\frac{\mathrm{tg}(\omega-\varphi)}{\sin\omega\cos(\omega-\varphi)}\,E^*\,d\omega$$

3.- APPLICATION AU CALCUL DE L'EFFICACITE DE PROTECTION PAR FILM INJECTE A PARTIR D'UNE OU PLUSIEURS RANGEES D'EVENTS.

Associées au calcul de pénétration qui fournit la loi de correspondance entre la distance longitudinale depuis le centre de l'orifice d'injection, $x = \xi\bar{\sigma}$ et l'angle ω de la ligne moyenne par rapport à l'axe Ox, les formules (10) et (11) permettent de déterminer l'évolution du taux de dilution global $\mu = \mu_T + \mu_D$.

En vue de l'application au calcul de l'efficacité de protection par film injecté à partir d'une rangée d'évents, on a d'abord admis que dans le cas de jets faiblement inclinés ($\omega_0 \leq 35°$), les deux processus concourent à provoquer le mélange des gaz chauds avec le fluide réfrigérant.

Au voisinage de l'injection, la croissance du paramètre μ_T est beaucoup plus rapide que celle de μ_D, et il paru légitime d'admettre que dans la mesure où l'espacement des orifices n'est ni trop faible ni trop important, les équations (10) et (11) pourraient fournir une approximation suffisante de l'effet moyen de dilution du flux réfrigérant.

Cette hypothèse a d'abord été confirmée d'après les résultats publiés par LIESS [11] pour une injection par une rangée d'évents espacés de $3D_0$ et inclinés de 35° dans le lit du vent ($\alpha_0 = 0$). L'efficacité adiabatique, en valeur moyenne transversale :

$$\bar{\eta} = \frac{T_f - \bar{T}_{PA}}{T_f - T_j}$$

avec T_f = température de frottement en amont des injections,

$\bar{T}_{PA}$ = température moyenne de paroi athermane, c'est-à-dire de frottement apparent, en aval des injections,

T_j = température totale du flux injecté, à la sortie des évents, était déduite du repérage des températures de barrettes de cuivre isolées thermiquement et insérées dans la paroi plane, transversalement à l'écoulement principal.

Les valeurs de $\bar{\eta}$ ainsi obtenues par LIESS et représentées figure 4 concordent bien avec celles qui résultent de l'application du premier principe de la Thermodynamique, en fonction du taux de dilution théorique :

$$(12)\qquad \bar{\eta} = \frac{1}{1 + \mu_T + \mu_D}$$

Cette concordance est toutefois moins satisfaisante lorsque le paramètre de soufflage ; défini comme le rapport $m = \rho_j v_{j_0}/\rho u$ des débits unitaires, a une valeur trop faible ou trop élevée par rapport à l'unité.

Les écarts observés entre les valeurs expérimentales et calculées pour les valeurs de m inférieures à environ 0,6 ou supérieures à l'unité sont essentiellement dûs à l'influence de trois facteurs qui ne sont pas pris en compte dans le schéma de dilution du jet unique :

- l'espacement relatif des orifices
- la coalescence des jets, qui intervient au-delà d'une distance liée à cet espacement
- la pénétration des jets

Pour $m < 0{,}6$, les valeurs expérimentales de $\bar{\eta}$ sont supérieures aux prévisions théoriques, surtout aux distances x/D_0 relativement importantes. Cela tient à ce que la longueur de référence $\bar{\sigma} = \frac{\pi}{4}\lambda m D_0$ variant sensiblement comme m^2, les valeurs de l'abscisse réduite $\xi = x/\bar{\sigma}$ dépassent alors le domaine de validité du schéma de calcul, valable essentiellement à proximité de l'injection.

Pour les grandes valeurs de m, la condition de proximité se trouve bien satisfaite, mais la pénétration plus accentuée des jets éloigne le domaine d'induction tourbillonnaire de la paroi, de telle sorte que la température du fluide à son voisinage immédiat ne peut plus être assimilée à celle du mélange uniforme.

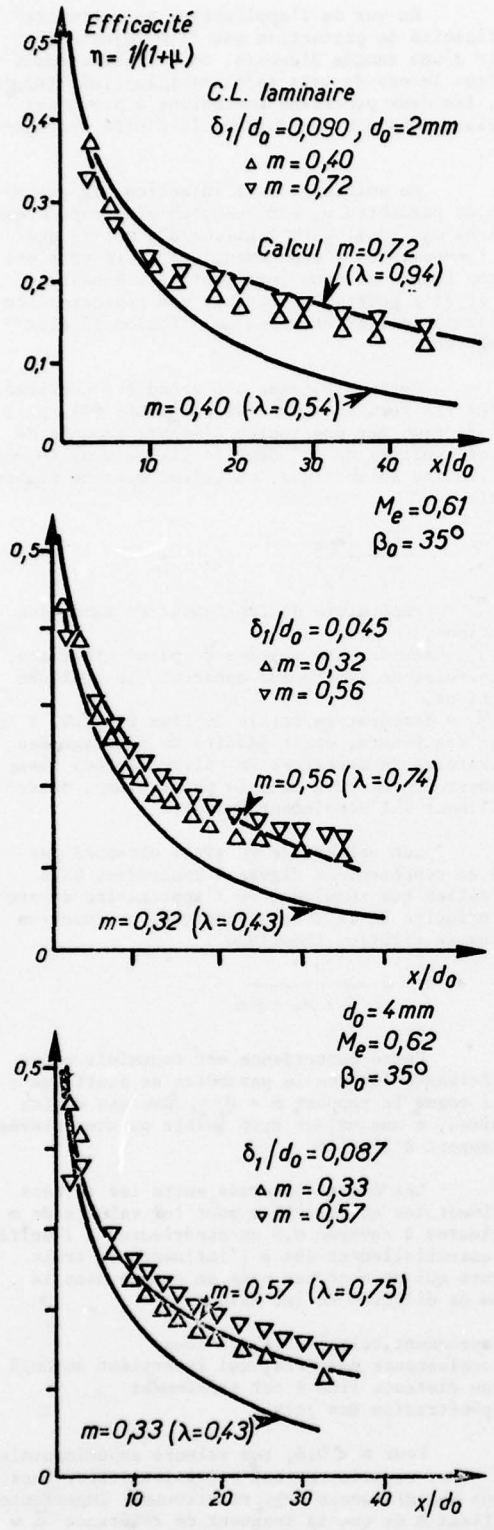

Fig. 4 — Valeurs calculées de l'efficacité pour un jet isolé comparées aux données expérimentales de Liess (une rangée, p = 3).

Influence du pas de perçage des évents

Lorsque les conditions de paroi strictement athermane sont réalisées, les repérages de température locale* en aval de l'injection par un seul orifice suivent une loi de distribution sensiblement gaussienne en fonction de la distance z, mesurée normalement à l'axe longitudinal $0x$ (Fig.5).

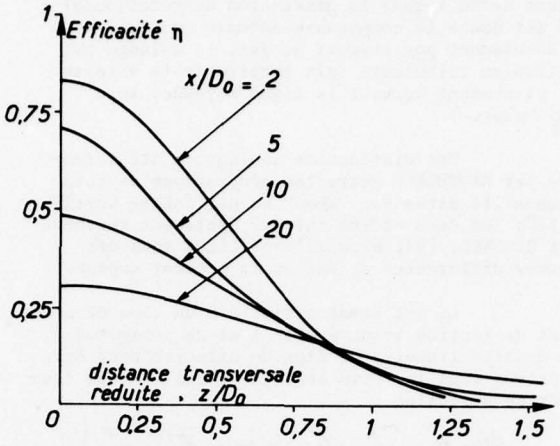

Fig. 5 — Distribution transversale de l'efficacité en aval d'un jet isolé, d'après Goldstein & al.

En aval d'une rangée d'orifices régulièrement espacés avec un entraxe de $2\,D_0$ à $3\,D_0$, on observe une loi de pénétration pratiquement identique à celle d'un jet unique [12]. Les sondages transversaux à proximité de la paroi révèlent des distributions périodiques d'efficacité qui résultent sensiblement de la sommation des lois gaussiennes qui s'appliqueraient derrière chaque orifice supposé isolé.

Des résultats récemment publiés [1] et obtenus par résolution numérique suivant une procédure de différences finies du domaine proche de l'injection révèlent toutefois une structure tourbillonnaire plus complexe que dans le cas du jet isolé. Dans les conditions d'injection par une rangée de canaux inclinés de $\beta_0 = 30°$, $\alpha_0 = 0$ et percés au pas $p = 2,5$ avec un coefficient de soufflage $m = 0,31$, les profils transversaux d'efficacité accusent une légère remontée au voisinage de l'axe moyen entre les évents ($z/D_0 = 1,25$) où s'établirait une structure rotationnelle secondaire de faible intensité, mais tendant néanmoins à induire elle aussi un flux de gaz chaud vers la paroi (Fig. 6).

L'équivalence approximative entre les efficacités mesurées en aval d'un orifice unique ou bien d'une rangée d'orifices, dans les mêmes conditions de rapports de vitesses (λ) et de quantités de mouvement (λm) a été signalée par ECKHERT [13]. Ainsi que l'a souligné cet auteur, une analogie formelle existe entre la loi de distribution applicable au jet unique

$$(13) \qquad \eta_j = \eta_{j\,ax.} \exp\left[-\ln 2 \left(\frac{z}{z_{1/2}}\right)^2\right]$$

$\eta_{j\,ax.}$ désignant la valeur maximale mesurée dans le plan x o y,

$z_{1/2}$ la valeur de la distance latérale z telle que $\eta_j = \eta_{j\,ax.}/2$ et la solution de l'équation de diffusion de la chaleur à partir d'une source ponctuelle placée au point origine O.

La moyenne transversale de η_j sur un segment $(-z_d, +z_d)$ tel que la valeur de l'expo-

---

* Les sondages en température d'arrêt à proximité immédiate de la paroi conduisent à des valeurs égales à celles des repérages effectués sur le métal au droit de ces sondages.

nentielle soit réduite à la fraction $\frac{1}{N}$ de l'unité ($N \gg 1$) s'écrit sensiblement :

$$\bar{\eta}_j = \eta_{jax} \cdot \frac{1}{z_j} \int_0^{\infty} \exp\left[-\ln 2 \left(\frac{z}{z_{1/2}}\right)^2\right] dz$$

$$(14) \quad \bar{\eta}_j = \eta_{jax} \cdot \frac{z_{1/2}}{z_j} \frac{1}{2} \sqrt{\frac{\pi}{\ln 2}}$$

où $\quad z_j / z_{1/2} = \sqrt{\ln N / \ln 2}$

d'où encore $\bar{\eta}_j = \frac{1}{2} \eta_{jax} \sqrt{\frac{\pi}{\ln N}}$

Dans le cas d'une rangée d'orifices d'espacement relatif $2z_0 = e/D_0$, e désignant l'entraxe de perçage des évents, la loi de distribution de l'efficacité prend la forme :

$$(15) \quad \eta = \eta_{jax} \cdot \left\{ \exp\left[-\ln 2 \left(\frac{z}{z_{1/2}}\right)^2\right] + \sum_{n=1}^{q} \exp\left[-\ln 2 \left(\frac{2nz_0 + z}{z_{1/2}}\right)^2\right] + \sum_{n=1}^{n=q-1} \exp\left[-\ln 2 \left(\frac{2nz_0 - z}{z_{1/2}}\right)^2\right] \right\}$$

l'origine des z étant au centre de l'orifice médian, de part et d'autre duquel sont supposés répartis 2 x q orifices alimentés identiquement.

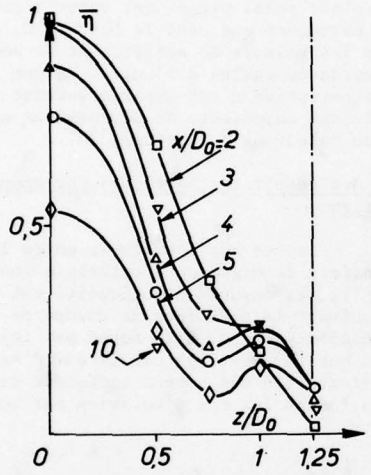

Fig. 6 – Distribution transversale de l'efficacité d'après le calcul [1], *en aval d'une rangée d'évents.*
$\alpha_0 = 0$; $\beta_0 = 30°$; $p = 2{,}5$; $m = 0{,}31$.

Le calcul de l'efficacité moyenne sur une distance égale au pas $2z_0$ conduit à l'expression :

$$\bar{\eta} = \eta_{jax} \cdot \frac{z_{1/2}}{z_0} \frac{1}{2} \sqrt{\frac{\pi}{\ln 2}} \left\{ 1 - \operatorname{erfc}\left[(2q+1) 2\sqrt{\ln 2} \frac{z_0}{z_{1/2}}\right] \right\}$$

le rapport $z_0 / z_{1/2}$ étant généralement de l'ordre de l'unité, cette expression peut être réduite dans le cas d'une rangée à nombre $(2q+1)$ assez grand d'orifices au terme principal

$$(16) \quad \bar{\eta} \simeq \eta_{jax} \frac{z_{1/2}}{z_0} \frac{1}{2} \sqrt{\frac{\pi}{\ln 2}}$$

semblable à celui de l'expression (14) de l'efficacité moyenne pour un seul orifice, au remplacement près de z_0 par z_j.

L'analogie avec la solution de l'équation de diffusion de la chaleur à partir d'une source ponctuelle conduit à représenter par l'expression

$$\frac{\pi}{2 \ln 2} \eta_{jax} \cdot z_{1/2}^2$$

l'intensité de la source ; l'examen des résultats expérimentaux [10] tend effectivement à confirmer l'invariance approximative du produit $z_{1/2}^2 \eta_{jax}$. en fonction de la distance axiale, au-delà de 5 diamètres D_0. Si l'on admet cette approximation, il vient moyennant un calcul simple :

$$(17) \quad \bar{\eta} = \frac{k}{z_0} \bar{\eta}_j^{\frac{1}{2}}$$

le facteur k ayant pour expression

$$k = \frac{(\pi \ln N)^{1/4}}{(2 \ln 2)^{1/2}} z_{1/2} \eta_{jax}^{\frac{1}{2}}$$

et étant par conséquent proportionnel à la puissance 1/2 de l'intensité de la source, dans la représentation analogique.

Il est plausible d'admettre que cette intensité de la source image de l'émission d'un jet doit être proportionnelle au débit massique injecté, c'est-à-dire au coefficient de soufflage $m = \rho_j v_j / \rho u$. Il s'ensuivrait que le coefficient k devrait être proportionnel à $m^{\frac{1}{2}}$; on constate qu'en réalité, les valeurs calculées de $\bar{\eta}$ selon la relation (17), avec $\bar{\eta}_j = (1 + \mu_T + \mu_D)^{-1}$, se comparent mieux avec les valeurs expérimentales si l'on admet que k est une fonction linéaire de $m^{\frac{1}{2}}$. Le fait que k ne s'annule pas avec m et dépend de l'angle d'injection peut s'expliquer par la dimension finie du jet, qui ne peut pas être assimilé à une source ponctuelle près de l'orifice.

Moyennant un choix approprié du coefficient k selon les conditions d'injection par une rangée d'orifices, la relation (17) rend bien compte de l'évolution de $\bar{\eta}$ avec la distance suivant Ox. On doit toutefois tenir compte de l'effet de diminution des sections de passage offertes à l'écoulement extérieur entre les jets, effet d'autant plus marqué que l'angle de dérapage α_0 est *plus important*.

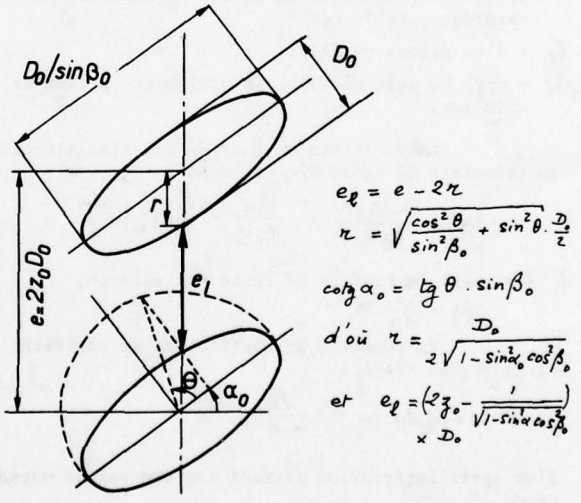

Fig. 7 – Effet d'obstruction d'une rangée de jets. Définition de la transparence.

Dans le cas le plus général, et suivant les notations de la figure 7, une valeur suffisamment approchée de la largeur minimale entre deux jets est donnée par l'expression de l'intervalle e_ℓ mesuré suivant la direction de la rangée, soit au voisinage immédiat de la paroi :

$$e_\ell = \left(p - \frac{1}{\sqrt{1 - \sin^2 \alpha_0 \cos^2 \beta_0}}\right) D_0$$

On peut admettre que le processus de dilution s'effectue comme suivant les hypothèses

du calcul précédemment proposé lorsque $e_\ell \geq D_o$, c'est-à-dire lorsque le pas de perçage $p = 2 s_o / D_o$ est tel que $p \geq 1 + (1 - \sin^2\alpha_o \cos^2\beta_o)^{-1/2}$.

Lorsque cette condition n'est pas satisfaite, le taux de dilution décroît suivant une loi qui peut être admise en première approximation comme de proportionnalité à e_ℓ. L'efficacité des films émis à travers une rangée de canaux est donc définie par l'une ou l'autre des relations

(18) $$\bar{\eta} = \frac{2k}{p}\,(1+\mu_T+\mu_D)^{-\frac{1}{2}} \qquad \text{lorsque } e_\ell \geq D_o$$

$$\bar{\eta} = \frac{2k}{p}\left\{1+(\mu_T+\mu_D)\left[p-(1-\sin^2\alpha_o\cos^2\beta_o)^{-\frac{1}{2}}\right]\right\}^{-\frac{1}{2}}$$

lorsque $e_\ell < D_o$

Influence de la coalescence des jets élémentaires

Les sondages transversaux en température d'arrêt effectués près de la paroi révèlent une uniformisation presque parfaite de cette grandeur au-delà d'une distance comprise entre 10 et 15 diamètres D_o, dans le cas des configurations d'injection étudiées expérimentalement. Parallèlement, un écart croissant aux distances plus grandes de l'injection est observé entre les efficacités calculées d'après les relations (18) et les données expérimentales.

Il est naturel que le caractère bidimensionnel qu'acquiert l'écoulement pariétal soit associé à un processus de dilution distinct de celui qui prévaut initialement, aussi longtemps que les jets élémentaires demeurent différenciés.

L'efficacité doit alors résulter d'un transfert de masse de la forme :

$$d\dot{m}_e = \rho u \mathcal{D} (T_e - T_f)\, dx$$

$\mathcal{D}$ désignant le nombre de transfert de masse

T la fraction massique de fluide de l'écoulement extérieur, telle que

T_e = 1 en dehors du film,

$T_f = \frac{\mu}{1+\mu}$ au sein du film, μ désignant le taux de dilution.

La variation du taux de dilution associée au transfert de masse $d\dot{m}_e$ est donc :

$$d\mu = \frac{d\dot{m}_e}{\rho_j v_{jo} h} = \frac{\rho u}{\rho_j v_{jo}} \mathcal{D} \left(\frac{1}{1+\mu}\right) \frac{dx}{h}$$

h désignant la hauteur de fente équivalente,

$$h = \frac{\pi}{4p} D_o$$

En fonction du coefficient de soufflage $m = \frac{\rho_j v_{jo}}{\rho u}$, il vient :

$$(1+\mu)\, d\mu = \mathcal{D} \frac{dx}{m h}$$

d'où après intégration portant sur une valeur moyenne de $\mathcal{D}$:

(19) $$(1+\mu)^2 - (1+\mu_{co})^2 = 2 \frac{\mathcal{D}}{m} \frac{(x - x_{co})}{h}$$

L'indice "co" se rapporte à la distance au-delà de laquelle l'effet de coalescence prévaut.

Compte tenu de l'expression $\eta = \frac{1}{1+\mu}$ de l'efficacité (la notation en valeur moyenne transversale n'étant plus nécessaire au-delà de x_{co}), l'équation (19) conduit à une loi d'évolution de η qui se traduit par un raccordement sans point anguleux avec les courbes calculées selon l'une ou l'autre des équations (18), et ce sur une plage assez étendue de valeurs de x/D_o.

Il est alors convenable d'adopter une valeur normalisée $x_{co}/D_o = 15$ comme limite de validité des équations (18) ; l'efficacité est ainsi bien représentée aux distances supérieures à x_{co} par la relation :

(20) $$\eta = \left[\frac{1}{\eta_{co}^2} + \frac{8\mathcal{D}}{m} \frac{p}{\pi} \left(\frac{x}{D_o} - 15\right)\right]^{-\frac{1}{2}}$$

avec $$\frac{1}{\eta_{co}^2} = \frac{p^2}{4k^2}(1+\mu_T+\mu_D)$$

ou $$\frac{1}{\eta_{co}^2} = \frac{p^2}{4k^2}\left\{1+(\mu_T+\mu_D)\left(1-\frac{1}{\sqrt{1-\sin^2\alpha_o\cos^2\beta_o}}\right)\right\}$$

Influence de la pénétration des jets

L'effet de la pénétration des jets n'est ressenti qu'au voisinage de l'injection, les résultats expérimentaux indiquant que le détachement des jets, d'ailleurs peu sensible lorsque l'angle ω_o reste inférieur à 30°, est suivi d'un recollement à une distance réduite x/D_o de l'ordre de 12.

Parmi les configurations d'injection étudiées sur paroi plane, cet effet n'est d'ailleurs apparu nettement que dans le cas $\alpha_o = 0$, $\beta_o = \omega_o = 30°$ et pour les valeurs du coefficient de soufflage supérieures ou égales à l'unité. Aucune influence de la pénétration n'est apparue lorsque l'injection présente une composante de dérapage α_o notable, même pour une valeur de β_o excédant 30°.

Examen des résultats théoriques par rapport à l'expérience

Basées sur l'analogie entre les équations de transfert de masse ou d'enthalpie (nombre de Lewis ≃ 1), des mesures d'efficacité ont été effectuées suivant la technique de dosage de la concentration en oxygène du film formé par injection d'azote pur [3] avec les conditions d'espacement et d'orientation des canaux indiquées dans le tableau I dans les cas d'émission par une rangée d'évents.

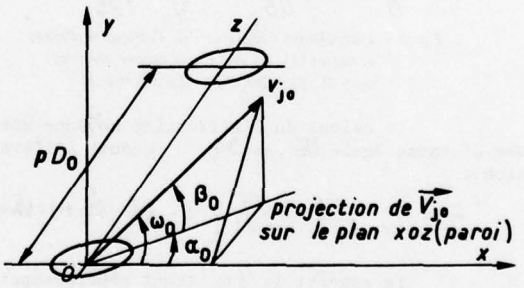

Tableau I

Configurations d'injection retenues pour les essais d'émission de film par une rangée d'évents sur paroi plane

α_o	β_o	ω_o	p
0	30	30	2
0	45	45	2
45	35, 26	54, 73	2
45	35, 26	54, 73	3
90	45	90	3

Les valeurs calculées d'après les relations (10), (11), (18), (20) conduisent aux courbes représentées figure 8 en fonction de x/D_o, pour les valeurs $m = 0{,}6$; 1 ; 1,5 du coefficient de soufflage. Sauf dans le cas où l'influence de la pénétra-

tion est sensible, dans un domaine d'ailleurs restreint ($2 < \frac{x}{D_0} < 8$ à 12), l'accord entre les prévisions et les données d'expérience est respecté avec un écart qui est au plus de l'ordre des erreurs de mesure.

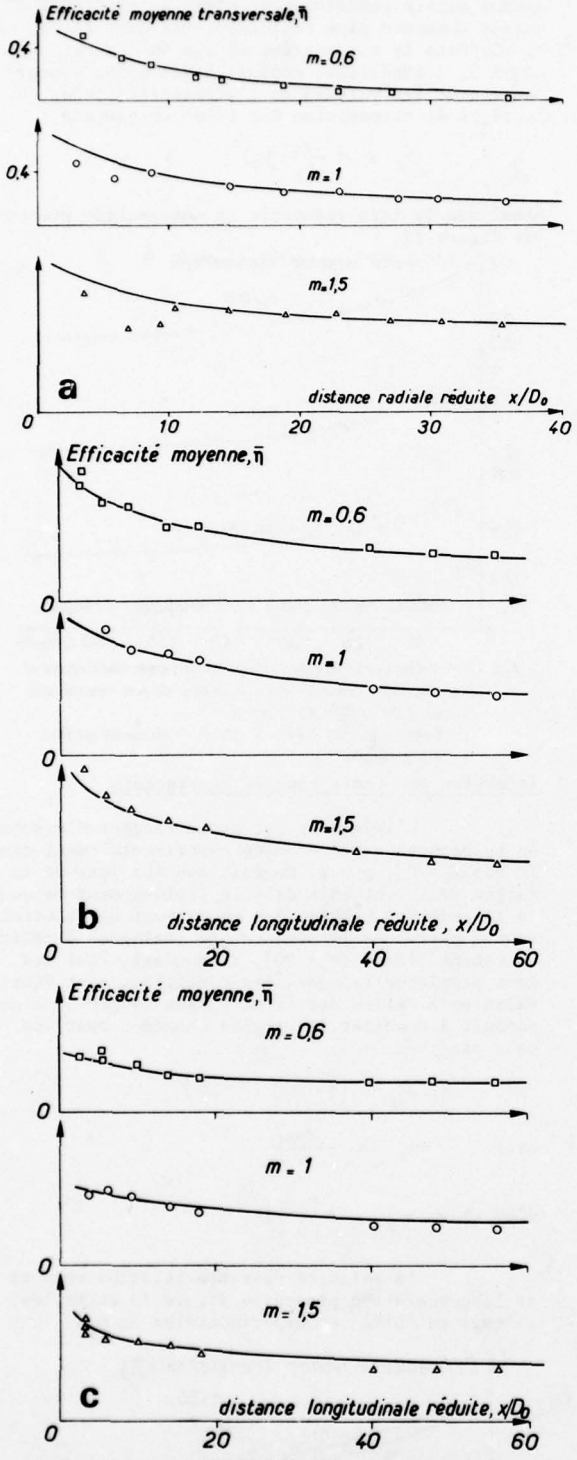

Fig. 8 – Valeurs calculées de l'efficacité moyenne transversale et résultats expérimentaux.

a. 1 rangée de jets. $p = 2$; $\alpha_0 = 0$; $\beta_0 = 30°$; $R_x = 1{,}3 \cdot 10^5$ $\delta_1/D_0 = 0{,}2$; $D_0 = 0{,}6$ mm.

b. 1 rangée de jets. $p = 2$; $\alpha_0 = 45°$ $\beta_0 = \text{arc sin } 1/\sqrt{3} \simeq 35°26$; $\omega_0 = 54°{,}74$; $\delta_1/D_0 = 0{,}1$ $D_0 = 1{,}2$ mm ; $R_x = 1{,}3 \cdot 10^5$.

c. 1 rangée de jets. $p = 3$; $\alpha_0 = 45°$; $\beta_0 = 35°26$; $R_x = 1{,}3 \cdot 10^5$; $\delta_1/D_0 = 0{,}1$; $D_0 = 1{,}2$ mm.

4.- CONFIGURATIONS D'INJECTION A PLUSIEURS RANGEES D'EVENTS

Les contraintes mécaniques, thermiques, aérodynamiques et les servitudes technologiques auxquelles sont soumises les aubes thermiquement très chargées imposent généralement de répartir l'injection entre plusieurs rangées rapprochées d'évents débouchant en quinconces, soit à injections espacées d'une zone à l'autre du profil (films en cascades), soit à injections réparties sur un nombre élevé de rangées régulièrement espacées de canaux en quinconces.

Selon une démarche complémentaire de celle qui a permis de passer du cas du jet unique à celui de la rangée de jets, il convient donc d'établir des lois de corrélation donnant le moyen de passer du cas de la rangée unique à celui de rangées multiples.

Injection par deux rangées rapprochées d'évents

Dans les conditions des essais avec injection à partir de deux ou trois rangées d'évents disposés en quinconces, indiquées dans le tableau II, les modalités d'interaction des jets issus de rangées successives diffèrent selon le pas de perçage p et selon l'orientation en dérapage α_0.

Tableau II

Configurations d'injection retenues pour les essais d'émission de film par deux ou trois rangées d'évents sur paroi plane

α_0	β_0	ω_0	p	2 rangées	3 rangées
0	30°	30°	2	+	+
90°	45°	90°	3	+	

Lorsque l'injection est effectuée sans composante de vitesse transversale ($\alpha_0 = 0$), les hypothèses du schéma de dilution restent vérifiées si la largeur libre de passage entre les jets reste au moins égale à leur diamètre initial $\mathcal{D}_0$, c'est-à-dire dans le cas de configurations à 2 rangées, si le pas p est supérieur ou égal à 4. Dans ce cas, l'efficacité peut être calculée comme pour une seule rangée de pas moitié du pas effectif.

Pour $p < 4$, le taux de dilution de chacune des rangées est approximativement diminué selon la proportion $\frac{p}{4}$, de telle sorte que l'efficacité résultante du film à 2 rangées se déduit de celle du film à une rangée par la règle simple :

$$\eta_2 \simeq \frac{1}{1 + \frac{p}{4}\mu_1} = \frac{4\eta_1}{p + (4-p)\eta_1} \quad \text{avec} \quad \eta_1 = \frac{1}{1+\mu_1}$$

Ainsi, pour $p = 2$, chacune des deux rangées participe pour moitié au processus théorique de dilution. La relation correspondante :

$$\eta_2 = \frac{2\eta_1}{1 + \eta_1}$$

est bien vérifiée d'après les résultats expérimentaux représentés figure 9, dans le domaine $x/D_0 \leqslant 15$. A distance plus grande, c'est-à-dire lorsque le film devient bidimensionnel, la relation (20) s'applique également bien à condition d'y introduire comme hauteur de fente équivalente $h = \frac{\pi}{4p}\mathcal{D}_0$, au lieu de $\frac{\pi}{4p}\mathcal{D}_0$. D'autre part, l'effet de pénétration qui était notable pour les valeurs m = 1 et 1,5 du coefficient de soufflage pour le film issu d'une seule rangée est beaucoup moins sensible dans le cas de deux rangées.

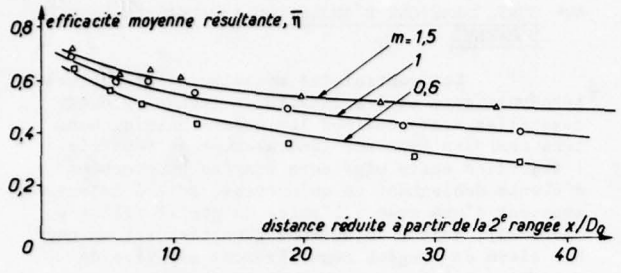

Fig. 9 – Valeurs calculées de l'efficacité moyenne transversale et résultats expérimentaux. 2 rangées rapprochées d'évents.
$\alpha_0 = 0$; $\beta_0 = 30°$; $p = 2$. Calcul : $\eta_2 = (2\,\eta_1)/(1 + \eta_1)$
$\delta_1/D_0 = 0{,}2$; $R_x = 1{,}3 \cdot 10^5$; $D_0 = 0{,}6$ mm.

Injection par deux ou plusieurs rangées écartées (films en cascade)

Dans le cas où la paroi de l'aube doit être protégée par une succession de films émis à partir de plusieurs rangées d'évents réparties avec des écartements de l'une à l'autre relativement grands par rapport au diamètre de perçage D_0, l'efficacité résultant des émissions en cascade peut être prévue très convenablement selon une règle simple, reposant sur l'hypothèse de stratification des films élémentaires. Le flux massique diffusant dans l'une quelconque de ces couches provient pour l'essentiel des couches extérieures, de telle sorte que la fraction de diluant résultant pour n émissions en cascade, soit $\frac{\mu_n}{1+\mu_n} = 1 - \eta_n$, est le produit des fractions de diluant des n films superposés :

$$1 - \eta_n = \prod_{l=1}^{l=n} (1 - \eta_l)$$

Cette règle de composition des efficacités se trouve bien confirmée d'après de nombreux résultats expérimentaux, dont deux exemples sont représentés figures 10 et 11.

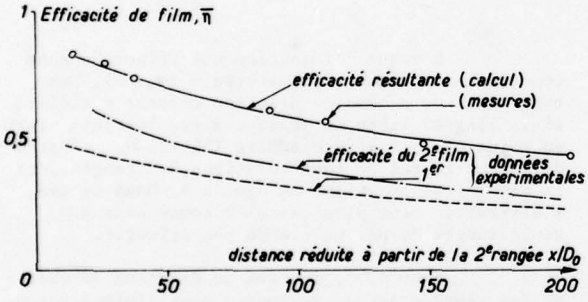

Fig. 10 – Efficacité résultant de l'émission de films par deux rangées en cascade. Calcul : $1 - \bar{\eta} = (1 - \bar{\eta}_1)(1 - \bar{\eta}_2)$.

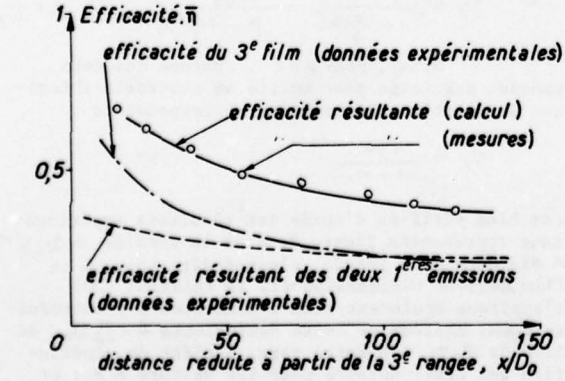

Fig. 11 – Efficacité résultant de l'émission de films par 3 rangées en cascade.
Calcul : $1 - \bar{\eta} = \prod_{i=1}^{3} (1 - \bar{\eta}_i)$.

Injection par deux ou plusieurs rangées rapprochées d'évents, avec une forte incidence en dérapage α_0

Lorsque l'angle de dérapage α_0 est important, le taux de dilution des jets issus d'une rangée suivie immédiatement d'une ou plusieurs autres augmente plus rapidement que dans le cas où $\alpha_0 = 0$. Dans le cas extrême où $\alpha_0 = 90°$, avec $\beta_0 = 45°$ et $p = 3$, l'expérience conduit à une bonne concordance avec les valeurs de l'efficacité tirées de la règle de composition des films en cascade

$$\eta_2 = 1 - (1 - \eta_1)^2$$

ainsi que le fait ressortir la comparaison présentée figure 12.

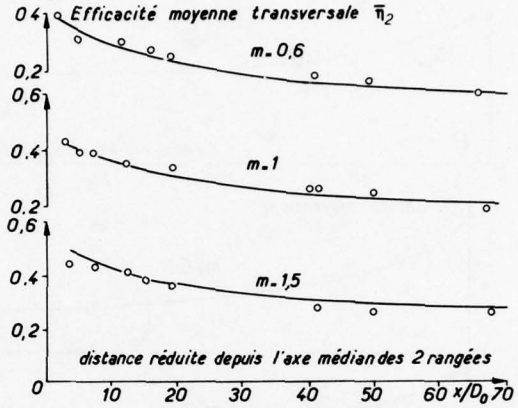

Fig. 12 – Valeurs calculées de l'efficacité moyenne transversale et résultats expérimentaux - 2 rangées de jets rapprochées.
$\alpha_0 = 90°$; $\beta_0 = 45°$; $p = 3$.
Calcul : $1 - \bar{\eta}_2 = (1 - \bar{\eta}_1)^2$; $\bar{\eta}_1$ = efficacité du film à une rangée.

Injection par trois rangées rapprochées

L'injection par trois rangées d'évents en quinconces a été étudiée expérimentalement dans le cas $\alpha_0 = 0°$, $p = 2$. Du fait que les jets de la rangée aval sont émis dans le prolongement de ceux de la première rangée, les conditions de dilution sont à partir de la 3ème rangée analogues à celles du cas précédent ($\alpha_0 = 90°$, 2 rangées). Pour les deux premières rangées, les conditions sont équivalentes à celles des films à deux rangées, ce qui conduit à combiner les règles énoncées pour les deux cas :

$$1 - \eta_3 = (1 - \eta_2)(1 - \eta_1)$$

avec $$\eta_2 = \frac{2\eta_1}{1 + \eta_1}$$

d'où $$1 - \eta_3 = \frac{(1 - \eta_1)^2}{1 + \eta_1}$$

La validité de cette relation ressort de la comparaison présentée figure 13 entre les valeurs calculées et expérimentales de η_3.

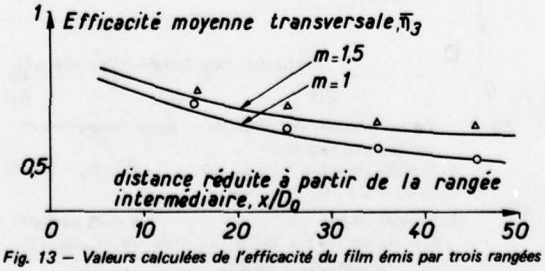

Fig. 13 – Valeurs calculées de l'efficacité du film émis par trois rangées en quinconces et résultats expérimentaux.
$\alpha_0 = 0$; $\beta_0 = 30°$; $p = 2$; $D_0 = 1$ mm.
Calcul : $1 - \bar{\eta}_3 = (1 - \bar{\eta}_1)^2 (1 + \bar{\eta}_1)$
($\bar{\eta}_1$ = efficacité du film à une rangée). $\delta_1/D_0 = 0{,}124$;
$R_x = 1{,}2 \cdot 10^5$.

Injection par un grand nombre de rangées réparties

Les conditions de refroidissement les plus efficaces d'une paroi exposée au flux de convection de gaz chauds sont obtenues par injection de réfrigérant à travers une multiplicité d'évents répartis en quinconce. L'expérience montre qu'il y a généralement avantage à retenir un espacement de 6 à 8 diamètres entre les évents. Bien que le transfert par convection au sein des perforations soit prépondérant dans le bilan de refroidissement, le film formé par les injections multiples a une efficacité adiabatique appréciable , qu'il est utile de pouvoir prédire dans les conditions imposées par les servitudes de tenue mécanique des aubes.

En raison de l'espacement relativement grand des orifices d'injection, il y a lieu d'une part de distinguer les films émis par les rangées impaires 1, 3, 5 ... et les rangées paires 2, 4, 6 ..., et d'autre part d'appliquer la règle de composition des efficacités de films en cascade aux films élémentaires alimentés par chacune des files d'évents, appartenant soit à une rangée impaire soit à une rangée paire. La valeur moyenne transversale de chacun des films est à prendre sur un quart de pas, et non sur un demi-pas comme précédemment.

Suivant cette approche, la relation donnant l'efficacité au-delà de m rangées d'ordre impair et n (compris entre $m-1$ et $m+1$) rangées d'ordre pair s'écrit :

$$\bar{\eta}_{(m+n)} = \left\{ 1 - \frac{1}{2} \left[\prod_{1}^{m} (1-\bar{\eta}_m) + \prod_{1}^{n} (1-\bar{\eta}_n) \right] \right\}$$

les efficacités moyennes $\bar{\eta}_m$ et $\bar{\eta}_n$ étant déduites de celles du jet unique par

$$\bar{\eta}_{m,n} = \frac{4k}{P} \sqrt{\bar{\eta}_j}$$

$$\bar{\eta}_j = \frac{1}{1 + \mu_T + \mu_D}$$

Les conditions d'injection aux faibles valeurs du coefficient de soufflage généralement adoptées dans le refroidissement par émission à travers des perforations multiples s'écartent toutefois sensiblement de celles pour lesquelles les hypothèses de calcul de μ_T et μ_D sont vérifiées. Afin de tenir compte de cette particularité, il convient d'affecter la valeur de $\bar{\eta}_{(m+n)}$ d'un coefficient d'atténuation f :

$$\bar{\eta}_{m+n} = \left\{ 1 - \frac{1}{2} \left[\prod_{1}^{m} (1-\bar{\eta}_m) + \prod_{1}^{n} (1-\bar{\eta}_n) \right] \right\} . f$$

f étant seulement fonction du coefficient de soufflage.

Les valeurs ainsi calculées sont en accord satisfaisant avec les résultats expérimentaux obtenus pour $m = 0,15$ à $m = 0,6$, avec un espacement des évents égal à 4;6 ou 8 (figure 14).

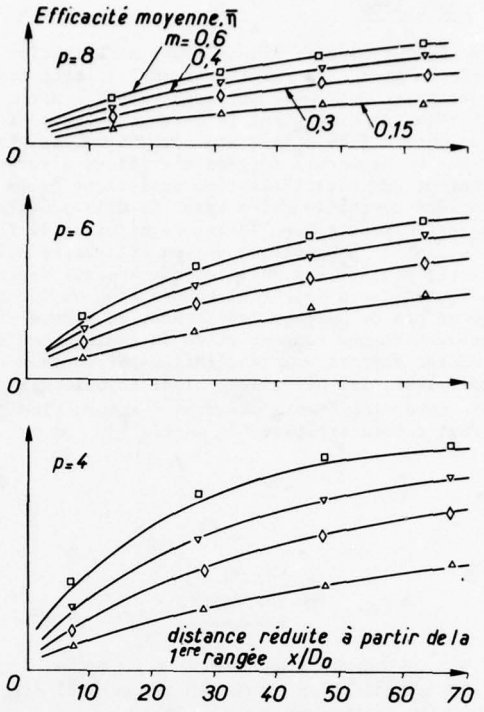

Fig. 14 — Valeurs calculées de l'efficacité de film à émission répartie par rangées multiples et résultats expérimentaux.
$\alpha_0 = 0$, $\beta_0 = 30°$; $D_0 = 0,6$ mm.

5.- AUTRES FACTEURS A PRENDRE EN COMPTE EN VUE DE L'APPLICATION A LA PROTECTION THERMIQUE DES AUBES DE TURBINES

Les schémas de calcul présentés ci-dessus se rapportent au cas d'émission de films sur paroi plane. Ils ne prennent en compte ni l'influence de la turbulence de l'écoulement extérieur, ni celle de la nature de la couche limite incidente. A ces facteurs particulièrement importants lorsqu'intervient un décollement de la couche limite s'ajoutent ceux qui sont liés à la courbure des aubes et aux gradients longitudinaux de pression. Les développements auxquels conduirait leur prise en considération sortiraient toutefois du cadre du présent exposé.

Selon les données actuellement disponibles, il n'apparait pas que les effets de la turbulence et ceux des décollements de couche limite sur l'efficacité de protection par film puissent être pris en compte au moyen de règles de corrélations assez générales.

En revanche, les effets de courbure de la paroi peuvent être assez bien représentés lorsque les gradients de pression longitudinaux sont négatifs(cas d'un extrados)ou modérés (cas d'un intrados).

L'analyse élémentaire de ces effets peut être abordée d'après le sens des forces centrifuges s'exerçant différentiellement sur les particules de fluide chaud ou réfrigérant ; l'effet résultant fait intervenir la différence entre les quantités de mouvement respectives des deux flux [14]. Il est possible de déduire de cette approche des règles simples de prévision de la variation correspondante du taux de dilution, donc de l'efficacité.

6.- CONCLUSION

La mise en oeuvre d'une modélisation simple du processus tridimensionnel d'interaction de jets avec un écoulement transversal a permis de décrire assez fidèlement le mélange progressif auquel donne lieu l'émission d'un film réfrigérant par une ou plusieurs rangées d'orifices discrets. Moyennant une caractérisation analytique de la structure tourbillonnaire associée à la pénétration des jets élémentaires, la loi de dilution du film, conduisant à la prévision de son efficacité adiabatique, peut être établie et adaptée aux diverses configurations d'injection compte tenu de l'influence du pas de perçage des évents, du nombre et de l'espacement des rangées et de la coalescence des jets. Par rapport aux résultats expérimentaux sur paroi plane, les prévisions ainsi formulées sont en bon accord, les écarts observés étant au plus de l'ordre des incertitudes de mesure.

- REFERENCES -

[1] G. BERGELES, A.D. GOSMAN, B.E.LAUNDER
The prediction of three dimensional discrete hole cooling processes
Journal of Heat Transfer, August 1976, pp 379 - 386.

[2] E. LE GRIVÈS - A. BENOÎT
Nouveau modèle théorique d'analyse de la pénétration d'un jet dans un écoulement subsonique.
La Recherche Aérospatiale 1972-3 pp 133-141.

[3] E. LE GRIVÈS
Refroidissement des aubes de turbine
Aspects fondamentaux
Revue Française de Mécanique N°55-56, 1975 pp 43-53.

[4] E. LE GRIVÈS
Mixing process induced by the vorticity associated with the penetration of a jet into a crossflow
CIMAC 12ème Congrès Intal des Machines à combustion, Tokyo 1977

[5] H. ZIEGLER and P.T. WOOLER
Multiple jets exhausting into a crossflow
Journal of Aircraft 8, 5, 1971, p. 414.

[6] G. RUDINGER and L.F. MOON
Laser Döppler measurements in a subsonic jet injected into a subsonic crossflow
Jal of Fluid Engineering Trans. ASME, vol. 981, Part 3 pp 516-520, 1976.

[7] R. FEARN and R.P. WESTON
Vorticity associated with a jet in a cross flow
AIAA Jal 12, n° 12, Déc. 1974, pp 1666-1671.

[8] H. WERLE
Le tunnel hydrodynamique au service de la recherche aérospatiale
Publ. ONERA n° 156, 1974, pp 48-49

[9] H. SNEL
The interaction between a jet and a non uniform main flow, and jet airframe interaction.
National Aerospace Laboratory The Netherlands NLR MP 75019 U 1975.

[10] J.F. KEFFER and W.D. BAINES
The round turbulent jet in a cross wind
Jal of Fluid Mechanics, 15, 4, 1963, pp 481-497.

[11] C. LIESS
Film cooling with ejection from a row of inclined circular holes.
An experimental study for the application to gas turbine blades
T.N. 97 VKI for Fluid Dynamics 1973

[12] V.L. ERIKSEN and R.J. GOLDSTEIN
Heat transfer and film cooling following injection through inclined circular tubes
Jal Heat Transfer 96, 239, 1974.

[13] E.R.G. ECKHERT
Film cooling with injection through holes
AGARD Conf "Proceedings on High Temperature Turbines n° 73, 1973.

[14] J. NICOLAS, A. LE MEUR
Curvature effects on a turbine blade cooling film. Paper 74 GT 156
ASME Gas Turbine Conference & Products Show Zurich, 1974.

DISCUSSION

C.H.Priddin, UK

You seem to have quite a good method for calculating effectiveness at some conditions. Could you please give the numerical limits of blowing rate (and pitch/diameter ratio) within which you would claim good accuracy?

Author's Reply

The proposed model has been checked with good accuracy in regard to our experimental results in the range of blowing rate and pitch/diameter parameters which are of interest for applications to film cooling of turbine blades or vanes:

Blowing rate	$m = 0.15$ to $m = 2$
Pitch/diameter	$p = 2$ to $p = 8$

THE EFFECT OF FREE-STREAM TURBULENCE UPON HEAT TRANSFER TO TURBINE BLADING

by

F.J. Bayley
Professor of Mechanical Engineering
University of Sussex
Falmer, BRIGHTON.

AND

R.W. Milligan
Formerly of Univ. of Sussex
Now, Associated Nuclear Service
Epsom. Surrey

SUMMARY

This report describes an initial investigation of the separate effects of free stream turbulence intensity and frequency upon the local heat transfer to a heavily loaded gas turbine blade section. It is shown that over the whole blade the rate of heat transfer is significantly increased by both these parameters, with the pressure surface showing the greatest response and the downstream half of the suction surface the least.

INTRODUCTION

In view of their importance in determining the life of gas turbine blading, the comparative rarity in the literature of data on local heat transfer rates from the main gas stream to representative blade sections is surprising. There are two possible explanations for this situation: First, the difficulty of measuring reliably the local heat transfer coefficients, particularly in the real engine environment; and second, the problems of reproducing and indeed defining, the relevant characteristics of the engine flow for laboratory investigations of the heat transfer process.

Turbine rotor blades, which represent the most critical heat transfer situation in terms of engine reliability, rotate at speeds up to 15000 rev/min in the wakes of a hundred or so stationary blades, upstream of which again there is a combustion system employing inevitably a highly turbulent mixing process between primary and secondary air streams. It is well established that convective heat transfer to even the simplest geometrical surfaces is susceptible to turbulent perturbations in main stream flow; what is not known, certainly for complex time-mean flows associated with modern heavily loaded gas turbine blading, with its sharp accelerations and curvature, are the precise roles in their effects upon heat transfer of the parameters which characterise the fluctuations in the real flow in an engine.

This paper reports an initial experimental study made in the Mechanical Engineering Laboratories of the University of Sussex with the objective of eliciting the relative effect of two of the parameters which at least are required to characterise the variations in a real gas flow; the amplitude of velocity variation, represented by turbulence intensity and its frequency.

2.0 EXPERIMENTAL TECHNIQUE

Turner (1) showed how, by utilising the modern high-speed digital computer, the heat transfer coefficients around a turbine blade (or indeed, any) section could be reliably determined from measurements of surface temperature and a knowledge of the internal heat transfer conditions. He showed that finite-element numerical Laplacian conduction equations, with insertion of the internal boundary conditions of heat transfer in cooling air passages in the blade section, and the distribution of external blade surface temperature, yielded stable values of the external gas-to-blade heat transfer coefficient. The procedure was sensitive enough to indicate clearly, as demonstrated in reference (1), the sharp change in heat transfer coefficient associated with transition from a laminar to turbulent boundary layer on the nozzle blade used for that work.

In the present programme Turner's procedure has been used to determine the local gas to blade heat transfer coefficients on the cascade of modern rotor blades shown in Fig.1 and Fig. 2 shows typical distributions of surface temperature as observed in the tests. The corresponding distribution of heat transfer coefficient at an outlet Reynolds number, Re, of 7.74×10^5 is shown as Fig.3, in which on this more heavily loaded section than Turner's nozzle blade, the transition to turbulence is clearly indicated at about the 50% position on the suction surface, which corresponds to the point of maximum velocity.

2.1 The turbulence Generator

The results shown as Fig. 2 and 3 were obtained from the centre blade of the cascade of three blades, 79mm span and 64mm chord mounted at a pitch/chord ratio of 0.78 downstream of a contraction in a wind tunnel which produced a mean velocity-time variation of less than one per cent. For the main programme a series of turbulence generators was fitted between the contraction and the cascade, and the mechanical development and calibration of these represented a major part of the present programme.

In essence the turbulence generators were conceived as squirrel cages in which the intention was to vary the turbulence intensity developed by using a range of bar diameters and the frequency of velocity fluctuations through the rotational speed. Originally two contra-rotating cages were used so that effects of downwash from each would be mutually cancelled and thus not distort the time-mean velocity distribution at the cascade entry. In practice velocity traverses downstream of a single cage showed an acceptably uniform

distribution, and this observation, together with the excessive power required to rotate the two cages in the full flow through the tunnel, to say nothing of continual problems with the gearing,led finally to the adoption of a single cage design. A 3.75kW electric motor with an infinitely variable speed control drove the cage at speeds up to 15000 rev/min, although to achieve this performance involved considerable mechanical development of the bearings and the bar support arrangements. Table I gives the geometrical arrangements and corresponding maximum bar passing frequencies of each of the cages tested.

TABLE I

CAGE	BAR DIAMETER	NUMBER AND CIRCUMFERENTIAL PITCH	MAX. FREQUENCY
1	2.3mm	60 - 2 rows staggered at 12mm	15kHz
2	7.9mm	6 - 40 mm	1.5
3	4.8mm	20 - 12 mm	5
4	6.4mm	20 - 12 mm	5

2.2 Characteristics of the Generated Turbulence

The turbulence characteristics from the generator cages of Table I were determined in a long series of calibration tests made over a range of rotational speeds and gas stream rates of flow using conventional anemometry. Considerable difficulty was experienced with probe breakage in the highly turbulent flows used and this problem has limited the range of data at present available. In particular X-array probes were not found suitable and most of the tests were made with standard miniature single wire probes with the wire axes normal to the flow so that directional resolution of the perturbations was consequently not possible. The output from the probes was recorded on magnetic tape for subsequent analysis.

Although some investigations of the length scales and energy content of the turbulence signals were made, the analysis has concentrated almost wholly upon what were seen as the two principle parameters in this initial investigation of the effects of the main stream turbulence upon heat transfer distribution. These were the root mean square turbulence intensity and the frequency spectra.

The turbulence intensities from the squirrel cages used in the present work were found to be remarkably constant. Over the full mass flow range of about 3:1 turbulence intensities varied in each case by about one percentage point either side of the mean value, with no consistent trend; cage (3) (20 x 4.8mm bars),for example showed a slightly rising trend with mass flow while cage (1) (60 x 2.4mm), showed the opposite tendency.

The effect of rotational speed was for three of the cages equally small as shown in Fig. 4, in which the observed mean turbulence intensities are plotted against this parameter in each case. The exception is cage (4) (20 x 6.4mm) bars which gave the highest mean turbulence intensity, but declining from about 47% at 2000 rev/min to about 36 at 12000 rev/min.

The measurements shown in Fig. 4 were made in the flow at a distance of 46mm downstream of the turbulence generator, which coincided with the plane of the blade leading edges when the cascade was in position for the heat transfer tests. Measurements at different streamwise positions in the tunnel showed the turbulence intensity to decrease as about the 0.8 power of the grid to probe distance. Traversing the anemometer probe across the tunnel indicated that the intensity of turbulence was vary uniform across the fluid stream.

The frequency spectra of the turbulence signals from the anemometers were derived using a computer programme developed in the Department of Engineering Science of the University of Warwick. Examples from the many signals analysed from each of the cages are given as Fig. 5a,b,c,d. These are represented as power spectral densities, in which the power, corresponding to the squared velocity fluctuations, is given over the full range of frequencies determinable from the signal. This is limited by the digitisation of the continuous signal on the tape, but covers the range of interest in the present work, up to 15kHz. In these figures the power is given as the ordinate at each frequency analysed, which is in fact the median of a finite sampling bandwidth.

From Fig. 5b it can be seen that cage 2 with only 6 bars, 8mm in diameter gave a power spectrum with a clearly identifiable dominant frequency corresponding to the bar passing rate, and analysis of all the signals obtained showed a similar result from each cage. In the cages with the smaller bars this effect did not persist far downstream, however, and cage I,(60 x 2.4mm bars) yielded a frequency spectrum with no salient frequency at the blade leading edges, as shown in Fig. 5a, and indeed little effect of frequency at all at this point. The few spatial correlations made suggested that the length of scales of the turbulence were consistent with bar size, and the more rapid decay of the initially dominant modes from the smaller bars of cage I might reasonably have been anticipated. The two intermediate cages showed dominant frequencies at the blade leading edges although in the case of cage 4 (fig. 5d)this appeared principally at half bar passing frequency while cage 3(Fig. 5c) showed additional harmonics. These observations are not easily explained but the totality of these results shows that the principal objective of this part of the work has been achieved; namely the attainment of a series of turbulent flows in which turbulence intensity and frequency characteristics are separately variable.

3.0 HEAT TRANSFER PERFORMANCE

3.1 Low Turbulence Data

To provide a base against which to compare the heat transfer coefficients in the streams with turbulence levels artifically increased by the generators, a series of tests was undertaken over the full range of flows available to the tunnel. In the air stream which was delivered from the blower at 100°C and with the blade chord of 64mm this correponded to outlet Reynolds numbers, Re, from about 3×10^5 to 10^6 and exit Mach numbers, M from 0.25 to 0.8.

A representative set of heat transfer distributions around the blade section for this range of variables is shown as Figure 6. Although these follow generally anticipated patterns there are nevertheless noteworthy features.

First, the fairly regular fluctuations in heat transfer coefficient with chordwise position have been observed over the full range of flow conditions, not only in the present experimental programme, but on all the blade sections investigated. This effect, first observed by Turner (1) was at one time attributed to the analytical technique used to derive the heat transfer coefficients, but variations in the finite element mesh and the disposition of internal cooling passages has not produced any substantial change in this pattern. A similar effect has also been observed when coefficients have been derived by an entirely different experimental and analytical procedure involving the measurement of the temperature difference across a blade section manufactured as a thin-walled (about 1mm) shell from a material of suitable thermal conductivity. It is difficult to see this 'geometric' fluctuation in heat transfer as other than a random effect arising from no immediately obvious fluid dynamic situation, especially since it was observed similarly in the tests with applied mainstream turbulence, generally with a comparable amplitude about the mean value.

A second noteworthy feature of the low turbulence heat transfer data of Figure 6 concerns the laminar-turbulent transition region on the suction surface of the blade. Generally this occurs as a well-defined increase in heat transfer coefficient at about 50 per cent along the suction surface. At the two highest Reynolds numbers used in the test programme, however, the transition is less sharp and occurs further downstream on the suction surface. This unexpected observation has the effect on the average coefficient for the whole section shown in Figure 7 which varies little over the range of Reynolds numbers tested. Indeed the downstream half of the suction surface (S2) exhibits a clear maximum heat transfer rate at a Reynolds number of about 7×10^5 , while the upstream section (S1) shows a steady decline in heat transfer with Reynolds number as the transition region moves away from this part of the blade surface. The leading edge radius and the pressure surface show more conventional variations in heat transfer with mainstream Reynolds numbers, each varying as approximately the one-half power of this parameter, as would be anticipated for laminar boundary layers. The coefficients in these regions and the average for the whole section, agreed satisfactorily with the few comparable published data.

3.2 Effects of Mainstream Turbulence

Figure 8 shows a typical distribution of heat transfer coefficient around the blade section for one of the higher turbulence intensities used in the present programme, and may be compared with the curve shown as Fig.3. The heat transfer coefficient is seen to be generally increased, by up to three times on the pressure surface, and by only a little less in the leading edge region. On the suction surface the changes are more complex; the average coefficient in this region is relatively little changed, although as will be shown, there are marked differences between the upstream and downstream surfaces. At this stage, the most striking observation is the suppression by the high mainstream turbulence of the clearly identified transition point associated with the undisturbed stream.

For a more detailed comparison between all the observations in the total programme, the measured heat transfer coefficients have been normalised by division by the low turbulence coefficient at the corresponding Reynolds number. Figure 9 represents all the results obtained and shows the normalised mean coefficient around the whole section plotted against the bar passing frequency, that is the product of the number of bars and the rotational speed, for each of the turbulence generating grids tested. There appears to be a marked effect of this parameter, particularly at the higher intensities of turbulence. Even with the lowest intensity of No. 1 grid there appears to be a small, but distinct, variation with frequency, although it must be remembered that with this grid no predominant frequency appeared in the power density spectrum at the blade leading edges.

The spread of results in Figure 9 is attributable to the effect of mainstream Reynolds number which was not entirely removed by the normalising procedure; in general it appeared that the increased turbulence had less effect at the highest Reynolds numbers at the leading edge, on the pressure surface and on the downstream half of the suction surface(S2) while on the upstream half (S1) the converse was true. These effects, however, were not conclusively observed, and were at times within the limits of experimental error.

Figures 10a,b,c and d show the effects observed with each of the turbulence

generating grids over the four principal regions into which the blade profile was divided for detailed examination. In this figure the average normalised coefficients are shown for each Reynolds number tested. The heat transfer at the leading edge of the blades is seen to be doubled with the highest turbulence intensities, at which conditions also there is a noticeable effect of bar passing frequency. This parameter affects the heat transfer rates over the pressure surface even more markedly and here also the greatest increase due to the turbulence intensity alone was found, with almost five fold increase in coefficient at the most severe conditions.

The smallest effect of turbulence was found in the downstream half of the suction surface, although there appeared again to be a small effect of frequency at the higher intensities. The normalised values appreciably less than unity which were observed in some cases are a consequence of the retarded and even suppressed rise in heat transfer associated with the laminar-turbulent transition. The upstream half of the suction surface, where the pressure gradient and surface curvature are greatest, showed effects of both frequency and amplitude generally between the extremes of the pressure surface and the rear suction surface.

4.0 CONCLUSIONS

The following principal conclusions may be drawn from the present work:

1. The squirrel cage type turbulence generator described in this paper has been shown to produce mainstream flows at entry to a cascade of turbine blades with separately variable turbulence intensities and frequency characteristics.

2. The low turbulence heat transfer performance of the blade section investigated has been shown to follow the trends associated with laminar boundary layers, certainly on the pressure surface and around the leading edge.

3. The local heat transfer rates on the suction surface in the unperturbed mainstream showed a clear transition to turbulence near the maximum velocity point for most of the experimental range, but the transition region moved downstream and became more extended at the highest exit Reynolds numbers used, $9 - 10 \times 10^5$.

4. The average heat transfer coefficient around the blade section was observed to increase with turbulence intensity and, especially at the higher intensities, with the dominant frequency.

5. The pressure surface of the blade was most affected by the variations in both turbulence intensity and frequency; the upstream half of the suction surface and the leading edge radius were little less affected but the downstream suction surface where a mainly turbulent boundary layer exists even with a low-turbulence mainstream responded less to either frequency or intensity.

6. Further work is clearly required in this technologically crucial area of artifically-generated turbulent flows. In particular the effects of frequency at the lower intensities, which will prevail in many practical situations, need to be examined. This is now being done with the present apparatus by modifying it to operate with the cascade of blades nearer the turbulence generator. In addition further work is required on the analysis and classification of the turbulent flows by determining the length and time scales with more certainty than has so far been possible, and to see whether these correlate with the heat transfer data. Further it seems important to extend the Reynolds number range of the test programme to nearer engine conditions to see if presently observed effects, at high and low turbulence intensities, persist.

REFERENCES

(1) Turner, A.B. 'Local heat transfer measurements on a gas turbine blade' I.Mech.E., Jnl. of Mech. Eng. Sci., Vol. 13, No.1, 1971

ACKNOWLEDGEMENTS

Our thanks are due to the University of Warwick for invaluable cooperation in analysing the turbulence signals; the Mechanical Engineering Workshop staff at Sussex University, and especially Mr C. Harvey, for the excellent workmanship involved in building and developing the test rig; and to the Bristol Engine Division of Rolls Royce (1971) Ltd for their support of this work.

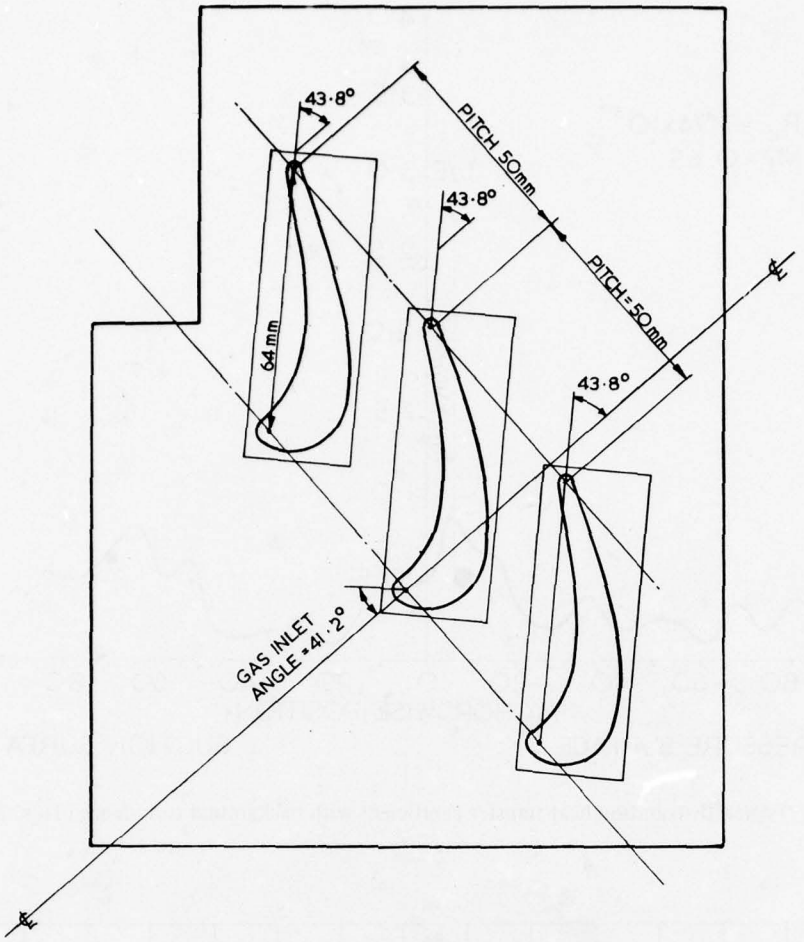

Fig.1 Arrangement of blade cascade

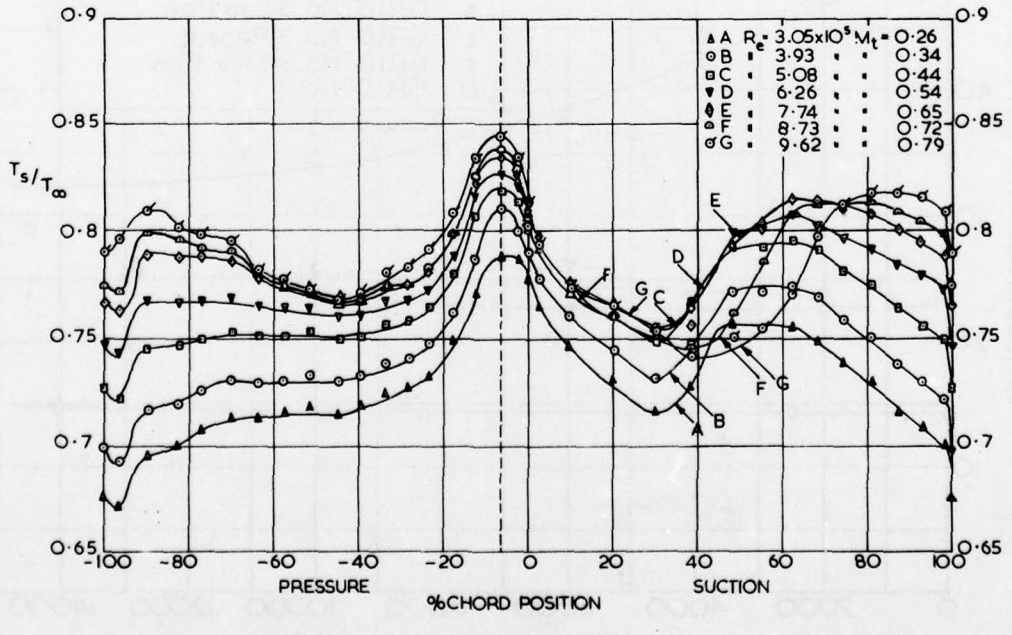

Fig.2 Distribution of blade surface temperature with background turbuience (Tu < 1%) for different R_e

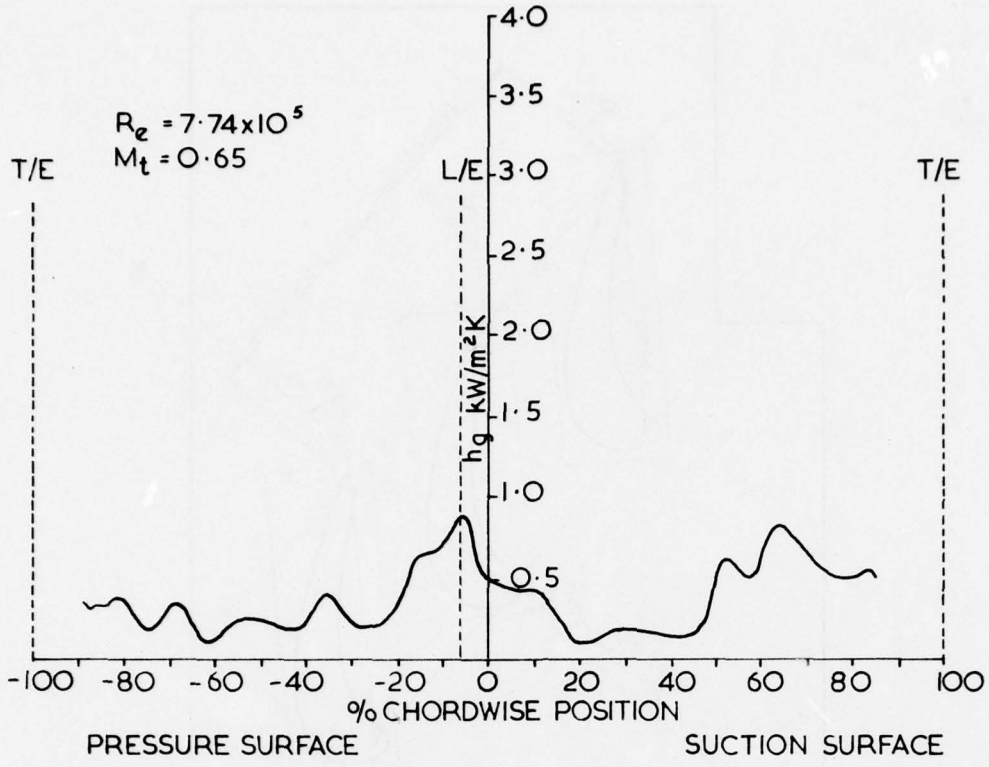

Fig.3 Typical distribution heat transfer coefficient with background turbulence (Tu < 1%)

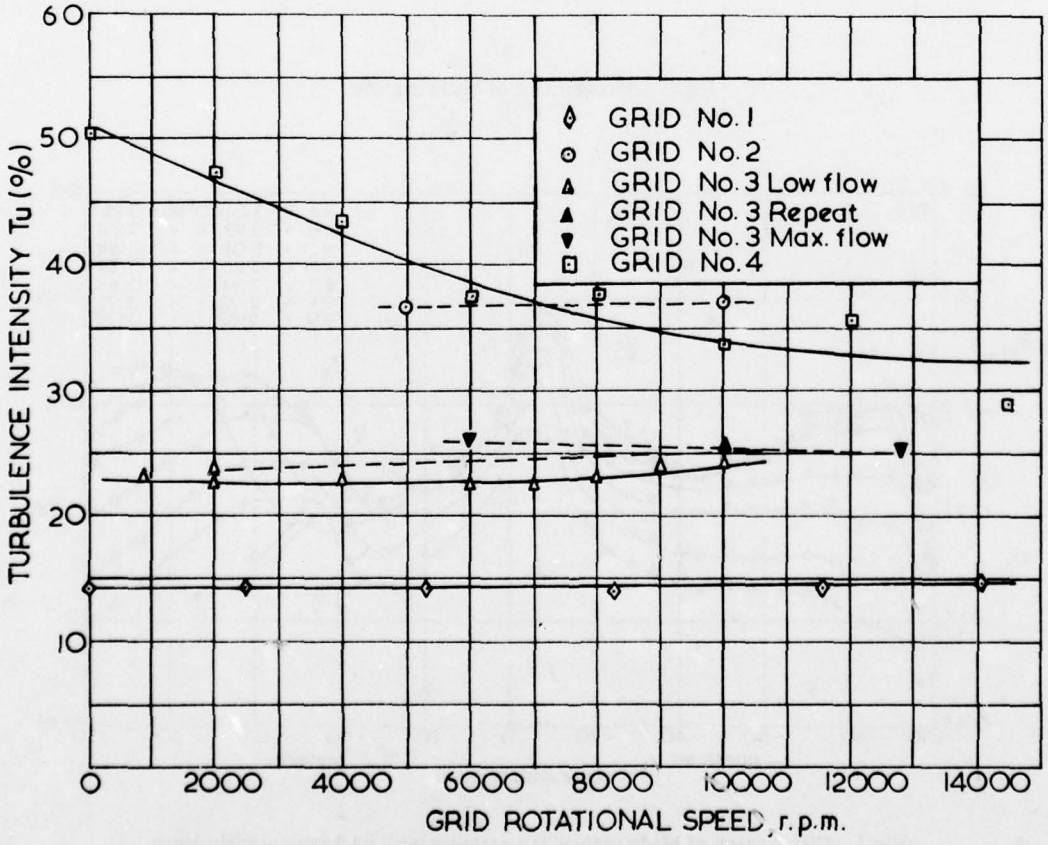

Fig.4 Turbulence intensity variation with rotational speed for all grids

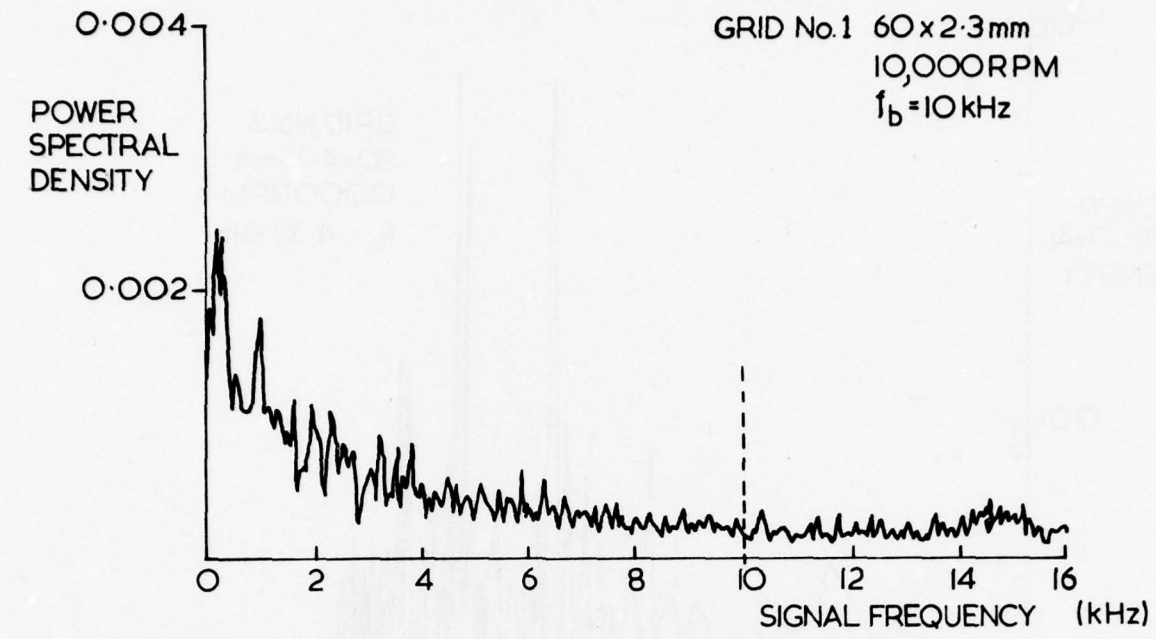

Fig.5(a) Auto-spectrum of hot wire signal for Grid No.1

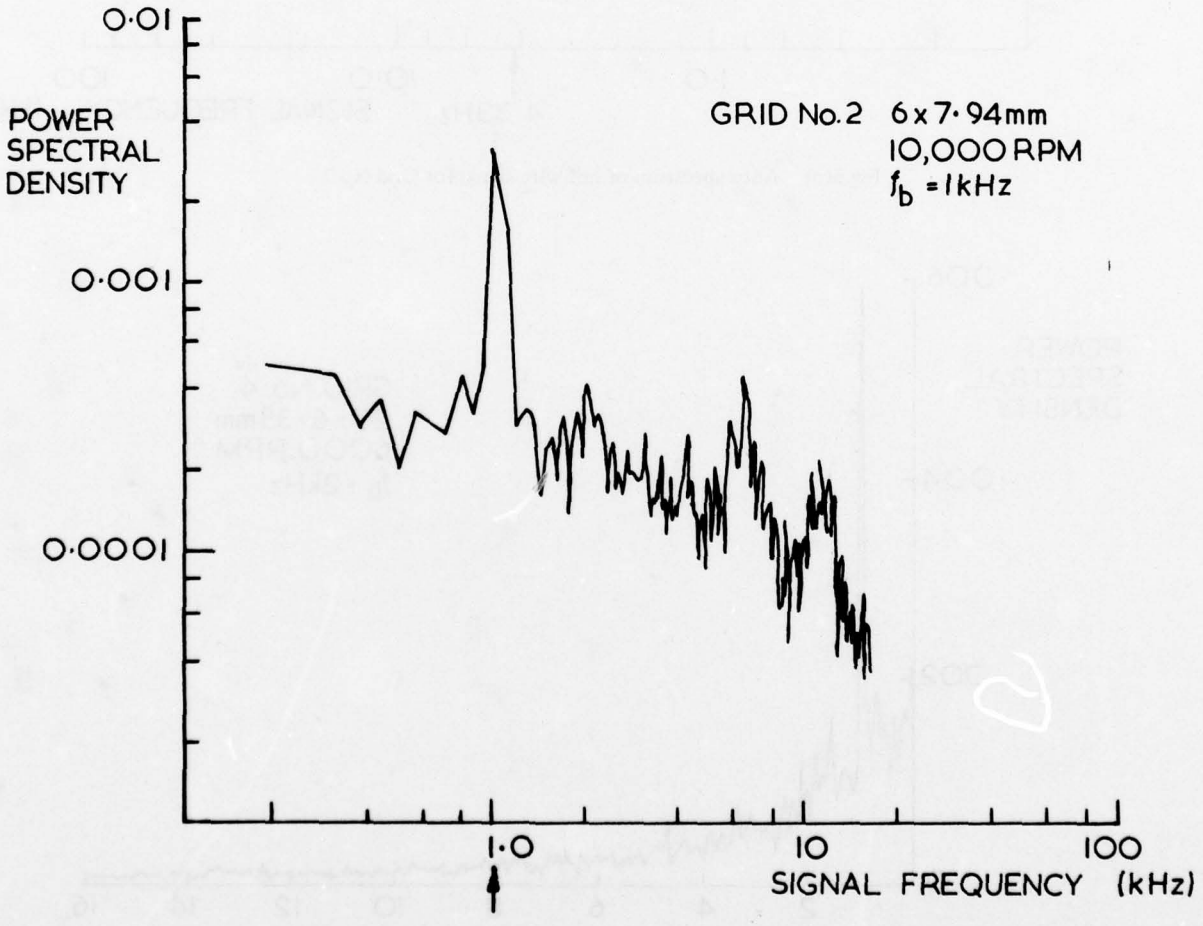

Fig.5(b) Auto-spectrum of hot wire signal for Grid No.2

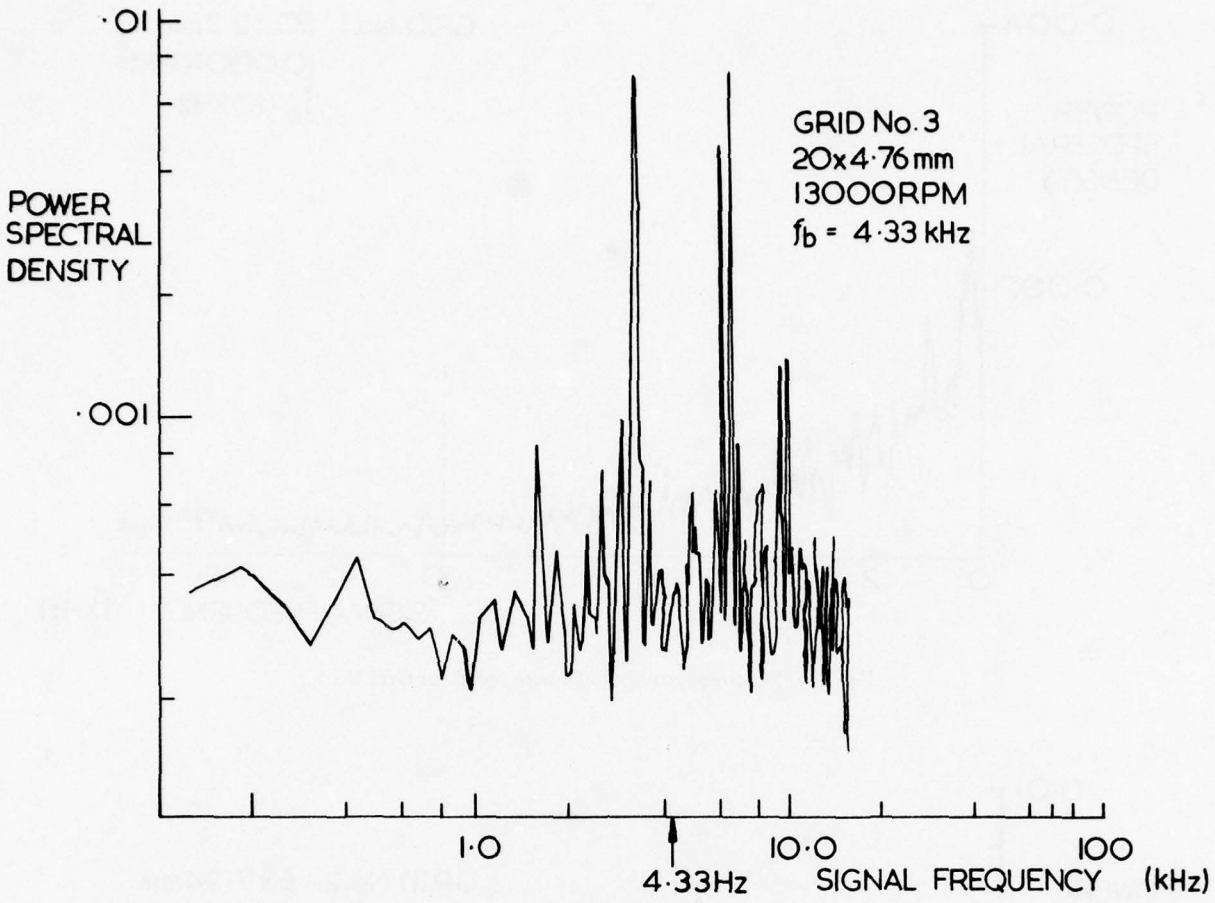

Fig.5(c) Auto-spectrum of hot wire signal for Grid No.3

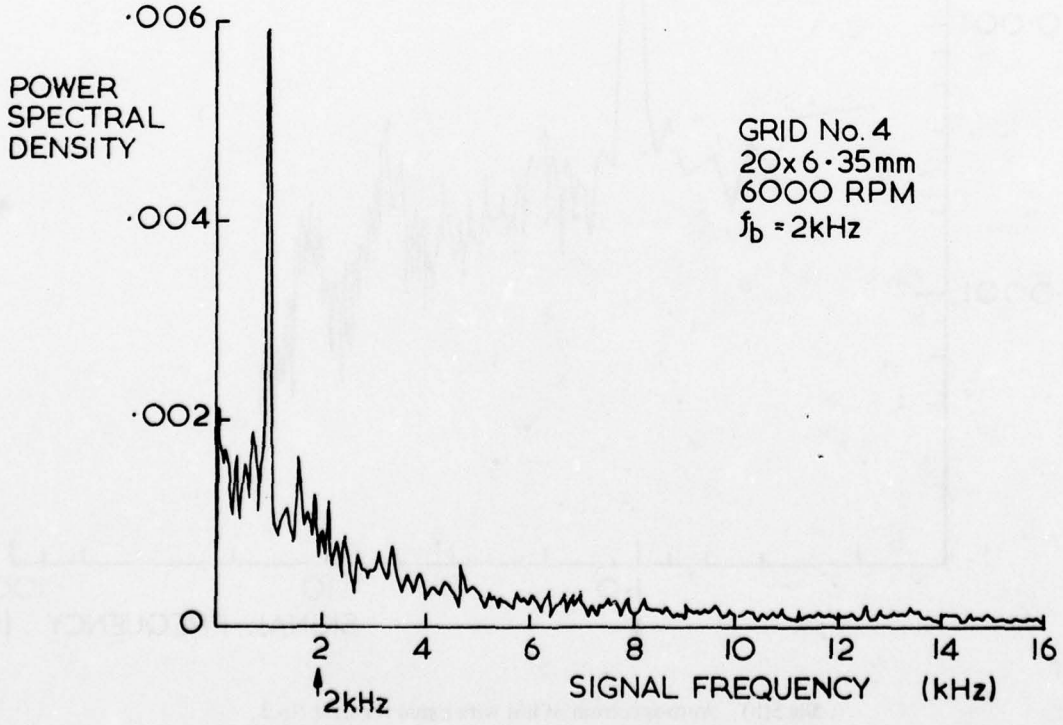

Fig.5(d) Auto-spectrum of hot wire signal for Grid No.4

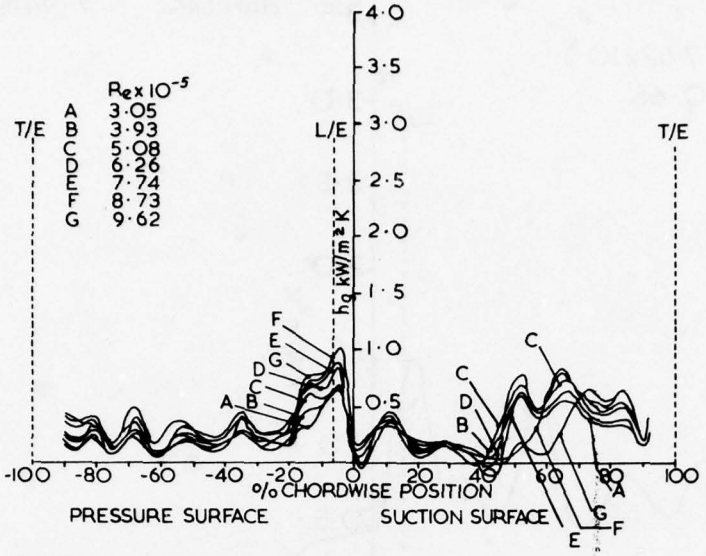

Fig.6 Distributions of heat transfer coefficients with low background turbulence – datum tests

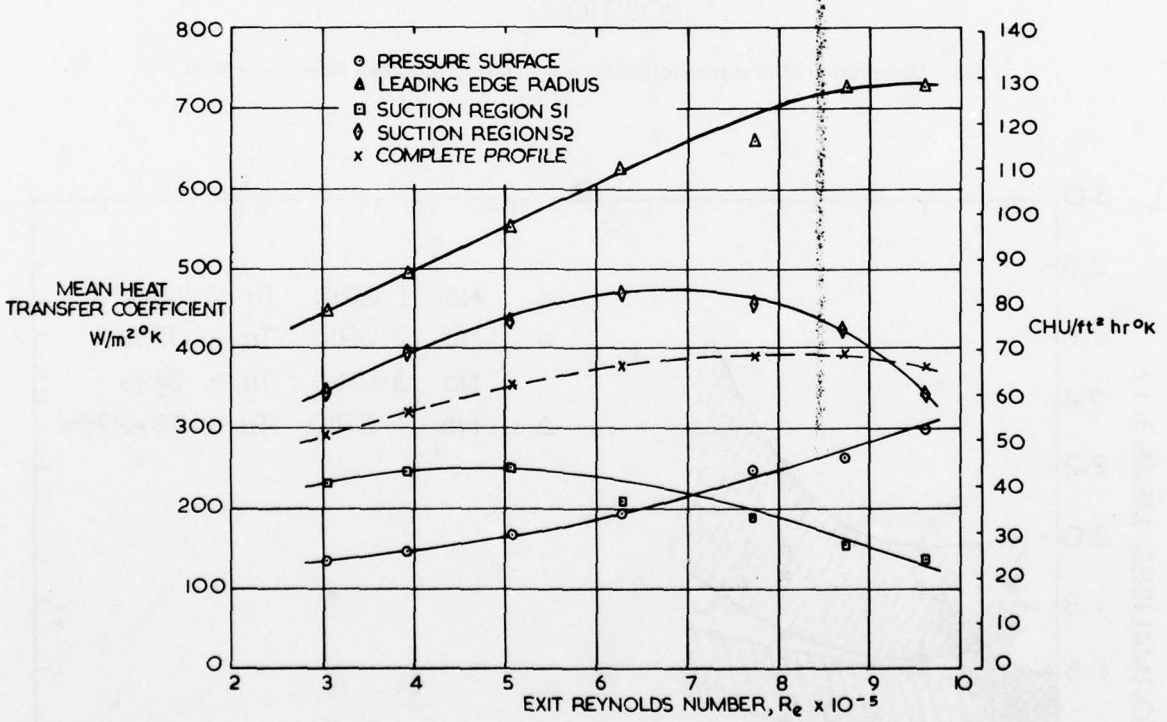

Fig.7 Variation with R_e of blade region mean h.t.c.'s with no applied turbulence (Tu < 1%)

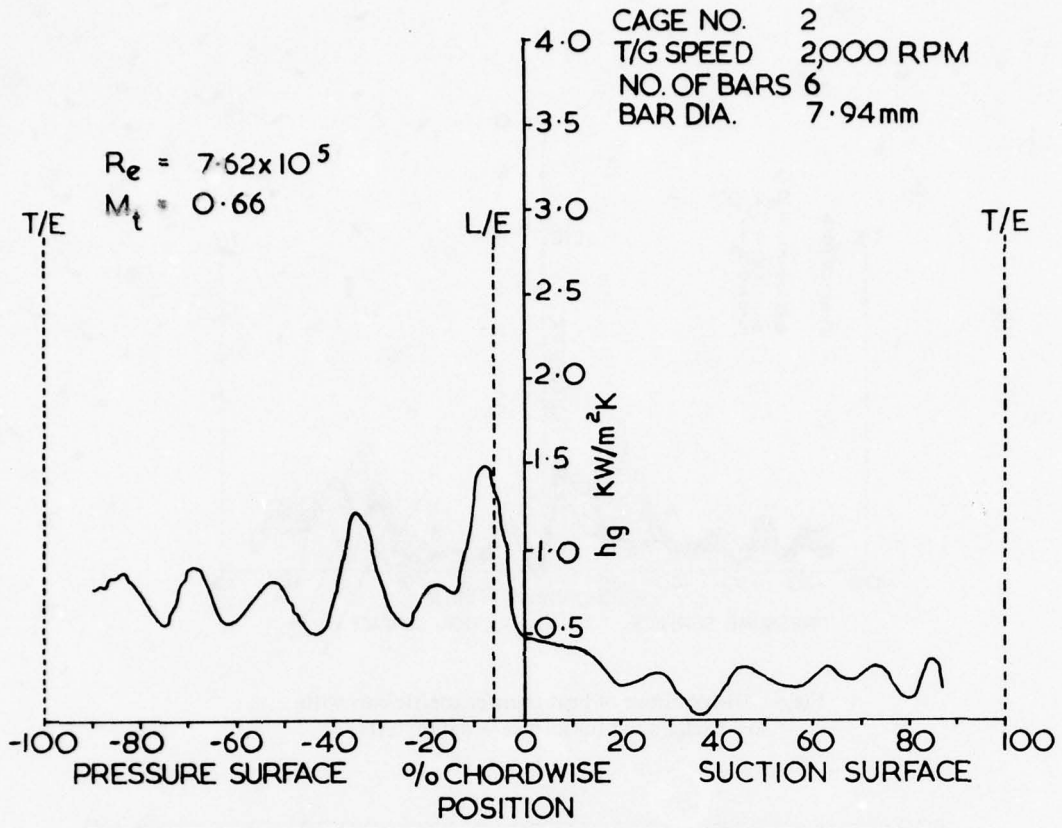

Fig.8 Distribution of heat transfer coefficient in highly turbulent flow (Tu ≃ 37%)

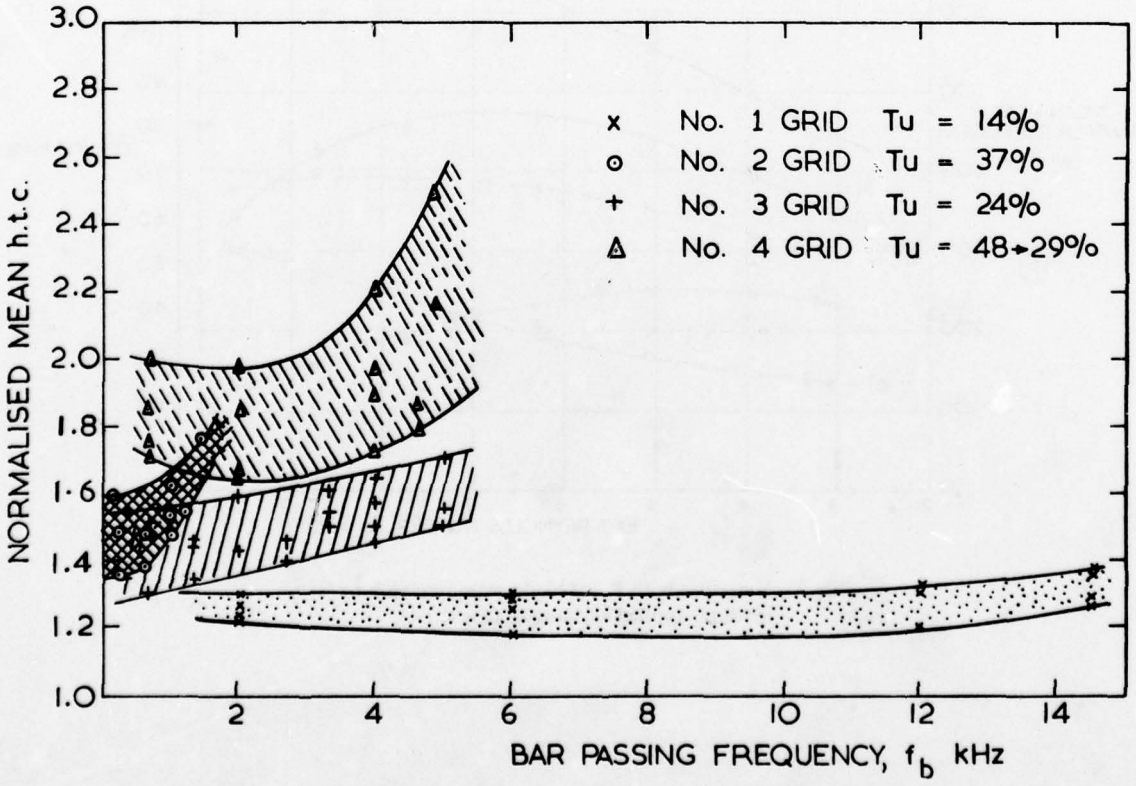

Fig.9 Variation of overall mean normalised h.t.c. with f_b for all grids

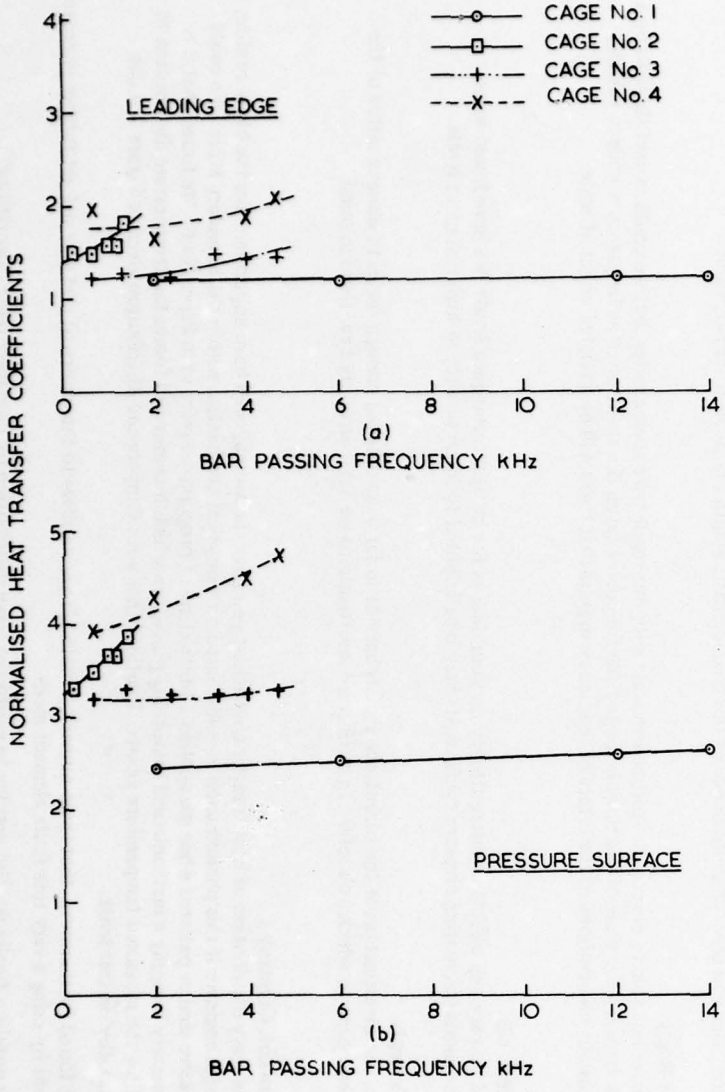

Fig.10 Variation of normalised coefficients in the selected blade regions

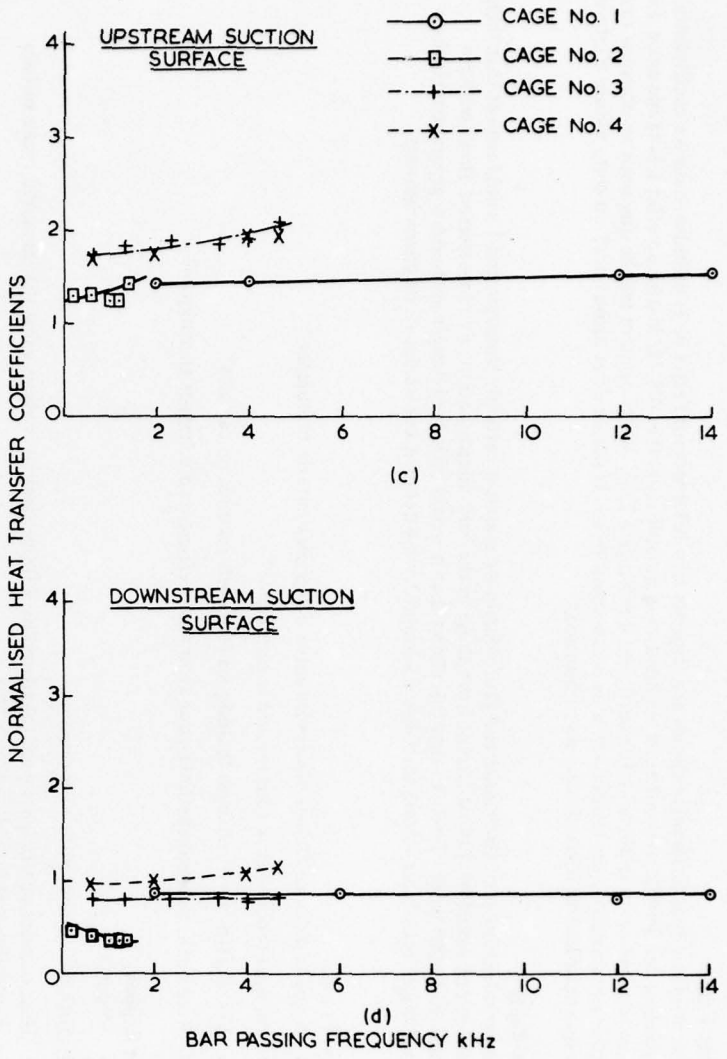

Fig.10 Variation of normalised coefficients in the selected blade regions

DISCUSSION

J.Francois, France

Nous avons eu dans différents exposés des résultats très différents sur l'effet de la turbulence sur les coefficients d'échange. Mr Schultz a montré une augmentation notable entre 0 et 4%, Mr Martin un effet très faible entre 4 et 9% et vous-même un triplement du coefficient d'échange à 37%. Votre opinion est-elle que nous ne pouvons tirer aucune conclusion de ces résultats si nous ne connaissons pas la nature de la turbulence? ou cette nature n'intervient-elle que pour les très forts niveaux de turbulence?

Author's Reply

The turbulent flows of Dr Schultz and Prof. Martin were almost certainly isotropic and I would expect that their observations would be quite different from those in the very intense and highly characterised flows we have examined in this work. I believe that this shows that it would be indeed dangerous to draw general conclusions about the effect of free stream turbulence without having detailed knowledge of its characteristics.

M.Pianko, France

(1) A quelle distance étaient placées les aubes des générateurs de turbulence?

(2) Par quel procédé avez-vous mesuré la turbulence?

(3) Les coefficients d'échanges thermiques étaient-ils mesurés ou calculés?

(4) Avec quelle précision estimez-vous avoir vos coefficients d'échanges thermiques?

Author's Replies

(1) 46 mm.

(2) With a single hot wire anemometer.

(3) Heat transfer coefficients were calculated by a finite element analysis using the measured blade surface temperatures as boundary conditions.

(4) This is a difficult question to answer since the calculated coefficients are sensitive to accuracy of surface temperature measurement. My belief is that they are certainly within ten per cent.

G.Winterfeld, Germany

When changing the turbulence level by varying the rod diameters, there is a change in characteristic length of turbulence. Did you observe an influence of this characteristic length on the heat transfer rate?

Author's Reply

We are not able to observe the turbulence scale with our single wire anemometer, but we could expect there to be a link between the scale of the turbulence and the frequency (even if not the obvious frequency x scale = velocity). Thus our observations of the effect of frequency suggest that there will be a related effect of scale.

E.E.Covert, US

Did you see any effects of intermittency on your data at the highest turbulence level? We have found some anomalous fluctuating pressure coefficients may be attributed to intermittency at high turbulent levels.

Author's Reply

No, our investigation of the turbulence signals has not so far been detailed enough for us to observe either of the phenomena to which you refer. In our future investigations we shall certainly bear them in mind.

R.Eggebrecht, Germany

The wavy distribution of heat transfer coefficient you have shown may well have importance for the blade cooling design engineer if this phenomenon is really based on a physical mechanism within the boundary layer. We could observe similar patterns when we applied a finite element program we refer to in Paper No.6. We found that it is necessary to apply a mathematical smoothing procedure which however still forces the temperature distribution to follow the measured temperature points. I noticed that your temperature distribution given in Figure 2 is not 'smoothy' in this sense.

We found furthermore, that these numerical methods are sensitive to the choice of grid size and get further improvement by using a very fine finite element mesh.

My question finally is: Did you try to verify the wavy distribution by boundary layer calculations?

Author's Reply

You raise a very important question, and the short answer is No, we have not been able to verify (or otherwise) by fluid mechanical analysis the 'wavy' heat transfer distribution. We have, however, varied our finite element grid size, and, indeed, used a quite different technique of measuring the distribution of heat transfer coefficient, and have still not removed the geometrical fluctuations.

D.K.Hennecke, Germany

In order to understand the effects of turbulence on the heat transfer in the various sections of the blade, one would have to know the variation of the turbulence as the flow passes through the cascade. Do you plan to measure this?

Author's Reply

This is a key point with which we wholly concur. We are currently making plans for a laser-doppler investigation of the variation of turbulence through the blade passage.

D.L.Schultz, UK

I have three comments to make:

(1) We have in fact measured the turbulence level in the passage of cascade and found that the turbulence level was in fact reduced by approximately the amount expected from the acceleration.

(2) It would now be well worthwhile for Sussex to use the pitot pressure fluctuation method outlined by Mr Le Bot.

(3) An alternative to the hot wire in such adverse environments is a circular cylinder on which the leading edge heat transfer rate is measured. There has been a great deal of experimental work done on this and quite satisfactory correlations available for the enhancement of the heat transfer rate due to free stream turbulence.

FLOW AND HEAT TRANSFER IN ROTATING COOLANT CHANNELS

by

W. D. Morris
Reader in Mechanical Engineering
Centre for Thermo-fluid Mechanics Research
School of Engineering & Applied Sciences
University of Sussex
Brighton BN1 9QT

SUMMARY

In this paper a selection of experimental results is presented which illustrates the influence of rotation on heat transfer in tubes which rotate about an axis either parallel to or perpendicular to the central tube axis. It is demonstrated that Coriolis and centripetal inertial effects can significantly alter the heat transfer characteristics in relation to the non-rotating case.

INTRODUCTION

Reliable operation of many prime movers, notably gas turbines, is dependent upon the provision of adequate cooling for certain crucial rotating components. In this respect the compressor and turbine discs are notable examples as are the rotor blades of the turbine stages. In some instances cooling of rotating components may be effectively achieved by circulating coolant over the external surfaces of the component itself. To exemplify, turbine discs may be cooled by the radially outward flow of relatively cool air forced between the disc and the neighbouring casing. However a number of instances occur in practice where the coolant is circulated through passages located within the component itself. With these so-called directly cooled systems the coolant is constrained to rotate with the component and is consequently subjected to Coriolis and centripetal components of acceleration which can influence an otherwise customary forced convection situation. It is with the effect of these rotationally induced acceleration components on the flow field and associated heat transfer that the present paper is concerned.

A flow circuit designed to transport coolant to an internally cooled rotating component will typically involve a combination of ducts having varying lengths, cross sectional shapes and orientations relative to the axis of rotation. Also bends, expansions, contractions, plenum chambers, etc are likely to be involved in the overall circuit. The flow through each of these geometric features will be influenced to some extent by rotation making prediction of the flow characteristics of the circuit, together with heat transfer, difficult.

This paper represents a selection of experimental data which illustrates the influence of rotation on heat transfer in two flow geometrics which are commonly encountered with cooling circuits designed for rotating components. Specifically the two geometric configurations discussed are shown in figure 1.

Firstly the case of flow in a heated tube constrained to rotate about an axis parallel to, but displaced from, its central axis is considered, see Figure 1. Results obtained with circular ducts will be presented for this case. This flow geometry may be encountered in the cooling of electrical auxiliaries, oil delivery systems to certain shaft bearings and the root fixing regions of turbine rotor blades.

The second class of rotating geometry considered involves flow in a heated tube constrained to rotate about an axis perpendicular to its central axis as shown in Figure 1. This geometry is particularly important in respect to gas turbines since it represents the spanwise coolant channels incorporated in convection cooled rotor blades. Results obtained with a circular sectioned duct in this configuration will be presented.

CASE 1 : Tube constrained to rotate about an axis parallel to its central axis

A qualitative description of the manner in which rotation effects the flow field and consequently the heat transfer may be explained by reference to the basic equations which control the problem. In this respect the treatment of laminar flow will serve the purposes of illustration. Consider the duct to be circular in cross section as shown in Figure 1 and that the velocity components at a typical point are u, v and w in the polar coordinate frame r, θ and z respectively. Note that the velocity components are measured relative to the tube itself so that it is necessary to modify the usual inertial terms in the equations expressing conservation of momentum to allow for this fact.

Eastthrope (1) demonstrates how the acceleration of a point referred to a rotating reference frame may be determined and when this is done the acceleration components f_r, f_θ and f_z in the three coordinate directions indicated by the subscripts may be expressed as

$$f_r = u\frac{\partial u}{\partial r} + \frac{v}{r}\frac{\partial u}{\partial \theta} + w\frac{\partial u}{\partial z} - \frac{v^2}{r} - 2\Omega v - (r + H\cos\theta)\Omega^2$$

$$f_\theta = u\frac{\partial v}{\partial r} + \frac{v}{r}\frac{\partial v}{\partial \theta} + w\frac{\partial v}{\partial z} + \frac{uv}{r} + 2\Omega u + H\Omega^2 \sin\theta \qquad (1)$$

$$f_z = u\frac{\partial w}{\partial r} + \frac{v}{r}\frac{\partial w}{\partial \theta} + w\frac{\partial w}{\partial z}$$

where H is the eccentricity between the tube central axis and the rotational axis and Ω is the angular velocity of the tube. The terms in equation (1) which involve products of the angular velocity with cross stream velocity components are known as the Coriolis acceleration components whereas those involving the square of the angular velocity are the centripetal components. The usual form of the Navier-Stokes equations must be modified for this rotating geometry to include these additional rotational acceleration components. If this is done for constant property flow the following physical features may be observed from the structure of the equations. At distances sufficiently far downstream of the entry region, where axial gradients of velocity are negligible, elimination of the pressure gradient terms from the radial and tangential momentum equations demonstrates that the Coriolis terms vanish identically as a source for the creation of secondary cross stream flow, see Morris (2). In this case the conservative centripetal terms impress a radial equilibrium-type pressure field onto the otherwise parabolic axial velocity profile.

In the entry region the Coriolis terms, via an interaction with a developing axial velocity profile, create secondary flow in the $r-\theta$ plane. Thus it is expected that in the entry region, even with constant property flow, the existence of Coriolis-generated secondary flow will influence the fluid temperature via the energy equation and hence the heat transfer.

Although the above arguements suggest that the effect of rotation on developed flow is manifest only as a cross stream pressure distribution arising from the conservative centripetal terms this is not the case if buoyancy effects are included. Under these circumstances the variable density interacts with the centripetal terms to create an additional source term for secondary flow. Modifications to the momentum conservation equations to include this buoyancy may be made using the so-called Boussinesq (3) approximation.

The basis of the Boussinesq approximation is to treat the pressure as a combination of the hydrostatic pressure, consistent with a stationary flow field relative to the tube and a reference density value, together with a pressure perturbation, p', which results from departures of the actual density from the assumed reference condition. When these assumptions are applied to the momentum equations expressed in terms of the rotating coordinate frame given in Figure 1, and local density variations with temperature are related to a volume expansion coefficient, it may be shown that the variable density effect need be included in the centripetal terms only and not in those arising from the Coriolis accelerations.

If, for convenience, the independent and dependent variables are non-dimensionalised according to

$$R = r/a\ ,\quad Z = z/a$$

$$U = u/w_m,\quad V = v/w_m\ ,\quad W = w/w_m \qquad (2)$$

$$X = P'/\rho w_m^2\ ,\qquad \eta = \frac{T-T_o}{T_w-T_o}$$

then the conservation equations for momentum, mass and energy may be written as

$$U\frac{\partial U}{\partial R} + \frac{V}{R}\frac{\partial U}{\partial \theta} + W\frac{\partial U}{\partial Z} - \frac{V^2}{R} - SV = -\frac{\partial X}{\partial R} + \frac{1}{4}\cdot\frac{Gr}{Re^2}\left[R + \frac{1}{\varepsilon}\cos\theta\right]\eta$$

$$+ \frac{2}{Re}\left[\nabla^2 U - \frac{U}{R^2} - \frac{2}{R^2}\frac{\partial V}{\partial \theta}\right] \qquad (3)$$

$$U\frac{\partial V}{\partial R} + \frac{V}{R}\frac{\partial V}{\partial \theta} + W\frac{\partial V}{\partial Z} + \frac{UV}{R} + SU = -\frac{1}{R}\frac{\partial \chi}{\partial \theta} - \frac{1}{4}\cdot\frac{Gr}{Re^2}\cdot\frac{1}{\varepsilon}\cdot\eta + \frac{2}{Re}\left[\nabla^2 V - \frac{V}{R^2} + \frac{2}{R^2}\frac{\partial U}{\partial \theta}\right] \quad (4)$$

$$U\frac{\partial W}{\partial R} + \frac{V}{R}\frac{\partial W}{\partial \theta} + W\frac{\partial W}{\partial Z} = -\frac{\partial \chi}{\partial Z} + \frac{2}{Re}\nabla^2 W \quad (5)$$

$$\frac{\partial (RU)}{\partial R} + \frac{\partial V}{\partial \theta} + \frac{\partial (RW)}{\partial Z} = 0 \quad (6)$$

$$U\frac{\partial \eta}{R} + \frac{V}{R}\frac{\partial \eta}{\partial \theta} + W\frac{\partial \eta}{\partial Z} = \frac{1}{RePr}\nabla^2 \eta \quad (7)$$

where

$$Re = \frac{w_m d}{\gamma} \quad \text{(Pipe flow Reynolds number)}$$

$$S = \frac{\Omega d}{w_m} \quad \text{(Rossby number)}$$

$$Gr = \frac{\Omega^2 d^4 \beta (T_w - T_o)}{\gamma^2} \quad \text{(Rotational Grashoff number)} \quad (8)$$

$$\varepsilon = \frac{a}{H} \quad \text{(Eccentricity Ratio)}$$

$$Pr = \gamma/\alpha \quad \text{(Prandtl number)}$$

All symbols used in the text are defined in the nomenclature.

Details of techniques available for the solution of the above equation set will not be discussed here since they form the topic of a paper to be presented later, see Spalding (4). However the important features which emerge from the equations at this stage may be itemised as follows. The flow and temperature fields depend on the dimensionless parameters cited in equation set (8). The associated heat transfer at any axial location may be expressed in terms of a customary local Nusselt number Nu_z. Thus the local Nusselt number will be functionally related to the Reynolds and Prandtl numbers associated with a conventional duct flow forced convection situation. However additional effects must be taken into consideration which account for rotation and this is made manifest in two ways.

Firstly the Coriolis acceleration is accounted for in the so-called Rossby number, S, which quantifies the relative magnitude of the Coriolis and inertial forces acting on the fluid. It is expected that this will be more important in the entry region of the duct. Secondly when the influence of buoyancy is included then the relative importance of the centripetal free convection is characterised by the rotational Grashoff number, Gr. This is similar to free convection effects of the earth's field but with the gravitational acceleration of the earth replaced by the centre-line centripetal acceleration of the rotating duct. Further, the geometric configuration characterised by the relative displacement of the duct axis from the rotational axis will have an effect on the heat transfer and flow behaviour. It is expected therefore that

$$Nu_z = \phi\ [\ Re, Pr, \varepsilon, Gr, S] \quad (9)$$

Where ϕ is some unknown functional relationship to be unravelled from the combined attack on the theoretical equations controlling the problem together with appropriate experimental work.

Morris (5), Mori and Nakayama (6,7), Woods and Morris (8) and Majumder et al(9) have presented solutions for this class of rotating duct. In each case the solutions were valid for conditions of established flow with a uniformly heated tube wall.

Morris (5) used a series expansion method of solution for laminar flow and obtained results which were valid for low rotational speeds and heating rates. Nevertheless, the main qualitative trends depicting the influence of rotation on developed flow were demonstrated. To exemplify, this work suggested that the cross stream buoyancy could give rise to significant increases in heat transfer with an attendent increase in flow resistance.

Mori and Nakayama (6) used a momentum integral-type of approach whereby they assumed a core flow region dominated by convection with a constant thickness boundary layer in the near-wall region. Solutions were matched at the interface of these two regions. These authors also confirmed the increases in heat transfer as rotation of the tube was introduced. This work was also extended, see reference (7), to turbulent flow.

Woods and Morris (8) resolved the equations used by Morris (5) using a numerical procedure based on the method proposed by Gosman et al (10). These numerical solutions were more general than those of Mori and Nakayama (6) since no assumptions concerning the nature of the secondary flow were necessary in the solution procedure. For this condition of established flow the following observations resulted from the analysis.

The eccentricity ratio, ε , had little influence on the heat transfer and flow resistance provided $\varepsilon < 0.2$. It was found that for eccentricity ratio values outside this range both Nusselt number and flow resistance increased slightly with the increases being greater at the high Prandtl number values. Thus only if the rotational axis is very close to the axis of the tube will eccentricity have any noticeable effect. Further details are given by Woods (11).

It is convenient with the truncated form of the differential equations, resulting from the assumptions of established flow, to measure the effect of buoyancy relative to the tube wall temperature at any axial location. This gives rise to a similarity solution for the temperature difference between any point in the flow and the corresponding wall value. Under these circumstances Morris (5) and Morris and Woods (8) used the product of the Grashoff number and the Prandtl number to characterise the buoyancy effect. This product, known as the Rayleigh number, was defined using the tube wall axial temperature gradient, τ, instead of a reference temperature difference between the wall and the fluid. Specifically the rotational Rayleigh number, Ra_τ , was defined as $Ra_\tau = H \Omega \beta a^4 \tau / \gamma \alpha$

A further interesting feature which emerges from the fully developed equation is that the Nusselt number and flow resistance, expressed as a Blassius friction factor, C , depend on the product of the Rayleigh and Reynolds numbers. Figure 2 demonstrates the predicted influence of rotation on fully developed flow for a range of Prandtl numbers together with experimental data obtained with air, water and glycerol. The sources of the experimental data together with salient details of the range of variables covered are given in Table I. In figure 2, Nu and Nu_o refer to the developed value of the Nusselt number obtained under rotating and stationary conditions respectively.

For air, see figure 2a, the numerical procedure tended to over-predict the experimental data for heat transfer. Here the heat transfer enhancement produced is expressed as a ratio of the Nusselt numbers obtained with rotating and stationary conditions with the non-rotating values for a specified Reynolds number taken from a series of datum experiments conducted with the test section held stationary. The general trend of the predictions, particularly the slope, was in good agreement with the observed results although the experimental data exhibited a Reynolds number effect with a tendency for the higher Nusselt numbers to occur at the higher Reynolds number values. It is difficult to isolate the effects of entry length completely with a realistic experimental facility and it is probable that the effects of Coriolis accelerations in the entry region are still influencing the test data to some extent.

Beyond Ra_τ Re values of about 10^6 there was a tendency for the increases in heat transfer to flatten off. This was not predicted by the theoretical analysis and could be possibly explained by a flow reversal situation. Woods (11) has suggested that this effect may be attributed to the influence of axial variations in density but as yet this has not been proved. Also shown in figure 2a is an empirical correlation proposed by Sakamoto and Fukui (12) for mean heat transfer. This correlation which has a Reynolds number effect additional to that included by the $Ra_\tau Re$ product is shown for a Reynolds number value of 2500 in the figure. It shows good agreement with the present data for air. Also shown is the prediction of Mori and Nakayama (6).

Figure 2b compares the results of the numerical prediction with the experimental data of Morris (13) obtained with water. This experimental data was taken during an investigation of the performance of a rotating thermosyphon incorporating the flow geometry being considered in the section of the report. The numerical solution is presented for Prandtl numbers of 4 and 6 respectively since the experimental data spanned this range. In this case the theoretical solution tended to underpredict the experimental data although the general tendency for rotation to increase the heat transfer was again apparent. There was a tendency for the enhancement in heat transfer to again flatten off at the higher values of the Ra_τ Re product.

In figure 2c the results of Morris (13) for glyceral are compared with the predicted values. For this high Prandtl number fluid, the viscosity variation with temperature is severe, and the actual Prandtl number for the experimental data fell in the range $10^3 - 10^4$. This range of values is used to compare the experimental and predicted results. All the experimental data was found to fall within this range as shown

in figure 2c.

Generally we see that the theoretical model was capable of predicting the correct qualitative trends as regards to the influence of rotation on fully developed heat transfer particularly the effect of Prandtl number.

We now consider the influence of rotation on heat transfer in the entry region of this rotating geometry. As mentioned earlier the Coriolis effect is most likely to influence the entry region, since even with constant property flow, it can sustain secondary flow in the cross stream direction. Although there will in practice always be a complex interaction of buoyant and Coriolis effects it is convenient to examine the entry region by considering the Coriolis effect alone. The coriolis effect has been quantified above by means of the Rossby number S. Some workers (e.g. Morris and Woods (8)), have alternatively used a rotational Reynolds number J, which is defined as $J = \Omega a^2 / 2\gamma$ to characterise Coriolis acceleration.

For laminar flow figure 3 typifies the influence of rotation on the mean Nusselt number, Nu_m for a range of heat flux levels. The data was obtained with test section A from Woods (11), see Table I. To avoid the usual effects of exit losses in ducted flow heat transfer experiments the mean Nusselt number was evaluated from the local data over a length/diameter range $0 < z/d < 34.65$. This figure shows that significant improvement in mean laminar flow heat transfer results from rotation of the tube.

Figure 4 shows similar plots obtained with turbulent flow. Again significant improvement in mean heat transfer results from rotation of the tube. Currently there is not sufficient data available with which to make confident assessments of the local response of heat transfer in rotation in this mode, but work with this aim in mind is progressing.

The detailed manner in which rotation typically influences the entrance region is shown in figure 5 where the variations in local Nusselt number along the tube are shown for a Reynolds number value of 13,500 and a nominal heat flux of 6.1 kW/m^2. As the rotational speed is increased the systematic increase in heat transfer is clearly evident.

Similar trends to those described above have also been detected by (Morris and Dias (14),) with a square sectional duct.

In conclusion this section of the paper demonstrates that rotation has a significant effect on heat transfer and flow resistance for a duct which is rotating about an axis parallel to its symmetry or central axis. Rotation must be taken into account in two ways reflecting the relative efffect of Coriolis and centripetal inertial effects. It is apparent that the centripetal effect is made mainly manifest as a free convection effect. There is still considerable research effort needed to fully understand these effects and their mutual interaction for ducts of practical importance.

CASE 2: Tube constrained to rotate about an axis perpendicular to its central axis

Consider now the case where the tube rotates about a perpendicular axis and, through which there is a radially outward flow as shown in figure 1. For this rotating geometry the acceleration components at a typical point in the flow may be shown to be

$$f_r = \frac{u\partial u}{\partial r} + \frac{v}{r}\frac{\partial u}{\partial \theta} + \frac{w\partial u}{\partial z} - \frac{v^2}{r} - 2\Omega w\sin\theta - r\Omega^2\sin^2\theta$$

$$f_\theta = \frac{u\partial v}{\partial r} + \frac{v}{r}\frac{\partial v}{\partial \theta} + \frac{w\partial v}{\partial z} + \frac{uv}{r} - 2\Omega w\cos\theta - r\Omega^2\sin\theta\cos\theta \qquad (10)$$

$$f_z = \frac{u\partial w}{\partial r} + \frac{v}{r}\frac{\partial w}{\partial \theta} + \frac{w\partial w}{\partial z} + 2\Omega(u\sin\theta + v\cos\theta) - z\Omega^2$$

where all symbols have the same meaning as before. Again rotational effects are manifest via the Coriolis and centripetal terms. When these additional inertial terms are included in the Navier-Stokes equations and the possibility of buoyancy effects included then the same non-dimensionalisation procedure used in Case 1, gives for laminar flow

$$U\frac{\partial U}{\partial R} + \frac{V}{R}\frac{\partial U}{\partial \theta} + W\frac{\partial U}{\partial Z} - \frac{V^2}{R} - SW\sin\theta$$

$$= -\frac{\partial \chi}{\partial R} + \frac{1}{4}\frac{Gr}{Re^2} R\eta\sin^2\theta + \frac{2}{Re}\left[\nabla^2 U - \frac{U}{R^2} - \frac{2}{R^2}\frac{V}{\partial\theta}\right] \qquad (11)$$

$$U\frac{\partial V}{\partial R} + \frac{V}{R}\frac{\partial V}{\partial \theta} + W\frac{\partial V}{\partial Z} + \frac{UV}{R} - SW\cos\theta = -\frac{1}{R}\frac{\partial \chi}{\partial \theta} + \frac{1}{4}\frac{Gr}{Re^2} R\eta\sin\theta\cos\theta$$

$$+ \frac{2}{Re}\left[\nabla^2 V - \frac{V}{R^2} + \frac{2}{R^2}\frac{\partial U}{\partial \theta}\right] \qquad (12)$$

$$U\frac{\partial W}{\partial R} + \frac{V}{R}\frac{\partial W}{\partial \theta} + W\frac{\partial W}{\partial Z} + S\left[U\sin\theta + V\cos\theta\right]$$

$$= -\frac{\partial \chi}{\partial Z} + \frac{1}{4}\frac{Gr}{Re^2} Z\eta + \frac{2}{Re}\nabla^2 W \qquad (13)$$

These equations, again presented for the purpose of illustration, permit the following observations. For constant property developed flow the Coriolis terms generate cross stream secondary flow which modifies the axial velocity profile. The conservative centripetal terms, not being directly linked to the flow field, impose a hydrostalic-type pressure distribution onto the flow. Thus when buoyancy is not taken into account the enhanced cross stream mixing induced by the Coriolis acceleration results in a consequential improvement in heat transfer.

For low rotational speeds Barua (15) quantified the nature of this secondary flow for isothermal developed flow using a series expansion solution technique. Estimates of the influence of rotation on flow resistance data were also made.

Mori and Nakayama (16) have, using the same integral method mentioned in references (6) and (7), also studied the effect of the Coriolis induced secondary flow on heat transfer. These authors confirmed that improved heat transfer resulted from rotation of the tube and presented some experimental data in support of the findings.

Lokai and Limanskii (17) have reported experimental data for this configuration which also indicates an improvement in heat transfer due to the Coriolis-induced secondary flow.

It is interesting now to comment on the effect of rotational buoyancy. When the flow is radially outward the buoyancy situation is analogous to a vertical tube influenced by the earth's field and having a downward flow. The axial buoyancy thus opposes the forced convection resulting in an impediment in heat transfer. The converse is true for upward flow in a vertical pipe. This suggests that with a radially outward flow the effect of centrifugal buoyancy will be to reduce the heat transfer and consequentially offset the previously suggested benefitial effects produced by the Coriolis acceleration. As far as the present author is aware there has been no previously reported experimental data available to demonstrate this effect. It is with this feature that the present section is mainly conerned.

A series of exploratory tests was undertaken with a test section 100mm in length with a bore diameter of 4.85mm constrained to rotate in this mode with its midspan position located 306mm from the axis of rotation. The tube could be electrically heated and was instrumented to permit local and mean Nusselt numbers to be evaluated for a range of heat flux levels, flow rates of air and rotational speeds up to 2000 rev/min giving a maximum mid-point centripetal acceleration of aproximately 1400g. Details of the complete experimental facility and data processing techniques are given by Morris and Ayhan (18). An initial program of experiments confirmed that the test section was behaving adequately in that, for a range of flow rates and heat flux levels, the experimental data compared favourably with accepted results for stationary tubes.

Figure 6 illustrates typical distributions of local Nusselt number measured along the tube for three values of Reynolds number in the lower turbulent range obtained with a rotational speed of 1000 rev/min. Each series of tests at a particular Reynolds number represents a range of heat flux levels or values of wall/coolant temperature difference. At zero rotational speed it had been found that for all heat flux levels with a specified Reynolds number, the heat transfer expressed as a local Nusselt number distribution had a strong tendency to collapse onto a single curve. This was not evident when the tube was rotated as shown by figure 6.

At each of the Reynolds numbers shown there was a systematic reduction in heat transfer as the wall/fluid temperature difference increased. Note for each series of tests shown that the individual variations in Reynolds numbers were of the order of 1% of the values quoted. Thus the bandwidth present on each series cannot be attributed to the simple forced convection Reynolds number effect. Similarly the peripheral speed of the rotor was constant so that each series shown in figure 6 corresponds to a fixed value of Rossby number. Thus the only variable not held constant is the Grashoff or Rayleigh number which is proportional to the wall/fluid temperature difference. Hence a possible explanation for the trends shown is that rotational buoyancy is progressively supressing the heat transfer.

Figure 7 illustrates the effect of rotation on the mean Nusselt number for a rotational speed of 1000 rev/min. The data is presented as the ratio of the Nusselt numbers obtained with and without rotation. The zero speed validation tests mentioned above were used for the reference condition at a particular Reynolds number value. The results again confirm the physical arguments discussed earlier that for relatively low heating rates with attendant low values of the Rayleigh number there can be significant improvements in heat transfer relative to the stationary tube. However as the heating rates become larger and buoyancy becomes more important there is a progressive reduction in mean heat transfer.

Also shown as figure 7 is the relative Nusselt number - Reynolds number correlation proposed by Lokai and Limanski (17). The important observation to note from the design viewpoint is that this Coriolis-based correlation can seriously overpredict heat transfer particularly at the lower Reynolds numbers. It is possible that the wide data scatter evident in the work of Lokai and Limanski could be partially explained in terms of buoyancy.

The systematic reduction in mean Nusselt number with increasing rotational Rayleigh number (Gr x Pr) is shown in figure 8. Also shown is the estimated mean Nusselt number based on the Lokai-Limanski correlation and the Kreith (19) correlation proposed for short stationary tubes. The Kreith correlation was actually in very good agreement with the zero speed tests of the present study.

The series of tests described above was repeated with a rotational speed of 2000 rev/min and the same trends were detectable. Figure 9 shows all the data obtained in the present study plotted in accordance with the suggestions of equations 11,12 and 13. Following customary practice the rotational Rayleigh number has again been used instead of the Grashoff number. This figure highlights clearly the two-fold manner in which rotation of the tube influences heat transfer.

At a specified value of the Reynolds and Rossby number the mean level of heat transfer is systematically reduced as the quotient Ra/Re^2 increases. This is a measure of the influence of rotationally induced free convection.

At a fixed value of the Reynolds and Rayleigh number the heat transfer is increased as the Rossby number increases. This is a measure of the influence of Coriolis forces as described above.

Over the range of variables covered in these exploratory experiments reductions in stationary pipe flow heat transfer up to 30% were typically produced as a result of the overall effect of rotation. Actual measured heat transfer could be up to 60% lower than that suggested from the correlation of Lokai and Limanski (17). Note that Fox (20) has demonstrated that a reduction of 10% in the heat transfer coefficient for a convection-cooled turbine blade can typically result in an increase of 20° C in the mean blade temperature. This, in turn, is equivalent to a sevenfold reduction in creep life. It is clear that accurate prediction of the coolant-side heat transfer is a vitally important consideration for turbine blade life predictions and appropriate account of rotational effects are necessary in design procedures. Further studies are consequently necessary to fully resolve the precise quantitative effect of Coriolis and centripetal effects on heat transfer.

CONCLUDING REMARKS

In conclusion the following remarks summarise the main observations presented in this paper.

1. The use of forced convection data obtained with stationary tubes for the prediction of heat transfer in rotating tubes can lead to significant errors of either positive or negative sense. The influence of rotation is generally made manifest in two ways. Coriolis terms under certain circumstances can induce secondary cross stream flow with attendant modifications to the axial flow profile which generally

tends to improve heat transfer. Centripetal terms via a buoyant-type interaction with a temperature dependent fluid density can also affect the flow field. In this respect the rotational free convection can give rise to either enhanced or impaired heat transfer depending on the relative location of the axis of rotation with respect to the tube and also the direction of the flow.

2. For a tube which rotates about an axis parallel to its central axis it is apparent that Coriolis effects are more dominant in the entrance region whereas rotational buoyancy is more important in the regions of developed flow. Both these individual effects tend to improve heat transfer.

3. With a tube which rotates about an axis perpendicular to its central axis Coriolis terms again tend to improve heat transfer in the developing and developed regions of flow. However for a radially outward flow it has been demonstrated that rotational buoyancy tends to offset and eventual reverse the increases brought about by the Coriolis interaction.

NOMENCLATURE

a	Tube radius
d	Tube diameter
f_r, f_θ, f_z	Radial, tangential and axial components of acceleration
L	Length of test section
p'	pressure correction
r	radial coordinate
R	Non-dimensional radial coordinate
T , T_w	Temperature and wall temperature
u	Dimensional radial velocity
U	Non-dimensional radial velocity
v	Dimensional tangential velocity
V	Non-dimensional tangential velocity
w	Dimensional axial velocity
W	Non-dimensional axial velocity
z	Dimensional azial coordinate
Z	Non-dimensional axial coordinate

GREEK SYMBOLS

Ω	angular velocity
θ	angluar coordinate
χ	non-dimensional pressure term
η	non-dimensional temperature
ρ	density
γ	kinematic viscosity
α	thermal diffusivity
β	expansion coefficient
ε	eccentricity parameter

NON-DIMENSIONAL GROUPS

Re	Reynolds number
Pr	Prandtl number
Gr	Rotational Groshoff number
Ra	Rotational Rayleigh number
S	Rossby number
J	Rotational Reynolds number
Nu	Nusselt number

SUBSCRIPTS

o stationary tube
m mean value

REFERENCES

1. Eastthorpe — Three Dimensional Dynamics. Butterworth Scientific Publications (1958)

2. Morris, W.D. — A Theoretical Analysis of the Influence of Rotation on Flow in a Tube Rotating about an Axis Parallel to Itself. Jour. Roy. Aero Soc. 69, 201, (1965)

3. Boussinesq, — Theorie Analytique de la Chaleur. Paris: Gathiers-Villars, Vol. 2 (1903).

4. Spalding, D.B. — Prediction of Heat Transfer in Rotating Systems. AGARD Conference, High Temperature Problems in Gas Turbines Ankara, Turkey. (1977)

5. Morris, W.D. — Laminar Convection in a Heated Vertical Tube Rotating About a Parallel Axis. Jour. Fluid Mech. 21, part 3, 453 (1965).

6. Mori, Y. and Nakayama, W. — Forced Convection Heat Transfer in a Straight Pipe Rotating About a Parallel Axis. (Lamwar) Int. Jour. Heat Mass Trans. II, 1179 (1967)

7. Nakayama, W. — Forced Convection Heat Transfer in a Straight Pipe Rotating about a Parallel Axis (Turbulent) Int. J. Heat Mass Transfer II, 1185 (1968)

8. Woods, J.L. and Morris W.D. — An Investigation of Laminar Flow in the Rotor Windings of Directly Cooled Electrical Machines. J.M.E.S. I.Mech E. 16 No 6, 408. (1974)

9. Skiadarsis, D. et al — Heat Transfer in Rotating Ducts. Euromech. Colloquium (Boundary Layers and Turbulence) Manchester (1976).

10. Gosman, A.D. et al — Heat and Mass Transfer in Recirculating Flows. Thermo-Fluids Section, Imp. Coll. Science Tech. SF/R/3

11. Woods, J.L. — Heat Transfer and Flow Resistance in an Rotating Duct System. D.Phil. Thesis, University of Sussex (1975)

12. Sakamoto, M. and Fukui, S. — Convective Heat Transfer of a Rotating Tube Revolving About an Axis Parallel to Itself. Elec and Nuclear Eng. Lab., Tokyo. Shibaura Elec Co. Ltd., Kawasaki, Japan.

13. Morris, W.D. — Heat Transfer Characteristics of a Rotating Thermosyphon. PhD. Thesis, University of Wales (1964).

14. Morris W.D. and Dias, F.M. — Unpublished Work. University of Sussex (1977)

15. Barra, S.N. — Secondary Flows in a Rotating Tube. Proc. Roy. Soc A227, 133 (1955)

16. Mori, Y. and Nakayama, W. — Convective Heat Transfer in Rotating Radial Circular Pipes (laminar) Int J. Heat Mass Trans, 11, 1027 (1968).

17. Lokai, V.I. and Limanski, A.S. — Influence of Rotation on Heat & Mass Transfer in Radial Cooling Channels of Turbine Blades. Izvestiya VUZ, Aviatsionnaya Tekhika, 18 No 3,69,(1975)

18. Morris W.D. and Ayhan, T. — Observations on the Influence of Rotation on Heat Transfer in the Cooling Channels of Gas Turbine Rotor Blades. Centre for Thermo-Fluid Mechanics Research, University of Sussex Report No (1977).

19. Kreith, F. — Principles of Heat Transfer. Int Textbook Co.,(1965)

20. Fox, M. — Some Implications of Heat Transfer in Turbine Blade Design:- A Framework for Comparison of Design Strategies. Aero. Res. Council Report No. ARC 35250, HMT 339 (1974).

ACKNOWLEDGEMENTS

The financial support of the Science Research Council and Rolls Royce (1971) Ltd for the investigations reported here is acknowledged with thanks.

FLUID	SOURCE	TEST SECTION DETAILS		
		LENGTH(mm)	DIAMETER(mm)	ECCENTRICITY RATIO
Air	Woods(11)	(A) 610	12.70	304.8
	Woods & Morris (8)	(B) 610	6.35	
Water	Morris (13)	304.8	6.35	152.4
Glycerol	Morris(13)	304.8	6.35	152.4

Table 1: Details of Test Sections used for Case 1 Experimental Data

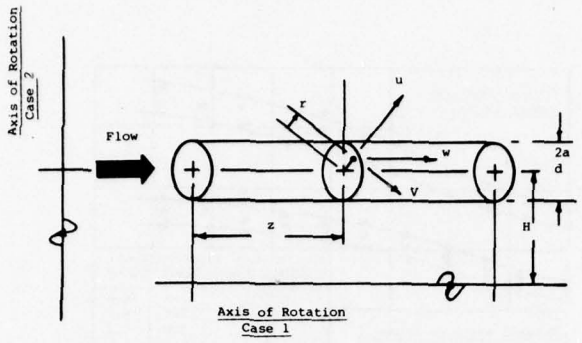

Figure 1: The Two Rotating Configurations Considered

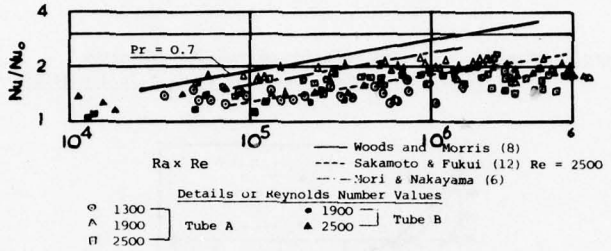

Figure 2a : Air (Woods & Morris (8))

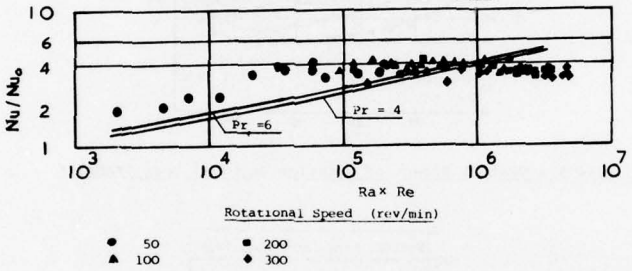

Figure 2b : Water (Morris (13))

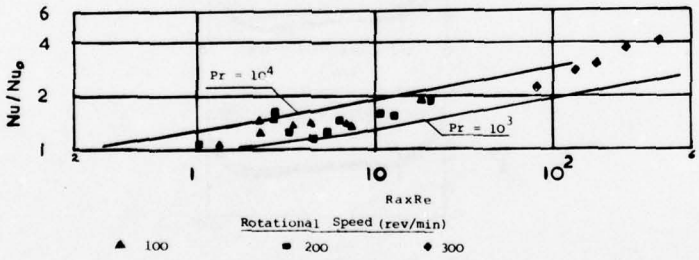

Figure 2c : Glycerol (Morris (13))

Figure 2 : Comparison of Theoretical and Experimental Developed Heat Transfer for a Variety of Fluids.

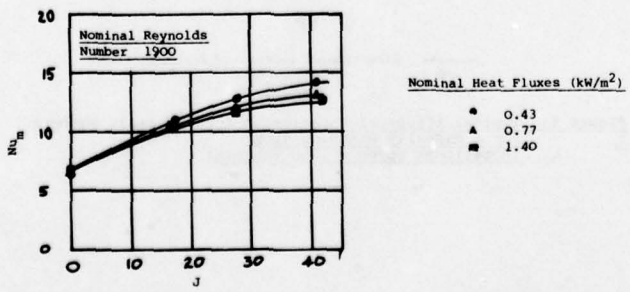

Figure 3 : Typical Effect of Rotation on Mean Entry Region Heat Transfer for Laminar Flow (Tube A, L/d = 34.65)

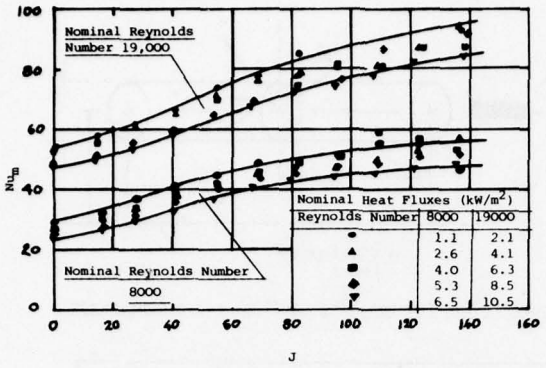

Figure 4 : Typical Effect of Rotation on Mean Entry Region Heat Transfer for Turbulent Flow (Tube A, L/d = 34.65)

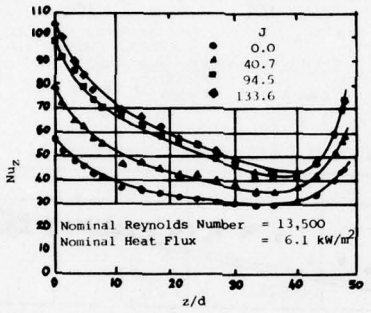

Figure 5 : Typical Effect of Rotation on Local Heat Transfer

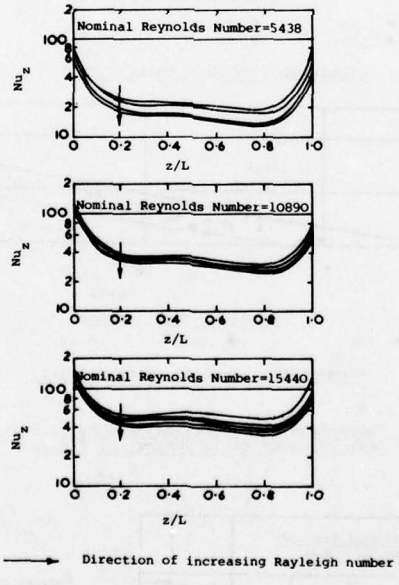

Figure 6: Typical Effect of Rotation on Local Nusselt Numbers for a Radially Rotating Tube (Rotational Speed = 1000 rev/min)

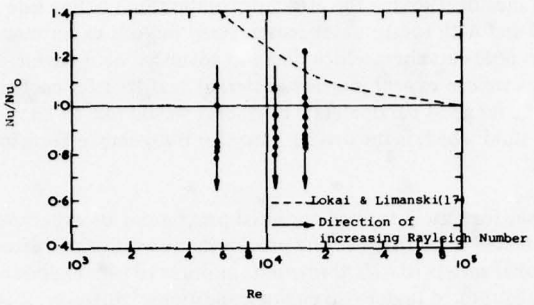

Figure 7: Experimentally Determinead Relative Mean Nusselt Numbers for a Radially Rotating Tube (Rotational Speed = 1000 rev/min)

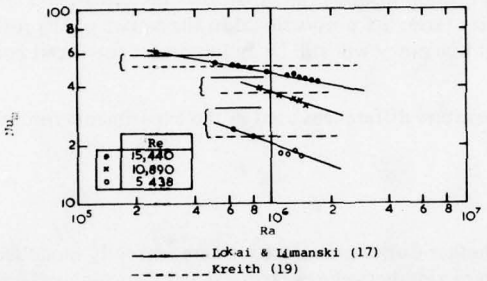

Figure 8: Typical Effect of Rotational Buoyancy on Heat Transfer in a Radially Rotating Tube (Rotational Speed = 1000 rev/min)

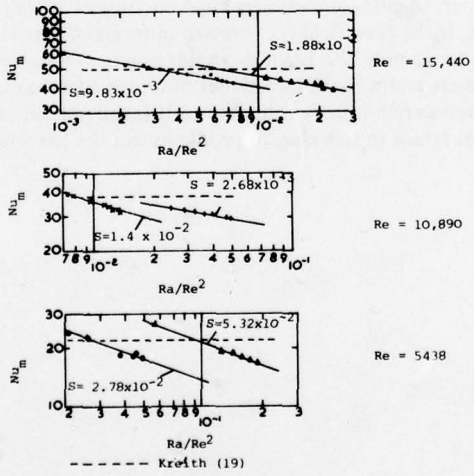

Figure 9 : Typical Effect of Coriolis Acceleration and Centrifugal Buoyancy on Heat Transfer in a Radially Rotating Tube

DISCUSSION

R.Eggebrecht, Germany

I fully appreciate the importance of studying the effect of rotation on cooling side heat transfer coefficients. From dimensions you have quoted and with rotational speeds covered in your experiments, I got the impression that we are far beyond rotational Reynolds numbers which occur in advanced aero engine turbines. So, we hopefully are on the better side, that means we can expect increased internal heat transfer coefficient. Would you please comment and do you plan to extend the range of parameters? Further, I would like to know the actual temperature difference between wall and fluid which is the driving force for buoyancy effects in your experiments.

Author's Reply

The tests reported in the paper for Case 2 formed an initial programme of experiments to see if any significant bouyancy effect could be detected in addition to the previously noted Coriolis effect. In this respect, it was decided to treat relatively low rotational speeds (0–2000 rev/min) in order to gain experience with the equipment before moving into higher speeds encountered under real engine conditions. However, it is intended to work towards engine conditions in the future programmes envisaged.

Although the Coriolis effect and its implied improvement in heat transfer will be increased at rotational speeds encountered in the turbine application it should be noted that the centripetal terms will tend to increase more rapidly due to the fact that these terms are proportional to the square of the rotational speed. It is the present author's opinion therefore that buoyancy will still be an important feature at conditions in the turbine operating range.

The average wall to fluid temperature differences used in the experiments for motivating heat transfer were typically in the range 20–60°Celsius.

B.W.Martin, UK

I am not quite clear how or whether Coriolis accelerations are correctly modelled by Rossby numbers incorporating the tip speed in view of the interaction between centrifugal and Coriolis accelerations.

Author's Reply

It is true that there is an interaction between the Coriolis and centripetal accelerations in the flow systems described in the paper. The choice of non-dimensional groups to aid quantification of these effects is to some extent within the control of the analyst. To amplify, if the basic conservation equations are non-dimensionalised according to the suggestion given in the paper, then the non-dimensional coefficient arising from the Coriolis terms has the so-called Rossby number character. If the flow field is expressed in terms of a local Reynolds number variation then the coefficient of the Coriolis terms now also has a Reynolds number character, but formed with a measure of peripheral speed as the velocity representation. Both techniques of representation can be used but do not overcome the fact that the two rotational effects are mutually interactive. It is the present author's opinion that only by a theoretical and extensive experimental attack in this class of problems can the two effects be unravelled.

CALCULATION OF TEMPERATURE DISTRIBUTION IN DISKS AND COOLING FLOW IN A TRANSIENT STATE

M. Caprili and R. Lazzeretti
Faculty of Engineering
University of Pisa
PISA - ITALY

SUMMARY

The present paper determines, for a transient state, the temperature distribution in irregularly shaped disks and that of the cooling fluid.
The method of calculation used is described, and the stability of the numerical solution is discussed.
The calculation program makes it possible to evaluate the influence of the functional parameters λ, P, α, etc., on temperature distribution.
Lastly, examples of the results obtained are shown in diagram form.

LIST OF SYMBOLS

- a = radius at disk bore
- b = radius at disk rim
- c_f = specific heat of cooling air
- c_s = specific heat of disk material
- d = thickness of cooling air
- P = mass flow rate of cooling air over disk (both faces)
- $s(x)$ = function for the variation of disk-thickness at radius
- t = time
- T_o = starting temperature of disk and inlet temperature of the cooling air
- T_1 = combustion gas temperature
- x = arbitrary radius
- y = temperature of disk at radius x
- z = temperature of cooling air at radius x
- α = heat-transfer coefficient between disk and cooling air
- α_g = heat-transfer coefficient between combustion gas and disk
- λ = thermal conductivity of disk material
- $\alpha' = \alpha g/\lambda$
- ρ_f = density of the cooling air
- ρ_s = density of disk material
- $k = 2\alpha/\lambda$
- $k' = \rho_s c_s/\lambda$
- $k_1 = 4\pi \alpha/c_f P$
- $k_1' = 2\pi d \rho_f/P$

INTRODUCTION

Reliable calculations of stress and predictions of component fatigue lives call for a precise knowledge of temperature distribution in the disk of the axial gas turbine engine.
A number of valuable papers deal with boundary layer behaviour on rotating disks.
One type of study investigates disk heating phenomena which, as is well known, are very complex and closely dependent on the specific characteristics of engine design. Two recently published papers - the first by Bailey and Owen [1] and the second by Evans [2] - have offered important contributions in this field. The first paper discusses the entrained flow question and heat transfer coefficients; the second is a survey of how the temperature distribution of axial gas turbine disks may be analysed. It includes a comparison between heat transfer correlations and boundary conditions applicable in the steady state.
A second type of study posits a simplified model and elaborates methods of calculation for the determination of analytical or numerical solutions to the differential equations governing heat-transfer phenomena. An early work by Oprecht [3] combines analytical and experimental considerations. Brown and Markland offer a range of solutions to a series of differential equations [4], while Cox [5] uses a step-by-step graphical construction to calculate the transient temperature distribution in a compressor disk.
In this paper a method is proposed for an approximate solution of the differential system governing the disk-fluid thermal equilibrium. In this procedure only the spatial variable has been made discrete, while the temporal variable has been left continuous. The ordinary differential system thus obtained has been analytically integrated by defining the exponential of a square matrix.
In addition, a method of unconditionally stable iterative calculation has been developed

by giving approximate values to this matrix exponential.
This method facilitates design studies, particularly those of a comparative nature. The calculation program makes it possible to evaluate the influence of functional parameters such as λ, P and α on temperature distribution.
A more complex geometrical model has been studied by us in an unpublished paper. Here the variables include shaft and seal arm attachments, and marked variations in disk section with radius. These features have demanded the application of two-dimensional techniques, using finite element solutions which appear to give satisfactory results.

2 - FUNDAMENTAL EQUATIONS AND NUMERICAL SOLUTION

Fig. 1 shows a disk whose thickness s(x) is a function of the radius. The periphery of the disk receives a supply of heat, which is removed by forcibly convected cooling air. The air reaches the inner radius at a known temperature To and moves outwards over both surfaces of the disk. The mass flow rate is P. Given the thickness of the disk, it is assumed that temperature variation along the axis is negligible. In this case, the differential systems which governs the disk-fluid thermal equilibrium, as deduced in [6], is:

$$\begin{cases} \dfrac{\partial}{\partial x}\left(xs(x)\dfrac{\partial y}{\partial x}\right) - kx(y-z) = k' xs(x)\dfrac{\partial y}{\partial t} & (2.1a) \\ -\dfrac{\partial z}{\partial x} + k_1 x(y-z) = k_1' x\dfrac{\partial z}{\partial t} \quad , \quad a<x<b,\ t>0 & (2.1b) \end{cases}$$

whose solution must satisfy the initial conditions:

$$\begin{cases} y(x,0) = T_o & (2.2a) \\ z(x,0) = T_o \quad , \quad a \leqslant x \leqslant b & (2.2b) \end{cases}$$

and the boundary conditions:

$$\begin{cases} \dfrac{\partial y(a,t)}{\partial x} = 0 & (2.3a) \\ \dfrac{\partial y(b,t)}{\partial x} + \alpha' y(b,t) = \alpha' T_1 & (2.3b) \\ z(a,t) = T_o \quad , \quad t \geqslant 0 & (2.3c) \end{cases}$$

where s(x) is a real positive function in [a,b], with continuous first derivative in (a,b). In the numerical results the outline of the disk is given by the function $s(x) = c\, x^{-\beta}$, where c and β are both positive constants and β is less than one.
From (2.2) and (2.3) it can immediately be seen whether the compatibility conditions are satisfied.
To obtain an approximate solution of the differential equations (2.1)-(2.3) by means of finite differences, we first render only the spatial variable discrete, leaving the time variable continuous.
The properties of the matrix, deriving from the system of differential equations (2.1)-(2.3) are studied in this semi-discrete form.
For the sake of simplicity, we will choose a uniform subdivision of the interval a,b and name any point at which subdivision may occur: $x_i = a + i\,\frac{b-a}{n+1} = a + i\,h$, $i = 0,1,..,n+1$.
Integrating (2.1) between $x_{i-\frac{1}{2}} = x_i - \frac{h}{2}$ and $x_{i+\frac{1}{2}} = x_i + \frac{h}{2}$, and naming $s_{i+\frac{1}{2}}$ as $s(x_i + \frac{h}{2})$, $y_{i+\frac{1}{2}}$ as $y(x_i + \frac{h}{2})$ etc., we obtain:

$$\begin{cases} x_{i+\frac{1}{2}}\, s_{i+\frac{1}{2}}\, \dfrac{\partial y_{i+\frac{1}{2}}}{\partial x} - x_{i-\frac{1}{2}}\, s_{i-\frac{1}{2}}\, \dfrac{\partial y_{i-\frac{1}{2}}}{\partial x} - k\displaystyle\int_{x_{i-\frac{1}{2}}}^{x_{i+\frac{1}{2}}} x(y-z)\,dx = \\ = k' \displaystyle\int_{x_{i-\frac{1}{2}}}^{x_{i+\frac{1}{2}}} xs(x)\frac{\partial y}{\partial t}\,dx & (2.4a) \\ -\displaystyle\int_{x_{i-\frac{1}{2}}}^{x_{i+\frac{1}{2}}} \frac{\partial z}{\partial x}\,dx + k_1 \int_{x_{i-\frac{1}{2}}}^{x_{i+\frac{1}{2}}} x(y-z)\,dx = k_1' \int_{x_{i-\frac{1}{2}}}^{x_{i+\frac{1}{2}}} x\frac{\partial z}{\partial t}\,dx & (2.4b) \end{cases}$$

Approximating the terms in (2.4) by:

$$\begin{cases} \dfrac{\partial y_{i+\frac{1}{2}}}{\partial x} = \dfrac{y_{i+1} - y_i}{h} + O(h^2) & (2.5a) \\ \dfrac{\partial y_{i-\frac{1}{2}}}{\partial x} = \dfrac{y_i - y_{i-1}}{h} + O(h^2) & (2.5b) \\ \displaystyle\int_{x_{i-\frac{1}{2}}}^{x_{i+\frac{1}{2}}} g(x)\,dx = g_i\,h + O(h^2) & (2.5c) \end{cases}$$

and, in particular, supposing that:

$$\int_{x_{i-\frac{1}{2}}}^{x_{i+\frac{1}{2}}} \frac{\partial z}{\partial x}\,dx = \frac{\partial z_i}{\partial x}\,h + O(h^2) = z_i - z_{i-1} + O(h^2)$$

equations (2.4) become:

$$\begin{cases} x_{i+\frac{1}{2}}\, s_{i+\frac{1}{2}}\, \dfrac{y_{i+1} - y_i}{h} - x_{i-\frac{1}{2}}\, s_{i-\frac{1}{2}}\, \dfrac{y_i - y_{i-1}}{h} - kx_i(y_i - z_i)\,h = \\ = -k' x_i\, s_i\, \dfrac{dy_i}{dt}\,h + \hat{r}'_i & (2.6a) \\ -z_i + z_{i-1} + k_1\, x_i (y_i - z_i)\,h = -k'_1\, x_i\, \dfrac{dz_i}{dt}\,h + \hat{r}''_i & (2.6b) \end{cases}$$

Overlooking the final terms within (2.6), we obtain the linear differential equations which are an approximation of the differential system (2.1) at the point x_i.
The (2.6) equations hold for all the x_i points within the interval [a,b].
When i=1 and i=n, unknowns y_0 and y_{n+1} appear in (2.6a); these may be eliminated using the boundary condition (2.3a),(2.3b).
In fact, giving approximate values the derivatives less than $O(h^2)$,(2.3a) and (2.3b) yeld:

$$\begin{cases} y_0 \cong \dfrac{4y_1 - y_2}{3} & (2.7a) \\ y_{n+1} \cong \dfrac{2h\alpha' T_1 + 4y_n - y_{n-1}}{2h\alpha' + 3} & (2.7b) \end{cases}$$

We thus obtain a system of 2n linear differential equations of the first order with constant coefficients where the unknown vector is:

$$\underline{u}^T(t) = [y_1, y_2, \ldots, y_n, z_1, z_2, \ldots, z_n]$$

which may be written in the matrix form:

$$C\,\frac{d\underline{u}(t)}{dt} = -A\,\underline{u}(t) + \underline{B} + \underline{\hat{r}}(t) \qquad (2.8)$$

where A and C are real matrices of the order of 2n and $\underline{B}$ a vector with 2n components.
We may now write the matrix A, the diagonal matrix C and the vector $\underline{B}$ in the differential problem (2.8).
Where the unknows are called u_i,(2.6a) becomes:

$$x_{i+\frac{1}{2}}\, s_{i+\frac{1}{2}}\, \frac{u_{i+1} - u_i}{h} - x_{i-\frac{1}{2}}\, s_{i-\frac{1}{2}}\, \frac{u_i - u_{i-1}}{h} - k\,x_i(u_i - u_{n+i})\,h = -k'\,x_i\,s_i\,h\,\frac{du_i}{dt} + \hat{r}'_i \qquad (2.9)$$

For i = 2,3,..., n-1, (2.9) may be rewritten:

$$-(D_i u_i - L_i u_{i-1} - U_i u_{i+1} - V_i u_{i+n}) = C_i\,\frac{du_i}{dt} + \hat{r}'_i$$

where:

$$\begin{cases} L_i = -\dfrac{x_{i-\frac{1}{2}}\ s_{i-\frac{1}{2}}}{h} \\ U_i = -\dfrac{x_{i+\frac{1}{2}}\ s_{i+\frac{1}{2}}}{h} \\ V_i = k\,h\,x_i \\ D_i = L_i + U_i + V_i \\ C_i = k'\,x_i\,s_i\,h \end{cases} \qquad (2.10)$$

Where the unknowns are called u_i, the boundary conditions (2.3a) becomes:

$$\frac{u_1 - y_0}{h} = \frac{u_2 - u_1}{3h} + O(h^2) \qquad (2.11)$$

When i=1 in (2.9), and using (2.11):

$$-(D_1 u_1 - U_1 u_2 - V_1 u_{n+1}) - C_1 \frac{du_1}{dt} + \hat{\tau}_1$$

where

$$\begin{cases} U_1 = \dfrac{1}{h}\left(x_{1+\frac{1}{2}}\ s_{i+\frac{1}{2}} - \dfrac{1}{3}\ x_{1-\frac{1}{2}}\ s_{1-\frac{1}{2}}\right) \\ V_1 = k\,x_1\,h \\ D_1 = V_1 + U_1 \\ C_1 = k'\,x_1\,s_1\,h \end{cases} \qquad (2.12)$$

Analogously, when the unknowns are called u_i, the boundary condition (2.3b) may be expressed as follows:

$$\frac{y_{n+1} - u_n}{h} = \frac{2\alpha' T_1}{2h\alpha' + 3} + \frac{(1 - 2h\alpha')\,u_n - u_{n-1}}{h(2h\alpha' + 3)} + O(h^2) \qquad (2.13)$$

When i=n in (2.9), and using (2.13): $-(D_n u_n - L_n u_{n-1} - V_n u_{2n}) + B_n - C_n \dfrac{du_n}{dt} + \hat{\tau}_n$

where

$$\begin{cases} L_n = \dfrac{1}{h}\left[x_{n-\frac{1}{2}}\ s_{n-\frac{1}{2}} - \dfrac{x_{n+\frac{1}{2}}\ s_{n+\frac{1}{2}}}{2h\alpha' + 3}\right] \\ V_n = k\,h\,x_n \\ D_n = L_n + V_n + \dfrac{2\alpha' x_{n+\frac{1}{2}}\ s_{n+\frac{1}{2}}}{2h\alpha' + 3} \\ B_n = \dfrac{2\alpha' T_1}{2h\alpha' + 3}\ x_{n+\frac{1}{2}}\ s_{n+\frac{1}{2}} \\ C_n = k'\,x_n\,s_n\,h \end{cases} \qquad (2.14)$$

The components $B_1, B_2, \ldots, B_{n-1}$ of vector $\underline{B}$ are zero.
Rows 1,2,...,n of matrices A and C, and components 1,2,...,n of vector B are now known.
We must now calculate rows n+1, n+2,...,2n of matrices A,C and components n+1, n+2,..., 2n of vector $\underline{B}$.
Where the unknowns in equation (2.6b) are called u_i, we obtain:

$$k_1 x_{i-n} h u_{i-n} - (1 + k_1 x_{i-n} h) u_i + u_{i-1} = k_1' x_{i-n} h \frac{du_i}{dt} + \hat{\tau}_i'' \qquad (2.15)$$

If $i = n + 2, n + 3, \ldots, 2n$, (2.15) may be expressed as:

$$- (D_i u_i - L_i u_{i-1} - V_i u_{i-n}) = C_i \frac{du_i}{dt} + \hat{\tau}_i''$$

where

$$\begin{cases} L_i = 1 \\ V_i = k_1 h x_{i-n} \\ D_i = L_i + V_i \\ C_i = k_1' h x_{i-n} \end{cases} \qquad (2.16)$$

The components $B_{n+2}, B_{n+3}, \ldots, B_{2n}$ of vector $\underline{B}$ are zero.
If $i = n + 1$, and considering the conditions given in (2.3c), (2.15) becomes:

$$- (D_{n+1} u_{n+1} - V_{n+1} u_1) + B_{n+1} = C_{n+1} \frac{du_{n+1}}{dt} + \hat{\tau}_{n+1}''$$

where

$$\begin{cases} V_{n+1} = k_1 h x_1 \\ D_{n+1} = 1 + V_{n+1} \\ C_{n+1} = k_1' h x_1 \\ B_{n+1} = T_o \end{cases} \qquad (2.17)$$

We have now determined matrices A and C, and vector B; these are now shown, in the same order, below

$$A = \left[\begin{array}{ccc|cc|cc} D_1 & -U_1 & & & & -V_1 & \\ -L_2 & D_2 & -U_2 & & & -V_2 & \\ \hline & & & -L_{n-1} & D_{n-1} \; -U_{n-1} & & -V_{n-1} \\ & & & & -L_n \quad D_n & & -V_n \\ -V_{n+1} & & & & & D_{n+1} & \\ & -V_{n+2} & & & & -L_{n+2} \; D_{n+2} & \\ \hline & & & -V_{2n-1} & & D_{2n-1} & \\ & & & & -V_{2n} & -L_{2n} \; D_{2n} & \end{array}\right]$$

$$C = h \begin{bmatrix} k'x_1 s_1 & & & & & \\ & k'x_2 s_2 & & & & \\ & & & & & \\ & & & k'x_n s_n & & \\ & & & & k_1' x_1 & \\ & & & & & k_1' x_2 \\ & & & & & \\ & & & & & k_1' x_n \end{bmatrix} \qquad \underline{B} = \begin{bmatrix} 0 \\ \cdot \\ \cdot \\ \cdot \\ \cdot \\ 2x_{n+\frac{1}{2}} s_{n+\frac{1}{2}} \alpha' T_{1/(2h\alpha'+3)} \\ T_c \\ 0 \\ \cdot \\ \cdot \\ 0 \end{bmatrix}$$

From (2.10),(2.12),(2.14),(2.16) and (2.17), it can immediately be seen that the matrix C is diagonal with positive elements, while matrix A is weakly diagonally dominant, and, as seen below, has a strongly connected graph.

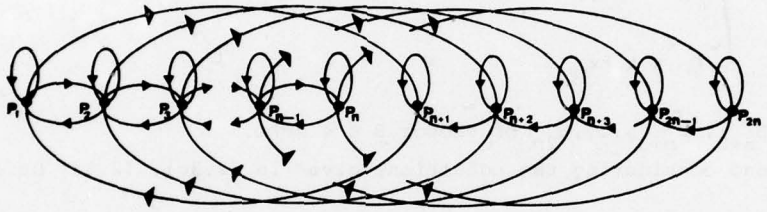

Matrices C and A are therefore non-singular. The solution of (2.8) must satisfy the initial conditions (2.2), which, in matrix notation, become:

$$\underline{u}(0) = \underline{R} \tag{2.18}$$

where $\underline{R}^T = \left[T_o, T_o, \ldots, T_o\right]$.

If T_o is a function r(x), the components of vector $\underline{R}$ are obtained using the mean integral of r(x) over the interval $\left[x_{i-\frac{1}{2}}, x_{i+\frac{1}{2}}\right]$.

The boundary conditions (2.3) are directly incorporated in matrix A and vector $\underline{B}$.

Pre-multiplying (2.8) by C^{-1}, we obtain

$$\frac{du}{dt} = -C^{-1}A\underline{u} + C^{-1}\underline{B} + \underline{\tau} \qquad , \qquad t>0 \tag{2.19}$$

where $\underline{\tau} \equiv C^{-1}\,\bar{\tau}(t)$.

To solve the linear differential system (2.19), we define the exponential series expansion

$$\exp(M) = 1 + M + \frac{M^2}{2!} + \frac{M^3}{3!} + \ldots \tag{2.20}$$

which is convergent for every square matrix M, as shown in Appendix A.
Using this definition, the only solution of (2.19) with initial condition (2.18) is:

$$\underline{u}(t) = \exp(-t\,C^{-1}A)\underline{u}(0) + \exp(-tC^{-1}A) \int_0^t \exp(\mu C^{-1}A)\,[C^{-1}\underline{B} + \underline{\tau}(\mu)]\,d\mu \qquad (2.21)$$

In this case the components of vector $\underline{B}$ are independent of time and (2.21) may be written in a simpler form:

$$\underline{u}(t) = A^{-1}\underline{B} + \exp(-tC^{-1}A)\,[\underline{u}(0) - A^{-1}\underline{B}] + \exp(-tC^{-1}A) \int_0^t \exp(\mu C^{-1}A)\underline{\tau}(\mu)d\mu \qquad (2.22)$$

Overlooking the term which includes the vector $\underline{\tau}(t)$ in (2.22), we obtain an approximate solution of the differential problem (2.1) - (2.3):

$$\underline{v}(t) = A^{-1}\underline{B} + \exp(-tC^{-1}A)\,[\underline{v}(0) - A^{-1}\underline{B}] \quad , \quad t>0 \qquad (2.23)$$

where $\underline{v}(o) = \underline{R}$.
It may be seen that (2.23) is actually the only solution to the differential equation:

$$C\,\frac{d\underline{v}(t)}{dt} = -A\,\underline{v}(t) + \underline{B} \quad , \quad t>0 \qquad (2.24)$$

obtained from (2.19) by neglecting the term $\underline{\tau}(t)$.
In (2.23) the right-hand terms correspond to the steady solution and the transient term, respectively.
Given the above properties of matrices A and C, the matrix $Q = -C^{-1}A$ is irreducible, containing non-diagonal, non-negative entries, so that the matrix exp(Qt) is positive [7]. It follows that the approximate solution to the differential equation (2.1),(2.3):

$$\underline{v}(t) = \exp(-t\,C^{-1}A)\,\underline{v}(0) + [I - \exp(-t\,C^{-1}A)]\quad A^{-1}\underline{B} \qquad (2.25)$$

associates - in line with the physical phenomena, and given that the coefficients are positive - a component of $\underline{v}(t)$ with each component of $\underline{v}(o)$, for t>o.
Another remarkable property may now be noted.
Since matrix C is positively diagonal, and matrix A is irreducible, given that it is weakly diagonally dominant with off-diagonal, non positive entries and positive diagonal entries, the only solution $\underline{v}(t)$ to (2.24) which satisfies condition (2.18) is uniformly bounded in norm for t≥o and satisfies the asymptotic relationship:

$$\lim_{t\to+\infty} \underline{v}(t) = A^{-1}\underline{B} \qquad (2.26)$$

In calculating, it is useful to approximate the exponential matrix in (2.23) using:

$$\exp(-\Delta t\,C^{-1}A) \cong (I + \frac{\Delta t}{2}\,C^{-1}A)^{-1}(I - \frac{\Delta t}{2}\,C^{-1}A) \quad , \quad \Delta t \geq 0 \qquad (2.27)$$

The approximation (2.27) not only maintains the above properties of the solution $\underline{v}(t)$, but also coincides with the expansion (2.20), if Δt is sufficiently small up to the squared term. Thus, if (2.27) is substituted in (2.23), and if we define the approximate solution at time t_o as vector $\underline{w}(t_o)$, we obtain:

$$\underline{w}(t_o + \Delta t) = (I + \frac{\Delta t}{2}\,C^{-1}A)^{-1}(I - \frac{\Delta t}{2}\,C^{-1}A) \cdot \left|\underline{w}(t_o) - A^{-1}\underline{B}\right| + A^{-1}\underline{B}\,, \Delta t > 0 \qquad (2.28)$$

where Δt is the time-interval.
If $t_o + \Delta t = (m+1)\,\Delta t$ e $\underline{w}^{(m)} = \underline{w}(t_o + m\,\Delta t)$, (2.28) defines the following iterative method:

$$\underline{w}^{(m+1)} = T(\Delta t) \left|\underline{w}^{(m)} - A^{-1}\underline{B}\right| + A^{-1}\underline{B} \qquad (2.29)$$

where $T(\Delta t) = (I + \frac{\Delta t}{2} C^{-1}A)^{-1}(I - \frac{\Delta t}{2} C^{-1}A)$, the iterative matrix.
From the recurring relationship (2.29) we obtain:

$$\underline{w}^{(m+1)} = [T(\Delta t)]^m [\underline{w}^{(o)} - A^{-1}\underline{B}] + A^{-1}\underline{B}$$

Since the iteration matrix $T(\Delta t)$, as shown in Appendix B, is unconditionally stable, the iterative procedure (2.29) converges for any initial vector $\underline{w}^{(o)}$ towards the steady solution:

$$\lim_{m \to \infty} \underline{w}^{(m)} = A^{-1}\underline{B}$$

The method outlined above has the basic advantage that no restriction is imposed on the time-interval as regards the stability of the solution. Thus a suitable choice of time-interval, as long as it is acceptable from a practical viewpoint, may offer a saving in computer-time without reducing the accuracy of the solution. This saving is considerable if, as in the present problem, the number of mesh points is large. Lastly, once the vector $\underline{w}^T = [w_1, w_2, \ldots, w_{2n}]$ has been obtained, the approximate values y_o and y_{n+1} has been calculated at time $t_o + \Delta t$, using (2.27):

$$\begin{cases} y_o \cong \dfrac{4w_1 - w_2}{3} & (2.29a) \\ y_{n+1} \cong \dfrac{2h\alpha' T_1 + 4w_n - w_{n-1}}{2h\alpha' + 3} & (2.29b) \end{cases}$$

Now that the temperature distribution has been calculated at time $m\Delta t$, it is calculated at time $(m+1)\Delta t$ and so on, until the steady solution is obtained. In practice, one stops when no appreciable variation - no more than a few degrees - is found between one solution and the next.

3 - RESULTS AND CONCLUSIONS

The calculating procedure outlined above allows a rapid and accurate evaluation of the temperature of the disk and of the cooling air, whether in transient or steady states. It also makes it possible to evaluate the influence of parameters α, β, P etc.. on changes in temperature, and to deduce which elements should be varied to maximise the efficiency of the system.
The approximation of the matrix $\exp(-\Delta t\, C^{-1} A)$, which has been adopted to obtain the approximate solution of the differential problem, provides an iterative method whose iteration matrix turns out to be unconditionally stable. It therefore follows that the iterative procedure converges, for any initial vector, towards the steady solution.
The calculating method, whose FORTRAN program is given in Appendix C, has another important advantage, that no restriction is imposed on the time-interval, as regards the stability of the solution. Thus a suitable choice of time-interval as long as this is acceptable on a practical basis, allows a saving in computer-time without reducing the accuracy of the solution.
Figs. 2-7 show some results obtained directly by the Plotter of the IBM 360/168 computer at the C.N.U.C.E., University of Pisa. These agree closely with the experimental results reported in [12].

APPENDIX A

The convergence of the matrix series (2.20) follows, as a specific case, from the THEOREM: *If A is a square matrix of order n, with complex entries, the eigenvalues of A belong to the circle of convergence of the series of powers*

$$f(z) = \sum_{k=0}^{\infty} a_k z^k \tag{A.1}$$

if and only if the series of powers

$$f(A) \equiv \sum_{k=0}^{\infty} a_k A^k \tag{A.2}$$

is convergent.

Supposing that S is a non-singular matrix which transforms matrix A by similarity transformation into the canonic form of Jordan:

$$SAS^{-1} \equiv \tilde{A} \equiv \begin{bmatrix} J_1 & & & 0 \\ & J_2 & & \\ & & \ddots & \\ 0 & & & J_r \end{bmatrix} \tag{A.3}$$

where each of the square submatrices J_l of order n, takes the form:

$$J_l = \begin{bmatrix} \lambda_l & 1 & & & 0 \\ & \lambda_l & 1 & & \\ & & \ddots & \ddots & \\ & & & \ddots & 1 \\ 0 & & & & \lambda_l \end{bmatrix}, \quad 1 \leqslant l \leqslant r \tag{A.4}$$

Since each submatrix J_l, is upper triangular, the matrix $\hat{A}$ is upper triangular, too. It follows that the set $\{\lambda_l\}_{l=1}^{r}$ is made up of all the separate eigenvalues of matrix A.

From (A.3) we obtain

$$(\hat{A})^m = \begin{bmatrix} J_1^m & & & \\ & J_2^m & & \\ & & \ddots & \\ & & & J_r^m \end{bmatrix}, \quad m \geqslant 1 \tag{A.5}$$

From (A.4), if $J_i^m \equiv (d_{i,j}^{(m)}(l)), 1 \leq i, j \leq n_l$, we obtain:

$$d_{i,j}^{(m)}(l) = \begin{cases} 0 , & j < i \\ \binom{m}{j-i} \lambda_l^{m-j+i} , & i \leq j \leq \min(n_l, m+i) \\ 0 , & m+i < j \leq n_l \end{cases} \tag{A.6}$$

where:

$$\binom{m}{k} = \frac{m!}{k!\,(m-k)!} \tag{A.7}$$

is the known binomial coefficient.
Equation (A.3) also yields:

$$A^m = S^{-1}(\hat{A})^m S \qquad , \qquad m \geq 1$$

when substituted in (A.2), this gives:

$$f(A) = S^{-1} f(\hat{A}) S$$

where

$$f(A) \equiv \sum_{k=0}^{\infty} a_k (\hat{A})^k \tag{A.8}$$

so that the theorem need be demonstrated for matrix $\hat{A}$.
Any element $f_{i,j}$ in matrix $f(\hat{A})$, using (A.5) and (A.6), yields:

$$f_{i,j} = \sum_{m=0}^{\infty} d_{i,j}^{(m)} = \begin{cases} 0 , & j < i \qquad \text{(A.9a)} \\ \sum_{m=0}^{\infty} a_m \lambda^m , & j = i \qquad \text{(A.9b)} \\ a_o + \frac{1}{s!} \sum_{m=s}^{\infty} a_m \frac{m!}{(m-s)!} \lambda^{m-s} , & j > i \qquad \text{(A.9c)} \end{cases}$$

where $s = j-i$ an λ is any eigenvalue in matrix A.
We may note that the s^{th} derivative of the series (A.1):

$$\frac{d^s}{dz^s} f(z) = \sum_{m=s}^{\infty} a_m \frac{m!}{(m-s)!} z^{m-s}$$

is identical with the summation which appears in (A.9c). Thus, if the eigenvalues in A belong to the circle of convergence of series (A.1), it may be inferred that the series (A.9b), (A.9c) and the matrix series (A.2) all converge.
On the other hand, if the series (A.2) converges, and if λ is any eigenvalue in A associated with the eigenvector $\underline{X}$, for the known equation giving the eigenvalues, we obtain:

$$\left(\sum_{m=0}^{\infty} a_m A^m\right) \underline{X} = \left(\sum_{m=0}^{\infty} a_m \lambda^m\right) \underline{X} \tag{A.10}$$

The convergence of the left-hand series in (A.10) implies the convergence of the series $\sum_{m=0}^{\infty} a_m \lambda^m$ for every eigenvalue λ in A.

Besides, it is known that this series of powers converges if the eigenvalue λ belongs to the circle of convergence the series (A.1). Q.E.D.
As a particular case of the theorem, it follows that the series (2.20):

$$\exp(A) = I + A + \frac{A^2}{2} + \dots ,$$

is convergent for any square matrix of order n with complex elements.

APPENDIX B

A matrix $T(\Delta t)$ is called unconditionally stable if its spectral radius $\rho(T(\Delta t))$ is less than one for each $\Delta t>o$.
Let us put forward the following THEOREM: *Suppose that $Q = (q_{i,j})$ is a square matrix of order n. If Q is irreducible and weakly diagonally dominant with positive diagonal entries, then the eigenvalues of Q possess the property:*

$$\mathrm{Re}\,\lambda_i > 0 \quad , \qquad 1 \leqslant i \leqslant n \tag{B.1}$$

We may note that $\lambda=o$ is now an eigenvalue of Q, so that the matrix turns out to be non-singular. It is known that the eigenvalues of Q belong to union of the circles

$$|z - q_{i,i}| \leqslant \eta_i \ , \qquad 1 \leqslant i \leqslant n \tag{B.2}$$

where

$$\eta_i = \sum_{j \neq i} {}_j \ |q_{i,j}|$$

and as matrix Q has been hypothesized as containing positive diagonal elements, it may be concluded that the union of the (B.2) contains only points on the complex plane, where the real part is positive. Q.E.D.
The matrix $C^{-1}A$ in section 2, satisfies the hypotheses of the theorem and thus has eigenvalues whose real part is positive.
From these properties it follows that the matrix $I + \frac{\Delta t}{2} C^{-1}A$ is non-singular for any $\Delta t>o$ and that the matrix:

$$T(\Delta t) = (I + \frac{\Delta t}{2} C^{-1}A)^{-1} (I - \frac{\Delta t}{2} C^{-1}A) \tag{B.3}$$

is unconditionally stable.
In fact, if λ_i is an eigenvalue of the matrix $C^{-1}A$, the eigenvalues of matrix (B.3) are:

$$(1 + \frac{\Delta t}{2} \lambda_i)^{-1} (1 - \frac{\Delta t}{2} \lambda_i)$$

Besides, the real part of $(1 + \frac{\Delta t}{2} \lambda_i)$ is greater than the real part $(1 - \frac{\Delta t}{2} \lambda_i)$ for any $\Delta t>o$, so that the spectral radius of matrix (B.3), as is now demonstrated, is less than one.

REFERENCES

1 - BAYLEY,F.J., and OWEN,J.M., "The Fluid Dynamics of a Shrouded Disk System With a radial Outflow of Coolant" J. of Eng. for Power, TRAS. ASME, Series A, Vol. 92, No.3, July 1970.

2 - EVANS, D.M. - "Calculation of Temperature Distribution in Multistage Axial Gas Turbine Rotor Assemblies When Blades Are Uncooled", ASME Paper No 73-GT-8.

3 - OPRECHT, U. - "Air Cooling of Small Gas Turbine Disks", Paper N. 21, Int. Develop. in Heat Transfer, 1961.

4 - BROWN,A., and MARKLAND, E. - "Temperature Distribution in Cooled Turbine Disks" Int. J. of Heat and Mass Transfer, Vol. 7, 1964.

5 - COX M. - "The Estimation of Transient Temperature Distributions and Thermal Stresses in Turbine and Compressor Discs. A.R.C.,C.P. n. 586, 1962.

6 - CAPRILI M. and LAZZERETTI R. - "Studio Analitico e Numerico della Distribuzione di Temperatura in dischi a Profilo Arbitrario e della Distribuzione di Temperatura nel Fluido di Raffredamento" Fac. di Ing. Università di Pisa STO0401, Settembre 1973.

7 - VARGA R.S. - "Matrix Iterative Analysis" Prentice-Hall, Inc., 1962.

8 - HOLLAND, M.J. - "Olympus 593 Turbine Cooling" Paper No 4, 36th AGARD Meeting on "High Temperature Turbines" Sept. 1970.

9 - METZGER, D.E. - "Heat Transfer and Pumping on a Rotating Disk With Freely Induced and Forced Cooling" J. of Eng. for Power, TRANS. ASME, Series A, Vol. 92, No 3, July 1970.

10 - KAPINOS, V.M. - "Heat Transfer From a Disc Rotating in a Housing With a Radial Flow of Coolant" J. of Eng. Physics, vol. 8, Jan. 1965.

11 - DORFMAN, L.A. - "Effect of Radial Flow Between the Rotating Disk and Housing on Their Resistance and Heat Transfer", Mekhanika i Mashinostroyeniye, N.4, 1961.

12 - LEWIS CENTER STAFF "Factor that Affect Operational Reliability of Turbojet Engines, NASA TR-54, 1960.

APPENDIX C

```
C       REGIME TRANSITORIC
        DIMENSION AA(3),AG(3),PA(3),IBUF(1024)
        COMMON/Z/SE,BETA,RE
        COMMON/SIS/PG,RI,C1,SF,CS,DENS,DENF,TG,TI,DT,E,M
C       RI    RAGGIO INTERNO DISCO
C       RE    RAGGIO ESTERNO DISCO
C       C1    CALORE SPECIFICO PRESSIONE COSTANTE FLUIDO
C       CS    CALORE SPECIFICO MATERIALE COSTITUENTE DISCO
C       SF    SPESSORE FLUIDO
C       P    PORTATA FLUIDO
C       T    TEMPO
C       TI    TEMPERATURA INIZIALE
C       TG    TEMPERATURA GAS COMBUSTI
C       ALFA    COEFFICIENTE CONVEZIONE FLUIDO RAFFREDDAMENTO DISCO
C       AGFA    COEFFICIENTE CONVEZIONE GAS COMBUSTI DISCO
C       SE    SPESSORE DISCO RAGGIO ESTERNO
C       DENS    DENSITA DISCO
C       DENF    DENSITA FLUIDO RAFFREDDAMENTO
C       AMDA    CONDUTTIVITA  MATERIALE DISCO
C       M    NUMERO NODI
C       DT    PASSO TEMPORALE
        CALL PLOTS (IBUF,1024,'0001-P021')
        CALL FACTOR(2.5)
        CALL PLOT(1.,1.,-3)
        L=1
        READ(5,887)PG,RI,C1,SF,CS,DENS,DENF,TG,TI,DT,E,M,SE,RE,ALFA,BETA,
       1AGFA,P,AMDA
        READ(5,888)(AA(I),I=1,3),(AG(I),I=1,2),(PA(I),I=1,2)
        WRITE(6,889)SE,RE,ALFA,BETA,AGFA,P,AMDA,PG,RI,C1,SF,CS,DENS,DENF,
       *TG,TI,DT,E,M
        DO 2 I=1,3
        ALFA=AA(I)
        CALL ROTORI (L,ALFA,AGFA,P,AMDA)
        L=L+1
 2      CONTINUE
        DO 3 I=1,2
        AGFA=AG(I)
        ALFA=0.06
        CALL ROTORI (L,ALFA,AGFA,P,AMDA)
        L=L+1
 3      CONTINUE
        DO 4 I=1,2
        P=PA(I)
        AGFA=0.2
        CALL ROTORI (L,ALFA,AGFA,P,AMDA)
        L=L+1
 4      CONTINUE
        CALL PLOT(40.,0.,999)
 887    FORMAT(F8.6,9F8.3/,F9.6,I2/,7F7.3)
 888    FORMAT(7F7.3)
 889    FORMAT(1H1,10X,'DATI',//10X,6E20.7/,10X,6E20.7/,10X,6E20.7//
       110X,'NUM.PUNTI',I3)
        STOP
        END

        SUBROUTINE ROTORI (IND,ALFA,AGFA,P,AMDA)
        COMMON/Z/SE,BETA,RE
        COMMON/SIS/PG,RI,C1,SF,CS,DENS,DENF,TG,TI,DT,E,M
        DIMENSION A(52,52),AP(52,52),SC(52),E(52),V1(52),V2(52),C(52),TA(2
       X8),TD(28),XAR(30),YAR(30)
 115    FORMAT(1H0,10X,18HTEMPERATURA ARIA  ,///(8E12.3))
 118    FORMAT(1H0,10X,18HTEMPERATURA DISCO  ,///(8E12.3))
 105    FORMAT( 1H1,10X,18HDETERMINANTE NULLO)
 110    FORMAT(1H1,10X,9HSOLUZIONE)
 111    FORMAT(1H0,5X,E10.1/,5X,(3E12.3))
 106    FORMAT(1H1,22H SOLUZIONE STAZIONARIA/)
 108    FORMAT(1H1(21HSOLUZIONE AL TEMPO T=),E12.3,15HMASSIMA V1-V2 E1=E12.3
       *)
        H=(RE-RI)/FLOAT(M)
        N=M-1
        N1=N-1
        N2=2*N
        M1=M+1
        XAR(1)=RI
        DO 101 I=2,M1
 101    XAR(I)=XAR(I-1)+H
        XAR(29)=RI
```

```
      XAR(30)=0.03
      YAR(29)=0.
      YAR(30)=80.
      CALL AXIS(0.,0.,6HRAGGIO,-6,9.,0.,XAR(29),XAR(30))
      CALL AXIS(0.,0.,18HTEMPERATURA  DISCO,18,10.,90.,YAR(29),YAR(30))
      CALL  AXIS(9.,0.,18HTEMPERATURA   ARIA,-18,10.,90.,YAR(29),
     *YAR(30))
      N3=N2+1
      CD=DENS*CS
      APFA=AGFA/AMDA
      ZK=2.*ALFA/AMDA
      ZK1=4.*PG*ALFA/(C1*F)
      N10=1
      ZKP=DENS*CS/AMDA
      ZK3=2.*PG*SF*DENF/F
      DO 100 I=1,N2
      DO100J=1,N2
  100 A(I,J)=0.
C     COSTRUZIONE MATRICE  A
      DO1I=2,N1
      X=RI+H*FLOAT(I)
      XM=X-H/2.
      XP=X+H/2.
      AL=XM*S(XM)/H
      AU=XP*S(XP)/H
      AV=ZK*H*X
      AD=AV+AL+AU
      K=I-1
      A(I,K)=-AL
      K=I+1
      A(I,K)=-AU
      A(I,I)=AD
      K=N+1
    1 A(I,K)=-AV
C     PRIMA RIGA
      X=RI+H

      XM=X-H/2.
      XP=X+H/2.
      AU=(XP*S(XP)-XM*S(XM)/3.)/H
      AV=ZK*H*X
      AD=AV+AL
      A(1,1)=AD
      A(1,2)=-AU
      K=N+1
      A(1,K)=-AV
C     N-MA RIGA
      X=RI+H*FLOAT(N)
      XM=X-H/2.
      XP=X+H/2.
      AL=(XM*S(XM)-XP*S(XP))/(2.*H*APFA+3.))/H
      AV=ZK*H*X
      AD=AV+AL+(2.*APFA/(2.*H*APFA+3.))*XP*S(XP)
      A(N,N1)=-AL
      A(N,N)=AD
      A(N,N2)=-AV
C     PARTE MATRICE  A  PER ALTRI PUNTI INTERNI. PER I=N-2 SI HA IL SECONDO
C     PUNTO INTERNO
      DO3I=M1,N2
      X=RI+H*FLOAT(I-N)
      AL=1.
      AV=ZK1*H*X
      AD=AL+AV
      K=I-1
      A(I,K)=-AL
      A(I,I)=AD
      K=I-N
    3 A(I,K)=-AV
C     N&1-MA RIGA
      X=RI+H
      AV=H*ZK1*X
      AD=1.+AV
      K=N+1
      A(K,K)=AD
      A(K,1)=-AV
C     COSTRUZIONE VETTORE  B
      DO201I=1,N2
  201 B(I)=0.
      X=RI+H*FLOAT(N)
      XP=X+H/2.
      B(N)=XP*S(XP)*2.*APFA*TG/(2.*H*APFA+3.)
      B(M)=TI
```

```
      DO 150 I=1,N2
      DO150J=1,N2
  150 AP(I,J)=A(I,J)
      DO14I=1,N2
   14 SC(I)=B(I)
      CALL GELG(SC,AP,N2,1,E,IER)
      IF(IER.NE.0) GO TO 400
C     TEMPERATURA AI BORDI
      TD(1)=(4.*SC(1)-SC(2))/3.
      TD(M1)=(2.*H*APFA*TG+4.*SC(N)-SC(N-1))/(2.*H*AFFA+3.)
      TA(1)=TI
      TA(M1)=(SC(N2)+H*ZK1*RE*TC(M1))/(1.+ZK1*H*RE)
      WRITE(6,106)
      DO 700 I=1,N
      J=I+1
      TD(J)=SC(I)
      I5=I+N
  700 TA(J)=SC(I5)
      WRITE(6,800)P,AGFA,ALFA
  800 FORMAT( 1H0,'PORTATA#',E12.3,'AGFA#',E12.3,'ALFA#',E12.3)
      WRITE(6,118) (TD(I),I=1,M1)
      WRITE(6,119) (TA(I),I=1,M1)
      DO 102 I=1,M1
  102 YAR(I)=TD(I)
      CALL LINE (XAR,YAR,28,1,4,0)
      DO 103 I=1,M1
  103 YAR(I)=TA(I)
      CALL LINE (XAR,YAR,29,1,4,2)
       CALL SYMBOL (1.,6.,0.3,7HALFA # ,0.0,7)
      CALL NUMBER (999.,999.,0.3,ALFA,0.,2)
      CALL SYMBOL (1.,5.4,0.3,7HAGFA # ,0.0,7)
      CALL NUMBER(999.,999.,0.3,AGFA,0.,2)
      CALL SYMBOL(1.,4.8,0.3,7HP     # ,0.0,7)
      CALL NUMBER(999.,999.,0.3,P,0.,3)
      DO32I=1,N
      X=RI+FLOAT(I)*H
      C (I)=H*ZKP*X*S(X)
      K=I+N
   32 C(K)=H*ZK3*X
C     E1#NORMA ERRORE
      E1=0.
      T=0.
      DO15I=1,N2
   15 V1(I)=TI
      WRITE(6,108) E1,T
      TD(1)=TI
      TD(M1)=TI
      TA(M1)=TI
      TA(1)=TI
      DO 301 I=1,N
      J=I+1
      TD(J)=V1(I)
      I5=I+N
  301 TA(J)=V1(I5)
      WRITE(6,118) (TD(I),I=1,M1)
      WRITE(6,119) (TA(I),I=1,M1)
      DO34I=1,N2
   34 C(I)=1./C(I)
C     VETTORE DT*C-1*B#B
      DO36I=1,N2
   36 B(I)=C(I)*B(I)*DT
C     MATRICE    I-DT*C-1*A/2*A
      DO38I=1,N2
      DO38J=1,N2
      A(I,J)=-DT*C(I)*A(I,J)/2.
      IF(I.EQ.J)A (I,J)=A (I,J)+1.
   38 CONTINUE
C     VETTORE DEI TERMINI NOTI
  300 DO 39 I=1,N2
      V2(I)=B(I)
      DO 39 J=1,N2
   39 V2(I)=A(I,J)*  V1(J)+V2(I)
C     MATRICE  I&DT*C-1*A/2*A
      DO 41 I=1,N2
      DO 41 J=1,N2
      A(I,J)=-A(I,J)
      IF(I.EQ.J) A(I,J)=A(I,J)+2.
   41  CONTINUE
      DO 42 I=1,N2
      DO 42 J=1,N2
   42 AP(I,J)=A(I,J)
```

```
      CALL GELG (V2,AP,N2,1,E,IER)
      IF(IER.NE.0) GO TO 400
      TD(1)=(4.*V2(1)-V2(2))/3.
      TD(M1)=(2.*H*APPA*TG+4.*V2(N)-V2(N-1))/(2.*H*APPA*3.)
      TA(1)=TI
      R1=RE*H
      TA(M1)=(V2(N2)+ZK1*R1*TD(M1)+ZK3*RE*H*V1(N2)/DT)/(1.+ZK1*R1+ZK3*
     XRE*H/DT)
      DO 302 I=1,N
      J=I+1
      TD(J)=V2(I)
      IS=I+N
  302 TA(J)=V2(IS)
      T=T+DT
C     CALCOLO DI NORMA |V2-V1|
      E1=ERR(V1,V2,N2)
      KS=MOD(N10,10)
      IF(KS.NE.0)GO TO146
      WRITE(6,108) T,E1
      WRITE(6,118) (TD(I),I=1,M1)
      WRITE(6,119) (TA(I),I=1,M1)
      DO 104 I=1,M1
  104 YAR(I)=TD(I)
      CALL LINE (XAR,YAR,28,1,4,0)
      DO 99 I=1,M1
   99 YAR(I)=TA(I)
      CALL LINE (XAR,YAR,28,1,4,2)
  146 IF(E1.LT.S.) GO TO 145
      E1=ERR(SC,V2,N2)
      IF(E1.LT.S.) GO TO 1000
  145 DO 115 I=1,N2
  115 V1(I)=V2(I)
C     TORNIAMO ALLA MATRICE   I-DT*C-1*A/2
      N10=N10+1
      IF(N10.GE.50)GO TO 1000
      DO 121 I=1,N2
      DO 121 J=1,N2
      A(I,J)=-A(I,J)
      IF(I.EQ.J) A(I,J)=A(I,J)+2.
  121 CONTINUE
      GO TO 300
  400 WRITE(6,105)
 1000 IF(IND.LT.2) GO TO 1001
      CALL PLOT(11.,-12.,-3)
      IND=0
      GO TO 1002
 1001 CALL PLOT(0.,12.,-3)
 1002 RETURN
      END

      FUNCTION S(X)
      COMMON/Z/SE,BETA,RE
      S=SE*(RE/X)**BETA
      RETURN
      END

      FUNCTION ERR(V1,V2,N2)
      DIMENSION V1(N2),V2(N2)
      AM=ABS(V1(1)-V2(1))
      ERR=AM
      DO 1 I=2,N2
      AM1=ABS(V1(I)-V2(I))
      IF(ERR.GE.AM1) GO TO 1
      ERR=AM1
    1 CONTINUE
      RETURN
      END
```

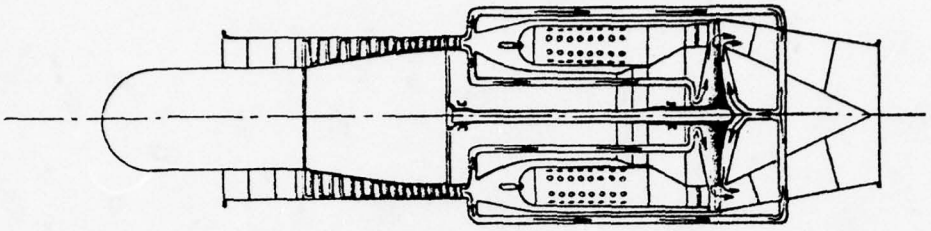

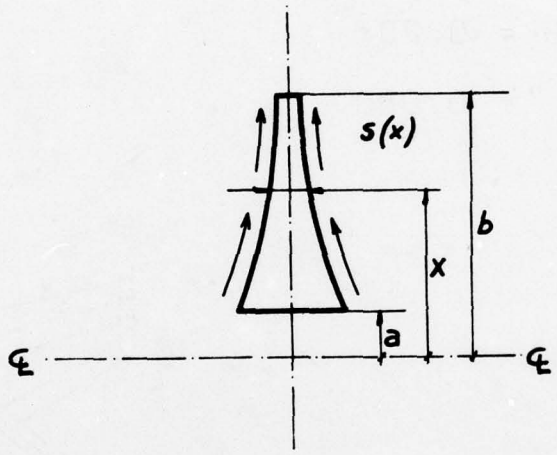

Figure 1

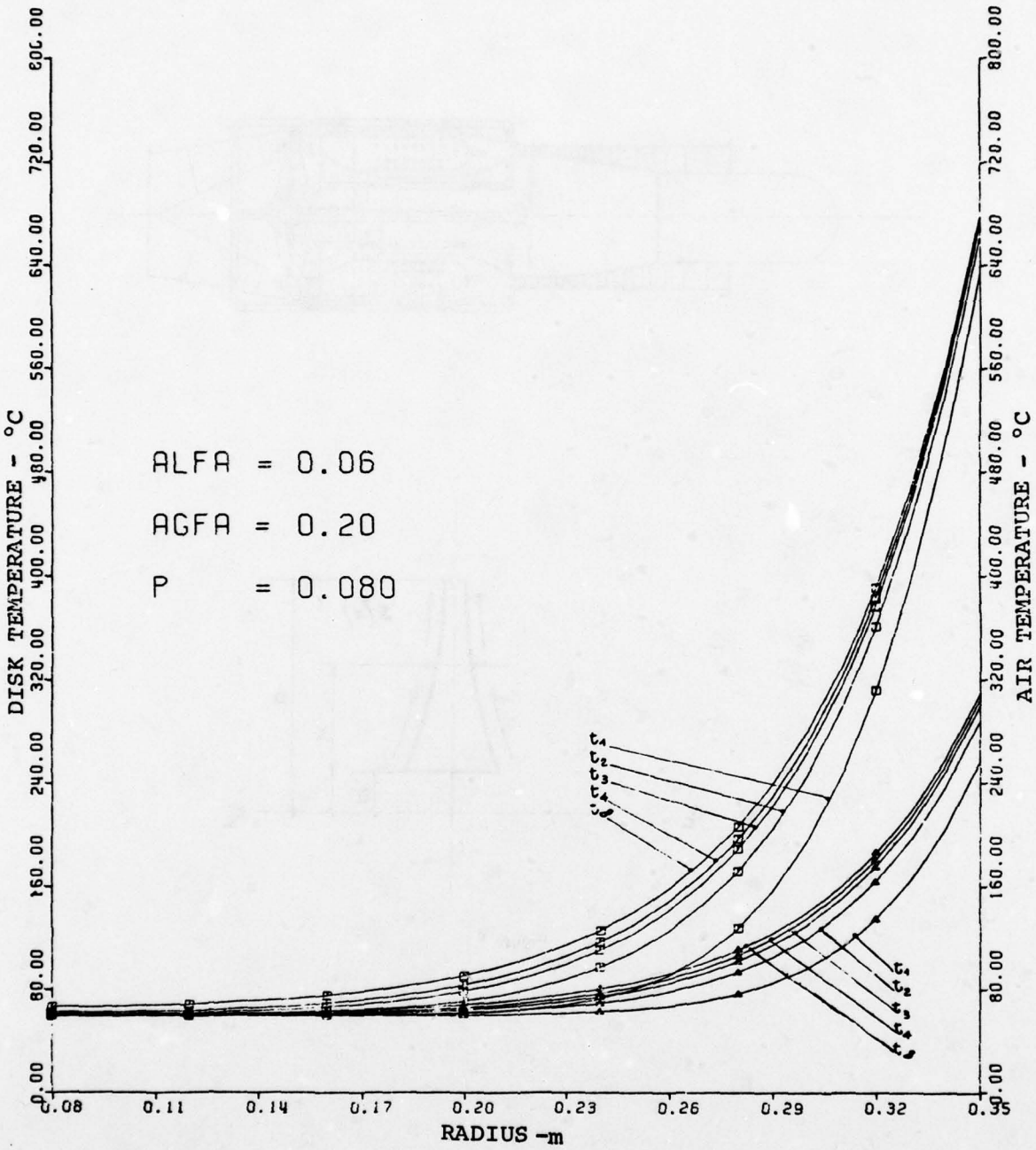

Fig.2 □ – Disk temp, △ – air temp, $t_1 = 5'$, $t_2 = 10'$, $t_3 = 15'$, $t_4 = 20'$, t_∞ = steady solution

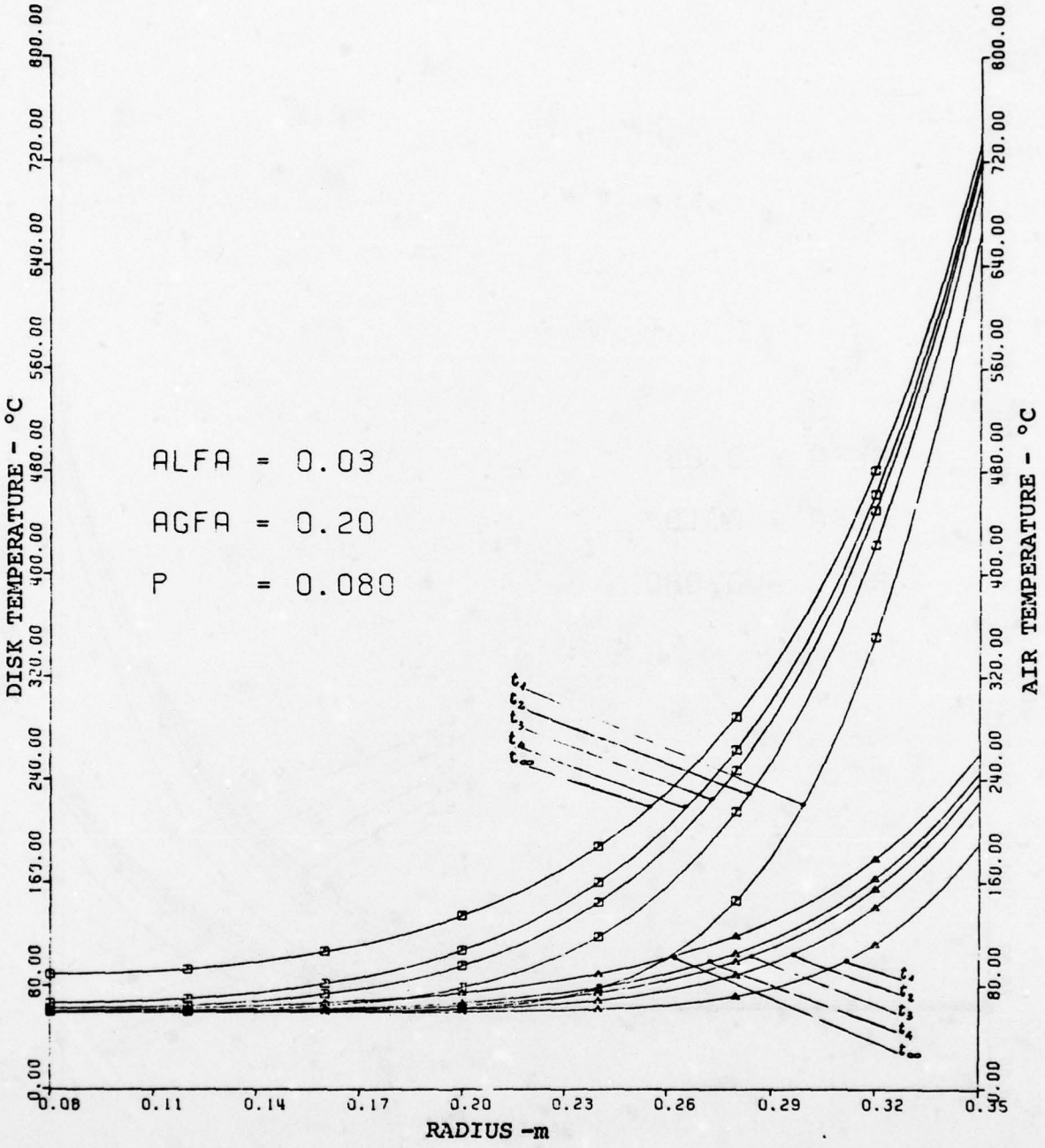

Fig.3 □ – Disk temp, △ – air temp, $t_1 = 5'$, $t_2 = 10'$, $t_3 = 15'$, $t_4 = 20'$, t_∞ = steady solution

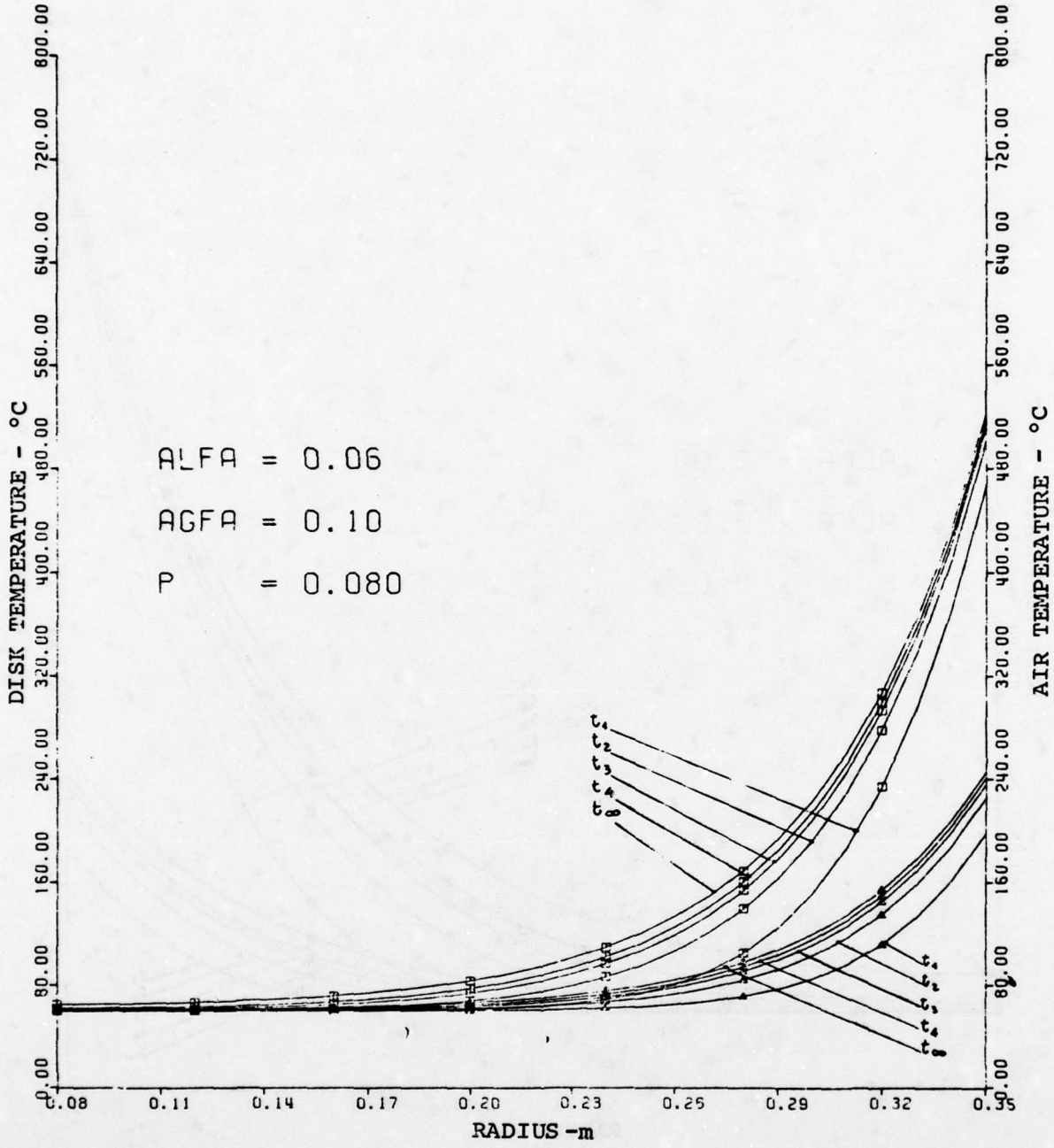

Fig.4 □ – Disk temp, △ – air temp, $t_1 = 5'$, $t_2 = 10'$, $t_3 = 15'$, $t_4 = 20'$, t_∞ = steady solution

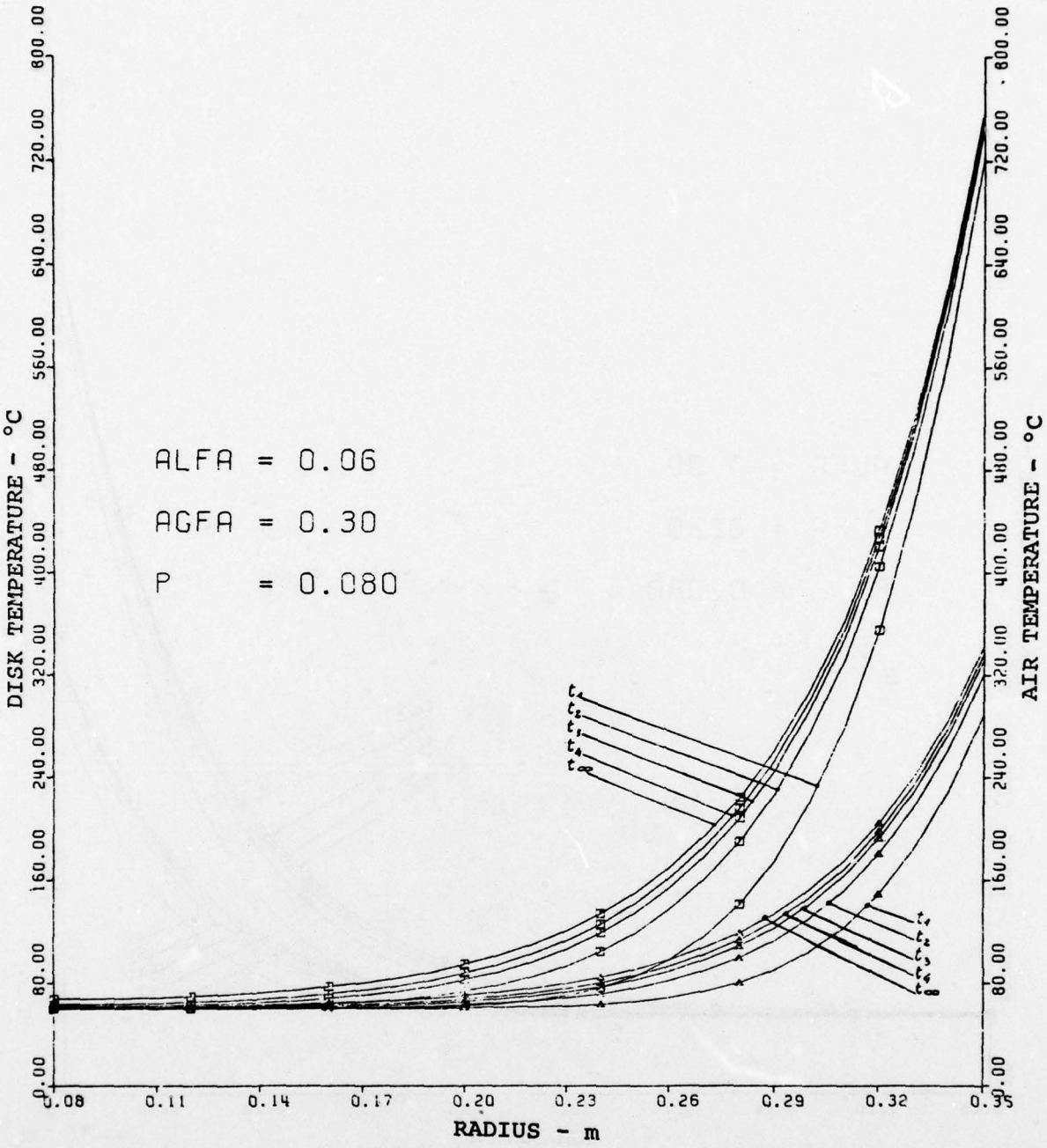

Fig.5 □ – Disk temp, △ – air temp, $t_1 = 5'$, $t_2 = 10'$, $t_3 = 15'$, $t_4 = 20'$, t_∞ = steady solution

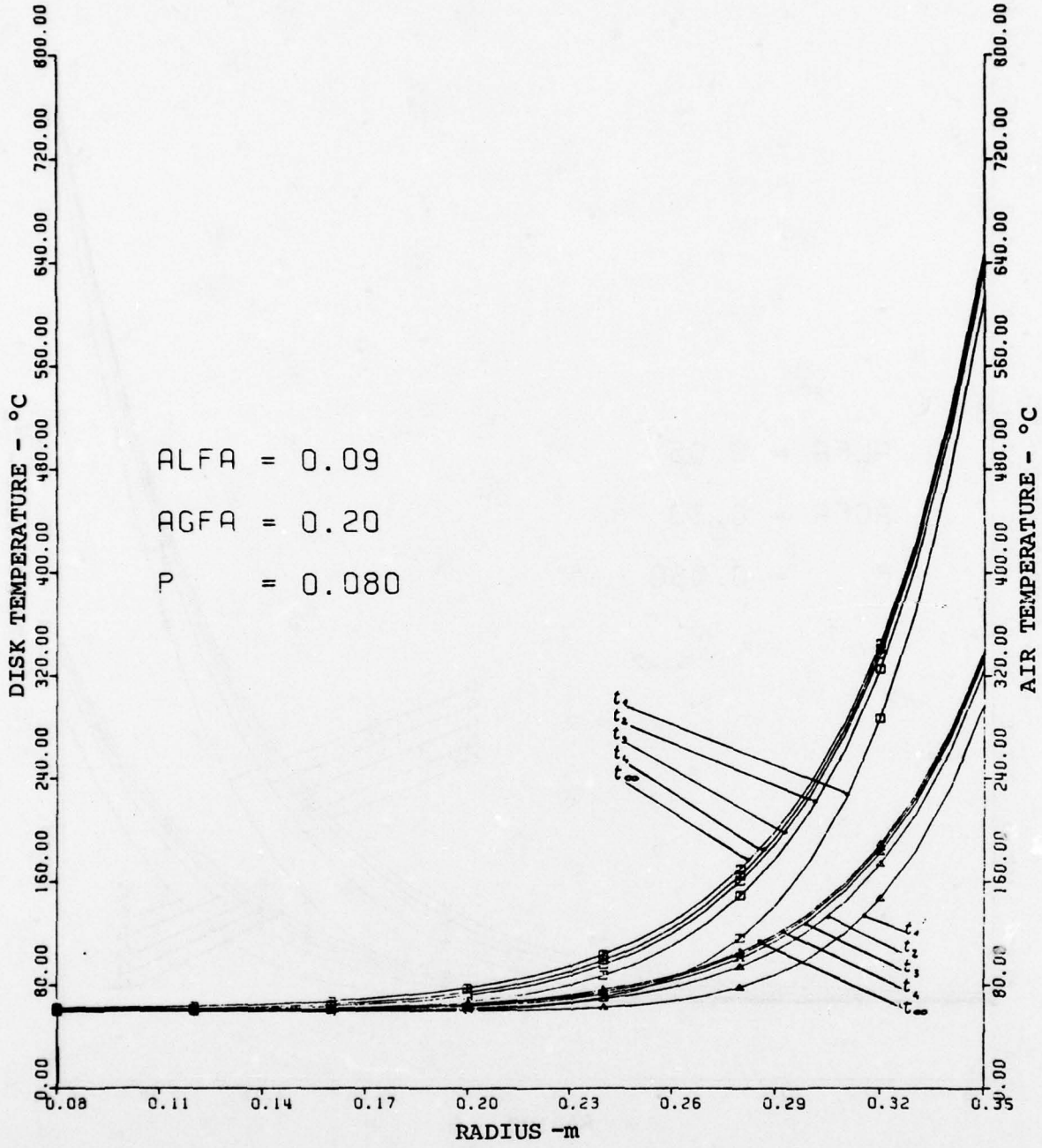

Fig.6 □ – Disk temp, △ – air temp, $t_1 = 5'$, $t_2 = 10'$, $t_3 = 15'$, $t_4 = 20'$, t_∞ = steady solution

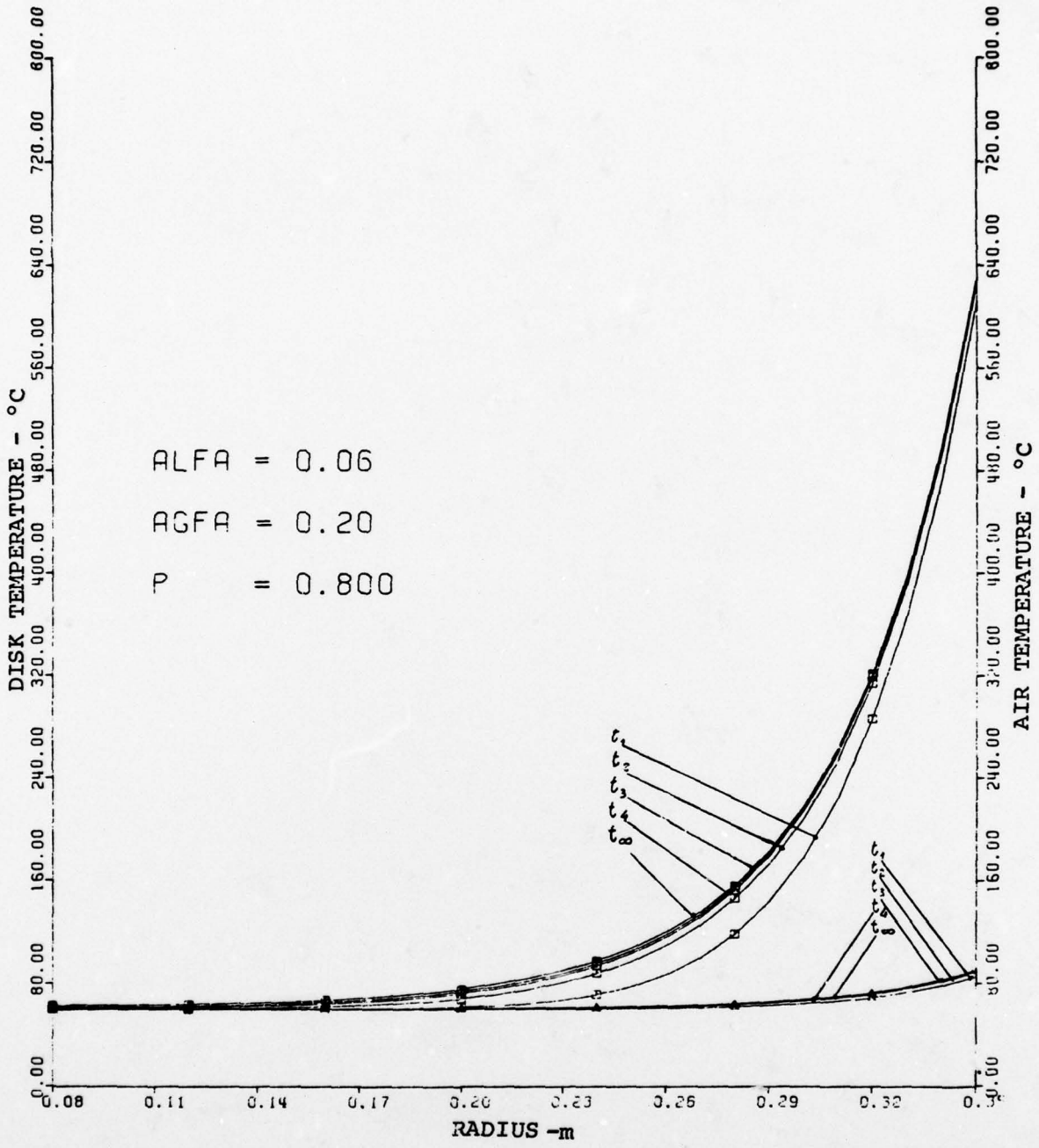

Fig.7 □ – Disk temp, △ – air temp, $t_1 = 5'$, $t_2 = 10'$, $t_3 = 15'$, $t_4 = 20'$ t_∞ = steady solution

A COMPARISON BETWEEN PREDICTED AND MEASURED SPECIES CONCENTRATIONS AND VELOCITIES IN A RESEARCH COMBUSTOR

Dr. W.P. Jones
Department of Chemical Engineering,
Imperial College, London SW7 2BX -
Formerly Rolls-Royce Ltd., Derby

W.C. Clifford
National Gas Turbine Establishment
Pyestock, Hampshire GU14 OLS

Dr. C.H. Priddin
Rolls-Royce Ltd. Aero Division
P.O. Box 31, Derby, DE2 8BJ

R de Chair,
Rolls-Royce Ltd. Aero Division
P.O. Box 3, Bristol, BS12 7QE

SUMMARY

A comparison is presented between the predictions of a mathematical model of chemically reacting flow and measurements of species concentrations and velocities in a small scale research combustor burning propane and air. The mathematical model is a three-dimensional finite difference method for solving the time-averaged conservation equations in turbulent flow. The Reynolds stress terms are modelled with a two-equation ($k - \epsilon$) model of turbulence and account is taken of the effect of turbulent fluctuations on the combustion reactions. Generally good agreement is obtained between predictions and measurements which include local gas velocities and the important chemical species (H_2O, O_2, N_2, CO_2, CO, and UHC). The tests were performed with an air inlet temperature of 570 K, a chamber pressure of 2.1 bar and an equivalence ratio of 0.69 in the primary zone (0.34 overall).

Nomenclature

a	Coefficient in equation 13
b	Constant in equation 21
C_B	Constant controlling dissipation of concentration fluctuations
C_{F1}	Constant controlling production of
C_{E2}	Constant controlling dissipation of
C_μ	Constant in turbulent viscosity (equation 9)
e	Deformation tensor
g	Metric tensor
k	Turbulence energy
h	Enthalpy
p	Static pressure
R_{CO2}	Rate of formation of CO_2 by chemical reaction
t	time
U	Velocity tensor
X_H	Mass fraction of hydrogen element
X_{CO2}	Mass fraction of CO_2
δ	Kronecker delta
δH	Fluctuation in hydrogen element
ϵ	Dissipation rate of turbulence energy
μ	Viscosity
ρ	Density
σ_k	"Prandtl/Schmidt number" for diffusion of k
σ_ϵ	"Prandtl/Schmidt number" for diffusion of E

Subscripts & Superscripts

i, j, l, m	Tensor indices
T	Turbulent
1, 2	Elements of probability distribution
$\widehat{\ }$	"Favre" average
$\overline{\ }$	Ensemble (or time) average
'	Fluctuating value
max	Maximum value
air	of air inlet stream
fuel	of fuel inlet stream

1. INTRODUCTION

For many years the design of gas turbine combustion chambers has been based on the use of empirical models of flame behaviour which attempt to correlate overall performance with inlet air conditions and simple geometrical factors such as chamber volume. These techniques have been successful, but only when used for the extrapolation of well proven designs to combustors of essentially similar shape. Any large scale departures from established geometries would require the development of new correlations to ensure reliable prediction.

Even in situations where the overall performance of a combustor design could be predicted with some confidence it has still been beyond the designer's capabilities to describe accurately the more detailed features of the flame such as outlet temperature traverse. There has always been, therefore, a motive for improvement in combustion prediction procedures but until recently neither the requirement nor the means available has been powerful enough to merit any large divergence from tradition. The current emphasis on research into combustion generated aircraft pollution and the availability of both advanced numerical methods and third-generation digital computers has swung this balance. There is now a great deal to be gained from a fundamental change in the way combustors are designed and good reason to believe that this change can be carried out successfully.

With the prediction of combustor based pollutant levels as an ultimate goal, Rolls-Royce Ltd and NGTE have been developing an advanced prediction procedure for gas turbine combustion. Concurrent with this development a small-scale high temperature and pressure combustor research facility was installed at NGTE and equipped with extensive gas analytical and other instrumentation.

2. THE EXPERIMENTAL ARRANGEMENT

2.1 The NGTE model combustor facility

The original version of the NGTE model was purpose-built for flame radiation measurements and a detailed description has been published (1)*. Throughput limitations of this early chamber resulted in high heat losses from the flame and provided the motive for the design and construction of the present model combustor facility. Five separately controlled and metered air inlet supplies are available, four at up to 50 bar and one at up to 100 bar. Total air mass flows at the two pressures are 0.9 kg/s and 0.12 kg/s respectively. Three of the 50 bar supplies may be heated independently, without vitiation, to provide air inlet temperatures ranging from $\sim$ 300 K to 1000 K. All supplied air is dried to a dewpoint of approximately 233 K. The facility includes three fuel supply systems, one for gaseous propane and two for aviation kerosine. The current design of combustor outer shell, exhaust valve and probe traversing system has allowed operation at up to 40 bar combustor operating pressure.

2.2 Combustion chamber

The experimental data reported in this paper were obtained from the combustion chamber shown in Figure 1. Primary zone air was admitted to the chamber by a straight-bladed 20° swirler fitted into the flat base-plate and fed from a high pressure-drop radial distribution system. Propane fuel was introduced, as vapour, by means of a simple burner, as shown, with equi-spaced holes around its periphery. These holes were aligned so as to direct the radial propane jets across the downstream edges of the corresponding swirler vanes. Remaining areas of the baseplate were either conduction or convection cooled with any cooling air exhausted separately to atmosphere.

The combustor liner was a cylinder manufactured from a fabricated transpiration-cooled material. Air supply to the cooled wall and the six equi-spaced dilution holes was via two plenum chambers surrounding the cylinder itself. The downstream, converging section of the chamber was non-porous and was a close sliding fit over the end of the main cylinder.

The rig was fitted with a multi-degree-of-freedom traversing apparatus which allows a probe to be positioned with its tip anywhere in the combustion space and with any orientation about its own axis. Operation of the combustor was entirely remote and measurement of inlet air and fuel flows and all other important rig parameters was carried out by a dedicated on-line computer system providing real-time display of operating conditions.

2.3 Gas Analysis

Gas samples were acquired by means of a water-cooled single-point cylindrical probe with the central tube temperature held at approximately 340 K. The sample was transferred from the probe to the instruments via 5 m of 5 mm bore stainless steel tube heated to 420 K. A wide range of gas analysis equipment is available in the facility. Results published in the paper were obtained from three instruments, as follows :-

a. A multi-component integrated chromatograph measuring H_2, O_2, N_2, CO_2 and CO concentrations in a dried sample.

b. A slug injection flame ionisation detector for determination of unburnt hydrocarbon levels as CH_4 equivalent.

c. A chemiluminescence NO meter equipped with a stainless steel reducing converter for NO_x (and hence NO_2) measurement.

* Numbers in brackets in the text designate references at end of paper.

Control of the instruments was automatic and data handling, including integration of chromatographic peaks, system calibration and noise rejection,was carried out on-line to the computer system mentioned above.

2.4 Velocity Measurement

Velocity measurements were performed with a 7-hole spherical-end pitot probe (2). The probe head is constructed of a platinum/rhodium alloy and is connected to a water-cooled stainless steel shaft of similar length and outside diameter to the gas sampling probe.

The design and operation of the probe allows it to sense velocity direction and magnitude at any point in the chamber while requiring only a single point of access. As for the gas analysis measurements, all velocity data were handled on-line by the computer system.

3. DISCUSSION OF EXPERIMENTS

In this section we discuss the experimental results obtained and comment on their accuracy and general suitability for comparison with numerical predictions. Only a limited fraction of the data is presented in the paper. Three major features are discussed; the accuracy of the data in absolute terms, the closeness of the flame to the required symmetry and the production of nitrogen oxides in relation to the theoretical model most commonly used for predictions.

3.1 Accuracy

Since all experimental data were obtained with physical sampling probes they are subject to the complication of flow disturbance by the probe and associated inaccuracy. The paper makes no attempt to shed light on this well known problem except to say that the probes used were as small as were consistent with rigidity and long life. A more subtle biasing of the data resulting from the use of physical probes is the influence of density fluctuations on the composition of the time-averaged sample. Once again, we make no attempt to assess this quantitatively but suggest that both the gas analytical and velocity data presented here will be closer to Favre (3) averages than simple time averages - they will tend to be mass weighted by the probes' sampling action. Having once acquired the sample, there exists, in the case of gas analysis, a further potential source of error from continuing reaction in the probe and transfer line itself. In practice this is minimised by thermostatic control of these items and in the current context is thought to result in negligible inaccuracy compared with, for instance, the flow disturbance caused by the probe.

We shall now consider the data from the point of view of repeatability and self-consistency. Both the gas analysis instrumentation and the velocity probe pressure transducers exhibited a mean repeatability of better than 0.5 per cent and estimated test point setting accuracy was ±2 per cent referred to outlet fuel/air ratio. Point-to-point repeatability of the gas analytical measurements was of the order of ±4 per cent of reading over the entire range of conditions covered.

A comparison between metered air mass flow and a mass flow integrated from the velocity measurements is given in Table I.

TABLE I

Distance from baseplate (mm)	Metered flow (g/s) (uniform cooling air injection)	Mass flow calculated from integrated velocity data (g/s)	
		Cold	Hot
17	48.9	25.0	57.7
27	49.9	35.3	58.1
47	52.1	37.7	61.1
67	54.3	38.0	-
87	56.5	38.2	-
107	58.7	72.2	-
137	88.9	67.7	-
165	92.0	109.3	-

This shows inconsistency in the probe data and generally poor agreement with the metered flow rates which may be attributable to two shortcomings in the velocity measurement technique. In the first place the rectangular sampling grid does not allow full coverage near the combustor wall and this could result in a finite proportion of the flow being ascribed an erroneous velocity during the integration process. Secondly, the performance of spherical probes is known to be suspect in regions of high total pressure gradient where yaw direction can be heavily biased. Despite manufacturing efforts to the contrary, the spherical probe still remains large in comparison with shear layer widths in the combustor and there is, perhaps, no reason to hope for better results.

The gas analytical results present a more successful picture, as can be seen from Figure 2. Here we are comparing metered and "measured" or "sampled" fuel/air ratios at a number of planes along the combustor. The metered line is based on the hypothesis that the cooling air is injected uniformly through the wall thus achieving the gradual reduction in fuel/air ratio. Both area weighted and a few mass weighted "sampled" fuel/air ratios are shown on this graph, the latter including the effect of the suspect velocity data discussed earlier. In general the agreement is good, improving as we progress along the chamber until the dilution zone where the relationship between metered and measured fuel/air ratios is excellent.

3.2 Traverse Symmetry

It is a well known feature of combustion chamber aerodynamics that an apparently trivial change in the boundary conditions of the flow can produce massive changes in the behaviour of the enclosed flame. An important achievement of the present work is that the flame as analysed does not depart to any significant degree from the symmetry to be expected from the chamber geometry. This is demonstrated in Figures 3 and 4 which show fuel/air ratio contours for stations 27 mm and 117 mm from the chamber baseplate, respectively. The former plot indicates a series of essentially concentric circles consistent with the swirler feed to the primary zone while Figure 4 corresponds to the dilution air entry plane. The six dilution jets are clearly visible. Circumferential averaging of the data forces axisymmetry and a comparison of such a plot with a typical diametral plane is shown in Figure 5. It is clear that this process of spatial data smoothing which is, of course, necessary (upstream of the dilution plane at least) prior to comparison with predictions does little to modify any of the salient features of the flame.

3.3 Oxides of Nitrogen

The study of NO_x production is of prime importance in the field of aero-engine pollution research because its minimisation requires the most radical departures from current combustor design practice. A comparison between adiabatic flame temperature and NO_x concentration is given in Figure 6. The region of highest temperature coincides broadly with the measured recirculation zone (Figure 9) but there is no similar relationship with the NO_x concentration. At first sight this is contrary to the well known dependence of NO_x production rate on local gas temperature but can in practice be explained on a number of counts, the principal one of which is thought to be the method used to calculate flame temperature from the gas analysis results which takes no account of turbulent fluctuations and instead uses time mean fuel/air ratios to calculate time mean temperatures. In addition the oxygen availability in the recirculation zone is very limited, and the gas analysis data in this region does show very small concentrations of oxygen and also quite large amounts of unburned hydrocarbons.

4. THE PREDICTION METHOD

The method is a fully three-dimensional finite difference solution of the Navier-Stokes equations for fluid flow, where recirculation is allowed in any of the three co-ordinate directions (i,e. it is fully elliptic). The solution variables are the three velocity components, pressure, turbulence energy and dissipation rate, a conserved scalar quantity and its variance. In the present work the scalar is taken to be the total mass fraction of hydrogen present in any molecular form. Another choice would be needed for fuels not containing hydrogen. In addition other equations may be solved to handle pollutant chemistry: for the data presented these are CO_2 concentration and its variance.

The finite difference method is a conservative, implicit scheme, with central differencing except in regions of large convection where upwind differencing is used to prevent negative coefficients arising. The resulting equations are solved in an ADI scheme such as may be found in Roache (4) and incorporated into a computer program called PACE. (Prediction of Aerodynamics and Combustor Emissions).

4.1 The Equations of Motion

The Navier-Stokes equations form the basis of the computation for fluid flow and these may be written in general tensor form as

$$\frac{\partial \rho u^i}{\partial t} + \left(\rho u^i u^j\right)_{,j} = T^{ij}_{,j} \qquad (1)$$

where T^{ij} is the complete stress tensor, which for a Newtonian fluid may be written as

$$T^{ij} = -\left(p + \tfrac{2}{3}\mu e^m_m\right) g^{ij} + 2\mu e^{ij} \qquad (2)$$

where $e^{ij} = \tfrac{1}{2}\left(g^{jl} u^i_{,l} + g^{il} u^j_{,l}\right)$ the deformation tensor (3)

Equations (1) and (2) apply to the instantaneous velocity distribution, and may be used directly in laminar flow, but have to be averaged for use in a turbulent flow (see Section 4.2).

To complete the description of the velocity field the continuity equation is used. This may be written in the form

$$\frac{\partial \rho}{\partial t} + (\rho u^i)_{,i} = 0 \qquad (4)$$

4.2 The Turbulence Model

Equations 1, 2 and 4 are first rewritten with the velocities decomposed into mean and fluctuating components in the manner used by Favre (3) such that

$$U^i = \hat{U}^i + u^i$$

and

$$\hat{U}^i = \overline{\rho U^i}/\bar{\rho} \qquad (5)$$

Equation (4) on averaging then becomes simply

$$(\bar{\rho} U^i)_{,i} = 0 \qquad (6)$$

and the momentum equations (1) become

$$(\bar{\rho}\hat{U}^i\hat{U}^j)_{,j} = T^{ij}_{,j} - (\overline{\rho u^i u^j})_{,j} \qquad (7)$$

From equation (2) the time averaged stress tensor is

$$\overline{T^{ij}} = -\left(\bar{p} + \tfrac{2}{3}\mu \overline{U^m_{,m}}\right) g^{ij} + \mu\left(g^{jl}\overline{U^i_{,l}} + g^{il}\overline{U^j_{,l}}\right) \qquad (8)$$

The Reynolds stress term in equation (7) is related to the mean rate of strain via the introduction of a turbulent viscosity to give:-

$$\overline{\rho u^i u^j} = \tfrac{2}{3} g^{ij}\left(\bar{\rho}k + \mu_T \hat{U}^m_{,m}\right) - \mu_T\left(g^{jl}\hat{U}^i_{,l} + g^{il}\hat{U}^j_{,l}\right) \qquad (9)$$

where k is the turbulence kinetic energy $\left(= \bar{\rho}\,\widehat{u^i u_i}\right)$

and the turbulent viscosity μ_T is given by

$$\mu_T = C_\mu \rho k^2/\epsilon \qquad (10)$$

following the two-equation model of Jones and Launder (5)

Examination of equation 8 shows that in the expression for $\overline{T}^{ij}$ only conventionally-averaged velocities appear. In order to relate these to the Favre-averaged velocities of the remaining terms, information about the velocity-density correlations would be required. Since the term represents only molecular shear effects, which are negligibly small in comparison with the turbulent terms in the flows considered, it would be justifiable to omit it altogether. In regions of flow where this term could be significant the turbulence intensity will be low and therefore the replacement of $\overline{U}^i$ with $\hat{U}^i$ is a reasonable approximation. This procedure has therefore been adopted.

The time-averaged momentum equation (7) becomes:

$$(\bar{\rho}\,\hat{U}^i\hat{U}^j)_{,j} = g^{ij}\left(p+\tfrac{2}{3}\bar{\rho}k\right)_{,j} + \left[(\mu+\mu_T)\left(g^{jl}\hat{U}^i_{,l}+g^{il}\hat{U}^j_{,l}\right)-\tfrac{2}{3}(\mu+\mu_T)\,g^{ij}\hat{U}^m_{,m}\right] \qquad (11)$$

The equations for the transport of turbulence energy and dissipation rate are, following Jones and Launder (5) :-

$$(\bar{\rho}\,\hat{U}^j k)_{,j} = \left[\left(\mu+\frac{\mu_T}{\sigma_k}\right)g^{ij}k_{,i}\right]_{,j} - \bar{\rho}\,\overline{u^i u^j}\cdot\hat{U}^j_{,i} - \rho\epsilon \qquad (12)$$

$$(\bar{\rho}\,\hat{U}^j \epsilon)_{,j} = \left[\left(\mu+\frac{\mu_T}{\sigma_\epsilon}\right)g^{ij}\epsilon_{,i}\right]_{,j} - C_1\bar{\rho}\epsilon a^i_j\hat{U}^j_{,i} - C_2\rho\epsilon^2/k \qquad (13)$$

where

$$a^i_j = \frac{\widehat{u^i u_j}}{k} - \tfrac{2}{3}\delta^i_j$$

The constants $C_\mu, \sigma_k, \sigma_\epsilon, C_{\epsilon 1}$ and $C_{\epsilon 2}$ appearing in the above expressions are given the values in Table II. The values are similar to those of Jones (6).

AD-A052 845 ADVISORY GROUP FOR AEROSPACE RESEARCH AND DEVELOPMENT--ETC F/G 21/5
HIGH TEMPERATURE PROBLEMS IN GAS TURBINE ENGINES.(U)
FEB 78

UNCLASSIFIED AGARD-CP-229 NL

7 OF 7
AD
A052845

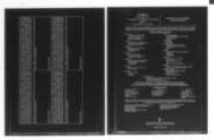

END
DATE
FILMED
5-78
DDC

TABLE II

Values of the empirical constants

C_μ	C_{ϵ_1}	C_{ϵ_2}	σ_k	σ_ϵ
0.09	1.44	1.92	1.0	1.3

The system of equations (10-13) represent a closed set provided that the fluid density is known. Calculation of this property will be discussed in Section 4.3

4.3 The Combustion Model

The model is required to predict mean temperatures, densities and compositions at each point in the flow. Four variables are used to characterise the composition. These are the hydrogen element mass fraction X_H, its variance, and the concentration of CO_2 and its variance. The equations describing the transport of X_H and its variance are:

$$\left(\bar{\rho}\,\hat{U}^j\hat{X}_H\right)_{,j} = \left[\left(\frac{\mu}{\sigma} + \frac{\mu_T}{\sigma_T}\right) g^{j\ell} X_{H,\ell}\right]_{,j} \tag{14}$$

$$\left(\bar{\rho}\,\hat{U}^j\hat{X''^2_H}\right)_{,j} = \left(\frac{\mu_T}{\sigma_T}\, g^{j\ell}\hat{X''^2_{H,\ell}}\right)_{,j} + \frac{2}{\sigma_T}\,\mu_T g^{ij}\hat{X}_{H,i}\hat{X}_{H,j} - C_\beta\,\bar{\rho}\,\frac{\epsilon}{k}\hat{X''^2_H} \tag{15}$$

and that for CO_2 concentration is

$$\left(\bar{\rho}\,\hat{U}^j\hat{X}_{CO_2}\right)_{,j} = \left[\left(\frac{\mu}{\sigma} + \frac{\mu_T}{\sigma_T}\right) g^{j\ell}\hat{X}_{CO_2,\ell}\right]_{,j} + \hat{R}_{CO_2} \tag{16}$$

where $\hat{R}_{CO_2}$ is the net formation rate of CO_2 by chemical reaction.

The equation for CO_2 fluctuation is:

$$\left(\bar{\rho}\,\hat{U}^j\hat{X''^2_{CO_2}}\right)_{,j} = \left(\frac{\mu_T}{\sigma_T}\, g^{j\ell}\hat{X''^2_{CO_2,\ell}}\right)_{,j} + \frac{2}{\sigma_T}\,\mu_T g^{ij}\hat{X}_{CO_2,i}\hat{X}_{CO_2,j} - C_\beta\bar{\rho}\,\frac{\epsilon}{k}\hat{X''^2_{CO_2}} + \widehat{R_{CO_2}X'_{CO_2}} \tag{17}$$

An assumption is needed about the shape of the probability density function of X_H, and in the present work it is assumed to be in the form of two δ-functions. The mean and variance of X_H together with the known maximum and minimum values * are sufficient to define the position of each δ-function and the fraction of time spent in each element. If the fluctuations are small enough to ensure that

---

* X_H takes its maximum when only fuel is present. For hydrocarbon fuels of the form CxHy, X_H max is given by $\frac{1.008y}{12.011x + 1.008y}$. Its minimum value is zero if the inlet streams contain no hydrogen.

the limits on X_H are not reached, then equal times are allowed in each element. The individual hydrogen mass fractions are then calculated by:

$$X_H^+ = \text{Maximum} \quad (X_H + \delta_H, X_{H\max})$$

$$X_H^- = \text{Minimum} \quad (X_H - \delta_H, 0) \qquad (18)$$

It is further assumed that fluctuations in CO_2 concentrations are perfectly correlated with the hydrogen atom fluctuations. Then in each of the gas states X_H and X_{CO_2} are known. All the other major chemical species present (H_2O, CO, N_2, O_2, CxHy) may then be found from the element mass balance, with the additional assumption that the initial hydrocarbon breakdown is very rapid in comparison with the CO consumption rate, i.e.

$$C_xH_y + O_2 \longrightarrow xCO + y/2\ H_2O \qquad \text{instantaneously}$$

This implies that instantaneously fuel and air cannot co-exist. However, it is quite possible that the fluctuations will cause one δ -function to contain fuel rich mixtures while the other is fuel weak, resulting in a mixture containing both fuel and oxygen on a mean basis.

Having obtained the major species concentrations, the temperature in each gas element is calculated by Newton-Raphson iteration of the JANAF enthalpy-temperature polynominals (7). The enthalpy is assumed to be linearly related to the hydrogen concentration, i.e.

$$h = \frac{X_H}{X_{H\max}} (h_{fuel} - h_{air}) + h_{air} \qquad (19)$$

The density in each gas element is calculated from the ideal gas law, with the assumption that pressure fluctuations are negligible (or uncorrelated with concentration). Reaction rates may now be calculated. The important reaction is taken to be

$$CO + OH \rightleftharpoons CO_2 + H \qquad (20)$$

In the rate equations the density, temperature CO, CO_2, O_2 and N_2 concentrations are known. The concentrations of O, H_2, OH and H are calculated by partial equilibrium assumptions. The rate constant for reaction 20 is taken from Baulch et al (8).

The mean fluid density, temperature, species concentrations and reaction rates are now computed knowing the time spent in each state, and these may be compared with measured mean concentrations, which will also be density weighted averages, since they were collected using a sampling probe as described in Section 4.1.

4.4 Fuel Droplets

The computer programme has the capability and has been used to calculate liquid fuel spray combustion chambers. However, since the present paper is concerned only with gaseous fuels no further details are presented here.

4.5 Solution Procedure

The method is a guess and correct procedure, similar to that of Chorin (9), Harlow & Welch (10) and Patankar & Spalding (11). The three momentum equations are solved sequentially, using a guessed pressure field. The continuity equation is then used to set up an equation for a pressure correction which can be used to correct the velocity field so that continuity is satisfied. This pressure correction added to the guessed pressure then provides the new guess for the next iteration cycle. Having obtained the corrected velocity field, the scalar variables (X_H, X_H^2 , droplet concentrations) are solved. Note that enthalpy is not solved explicitly: the assumptions are made that fluctuations in enthalpy are produced only by

fluctuating chemical composition, and not by direct heat conduction, and also that the combustion chamber side walls are adiabatic. With these assumptions the enthalpy equation is identical to that for the hydrogen concentration, and the calculated X_H in each gas element is sufficient to determine the element enthalpy also (Equation 19).

5. COMPARISON OF PREDICTIONS WITH EXPERIMENT

5.1 The Computing Grid and Boundary Conditions

Predictions were only performed in the cylindrical measurement region. The conical nozzle was not included, and so the geometric mesh boundaries were set up along the chamber walls. This greatly simplified the boundary treatment required. The solid obstruction of the injector was handled by fixing values of all the variables inside the injector.

To obviate the need to solve a complete (or half section) chamber, the 20 propane jets and swirl vanes were simulated by 18 of equivalent total area. Thus a 60° sector could be used containing one dilution jet, and three injector holes and swirl vanes, representing one-sixth of the chamber. This allows the available mesh to be distributed more finely in the circumferential direction.

A grid size of 18 x 15 x 12 was used in the axial, circumferential and radial directions respectively, compressed where necessary to give resolution of the swirler, injector and dilution jet details.

The boundary conditions for all the fluid entry points were known from the mass flows and fluid composition provided. The solid areas of the baseplate were assumed adiabatic and so the normal gradient of all species concentrations was taken to be zero. For the transpired wall, the values of the variables were taken to be given by the properties of the entering flow, and the surface assumed shear - free. At the exit of the chamber the axial gradient of all variables was set to zero.

5.2 Fuel/Air Ratio and Velocity Comparisons

These two comparisons are grouped together because they are not primarily dependent on the details of the chemistry as are the composition comparisons shown later. Attention is drawn first to the radial profiles of fuel/air ratio (Figure 7) because of some features here which directly influence all other comparisons. The predicted profiles do display the correct behaviour - high (rich) values in the centre of the duct, which at the lowest plane of measurement are at a fairly constant level, a slight peak around 20 mm radius followed by a fall to a much lower, constant level in the outer region of the chamber. The gradient reduces with downstream distance, while the maximum value remains close to the centre.

Some defects are apparent however. The most important of these is that the prediction does not have sufficient penetration of fuel into the swirler air stream. This is responsible for both the low values in the outer region and the high values near the centre at the first plane of comparison. It is worth noting that earlier runs of the program were done with no allowance for the wakes of the swirl vanes, and in those cases the fuel concentration fell to virtually zero at the outside of the chamber. In the predictions presented, the swirler wakes were simulated by setting the axial velocity to zero at the circumferential location of the swirl vanes. The relative angular positions of the propane jets and swirler wakes does not appear significant, since the jets have spread to coalescence before reaching the swirler radius. In fact the spreading angle of these jets is somewhat greater than that of a free jet in stagnant surroundings. The available grid resolution does not allow many grid lines in any one propane jet, and this is probably the reason for the large spreading rate predicted. A consequence of the spreading is that the proportion of the jet which penetrates the swirler wake will contain less propane than in the experiment, and this is likely to be the cause of both the rich centre and the weak outer region of the predicted profiles at the lowest plane of comparison. The recirculation zone is too rich therefore, but downstream of the end of the recirculation, profiles of fuel/air ratio are in excellent agreement with the measurements. The lack of further smoothing of the profile at the end of the chamber is due to the spareness of axial grid nodes in this region: an additional mesh line here would undoubtedly improve the exit profile. Figure 8 shows that the axial variation of fuel/air ratio is well predicted (as indeed it should be). The addition of dilution air between 117 and 128 mm from the baseplate may be clearly seen in this figure.

Turning now to the axial velocity contours (Figure 9) it may be seen that the recirculation length is fairly well predicted. This is quite a critical test and indicates that the numerical method and turbulence model are producing the correct behaviour. Of course, the numerical method itself has been subjected to a number of verification tests for flows with analytically known solutions - however, the real test must always be comparison with a detailed experiment such as reported here. It is worth noting here that the recirculation length was found to be sensitive to the turbulence intensity level of the swirler airstream. The predictions reported here are with 20% turbulence: a much longer recirculation was found with low inlet turbulence. Some experimental work is being pursued currently to measure the swirler exit air velocity and turbulence intensity distribution to enable a realistic specification of boundary conditions to be supplied. It is likely, however, that turbulence generation in the region of the swirler wakes will produce values in the region of the 20% assumed. The 10 and 20 m/s contours are apparently much longer than measurements indicate. This can be attributed partly to the inaccuracies involved in measuring low velocities in a highly turbulent flow with the type of probe used. The actual location of zero axial velocity should however be quite correct. At 47mm from the baseplate measured velocities are higher than predicted everywhere: the integrated velocity data gives a mass flow about 18% too high at this plane (Table I) whereas the integrated

predictions do give the correct mass flow. This is an indication of the difficulties in measuring velocity accurately in a turbulent combusting flow. In addition since the velocity probe actually records dynamic head, the density used will influence the velocities quoted.

One feature which is apparent from the limited data available is that the high velocity ($>$ 40 m/s) region does not extend sufficiently far downstream. This high-velocity area is associated with the swirler air stream, and it is quite likely that the lack of penetration of fuel mentioned earlier is responsible, since the predicted local gas density will be higher than it should be in the outer regions, and hence higher velocity will be lower. The overall measured mass error must also be borne in mind here however.

In general, therefore the aerodynamic features of the flame have been reasonably well predicted, and the model is quite satisfactory in these respects.

5.3 Composition Comparisons

The discrepancies noted earlier in connection with the fuel/air ratio profiles should be borne in mind while judging the comparisons made here. The carbon monoxide and unburned hydrocarbon concentrations predicted are a direct result of the chemical aspect of the model chosen, and so if fuel-air ratio and velocity distributions were correct, these comparisons will indicate whether the simple chemistry is adequate.

However, because of the peaks in fuel/air ratio which persist, there are regions of the predicted flow which are richer than stoichiometric, and it is these, in combination with the rich element of the probability distribution, which are responsible for some of the defects in the unburned hydrocarbon and CO predictions. Figure 10 shows the mean radial profiles of unburned hydrocarbon concentration, and it is clear that this mechanism has caused peak values nearer the centre than the measurements show. The predictions indicate that the unburned hydrocarbons persist in the mixing region between the swirler air and the propane stream and are subsequently carried into the recirculation zone. The measurements on the other hand indicate that unburnt fuel is being swept directly downstream in the swirler air stream itself. Improved penetration of propane into the swirler air stream would reduce the rich centre region and hence the concentration of unburned hydrocarbons there, and increase the concentrations in the swirler streams. The plane-averaged values are plotted against axial distance on Figure 11.

The incorrect profiles are seen to be irrelevant in determining the mean level- in fact, excellent agreement is obtained, demonstrating that the "instant reaction" assumption, together with the fluctuation model, does in fact give a very realistic mean rate of reaction for the unburned fuel. This may appear strange, since the instantaneous hydrocarbon reaction rate is infinite, but the effective reaction rate is governed by the decay of fluctuations. The good agreement here is a justification of both the infinite rate model and the modelling of the fluctuations themselves.

The carbon monoxide concentration is shown in profile form on Figure 12 and in plane-averaged form on Figure 13. CO concentration increases initially in the region where fuel breakdown is occurring, but has levelled off at 27mm from the baseplate. It then decreases as CO is oxidised to CO_2 but more slowly than the hydrocarbon concentration because of its finite reaction rate. These features correspond well with the measurements, but the CO levels are considerably too high at all planes. There are two reasons for this. First, the over rich recirculation zone will allow too high levels of CO to build up initially, but probably more important is the slow CO consumption rate in the later stages. This is a consequence of the simple probability distribution assumed, in conjunction with the assumption that the initial fuel breakdown is to CO and H_2O. The effect of these assumptions is that in the rich element of the probability distribution any unburned fuel remaining will react with O_2 until either O_2 or unburned fuel concentration is zero. Thus the presence of UHC prohibits any CO reaction taking place in the rich elements, and this is probably the cause of the high predicted CO levels.

An improved probability distribution such as described in Section 6.2 would improve predictions but it may be that a more complex kinetic scheme is required which would allow OH radicals to exist even in rich mixtures. This feature of the model requires further study.

The other two comparisons shown (temperature and combustion efficiency) are not strictly independent of the other variables, but they do represent parameters of importance to the combustion engineer. The "measured" temperature is found from the measured species concentrations, assuming no heat losses, and a temperature calculated in a similar way from the predictions is plotted on Figure 14 for comparison. This is not the temperature actually used for computing densities and reaction rates in the program, since these are calculated separately for each element of the probability density function. Better agreement is obtained here than for fuel/air ratio at 27mm from the baseplate, because of the flattening temperature versus fuel/air ratio characteristic near stoichiometric conditions. In the bulk of the flow away from the wall a fairly constant level is found and the predictions follow this trend. The general temperature levels predicted are everywhere too low, because of the presence of large quantities of CO up to 147mm from the baseplate. There is good agreement at the last two planes where most of the CO has been consumed.

Combustion efficiency plots (plane averaged) are given in Figure 15. This parameter is also calculated from the species concentrations. The shape of the curve is well predicted, again showing that this kind of model does possess the correct features. However, the approach to high efficiency is too slow, because of the excess CO mentioned earlier. The rapid rise in efficiency between the 100 and 140 mm planes is because of the addition of dilution air which

has the effect of making oxygen available in the rich elements, allowing the CO to react. The inefficiency at the exit plane is a result of low temperature in the weak element of the probability distribution preventing further CO oxidation. It is likely that an improved probability distribution would considerably benefit the efficiency prediction.

6. FUTURE DEVELOPMENTS OF THE MODEL

6.1 Arbitrary Boundaries

The major limitation of the method as it stands for the prediction of realistic combustor flows is that the geometry of the boundaries has to conform to the edge of the mesh, i.e. it is restricted to cylindrical or rectangular combustors. Work is well underway to expand the boundary capability to enable boundaries of arbitrary shape to be handled. The boundary will be approximated by a series of planes through each computational cell (but at any angle to the mesh). The finite-difference equations are modified for boundary cells, and all geometric data is calculated once only at the start of a computation. Some simple test cases have already been run with this model, but without combustion.

6.2 The Combustion Model

The first (and probably simplest) improvement which could be made here would be to replace the double-delta function probability distribution function (p.d.f.) with a more physically realistic p.d.f. which can still be defined by a mean and standard deviation. One function which would be suitable is the Beta function which Rhodes (12) showed to be a very good approximation to measured concentration distributions in a turbulent flow. This has the form:

$$p(X) = b X^{\alpha} (1-X)^{\beta} \qquad (21)$$

where α and β are determined from the mean and standard deviation of a scaler concentration X, and b is a constant chosen such that $\int_0^{X_{max}} p(X)\,dX = 1$

A second improvement being pursued is to solve a separate equation for unburned hydrocarbon concentration and to allow the "instant reaction" assumption to be relaxed. The equations to be solved then become much more complex, since more chemical species are present, and their fluctuations are not simply correlated. Additional equations are required for some of the species correlations. This approach is likely to be rather more long term because of its complexity, but does offer the possibility of predicting unburned hydrocarbon emissions in situations where the rate of initial breakdown may be important (extinction, high altitude operation, ignition) in addition to those of CO and NOx. The present method appears to predict unburned hydrocarbons well in the present situation.

The addition of the Zeldovich reaction mechanism for NOx formation is quite straightforward, and only lack of time has prevented its inclusion in the present paper. It is hoped that NOx comparisons will be presented at a later date.

Improvements in the chemical kinetics may also be possible but probably at the expense of large increases in computer time.

7. CONCLUSIONS

A prediction method has been developed with some novel features in the combustion model used, and a comparison performed with a set of measurements of velocity and species concentrations in a research combustor. The method has been shown to be capable of predicting recirculation zone length profiles of fuel/air ratio and to give the correct trends of hydrocarbon and CO concentration. In spite of the instantaneous hydrocarbon breakdown assumed, the net consumption of HC is well predicted. However, because of the lack of oxygen in the rich elements, CO consumption is too slow. There is evidence that a more realistic probability distribution function is required, the Beta function being the most likely candidate. The high CO levels have caused both temperature and combustion efficiency to be too low, but general features of both are well predicted.

It has been found that the treatment of the swirler wake region is important in determining the initial mixing of fuel and air, and further improvement is required in this region to obtain more accurate predictions. Nitric oxide predictions have not yet been incorporated into the method, but this can be done easily and will be added when more accurate fuel/air ratio profiles and CO consumption rates can be obtained.

With a little further development the method should prove a powerful and useful tool in the development of combustion systems.

8. REFERENCES

1. F.H. Holderness, J.J. Macfarlane — Soot formation in rich kerosine flames at high pressure. AGARD Propulsion and Energetics Panel 41st Meeting 1972

2. J.J. Macfarlane — An omni-directional velocity vector probe suitable for use in gas turbine combustors. NGTE Report No. R.317, 1971

3. A Favre — Statistical equations of turbulent gases - in - Problems of hydrodynamics and continuum mechanics. SOC. Indust & Appl Math, Philadelphia (1969)

4. P.J. Roache — Computational fluid dynamics. Hermosa, Albuquerque (1976)

5. W.P. Jones, B.E. Launder — The prediction of laminarisation with a two equation model of turbulence. Int J Heat and Mass Transfer 15, 301, 1972

6. W.P. Jones — Laminarisation in a strongly accelerated boundary layer. PhD Thesis, University of London, 1971

7. S. Gordon, B.J. Mcbride — Computer program for calculation of complex chemical equilibrium compositions. NASA SP 273, 1971

8. D.L. Baulch, D.D. Drysdale, J. Duxbury, A.C. Lloyd — Evaluated kinetic data for high temperature reactions. Vol 3, Homogenous gas phase reactions of the O_2-O_3 system, the CO-O_2-H_2 system and of sulphur containing species. Butterworth, London (1976)

9. A.J. Chorin — Numerical solution of the Navier-Stokes equations. Math Comp 22, 745, 1968

10. F.H. Harlow, J.E. Welch — Numerical calculations of time-dependent viscous incompressible flow of fluid with free surface. Phys Fluids 10, 314, 1967

11. S.V. Patankar, D.B. Spalding — A calculation procedure for heat, mass and momentum transfer in three-dimensional parabolic flows

12. R.P. Rhodes — A probability distribution function for turbulent flows. In Project Squid workshop - Turbulent mixing in non-reactive and reactive flows. Plenum Press, New York

Reports quoted are not necessarily available to members of the public or to commercial organisations.

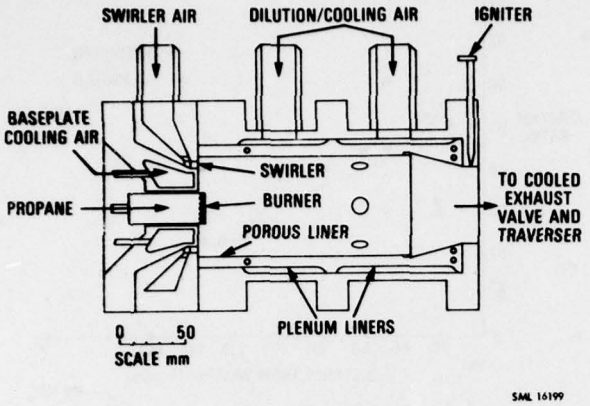

FIG.1 NGTE RESEARCH COMBUSTOR

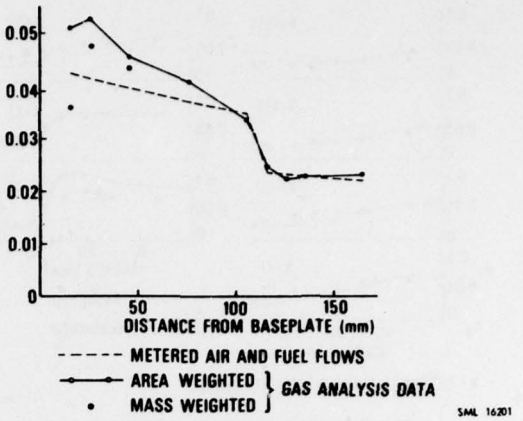

FIG.2 COMPARISON OF METERED AND SAMPLED FUEL/AIR RATIO

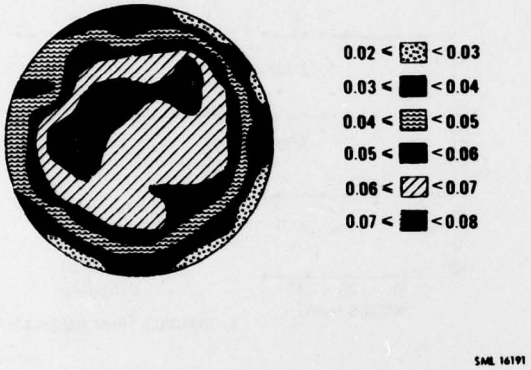

FIG.3 PRIMARY ZONE FUEL/AIR RATIO CONTOURS

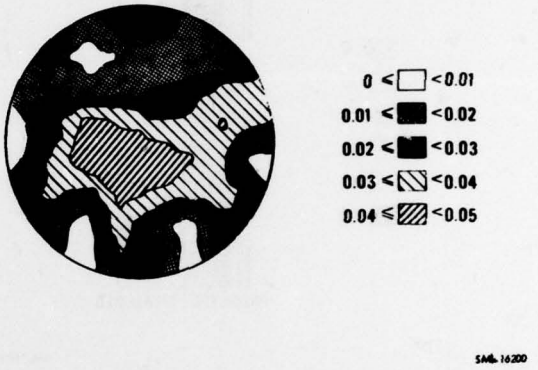

FIG.4 DILUTION ZONE FUEL/AIR RATIO CONTOURS

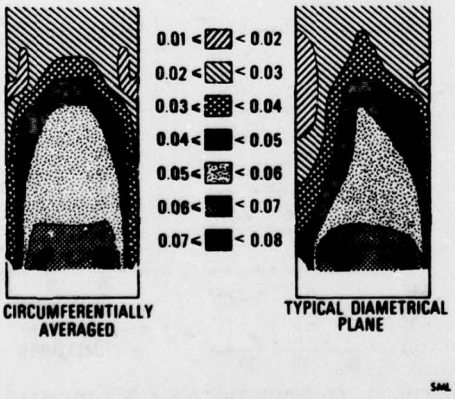

FIG.5 COMPARISON OF AVERAGED AND AS MEASURED FUEL/AIR RATIO CONTOURS

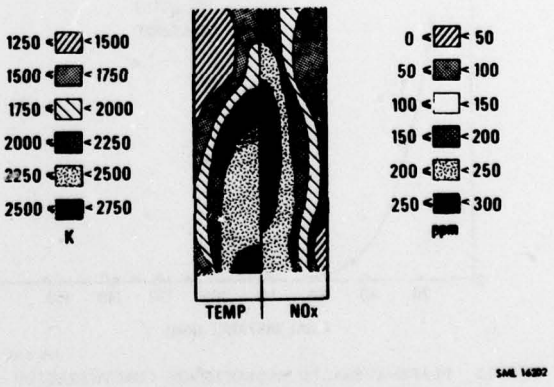

FIG.6 ADIABATIC FLAME TEMPERATURE & NOx CONCENTRATION CONTOURS

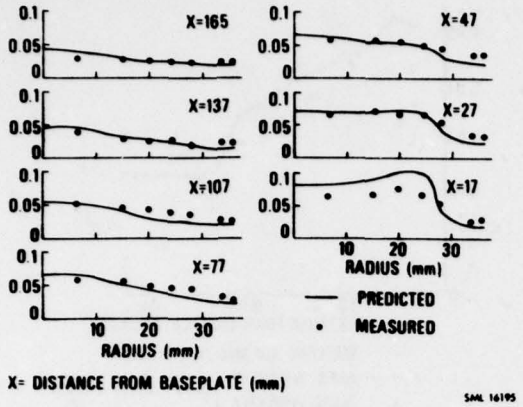

FIG.7 FUEL/AIR RATIO PROFILES

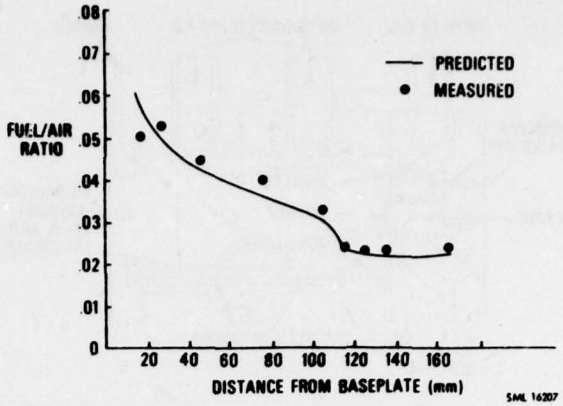

FIG.8 PLANE-AVERAGED FUEL/AIR RATIO

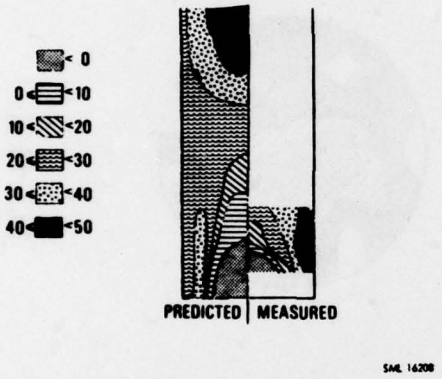

FIG.9 AXIAL VELOCITY CONTOURS

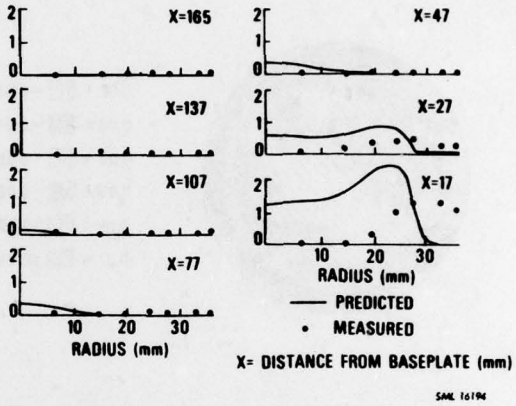

FIG.10 UHC CONCENTRATION (%) PROFILES

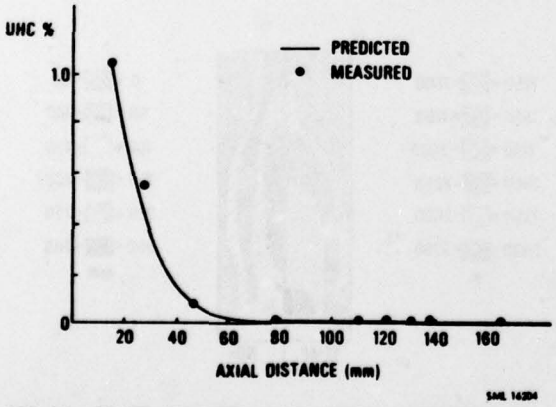

FIG.11 PLANE-AVERAGED HYDROCARBON CONCENTRATION

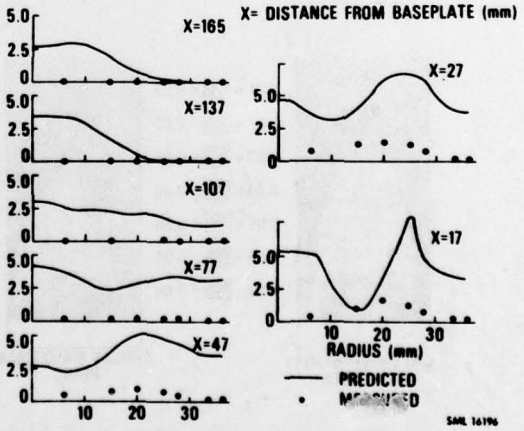

FIG.12 CO CONCENTRATION (%) PROFILES

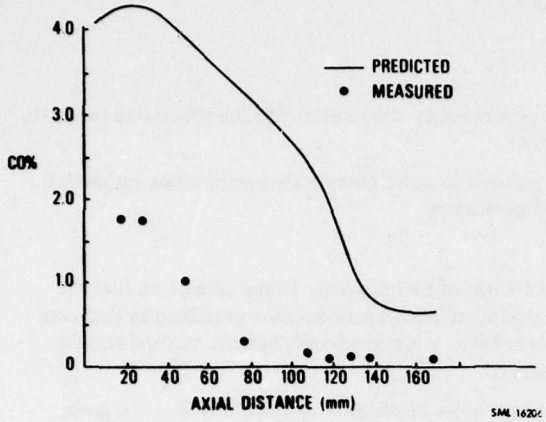

FIG.13 PLANE-AVERAGED CO CONCENTRATION

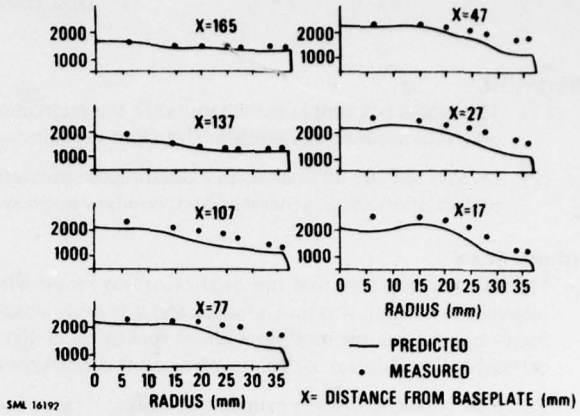

FIG.14 TEMPERATURE PROFILES (K)

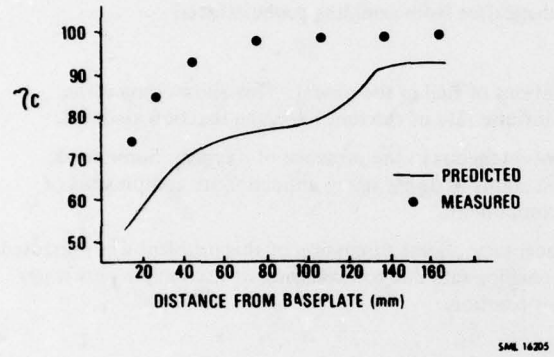

FIG.15 COMBUSTION EFFICIENCY

DISCUSSION

J.Winter, UK

(1) The model is a simple combustor with the recirculation generated by the swirler. Do the prediction methods take into account any entrainment from the dilution flow?

(2) Do you see any difficulties in extending the prediction method to more complicated geometries e.g. with the recirculation zones generated by secondary holes as well as swirlers?

Author's Reply

I should mention here that the combustor was tested with and without fuel flowing. In the case of no fuel the recirculation length was much longer and it is quite possible that some dilution air become entrained in that case. I have not yet run the method without fuel to check that this behaviour is reproduced, but the method should certainly allow dilution air to be entrained if conditions require it.

There are no difficulties in principle in adding a row of secondary holes in addition to the dilution – the main difficulty in modelling real combustors is the fitting of arbitrary wall geometry, and this work is in hand.

G.Winterfeld, Germany

(1) Does your model take into account the effect of unmixedness?

(2) Does your reaction kinetic scheme take care of the time-dependent decomposition of the fuel?

(3) How do you check that your CO – measurements do not suffer from sampling probe effects?

Author's Reply

(1) Unmixedness is taken into account through the fluctuations of fuel in the model. This allows time mean values of both fuel and oxygen to exist in spite of the infinite rate of the fuel + oxygen reaction assumed.

(2) At present, the fuel decomposition is assumed to be instantaneous in the presence of oxygen. Some work is being pursued to relax this assumption, but the implications of doing so are a much more complex set of equations and many more correlations of fluctuating components.

(3) It is always difficult to be categorical about sampling accuracy. Some discussion of this problem was presented in Section 3.1, and I would only comment that the quenching rate due to expansion of the sample plus water cooling is believed to be fast enough to preclude further reaction.

J.F.Chevalier, France

Dans le calcul du fuel/air ratio, que mettez-vous dans le fuel?

Author's Reply

One of the quantities which we have in the solution is the total mass fraction of the hydrogen element present in all molecular forms, and from this one can calculate fuel/air ratio directly

$$\text{Fuel/air ratio} = \frac{X_H}{\text{Fraction of H in fuel} - X_H}$$

The other equation solved is for CO_2, and from these two one can generate the concentrations of all the other chemical compounds. So you see it is not a question of putting various compounds together to find fuel/air ratio, but rather of extracting the composition from the fuel/air ratio which we know.

J.Odgers, Canada

You obviously have a very large amount of experimental data. Have you attempted to assess the performance of the combustor using any of the alternative theories which are available. Also, is it possible that the data may be made available for general testing?

Author's Reply

We have developed the prediction method systematically selecting what we believe to be the most suitable models available for this purpose, and the data was obtained specifically to use as a test case for this model. So the answer to your first question is no, only the current method has been used to date.

As to your second question, the data concerned is the property of NGTE, and so I must refer to my colleagues there. (I have since been informed that it will be released for general use.)

REPORT DOCUMENTATION PAGE

1. Recipient's Reference	2. Originator's Reference	3. Further Reference	4. Security Classification of Document
	AGARD-CP-229	ISBN 92-835-0209-4	UNCLASSIFIED

5. Originator Advisory Group for Aerospace Research and Development
North Atlantic Treaty Organization
7 rue Ancelle, 92200 Neuilly sur Seine, France

6. Title

HIGH TEMPERATURE PROBLEMS IN GAS TURBINE ENGINES

7. Presented at the 50th Meeting of the AGARD Propulsion and Energetics Panel held at the Faculty of Engineering, Middle East Technical University, Ankara, Turkey from 19–23 September 1977.

8. Author(s)	9. Date
Various	February 1978
10. Author's Address	**11. Pages**
Various	602

12. Distribution Statement This document is distributed in accordance with AGARD policies and regulations, which are outlined on the Outside Back Covers of all AGARD publications.

13. Keywords/Descriptors

Gas turbine engines	Performance	Nozzles
High temperature tests	Cooling	Afterburners
Mathematical prediction	Combustion chambers	Heat transfer

14. Abstract

These Conference Proceedings contain 39 papers presented at the 50th Meeting of the AGARD Propulsion and Energetics Panel, held at Ankara, Turkey on 19–23 September 1977. The papers were grouped into eight sessions on motivation and survey, turbine cooling techniques, combustors, afterburners and nozzles, materials and coatings, mechanical problems, effect of cooling on aerodynamic performance, measuring techniques, and on prediction methods.

The purpose of this meeting was to review and highlight the main problems associated with the attainment of high temperatures in aircraft gas turbines. Attention was focussed on methods of cooling components in the hot portion of the engine, notably the combustor and reheat liners, nozzle guide vanes and turbine components. Progress in new materials and protective coatings was discussed. Fuel and combustion problems associated with operation at high gas temperatures were considered as well. Furthermore, new measuring techniques and heat transfer prediction methods were discussed.

Also included are the Technical Evaluation Report and the discussions which took place after most of the presentations.

AGARD Conference Proceedings No.229 Advisory Group for Aerospace Research and Development, NATO HIGH TEMPERATURE PROBLEMS IN GAS TURBINE ENGINES Published February 1978 602 pages These Conference Proceedings contain 39 papers presented at the 50th Meeting of the AGARD Propulsion and Energetics Panel, held at Ankara, Turkey on 19–23 September 1977. The papers were grouped into eight sessions on motivation and survey, turbine cooling techniques, combustors, afterburners and nozzles, materials and coatings, mechanical problems, effect of cooling on aerodynamic performance, measuring techniques, and on prediction methods. P.T.O.	AGARD-CP-229 Gas turbine engines High temperature tests Mathematical prediction Performance Cooling Combustion chambers Nozzles Afterburners Heat transfer	AGARD Conference Proceedings No.229 Advisory Group for Aerospace Research and Development, NATO HIGH TEMPERATURE PROBLEMS IN GAS TURBINE ENGINES Published February 1978 602 pages These Conference Proceedings contain 39 papers presented at the 50th Meeting of the AGARD Propulsion and Energetics Panel, held at Ankara, Turkey on 19–23 September 1977. The papers were grouped into eight sessions on motivation and survey, turbine cooling techniques, combustors, afterburners and nozzles, materials and coatings, mechanical problems, effect of cooling on aerodynamic performance, measuring techniques, and on prediction methods. P.T.O.	AGARD-CP-229 Gas turbine engines High temperature tests Mathematical prediction Performance Cooling Combustion chambers Nozzles Afterburners Heat transfer
AGARD Conference Proceedings No.229 Advisory Group for Aerospace Research and Development, NATO HIGH TEMPERATURE PROBLEMS IN GAS TURBINE ENGINES Published February 1978 602 pages These Conference Proceedings contain 39 papers presented at the 50th Meeting of the AGARD Propulsion and Energetics Panel, held at Ankara, Turkey on 19–23 September 1977. The papers were grouped into eight sessions on motivation and survey, turbine cooling techniques, combustors, afterburners and nozzles, materials and coatings, mechanical problems, effect of cooling on aerodynamic performance, measuring techniques, and on prediction methods. P.T.O.	AGARD-CP-229 Gas turbine engines High temperature tests Mathematical prediction Performance Cooling Combustion chambers Nozzles Afterburners Heat transfer	AGARD Conference Proceedings No.229 Advisory Group for Aerospace Research and Development, NATO HIGH TEMPERATURE PROBLEMS IN GAS TURBINE ENGINES Published February 1978 602 pages These Conference Proceedings contain 39 papers presented at the 50th Meeting of the AGARD Propulsion and Energetics Panel, held at Ankara, Turkey on 19–23 September 1977. The papers were grouped into eight sessions on motivation and survey, turbine cooling techniques, combustors, afterburners and nozzles, materials and coatings, mechanical problems, effect of cooling on aerodynamic performance, measuring techniques, and on prediction methods. P.T.O.	AGARD-CP-229 Gas turbine engines High temperature tests Mathematical prediction Performance Cooling Combustion chambers Nozzles Afterburners Heat transfer

The purpose of this meeting was to review and highlight the main problems associated with the attainment of high temperatures in aircraft gas turbines. Attention was focussed on methods of cooling components in the hot portion of the engine, notably the combustor and reheat liners, nozzle guide vanes and turbine components. Progress in new materials and protective coatings was discussed. Fuel and combustion problems associated with operation at high gas temperatures were considered as well. Furthermore new measuring techniques and heat transfer prediction methods were discussed.

Also included are the Technical Evaluation Report and the discussions which took place after most of the presentations.

ISBN 92-835-0209-4

The purpose of this meeting was to review and highlight the main problems associated with the attainment of high temperatures in aircraft gas turbines. Attention was focussed on methods of cooling components in the hot portion of the engine, notably the combustor and reheat liners, nozzle guide vanes and turbine components. Progress in new materials and protective coatings was discussed. Fuel and combustion problems associated with operation at high gas temperatures were considered as well. Furthermore new measuring techniques and heat transfer prediction methods were discussed.

Also included are the Technical Evaluation Report and the discussions which took place after most of the presentations.

ISBN 92-835-0209-4

The purpose of this meeting was to review and highlight the main problems associated with the attainment of high temperatures in aircraft gas turbines. Attention was focussed on methods of cooling components in the hot portion of the engine, notably the combustor and reheat liners, nozzle guide vanes and turbine components. Progress in new materials and protective coatings was discussed. Fuel and combustion problems associated with operation at high gas temperatures were considered as well. Furthermore new measuring techniques and heat transfer prediction methods were discussed.

Also included are the Technical Evaluation Report and the discussions which took place after most of the presentations.

ISBN 92-835-0209-4

The purpose of this meeting was to review and highlight the main problems associated with the attainment of high temperatures in aircraft gas turbines. Attention was focussed on methods of cooling components in the hot portion of the engine, notably the combustor and reheat liners, nozzle guide vanes and turbine components. Progress in new materials and protective coatings was discussed. Fuel and combustion problems associated with operation at high gas temperatures were considered as well. Furthermore new measuring techniques and heat transfer prediction methods were discussed.

Also included are the Technical Evaluation Report and the discussions which took place after most of the presentations.

ISBN 92-835-0209-4

D125
5

AGARD
NATO OTAN
7 RUE ANCELLE · 92200 NEUILLY-SUR-SEINE
FRANCE
Telephone 745.08.10 · Telex 610176

DISTRIBUTION OF UNCLASSIFIED AGARD PUBLICATIONS

AGARD does NOT hold stocks of AGARD publications at the above address for general distribution. Initial distribution of AGARD publications is made to AGARD Member Nations through the following National Distribution Centres. Further copies are sometimes available from these Centres, but if not may be purchased in Microfiche or Photocopy form from the Purchase Agencies listed below.

NATIONAL DISTRIBUTION CENTRES

BELGIUM
Coordonnateur AGARD – VSL
Etat-Major de la Force Aérienne
Quartier Reine Elisabeth
Rue d'Evere, 1140 Bruxelles

CANADA
Defence Scientific Information Service
Department of National Defence
Ottawa, Ontario K1A OZ2

DENMARK
Danish Defence Research Board
Østerbrogades Kaserne
Copenhagen Ø

FRANCE
O.N.E.R.A. (Direction)
29 Avenue de la Division Leclerc
92 Châtillon sous Bagneux

GERMANY
Zentralstelle für Luft- und Raumfahrt-
dokumentation und -information
Postfach 860880
D-8 München 86

GREECE
Hellenic Armed Forces Command
D Branch, Athens

ICELAND
Director of Aviation
c/o Flugrad
Reykjavik

ITALY
Aeronautica Militare
Ufficio del Delegato Nazionale all'AGARD
3, Piazzale Adenauer
Roma/EUR

LUXEMBOURG
See Belgium

NETHERLANDS
Netherlands Delegation to AGARD
National Aerospace Laboratory, NLR
P.O. Box 126
Delft

NORWAY
Norwegian Defence Research Establishment
Main Library
P.O. Box 25
N-2007 Kjeller

PORTUGAL
Direccao do Servico de Material
da Forca Aerea
Rua de Escola Politecnica 42
Lisboa
Attn: AGARD National Delegate

TURKEY
Department of Research and Development (ARGE)
Ministry of National Defence, Ankara

UNITED KINGDOM
Defence Research Information Centre
Station Square House
St. Mary Cray
Orpington, Kent BR5 3RE

UNITED STATES
National Aeronautics and Space Administration (NASA),
Langley Field, Virginia 23365
Attn: Report Distribution and Storage Unit

THE UNITED STATES NATIONAL DISTRIBUTION CENTRE (NASA) DOES NOT HOLD STOCKS OF AGARD PUBLICATIONS, AND APPLICATIONS FOR COPIES SHOULD BE MADE DIRECT TO THE NATIONAL TECHNICAL INFORMATION SERVICE (NTIS) AT THE ADDRESS BELOW.

PURCHASE AGENCIES

Microfiche or Photocopy
National Technical
Information Service (NTIS)
5285 Port Royal Road
Springfield
Virginia 22151, USA

Microfiche
Space Documentation Service
European Space Agency
10, rue Mario Nikis
75015 Paris, France

Microfiche
Technology Reports
Centre (DTI)
Station Square House
St. Mary Cray
Orpington, Kent BR5 3RF
England

Requests for microfiche or photocopies of AGARD documents should include the AGARD serial number, title, author or editor, and publication date. Requests to NTIS should include the NASA accession report number. Full bibliographical references and abstracts of AGARD publications are given in the following journals:

Scientific and Technical Aerospace Reports (STAR),
published by NASA Scientific and Technical
Information Facility
Post Office Box 8757
Baltimore/Washington International Airport
Maryland 21240, USA

Government Reports Announcements (GRA),
published by the National Technical
Information Services, Springfield
Virginia 22151, USA

Printed by Technical Editing and Reproduction Ltd
Harford House, 7–9 Charlotte St, London W1P 1HD

ISBN 92-835-0209-4